

AFRL-PR-WP-TP-2002-200, V2

**ADVANCED LASER DIAGNOSTIC
APPLICATIONS**

Volume 2 of 3 (Pages 218 – 693)

Larry P. Goss, Ph.D.

**Innovative Scientific Solutions, Inc.
2766 Indian Ripple Road
Dayton, OH 45440-3638**



MARCH 2001

FINAL REPORT FOR 18 SEPTEMBER 1995 – 28 SEPTEMBER 2000

Approved for public release; distribution is unlimited.

**PROPULSION DIRECTORATE
AIR FORCE RESEARCH LABORATORY
AIR FORCE MATERIEL COMMAND
WRIGHT-PATTERSON AIR FORCE BASE, OH 45433-7251**

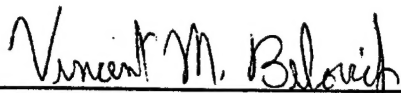
20021008 166

NOTICE

USING GOVERNMENT DRAWINGS, SPECIFICATIONS, OR OTHER DATA INCLUDED IN THIS DOCUMENT FOR ANY PURPOSE OTHER THAN GOVERNMENT PROCUREMENT DOES NOT IN ANY WAY OBLIGATE THE U.S. GOVERNMENT. THE FACT THAT THE GOVERNMENT FORMULATED OR SUPPLIED THE DRAWINGS, SPECIFICATIONS, OR OTHER DATA DOES NOT LICENSE THE HOLDER OR ANY OTHER PERSON OR CORPORATION; OR CONVEY ANY RIGHTS OR PERMISSION TO MANUFACTURE, USE, OR SELL ANY PATENTED INVENTION THAT MAY RELATE TO THEM.

THIS REPORT IS RELEASABLE TO THE NATIONAL TECHNICAL INFORMATION SERVICE (NTIS). AT NTIS, IT WILL BE AVAILABLE TO THE GENERAL PUBLIC, INCLUDING FOREIGN NATIONS.

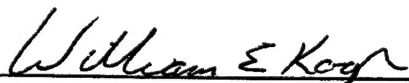
THIS TECHNICAL REPORT HAS BEEN REVIEWED AND IS APPROVED FOR PUBLICATION.



VINCENT M. BELOVICH, Ph.D.
Contract Monitor
Combustion Science Branch (AFRL/PRTS)



ROBERT D. HANCOCK, Ph.D.
Chief
Combustion Science Branch, AFRL/PRTS



WILLIAM E. KOOP
Chief of Technology
Turbine Engine Division
Propulsion Directorate

Do not return copies of this report unless contractual obligations or notice on a specific document require its return.

REPORT DOCUMENTATION PAGE

Form Approved
OMB No. 0704-0188

The public reporting burden for this collection of information is estimated to average 1 hour per response, including the time for reviewing instructions, searching existing data sources, gathering and maintaining the data needed, and completing and reviewing the collection of information. Send comments regarding this burden estimate or any other aspect of this collection of information, including suggestions for reducing this burden, to Department of Defense, Washington Headquarters Services, Directorate for Information Operations and Reports (0704-0188), 1215 Jefferson Davis Highway, Suite 1204, Arlington, VA 22202-4302. Respondents should be aware that notwithstanding any other provision of law, no person shall be subject to any penalty for failing to comply with a collection of information if it does not display a currently valid OMB control number. PLEASE DO NOT RETURN YOUR FORM TO THE ABOVE ADDRESS.

1. REPORT DATE (DD-MM-YY) March 2001			2. REPORT TYPE Final		3. DATES COVERED (From - To) 09/18/1995 - 09/28/2000	
4. TITLE AND SUBTITLE ADVANCED LASER DIAGNOSTIC APPLICATIONS Volume 2 of 3 (Pages 218 - 693)					5a. CONTRACT NUMBER F33615-95-C-2507	
					5b. GRANT NUMBER	
					5c. PROGRAM ELEMENT NUMBER 62203F	
6. AUTHOR(S) Larry P. Goss, Ph.D.					5d. PROJECT NUMBER 3048	
					5e. TASK NUMBER 04	
					5f. WORK UNIT NUMBER AI	
7. PERFORMING ORGANIZATION NAME(S) AND ADDRESS(ES) Innovative Scientific Solutions, Inc. 2766 Indian Ripple Road Dayton, OH 45440-3638					8. PERFORMING ORGANIZATION REPORT NUMBER 2507 Final	
9. SPONSORING/MONITORING AGENCY NAME(S) AND ADDRESS(ES) Propulsion Directorate Air Force Research Laboratory Air Force Materiel Command Wright-Patterson Air Force Base, OH 45433-7251					10. SPONSORING/MONITORING AGENCY ACRONYM(S) AFRL/PRTS	
					11. SPONSORING/MONITORING AGENCY REPORT NUMBER(S) AFRL-PR-WP-TP-2002-200, V2	
12. DISTRIBUTION/AVAILABILITY STATEMENT Approved for public release; distribution is unlimited.						
13. SUPPLEMENTARY NOTES This is Volume 2 of 3. See also AFRL-PR-WP-TP-2002-200, V1 and AFRL-PR-WP-TP-2002-200, V3. Report contains color. Report is comprised of numerous publications, such as journal articles and conference papers.						
14. ABSTRACT Reported are results of experimental and numerical investigations on gas turbine combustion and fuel processes, including: 1) Development, evaluation, and utilization of advanced laser diagnostic and analytical techniques for studying combustion and fuel processes important to current and future military aircraft; 2) Determination of cause and investigation of schemes to eliminate combustion and thermal-stability-related problems resulting from change from JP-4 to JP-8 fuel; 3) Proposal and evaluation of advanced combustor concepts and design characteristics to optimize tradeoffs in performance, visual observables, durability, and pollutants; 4) Investigation of methods for reducing emissions of carbon monoxide, hydrocarbons, oxides of nitrogen, and smoke in current and future gas turbine combustors; 5) Design and completion of experiments for establishing a database for developing and evaluating combustor and fuel-system-component design models; 6) Development of computational-fluid-dynamics (CFD) models for gas turbine combustor and fuel-system-component design; 7) Evaluation of additive and advanced thermally stable fuels that provide thermal stability up to 900 °F; 8) Evaluation of thermally stable and environmentally safe anti-icing additives for JP-8 and JP-900 fuels; 9) Investigation of methods of using fuel to cool hot engine components and determination of impact of fuel phase change on combustion, and 10) Investigation of new military and commercial applications for combustion and fuels technology developed in this program, including high-cycle fatigue and aging aircraft.						
15. SUBJECT TERMS Advanced laser diagnostics, fuel thermal stability, computational fluid dynamics with chemistry, vortex-flame interactions, pulse-detonation engines, trapped-vortex combustor, fuel additives, spray combustion						
16. SECURITY CLASSIFICATION OF:			17. LIMITATION OF ABSTRACT: SAR	18. NUMBER OF PAGES 484	19a. NAME OF RESPONSIBLE PERSON (Monitor) Vincent M. Belovich, Ph.D. 19b. TELEPHONE NUMBER (Include Area Code) (937) 255-4229	
a. REPORT Unclassified	b. ABSTRACT Unclassified	c. THIS PAGE Unclassified				

TABLE OF CONTENTS

<u>Section</u>		<u>Page</u>
1	INTRODUCTION	1
2	DIAGNOSTIC AND ANALYTICAL INSTRUMENTATION DEVELOPMENT	2
2.1	COMBUSTION DIAGNOSTICS	2
2.1.1	Overview	2
2.1.2	Two-Dimensional Flow-Visualization Technique	2
2.1.3	Three-Dimensional Flow-Visualization Technique	35
2.1.4	Ultrafast-Imaging Technique	56
2.1.5	Phase-Sensitive-Imaging Technique	71
2.1.6	Particle-Image-Velocimetry Technique	83
2.1.7	Pressure-Sensitive-Paint Technique	136
2.2	FUEL DIAGNOSTICS	179
2.2.1	Overview	179
2.2.2	Particle-Sizing, Oxygen-Concentration, and Mass- Deposition Methods	179
2.2.3	Picosecond Pump/Probe Diagnostics	196
2.2.4	Spectroscopic Techniques	213
3	DIAGNOSTIC APPLICATIONS	218
3.1	COMBUSTION STUDIES	218
3.1.1	Overview	218
3.1.2	Fundamental Combustion Studies	218
3.1.2.1	Jet Diffusion Flames	218
3.1.2.2	Counterflow Diffusion Flames	284
3.1.3	Large-Scale Combustion Studies	369
3.1.3.1	Trapped-Vortex Combustor	369
3.1.3.2	Lean Blowout and Emission	416
3.1.3.3	Combustor Design Trends	542
3.1.3.4	Active Combustion Control	571
3.1.3.5	Pulse Detonation Engines	623

TABLE OF CONTENTS (CONTINUED)

<u>Section</u>	<u>Page</u>
3.2 FUEL STUDIES	644
3.2.1 Overview	644
3.2.2 Fuel Thermal Stability	644
3.2.2.1 Autoxidation of Jet-A Fuels	644
3.2.2.2 Kinetics	656
3.2.2.3 Fuel Blends	657
3.2.2.4 Fuel Recirculation	658
3.2.2.5 Fuel Pyrolysis	666
3.2.2.6 Lubricants	671
3.2.3 Effect of Additives on Fuel Thermal Stability	676
3.2.4 Icing Inhibitors	689
4 MODEL DEVELOPMENT	694
4.1 COMBUSTION MODELING	694
4.1.1 Overview	694
4.1.2 Jet Diffusion Flames	694
4.1.3 Opposing-Jet Diffusion Flames	913
4.1.4 Trapped-Vortex Combustor	941
4.1.5 Pulse Detonation Waves	981
4.1.6 Droplet and Two-Phase Flows	986
4.2 MODELING OF FUEL THERMAL STABILITY	1132
4.2.1 Overview	1132
4.2.2 Fuel Thermal Stability	1132
APPENDIX: Presentations, Publications, and Patents	1196

3. DIAGNOSTIC APPLICATIONS

3.1 COMBUSTION STUDIES

3.1.1 Overview

The demands for high thrust-to-weight ratio and low emissions of future military aircraft make the use of current gas turbine engines uneconomical and environmentally unsafe and render the operation of the engine unstable. To meet these demands, combustors must be designed based on advanced concepts in combustor technology. The objectives of this portion of the program were as follows: 1) to gain a fundamental understanding of reacting flows by conducting experimental/numerical investigations of controlled combustion processes, 2) to develop new and innovative combustor concepts that might improve performance and emissions characteristics, and 3) to test and evaluate these advanced concepts in realistic engine environments. The combustion studies conducted during this program were focused on small-scale fundamental experiments and large-scale practical demonstrations of advanced combustor concepts. The results of efforts in each of these areas are discussed below.

3.1.2 Fundamental Combustion Studies

3.1.2.1 Jet Diffusion Flames. Jet diffusion flames have been the subjects of many combustion studies because they are simple to set up, yet display many of the important chemical and physical properties of more complex combustors. Numerous experimental and numerical studies were performed on jet diffusion flames during this program. In particular, H_2 -air, methane-air, and $CO/H_2/N_2$ -air jet diffusion flames were investigated.

3.1.2.1.1 H_2 -Air Flames. The paper entitled "The Structure of a Dynamic Nonpremixed H_2 -Air Flame" (see pp. 220-230) discusses the use of advanced laser diagnostic techniques to characterize the dynamic structure of a jet diffusion flame. In the publication entitled "Thermal Diffusion Effects and Vortex-Flame Interactions in Hydrogen Jet Diffusion Flames" (see pp. 231-237), the results of using both experimental and numerical techniques to study induced vortex-flame interactions are discussed. A later paper entitled "Flame Structure of Stabilization Region in a Laminar Hydrogen Jet Diffusion Flame" (see pp. 238-243) documents the results of an experimental and computational investigation on a laminar, hydrogen jet diffusion flame to determine the structure of the stabilization region below the nozzle.

3.1.2.1.2 Methane-Air Flames. Induced vortex-flame interactions in a methane-air flame were reported in the paper entitled "An Experimental and Numerical Investigation on Local Extinction in Jet Diffusion Flames" (see pp. 244-249). A second paper entitled "Simulation of Local Quenching in a Methane-Air Jet Diffusion Flame" (see pp. 250-253) discusses the local quenching processes that occur during strong vortex-flame interactions. The publication entitled "NO_x in Methane-Air Jet Diffusion Flames" (see pp. 254-262) documents the investigation into NO_x formation in an unsteady laminar flame.

3.1.2.1.3 CO/H₂/N₂ Flames. Scalar and velocity measurements are documented for two turbulent jet flames of CO/H₂/N₂ in the article entitled "Experiments on the Scalar Structure of Turbulent CO/H₂/N₂ Jet Flames" (see pp. 263-283). Simultaneous measurements of temperature and the major species OH and NO were made using a combination of Rayleigh-scattering, Raman-scattering, and laser-induced-fluorescence techniques.

The Structure of a Dynamic Nonpremixed H₂-Air Flame

C. D. Carter
Systems Research Laboratories, Inc.
2800 Indian Ripple Rd.
Dayton, OH 45440-3696
E-mail: cartercd@possum.appl.wpafb.af.mil

R. D. Gould
Mechanical and Aerospace Engineering Department
North Carolina State University
Raleigh, NC 27695

L. P. Goss, V. R. Katta, and K.-Y. Hsu
Innovative Scientific Solutions, Inc
3845 Woodhurst Ct.
Dayton, OH 45430

INTRODUCTION

Studies of simple, vertically oriented, nonpremixed jet flames have shown that when the co-flow velocity is sufficiently low, buoyancy-induced, periodic toroidal vortices form outside the flame surface [1-4]. These vortices wrinkle the flame surface and produce stretched and compressed flamelets, thereby providing a relatively simple means of studying flame-vortex interactions. Recent direct numerical simulations of these unsteady laminar flames (with H₂ as the fuel) suggest that preferential diffusion—due to nonunity Lewis number (Le , the ratio of rates of heat and species diffusion)—acting in concert with flame curvature influences the gas temperature along the flame surface [1,2,5]. In particular, Katta *et al.* [1,2] find that the flame temperature increases in the compressed regions of the flame and decreases in the stretched regions. That the flame temperature varies in this manner has been confirmed, in part, by previous experimental studies showing increased temperature within the compressed regions [3-4,6-7].

To characterize the structure of a dynamic nonpremixed H₂-air flame, we have made sequential point measurements of temperature using thin-filament pyrometry (TFP) and of concentrations of hydroxyl (OH) and nitric oxide (NO) using laser-induced fluorescence (LIF). Because the NO production rate is strongly temperature sensitive (e.g., at flame temperatures the production rate for thermal NO increases by a factor of ~2 for increases in temperature of 100 K), NO is a good marker for the higher temperature zones. We have chosen three downstream locations, 50, 85, and 135 mm from the jet exit, that illustrate the downstream development of the buoyant flame structure. For each of these positions, we have recorded the radial and temporal variation of these scalars.

EXPERIMENTAL METHODS

Facilities and Techniques

Shown in Fig. 1 is a schematic of the experimental facility. The burner consists of a tapered fuel tube (1.0-cm ID) surrounded by a co-annular air section (15.0-cm ID); both the burner and the co-annular section are mounted to an x - y - z translation system employing stepper motors. The area-averaged flow velocities for the fuel and air were 4.6 and 0.42 m/s, respectively. Recent velocity measurements (employing LDV) across the co-annular region show that the air velocity is reasonably uniform (at ~0.44 m/s) away from the fuel nozzle; however, a significant lower-speed region (due to the boundary layer and the taper of the fuel nozzle) exists adjacent to the fuel tube. The selected air and fuel flow rates result in a buoyant frequency of 15.2 Hz. Although a range of frequencies (10 to 20 Hz) can be obtained by varying

the gas flow rates, the 15-Hz frequency is optimum for the available laser system, a 30-Hz Nd:YAG pump laser, insofar as the laser is triggered at twice the frequency of the buoyant fluctuations. The laser and detection electronics were phase locked to the 15.2-Hz buoyant frequency using the passage of these structures through a cw laser beam; the beam steering induced by the passage of the flame bulge moved the laser beam on and off a photodiode at the 15.2-Hz frequency. With the flame isolated from disturbances, the variation in the trigger frequency was within ± 0.2 Hz. To maintain a consistent trigger-flame phase relationship while probing different regions of the flow, we mounted both the cw laser and the photodiode detector to the burner/co-flow housing. Thus, the detection electronics were triggered from the same flame structure, regardless of the burner position. Finally, to reduce the maximum temperatures and, thereby, extend the lifetimes of the filaments, we employed a diluted fuel mixture in the ratio of 2.22 parts H_2 to 1 part N_2 ; the corresponding maximum adiabatic equilibrium temperature is ~ 2220 K.

Originally the filament emission and NO fluorescence were recorded simultaneously. However, the flame proved to be reproducible, and subsequent to our initial simultaneous measurements, each (NO fluorescence, OH fluorescence, and temperature) was recorded sequentially. The β -SiC filaments, due to their small diameter (14 μm) and low thermal conductivity (10 kcal/m-hr-K or about 40 times lower than that of a Type-S or -R thermocouple), exhibit excellent temporal response and spatial resolution. The filament acts as a graybody with an emissivity of 0.88. The detection limit for the filament is detector dependent and was ~ 900 K for the sandwiched Si and InGaAs photodiodes employed in this experiment; the high-temperature limit, ~ 2350 K in practice (depending on the tension on the filament), is determined by the sublimation point of the β -SiC material. The InGaAs and Si photodiodes have respective spectral ranges of about 0.9 to 1.8 μm and 0.45 to 1.0 μm ; and because the temperature is derived from a ratio of the photodiode signals, the measurement is less sensitive to any variation in the filament emissivity and to small variations in the optical alignment. The frequency response of the filament is better than 1 kHz for flame conditions. Therefore, we expect that the filament will accurately reflect the temporal variations in gas temperature.

We overlapped the filament and LIF probe volumes using a 500- μm pinhole—which was mounted on a kinematic magnetic base assembly—in combination with a He-Ne alignment laser; the pinhole defined the spatial resolution of both the LIF and the TFP measurements. The light from the He-Ne laser was split into two beams which were directed through the alignment pinhole. The intersection of the two beams was then used as a marker for the probe volume, and the filament was properly aligned when scattering from both He-Ne beams was observable. With all three measurements, we translated the burner to the axial and radial position of interest. The signals were then recorded as a function of delay relative to the trigger signal; the 2-D maps (signal versus time and radius) were then constructed from the individual signal-versus-time traces. With temperature we recorded the signals in real time; that is, we sampled the filament emission at a frequency of 1 kHz. Typically, we averaged the filament emission over 30 cycles for each spatial location. Strong emission originates from H_2O within the hottest regions of the flame; consequently, we simultaneously recorded the background flame emission and the filament emission. The emission was collected and focused by a concave spherical mirror (to eliminate chromatic aberration present with the available transmissive-lens systems) and then directed onto two optical fibers (one fiber specifically for filament emission and the other for flame emission), which routed the radiation to *two* dual-photodiode detectors. The spatial resolution of the temperature measurement, which was determined by the magnification of the mirror system (0.5) and the fiber core diameter (0.55 mm), was ~ 1.1 mm. The effective separation of the background and filament fibers was ~ 3 mm. To account for differences in optical efficiencies and detector gain, the recorded signals for the two detectors were *matched* with the filament well away from the flame, to ensure that both detectors recorded only background flame emission. Unfortunately, we did observe the effects of movement of the filament (due to gas velocity variations), not only within the unsteady flame but also in the transition from the unsteady flame to the calibration flame; of course movement of the filament can bias the temperature measurements.

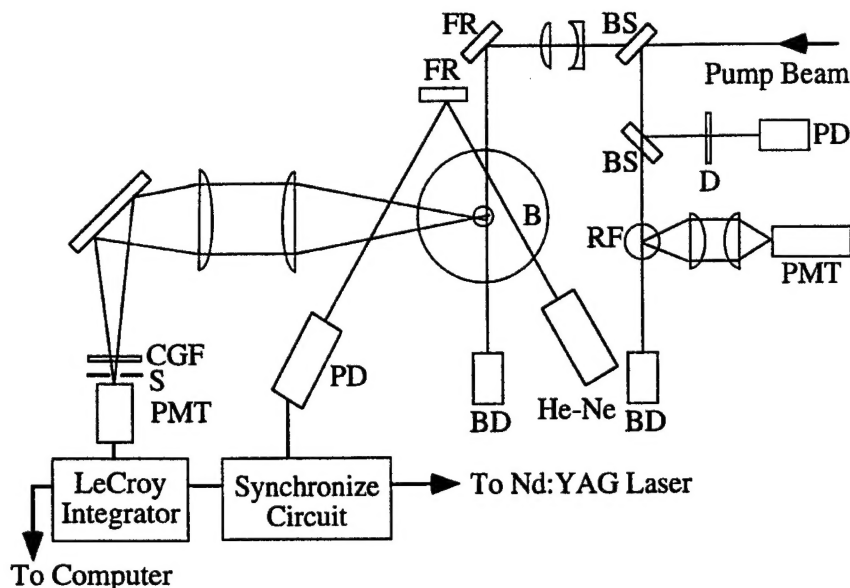


Fig. 1. Schematic of experimental setup. For the filament measurements, the fluorescence lenses were replaced by a spherical concave mirror and two optical fibers were employed to transmit the filament and background flame emissions to two dual-photodiode detectors.

With the LIF measurements, we were limited by the 30-Hz pulse repetition frequency of the pump laser; and typically, we averaged the fluorescence from 30 laser pulses—corresponding to 30 successive buoyant cycles—for each temporal and spatial location. The laser-beam diameters for OH and NO excitation were adjusted to allow $\sim 90\%$ of the beam energy to pass through the 500- μm -diameter alignment pinhole. We limited the probe-volume beam energies for OH and NO to 10 μJ (less for NO excitation) to ensure that the fluorescence would remain within the linear regime. We collected the fluorescence with two 100-mm-diameter fused-silica lenses—a 250-mm focal-length collection lens and a 500-mm focal-length focusing lens—which resulted in a system magnification of ~ 2 . A slit-and-photomultiplier-tube housing was positioned at the focus of the fluorescence beam. For both NO and OH fluorescence collection, the slit width was set to ~ 1.0 mm, resulting in a resolution of ~ 0.5 mm along the axis of the LIF laser beams.

To generate the wavelength for NO excitation, the frequency-doubled output of the dye laser was mixed with the residual IR radiation from the Nd:YAG. We tuned this system to the $Q_1(28)$ transition of the $A^2\Sigma^+-X^2\Pi(0,0)$ band ($\lambda = 225.20$ nm). A Schott UG-5 colored-glass filter, a KrF excimer-laser turning mirror, and the spectral response of a solar-blind PMT photocathode were used to isolate the NO fluorescence from the ($v' = 0$, $v'' = 1-5$) bands and reject background radiation. Although interfering fluorescence from vibrationally hot O_2 is present, the level of interference in this flame is small relative to the NO fluorescence [8]. For OH excitation, we tuned the same laser system (using the frequency-doubled dye laser beam) to the $S_{21}(8)$ line of the $A^2\Sigma^+-X^2\Pi(1,0)$ band ($\lambda = 278.91$ nm). By pumping a satellite transition, we greatly reduced absorption of the laser beam propagating through the flame [9]. Schott colored-glass filters, WG-295 and UG-11, blocked scattered radiation and transmitted fluorescence from the dominant (1,1) and (0,0) bands, where the (0,0)-band fluorescence is preceded by vibrational energy transfer from $v' = 1$ to $v' = 0$ [10]. Some of the fluorescence, principally the (0,0)-band component, is strongly absorbed as it propagates through the flame. For this reason, we collected fluorescence from the *near* half of the flame; furthermore, the OH layers are thin (see Figs. 3-6 below), and thus we expect that the OH fluorescence from the unsteady flame is minimally affected by absorption. For both LIF

measurements, we recorded the laser energy in addition to the OH or NO fluorescence from a laminar, near-adiabatic reference flame (Fig. 1). The reference flame served two purposes: first, the LIF signal allowed easy tuning of the laser wavelength to the desired transition; second, the recorded fluorescence allowed correction of the LIF signal from the unsteady flame for minor wavelength drift of the dye laser.

Calibrations and Corrections

The filament was calibrated using a near-adiabatic H₂-air flame produced by a Hencken burner [11]. This 25-mm-square burner consists of an array of small fuel tubes within a Hastelloy honeycomb matrix which provides for the flow of air. The uncooled burner thus produces an array of nonpremixed flames; with sufficiently high flow rates of H₂ and air (total cold-gas flow rates of ~50 slpm for this 25-mm-square burner), the heat loss to the burner is negligible and the temperature is near the adiabatic value [11]. The hot-gas velocity—which is necessary for calculation of the radiation correction—can easily be calculated because of the approximate 1-D nature of the flow field; additionally, the gas properties can be obtained from equilibrium calculations. Because of the nonpremixed nature of the burner, one can obtain a wide range of temperatures (from < 900 K to > 2300 K) simply through variation of the H₂ flow rate [11]. In Fig. 2, we show a comparison between the derived filament temperatures (calibrating the filament at one Hencken flame condition) and the calculated adiabatic equilibrium temperatures.

To convert the emission measurement into gas temperature, the measured filament temperature must be corrected for radiative losses [7]. The numerical simulation of the flame (described below) shows that the velocity field is relatively uniform (i.e., a factor of two variation) in the region of interest; thus, we have simply used a constant velocity of 3.6 m/s for all the radiation corrections. However, to assess the sensitivity of the derived temperature to the time-varying velocity and temperature fields, we have used the calculated fields and gas properties as inputs for the radiation-correction algorithm. The difference in temperatures derived by the two approaches—one using uniform velocity and gas properties and the other using the time-varying values—is small because of the relatively high velocity of the gas. This effect is illustrated in Fig. 2 where the temperatures derived using 1) a velocity of 6 m/s (for all the TFP measurements) and 2) the calculated burnt-gas velocity—which varies from 4 to 12 m/s—are virtually identical.

To calibrate the OH fluorescence, we used the same burner. At heights ≥ 3 cm above the burner, the OH fluorescence is constant, indicating that the OH has equilibrated. We recorded OH absorption spectra in a lean ($\phi = 0.94$) H₂-air flame by scanning the dye laser over several transitions in the (0,0) band. We derived the absorption pathlength (about 28 mm) from a measurement of the OH LIF across the burner. The resulting concentration, $[\text{OH}] = 2.18 \times 10^{16} \text{ cm}^{-3}$, compares well with the adiabatic equilibrium value of $2.37 \times 10^{16} \text{ cm}^{-3}$ (with $T_{ad,eq} = 2340 \text{ K}$) and is consistent with a temperature only ~25 K below the adiabatic value. A comparison of the OH LIF data (calibrated using this absorption measurement) and the adiabatic equilibrium value is also shown in Fig. 2. The OH fluorescence signal has been corrected for variations in Boltzmann fraction and quenching (see the equation below), although both of these corrections are relatively small. This figure demonstrates that OH concentrations are indeed close to the adiabatic equilibrium values. Note that in correcting the fluorescence, we have not taken into account fluorescence trapping, either in the calibration flame or in the unsteady flame (although we expect that this correction is relatively small).

Unlike the concentrations of OH, those of NO are too small for reliable absorption measurements and are typically far below equilibrium at reasonable distances above the burner. Consequently, the approach we took was to dope a lean laminar flame with a small, known concentration of NO (from a bottle with ~200 ppm of NO in N₂). The calibration procedure consists of measuring NO fluorescence signals in a doped flame and in an undoped flame, where a portion of the pure N₂ is substituted for the NO-doped N₂.

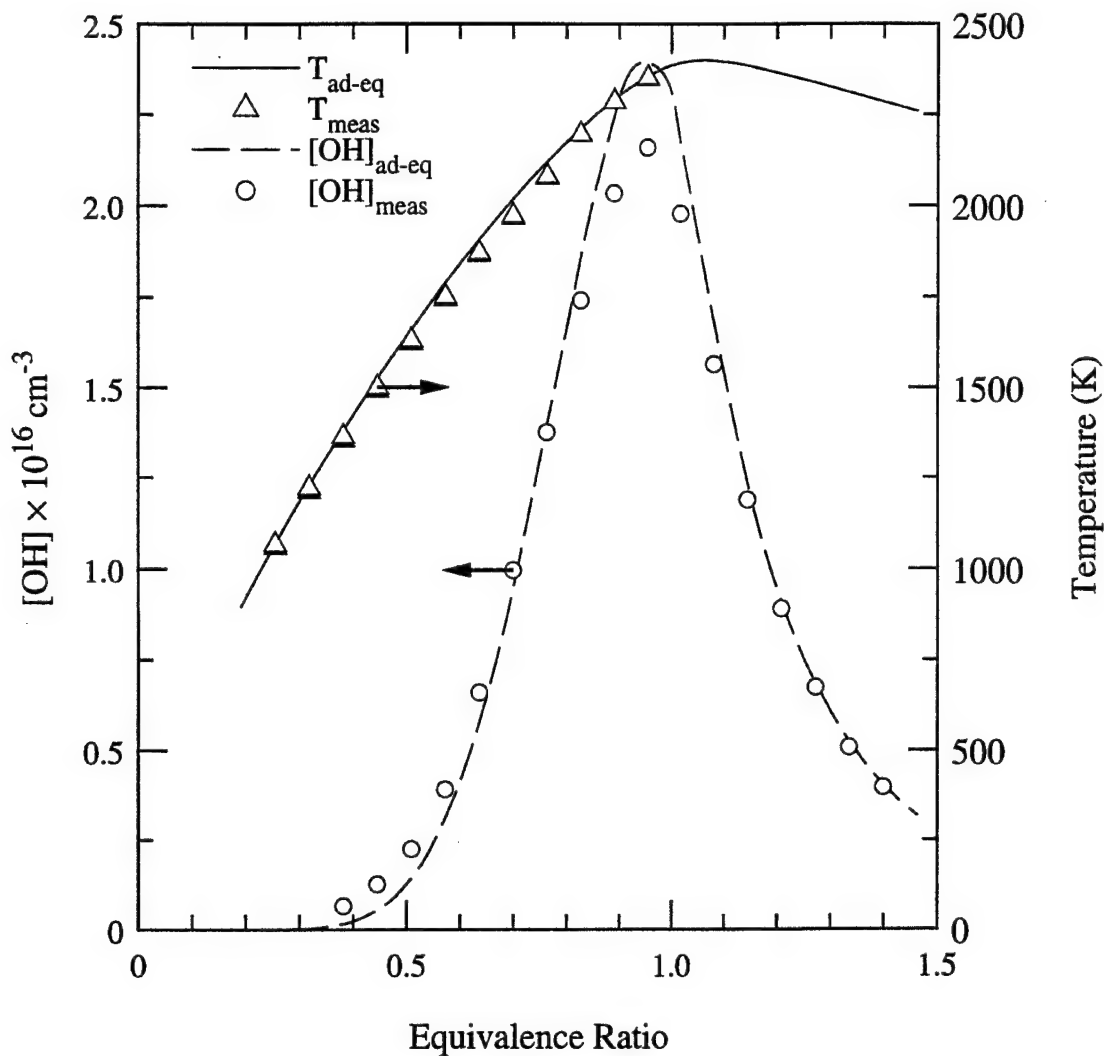


Fig. 2. Temperature and OH concentration over a near-adiabatic H_2 -air Hencken flame. The experimental temperatures and OH concentrations were recorded with TFP and LIF, respectively. The filament emission was calibrated using the adiabatic equilibrium temperature at $\phi = 0.95$, while the OH was calibrated with an independent absorption measurement. The TFP temperatures derived using the burnt-gas velocity are represented by open triangles, while those derived using a single velocity are represented by closed triangles.

Thus, except for the NO levels, the flames are identical; by subtracting the signal from the undoped flame from that of the doped flame, we obtain the signal corresponding to the doped NO.

Using quantities obtained from the calibration flame (denoted with the subscript *cal*), we convert the linear fluorescence signals S_f to mole fraction with the following equation:

$$X_i = \frac{S_f}{N_T} \left[\frac{N_i}{S_f} \right]_{cal} \left(\frac{[F_B]_{cal}}{F_B} \right) \left(\frac{[E_L/Q]_{cal}}{E_L/Q} \right).$$

Here, N_T is the total number density, $[N_i/S_f]_{cal}$ the fluorescence calibration factor (species number density divided by fluorescence signal), F_B the Boltzmann fraction, E_L the laser energy, and Q the net quenching rate. For the NO fluorescence, we also took into account the effect of line broadening; however, its effect on the derived concentrations is small for the range of temperatures recorded with the filament. Of course, for both OH and NO LIF, we chose transitions to minimize the temperature sensitivity of the respective ground-state populations over the temperature range appropriate for the filament (i.e., 900 - 2300 K).

Currently we can only approximate the quenching variation using the recorded temperatures. Because one can distinguish fuel-rich from fuel-lean regions, the mix of species necessary to produce the measured temperatures can be estimated from equilibrium calculations. Because OH exists over only a limited range of conditions, its fluorescence is minimally affected by the accuracy of this estimate; for NO fluorescence, however, the quenching rate can vary by a factor of two over the range 900 - 2300 K. Consequently, to correct the fluorescence for the quenching variation across the flame, we constructed a *look-up* table of the quenching rate as a function of temperature, which was based on an adiabatic equilibrium temperature and the corresponding mixture of species. The corrections differ for rich and lean conditions; thus, the correction algorithm must distinguish between the fuel-rich (inner) and fuel-lean (outer) regions of the flame. The models for OH and NO quenching include the quenching cross sections recently described by Paul *et al.* [12, 13 for NO; 14, 15 for OH].

RESULTS AND DISCUSSION

The numerical model that we employ has been described in detail by Katta *et al.* [1,2], although we note the following: 1) the time-dependent Navier-Stokes equations, along with the species- and energy-conservation equations, are integrated on a nonuniform staggered-grid system; 2) the detailed chemistry model includes 13 species and 52 elementary reactions; and 3) the effective binary-diffusion coefficient of the individual species in the local mixture is calculated using molecular dynamics and Lennard-Jones potentials. The numerical results presented herein are for a uniform air co-flow velocity of 0.3 m/s rather than the area-averaged value of 0.42 m/s. Use of the area-averaged value, though, results in a flow development that does not match the experimental observations. Recently, we have attempted to remedy this discrepancy by recording an inlet co-flow velocity profile with laser-Doppler velocimetry; however, updated calculations were not available for this paper. Nevertheless, we show Figs. 3, 4, and 5 the experimental and numerical values (using the 0.3-m/s co-flow velocity) of temperature and mole fraction of OH and NO at the three downstream locations of 50, 85, and 135 mm, respectively, versus radial position and time (relative to the photodiode trigger signal). These figures show the development of the flame bulge as the observation point moves downstream. The NO and temperature data were acquired in 1-mm radial steps, while the OH was recorded in 0.5-mm (at 50 and 85 mm downstream) and 0.75-mm (at 135 mm downstream) radial increments; however, linear interpolation has been used to *smooth* the images. Note that for purposes of comparison, we have displayed the measured (left-hand side) and calculated (right-hand side) values in a *mirror-image* format; in addition, we have shown only the computed and measured contours above 1000 K, since we were limited to measuring temperatures above 900 K with our TFP apparatus.

At 50 mm (Fig. 3), the flame resembles a steady flame, though we note some temporal variation in the position of the flame surface; furthermore, the measurements and calculations show a small variation (temporal) in temperature along the flame surface and a concomitant variation in X_{NO} . Maximum concentrations of NO in the measurements and calculations are similar at about ~300 ppm. Consistently (at the three downstream locations), we obtain slightly greater measured X_{OH} (~1.1 percent by volume) than calculated X_{OH} (~0.9 to 1.0); however, fluorescence trapping in the *calibration flame* presumably results in a small error (perhaps +10%) in the calibration factor. As expected, OH exists only over a relatively narrow region of space. This region matches well that bracketed by the $T > 1800$ K contour; consequently, the OH marks the high-temperature regions where we expect NO to be produced. In addition, we

consistently observed somewhat greater experimental flame temperatures, 2350 K measured versus ~2200 K calculated, at each downstream position; this, however, may be the result of movement of the filament in the calibration process (due to the high burnt-gas velocity in the Hencken flame).

At 85 mm downstream of the jet exit (Fig. 4), the development of the flame bulge continues. The effect of the nonunity Le is now clearly seen in the NO image; within the bulge the NO concentration peaks at greater than 400 ppm (with the calculated values being slightly higher than the measured ones). Away from the bulge, however, the NO concentration across the flame is much reduced (i.e., $X_{NO} \approx 200$ ppm from the measurements and calculations at about 28 ms). The width of the OH zone is maximum within the bulge, but the peak concentration across the flame drops slightly ($X_{OH} \approx 0.008$ near the bulge vs. $X_{OH} \approx 0.009$ away from the bulge). Again, the maximum measured temperature is ~2350 K, while the maximum calculated value is ~2200 K. In general, however, the agreement between the measurements and calculations is good, not only in terms of peak concentrations and temperatures, but also in terms of the shapes of the concentration and temperature maps (although there are some differences, particularly with the X_{NO} and temperature at ~40 ms).

At 135 mm downstream of the jet exit (Fig. 5), the flame bulge is fully developed. The maximum observed temperature, ~2350 K from the measurements and ~2200 K from the calculations, occurs at the location of the flame bulge, i.e., the compressed region of the flame; in the stretched regions of the flame, the maximum temperatures across the flame drop to ~2100 K. The discrepancy between the measured and calculated temperature aside, there is reasonably good agreement between the calculated and measured temperature. We also observe good agreement between the measured and computed values of X_{OH} and X_{NO} . Of course, flame disturbances from room drafts are more evident at this position than at 50 and 85 mm; thus, the X_{OH} map in particular (due to the small region over which OH exists) appears somewhat *noisy*. The maximum measured X_{OH} are somewhat higher than the calculated ones; however, across the flame bulge, the measured X_{OH} are somewhat lower than the calculated values. The X_{NO} peaks in the compressed regions (at $X_{NO} \approx 490$ ppm from the measurements and $X_{NO} \approx 550$ ppm from the calculations), as expected based on the high temperatures within the bulge. In the stretched regions, the X_{NO} decreases significantly; for example at ~25 ms, the measurements show that $X_{NO} \approx 180$ ppm (the calculated value is somewhat higher, however). Of course, once the NO is produced, it is transported as a relatively stable product, and thus we observe considerable concentrations of NO even in fuel-rich regions

CONCLUSIONS

We have investigated the structure of a dynamic nonpremixed H_2 -air flame through experiments and a direct numerical simulation. In particular, we have recorded in space and time through sequential phase-locked point measurements the temperature using TFP and the concentrations of OH and NO using LIF. The measurements and calculations show the evolution of the flame with increasing distance from the jet exit. Near the jet exit the flame resembles its steady counterpart; however, even at 50 mm downstream, we observe some temporal structure that includes small broadening and narrowing of the high-temperature and high- X_{NO} zones; this effect is less pronounced with the thin OH region. Accompanying the broadening of the temperature/ X_{NO} zones is a modest increase in the NO concentration. The comparison between measurements and computations is good, especially for OH and NO concentrations. Consistently, the temperature recorded with TFP was 100 to 150 K higher than expected; this may result from movement of the filament. With increasing downstream distance, the dynamic character of the flame continues to develop. At 85 mm above the jet, the compressed and stretched regions are now clearly visible, as are the effects of the flame curvature and nonunity Le on the X_{NO} and X_{OH} ; whereas the NO concentrations are maximum within the compressed region, the OH concentrations across the flame zone are at their minimum values. Again, the comparison between modelling and experimental results is good, not only in terms of the magnitudes of the concentrations and temperatures but also in terms of the shapes of the concentration and

temperature maps. Finally, at 135 mm downstream, we find the bulge to be fully developed, and the combined effects of flame curvature and nonunity Le are most evident from the NO map, due to the temperature sensitivity of the thermal-NO mechanism. With both measurements and calculations, the X_{NO} within the bulge is in excess of 450 ppm. Within the stretched regions of the flame, the X_{NO} is greatly reduced. Again, the measured temperatures are somewhat high across the reaction zone, and our future work will focus on improving the accuracy of the recorded temperatures. In addition, for the numerical simulation, we selected a co-flow velocity (one somewhat less than the area-averaged value) such that the simulation matched the general observations of the flame development; of course, future calculations will incorporate the measured velocity profile.

ACKNOWLEDGMENTS

This work was supported by Wright Laboratory, Aero Propulsion and Power Directorate, Wright-Patterson Air Force Base, OH, under Contract Nos. F33615-90-C-2033 and F33615-95-C-2507.

REFERENCES

1. Katta, V. R., Goss, L. P., and Roquemore, W. M., *Combust. Flame* **96**: 60-74 (1994).
2. Katta, V. R. and Roquemore, W. M., *Combust. Flame* **100**: 61-70 (1995).
3. Katta, V. R., Grisch, F., Attal-Tretout, B., Bouchardy, P., and Roquemore, W. M. "Vortex-Flame Interactions in a Hydrogen Jet Diffusion Flame," Presented at 1995 Joint Technical Meeting (Central and Western States and Mexican National Sections) of the Combustion Institute, April 23-26, 1995, San Antonio, TX.
4. Carter, C. D., Goss, L. P., Hsu, K.-Y., Katta, V. R., and Trump, D. D., "The Structure of a Dynamic Nonpremixed H_2 -air Flame," Presented at 1995 Joint Technical Meeting (Central and Western States and Mexican National Sections) of the Combustion Institute, April 23-26, 1995, San Antonio, TX.
5. Law, C. K. and Chung, S. H., *Combust. Sci. Technol.* **29**: 129-145 (1982).
6. Vilimpoc, V. and Goss, L. P., *Twenty-Second Symposium (International) on Combustion*. The Combustion Institute, Pittsburgh, 1988, pp. 1907-1914.
7. Goss, L. P., Vilimpoc, V., Sarka, B., and Lynn, W. F., *ASME Trans.* **111**: 46-52 (1989).
8. Carter, C. D. and Barlow, R. S., *Opt. Lett.* **19**: 299-301 (1994).
9. Chidsey, I. L. and Crosley, D. R., *J. Quant. Spectrosc. Radiat. Transfer* **23**: 187-199 (1980).
10. Smith, G. P. and Crosley, D. R., *Appl. Opt.* **22**: 1428-1430 (1983).
11. Barlow, R. S. and Carter, C. D., *Combust Flame* **97**: 261-280 (1994).
12. Paul, P. H., Carter, C. D., Gray, J. A., Durant Jr., J. L., and Furlanetto, M. R., *Correlations for the $NO A^2\Sigma^+(v'=0)$ Electronic Quenching Cross-section*, Sandia Report SAND94-8237, Sandia National Laboratories, Livermore, CA, 1995.
13. Paul, P. H., Gray, J. A., Durant Jr., J. L., and Thoman Jr., J. W., *AIAA J.* **32**: 1670 (1994).
14. Paul, P. H., Carter, C. D., Gray, J. A., Durant Jr., J. L., Thoman, J. W., and Furlanetto, M. R., *Correlations for the $OH A^2\Sigma^+(v'=0)$ Electronic Quenching Cross-section*, Sandia Report SAND94-8244, Sandia National Laboratories, Livermore, CA, 1994.
15. Paul, P. H., *J. Quant. Spectrosc. Radiat. Transfer* **51**: 511 (1994).

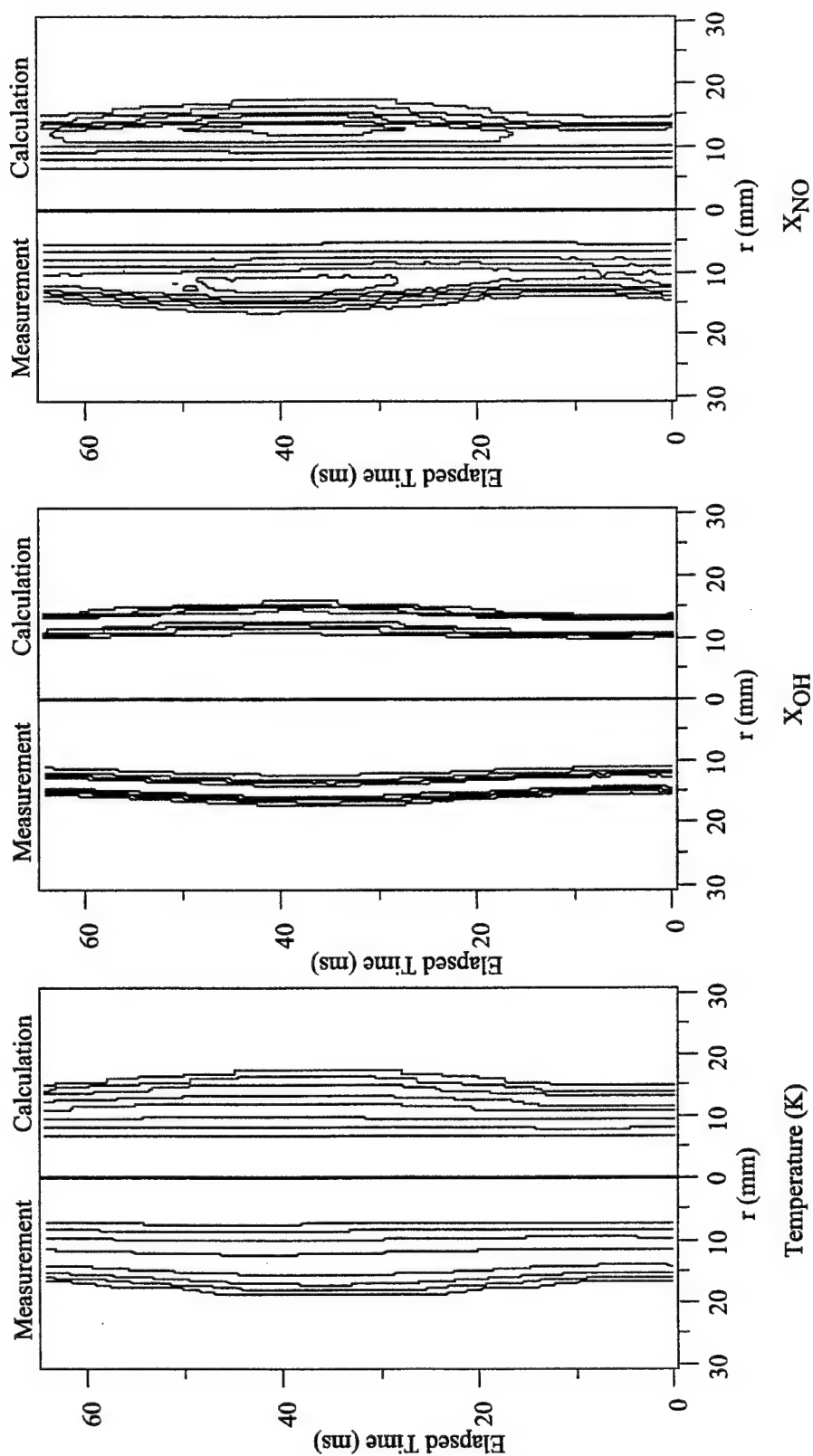


Fig. 3. Contour plots of measured (left-hand side) and calculated (right-hand side) (1) temperature (left), (2) OH concentration (middle), and (3) NO concentration (right) in space (radius) and time at 50 mm downstream of the jet exit. The description of the contours is as follows: (1) temperature, from 1000 to 2200 K with 400 K intervals; (2) OH mole fraction, X_{OH} , from 0.002 to 0.008 with 0.002 intervals; (3) NO mole fraction, X_{NO} , from 50 to 300 ppm with 50 ppm intervals.

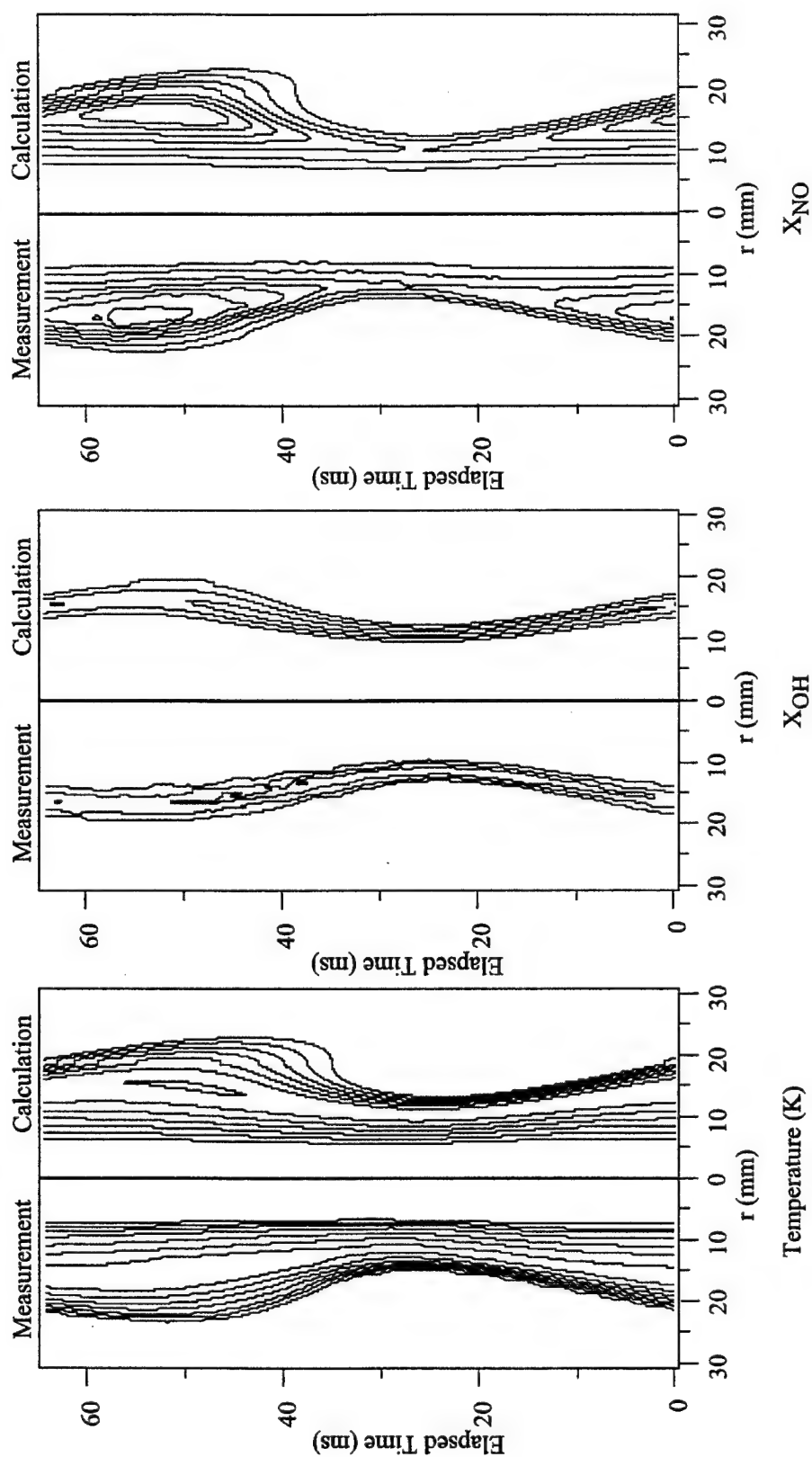


Fig. 4. Contour plots of measured (left-hand side) and calculated (right-hand side) (1) temperature (left), (2) OH concentration (middle), and (3) NO concentration (right) in space (radius) and time at 85 mm downstream of the jet exit. The description of the contours is as follows: (1) temperature, from 1000 to 2000 K with 200 K intervals; (2) OH mole fraction, X_{OH} , from 0.003 to 0.009 with 0.003 intervals; (3) NO mole fraction, X_{NO} , from 100 to 400 ppm with 50 ppm intervals.

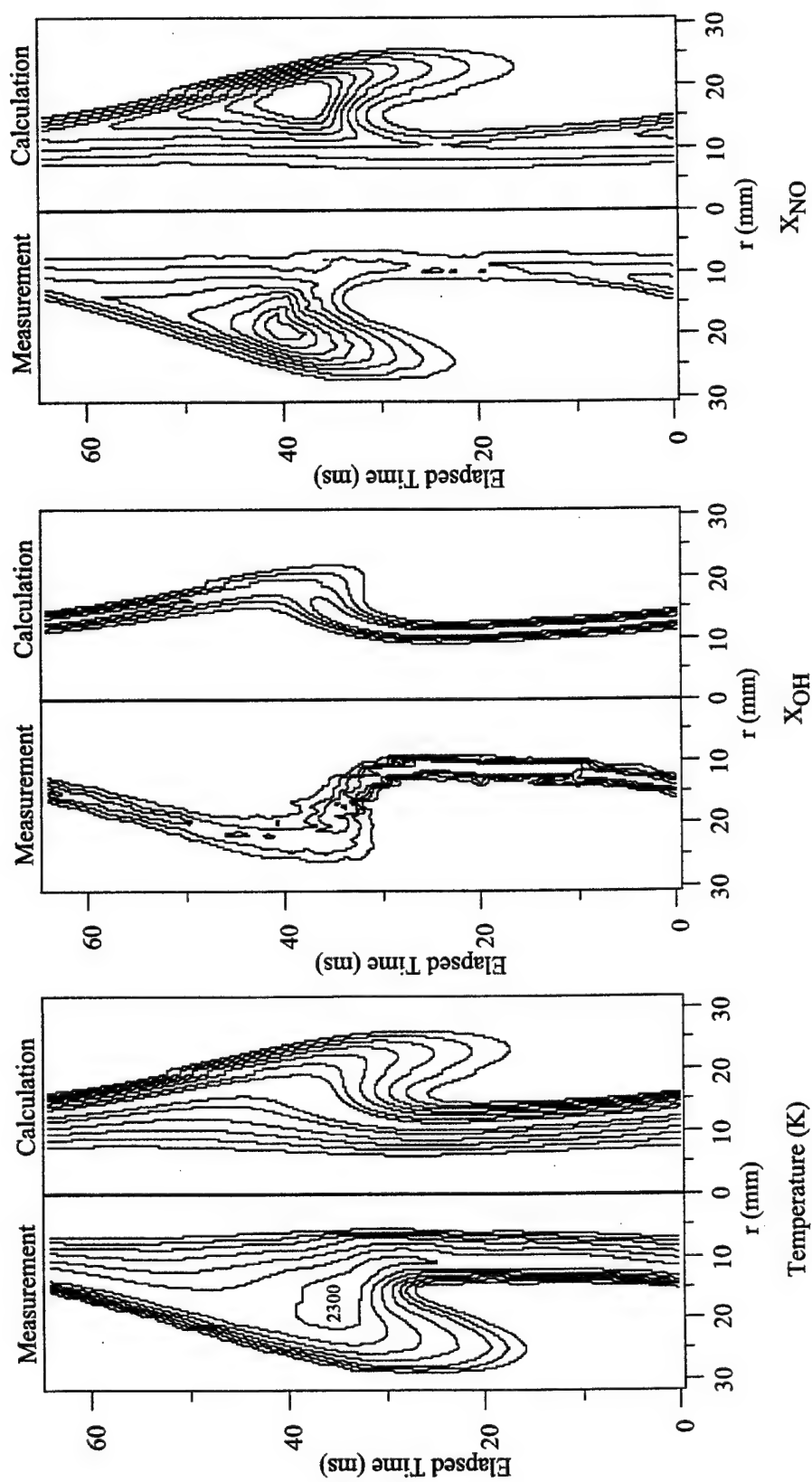


Fig. 5. Contour plots of measured (left-hand side) and calculated (right-hand side) (1) temperature (left), (2) OH concentration (middle), and (3) NO concentration (right) in space (radius) and time at 135 mm downstream of the jet exit. The description of the contours is as follows: (1) temperature, from 1000 to 2000 K with 200 K intervals (the measured temperatures > 2300 K are also shown); (2) OH mole fraction, X_{OH} , from 0.002 to 0.008 with 0.002 intervals; (3) NO mole fraction, X_{NO} , from 100 to 450 ppm with 50 ppm intervals.

THERMAL DIFFUSION EFFECTS AND VORTEX-FLAME INTERACTIONS IN HYDROGEN JET DIFFUSION FLAMES

R. D. HANCOCK*, F. R. SCHAUER* AND R. P. LUCHT

Department of Mechanical and Industrial Engineering, University of Illinois, 1206 W. Green St., Urbana, IL 61801

V. R. KATTA AND K. Y. HSU

Innovative Scientific Solutions, Inc., 3845 Woodhurst Ct., Dayton, OH 45433

The structure of hydrogen jet diffusion flames has been investigated using coherent anti-Stokes Raman scattering (CARS) to obtain temperature profiles in both steady laminar flames and during the interaction of an induced fuel-side vortex with the diffusion flame sheet. The experimental profiles are compared with the results of direct numerical simulations (DNS) of the diffusion flames. The accuracy of the CARS system was evaluated by comparing experimental temperature measurements from hydrogen-air flames produced with a Hencken burner, with adiabatic flame temperatures found using the NASA Lewis equilibrium code. The CARS measurements and equilibrium code calculations are in excellent agreement. Temperature profiles were then obtained in steady, laminar hydrogen (H_2), hydrogen-nitrogen (H_2/N_2), and hydrogen-nitrogen-helium ($H_2/N_2/He$) jet diffusion flames. Thermal diffusion has been found to be very significant in these hydrogen jet diffusion flames and has therefore been incorporated into our DNS model. The experimental and computational results for the steady flames show good quantitative agreement in terms of peak temperature and flame location when thermal diffusion is included in the model.

CARS was also used to measure radial temperature profiles at several axial positions and at one specific time during vortex-flame interactions in the H_2/N_2 and $H_2/N_2/He$ flames. It has been predicted by Katta and Roquemore [*Combust. Flame* 100:61-70 (1995)] that the local flame temperature in nonunity Lewis number flames can depart significantly from the local steady-state temperature during vortex-flame interactions. The CARS and DNS model results support this prediction and show similar temperature departures from the steady-state solution. The high mole fraction and temperature gradients that are created during vortex-flame interactions probably increase the importance of thermal diffusion in these flames.

Introduction

In gaseous diffusion flames, the fuel and oxidant mix and react in a region of finite thickness called the reaction zone or flame sheet. According to Hotte and Hawthorne [1], a flame is considered to be turbulent when its entire flame surface becomes wrinkled and bumpy. Photographs and images of these flames indicate that many of these wrinkles and bumps are caused by small- and large-scale vortical structures that collide and interact with the flame sheet. It has been predicted by Katta and Roquemore [2] that when a vortex collides with the flame sheet, a curved flame surface with regions of positive and negative stretch is produced in which significant deviations in the local peak flame temperature and NO concentration from the equilibrium flame conditions are observed. Here, we describe a combined experimental and computational study of flame structure for both steady, laminar jet diffusion flames and during the interaction of an in-

duced fuel-side vortex with a diffusion flame sheet. The primary experimental tool that was used to investigate flame structure is coherent anti-Stokes Raman scattering (CARS) temperature measurements. An accurate and precise CARS system was developed and tested with detailed temperature measurements in a near-adiabatic Hencken calibration burner [3,4]. These CARS measurements were compared with calculations from the NASA-Lewis equilibrium code [5] and the direct numerical simulations (DNS) model developed by Katta et al. [6] and found to be in excellent agreement. Detailed CARS temperature measurements in several steady (undriven) hydrogen diffusion flames were compared with the results of the DNS model (with and without thermal diffusion) to evaluate the level of absolute agreement between the experiment and the model; we found that it was necessary to include thermal diffusion in the model to obtain good agreement. The vortex-flame interactions were produced by pulsing a loudspeaker located in a chamber under the fuel tube at a frequency of 20 Hz. This resulted in a repeatable vortex that is similar to a single tur-

*Wright Laboratory, Wright-Patterson AFB, OH 45433.

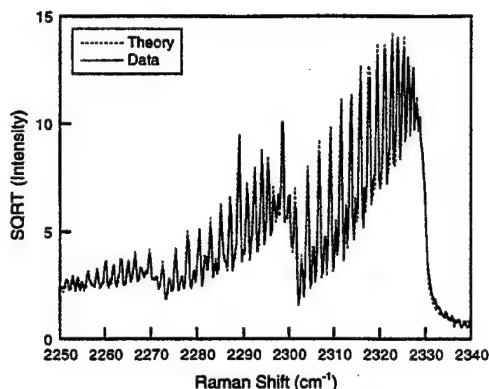


FIG. 1. Typical fit of a CARS nitrogen spectra from the hydrogen-nitrogen jet diffusion flame. The fit temperature is 2303 K and the nitrogen mole fraction is 0.63. The spectral resolution is 0.59 cm^{-1} .

bulent event and extremely reproducible [7]. CARS data was then collected during a single vortex-flame interaction in a driven jet diffusion flame.

The jet fluid for the diffusion flames studied consisted of various mixtures of hydrogen, nitrogen, and helium gases. Hydrogen was selected because its chemistry is fairly simple compared to other gaseous fuels, it departs significantly from unity Lewis number behavior, and it produces highly stable flames. Nitrogen is the gas species probed for CARS temperature measurements and is added to the jet fluid to move the stoichiometric contour closer to the shear layer. Helium has diffusive characteristics similar to hydrogen and can also be used to move the stoichiometric contour.

Experimental Systems

The accuracy and precision of the CARS system were investigated by performing measurements in a Hencken burner [3]. The Hencken burner has an array of fuel tubes that are inserted into a stainless steel honeycomb structure. Air flows through the remaining holes of the honeycomb structure and the resulting flames are flat, uniform, steady, and nearly adiabatic for sufficiently high flow rates. The airflow was held constant at 60.6 standard L/min (SLPM), with a 0°C reference, and the hydrogen flow rate was varied to produce fuel equivalence ratios ranging from 0.5 to 2.5 [5]. Temperature measurements were made at a position 3.81 cm directly above the center of the burner.

The jet diffusion flame apparatus consists of a 2.54-cm diameter axisymmetric fuel tube that contracts to a 1.00-cm diameter sharp-edged nozzle. The fuel tube is surrounded by a 15.24-cm diameter

coflow of air at 0.48 m/s. Three different flames with the same total jet fluid flow rate of 21.25 SLPM were investigated. The flow rate for the first flame was 21.25 SLPM of pure hydrogen (H_2), for the second flame the flow rates were 15.0 SLPM of hydrogen and 6.25 SLPM of nitrogen (H_2/N_2), and for the third flame they were 15.0 SLPM of hydrogen, 2.25 SLPM of nitrogen, and 4.0 SLPM of helium ($\text{H}_2/\text{N}_2/\text{He}$). The average exit velocity was 4.9 m/s. The vortex-flame interactions were created by pulsing the flow with a loud speaker located in a chamber underneath the fuel tube at a rate of 20 Hz. Simultaneous reactive Mie scattering (RMS) [8] and OH laser-induced fluorescence images of these flames indicate that the vortex and flame structures are reproducible to within about $100 \mu\text{m}$ from cycle to cycle over the axial region investigated.

Figure 1 shows an example of a broadband CARS spectrum obtained with this system in the H_2/N_2 flame. A detailed treatment of CARS can be found in other sources [9,10]. Over 95% of the CARS signal beam was generated in a diagnostic volume less than 2.0 mm long and ca. $50 \mu\text{m}$ in diameter. The CARS signal was focused into a 1-m spectrometer where it was spectrally dispersed and detected using a 512×512 , back-illuminated, unintensified CCD array (Photometrics). The flame was moved radially through the diagnostic volume in the direction perpendicular to the 2.0 mm length in order to maintain the highest possible spatial resolution.

All of the nitrogen CARS spectra obtained were the average of 100 laser shots. Averaging is acceptable in the driven jet diffusion flame because the vortex-flame interaction event and laser pulse are temporally phase locked and spatially repeatable. The nitrogen CARS spectra were fit using the CARSFT code developed at Sandia National Laboratories [11]. Based on the quality and high spectral resolution of the CARS spectra obtained, and on the results of the Hencken burner validations, it is conservatively estimated that the accuracy and precision of the nitrogen CARS temperature measurements are better than 2% ($\pm 40 \text{ K}$ at 2000 K) and 0.5% ($\pm 10 \text{ K}$ at 2000 K), respectively.

Numerical Model

The direct numerical simulations of the diffusion flames were performed using a code developed by Katta et al. [6] and since modified to use the CHEMKIN chemistry model. Time-dependent, axisymmetric Navier-Stokes equations are solved along with species and energy conservation equations in the cylindrical coordinate system. Finite-difference forms of the momentum equations are obtained by an implicit QUICKEST scheme, and finite-difference forms of the species and energy equations are found by a hybrid scheme of upwind and central differencing with a 151×61 mesh grid.

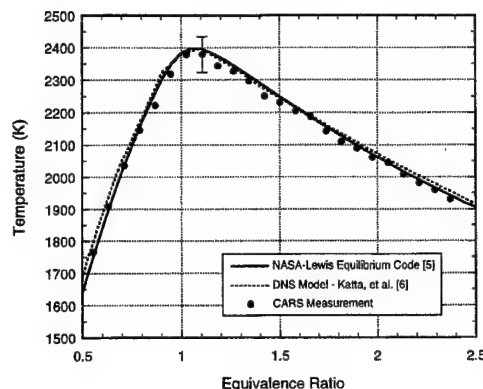


FIG. 2. Comparison of temperature versus equivalence ratio for CARS measurements in a Hencken burner with predicted adiabatic flame temperatures using the NASA Lewis equilibrium code [5] and Katta et al. [6] DNS model.

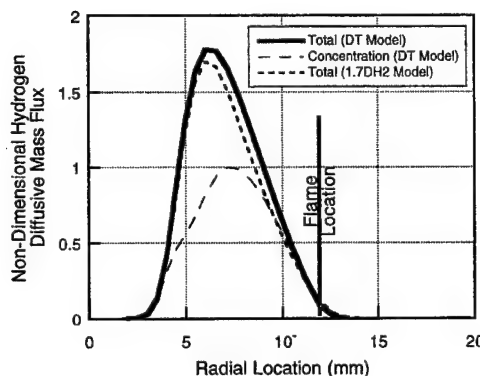


FIG. 3. Nondimensional hydrogen diffusive mass fluxes in hydrogen-nitrogen jet diffusion flame models at 15.24 mm axial location.

The binary diffusion coefficients were determined from Chapman-Enskog collision theory and Lennard-Jones potentials, and effective multicomponent diffusion coefficients were calculated as shown by Williams [12]. Although often negligible, thermal diffusion was found to be significant in these hydrogen jet diffusion flames. The thermal diffusion ratio, k_T , was computed with the high-temperature, rigid-sphere formulation of Furth using a collision factor within 10% of that recommended by Penner, which produces results in fair agreement with Grew's experimental data for H_2/N_2 mixtures [13,14]. Further details concerning the thermal diffusion model used in the CFD model may be found elsewhere [15]. The hydrogen-air chemical kinetics model includes 14 species and 54 reactions, and both temperature

and species-dependent properties are incorporated. The pressure field is calculated at every time step. The required input parameters include mass fractions, boundary conditions, and the time-dependent jet velocity profile.

Results and Discussion

Hencken Burner Results

The Hencken burner results were used to test the accuracy and precision of the CARS system and to check the chemical mechanism in the DNS model. Flame temperatures were measured in the Hencken burner with broadband CARS, and adiabatic flame temperatures were calculated with both the NASA Lewis equilibrium code [5] and the DNS model [6]. Equivalence ratios ranged from 0.5 to 2.5 for the H_2 -air flame. As illustrated in Fig. 2, the nitrogen CARS temperatures are within 1% of the predicted adiabatic flame temperatures. The results indicate that, for sufficiently high flow rates, the Hencken burner flames are nearly adiabatic, that the CARS temperature measurements are very accurate, and that the chemical mechanism in the CFD model is in excellent agreement with the NASA Lewis equilibrium code.

Steady Laminar Diffusion Flame Results

In order to investigate complex vortex-flame interactions, it was first essential that the steady jet diffusion flames be modeled accurately. The DNS code should be very accurate provided that the chemistry and transport submodels are correct, and that the experimental inputs to the code, such as the jet and coflow mass flow rates, are accurate. However, the initial DNS calculations showed poor agreement with the experiment in terms of the peak flame temperature and flame location. After a thorough investigation of experimental parameters such as the fuel and coflow velocities and velocity profiles, and the chemistry model in the DNS code, we turned our attention to the diffusive transport mechanisms. By multiplying the concentration diffusion coefficient of diatomic hydrogen by a factor of 1.7, excellent agreement between the DNS code and experiment was achieved. The apparent diatomic hydrogen diffusion coefficient enhancement suggested that thermal diffusion, which acts to raise the mass flux of "light" species such as H_2 in the direction of increasing temperature, may be an important factor in the high-temperature-gradient regions of these diffusion flames. Figure 3 shows the calculated radial mass flux of hydrogen in our hydrogen-air diffusion flames at an axial location of 15.24 mm above the nozzle. The mass flux is calculated (1) without thermal diffusion and with the hydrogen concentration

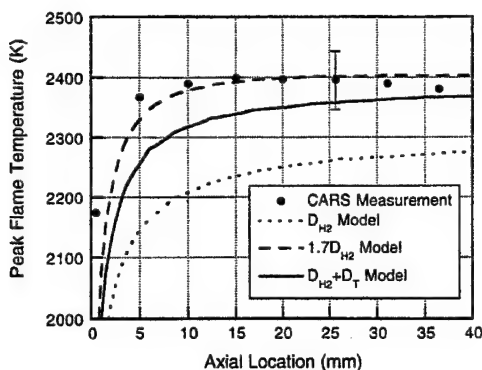


FIG. 4. Measured and modeled peak flame temperatures from the pure hydrogen jet diffusion flame. Model results shown for three hydrogen diffusion formulations.

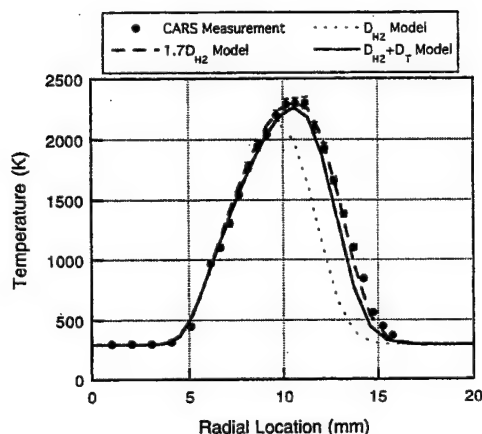


FIG. 5. Hydrogen-nitrogen flame radial CARS measurements and model temperature profiles at 15.24 mm axial location. Model results shown for three hydrogen diffusion formulations.

diffusion coefficient multiplied by 1.7, and (2) with unmodified concentration diffusion coefficients but including thermal diffusion. The contribution of concentration diffusion alone is also shown in Fig. 3, and it is apparent that the diffusive mass flux is drastically increased by thermal diffusion. As illustrated in Fig. 4, when thermal diffusion is included in the model, the pure hydrogen flame temperature rises about 100 K to within the experimental error of the CARS temperature measurements. Because of the impact of the diffusion coefficients on the flame structure, a thorough investigation of the transport coefficients found in the literature and used in the DNS model is warranted.

Measured and calculated radial temperature pro-

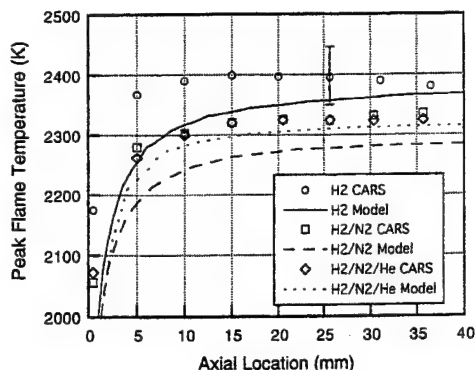


FIG. 6. Measured (CARS) and modeled peak flame temperatures for three hydrogen jet diffusion flames. Thermal diffusion included in all models.

files are shown in Fig. 5 for the H_2/N_2 flame at the 15.24-cm axial location. When the effects of thermal diffusion are not included, the flame temperatures are lower and the radial profile is both narrower and significantly inside the experimental results. The addition of thermal diffusion dramatically improves agreement between the experiment and the model. Axial temperature profiles of peak radial temperatures for the H_2 , H_2/N_2 , and $H_2/N_2/He$ flames are shown in Fig. 6. The model results are about 50 K lower than the experimental results for the H_2 and H_2/N_2 flames. For these flames, thermal diffusion was incorporated in the model calculations. Convergence problems were encountered in the DNS solution but these were overcome by phasing in the thermal diffusion slowly as the calculation proceeded. The peak flame temperature locations are shown in Fig. 7 for the same three flames; again there is good agreement between model and experiment for all three flames.

Vortex-Flame Interactions

The physics and chemistry of vortex-flame interactions is extremely complex. There are several processes that complement, or compete, with one another to influence the local flame temperature and chemical composition during a vortex-flame interaction. The DNS model is a powerful tool for investigating the physics and chemistry of vortex-flame interactions. The effects of factors such as nonunity Lewis number, finite rate chemical kinetics, flame stretch, and curvature can be investigated in detail by examining the DNS solutions. Here, we discuss only fuel-side vortex-flame interactions in hydrogen jet diffusion flames; in these flames, nonunity Lewis number effects should be important. The use of the DNS code to model premixed flames, counterflow diffusion flames, and the interaction of an air-side

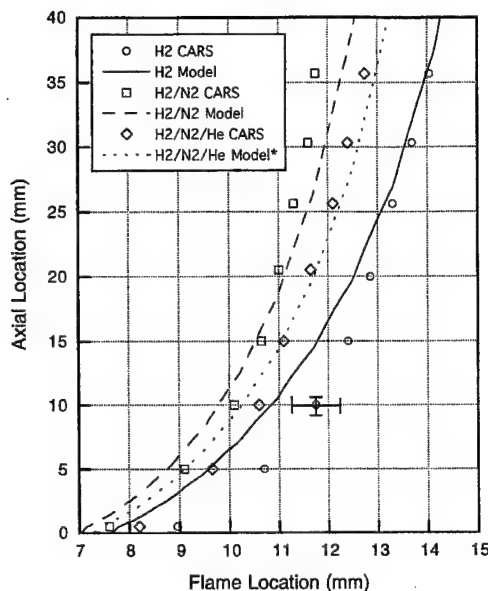


FIG. 7. Measured (CARS) and modeled peak flame temperatures locations for three hydrogen jet diffusion flames. *Hydrogen thermal diffusion included in all models except $H_2/N_2/He$ flame model which uses $1.7D_{H_2}$.

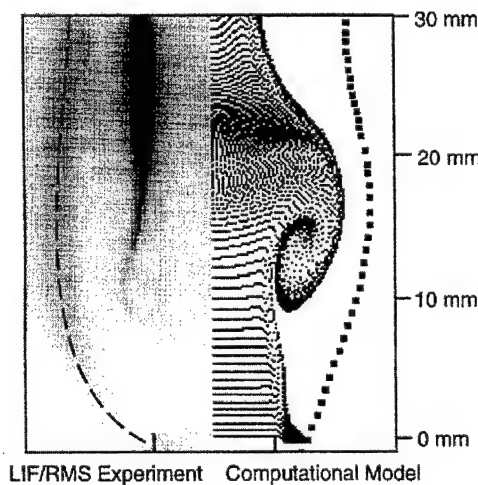


FIG. 8. Comparison of experimental and computational images of a vortex-flame interaction in the H_2/N_2 flame.

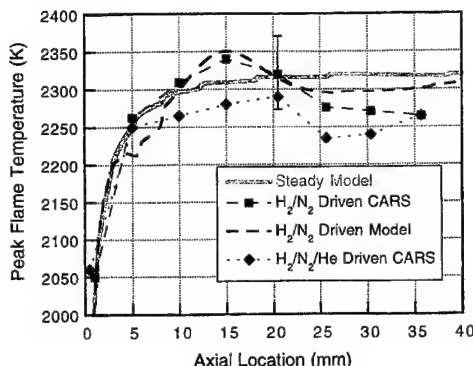


FIG. 9. Measured (CARS) and modeled peak flame temperatures for driven jet diffusion flames. $1.7D_{H_2}$ diffusion formulation used for all models.

vortex with a diffusion flame sheet is discussed elsewhere [2,16–19].

Figure 8 is a split experimental and computational image of the driven H_2/N_2 flame. The left half of the image shows both the flame zone as indicated by OH laser-induced fluorescence and the shear layer as marked by TiO_2 particles formed using reactive Mie scattering. The right side is an image from the computational model. The vortex is marked using particle traces and the peak flame temperature locations are marked by dots. After a great deal of effort, we produced a computational vortex that was similar to the vortex observed experimentally, and likewise, also produced similar flame front curvature.

The addition of thermal diffusion to the model results in significant cross-transport terms in the conservation equations, making it more difficult to obtain converged solutions. This problem was overcome for the steady flames. However, more difficulty was encountered when modeling the driven flames due to the additional numerical complications resulting from subjecting the flow to large time-dependent fluctuations. Therefore, in modeling the unsteady vortex-flame interactions we have multiplied the hydrogen concentration diffusion coefficient by 1.7 to approximate the effects of thermal diffusion.

Figure 9 is a plot of the measured peak radial flame temperatures versus axial location for two driven jet diffusion flames. The H_2/N_2 flame DNS results are also shown, and the axial variations of the calculated and measured peak radial temperatures are remarkably similar. The calculated and measured temperature profiles for this flame both exhibit a 40 K temperature rise above the peak steady flame temperature at the 15.24-mm axial location, and both show a drop in temperature further downstream of the vortex in the negatively stretched region of the flame. Katta and Roquemore [2] predict that the lo-

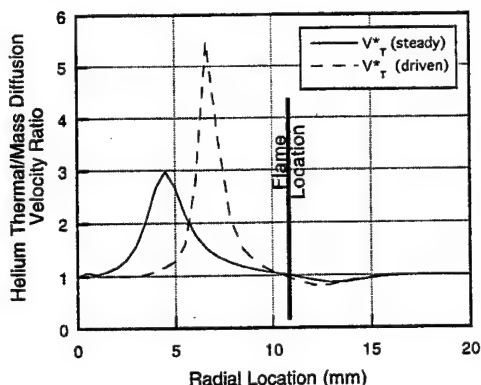


FIG. 10. Helium thermal/concentration diffusion velocity ratio ($V^*_T = 1 + V_{DT}/V_{DH_2}$) for steady and driven $H_2/N_2/He$ flame at 15.24 mm axial location.

cation of maximum positive stretch and maximum temperature exists just ahead of the vortex and that the peak temperature drops significantly in the negatively stretched regions of the flame upstream and downstream of the vortex. For this particular flame, the vortex center is at an axial location of 10 mm and the location of the peak stretch and temperature is at 15 mm. The shape and magnitude of the measured axial temperature profile and the measurement of a peak bulge temperature above the steady-state value support the predictions of Katta and Roquemore [2].

The measured axial profile of peak radial temperatures for the $H_2/N_2/He$ flame shown in Fig. 9 has a shape similar to that for the H_2/N_2 flame, but the local flame temperature is below the steady-state temperature near the bulge region. An increase of the helium mass flux to the flame zone could be the cause of this decrease in temperature at the bulge; the additional helium in this region may serve as a diluent to reduce the local flame temperature. Figure 10 shows the calculated enhancement in the radial helium diffusion velocity due to thermal diffusion for both the steady and driven flames. The steeper gradients in the compressed region of the driven flame act to further enhance thermal diffusion of helium to the flame zone. Thermal diffusion for species other than hydrogen and helium has been found to be negligible due to either low concentrations or molecular weights too close to those of the surrounding gases.

Conclusions

Experimental and computational temperature profiles of laminar hydrogen jet diffusion flames have been obtained and compared for both steady

flames and driven flames with vortex-flame interactions. The experimental temperature profiles were obtained with a broadband CARS system that was carefully validated using a Hencken burner; measured CARS temperatures were within 1% of calculated adiabatic equilibrium temperatures. Three different flames were investigated. With the inclusion of thermal diffusion in the transport model, the DNS model calculations were in good agreement with experimental measurements for the H_2 and H_2/N_2 flames. The mass flux of hydrogen to the flame zone was increased significantly by thermal diffusion, resulting in an increase of approximately 100 K in the peak radial temperature, moving the radial location of peak temperature outward and broadening the temperature profile. Vortex-flame interaction results from the H_2/N_2 driven flame indicate that the local temperature is higher than the steady-state undriven flame temperature at the bulge where the flame is positively stretched and flame curvature is concave toward the fuel-side of the flame surface. The overall shape of the axial temperature profiles for the experiment and the model are similar. Experimental results from the driven $H_2/N_2/He$ flame indicate that the temperature at the bulge is slightly below the steady-state flame temperature, but the overall shape of the axial profile of peak radial temperature is similar to that for the H_2/N_2 flame.

Acknowledgments

Financial support was provided by Systems Research Laboratories, Inc. and the Aero Propulsion and Power Directorate of Wright Laboratory (USAF). The authors also wish to thank Dr. Mel Roquemore of Wright Laboratory for his technical guidance and numerous stimulating discussions during this research program.

REFERENCES

1. Hottel, H. C., and Hawthorne, W. R., *Third Symposium on Combustion, Flame, and Explosion Phenomena*, The Combustion Institute, Pittsburgh, PA, 1949, pp. 254-256.
2. Katta, V. R., and Roquemore, W. M., *Combust. Flame* 100:61-70 (1995).
3. Hencken, K., Research Technologies, Inc., personal communication, 1995.
4. Hancock, R. D., Bertagnolli, K. E., and Lucht, R. P., *Nitrogen and Hydrogen CARS Temperature Measurements in a Hydrogen/Air Flame Using a Near-Adiabatic Flat-Flame Burner*, *Combust. Flame* (1996). Accepted.
5. Gordon, S., and McBride, B. J., *Computer Program for Calculation of Complex Chemical Equilibrium Compositions, Rocket Performance, Incident and Reflected Shocks, and Chapman-Jouguet Detonations*, NASA Technical Report SP-273 (1976).

6. Katta, V. R., Goss, L. P., and Roquemore, W. M., *Combust. Flame* 96:60-74 (1994).
7. Hsu, K. Y., Chen, L. D., Katta, V. R., Goss, L. P., and Roquemore, W. M., *Experimental and Numerical Investigations of the Vortex-Flame Interactions in a Driven Jet Diffusion Flame*, AIAA Paper 93-0455, 31st Aerospace Sciences Meeting, Reno (1993).
8. Chen, L.-D., and Roquemore, W. M., *Combust. Flame* 66(1): 81-86 (1986).
9. Eckbreth, A. C., *Laser Diagnostics for Combustion Temperature and Species*, Abacus Press, Cambridge, (1988).
10. Greenhalgh, D. A., in *Optical Diagnostics for Flow Processes*, (L. Lading et al., Eds.) Plenum Press, New York, 1994, pp. 357-389.
11. Palmer, R. E., *The CARSFT Computer Code for Calculating Coherent Anti-Stokes Raman Spectra: User and Programmer Information*, Sandia Report SAND89-8206, 1989.
12. Williams, F. A., *Combustion Theory*, Addison-Wesley Publishing Co., Redwood City, CA, 1985.
13. Grew, K. E., and Ibbs, T. L., *Thermal Diffusion in Gases*, University Press, Cambridge, 1952.
14. Penner, S. S., *Chemistry Problems in Jet Propulsion*, Pergamon Press, New York, 1957.
15. Schauer, F. R., Hancock, R. D., Lucht, R. P., and Katta, V. R., "Thermal Diffusion and Non-Unity Lewis Number Effects in Hydrogen Jet Diffusion Flames," Central States Section of the Combustion Institute, St. Louis, Paper 16 (1996).
16. Katta, V. R., Grisch, F., Attal-Tretout, B., Bouchardy, P., Roquemore, W. M., *Vortex-Flame Interactions in a Hydrogen Jet Diffusion Flame*, Central States/Western States/Mexican National Sections of the Combustion Institute, San Antonio, Paper 95 S-034, 1995.
17. Carter, C. D., Gould, R. D., Goss, L. P., Katta, V. R., and Hsu, K. Y., "The Structure of a Dynamic Nonpremixed H₂-Air Flame," 1995 Meeting of the Western States Section of the Combustion Institute, Stanford, Paper 95F-222 (1995).
18. Law, C. K., *Twenty-Second Symposium (International) on Combustion*, The Combustion Institute, Pittsburgh, PA, 1988, pp. 1381-1402.
19. Chung, S. H., and Law, C. K., *Combust. Flame* 52:59-79 (1983).

COMMENTS

Dr. K. H. Luo, Queen Mary and Westfield College, UK. The peak temperature vs. the axial location profiles predicted by the numerical method show substantial jumps from one point to another. I believe that the calculations involve significant numerical errors due to the use of coarse grids. In no circumstances could such poor-resolution calculations be called DNS. The comparison with experimental data is therefore meaningless.

Author's Reply. The plots of peak temperature versus axial temperature in the presentation did show jumps of

~10K (of 2300K) in the DNS model temperature. The jumps occurred because of the plotting routine that we used to extract the data from the DNS output. We are plotting the peak radial temperature as a function of axial position in Figs. 4, 6, and 9. The jumps occurred when the peak radial temperature moved from one radial spatial grid point to another. The authors would like to point out that over twenty radial points are within the flame zone of the DNS computation, resulting in smooth radial profiles as seen in Fig. 7. There are no such jumps in the raw, axial DNS data, and the plotting routine was re-written for the figures in the published paper to reflect this.

Flame Structure of Stabilization Region in a Laminar Hydrogen Jet Diffusion Flame

F. R. Schauer[†], S. M. Green, R. P. Lucht*

Department of Mechanical and Industrial Engineering, University of Illinois, 1206 W. Green St., Urbana, IL 61801
(Phone: 217-333-5056, Fax: 217-244-6534)

[†]Also with Wright Laboratory, Wright-Patterson AFB, OH 45433

R. D. Hancock

Wright Laboratory, Wright-Patterson AFB, OH 45433
(Phone: 937-255-7487, Fax: 937-255-1125)

V. R. Katta

Innovative Scientific Solutions, Inc., 3845 Woodhurst Ct., Dayton, OH 45433
(Phone: 937-255-8781, Fax: 9373-255-1125)

A laminar hydrogen jet diffusion flame was investigated experimentally and computationally to determine the structure of the stabilization region below the nozzle. Temperature and concentration measurements in the flames were obtained with a coherent anti-Stokes Raman scattering (CARS) system. Modeling of the flame was performed with a finite-rate chemistry, computational fluid dynamics (CFD) code developed for the study of diffusion flames. A dual-pump CARS instrument was developed for the simultaneous measurement of gas-phase temperature and concentrations of molecular nitrogen and oxygen. Detailed temperature and oxygen/nitrogen mole fraction ratio measurements have been performed in the stabilization region of the hydrogen-nitrogen jet diffusion flame. Measurements were also completed using a different dual-pump CARS setup to simultaneously measure temperature and concentrations of molecular hydrogen and nitrogen. CARS temperature and concentration measurements, which have very high precision and spatial resolution, were then compared to the CFD model. These experimental and computational results indicate that there exists a region below the nozzle exit where significant amounts of oxygen are found on the fuel side of the peak flame temperature profile. The flame structure is observed to be essentially 'premixed' in the stabilization region of the laminar diffusion flame.

Introduction

The stabilization region of a laminar diffusion flame is of great interest to many researchers in the combustion community and flame stabilization is obviously a subject of great practical as well as scientific interest. It has been observed that under a wide range of flow conditions in hydrogen jet diffusion flames, the flame will attach to the outside of the fuel tube several millimeters below the exit of the nozzle. Close visual inspection of these flames would indicate that as the fuel exits the nozzle some of the fuel diffuses away from the nozzle and down the outside of the nozzle. The modeling results of Fukatani, et al. [1] show that at the lowest part of the hydrogen flame, the upward-flowing air and the hydrogen diffusing downward meet and react like premixed gas mixtures. Takahashi and Katta [2-4] show similar modeling results for methane flames and observe air passing through a narrow "dark space" between the flame and nozzle producing a premixed region on the fuel side of the flame. In order to investigate these predictions we

used dual-pump coherent anti-Stokes Raman scattering (CARS) to probe this region in detail to determine the temperature distribution and the structure of this premixed flame zone.

High spatial gradients in temperature and concentrations in the stabilization region have previously made quantitative measurements difficult. The entire stabilization zone is only a couple of millimeters in thickness and length for these flame and thus requires an experimental technique with excellent spatial resolution and precision.

In order to overcome these difficulties, a dual-pump CARS technique was developed to simultaneously measure temperature and multiple species concentrations. CARS is a laser diagnostic technique that has been used extensively for measuring gas temperature and major species concentrations in harsh combustion environments. Early applications of the CARS technique allowed for the detection of only one species at a time. Techniques which probe more than one species at a time have since been developed.

*Corresponding author

Proceedings of the 1997 Technical Meeting of the Central States Section of the Combustion Institute

Dual-pump CARS was first introduced by Teets [5] using two pump beams at different but fixed frequencies ω_1 and ω_2 . The technique was further developed by Lucht [6] who used a tunable dye laser as the second pump beam for the detection of nitrogen and oxygen in a pressure cell and the detection of propane and nitrogen in a fuel-injected engine. A short time later Lucht et al. [7] demonstrated pure rotational and vibrational dual-pump CARS and the use of polarization techniques to vary the relative intensities of the two CARS signals.

The dual-pump CARS technique permits two species, independent of their vibrational Raman resonances, to be probed simultaneously. The spectra for the two species are generated with the same three laser beams in precisely the same spatial location and instant of time. This helps to reduce the effects of beam steering in high-temperature gradient regions in flames. Furthermore, the CARS signals from the two species can be generated at nearly the same frequency, and therefore both species can be detected using a single array detector. Furthermore, the frequency resolution and separation of the two CARS spectra generated using dual-pump CARS can be adjusted to optimize temperature and concentration measurement accuracy.

In this study, two different dual-pump CARS systems were used to investigate the structure of the jet diffusion flame below the nozzle of a laminar axisymmetric hydrogen/nitrogen jet diffusion flame. Temperature and the concentrations of N_2 and O_2 were measured using the first of the two setups. Then temperature and the concentration ratios of N_2 and H_2 were measured using the second dual-pump CARS setup. Comparisons of the temperature and species concentration measurements to direct numerical simulation (DNS) models of the diffusion flame were used to study the stabilization region.

Experimental Facility

The jet diffusion flame apparatus consisted of a 2.54 cm diameter axisymmetric fuel tube that contracts to a 1-cm-diameter sharp-edged nozzle. The fuel tube is surrounded by a 15.24 cm diameter co-flow of air at 0.48 m/s, which helps to remove room air disturbances. The diffusion flame investigated in this experiment consisted of 15.0 SLPM of hydrogen and 6.25 SLPM of nitrogen. The resulting calculated average peak centerline axial velocity was 4.9 m/s at room temperature. The jet and annulus air velocity profiles were also measured using a hot wire anemometer and found to be nearly top-hat and within 5% of volume-based calculations over the center 8 mm of the jet. Since this flame was stable, local gas

temperature and concentration measurements could be accurately made with averaged CARS spectra.

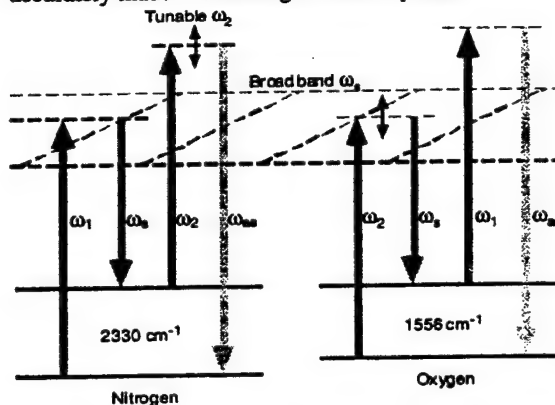


Figure 1. Energy-level schematic for dual-pump measurements of O_2 and N_2 .

The energy level diagrams for the dual-pump CARS techniques used are shown in Fig. 1 for the N_2/O_2 CARS system and Fig. 2 for the N_2/H_2 CARS system. The left sides of both figures illustrate that a CARS polarization is established for nitrogen when the frequency difference $\omega_1 - \omega_3$ corresponds to the vibrational Raman resonance 2330 cm^{-1} . The induced vibrational Raman polarization scatters the incident ω_2 beam to produce anti-Stokes radiation at frequency $\omega_{as} = \omega_1 - \omega_3 + \omega_2$. The right side of Fig. 1 illustrates that for oxygen the frequency difference $\omega_2 - \omega_3$ corresponds to the vibrational Raman resonance 1556 cm^{-1} . The vibrational Raman polarization of the oxygen molecule scatters the incident ω_1 beam to produce the anti-Stokes signal at a frequency of $\omega_{as} = \omega_2 - \omega_3 + \omega_1$. Similarly in Fig. 2, the Raman resonance, $\omega_2 - \omega_3 = 4070\text{ cm}^{-1}$, produces the anti-Stokes signal for H_2 .

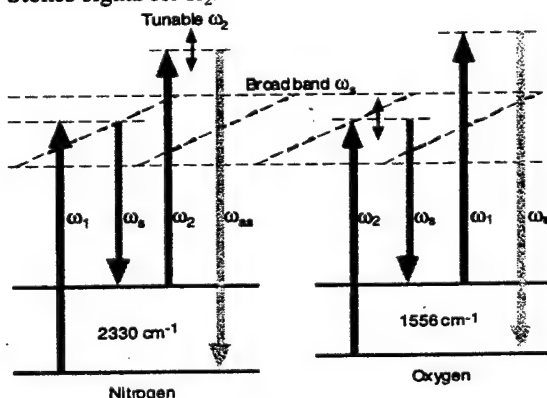


Figure 2. Energy-level schematic for dual-pump CARS measurements of H_2 and N_2 .

[illegible]

A three-dimensional "folded BOXCARS" phase-matching geometry was used to generate the CARS signal [10]. The three laser beams were crossed and focused in the flame producing a diagnostic volume in which over 95% of the CARS signal beam was generated in a region less than 2.0 mm long and ~50 μm in diameter. The resulting CARS signal was focused into a 1-meter double spectrometer where it was spectrally dispersed and detected using a 512 x 512, back-illuminated, unintensified CCD array (Photometrics) [11].

high signal-to-noise ratio for the CARS spectra was maintained and the broadband dye laser spectral profile was frequently monitored.

Numerical Model

Axial diffusion, important in the stabilization region of this flame, was included. The effects of hydrogen thermal diffusion, which augments the

concentration diffusion of hydrogen by approximately 70% in these flames, were accounted for [16]. Radiation, which is not very strong in hydrogen flames, is neglected as well as heat transfer to the nozzle. The required inputs included mass fractions, boundary conditions, and the time-dependent jet velocity profile. For the results presented within this paper, all modeling was steady-state.

Results and Discussion

CARS Systems

Validation of the CARS instrument used in this study have been previously performed by the authors and Bertagnoli [14]. N_2 CARS temperature measurements used herein have consistently provided better than 2% accuracy and 1% precision (± 40 K and ± 20 K at 2000 K respectively). H_2 CARS temperature measurements have demonstrated the same level of precision but with slightly worse accuracy ($\sim 4\%$) primarily due to lack of information about H_2 CARS line shapes.

A similar lack of basic scientific knowledge about CARS lineshapes was encountered when N_2/O_2 dual pump CARS measurements were validated in the Hencken burner by the authors [Optics]. Dreier and Schiff [31] found similar problems in their high temperature oxygen CARS spectra. The authors found that adiabatic flame temperature measurements in a Hencken burner using the N_2/O_2 CARS spectra were within 1% of the value predicted by the NASA Lewis equilibrium code [14, 18, and 19]. But, the O_2 concentration measurements were $\sim 25\%$ high despite the measurement's excellent precision. Clearly further basic CARS spectroscopy research needs to be done in order to model hydrogen and oxygen line shapes as accurately as nitrogen.

Flame Stabilization Region

CARS spectra were obtained at several hundred points in the stabilization region of the diffusion flame. Data was collected every 254 microns in the axial and radial directions around the stabilization region. Typical N_2/O_2 CARS spectra are shown in Fig. 5a, b, and c demonstrating the radial variation of temperature and oxygen concentration from inside the flame zone, at the peak temperature region of the flame zone, and outside the flame zone respectively. The increased oxygen concentration outside the flame zone is clearly evident from the stronger O_2 spectra evident in Fig 5c, but oxygen is also present in significant quantities well within the flame zone.

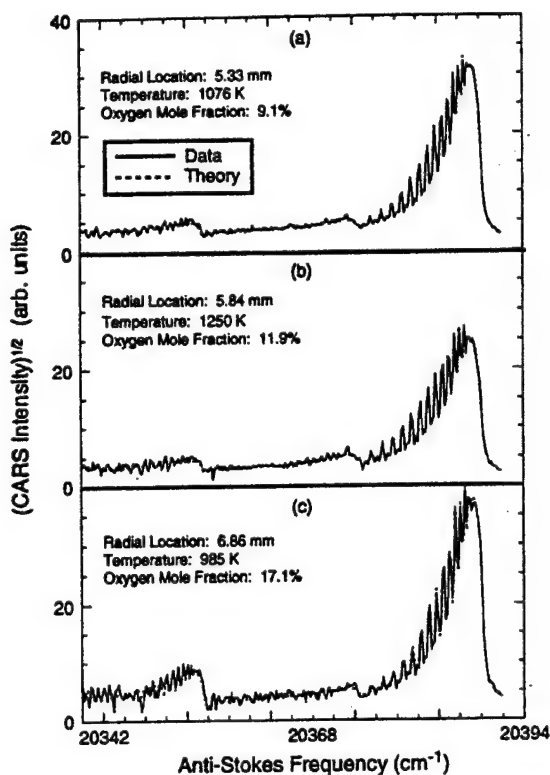


Figure 5. N_2/O_2 dual-pump CARS spectra showing the presence of oxygen on the fuel side of the flame zone. All three spectra were obtained 1.27 mm below the lip of the 10 mm diameter nozzle. Spectrum 5a is a point on the fuel side of the flame zone, 5b is at the peak temperature region of the flame zone, and 5c is on the air side of the flame zone.

H_2/N_2 dual-pump CARS spectra are shown in Fig. 6 near the nozzle tip. Again, spectra are shown for a location on the fuel side of the flame zone, near the peak temperature region of the flame zone, and outside the flame zone on the air side of the diffusion flame. Several interesting phenomena can be noted from these spectra. Firstly, hydrogen is diffusing below the nozzle against the convective flow. It is evident that since hydrogen appears on the air side of the fuel zone below the nozzle there exists a premixed region in this stabilization region. By comparing nitrogen spectra with Fig. 5 it is also apparent that the intensity of the nitrogen CARS signal with the H_2/N_2 CARS system is not as strong as the signal in the N_2/O_2 CARS system. This is because the broadband Stokes laser is much less efficient when tuned to the H_2 CARS resonances. Despite this it is still possible to extract the relative concentrations of H_2 and N_2 from the data.

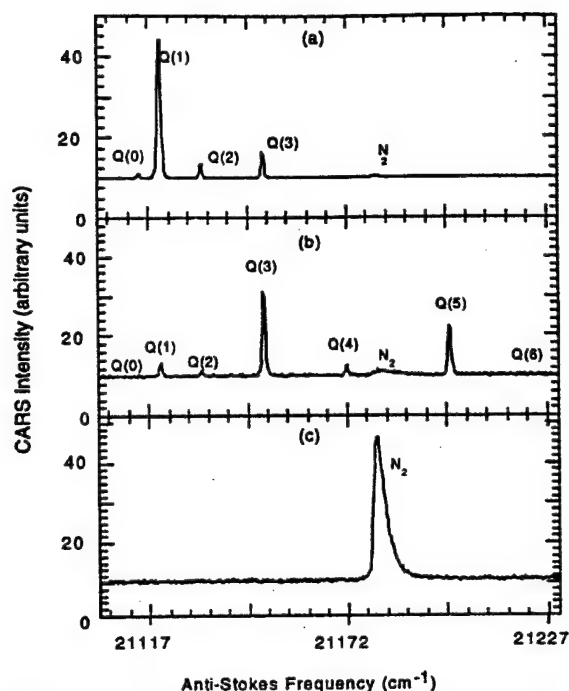


Figure 6. H_2/N_2 dual-pump CARS spectra showing the radial variation of concentrations. All three spectra were obtained at the axial location of the tip of the nozzle. Spectrum 6a is a point on the fuel side of the flame zone, 6b is near the peak temperature region of the flame zone, and 6c is on the air side of the flame zone.

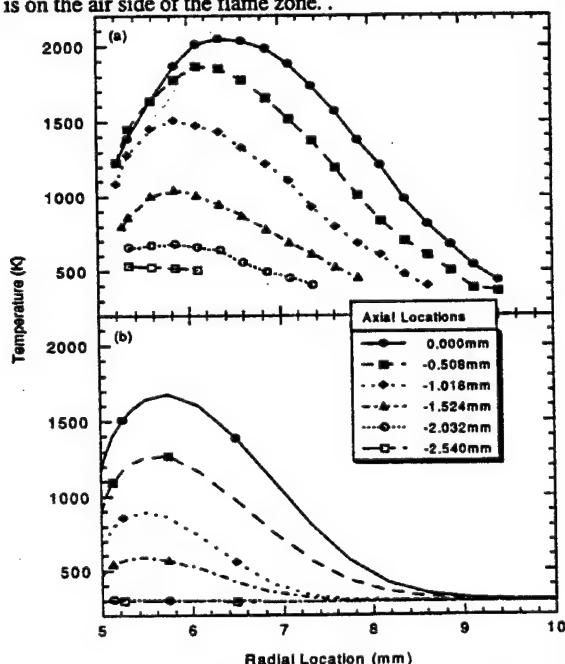


Figure 7. Dual-pump CARS measurements (a) and DNS (b) radial temperature profiles in the stabilization region of a hydrogen-nitrogen jet diffusion flame at various axial locations

Results for the entire flame stabilization region of the hydrogen-nitrogen jet diffusion flame are shown in Figs. 8 and 9. DNS model is shown alongside the N_2/O_2 dual-pump CARS measurements. Temperature and O_2 mole fraction are shown in Figs. 8 and 9 respectively. It is evident that the temperature falls off quickly below the nozzle and the oxygen can diffuse through this region without being consumed due to chemical reaction [20].

The CARS data and DNS qualitatively predict the same premixed flame structure in the stabilization region. Contributions to quantitative discrepancies include possible errors in boundary conditions, uncertainties in diffusion modeling, neglecting heat transfer to the nozzle, and problems with the lineshape models in the CARSFT code.

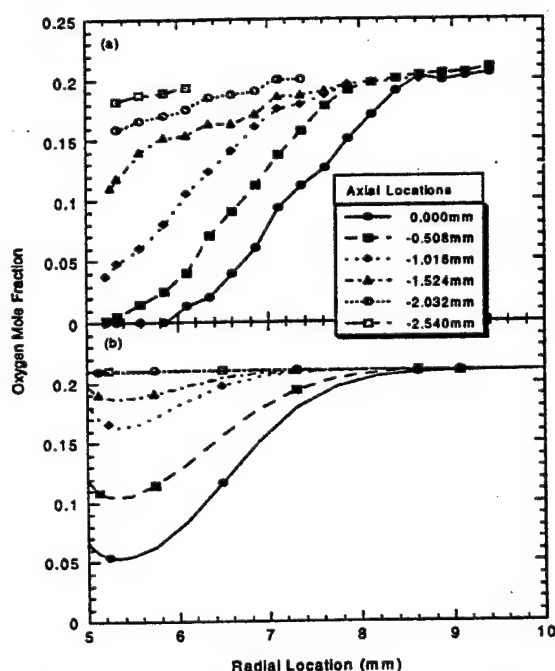


Figure 8. Dual-pump CARS measurements (a) and DNS (b) O_2 mole fractions in the stabilization region of a hydrogen-nitrogen jet diffusion flame.

Conclusions

Dual-pump CARS for N_2/O_2 and H_2/N_2 measurements have been developed and used to obtain gas phase temperatures and mole fractions of major hydrogen combustion species. Simultaneous measurements of temperature and species concentrations are possible with this system. Problems with beam steering in the high gradient regions are largely avoided because relative intensities of the different species CARS spectra do not depend on beam

overlap. Although only two species can be probed simultaneously, this non-intrusive experimental technique is well suited for combustion studies due to its high precision and spatial resolution.

Detailed temperature, O_2 mole fraction, and H_2 fraction measurements were made in the stabilization region of a laminar hydrogen-nitrogen/air jet diffusion flame. Results indicate the presence of a premixed region below the jet nozzle where the hydrogen diffuses against the convective flow to mix with oxygen. O_2 was observed on the fuel side of the flame zone while H_2 was observed on the air side of the flame zone. These results are in agreement with the DNS code predictions and provide quantitative insight into the stabilization of a hydrogen diffusion flame.

Acknowledgments

Financial support for this work was provided in part by Systems Research Laboratories, Inc., the Aero Propulsion and Power Directorate of Wright Laboratory (USAF), and the Air Force Palace Knight program.

References

1. Fukatani, S., Kunioishi, N., and Jinno, H., *Dynamics of Deflagrations and Reactive Systems: Flames* 131,111-124 (1992).
2. Takahashi, F. and Katta, V.R., "A Numerical Study of the Stability of Methane Jet Diffusion Flames" presented at Central States Section/The Combustion Institute, St. Louis, MO (1996).
3. Takahashi, F. and Katta, V.R., "A Further Analysis of the Stabilizing Region of Methane Jet Diffusion Flames" presented at Eastern States Section/The Combustion Institute, Hilton Head, SC (1996).
4. Takahashi, F., Schmoll, W.J., Vangress, M.D., Katta, V.R., "The Stabilizing Region of Methane Jet Diffusion Flames" presented at the 26th International Symposium on Combustion/The Combustion Institute, 02-013 (1996).
5. Teets, R.E., paper presented at International Laser Science Conference, Dallas, TX, November 18-22, (1985).
6. Lucht, R.P., "Three-Laser Coherent Anti-Stokes Raman Scattering Measurements of Two Species," *Optics Letters* 12,78-80 (1987).
7. Lucht, R.P., Palmer, R.E., and Maris, M.A., "Simultaneous Acquisition of Pure Rotational and Vibrational Nitrogen Spectra Using Three-Laser Coherent Anti-Stokes Raman Spectroscopy," *Optics Letters* 12,386-388 (1987).
8. Eckbreth, A.C., *Laser Diagnostics for Combustion Temperature and Species*, Cambridge: Abacus Press, (1988).
9. Greenhalgh, D., in *Optical Diagnostics for Flow Processes*. (Eds. L. Lading, et al.) New York: Plenum Press, pp. 357-389 (1994).
10. Shirley, J.A., Hall, R.J. and Eckbreth, A. J., "Folded BOXCARS for Rotational Raman Studies," *Optics Letters* 5,380-382, (1980).
11. Rakestraw, D.J., Lucht, R. P., and Dreier, T., "Use of a charge-coupled device camera for broadband coherent anti-Stokes Raman scattering measurements," *Applied Optics* 28,4116-4120 (1989).
12. Palmer, R. E. , *The CARSFT Computer Code for Calculating Coherent Anti-Stokes Raman Spectra: User and Programmer Information*, Sandia National Laboratories, Sandia Report SAND89-8206 (1989).
13. Hancock, R.D., Schauer, F.R., Lucht, R.P., and Farrow, R.L., "Dual-Pump Coherent Anti-Stokes Raman Scattering (CARS) Measurements of Nitrogen and Oxygen in a Laminar Jet Diffusion Flame", accepted for publication in *Applied Optics* (1997).
14. Hancock, R.D., Bertagnolli, K.E., and Lucht, R.P., "Nitrogen and hydrogen CARS temperature measurements in a hydrogen/air flame using a near adiabatic flat-flame burner", accepted for publication in *Combustion and Flame* (1997).
15. Katta, V. R., Goss, L. P., and Roquemore, W. M., *Combustion and Flame* 96, 60-74 (1994).
16. Hancock, R.D., Schauer, F.R., Lucht, R.P., Katta, V.R., and Hsu, K.Y., "Thermal diffusion effects and vortex-flame interactions in hydrogen jet diffusion flames", *Proceedings of the 26th International Symposium on Combustion*, The Combustion Institute, 29-322 (1996).
17. Dreier, T. and Schiff, G., *Applied Physics B* 55, 388-390 (1992).
18. Hencken, K., Research Technologies, Inc. (1995).
19. Gordon, S., and McBride, B.J., *Computer Program for Calculation of Complex Chemical Equilibrium Compositions, Rocket Performance, Incident and Reflected Shocks, and Chapman-Jouguet Detonations*, NASA SP-273 (1976).
20. Smooke, M.D., Mitchell, R.E., and Keyes, D.E., *Combustion Science and Technology* 67,85-122 (1989).

An Experimental and Numerical Investigation on Local Extinction in Jet Diffusion Flames

K. Y. Hsu* and V.R. Katta
Innovative Scientific Solutions, Inc.
3845 Woodhurst Court
Dayton, OH 45430

W. M. Roquemore
Aero Propulsion Directorate
Wright Laboratory
Wright-Patterson Air Force Base, OH 45433

Vortex-flame interactions are important elements of a turbulent flame and are building blocks for the development of turbulent-flame models. Experimental studies have been initiated recently at Wright Laboratory to establish a data base of vortex-flame interactions for the validation of time-dependent CFDC codes. In the previous experiment, a methane jet diffusion flame is driven by a loud speaker to create local flame extinction during the vortex-flame interaction. Alternative approach is to inject a vortex directly in a jet flame; this offers the potential in furthering the study of vortex-flame interactions for vortices of different sizes and strengths. A time-dependent CFDC code with detailed chemistry model has been developed for simulation of the local and temporal quenching processes during vortex-flame interactions in methane jet flames. An order of magnitude increase was found in the production and destruction rates of methyl and hydrogen radicals, respectively, in the flame zone under highly strained conditions.

Introduction

Lean blowout, high-altitude relight, emissions, and combustion efficiency are of practical importance in the design of modern gas turbine combustors. Turbulent jet diffusion flames are used to gain insight into turbulent combustion processes and to develop numerical models for use in combustor design. The conceptual view of turbulent reaction zones and the interplay between turbulence and chemistry are germane to the modeling approaches. Recent research has focused on whether turbulent flames can be viewed as an ensemble of strained laminar flamelets or distributed reaction zones.^{1,2}

Many of the basic features of turbulent jet diffusion flames have been characterized.³⁻⁵ Improved visualization techniques have provided additional insights into the structure of a turbulent flame.⁶ At transitional jet velocities, well organized, axisymmetric vortex structures are observed inside the laminar flame surface for distance of several jet diameters downstream. As the jet velocity increases, the inner vortices begin to coalesce at a downstream location in the flame. The coalescence process is highly unstable and results in the breakdown of the organized vortices into smaller but identifiable three dimensional fluid elements. The flame becomes turbulent when these small three-dimensional structures interact with the flame, creating the turbulent flame brush. The wrinkles or bumps in the flame are localized distortions of the flame surface that result when three-dimensional fluid

elements of different sizes, shapes, velocities, and rotational strengths interact with reaction zones of different thicknesses.

It is important to understand individual vortex-flame interactions for several reasons. First, they can increase or decrease the turbulent reaction rate. When the vortex-flame interaction is moderate, they increase the surface area of the flame which leads to an overall increase in the global reaction rate and a reduction in the length of the flame. However, if a vortex has a sufficiently high radial velocity, it can penetrate the flame, creating a localized hole in which no chemical reactions take place.⁷⁻¹⁰ These holes can cause the flame to split or lift when they form near the jet exit. If the holes cover excessive area of the flame surface the global reaction rate decrease which lead to reduction in combustion efficiency and blow-out. Second, flame-vortex interactions may be building blocks for statistical theories of turbulent flames. It is conceivable that an ensemble of only a relatively few basic types of vortex-flame interactions need to be considered for an accurate representation of the statistical result of what, at first glance, might appear to be an endless number of interactions. If this idea is supported by experimental results, it may be feasible to construct a statistical turbulent combustion model.

This paper presents the results of experimental and numerical studies of the individual vortex-flame

* Corresponding author

Proceedings of the 1996 Technical Meeting of the Central States Section of the Combustion Institute

interactions produced in methane jet diffusion flame using two vortex-generation schemes.

Experimental

A specific vortex-flame interaction in a driven methane jet diffusion flame has been studied. The fuel jet velocity was modulated by a loud speaker under a specific driving condition. The detailed descriptions of the experiment are discussed in Ref. 11. The experiment was very repeatable in creating local extinction; however, it was specific to certain driving frequency as well as the size and strength of the vortex. The structure of higher harmonics resulting from mechanical damping from the loud speaker further complicates the interaction process and creates difficulty in specifying the conditions for numerical simulation.

Currently, an alternative experiment has been initiated for continuing the studies of vortex-flame interactions in a jet diffusion flame. The vortices are injected directly toward a jet flame using an injection tube inside a 13-mm-diameter fuel tube as shown in Fig. 1. The 6.4-mm-diameter injection tube has a piston-like cap mounted at the tip. The gap between the tip of the tube and the cap creates a radial passage for fuel injection. By modulating the fuel flow through the injection stream, the fuel is injected periodically and travels radially toward the flame surface. The injection location can be adjusted by traversing the injection tube in the axial direction. Low speed coflowing air around the fuel tube is used to reduce the disturbance from the surrounding.

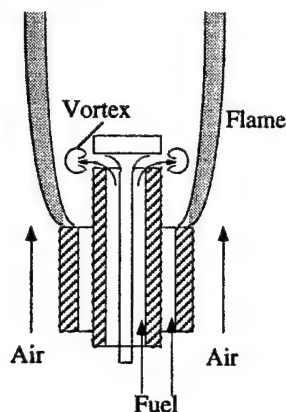


Figure 1. Direct vortex-injection in a jet flame

To prove the concept, a simplified modulation scheme was employed, with a solenoid valve being used to control the injected fuel. A function generator was used to drive a relay that controls the solenoid valve that opens and closes the fuel flow periodically. Reactive Mie scattering (RMS) technique was used to visualize the instantaneous vortical structure. Sub-micron particles of TiO_2 were formed from the reaction between TiCl_4 vapor seeded in the fuel and the water vapor produced in the

flame zone. A laser sheet expanded from a pulsed Nd:YAG laser operated at second-harmonic was used for illumination. The laser and vortex injection were synchronized using an electronic circuit with variable time delay. A gated intensified CCD camera synchronized with the laser was used to capture the sequential process during the vortex-flame interaction.

Mathematical Model

In the mathematical model,¹²⁻¹³ time-dependent Navier-Stokes equations are solved along with species- and energy-conservation equations in an uncoupled manner on a staggered-grid cylindrical coordinate system. The species equations are solved by coupling them through the production terms. A detailed chemical-kinetics model proposed by Peters for methane-air combustion¹⁴ is used in this formulation. It consists of 17 species involved in 52 elementary reactions. The C_2 chemistry is not considered in this study. Thermo-physical properties such as enthalpy, viscosity, thermal conductivity, and binary molecular diffusion coefficients of all 17 species are calculated. The solution scheme and treatment of boundary conditions as well as the validation of the code are discussed in Ref. 15.

Results and Discussion

In the former driven flame study, a specific vortex-flame interaction was produced when the fuel flow rate was maintained at a mean mass velocity of 1.5 m/s and an annulus air velocity of 0.4 m/s. The methane jet was modulated at a frequency of 30 Hz using a loud speaker. Phase-locked LDA measurement with a 5-ms sampling window showed that the jet velocity was accelerated from 1 m/s to around 8 m/s within a driving cycle. A symmetric vortex was generated periodically inside the flame, and the temporal images of vortex-flame interaction are shown in Figs. 2 (a), (b), and (c) for t_0+10 , t_0+14 , and t_0+16 ms, respectively. The fuel accelerated out of the tube interacts with the near-stagnant fluid ahead of it and, as a result, turns radially toward the flame and form a toroidal vortex [Fig. 2(a)]. The near-stagnant point can be observed ahead of the vortex. The local extinction occurred at the maximum radius, as evident from the disappearance of the flame. The vortex is then convected downstream and deformed as a result of velocity gradient. A part of the vortex on the low speed air side is convected more slowly and continues to interact with the flame [cf Figs. 2 (b) and (c)]. The extinction process was verified by OH imaging, as reported in Ref. 11.

The time-dependent CFDC code was used to simulate the vortex-flame interaction process as observed in the experiment. It was found that the inclusion of nozzle in the calculation domain was very important in anchoring the flame around the nozzle in the shear layer for this study. Hence, a straight tube of 1 cm height and 0.2 mm wall thickness was used with adiabatic wall boundary conditions being imposed along the tube walls. Flat initial-velocity profiles were specified based on the

measured values at the entrance plane of the fuel tube and the exit plane of the annulus air duct. A mesh size of 171×71 was used for a 250×150 mm computational domain.

The computational flame was driven periodically by perturbing the fuel mass-flow rate at the entrance of the fuel tube at a frequency of 30 Hz. The temporal velocity profile was obtained by modifying the experimentally measured velocities at the center of the nozzle exit in a non-reacting environment.

Evolution of the computed flame is shown in Figs. 3(a), (b), and (c) through instantaneous plots of temperature and particle locations at $t_0+44.7$, t_0+48 , and t_0+51 ms, respectively. Sets of massless particles were released continuously along the exit plane of the nozzle, and the instantaneous locations of all the particles are plotted in the left half of each figure. Radial locations of the peak temperatures are shown with large black solid circles. When the peak temperature of the flame fell below 1500 K (approximate quenching limit), the peak-temperature surface location was not shown at that height. Temperature fields between 300 and 2200 K are shown on the right half of each figure.

Particle-trace plots clearly identify the structure of the vortex associated with the mass ejection. When the fluctuating velocity was superimposed on the steady-fuel flow of 1.5 m/s, the resulting velocity at the tube entrance temporarily became very low, between t_0+30 and t_0+43 ms. This near-stagnant flow condition at the nozzle entrance caused the flame surface--and, thereby, the viscous fluid--to approach the centerline of the flame [cf Fig. 3(a)]. The additional fuel injected suddenly with a velocity of 14 m/s (modified velocity of 15.5 m/s) collided with the column of viscous combustion products and then traveled radially outward [cf Fig. 3(b)], forming a toroidal vortex. At this instant (t_0+48 ms), the flame surface at an axial height of $z = 20$ mm has been moved radially outward from 7 to 12 mm. The interaction of the vortex with the flame surface caused the flame temperature to decrease; however, no local quenching was noted. After $t_0+48.5$ ms, the flame between $z = 22.5$ and 26 mm became extinguished, and a hole in the flame surface formed. Since the velocity in the potential core is higher than that near the flame surface, by t_0+51 ms, the vortex has moved farther downstream compared to the movement of the hole--leaving the tail of the vortex in the hole region [Fig. 3(c)]. The flame and vortex shape at this time compares favorably with that of the experiment shown in Fig. 2(c). Re-ignition is then taking place in the hole region as the influence of the vortex on the flame surface diminishes, the flame slowly returns to its unperturbed position, and another driving cycle begins.

The instantaneous images shown in Fig. 3 clearly demonstrate that the calculations have captured the important aspects of the local quenching process observed during vortex-flame interactions in a jet diffusion flame. The flame structures at $z=22$ mm for times $t_0+44.7$ ms (weakly strained flame) and t_0+48 ms (near-extinction-

limit flame) are plotted in Figs. 4 and 5, respectively. A comparison of Figs. 4(a) and 5(a) suggests that the methyl-radical concentration in the flame zone increases as the flame is strained to near-quenching limits. This higher concentration seems to be destroying the radical pool that is crucial for the stability of the flame. This is also evident from the molar-production-rate plots [Figs. 4(b) and 5(b)]. The production rate of CH_3 has increased nearly an order of magnitude, and the destruction rate of the H radical has increased by an order of magnitude.

A preliminary test has been conducted for the vortex-flame interaction using the direct vortex injection scheme. To reduce the luminosity of the flame, the methane is diluted with N_2 at a 2:1 volume ratio. The mean fuel jet velocity is 1.7 m/s at the exit. The internal vortices are created by injecting methane at an axial location 20 mm downstream of the fuel jet at a frequency of 10 Hz. The phase-locked RMS images obtained during the vortex-flame interaction at different instants are shown in Fig. 6. Figure 6(a) shows a vortex, marked by the TiO_2 scattered particles, traveling radially toward the flame zone. The flame bulge is observed as the vortex interacts with the flame surface. After 0.5 ms [cf Fig. 6(b)], the vortex stretches the flame zone and locally creates a hole on the flame surface, as evident from the disappearance of the flame. The vortical structure is moving at a speed of 3 m/s as estimated from the sequential images. The duration time and the velocity of the injected fuel have not been characterized at this time.

A numerical simulation for the direct-injection vortex-flame interaction has also been conducted. At a jet velocity of 1.7 m/s, a typical laminar flame is established around the fuel tube, as shown in Fig. 7 (a), with instantaneous velocity and temperature fields. The flow recirculation in the wake region downstream of the cap is evident from the velocity plot. The injection tube is also included in the calculation domain along with the adiabatic wall condition. The fuel is injected at time t_0 with an initial radial velocity of 5 m/s through a 3-mm gap, as shown in the figures. The axial location of the injection is 20 mm downstream measured from the tip of the fuel tube. At t_0+10 ms, a vortex has grown and interacts with the flame zone, as shown in Fig. 7 (b). The flame zone has been distorted similar to that observed in the experiment (Fig. 6). At the maximum flame radius, the flame is strained with a local reduction in temperature, as shown in Fig. 7 (b). The interaction between the injected fluid and the wake behind the cap has been observed in both experiment and simulation. The wake region appears to have a strong influence on the vortex-flame interaction. The basic feature of the interaction process is captured using numerical simulation.

Conclusions

Vortex-flame interactions are important elements of a turbulent flame and are building blocks for the development of turbulent-flame models. An experimental

study was initiated recently at Wright Laboratory to establish a data base of vortex-flame interactions for the validation of time-dependent CFDC codes.

A time-dependent CFDC code that incorporates 17 species involved in 52 reactions was developed for simulation of the local and temporal quenching processes observed during vortex-flame interactions in methane jet flames. Inclusion of the fuel tube in the computational domain was found to be necessary to avoid lift-off of the flame during the driving sequence of the fuel jet. The large torroidal vortex formed from the fuel puff pushed the flame radially outward and created a hole on the flame surface. As the vortex convected downstream, re-ignition took place in the hole region and the flame returned to its unperturbed position. It is observed that the large increase in CH_3 radicals in the strained flame zone depleted the radical pool and, hence, quenched the flame locally. Detailed studies on the quenching associated with stretch factors and species fluxes into the flame zone should be performed using both numerical and experimental approaches.

The vortex-flame interaction was studied using direct injection scheme. The preliminary results demonstrate the potential for further investigation of vortex-flame interactions of vortices with various size and speed. The wake region appears to have strong impact on the vortex-flame interaction. To eliminate possible complication of the process, a new injection cap with a longer body and conical tip will be used to remove the wake flow. In order to perform a detail study and establish a data base of vortex-flame interactions, precise control of the injection speed and volume will be implemented.

Acknowledgments

This work was supported, in part, by Air Force Contract F33615-95-C-2507 and the Air Force Office of Scientific Research. The authors would like to thank Messrs. H. Day, D. Trump, and B. Sarka for their assistance in experiment and Mrs. Marian Whitaker for the editorial help.

References

1. Bilger, R. W., Twenty-second International Symposium on Combustion, pp. 475-488, (1989).
2. Correa, S. M., Major Research Topics in Combustion, Hussaini, M. Y., Kumar, A., and Voight, R. G., Eds., Springer-Verlag (1992).
3. Hottel, H. C. and W. R. Hawthorne, Third Symposium International on Combustion, Flame and Explosive Phenomena, pp. 254-266 (1949).
4. Schuelefield D. A., and J. E. Garside, Third Symposium International on Combustion, Flame and Explosive Phenomena, pp. 102-110 (1949).
5. Wohl, K., Kapp, N. M., and C. Gazley, Third Symposium International on Combustion, Flame and Explosive Phenomena, PP 3-21 (1949).
6. Roquemore, W. M., L.-D. Chen, L. P. Goss and W. F. Lynn, Lecture Notes in Engineering. Vol. 40, pp. 49-63 (1988).
7. Takahashi, F., Schmoll, W. J., Twenty-third Symposium International on Combustion (1991).
8. Chen, T. H. and Goss, L. P., Combust. Sci. and Tech., Vol. 79, pp. 311-324 (1991).
9. Takahashi, F. and Goss L., Twenty-fourth Symposium International on Combustion (1992).
10. Takahashi, F. and Katta, V.R., AIAA paper No 93-046 (1993).
11. Hsu, K. Y., Chen, L.-D., Katta, V. R., Goss, L. P., and Roquemore, W. M., AIAA Paper 93-0455 (1993).
12. Katta, V. R., Goss, L. P., and Roquemore, W. M., AIAA J. 32:84 (1994).
13. Katta, V. R., Goss, L. P., and Roquemore, W. M., Combustion and Flame 96:60 (1994).
14. Peters, N., in Reduced Kinetic Mechanisms for Applications in Combustion Systems, Lecture notes in Physics (N. Peters and B. Rogg, Eds.), Springer-Verlag, Berlin (1993).
15. Katta, V.R., Hsu, K.Y. and Roquemore, W.M., submitted to Twenty-sixth International Symposium on Combustion (1996).

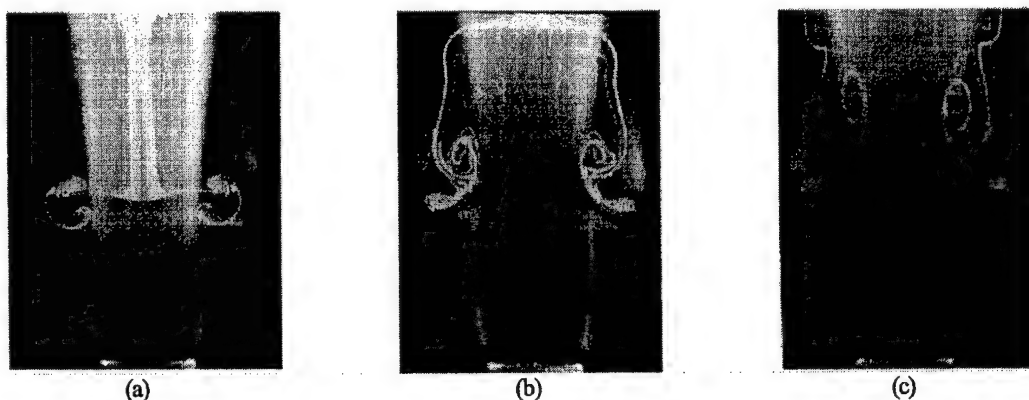


Figure 2. Flame images at (a) t_0+10 , (b) t_0+14 , and (c) t_0+16 ms during vortex-flame interaction.

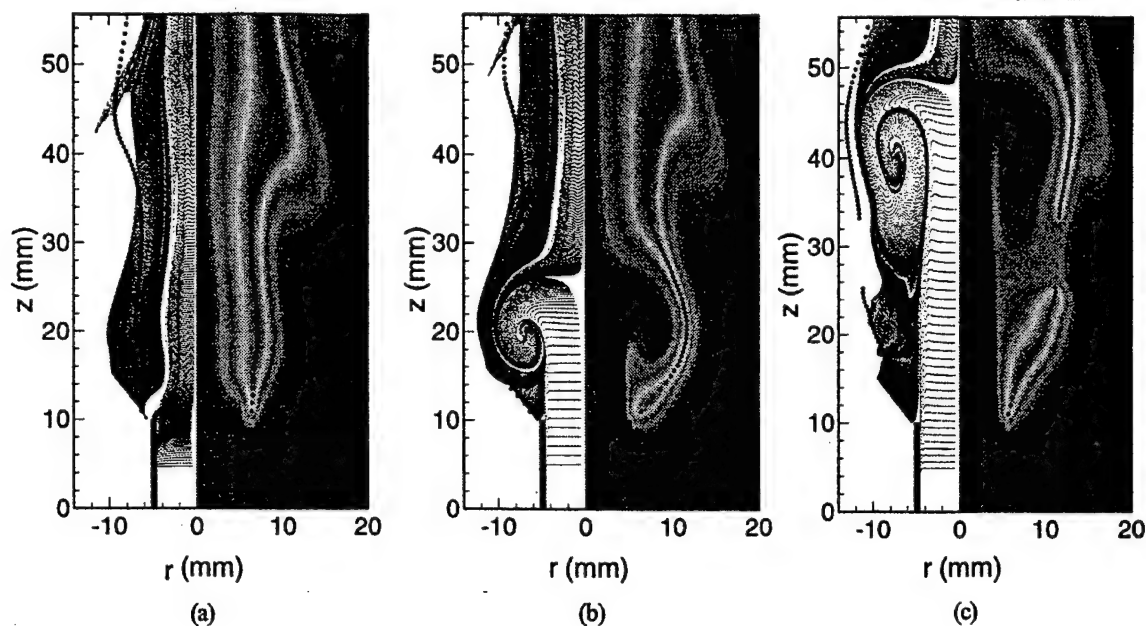


Figure 3. Computed vortex-flame interaction and local quenching in a methane jet diffusion flame.

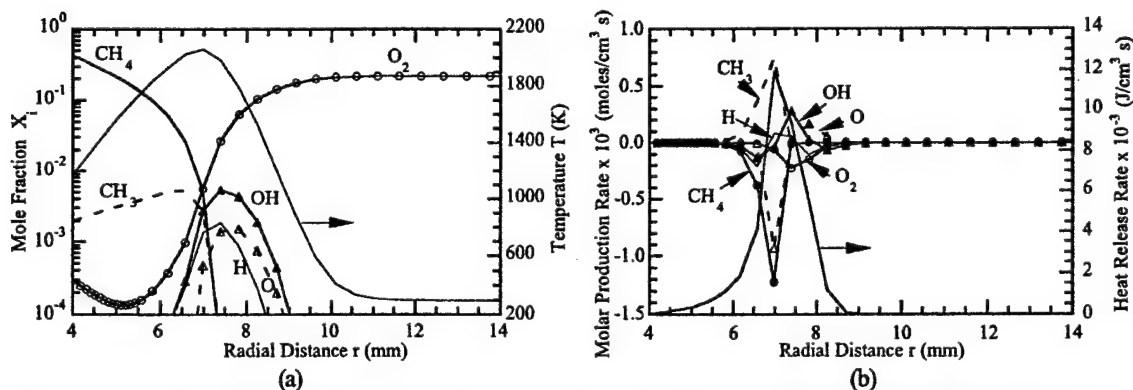


Figure 4. A weakly strained flame structure ($t_0+44.7$ ms) at a height of 22 mm. Radial profiles of (a) temperature and molar concentrations and (b) molar production rates and total heat-release rates.

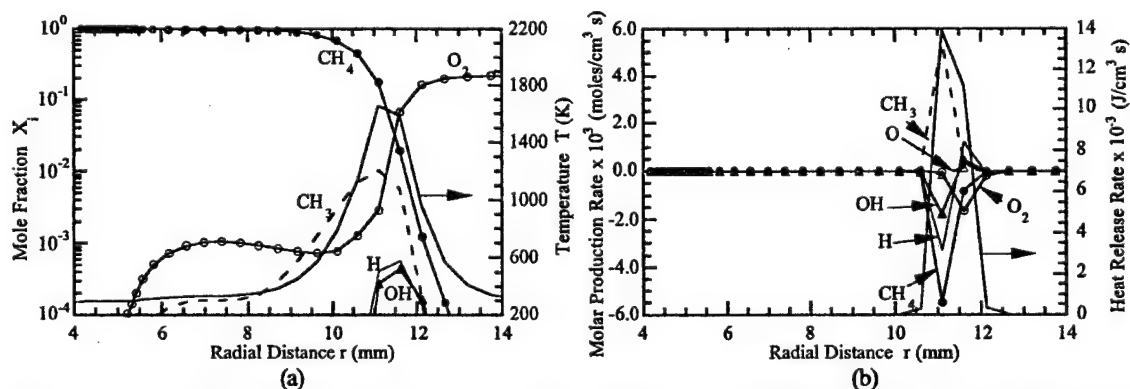


Figure 5. A near-quenched flame structure (t_0+48 ms) at a height of 22 mm. Radial profiles of (a) temperature and molar concentrations and (b) molar production rates and total heat-release rates.

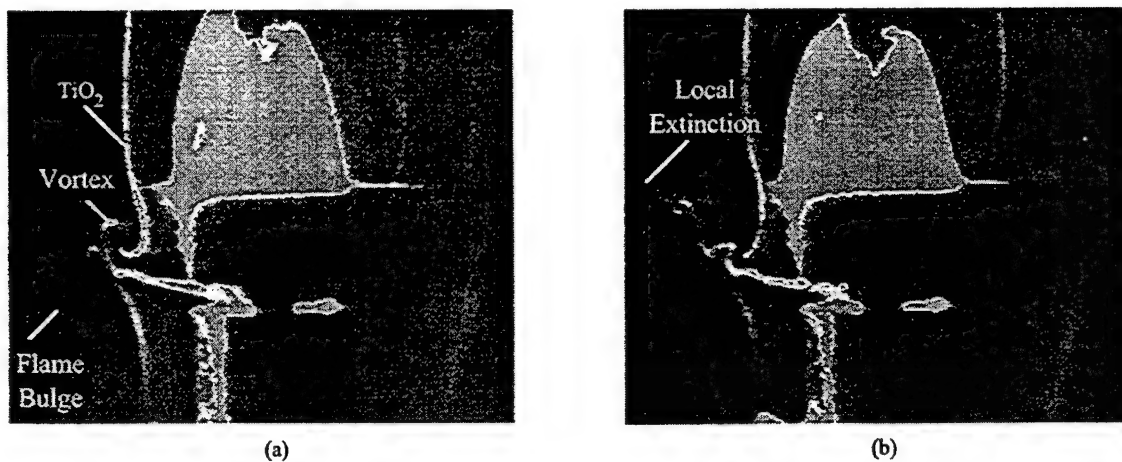


Figure 6. Images of vortex-flame interaction using the direct injection in a methane jet diffusion flame.

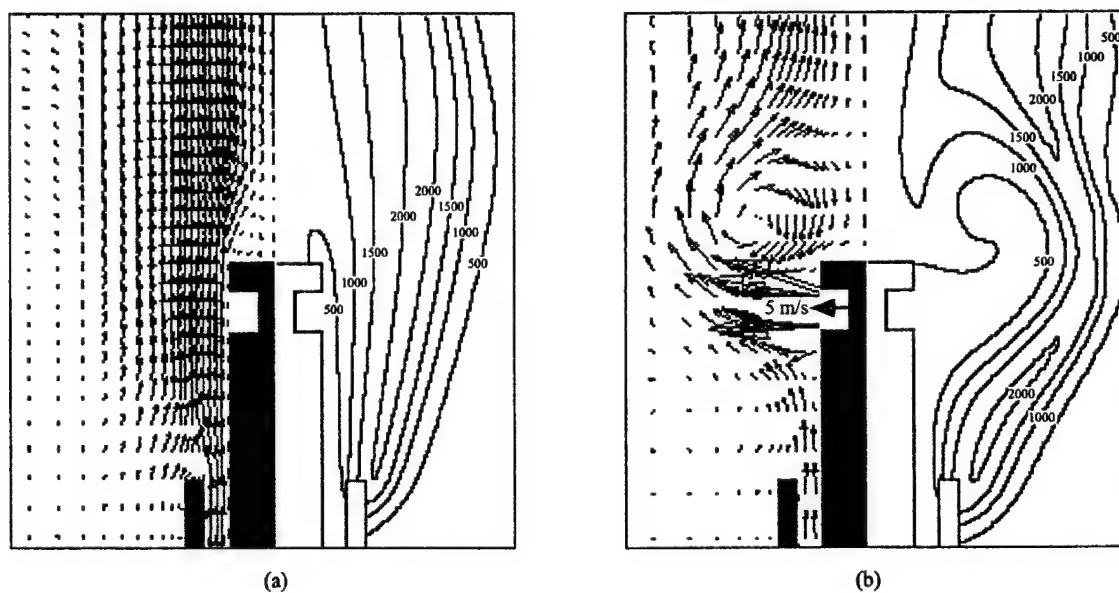


Figure 7. Velocity and temperature fields of the computed methane jet diffusion flame at (a) no injection and (b) 5 m/s injection at t_0+10 ms.

Simulation of Local Quenching in a Methane-Air Jet Diffusion Flame

V. R. Katta, K. Y. Hsu
Innovative Scientific Solutions, Inc.
3845 Woodhurst Court
Dayton, OH 45430

and

W. M. Roquemore
Wright Laboratory
Aero Propulsion and Power Directorate
Wright-Patterson Air Force Base, OH 45433

INTRODUCTION

Dynamic jet diffusion flames are often studied to gain the knowledge needed to develop models for turbulent-chemistry interactions. Improved visualization techniques have provided insight into the complex structure of a turbulent flame and the events occurring as the flame becomes turbulent [1]. The wrinkles or bumps in the flame are observed to be localized protrusions of the flame surface that result when three-dimensional fluid elements (often associated with vortices) of different size, shape, velocity, and rotational strength interact with reaction zones of different thickness. This interaction processes is commonly referred to as the vortex-flame interaction.

An understanding of vortex-flame interactions is important for several reasons. First, these interactions can increase or decrease the turbulent reaction rate. When vortex-flame interactions are moderate, they increase the surface area of the flame which leads to an overall increase in the global reaction rate and a reduction in the length of the flame. However, if a vortex has a sufficiently high radial velocity, it can pass through the flame, creating a localized hole in which no chemical reactions take place [2,3]. When these holes form near the jet exit, they can cause the flame to split or lift. If the holes cover a significant portion of the flame surface, the global reaction rate can decrease, which can lead to reduction in combustion efficiency and blow-out. Secondly, vortex-flame interactions are considered as building blocks for statistical theories of turbulent flames. It is conceivable that an ensemble of only a relatively few basic types of vortex-flame interactions need to be considered for accurate representation of the statistical result of what, on first sight, might appear to be an endless number of interactions. If this idea is supported by experimental results, it may be feasible to construct a statistical turbulent-combustion model.

This paper describes a numerical and experimental study on a particular type of vortex-flame interaction that was obtained in a methane jet diffusion flame [4]. A CFDC code that was validated by directly simulating axisymmetric counterflow diffusion flames up to the quenching limits is used for the investigation of local quenching process during vortex-flame interactions. The structures of weakly strained, near-quenching-limit, and just-quenched flames were investigated for the coflow configuration.

MATHEMATICAL MODEL

In the mathematical model [5,6], time-dependent Navier-Stokes equations are solved along with species- and energy-conservation equations in an uncoupled manner on a staggered-grid cylindrical coordinate system. However, the species equations are solved by coupling them through the production terms. The body-force term due to the gravitational field is included in the axial-momentum equation. A clustered mesh system is employed to trace the large gradients in flow variables near the flame surface. A detailed chemical-kinetics model proposed by Peters for methane-air combustion [7] is used in this formulation. It consists of 17 species (CH_4 , O_2 , CH_3 , CH_2 , CH , CH_2O , CHO , CO_2 , CO , H_2 , H , O , OH , H_2O , HO_2 , H_2O_2 , and N_2) that are involved in 52 elementary reactions. The C_2 chemistry is not considered in this study. Reaction rates for these elementary reactions have been obtained from Reference 7. The thermo-physical properties such as enthalpy, viscosity, thermal conductivity and binary molecular diffusion coefficients of all 17 species are calculated from the polynomial curve fits developed for the temperature range 300 - 5000 K. Mixture viscosity and thermal conductivity are then estimated using the Wilke and Kee expressions, respectively. Molecular diffusion is assumed to be of the binary-diffusion type, and the diffusion velocity of a species is calculated according to Fick's law and using the effective-diffusion coefficient of that species.

The finite-difference forms of the momentum equations are obtained using an implicit QUICKEST scheme [5,8], and those of the species and energy equations are obtained using a hybrid scheme of upwind and central differencing. At every time-step, the pressure field is accurately calculated by solving all the pressure Poisson equations simultaneously and utilizing the LU (Lower and Upper diagonal) matrix-decomposition technique. Treatment of the boundary conditions is identical to that reported in earlier papers [5,9].

The CFDC code used in the present study was validated [10] by predicting the flame structures for the counterflow diffusion flames investigated by Sung et al [11] and Smooke et al. [12] and the coaxial jet diffusion flames studied by Mitchell et al [13]. And also, the CFDC codes developed using the same methodology for $\text{H}_2\text{-O}_2\text{-N}_2$ combustion yielded excellent predictions for the vortex-flame interactions in hydrogen jet diffusion flames [6,14].

RESULTS AND DISCUSSION

Experiment on a Driven Jet Diffusion Flame

The experimental setup used to generate vortices inside a laminar jet diffusion flame is described in detail in Ref. 4. This simple, axisymmetric unconfined burner consists of a central fuel nozzle and a coannular air duct with exit diameters of 10 and 152 mm, respectively. The fuel nozzle is connected to the speaker chamber by means of a long tapered tube. Fuel is pumped through the side ports of the speaker chamber. An audio speaker is mounted in this chamber in such a way that the hollow cone of the diaphragm is toward the nozzle exit. While a steady flow of fuel is maintained throughout the experiment, puffs of fuel are periodically ejected from the nozzle by driving the speaker with a pulse generator. The flame is shielded from room-air disturbances using a low-speed air flow in the coannular duct. This system permits precise control of the frequency, strength, and shape of the vortex that emerges from the fuel nozzle.

Several visualization and measurement techniques are used to capture the vortex-flame interaction process. An instantaneous (phase) image obtained with the Reactive-Mie-Scattering (RMS) technique [1] is shown in Fig. 1(a). With this method micron-sized TiO_2 particles, formed from the spontaneous reaction between the seeded- TiCl_4 vapor and the water vapor produced during combustion, are visualized using the Mie-scattered light from a laser sheet. TiCl_4 is seeded into the fuel flow, and the laser firing is synchronized with the speaker driving signal. Images at different phases are obtained by changing the delay between the laser firing and the speaker driving signals. The luminous flame surface is also captured in Fig. 1(a); however, it represents the flame integrated over the period during which the camera shutter is open. Figure 1(a) illustrates that the vortices generated are quite symmetric. The vortices are introduced into the flame at a rate of 30/sec which corresponds to the driving frequency set for the speaker pulse generator. The thin lines surrounding the vortices result from the green light scattered by the TiO_2 particles. The motion of the vortices has pushed the flame surface radially outward to the point where it is locally and temporally quenched.

Numerical Simulations on a Driven Jet Diffusion Flame

Typically, a methane jet diffusion flame anchors on the outer side of the fuel nozzle or tube. Simulation of this feature is very important for the driven jet flames since flames simulated without the nozzle lip anchor in the shear layer and tend to lift off easily with the driving pulses. Hence, a straight tube of 1-cm height and 0.2-mm wall thickness is included in the calculation domain. Adiabatic wall boundary conditions are imposed along the tube walls.

The jet flame described in the previous section is numerically simulated using the time-dependent CFDC code. Flat initial-velocity profiles with measured mass-averaged values of 1.5 and 0.4 m/s were used at the entrance plane of the fuel tube and the exit plane of the annulus air duct, respectively. Using a mesh size of 171×71 , calculations were first made for the unsteady flow in a 250×150 mm computational domain. The buoyancy-influenced instability resulted in a weak, low-frequency flame oscillation (~ 20 Hz), but no vortex roll up [4] developed outside the flame surface. This is a result of the relatively high air-flow rate (0.4 m/s) used in the annulus duct.

The computational flame was then driven periodically by perturbing the fuel mass-flow rate at the entrance of the fuel tube at a frequency of 30 Hz. The resulting velocity contains a weak-suction pulse for about 13 ms, followed by a sharp mass ejection for a period of 14 ms. This velocity profile was obtained by modifying the experimentally measured velocities at the center of the nozzle exit under a non-reacting environment to achieve a vortex structure similar to that observed in the flame experiment.

Vortex-Flame Interaction and Local Quenching

Evolution of the computed flame is shown in Figs. 1(b), 1(c) and 1(d) through instantaneous plots of temperature and particle locations at $t_0+44.7$, t_0+48 and $t_0+48.5$ ms, respectively. Calculations were performed for several perturbation cycles prior to the solutions shown in these figures. Sets of massless particles were released continuously along two lines—one inside the fuel tube and the other outside the flame surface—and the instantaneous locations of all the particles are plotted on the left half of each figure. Locations of the flame surface obtained by radially scanning for the peak temperature are shown with large black solid circles. When the temperature of the flame fell below 1500 K (approximate quenching limit), the peak-temperature surface location was not shown at that height. Iso temperature contours representing values that are evenly spaced between 400 and 2200 K are shown on the right half of each figure.

Particle-trace plots clearly identify the structure of the vortex associated with the mass ejection. When the fluctuating velocity was superimposed on the steady-fuel flow of 1.5 m/s, the resulting velocity at the tube entrance temporarily became very low, between t_0+30 and t_0+43 ms. This near-stagnant flow condition at the nozzle entrance caused the flame surface—and, thereby, the viscous fluid—to approach the centerline of the flame [cf Fig. 1(b)]. The additional fuel ejected suddenly with a velocity of 14 m/s (modified velocity of 15.5 m/s) collided with the column of viscous combustion products and then traveled radially outward [cf Fig. 1(c)], forming a toroidal vortex. At this instant (t_0+48 ms), the flame surface at an axial height of $z = 20$ mm has been moved radially outward from 7 to 12 mm. The interaction of the vortex with the flame surface caused the flame temperature to decrease; however, no local quenching was noted. At $t_0+48.5$ ms, the vortex convected downstream by about 2 mm, the flame between $z = 22.5$ and 26 mm became extinguished [Fig. 1(d)], and a hole in the flame surface formed. Since the velocity in the potential core is higher than that near the flame surface, by t_0+51 ms the vortex has moved farther downstream compared to the movement of the hole—leaving the tail of the vortex in the hole region (not shown here). The flame and vortex shape at this time compares favorably with that of the experiment shown in Fig. 1(a). At

later times re-ignition takes place in the hole region as the influence of the vortex on the flame surface diminishes, the flame slowly returns to its unperturbed position, and another driving cycle follows.

The instantaneous images shown in Fig. 1 clearly demonstrate that the present calculations have captured the important aspects of the local quenching process observed during vortex-flame interactions in a jet diffusion flame. In order to investigate the structural changes that a diffusion flame might undergo when it was stretched to extinction limits, flame structures at $z = 22$ mm for times $t_0 + 44.7$ ms (weakly strained flame) and $t_0 + 48$ ms (near-extinction-limit flame) and at $z = 24$ mm for time $t_0 + 48.5$ ms (just-quenched flame) are plotted in Fig. 2.

A comparison of Figs. 2(a) and 2(c) suggests that concentration of methyl radical in the flame zone increases as the flame is strained to near-quenching limits; while the concentrations of other radicals such as H, O and OH decrease. The former is, in part, resulting from the vortex-induced convective flow. The higher concentration of methyl radicals seems to be destroying the radical pool that is crucial for the stability of the flame. This is also evident from the molar-production-rate plots [Figs. 2(b) and 2(d)]. The production rate of CH_3 has increased nearly an order of magnitude, and the destruction rate of the H radical increased by an order of magnitude. This is in contrast to the behavior observed in counterflow flames in which only a slight increase in production and destruction rates of the CH_3 and H radicals was found when the flame was strained to the extinction limits. While the higher fuel and oxidizer fluxes (concentration gradients) into the diffusion flame due to flame stretching led to lower flame temperatures, they also caused the heat-release rate to increase. Local quenching of the flame at $z = 24$ mm [Fig. 2(f)] may be characterized with the rapid drop in heat release rate and disappearance of H, O, and OH radicals. Interestingly, the gas temperature at this location is still about 1400 K and not much change in methyl-radical distribution was noted with flame quenching.

CONCLUSION

Vortex-flame interactions are important elements of a turbulent flame and are building blocks for the development of turbulent-flame models. An experimental study was initiated recently at Wright Laboratory to establish a data base of vortex-flame interactions for the validation of time-dependent CFDC codes. Axisymmetric vortices were periodically generated inside a coflowing methane jet diffusion flame by driving the fuel jet using a speaker, and phase-locked images of interactions with the flame surface are recorded.

A time-dependent CFDC code that incorporates 17 species involved in 52 reactions was developed for simulation of the local and temporal quenching process observed during vortex-flame interactions in methane jet flames. The model was validated by directly simulating axisymmetric counterflow diffusion flames and by comparing the experimental results for flame structure and extinction limits. Calculations were made for the vortex-flame interactions in a coflowing jet diffusion flame. Inclusion of the fuel tube in the computational domain is found to be necessary to avoid lift-off of the flame during the driving sequence of the fuel jet. The large toroidal vortex formed from the fuel puff pushed the flame radially outward and created a hole on the flame surface. As the vortex convected downstream, re-ignition took place in the hole region and the flame returned to its unperturbed position. It is observed that the large increase in CH_3 radicals in the strained flame zone depleted the radical pool and hence, quenched the flame locally. Detailed studies on the quenching process through calculating the stretch factors and species fluxes into the flame zone should be performed in follow-up investigations.

ACKNOWLEDGMENT

This work was supported, in part, by Air Force Contract F33615-90-C-2033 and the Air Force Office of Scientific Research. The authors would like to thank Dr. Takahashi for stimulating discussions on quenching mechanisms and Mrs. Whitaker for editorial help.

REFERENCES

1. Roquemore, W. M., Chen, L.-D., Goss, L. P., and Lynn, W. F. in *Turbulent Reactive Flows*, Lecture Notes in Engineering (R. Borghi and S. N. B. Murthy, Eds.), Springer-Verlag, Berlin, 1989, Vol. 40, p. 49.
2. Takahashi, F., and Goss, L. P., in *Twenty-Fourth Symposium (International) on Combustion*, The Combustion Institute, Pittsburgh, 1992, p. 351.
3. Chen, T. H., and Goss, L. P., *Combustion Science and Technology*, 79:311 (1991).
4. Hsu, K. Y., Chen, L.-D., Katta, V. R., Goss, L. P., and Roquemore, W. M., AIAA Paper 93-0455, Reno, Jan., 1993.
5. Katta, V. R., Goss, L. P., and Roquemore, W. M., AIAA J. 32:84 (1994).
6. Katta, V. R., Goss, L. P., and Roquemore, W. M., *Combustion and Flame* 96:60 (1994).
7. Peters, N., in *Reduced Kinetic Mechanisms for Applications in Combustion Systems*, Lecture notes in Physics (N. Peters and B. Rogg, Eds.), Springer-Verlag, Berlin, 1993, Vol. m15, p. 3-14.
8. Leonard, B. P., *Computer Methods in Applied Mechanics and Engineering*, 19:59 (1979).
9. Katta, V. R., Goss, L. P., and Roquemore, W. M., *Int. J. Num. Meth. Heat Fluid Flow*, 4:413 (1994).
10. Katta, V. R., and Roquemore, W. M., in *Proceedings of the Spring Technical Meeting of the Central States Section of the Combustion Institute*, St. Louis, May 5-7, 1996, pp. 449-454.
11. Sung, C. J., Liu, J. B., and Law, C. K., *Combustion and Flame*, 102:481 (1995).
12. Smooke, M. D., in *Numerical Approaches to Combustion Modeling*, (S. Oran and J. Boris, Eds.), Progress in Astronautics and Aeronautics, Vol. 135, 1991, p. 183.
13. Mitchell, R. E., Sarofim, A. F., and Clomberg, L. A., *Combustion and Flame* 37:227 (1980).
14. Katta, V. R., and Roquemore, W. M., *Combustion and Flame*, 100:61 (1995).

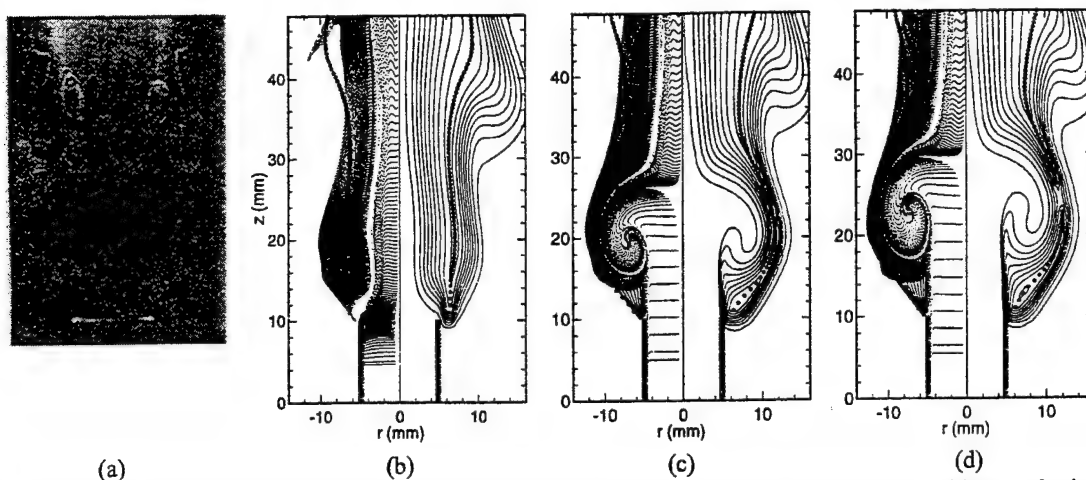


Fig. 1. Vortex-flame interaction and local quenching in methane jet diffusion flame. (a) Experimental image obtained using Reactive-Mie-Scattering technique. Computed flames obtained at instants (b) $t_0 + 44.7$, (c) $t_0 + 48$ and (d) $t_0 + 48.5$ ms

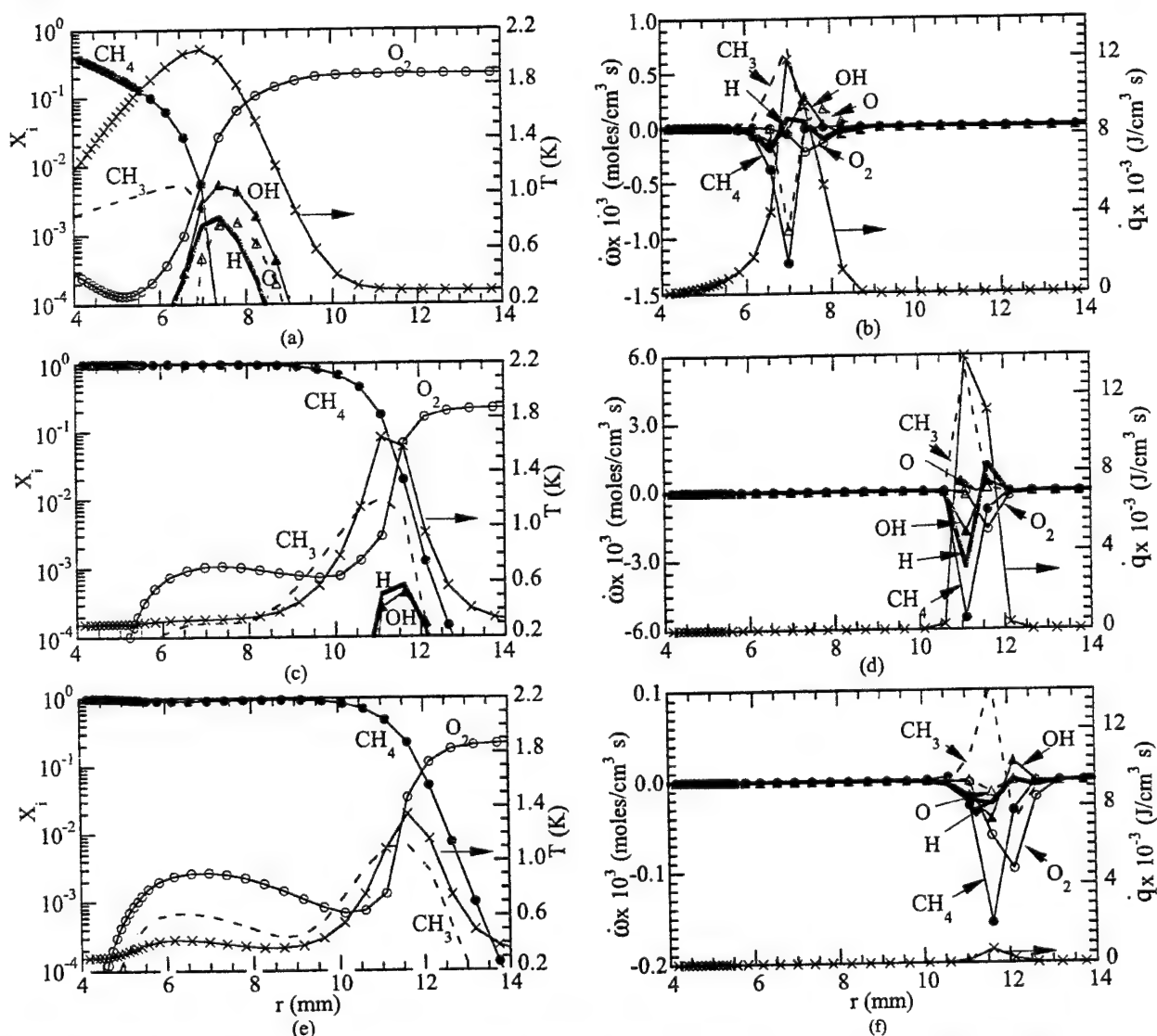


Fig. 2. Flame structure obtained at instants (a),(b) when flame is weakly strained at $t_0 + 44.7$ ms, (c),(d) when flame is strained to extinction limit at $t_0 + 48$ ms, and (e),(f) when flame is just quenched at $t_0 + 48.5$ ms.



AIAA 98-0155

NO_x in Methane-Air Jet Diffusion Flames

V. R. Katta
Innovative Scientific Solutions, Inc
Dayton, OH

W. M. Roquemore
Air Force Research Laboratory
Wright-Patterson AFB, OH

**36th Aerospace Sciences
Meeting & Exhibit**
January 12–15, 1998 / Reno, NV

For permission to copy or republish, contact the American Institute of Aeronautics and Astronautics
1801 Alexander Bell Drive, Suite 500, Reston, Virginia 20191-4344

NOx in Methane-Air Jet Diffusion Flames

Viswanath R. Katta*
Innovative Scientific Solutions, Inc.
2786 Indian Ripple Road
Dayton, OH 45440-3638

and

W. M. Roquemore*
Propulsion Directorate
Air Force Research Laboratory
Wright-Patterson Air Force Base, OH 45433-7103

Abstract

Dynamic simulations for NOx formation in an unsteady laminar, methane jet flame are made using an axisymmetric, time-dependent CFDC code and a detailed-chemical-kinetics model. Due to the buoyancy-induced instability vortical structures developed outside the flame surface and caused the flame to wrinkle. These simulations indicate that the temperature of the flame increases locally when it is compressed by the outer vortex and decreases when it is stretched. These effects are similar to those observed in a hydrogen diffusion flame and are attributed to the local non-unity Lewis numbers. Previous studies on dynamic hydrogen flames further revealed that the concentration of NO increases significantly in the compressed flame regions where temperature increases. For understanding the flame stretching and compression effects on the production of NO in methane diffusion flames calculations are made using different NOx chemistry models. It is observed that the thermal NO increases in the compressed flame regions; however, the flame stretch effect seems to be weak on the total NO (thermal + prompt) production.

Introduction

Studies of jet diffusion flames are important in understanding combustion phenomena in practical systems and for developing theories of combusting processes. Because of this, jet flames have been actively investigated since the classic works of Hotel et al¹ published in the Third Symposium on Combustion and Flame Explosion Phenomena in 1949. Considerable data on statistical quantities such as time averaged and rms values of velocity, temperature, and species concentrations have been obtained with single point measurement techniques. These data have formed the bases for understanding many of the processes

occurring in jet diffusion flames. Because of the success of the statistical approach there is a tendency to think about combustion processes in terms of time-averaged parameters. For engineering applications, there is a definite value, and in several situations, there is a necessity of thinking in terms of mean values of parameters. However, there is a danger to this line of thinking in that the mean and fluctuating quantities can, in many cases, mask the physics and chemistry that are germane to understanding the fundamental processes that give rise to the statistical results. This is particularly true for laminar and near-transitional jet flames in which the impact of large-scale, organized, buoyancy-induced vortices on the air side of the flame and the Kelvin-Helmholtz type vortex structures on the fuel side of the flame dominate the flame characteristics. To gain an insight into these processes, it is helpful and perhaps essential to think in terms of the dynamic characteristics of jet flames.

Several numerical investigations made in the past for dynamic jet flames using conserved-scalar approach, global-chemistry and detailed chemistry models have revealed important aspects of combustion such as effect of heat-release rate,² role of buoyancy,^{3,4} enhancement of soot formation⁵ and Lewis-number effects.⁶ However, most of these studies involving finite-rate chemistry are limited to hydrogen fuel as the kinetic models for this fuel are relatively simple. On the other hand, because of the complex nature of the reaction mechanisms, flame calculations for hydrocarbon fuels are restricted to either steady-state problems or chemically lazy flames in which chemistry is not important. Simulation of dynamic hydrocarbon flames with sufficiently accurate models for physical and chemical processes is required for understanding the processes that are leading to the formation Nitric Oxides. Recently, the authors have developed a time-accurate CFDC (computational Fluid Dynamics with Chemistry) code⁷ known as UNICORN (UNsteady Ignition and COMbustion with ReactionNs) for investigating methane diffusion flames by incorporating detailed-chemical-kinetics

*Senior Engineer, AIAA Member

+Senior Scientist, AIAA Member

This paper declared a work of the U. S. Government and is not subjected to copyright protection in the United States.

model. This paper describes a numerical study conducted using UNICORN on the formation of NO_x in a co-axial methane jet diffusion flame. Results are discussed to emphasize the effects of flame dynamics on the production of thermal and prompt NO_x.

Modeling

In the mathematical model, time-dependent Navier-Stokes equations are solved along with the species- and energy-conservation equations in an uncoupled manner on a staggered-grid cylindrical coordinate system. However, the species equations are solved by coupling them through the production terms. The body-force term due to the gravitational field is included in the axial-momentum equation. A clustered mesh system is employed to trace the large gradients in flow variables near the flame surface. The detailed chemical-kinetics models GRI Versions 1.2 and 2.11⁸ compiled by the Gas Research Institute (GRI) are used in the present study. These are the most comprehensive mechanisms (Version 1.2 with out and Version 2.11 with NO_x chemistry) available for methane combustion. These two versions are having 31 and 48 species, respectively, and 346 and 550 elementary-reaction steps, respectively and are recommended by several investigators for computing methane flames. The enthalpies of all the species are calculated from the polynomial curve fits developed for the temperature range 300 - 5000 K. The physical properties such as viscosity, thermal conductivity and binary molecular diffusion coefficients of the species are calculated using molecular dynamics. Mixture viscosity and thermal conductivity are then estimated using the Wilke and Kee expressions, respectively. Molecular diffusion is assumed to be of binary type, and the diffusion velocity of a species is calculated according to Fick's law and using the effective-diffusion coefficient of that species. The Lennard-Jones potentials, effective temperatures and the coefficients for the enthalpy polynomials for each species are obtained from the CHEMKIN libraries.⁹

While the governing equations for momentum are integrated using an implicit QUICKEST (Quadratic Upstream Interpolation for Convective Kinematics with Estimated Streaming Terms) numerical scheme^{10,11} which is third-order accurate in both space and time and has a low numerical diffusion error, the species and energy equations are integrated using an hybrid scheme of upwind and central differencing. An orthogonal, staggered grid system with rapidly expanding cell sizes in both the *z* and *r* directions is utilized for discretizing the governing equations. The pressure field at every time step is accurately calculated by simultaneously solving the system of algebraic pressure

Poisson equations at all grid points using the LU (Lower-Upper) decomposition technique.

Unsteady axisymmetric calculations are made on a physical domain of 250 x 150 mm utilizing a 171 x 61 non-uniform grid system. Generally, the computational domain is bounded by the axis of symmetry and an outflow boundary in the radial direction and by the inflow and another outflow boundary in the axial direction. Flat velocity profiles were imposed at the fuel and air inflow boundaries. The outer boundaries in the *z* and *r* directions are located sufficiently far from the nozzle exit (~ 25 nozzle diameters) and the symmetry axis (~ 15 nozzle diameters), respectively, that the propagation of boundary-induced disturbances into the region of interest is minimized. An extrapolation procedure with weighted zero- and first-order terms is used to estimate the flow variables at the outflow boundary.

Results and Discussion

The experimental setup consist of vertically mounted coannular jets and is described in Ref. 12. The central fuel jet is a 25.4 mm diameter tube which contracts to a 10 mm diameter nozzle. The nozzle is designed to provide a flat mean velocity profile with low velocity fluctuations at the nozzle exit. The annulus air jet has a diameter of 245 mm. An air velocity of 15 cm/s is used to reduce the room air disturbances in the first 15 diameters of the jet exit while not causing a significant effect on the dynamic flame structure. The pure methane flame investigated in this paper has a fuel jet velocity of 0.5 m/s.

Calculations are made for this flame using GRI Version 1.2 chemistry mechanism. The computed instantaneous temperature and OH-concentration fields are shown in Fig. 1(a) on the right and left sides of the symmetry line, respectively. The temperature field is plotted using contour lines having an initial value of 500 K and a spacing of 300 K. Because of the gravity term in the axial-momentum equation and the low-speed annulus air flow, solution of the governing equations resulted in a dynamic flame, with large toroidal vortices forming naturally outside the flame surface. It is important to note that no artificial perturbation is required for the formation of the outer vortices. In the presence of gravitational force, acceleration of hot gases along the flame surface generated the outer structures as part of the solution. The frequency corresponding to the passage of these outer vortices (also known as flame flickering frequency) is close to 12 Hz.

The interaction of outer vortices with the flame surface caused the latter to wrinkle. It is also evident from Fig. 1(a) that the aerodynamic stretch along the flame surface is not constant. Flame is locally compressed at *z* = 30 and 100

mm and stretched at $z = 80$ and 150 mm. The closed contour No. 7 in Fig. 1(a) further suggests that the temperature is locally increased in the compressed region of the flame. Tendency of flame temperature to increase in the compressed regions during outside-vortex/flame interaction was recognized in the earlier studies on hydrogen flames. However, the increase in temperature in the case of methane flames is only 40 K compared to about 100 K rise seen in pure hydrogen flames. The rise in temperature in hydrogen flames further led to an increase in NO production in the compressed regions.

It is known that NO in a hydrogen flame is generated only from thermal mechanism, where as, in a methane flame it is primarily produced due to both the thermal and prompt mechanisms. To investigate the effect of flame stretching and compression on the production of NO in a methane diffusion flame, calculations are made incorporating different NOx chemistry mechanisms. Results obtained with GRI Version 2.11 mechanism, which is a combination of GRI Version 1.2 mechanism for methane combustion and a comprehensive mechanism for NOx are shown in Fig. 1(b). It may be noted that the vortex locations for the flame in Fig. 1(b) are slightly shifted downstream compared to those in Fig. 1(a). This is because of a small difference in the phases of the two flames. In general, the flames predicted by GRI Versions 1.2 and 2.11 are quite similar. These calculations suggest that the temperature and concentrations of radicals such as H, O and OH are not affected by the inclusion of NOx chemistry to GRI Version 1.2 combustion chemistry.

Calculations are also made by switching off the prompt mechanism for NOx in GRI Version 2.11 chemistry and the resulting flame structure in the form of temperature and OH-concentration fields is shown in Fig. 1(c). This flame structure is identical to that predicted with the complete NOx chemistry. A commonly used simple mechanism for thermal NO (Zel'dovich mechanism) is used in conjunction with GRI Version 1.2 chemistry in the final calculation and the resulted flame in terms of temperature and major species concentrations (not shown here) is found to be identical to those shown in Fig. 1.

Detailed flame structures obtained with the two versions of GRI methane-chemistry mechanisms (with and without NOx chemistry) are shown in Fig. 2. Here, instantaneous radial distributions of major radicals (CH_3 , H_2 , H, O, and OH) and some minor radicals (C_2H_6 , C_2H_3 , C_2H , CHO, and CH) are plotted at a height of 80 mm above the burner in Figs. 2(a) and 2(b), respectively. As mentioned previously, there exists a small phase difference in the two instantaneous solutions used for the analysis [cf Figs. 1(a) and 1(b)]. This phase difference caused a shift in the radial distributions of species obtained with GRI Version 2.11

chemistry toward the axis of symmetry. Figure 2 suggests that NOx chemistry in the GRI Version 2.11 mechanism is not affecting the basic structure of the low-speed jet diffusion flame obtained with GRI Version 1.2 mechanism.

The major contributors for NOx in methane flames are NO and NO_2 , and other forms of nitric oxides appear only in relatively low concentrations. The distributions of NO and NO_2 in the dynamic methane flame predicted by previously mentioned three types of NOx mechanisms (GRI Version 2.11 as it is and without prompt mechanism, and Zel'dovich thermal NO mechanism) are shown in Figs. 3(a), 3(b) and 3(c), respectively. Concentration of NO is plotted on the left side of the symmetry line and that of NO_2 is plotted on the right side. The flame (or peak-temperature) surface that is identified from the temperature field is also shown in this figure using open circles. As expected, the concentrations of NO and NO_2 are increasing with the flame height. Interestingly, by responding to the variations in temperature along the flame surface, the thermal NO in Figs. 3(b) and 3(c) is showing peaks in the compressed regions ($z = 40$ and 100 mm). However, inclusion of prompt NOx in Fig. 3(a) resulted in a monotonically increasing NO along the flame surface. Another interesting aspect of this flame is that almost all NO_2 is located well outside the high-temperature flame.

Radial distributions of NOx and other important species in NOx chemistry are shown in Figs. 4 and 5 at flame heights of 80 and 150 mm, respectively. These two locations represent similarly stretched flame zones but, located at different heights. Here, complete chemistry represents GRI Version 2.11, Thermal mechanism represents GRI Version 2.11 without prompt chemistry and finally, Thermal* represents the simple form of thermal NO (or Zel'dovich) chemistry. At $z = 80$ mm, the thermal NO in the flame zone is only 30 ppm compared to that of 80 ppm total (i.e., thermal + prompt). This difference is becoming less at downstream locations. For example, at $z = 150$ mm the thermal NO has increased to 60 ppm where as the total NO has increased only to 120 ppm. Over all, the thermal NOx predicted by the simple chemistry model follows closely with that of GRI Version 2.11 (without prompt mechanism).

Figure 6 shows the evaluations of temperature, OH, N and NOx species at a height of 80 mm above the burner. As the flame is flickering at a frequency of ~ 12 Hz temporal variations for a period of 83 ms are plotted. Results obtained with GRI Version 2.11 are shown on the left side while those obtained by neglecting prompt NOx are shown on the right side. The iso-contour levels used for plotting the distributions of the variables on the left and right sides are identical except in Figs. 6(c). As the concentration of N radical generated without the prompt

mechanism is significantly lower than that generated with the prompt mechanism, an order of lower level contours are used on the right side of Fig. 6(c). In general, the prompt-NO_x mechanism seems to be increasing the spreading of NO, NO₂, and N₂O in the high-temperature region. It is evident from Fig. 6(d) that the change in concentration of NO as the aerodynamic stretch on the flame is altered from compression to stretch is more for thermal NO compared to that of total NO.

Summary and Conclusions

Accurate dynamic simulations using detailed-chemical-kinetics models for hydrocarbon fuels are needed for understanding flame structure and various mechanisms involved in the production of pollutants in jet diffusion flames. An axisymmetric, time-dependent CFDC code is developed for the simulation of methane jet diffusion flames. The basic structure of a low-speed, buoyancy-dominated flame is obtained using GRI Version 1.2 chemistry mechanism. Due to the buoyancy-induced instability vortical structures developed outside the flame surface which caused the flame to wrinkle. These simulations indicate that the temperature of the flame increases locally when it is compressed by the outer vortex and decreases when it is stretched. These effects are similar to those observed in a hydrogen diffusion flame and are attributed to the local non-unity Lewis numbers. For understanding the flame stretching and compression effects on the production of NO_x in methane diffusion flames calculations are made using 1) GRI Version 2.11 mechanism (Version 1.2 + NO_x chemistry), 2) GRI Version 2.11 mechanism without prompt NO_x mechanism, and 3) GRI Version 1.2 plus Zel'dovich thermal NO_x mechanism. It is observed that the production of NO_x in this low-speed flame did not affect the basic flame structure. It is also found that the thermal NO increases in the compressed flame regions; however, the flame stretch effect seems to be weaker on the total NO (thermal + prompt) production.

Acknowledgment

This work was supported, in part, by Air Force Contract F33615-95-C-2507 and the Air Force Office of Scientific Research.

References

1. Hottel, H. C. and Hawthorne, W. R., "Diffusion in Laminar Flame Jets," *Third Symposium (International) on Combustion, Flame and Explosive Phenomena*, pp 254-266, 1949.
2. Ellzey, J. L., Laskey, K. J., and Oran, E. S., *Progress in Astronautics and Aeronautics*. American Institute of Aeronautics and Astronautics, Washington, D. C., 1989, Vol. 131, p. 179.
3. Davis, R. W., Moore, E. F., Roquemore, W. M., Chen, L.-D., Vilimpoc, V., and Goss, L. P. *Combust. Flame*, Vol. 83, 1991, p. 263.
4. Katta V. R., Goss, L. P., and Roquemore, W. M., *Combustion and Flame* 96:60-74 (1994).
5. Katta, V. R., Goss, L. P., and Roquemore W. M., *Combustion and Flame*, Vol. 96, No. 1-2, 1994, pp. 60-74.
6. Kaplan, C. R., Oran, E. S., Kailasnath, K., and Ross, H. D., Gravitational Effects on Sooting Diffusion Flames, Presented at the 26th International Symposium on Combustion, Napoli, Italy, July 28-August 2, 1996.
7. Katta, V. R., Goss, L. P., and Roquemore W. M., "Simulation of Dynamic Methane Jet Diffusion Flame Using Finite-Rate Chemistry Model," AIAA Paper 97-0904, Jan. 6-10, 1997, Reno, NV.
8. Frenklach, M., Wang, H., Bowman, C. T., Hanson, R. K., Smith, G. P., Golden, D. M., Gardiner, W. C., and Lissianski, V., "An Optimized Kinetics Model for Natural Gas Combustion," Work-In-Progress Poster Session 3, Number 26, 25th International Symposium on Combustion, Irvine, CA.
9. Kee, R. J., Rupley, F. M., and Miller, J. A., "The Chemkin Thermodynamic Data Base," Sandia National Laboratories Report, SAND87-8215, 1987.
10. Katta, V. R., Goss, L. P., and Roquemore, W. M.; Numerical Investigations of Transitional H₂/N₂ Jet Diffusion Flames, *AIAA Journal*, Vol. 32, No. 1, 1994, pp. 84-94.
11. Leonard, B. P., *Computational Methods in Applied Mechanics and Engineering*, Vol. 19, p. 59, 1979.
12. Roquemore, W. M., Chen, L.-D., Goss, L. P., and Lynn, W. F., "Structure of Jet Diffusion Flames," *Turbulent Reactive Flows*. Lecture Notes in Engineering. Vol. 40, pp. 49-63, 1988.

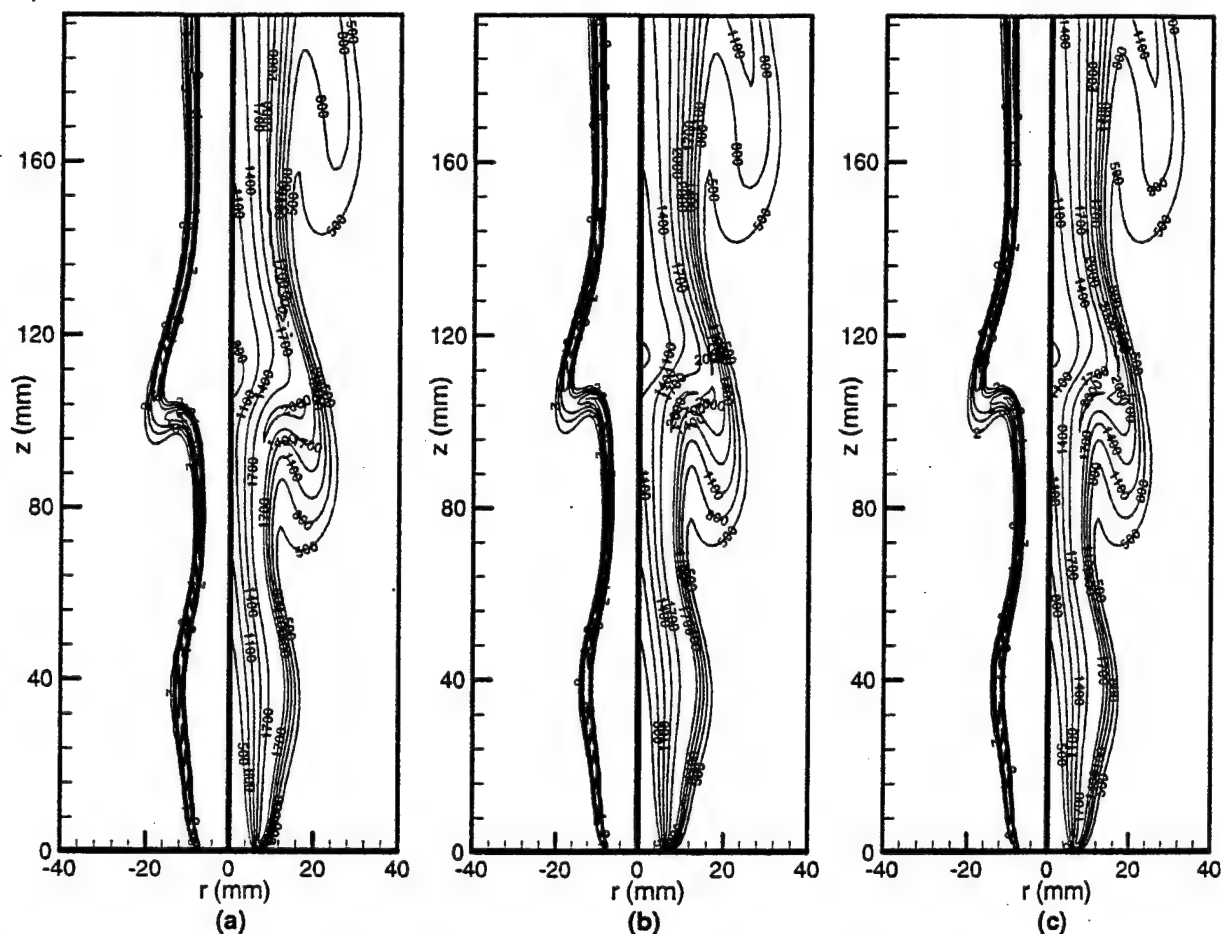


Fig. 1. Unsteady methane flame simulated using (a) GRI Version 1.2, (b) GRI Version 2.11, and (c) GRI Version 2.11 without prompt NOx. Temperature and OH-concentration fields are shown on left and right halves, respectively.

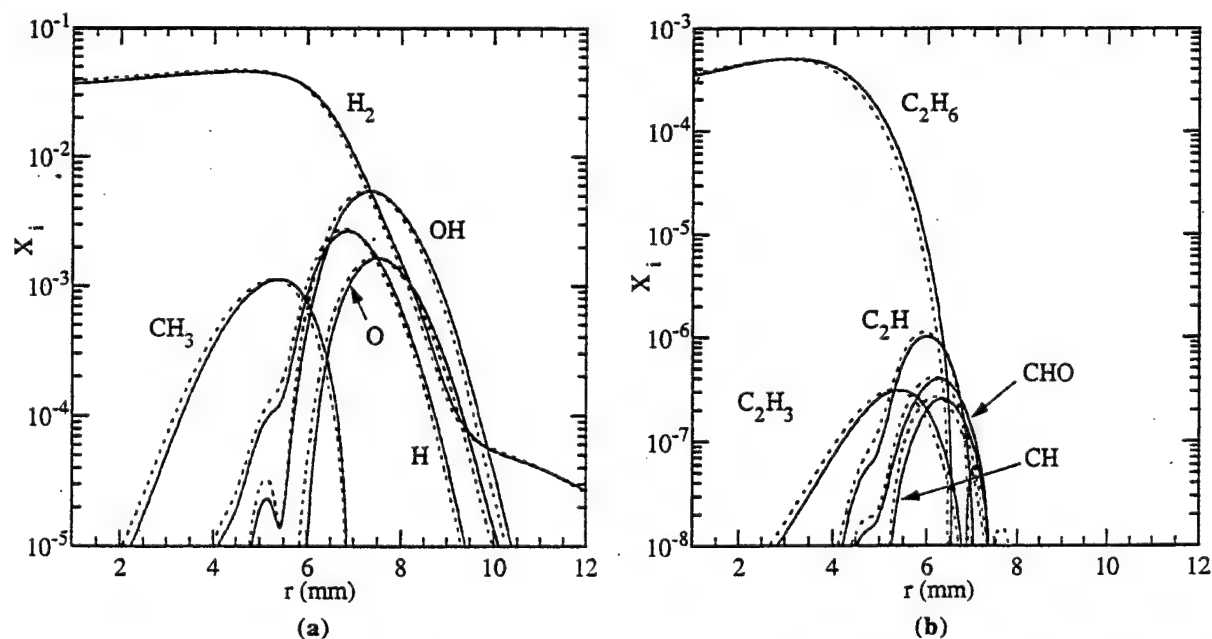


Fig. 2. Radial distributions of (a) major-radical and (b) minor-radical concentrations in the flame at a height of 80 mm obtained using GRI Version 1.2 (—) and GRI Version 2.11(- - -).

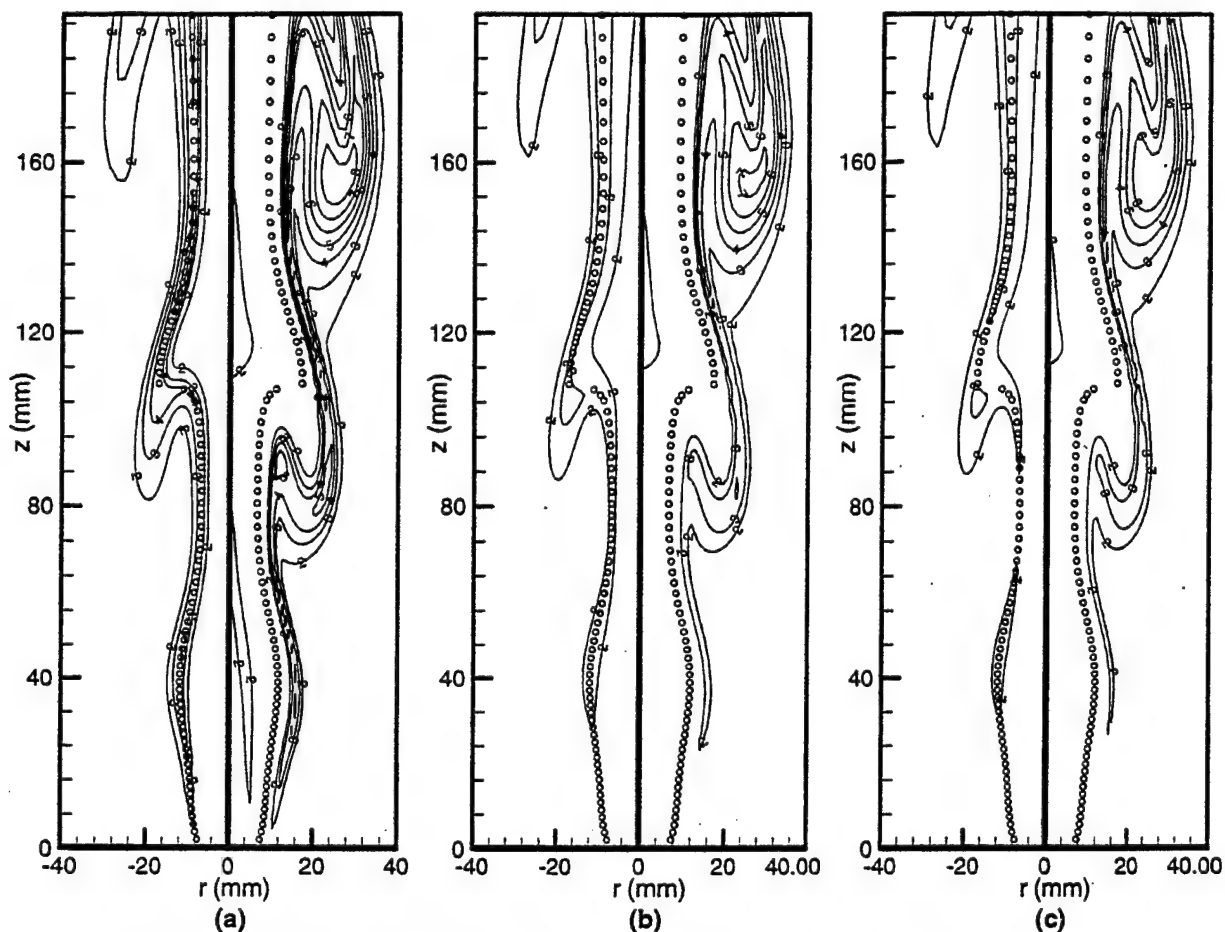


Fig. 3. NOx in unsteady methane flame predicted using (a) GRI Version 2.11, (b) GRI Version 2.11 without prompt NOx, and (c) GRI Version 1.2 plus Zel'dovich thermal NOx. Iso-contours of NO and NO₂ concentrations are shown on left and right halves, respectively.

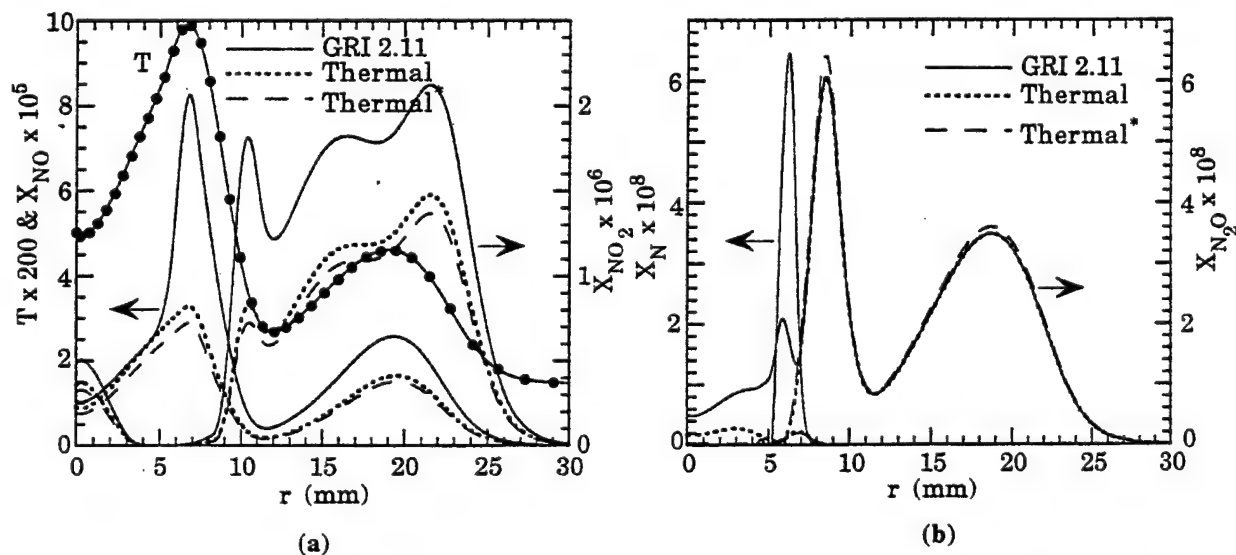


Fig. 4. Radial distributions of (a) temperature, NO, and NO₂ and (b) N and N₂O in stretched flame at a height of 80 mm.

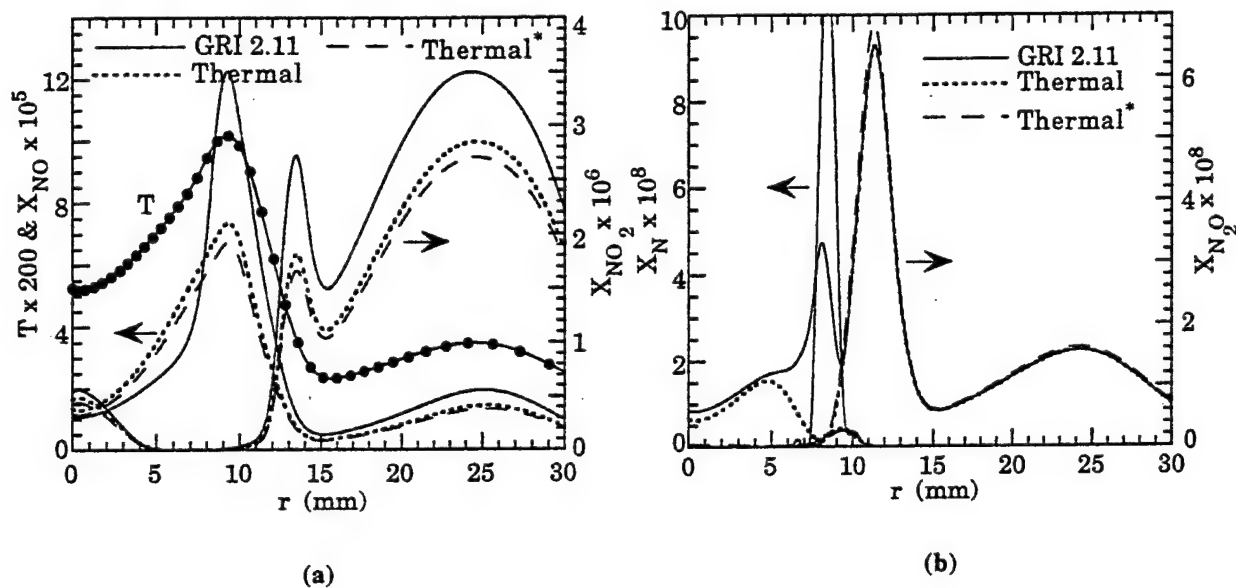


Fig. 5. Radial distributions of (a) temperature, NO , and NO_2 and (b) N and N_2O in stretched flame at a height of 150 mm.

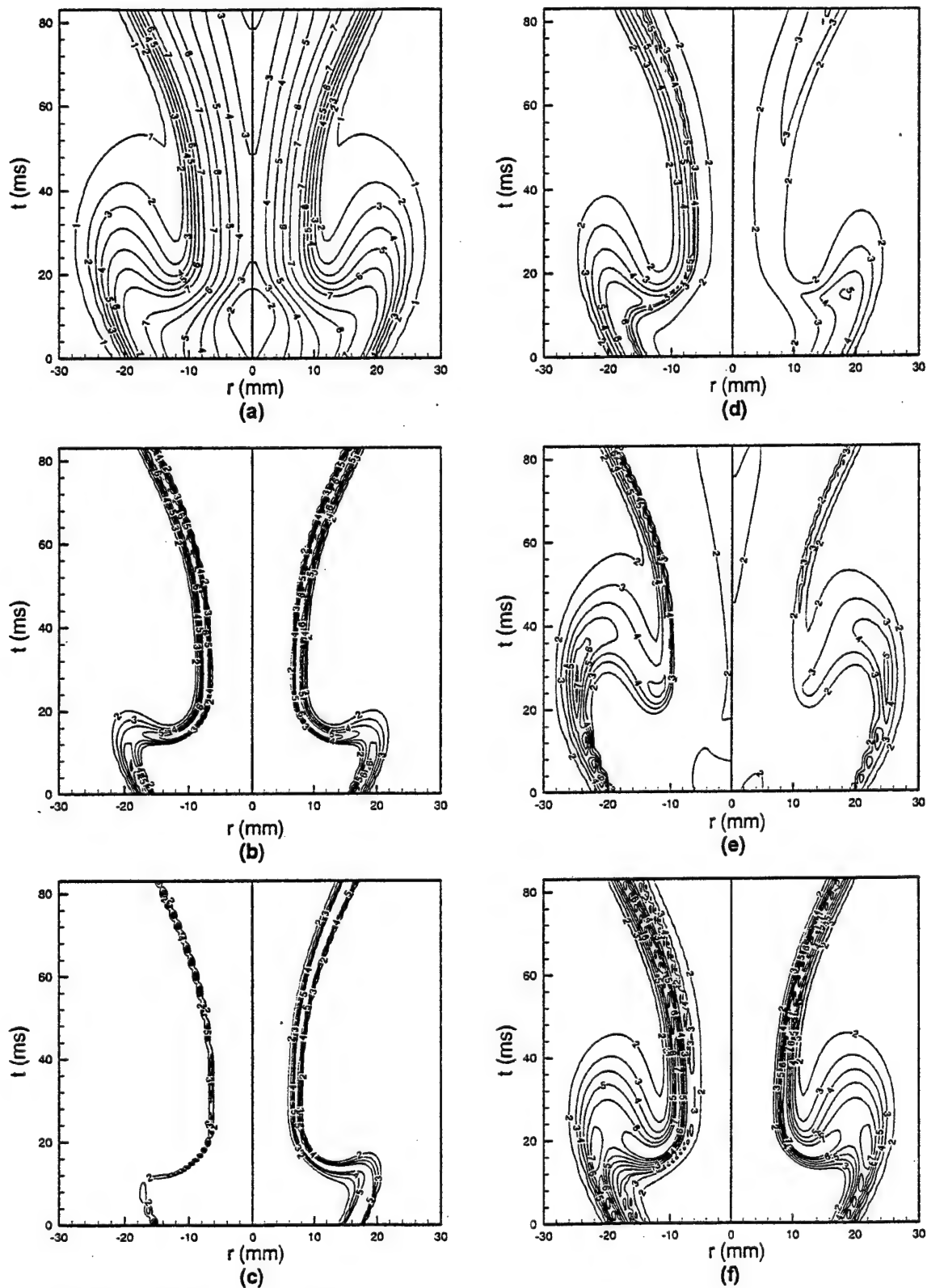


Fig. 6. Temporal variations of (a) temperature, (b) OH, (c) N, (d) NO, (e) NO₂, and (f) N₂O at a height of 80 mm. Predictions made using GRI Version 2.11 (left side) and GRI Version 2.11 without prompt NO_x (right side).

Experiments on the Scalar Structure of Turbulent CO/H₂/N₂ Jet Flames

R. S. BARLOW

Combustion Research Facility, Sandia National Laboratories, Livermore, CA 94551-0969

G. J. FIECHTNER, C. D. CARTER

Innovative Scientific Solutions, Inc., Dayton, OH 45440-3638

and

J.-Y. CHEN

Mechanical Engineering Department, University of California, Berkeley, CA 94720

Scalar and velocity measurements are reported for two turbulent jet flames of CO/H₂/N₂ (40/30/30 volume percent) having the same jet Reynolds number of 16,700 but different nozzle diameters (4.58 mm and 7.72 mm). Simultaneous measurements of temperature, the major species, OH, and NO are obtained using the combination of Rayleigh scattering, Raman scattering, and laser-induced fluorescence. Three-component laser-Doppler velocimetry measurements on the same flames were performed at ETH Zurich and are reported separately. This paper focuses on the scalar results but includes some limited velocity data. Axial profiles of mixture fraction, major species mole fractions, and velocity in these two flames are in close agreement when streamwise distance is scaled by nozzle diameter. However, OH mole fractions are lower and NO mole fractions are higher near the stoichiometric flame length in the larger flame due to the lower scalar dissipation rates and longer residence times. Turbulent flame measurements are compared with steady strained laminar flame calculations. Laminar calculations show remarkably close agreement with measured conditional means of the major species when all diffusivities are set equal to the thermal diffusivity. In contrast, laminar flame calculations that include the normal Chemkin treatment of molecular transport are clearly inconsistent with the measurements. These results suggest that turbulent stirring has a greater influence than molecular diffusion in determining major species concentrations at the flow conditions and locations considered in the present experiments, which begin at an axial distance of 20 nozzle diameters. Analysis of the conditional statistics of the differential diffusion parameter supports this conclusion, though some evidence of differential diffusion is observed. With regard to validation of turbulent combustion models, this data set provides a target that retains the geometric simplicity of the unpiloted jet flame in coflow, while including a chemical kinetic system of intermediate complexity between hydrogen flames and the simplest hydrocarbon flames. Aspects of the measurements, including Favre-averaged profiles, conditional statistics, mixture fraction pdf's, and departures from partial equilibrium, are presented and discussed in terms of their relevance to the testing of turbulent combustion submodels. The complete data are available on the World Wide Web for use in model validation studies. © 2000 by The Combustion Institute

INTRODUCTION

Detailed scalar and velocity data sets are essential for the process of testing and improving computational models for turbulent nonpremixed combustion. Laser diagnostics can provide nonintrusive measurements of the instantaneous velocities and species concentrations, and statistical information from such measurements may be used to evaluate a variety of modeling approaches. Despite the very productive history of laser diagnostics in combustion,

the number of data sets available in the literature that are appropriate for the quantitative evaluation of fundamental aspects of turbulent combustion models is relatively small. It is important for such data sets to include well-defined boundary conditions and relatively simple geometric configurations. It is also important that both velocity and scalar measurements be available for the same flames. Multicomponent velocity measurements are preferable, as are multiscalar measurements that include minor species. Minor species, such as combustion intermediates, radicals, and pollutants, tend to be sensitive to the details of

*Corresponding author. E-mail: barlow@ca.sandia.gov

interactions between fluid dynamics and chemical kinetics. Consequently, measurements of minor species can provide information on the fundamental nature of these interactions, and the prediction of minor species along with velocity, temperature, and major species constitutes a useful test of combustion models.

There are at least three detailed scalar and velocity data sets for hydrogen jet flames [1-4]. Model calculations of some of these flames have been compared [5-7], and it appears that state-of-the-art models are capable of yielding accurate calculations of such flames, including difficult details such as nitric oxide formation. The present paper focuses on simple, attached jet flames of 40% CO/30% H₂/30% N₂ (also referred to as syngas in the literature), which add a modest increment in chemical kinetic complexity, while retaining the simple geometry of the hydrogen jet flames. This study is part of a larger collaborative effort under the framework of the International Workshop on Measurement and Computation of Turbulent Nonpremixed Flames (TNF) [4] to develop a library of well-documented data sets that covers a progression in geometric and chemical kinetic complexity.

The fuel combination of carbon monoxide and hydrogen allows for the study of interactions of turbulent mixing and chemical reaction over a range of chemical time scales, including those associated with the binary reactions of the hydrogen-oxygen system, the oxidation of CO, the decay of OH through the three-body recombination reactions, and the thermal formation of nitric oxide. The flames considered here do not exhibit localized extinction or liftoff. Therefore, they can be addressed by a wide range of modeling approaches.

Reviews of the available experimental data sets on turbulent nonpremixed flames have been provided by Strahle [8], Faeth and Samuelsen [9], Drake and Kollmann [10], and more recently by Masri et al. [11]. Several experiments involving simultaneous multiscalar measurements based on Raman/Rayleigh or Raman/Rayleigh/LIF (laser-induced fluorescence) techniques have been conducted on flames having CO as a major fuel component. These include studies of piloted and bluff-body stabilized flames of CO/H₂/N₂ by Masri and Dibble

[12] and Correa and Gulati [13, 14]. The paper by Masri et al. [15] on hydrogen jet flames diluted with CO₂ is closely related, in a chemical kinetic sense, because the CO₂ is partially converted to CO at high temperatures within the flame. These experimental studies have provided useful insights on turbulence-chemistry interactions, particularly with regard to differences in extinction behavior among flames of H₂, CO/H₂, and hydrocarbon fuels. However, they are of limited utility with regard to rigorous, quantitative testing of turbulent combustion models because of the lack of complementary information on the velocity field.

We believe that the present data set has sufficient completeness and accuracy to make it useful for quantitative testing of turbulent combustion models. Raman/Rayleigh/LIF experiments were conducted at Sandia and include simultaneous point measurements of temperature, N₂, O₂, CO, H₂, CO₂, H₂O, OH, and NO. Subsequently, through the collaborative framework of the TNF Workshop, three-component laser-Doppler velocity (LDV) measurements were undertaken at ETH Zurich, Switzerland, and those experiments are reported separately by Flury [16]. The present paper focuses on the scalar measurements and includes only limited velocity data. Complete scalar and velocity data, together with documentation on boundary conditions and experimental uncertainties, are available on the Internet [17].

The following sections provide a description of experimental methods for the scalar measurements and present results in several forms, including averaged profiles, conditional statistics, probability density functions (pdf's), and derived quantities related to differential diffusion, and partial equilibrium. Measured conditional means are compared with steady laminar flame calculations to extract insights on the relative importance of turbulent stirring and molecular diffusion in determining the scalar structure of these flames.

EXPERIMENTAL METHODS AND MEASUREMENT UNCERTAINTIES

Multiscalar experiments were conducted in the Turbulent Diffusion Flame (TDF) laboratory at

Sandia's Combustion Research Facility. The flow facility, diagnostic systems, and calibration procedures have been described in previous publications [18–20]. The combination of spontaneous Raman scattering and Rayleigh scattering was used to measure the major species concentrations (N₂, O₂, CO, H₂, CO₂, H₂O) and temperature. Linear LIF was used to measure the concentrations of OH and NO. Fluorescence signals were corrected on a shot-to-shot basis for variations in the Boltzmann fraction and collisional quenching rate, based on measured temperature and major species concentrations in the probe volume. Collisional quenching cross sections for OH and NO were based on the work of Paul et al. [21, 22]. Spatial resolution of the scalar measurements was roughly 0.75 mm.

A system for two-photon LIF of CO was also implemented for this study, and part of the original motivation for investigating turbulent CO/H₂/N₂ flames was to allow direct comparison of the CO fluorescence and CO Raman methods in flames with a wide range of CO concentrations and without interferences from hydrocarbons. However, the signal-to-noise ratio (SNR) for the CO LIF measurements in the turbulent CO/H₂/N₂ flames was worse than for the Raman measurements, even though the LIF technique showed superior SNR in cold flows and calibration flames. The reasons are not known at this time. Beam steering effects and the differences in spatial resolution (beam diameters) were considered as possible causes, but tests showed that results were insensitive to these effects. This excess noise problem is not observed in turbulent methane flames [23]. CO results included in this paper are from Raman scattering measurements.

The precision of the scalar measurements is represented Fig. 1, which shows results of processed data from a series of CO/H₂-air flat flames (50/50 fuel mixture) operated on a Hencken burner [19]. The symbols show mean temperature and species mole fractions from each operating condition of the burner, and each symbol is surrounded by an ellipse having major and minor axes of twice the standard deviations ($\pm\sigma$) of the scalar and the mixture fraction. The standard deviations in these calibrations may be used to estimate the contribu-

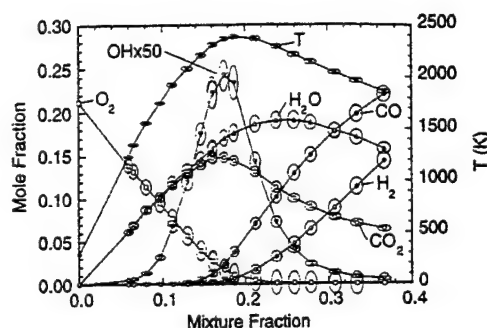


Fig. 1. Measured temperature and species mole fractions in the product gases above a series of CO/H₂-air calibration flames stabilized on a Hencken burner. Symbols show mean values from the Raman/Rayleigh/LIF data reduction process. Ellipses show standard deviations ($\pm\sigma$) for single-shot measurements of the scalars and for the resultant mixture fraction at each calibration condition.

tion of random error (primarily shot noise) to the conditional fluctuations reported below. Representative values of precision are listed in Table 1 for specific flame conditions.

Estimates of systematic uncertainties (absolute accuracy of averaged values) are also listed in Table 1 and are based on analysis of the calibration methods, repeatability of calibrations, considerations of calibration drift, allowances for greater uncertainties within the interpolated regions (approx. 900 K to 1600 K) of the calibration curves for H₂ and CO, and uncertainties in gas flow rates. Flow controllers were

TABLE 1

Standard Deviations of Scalars Measured in Flat Flames and Estimated Systematic Uncertainties

Scalar	σ (rms)	Conditions (mass fraction, T)	Systematic Uncertainty
T	1%	2140 K ^a	2%
Y _{N₂}	2%	0.73, 2140 K ^a	3%
Y _{H₂O}	5%	0.12, 2140 K ^a	3–5%
Y _{CO₂}	6%	0.14, 2140 K ^a	3–5%
Y _{CO}	13%	0.062, 2020 K ^b	5–10%
Y _{H₂}	17%	0.003, 2020 K ^b	5–10%
Y _{OH}	8%	0.0016, 2140 K ^a	10%
Y _{NO}	10%	8 ppm, 1760 K ^c	10–15%

^a Premixed CH₄/air, $\phi = 0.96$, uncooled (Hencken) burner.

^b Premixed CH₄/air, $\phi = 1.27$, uncooled (Hencken) burner.

^c Premixed CH₄/O₂/N₂, $\phi = 0.72$, cooled (McKenna) burner.

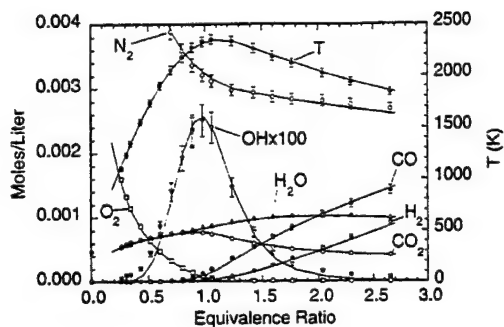


Fig. 2. Processed mean values of temperature and concentration in the CO/H₂-air Hencken-burner flames. Error bars show estimated systematic uncertainties, as listed in Table 1. Solid lines connect nonadiabatic equilibrium values calculated at the measured Rayleigh temperatures.

calibrated using laminar flow elements (Meriam Instrument), and these calibrations were repeatable to within $\pm 1\%$ over the range of flows used in the present experiments. The estimated uncertainties in averaged temperature and concentration measurements are illustrated in Fig. 2. Here, averaged results are plotted versus the equivalence ratio for 18 CO/H₂-air flame conditions. The lower values from Table 1 are plotted as error bars. Where no error bars are visible the uncertainty is represented approximately by the size of the plotting symbol. The solid curves in Fig. 2 show results of nonadiabatic equilibrium calculations computed at temperatures representing the average Rayleigh temperature from several calibration sets. These averaged Rayleigh temperatures are about 50 K below adiabatic equilibrium in these calibration flames. The OH calibration is based on independent laser absorption measurements in a CH₄-air flame, and this is consistent with the calculated nonadiabatic equilibrium OH levels in the CO/H₂-air flames, as shown in Fig. 2.

Experiments were conducted on two jet flames with different nozzle diameters but equal Reynolds numbers based on the cold-jet exit conditions. The fuel composition for both flames was 40% CO, 30% H₂, and 30% N₂ by volume. Nozzle dimensions and jet flow conditions are listed in Table 2. The nozzles were constructed from straight tubing with squared-off ends. The thick wall of the tubing provided a small recirculation zone that helped to stabilize

TABLE 2

Nozzle Dimensions and Flow Conditions^a

Flame	<i>d</i> , Nozzle ID (mm)	Nozzle OD (mm)	<i>U</i> _{jet} (m/s)	<i>Re</i> _{jet}
A	4.58	6.34	76.0 ± 1.5	~16,700
B	7.72	9.46	45.0 ± 0.9	~16,700

^a $Re = U_{jet}d/\nu$, where $\nu = 2.083 \times 10^{-5} \text{ m}^2/\text{s}$.

the flames without a pilot. This experimental convenience may lead to computational inconvenience, in that most turbulence models would not be expected to resolve the details of the near-nozzle flow. However, we do not expect this to be a significant liability for these data. The flames were unconfined, and each burner tube was mounted such that the flame base was above the level of the 30-cm by 30-cm exit of the wind tunnel. The coflow air conditions were 0.75 m/s \pm 0.05 m/s velocity, 290 K \pm 2 K temperature, 0.012 \pm 0.002 mole fraction of H₂O vapor, and 100.6 \pm 0.4 kPa pressure.

RESULTS AND DISCUSSION

Both flames appeared to be fully attached to the nozzle, and there is no evidence in the data that oxygen is entrained into the fuel jet through extinguished zones near the nozzle. Axial profiles were obtained in both flames and include measurements from $x/d = 20$ to $x/d = 75$ with steps of $5d$, where d is the nozzle inner diameter. Radial profiles were obtained at axial positions of $x/d = 20, 30, 40, 50$, and 60 in each flame. Typically, 800 to 1000 shots were collected at each location in these profiles. Measurements were not taken closer to the nozzle due to considerations of spatial resolution. The smallest scalar length scale, λ_B , was estimated following the approach outlined by Smith et al. [24]. At $x/d = 20$ in the smaller flame the estimated λ_B is approximately equal to the 0.75-mm size of the laser probe volume. Better spatial resolution is achieved further downstream and in the larger flame. There may be some influence of spatial averaging on the measurements, but we would not expect this to alter any of the conclusions of this paper.

The sections that follow report Favre- and conditionally averaged mole fractions of the

measured scalars, as well as several derived quantities based on measured mass fractions. The data base available on the web includes Favre, Reynolds, and conditional statistics of both mole fractions and mass fractions. In ad-

dition, the complete files of single-shot mass fractions and mole fractions are available.

Here and in the archived data files the mixture fraction is calculated from the data following the method of Bilger et al. [25].

$$F = \frac{2(Y_C - Y_{C,2})/w_C + (Y_H - Y_{H,2})/2w_H - (Y_O - Y_{O,2})/w_O}{2(Y_{C,1} - Y_{C,2})/w_C + (Y_{H,1} - Y_{H,2})/2w_H - (Y_{O,1} - Y_{O,2})/w_O},$$

where Y 's are elemental mass fractions of carbon, hydrogen, and oxygen; w 's are atomic weights; and the subscripts 1 and 2 refer to the fuel stream and coflowing air stream, respectively. The fuel and air boundary conditions for the elemental mass fractions are listed in Table 3. Bilger's formulation preserves the stoichiometric value of the mixture fraction, independent of the effects of differential molecular diffusion. The stoichiometric value of the mixture fraction, F_{st} , is 0.295 in the present flames.

Axial and Radial Profiles

Axial (centerline) profiles of Favre-averaged mixture fraction, temperature, and species mole fractions are plotted in Fig. 3 (left side) for the two flames, with the axial coordinate, x , normalized by nozzle diameter, d . In these fully connected flames with low coflow velocity, the scaling by nozzle diameter works well for all measured scalars except for the mole fractions of OH and NO. The OH and NO mole fractions are more strongly influenced by local scalar dissipation and by convective residence time than are temperature and the major species concentrations. Consequently, OH mole fractions are 20–25% lower in flame B than in flame A, and NO levels are about 40% higher. It is this greater sensitivity of some minor species to fluid-dynamic scaling that makes them useful for the evaluation of turbulent combustion

models. Axial profiles of scalar fluctuations are also plotted in Fig. 3 (right side). Again, the scaling of axial distance by nozzle diameter demonstrates the similarity of the two flames. Note also that the fluctuations in temperature, H₂O, and CO₂ pass through local minima at the streamwise locations where the corresponding mean values reach their peaks.

Radial profiles of Favre-averaged scalars at streamwise locations of $x/d = 20$ and $x/d = 50$ are plotted in Fig. 4. Again the simple scaling by nozzle diameter works well for temperature and major species in these flames. However, OH levels are lower and NO levels are higher in flame B than in flame A, due to the lower scalar dissipation rates and longer residence times in the larger flame. Axial and radial profiles of the normalized mean and fluctuation of the streamwise component of velocity, as reported by Flury [16], are shown in Figs. 5 and 6 to emphasize the availability of velocity measurements in these flames. The archive [17] of velocity data includes axial profiles and radial profiles at $x/d = 0, 10, 20, 30, 40, 50$, and 60 in each flame.

Axial and radial profiles of velocity and scalars provide an important first level of information on jet flame structure that may be used in the testing and evaluation of turbulent combustion models. However, such profiles yield little information on the details of the relationships among species and the influence of turbulence on scalar transport and reaction progress. Consequently, these profiles are necessary but not sufficient for the establishment of a complete quantitative understanding of the capabilities and limitations of turbulent combustion models, nor are such profiles particularly useful for developing fundamental insights on the effects of turbulence–chemistry interactions. Issues of chemistry and turbulence–chemistry interac-

TABLE 3

Elemental Mass Fraction Boundary Conditions^a

Stream	Y_C	Y_H	Y_O
Fuel, 1	0.2377	0.0299	0.3167
Coflow, 2	0.0	7.7×10^{-4}	0.2356

^a Coflow humidity included, CO₂ content in air neglected, balance is N₂.

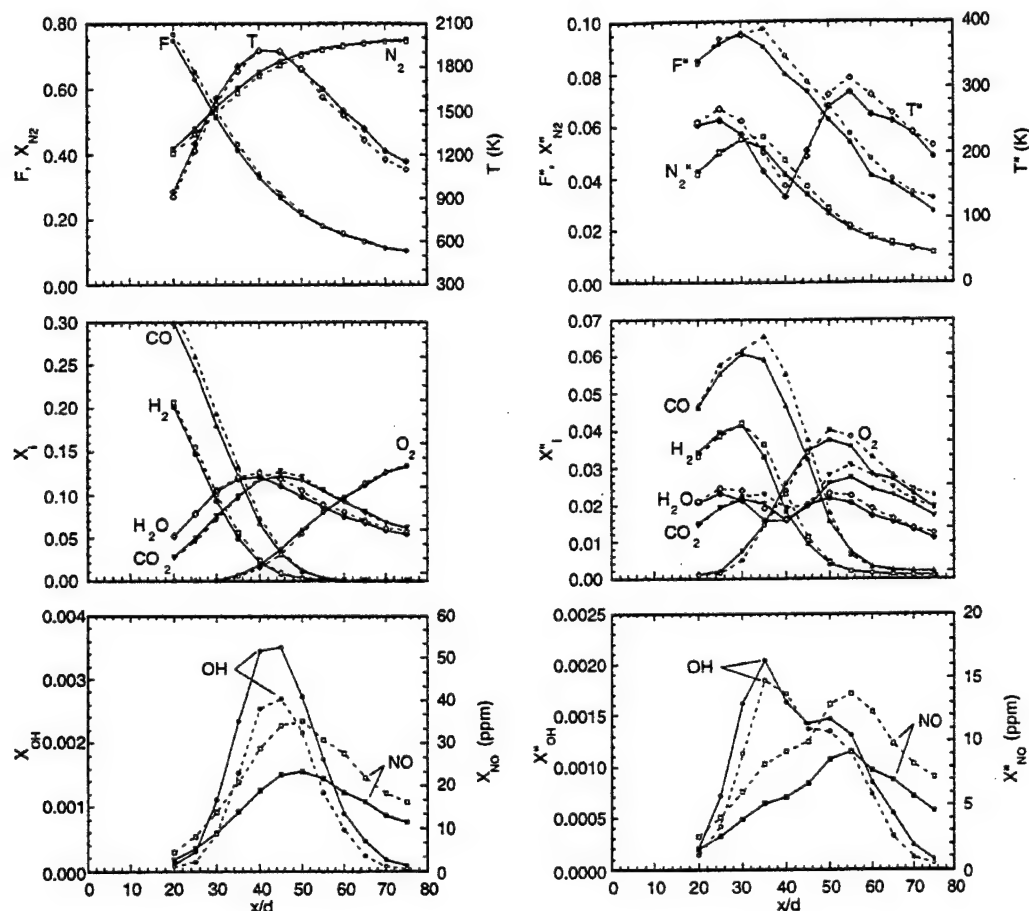


Fig. 3. Axial profiles of Favre-averaged scalars (left side) and rms fluctuations (right side) for the two flames, A (solid lines) and B (dashed lines).

tions may be better explored in mixture-fraction space, as is done in the following sections.

Conditional Statistics and Issues of Scalar Transport

In the present flames there is no evidence of localized extinction at the measured locations or of the entrainment of oxygen into the fuel jet through extinguished or lifted regions at the flame base. This is demonstrated in Fig. 7, which is a scatter plot of temperature and the mole fraction of O_2 . In these fully connected flames the scalar structure in mixture-fraction space may be represented conveniently by the conditional mean and rms fluctuation, rather than the

complete scatter plots or pdf's. As an illustration, Fig. 8 shows the conditional means of temperature and O_2 mole fraction corresponding to the scatter data in Fig. 7, with the conditional rms fluctuations ($\pm\sigma$) plotted as "error" bars. Conditional statistics presented in this paper are determined using all data from a given radial profile. Previous work has shown some radial dependence of the conditional statistics in hydrogen jet flames, particularly in the upstream region of the flame, and we will consider this detail later in this paper.

Scatter data and conditional means of scalars measured in turbulent flames have often been compared with results of steady, strained, laminar flame calculations. Initial comparisons for

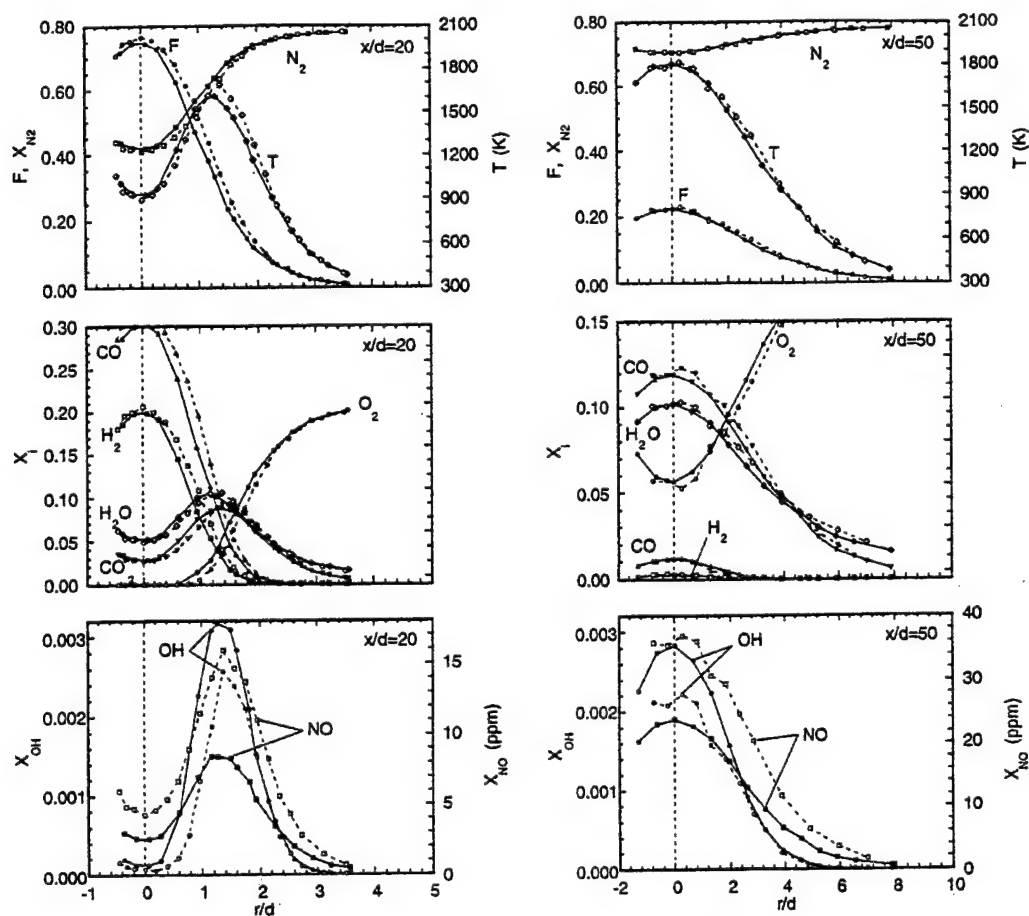


Fig. 4. Radial profiles of Favre-averaged scalars in the two flames, A (solid lines) and B (dashed lines), measured at axial locations $x/d = 20$ (left) and $x/d = 50$ (right). The Favre-averaged stoichiometric flame length is $\sim 44d$ in both flames.

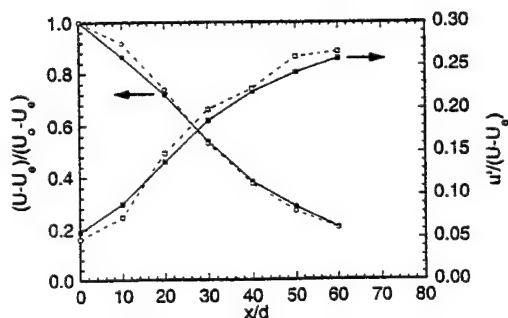


Fig. 5. Centerline profiles of mean and fluctuating axial velocity from LDV measurements by Flury [16] for flames A (solid lines) and B (dashed lines). U_0 is the coflow velocity, and U_0 is the nozzle exit velocity on the centerline.

these CO/H₂/N₂ flames, using the CO mechanism from Peters and Rogg [26], revealed large differences between measurements and laminar calculations that included the Chemkin treatment of species transport. This was true for all measured locations in both turbulent flames. Laminar calculations were repeated with all species diffusivities set equal to the thermal diffusivity, and results of both sets of calculations are shown in Fig. 9. The different treatments of scalar transport result in large differences in the mole fractions of H₂, CO, H₂O, and CO₂. The most obvious effect is that the H₂O/CO₂ ratio decreases by roughly a factor of 2 near the stoichiometric value of the mixture fraction when equal diffusivities are prescribed. Values of scalar dissipation at the stoichiomet-

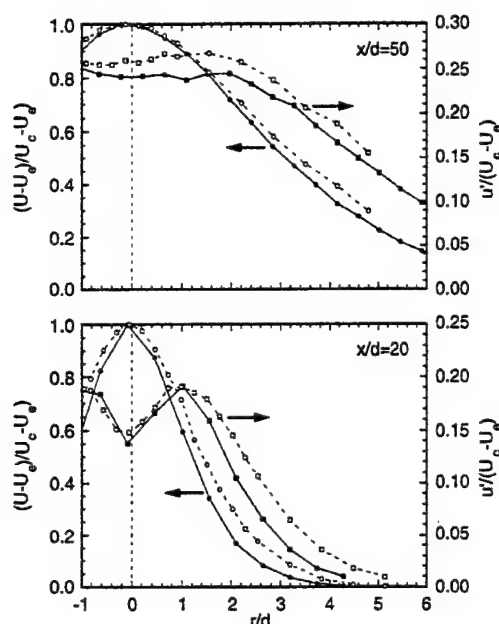


Fig. 6. Radial profiles of mean and fluctuating axial velocity from LDA measurements by Flury [16] for flames A (solid lines) and B (dashed lines) at $x/d = 20$ (lower graph) and $x/d = 50$ (upper graph). U_c is the coflow velocity, and U_c is the axial velocity on the centerline.

ric condition are given in Table 4 for all cases. Note that the scalar dissipation values in the flames with equal diffusivities are about 50% higher than in the corresponding flames with the normal Chemkin treatment of molecular transport. This is related to the fact that, in the presence of differential diffusion, scalar dissipa-

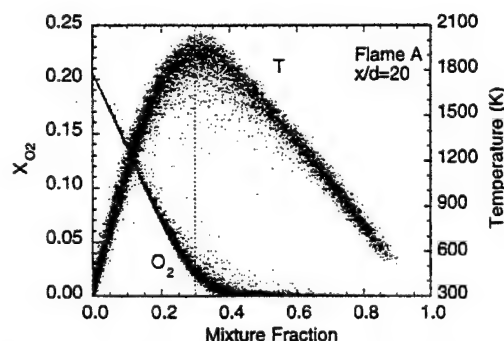


Fig. 7. Scatter plot of single-shot temperature and O_2 measurements in flame A at $x/d = 20$, including approximately 15,000 samples from the complete radial profile. The vertical dashed line indicates the stoichiometric value of the mixture fraction.

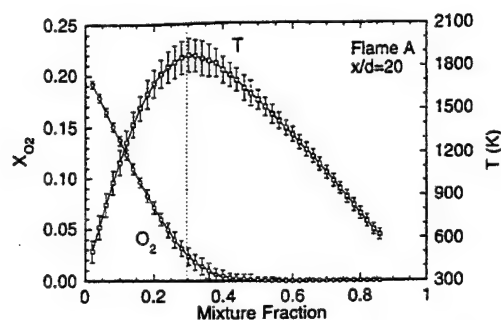


Fig. 8. Conditional mean and rms fluctuation (plotted as uncertainty bars) calculated from the data of Fig. 7, using evenly spaced intervals of 0.02 in mixture fraction. The vertical dashed line indicates the stoichiometric value of the mixture fraction.

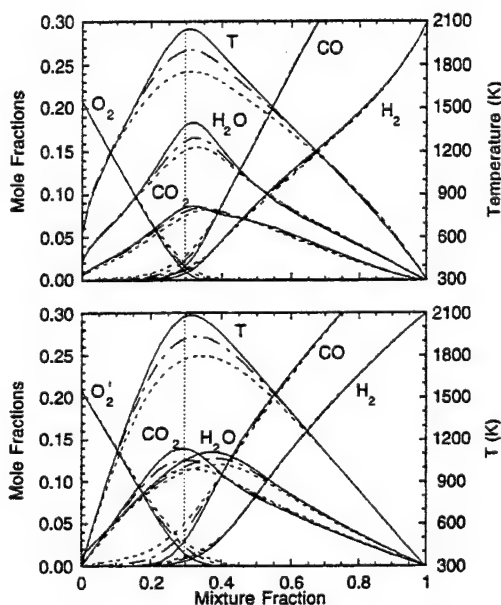


Fig. 9. Results of steady strained opposed-flow laminar flame calculations corresponding to the fuel and air boundary conditions of these turbulent jet flame experiments. Curves for three values of the strain parameter (Tsuji geometry) are plotted in each graph, $a = 10 \text{ s}^{-1}$ (solid), 100 s^{-1} (chain-dash), and 400 s^{-1} (dash). Values of the scalar dissipation at the stoichiometric condition in these laminar flames are listed in Table 4. The results in the upper graph include full molecular transport (Chemkin), while the lower graph shows the effect of setting all species diffusivities equal to the thermal diffusivity. The vertical dashed line indicates the stoichiometric value of the mixture fraction.

TABLE 4

Scalar Dissipation Rates at Stoichiometric in the Laminar Flames

Strain Parameter, a (s ⁻¹)	10	100	400
χ_{st} , Full transport (s ⁻¹)	3.0	30	120
χ_{st} , Equal diffusivities (s ⁻¹)	4.6	46	184

tion is sensitive to the definition of mixture fraction.

The equal diffusivity calculations yield better agreement with the measurements. This is illustrated in Fig. 10, which compares measurements from flame A at $x/d = 30$ with the two types of laminar calculations, both with strain parameter $a = 100$ s⁻¹. Comparison of the measured and calculated H₂O and CO₂ mole fractions near the stoichiometric value of the mixture fraction gives clear evidence of the failure of the laminar flame calculation that includes differential diffusion to approximate the turbulent flame results. Changing the strain rate of the compared flame would not alter this conclusion. The agreement between the equal-diffusivity calculation and the turbulent flame data is remarkable, particularly with regard to the H₂O/CO₂ ratio, suggesting that turbulent stirring has a greater influence than molecular diffusion in determining the major species mole fractions at the jet flame conditions considered here. We would not expect the conditional means in Fig. 10 or the measured H₂O/CO₂ ratio to be altered

significantly by improved spatial resolution of the measurements because the measurement resolution is already smaller than the estimated smallest scalar length scale at this location.

Figure 11 shows the streamwise evolution of the conditional mean and rms fluctuation of temperature and major species in the two flames. Equal-diffusivity calculations are included in each plot with $a = 10$ s⁻¹ or $a = 100$ s⁻¹ depending on which result better approximates the local measurements. (We did not run additional calculations to obtain closer matches at each location.) The values of scalar dissipation at the stoichiometric mixture fraction in these two laminar calculations are $\chi_{st} = 4.6$ s⁻¹ and $\chi_{st} = 46$ s⁻¹, respectively. The measurements are consistent with the expected trend of decreasing strain and scalar dissipation rates with increasing streamwise distance. It is also evident that there are greater effects of finite rate chemistry in flame A than in flame B, especially at $x/d = 20$, where the conditional mean temperature is significantly lower in flame A than in flame B. There is some evidence of differential species diffusion in fuel-rich portions of both jet flames. In particular, the measured CO/H₂ ratio in fuel-rich mixtures is somewhat greater than indicated by the equal-diffusivity results. Nevertheless, Figs. 9–11 support the conclusion that for all measured locations in the present flames the equal-diffusivity calculations yield better approximations of the measure conditional means of temperature and the major species mole fractions than do the calculations that include differential diffusion.

The conclusion that turbulent stirring has a greater role than molecular diffusion in determining the conditional mean compositional structure of the present flames is consistent with the results of several experimental, theoretical, and computational studies [e.g., 1, 2, 24, 27–33] that point to a progressive reduction in the effects of differential species diffusion as Reynolds number increases or as one moves downstream in a turbulent jet or flame. Differential-diffusion effects can be strong near the base of a turbulent flame, particularly in cases where H₂ is mixed with a heavier gas in the fuel stream and the cold-jet Reynolds number is in the neighborhood of 10,000 or lower [2]. It appears

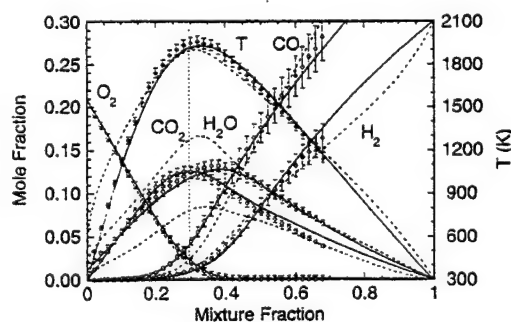


Fig. 10. Measured conditional means at $x/d = 30$ in flame A compared with the two types of laminar calculations for $a = 100$ s⁻¹: full transport (dash lines) and equal diffusivities (solid lines). Indicated experimental uncertainties correspond to the larger values in Table 1. The vertical dashed line indicates the stoichiometric value of the mixture fraction.

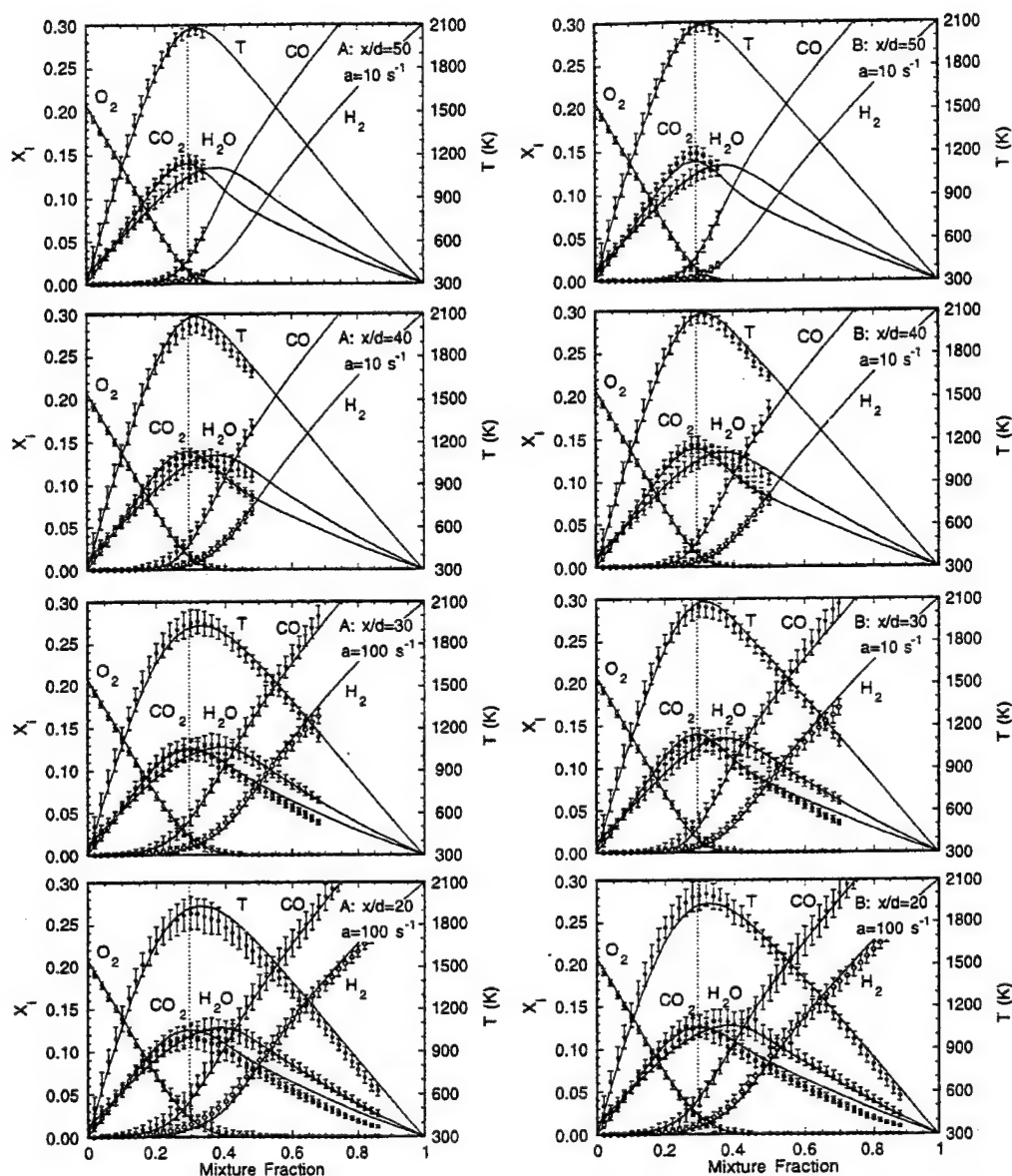


Fig. 11. Streamwise evolution of conditional statistics in the two jet flames. Solid curves show results of equal diffusivity laminar flame calculations at strain rates of $a = 10 \text{ s}^{-1}$ ($\chi_{st} = 4.6 \text{ s}^{-1}$) or $a = 100 \text{ s}^{-1}$ ($\chi_{st} = 46 \text{ s}^{-1}$).

that the Reynolds number is sufficiently high in the present flames to allow turbulent stirring to overshadow or "wash out" the influence of differential diffusion on the conditional means of the major species before the first measurement location of $x/d = 20$ is reached.

The degree of differential diffusion may be quantified by defining and comparing elemental

mixture fractions. Here, we define mixture fractions for hydrogen and carbon as:

$$F_H = \frac{Y_H - Y_{H,1}}{Y_{H,2} - Y_{H,1}} \quad \text{and} \quad F_C = \frac{Y_C - Y_{C,1}}{Y_{C,2} - Y_{C,1}},$$

where subscripts 1 and 2 refer to fuel and air streams, respectively. A differential diffusion

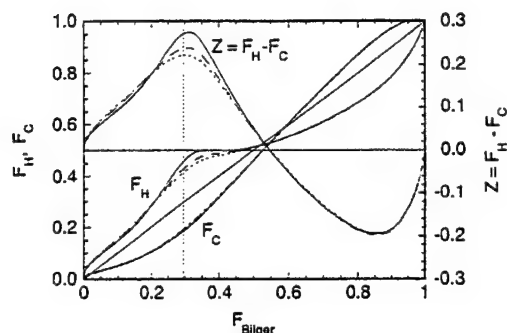


Fig. 12. Elemental mixture fractions, F_H and F_C , and the differential diffusion parameter, z , plotted versus the Bilger mixture fraction. Results are from steady laminar flame calculations with full transport at strain rates of $a = 10 \text{ s}^{-1}$ (solid), 100 s^{-1} (long dash), and 400 s^{-1} (short dash).

parameter, $z = F_H - F_C$, can then be calculated as the difference between these elemental mixture fractions. Figure 12 shows calculated results for F_H , F_C , and z plotted versus the Bilger mixture fraction from steady laminar flame calculations using the conventional Chemkin molecular transport package. Preferential diffusion of H₂ toward the reaction zone causes a deficit in hydrogen relative to carbon in region $0.55 < F_{\text{Bilger}} < 1$, and there is a positive peak in z just on the rich side of the stoichiometric condition. These calculated flames show strong effects of differential diffusion which are not very sensitive to the applied strain rate.

In the experiments, z is determined by subtracting two uncertain quantities that may have similar values. It is, therefore, important to consider the contributions of random and systematic errors in the differential diffusion results. A relatively simple test is to apply the differential diffusion analysis to measurements from the flat calibration flames, where differential diffusion is expected to be negligible because measurements are made in product gases 3 cm above the burner. Figure 13 shows results for F_H , F_C , and z in each of the CO/H₂/air calibration flames, with mean values shown as symbols and rms fluctuations ($\pm\sigma$) shown as "error" bars. Note that the stoichiometric value of the mixture fraction in the calibration flames is lower than in the turbulent flames ($F_{\text{Bilger}} = 0.179$ versus $F_{\text{Bilger}} = 0.295$). On the fuel-lean side, where results depend mainly on the H₂O and CO₂ Raman calibrations, z is nearly zero. In

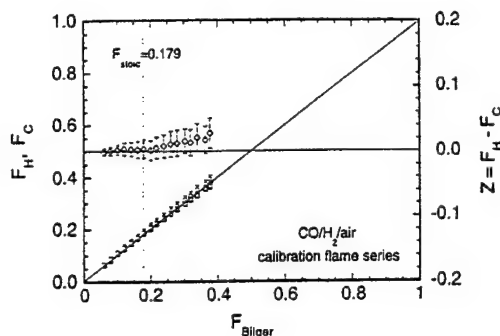


Fig. 13. Mean and rms values of the elemental mixture fractions F_H (squares) and F_C (circles) and the differential diffusion parameter z (diamonds) in the same CO/H₂-air flat flame calibration series as plotted in Figs. 1 and 2. The stoichiometric value of the mixture fraction is lower than in the turbulent flames because there is no N₂ dilution of the fuel.

fuel-rich flames, where the calibrations for H₂ and CO become increasingly important, z becomes slightly positive. The difference of the averaged z from zero is within the bounds corresponding to the estimated systematic uncertainties for the CO and H₂ Raman measurements. Note that uncertainties in flow meter calibrations, which are typically $\pm 1\%$ for each gas, can contribute to nonzero z values. Results in Fig. 13 indicate that we can expect uncertainties of 0.02 to 0.03 in conditionally averaged values of z in the turbulent flames. Fluctuations in F_H , F_C , and z in the calibration flames are due mainly to shot noise in the species measurements.

Figure 14 shows the streamwise evolution of F_H , F_C , and z in each of the two turbulent flames. Here, again, the symbols show conditional means, and the conditional rms fluctuations are plotted as error bars. Several observations may be made. First, for the turbulent flame conditions and locations considered in the present experiments, the measured effects of differential diffusion are much smaller than in the laminar calculations. Second, the largest differential diffusion effects are observed in the richest samples at each streamwise location, such that the conditional mean z is close to zero for lean and near-stoichiometric samples, but drops toward negative values at the fuel-rich end of each data set. The measured magnitude of z remains small relative to that in the laminar calculations, and it is not completely clear that

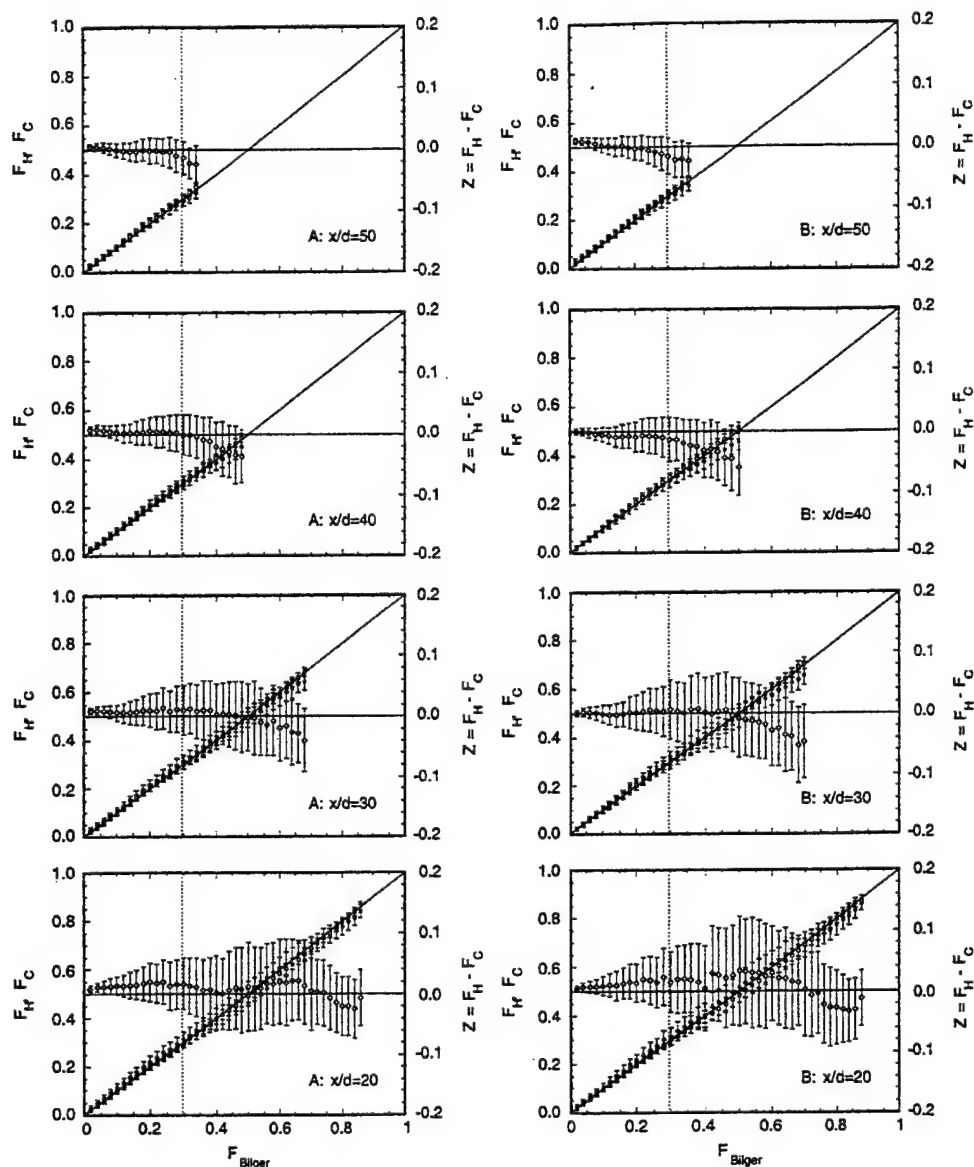


Fig. 14. Streamwise evolution of conditional mean values and rms fluctuations of F_H (squares), F_C (circles), and z (diamonds) in flames A and B. Note expanded scale for z .

the measured streamwise trends in z are significant relative to the accuracy of the measurements. However, the fact that the negative dip in z at the fuel-rich end appears consistently in all plots, with the effect moving across the mixture fraction coordinate, suggests that it is not caused by systematic error in the Raman calibrations or flow meter calibrations. The

observed streamwise evolution of the conditional mean of z is believed to reflect a mixing history that involves preferential diffusion of H_2 out of the core of the jet near the flame base [24], where heat release tends to laminarize the flow, particularly at lower Reynolds numbers. Once this initial deficit of hydrogen is created in the richest samples, it appears to be preserved

far downstream because the richest samples at any streamwise location are those which have been least affected by turbulent stirring.

A third observation regarding Fig. 14 is that the conditional fluctuations in z tend to decrease with downstream distance. In fact, the level of fluctuation at $x/d = 50$ is comparable to the noise in measurements above the calibration flames (Fig. 13), and any fluctuations in z that exist near the tips of these jet flames are too small to be measured accurately by the present diagnostics. It is possible to subtract out (approximately) the shot noise contribution to the conditional fluctuations of z , as done by Smith et al. [24]. This procedure is based upon the reasonable assumption that random errors in z are statistically independent of the actual turbulent fluctuations. The noise contribution can then be determined from the rms fluctuations of z obtained from the flat-flame calibration data. However, we have not applied this procedure here.

Larger differential diffusion effects are expected to be present closer to the nozzle, as reported by Meier et al. [2] for nitrogen-diluted H₂ flames and by Bergmann et al. [28] for CH₄/H₂/N₂ flames. However, it is clear that the influence of differential diffusion on major species mole fractions is relatively small in the present flames for $x/d \geq 20$ and that turbulent stirring is sufficiently strong to make the effective turbulent diffusivities nearly equal for the measured scalars. One might expect turbulent combustion models built on an assumption of equal diffusivities to perform well in predicting these flames. Conversely, one would expect a flamelet approach to perform poorly if the flamelet library is based on calculations that include full molecular transport.

Trends Related to Damköhler Number

Trends in the conditional means of each measured scalar may be related qualitatively to changes in the relevant Damköhler number ($Da = \tau_{\text{flow}}/\tau_{\text{chem}}$) between the two flames or among the different locations in a given flame. Such trends have been reported and discussed in many papers. We consider these trends in the context of the present flames not because they provide new fundamental insights but because

the quantitative prediction of these results constitutes an important test of submodels for mixing and for the coupling of turbulence and chemistry.

A broad range of chemical reaction rates or time scales is represented by these flames, including the time scales associated with the binary reactions of the H₂/O₂ system, oxidation of CO, decay of OH through the three-body recombination reactions, and formation of NO via the extended Zeldovich mechanism. There is also a broad range of fluid-dynamic time scales in these flames. At the simplest level one might consider the convective residence time from the nozzle to the measurement location (proportional to x/U_{jet}) and the local large-eddy time scale [34–36], which is associated with the large-scale strain rate (and arguably the large-scale turbulent stirring process) and scales as $\tau_{\text{large-eddy}} \propto \delta_{1/2}/(U_c - U_e)$, where $\delta_{1/2}$ is the half-width of the velocity profile.

While it may not be appropriate to assign precise flow and chemical times in turbulent flames, the consideration of Damköhler numbers based on representative time scales can be useful in understanding the potential for coupling between various flow processes and specific reactions or species. Consider CO oxidation as an example. Drake and Blint [37] tabulated chemical time scales (based on peak forward reaction rates) for specific reactions in laminar calculations of CO/H₂/N₂ flames with the same fuel volume fractions as used here. For their case with $\alpha = 10 \text{ s}^{-1}$, which Fig. 11 has shown to be representative of conditions in portions of the present jet flames, τ_{reaction} is given as 0.73 ms for the reaction $\text{CO} + \text{OH} \rightleftharpoons \text{CO}_2 + \text{H}$. In the present experiments the convective times range from roughly 3 ms ($x/d = 20$, flame A) up to 10's of ms, whereas the local large-eddy times fall in the approximate range of 0.3 ms ($x/d = 20$, flame A) to 5 ms ($x/d = 60$, flame B). Taking $\tau_{\text{chem}} \sim 0.73 \text{ ms}$ for CO oxidation and $\tau_{\text{flow}} \sim 0.7 \text{ ms}$ from the large-eddy time at $x/d = 20$ in flame B yields $Da_{\text{CO}} \sim 1$. This suggests that CO oxidation may be strongly coupled with large-scale mixing processes. Qualitatively, the chemical times for CO oxidation and radical recombination are comparable to flow times within the present flames, the main path for H₂O formation is fast relative

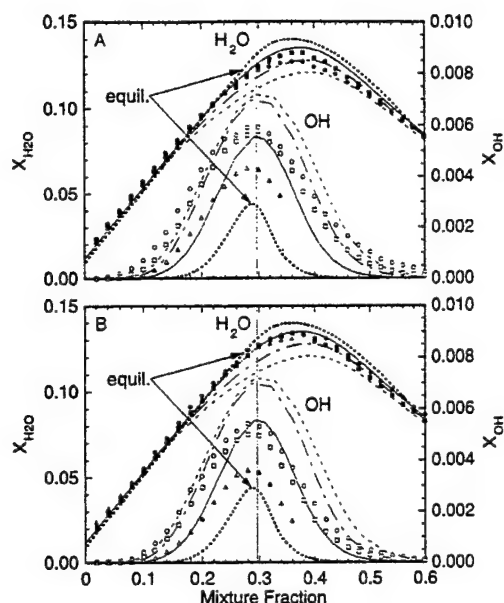


Fig. 15. Conditional means of X_{H_2O} and X_{OH} in flames A (upper) and B (lower) at streamwise locations $x/d = 20$ (circles), $x/d = 30$ (squares), and $x/d = 50$ (triangles). Curves are plotted for the equal-diffusivity flame calculations at strain rates of $a = 10\text{ s}^{-1}$ (solid), $a = 100\text{ s}^{-1}$ (chain-dash), and $a = 400\text{ s}^{-1}$ (dash). Values of the scalar dissipation at the stoichiometric condition in these three laminar flames are $\chi_{st} = 4.6\text{ s}^{-1}$, 46 s^{-1} , and 184 s^{-1} , respectively. Adiabatic equilibrium curves (short dash) are included.

to fluid-dynamic times, and thermal formation of NO is relatively slow. These relationships are reflected in the measured conditional means, as discussed below.

Figure 15 shows the measured condition means of the mole fractions of H_2O and OH at streamwise locations of $x/d = 20, 30$, and 50 in each of the two flames A and B. Curves representing adiabatic equilibrium conditions and steady strained laminar flame solutions are also plotted. The laminar flame curves correspond to equal-diffusivity calculations with three values of the strain parameter, $a = 10\text{ s}^{-1}$, 100 s^{-1} , and 400 s^{-1} ($\chi_{st} = 4.6\text{ s}^{-1}$, 46 s^{-1} , and 184 s^{-1} , respectively). The conditional mean of X_{H_2O} is relatively insensitive to location, indicating that H_2O formation via the binary reactions is fast relative to the fluid-dynamic time scales. The relatively small differences in the X_{H_2O} curves are believed to be controlled mainly by progress of the slower radical recombination reactions.

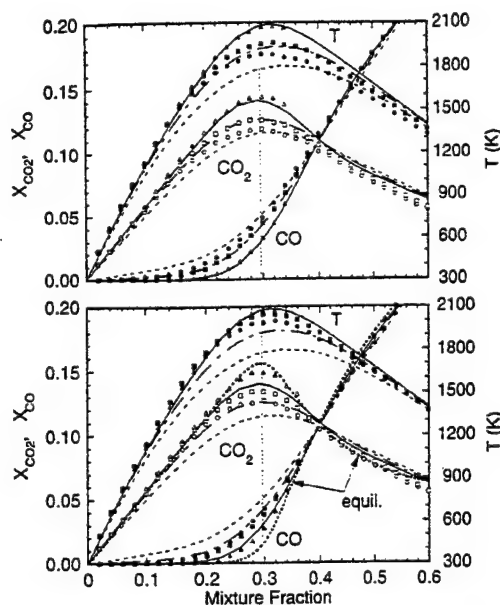


Fig. 16. Conditional means of X_{CO_2} , X_{CO} , and T in flames A (upper) and B (lower) at streamwise locations $x/d = 20$ (circles), $x/d = 30$ (squares), and $x/d = 50$ (triangles). Curves are plotted for the equal-diffusivity flame calculations at strain rates of $a = 10\text{ s}^{-1}$ (solid), $a = 100\text{ s}^{-1}$ (chain-dash), and $a = 400\text{ s}^{-1}$ (dash). Values of the scalar dissipation at the stoichiometric condition in these three laminar flames are $\chi_{st} = 4.6\text{ s}^{-1}$, 46 s^{-1} , and 184 s^{-1} , respectively. Adiabatic equilibrium curves (short dash) for X_{CO_2} and X_{CO} are included in the lower graph.

The conditional mean of X_{OH} changes significantly from a peak of roughly twice equilibrium at $x/d = 20$ in flame A to roughly 20% above equilibrium at $x/d = 50$ in flame B. This result indicates that the time scales for radical recombination are comparable to time scales of the flow.

Figure 16 includes the corresponding results for CO_2 , CO , and temperature. There is a distinct progression in the conditional mean results for X_{CO} and X_{CO_2} as one moves downstream in a given flame or compares flames A and B at a given value of x/d . At $x/d = 20$ in flame A the CO and CO_2 levels are comparable to those in a laminar flame at a moderate strain rate between 100 and 400 s^{-1} . At $x/d = 50$ in flame B the CO and CO_2 results fall between the curves for equilibrium and for the $a = 10\text{ s}^{-1}$ strained laminar flame. Trends in the measured conditional means of CO , CO_2 , and OH indicate a strong coupling between flow and reaction (effective Damköhler numbers are of

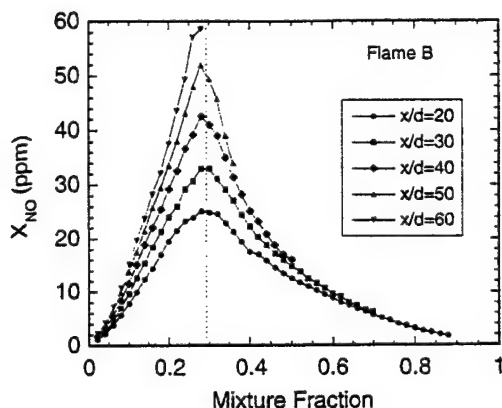


Fig. 17. Streamwise evolution of the conditional mean of nitric oxide mole fraction in flame B.

order unity). Thus, the quantitative prediction of the conditional statistics of these species is expected to be a useful test of submodels for coupling turbulence and chemistry.

Figure 17 shows the measured conditional means of NO mole fraction in flame B. Thermal NO formation is sufficiently slow that NO concentrations remain far below equilibrium everywhere in these flames ($Da_{NO} \ll 1$). Consequently, there is a steady increase in conditional mean NO mole fraction as one moves downstream in each flame, so long as there is some fluid within the NO-forming interval in mixture fraction near the stoichiometric condition.

Radial Dependence of Conditional Means

All of the conditional mean results discussed until now were generated using data from complete radial profiles. Some radial dependence of the conditional statistics is expected in turbulent jet flames, but previous experimental studies have indicated that this dependence is relatively weak. Barlow and Carter [38] examined this issue in hydrogen jet flames and reported that the radial dependence of conditional means of measured scalars was minor in the lower half of the flames and negligible in the upper half. Figure 18 shows conditional mean curves for selected scalars from seven separate radial locations at $x/d = 30$ in flame A. The statistical sample size is limited (typically 30 to 60 samples per mixture-fraction bin), but these data confirm that there is only a relatively weak radial

dependence of the measured conditional means at this location in flame A. OH shows the greatest variation, with a spread of about 10% between the different curves near the stoichiometric mixture fraction and larger percentage differences for fuel-lean conditions.

Near the stoichiometric mixture fraction and at lean conditions, the OH curves in Fig. 18 tend to shift downward as radius increases from 5 mm to 15 mm. This is the region where the radial gradient of the mean axial velocity is steepest. Therefore, larger radius corresponds on average to lower velocity, longer residence time, and more time for the three-body recombination reactions to bring OH levels down toward equilibrium at a given mixture fraction. Thus, the trend in X_{OH} in Fig. 18 is consistent with the effects of Damköhler number discussed above. The curves for X_{CO} in Fig. 18 show some separation near the stoichiometric condition, and the CO_2 trend is also qualitatively consistent with changes in Damköhler number. CO_2 mole fraction tends to increase with increasing radius, corresponding to the increase in effective Damköhler number. Curves for the other measured scalars are generally within $\pm 5\%$ of the result based on averaging all data from the full radial profile, and such Damköhler-related trends are less obvious.

The radial dependence of conditional means is slightly greater at $x/d = 20$ in flame A (not shown) than at $x/d = 30$ but less at all other measured streamwise locations in the two flames. These results indicate that for fully connected simple jet flames, such as the present cases, the assumption of radial independence of conditional means is a reasonable approximation. One would not expect significant modeling errors to result from the use of this assumption in the context of conditional moment closure (CMC) calculations of this type of flame. Similarly, in the context of flamelet models, one would not expect significant errors to result from the use of a single value of the scalar dissipation rate to represent the mean scalar values at a given streamwise location. This latter conclusion was already apparent from Fig. 11. At the same time, the data confirm that in this jet flame the radial dependence of conditional means is greater than the axial dependence. For example, a radial displacement of less than one

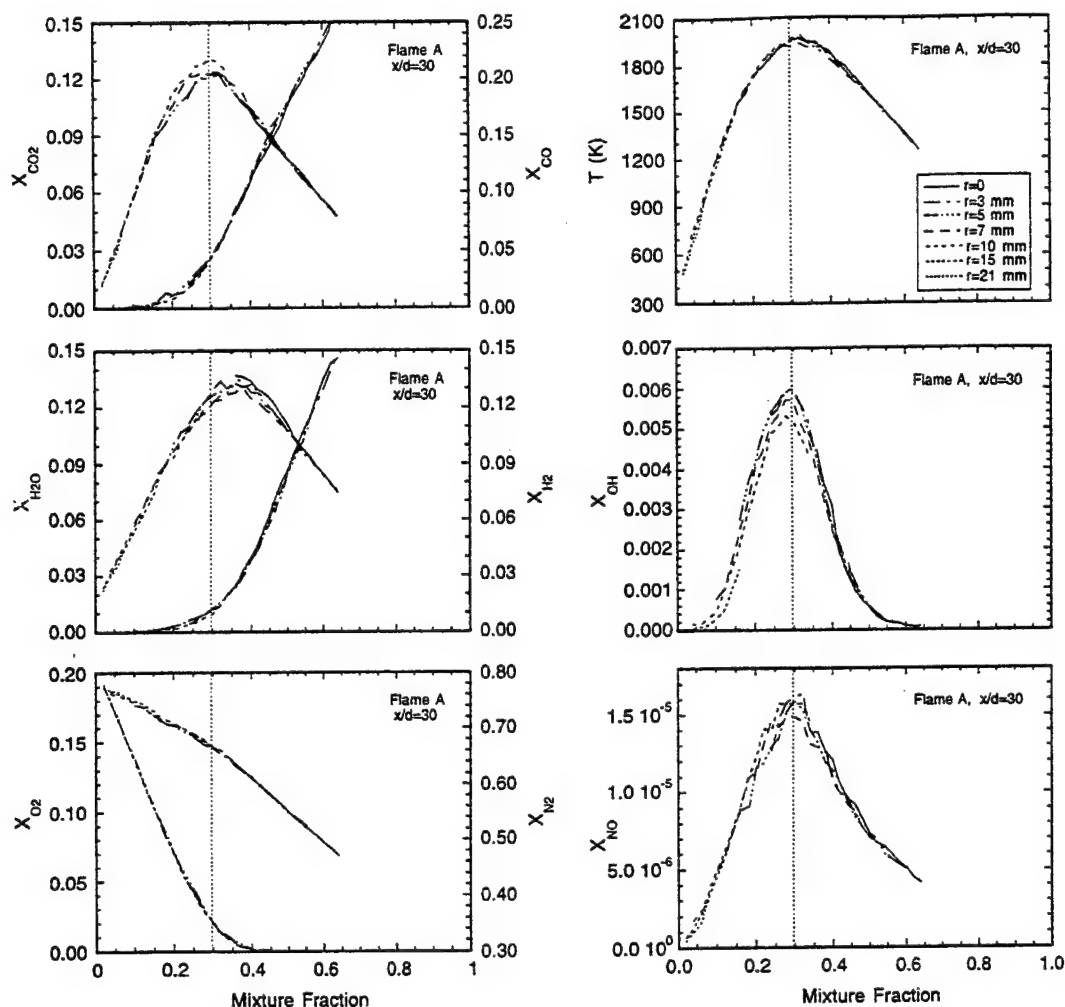


Fig. 18. Conditional means of selected scalars determined at seven separate radial locations at $x/d = 30$ in flame A.

nozzle diameter from $r = 3$ mm to $r = 7$ mm (Fig. 18) causes changes in X_{CO_2} and X_{OH} at the stoichiometric mixture fraction that are comparable to the effects of moving more than 10 times that distance in the axial direction from $x/d = 20$ to $x/d = 30$ (Figs. 16 and 17).

The conditional mean curves in Fig. 18 each span a limited interval in mixture fraction because the mixing characteristics of this flame do not bring all values of the mixture fraction to any single location. Very lean samples do not penetrate to the centerline, and the richest samples do not stray far from the centerline. The pdf's of mixture fraction at each of the

radial locations shown in Fig. 18 are plotted in Fig. 19. Here, the pdf's are not smooth because of the relatively small sample size of 800–1000 for each location, and they are broadened somewhat by noise, the magnitude of which can be estimated from the calibration results in Fig. 1. However, these pdf's serve to quantify the mixing statistics in these flames, and they provide another important point of comparison with turbulent combustion models. Corresponding pdf's for other locations may be generated from the data base [17], as radial position is tabulated in the single-shot data files.

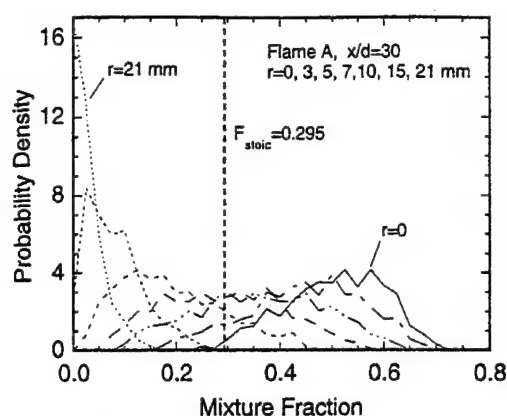
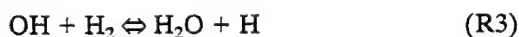


Fig. 19. Pdfs of mixture fraction at the seven locations from Fig. 18.

Deviation from Partial Equilibrium

Partial equilibrium assumptions, when valid, can be useful for combustion models and for the analysis of experimental data because they allow the concentrations of certain species that are not calculated or measured to be derived from those that are. If one or more of the rapid binary reactions

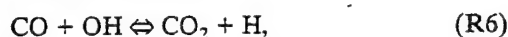


is in equilibrium, then a state of partial equilibrium exists, even if other slower reactions in the system are far from being equilibrated. Note that R5 is the sum of R1 and R2, rather than an elementary reaction in itself.

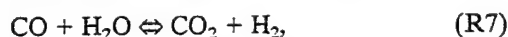
Partial equilibrium of these reactions in laminar and turbulent flames of various fuels has been considered by many authors [5, 20, 24, 37–41, and references therein]. Detailed laminar flame calculations have indicated that these reactions are equilibrated, or nearly so, only at temperatures above ~1700 K in hydrogen flames and under more restrictive conditions in methane flames. Barlow et al. [20] used reaction R4 to determine O atom concentrations at high-temperature conditions in a turbulent hydrogen jet flame, based on simultaneous mea-

surements of OH, H₂O, and temperature. However, experimental verification of the conditions under which partial equilibrium is achieved is difficult because it requires accurate measurements of temperature and multiple species. Still, quantitative information on deviations from partial equilibrium in turbulent flames is expected to be useful for the process of evaluating models for the coupling of turbulence and chemistry and for understanding the limitations of some reduced mechanisms.

Drake and Blint [37] provide an extensive discussion of the structure of opposed-flow laminar flames of CO/H₂/N₂ fuel (same ratios as used here), including effects of differential diffusion, superequilibrium radical formation, and deviations from partial equilibrium. The CO oxidation reaction



which is slower than the shuffle reactions R1–R5, is an important heat release step in CO and hydrocarbon flames. Combining R6 and R3 yields the water–gas shift reaction



in which all species are measured in the present experiments. Drake and Blint [37] observed that the water–gas shift reaction achieved partial equilibrium in laminar calculations of CO/H₂/N₂ flames only at low strain rates and for temperatures above 1900 K.

Here we consider deviations from partial equilibrium in the turbulent flames and compare the results with laminar flame calculations at intermediate strain rates, which appear to be representative of conditions within these turbulent flames. For this purpose we define the ratio

$$R_{\text{wg}} = ([\text{CO}_2][\text{H}_2]/[\text{CO}][\text{H}_2\text{O}])/K_{\text{EQ7}},$$

where the species concentrations are either measured or taken from the laminar flame calculations and K_{EQ7} is the equilibrium constant for the water–gas shift reaction, R7. R_{wg} is unity when this reaction is equilibrated. An analogous ratio for the shuffle reaction R5 may be defined as

$$R_{\text{sh}} = ([\text{OH}]^2/[\text{O}_2][\text{H}_2])/K_{\text{EQ5}}.$$

However, we do not report results on R_{sh} in the present turbulent flames because the uncertain-

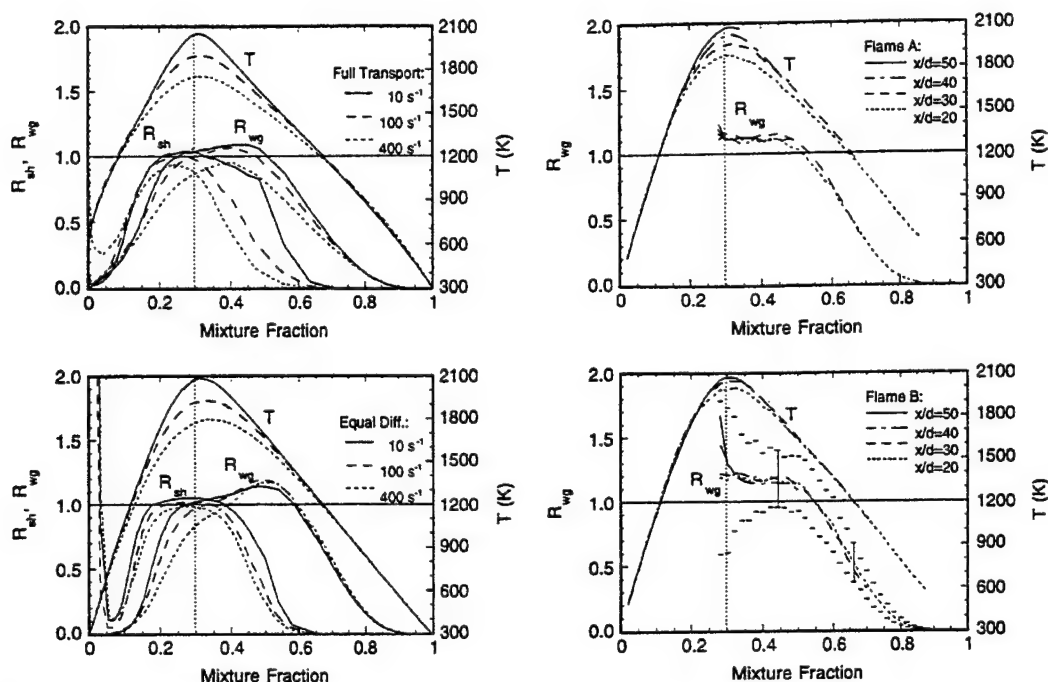


Fig. 20. Results for the partial equilibrium ratios R_{wg} and R_{sh} and the temperature in laminar flame calculations (left) and turbulent flame measurements (right) at the strain rates and streamwise locations indicated. The vertical dashed line corresponds to the stoichiometric value of the mixture fraction.

ties are too large for the results to be quantitatively useful. The reason is that, for all conditions in the present jet flames, at least one of the species, OH, O_2 , or H_2 , is present only in low concentration.

Figure 20 (left side) shows curves of R_{wg} and R_{sh} versus mixture fraction for laminar flame calculations at strain rates of $a = 10 \text{ s}^{-1}$, 100 s^{-1} , and 400 s^{-1} , with full transport and with equal diffusivities. Corresponding curves of temperature are also plotted. (Note that for the full transport calculations the scalar dissipation at the stoichiometric condition depends on the definition of mixture fraction. The Bilger formulation for mixture fraction yields scalar dissipation values in the full transport cases that are roughly 30% lower than those in the equal diffusivity cases.) It is clear that deviations from partial equilibrium in these laminar calculations depend on stoichiometry and transport, as well as on temperature. Consider first the shuffle reaction R5. Taking 10% deviation of R_{sh} from unity as an arbitrary criteria for departure from equilibrium, it is apparent that partial equilib-

rium of R5 holds over a wider temperature range when all species diffusivities are set equal to the thermal diffusivity. Regardless of the transport assumption, partial equilibrium of R5 holds to a lower temperature on the fuel-lean side than on the fuel-rich side. On the fuel-rich side there are significant differences between the curves for the full-transport and equal-diffusivity calculations. The graphs on the right side of Fig. 20 show the conditional mean curves of R_{wg} in turbulent flames A and B at streamwise locations of $x/d = 20, 30, 40$, and 50 . R_{wg} is not plotted for fuel-lean mixture fractions because concentrations of CO and H_2 become too low to be measured with useful accuracy. The conditional rms fluctuations in R_{wg} at $x/d = 40$ are plotted as error bars ($\pm\sigma$), and it is apparent that these fluctuations increase rapidly as CO and H_2 disappear near the stoichiometric mixture fraction.

In Fig. 21 the same results for R_{wg} in the laminar and turbulent flames are plotted versus temperature. The temperature coordinate makes even more obvious the influences of stoichiometry and transport on departures from equilib-

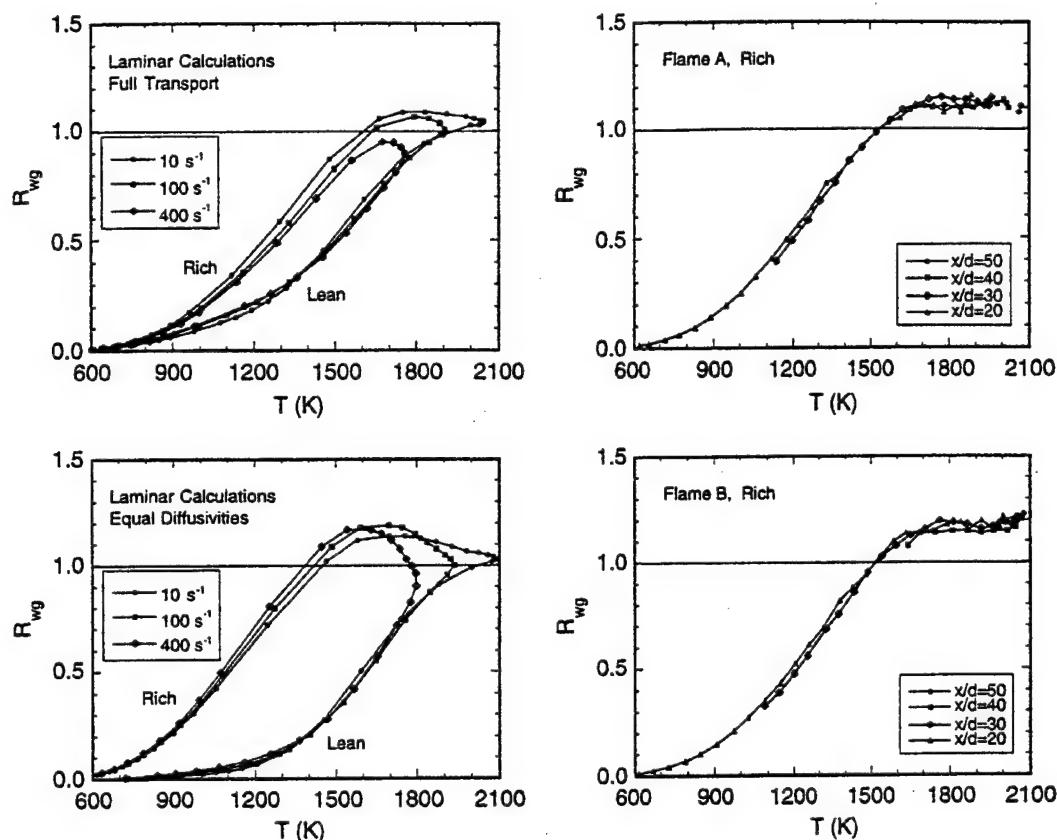


Fig. 21. Results for R_{wg} plotted vs. temperature for laminar flame calculations (left) and turbulent flame measurements (right). Only fuel-rich results are plotted for the turbulent flames.

rium of the water-gas shift reaction in the laminar flame calculations. There are distinct lean and rich legs, and the curves are quite different for the two transport scenarios. There is not a clear asymptotic trend toward partial equilibrium ($R_{wg} = 1$) at the highest temperatures for the strain rates covered by these laminar calculations.

Systematic uncertainty in the conditional means of R_{wg} may be estimated at selected points based on the individual uncertainties in Table 1 and the sensitivity of the equilibrium constant to error in the conditional mean temperature. Errors in species and temperature are assumed to be independent for this purpose. For the conditions in flame A at $x/d = 30$ and 0.4 mixture fraction the uncertainty in R_{wg} is estimated to be $\pm 9\%$ or about ± 0.01 , based on lower values from Table 1. At a mixture fraction of 0.6, the estimated uncertainty in R_{wg} roughly

doubles because temperatures are in the middle of the range where the CO and H₂ calibrations are interpolated and the higher uncertainties in Table 1 apply. Uncertainty in R_{wg} also increases as mixture fraction approaches the stoichiometric condition and the concentrations of CO and H₂ become small. This trend is most obvious in Fig. 20 at the fuel-lean ends of the curves for $x/d = 40$ and $x/d = 50$ in flame B, where scalar dissipation rates are lowest. Away from the stoichiometric condition, the relative uncertainty in comparing curves at different streamwise locations in the same flame depends on calibration drift and is expected to be below 5%.

Within the limits imposed by these experimental uncertainties, there are a few observations to be made regarding the conditional mean results for R_{wg} in the turbulent flames. First, there is no significant streamwise evolution within each flame in the partial-equilibrium

behavior of the water-gas shift reaction. Second, R_{wg} reaches a plateau between 1.1 and 1.2 at temperatures above 1700 K. The failure of the measured values to approach unity at the highest measured temperatures may result from errors in background and crosstalk corrections that become important when concentrations of CO and H_2 become small. Third, with the exception of these near-stoichiometric results, the conditional means from the turbulent flames fall between the curves for the full-transport and equal-diffusivity calculations. Finally, partial equilibrium of the water-gas shift reaction does not appear to be a good approximation for these jet flames. If it is achieved at all (within 10%), partial equilibrium of the water-gas shift reaction will only hold for a small fraction of conditions in these flames.

CONCLUSIONS

Detailed scalar measurements have been reported for two simple turbulent jet flames of $CO/H_2/N_2$ fuel (40%/30%/30%) having the same Reynolds number of 16,700 but different nozzle diameters. The flames are both fully attached, and there is no evidence of localized extinction at the measured locations or of the penetration of oxygen into the jet core due to lift off or extinction near the flame base. These results, combined with the three-component velocity measurements reported separately by Flury [16], are believed to constitute the most complete data set available for this type of flame. With regard to the systematic evaluation of turbulent combustion models, these geometrically simple flames represent a modest increment in chemical kinetic complexity over hydrogen jet flames, and they may be addressed by a wide range of nonpremixed combustion models. The complete data archives, including both mole fractions and mass fractions, have been made available on the Internet to facilitate comparisons with model calculations. Aspects of the measured results have been presented and discussed in terms of their relevance to the testing of turbulent combustion submodels. The main conclusions of this study are as follows:

Axial and radial profiles of Favre-averaged temperature and major species mole fractions

are similar when distance is scaled by the nozzle diameter. However, at a given streamwise distance, x/d , the OH levels are lower and the NO levels are higher in the larger flame, due to the lower scalar dissipation rates and longer residence times.

Comparisons with two types of laminar flame calculations have shown that the conditional means of major species mole fractions in the turbulent flames are better approximated by laminar flame calculations that prescribe equal diffusivities. This indicates that turbulent stirring has a greater influence than molecular diffusion in determining major species mole fractions for the flow conditions and measurement locations considered in the present experiments.

Analysis of elemental mixture fractions of hydrogen and carbon and of the differential diffusion parameter z , defined as the difference between these elemental mixture fractions, has confirmed that differential diffusion effects in the turbulent flames are small compared to those in laminar flames computed with the usual Chemkin treatment of molecular transport.

The streamwise evolution of conditional means of CO, CO_2 , and OH in each flame, as well as the differences in the two flames between conditional means of these species at a given streamwise location, x/d , indicate a strong coupling between time scales of the flow and time scales of the reactions that control departure of these species from equilibrium (effective Damköhler number of order unity). Thus, the quantitative prediction of conditional statistics of CO, CO_2 , and OH in these flames is expected to be a useful test of submodels for coupling turbulence and chemistry.

There is some radial dependence of the conditional means of measured scalars in these flames, and this dependence is consistent with considerations of the effective Damköhler numbers of the reactions controlling those species. However, the radial variations in conditional means remain relatively small, such that statistics based on data from a complete profile yield a reasonable representation of scalar structure.

Partial equilibrium of the water-gas shift reaction is not achieved in these flames (greater than 10% deviation), except perhaps in the small fraction of samples corresponding to the highest temperatures.

Work at Sandia was supported by the United States Department of Energy, Office of Basic Energy Sciences. C.D.C. was supported by the AFOSR under Air Force Contract F33615-92-2202. Informative discussions with R. Bilger, G. Kosály, and H. Pitsch during the preparation of this paper are gratefully acknowledged. Velocity measurements by M. Flury at ETH Zurich were supported by the Bundesamt für Energiewirtschaft.

REFERENCES

- Barlow, R. S., and Carter, C. D., *Combust. Flame* 97:261–280 (1994); and *Combust. Flame* 104:288–299 (1996).
- Meier, W., Vydorov, A. O., Bergmann, V., and Stricker, W., *Appl. Phys. B* 63:79–90 (1996).
- Neuber, A., Krieger, G., Tacke, M., Hassel, E. P., and Janicka, J., *Combust. Flame* 113:198–211 (1998).
- Web site of the International Workshop on Measurement and Computation of Turbulent Nonpremixed Flames, www.ca.sandia.gov/tdf/Workshop.html, includes data archives, information on computational submodels, and results of collaborative comparisons of measured and modeled results for various turbulent flames.
- Chen, J.-Y., Chang, Y.-C., and Koszykowski, M., *Combust. Sci. Technol.* 110:505 (1996).
- Barlow, R. S., Smith, N. S. A., Chen, J.-Y., and Bilger, R. W., *Combust. Flame* 117:4–31 (1999).
- Schlatter, M., Ferreira, J. C., Flury, M., and Gass, J., *Twenty-Sixth Symposium (International) on Combustion*, The Combustion Institute, Pittsburgh, 1996, pp. 2215–2222.
- Strahle, W. C., *Prog. Energy Combust. Sci.* 12:253–255 (1986).
- Faeth, G. M., and Samuelsen, G. S., *Prog. Energy Combust. Sci.* 12:305–372 (1986).
- Drake, M. C., and Koilman, W., *Prog. Energy Combust. Sci.* 12:373–392 (1986).
- Masri, A. R., Dibble, R. W., and Barlow, R. S., *Prog. Energy Combust. Sci.* 22:307–362 (1996).
- Masri, A. R., and Dibble, R. W., *Twenty-Second Symposium (International) on Combustion*, The Combustion Institute, Pittsburgh, 1988, pp. 607–618.
- Correa, S. M., and Gulati, A., *Twenty-Second Symposium (International) on Combustion*, The Combustion Institute, Pittsburgh, 1988, pp. 599–606.
- Correa, S. M., and Gulati, A., *Combust. Flame* 89:195–213 (1992).
- Masri, A. R., Dibble, R. W., and Barlow, R. S., *Combust. Flame* 91:285–309 (1992).
- Flury, M., Ph.D. thesis and paper in preparation, ETH Zurich, Switzerland.
- CO/H₂/N₂ jet flame data base under Experimental Data Archives on the web site for the International Workshop on Measurement and Computation of Turbulent Nonpremixed Flames, www.ca.sandia.gov/tdf/Workshop.html.
- Carter, C. D., and Barlow, R. S., *Optics Lett.* 19:299–301 (1993).
- Nguyen, Q. V., Dibble, R. W., Carter, C. D., Fiechtner, G. J., and Barlow, R. S., *Combust. Flame* 105:499–510 (1996).
- Barlow, R. S., Fiechtner, G. J., and Chen, J.-Y., *Twenty-Sixth Symposium (International) on Combustion*, The Combustion Institute, Pittsburgh, 1996, pp. 2199–2205.
- Paul, P. H., *JQSRT* 51:511–524 (1994).
- Paul, P. H., Gray, J. A., Durant Jr., J. L., and Thoman Jr., J. W., *ALAA J.* 32:1670–1675 (1994).
- Barlow, R. S., and Frank, J. H., *Twenty-Seventh Symposium (International) on Combustion*, The Combustion Institute, Pittsburgh, 1998, pp. 1087–1095.
- Smith, L. L., Dibble, R. W., Talbot, L., Barlow, R. S., and Carter, C. D., *Combust. Flame* 100:153–160 (1995).
- Bilger, R. W., Stårner, S. H., and Kee, R. J., *Combust. Flame* 80:135–149 (1990).
- Peters, N., and Rogg, B., *Reduced Mechanisms for Applications in Combustion Systems*, Springer-Verlag, Heidelberg, 1993.
- Bilger, R. W., and Dibble, R. W., *Combust. Sci. Technol.* 28:161–172 (1982).
- Bergmann, V., Meier, W., Wolff, D. and Stricker, W., *Appl. Phys. B* 66:489–502 (1998).
- Dally, B. B., Masri, A. R., Barlow, R. S., and Fiechtner, G. J., *Combust. Flame* 114:119–148 (1998).
- Kerstein, A. R., *J. Fluid Mech.* 216:411–435 (1990).
- Kosály, G., Personal communication of notes on “Mixture fraction based closure models of turbulent nonpremixed combustion,” May 1997.
- Nilsen, V., and Kosály, G., *Combust. Flame* 117:493–513 (1999).
- Pitsch, H., “Unsteady Flamelet Modeling of Differential Diffusion in Turbulent Diffusion Flames,” submitted to *Combust. Flame*.
- Barlow, R. S., Dibble, R. W., Chen, J.-Y., and Lucht, R. P., *Combust. Flame* 82:235–251 (1990).
- Mungal, M. G., and Frieler, C. E., *Combust. Flame* 71:23–34 (1988).
- Broadwell, J. E., and Mungal, M. G., *Twenty-Second Symposium (International) on Combustion*, The Combustion Institute, Pittsburgh, 1988, pp. 579–587.
- Drake, M. C., and Blint, R. J., *Combust. Sci. Technol.* 61:187–224 (1988).
- Barlow, R. S., and Carter, C. D., *Combust. Flame* 104:288–299 (1996).
- Warnatz, J., Maas, U., and Dibble, R. W., *Combustion*, Springer-Verlag, Berlin, 1996.
- Smyth, K. C., and Tjossem, P. J. H., *Combust. Flame* 79:366–380 (1990).
- Barlow, R. S., Dibble, R. W., Stårner, S. H., and Bilger, R. W., *Twenty-Second Symposium (International) on Combustion*, The Combustion Institute, Pittsburgh, PA, 1988, pp. 579–587.

Received 15 January 1999; revised 20 August 1999; accepted 26 August 1999

3.1.2.2 Counterflow Diffusion Flames. Studies on counterflow diffusion flames have provided benchmark experimental data and yielded valuable insight into the response of the flame to strain rate. However, in practical combustion devices, flames are subject to severe unsteadiness resulting from the random motion of vortices. To retain the simplicity offered by planar diffusion flames, unsteadiness is imposed on counterflow flames by modulating the air flow. A piston is used to produce a vortex that travels within the surrounding oxidizer flow. The interaction of this vortex and the planar diffusion flame was the focus of this effort. In the paper entitled "Interaction of a Vortex with a Flat Flame Formed Between Opposing Jets of Hydrogen and Air" (see pp. 285-292), the dynamic interactions of an induced vortex and a planar diffusion flame are reported. Numerical and experimental results are compared for vortex-flame interactions in the publication entitled "Dynamic Interactions of a Flame and an Isolated Vortex" (see pp. 293-313). Rayleigh, PLIF, and PIV techniques were applied to the study of the flame-vortex interaction, and the results are documented in the paper entitled "Regimes of Interaction Between a Nonpremixed Hydrogen-Air Flame and an Isolated Vortex" (see pp. 314-326). The integration of diagnostic techniques led to the simultaneous measurement of OH concentration and velocity fields, which is reported in the publication entitled "Application of Imaging Techniques to the Study of Vortex-Flame Interactions" (see pp. 327-338). The effects of injecting noble gases into the planar laminar flame are reported in the paper entitled "Vortex Injection of Noble Gases in an Opposed-Jet Burner" (see pp. 339-342). The injection of multiple vortices into the planar laminar flame was investigated, and the results are reported in the publication entitled "Injection of a Single and Multiple Vortices in an Opposed-Jet Burner" (see pp. 343-354). Comparison of numerical and experimental results on vortex-flame interactions led to the construction of a spectral interaction diagram. Eight interaction types have been found, emphasizing the relative importance of competing physical phenomena such as straining, curvature, wrinkling, rollup, and extinction. The results of this study are reported in the paper entitled "Regimes of Nonpremixed Flame/Vortex Interactions" (see pp. 355-368).

INTERACTION OF A VORTEX WITH A FLAT FLAME FORMED BETWEEN OPPOSING JETS OF HYDROGEN AND AIR

V. R. KATTA,¹ C. D. CARTER,¹ G. J. FIECHTNER,¹ W. M. ROQUEMORE,² J. R. GORD² AND J. C. ROLON³

¹*Innovative Scientific Solutions, Inc.*

2766 Indian Ripple Road

Dayton, OH 45440-3638, USA

²*Propulsion Directorate*

Air Force Research Laboratory

Wright-Patterson Air Force Base, OH 45433-7103, USA

³*E.M2.C Laboratory, CNRS*

Ecole Centrale Paris

92295 Chatenay-Malabry Cedex, France

Studies on individual vortex-flame interactions constitute important elements for the understanding of the turbulent-flame structure. Vortices having sufficiently high normal velocity can pass through the flame by extinguishing it locally. In several circumstances, they deform the flame surface significantly before attaining extinction conditions. The development of curvature on the flame surface, especially in hydrogen flames, could lead to different quenching patterns. An experimental/numerical investigation is performed to explore possible quenching patterns in opposing-jet diffusion flames. A diluted hydrogen-nitrogen mixture is used as the fuel. Vortices are driven toward the flame surface with different velocities from the air side. The changes in the structure of the flame during its interaction with the incoming vortex are recorded by measuring instantaneous OH-concentration fields using the laser-induced fluorescence (LIF) technique. A time-dependent CFDC code that incorporates 13 species and 74 reactions is used for the simulation of these vortex-flame interactions. Both the experiments and calculations have identified two types of quenching patterns; namely, point and annular. It is found that when an air-side vortex is forced toward the flame at a relatively high speed, then the flame at the stagnation line quenches, resulting in a well-known point-quenching pattern. On the other hand, when the vortex is forced at a moderate speed, the flame surface deforms significantly, and quenching develops in an annular ring away from the stagnation line, resulting in an unusual annular-quenching pattern. Detailed analyses performed just before the development of annular quenching and 1 ms later suggest that this unusual annular quenching did not result from the strain rate. Based on the understanding gained from previous investigations on curvature effects in coaxial hydrogen jet flames and the findings made in the present study, it is argued that such quenching develops as a result of the combined effect of preferential diffusion and flame curvature.

Introduction

Recently, numerous investigations (experimental and numerical) [1-3] have been performed to quantify the scalar structure of steady state, aerodynamically strained, planar diffusion flames. Such studies on counterflow diffusion flames have not only provided benchmark experimental data but also yielded valuable insight into the flame behavior in response to strain rate. However, in practical combustion devices, flames are subjected to severe unsteadiness resulting from the random motion of vortices [4,5]; this has led to studies of unsteady counterflow flames. To retain the simplicity offered by planar diffusion flames, unsteadiness is imposed on counterflow flames by fluctuating the fuel and air jets simultaneously and sinusoidally [6,7]. These studies have demonstrated that the unsteady flames can be stretched beyond the steady-state extinction limit.

During vortex-flame interactions, which are often considered as the building blocks for statistical theories of turbulence, the flame surface is subjected not only to unsteadiness but also to deformation. Studies of Law [8], Mizomoto et al. [9], and Takagi and Xu [10] have shown that the structure of a flamelet depends on the curvature and the preferential diffusion associated with species having different molecular weights. To investigate the effects of curvature on flame structure, both theoretical and experimental studies have been initiated. In particular, experiments designed by Roberts et al. [11] and Rolon [12] have created great interest, especially because of their unique abilities to shoot a well-characterized vortex toward the flame surface.

Several investigators have developed models [13-15] for the study of vortex-flame interactions in opposing-jet flames. In all of these models, it is

assumed that an artificially created vortex pair (by specifying the vorticity field) interacts with a flat flame formed in a parallel flow. Although such an assumption has advantages in exploring interesting aspects of the vortex-flame interactions, these investigations do not represent the actual interactions in opposing-jet flames; hence, they could not yield direct comparisons between predictions and measurements.

Recent advances in computer-hardware technology and the need for improving the understanding of combustion phenomena under complex practical situations have led to the development of two- and three-dimensional computational fluid dynamics models that incorporate detailed chemical kinetics [16,17]. However, to our knowledge, no complete simulation of the counterflow diffusion flame has yet been reported. Such simulations would not only eliminate the concerns of the simplified analyses but also provide a valuable tool for studies of vortex-flame interactions in counterflow premixed [11] and diffusion [12] flames.

This paper describes a numerical and experimental study performed on the vortex-flame interactions in a hydrogen opposing-jet diffusion flame. The Computational Fluid Dynamics with Chemistry (CFDC) code was validated by direct simulation of the steady-state counterflow diffusion flame. The calculated instantaneous flowfield that reveals the annular-quenching pattern is compared with the measured OH-concentration image. The processes leading to annular quenching during the vortex-flame interaction are investigated by analyzing the flame structures obtained at different locations and times.

Mathematical Model

Time-dependent, axisymmetric Navier-Stokes equations written in the cylindrical-coordinate (z - r) system are solved along with species- and energy-conservation equations [18]. A detailed chemical-kinetics model has been used to describe hydrogen-air combustion. This model consists of 13 species; namely, H_2 , O_2 , H , O , OH , H_2O , HO_2 , H_2O_2 , N , NO , NO_2 , N_2O , and N_2 . A detailed chemical-kinetics model having 74 reactions among the constituent species is used, and the rate constants for this H_2 - O_2 - N_2 reaction system were obtained from Ref. [19].

Temperature- and species-dependent property calculations are incorporated in the model. The enthalpy of each species is calculated from polynomial curve fits that were developed for the temperature range of 300–5000 K. The viscosity and thermal conductivity of individual species are estimated from the Chapman-Enskog collision theory, and the mixture properties are obtained using Wilke's semiempirical formulae. The effective binary-diffusion coefficient

of the individual species in the local mixture is calculated using molecular dynamics and the Lennard-Jones potentials.

The governing equations are integrated on a non-uniform staggered-grid system. An orthogonal grid having rapidly expanding cell sizes in both the axial and radial directions is employed. The finite-difference forms of the momentum equations are obtained using an implicit QUICKEST scheme [20,21], and those of the species and energy equations are obtained using a hybrid scheme of upwind and central differencing. At every time step, the pressure field is calculated by solving the pressure Poisson equations simultaneously and utilizing the LU (Lower and Upper diagonal) matrix-decomposition technique.

Experimental Setup

The burner geometry used for the vortex-flame-interaction studies in opposing-jet flames was initially designed by Rolon [12]. It consists of 25-mm-diameter inner nozzles, 40-mm-diameter outer nozzles, and syringe tubes of 5-mm diameter. Fuel (a mixture of hydrogen and nitrogen) and air are fed through the upper- and lower-inner nozzles, respectively. Nitrogen was used in the outer nozzles to shield the flame from the ambient air. Even though the tip of the syringe tube is placed 5 mm upstream of the inner nozzle exit in the experiment, it has been assumed to be flush with the nozzle exit in the present numerical investigations. In a typical experiment, a steady-state opposing-flow jet flame is initially established by flowing fuel and air at specified flow rates through the respective nozzles. Vortices are shot toward the flame surface from either the fuel or the air side by rapidly injecting a specified amount of fluid from the respective syringe tube. The vortices are usually characterized [12] by the amount and duration of fluid injection. The resulting changes in the structure of the flame because of its interaction with the approaching vortex are recorded by measuring instantaneous relative OH-concentration fields using the laser-induced fluorescence (LIF) technique.

Results and Discussion

Experiments were performed using this burner for different flow conditions and vortex sizes and shapes. In the present study, the flat flame formed between the fuel and air jets having velocities of 0.69 and 0.5 m/s, respectively, is considered. The hydrogen-to-nitrogen molar ratio used for the fuel jet is 0.38. Calculations for this axisymmetric flame were made using a nonuniform 301×121 mesh system that yielded a mesh spacing of 0.1 mm in both axial (z) and radial (r) directions in the region of interest.

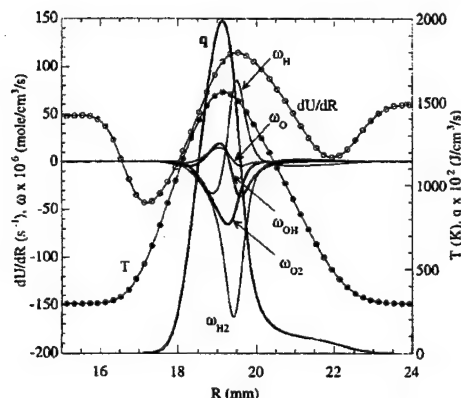


FIG. 1. Structure of steady-state flame established between 37.6% H_2 diluted with N_2 and air jets. Air-side strain rate induced on the flame is 48 s^{-1} .

Steady-State Flame Structure

The CFDC model developed for the simulation of a time-dependent jet diffusion flame was previously validated by simulating the counterflow jet diffusion flames studied by Sung et al. [22] and the coaxial flames investigated by Grisch et al. [23]. The computed flame structure at the stagnation line of the steady-state flame used in this study is shown in Fig. 1 in the form of distributions of velocity gradient normal to the flame (dU/dR), molar production rates of various species (ω_i), temperature (T), and heat release rate (q). Here R represents the line that is normal to the flame surface. Note that since the flame is symmetric, the normal to the flame surface at this location coincides with the stagnation line. The flame structure shown in Fig. 1 is not compared with the experimental one because of the lack of quantitative data; however, it compares well with that of a typical opposing-jet diffusion flame [22]. On the other hand, the calculations made for slightly different flow rates yielded good agreement with the experimental data of Rolon [12].

An opposing-jet flame is usually characterized by the air-side strain rate (K_{air}), which may be obtained by calculating the maximum velocity gradient on the air side of the flame [3]. The 48 s^{-1} strain rate of the steady-state flame in Fig. 1 represents that of a weakly strained flame. In general, the peak strain rate on the fuel side (60 s^{-1}) will be greater than that on the air side as a result of the difference in the density of the two jets. Although the peaks in production rates of O and OH radicals appear on the air side of the flame (peak temperature or heat-release-rate location), the H radicals are produced at the highest rate on the fuel side. Because the flame surface is flat (zero curvature) at this location, the

flame structure is not affected by the preferential diffusion of various species having different Lewis numbers in a hydrogen flame.

The steady-state strain rate on the opposing-jet flame can be increased by gradually increasing the velocities of the fuel and air jets. Calculations were repeated by varying jet velocities, and it was found that a stable steady-state flame can be obtained for maximum fuel and air jet velocities of 16 and 14 m/s, respectively. These velocities yielded an air-side strain rate (K_{air}) and flame temperature of 1410 s^{-1} and 1130 K, respectively; these values agree favorably with calculations made by Gutheil et al. [24] using full chemistry for hydrogen-air combustion.

Vortex-Flame Interaction

As discussed earlier, vortices are shot toward the flame surface from the air side by injecting a specified amount of fluid (2.2 cm^3 of air) through the syringe tube. Vortex evolution and its interaction with the flame surface depend on the injection time. In general, with the shorter injection times, the generated vortices travel faster toward the flame surface and affect its structure as the local flow time scales approach the chemical time scales. When the former time scales decrease to a certain level, one might expect localized quenching on the flame surface. On the other hand, the flame surface develops more curvature during the vortex-flame interaction with a slower vortex as the flow time scales become comparable to the diffusion time scales. Because of the preferential diffusion of different species in hydrogen flames, the curvature of the flame can also affect its chemical structure, which means that in hydrogen flames both the faster- and slower-moving vortices could affect the flame structure.

Experiments were conducted on vortex-flame interactions by changing the injection time. Instantaneous flame structures were obtained by recording OH-concentration distributions. As expected, for shorter injection times, the vortex was able to quench the flame at the stagnation line (point quenching) and penetrate through the hole formed on the flame surface. Interestingly, for longer injection times, the vortex deformed the flame surface significantly, and it was observed that quenching on the flame surface first occurs annularly at a location 5-mm radially outward from the stagnation line and then propagates toward the stagnation line ($r = 0$). The OH image obtained for the 10-ms injection-time condition is shown in Fig. 2. This instantaneous image was obtained using the LIF technique. It is known that the concentration of OH in a flame correlates well with the reaction zone. Fig. 2 suggests that the vortex, having a diameter of 13 mm, traveling from the air side has shifted the flame (reaction zone) at the stagnation line by about 0.6 diameter. Note that because the steady-state flame used in this

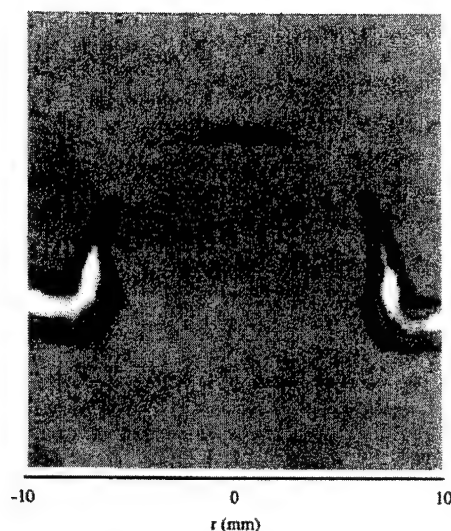


FIG. 2. Relative concentration of OH measured 10 ms after firing the vortex toward the flame. Experiment was performed using the LIF technique.

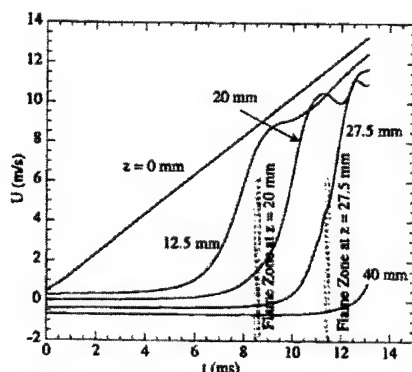


FIG. 3. Variation of local normal velocities with time obtained at four locations along the stagnation line. Straight line with a slope of 10^3 m/s/s at $z = 0$ represents the perturbation velocity imposed at the exit of the air nozzle.

study is a weakly strained one, the OH concentration in the unperturbed flame section (bright yellow) is much higher than that in the highly strained flame zone (dark blue) at the center. Disappearance of OH in the region $4.2 \text{ mm} < r < 5.2 \text{ mm}$ suggests that the flame is quenched. A few milliseconds later the flame in the region $r < 5.3 \text{ mm}$ is completely extinguished.

The phenomenon of flame extinction in an annular

region rather than in the intuitively expected region around the stagnation line could result from either (1) maximum strain rate developing in the region other than at the stagnation line or (2) combined effect of preferential diffusion and flame curvature reducing the reaction rates at a location other than the maximum-strain-rate region. To investigate the role of these possible effects during the vortex-flame interaction shown in Fig. 2, calculations were performed using the time-dependent CFDC code discussed earlier. Flow conditions for the steady-state flame were matched with those used in the experiment, and the computed flame structure is shown in Fig. 1. The unsteady simulations were then performed by injecting air through the central syringe tube in such a way that the velocity at the exit increased linearly at a rate of 10^3 m/s/s.

The axial velocities recorded at four locations along the stagnation line ($z = 0, 12.5, 20,$ and 27.5 mm) are plotted with respect to time in Fig. 3. The profile at $z = 0$ represents the one used as the transient boundary conditions for the vortex-flame interaction simulation. At $t = 0$ the flame was located at $z = 19.2$ mm (cf. Fig. 1). In the opposing-flow configuration, the linearly increasing velocity profile transformed into a wave-like profile as the injected mass approached the stagnation point. The times at which the flame surface passed through the axial locations $z = 20$ and 27.5 mm are indicated in Fig. 3 by shaded regions. The increasing velocity in the flame zones (shaded areas) located farther upstream suggests that the separation between the vortex and the flame surface is decreasing with time.

The computed flowfields at four instants (9.1, 11.1, 12.1 and 12.54 ms) during the vortex-flame interaction are shown in Fig. 4. Here, temperature and OH-concentration fields are plotted on the right and left halves, respectively. The instantaneous locations of all the particles that were injected from the air-side nozzles are shown in white, and those injected from the fuel-side nozzles are shown in yellow. Note that the z axis in Figs. 4a to 4d is shifted to accommodate the vortex. A few observations that can be made from these instantaneous plots: (1) the OH zone is thinner than the temperature field and is shifted toward the air side (from which the vortex is coming) of the peak-temperature surface, (2) as the stagnation plane (surface that separates the convective flows from the fuel and air sides) forms on the fuel side of the peak-temperature surface, the vortex (marked with white particles) is penetrating into the flame zone, and (3) the thinned flame is shifted with the vortex significantly before being quenched.

A closer look at the flame structures in Figs. 4a to 4d suggests that up to $t = 11.1$ ms, the peak OH concentration and temperature decreased more at the axis of symmetry than at any other location in the flame zone as a result of the vortex-flame interaction. However, as the flame developed more

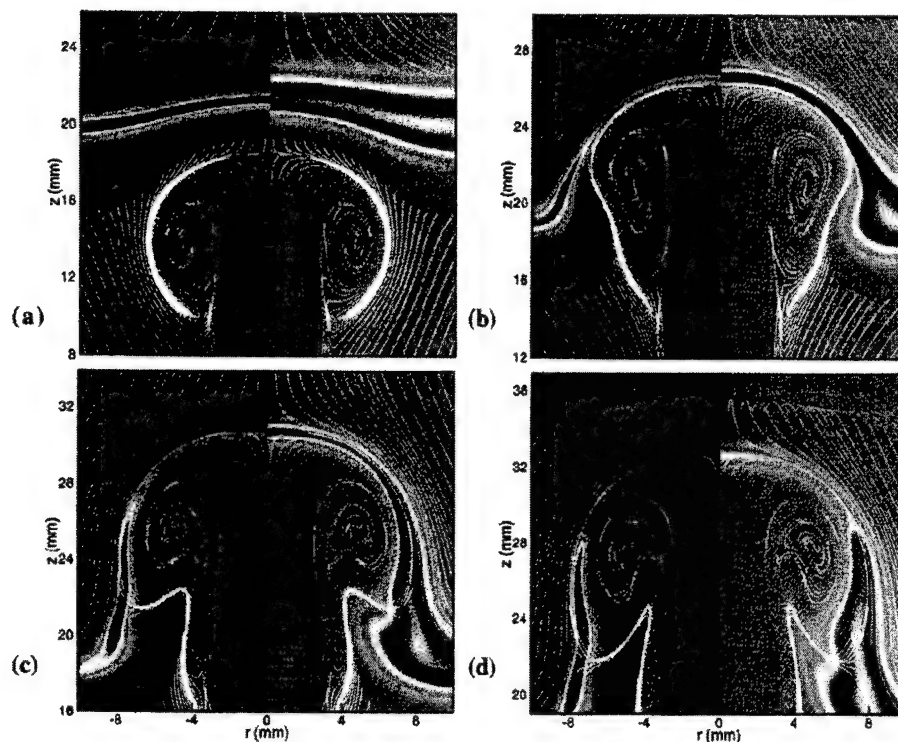


FIG. 4. Computed flames and flowfields obtained at instants (a) 9.1 ms, (b) 11.1 ms, (c) 12.1 ms, and (d) 12.54 ms. OH-concentration and temperature fields are shown on left and right halves, respectively. Instantaneous locations of particles that were injected from air and fuel nozzle are shown in white and yellow, respectively.

curvature for $t > 11.1$ ms, the lowest OH concentration and temperature locations shifted away from the axis. In Fig. 4c, the concentration of OH at $r = 5.3$ mm decreased below that of a stable flame (0.08%), whereas its concentration elsewhere is still above this level, suggesting that the flame is first quenched annularly at $r = 5.3$ mm. After another 0.44 ms of interaction (Fig. 4d), the flame is quenched in the region $r < 6$ mm. Interestingly, the combustion products are still present near the axis, while they are almost dissipated at $r = 5.3$ mm.

The computed flame in Fig. 4c qualitatively matches the OH image (Fig. 2) obtained during the experiments. In both flames, the diameter of the interacting vortex is the same (16 mm), and quenching is initiated at $r \sim 5.3$ mm. However, the computed flame appears to be pushed farther in the axial direction than the flame in the experiment. This difference could result from the flush-mounted syringe tube used in the model. The annular quenching process in the simulations is quantitatively shown in Fig.

5 by plotting the flame shape (broken line) and its temperature distribution (solid line) at different times during the vortex-flame-interaction process. The steady-state flame represented by line "a" is curved concave with respect to the fuel jet as a result of the difference in the densities and, hence, the velocities of the fuel and air jets. Nevertheless, the flame is at a uniform temperature of 1565 K (Line "1"). As the vortex pushes the flame toward the fuel jet, the flame temperature begins to decrease at the axis of symmetry. For $t > 11.1$ ms, the flame temperature is decreasing more in the region $4 \text{ mm} < r < 6 \text{ mm}$ than at the axis of symmetry. At $t = 12.1$ ms, the flame temperature of 1085 K at $r = 5 \text{ mm}$ is $\sim 70 \text{ K}$ lower than that at $r = 0 \text{ mm}$ and is $\sim 45 \text{ K}$ lower than that of the stable flame.

Time-accurate calculations using detailed chemistry and transport models can capture the annular-quenching pattern observed in the experiments. To further investigate the cause for annular quenching during the vortex-flame interaction, detailed flame

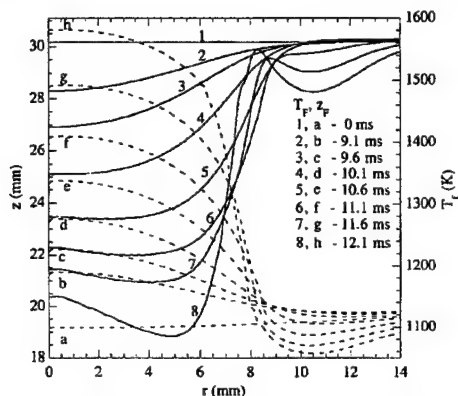


FIG. 5. Evolution of flame surface and changes in temperature during interaction with the vortex that originated on the air side.

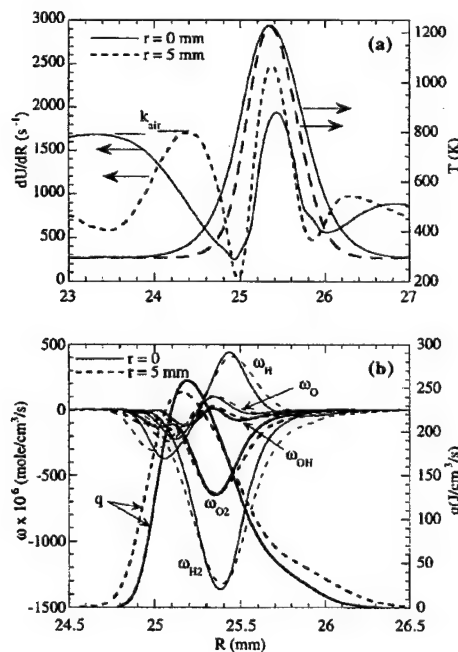


FIG. 6. Comparison of flame structure at the stagnation line with that located 5 mm away from the stagnation line obtained at $t = 11.1$ ms. (a) Velocity gradient and temperature variation normal to the flame surface and (b) variations in molar production and heat-release rates.

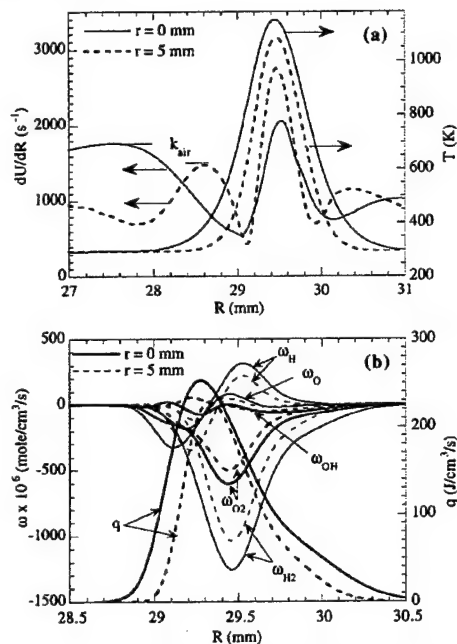


FIG. 7. Comparison of flame structure at the stagnation line with that located 5 mm away from the stagnation line obtained at $t = 12.1$ ms. (a) Velocity gradient and temperature variation normal to the flame surface and (b) variations in molar production and heat-release rates.

structures obtained from the data shown in Figs. 4b and 4c are plotted in Figs. 6 and 7, respectively. In each case the local flame structures obtained along the lines normal to the flame surface at $r = 0$ and 5 mm are compared. To gain a better understanding, the value of R (the distance in the direction normal to the flame) is adjusted to align the peak temperature locations.

Figure 6 suggests that the flame structures obtained at $r = 0$ and 5 mm are quite similar, except that the flame at 5 mm is slightly thicker. The flame at this instant is not extinguished at any radial location, and the flame temperature of 1228 K at $r = 0$ and 5 mm is greater than the quenching limit. Air-side strain rates calculated at both locations are nearly the same (~ 1700 s⁻¹), and are higher than the extinction limit (1410 s⁻¹) for the steady-state flame. It is known that unsteady flames can withstand to higher strain rates because of non-equilibrium-chemistry effects [6].

The flame temperature of 1085 K at $r = 5$ mm in Fig. 7 is below the quenching limit, whereas that at $r = 0$ mm is still above it. Interestingly, the strain rate (K_{air}) at $r = 5$ mm is lower than that at 0 mm, which suggests that the vortex-induced strain rate is

not totally responsible for the quenching at the former location. Close inspection of Fig. 5 reveals that the curvature (dz/dr) of the flame surface increases rapidly in the region $5 \text{ mm} > r > 8 \text{ mm}$ for times greater than 11.1 ms. In earlier studies of unsteady coflowing hydrogen jet diffusion flames [18,25], it was found that the temperature of the flame can increase or decrease as a result of the combination of preferential diffusion and curvature. Therefore, by use of the understanding gained in those studies and the analysis presented in this paper, the annular quenching observed during the vortex-flame interactions in opposing-flow hydrogen diffusion flames is thought to result from preferential diffusion and curvature—not strain rate.

Conclusion

Individual vortex-flame interactions are often studied to gain better understanding of turbulent-flame structures and, hence, to develop accurate turbulence-chemistry interaction models. A time-dependent CFD code that incorporates 13 species and 74 reactions among the constituent species has been developed for the simulation of vortex-flame interactions in opposing-flow hydrogen jet diffusion flames. The model has been validated by directly simulating several steady-state axisymmetric counterflow diffusion flames and comparing the results obtained along the stagnation line with those computed with standard one-dimensional models and experiments.

Experiments were conducted to investigate the different quenching patterns one might expect during vortex-flame interactions in opposing-flow hydrogen jet diffusion flames. It was observed that when an air-side vortex is forced toward the flame at a relatively high speed, the flame at the stagnation line quenches, as expected, and the vortex passes through that hole. On the other hand, when the vortex is forced at a moderate speed, the flame surface deforms significantly and quenching develops in an annular manner away from the stagnation line. To investigate the processes involved in the development of such annular quenching, time-dependent calculations were performed for the opposing-flow jet flame using the axisymmetric CFD code.

A steady-state opposing-flow jet flame was simulated first, and then a vortex was injected into the flow by ramping the velocity at the center portion of the air-jet exit to represent the syringe injection used in the experiment. Calculations performed with different injection times successfully captured the two extinction patterns (point and annular) observed in the experiments. Detailed analysis performed on the instantaneous data obtained just before the development of annular quenching and 1 ms later revealed that (1) the strain rate in the annular region

is equal to or lower than that at the stagnation line, and (2) the flame curvature increases significantly in the annular region where the flame has begun to quench. Based on the understanding gained from previous investigations of curvature effects in coaxial hydrogen jet flames and the findings of this study, it is thought that the unusual annular quenching observed during the vortex-flame interactions in opposing-jet diffusion flames is caused by the combined effect of preferential diffusion and flame curvature.

REFERENCES

1. Kee, R. J., Miller, J. A., Evans, G. H., and Dixon-Lewis, G., in *Twenty-Second Symposium (International) on Combustion*, The Combustion Institute, Pittsburgh, 1988, pp. 1479–1494.
2. Dixon-Lewis, G., in *Twenty-Third Symposium (International) on Combustion*, The Combustion Institute, Pittsburgh, 1990, pp. 305–324.
3. Chelliah, H. K., Law, C. K., Ueda, T., Smooke, M. D., and Williams, F. A., in *Twenty-Third Symposium (International) on Combustion*, The Combustion Institute, Pittsburgh, 1990, pp. 503–511.
4. Hottel, H. C., and Hawthorne, W. R., "Flame and Explosive Phenomena," in *Third Symposium (International) on Combustion*, The Combustion Institute, Pittsburgh, 1949, pp. 254–266.
5. Roquemore, W. M., Chen, L.-D., Goss, L. P., and Lynn, W. F., in *Turbulent Reactive Flows, Lecture Notes in Engineering* (R. Borghi and S. N. B. Murthy, eds.), Springer-Verlag, Berlin, 1989, Vol. 40, p. 49.
6. Darabiha, N., *Combust. Sci. Technol.*, 86:163 (1992).
7. Egolfopoulos, F. N., and C. S. Campbell, *J. Fluid Mech.*, 318:1 (1996).
8. Law, C. K., *Prog. Energy Combust. Sci.*, 10:295 (1984).
9. Mizomoto, M., Asaka, Y., Ikai, S., and Law, C. K., in *Twentieth Symposium (International) on Combustion*, The Combustion Institute, Pittsburgh, 1984, pp. 1933–1939.
10. Takagi T. and Xu, Z., *Combust. Flame* 96:50 (1994).
11. Roberts, W. L., Driscoll, J. F., Drake, M. C., and Ratcliffe, J. W., in *Twenty-Fourth Symposium (International) on Combustion*, The Combustion Institute, Pittsburgh, 1992, pp. 169–176.
12. Rolon, J. C., Aguerre, F., and Candel, S., *Combust. Flame* 100:422 (1995).
13. Ashurst, W. T., *Combust. Sci. Technol.* 92:87 (1993).
14. Poinot, T., Trouve, A., Veynante, D., Candel, S., and Esposito, E., *J. Fluid Mech.* 177:265 (1987).
15. Rutland, C. J. and Ferziger, J. H., *Combust. Flame* 84:343 (1991).
16. Smooke, M. D., Ern, A., Tanoff, M. A., Valdati, B. A., Mohammed, R. K., Marran, D. F., and Long, M. B., in *Twenty-Sixth Symposium (International) on Combustion*, The Combustion Institute, Pittsburgh, 1996, p. 2161.

17. Katta, V. R. and Roquemore, W. M., AIAA paper 97-0904, Reno, Jan., 1997.
18. Katta, V. R., Goss, L. P., and Roquemore, W. M., *Combust. Flame* 96:60 (1994).
19. Frenklach, M., Wang, H., Goldenberg, M., Smith, C. P., Golden, D. M., Bowman, C. T., Hanson, R. K., Gardiner, W. C., and Lissianski, V., Gas Research Institute technical report GRI-95/0058, November 1, 1995.
20. Leonard, B. P., *Comput. Meth. Appl. Mech. Eng.* 19:59 (1979).
21. Katta, V. R., Goss, L. P., and Roquemore, W. M., *AIAA J.*, 32:84 (1994).
22. Sung, C. J., Liu, J. B., and Law, C. K., *Combust. Flame* 102:481 (1995).
23. Grisch, F., Attal-Tretout, B., Bouchardy, P., Katta, V. R., and Roquemore, W. M., *J. Nonlin. Opt. Phys. Mater.* 5:505 (1996).
24. Gutheil, E., Balakrishnan, G., and Williams, F. A., "Structure and Extinction of Hydrogen-Air Diffusion Flames," in *Lecture Notes in Physics* (N. Peters and B. Rogg, eds.), Springer-Verlag, New York, 1993, pp. 177-195.
25. Katta, V. R., and Roquemore, W. M., *Combust. Flame*, 100:61 (1995).

COMMENTS

Bernard Zanuner, French Aerospace Research Institute, (ONERA) France. Computational results of a steady laminar counter flow diffusion flame with a 1-D solver is often sensitive to the grid size. If your discretization is too rough, you may observe, for a particular stretch rate, extinction where the flame should survive. Did you perform grid dependence analyses in your 2-D computation?

Author's Reply. Numerical results, in general, are sensitive to the grid distribution. In the flame calculations, one might see extinction due to insufficient grid spacing, the exact grid spacing required to capture accurately the extinction process depends on the numerical schemes used. After performing calculations using different grid spacings, we found that 0.1-mm spacing in the axial and radial directions is sufficient to capture the extinction process that is independent of grid spacing.

Tadao Takeno, Nagoya University, Japan. Have you studied what is the appropriate parameter to predict the local extinction? We found the local dissipation rate can predict the occurrence of the local extinction [1].

REFERENCE

1. Yamashita, H., Shimada, M., and Takeno, T., in *Twenty-Sixth Symposium (International) on Combustion*, The Combustion Institute, Pittsburgh, 1996, pp. 27-34.

Author's Reply. We have not characterized the extinction conditions using local flow parameters. Although the local dissipation rate seems to predict extinction of a steady, nearly flat flame, it may not be sufficient to describe the extinction processes in a curved hydrogen flame. Some type of correction to the dissipation-rate vs. temperature relationship based on the local Lewis number and flame curvature is required.

H. N. Najm, Sandia National Laboratories, USA. The disappearance of OH radical is used in this work as an indicator of extinction. On the other hand, chemical production and consumption rates are available from this numerical simulation. In fact, the consumption rate of the fuel (H_2) was presented in the talk and was clearly nonzero in locations where OH disappeared. The results indicate little change (about 20% apparently) in H_2 consumption rate between flame regions where OH has disappeared and where it is still present. This suggests that the disappearance of OH in this flame is not an adequate indication of local extinction, at least as far as the model and chemical mechanism used in this work are concerned.

Author's Reply. Extinction represents a process in which the chemical kinetics transform from flame to no-flame reactions. Extinction does not occur instantaneously; rather, it occurs over a period of time (typically in several hundred μs). OH concentration, heat release rate, or any other quantity represents only a particular state in this extinction process. It is obvious that the first sign of the disappearance of the OH radical does not represent an extinguished flame; nevertheless, it does indicate a well-advanced state in the extinction process. The temperature and H_2 consumption rate in Fig. 7 suggest that the flame in region $r = 5$ mm is going through the extinction process, while stable burning is taking place in the region $r = 0$ mm. Figures 4c and 4d show that changes in temperature are evident only 440 μs after the changes in OH are observed. In the simple diffusion flames investigated in this paper, disappearance of the OH radical always leads to complete extinction in a few microseconds. On the other hand, in certain premixed flames, the extinction process may be terminated after the disappearance of the OH radical—in those situations, tagging the OH radical to extinction is not sufficient.

Dynamic Interactions of a Flame and an Isolated Vortex

G. J. Fiechtner,^{1,2} C. D. Carter,^{1,2} K. D. Grinstead, Jr.,^{1,2} J. R. Gord,¹
J. M. Donbar,¹ and J. C. Rolon³

¹ Air Force Research Laboratory, Wright-Patterson Air Force Base, OH 45433-7103, USA.

² Innovative Scientific Solutions, Inc., 2766 Indian Ripple Road, Dayton, OH 45440-3638, USA.

³ Laboratoire d'Énergétique Moléculaire et Macroscopique, Combustion, École Centrale Paris,
Grande Voie des Vignes, 92295 Châtenay-Malabry Cedex, France.

Abstract: The dynamic interaction of a laminar flame and a vortex is examined. The hydroxyl (OH) layer produced by the flame is imaged using planar laser-induced fluorescence (PLIF), and preliminary vortex-characterization data are acquired using acetone PLIF and digital, two-color particle-image velocimetry (PIV). The PIV and PLIF measurements of OH are performed simultaneously. The hydrogen-air flame is supported in a nonpremixed opposed-jet burner. The apparatus is found to produce highly repeatable events, making it ideal for studying the interaction of a flame and an isolated vortex. A distinct annular extinction of the OH layer is observed, in good agreement with previous computational modeling predictions for the apparatus.

1. Introduction

Recent results in numerical modeling combined with experimental measurements have led to important advances in the understanding of combustion. Numerous investigations have contributed to these advances, including a particular type of study in which the interaction of a laminar, nonpremixed flame and a vortex is examined. These efforts involve repeatable, carefully controlled conditions that are highly amenable to experimental study.

In recent computational calculations, Katta (Katta et al., 1998) predicted that, during the interaction of a nonpremixed hydrogen-air flame and an isolated vortex, the extinction of the OH layer would occur in an annular pattern. The experiments detailed in the present paper are performed to examine, in part, the validity of this prediction. Experimental results obtained with planar laser-induced fluorescence (PLIF) of OH are used to determine regimes in which the annular extinction occurs. The nonpremixed flame is supported by air and fuel in an opposed-jet burner. The fuel consists of hydrogen diluted with nitrogen. The amount of hydrogen in nitrogen is varied, along with the strength of the vortex. The temporal evolution of the vortex-flame interactions is imaged with the PLIF system.

Additional measurements are performed to characterize the vortices. First, acetone is seeded into the vortex, and its laser-induced fluorescence is detected. Second, particles are seeded into the flowfield and the scattering is used for digital, two-color particle-image velocimetry (PIV) measurements. Digital PIV measurements are made simultaneously with PLIF measurements of OH. Preliminary vortex-characterization results are discussed in this paper.

2. Background

Numerous experimental studies of the interaction dynamics of vortices and flames have been conducted, and many of these investigations employed two-dimensional imaging to study the interaction. For premixed flame fronts, most measurements have been made using two types of flames. Hertzberg et al. (1984) and Escudie (1988) conducted an experiment in which a Karman vortex street was produced using a cylindrical rod in a cross flow of premixed gases. A V-flame was supported behind a wire positioned downstream of the rod that produced the vortex street. Planar tomographic imaging was used to study the interaction of the vortex street and the flame. A similar interaction of a Karman vortex street and a flame was investigated by Lee et al. (1993) using PLIF imaging of OH and by Nye et al. (1996) using both OH

PLIF and PIV. A disadvantage of using the vortex street is the difficulty in isolating a single vortex. Samaniego (1992a) developed a means of injecting an isolated line vortex through a horizontal slot in the wall of a vertical wind tunnel; this was pursued as a means of replacing the vortex street in experiments with V-flames. A year later, Samaniego (1992b) presented results on the interaction of a line vortex and a V-flame. Schleiren images of the time-dependent vortex-flame interaction along with CH emission data from the entire flame were presented. Nguyen and Paul (1996) also studied vortex-flame interactions using the Samaniego burner, reporting results of PLIF measurements of OH and CH radicals.

In a second type of study involving premixed combustion, Jarosinski et al. (1988) studied a flame that was ignited at one end of a tube of premixed gases. A vortex was injected at the other end of the tube. The interaction dynamics were then photographed using a mercury-xenon arc lamp and a rotating-drum streak camera with a rotating-disc shutter. Recently, Driscoll and co-workers produced an impressive series of papers concerning a similar vortex-flame facility in which PIV, OH PLIF, or a combination of these imaging techniques was applied (Driscoll et al., 1993; Driscoll et al., 1994; Mueller et al., 1995; Mueller et al., 1996; Mueller, 1996; Mueller et al., 1998; Roberts and Driscoll, 1991; Roberts, 1992; Roberts et al., 1992; Roberts et al., 1993; Sinibaldi et al., 1997; Sinibaldi et al., 1998).

Nonpremixed flames have also been the subject of experimental study. Rolon and co-workers (Renard et al., 1998a; Renard et al., 1998b; Rolon et al., 1995; Thevenin et al., 1996; Thevenin et al., 1998) recently developed an apparatus in which a vortex is injected into a flame supported between the nozzles of an opposed-jet burner. This geometry has numerous advantages. First, unlike the above geometries, a stationary nonpremixed flame can easily be produced and isolated. Second, the flame thickness can be varied by changing either the nozzle velocities or the spacing between the upper and lower burner nozzles. The device has also been extended to the study of vortices that interact with premixed opposed-jet flames (Renard et al., 1998a). Takagi and coworkers (Takagi et al., 1996; Yoshida and Takagi, 1998) performed planar Rayleigh-scattering measurements of temperature in a similar type of opposed-jet burner in which a small jet of fuel or air was injected using a micro-nozzle with an inner diameter of only 0.25 mm. Either a jet of air was injected from the air side of the diffusion flame or a jet of fuel was injected from the fuel side.

In a different class of measurements, Hsu et al., (1993) modulated the axial velocity of a laminar jet diffusion flame using a loud speaker to produce vortex-flame interactions. This apparatus was further studied by Hancock and coworkers (Hancock, 1996; Hancock et al., 1996; Hancock et al., 1997; Schauer, 1998; Schauer et al., 1998) using a number of techniques including reactive Mie scattering, PLIF, and digital PIV. These studies have provided large quantities of data for comparison with numerical-modeling predictions. A potential disadvantage of this burner is the complicated geometry (when compared to the above geometries, which involve completely isolated vortex injection) due to the convective velocity field associated with rotation of the vortex and translation of the flame zone (Hancock, 1996). In a similar type of study, Mueller and Scheffer (1998) recently performed OH PLIF measurements in a Wolfhard-Parker slot burner that was acoustically forced by loudspeakers on the side walls of the upstream fuel duct. PLIF imaging of acetone was used as a marker of the fuel.

More recently, Chen and Dahm (1997, 1998) developed a facility for generating a nonpremixed burning layer that wraps into a vortex ring. The facility permits experiments to be performed under conditions of both normal gravity and microgravity, allowing the study of the influence of buoyancy.

The experiments described in the present paper are based on the counterflow geometry of Rolon and co-workers, and the observations described below rely heavily on the progress outlined in their papers (Renard et al., 1998a; Renard et al., 1998b; Rolon et al., 1995; Thevenin et al., 1996; Thevenin et al., 1998). A fuel mixture of hydrogen and nitrogen permits the use of laser diagnostics in the absence of hydrocarbon interferences, and the reaction zone of these nonpremixed flames is generally much thicker than that for premixed flames. Hydrogen chemistry simplifies the numerical calculations that are the subject of comparison with experimental results.

3. Apparatus and Procedure

3.1 Burner Facility

A picture (a) and diagram (b) of the Rolon burner are shown in Figure 1. The flame is supported between upper and lower nozzles separated by 40 mm, each with an exit diameter of 25 mm. The fuel consists of hydrogen diluted with nitrogen and flows from the upper nozzle. Air flows from the lower nozzle. Unique to this type of apparatus is a tube with 5-mm inner diameter that is installed concentrically within the lower nozzle. This tube is attached to a cylinder that contains a piston which, in turn, is attached to an actuator. Feeding an appropriate current to the actuator causes a solenoid to force the piston upward abruptly, resulting in the emergence of a vortex from the tube. The vortex travels upward within the surrounding oxidizer flow. A flow of air is supplied to the vortex tube such that, in the absence of a vortex, the exit velocity matches the velocity of the air from the surrounding nozzle. To minimize the impact of room-air disturbances, upper and lower guard flows of nitrogen are supported through outer nozzles, which are concentric with the respective upper and lower inner nozzles that support the flame.

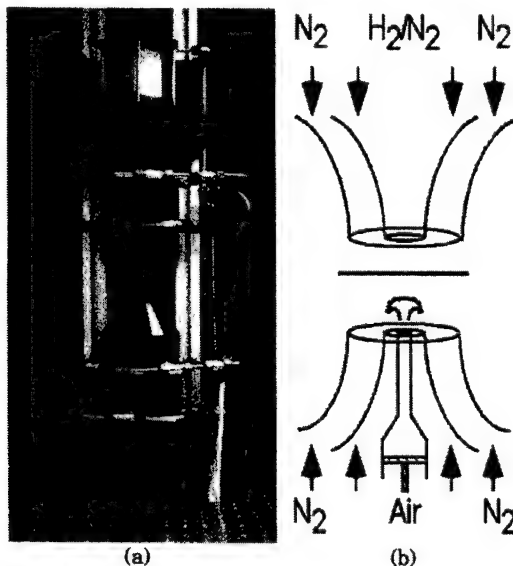


Figure 1: (a) Digital photograph of opposed-jet burner. (b) Cross-sectional diagram of burner nozzles and piston.

The hydrogen, nitrogen-diluent, and oxidizer-air flows are furnished by mass-flow controllers with respective full-scale ranges of 20, 20, and 30 l/min. A continuous flow of air is provided to the vortex tube by a 5-l/min controller, while the guard flows for the upper and lower guard (outer) nozzles is furnished by two 50-l/min mass-flow controllers. The flow rates of the controllers are accurate to $\pm 1\%$ of the full-scale range. The experiments have been repeated for six flame conditions, as summarized in Table I.

The vortex properties can be varied by changing the magnitude and the rise time of the current that is fed to the actuator. The impedance of the actuator ranges from 1 to 1.5 Ω , depending on the frequency content of the current. At full displacement, a current of up to 6 A is provided to the solenoid by a specially designed, high-speed power amplifier. This can result in considerable power consumption by the actuator if the full-displacement condition is maintained for long periods. Consequently, an AC waveform is supplied by initial application of a negative potential, causing the piston to be withdrawn from the flame. The negative potential is applied for about 0.5 s to allow the flame to recover from this initial disturbance, as verified by digital, two-color PIV. The potential is then quickly changed to a positive value of the same magnitude with a carefully controlled rise time, τ_r . The strength of the vortex can be increased by increasing the current magnitude, which results in a larger volume of displaced fluid through the exit of the tube. Eventually, the maximum displacement of the solenoid is reached. In this case the vortex strength can be

Table I: Flow rates (l/min) at 21.5°C and 724 mm Hg for six flame conditions. X_{H_2} is volume fraction of hydrogen in nitrogen diluent.

Gas	Flame					
	A	B	C	D	E	F
H ₂	2.76	3.40	4.04	4.67	5.31	5.94
N ₂						
Diluent	17.1	17.1	17.1	17.0	17.0	16.9
X_{H_2}	0.14	0.17	0.19	0.22	0.24	0.26
Air	11.2	11.2	11.2	11.2	11.2	11.2

further increased using a smaller value of τ_r . The relationship among volume displacement, τ_r , and the vortex characteristics has been discussed in numerous papers, including those by Rolon et al. (1995), Rob-

erts (1992), and Chen and Dahm (1997, 1998). The drive current for the solenoid is obtained by power amplifying the output of a digital arbitrary-waveform generator. This generator is operated at its maximum number of 10,000 quantized steps, resulting in a minimum step size of 0.1 ms. For all measurements discussed in this paper, τ_r is set at 10 ms.

Visualization of the vortex formation and propagation via acetone PLIF is accomplished using a vaporizer that is installed between the vortex tube and the mass-flow controller. A bypass valve allows adjustment of the acetone seeding level. Because the acetone changes the flame characteristics, these visualization studies are limited to nonreacting flows. When the acetone studies are not required, the acetone vaporizer is removed from the apparatus.

Seed particles are introduced into the burner flows when digital PIV measurements of the vortex velocity are performed. Three particle seeders are installed; one is placed after the air mass-flow controller, another after the vortex-air mass flow controller, and a third after the junction where the hydrogen and nitrogen gases are mixed. With the use of three seeders, each flow can be seeded with particles individually, or combinations of the different flowfields can be seeded. Each seeder contains hollow spherical ceramic particles with an approximate mean diameter of 2.4 μm . When PIV studies are not required, the seeders are removed from the apparatus.

3.2 OH PLIF Imaging

The PLIF system contains a frequency-doubled, Q-switched Nd:YAG laser that is used to pump a dye laser which, in turn, is frequency doubled. The UV radiation is directed through a telescope that is adjusted to produce a light sheet with a height that matches as nearly as possible the 40-mm burner separation. The resulting beam thickness is $\sim 300 \mu\text{m}$, which corresponds to the full width (defined as the distance between the locations of the 25% peak intensity points).

Hydroxyl radicals absorb the laser radiation at 281.3414 nm via the $R_1(8)$ transition of the (1,0) band in the A-X system. Fluorescence from the A-X (1,1) and (0,0) bands is detected at right angles through WG-295 and UG-11 colored-glass filters, using a 105-mm-focal-length f/4.5 UV lens. The resulting light is recorded on an intensified CCD camera with an intensifier gate width of 100 ns. CCD pixels are binned in 2x2 groups, resulting in an effective array size of 288 x 192 pixels, with an imaged area of 25.6 x 38.4 mm^2 . The bottom of the image is 0.25 mm above the surface of the lower nozzle. A color table is used with a maximum value set to 95% of the maximum signal for all images taken at a given flame condition. The low-signal color is assigned by calculating the background noise and selecting a minimum value that is two standard deviations above this level. Therefore, in cases where "extinction" of the OH layer is observed, "extinction" refers to signal levels that fall below this minimum value and are, therefore, assigned the last color in the table. All images represent the signal collected during a single laser shot, and no smoothing of the resulting images is attempted.

In studies of vortex-flame interactions conducted by other investigators [see, for example, Najm et al., (1998)], LIF was applied as a marker of some other quantity such as heat release or burning rate. In the present experiments, the OH image is obtained for direct comparison with numerical computations of the OH distribution (Katta et al., 1998); therefore, no attempt is made to correlate the images with any other quantities, although it has recently been shown that the OH concentration may be a good indicator of flame extinction in this configuration (Renard et al., 1998b).

Acetone PLIF imaging is accomplished using the OH PLIF imaging system. Here, the UG-11 colored-glass filter is removed to permit collection of the acetone fluorescence.

3.3 Digital, Two-Color PIV

Measurements of the velocity field are carried out using digital, two-color PIV (Gogenini et al., 1998a; Gogenini et al., 1998b; Donbar, 1998). Here, a color digital CCD (Khosla, 1992) with an array of 3060 x 2036 pixels is used. A magnification of 78,368 pixels/m is employed, resulting in an imaged area of 26.0 x 39.0 mm^2 . The color CCD camera and the intensified CCD array are aligned using a transparent mask printed with a graduated scale. Further alignment between images is performed after each experi-

ment employing software; a transformation in two-dimensional space is applied to the PIV images relative to the PLIF images. Two lasers are used, with one PIV light sheet produced by directly doubling the output of a Q-switched Nd:YAG laser (30 mJ/pulse at the test section). The remainder of this beam is used to pump the dye laser that is frequency doubled to excite OH fluorescence. The second PIV light sheet is produced by pumping a dye laser (employing DCM laser dye) with a second frequency-doubled, Q-switched Nd:YAG laser, resulting in laser radiation at 640 nm (40 mJ/pulse at the test section). The thickness of both the red and green light sheets is set to $\sim 700 \mu\text{m}$ at the probe region. A digital delay generator is used to drive the timing of the two lasers such that the red pulses are delayed precisely with respect to the green ones. In the absence of a vortex, the underlying counterflow velocity field is probed with red pulses that are delayed by up to 1 ms with respect to the corresponding green pulses. For the fastest vortices studied, the delay between red and green pulses is reduced to 10 μs . The camera shutter is set to open for 1/15 s to permit both laser pulses to be detected by the color CCD. Most of the flame emission and light from other devices in the laboratory (monitors, etc.) is greatly attenuated by the shutter.

Velocity vectors are calculated using the correlation software described by Gogenini et al., (1998a). A correlation area of 128 x 128 pixels is used in the calculation, corresponding to a correlation area of 0.269 cm^2 and a spatial resolution of 1.6 mm. In these preliminary studies, the main interest in digital PIV measurements is to obtain the propagation velocity of the vortex, and this correlation area is acceptable for such purposes. We have also obtained acceptable results using correlation areas as small as 32 x 32 pixels, which will be utilized in future studies in which quantities such as strain will be calculated. Neighboring correlation boxes are overlapped by 75%, resulting in a velocity field with an area containing 95 x 60 vectors, or 5700 total vectors over the area of the color CCD. In some portions of each image, a small percentage of errant vectors results from low seed levels, scattering of light into the camera, flame emission, and other effects. Because the vortex-flame interactions are repeatable, digital PIV images can be recorded until an image with an extremely small percentage of incorrect vectors is obtained. For this reason, nearly 15 gigabytes of digital color image data were acquired.

Characterization of vortices is illustrated in Figure 2; a single, idealized vortex ring is superimposed over an axisymmetric cylindrical coordinate system using the coordinates z and u to illustrate the forward position and velocity, respectively. The coordinates r and v represent the radial position and velocity, respectively. In this coordinate representation, the vorticity simplifies to

$$\vec{\zeta} = \Delta \times \vec{V} = \frac{\partial v}{\partial z} - \frac{\partial u}{\partial r}. \quad (1)$$

In these preliminary studies, evaluation of the derivatives in Eq. (1) is carried out without smoothing of the velocity field. Because this can cause amplification of noise, future calculations will be performed using an appropriate smoothing algorithm (Luff et al., 1996; Luff et al., 1998). When the velocity field represents the final desired result from reduction of digital PIV images, it is common to filter out incorrect vectors; this results in "holes" in the field that must be filled using a variety of techniques such as interpolation (Gogenini et al., 1998b). However, the resulting interpolated holes will represent a source of significant error in vorticity computations (Luff et al., 1996; Luff et al., 1998). Therefore, images with more than a few holes are discarded before attempts are made to compute the vorticity. In the future, an optimum method of computing the velocity field will be implemented to reduce the uncertainty in vorticity produced by the holes. Before images of vorticity are plotted, a 3 x 3 smoothing function, that is provided with the commercially available Transform® software, is applied four times. In these preliminary studies, the resulting images are used to examine the relative distribution of vorticity as a vortex propagates upward from the lower nozzle. In future studies in which the influence of the flame on the vorticity will be examined and quantitative vorticity information extracted, a more accurate method of computing and displaying the vorticity will be implemented (Luff et al., 1996; Luff et al., 1998).

The vortex circulation is computed using the integral over the contour shown in Figure 2 (Sullivan et al., 1973a; Sullivan et al., 1973b), yielding (Fox and MacDonald, 1985; Daily and Harleman, 1966; Luff et al., 1996; Luff et al., 1998)

$$\Gamma = \oint_C \vec{v} \cdot d\vec{s} = \sum_i \sum_j \vec{v}_{ij} \cdot \vec{s}_{ij} = \sum_i \sum_j \zeta_{ij} A_{\text{cell}} \quad (2)$$

where C represents a contour box whose sides are drawn along lines where the vorticity remains below ~10% of its peak value (found at the core). The line-integral method (first double summation) and the vorticity-integral method (second double summation) are found to agree within 20%. To confirm the choice of contour and the integration process, the integration is performed over each side of the vortex depicted in Figure 2, and the resulting sum is determined to approach zero.

3.4 Planar Rayleigh Scattering

The above analysis of velocity fields has been used to estimate the forward propagation velocity of vortices or to compute vorticity in cold flows. Recent efforts have been made to examine digital, two-color PIV data in greater detail, including calculations of vorticity, strain, etc., in the vicinity of the flame front. Unfortunately, sharp temperature gradients can cause errors in PIV results because of thermophoresis, which has the greatest influence for injection of comparatively slow vortices and for counterflow flames without vortex injection (Gomez and Rosner, 1993; Nichols, 1986; Pellet et al., 1995; Sung et al., 1994 and 1996;

Talbot et al., 1980; Waldmann and Schmitt, 1980; and Walsh, 1976). Knowledge of the temperature field would enable reduction of the velocity error introduced by thermophoresis. In addition, measurement of the temperature field would be advantageous for comparison with numerical computations. Because point temperature measurements would be extremely cumbersome in the present experiments, recent implementation of planar thermometry by Rayleigh scattering has been explored. Based on experimental observations of other researchers (Dibble and Hollenbach, 1980; Everest 1994; Everest et al, 1995; Komiyama et al., 1996, Takagi et al., 1996; and Yoshida and Takagi, 1998), Rayleigh scattering thermometry should be an excellent diagnostic for studies of vortex-flame interactions in the Rolon burner. In addition, the planar Rayleigh scattering signal can be collected using unintensified CCD cameras, allowing extended linear range and improved spatial resolution (Paul et al, 1990; Paul, 1991; and Williams et al, 1995).

Rayleigh scattering images are collected using a thinned, back-illuminated CCD with an image area of 550 x 550 pixels. The digital color camera is removed to make room for this CCD. Doubled Nd:YAG pulses of 400 mJ are scattered off the burner gases, and the scattering is directed through a four-cavity, 10-nm bandpass filter with a central wavelength of 532 nm. The bandpass filter is required to remove almost all background flame emission and synchronous fluorescence and scattering from simultaneous PLIF measurements of OH. The Rayleigh cross section is calibrated by passing Helium through the burner nozzles at room temperature and recording a scattering image. Next, room-temperature nitrogen is fed to the burner nozzles, and a scattering image is recorded. Because Rayleigh scattering data have only recently been collected, no images have been converted from pixel counts to temperature. Instead, each pixel is normalized to the scattering image of room-temperature nitrogen.

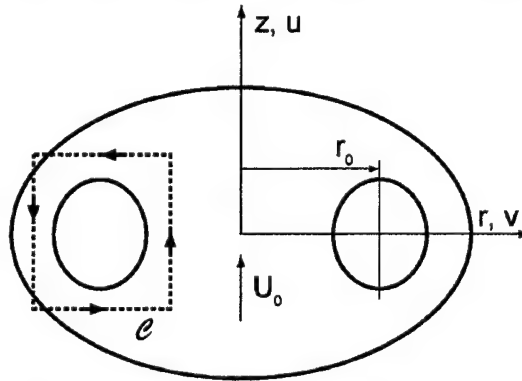


Figure 2. Coordinate system and integration contour used during computation of vortex properties (Daily and Harleman, 1966; Fox and MacDonald, 1985; Sullivan et al., 1973a; Sullivan et al., 1973b).

3.5 Synchronization and Timing

Precise synchronization of several experimental events is required, including vortex generation and propagation, production of laser pulses, and activation of the camera shutter and intensifier. Figure 3 contains a block diagram of the synchronization scheme.

Because the Nd:YAG lasers are designed to operate at a nominal repetition rate of 10 Hz, the experimental sequence must be synchronized to a 10-Hz master clock that drives the flash lamps and the Pockels cells of the lasers. To trigger the lasers, the clock sends two signals—one traveling to a 50- Ω power combiner and then to the laser digital delay generator (DDG). The 10-Hz clock also provides a TTL signal to one of two inputs of a coincidence unit. The second input of this unit is driven by a TTL pulse from the PLIF camera controller. The coincidence unit outputs a pulse only when pulses from both the 10-Hz clock and the PLIF camera controller are present. When a vortex-flame event is initiated using a personal computer, the PLIF camera controller outputs a pulse ~ 1.3 s in duration. The corresponding output of the coincidence unit is a 1.3-s envelope of TTL pulses separated by 100 ms. The first pulse in this envelope triggers a master DDG, synchronizing it with the 10-Hz clock and the laser pulse train. This DDG triggers an arbitrary-waveform generator (AWG) that outputs a 1-s waveform; this waveform is amplified and fed to the piston actuator to generate a vortex. Approximately 0.5 s after the AWG waveform is initiated, the vortex is fired; therefore, five laser pulses are generated during the time between computer initiation and the vortex-flame interaction.

When the DDG is externally triggered, the jitter between the trigger and a DDG output pulse is 60 ps plus the output delay divided by 10^8 . Over the 0.5-s period between the first and fifth laser pulses, this corresponds to a jitter of 5.06 ns. The 10-Hz-clock jitter specifications are not nearly so good. The jitter

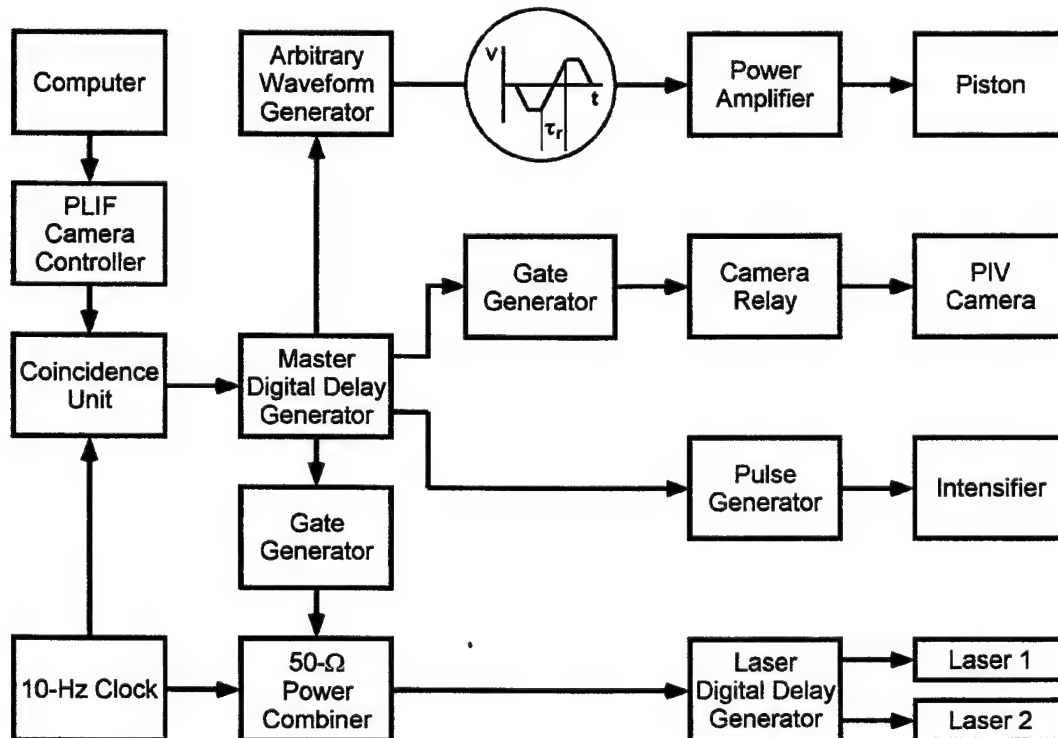


Figure 3: Diagram of electronic timing connections for simultaneous OH PLIF, digital PIV, and Rayleigh scattering measurements.

between clock outputs is one part in 10,000, corresponding to a jitter of 50 μ s over the same 0.5-s period. Attempting to synchronize the piston with the clock severely limits the temporal resolution available to "freeze" vortex-flame events in time and requires an intensifier gate width significantly larger than 50 μ s. The master DDG is, therefore, configured to trigger the fifth laser pulse preemptively. A delayed pulse from the master DDG arrives at the 50- Ω power combiner just before the fifth pulse in the clock pulse train, preemptively triggering the laser(s). If no initiation pulse is output from the computer, the laser(s) are triggered by the 10-Hz clock as usual. This approach reduces the jitter in the timing of the fifth laser pulse from 50 μ s to \sim 5 ns while maintaining the nominal 10-Hz repetition rate required by the lasers.

Other outputs of the master DDG are suitably delayed and directed to the image detectors. For PIV experiments, the width of a TTL pulse is adjusted using a gate generator, which closes a relay to trigger the digital PIV camera system. For simultaneous PLIF experiments, another master-DDG output triggers a pulse generator which, in turn, activates the intensifier of an ICCD camera.

The scheme depicted in Figure 3 provides precise control of the relative timing between the laser diagnostics and the vortex-flame event. To explore the temporal evolution of the event, data are captured utilizing the following phase-locked timing sequence: 1) an image is recorded, 2) the delay between vortex production and the laser/camera events is adjusted, and 3) another vortex is initiated and a second image recorded. This process is repeated to acquire numerous images, obtained at increasing delays; then an animation is created by assembling the individual images in temporal order. Effective temporal separation between images is selected between 10 and 200 μ s, depending on the time scale of the event under study. The resulting animations are a testament to the high degree of repeatability achievable with this apparatus.

3.6 Computational Model

Time-dependent, axisymmetric Navier-Stokes equations written in cylindrical coordinates are solved along with species- and energy-conservation equations. A detailed chemical kinetics model containing thirteen species (H_2 , O_2 , H , O , OH , H_2O , HO_2 , H_2O_2 , N , NO , NO_2 , N_2O , and N_2) is used to describe hydrogen-air combustion. Seventy-four reactions among the constituent species are used, with rate constants obtained from Frenklach et al. (1995). Temperature- and species-dependent property calculations are also incorporated into the model; the enthalpy of each species is calculated from polynomial curve fits that were developed for the temperature range 300-5000 K. The viscosity and the thermal conductivity of individual species are estimated from the Chapman-Enskog collision theory, and the mixture properties are obtained employing Wilke's semi-empirical formula. The effective binary diffusion coefficient of the individual species in the local mixture is calculated using molecular dynamics and Lennard-Jones potentials.

The governing equations are integrated on a nonuniform staggered-grid system. An orthogonal grid with rapidly expanding cell sizes in the axial and the radial directions is employed. The finite-difference forms of the momentum equations are obtained using an implicit QUICKEST scheme (Leonard, 1979; Katta et al., 1994), and those of the species and energy equations are obtained using a hybrid scheme of upwind and central differencing. At every time step, the pressure field is calculated by solving the pressure Poisson equations simultaneously and utilizing the LU matrix decomposition technique. Calculations are made using a non-uniform 301 x 121 mesh system with a spacing of 0.1 mm in both the axial and radial directions. The fuel and air jets are assumed to have velocities of 0.69 and 0.5 m/s, respectively, and the hydrogen-to-nitrogen ratio used for the fuel jet is 0.38. The vortex is modeled by forcing 2.2 cm³ of air through the exit of a nozzle with an exit velocity that increases linearly at a rate of 10³ m/s/s. Further details are given by Katta et al. (1998).

4. Results and Discussion

4.1 Vortex Characterization

The series of acetone images in Figure 4 is typical of the sequential images used to measure the vortex-propagation velocity for a given amplitude and rise time of the solenoid drive current. The six images in the figure are selections from a sequence of fifty images, each delayed by 100 μ s relative to the previous one. If the location of the flame front in the absence of a vortex is known, the acetone-PLIF image

sequence can be used to estimate the velocity of the vortex at this location. In this case, the propagation velocity is ~ 5 m/s. Recently, characterization of vortex properties has been initiated using PIV, which is accomplished simultaneously with OH PLIF. Digital, two-color PIV measurements are readily made when the flame is burning, offering a significant advantage over the acetone-PLIF measurements of the vortex propagation velocity. Figure 5 shows the scattering signal obtained when the vortex-tube flow is seeded with a slightly higher particle density than that produced by the upper- and lower-burner. The corresponding set of vectors is shown in Figure 6. The maximum vector length in the forward direction yields a propagation velocity of 0.77 m/s in this case.

It is now well known that the a strained field can have significant influence on the history of a vortex (Brickman and Ruddick, 1990; Dritchel, 1989; Legras and Dritchel, 1993; Mariotti et al., 1994; Trieleng et al., 1997; Trieleng et al., 1998). There-

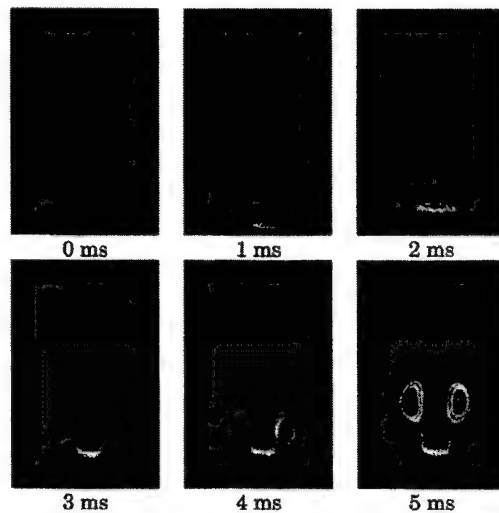


Figure 4: Acetone-PLIF images of vortex.

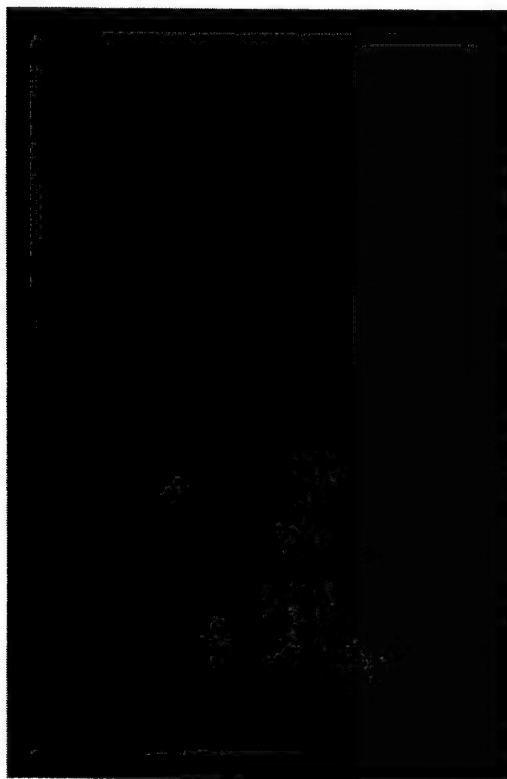


Figure 5: Scattering from particles in vortex flow.

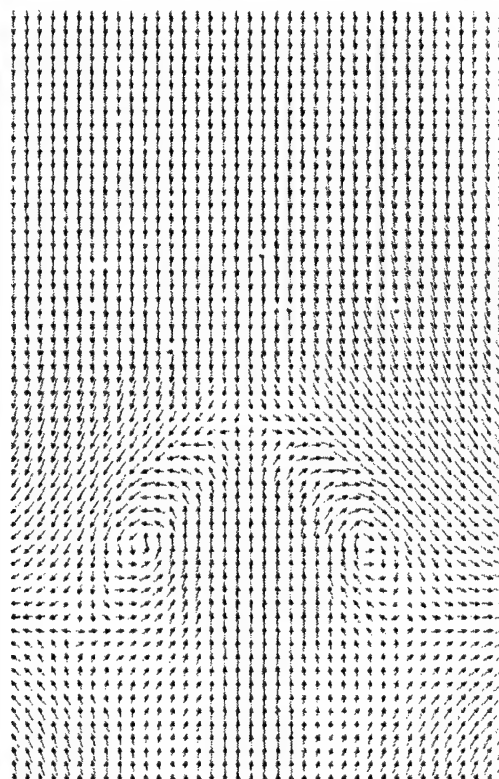


Figure 6: Vectors calculated from PIV image of Figure 5.

fore, it is extremely important that the vortices be characterized. Three different vortices are shown in Figure 7 by their respective vorticity fields, including a "weak," an "intermediate," and a "strong" vortex in row (a), (b), and (c), respectively. The weak vortex has a circulation of $\sim 76 \text{ cm}^2/\text{s}$ and an initial propagation velocity of 1 m/s. However, the propagation velocity of this vortex slows to only 0.6 m/s by the fifth frame (labelled "50 ms"). Meanwhile, the separation between cores is $2r_0=7 \text{ mm}$ in the first frame (labeled "0 ms") and increases to nearly 15 mm in the fifth frame.

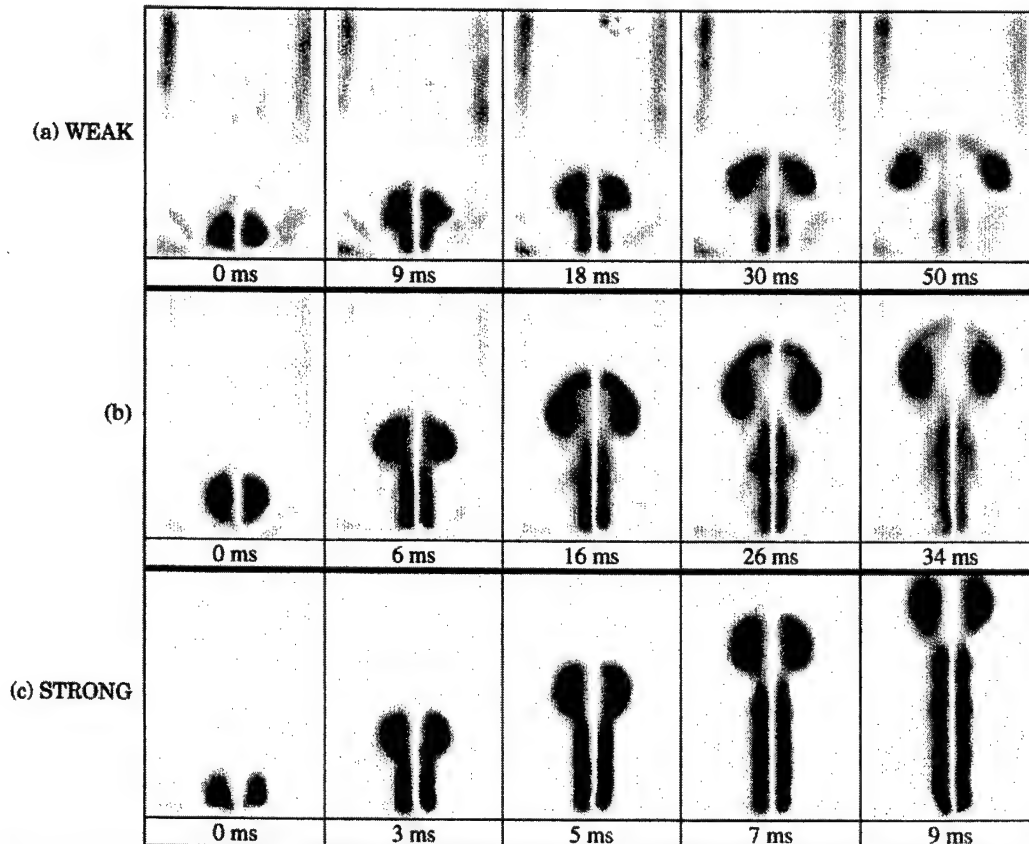


Fig. 7. Vorticity fields for three vortices, with each being shown in a different row [(a), (b), and (c)].

In contrast, the intermediate vortex shown in row (b) of Figure 7 has a circulation of $170 \text{ cm}^2/\text{s}$ and an initial propagation velocity of 2.2 m/s. By the time the vortex reaches the position shown in the fifth frame of row (b), the propagation velocity has decreased to 1.8 m/s. The intermediate vortex shown in the first frame of row (b) has a core separation of $2r_0=7.8 \text{ mm}$, which increases to $\sim 12 \text{ mm}$ by the fifth frame of row (b). Row (c) contains the time-resolved vorticity field for a "strong" vortex, which has a circulation of $1200 \text{ cm}^2/\text{s}$. This vortex has a propagation velocity of 8.4 m/s in the first frame. The velocity increases to a value of 10 m/s in the fourth frame and then decreases to 9.5 m/s in the fifth frame of row (c). The strong vortex has a core separation of $2r_0=8 \text{ mm}$ in the first frame, and the diameter grows to a value of $\sim 10.5 \text{ mm}$ by the fifth frame of row (c). The strong vortex is observed to enter the upper-burner nozzle after the fifth frame. Care must be taken when attempting to generate a vortex that is stronger than case (c) since a three-dimensional lobe structure may result (Widnall, 1975).

Vortex characterization is also essential in choosing the amount of volume that is discharged from the piston/cylinder when generating a vortex. For a cylindrical volume that emanates from a nozzle having

length L and diameter D , Gharib et al. (1998) have shown that the maximum circulation that a vortex ring can attain is reached for L/D at ~ 4 and that for larger ratios, additional trailing vortex rings form. For the present 0.5-cm nozzle, the volume that a vortex can contain as estimated from the results of Gharib et al. (1998) is $\sim 0.4 \text{ cm}^3$. The present vortex generator can sweep a maximum volume of $\sim 3 \text{ cm}^3$, for a maximum attainable L/D ratio of ~ 30 . An example of the consequences of overfilling the vortex is shown in Figure 8, which contains Mie scattering images from PIV particles as viewed with the color digital camera. The first frame (labelled "0 ms") corresponds to the instance in which the vortex reaches the flame and begins to induce flame curvature. After 2 ms, when this vortex has clearly passed the initial flame-front position, a second vortex has obviously formed. After another 2 ms, a third vortex

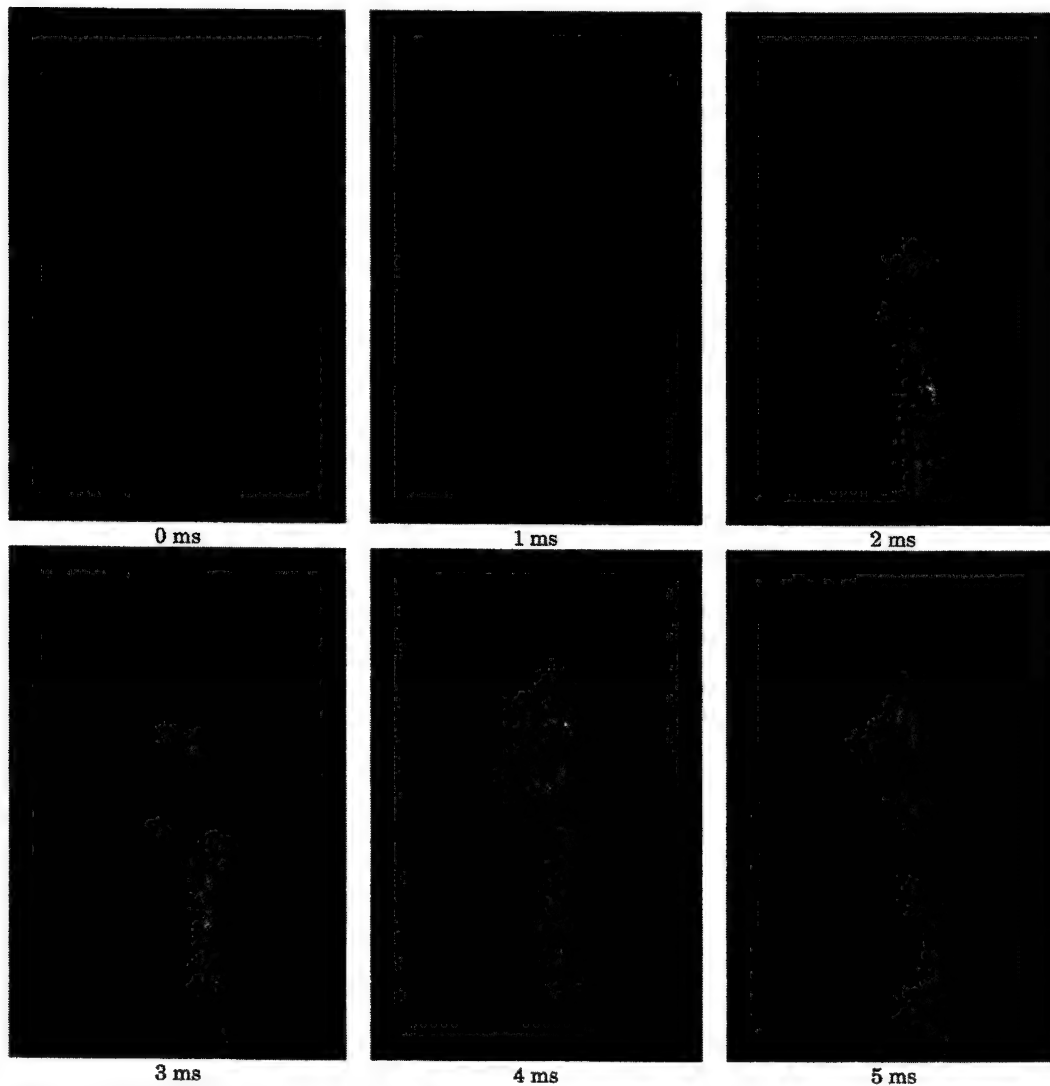


Figure 8: Mie scattering images of an attempt to overfill the vortex. Secondary and tertiary vortices are formed.

is observed, and after 5 ms, the second vortex is observed to overtake the leading vortex and reach the flame front. This vortex leap-frogging process is found to be highly repeatable and, in future studies, may also prove valuable because of the unique curvature and strain regions formed by these events.

4.2 Regimes of Vortex-Flame Interaction

The PLIF images of OH shown in Figure 9 correspond to a vortex-flame interaction in which extinction of the OH layer is absent. Initially, the vortex creates a small dent in the flame, and this dent begins to grow. Eventually the flame nearly surrounds the advancing vortex as it approaches the upper nozzle. In the later interaction stages, the OH PLIF signal level is observed to increase by more than a factor of five over the levels observed without a vortex. The increased signal level is indicated by the light colors in the frames of Figure 9. This change in OH signal level is thought to indicate enhanced burning. For this particular example, the flow rates of Flame D in Table I are used.

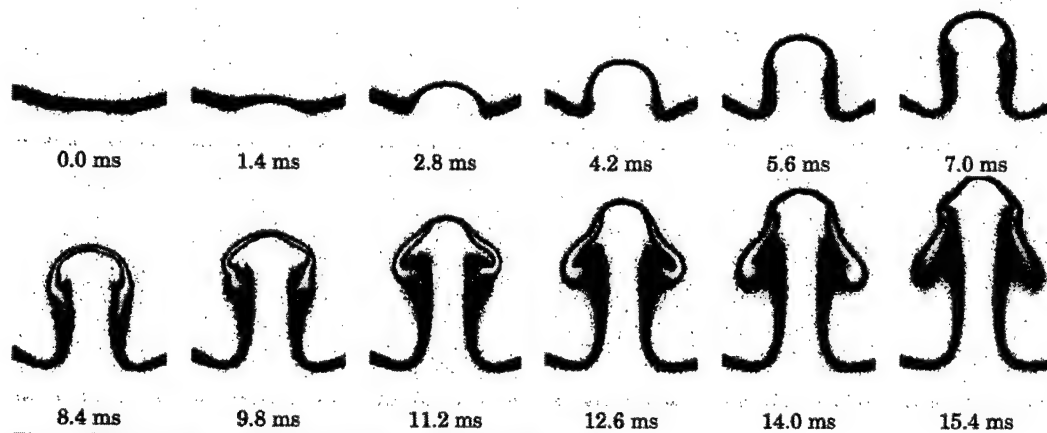


Fig. 9. OH PLIF images when the OH layer remains intact.

The images of Figure 10 correspond to Flame E in Table I and a vortex that is considered to be "strong." Extinction of the OH layer takes place in an annular pattern around the sides of the vortex, leaving a burning layer at its leading edge. After extinction, the isolated island of flame burns away, and the vortex travels upward toward the other nozzle. The flame follows the vortex, traveling up the stem. As the flame overtakes the vortex, it wraps up and turns in upon itself. An additional effect can be seen in flames that exhibit the annular extinction if the vortex strength is slightly decreased: The isolated island at first shrinks in size, but does not completely disappear; it then begins to grow, and burns back around the vortex as it propagates upward. This process is demonstrated in the images of Figure 11.

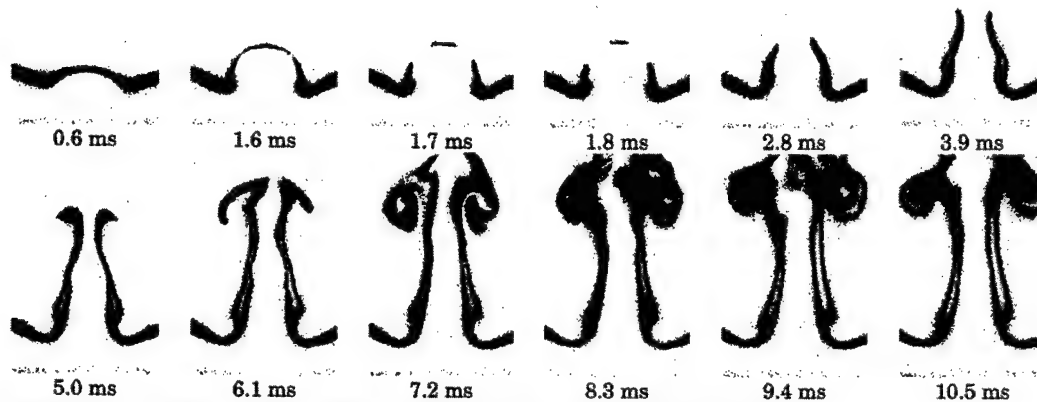


Figure 10: Sequence of images before and after annular extinction of the OH layer.

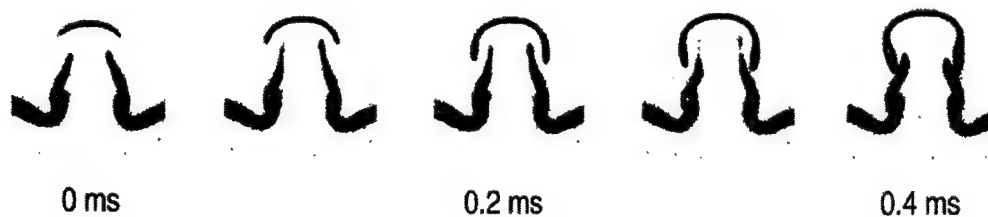


Figure 11. Sequences of images in which the island of flame that is isolated after the annular break in the OH layer begins to grow. Eventually the isolated island recombines with the sides of the flame.

3.7 Preliminary Rayleigh Scattering Measurements

Typical planar Rayleigh scattering images are shown in Figure 12. The flame conditions and vortex strength are similar to those for Figure 11. As shown, Rayleigh scattering images indicate an isolated island of high-temperature gas in front of the advancing vortex. Eventually this island burns around the vortex, and the island flame again contacts the outer flame at the vortex stem.

3.8 Simultaneous PLIF and PIV Results

Although the flame-vortex interactions produced in a Rolon burner are found to be highly repeatable, simultaneous image acquisition of PLIF and PIV and of Rayleigh scattering and PLIF is necessary if the images are to be matched properly. An example of a PLIF image with an overlaid, simultaneously acquired velocity field is shown in Figure 13. The image to the right is an expanded view corresponding to the box drawn in the left image. Again, the PIV results are of high quality, as no vector "holes" exist in this image.

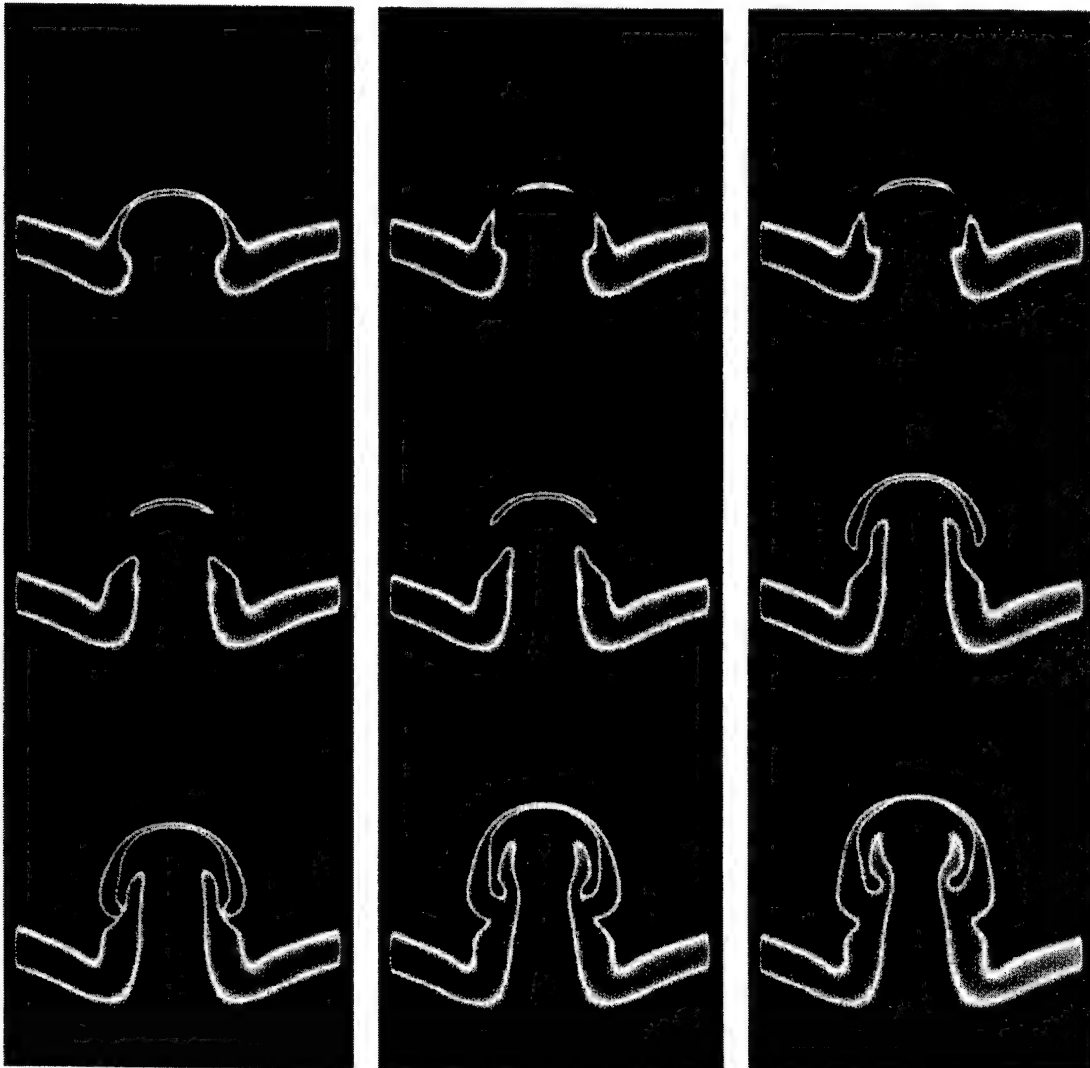


Figure 12. Rayleigh scattering images of the Katta-type annular extinction followed by burnback.

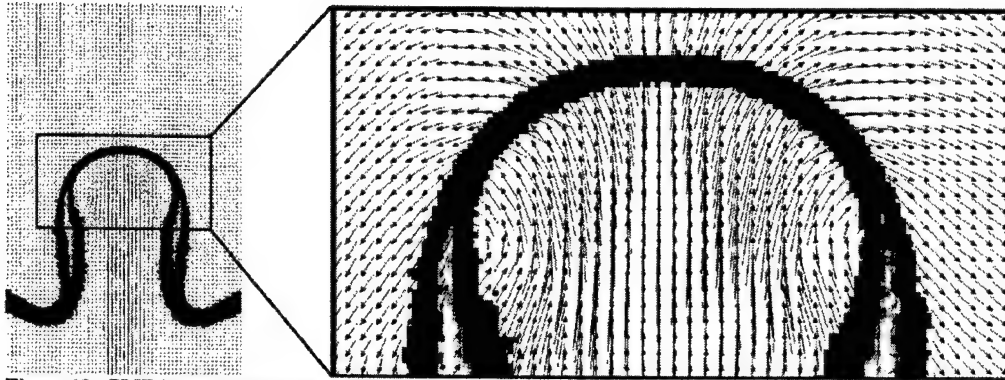


Figure 13. PLIF image of OH with superimposed two-color digital PIV vectors. Full image is shown on the left (approximately 25-mm wide) with expanded cutout shown on the right. The velocity field of the vortex has been severely distorted by the surrounding flame.

3.9 Computational Results

A typical computational result obtained by Katta (Katta et al., 1998) is shown in Figure 12, which contains images of the streakline, temperature, OH, and H fields. The annular decrease in the OH layer is quite similar to the experimental results shown in Figure 10. In fact, the numerical results were obtained before the experiments were initiated, attesting to the utility of the code. Detailed analysis of the numerical results reveals that the strain rate in the annular region is equal to or lower than that at the stagnation line, and the flame curvature increases significantly in the annular region where the break in the OH layer appears. Based on these observations, it is postulated that the annular mechanism results from the combined effect of preferential diffusion and flame curvature. Indeed, Yoshida and Takagi (1998) have found that, in nonpremixed counterflow flames of hydrogen and air into which a microjet is injected, preferential diffusion can cause enhanced H_2 concentrations in regions with concave curvature, greatly influencing extinction and reignition processes.

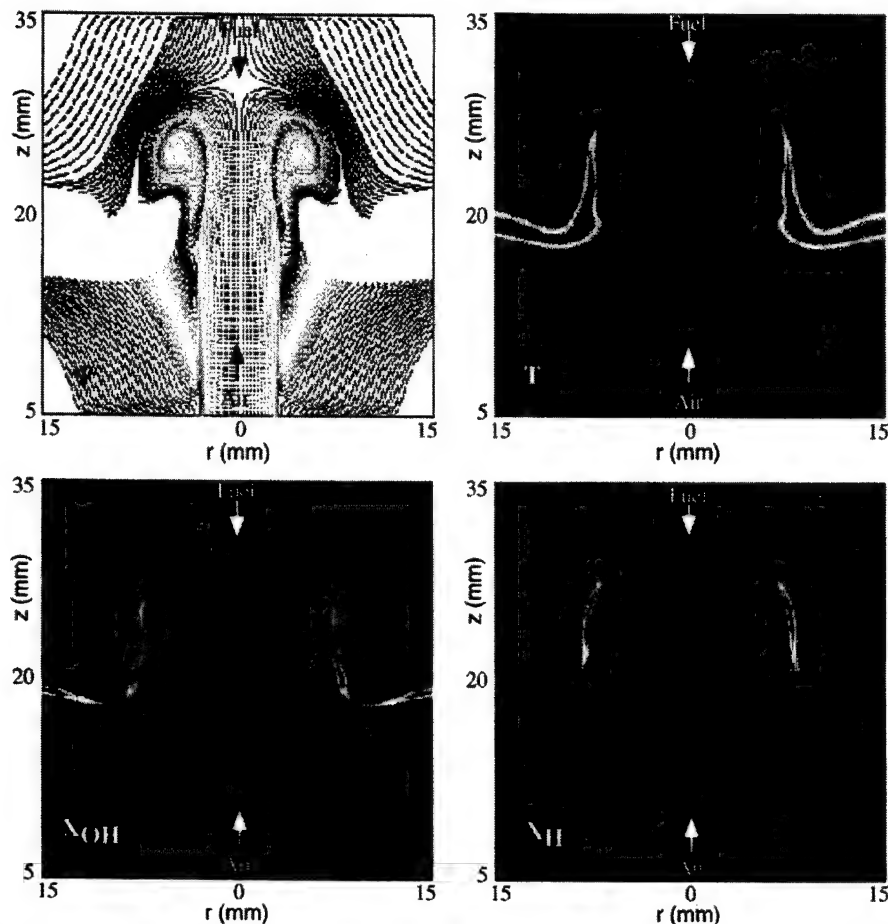
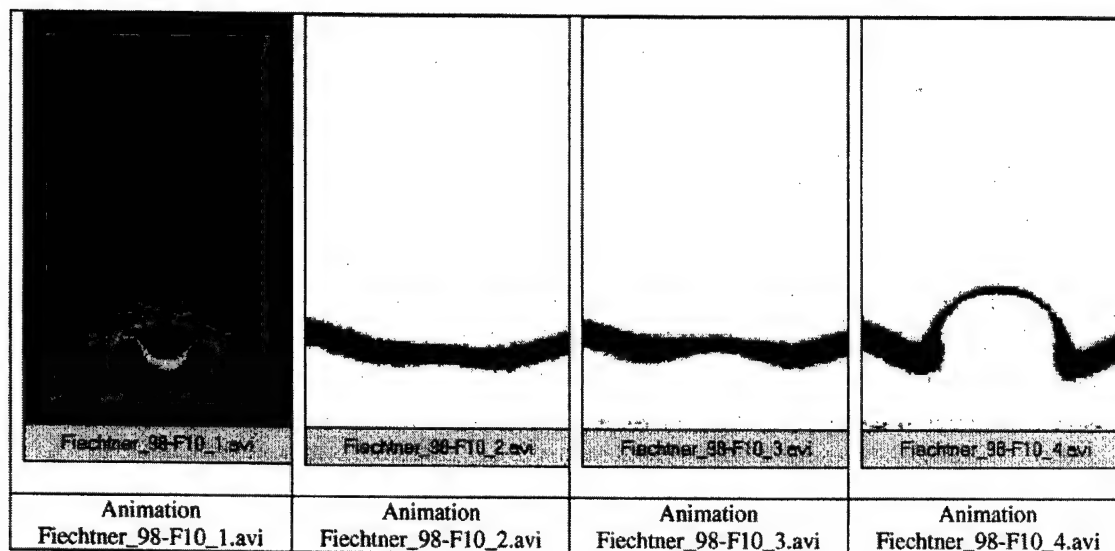


Figure 14. Computational result of Katta (Katta et al., 1998). The image in the upper left hand corner depicts a particle trace of the streamlines. The image in the upper right hand corner shows the temperature field, while the lower left and right images contain the OH and H fields, respectively.

3.10 Animations of Experimental Results

Animations are made from sequences of experimental images. Animation Fiechtner_98-F10_1.avi corresponds to the acetone PLIF results of Figure 4. Animation Fiechtner_98-F10_2.avi corresponds to the OH PLIF results of Figure 9 where no break in the OH layer is observed. Animation Fiechtner_98-F10_3.avi corresponds to the OH PLIF results of Figure 10, which demonstrate an annular "extinction" of the OH layer. The delay between images in these three cases is 100 μ s. To focus on the regime of annular extinction, the measurements corresponding to Figure 10 were repeated using a delay of only 10 μ s. The corresponding results are shown in Animation Fiechtner_98-F10_4.avi. The 50 frames in this animation were obtained in sequential order; images were not reshuffled to make the animation smoother. As demonstrated in Animation Fiechtner_98-F10_4.avi, the repeatability of the Rolon burner is exceptional.



5. Conclusions and Future Research

The apparatus of Rolon and co-workers (Renard et al., 1998a; Renard et al., 1998b; Rolon et al., 1995; Thevenin et al., 1996; Thevenin et al., 1998) has been implemented to study of the interaction of a vortex and a flame. PLIF measurements of acetone and digital, two-color PIV have been applied to characterize the vortices injected into the opposed-jet flow. PLIF images of OH have been used to observe the dynamics of the interaction of the vortex and the flame. An annular break in the OH layer has been observed in excellent agreement with the numerical computations of Katta (Katta et al., 1998).

Future work will be directed toward understanding phenomena such as the annular extinction. A variety of parameters can be studied, such as extended ranges of nitrogen dilution in hydrogen, various flame-thickness regimes and vortex sizes, and different fuels. To aid in these studies, simultaneous OH PLIF and digital, two-color PIV will continue to be employed, along with measurements of the temperature field.

Acknowledgements

The authors thank Dr. V. R. Katta for providing Figure 14. The authors also acknowledge the advice of Drs. L. P. Goss, S. Gogineni, J. Estevadeordal, M. A. Linne, and Mr. T. Drouillard concerning the reduction of two-color PIV data. The authors thank Dr. R. D. Hancock and Mr. I. Vihinen for assistance in assembly and construction of the burner. The authors also acknowledge Mr. P.-H. Renard and Drs. R. D. Hancock, W. M. Roquemore, V. R. Katta, and K.-Y. Hsu for the stimulating discussions of vortex-flame dynamics. Finally, the authors wish to thank Ms. M. M. Whitaker for editorial comments. This work is supported by U. S. Air Force Contracts F33615-95-C-2507 and F33615-97-C-2702.

References

- Brickman, D., and Ruddick, B., 1990, "The Behavior and Stability of a Lens in a Strain Field," *Journal of Geophysical Research*, Vol. 95, No. C6, pp. 9657-9670.
- Chen, S.-J., and Dahm, W. J. A., 1997, "Vortex Ring/Diffusion Flame Interactions in Microgravity Conditions," *Proceedings of the Fourth International Microgravity Combustion Workshop*, Cleveland, OH, pp. 191-196. NASA Conference Publication No. 10191.
- Chen, S.-J., and Dahm, W. J. A., 1998, "Diffusion Flame Structure of a Laminar Vortex Ring Under Microgravity Conditions," accepted for publication in *Twenty-Seventh Symposium (International) on Combustion*, The Combustion Institute, Pittsburgh, PA.
- Daily, J. W., and Harleman, D. R. F., 1966, "Fluid Dynamics," Addison-Wesley Publishing, Reading, MA.

- Dibble, R. W., and Hollenback, R. E., 1981, "Laser Rayleigh Thermometry in Turbulent Flames," *Eighteenth Symposium (International) on Combustion*, The Combustion Institute, Pittsburgh, PA, pp. 1489-1499.
- Donbar, J. M., 1998, "Reaction Zone Structure and Velocity Measurements in Permanently Blue Nonpremixed Jet Flames," Ph.D. Dissertation, University of Michigan, Ann Arbor, MI.
- Driscoll, J. F., Suktus, D. J., Roberts, W. L., Post, M. E., and Goss, L. P., 1993, "The Strain Exerted by a Vortex on a Flame - Determined from Velocity Field Images," AIAA Paper No. 93-0362.
- Driscoll, J. F., Suktus, D. J., Roberts, W. L., Post, M. E., and Goss, L. P., 1994, "The Strain Exerted by a Vortex on a Flame - Determined from Velocity Field Images," *Combustion Science and Technology*, Vol. 4/6, pp. 213-229.
- Dritschel, D. G., 1989, "Strain-Induced Vortex Stripping," in *Mathematical Aspects of Vortex Dynamics*, R. E. Caflisch, ed., SIAM, Philadelphia, PA, pp. 107-119.
- Escudie, D., 1988, "Stability of a Premixed Laminar V-Shaped Flame," *Progress in Astronautics and Aeronautics*, Vol. 113, pp. 215-239.
- Everest, D. A., 1994, "The Effect of Strain Rate on the Temperature Field Structure in a Turbulent Non-Premixed Flame Using Planar Rayleigh Scattering," Ph.D. Dissertation, University of Michigan, Ann Arbor, MI.
- Everest, D. A., Driscoll, J. F., Dahm, W. J. A., and Feikema, D. A., 1995, "Images of the Temperature Field and Temperature Gradients to Quantify Mixing Rates within a Non-Premixed Turbulent Jet Flame," *Combustion and Flame*, Vol. 101, pp. 58-68.
- Fox, R. W., and McDonald, A. T., 1985, "Introduction to Fluid Mechanics," John Wiley & Sons, New York.
- Frenklach, M., Wang, H., Goldenberg, M., Smith, G. P., Golden, D. M., Bowman, C. T., Hanson, R. K., Gardiner, W. C., Lissianski, V., 1995, *Gas Research Institute Technical Report* No. GRI-95/0058.
- Gharib, M., Rambod, E., and Shariff, K., 1988, "A Universal Time Scale for Vortex Ring Formation," *Journal of Fluid Mechanics*, Vol. 360, pp. 121-140.
- Gogineni, S., Goss, L. P., and Roquemore, W. M., 1998a, "Manipulation of a Jet in a Cross Flow," *Experimental Thermal and Fluid Science*, Vol. 16, pp. 209-219.
- Gogineni, S., Goss, L., Pestian, D., and Rivir, R., 1998b, "Two-Color Digital PIV Employing a Single CCD Camera," *Experiments in Fluids*, in press.
- Gomez, A., and Rosner, D. E., 1993, "Thermophoretic Effects on Particles in Counterflow Laminar Diffusion Flames," *Combustion Science and Technology*, Vol. 89., Nos. 5-6, pp. 335-362.
- Hancock, R. D., 1996, "Laser Diagnostic Investigation of the Structure of Steady and Driven Hydrogen Jet Diffusion Flames," Ph.D. Dissertation, University of Illinois, Urbana.
- Hancock, R. D., Schauer, F. R., Lucht, R. P., Katta, V. R., and Hsu, K. Y., 1996, "Thermal Diffusion Effects and Vortex-Flame Interactions in Hydrogen Jet Diffusion Flames," *Twenty-Sixth Symposium (International) on Combustion*, The Combustion Institute, Pittsburgh, PA, pp. 1087-1093.
- Hancock, R. D., Schauer, F. R., Lucht, R. P., and Farrow, R. L., 1997, "Dual-Pump Coherent Anti-Stokes Raman Scattering (CARS) Measurements of Nitrogen and Oxygen in a Laminar Jet Diffusion Flame," *Applied Optics*, Vol. 36, No. 15, pp. 3217-3226.
- Hertzberg, J. R., Namazian, M., and Talbot, L., 1984, "A Laser Tomographic Study of a Laminar Flame in a Karman Vortex Street," *Combustion Science and Technology*, Vol. 38, No. 3/4, pp. 205-216.
- Hsu, K. Y., Chen, L. D., Katta, V. R., Goss, L. P., and Roquemore, W. M., 1993, "Experimental and Numerical Investigations of the Vortex-Flame Interactions in a Driven Jet Diffusion Flame," AIAA Paper No. 93-0455.
- Jarosinski, J., Lee, J. H. S., and Knystautas, R., 1988, "Interaction of a Vortex Ring and a Laminar Flame," *Twenty-Second Symposium (International) on Combustion*, Pittsburgh, PA, pp. 505-514.
- Katta, V. R., Goss, L. P., and Roquemore, W. M., 1994, "Numerical Investigations of Transitional H₂/N₂ Jet Diffusion Flames," *AIAA Journal*, Vol. 32, No. 1, pp. 84-94.
- Katta, V.R., Carter, C. D., Fiechtner, G. J., Roquemore, W. M., Gord, J. R. and Rolon, J. C., 1998, "Inter-

- action of a Vortex With a Flat Flame Formed Between Opposing Jets of Hydrogen and Air," accepted for publication in *Twenty-Seventh Symposium (International) on Combustion*, The Combustion Institute, Pittsburgh, PA.
- Khosla, R. P., 1992, "From Photons to Bits," *Physics Today*, Vol. 45, No. 12, pp. 42-49.
- Komiyama, M., Miyafuji, A., and Takagi, T., 1996, "Flamelet Behavior in a Turbulent Diffusion Flame Measured by Rayleigh Scattering Image Velocimetry," *Twenty-Sixth Symposium (International) on Combustion*, The Combustion Institute, Pittsburgh, PA, pp. 339-346.
- Lee, T.-W., Lee, J. G., Nye, D. A., and Santavicca, D. A., 1993, "Local Response and Surface Properties of Premixed Flames During Interactions with Karman Vortex Streets," *Combustion and Flame*, Vol. 94, No. 1/2, pp. 146-160.
- Legras, B., and Dritschel, D. G., 1993, "Vortex Stripping and the Generation of High Vorticity Gradients in Two-Dimensional Flows," *Applied Scientific Research*, Vol. 51, pp. 445-455.
- Leonard, B. P., 1979, "A Stable and Accurate Convective Modeling Procedure Based on Quadratic Upstream Interpolation," *Computer Methods in Applied Mechanics and Engineering*, Vol. 19, pp. 59-98.
- Luff, J. D., Rompage, A. M., Linne, M. A., and Hertzberg, J. R., 1996, "Uncertainties Associated with the Post-Processing of 2-D Particle Image Velocimetry (PIV) Velocity Data of Unsteady Flow Fields," presented at the *Spring Technical Meeting of the Western States Section/ The Combustion Institute*, Tempe, AZ, March, 1996. Paper No. WSS 96S-005.
- Luff, J. D., Drouillard, T., Rompage, A. M., Linne, M. A., and Hertzberg, J. R., 1998, "Experimental Uncertainties Associated with Particle Image Velocimetry (PIV) Based Vorticity Algorithms," to appear in *Experiments in Fluids*, Vol. 25.
- Mariotte, A., and Legras, B., 1994, "Vortex Stripping and the Erosion of Coherent Structures in Two-Dimensional Flows," *Physics of Fluids*, Vol. 6, No. 12, pp. 3954-3962.
- Mueller, C. J., Driscoll, J. F., Sutkus, D. J., Roberts, W. L., Drake, M. C., and Smooke, M. D., 1995, "Effect of Unsteady Stretch Rate on OH Chemistry During a Vortex-Flame Interaction: To Assess Flamelet Models," *Combustion and Flame*, Vol. 100, No. 1/2, pp. 323-331.
- Mueller, C. J., Driscoll, J. F., Ruess, D. L., and Drake, M. C., 1996, "Effects of Unsteady Stretch on the Strength of a Freely-Propagating Flame Wrinkled by a Vortex," *Twenty-Sixth Symposium (International) on Combustion*, The Combustion Institute, Pittsburgh, PA, pp. 347-355.
- Mueller, C. J., 1996, "Measurements of Vortex-Flame Interaction Dynamics and Chemistry," Ph.D. Dissertation, University of Michigan, Ann Arbor.
- Mueller, C. J., Driscoll, J. F., Ruess, D. L., Drake, M. C., and Rosalik, M. E., 1998, "Vorticity Generation and Attenuation as Vortices Convect Through a Premixed Flame," *Combustion and Flame*, Vol. 112, No. 3, pp. 342-358.
- Mueller, C. J., and Schefer, R. W., 1998, "Coupling of a Diffusion Flame Structure to an Unsteady Vortical Flowfield," accepted for publication in *Twenty-Seventh Symposium (International) on Combustion*, The Combustion Institute, Pittsburgh, PA.
- Najm, H. N., Paul, P. H., Mueller, C. J., and Wyckoff, P. S., 1998, "On the Adequacy of Certain Experimental Observables as Measurements of Flame Burning Rate," *Combustion and Flame*, Vol. 113, No. 3, pp. 312-332.
- Nguyen, Q.-V., and Paul, P. H., 1996, "The Time Evolution of a Vortex-Flame Interaction Observed via Planar Imaging of CH and OH," *Twenty-Sixth Symposium (International) on Combustion*, The Combustion Institute, Pittsburgh, PA, pp. 357-364.
- Nichols, R. H., 1986, "The Effects of Particle Dynamics on Turbulence Measurements with the Laser Doppler Velocimeter," Ph.D. Dissertation, University of Tennessee, Knoxville, TN.
- Nye, D. A., Lee, J. G., Lee, T.-W., and Santavicca, D. A., 1996, "Flame Stretch Measurements During the Interaction of Premixed Flames and Karman Vortex Streets Using PIV," *Combustion and Flame*, Vol. 94, No. 1/2, pp. 167-176.
- Paul, P. H., 1991, "The Application of Intensified Array Detectors to Quantitative Planar Laser-Induced Fluorescence Imaging," AIAA 91-2315.

- Paul, P. H., van Cruyningen, I., Hanson, R. K., and Kychakoff, G., 1990, "High Resolution Digital Flow-field Imaging of Jets," *Experiments in Fluids*, Vol. 9, pp. 241-251.
- Pellet, G. J., Wilson, L. G., Humphreys, W. J., Jr., Batram, S. M., Gatrell, L. R., and Issac, K. M., 1995, "Velocity Fields of Axisymmetric Hydrogen-Air Counterflow Diffusion Flames from LDV, PIV, and Numerical Computation," AIAA 95-3112.
- Renard, P.-H., Rolon, J. C., Thevenin, D., and Candel, S., 1998a, "Wrinkling, Pocket Formation and Double Premixed Flame Interaction Processes," accepted for publication in *Twenty-Seventh Symposium (International) on Combustion*, The Combustion Institute, Pittsburgh, PA.
- Renard, P.-H., Rolon, J. C., Thevenin, D., and Candel, S., 1998b, "Investigations of Heat Release, Extinction, and Time Evolution of the Flame Surface for a Non-Premixed Flame Interacting with a Vortex," accepted for publication, *Combustion and Flame*.
- Roberts, W. L., and Driscoll, J. F., 1991, "A Laminar Vortex Interacting with a Premixed Flame: Measured Formation of Pockets of Reactants," *Combustion and Flame*, Vol. 87, No. 3/4, pp. 245-256.
- Roberts, W. L., 1992, "A Premixed Laminar Flame Interacting With a Vortex Resulting in Flame Stretch and Quenching," Ph.D. Dissertation, University of Michigan, Ann Arbor, MI.
- Roberts, W. L., Driscoll, J. F., Drake, M. C., and Ratcliffe, J. W., 1992, "OH Fluorescence Images of the Quenching of a Premixed Flame During an Interaction with a Vortex," *Twenty-Fourth Symposium (International) on Combustion*, The Combustion Institute, Pittsburgh, pp. 169-176.
- Roberts, W. L., Driscoll, J. F., Drake, M. C., and Goss, L. P., 1993, "Images of the Quenching of a Flame by a Vortex - To Quantify Regimes of Turbulent Combustion," *Combustion and Flame*, Vol. 94, No. 1/2, pp. 58-69.
- Rolon, J. C., Aguerre, F., and Candel, S., 1995, "Experiments on the Interaction Between a Vortex and a Strained Diffusion Flame," *Combustion and Flame*, Vol. 100, No. 3, pp. 422-429.
- Samaniego, J.-M., 1992a, "Generation of Two-Dimensional Vortices in a Cross Flow," *Annual Research Briefs - 1992*, Center for Turbulence Research, NASA Ames Research Center/Stanford University, pp. 431-441.
- Samaniego, J.-M., 1992b, "Stretch-Induced Quenching in Vortex-Flame Interactions," *Annual Research Briefs - 1993*, Center For Turbulence Research, NASA Ames Research Center/Stanford University, pp. 205-218.
- Schauer, F. R., 1998, "Thermal Diffusion and Flame Structure in a Laminar Hydrogen Jet Diffusion Flame," Ph.D. Thesis, University of Illinois, Urbana.
- Schauer, F. R., Hancock, R. D., Gogineni, S., and Lucht, R. P., 1998, "Vortex-Flame Interactions in Hydrogen Jet Diffusion Flames: A DPIV and DNS Investigation," submitted to *Experiments in Fluids*.
- Sinibaldi, J. O., Mueller, C. J., and Driscoll, J. F., 1997, "Measured Local Propagation Velocities of Wrinkled Premixed Flames," Proceedings of the *Fall Technical Meeting*, The Eastern States Section of the Combustion Institute, Hartford, CT, pp. 179-182.
- Sinibaldi, J. O., Driscoll, J. F., Mueller, C. J., and Tulkki, A. E., 1997 "Flame-Vortex Interactions: Effects of Buoyancy from Microgravity Imaging Studies," AIAA 97-0669.
- Sinibaldi, J. O., Mueller, C. J., Tulkki, A. E., and Driscoll, J. F., 1998, "Suppression of Flame Wrinkling by Buoyancy: The Baroclinic Stabilization Mechanism," *AIAA Journal*, Vol. 36, No. 8, pp. 1432-1438.
- Sinibaldi, J. O., Mueller, C. J., and Driscoll, J. F., 1998, "Local Flame Propagation Speeds Along Wrinkled, Unsteady, Stretched Premixed Flames," accepted for publication in *Twenty-Seventh Symposium (International) on Combustion*, The Combustion Institute, Pittsburgh, PA.
- Sullivan, J. P., Widnall, S. E., and Ezekiel, S., 1973a, "Study of Vortex Rings Using a Laser Doppler Velocimeter," AIAA Paper No. 73-105.
- Sullivan, J. P., Widnall, S. E., and Ezekiel, S., 1973b, "Study of Vortex Rings Using a Laser Doppler Velocimeter," *AIAA Journal*, Vol. 11, No. 10, pp. 1384-1389.
- Sung, C. J., Law, C. K., and Axelbaum, R. L., 1994, "Thermophoretic Effects on Seeding Particles in LDV Measurements of Flames," *Combustion Science and Technology*, Vol. 99, pp. 119-132.

- Sung, C. J., Kistler, J. S., Nishioka, M., and Law, C. K., 1996, "Further Studies on Effects of Thermophoresis on Seeding Particles in LDV Measurements of Strained Flames," *Combustion and Flame*, Vol. 105, pp. 189-201.
- Takagi, T., Yoshikawa, Y., Yoshida, K., Komiyama, M., and Kinoshita, S., 1996, "Studies on Strained Non-Premixed Flames Affected by Flame Curvature and Preferential Diffusion," Twenty-Sixth Symposium (International) on Combustion, The Combustion Institute, Pittsburgh, PA, pp. 1103-1110.
- Talbot, L., Cheng, R. K., Schefer, R. W., and Willis, D. R., 1980, "Thermophoresis of Particles in a Heated Boundary Layer," *Journal of Fluid Mechanics*, Vol. 101, No. 4, pp. 737-758.
- Thevenin, D., Rolon, J. C., Renard, P.-H., Kendrick, D. W., Veynante, D., and Candel, S., 1996, "Structure of a Nonpremixed Flame Interacting with Counterrotating Vortices," *Twentieth-Sixth Symposium (International) on Combustion*, The Combustion Institute, Pittsburgh, PA, pp. 1079-1086.
- Thevenin, D., Renard, P.-H., Rolon, J. C., and Candel, S., 1998, "Extinction Processes During a Non-Premixed Flame/Vortex Interaction," accepted for publication in *Twenty-Seventh Symposium (International) on Combustion*, The Combustion Institute, Pittsburgh, PA.
- Trieling, R. R., Beckers, M., and van Heijst, G. J. F., 1997, "Dynamics of Monopolar Vortices in a Strain Flow," *Journal of Fluid Mechanics*, Vol. 345, pp. 165-201.
- Trieling, R. R., van Wesenbeeck, J. M. A., and van Heijst, G. J. F., 1998, "Dipolar Vortices in a Strain Flow," *Physics of Fluids*, Vol. 10, No. 1, pp. 144-159.
- Yoshida, K., and Takagi, T., 1998, "Transient Local Extinction and Reignition Behavior of Diffusion Flames Affected by Flame Curvature and Preferential Diffusion," accepted for publication in *Twenty-Seventh Symposium (International) on Combustion*, The Combustion Institute, Pittsburgh, PA.
- Waldmann, L., and Schmitt, K. H., 1966, "Thermophoresis and Diffusiophoresis of Aerosols," in *Aerosol Science*, C. N. Davies, ed., Academic Press, New York, pp. 137-162.
- Walsh, M. J., 1976, "Influence of Particle Drag Coefficient on Particle Motion in High Speed Flow with Typical Laser Velocimetry Applications," NASA TN D-8120.
- Widnall, S. E., 1975, "The Structure and Dynamics of Vortex Filaments," *Annu. Rev. Fluid. Mech.*, Vol. 7, pp. 141-165.
- Williams, G. A., Jr., Reihheimer, A. L., Johnson, C. B., Wheeler, K. D., Wodecki, N. D., Aebi, V. W., and Costello, K. A., 1995, "Back-Illuminated and Electron-Bombarded CCD's Low Light Level Imaging System Performance," SPIE Volume 2551, pp. 208-223.



AIAA 99-0320

Regimes of Interaction Between a Nonpremixed Hydrogen-Air Flame and an Isolated Vortex

G. J. Fiechtner,^{1,2} C. D. Carter,^{1,2} V. R. Katta,^{1,2}
J. R. Gord,¹ J. M. Donbar,¹ and J. C. Rolon³

¹Air Force Research Laboratory
Wright-Patterson AFB, OH 45433-7103

²Innovative Scientific Solutions, Inc.
2766 Indian Ripple Road, Dayton, OH 45440-3638

³Laboratoire d'Énergétique Moléculaire et
Macroscopique, Combustion, École Centrale Paris
and CNRS, Grande Voie des Vignes 92295,
Châtenay-Malabry Cedex, France

**37th AIAA Aerospace Sciences
Meeting and Exhibit
January 11-14, 1999 / Reno, NV**

REGIMES OF INTERACTION BETWEEN A NONPREMIXED HYDROGEN-AIR FLAME AND AN ISOLATED VORTEX

G. J. Fiechtner,^{1,4,5} C. D. Carter,^{1,4} V.R. Katta,^{1,4} James R. Gord,^{2,4}
J. M. Donbar,^{2,4} and J. C. Rolon³

Abstract

The dynamic interaction of a laminar flame and a vortex is examined. The hydroxyl (OH) layer produced by the flame is imaged using planar laser-induced fluorescence (PLIF), and vortex-characterization data are acquired using digital, two-color particle-image velocimetry (PIV). The PIV and PLIF measurements of OH are performed simultaneously. The hydrogen-air flame is supported in a nonpremixed opposed-jet burner. The apparatus is found to produce highly repeatable events, making it ideal for studying the interaction of a flame and an isolated vortex. A distinct annular extinction of the OH layer is observed, in good agreement with previous computational modeling predictions for the apparatus.

Introduction

Recent results in numerical modeling combined with experimental measurements have led to important advances in the understanding of combustion. Numerous investigations have contributed to these advances, including a particular type of study in which the interaction of a laminar, nonpremixed flame and a vortex is

examined. These efforts involve repeatable, carefully controlled conditions that are highly amenable to experimental study. The resulting data can be used for a variety of purposes, such as identifying fundamental regimes of vortex-flame interactions (Renard et al., 1998a). This paper contains experimental results that are used to validate numerical computations.

In recent computational calculations, Katta (Katta et al., 1998) predicted that during the interaction of a nonpremixed hydrogen-air flame and an isolated vortex, the extinction of the OH layer would occur in an annular pattern. The experiments detailed in the present paper are performed to examine, in part, the validity of this prediction. Experimental results obtained with planar laser-induced fluorescence (PLIF) of OH are used to determine regimes in which the annular extinction occurs. The nonpremixed flame is supported by air and fuel in an opposed-jet burner. The fuel consists of hydrogen diluted with nitrogen. The amount of hydrogen in nitrogen is varied, along with the strength of the vortex. The temporal evolution of the vortex-flame interactions is imaged with the PLIF system. Additional measurements are performed to characterize the vortices. Particles are seeded into the flowfield, and the scattering is used for digital, two-color particle-image velocimetry (PIV) measurements. Digital PIV measurements are made simultaneously with PLIF measurements of OH.

Background

Numerous experimental studies of the interaction dynamics of vortices and flames have been conducted, and many of these investigations employed two-dimensional imaging to study the interaction. For premixed flame fronts, most measurements have been made using two types of flames. Hertzberg et al. (1984) and Escudie (1988) conducted an experiment in which a Karman vortex street was produced using a cylindrical rod in a cross flow of premixed gases. A V-flame was supported behind a wire positioned downstream of the rod that produced the vortex street. Planar tomographic imaging was used to study the interaction of the vortex street and the flame. A similar

¹Air Force Research Laboratory, Wright-Patterson Air Force Base, OH 45433-7103, USA.

²Innovative Scientific Solutions, Inc., 2766 Indian Ripple Road, Dayton, OH 45440-3638, USA.

³Laboratoire d'Énergétique Moléculaire et Macroscopique, Combustion, École Centrale Paris and CNRS, Grande Voie des Vignes, 92295 Châtenay-Malabry Cedex, France.

⁴Member, AIAA.

⁵Corresponding author and presenter.

This paper is declared a work of the U.S. Government and is not subject to copyright protection in the United States.

interaction of a Karman vortex street and a flame was investigated by Lee et al. (1993) using PLIF imaging of OH and by Nye et al. (1996) using both OH PLIF and PIV. A disadvantage of using the vortex street is the difficulty in isolating a single vortex. Samaniego (1992a) developed a means of injecting an isolated line vortex through a horizontal slot in the wall of a vertical wind tunnel; this was pursued as a means of replacing the vortex street in experiments with V-flames. A year later, Samaniego (1992b) presented results on the interaction of a line vortex and a V-flame. Schleißen images of the time-dependent vortex-flame interaction along with CH emission data from the entire flame were presented. Nguyen and Paul (1996) also studied vortex-flame interactions using the Samaniego burner, reporting results of PLIF measurements of OH and CH radicals.

In a second type of study involving premixed combustion, Jarosinski et al. (1988) studied a flame that was ignited at one end of a tube of premixed gases. A vortex was injected at the other end of the tube. The interaction dynamics were then photographed using a mercury-xenon arc lamp and a rotating-drum streak camera with a rotating-disc shutter. Recently, Driscoll and co-workers produced an impressive series of papers concerning a similar vortex-flame facility in which PIV, OH PLIF, or a combination of these imaging techniques was applied (Driscoll et al., 1994; Mueller et al., 1995; Mueller et al., 1996; Mueller et al., 1998; Roberts and Driscoll, 1991; Roberts et al., 1992; Roberts et al., 1993; Sinibaldi et al., 1998a; Sinibaldi et al., 1998b).

Nonpremixed flames have also been the subject of experimental study. Rolon and co-workers (Renard et al., 1998a; Renard et al., 1998b; Rolon et al., 1995; Thevenin et al., 1996; Thevenin et al., 1998) recently developed an apparatus in which a vortex is injected into a flame supported between the nozzles of an opposed-jet burner. This geometry has numerous advantages. First, unlike the above geometries, a stationary nonpremixed flame can be produced and isolated easily. Second, the flame thickness can be varied by changing either the nozzle velocities or the spacing between the upper and lower burner nozzles. The device has also been extended to the study of vortices that interact with premixed opposed-jet flames (Renard et al., 1998a). Takagi and coworkers (Takagi et al., 1996; Yoshida and Takagi, 1998) performed planar Rayleigh-scattering measurements of temperature in a similar type of opposed-jet burner in which a small jet of fuel or air was injected using a micro nozzle with an inner diameter of only 0.25 mm. Either a jet of air was injected from the air side of the diffusion flame or a jet of fuel was injected from the fuel side.

In a different class of measurements, Hsu et al. (1993) modulated the axial velocity of a laminar jet diffusion flame using a loud speaker to produce vortex-

flame interactions. This apparatus was further studied by Hancock and coworkers (Hancock et al., 1996) using a number of techniques including reactive Mie scattering, PLIF, and digital PIV. These studies have provided large quantities of data for comparison with numerical-modeling predictions. A potential disadvantage of this burner is the complicated geometry (when compared to the above geometries, which involve completely isolated vortex injection) due to the convective velocity field associated with rotation of the vortex and translation of the flame zone. In a similar type of study, Mueller and Schefer (1998) recently performed OH PLIF measurements in a Wolfhard-Parker slot burner that was acoustically forced by loudspeakers on the side walls of the upstream fuel duct. PLIF imaging of acetone was used as a marker of the fuel.

More recently, Chen and Dahm (1998) developed a facility for generating a nonpremixed burning layer that wraps into a vortex ring. The facility permits experiments to be performed under conditions of both normal gravity and microgravity, allowing the study of the influence of buoyancy.

The experiments described in the present paper are based on the counterflow geometry of Rolon and co-workers (Renard et al., 1998a; Renard et al., 1998b; Rolon et al., 1995; Thevenin et al., 1996; Thevenin et al., 1998). A fuel mixture of hydrogen and nitrogen permits the use of laser diagnostics in the absence of hydrocarbon interferences, and the reaction zone of these nonpremixed flames is generally much thicker than that for premixed flames. Hydrogen chemistry simplifies the numerical calculations that are the subject of comparison with experimental results.

Apparatus and Procedure

Burner Facility

A picture (a) and diagram (b) of the Rolon burner are shown in Figure 1. The flame is supported between upper and lower nozzles separated by 40 mm, each with an exit diameter of 25 mm. The fuel consists of hydrogen diluted with nitrogen and flows from the upper nozzle. Air flows from the lower nozzle. Unique to this type of apparatus is a tube with 5-mm inner diameter that is installed concentrically within the lower nozzle. This tube is attached to a cylinder that contains a piston which, in turn, is attached to an actuator. Feeding an appropriate current to the actuator causes a solenoid to force the piston upward abruptly, resulting in the emergence of a vortex from the tube. For a cylindrical volume of fluid that emanates from a nozzle having length L and diameter D , Gharib et al. (1998) have shown that the maximum circulation which a vortex ring can attain is reached for L/D at ~ 4 and that

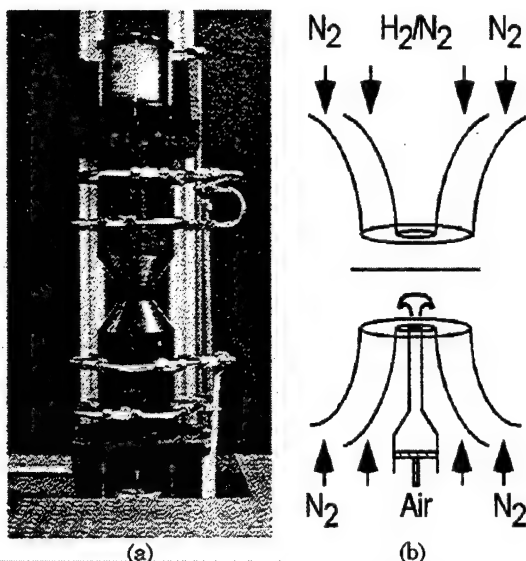


Figure 1: (a) Digital photograph of opposed-jet burner. (b) Cross-sectional diagram of burner nozzles and piston.

for larger ratios additional trailing vortex rings form. For the present 0.5-cm nozzle, the volume that a vortex can contain as estimated from the results of Gharib et al. (1998) is $\sim 0.4 \text{ cm}^3$. The present vortex generator can sweep a maximum volume of $\sim 3 \text{ cm}^3$, for a maximum attainable L/D ratio of ~ 30 . For the experiments described in this paper, comparatively strong vortices are generated using a 0.1-ms piston risetime. The piston is allowed to travel through its maximum range, but the tube is placed such that the diagnostics are triggered before a secondary or tertiary vortex exits the tube. The resulting leading vortex travels upward within the surrounding oxidizer flow. A flow of air is supplied to the vortex tube such that in the absence of a vortex, the exit velocity matches the velocity of the air from the surrounding nozzle. To minimize the impact of room-air disturbances, upper and lower guard flows of nitrogen are supported through outer nozzles, which are concentric with the respective upper and lower inner nozzles that support the flame.

The hydrogen, nitrogen-diluent, and oxidizer-air flows are furnished by mass-flow controllers with respective full-scale ranges of 20, 20, and 30 l/min. A continuous flow of air is provided to the vortex tube by a 5-l/min controller, while the guard flows for the upper and lower guard (outer) nozzles are furnished by two 50-l/min mass-flow controllers. The flow rates of the controllers are accurate to $\pm 1\%$ of the full-scale range. The experiments have been repeated for six flame conditions, as summarized in Table I.

Seed particles are introduced into the burner flows when digital PIV measurements of the vortex velocity are performed. Three particle seeders are

Table I: Flow rates (l/min) at 21.5°C and 724 mm Hg for six flame conditions. X_{H_2} is the volume fraction of hydrogen in nitrogen diluent.

Gas	Flame					
	A	B	C	D	E	F
H_2	2.76	3.40	4.04	4.67	5.31	5.94
N_2	17.1	17.1	17.1	17.0	17.0	16.9
X_{H_2}	0.14	0.17	0.19	0.22	0.24	0.26
Air	11.2	11.2	11.2	11.2	11.2	11.2

installed; one is placed after the air mass-flow controller, another after the vortex-air mass flow controller, and a third after the junction where the hydrogen and nitrogen gases are mixed. With the use of three seeders, each flow can be seeded with particles individually, or combinations of the different flowfields can be seeded. Each seeder contains hollow spherical ceramic particles with an approximate mean diameter of $2.4 \mu\text{m}$. When PIV studies are not required, the seeders are removed from the apparatus.

Laser Diagnostics: OH PLIF Imaging

The PLIF system contains a frequency-doubled, Q-switched Nd:YAG laser that is used to pump a dye laser which, in turn, is frequency doubled. The UV radiation is directed through a telescope that is adjusted to produce a light sheet with a height that matches as nearly as possible the 40-mm burner separation. The resulting beam thickness is $\sim 300 \mu\text{m}$, which corresponds to the full width (defined as the distance between the locations of the 25% peak intensity points).

Hydroxyl radicals absorb the laser radiation at 281.3414 nm via the $R_1(8)$ transition of the (1,0) band in the A-X system. Fluorescence from the A-X (1,1) and (0,0) bands is detected at right angles through WG-295 and UG-11 colored-glass filters, using a 105-mm-focal-length $f/4.5$ UV lens. The resulting light is recorded on an intensified CCD camera with an intensifier gate width of 100 ns. CCD pixels are binned in 2×2 groups, resulting in an effective array size of 288×192 pixels, with an imaged area of $25.6 \times 38.4 \text{ mm}^2$. The bottom of the image is 0.25 mm above the surface of the lower nozzle. A color table is used with a maximum value set to 95% of the maximum signal for all images taken at a given flame condition. The low-signal color is assigned by calculating the background noise and selecting a minimum value that is two standard deviations above this level. Therefore, in cases where "extinction" of the OH layer is observed, "extinction" refers to signal levels that fall below this minimum value and are, therefore, assigned the last color in the table. All images represent the signal collected during a single laser shot, and no smoothing of the resulting images is attempted.

In studies of vortex-flame interactions conducted by other investigators [see, for example, Najm et al. (1998)], LIF was applied as a marker of some other quantity such as heat release or burning rate. In the present experiments, the OH image is obtained for direct comparison with numerical computations of the OH distribution (Katta et al., 1998); therefore, no attempt is made to correlate the images with any other quantities, although it has recently been shown that the OH concentration may be a good indicator of flame extinction in this configuration (Renard et al., 1998b).

Laser Diagnostics: Digital, Two-Color PIV

Measurements of the velocity field are carried out using digital, two-color PIV (Gogenini et al., 1998a; Gogenini et al., 1998b; Donbar, 1998). Here, a color digital CCD (Khosla, 1992) with an array of 3060 x 2036 pixels is used. A magnification of 78,368 pixels/m is employed, resulting in an imaged area of 26.0 x 39.0 mm². The color CCD camera and the intensified CCD array are aligned using a transparent mask printed with a graduated scale. Further alignment between images is performed after each experiment employing software; a transformation in two-dimensional space is applied to the PIV images relative to the PLIF images. Two lasers are used, with one PIV light sheet produced by directly doubling the output of a Q-switched Nd:YAG laser (30 mJ/pulse at the test section). The remainder of this beam is used to pump the dye laser that is frequency doubled to excite OH fluorescence. The second PIV light sheet is produced by pumping a dye laser (employing DCM laser dye) with a second frequency-doubled, Q-switched Nd:YAG laser, resulting in laser radiation at 640 nm (40 mJ/pulse at the test section). The thickness of both the red and green light sheets is set to ~700 μm at the probe region. A digital delay generator is used to drive the timing of the two lasers such that the red pulses are delayed precisely with respect to the green ones. In the absence of a vortex, the underlying counterflow velocity field is probed with red pulses that are delayed by up to 1 ms with respect to the corresponding green pulses. For the fastest vortices studied, the delay between red and green pulses is reduced to 10 μs. The camera shutter is set to open for 1/15 s to permit both laser pulses to be detected by the color CCD. Most of the flame emission and light from other devices in the laboratory (monitors, etc.) is greatly attenuated by the shutter.

Velocity vectors are calculated using the correlation software described by Gogenini et al., (1998a). A correlation area of 128 x 128 pixels is used in the calculation, corresponding to a correlation area of 0.269 cm² and a spatial resolution of 1.6 mm. In these preliminary studies, the main interest in digital PIV measurements is to obtain the propagation velocity of the

vortex, and this correlation area is acceptable for such purposes. We have also obtained acceptable results using correlation areas as small as 32 x 32 pixels, which will be utilized in future studies in which quantities such as strain will be calculated. Neighboring correlation boxes are overlapped by 75%, resulting in a velocity field with an area containing 95 x 60 vectors, or 5700 total vectors over the area of the color CCD. In some portions of each image, a small percentage of errant vectors results from low seed levels, scattering of light into the camera, flame emission, and other effects. Because the vortex-flame interactions are repeatable, digital PIV images can be recorded until an image with an extremely small percentage of incorrect vectors is obtained. For this reason, nearly 15 gigabytes of digital color image data were acquired.

Characterization of vortices is illustrated in Figure 2; a single, idealized vortex ring is superimposed over an axisymmetric cylindrical coordinate system using the coordinates z and u to illustrate the forward position and velocity, respectively. The coordinates r and v represent the radial position and velocity, respectively. In this coordinate representation, the vorticity simplifies to

$$\bar{\zeta} = \Delta \times \bar{V} = \frac{\partial v}{\partial z} - \frac{\partial u}{\partial r} \quad (1)$$

In these preliminary studies, evaluation of the derivatives in Eq. (1) is carried out without smoothing of the velocity field. Because this can cause amplification of noise, future calculations will be performed using an appropriate smoothing algorithm (Luff et al., 1996; Luff et al., 1998). When the velocity field represents the final desired result from reduction of digital PIV images, it is common to filter out incorrect vectors; this results in "holes" in the field that must be filled using a variety of techniques such as interpolation (Gogenini et al., 1998b). However, the resulting interpolated holes

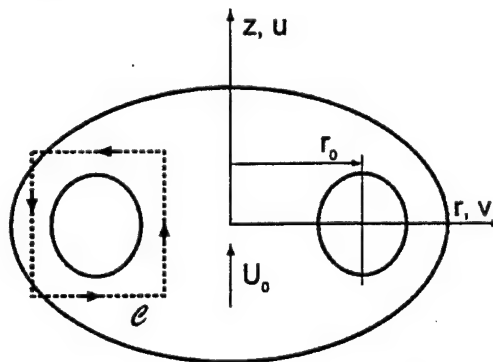


Figure 2. Coordinate system and integration contour used during computation of vortex properties (Daily and Harleman, 1966; Fox and MacDonald, 1985; Sullivan et al., 1973a; Sullivan et al., 1973b).

will represent a source of significant error in vorticity computations (Luff et al., 1996; Luff et al., 1998). Therefore, images with more than a few holes are discarded before attempts are made to compute the vorticity. In the future, an optimum method of computing the velocity field will be implemented to reduce the uncertainty in vorticity produced by the holes. Before images of vorticity are plotted, a 3×3 smoothing function, that is provided with the commercially available Transform® software, is applied four times. In these preliminary studies, the resulting images are used to examine the relative distribution of vorticity as a vortex propagates upward from the lower nozzle. In future studies in which the influence of the flame on the vorticity will be examined and quantitative vorticity information extracted, a more accurate method of computing and displaying the vorticity will be implemented (Luff et al., 1996; Luff et al., 1998).

The vortex circulation is computed using the integral over the contour shown in Figure 2 (Sullivan et al., 1973a; Sullivan et al., 1973b), yielding (Fox and MacDonald, 1985; Daily and Harleman, 1966; Luff et al., 1996; Luff et al., 1998)

$$\Gamma = \oint_C \vec{V} \cdot d\vec{s} = \sum_i \sum_j \vec{V}_{ij} \cdot \vec{s}_{ij} = \sum_i \sum_j \zeta_{ij} A_{\text{cell}} \quad (2)$$

where C represents a contour box whose sides are drawn along lines where the vorticity remains below ~10% of its peak value (found at the core). The line-integral method (first double summation) and the vorticity-integral method (second double summation) are found to agree within 20%. To confirm the choice of contour and the integration process, the integration is performed over each side of the vortex depicted in Figure 2, and the resulting sum is determined to approach zero.

Planar Rayleigh Scattering

The above analysis of velocity fields has been used to estimate the forward propagation velocity of vortices or to compute vorticity in cold flows. Recent efforts have been made to examine digital, two-color errors in PIV results because of thermophoresis, which has the greatest influence for injection of comparatively slow vortices and for counterflow flames without vortex injection (Gomez and Rosner, 1993; Nichols, 1986; Pellet et al., 1995; Sung et al., 1994 and 1996; Talbot et al., 1980; Waldmann and Schmitt, 1980; and PIV data in greater detail, including calculations of vorticity, strain, etc., in the vicinity of the flame front. Unfortunately, sharp temperature gradients can cause Walsh, 1976). Knowledge of the temperature field would enable reduction of the velocity error introduced by thermophoresis. In addition, measurement of the temperature field would be advantageous for compari-

son with numerical computations. Because point temperature measurements would be extremely cumbersome in the present experiments, recent implementation of planar thermometry by Rayleigh scattering has been explored. Based on experimental observations of other researchers (Dibble and Hollenbach, 1980; Everest 1994; Everest et al., 1995; Komiyama et al., 1996; Takagi et al., 1996; and Yoshida and Takagi, 1998), Rayleigh scattering thermometry should be an excellent diagnostic for studies of vortex-flame interactions in the Rolon burner. In addition, the planar Rayleigh scattering signal can be collected using unintensified CCD cameras, allowing extended linear range and improved spatial resolution (Paul et al., 1990; Paul, 1991; and Williams et al., 1995).

Rayleigh scattering images are collected using a thinned, back-illuminated CCD with an image area of 550×550 pixels. The digital color camera is removed to make room for this CCD. Doubled Nd:YAG pulses of 400 mJ are scattered off the burner gases, and the scattering is directed through a four-cavity, 10-nm bandpass filter with a central wavelength of 532 nm. The bandpass filter is required to remove almost all background flame emission and synchronous fluorescence and scattering from simultaneous PLIF measurements of OH. The Rayleigh cross section is calibrated by passing Helium through the burner nozzles at room temperature and recording a scattering image. Next, room-temperature nitrogen is fed to the burner nozzles, and a scattering image is recorded. Because Rayleigh scattering data have only recently been collected, no images have been converted from pixel counts to temperature. Instead, each pixel is normalized to the scattering image of room-temperature nitrogen.

Synchronization and Timing

Precise synchronization of several experimental events is required, including vortex generation and propagation, production of laser pulses, and activation of the camera shutter and intensifier. Figure 3 contains a block diagram of the synchronization scheme.

Because the Nd:YAG lasers are designed to operate at a nominal repetition rate of 10 Hz, the experimental sequence must be synchronized to a 10-Hz master clock that drives the flash lamps and the Pockels cells of the lasers. To trigger the lasers, the clock sends two signals—one traveling to a 50- Ω power combiner and then to the laser digital delay generator (DDG). The 10-Hz clock also provides a TTL signal to one of two inputs of a coincidence unit. The second input of this unit is driven by a TTL pulse from the PLIF camera controller. The coincidence unit outputs a pulse only when pulses from both the 10-Hz clock and the PLIF camera controller are present. When a vortex-flame event is initiated using a personal computer, the PLIF

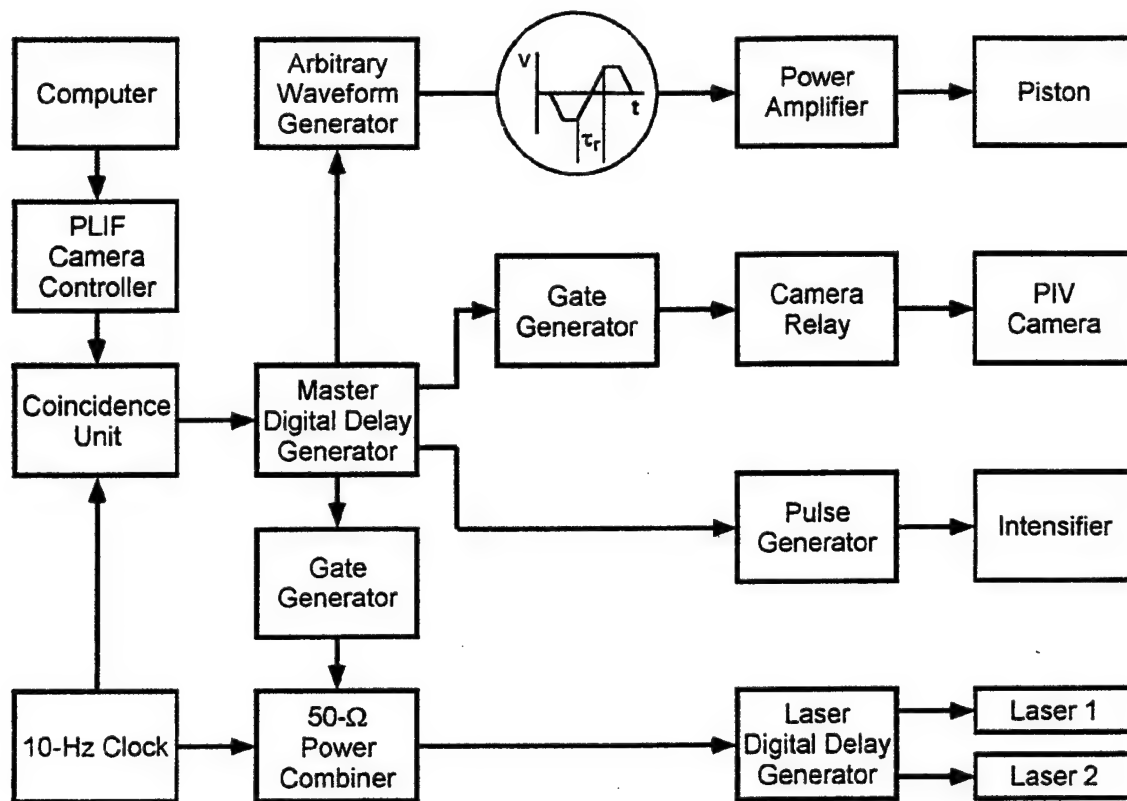


Figure 3: Diagram of electronic timing connections for simultaneous OH PLIF, digital PIV, and Rayleigh scattering measurements.

camera controller outputs a pulse ~ 1.3 s in duration. The corresponding output of the coincidence unit is a 1.3-s envelope of TTL pulses separated by 100 ms. The first pulse in this envelope triggers a master DDG, synchronizing it with the 10-Hz clock and the laser pulse train. This DDG triggers an arbitrary-waveform generator (AWG) that outputs a 1-s waveform; this waveform is amplified and fed to the piston actuator to generate a vortex. Approximately 0.5 s after the AWG waveform is initiated, the vortex is fired; therefore, five laser pulses are generated during the time between computer initiation and the vortex-flame interaction.

When the DDG is externally triggered, the jitter between the trigger and a DDG output pulse is 60 ps plus the output delay divided by 10^8 . Over the 0.5-s period between the first and fifth laser pulses, this corresponds to a jitter of 5.06 ns. The 10-Hz-clock jitter specifications are not nearly so good. The jitter between clock outputs is one part in 10,000, corresponding to a jitter of 50 μ s over the same 0.5-s period. Attempting to synchronize the piston with the clock severely limits the temporal resolution available to "freeze" vortex-flame events in time and requires an intensifier gate width significantly larger than 50 μ s.

The master DDG is, therefore, configured to trigger the fifth laser pulse preemptively. A delayed pulse from the master DDG arrives at the 50- Ω power combiner just before the fifth pulse in the clock pulse train, preemptively triggering the laser(s). If no initiation pulse is output from the computer, the laser(s) are triggered by the 10-Hz clock as usual. This approach reduces the jitter in the timing of the fifth laser pulse from 50 μ s to ~ 5 ns while maintaining the nominal 10-Hz repetition rate required by the lasers.

Other outputs of the master DDG are suitably delayed and directed to the image detectors. For PIV experiments, the width of a TTL pulse is adjusted using a gate generator, which closes a relay to trigger the digital PIV camera system. For simultaneous PLIF experiments, another master-DDG output triggers a pulse generator which, in turn, activates the intensifier of an ICCD camera.

The scheme depicted in Figure 3 provides precise control of the relative timing between the laser diagnostics and the vortex-flame event. To explore the temporal evolution of the event, data are captured utilizing the following phase-locked timing sequence: 1) an image is recorded, 2) the delay between vortex

production and the laser/camera events is adjusted, and 3) another vortex is initiated and a second image recorded. This process is repeated to acquire numerous images, obtained at increasing delays; then an animation is created by assembling the individual images in temporal order. Effective temporal separation between images is selected between 10 and 200 μ s, depending on the time scale of the event under study. The resulting animations are a testament to the high degree of repeatability achievable with this apparatus.

Results and Discussion

Vortex Characterization

Figure 4 shows the scattering signal obtained when the vortex-tube flow is seeded with a slightly higher particle density than that produced by the upper and lower burners. The corresponding set of vectors is shown at the right in Fig. 4. The vector field contains only six positions from a total of 5700 vectors where the software cannot be used to assign a velocity. The maximum vector length in the forward direction yields a propagation velocity of 0.77 m/s in this case.

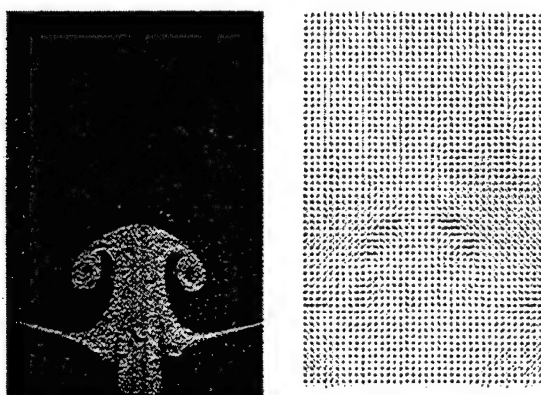


Figure 4. Scattering from particles in vortex flow and vectors calculated from scattering image.

The high quality of the velocity data enables the calculation of flowfield quantities such as vorticity. The temporal evolution of three different vortices is shown in Figure 5 using plots of vorticity fields. A "weak," an "intermediate," and a "strong" vortex are shown in rows (a), (b), and (c), respectively. The weak vortex has a circulation of ~ 76 cm^2/s and an initial propagation velocity of 1 m/s. However, the propagation velocity of this vortex slows to only 0.6 m/s by the fifth frame (labeled "50 ms"). Meanwhile, the separation between cores is 7 mm in the first frame (labeled "0 ms") and increases to nearly 15 mm in the fifth frame.

In contrast, the intermediate vortex shown in row (b) of Figure 5 has a circulation of 170 cm^2/s and an initial propagation velocity of 2.2 m/s. By the time the

vortex reaches the position shown in the fifth frame of row (b), the propagation velocity has decreased to 1.8 m/s. The intermediate vortex shown in the first frame of row (b) has a core separation of 7.8 mm, which

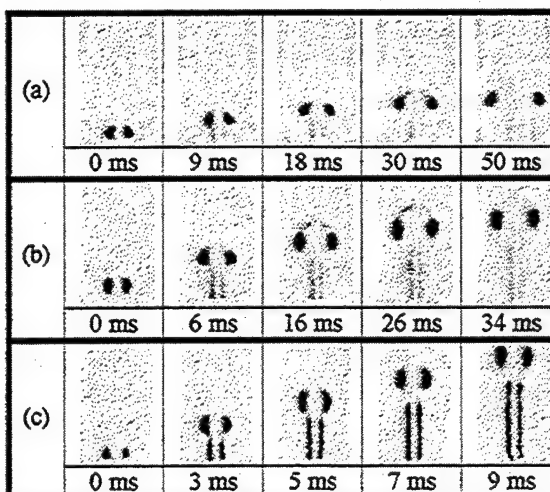


Figure 5. Vorticity fields for three vortices denoted by (a), (b), and (c). Times correspond to delays between the laser diagnostics trigger and the piston trigger.

increases to 12 mm by the fifth frame of row (b). Row (c) contains the time-resolved vorticity field for a "strong" vortex, which has a circulation of 1200 cm^2/s . This vortex has a propagation velocity of 8.4 m/s in the first frame. The velocity increases to a value of 10 m/s in the fourth frame and then decreases to 9.5 m/s in the fifth frame of row (c). The strong vortex has a core separation of 8 mm in the first frame, and the diameter grows to a value of 10.5 mm by the fifth frame of row (c). The strong vortex is observed to enter the upper-burner nozzle after the fifth frame. Care must be taken when attempting to generate a vortex that is stronger than case (c) since a three-dimensional lobe structure may result (Widnall, 1975).

Regimes of Flame-Vortex Interaction

The PLIF images of OH shown in Figure 6 correspond to a flame-vortex interaction in which extinction of the OH layer is absent. Initially, the vortex creates a small dent in the flame, and this dent then grows. Eventually the flame nearly surrounds the advancing vortex as it approaches the upper nozzle. In the later interaction stages, the OH PLIF signal level is observed to increase by greater than a factor of five over the levels observed without a vortex. The increased signal level is indicated by the light colors in the frames of Figure 6. This change in OH signal level is thought to indicate enhanced burning. For this particular example, the flow rates of Flame D in Table I are used.

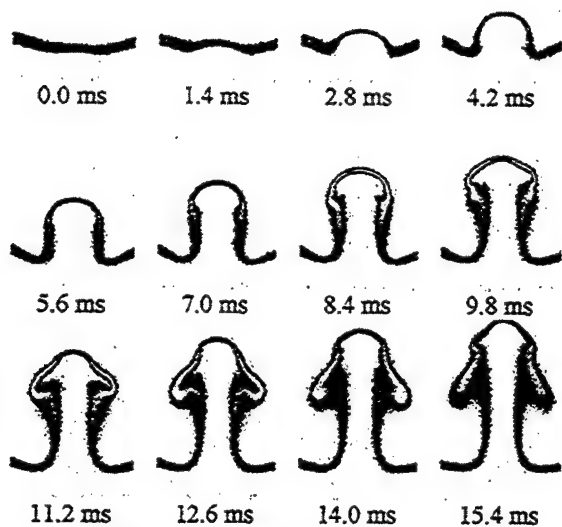


Fig. 6. OH PLIF images when OH layer remains intact.

The images of Figure 7 are obtained with flow conditions corresponding to Flame E in Table I and a vortex that is considered to be "strong". Extinction of the OH layer takes place in an annular pattern around the sides of the vortex, leaving a burning layer at its leading edge. This behavior was first predicted numerically by Katta,¹ well before these experiments were initiated, attesting to the utility of his code. After

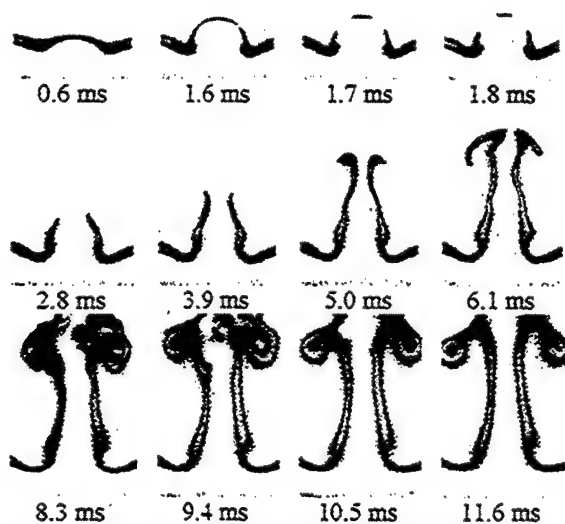


Figure 7: Sequence of images before and after extinction of the OH layer.

extinction, the isolated island of flame burns away, and the vortex travels upward toward the other nozzle. The flame follows the vortex, traveling up the stem. As the flame overtakes the vortex, it wraps up and turns in upon itself.

Typical planar Rayleigh-scattering images are shown in Figure 8. The flame conditions are similar to those for Figure 7; however, the vortex strength has been decreased slightly. As shown, Rayleigh-scattering images indicate an isolated island of high-temperature gas in front of the advancing vortex. Eventually this island burns around the vortex, and the island flame again contacts the outer flame at the vortex stem.

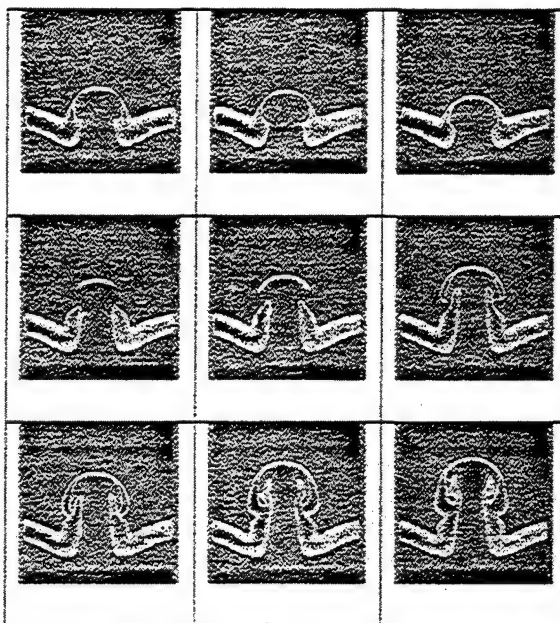


Figure 8. Rayleigh-scattering images of annular

Future Investigations

Based on the success of the studies described in this paper, we plan to extend experiments in several ways. First, although the agreement between the computations and the experiments regarding the annular extinction is good, more extensive measurements will be taken to identify a cause for this phenomenon. For instance, the extinction pattern may result from a flowfield boundary condition that is peculiar to this particular apparatus. Indeed, an advantage of the model of Katta is that the vortex-injection boundary conditions can be included in the numerical-solution process. In addition, a more fundamental interaction, such as preferential diffusion (Yoshida and Takagi, 1998) may cause this phenomenon.

Second, the Rolon burner configuration may prove to be ideal for studying other interactions of importance to combustion. One example that we have

recently begun to study is the behavior of fire suppressants injected into a laminar hydrocarbon flame. Here, the vortex-injection tube is fitted with a three-way solenoid valve having two inlets. The first inlet provides the air flow described in this paper. The second inlet provides some other gas mixture or a droplet-containing flow. The current to the solenoid valve is timed such that it switches to the second inlet only for a period of time sufficient to fill the vortex tube. The piston is then triggered to produce a carefully-controlled vortex or jet. The interaction with the flame is monitored using the diagnostics described in this paper.

Finally, the measurement techniques are being improved to aid in interpretation of the data. For example, simultaneous acquisition of PLIF and PIV data enables careful examination of quantities such as flame stretch by overlapping images from two cameras. An image containing overlapped vectors and a PLIF image of OH is shown in Figure 9. These vectors were calculated using an effective spatial resolution of ~ 1.6 mm, which may be inadequate for spatial derivatives in the vicinity of the flamefront. We are presently working to improve the spatial resolution. More importantly, thermophoresis may introduce a bias into velocity vectors where temperature gradients are large (Gomez and Rosner, 1993; Sung et al, 1996). Using simultaneous PLIF and Rayleigh-scattering measurements, we hope to use overlapped flame fronts to overlap corresponding velocity and temperature fields. The resulting images should permit an examination of thermophoretic bias on the velocity field.

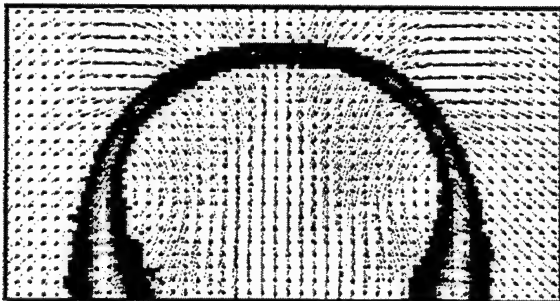


Figure 9. Simultaneous PIV and OH PLIF.

Conclusions

The apparatus of Rolon and co-workers (Renard et al., 1998a; Renard et al., 1998b; Rolon et al., 1995; Thevenin et al., 1996; Thevenin et al., 1998) has been implemented to study the interaction of a vortex and a flame. Digital two-color PIV has been applied to characterize the vortices injected into the opposed-jet flow. PLIF images of OH have been used to observe the dynamics of the interaction of the vortex and the flame. An annular break in the OH layer has been

observed, in excellent agreement with the numerical computations of Katta (Katta et al., 1998).

Acknowledgements

The authors thank Mr. K. D. Grinstead, Jr., for technical assistance in setting up the experiments. The authors also acknowledge the advice of Drs. L. P. Goss, S. P. Gogineni, J. Estevadeordal, M. A. Linne, and Mr. T. Drouillard concerning the reduction of two-color PIV data. The authors thank Dr. R. D. Hancock and Lt. I. Vihinen for assistance in assembly and construction of the burner. The authors also acknowledge Mr. P.-H. Renard, Drs. R. D. Hancock, W. M. Roquemore, and K.-Y. Hsu for the stimulating discussions of vortex-flame dynamics. Finally, the authors wish to thank Ms. M. M. Whitaker for editorial assistance. This work is supported by U. S. Air Force Contracts F33615-95-C-2507 and F33615-97-C-2702.

References

- Brickman, D., and Ruddick, B., 1990, "The Behavior and Stability of a Lens in a Strain Field," *Journal of Geophysical Research*, Vol. 95, No. C6, pp. 9657-9670.
- Chen, S.-J., and Dahm, W. J. A., 1997, "Vortex Ring/Diffusion Flame Interactions in Microgravity Conditions," *Proceedings of the Fourth International Microgravity Combustion Workshop*, Cleveland, OH, pp. 191-196. NASA Conference Publication No. 10191.
- Chen, S.-J., and Dahm, W. J. A., 1998, "Diffusion Flame Structure of a Laminar Vortex Ring Under Microgravity Conditions," accepted for publication in *Twenty-Seventh Symposium (International) on Combustion*, The Combustion Institute, Pittsburgh, PA.
- Daily, J. W., and Harleman, D. R. F., 1966, "Fluid Dynamics," Addison-Wesley Publishing, Reading, MA.
- Dibble, R. W., and Hollenback, R. E., 1981, "Laser Rayleigh Thermometry in Turbulent Flames," *Eighteenth Symposium (International) on Combustion*, The Combustion Institute, Pittsburgh, PA, pp. 1489-1499.
- Donbar, J. M., 1998, "Reaction Zone Structure and Velocity Measurements in Permanently Blue Non-premixed Jet Flames," Ph.D. Dissertation, University of Michigan, Ann Arbor, MI.
- Driscoll, J. F., Sutkus, D. J., Roberts, W. L., Post, M. E., and Goss, L. P., 1993, "The Strain Exerted by a Vortex on a Flame - Determined from Velocity Field Images," AIAA Paper No. 93-0362.

- Driscoll, J. F., Sutkus, D. J., Roberts, W. L., Post, M. E., and Goss, L. P., 1994, "The Strain Exerted by a Vortex on a Flame - Determined from Velocity Field Images," *Combustion Science and Technology*, Vol. 4/6, pp. 213-229.
- Dritschel, D. G., 1989, "Strain-Induced Vortex Stripping," in *Mathematical Aspects of Vortex Dynamics*, R. E. Caflisch, ed., SIAM, Philadelphia, PA, pp. 107-119.
- Escudie, D., 1988, "Stability of a Premixed Laminar V-Shaped Flame," *Progress in Astronautics and Aeronautics*, Vol. 113, pp. 215-239.
- Everest, D. A., 1994, "The Effect of Strain Rate on the Temperature Field Structure in a Turbulent Non-Premixed Flame Using Planar Rayleigh Scattering," Ph.D. Dissertation, University of Michigan, Ann Arbor, MI.
- Everest, D. A., Driscoll, J. F., Dahm, W. J. A., and Feikema, D. A., 1995, "Images of the Temperature Field and Temperature Gradients to Quantify Mixing Rates within a Non-Premixed Turbulent Jet Flame," *Combustion and Flame*, Vol. 101, pp. 58-68.
- Fox, R. W., and McDonald, A. T., 1985, "Introduction to Fluid Mechanics," John Wiley & Sons, New York.
- Frenklach, M., Wang, H., Goldenberg, M., Smith, G. P., Golden, D. M., Bowman, C. T., Hanson, R. K., Gardiner, W. C., Lissianski, V., 1995, *Gas Research Institute Technical Report No. GRI-95/0058*.
- Gharib, M., Rambod, E., and Shariff, K., 1988, "A Universal Time Scale for Vortex Ring Formation," *Journal of Fluid Mechanics*, Vol. 360, pp. 121-140.
- Gogineni, S., Goss, L. P., and Roquemore, W. M., 1998a, "Manipulation of a Jet in a Cross Flow," *Experimental Thermal and Fluid Science*, Vol. 16, pp. 209-219.
- Gogineni, S., Goss, L., Pestian, D., and Rivir, R., 1998b, "Two-Color Digital PIV Employing a Single CCD Camera," *Experiments in Fluids*, in press.
- Gomez, A., and Rosner, D. E., 1993, "Thermophoretic Effects on Particles in Counterflow Laminar Diffusion Flames," *Combustion Science and Technology*, Vol. 89, Nos. 5-6, pp. 335-362.
- Hancock, R. D., 1996, "Laser Diagnostic Investigation of the Structure of Steady and Driven Hydrogen Jet Diffusion Flames," Ph.D. Dissertation, University of Illinois, Urbana.
- Hancock, R. D., Schauer, F. R., Lucht, R. P., Katta, V. R., and Hsu, K. Y., 1996, "Thermal Diffusion Effects and Vortex-Flame Interactions in Hydrogen Jet Diffusion Flames," *Twenty-Sixth Symposium (International) on Combustion*, The Combustion Institute, Pittsburgh, PA, pp. 1087-1093.
- Hancock, R. D., Schauer, F. R., Lucht, R. P., and Farrow, R. L., 1997, "Dual-Pump Coherent Anti-Stokes Raman Scattering (CARS) Measurements of Nitrogen and Oxygen in a Laminar Jet Diffusion Flame," *Applied Optics*, Vol. 36, No. 15, pp. 3217-3226.
- Hertzberg, J. R., Namazian, M., and Talbot, L., 1984, "A Laser Tomographic Study of a Laminar Flame in a Karman Vortex Street," *Combustion Science and Technology*, Vol. 38, No. 3/4, pp. 205-216.
- Hsu, K. Y., Chen, L. D., Katta, V. R., Goss, L. P., and Roquemore, W. M., 1993, "Experimental and Numerical Investigations of the Vortex-Flame Interactions in a Driven Jet Diffusion Flame," *AIAA Paper No. 93-0455*.
- Jarosinski, J., Lee, J. H. S., and Knystautas, R., 1988, "Interaction of a Vortex Ring and a Laminar Flame," *Twenty-Second Symposium (International) on Combustion*, Pittsburgh, PA, pp. 505-514.
- Katta, V. R., Goss, L. P., and Roquemore, W. M., 1994, "Numerical Investigations of Transitional H_2/N_2 Jet Diffusion Flames," *AIChE Journal*, Vol. 32, No. 1, pp. 84-94.
- Katta, V. R., Carter, C. D., Fiechtner, G. J., Roquemore, W. M., Gord, J. R. and Rolon, J. C., 1998, "Interaction of a Vortex With a Flat Flame Formed Between Opposing Jets of Hydrogen and Air," accepted for publication in *Twenty-Seventh Symposium (International) on Combustion*, The Combustion Institute, Pittsburgh, PA.
- Khosla, R. P., 1992, "From Photons to Bits," *Physics Today*, Vol. 45, No. 12, pp. 42-49.
- Komiyama, M., Miyafuji, A., and Takagi, T., 1996, "Flamelet Behavior in a Turbulent Diffusion Flame Measured by Rayleigh Scattering Image Velocimetry," *Twenty-Sixth Symposium (International) on Combustion*, The Combustion Institute, Pittsburgh, PA, pp. 339-346.
- Lee, T.-W., Lee, J. G., Nye, D. A., and Santavica, D. A., 1993, "Local Response and Surface Properties of Premixed Flames During Interactions with Karman Vortex Streets," *Combustion and Flame*, Vol. 94, No. 1/2, pp. 146-160.
- Legras, B., and Dritschel, D. G., 1993, "Vortex Stripping and the Generation of High Vorticity Gradients in Two-Dimensional Flows," *Applied Scientific Research*, Vol. 51, pp. 445-455.
- Leonard, B. P., 1979, "A Stable and Accurate Convective Modeling Procedure Based on Quadratic Upstream Interpolation," *Computer Methods in Applied Mechanics and Engineering*, Vol. 19, pp. 59-98.
- Luff, J. D., Rompage, A. M., Linne, M. A., and Hertzberg, J. R., 1996, "Uncertainties Associated with the Post-Processing of 2-D Particle Image Velocimetry (PIV) Velocity Data of Unsteady Flow Fields," presented at the *Spring Technical Meeting of the Western States Section/ The Combustion In-*

- stitute, Tempe, AZ, March, 1996. Paper No. WSS 96S-005.
- Luff, J. D., Drouillard, T., Rompage, A. M., Linne, M. A., and Hertzberg, J. R., 1998, "Experimental Uncertainties Associated with Particle Image Velocimetry (PIV) Based Vorticity Algorithms," to appear in *Experiments in Fluids*, Vol. 25.
- Mariotte, A., and Legras, B., 1994, "Vortex Stripping and the Erosion of Coherent Structures in Two-Dimensional Flows," *Physics of Fluids*, Vol. 6, No. 12, pp. 3954-3962.
- Mueller, C. J., Driscoll, J. F., Sutkus, D. J., Roberts, W. L., Drake, M. C., and Smooke, M. D., 1995, "Effect of Unsteady Stretch Rate on OH Chemistry During a Vortex-Flame Interaction: To Assess Flamelet Models," *Combustion and Flame*, Vol. 100, No. 1/2, pp. 323-331.
- Mueller, C. J., Driscoll, J. F., Ruess, D. L., and Drake, M. C., 1996, "Effects of Unsteady Stretch on the Strength of a Freely-Propagating Flame Wrinkled by a Vortex," *Twenty-Sixth Symposium (International) on Combustion*, The Combustion Institute, Pittsburgh, PA, pp. 347-355.
- Mueller, C. J., 1996, "Measurements of Vortex-Flame Interaction Dynamics and Chemistry," Ph.D. Dissertation, University of Michigan, Ann Arbor.
- Mueller, C. J., Driscoll, J. F., Reuss, D. L., Drake, M. C., and Rosalik, M. E., 1998, "Vorticity Generation and Attenuation as Vortices Convect Through a Premixed Flame," *Combustion and Flame*, Vol. 112, No. 3, pp. 342-358.
- Mueller, C. J., and Schefer, R. W., 1998, "Coupling of a Diffusion Flame Structure to an Unsteady Vortical Flowfield," accepted for publication in *Twenty-Seventh Symposium (International) on Combustion*, The Combustion Institute, Pittsburgh, PA.
- Najm, H. N., Paul, P. H., Mueller, C. J., and Wyckoff, P. S., 1998, "On the Adequacy of Certain Experimental Observables as Measurements of Flame Burning Rate," *Combustion and Flame*, Vol. 113, No. 3, pp. 312-332.
- Nguyen, Q.-V., and Paul, P. H., 1996, "The Time Evolution of a Vortex-Flame Interaction Observed via Planar Imaging of CH and OH," *Twenty-Sixth Symposium (International) on Combustion*, The Combustion Institute, Pittsburgh, PA, pp. 357-364.
- Nichols, R. H., 1986, "The Effects of Particle Dynamics on Turbulence Measurements with the Laser Doppler Velocimeter," Ph.D. Dissertation, University of Tennessee, Knoxville, TN.
- Nye, D. A., Lee, J. G., Lee, T.-W., and Santavicca, D. A., 1996, "Flame Stretch Measurements During the Interaction of Premixed Flames and Karman Vortex Streets Using PIV," *Combustion and Flame*, Vol. 94, No. 1/2, pp. 167-176.
- Paul, P. H., 1991, "The Application of Intensified Array Detectors to Quantitative Planar Laser-Induced Fluorescence Imaging," AIAA 91-2315.
- Paul, P. H., van Cruyningen, I., Hanson, R. K., and Kychakoff, G., 1990, "High Resolution Digital Flowfield Imaging of Jets," *Experiments in Fluids*, Vol. 9, pp. 241-251.
- Pellet, G. J., Wilson, L. G., Humphreys, W. J., Jr., Batram, S. M., Gatrell, L. R., and Issac, K. M., 1995, "Velocity Fields of Axisymmetric Hydrogen-Air Counterflow Diffusion Flames from LDV, PIV, and Numerical Computation," AIAA 95-3112.
- Renard, P.-H., Rolon, J. C., Thevenin, D., and Candel, S., 1998a, "Wrinkling, Pocket Formation and Double Premixed Flame Interaction Processes," accepted for publication in *Twenty-Seventh Symposium (International) on Combustion*, The Combustion Institute, Pittsburgh, PA.
- Renard, P.-H., Rolon, J. C., Thevenin, D., and Candel, S., 1998b, "Investigations of Heat Release, Extinction, and Time Evolution of the Flame Surface for a Non-Premixed Flame Interacting with a Vortex," accepted for publication, *Combustion and Flame*.
- Roberts, W. L., and Driscoll, J. F., 1991, "A Laminar Vortex Interacting with a Premixed Flame: Measured Formation of Pockets of Reactants," *Combustion and Flame*, Vol. 87, No. 3/4, pp. 245-256.
- Roberts, W. L., 1992, "A Premixed Laminar Flame Interacting With a Vortex Resulting in Flame Stretch and Quenching," Ph.D. Dissertation, University of Michigan, Ann Arbor, MI.
- Roberts, W. L., Driscoll, J. F., Drake, M. C., and Ratcliffe, J. W., 1992, "OH Fluorescence Images of the Quenching of a Premixed Flame During an Interaction with a Vortex," *Twenty-Fourth Symposium (International) on Combustion*, The Combustion Institute, Pittsburgh, pp. 169-176.
- Roberts, W. L., Driscoll, J. F., Drake, M. C., and Goss, L. P., 1993, "Images of the Quenching of a Flame by a Vortex - To Quantify Regimes of Turbulent Combustion," *Combustion and Flame*, Vol. 94, No. 1/2, pp. 58-69.
- Rolon, J. C., Aguerre, F., and Candel, S., 1995, "Experiments on the Interaction Between a Vortex and a Strained Diffusion Flame," *Combustion and Flame*, Vol. 100, No. 3, pp. 422-429.
- Samaniego, J.-M., 1992a, "Generation of Two-Dimensional Vortices in a Cross Flow," *Annual Research Briefs - 1992*, Center for Turbulence Research, NASA Ames Research Center/Stanford University, pp. 431-441.
- Samaniego, J.-M., 1992b, "Stretch-Induced Quenching in Vortex-Flame Interactions," *Annual Research Briefs - 1993*, Center For Turbulence Research, NASA Ames Research Center/Stanford University, pp. 205-218.

- Schauer, F. R., 1998, "Thermal Diffusion and Flame Structure in a Laminar Hydrogen Jet Diffusion Flame," Ph.D. Thesis, University of Illinois, Urbana.
- Schauer, F. R., Hancock, R. D., Gogineni, S., and Lucht, R. P., 1998, "Vortex-Flame Interactions in Hydrogen Jet Diffusion Flames: A DPIV and DNS Investigation," submitted to *Experiments in Fluids*.
- Sinibaldi, J. O., Mueller, C. J., and Driscoll, J. F., 1997, "Measured Local Propagation Velocities of Wrinkled Premixed Flames," Proceedings of the *Fall Technical Meeting*, The Eastern States Section of the Combustion Institute, Hartford, CT, pp. 179-182.
- Sinibaldi, J. O., Driscoll, J. F., Mueller, C. J., and Tulkki, A. E., 1997 "Flame-Vortex Interactions: Effects of Buoyancy from Microgravity Imaging Studies," AIAA 97-0669.
- Sinibaldi, J. O., Mueller, C. J., Tulkki, A. E., and Driscoll, J. F., 1998, "Suppression of Flame Wrinkling by Buoyancy: The Baroclinic Stabilization Mechanism," AIAA Journal, Vol. 36, No. 8, pp. 1432-1438.
- Sinibaldi, J. O., Mueller, C. J., and Driscoll, J. F., 1998, "Local Flame Propagation Speeds Along Wrinkled, Unsteady, Stretched Premixed Flames," accepted for publication in *Twenty-Seventh Symposium (International) on Combustion*, The Combustion Institute, Pittsburgh, PA.
- Sullivan, J. P., Widnall, S. E., and Ezekiel, S., 1973a, "Study of Vortex Rings Using a Laser Doppler Velocimeter," AIAA Paper No. 73-105.
- Sullivan, J. P., Widnall, S. E., and Ezekiel, S., 1973b, "Study of Vortex Rings Using a Laser Doppler Velocimeter," *AIAA Journal*, Vol. 11, No. 10, pp. 1384-1389.
- Sung, C. J., Law, C. K., and Axelbaum, R. L., 1994, "Thermophoretic Effects on Seeding Particles in LDV Measurements of Flames," *Combustion Science and Technology*, Vol. 99, pp. 119-132.
- Sung, C. J., Kistler, J. S., Nishioka, M., and Law, C. K., 1996, "Further Studies on Effects of Thermophoresis on Seeding Particles in LDV Measurements of Strained Flames," *Combustion and Flame*, Vol. 105, pp. 189-201.
- Takagi, T., Yoshikawa, Y., Yoshida, K., Komiyama, M., and Kinoshita, S., 1996, "Studies on Strained Non-Premixed Flames Affected by Flame Curvature and Preferential Diffusion," *Twenty-Sixth Symposium (International) on Combustion*, The Combustion Institute, Pittsburgh, PA, pp. 1103-1110.
- Talbot, L., Cheng, R. K., Schefer, R. W., and Willis, D. R., 1980, "Thermophoresis of Particles in a Heated Boundary Layer," *Journal of Fluid Mechanics*, Vol. 101, No. 4, pp. 737-758.
- Thevenin, D., Rolon, J. C., Renard, P.-H., Kendrick, D. W., Veynante, D., and Candel, S., 1996, "Structure of a Nonpremixed Flame Interacting with Counter-rotating Vortices," *Twentieth-Sixth Symposium (International) on Combustion*, The Combustion Institute, Pittsburgh, PA, pp. 1079-1086.
- Thevenin, D., Renard, P.-H., Rolon, J. C., and Candel, S., 1998, "Extinction Processes During a Non-Premixed Flame/Vortex Interaction," accepted for publication in *Twenty-Seventh Symposium (International) on Combustion*, The Combustion Institute, Pittsburgh, PA.
- Trieling, R. R., Beckers, M., and van Heijst, G. J. F., 1997, "Dynamics of Monopolar Vortices in a Strain Flow," *Journal of Fluid Mechanics*, Vol. 345, pp. 165-201.
- Trieling, R. R., van Wesenbeeck, J. M. A., and van Heijst, G. J. F., 1998, "Dipolar Vortices in a Strain Flow," *Physics of Fluids*, Vol. 10, No. 1, pp. 144-159.
- Yoshida, K., and Takagi, T., 1998, "Transient Local Extinction and Reignition Behavior of Diffusion Flames Affected by Flame Curvature and Preferential Diffusion," accepted for publication in *Twenty-Seventh Symposium (International) on Combustion*, The Combustion Institute, Pittsburgh, PA.
- Waldmann, L., and Schmitt, K. H., 1966, "Thermophoresis and Diffusiophoresis of Aerosols," in *Aerosol Science*, C. N. Davies, ed., Academic Press, New York, pp. 137-162.
- Walsh, M. J., 1976, "Influence of Particle Drag Coefficient on Particle Motion in High Speed Flow with Typical Laser Velocimetry Applications," NASA TN D-8120.
- Widnall, S. E., 1975, "The Structure and Dynamics of Vortex Filaments," *Annu. Rev. Fluid. Mech.*, Vol. 7, pp. 141-165.
- Williams, G. A., Jr., Reihheimer, A. L., Johnson, C. B., Wheeler, K. D., Wodecki, N. D., Aebi, V. W., and Costello, K. A., 1995, "Back-Illuminated and Electron-Bombarded CCD's Low Light Level Imaging System Performance," SPIE Volume 2551, pp. 208-223.

Application of imaging techniques to the study of vortex-flame interactions

Gregory J. Fiechtner,^{a,b*} Paul-Henri Renard,^c James R. Gord,^a
Keith D. Grinstead, Jr.,^{a,b} Campbell D. Carter,^{a,b} and Juan Carlos Rolon^c

^aAir Force Research Laboratory, Propulsion Sciences and Advanced Concepts Division,
Wright-Patterson Air Force Base, OH 45433-7103, USA

^bPresent Address: Innovative Scientific Solutions, Inc., 2766 Indian Ripple Road,
Dayton, OH 45440-3638, USA

^cLaboratoire d'Énergétique Moléculaire et Macroscopique, Combustion,
École Centrale Paris and CNRS, Grande Voie des Vignes
92295 Châtenay-Malabry Cedex, France

ABSTRACT

A thorough understanding of turbulent reacting flows is essential to the continued development of practical combustion systems. Unfortunately, these studies represent a tremendous research challenge owing to the inherent complexity of such flows. In an effort to reduce the complexity of these systems while capturing the essential features that define the physics and chemistry of turbulent reacting flows, we have been studying the interaction of a vortex with a laminar flame. The experimental apparatus includes a piston-cylinder device configured to provide a controlled toroidal vortex. The generated vortex/jet interacts with a nonpremixed hydrogen-air flame supported in a counterflow burner. The counterflow configuration permits precise selection of the flame and the associated strain field. Vortex characterization is essential to interpreting the experimental observations and accomplishing numerical modeling of vortex-flame interactions. Two-color particle-image velocimetry (PIV) has been employed to characterize the vortex and to describe the underlying counterflow velocity field. The hydroxyl (OH) layer produced by the flame is imaged using planar laser-induced fluorescence (PLIF). The PIV and PLIF measurements of OH are performed simultaneously. A distinct annular extinction of the OH layer is observed, in good agreement with previous computational modeling predictions for the apparatus.

Keywords: PIV, PLIF, Laser-Induced Fluorescence, Vortex, Turbulence, Combustion

1. INTRODUCTION

Recent results in numerical modeling combined with experimental measurements have led to important advances in the understanding of combustion. Numerous investigations have contributed to these advances, including a particular type of study in which the interaction of a laminar, nonpremixed flame and a vortex is examined. These efforts involve repeatable, carefully controlled conditions that are highly amenable to experimental study. The resulting data can be used for a variety of purposes, such as identifying fundamental regimes of vortex-flame interactions.¹ Vortical structures are an important feature in unsteady and turbulent combustion,²⁻⁵ and experimental data can be used to develop models for use in practical combustion topics such as experimental gas turbine combustors.⁶⁻⁹ This paper contains experimental results that are used to validate prior numerical computations.

In recent computational calculations, Katta¹⁰ predicted that during the interaction of a nonpremixed hydrogen-air flame and an isolated vortex, the extinction of the OH layer would occur in an annular pattern. The experiments detailed in the present paper are performed to examine, in part, the validity of this prediction. Experimental results obtained with planar laser-induced fluorescence (PLIF) of OH are used to determine regimes in which the annular extinction occurs. The nonpremixed flame is supported by air and fuel in an opposed-jet burner. The fuel consists of hydrogen diluted with nitrogen. The temporal evolution of the vortex-flame interactions is imaged with the PLIF system. Additional measurements are performed to characterize the vortices. Particles are seeded into the flowfield, and the scattering is used for digital, two-color particle-image velocimetry (PIV) measurements. Digital PIV measurements are made simultaneously with PLIF measurements of OH.

* Further author information: (Send correspondence to G.J.F.)

G.J.F.: E-mail: gjfiech@ward.appl.wpafb.af.mil, Tel: (937) 255-8373, WWW: www.innssi.com

An annular break in the OH layer is observed, in agreement with the predictions of Katta using numerical computations.¹⁰ The annular pattern is accompanied by comparatively large flame curvature. The temporal resolution that is necessary to resolve the annular break experimentally is found to agree with the magnitude of the computational time step used by Katta.

2. BACKGROUND

Numerous experimental studies of the interaction dynamics of vortices and flames have been conducted, and many of these investigations employed two-dimensional imaging to study the interaction. For premixed flame fronts, most measurements have been made using two types of flames. Hertzberg et al.¹¹ and Escudie¹² conducted an experiment in which a Karman vortex street was produced using a cylindrical rod in a cross flow of premixed gases. A V-flame was supported behind a wire positioned downstream of the rod that produced the vortex street. Planar tomographic imaging was used to study the interaction of the vortex street and the flame. A similar interaction of a Karman vortex street and a flame was investigated by Lee et al.¹³ using PLIF imaging of OH and by Nye et al.¹⁴ using both OH PLIF and PIV. A disadvantage of using the vortex street is the difficulty in isolating a single vortex. Samaniego¹⁵ developed a means of injecting an isolated line vortex through a horizontal slot in the wall of a vertical wind tunnel; this was pursued as a means of replacing the vortex street in experiments with V-flames. A year later, Samaniego¹⁶ presented results on the interaction of a line vortex and a V-flame. Schlieren images of the time-dependent vortex-flame interaction along with CH emission data from the entire flame were presented. Nguyen and Paul¹⁷ also studied vortex-flame interactions using the Samaniego burner, reporting results of PLIF measurements of OH and CH radicals.

In a second type of study involving premixed combustion, Jarosinski et al.¹⁸ studied a flame that was ignited at one end of a tube of premixed gases. A vortex was injected at the other end of the tube. The interaction dynamics were then photographed using a mercury-xenon arc lamp and a rotating-drum streak camera with a rotating-disc shutter. Recently, Driscoll and co-workers produced an impressive series of papers concerning a similar vortex-flame facility in which PIV, OH PLIF, or a combination of these imaging techniques was applied.¹⁹⁻²⁷

Nonpremixed flames have also been the subject of experimental study. Rolon and co-workers^{1,28-31} recently developed an apparatus in which a vortex is injected into a flame supported between the nozzles of an opposed-jet burner. This geometry has numerous advantages. First, unlike the above geometries, a stationary nonpremixed flame can be produced and isolated easily. Second, the flame thickness can be varied by changing either the nozzle velocities or the spacing between the upper and lower burner nozzles. The device has also been extended to the study of vortices that interact with premixed opposed-jet flames.¹ Takagi and coworkers^{32,33} performed planar Rayleigh-scattering measurements of temperature in a similar type of opposed-jet burner in which a small jet of fuel or air was injected using a micro nozzle with an inner diameter of only 0.25 mm. Either a jet of air was injected from the air side of the diffusion flame or a jet of fuel was injected from the fuel side. Santoro and coworkers³⁴ modified a vortex counterflow burner so that either gaseous or spray flames can be studied.

In a different class of measurements, Hsu et al.^{35,36} modulated the axial velocity of a laminar jet diffusion flame using a loud speaker to produce vortex-flame interactions. This apparatus was further studied by Hancock and coworkers³⁷ using a number of techniques including reactive Mie scattering, PLIF, and digital PIV. These studies have provided large quantities of data for comparison with numerical-modeling predictions. A potential disadvantage of this burner is the complicated geometry (when compared to the above geometries, which involve completely isolated vortex injection) due to the convective velocity field associated with rotation of the vortex and translation of the flame zone. In a similar type of study, Mueller and Schefer³⁸ performed OH PLIF measurements in a Wolfhard-Parker slot burner that was forced acoustically by loud speakers on the side walls of the upstream fuel duct. PLIF imaging of acetone was used as a marker of the fuel.

More recently, Chen and Dahm³⁹ developed a facility for generating a nonpremixed burning layer that wraps into a vortex ring. The facility has been operated under conditions of both normal gravity and microgravity, allowing the study of the influence of buoyancy. In contrast, You et al.⁴⁰ have designed a facility in which the vortex is ignited just as the fluid begins to exit a tube.

The experiments described in the present paper are based on the counterflow geometry of Rolon and co-workers.^{1,28-31} A fuel mixture of hydrogen and nitrogen permits the use of laser diagnostics in the absence of hydrocarbon interferences. Hydrogen chemistry simplifies the numerical calculations that are the subject of comparison with experimental results.^{2,3,10,41}

3. APPARATUS AND PROCEDURE

3.1 Burner Facility

A picture (a) and diagram (b) of the Rolon burner are shown in Figure 1. The flame is supported between upper and lower nozzles separated by 40 mm, each with an exit diameter of 25 mm. The fuel consists of hydrogen diluted with nitrogen and flows from the upper nozzle. Air flows from the lower nozzle. Unique to this type of apparatus is a tube with 5-mm inner diameter that is installed concentrically within the lower nozzle. This tube is attached to a cylinder that contains a piston which, in turn, is attached to an actuator. Feeding an appropriate current to the actuator causes a solenoid to force the piston upward abruptly, resulting in the emergence of a vortex from the tube. For a cylindrical volume of fluid that emanates from a nozzle having length L and diameter D , Gharib et al.⁴² have shown that the maximum circulation which a vortex ring can attain is reached for L/D at ~ 4 and that for larger ratios additional trailing vortex rings form. For the present 0.5-cm nozzle, the volume that a vortex can contain as estimated from the results of Gharib et al.⁴² is $\sim 0.4 \text{ cm}^3$. The present vortex generator can sweep a maximum volume of $\sim 3 \text{ cm}^3$, for a maximum attainable L/D ratio of ~ 30 . For the experiments described in this paper, comparatively strong vortices are generated using a 0.1-ms piston risetime.

The piston is allowed to travel through its maximum range, but the tube is placed such that the diagnostics are triggered

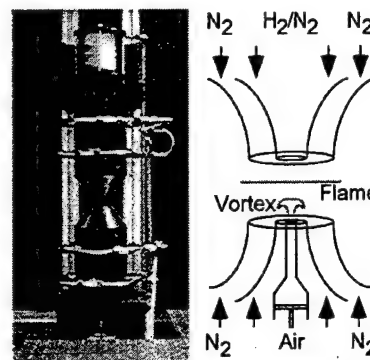


Figure 1. (a) Digital photograph of opposed-jet burner. (b) Cross-sectional diagram of burner nozzles and piston.

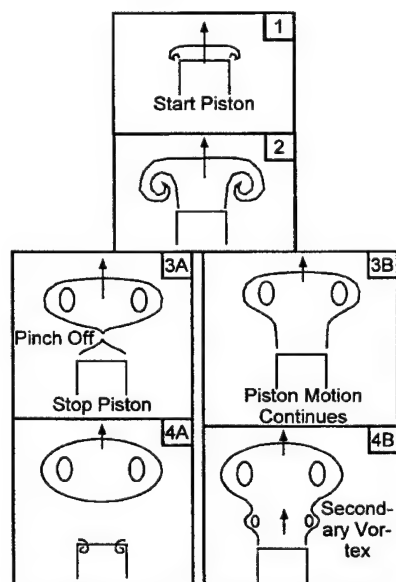


Figure 2. Diagram of vortex-formation processes.

before a secondary or tertiary vortex exits the tube. This process is illustrated in Figure 2. In frame 1 of Figure 2, a slug of fluid begins to exit the tube, while in frame 2, the vortex begins to form. After frame 2, one of two paths is followed depending on the motion of the piston. If the piston is stopped (path A), the vortex pinches off as it travels upward, as illustrated in frames 3A and 4A of Figure 2. If the piston motion is allowed to continue (path B), the vortex travels initially above a column of fluid, as shown in frame 3B. This condition is selected for the present experiments because the resulting vortex resembles closely the corresponding vortices used in the computations of Katta.^{2,3,41} Therefore, models that rely on an artificially created vortex pair by specifying the vortex field may not be well-represented by our experimental conditions.⁴³ If the piston is allowed to pump fluid from the nozzle at later times, multiple vortices can be produced from the tube, as illustrated in frame 4B of Figure 2. Vortex conditions are monitored carefully by examining scattering images acquired with a color digital camera; the multiple-vortex condition is avoided in this manner. It is also possible for vortices that are initially laminar to then become unsteady and turbulent,⁴⁴ conditions that are carefully avoided. In addition, if the piston/cylinder is not properly aligned and lubricated, an undesired turbulent puff of fluid exits the tube.^{45,46}

The laminar vortices travel upward within the surrounding oxidizer flow. A flow of air is supplied to the vortex tube such that in the absence of a vortex, the exit velocity matches the velocity of the air from the surrounding nozzle. To minimize the impact of room-air disturbances, upper and lower guard flows of nitrogen are supported through outer nozzles, which are concentric with the respective upper and lower inner nozzles that support the flame. The hydrogen,

nitrogen-diluent, and oxidizer-air flows are furnished by mass-flow controllers with respective full-scale ranges of 20, 20, and 30 l/min. A continuous flow of air is provided to the vortex tube by a 5-l/min controller, while the guard flows for the upper and lower guard (outer) nozzles are furnished by two 50-l/min mass-flow controllers. The flow rates of the controllers are accurate to $\pm 1\%$ of the full-scale range. The experiments have been completed for a volume fraction of H_2 in N_2 of 0.19, with flow rates for H_2 , N_2 , and Air of 4.04, 17.1, and 11.2 l/min, respectively.

Seed particles are introduced into the burner flows when digital PIV measurements of the vortex velocity are performed. Three particle seeders are installed; one is placed after the air mass-flow controller, another after the vortex-air mass flow controller, and a third after the junction where the hydrogen and nitrogen gases are mixed. With the use of three seeders, each flow can be seeded with particles individually, or combinations of the different flowfields can be seeded. Each seeder

contains hollow spherical ceramic particles with an approximate mean diameter of $2.4\text{ }\mu\text{m}$. When PIV studies are not required, the seeders are removed from the apparatus. Experiments are repeated for both seeded and unseeded flows, and no significant change in the results is caused by the presence of seed particles.

3.2 Synchronization and Timing

The time-dependent nature of vortex-flame interactions is compared to computational predictions. Precise synchronization of several experimental events is required, including vortex generation and propagation, production of laser pulses, and activation of the camera shutter and intensifier. A block diagram of the synchronization scheme is included in Figure 3.

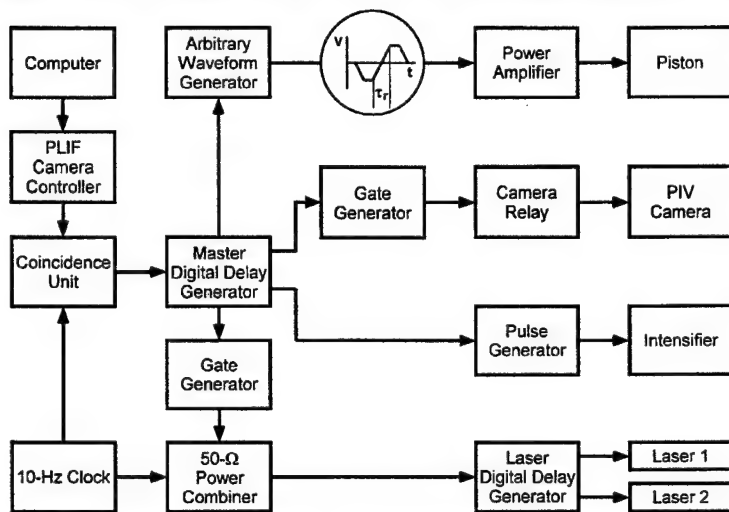


Figure 3. Diagram of electronic timing connections for simultaneous OH PLIF and digital PIV measurements.

synchronizing it with the 10-Hz clock and the laser pulse train. This DDG triggers an arbitrary-waveform generator (AWG) that outputs a 1-s waveform; this waveform is amplified and fed to the piston actuator to generate a vortex. Approximately 0.5 s after the AWG waveform is initiated, the vortex is fired; therefore, five laser pulses are generated during the time between computer initiation and the vortex-flame interaction.

When the DDG is externally triggered, the jitter between the trigger and a DDG output pulse is 60 ps plus the output delay divided by 10^8 . Over the 0.5-s period between the first and fifth laser pulses, this corresponds to a jitter of 5.06 ns. The 10-Hz-clock jitter specifications are not nearly so good. The jitter between clock outputs is one part in 10,000, corresponding to a jitter of 50 μs over the same 0.5-s period. Attempting to synchronize the piston with the clock limits the temporal resolution available to "freeze" vortex-flame events in time and requires an intensifier gate width significantly larger than 50 μs . The master DDG is, therefore, configured to trigger the fifth laser pulse preemptively. A delayed pulse from the master DDG arrives at the 50- Ω power combiner just before the fifth pulse in the clock pulse train, triggering the laser(s) preemptively. If no initiation pulse is output from the computer, the laser(s) are triggered by the 10-Hz clock as usual. This approach reduces the jitter in the timing of the fifth laser pulse from 50 μs to ~ 5 ns while maintaining the nominal 10-Hz repetition rate required by the lasers.

Other outputs of the master DDG are delayed suitably and directed to the image detectors. For PIV experiments, the width of a TTL pulse is adjusted using a gate generator, which closes a relay to trigger the digital PIV camera system. For simultaneous PLIF experiments, another master-DDG output triggers a pulse generator which, in turn, activates the intensifier of an ICCD camera.

The scheme depicted in Figure 3 provides precise control of the relative timing between the laser diagnostics and the vortex-flame event. To explore the temporal evolution of the event, data are captured utilizing the following phase-locked timing sequence: 1) an image is recorded, 2) the delay between vortex production and the laser/camera events is adjusted, and 3) another vortex is initiated and a second image recorded. This process is repeated to acquire numerous images, obtained at increasing delays. Effective temporal separation between images is selected between 10 and 3 ms, depending on

Because the Nd:YAG lasers are designed to operate at a nominal repetition rate of 10 Hz, the experimental sequence must be synchronized to a 10-Hz master clock that drives the flash lamps and the Pockels cells of the lasers. To trigger the lasers, the clock sends two signals—one traveling to a 50- Ω power combiner and then to the laser digital delay generator (DDG). The 10-Hz clock also provides a TTL signal to one of two inputs of a coincidence unit. The second input of this unit is driven by a TTL pulse from the PLIF camera controller. The coincidence unit outputs a pulse only when pulses from both the 10-Hz clock and the PLIF camera controller are present. When a vortex-flame event is initiated using a personal computer, the PLIF camera controller outputs a pulse ~ 1.3 s in duration. The corresponding output of the coincidence unit is a 1.3-s envelope of TTL pulses separated by 100 ms. The first pulse in this envelope triggers a master DDG,

the time scale of the event under study. The resulting temporal sequences of images are a testament to the high degree of repeatability achievable with this apparatus.

3.3 Measurement Techniques and Data Collection

The PLIF system contains a frequency-doubled, Q-switched Nd:YAG laser that is used to pump a dye laser which, in turn, is frequency doubled. The UV radiation is directed through a telescope that is adjusted to produce a light sheet with a height that matches as nearly as possible the 40-mm burner separation. The resulting beam thickness is $\sim 300\text{ }\mu\text{m}$, which corresponds to the full width (defined as the distance between the locations of the 25% peak intensity points).

Hydroxyl radicals absorb the laser radiation at 281.3414 nm via the $R_1(8)$ transition of the (1,0) band in the A-X system. Fluorescence from the A-X (1,1) and (0,0) bands is detected at right angles through WG-295 and UG-11 colored-glass filters, using a 105-mm-focal-length $f/4.5$ UV lens. The resulting light is recorded on an intensified CCD camera with an intensifier gate width of 100 ns. CCD pixels are binned in 2×2 groups, resulting in an effective array size of 288×192 pixels, with an imaged area of $25.6 \times 38.4\text{ mm}^2$. The images are cropped such that the bottom of each image coincides with the top surface of the lower nozzle. A color table is used with a maximum value set to 95% of the maximum signal for all images taken at a given flame condition. The low-signal color is assigned by calculating the background noise and selecting a minimum value that is two standard deviations above this level. Therefore, in cases where "extinction" of the OH layer is observed, "extinction" refers to signal levels that fall below this minimum value and are, therefore, assigned the last color in the table. The last color is chosen to be white to facilitate easy viewing of images when overlaid with velocity vectors.

In studies of vortex-flame interactions conducted by other investigators (see, for example, Najm et al.^{47,48}), PLIF was applied as a marker of some other quantity such as heat release or burning rate. In the present experiments, the OH image is obtained for direct comparison with numerical computations of the OH distribution with respect to certain spatial features;¹⁰ therefore, no attempt is made to correlate the images with any other quantities, although it has been shown recently that the OH concentration may be a good indicator of flame extinction in this configuration.²⁸ The presence of a break in the OH layer is ascertained by repeating measurements at later delays, for which it is obvious that the vortex passes through a hole in the flame zone. We do not attempt to map the detailed OH concentration profiles across the flame zone in the vicinity of the perceived break.

Measurements of the velocity field are carried out using digital, two-color PIV.^{49,50} Here, a color digital CCD with an array of 3060×3036 pixels is used. A magnification of 78,368 pixels/m is employed, resulting in an imaged area of $26.0 \times 39.0\text{ mm}^2$. The color CCD camera and the intensified CCD array are aligned using a transparent mask printed with a graduated scale. Further alignment between images is performed after each experiment employing software; a transformation in two-dimensional space is applied to the PIV images relative to the PLIF images. Two lasers are used, with one PIV light sheet produced by doubling the output of a Q-switched Nd:YAG laser directly (30 mJ/pulse at the test section). The remainder of this beam is used to pump the dye laser that is frequency doubled to excite OH fluorescence. The second PIV light sheet is produced by pumping a dye laser (employing DCM laser dye) with a second frequency-doubled, Q-switched Nd:YAG laser, resulting in laser radiation at 640 nm (40 mJ/pulse at the test section). The thickness of both the red and green light sheets is set to $\sim 700\text{ }\mu\text{m}$ at the probe region. A digital delay generator is used to drive the timing of the two lasers such that the red pulses are delayed precisely with respect to the green ones. In the absence of a vortex, the underlying counterflow velocity field is probed with red pulses that are delayed by up to 1 ms with respect to the corresponding green pulses. For the fastest vortices studied, the delay between red and green pulses is reduced to 10 μs . The camera shutter is set to open for 1/15 s to permit both laser pulses to be detected by the color CCD. Most of the flame emission and light from other devices in the laboratory (monitors, etc.) is greatly attenuated by the shutter.

Velocity vectors are calculated using the correlation software described by Gogineni and coworkers.^{49,50} A correlation area of 128×128 pixels is used in the calculation, corresponding to a correlation area of 0.269 cm^2 and a spatial resolution of 1.6 mm. The digital PIV measurements are performed to obtain the propagation velocity of the vortex to match experimental and computational conditions; this correlation area is acceptable for such purposes. Neighboring correlation boxes are overlapped by 75%, resulting in a velocity field with an area containing 95×60 vectors, or 5700 total vectors over the area of the color CCD. In some portions of each image, a small percentage of errant vectors results from low seed levels, scattering of light into the camera, flame emission, and other effects. Because the vortex-flame interactions are repeatable, digital PIV images can be recorded until an image with an extremely small percentage of incorrect vectors is obtained. For presentation purposes, most vectors are not plotted, with fields of 15×32 vectors selected for the present images.

Color digital images acquired using the PIV system can also be used without further computation of velocity vectors. By adjusting the seed level in the vortex-tube flow so that it is either noticeably larger or smaller than the seed levels for the rest

of the burner, flow visualization of the vortex-formation process is possible. Because of the temporal separation between the red and green laser pulses, these images may appear to be slightly blurred.

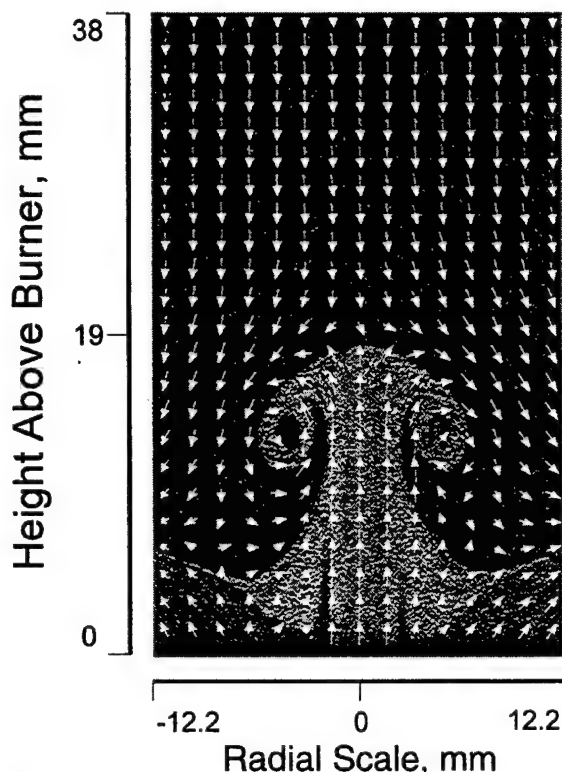


Figure 4. Scattering from particles in vortex flow with PIV velocity field superimposed.

4. RESULTS AND DISCUSSION

The scattering image of Fig. 4 is obtained when the vortex-tube flow is seeded with a slightly higher particle density than that produced by the upper and lower burners. As shown, the "mushroom" vortex advances ahead of a column of fluid because the piston continues to push fluid from the vortex nozzle. The fluid column takes on the appearance of the stem of a mushroom. The scattering image of Fig. 4 is taken in a cold flow. Vortices produced in reacting flows also exhibit the laminar stem-like appearance in the wake. The vortex has a propagation velocity of 1.5 m/s.

The PLIF images of OH shown in Figure 5 correspond to a vortex-flame interaction in which extinction of the OH layer is not observed. Initially, the vortex creates a small dent in the flame, and this dent begins to grow. Eventually the flame engulfs the advancing vortex as it approaches the upper nozzle. The vortex of Figure 5 has a propagation velocity of 3.9 m/s.

The images of Figure 6 correspond a vortex that has a propagation velocity of 5.0 m/s. Extinction of the OH layer is observed. After extinction the vortex travels upward toward the other nozzle. The flame follows the vortex, traveling up the stem. The temporal resolution of the sequence plotted in Figure 6 is not sufficient to observe the local structure of the extinction of the OH layer. We have found that a temporal resolution of 10 μ s is often necessary to study these regimes adequately for hydrogen/air flames.⁵¹ This temporal resolution agrees with the resolution used by Katta¹⁰ during numerical simulations of these

interactions. An image of the spatial structure taken at the instant of extinction of the OH layer is shown in Figure 7. The annular break in the OH layer was first predicted numerically by Katta¹⁰ attesting to the utility of his code. The annular pattern is also observed in experiments in which Rayleigh scattering images of temperature are recorded.⁵¹

5. FUTURE INVESTIGATIONS

The Rolon burner may prove to be ideal for studying other interactions of importance to combustion. One example that we have recently begun to study is the behavior of fire suppressants injected into a laminar hydrocarbon flame. Here, the vortex-injection tube is fitted with a three-way solenoid valve having two inlets. The first inlet provides the air flow described in this paper. The second inlet provides some other gas mixture or a droplet-containing flow. The current to the solenoid valve is timed such that it switches to the second inlet only for a period of time sufficient to fill the vortex tube. The piston is then triggered to produce a carefully-controlled vortex or jet. The interaction with the flame is monitored using the diagnostics described in this paper.

Measurement techniques are being improved to aid in interpretation of the data. For example, simultaneous acquisition of PLIF and PIV data enables careful examination of quantities such as flame stretch by overlapping images from two cameras. Vectors were calculated using an effective spatial resolution of ~ 1.6 mm, which may be inadequate for spatial derivatives in the vicinity of the flamefront. We are presently working to improve the spatial resolution. More importantly, thermophoresis may introduce a bias into velocity vectors where temperature gradients are large.^{52,53} Using simultaneous PLIF and Rayleigh-scattering measurements of temperature, we hope to use overlapped flame fronts to overlap corresponding velocity and temperature fields. The resulting images should permit an examination of thermophoretic bias on the velocity field.

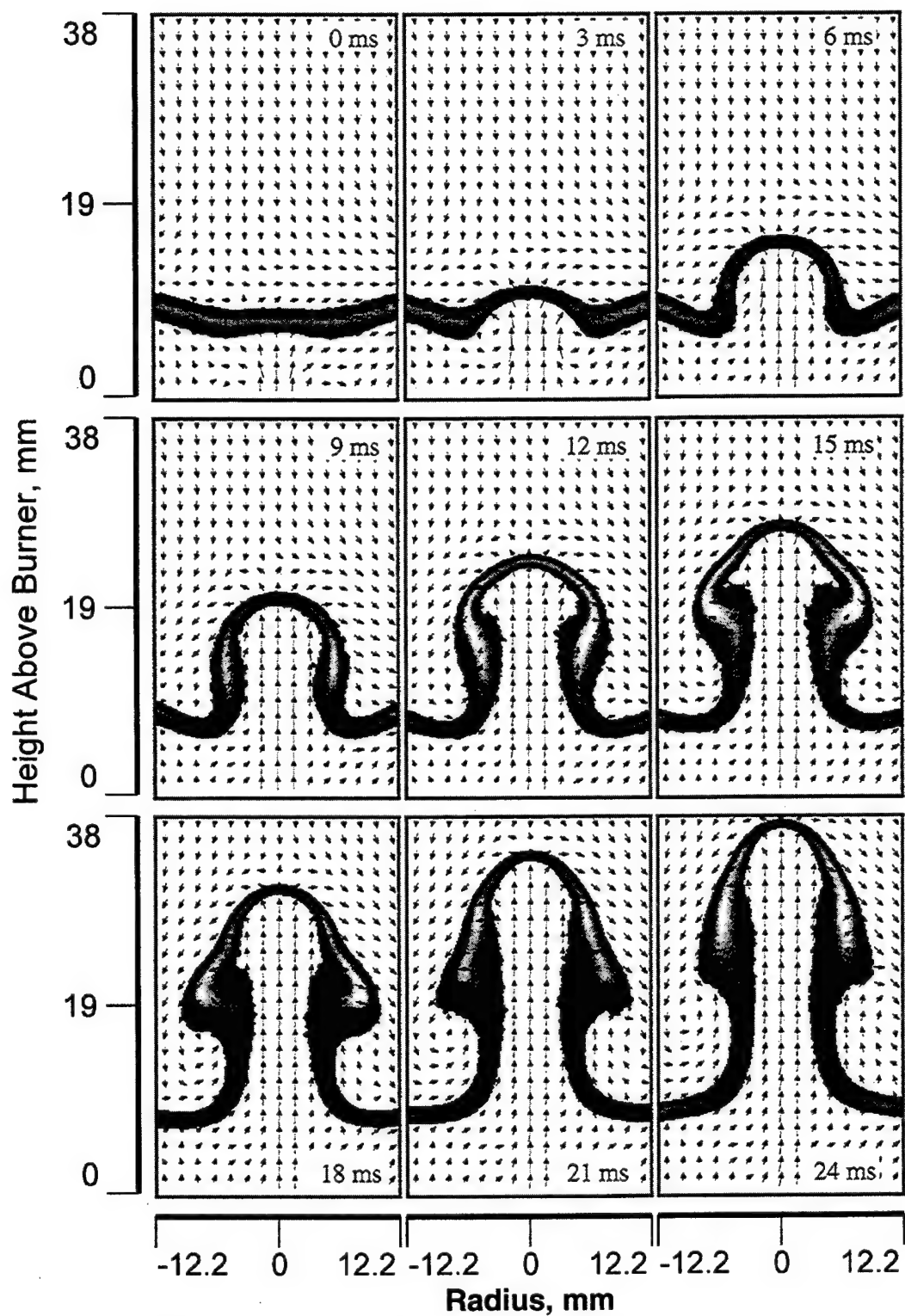


Figure 5. Sequence of PIV/OH PLIF images taken when the OH layer remains intact.

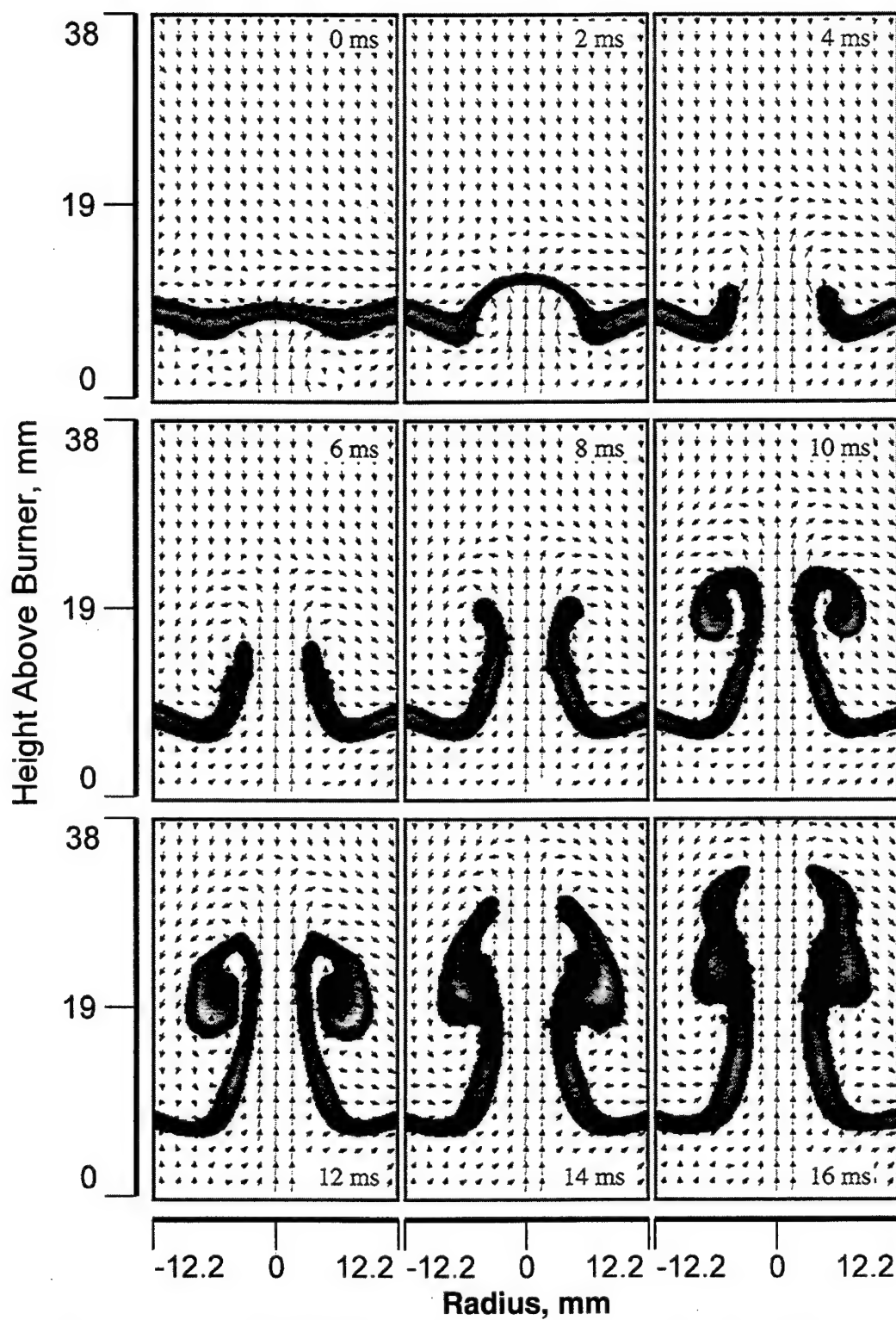


Figure 6. Sequence of PIV/OH PLIF images taken before and after local extinction of the OH layer.

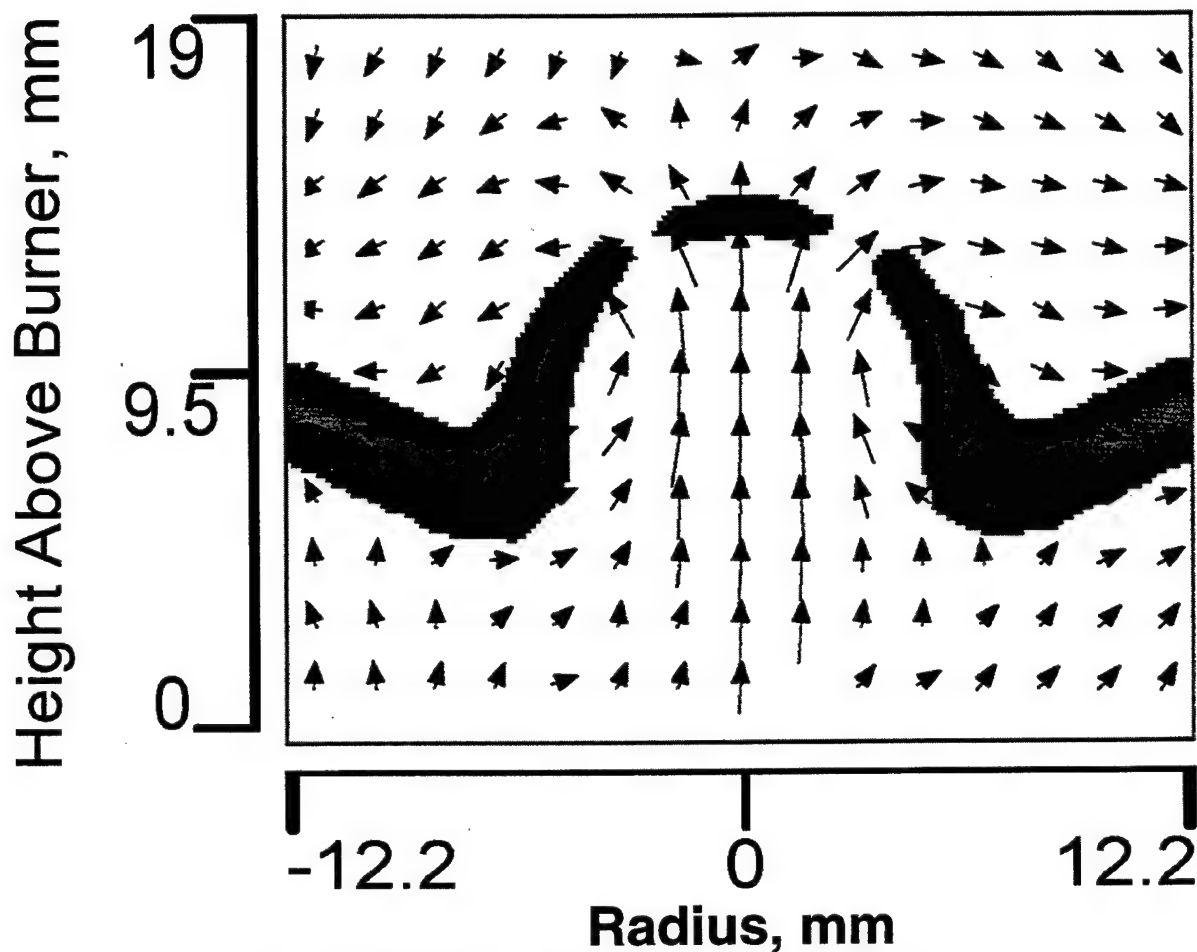


Figure 7. PIV/OH PLIF image of the annular extinction of the OH layer.

6. CONCLUSIONS

The apparatus of Rolon and co-workers^{1,28-31} has been implemented to study the interaction of a vortex and a flame. Digital two-color PIV has been applied to characterize the vortices injected into the opposed-jet flow. Simultaneous PLIF images of OH have been used to observe the dynamics of the interaction of the vortex and the flame. An annular break in the OH layer has been observed, in excellent spatial and temporal agreement with the numerical computations of Katta.¹⁰

ACKNOWLEDGEMENTS

The authors thank Dr. J. M. Donbar for technical assistance in setting up the experiments. The authors also acknowledge the advice of Drs. L. P. Goss, S. P. Gogineni, J. Estevadeordal, M. A. Linne, and Mr. T. Drouillard concerning the reduction of two-color PIV data. The authors thank Dr. R. D. Hancock and Lt. I. Vihinen for assistance in assembly and construction of the burner. The authors also acknowledge Drs. J. M. Donbar, R. D. Hancock, W. M. Roquemore, V. R. Katta, and K.-Y. Hsu for the stimulating discussions of vortex-flame dynamics. Finally, the authors wish to thank Ms. M. M. Whitaker for editorial assistance. This work is supported by U. S. Air Force Contracts F33615-95-C-2507 and F33615-97-C-2702.

REFERENCES

1. P.-H. Renard, J. C. Rolon, D. Thevenin, and S. Candel, "Wrinkling, Pocket Formation and Double Premixed Flame Interaction Processes," *Twenty-Seventh Symposium (International) on Combustion*, The Combustion Institute, Pittsburgh, PA, pp. 659-666, 1998.
2. W. M. Roquemore and V. R. Katta, "Role of Flow Visualization in the Development of UNICORN," *International Conference on Optical Technology and Image Processing in Fluid, Thermal, and Combustion Flow*, Yokohama, Japan, Paper No. KL-310, 1998.
3. W. M. Roquemore and V. R. Katta, "Role of Flow Visualization in the Development of UNICORN," *Journal of Visualization*, in press, 1999.
4. F. Takahashi, W. J. Schmoll, D. D. Trump, and L. P. Goss, "Vortex-Flame Interactions and Extinction in Turbulent Jet Diffusion Flames," *Twenty-Sixth Symposium (International) on Combustion*, The Combustion Institute, Pittsburgh, PA, pp. 145-152, 1996.
5. W. M. Roquemore, V. K. Reddy, P. O. Hedman, M. E. Post, T. H. Chen, L. P. Goss, D. Trump, V. Vilimpoc, and G. J. Sturgess, "Experimental and Theoretical Studies in a Gas-Fueled Research Combustor," *29th AIAA Aerospace Sciences Meeting*, Reno, NV, AIAA 91-0639, 1991.
6. V. R. Katta and W. M. Roquemore, "Numerical Studies on Trapped-Vortex Concepts for Stable Combustion," *Trans. ASME* **120**, pp. 60-68, 1998.
7. V. R. Katta and W. M. Roquemore, "Study on Trapped-Vortex Combustor--Effect of Injection on Dynamics of Non-Reacting and Reacting Flows in a Cavity," *33rd AIAA/ASME/SAE/ASEE Joint Propulsion Conference & Exhibit*, Seattle, WA, AIAA 97-3256, 1997.
8. M. D. Durbin, M. D. Vangsness, D. R. Ballal, and V. R. Katta, "Study of Flame Stability in a Step Swirl Combustor," *Trans. ASME* **118**, pp. 308-315, 1996.
9. K. Y. Hsu, C. D. Carter, V. R. Katta, and W. M. Roquemore, "Characteristics of Combustion Instability Associated with Trapped-Vortex Burner," *37th AIAA Aerospace Sciences Meeting and Exhibit*, Reno, NV, AIAA 99-0488, 1999.
10. V. R. Katta, C. D. Carter, G. J. Fiechtner, W. M. Roquemore, J. R. Gord, and J. C. Rolon, "Interaction of a Vortex With a Flat Flame Formed Between Opposing Jets of Hydrogen and Air," *Twenty-Seventh Symposium (International) on Combustion*, The Combustion Institute, Pittsburgh, PA, pp. 587-594, 1998.
11. J. R. Hertzberg, M. Namazian, and L. Talbot, "Tomographic Study of a Laminar Flame in a Karman Vortex Street," *Combust. Sci. Technol.* **38**, pp. 205-216, 1984.
12. D. Escudie, "Stability of a Premixed Laminar V-Shaped Flame," *Prog. Astronaut. Aeronaut.* **113**, pp. 215-239, 1988.
13. T.-W. Lee, J. G. Lee, D. A. Nye, and D. A. Santavicca, "Local Response and Surface Properties of Premixed Flames During Interactions with Karman Vortex Streets," *Combust. Flame* **94**, pp. 146-160, 1993.
14. D. A. Nye, J. G. Lee, T.-W. Lee, and D. A. Santavicca, "Flame Stretch Measurements During the Interaction of Premixed Flames and Karman Vortex Streets Using PIV," *Combust. Flame* **94**, pp. 167-176, 1996.
15. J.-M. Samaniego, "Generation of Two-Dimensional Vortices in a Cross Flow," *Annual Research Briefs--1992*, Center for Turbulence Research, NASA Ames Research Center/Stanford University, pp. 431-441, 1992.
16. J.-M. Samaniego, "Stretch-Induced Quenching in Vortex-Flame Interactions," *Annual Research Briefs--1993*, Center for Turbulence Research, NASA Ames Research Center/Stanford University, pp. 205-218, 1992.
17. Q.-V. Nguyen and P. H. Paul, "The Time Evolution of a Vortex-Flame Interaction Observed via Planar Imaging of CH and OH," *Twenty-Sixth Symposium (International) on Combustion*, The Combustion Institute, Pittsburgh, PA, pp. 357-364, 1996.
18. J. Jarosinski, J. H. S. Lee, and R. Knystautas, "Interaction of a Vortex Ring and a Laminar Flame," *Twenty-Second Symposium (International) on Combustion*, The Combustion Institute, Pittsburgh, PA, pp. 505-514, 1988.
19. J. F. Driscoll, D. J. Suktus, W. L. Roberts, M. E. Post, and L. P. Goss, "The Strain Exerted by a Vortex on a Flame--Determined from Velocity Field Images," *Combust. Sci. Technol.* **96**, pp. 213-229, 1994.
20. C. J. Mueller, J. F. Driscoll, D. J. Suktus, W. L. Roberts, M. C. Drake, and M. D. Smooke, "Effect of Unsteady Stretch Rate on OH Chemistry During a Vortex-Flame Interaction: To Assess Flamelet Models," *Combust. Flame* **100**, pp. 323-331, 1995.
21. C. J. Mueller, J. F. Driscoll, D. L. Ruess, and M. C. Drake, "Effects of Unsteady Stretch on the Strength of a Freely-Propagating Flame Wrinkled by a Vortex," *Twenty-Sixth Symposium (International) on Combustion*, The Combustion Institute, Pittsburgh, PA, pp. 347-355, 1996.
22. C. J. Mueller, J. F. Driscoll, D. L. Ruess, and M. C. Drake, "Vorticity Generation and Attenuation as Vortices Convect Through a Premixed Flame," *Combust. Flame* **112**, pp. 342-358, 1998.
23. W. L. Roberts and J. F. Driscoll, "A Laminar Vortex Interacting with a Premixed Flame: Measured Formation of Pockets of Reactants," *Combust. Flame* **87**, pp. 245-256, 1991.

24. W. L. Roberts, J. F. Driscoll, M. C. Drake, and J. W. Ratcliffe, "OH Fluorescence Images of the Quenching of a Premixed Flame During an Interaction with a Vortex," *Twenty-Fourth Symposium (International) on Combustion*, The Combustion Institute, Pittsburgh, PA, pp. 169-176, 1992.
25. W. L. Roberts, J. F. Driscoll, M. C. Drake, and L. P. Goss, "Images of the Quenching of a Flame by a Vortex—To Quantify Regimes of Turbulent Combustion," *Combust. Flame* **94**, pp. 58-69, 1993.
26. J. O. Sinibaldi, C. J. Mueller, A. E. Tulkki, and J. F. Driscoll, "Suppression of Flame Wrinkling by Buoyancy: The Baroclinic Stabilization Mechanism," *AIAA J.* **36**, pp. 1432-1438, 1998.
27. J. O. Sinibaldi, C. J. Mueller, and J. F. Driscoll, "Local Flame Propagation Speeds Along Wrinkled, Unsteady, Stretched Premixed Flames," *Twenty-Seventh Symposium (International) on Combustion*, The Combustion Institute, Pittsburgh, PA, pp. 827-832, 1998.
28. P.-H. Renard, J. C. Rolon, D. Thevenin, and S. Candel, "Investigations of Heat Release, Extinction, and Time Evolution of the Flame Surface for a Non-Premixed Flame Interacting With a Vortex," *Combust. Flame* **117**, pp. 189-205, 1999.
29. J. C. Rolon, F. Aguerre, and S. Candel, "Experiments on the Interaction Between a Vortex and a Strained Diffusion Flame," *Combust. Flame* **100**, pp. 422-429, 1995.
30. D. Thevenin, P.-H. Renard, J. C. Rolon, and S. Candel, "Structure of a Nonpremixed Flame Interacting with Counterrotating Vortices," *Twenty-Sixth Symposium (International) on Combustion*, The Combustion Institute, Pittsburgh, PA, pp. 1079-1086, 1996.
31. D. Thevenin, P.-H. Renard, J. C. Rolon, and S. Candel, "Extinction Processes During a Non-Premixed Flame/Vortex Interaction," *Twentieth-Seventh Symposium (International) on Combustion*, The Combustion Institute, Pittsburgh, PA, pp. 719-726, 1998.
32. T. Takagi, Y. Yoshikawa, K. Yoshida, M. Komiyama, and S. Kinoshita, "Studies on Strained Non-Premixed Flames Affected by Flame Curvature and Preferential Diffusion," *Twenty-Sixth Symposium (International) on Combustion*, The Combustion Institute, Pittsburgh, PA, pp. 1103-1110, 1996.
33. K. Yosida and T. Takagi, "Transient Local Extinction and Reignition Behavior of Diffusion Flames Affected by Flame Curvature and Preferential Diffusion," *Twenty-Seventh Symposium (International) on Combustion*, The Combustion Institute, Pittsburgh, PA, pp. 685-692, 1998.
34. V. S. Santoro, D. C. Kyritsis, and A. Gomez, "A Comparison of the Interaction of Laminar Vortices with Either Gaseous or Spray Counterflow Diffusion Flames," *First Joint Meeting of the United States Sections of the Combustion Institute*, Washington, DC, Paper No. 21, 1999.
35. K. Y. Hsu, Chen. L. D., V. R. Katta, L. P. Goss, and W. M. Roquemore, "Experimental and Numerical Investigations of the Vortex-Flame Interactions in a Driven Jet Diffusion Flame," *31st AIAA Aerospace Sciences Meeting & Exhibit*, Reno, NV, AIAA 93-0455, 1993.
36. V. R. Katta, K. Y. Hsu, and W. M. Roquemore, "Local Extinction in an Unsteady Methane-Air Jet Diffusion Flame," *Twenty-Seventh Symposium (International) on Combustion*, The Combustion Institute, Pittsburgh, PA, pp. 1121-1129, 1998.
37. R. D. Hancock, F. R. Schauer, R. P. Lucht, V. R. Katta, and K. Y. Hsu, "Thermal Diffusion Effects and Vortex-Flame Interactions in Hydrogen Jet Diffusion Flames," *Twenty-Sixth Symposium (International) on Combustion*, The Combustion Institute, Pittsburgh, PA, pp. 1087-1093, 1996.
38. C. J. Mueller and R. W. Schefer, "Coupling of a Diffusion Flame Structure to an Unsteady Vortical Flowfield," *Twenty-Seventh Symposium (International) on Combustion*, The Combustion Institute, Pittsburgh, PA, pp. 1105-1112, 1998.
39. S.-J. Chen and W. J. A. Dahm, "Diffusion Flame Structure of a Laminar Vortex Ring Under Microgravity Conditions," *Twenty-Seventh Symposium (International) on Combustion*, The Combustion Institute, Pittsburgh, PA, pp. 2579-2586, 1998.
40. Y. H. You, D. K. Lee, and H. D. Shin, "Visual Investigation of a Vortex Ring Interacting with a Nonpremixed Flame," *Combust. Sci. Technol.* **139**, pp. 365-383, 1998.
41. V. R. Katta and W. M. Roquemore, "Studies on Unsteady Opposing-Jet Diffusion Flames," *37th AIAA Aerospace Sciences Meeting and Exhibit*, Reno, NV, AIAA 99-0322, 1999.
42. M. Gharib, E. Rambod, and K. Shariff, "A Universal Time Scale for Vortex Ring Formation," *J. Fluid. Mech.* **360**, pp. 121-140, 1998.
43. W. T. Ashurst, "Flame Propagation Through Swirling Eddies, a Recursive Pattern," *Combust. Sci. Technol.* **92**, 87, 1993.
44. S. E. Widnall, "The Structure and Dynamics of Vortex Filaments," *Ann. Rev. Fluid. Mech.* **7**, pp. 141-165, 1975.
45. T. Poinso, A. Trounev, D. Veynante, S. Candel, and E. Esposito, "Vortex-Driven Acoustically Coupled Combustion Instabilities," *J. Fluid Mech.* **177**, pp. 265-292, 1987.

46. C. J. Rutland and J. H. Ferziger, "Simulations of Flame-Vortex Interactions," *Combust. Flame* **84**, pp. 343-360, 1991.
47. H. N. Najm, P. H. Paul, C. J. Mueller, and P. S. Wyckoff, "On the Adequacy of Certain Experimental Observables as Measurements of Flame Burning Rate," *Combust. Flame* **113**, pp. 312-332, 1998.
48. P. H. Paul and H. N. Najm, "Planar Laser-Induced Fluorescence Imaging of Flame Heat Release Rate," *Twenty-Seventh Symposium (International) on Combustion*, The Combustion Institute, Pittsburgh, PA, pp. 43-50, 1998.
49. S. Gogineni, L. P. Goss, and W. M. Roquemore, "Manipulation of a Jet in a Cross Flow," *Exper. Therm. Fluid. Sci.* **16**, pp. 209-219, 1998.
50. S. Gogineni, L. Goss, D. Pestian, and R. Rivir, "Two-Color Digital PIV Employing a Single CCD Camera," *Exper. Fluids* **25**, pp. 320-328, 1998.
51. G. J. Fiechtner, C. D. Carter, V. R. Katta, J. R. Gord, J. M. Donbar, and J. C. Rolon, "Regimes of Interaction Between a Nonpremixed Hydrogen-Air Flame and an Isolated Vortex," *37th AIAA Aerospace Sciences Meeting and Exhibit*, Reno, NV, AIAA 99-0320, 1999.
52. A. Gomez and D. E. Rosner, "Thermophoretic Effects on Particles in Counterflow Laminar Diffusion Flames," *Combust. Sci. Technol.* **89**, pp. 355-362, 1993.
53. C. J. Sung, J. S. Kistler, M. Nishioka, and C. K. Law, "Further Studies on Effects of Thermophoresis on Seeding Particles in LDV Measurements of Strained Flames," *Combust. Flame* **105**, pp. 189-201, 1996.

Vortex Injection of Noble Gases in an Opposed-Jet Burner

G. J. Fiechtner,^{1,2} J. R. Gord,¹ C.D. Carter,^{1,2} K. D. Grinstead, Jr.,^{1,2} V. R. Katta,^{1,2} P.-H. Renard,³
and J. C. Rolon³

¹Air Force Research Laboratory, Propulsion Directorate,
Wright-Patterson Air Force Base, OH 45433-7103, USA.

²Present Address: Innovative Scientific Solutions, Inc., 2766 Indian Ripple Road, Dayton, OH 45440-3638,
USA. G.J.F. Contact E-Mail: gjfiech@ward.appl.wpafb.af.mil, Tel: (937) 255-8373.

³Laboratoire d'Énergétique Moléculaire et Macroscopique, Combustion, École Centrale Paris and CNRS,
Grande Voie des Vignes, 92295 Châtenay-Malabry Cedex, France.

1. Introduction

Numerical modeling and experimental measurements of reacting flows have led to important advances in the understanding of combustion. Numerous investigations, including those on the interaction of a laminar flame and a vortex, have contributed to these advances. The resulting data are useful in a variety of applications such as the identification of fundamental regimes of vortex-flame interactions.¹ Vortical structures are an important feature in unsteady and turbulent combustion, and experimental data can be used to develop models for use in practical combustion areas such as experimental gas turbine combustors. Using a burner developed at École Centrale Paris and CNRS, we recently performed a series of studies in which numerical predictions² were later validated using measurements of flame extinction in a nonpremixed hydrogen/air flame by an air-filled vortex.³ The recent ban on the manufacture of halon has led to the need for alternative fire suppressants. In this study, we explore the possibility of extending vortex-flame extinction studies to basic research in fire-suppression dynamics. A valve-switching mechanism is demonstrated for filling a vortex with a fluid. Synchronization of the filled-vortex injector with laser diagnostics is then demonstrated. In the preliminary results presented here, local flame extinction is promoted with a helium-filled vortex. We propose that carefully-controlled vortex-flame experiments and modeling can be a useful tool in the search for Halon replacements.

2. Background

The search for replacements for bromine-containing fluorocarbons has resulted in intense research. These studies⁴ have addressed the effect of halon replacements on global parameters such as burning velocity, HF and CF₂O production, extinction strain rate, flame temperature, and species concentration profiles (see, for example, Reference 4 and the references therein). During past development of combustion codes for gas turbine combustor modelling, experimental studies of vortex-flame interactions have been of great benefit.⁵ Similar benefit may result from vortex-flame studies when applied to the problem of fire suppression. Numerous experimental studies of the interaction dynamics of vortices and flames have been conducted. For premixed flame fronts, most measurements have been made using two types of flames. Hertzberg et al.⁶ and Escudie⁷ conducted an experiment in which a Karman vortex street was produced using a cylindrical rod in a cross flow of premixed gases. A V-flame was supported behind a wire positioned downstream of the rod that produced the vortex street. Planar tomographic imaging was used to study the interaction of the vortex street and the flame. A similar interaction of a Karman vortex street and a flame was investigated by Lee et al.⁸ using PLIF imaging of OH and by Nye et al.⁹ using both OH PLIF and PIV. A disadvantage of using the vortex street is the difficulty in isolating a single vortex. Samaniego^{10,11} developed a means of injecting an isolated line vortex through a horizontal slot in the wall of a vertical wind tunnel and presented results on the interaction of a line vortex and a V-flame. Schlieren images of the time-dependent vortex-flame interaction along with CH emission data from the entire flame were presented. Paul and coworkers¹²⁻¹⁴ studied vortex-flame interactions using the Samaniego burner; PLIF measurements of OH and CH radicals were reported initially, and quantities such as heat release were presented during later studies.

In a second type of study involving premixed combustion, Jarosinski et al.¹⁵ studied a flame that was ignited at one end of a tube of premixed gases. A vortex was injected at the other end of the tube. The interaction dynamics were then photographed using a mercury-xenon arc lamp and a rotating-drum streak camera with a rotating-disc shutter. Recently, Driscoll and co-workers produced an impressive series of papers concerning a similar vortex-flame facility in which PIV, OH PLIF, or a combination of these imaging techniques was applied (see Driscoll et al.,¹⁶ Mueller et al.,¹⁷ Sinibaldi et al.,¹⁸ and the references therein).

Nonpremixed flames have also been the subject of experimental study. Rolon and co-workers (see Renard et al.,¹⁹ Thevenin et al.,²⁰ and the references therein) recently developed an apparatus in which a vortex was injected into a flame supported between the nozzles of an opposed-jet burner. Takagi and coworkers^{21,22} performed planar Rayleigh-scattering measurements of temperature on a similar type of opposed-jet burner in which a small jet of fuel or air was injected using a micro-nozzle with an inner diameter of only 0.25 mm. Either a jet of air was injected from the air side of the diffusion flame or a jet of fuel was injected from the fuel side. Chen and Dahm²³ developed a facility for generating a nonpremixed burning layer that wraps into a vortex ring. The facility permits experiments to be performed under conditions of both normal gravity and microgravity, allowing the study of the influence of buoyancy.

3. Apparatus and Procedure

The opposed-jet burner used in these experiments has been described elsewhere.³ The flame is supported between upper and lower nozzles that are separated by 40 mm, each with an exit diameter of 25 mm. The fuel consists of hydrogen diluted with nitrogen and flows from the upper nozzle. Air flows from the lower nozzle. Unique to this type of apparatus is a tube with ~2-mm inner diameter that is installed concentrically within the lower nozzle. This tube is attached to a cylinder that contains a piston which, in turn, is attached to an actuator. Feeding an appropriate current to the actuator causes a solenoid to force the piston upward abruptly, resulting in the emergence of a vortex from the tube. The vortex travels upward within the surrounding oxidizer flow. As configured during past experiments, a flow of air is supplied to the vortex tube such that, in the absence of a vortex, the exit velocity matches the velocity of the air from the surrounding nozzle. The air supply has been modified for the present experiments by inserting two three-way valves—one connected to the air supply and the other connected to the helium supply. For filling a vortex with helium, the vortex piston is moved to its farthest position from the flame, at which time the currents supplied to the two three-way valves are reversed. The air valve switches to vent air to the fume hood, and the helium valve switches to provide a flow of helium to the vortex nozzle. When the desired amount of helium has been delivered, the solenoid currents are again reversed such that the air valve admits air to the vortex nozzle and helium is vented to the fume hood. At this instant, upward motion of the vortex piston is initiated, forcing a vortex into the opposed-jet burner. To minimize the impact of room-air disturbances, upper and lower guard flows of nitrogen are supported through outer nozzles, which are concentric with the respective upper and lower inner nozzles that support the flame.

PLIF measurements are accomplished by exciting hydroxyl radicals at 281.3414 nm via the $R_1(8)$ transition of the (1,0) band in the A-X system. Fluorescence from the A-X (1,1) and (0,0) bands is detected at right angles using WG-295 and UG-11 colored-glass filters, a 105-mm-focal-length $f/4.5$ UV lens, an image intensifier, and CCD pixels that are binned in 2x2 groups, resulting in an imaged area of 25.6 x 38.4 mm². The bottom of the image is 0.25-mm above the surface of the lower nozzle. A color table is used, with a maximum value set to 120% of the maximum signal for the flame condition in which a vortex is not injected. The low-signal color is assigned by calculating the background noise and selecting a minimum value that is two standard deviations above this level. Therefore, in cases where "extinction" of the OH layer is observed, "extinction" refers to signal levels that fall below this minimum value and are, therefore, assigned the last color in the table. All images represent the signal collected during a single laser shot, and no smoothing of the resulting images is attempted.

4. Results and Discussion

The PLIF images of OH shown in Figure 1 correspond to an air-filled vortex that interacts with the hydrogen-air flame. An effective temporal delay of 1 ms is used between images. "Extinction" of the OH layer is absent. Initially, the vortex creates a small dent in the flame, and this dent begins to grow. In the later interaction stages, the OH PLIF signal level is observed to increase by more than a factor of five over the levels observed without a vortex.

The images of Figure 2 are taken under experimental conditions identical to those for the images of Figure 1, except that the vortex is filled with helium. Local extinction of the OH layer takes place at a point on the top surface of the vortex. After extinction, the vortex travels upward toward the other nozzle through the hole created in the flame. The flame then burns back behind the vortex and closes the hole.

While acquiring the data in Figures 1 and 2, simultaneous images were captured using Rayleigh scattering. Rayleigh scattering can be used to compute the temperature in the vicinity of the flame; this temperature is needed to place OH images on a quantitative basis.³ In addition, the helium vortex entrains surrounding air before

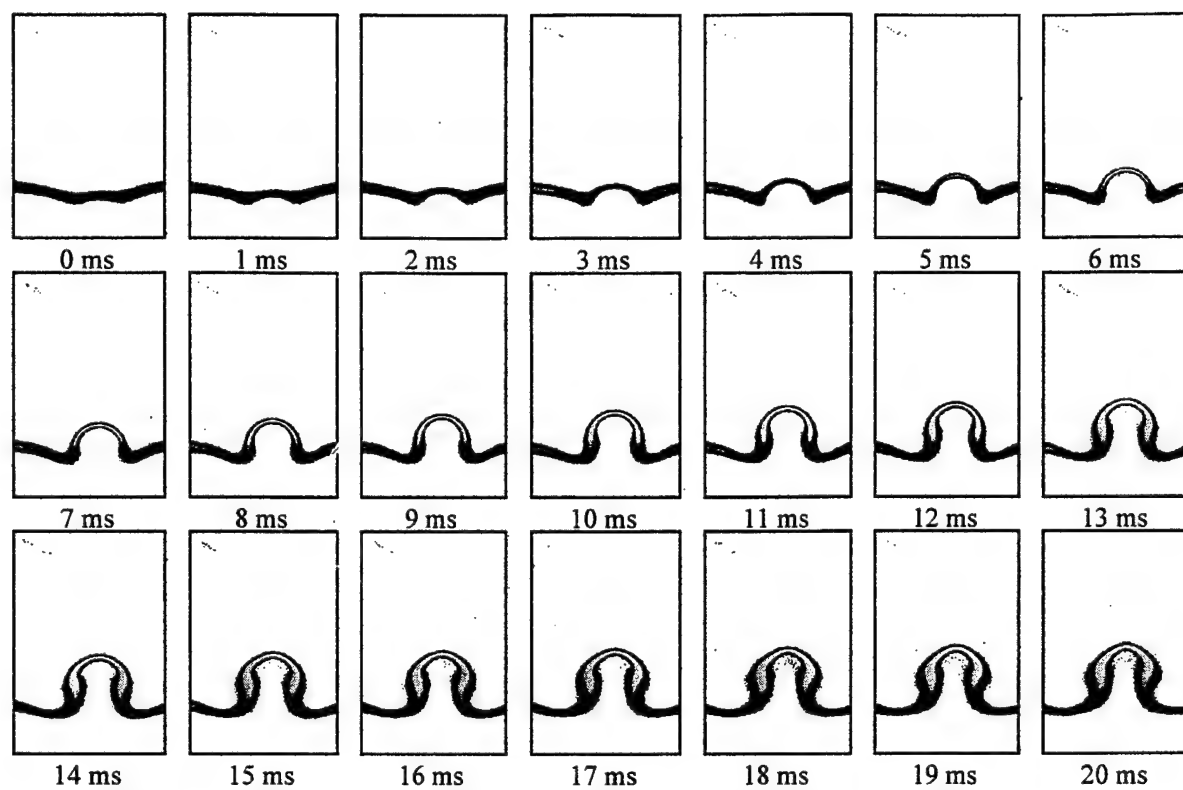


Figure 1. Temporal sequence of images acquired during interaction of air vortex and flame.

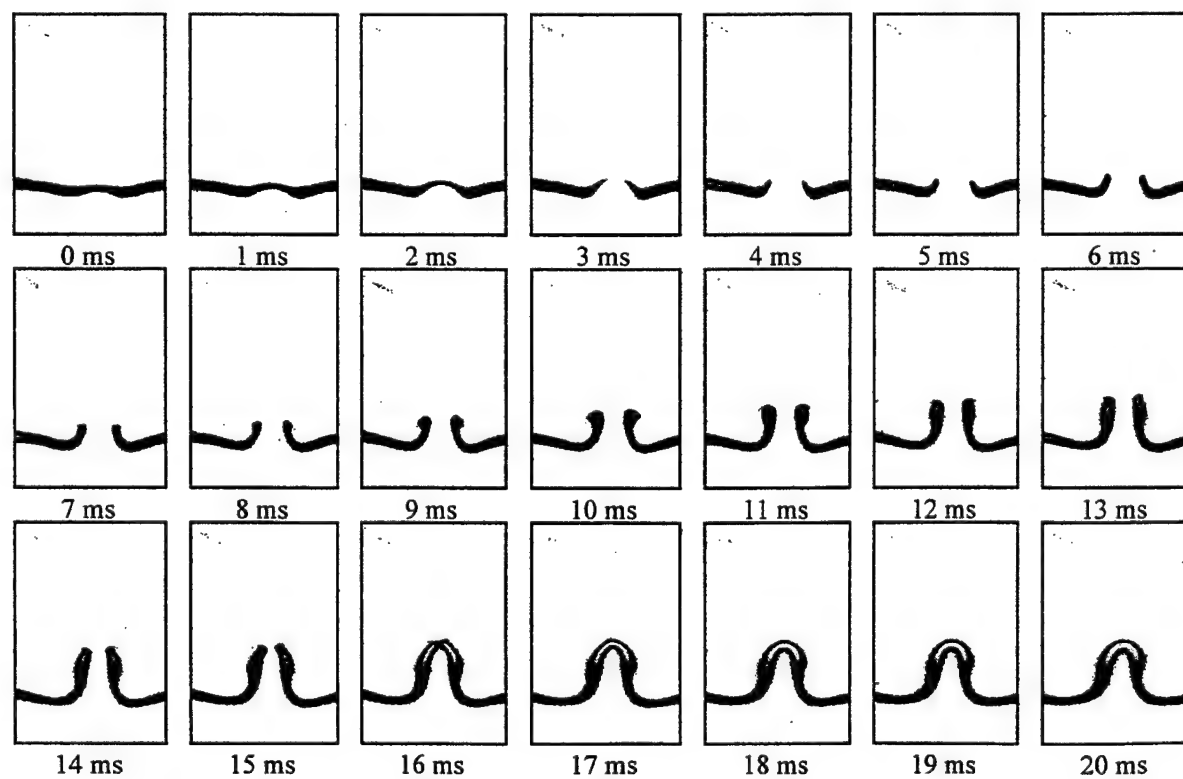


Figure 2. Temporal sequence of images acquired during interaction of helium-air vortex and flame.

reaching the flame, and Rayleigh scattering can be used to estimate the concentration of helium in the vortex. Future studies will utilize hydrocarbon fuels, and more realistic suppressants will be used to fill vortices.

5. Conclusions

The apparatus of Rolon and co-workers^{1,20} has been used to study the interaction of a vortex and a flame using PLIF measurements of OH. The process of filling the vortex has been demonstrated to be highly repeatable. A preliminary experiment has been completed in which a helium-air vortex extinguished a hydrogen-air flame locally at a point. An analogous vortex filled exclusively with air does not extinguish the flame.

Acknowledgements

The authors thank Dr. R. D. Hancock and Capt. I. Vihinen for assistance in assembly and construction of the burner. The authors also acknowledge Drs. R. D. Hancock, W. M. Roquemore, and K.-Y. Hsu for the stimulating discussions of vortex-flame dynamics. Finally, the authors wish to thank Ms. M. M. Whitaker for editorial comments. This work is supported by U. S. Air Force Contracts F33615-95-C-2507 and F33615-97-C-2702.

References

1. P.-H. Renard, J. C. Rolon, D. Thevenin, and S. Candel, *Combust. Flame* **117**, pp. 189-205, 1999.
2. V. R. Katta, C. D. Carter, G. J. Fiechtner, W. M. Roquemore, J. R. Gord, and J. C. Rolon, *Twenty-Seventh Symposium (International) on Combustion*, The Combustion Institute, Pittsburgh, PA, pp. 587-594, 1998.
3. G. J. Fiechtner, C. D. Carter, V. R. Katta, J. R. Gord, J. M. Donbar, and J. C. Rolon, *37th AIAA Aerospace Sciences Meeting and Exhibit*, Reno, NV, AIAA 99-0320, 1999.
4. D. L'Espérance, B. A. Williams, and J. W. Fleming, *Combust. Flame* **117**, pp. 709-731, 1999.
5. W. M. Roquemore and V. R. Katta, *International Conference on Optical Technology and Image Processing in Fluid, Thermal, and Combustion Flow*, Yokohama, Japan, Paper No. KL-310, 1998.
6. J. R. Hertzberg, M. Namazian, and L. Talbot, *Combust. Sci. Technol.* **38**, pp. 205-216, 1984.
7. D. Escudie, *Prog. Astronaut. Aeronaut.* **113**, pp. 215-239, 1988.
8. T.-W. Lee, J. G. Lee, D. A. Nye, and D. A. Santavicca, *Combust. Flame* **94**, pp. 146-160, 1993.
9. D. A. Nye, J. G. Lee, T.-W. Lee, and D. A. Santavicca, *Combust. Flame* **94**, pp. 167-176, 1996.
10. J.-M. Samaniego, *Annual Research Briefs--1992*, Center for Turbulence Research, NASA Ames Research Center/Stanford University, pp. 431-441, 1992.
11. J.-M. Samaniego, *Annual Research Briefs--1993*, Center for Turbulence Research, NASA Ames Research Center/Stanford University, pp. 205-218, 1992.
12. Q.-V. Nguyen and P. H. Paul, *Twenty-Sixth Symposium (International) on Combustion*, The Combustion Institute, Pittsburgh, PA, pp. 357-364, 1996.
13. H. N. Najm, P. H. Paul, C. J. Mueller, and P. S. Wyckoff, *Combust. Flame* **113**, pp. 312-332, 1998.
14. P. H. Paul and H. N. Najm, *Twenty-Seventh Symposium (International) on Combustion*, The Combustion Institute, Pittsburgh, PA, pp. 43-50, 1998.
15. J. Jarosinski, J. H. S. Lee, and R. Knystautas, *Twenty-Second Symposium (International) on Combustion*, The Combustion Institute, Pittsburgh, PA, pp. 505-514, 1988.
16. J. F. Driscoll, D. J. Sutkus, W. L. Roberts, M. E. Post, and L. P. Goss, *Combust. Sci. Technol.* **96**, pp. 213-229, 1994.
17. C. J. Mueller, J. F. Driscoll, D. L. Reuss, and M. C. Drake, *Combust. Flame* **112**, pp. 342-358, 1998.
18. J. O. Sinibaldi, C. J. Mueller, and J. F. Driscoll, *Twenty-Seventh Symposium (International) on Combustion*, The Combustion Institute, Pittsburgh, PA, pp. 827-832, 1998.
19. P.-H. Renard, J. C. Rolon, D. Thevenin, and S. Candel, *Twenty-Seventh Symposium (International) on Combustion*, The Combustion Institute, Pittsburgh, PA, pp. 659-666, 1998.
20. D. Thevenin, P.-H. Renard, J. C. Rolon, and S. Candel, *Twenth-Seventh Symposium (International) on Combustion*, The Combustion Institute, Pittsburgh, PA, pp. 719-726, 1998.
21. T. Takagi, Y. Yoshikawa, K. Yoshida, M. Komiyama, and S. Kinoshita, *Twenty-Sixth Symposium (International) on Combustion*, The Combustion Institute, Pittsburgh, PA, pp. 1103-1110, 1996.
22. K. Yosida and T. Takagi, *Twenty-Seventh Symposium (International) on Combustion*, The Combustion Institute, Pittsburgh, PA, pp. 685-692, 1998.
23. S.-J. Chen and W. J. A. Dahm, *Twenty-Seventh Symposium (International) on Combustion*, The Combustion Institute, Pittsburgh, PA, pp. 2579-2586, 1998.

Injection of Single and Multiple Vortices in an Opposed-Jet Burner

Fiechtner, G. J.*1.*2, Renard, P.-H.*3, Carter, C. D.*1.*2, Gord, J. R.*1 and Rolon, J. C.*3

*1 Air Force Research Laboratory, Propulsion Directorate, Wright-Patterson Air Force Base, OH 45433-7103, USA.

*2 Innovative Scientific Solutions, Inc., 2766 Indian Ripple Road, Dayton, OH 45440-3638, USA.

*3 Laboratoire d'Énergétique Moléculaire et Macroscopique, Combustion, École Centrale Paris and CNRS, Grande Voie des Vignes, 92295 Châtenay-Malabry Cedex, France.

Received 9 July 1999.

Revised 27 September 1999.

Abstract: A thorough understanding of turbulent reacting flows is essential to the continued development of practical combustion systems. Combustor codes can be validated using data such as those generated in this study of a vortex interacting with a nonpremixed, opposed-jet hydrogen-air flame. When experimental results are compared with model predictions, the underlying flowfield must be matched carefully. Since the vortex-injection process used in the present experiments can result in many types of vortices, including multiple vortices, restrictions on the experimental operation of the burner are required as well as careful vortex characterization. Vortex-characterization data are acquired using digital, two-color particle-image velocimetry (PIV), and the hydroxyl (OH) layer produced by the flame is imaged using planar laser-induced fluorescence (PLIF). The PIV and OH PLIF measurements are performed simultaneously. Good agreement with previous numerical-modeling predictions is obtained when experiments and computations are performed using similar vortex conditions.

Keywords: visualization, turbulence, vortex, flamelet, PLIF, PIV.

1. Introduction

Recent predictions from numerical modeling combined with results of experimental measurements have led to important advances in the understanding of combustion. Numerous investigations have contributed to these advances, including a particular type of study in which the interaction of a laminar nonpremixed flame and a vortex is examined. The resulting data can be used for a variety of purposes such as identifying fundamental regimes of vortex-flame interactions (Renard et al., 1999). Vortical structures play an important role in unsteady and turbulent combustion (Takahashi et al., 1996; Roquemore and Katta, 1998; Roquemore and Katta, 1999), and experimental data from studies of these structures can be used to develop models for application to practical combustion devices such as experimental gas-turbine combustors (Roquemore et al., 1991; Durbin et al., 1996; Katta and Roquemore, 1997; Katta and Roquemore, 1998; Hsu et al., 1999).

In recent numerical calculations, Katta predicted that during the interaction of a nonpremixed hydrogen-air flame and an isolated vortex, the extinction of the OH layer would occur in an annular pattern (Katta et al., 1998a). Later experimental results confirmed this computational prediction (Katta et al., 1998a; Fiechtner et al., 1998; Fiechtner et al., 1999). Agreement of experimental and computational results relies on careful matching of the underlying flowfields of the techniques. Because the vortex-injection process used in the present study can result in many types of vortices, including multiple vortices, careful vortex characterization is necessary. This is accomplished by seeding particles into the flowfield and detecting the scattered light during digital, two-color

particle-image velocimetry (PIV) measurements. Digital PIV measurements are made simultaneously with planar laser-induced fluorescence (PLIF) measurements of the hydroxyl radical (OH), which is formed during combustion in a nonpremixed, hydrogen-air opposed-jet burner. Good agreement with previous computational-modeling predictions is obtained when vortex conditions are matched.

2. Background

The experiments described in this paper concern vortex-flame interactions, and the importance of the vortex-injection process is emphasized; therefore, a review of vortex-flame studies is presented, followed by a review of vortex-formation measurements.

2.1 Vortex-flame Experiments

Numerous experimental studies of the interaction dynamics of vortices and flames have been conducted. For premixed flame fronts, most measurements have been made using two experimental configurations: V-flames can be supported behind a wire, or flames can be propagated inside a cylinder. A variety of vortex-injection methods can be applied. In one case, a Karman vortex street was produced using a cylindrical rod in a cross flow of premixed gases (Hertzberg et al., 1984; Escudie, 1988), and the resulting vortices interacted with a V-flame. Planar tomographic imaging was used to study the interaction of the vortex street and the flame. A similar interaction of a Karman vortex street and a flame was investigated using PLIF imaging of OH (Lee et al., 1993) and using both OH PLIF and PIV (Nye et al., 1996). A disadvantage of using the vortex street is the difficulty in isolating a single vortex. To replace the vortex street in experiments with V-flames, a means of injecting an isolated line vortex through a horizontal slot in the wall of a vertical wind tunnel was developed (Samaniego, 1992a). A year later, schlieren images of the time-dependent vortex-flame interaction along with CH emission data from the entire V-flame were presented (Samaniego, 1992b). Paul and co-workers also studied vortex-flame interactions using the Samaniego burner, initially reporting results of PLIF measurements of OH and CH radicals (Nguyen and Paul, 1996), with more recent results including images of quantities such as heat release (Najm et al., 1998; Paul and Najm, 1998).

In a second configuration involving premixed combustion, a flame was ignited at one end of a tube of premixed gases, and a vortex was injected at the other end of the tube (Jarosinski et al., 1988). The vortex-flame interaction was photographed using a mercury-xenon arc lamp and a rotating-drum streak camera with a rotating-disc shutter. Recently, Driscoll and co-workers produced an impressive series of papers concerning a similar vortex-flame facility in which PIV, OH PLIF, or a combination of these imaging techniques was applied (Roberts and Driscoll, 1991; Roberts et al., 1992; Roberts et al., 1993; Driscoll et al., 1994; Mueller et al., 1995; Mueller et al., 1996; Mueller et al., 1998; Sinibaldi et al., 1998a; Sinibaldi et al., 1998b).

Nonpremixed flames have also been the subject of experimental study. Rolon and co-workers (Rolon et al., 1995; Thevenin et al., 1996; Renard et al., 1998; Thevenin et al., 1998; Renard et al., 1999) developed an apparatus in which a vortex is injected into a flame supported between the nozzles of an opposed-jet burner. This geometry has numerous advantages. First, a stationary nonpremixed flame can be produced and isolated easily, which is not possible with the above geometries. Second, the flame thickness can be varied by changing either the nozzle velocities or the spacing between the upper- and lower-burner nozzles. The device has also been extended to the study of vortices that interact with premixed opposed-jet flames (Renard et al., 1998). Takagi and co-workers (Takagi et al., 1996; Yoshida and Takagi, 1998) performed planar Rayleigh-scattering measurements of temperature in a similar type of opposed-jet burner in which a small jet of fuel or air was injected using a micro-nozzle with an inner diameter of only 0.25 mm. Santoro and co-workers modified a vortex counterflow burner to permit the study of spray flames (Santoro et al., 1999).

In a different class of measurements, Hsu and co-workers modulated the axial velocity of a laminar jet diffusion flame using a loud speaker to produce vortex-flame interactions (Hsu et al., 1993; Katta et al., 1998b). Additional studies were performed with this apparatus using a number of techniques including reactive Mie scattering, PLIF, and digital PIV (Hancock et al., 1996). In a similar type of study, OH PLIF measurements were performed in a Wolfhard-Parker slot burner that was forced acoustically by loud speakers on the side walls of the upstream fuel duct (Mueller and Schefer, 1998). PLIF imaging of acetone was used as a marker for the fuel.

A facility was developed recently for generating a nonpremixed burning layer that wraps into a vortex ring (Chen and Dahm, 1998). The facility has been operated under conditions of both normal gravity and microgravity, allowing the study of the influence of buoyancy. In contrast, a facility has been developed in which the vortex is

ignited just as the fluid begins to exit a tube (You et al., 1998). The experiments described in the present paper are based on the counterflow geometry of Rolon and co-workers (Rolon et al., 1995; Thevenin et al., 1996; Renard et al., 1998; Thevenin et al., 1998; Renard et al., 1999).

2.2 Vortex-production Process

Vortex formation has been the subject of intense study for many years (Magarvey and MacLachy, 1964; Widnall, 1975; Maxworthy, 1977; Pullin, 1979; Didden, 1979; Glezer, 1988; Glezer and Coles, 1990; Southerland et al., 1991; Saffman, 1992; Shariff and Leonard, 1992; Nitsche and Krasny, 1994; Nitsche, 1996; Weigand and Gharib, 1997; Fabris and Leipmann, 1997; Heeg and Riley, 1997); thus, a large amount of information is available for analyzing the results of the present experiments. The mechanism used to create vortices during the present experiments relies on a piston/cylinder with stroke length L attached to a nozzle with diameter D . The maximum circulation which a vortex ring can attain is reached for a formation number, L/D , of ~ 4 ; additional trailing vortex rings form for larger ratios (Gharib et al., 1998). Use of larger formation numbers results in the formation of a starting jet (Garside et al., 1943; Rizk, 1958; Abramovich and Solan, 1973; Yaros, 1977; List, 1982; Witze, 1983; Kuo et al., 1986; Cattolica and Vosen, 1987; Brombacher, 1997; Johari et al., 1997; Hill and Ouellette, 1999). The vortex-formation process is illustrated in Fig. 1. In Frame 1 a slug of fluid begins to exit the tube, while in Frame 2 the vortex begins to form. After Frame 2 one of two paths is followed, depending on the motion of the piston. If the piston is stopped after a comparatively small value of the formation number (Path A), the vortex pinches off as it travels upward, as illustrated in Frames 3A and 4A of Fig. 1. This case has been reported numerous times in the literature (Magarvey and MacLachy, 1964; Widnall, 1975; Maxworthy, 1977; Pullin, 1979; Didden, 1979; Glezer, 1988; Glezer and Coles, 1990; Southerland et al., 1991; Saffman, 1992; Shariff and Leonard, 1992; Nitsche and Krasny, 1994; Nitsche, 1996; Weigand and Gharib, 1997; Fabris and Leipmann, 1997; Heeg and Riley, 1997). The trailing fluid is entrained into the vortex during the pinch-off process (Gharib et al., 1998), resulting in a "bubble" defined by leading and trailing stagnation points (James and Mandia, 1996). The pinch-off process can require up to two formation numbers for completion (Gharib et al., 1998).

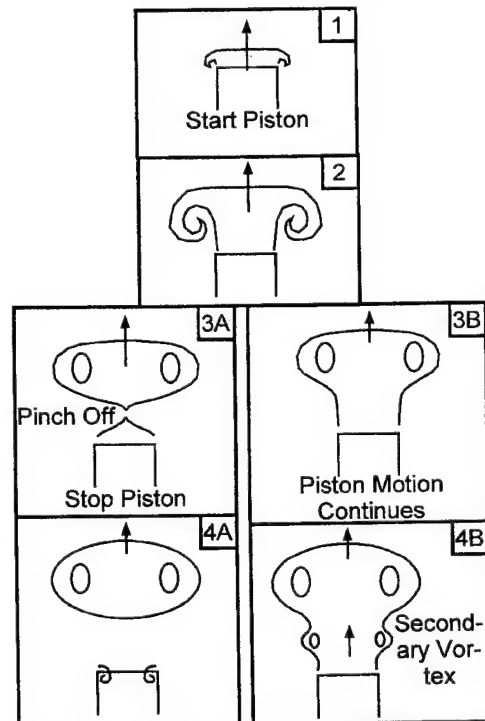


Fig. 1. Schematic diagram of vortex-formation processes.

If the piston motion is allowed to continue (Path B), the developing vortex travels initially above a column of fluid, as shown in Frame 3B. If the piston motion continues, multiple vortices can be produced from the tube, as illustrated in Frame 4B of Fig. 1 (Auerbach, 1991; Gharib et al., 1998). The trailing vortex may eventually overtake the leading vortex, resulting in the interaction of two coaxial vortices. Additional vortices can also interact with the leading vortex. Interactions of multiple coaxial vortices have received considerable attention in the literature (Oshima et al., 1975; Yamada and Matsui, 1978; Maxworthy, 1979; Yamada and Matsui, 1979a; Yamada and Matsui, 1979b; Oshima et al., 1986; Shariff and Leonard, 1992; Riley, 1993; Weidman and Riley, 1993; Leung et al., 1996; Konstantinov, 1997; Lim, 1997; Leung et al., 1997).

3. Apparatus and Procedure

3.1 Burner Facility

A photograph of the opposed-jet burner can be found in the literature (Gord et al., 1998; Renard et al., 1999; Fiechtner et al., 1999). The flame is supported between upper and lower nozzles separated by 40 mm, each with an exit diameter of 25 mm. The fuel consists of hydrogen diluted with nitrogen and flows from the upper nozzle. Air flows from the lower nozzle. Unique to this type of apparatus is a tube with 5-mm inner diameter that is installed concentrically within the lower nozzle. This tube is attached to a cylinder containing a piston that, in turn, is attached to an actuator. When an appropriate current is delivered to the actuator, a solenoid forces the piston upward abruptly, resulting in the emergence of a vortex from the tube. In the present study, vortices are generated using a 10-ms piston risetime.

Studies comparing vortex production via nozzles and orifices have revealed subtle differences in parameters such as vortex size (James and Mandia, 1996); this must be considered when comparing the results of the present study with those obtained during experiments in which vortices are generated using orifices (Roberts and Driscoll, 1991; Roberts et al., 1992; Roberts et al., 1993). When vortices are characterized fully, such concerns are minimized. The volume that a vortex can contain based on the diameter of our nozzle is $\sim 0.4 \text{ cm}^3$ (Gharib et al., 1998). Our vortex generator can sweep a maximum volume of $\sim 3 \text{ cm}^3$, for a maximum attainable formation number of ~ 30 . The condition illustrated in Frame 3B of Fig. 1 was chosen in our experiments to match the vortices used in the computations of Katta (Roquemore and Katta, 1998; Roquemore and Katta, 1999; Katta and Roquemore, 1999). An example of such a vortex is shown in Fig. 2, where the numerically computed vortex is observed to travel above a column of fluid. Numerical routines that rely on an artificially created vortex pair by specifying the vortex field (Poinsot et al., 1987; Rutland and Ferziger, 1991; Ashurst, 1993) may not model our experimental conditions properly. It is also possible for vortices that are initially laminar to become unsteady and turbulent (Widnall, 1975; Glezer and Coles, 1990; Shariff and Leonard, 1992; You et al., 1998)—conditions that are avoided in the present study. In addition, if the piston/cylinder is not aligned and lubricated properly, an undesired turbulent puff of fluid may exit the tube.

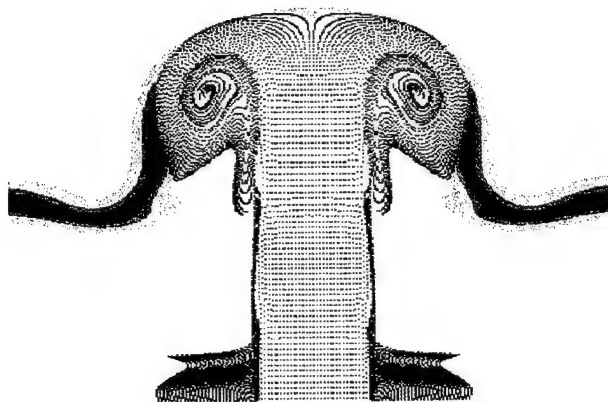


Fig. 2. Example of numerically computed vortex interacting with laminar flame.

The laminar vortices travel upward within the surrounding oxidizer flow. A flow of air is supplied to the vortex tube such that in the absence of a vortex, the exit velocity matches the velocity of the air from the surrounding nozzle. To minimize the impact of room-air disturbances, upper and lower guard flows of nitrogen are supported through outer nozzles that are concentric with the respective upper and lower inner nozzles supporting the flame. The hydrogen, nitrogen-diluent, and oxidizer-air flows are furnished by mass-flow controllers with respective full-scale ranges of 20, 20, and 30 l/min. A continuous flow of air is provided to the vortex tube by a 5-l/min controller, while the guard flows for the upper and lower guard (outer) nozzles are furnished by two 50-l/min mass-flow controllers. The flow rates of the controllers are accurate to $\pm 1\%$ of the full-scale range.

Hollow ceramic seed particles with an approximate mean diameter of $2.4\text{ }\mu\text{m}$ are introduced into the burner flows when digital PIV measurements of the vortex velocity are performed. Three particle seeders are installed – one placed after the air mass-flow controller, another after the vortex-air mass flow controller, and a third after the junction where the hydrogen and nitrogen gases are mixed.

3.2 Laser Diagnostics

The PLIF system includes a frequency-doubled, Q-switched Nd:YAG laser that is used to pump a dye laser which, in turn, is frequency doubled. The UV radiation is directed through a telescope that is adjusted to produce a light sheet with a height that matches as nearly as possible the 40-mm burner separation. The resulting beam thickness is $\sim 300\text{ }\mu\text{m}$, which corresponds to the full width (defined as the distance between the locations of the 25% peak-intensity points).

Hydroxyl radicals absorb the laser radiation at 281.3414 nm via the $R_1(8)$ transition of the (1,0) band in the A-X system. Fluorescence from the A-X (1,1) and (0,0) bands is detected at right angles through WG-295 and UG-11 colored-glass filters using a 105-mm-focal-length $f/4.5$ UV lens. The resulting light is recorded on an intensified CCD camera with an intensifier gate width of 100 ns. CCD pixels are binned in 2×2 groups, resulting in an effective array size of 288×192 pixels with an imaged area of $25.6 \times 38.4\text{ mm}^2$. The bottom of the image rests immediately above the surface of the lower nozzle. A color table is used with a maximum value set to 95% of the maximum signal for all images taken at a given flame condition. The low-signal color is assigned by calculating the background noise and selecting a minimum value that is two standard deviations above this level.

Measurements of the velocity field are carried out using digital, two-color PIV (Gogineni et al., 1998a; Gogineni et al., 1998b). Here, a color digital CCD with an array of 3060×2036 pixels is used. A magnification of 78,368 pixels/m is employed, resulting in an imaged area of $26.0 \times 39.0\text{ mm}^2$. The color CCD camera and the intensified CCD array are aligned using a transparent mask printed with a graduated scale. Two lasers are used; one PIV light sheet is produced by doubling the output of a Q-switched Nd:YAG laser (30 mJ/pulse at the test section). The remainder of this beam is used to pump the dye laser that is frequency doubled to excite OH fluorescence. The second PIV light sheet is produced by pumping a dye laser (employing DCM laser dye) with a second frequency-doubled, Q-switched Nd:YAG laser, resulting in laser radiation at 640 nm (40 mJ/pulse at the test section). The thickness of both the red and green light sheets is set to $\sim 700\text{ }\mu\text{m}$ at the probe region. A digital delay generator is used to drive the timing of the two lasers such that the red pulses are delayed precisely with respect to the green ones. Velocity vectors are calculated using correlation software (Gogineni et al., 1998a). A correlation area of 128×128 pixels is used in the calculation, corresponding to a correlation area of 0.269 cm^2 and a spatial resolution of 1.6 mm . Digital PIV measurements are applied to obtain the propagation velocity of the primary vortex, and this correlation area is acceptable for such purposes.

3.3 Synchronization and Timing

For the present experiments, precise synchronization of several experimental events is required, including vortex generation and propagation, production of laser pulses, and activation of the camera shutter or intensifier. As described in previous papers (Fiechtner et al., 1998; Gord et al., 1998; Fiechtner et al., 1999), lasers, cameras, and the vortex injector are synchronized electronically with an effective temporal jitter of $\sim 10\text{ ns}$. This electronic jitter is much smaller than the fastest event probed to date, which occurs on an $\sim 10\text{-}\mu\text{s}$ time scale. Temporally resolved data are acquired utilizing the following phase-locked timing sequence: 1) an image is recorded, 2) the delay between vortex production and laser/camera events is adjusted, and 3) another vortex is initiated and a second image recorded.

This process is repeated to acquire numerous images at increasing delays, and an animation is created by assembling the individual images in temporal order. The burner facility results in highly reproducible events, even at delays as short as $10\ \mu\text{s}$.

4. Results and Discussion

Simultaneous and superimposed images of the OH PLIF signal and the PIV velocity field are shown in Fig. 3. The annular break of the OH layer corresponds closely to that predicted during previous numerical computations (Katta et al., 1998a).

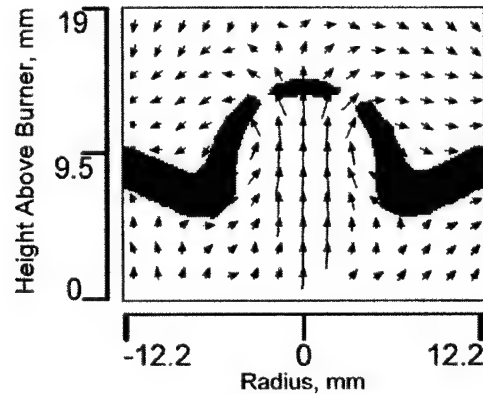


Fig. 3. OH PLIF image and superimposed velocity field demonstrating annular extinction of OH layer. OH PLIF image and digital PIV data are acquired simultaneously. Vortex propagates upward at velocity of 4.2 m/s.

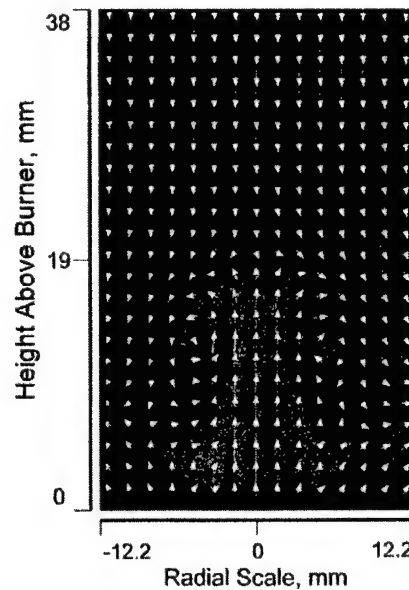


Fig. 4. Vortex injected into cold flow. Vortex propagates upward at velocity of 1.5 m/s.

The scattering image of Fig. 4 was obtained when the vortex-tube flow was seeded with a slightly higher particle density than that produced by the upper and lower burners. As shown, the "mushroom" vortex advances ahead of a column of fluid because the piston continues to push fluid from the vortex nozzle. The scattering image of Fig. 4 was acquired in a cold flow. If the flame is ignited, a vortex such as that depicted in the scattering image of Fig. 5 is obtained. Here, the flame causes the vortex to take on a shape much like that observed in the numerical simulation of Fig. 2, which also corresponds to a reacting flow. However, the vortex images of Figs. 4 and 5 have additional wing-like structure about their stems. This structure results from the pattern formed by the seed particles that exit the vortex tube prior to injection of a vortex, as demonstrated in the scattering image in the upper half of Fig. 6. The velocity vectors superimposed on the OH PLIF image in the lower half of Fig. 6 demonstrate that in

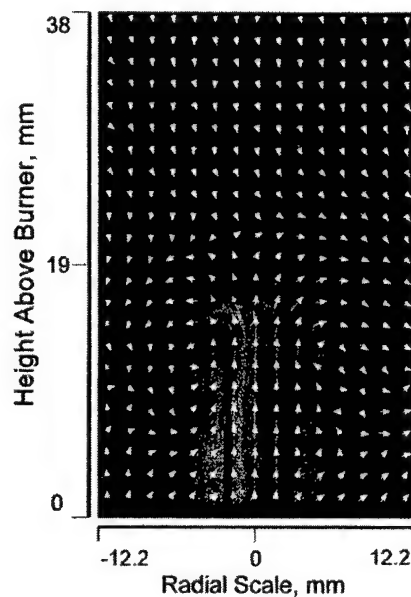


Fig. 5. Vortex injected into opposed-jet flame. Vortex propagates upward at velocity of 8.3 m/s.

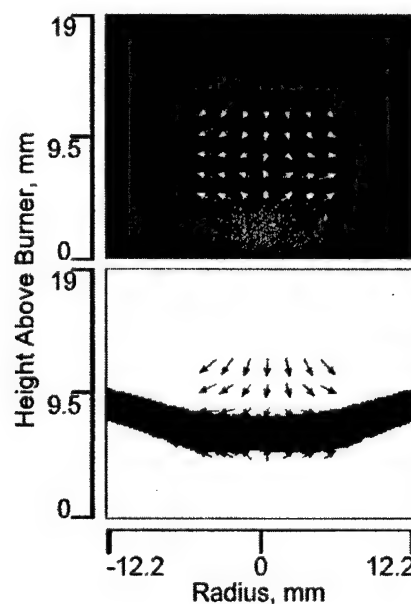


Fig. 6. Simultaneous scattering (upper) and OH PLIF (lower) images. Superimposed vectors demonstrate that stagnation point is located slightly above location of peak OH signal.

the absence of a vortex, the stagnation plane is located slightly above the position of the peak OH signal.

The sequence of four scattering images in Fig. 7 demonstrates the temporal development of an overfilled leading vortex (Gharib et al., 1998; Chen and Dahm, 1998), in which a second and a third vortex are observed. In addition, the high temperatures caused by combustion produce a low-density region that is identified by a smaller scattering signal around the vortices and the stem. This rich structure is repeatable and, therefore, may provide precisely controlled regions of flame curvature and additional regions in which multiple flame layers can interact (Petrov and Ghoniem, 1998). The rainbow appearance of the images results from variations in the irradiance of the red and green lasers across the respective light sheets; these variations were less pronounced when the images of Figs. 4-6 were recorded. Variations in image brightness are caused by different particle seed levels (for each of the three seeders) from image to image.

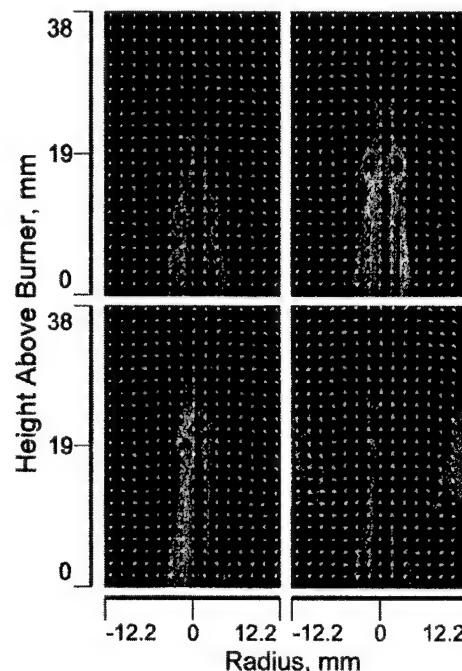


Fig. 7. Multiple-vortex injection observed using temporal sequence of scattering images, with time increasing from left to right, top to bottom: Relative to the first image, subsequent images are delayed by 1, 2.5, and 3.5 ms. Primary vortex in the first image propagates upward at velocity of 9.1 m/s.

5. Conclusions and Future Research

The apparatus of Rolon and co-workers (Rolon et al., 1995; Thevenin et al., 1996; Renard et al., 1998; Thevenin et al., 1998; Renard et al., 1999) has been implemented to study the interaction of a vortex and a flame. Digital, two-color PIV has been applied to characterize the vortices injected into the opposed-jet flow. PLIF images of OH have been used to observe the dynamics of the interaction of the vortex and the flame. An annular break in the OH layer has been observed experimentally, in excellent agreement with prior predictions from numerical computations (Katta et al., 1998a). This agreement results from careful experimental characterization of the vortical flowfield, with the chosen conditions matching those of the corresponding vortex-injection process in the numerical computations.

The present discussion of multiple-vortex formation is limited to a preliminary example. Indeed, most of our previous studies have been limited to the interaction of an isolated vortex and a flame (Fiechtner et al., 1998; Gord et al., 1998; Katta et al., 1998a; Fiechtner et al., 1999). Further investigations of multiple-vortex formation dynamics are being performed to address a wider range of formation numbers. Vortex-vortex interactions are

being studied in greater detail, and regions suitable for studying flame-flame interactions are being probed. These studies are being accomplished simultaneously with numerical modeling.

Acknowledgments

The authors thank Mr. K. D. Grinstead, Jr. and Dr. J. M. Donbar for technical assistance in setting up the experiments; Dr. V. R. Katta for providing the numerically computed vortex shown in Fig. 2; Drs. L. P. Goss, S. Gogineni, J. Estevadeordal, M. A. Linne and Mr. T. Drouillard for advice concerning the reduction of two-color PIV data; Dr. R. D. Hancock and Capt. I. Vihinen for assistance in construction and assembly of the burner; and Ms. M. M. Whitaker for editorial comments. The authors also acknowledge stimulating discussions of vortex-flame dynamics with Drs. R. D. Hancock, W. M. Roquemore, V. R. Katta and K.-Y. Hsu. This work is supported by U. S. Air Force Contracts F33615-95-C-2507 and F33615-97-C-2702.

References

- Abramovich, S. and Solan, A., The Initial Development of a Submerged Laminar Round Jet, *Journal of Fluid Mechanics*, 59 (1973), 791-801.
- Ashurst, W. T., Flame Propagation Through Swirling Eddies, A Recursive Pattern, *Combustion Science and Technology*, 92 (1993), 87.
- Auerbach, D., Stirring Properties of Vortex Rings, *Physics of Fluids A*, 3 (1991), 1351-1355.
- Brombacher, E. J., Flow Visualisation of Natural Gas Fuel Injection, M.S. Thesis, University of Toronto (1997).
- Cattolica, R. and Vosen, S., Combustion-Torch Ignition: Fluorescence Imaging of OH Concentration, *Combustion and Flame*, 68 (1987), 267-281.
- Chen, S.-J. and Dahm, W. J. A., Diffusion Flame Structure of a Laminar Vortex Ring Under Microgravity Conditions, Twenty-Seventh Symposium (International) on Combustion, (1998), 2579-2586, The Combustion Institute, Pittsburgh, PA.
- Didden, N., On the Formation of Vortex Rings Rolling-Up and Production of Circulation, *Zeitschrift für Angewandte Math. physik*, 30 (1979), 101-116.
- Driscoll, J. F., Sutkus, D. J., Roberts, W. L., Post, M. E. and Goss, L. P., The Strain Exerted by a Vortex on a Flame - Determined from Velocity Field Images, *Combustion Science and Technology*, 96 (1994), 213-229.
- Durbin, M. D., Vangsness, M. D., Ballal, D. R. and Katta, V. R., Study of Flame Stability in a Step Swirl Combustor, *Transactions of the ASME*, 118 (1996), 308-315.
- Escudie, D., Stability of a Premixed Laminar V-Shaped Flame, *Progress in Astronautics and Aeronautics*, 113 (1988), 215-239.
- Fabris, D. and Leipmann, D., Vortex Ring Structure at Late Stages of Formation, *Physics of Fluids*, 9 (1997), 2801-2803.
- Fiechtner, G. J., Carter, C. D., Grinstead, K. D., Gord, J. R., Roquemore, W. M. and Rolon, J. C., Flame-Vortex Interactions in a Non-Premixed H₂/N₂/Air Counterflow Burner, 34th AIAA/ASME/SAE/ASEE Joint Propulsion Conference & Exhibit (Cleveland, OH), (1998), AIAA 98-3770.
- Fiechtner, G. J., Carter, C. D., Katta, V. R., Gord, J. R., Donbar, J. M. and Rolon, J. C., Regimes of Interaction Between a Nonpremixed Hydrogen-Air Flame and an Isolated Vortex, 37th AIAA Aerospace Sciences Meeting and Exhibit (Reno, NV), (1999), AIAA 99-0320.
- Garside, J. E., Hall, A. R. and Townsend, D. T. A., Flow States in Emergent Gas Streams, *Nature*, 152 (1943), 748.
- Gharib, M., Rambod, E. and Shariff, K., A Universal Time Scale for Vortex Ring Formation, *Journal of Fluid Mechanics*, 360 (1998), 121-140.
- Glezer, A., The Formation of Vortex Rings, *Physics of Fluids*, 31 (1988), 3532-3542.
- Glezer, A. and Coles, D., An Experimental Study of a Turbulent Vortex Ring, *Journal of Fluid Mechanics*, 221 (1990), 243-283.
- Gogineni, S., Goss, L., Pestian, D. and Rivir, R., Two-Color Digital PIV Employing a Single CCD Camera, *Experiments in Fluids*, 25 (1998a), 320-328.
- Gogineni, S., Goss, L. P. and Roquemore, W. M., Manipulation of a Jet in a Cross Flow, *Experimental Thermal Fluid Science*, 16 (1998b), 209-219.
- Gord, J. R., Donbar, J. M., Fiechtner, G. J., Carter, C. D., Katta, V. R. and Rolon, J. C., Experimental and Computational Visualization of Vortex-Flame Interactions in an Opposed-Jet Burner, International Conference on Optical Technology and Image Processing in Fluid, Thermal, and Combustion Flow (Yokohama, Japan), (1998), Paper No. AB-082.
- Hancock, R. D., Schauer, F. R., Lucht, R. P., Katta, V. R. and Hsu, K. Y., Thermal Diffusion Effects and Vortex-Flame Interactions in Hydrogen Jet Diffusion Flames, Twenty-Sixth Symposium (International) on Combustion, (1996), 1087-1093, The Combustion Institute, Pittsburgh, PA.
- Heeg, R. S. and Riley, N., Simulations of the Formation of an Axisymmetric Vortex Ring, *Journal of Fluid Mechanics*, 339 (1997), 199-211.
- Hertzberg, J. R., Namazian, M. and Talbot, L., Tomographic Study of a Laminar Flame in a Karman Vortex Street, *Combustion Science and Technology*, 38 (1984), 205-216.
- Hill, P. G. and Ouellette, P., Transient Turbulent Gaseous Fuel Jets for Diesel Engines, *Journal of Fluids Engineering*, 121 (1999), 93-101.
- Hsu, K. Y., Carter, C. D., Katta, V. R. and Roquemore, W. M., Characteristics of Combustion Instability Associated with Trapped-Vortex Burner, 37th AIAA Aerospace Sciences Meeting and Exhibit (Reno, NV), (1999), AIAA-99-0488.
- Hsu, K. Y., Chen, L. D., Katta, V. R., Goss, L. P. and Roquemore, W. M., Experimental and Numerical Investigations of the Vortex-Flame Interactions in a Driven Jet Diffusion Flame, 31st AIAA Aerospace Sciences Meeting & Exhibit (Reno, NV), (1993), AIAA-93-0455.
- James, S. and Mandia, C. K., Direct Numerical Simulation of a Laminar Vortex Ring, *Physics of Fluids*, 8 (1996), 2400-2414.
- Jarosinski, J., Lee, J. H. S. and Knystautas, R., Interaction of a Vortex Ring and a Laminar Flame, Twenty-Second Symposium (International) on Combustion, (1988), 505-514, The Combustion Institute, Pittsburgh, PA.
- Johari, H., Zhang, Q., Rose, M. J. and Bourque, S. M., Impulsively Started Turbulent Jets, *AIAA Journal*, 35 (1997), 657-662.
- Katta, V. R., Carter, C. D., Fiechtner, G. J., Roquemore, W. M., Gord, J. R. and Rolon, J. C., Interaction of a Vortex With a Flat Flame Formed Between Opposing Jets of Hydrogen and Air, Twenty-Seventh Symposium (International) on Combustion, (1998a), 587-594, The Combustion Institute, Pittsburgh, PA.
- Katta, V. R., Hsu, K. Y. and Roquemore, W. M., Local Extinction in an Unsteady Methane-Air Jet Diffusion Flame, Twenty-Seventh Symposium (International) on Combustion, (1998b), 1121-1129, The Combustion Institute, Pittsburgh, PA.

- Katta, V. R. and Roquemore, W. M., Study on Trapped-Vortex Combustor—Effect of Injection on Dynamics of Non-Reacting and Reacting Flows in a Cavity, 33rd AIAA/ASME/SAE/ASEE Joint Propulsion Conference & Exhibit (Seattle, WA), (1997), AIAA-97-3256.
- Katta, V. R. and Roquemore, W. M., Numerical Studies on Trapped-Vortex Concepts for Stable Combustion, Transactions of the ASME, 120 (1998), 60-68.
- Katta, V. R. and Roquemore, W. M., Studies on Unsteady Opposing-Jet Diffusion Flames, 37th AIAA Aerospace Sciences Meeting and Exhibit (Reno, NV), (1999), AIAA 99-0322.
- Konstantinov, M., Numerical Investigation of the Interaction of Coaxial Vortex Rings, International Journal of Numerical Methods for Heat & Fluid Flow, 7 (1997), 120-140.
- Kuo, T.-W., Syed, S. A. and Bracco, F. V., Scaling of Impulsively Started, Incompressible, Laminar Round Jets and Pipe Flows, AIAA Journal, 24 (1986), 424-428.
- Lec, T.-W., Lee, J. G., Nye, D. A. and Santavica, D. A., Local Response and Surface Properties of Premixed Flames During Interactions with Karman Vortex Streets, Combustion and Flame, 94 (1993), 146-160.
- Leung, R. C. K., Chu, W. F., Tang, S. K. and Ko, N. W. M., Control of Vortex Pairing with Sound, AIAA Journal, 35 (1997), 802-809.
- Leung, R. C. K., Tang, S. K., Ho, I. C. K. and Ko, N. W. M., Vortex Pairing as a Model for Jet Noise Control, AIAA Journal, 34 (1996), 669-677.
- Lirn, T. T., On the Role of Kelvin-Helmholtz-Like Instability in the Formation of Turbulent Vortex Rings, Fluid Dynamics Research, 21 (1997), 47-56.
- List, E. J., Turbulent Jets and Plumes, Annual Reviews of Fluid Mechanics, 14 (1982), 189-212.
- Magarvey, R. H. and MacLachy, C. S., The Formation and Structure of Vortex Rings, Canadian Journal of Physics, 42 (1964), 678-683.
- Maxworthy, T., Some Experimental Studies of Vortex Rings, Journal of Fluid Mechanics, 81 (1977), 465-495.
- Maxworthy, T., Comments on 'Preliminary Study of Mutual Slip-Through of a Pair of Vortices', Physics of Fluids, 22 (1979), 200.
- Mueller, C. J., Driscoll, J. F., Reuss, D. L. and Drake, M. C., Vorticity Generation and Attenuation as Vortices Convect Through a Premixed Flame, Combustion and Flame, 112 (1998), 342-358.
- Mueller, C. J., Driscoll, J. F., Ruess, D. L. and Drake, M. C., Effects of Unsteady Stretch on the Strength of a Freely-Propagating Flame Wrinkled by a Vortex, Twenty-Sixth Symposium (International) on Combustion, (1996), 347-355, The Combustion Institute, Pittsburgh, PA.
- Mueller, C. J., Driscoll, J. F., Sutkus, D. J., Roberts, W. L., Drake, M. C. and Smooke, M. D., Effect of Unsteady Stretch Rate on OH Chemistry During a Vortex-Flame Interaction: To Assess Flamelet Models, Combustion and Flame, 100 (1995), 323-331.
- Mueller, C. J. and Schefer, R. W., Coupling of a Diffusion Flame Structure to an Unsteady Vortical Flowfield, Twenty-Seventh Symposium (International) on Combustion, (1998), 1105-1112, The Combustion Institute, Pittsburgh, PA.
- Najm, H. N., Paul, P. H., Mueller, C. J. and Wyckoff, P. S., On the Adequacy of Certain Experimental Observables as Measurements of Flame Burning Rate, Combustion and Flame, 113 (1998), 312-332.
- Nguyen, Q.-V. and Paul, P. H., The Time Evolution of a Vortex-Flame Interaction Observed via Planar Imaging of CH and OH, Twenty-Sixth Symposium (International) on Combustion, (1996), 357-364, The Combustion Institute, Pittsburgh, PA.
- Nitsche, M., Scaling Properties of Vortex Ring Formation at a Circular Tube Opening, Physics of Fluids, 8 (1996), 1848-1855.
- Nitsche, M. and Krasny, R., A Numerical Study of Vortex Ring Formation at the Edge of a Circular Tube, Journal of Fluid Mechanics, 276 (1994), 139-161.
- Nye, D. A., Lee, J. G., Lee, T.-W. and Santavica, D. A., Flame Stretch Measurements During the Interaction of Premixed Flames and Karman Vortex Streets Using PIV, Combustion and Flame, 94 (1996), 167-176.
- Oshima, Y., Kambe, T. and Saburo, A., Interaction of Two Vortex Rings Moving along a Common Axis of Symmetry, Journal of the Physical Society of Japan, 38 (1975), 1159-1166.
- Oshima, Y., Noguchi, T. and Oshima, K., Numerical Study of Interaction of Two Vortex Rings, Fluid Dynamics Research, 1 (1986), 215-227.
- Paul, P. H. and Najm, H. N., Planar Laser-Induced Fluorescence Imaging of Flame Heat Release Rate, Twenty-Seventh Symposium (International) on Combustion, (1998), 43-50, The Combustion Institute, Pittsburgh, PA.
- Petrov, C. and Ghoniem, A. F., Dynamics and Structure of Interacting Nonpremixed Flames, Combustion and Flame, 115 (1998), 180-194.
- Poinsot, T., Trounev, A., Veynante, D., Candel, S. and Esposito, E., Vortex Driven Acoustically Coupled Combustion Instabilities, Journal of Fluid Mechanics, 177 (1987), 265-292.
- Pullin, D., Vortex Ring Formation at Tube and Orifice Openings, Physics of Fluids, 22 (1979), 401-403.
- Renard, P.-H., Rolon, J. C., Thevenin, D. and Candel, S., Wrinkling, Pocket Formation and Double Premixed Flame Interaction Processes, Twenty-Seventh Symposium (International) on Combustion, (1998), 659-666, The Combustion Institute, Pittsburgh, PA.
- Renard, P.-H., Rolon, J. C., Thevenin, D. and Candel, S., Investigations of Heat Release, Extinction, and Time Evolution of the Flame Surface for a Non-Premixed Flame Interacting with a Vortex, Combustion and Flame, 117 (1999), 189-205.
- Riley, N., On the Behaviour of Pairs of Vortex Rings, Quarterly Journal of Mechanics and Applied Mathematics, 46 (1993), 521-539.
- Rizk, W., Experimental Studies of the Mixing Processes and Flow Configurations in Two-Cycle Engine Scavenging, Proceedings of the Institution of Mechanical Engineers, Series E, 172 (1958), 417-424.
- Roberts, W. L. and Driscoll, J. F., A Laminar Vortex Interacting with a Premixed Flame: Measured Formation of Pockets of Reactants, Combustion and Flame, 87 (1991), 245-256.
- Roberts, W. L., Driscoll, J. F., Drake, M. C. and Goss, L. P., Images of the Quenching of a Flame by a Vortex—To Quantify Regimes of Turbulent Combustion, Combustion and Flame, 94 (1993), 58-69.
- Roberts, W. L., Driscoll, J. F., Drake, M. C. and Ratcliffe, J. W., OH Fluorescence Images of the Quenching of a Premixed Flame During an Interaction with a Vortex, Twenty-Fourth Symposium (International) on Combustion, (1992), 169-176, The Combustion Institute, Pittsburgh, PA.
- Rolon, J. C., Aguerre, F. and Candel, S., Experiments on the Interaction Between a Vortex and a Strained Diffusion Flame, Combustion and Flame, 100 (1995), 422-429.
- Roquemore, W. M. and Katta, V. R., Role of Flow Visualization in the Development of UNICORN, International Conference on Optical Technology and Image Processing in Fluid, Thermal, and Combustion Flow (Yokohama, Japan), (1998), Paper No. KL-310.
- Roquemore, W. M. and Katta, V. R., Role of Flow Visualization in the Development of UNICORN, to appear in Journal of Visualization, 2-314, 1999.
- Roquemore, W. M., Reddy, V. K., Hedman, P. O., Post, M. E., Chen, T. H., Goss, L. P., Trump, D., Vilimpoc, V. and Sturgess, G. J., Experimental and Theoretical Studies in a Gas-Fueled Research Combustor, 29th AIAA Aerospace Sciences Meeting (Reno, NV), (1991), AIAA-91-0639.

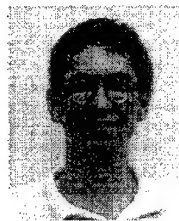
- Rutland, C. J. and Ferziger, J. H., Simulations of Flame-Vortex Interactions, *Combustion and Flame*, 84 (1991), 343-360.
- Saffman, P. G., *Vortex Dynamics*, (1992), Cambridge University Press, New York.
- Samaniego, J.-M., Generation of Two-Dimensional Vortices in a Cross Flow, *Annual Research Briefs-1992*, Center for Turbulence Research (NASA Ames Research Center/Stanford University), (1992a), 431-441.
- Samaniego, J.-M., Stretch-Induced Quenching in Vortex-Flame Interactions, *Annual Research Briefs-1993*, Center for Turbulence Research (NASA Ames Research Center/Stanford University), (1992b), 205-218.
- Santoro, V. S., Kyritsis, D. C. and Gomez, A., A Comparison of the Interaction of Laminar Vortices with Either Gaseous or Spray Counterflow Diffusion Flames, *First Joint Meeting of the United States Sections of the Combustion Institute* (Washington, DC), (1999), Paper No. 21.
- Shariff, K. and Leonard, A., Vortex Rings, *Annual Reviews of Fluid Mechanics*, 24 (1992), 235-279.
- Sinibaldi, J. O., Mueller, C. J. and Driscoll, J. F., Local Flame Propagation Speeds Along Wrinkled, Unsteady, Stretched Premixed Flames, *Twenty-Seventh Symposium (International) on Combustion*, (1998a), 827-832, The Combustion Institute, Pittsburgh, PA.
- Sinibaldi, J. O., Mueller, C. J., Tulkki, A. E. and Driscoll, J. F., Suppression of Flame Wrinkling by Buoyancy: The Baroclinic Stabilization Mechanism, *AIAA Journal*, 36 (1998b), 1432-1438.
- Southerland, K. B., Porter, J. R., Dahm, W. J. A. and Buch, K. A., An Experimental Study of the Molecular Mixing Process in an Axisymmetric Laminar Vortex Ring, *Physics of Fluids A*, 3 (1991), 1385-1392.
- Takagi, T., Yoshikawa, Y., Yoshida, K., Komiya, M. and Kinoshita, S., Studies on Strained Non-Premixed Flames Affected by Flame Curvature and Preferential Diffusion, *Twenty-Sixth Symposium (International) on Combustion*, (1996), 1103-1110, The Combustion Institute, Pittsburgh, PA.
- Takahashi, F., Schmoll, W. J., Trump, D. D. and Goss, L. P., Vortex-Flame Interactions and Extinction in Turbulent Jet Diffusion Flames, *Twenty-Sixth Symposium (International) on Combustion*, (1996), 145-152, The Combustion Institute, Pittsburgh, PA.
- Thevenin, D., Renard, P.-H., Rolon, J. C. and Candel, S., Structure of a Nonpremixed Flame Interacting with Counterrotating Vortices, *Twenty-Sixth Symposium (International) on Combustion*, (1996), 1079-1086, The Combustion Institute, Pittsburgh, PA.
- Thevenin, D., Renard, P.-H., Rolon, J. C. and Candel, S., Extinction Processes During a Non-Premixed Flame/Vortex Interaction, *Twenty-Seventh Symposium (International) on Combustion*, (1998), 719-726, The Combustion Institute, Pittsburgh, PA.
- Weidman, P. D. and Riley, N., Vortex Ring Pairs: Numerical Simulation and Experiment, *Journal of Fluid Mechanics*, 257 (1993), 311-337.
- Weigand, A. and Gharib, M., On the Evolution of Laminar Vortex Rings, *Experiments in Fluids*, 22 (1997), 447-457.
- Widnall, S. E., The Structure and Dynamics of Vortex Filaments, *Annual Review of Fluid Mechanics*, 7 (1975), 141-165.
- Witze, P. O., Hot-Film Anemometer Measurements in a Starting Turbulent Jet, *AIAA Journal*, 21 (1983), 308-309.
- Yamada, H. and Matsui, T., Preliminary Study of Mutual Slip-Through of a Pair of Vortices, *Physics of Fluids*, 21 (1978), 292-294.
- Yamada, H. and Matsui, T., Mutual Slip-Through of a Pair of Vortex Rings, *Physics of Fluids*, 22 (1979a), 1245-1249.
- Yamada, H. and Matsui, T., Reply to Comments of T. Maxworthy, *Physics of Fluids*, 22 (1979b), 201.
- Yaros, R., The Evolution of a Suddenly Initiated Semiconfined, Two-Dimensional, Turbulent Jet, Ph.D. Dissertation, Pennsylvania State University (1977).
- Yoshida, K. and Takagi, T., Transient Local Extinction and Reignition Behavior of Diffusion Flames Affected by Flame Curvature and Preferential Diffusion, *Twenty-Seventh Symposium (International) on Combustion*, (1998), 685-692, The Combustion Institute, Pittsburgh, PA.
- You, Y. H., Lee, D. K. and Shin, H. D., Visual Investigation of a Vortex Ring Interacting with a Nonpremixed Flame, *Combustion Science and Technology*, 139 (1998), 365-383.

Author Profile

Gregory J. Fiechtner: He is a senior mechanical engineer at Innovative Scientific Solutions, Inc. He received his B.S. in Mechanical Engineering from the University of Nebraska (Lincoln) in 1986 and both his M.S. in Mechanical Engineering (1989) and his Ph.D. in Mechanical Engineering (1992) from Purdue University. He pursued postdoctoral studies at the University of Colorado and the Colorado School of Mines from 1992 to 1994 and at Sandia National Laboratories (Livermore) from 1994 to 1996. His research experience involves measurements and modeling of combustion, including the development and application of advanced laser-based diagnostic techniques for the characterization and improvement of gas-turbine-engine combustion. He is an active member of the American Institute of Aeronautics and Astronautics, the American Society of Mechanical Engineers, the Institute of Electrical and Electronics Engineers, the Optical Society of America, and the Combustion Institute. Dr. Fiechtner has 105 publications and presentations in the areas of combustion diagnostics, fluid mechanics, lasers, and instrumentation.



Paul-Henri Renard: He received his M.Sc. degree in Mechanical Engineering in 1995 from École Centrale Nantes and is completing requirements for his Ph.D. in combustion sciences at École Centrale Paris. He worked one year at ONERA (National Aerospace Research Agency) in the field of spectroscopic numerical simulation and at the United States Air Force Research Laboratory in 1998.



Campbell D. Carter: He has been a research scientist at Innovative Scientific Solutions, Inc., since 1994 and received his B.S. in Mechanical Engineering from the University of Texas at Austin, his M.S. in Mechanical Engineering from the University of California, Berkeley, and his Ph.D. in Mechanical Engineering from Purdue University. He then served as a postdoctoral researcher at the Combustion Research Facility, Sandia National Laboratories (Livermore). His interests include the application and development of advanced laser diagnostics for reacting flows and combustors, a field in which he has published over 20 archival journal articles and more than 70 additional papers and presentations. Dr. Carter is a member of the American Institute of Aeronautics and Astronautics and serves on the Advanced Measurements Technology Technical Committee; he is also an active member of the Combustion Institute.



James R. Gord: He is a senior research chemist with the Propulsion Sciences and Advanced Concepts Division of the Air Force Research Laboratory's Propulsion Directorate and received his B.S. in Chemistry from Miami University in 1986 and his Ph.D. in Analytical Chemistry from Purdue University in 1990. He pursued postdoctoral studies at the Joint Institute for Laboratory Astrophysics from 1990 to 1991 and then joined the Air Force research team, first as an on-site contractor at Wright-Patterson Air Force Base with Systems Research Laboratories, Inc., and then as a civil servant in his current position. He directs the development and application of advanced laser-based diagnostic techniques for the characterization and improvement of gas-turbine-engine combustion and thermally stable aviation fuels. He is a member of the American Chemical Society, the American Institute of Physics, the Combustion Institute, the Optical Society of America, Phi Beta Kappa, Sigma Xi, and the Society for Applied Spectroscopy.



Juan Carlos Rolon: He has been on the teaching staff at École Centrale Paris since 1982 and has been a professor at that institution since 1989. He teaches fluid mechanics, combustion, signal processing, control systems, and optical diagnostics. He earned his M.S. in Theoretical Physics from the University of Moscow in 1970, his D.E.A. in Fluid Mechanics from the University of Paris in 1973, and his Ph.D. from École Centrale Paris in 1988. He was a research engineer at École Centrale Paris from 1973 to 1975 and an invited research scientist at CNRS for two years. Before his return to École Centrale, he was a Professor of Physics at the École Normale Supérieure in Oran (Algeria) from 1976 to 1982. He leads a team conducting research in the area of flame structures and optical diagnostics. His current interests lie in flame spectroscopy, radical imaging, combinations of imaging and digital processing, light scattering, laser-induced fluorescence, and laser Doppler velocimetry. He has published more than 30 papers in these areas. His research has been supported by governmental agencies and industry, and he was the Principal Investigator on three European contracts. He was recently selected by the European Office of Research and Development to be an invited professor; he was selected as a leading speaker for the Window on Science program of the United States Air Force Research Laboratory. He was awarded by the Grand Prix of the French Academy of Sciences in 1997. During the same year, along with Dr. D. Thevenin and P.-H. Renard, he received the first award from the Seymour Cray competition on industrial applications of intensive computing.

Presented at the Twenty-Eighth International Symposium on Combustion, Edinburgh, Scotland,
30 July - 4 August 2000; published in Proceedings of the Combustion Institute, Vol. 28, 2000.

PUBLISHED WITH PERMISSION

REGIMES OF NONPREMIXED FLAME/VORTEX INTERACTIONS

D. Thévenin^{†*}, P.H. Renard[†], G.J. Fiechtner^{*}, J.R. Gord[‡] and J.C. Rolon[†]

[†] : *Laboratoire EM2C
Ecole Centrale Paris and CNRS
Grande Voie des Vignes
F-92295 Châtenay-Malabry, FRANCE*

^{*} : *Innovative Scientific Solutions, Inc.
2766 Indian Ripple Road
Dayton, OH 45440-3638, USA*

[‡] : *Propulsion Directorate
Air Force Research Laboratory
Wright-Patterson Air Force Base
OH 45433-7103, USA*

ABSTRACT

Detailed studies of flame/vortex interactions are extremely valuable to improve our understanding of turbulent combustion regimes. Combined experimental and numerical studies have already been performed in the premixed case during previous investigations. Therefore, we have decided to carry out a detailed experimental investigation on the regimes observed during interaction of a vortex ring and a nonpremixed, diluted, hydrogen-air, laminar counterflow flame. To obtain the needed information, several optical diagnostic techniques have been used, in particular, Planar Laser-Induced Fluorescence (PLIF) of acetone to quantify vortex structure and speed, simultaneous OH PLIF and Rayleigh measurements, and simultaneous OH PLIF and Particle-Imaging Velocimetry (PIV) measurements. A post-processing of the results combined with direct simulations using detailed chemistry and transport models to check the quality of the post-processing procedures, has led to the construction of a spectral interaction diagram. Eight interaction types are found, emphasizing the relative importance of competing physical phenomena such as straining, curvature, wrinkling, roll-up, and extinction. In particular, we observe two different types of extinction, one due to the combined action of curvature and straining, and the other purely due to straining effects. It is also observed that many vortices are too small or dissipate too rapidly to influence the flame. In other cases the vortex ring can lead to the formation of pockets of oxidizer burning in the fuel part of the domain. These regimes and the limits between them have important implications for the modeling of turbulent nonpremixed combustion.

Introduction

The interaction of flames and vortices is a problem of theoretical and practical interest. In particular, if a field of turbulence is considered to be a collection of vortices of different sizes and strengths, it is possible to use the flame-vortex interaction as a model problem to investigate basic processes associated with turbulent combustion. Flame-vortex interactions often govern the combustion rate or lead to combustion instabilities. Vortices are observed in free flames and in flames stabilized on bluff-bodies or are used to enhance mixing.

Numerous publications can be found concerning flame-vortex interactions, and we refer to our previous papers on the subject [1-4]. Complementary information can be found for example in [5-10]. Considering these publications, one may conclude that the interaction of a premixed flame with a vortex ring or a counter-rotating vortex pair has been studied extensively. Efforts to identify different regimes and to compare experimental and numerical results in particular concerning the extinction limits have been successful [9,11,12].

Experiments using non-premixed flames are more difficult and initially were carried out in water using an acid-base reaction to simulate the flame [13] or employed quite different configurations such as jet flames submitted to natural or forced vortical instabilities [14-17]; more recently burning rings [18,19] were studied under microgravity conditions. Considering that experiments on diffusion flames are highly needed, a counterflow burner was built in our laboratory to investigate the effect of vortices in non-premixed cases [1,20]. An international collaboration was initiated to obtain as many experimental measurements as possible for this configuration.

The present article begins by providing details on the experimental setup. The post-processing of the measurements is then described. Identified interaction regimes are subsequently shown and used to construct an interaction diagram. Finally, the implications of these results for nonpremixed turbulent combustion are discussed.

Experimental Apparatus and Procedure

A detailed description of the counterflow burner is given in Ref.[20] and a schematic illustration of the setup may be found in Ref.[1] and [3]. Experiments are performed with hydrogen diluted with nitrogen on the upper side and air on the lower side, at room temperature and pressure. Each injection nozzle has a diameter of 25 mm and is surrounded by another nozzle issuing nitrogen to isolate the reactive stream from outer perturbations. A steady, non-premixed flame featuring a one-dimensional structure around the stagnation point is initiated. This flame is subjected to a constant low-level strain acting along its plane. The resulting strain-rate is negligible compared to that exerted by the vortex rings.

We have changed the global mixture ratio ϕ , defined as the ratio between initial mass fraction of fuel on the fuel side $Y_{fu,0}$ and initial mass fraction of oxidizer on the oxidizer side $Y_{ox,0}$, divided by corresponding values for stoichiometric combustion [1]. Values of ϕ vary between 0.5 and 1.6.

The lower nozzle contains a cylindrical tube of constant internal diameter. To vary the size of the generated vortex ring, 4 different tubes, of inner diameter 0.5, 2, 5, and 10 mm can be used. This tube is connected to a cylindrical plenum chamber in which a piston is moved by an actuator. We can vary the volume of fluid pushed by the piston as well as the

piston rise time, allowing control of the vortex speed. By changing separately the tube size and the actuation parameters, we have generated vortex rings with an external radius R_H that varies from 0.76 mm to 11.2 mm and with a propagation speed U_T that varies from 0.22 m/s to 5.05 m/s. Both the vortex size and the vortex speed have been measured using the same setup (with pure nitrogen injection in the upper burner) by Planar Laser-Induced Fluorescence (PLIF) of acetone, with acetone being injected through the vortex generator and all other conditions being similar to the standard experiment [21]. It is known that the rotational velocity and the propagation speed of a vortex ring are closely connected in this configuration.

Measurements are carried out mainly using PLIF of the OH radical simultaneously with Rayleigh scattering. The PLIF of OH relies on a frequency-doubled Nd:YAG laser at 532 nm (800 mJ power), which is used to excite OH (281.3 nm absorption line) via a frequency-doubled Rhodamine dye laser. The fluorescence signal is filtered using WG 295 and UG 11 filters and is subsequently collected on an intensified CCD camera with 576×384 pixels. For simultaneous Rayleigh measurements, 300 mJ of energy is employed to pump the dye laser used to excite the OH radical. The remaining 500 mJ is separated at the output of the frequency doubler and used for Rayleigh scattering measurements. The Rayleigh signal is collected on a CCD camera (512×512 array) with a band-pass filter centered at 532 nm [22,23].

We have also made simultaneous OH PLIF and PIV measurements. Here, the OH PLIF technique is identical to that described previously, with 30 mJ of energy at 532 nm after the frequency-doubled Nd:YAG laser being used to pump the dye laser for the OH PLIF measurements. At the output of a DCM dye laser pumped by a second Nd:YAG system, 40 mJ of energy is produced at 640 nm. The resulting green and red light sheets induce Mie scattering signals that are collected on a Kodak DCS 460 Color CCD camera with 3060×2036 pixels. The PIV system relies on a two-colour numerical intercorrelation technique. The delay between the two laser shots is equal to 10 μ s. All details concerning the simultaneous OH PLIF and PIV measurements are described elsewhere [21,24].

Experiments are conducted as follows: a steady flame is first established; then, at a selected instant t_0 , a toroidal vortex is injected impulsively by the action of the piston, and accelerates rapidly toward the flame. At a well-defined instant $t_1 \geq t_0$, the signals (either OH PLIF and Rayleigh or OH PLIF and PIV) are collected. Since the experiment is reproducible within less than 10 μ s, the whole temporal interaction sequence is obtained by choosing different delays, $t_1 - t_0$.

Post-Processing of Experimental Results

To increase the signal-to-noise ratio, the pixels of the CCD camera used to collect the OH PLIF signal are paired in two directions, resulting in a real image of 288×192 pixels. As explained in Ref.[3] and demonstrated in Ref.[2], it is possible to analyze the PLIF results for the OH radical to compute an instantaneous flame-surface area. This information is used as a complement to a visual examination of the raw results obtained with the CCD camera, allowing us to quantify the wrinkling of the flame front by the vortices and to determine whether extinction is occurring.

Computation of the flame-surface area is automated using MATLAB and has been validated on test pictures. We compute the instantaneous flame-surface area $\mathcal{A}(t)$ in this manner. We remove from $\mathcal{A}(t)$ the initial value of the flame-surface area for the unperturbed flame, $\mathcal{A}(0)$, to obtain $\mathcal{A}_n(t)$. To take into account the varying size of the vortex rings, we have also considered a normalized flame-surface area, which is more appropriate for examining the influence of small vortices. To accomplish this, $\mathcal{A}_n(t)$ is divided by a reference surface \mathcal{A}_{ref} associated with the employed vortex ring. We have checked that the structure of our vortex rings is similar to Hill's spherical vortices [25]; therefore, we choose to define \mathcal{A}_{ref} as $2\pi R_H^2$, with R_H being the radius of the vortex ring. We then follow in time the evolution of the normalized flame-surface area $\mathcal{A}^*(t) = (\mathcal{A}(t) - \mathcal{A}(0))/\mathcal{A}_{ref}$. Using \mathcal{A}^* , a small vortex ring may have a large (relative) influence on the flame front, which is not visible with \mathcal{A}_n . In particular, we have often observed that quite small vortices may increase the flame-surface area by more than ten times \mathcal{A}_{ref} . This confirms that a large number of small vortices may play an important role in the mixing process, showing the importance of taking micro-mixing into account for nonpremixed turbulent flames. Nevertheless, the global impact of a single vortex on the flame is given by the evolution of $\mathcal{A}_n(t)$.

Because the inhomogeneities across the laser sheet have not been measured and the cross sections of the different species in the flame differ, our Rayleigh measurements are of a qualitative nature. An example of simultaneous OH PLIF/Rayleigh measurements is shown in Fig.1. Both diagnostics give complementary pictures of the same interaction process. The OH PLIF signal is associated with the perturbation of the reaction zone, while the Rayleigh signal corresponds to changes in temperature.

The velocity field obtained from PIV measurements is determined by an intercorrelation procedure, with a variable mesh size that depends on the seeding density, the local velocity gradients, and the size of the particle images. To obtain acceptable results, we make sure that the displacement of the particles between the two images is less than half the mesh size. Four or five pairs of particles are then sufficient to obtain accurate results [26]. The intercorrelation peak is found by a search of maximum intensity. Erroneous velocity vectors are then eliminated. This procedure has been described elsewhere [21,24].

Because of the amount of information associated with the PIV measurements, we have to date been unable to post-process them further. Therefore, we have taken into account in our interpretation only the observed velocity field (Fig.2). In the near future we will compute quantities of interest such as instantaneous local strain rate and combine it with an estimation of the curvature to obtain values of the stretch rate exerted on the flame.

Observed Regimes and Interaction Diagram

Using theoretical results along with the information described above, we have identified eight interaction regimes for the nonpremixed flame/vortex interaction (Fig.3). These regimes reflect the relative importance of the physical phenomena that play a major role in this configuration: dissipation, straining, curvature, wrinkling, roll-up, and quenching. We have plotted the results in a spectral diagram, similar to that in Refs.[9,11,27]. To facilitate comparison, we keep the coordinates used in Ref.[27]. The domain accessed using our experimental setup is also displayed in Fig.3

The horizontal axis of this diagram corresponds to the ratio of the diameter of the vortex ring $2R_H$ to the initial thermal flame width δ_f . The vertical axis is associated with the ratio of the characteristic flame time t_c to the propagation time of the vortex through the flame δ_f/U_T . The flame time t_c is not easy to define and cannot be measured in our experimental setup. We have chosen here to use the asymptotic theory results of Ref.[28] to compute this flame time as a function of the global mixture ratio ϕ . We obtain

$$\frac{1}{t_c} = \phi A \left(\frac{\rho_f}{\rho_{ox,0}} \right)^2 \text{Le}_F K^2 \left(\frac{C_p T_f^2}{Q Y_{fu,0} T_a} \right)^2 \exp \left(-\frac{T_a}{T_f} \right) \quad (1)$$

where T_f and ρ_f correspond to the temperature and density at the flame [28]. The fuel Lewis number Le_F introduced here is taken to be equal to 0.3 [29]. The factor K is necessary for taking into account the different Lewis numbers of the fuel and oxidizer [28]. Finally, the activation temperature T_a is taken to be 8000 K and the ratio of specific heat release to heat capacity Q/C_p is taken to be $5 \cdot 10^4$ K [30,31]. The Arrhenius preexponential factor A of the single reaction used to describe the chemical processes has been chosen to obtain the correct extinction limit for a global mixture ratio $\phi = 0.7$. Since these values of t_c are obtained by high-activation-energy asymptotics with a single-step irreversible reaction, they yield only an order of magnitude approximation. The computed characteristic flame times using our set of parameters are given in Table 1.

In Fig.3, we have also plotted some theoretical lines given in Ref.[27], corresponding to different values of the Reynolds number Re and Damköhler number Da . The line associated with $\text{Re} = (2R_H)U_T/\nu = 1$ is the limit of instantaneous vortex dissipation by viscosity (for $\text{Re} < 1$). This line has a slope of -1 in this log-log diagram.

The line $\text{Da} = \text{Da}_q$ corresponds to the quenching limit. It can also be defined as

$$\frac{U_T t_c}{\delta_f} = \frac{1}{\text{Da}_q} \frac{2R_H}{\delta_f} \quad (2)$$

Extinction is observed for $\text{Da} < \text{Da}_q$.

The line $\text{Da} = \text{Da}_u$ corresponds to the limit for unsteady effects. It can also be defined as $U_T t_c / \delta_f = (1/\text{Da}_u)(2R_H/\delta_f)$. Unsteady effects should be strong for $\text{Da} < \text{Da}_u$.

We have also plotted the vertical line $(2R_H)/\delta_f = 2$. It corresponds intuitively to the limit for cases where curvature effects are strong (for $(2R_H)/\delta_f < 2$) since larger vortices will not curve the flame front significantly.

Zone (I) corresponds to values of the vortex Reynolds number below 1. It is well known from theoretical considerations that such vortices are dissipated immediately by viscosity [32] and, therefore, do not influence the flame. We do not observe this behaviour precisely in our experiments. In fact, it appears that this no-effect zone is not associated with $\text{Re} = 1$, but with a somewhat higher cut-off value of the Reynolds number $\text{Re} = \text{Re}_c$. If we choose arbitrarily as a definition of *no-effect* that the maximum increase of flame surface area $\mathcal{A}_n(t)$ during the interaction is less than $8\pi R_H^2$, we obtain $\text{Re}_c = 23$ experimentally for our setup. Zone (II) corresponds to that part of the domain between $\text{Re} = 1$ and $\text{Re} = \text{Re}_c$.

In Zone (III), the Reynolds number of the vortices is larger than 1, but these vortices do not survive sufficiently long to perturb the flame before being dissipated by viscosity. This

corresponds to a condition

$$\frac{(2R_H)^2}{\nu} < t_c \quad (3)$$

After introducing the Prandtl number Pr and the Damköhler number Da_d that is characteristic of thermal-diffusion effects, i.e. $Da_d = \rho C_p \delta_f^2 / (\lambda t_c)$, the limit of this zone corresponds to a ratio of vortex size to flame width equal to

$$\frac{2R_H}{\delta_f} = \left(\frac{Pr}{Da_d} \right)^{1/2} \quad (4)$$

This line marks the limit between Zone (III) and Zone (IV). This limit could not be verified in our experiments because it is impossible to generate sufficiently small vortices. In fact, we have verified that it would still be impossible to reach this limit in our setup by increasing the flame width significantly by changing the diluent or placing the entire experiment in a low-pressure vessel.

In Zone (IV), we have $(2R_H)/\delta_f < 2$. Curvature effects are therefore important. However, extinction is not observed because the vortex ring is not sufficiently large to separate the two sides of the induced wrinkle, since $(2R_H) < \delta_f/2$. For the same reason, the increase in flame-surface area is not very large, since the produced flame surface remains in the vicinity of the symmetry axis.

Zone (V) is limited in the horizontal direction by the vertical lines $(2R_H)/\delta_f = 1/2$ on the left and $(2R_H)/\delta_f = 2$ on the right. Therefore, in this zone curvature effects are still important. However, since the dimensions of the vortices are of the same order of magnitude as the flame width, we also observe an important thickening of the reaction zone. At the same time, wrinkling effects are now important. As a consequence of curvature effects and of stronger vortices, extinction is observed in this zone, although the corresponding vortices are still small. PLIF images illustrating the thickening of the reaction zone can be found in Ref.[3].

In Zone (VI), wrinkling effects become strong in comparison with Zone (II), and curvature effects do not play an important role since the vortices are much larger than the flame thickness. However, an important roll-up of the flame is observed to participate in the increase in flame surface area. No quenching is observed in this zone. Images illustrating this roll-up can be found in Ref.[3].

Zone (VII) is separated from Zone (VI) by a slanted line $Da = Da_p$. The pinch-off of the flame front behind the vortex is essential for generating a pocket and occurs when the vortex characteristic time is shorter than a chemical time t_p associated with this phenomenon. This condition can be written in terms of the Damköhler number Da_p , that compares the characteristic time of pocket formation to the flame time as $(U_T t_c)/\delta_f > (1/Da_p)(2R_H/\delta_f)$ which also corresponds to the condition $Da = Da_p$. Since $Da > Da_q$ there, we observe no extinction. The wrinkling effect of the vortices on the flame-surface area is still strong in this zone, as in Zone (VI). Curvature effects are still negligible, but roll-up is again considerable. In Zone (VII), this roll-up leads eventually to the formation of pockets of oxidizer inside the upper part of the setup, which is filled with diluted fuel. These pockets are continuously surrounded by an active reaction zone.

The theoretical line $Da = Da_u$ of Ref.[27] runs through Zones (II), (V) and (VII). It is not possible in our setup to identify unsteady effects (*unsteady* meaning here that the flame

structure is not in equilibrium with the flow field imposed by the vortex). We are, therefore, unable to verify the validity and the importance of this separation in our experiments.

Finally, Zone (VIII) is separated from Zone (VII) by the slanted line $Da = Da_q$. We, therefore, observe extinction due to strain in Zone (IX), since $Da < Da_q$. The results shown in Fig.1 correspond to this zone, while Fig.2 is associated with the boundary between Zones (V), (VII), and (VIII). The influence of the vortices on the flame-surface area is still strong; roll-up effects are observed again, while curvature effects are negligible. As a result of extinction of the flame induced by strain and although pockets of oxidizer can still be formed in this zone, we do not observe the burning of such pockets in the fuel side of the setup.

These results are summarized in Fig.3. This spectral diagram can be used to establish a turbulent, nonpremixed combustion diagram. To accomplish this, we consider that a nonpremixed flame front interacting with a turbulence field is submitted to the effect of a continuous distribution of vortices, the size and velocity of which varies from the Kolmogorov scale to the integral scale. This means that at each point of a turbulent combustion diagram, we must associate information from the spectral diagram, where the influence of all the corresponding turbulent scales is taken into account [11,33]. By doing so, we assume that each vortex acts independently on the flame front. Possible non-linear interactions between several vortices are lost in this procedure. Nevertheless, it constitutes an interesting step toward a more accurate description of turbulent, nonpremixed combustion.

If one considers the classical relations for homogenous isotropic turbulence [32], the relation between the integral length scale l_t and the Kolmogorov length scale l_k is $l_t = Re_r^{3/4} l_k$. Similarly, the integral velocity fluctuation u' is related to the Kolmogorov velocity u_k by $u' = Re_r^{1/4} u_k$. As a consequence, the energetic cascade for homogeneous, isotropic turbulence is represented by a straight line of slope 1/3 in our spectral diagram. Moreover, the existing line $Re = 1$ corresponds readily to the Kolmogorov scales, which means that the starting point of the segment representing the turbulent energy distribution will be located on this line. We need only to compute the point on the spectral diagram associated with the integral scales to determine the information needed to place this segment. Depending on the different zones that this segment will cross, it is then possible to deduce the turbulent, nonpremixed combustion regime associated with these turbulence parameters. This work and the associated interpretation are presently underway.

Conclusions

Using various optical diagnostic techniques on a flexible setup, we have investigated in detail the interaction of a vortex ring and a planar, nonpremixed, diluted hydrogen/air flame. Data were obtained by varying mainly the global mixture ratio of the flame and the size and propagation speed of the vortex ring. Plotting these results in a single spectral interaction diagram and using theoretical considerations for zones where no experimental points are available, we have identified eight interaction regimes. These regimes correspond to the balance between the physical phenomena that control nonpremixed flame/vortex interactions: dissipation, straining, curvature, wrinkling, roll-up, and extinction. This spectral diagram can be employed eventually to build a turbulent, nonpremixed combustion diagram.

Acknowledgements

Travel of researchers between Ecole Centrale and Wright-Patterson has been supported by the Windows-on-Science program. The PhD work of P.-H. Renard has been supported financially by DRET. This work is also supported partly by US Air Force Contract F33615-95-C-2507. The authors thank Drs. Cam Carter (ISSI) and Jeff Donbar (AFRL) for their advice and assistance with PLIF, PIV and Rayleigh-scattering measurements [34].

REFERENCES

- [1] Thévenin, D., Rolon, J. C., Renard, P. H., Kendrick, D. W., Veynante, D. and Candel, S., *Proc. Combust. Inst.* 26:1079-1086 (1996).
- [2] Thévenin, D., Renard, P. H., Rolon, J. C. and Candel, S., *Proc. Combust. Inst.* 27:719-726 (1998).
- [3] Renard, P. H., Rolon, J. C., Thévenin, D. and Candel, S., *Combust. Flame* 117:189-205 (1999).
- [4] Renard, P. H., Thévenin, D., Rolon, J. C. and Candel, S., *Prog. Energ. Combust. Sci.* in press (2000).
- [5] Karagozian, A. R. and Manda, B. V. S., *Combust. Sci. Tech.* 49:185-200 (1986).
- [6] Jarosinski, J., Lee, J. H. S. and Knystautas, R., *Proc. Combust. Inst.* 22:505-514 (1988).
- [7] Roberts, W. L. and Driscoll, J. F., *Combust. Flame* 87:245-256 (1991).
- [8] Rutland, C. J. and Ferziger, J. H., *Combust. Flame* 84:343-360 (1991).
- [9] Roberts, W. L., Driscoll, J. F., Drake, M. C. and Goss, L. P., *Combust. Flame* 94:58-69 (1993).
- [10] Katta, V. R., Carter, C. D., Fiechtner, G. J., Roquemore, W. M., Gord, J. R. and Rolon, J. C., *Proc. Combust. Inst.* 27:587-594 (1998).
- [11] Poinso, T., Veynante, D. and Candel, S., *J. Fluid Mech.* 228:561-606 (1991).
- [12] Renard, P. H., Rolon, J. C., Thévenin, D. and Candel, S., *Proc. Combust. Inst.* 27:659-666 (1998).
- [13] Karagozian, A. R., Suganuma, Y. and Strom, B. D., *Phys. Fluids* 31:1862-1871 (1988).
- [14] Strawa, A. and Cantwell, B., *Phys. Fluids* 28(8):2317-2320 (1985).
- [15] Gutmark, E., Parr, T. P., Parr, D. M. and Shadow, K. C., *Sixth Symposium on Turbulent Shear Flows*, Toulouse, France, Paper 7-3, 1987.
- [16] Chen, L. D., Roquemore, W., Goss, L. P. and Vilimpoc, V., *Combust. Sci. Tech.* 77:41-57 (1991).
- [17] Hsu, K. Y., Chen, L. D., Katta, V. R., Goss, L. P. and Roquemore, W. M., *31st Aerospace Sciences Meeting*, AIAA 93-0455, 1993.
- [18] Park, J. and Shin, H. D., *Combust. Flame* 110:67-77 (1997).
- [19] Chen, S. and Dahm, W., *Proc. Combust. Inst.* 27:2579-2586 (1998).
- [20] Rolon, J. C., Aguerre, F. and Candel, S., *Combust. Flame* 100:422-429 (1995).
- [21] Fiechtner, G. J., Renard, P. H., Carter, C. D., Gord, J. R. and Rolon, J. C., *J. Visualization* 2(3):331-342, (1999).
- [22] Gord, J. R., Donbar, J. M., Fiechtner, G. J., Carter, C. D., Katta, V. R. and Rolon, J. C., *International Conference on Optical Technology and Image Processing in Fluid, Thermal and Combustion Flow*, Visualization Society of Japan and SPIE, Yokohama, Japan, 1998.
- [23] Gord, J. R., Donbar, J. M., Fiechtner, G. J., Carter, C. D. and Rolon, J. C., *Ninth International Symposium on Applications of Laser Techniques to Fluid Mechanics*, Lisbon, Portugal, 1998, pp.35.1.1-35.1.8.
- [24] Fiechtner, G. J., Carter, C. D., Grinstead, J., Gord, J. R., Roquemore, W. M. and

Rolon, J. C., *AIAA/ASME/SAE/ASEE 34th Joint Propulsion Conference*, AIAA 98-3770, 1998.

[25] Saffman, P., *Vortex Dynamics* Cambridge University Press, Cambridge, UK, 1992.

[26] Gogineni, S., Goss, L., Pestian, D. and Rivir, R., *Exper. Fluids* 25:320-328 (1998).

[27] Cuénot, B. and Poinso, T., *Proc. Combust. Inst.* 25:1383-1390 (1994).

[28] Cuénot, B. and Poinso, T., *Combust. Flame* 104:111-137 (1996).

[29] Zhao, J., Isaac, K. and Pellett, G., *J. Propul. Power* 12(3):534-542 (1996).

[30] Coffee, T. P., Kotlar, A. J. and Miller, M. S., *Combust. Flame* 54:155 (1983).

[31] Thévenin, D. and Candel, S. M., *Phys. Fluids A* 7(2):434-445 (1995).

[32] Hinze, J. O., *Turbulence* McGraw Hill Book Company, NY, 2nd Ed., 1975.

[33] Poinso, T., Veynante, D. and Candel, S., *Proc. Combust. Inst.* 23:613-619 (1990).

[34] Carter, C.D., Donbar, J.M. and Driscoll, J.F., *Appl. Phys. B* 66:129-132 (1998).

ϕ	0.5	0.6	0.7	0.8	0.9	1.0
$t_c^{-1} (s^{-1})$	$1.42 \cdot 10^2$	$4.30 \cdot 10^2$	$1.21 \cdot 10^3$	$2.11 \cdot 10^3$	$3.84 \cdot 10^3$	$6.29 \cdot 10^3$
ϕ	1.1	1.2	1.3	1.4	1.5	1.6
$t_c^{-1} (s^{-1})$	$9.58 \cdot 10^3$	$1.40 \cdot 10^4$	$1.97 \cdot 10^4$	$2.63 \cdot 10^4$	$3.37 \cdot 10^4$	$4.27 \cdot 10^4$

Table 1: Characteristic flame time obtained by asymptotic analysis for a nonpremixed hydrogen-air flame. The Arrhenius preexponential factor has been adapted to obtain the correct extinction limit for $\phi = 0.7$.

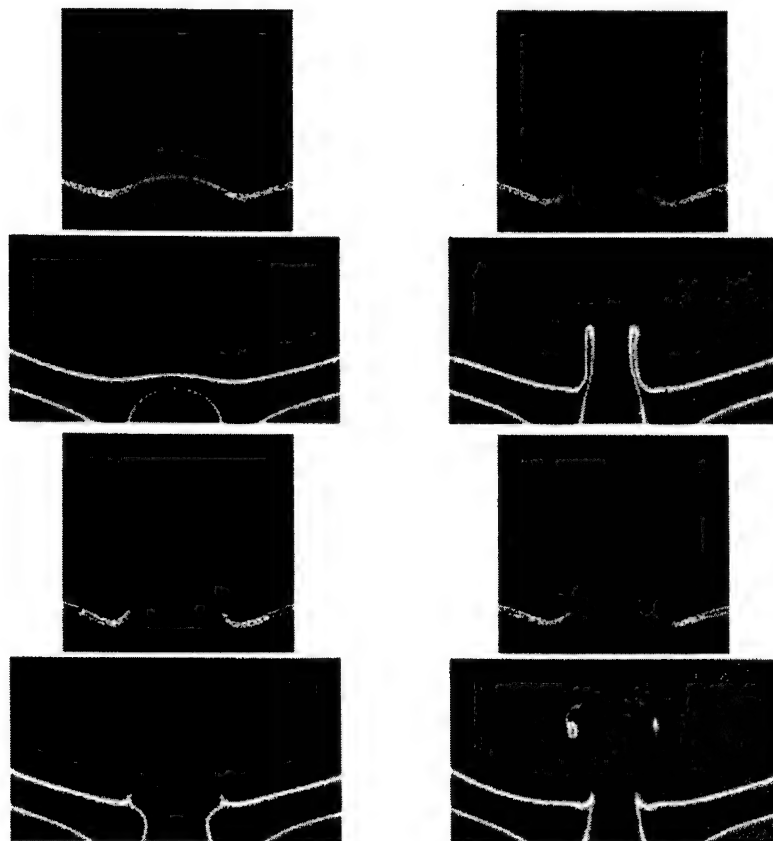


Figure 1: Simultaneous OH PLIF and Rayleigh measurements. In this case (injector of 5 mm, $\phi = 0.5$), extinction is observed on the symmetry axis. We show at four different interaction times ($t = 16$ ms, top left; $t = 18$ ms, bottom left; $t = 20$ ms, top right; $t = 22$ ms, bottom right) the OH PLIF image on top and the corresponding Rayleigh diffusion image below it. Note that the colours have been inverted for the Rayleigh signal.

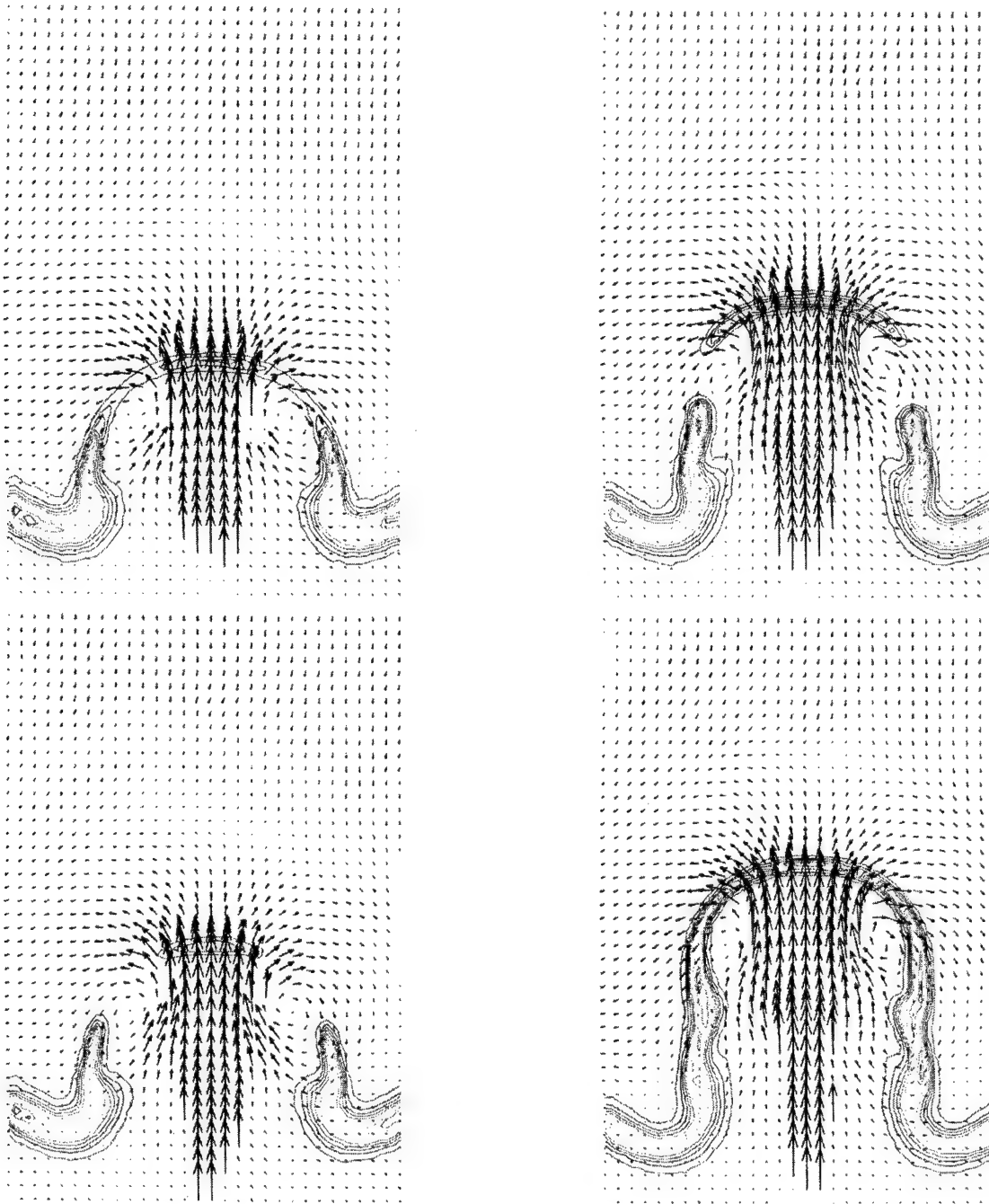


Figure 2: Simultaneous OH PLIF and PIV measurements. In this case (injector of 5 mm, $\phi = 1.0$), an annular extinction is observed. Shown at four different interaction times ($t = 8.3$ ms, top left; $t = 8.5$ ms, bottom left; $t = 9.0$ ms, top right; $t = 9.4$ ms, bottom right) are the isolevels of OH obtained by PLIF and the corresponding velocity vectors obtained by PIV. The lowest OH isolevel corresponds to the extinction limit [3].

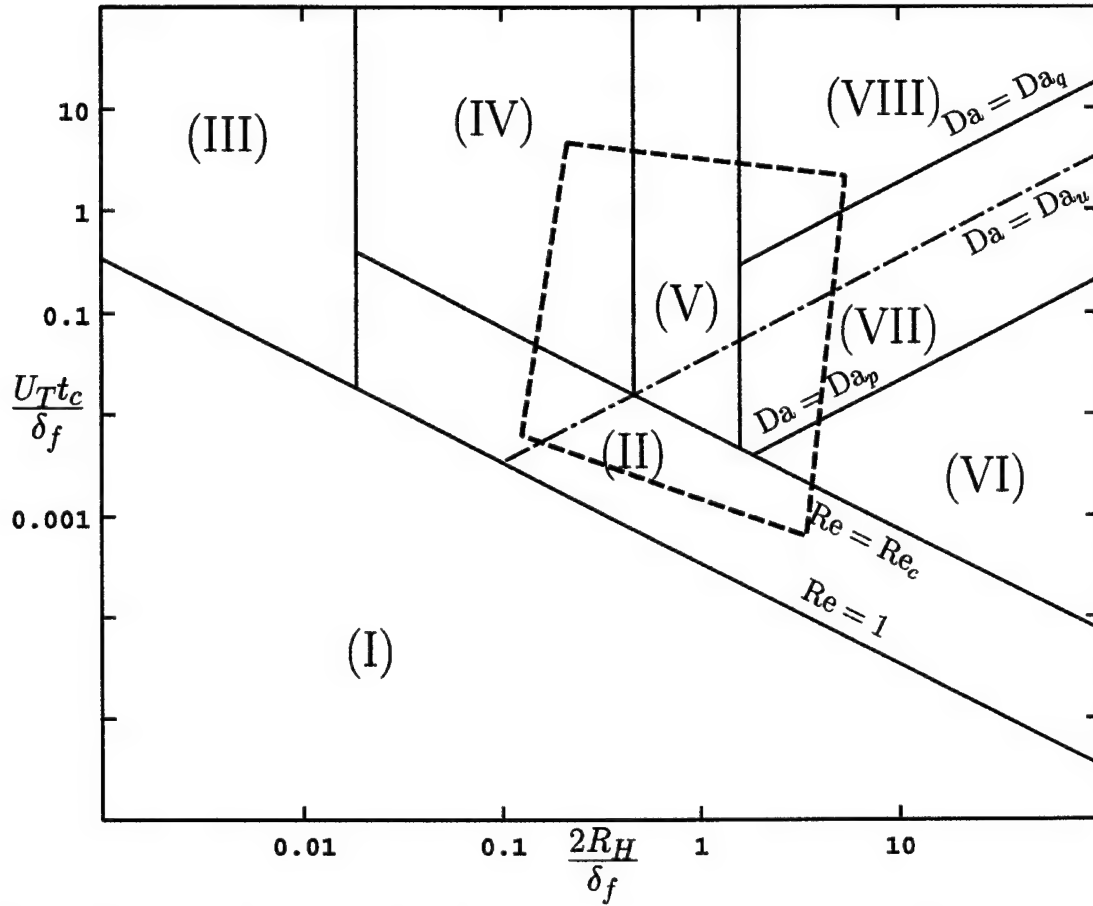


Figure 3: Spectral diagram for the nonpremixed flame/vortex interaction (log-log scale). This diagram is a synthesis of our experimental results along with theoretical considerations. Eight interaction types are identified. In Zones (I), (II), and (III), the vortices have no effect or a very weak effect on the flame. In Zone (IV), moderate curvature and wrinkling effects are observed. In Zone (V), a thickening of the reaction zones along with strong curvature effects and wrinkling is observed, leading to extinction. Zone (VI) is associated with wrinkling effects and a strong roll-up of the reaction zones, without extinction. Zone (VII) is similar to Zone (VI) except that pockets of oxidizer are formed and burn in the fuel part of the domain. Finally, in Zone (VIII), wrinkling and roll-up are still important, but extinction is observed always on the centerline. The domain limited by the dashed line corresponds to the zone accessible with our experimental setup.

3.1.3 Large-Scale Combustion Studies

3.1.3.1 Trapped-Vortex Combustor. The construction and testing of a trapped-vortex combustor are reported in the paper entitled "Entrainment of Mainstream Flow in a Trapped-Vortex Combustor" (see pp. 370-383). This early study concentrated on indirect estimates of cavity entrainment over a wide range of operating conditions for several cavity sizes. In a second study, documented in the paper entitled "Characteristics of a Trapped-Vortex Combustor" (see pp. 384-392), detailed temperature (CARS), species-concentration (gas-sampling), and velocity (PIV) data were obtained in the combustor to aid the understanding of the dynamics associated with the cavity. Peak combustion efficiencies of 99 percent were obtained with the combustor. The lean blowout stability of the trapped-vortex combustor is discussed in the paper entitled "Combustion Characteristics of a Trapped Vortex Combustor" (see pp. 393-405). In the publication entitled "Characteristics of Combustion Instability Associated with Trapped-Vortex Burner" (see pp. 406-415), a detailed study to identify and understand the dynamic behavior and acoustic noise associated with the trapped-vortex combustor is documented.



AIAA 97-0261

Entrainment of Mainstream Flow in a Trapped-Vortex Combustor

G.J. Sturgess and K-Y Hsu
Innovative Scientific Solutions, Inc.
Beavercreek, OH

**35th Aerospace Sciences
Meeting & Exhibit**
January 6-10, 1997 / Reno, NV

ENTRAINMENT OF MAINSTREAM FLOW IN A TRAPPED-VORTEX COMBUSTOR

G.J. Sturgess*

K-Y Hsu*

*Innovative Scientific Solutions, Inc.,
Beavercreek, Ohio*

Abstract

A laboratory-scale combustor is described. To provide good flame stabilization the combustor uses a vortex formed and trapped inside an annular cavity introduced into a centerbody that is placed in a concentric, axially flowing mainstream which is confined by a circular duct. Separately-controlled primary air and gaseous propane are directly injected unpremixed into the cavity for combustion purposes. The stability of the vortex in a driven-cavity is determined by the cavity dimensions. For a cavity that is additionally pumped by the directly-injected primary air and fuel flows, the relative momenta of the mainstream and injected cavity flows will also determine the combustion stability through the entrainment of mainstream flow into the cavity. Direct measurements of cavity entrainment are difficult to make. However, indirect assessments of entrainment are possible from other measurements with a few plausible assumptions. Indirect estimates of entrainment are provided over wide ranges of operating conditions at atmospheric temperature and pressure for several cavity sizes.

Introduction

In an introductory paper¹ a laboratory-scale combustor of unique form was described. The combustor uses a trapped vortex (TV) in a cavity for flame stabilization. The arrangement was such as to expose an axisymmetric annular cavity formed in a centerbody, to a by-passing co-axial mainflow of air that was confined by an enclosing circular cross-section duct. Primary air was injected into the cavity to

strengthen the naturally occurring vortex. In addition, a gaseous propane fuel supply was directly injected into the cavity, in close association with the primary air. Combustion took place within the cavity, to a degree determined by the cavity loading and equivalence ratio. The combustion efficiency achieved and the gaseous emissions generated both depended strongly on these quantities. However, cavity loading and equivalence ratio cannot be defined directly from the metered fuel and air masses supplied to the combustor. A quantity of mainstream air is entrained into the cavity by the action of the cavity vortex and by the additional pumping action of the primary air and the fuel jets.

If reliable performance is to be designed into a TV combustor it is essential to have reasonably accurate values of entrained air as functions of the combustor operating conditions and the cavity dimensions.

Background

Performance trends for future advanced aircraft gas turbine engines such as are being developed for the commercial market place, and especially for the IHPTET (*Integrated High Performance Turbine Engine Technology*) technology demonstrator program of the United States Air Force², will demand the design and use of lightweight combustion systems that are also compact and which have high combustion intensities of the order³ of $(10-16) \times 10^6 \text{ BTU/hr.ft}^3 \text{ atm}$. $[(10-16) \times 10^4 \text{ kW/m}^3 \text{ bar}]$. Furthermore, engines for military application will be expected to have much-expanded operating envelopes. Therefore, combustion

* AIAA Senior Member

+ AIAA Member

stability, always important, will become a key design concern.

In order to achieve such elevated combustion intensities as will be required, without losses in efficiency or generation of excess gaseous pollutants, fuel and air mixing prior to reaction must not only be improved but must take place at accelerated rates. This does not necessarily imply premixed systems will be used. The mixing process might take place concurrently with combustion as in a conventional fuel-rich primary zone, or as a partial-premixing direct injection system. Details of the mixing process will always be constrained by considerations of autoignition. When mixed or partially-mixed, combustion of the fuel/air mixture will also have to be completed as rapidly as possible. Rapid combustion is achieved via a combination of good fuel/air mixing, high flow turbulence and provision of adequate piloting. Unfortunately, such high-rate processes and good mixing are not readily conducive to ensuring good flame-holding with improved combustion stability.

The trapped vortex combustor concept, with its great potential for enhanced stability, appears to be a natural choice for providing the stabilization capability of such future combustion systems. A TV combustor module arranged in parallel could form the pilot for a fuel-staged combustor, the main stage of which could be operated lean and with short residence time in order to minimize the formation of thermal nitric oxide, an atmospheric pollutant.

Previous Work

In nature trapped vortices can be identified on the lee-sides of exposed mountain ridges, from the elegant cusp-geometries sculpted in the snow banks by wind action. Similar behavior can also be observed with sand dunes. This natural formation was manifested in the Griffith experimental low drag airfoil⁴ of the 1930's. It was also shown^{5,6} that substantial reductions in body base-drag could be achieved by locking a vortex at an axisymmetric body trailing-edge by means of one or more sting-mounted disks.

The use of a trapped vortex as an internal flow control device has a long history. The Dall flow tube⁷ was an example of a flow-metering device that used a vortex trapped in an annular cavity placed in a venturi throat to achieve flow measurements with very low losses in total pressure. Observations of the snow cornice and experiences with the Dall tube idea applied

to diffusers⁸, led to the proposal to use trapped vortices in combustion section dump diffusers⁹. The dump diffuser was originally introduced in the Rolls Royce Pegasus 5 V/STOL engine to address the problem of flow split deviations in the combustor arising from severe distortions at the engine inlet during transition from vertical to horizontal flight. With General Electric Aircraft Engines quickly realizing the advantages, the dump diffuser has subsequently become ubiquitous to ameliorate combustor flow split changes that take place due to compressor exit profile shifts in aging engines.

Combustion use of the trapped vortex concept extends back to the nineteenth century when wind-resistant kerosene-fueled table lamps were produced in Russia¹⁰. Later, a wall-recess was considered as a possible flameholder for aircraft engine afterburners¹¹, but did not find favor due to excess heat losses to the wall from the recirculation zone, that impaired flame stability. More recently scramjet engine technology in the former Soviet Union has explored the use of the trapped vortex as a flameholder¹² in low Mach number supersonic flows. Similar studies were conducted in Japan^{13,14}, where the vortex cavity was located in a strut, and the flame holding capability was explored.

In any study of the detailed behavior of the trapped vortex the vortex dynamics are found to be extremely important. The basic stability of the vortex is dependent on the cavity dimensions. Proper sizing rules of the cavity to successfully trap a vortex over a wide range of operating conditions have been established in isothermal, non-reacting flow⁶. With the vortex fully trapped within the cavity, a minimum base drag condition is reached.

The effects of the vortex dynamics on drag have also been explored¹⁵. For non-combusting and combusting flows our colleagues have studied the aspect of the vortex dynamics numerically¹⁶. It was shown that vortex shedding behind a bluff body leads to a higher drag coefficient. The dynamic behavior is complex, and can consist of more than a single dominant vortex, depending on the cavity dimensions. Entrainment into the cavity and residence time within the cavity were found to depend on the shedding characteristics.

Present Contribution

Data from the original report¹ with fixed cavity dimensions have been analyzed to provide parametric information for the effects on entrainment of mainstream air into the cavity, of mainstream air

velocity for zero primary air and, for a fixed value of primary air velocity. The effect on cavity entrainment of mainstream air by primary air jet velocity at fixed mainstream air velocity is also given. Additional experiments have been conducted to cover a number of cavity dimensions. The collected data have been correlated to provide preliminary design curves for determining the separate effects of operating variables and cavity dimensions on entrainment.

Combustor Arrangement

The original laboratory-scale TV combustor was described in Reference 1. The combustor consists of two major portions: a centerbody assembly and, a housing assembly.

The centerbody assembly is formed from a long central shaft of stainless steel that is made up of an inner fuel tube surrounded by a concentric air passage with outer diameter d_i , of 12.7mm, and which passes with a sliding fit through a solid disk of 70mm diameter, d_f , that forms a forebody. On the downstream end of the shaft is permanently mounted a short, hollow drum of 50.8 mm diameter, d_a , that forms an afterbody.

The drum contains two inner compartments that form respectively, primary air and fuel manifolds. These manifolds are supplied through the supporting double-tube shaft. The adjustable spacing H , between the forebody, the afterbody and the shaft forms an annular cavity within which a vortex may be trapped.

Fuel is discharged upstream into the vortex cavity from the upstream face of the drum via a ring of 8 circular jets each of 1.75mm diameter; tubes from the fuel manifold pass through the air manifold to feed these jets. Air from the air manifold is discharged upstream into the vortex cavity from the upstream face of the drum via two concentric rings of circular jets each of 2.286mm diameter. There are 8 air jets in the inner ring and 16 air jets in the outer. The ring of fuel jets is concentric with and between, the rings of air jets. The fuel jets are circumferentially oriented to place a fuel jet midway between adjacent pairs of inner and outer air jets.

The forebody is supported concentric in a duct of 80 mm internal diameter, d_c , that supplies main air to the combustor from an air conditioning unit similar to that described in Reference 17. The combustor main body is a length of 80mm internal diameter Pyrex

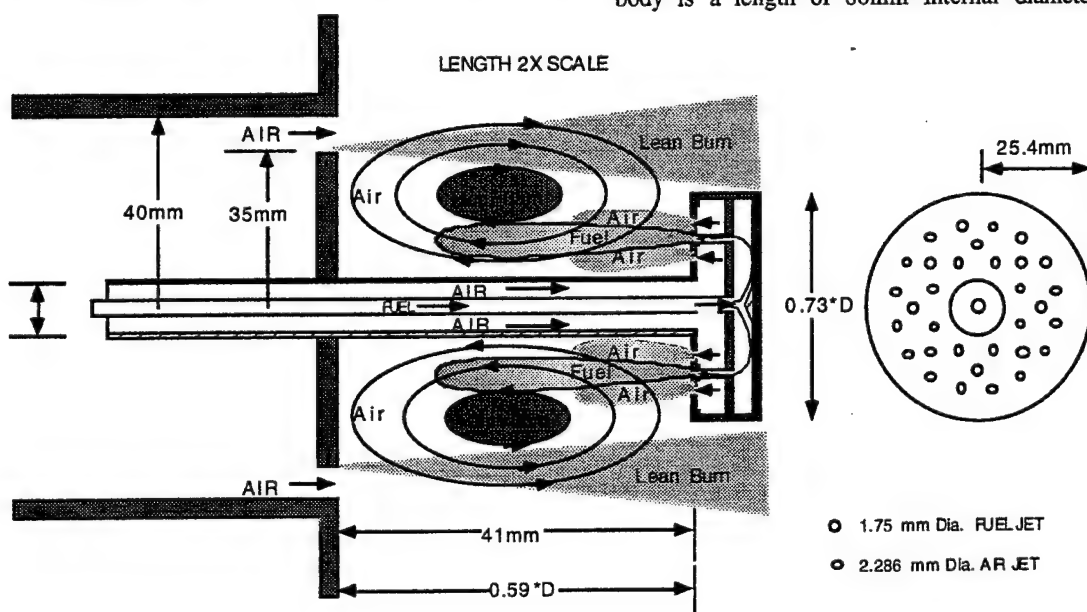


Figure 1: Schematic of Combustor Centerbody Assembly, Showing Operation

tubing. The length of the combustor in the original experiment was 910mm; for the present set of experiments a replacement (due to breakage) length was 780mm.

The complete centerbody assembly is cooled by the flows of air and fuel internally through it. The combustor main wall is protected initially from direct exposure to flame temperatures by the cool annular jet of main air that is in contact with it. No downstream external cooling of the main wall was provided. The forebody has no direct cooling, other than that provided by the annular flow of main air passing its outer edge.

The combustor and its conditioning unit for main air are mounted vertically in a test bay at Wright Laboratory. The main air and pilot air originated from two air supplies, and are metered and controlled separately. The gaseous propane is supplied from bottles. Exhaust from the combustor is collected and removed through a conventional exhaust hood.

A schematic view of the combustor is given in Figure 1. The sketch shows fuel and air paths, and suggests the modes of burning.

Emissions Measurements

The axial plane downstream for the emissions measurements was fixed at 756.5mm, or 9.46 combustor diameters from the downstream face of the forebody. At this distance the exhaust was well-mixed. All air supplies to the combustor were dried to a dew point of less than -55F (225K).

The emissions probe extended across the combustor diameter, and contained 5 sampling ports of 0.5mm diameter. The sampling ports were distributed along the probe to give an area-weighted sample. The probe had provision for water-cooling, although at the conditions of the present testing there were no significant differences in the gas sample temperatures at the meter with or without the cooling.

An Ecom-S+ microprocessor-based portable emissions sampling/analyzer unit was used to measure the concentrations of CO , NO , NO_2 , O_2 and unburned hydrocarbons (UHC). The differences between the metered equivalence ratios and the emissions-based equivalence ratios were generally in the range of 5-10%. Near blowout conditions this difference rose to about 20%, due to inaccuracies in the derived value of CO_2

which was obtained from the measured O_2 concentration, assuming equilibrium.

Entrainment Measurement

Direct measurement of mainstream entrainment into the cavity is not easy. Several obvious approaches exist, but are all subject to potential difficulties. Some example methods are briefly given below.

If an axisymmetric interface is imagined between the downstream corner of the forebody to the upstream corner of the afterbody (see Figure 1), simultaneous surface measurements of temperature, composition and velocities normal to the surface, for integration over the entire interface surface, would be necessary.

Alternatively, an average cavity residence time τ , could be found from the timing of decay of an inert tracer directly introduced into the cavity in pulsed fashion. Then,

$$\tau = \ell_f / \bar{V} \quad (1.)$$

where the average velocity \bar{V} , is given by,

$$\bar{V} = \frac{\dot{m}_{tot}}{\rho A_{cavity}} \quad (2.)$$

and, the total mass flow rate in the cavity is the sum of the fuel and air mass flow rates,

$$\dot{m}_{tot} = \dot{m}_f + \dot{m}_a \quad (3.)$$

Finally, the cavity air mass flow rate is the sum of the metered primary air directly introduced into the cavity, and the sought for entrained mass flow rate, \dot{m}_{ent} ,

$$\dot{m}_a = \dot{m}_{pri} + \dot{m}_{ent} \quad (4.)$$

Measurement of the cavity temperature and determination of the path length ℓ_f , of the fuel say, from flow visualization are also needed to determine the entrainment. This latter step presents some difficulties.

Measurements in the cavity of the concentration of an inert tracer that was introduced into the mainstream might also yield a suitable entrainment measurement, provided that representative sampling could be obtained.

With "direct" measurement of entrainment being potentially so difficult, indirect estimates of entrainment can be usefully and conveniently based on more easily-made measurements of other quantities through invoking a few plausible assumptions. If two or more independent types of such entrainment estimates can be produced, based on primary measurements of different quantities, they can then be used as a mutual check of the underlying assumptions upon which the estimated entrainments rest. If good agreements are attained then sufficient accuracy should be present to provide good indications of the quantity of entrained air.

Two types of basic measurement are given in Reference 1 that can be used for making estimates of mainstream air which is entrained into the vortex cavity. First, lean blowout (*LBO*) data, and second, gaseous emissions by gas sampling. Use of both types of measurement for the purposes of estimating cavity entrainment involves some assumptions concerning the nature of the flows within the cavity. However, entrainment estimates based on three measured quantities - *CO*, *NOx* and *LBO* - are then possible, with the emissions and *LBO* 's being quite different types of measurement.

For the *LBO* data it is first assumed that for *LBO* 's under the present operating conditions the cavity mass loading is relatively low so that blowout always takes place well away from the peak heat release rate condition. It is then assumed that the fuel and air within the cavity are sufficiently well mixed that blowouts always occur at the flammability limits of propane/air mixtures, i.e. at a cavity equivalence ratio of 0.5¹⁸ for reactants at atmospheric temperature and pressure. A final assumption is made that the flame is always confined to the cavity at blowout conditions.

For the emissions data two assumptions are necessary also. First, that the total oxides of nitrogen (*NOx*) and carbon monoxide (*CO*) are generated solely within the vortex cavity. The validity of this assumption can be improved by always operating with relatively low mass flow rates so that the observed flame is confined to the cavity. (The low mass flow rate condition also improves the validity of the assumption above concerning peak heat release rates.) The second assumption is that the reactions taking place in the cavity do so with fuel/air mixing levels such that minimum *CO* and maximum *NOx* (thermal *NO*) are attained at a nominal cavity equivalence ratio of unity¹⁹.

Heat losses from the combustor will increase the validity of these assumptions.

To assess the approximate level of fuel/air mixing within the cavity the CARS (Coherent Anti-Stokes Raman Spectroscopy) temperature measurements and PIV (Particle Imaging Velocimetry) flow visualization information gathered in the original report¹ were used. Both sets of measurements demonstrated for the H/d_f equal to 0.59 cavity, that the individual fuel and air jets, which are introduced through the cavity aft-wall, had essentially lost their identities before the forebody was reached. This is indicative of relatively high levels of mixing being achieved in the cavity. The fuel flow rate used in the earlier experiments was higher than the rates used in the current experiments. Therefore, mixing under most conditions in the present work should also be good. As an *LBO* is approached by reducing the fuel flow rate at fixed airflow conditions in both series of experiments, mixing should improve further for blowouts. Therefore, the assumption of good fuel/air mixing on a global basis in the cavity, under most operating conditions of interest, is not unreasonable.

To help test the well-mixed assumption in the case of *LBO*'s the cavity fuel distribution was varied through replacing the 8 fuel jets by a similar array of 12 jets of 1.98mm individual diameter placed on a pitch circle of 12.7mm diameter. Blowouts were obtained for this system at 14, 28 and 42m/s mainstream air velocity and for zero primary air; the overall cavity length was also varied at each condition from 14.6mm to 63.5mm, giving H/d_f values from 0.21 to 0.907.

The blowouts for the two fuel jet systems agreed closely over all H 's for the 28 and 42m/s mainstream velocities. For the 14m/s mainstream velocity the blowout fuel flow rates were within the data uncertainty for H/d_f 's less than about 0.54. These data imply that around the optimum (minimum drag) cavity dimensions and for the higher values of mainstream velocity, the fuel is reasonably well-distributed around the cavity circumference with the 8-jet system.

The apparent equivalence ratio for minimum *CO* is not as sensitive to unmixedness as is the *NOx* peak, being more sensitive to heat losses rather. The apparent equivalence ratio for maximum *NOx* can typically vary between 0.8 and 1.3 due to unmixedness effects. Such a range of variation could exert noticeable

influence on the entrainment estimated from the position of the NO_x peaks.

The assumptions that the measured gaseous emissions were generated totally within the cavity was checked for the original results by comparing at identical operating conditions, between the single cavity and some double cavity results given in Reference 1. Almost no effect was found on CO at all mainstream velocities; there was a somewhat greater effect of the double cavity on NO_x , especially at lower mainstream velocities. For the present results care was taken to use mass flow rates such that the visible flame was always confined to the cavity.

From the above, it would be expected that the estimated entrainment values should be in reasonable agreement for the LBO and CO methods, with an expected difference for the NO_x method. The estimates based on CO and LBO should be reasonably accurate.

The technique used is the same for all three bases of estimation: The observed equivalence ratios at LBO , minimum CO and maximum NO_x respectively, are corrected to the postulated "theoretical" values by adding (or subtracting) additional air to the metered primary air in the cavity. The quantity of additional air added is the entrained mainstream air that **must be present to satisfy the assumptions.**

Estimated Entrainment from Reference 1

Figure 2 presents the estimated cavity entrainment air, expressed as a percentage of mainstream air, for the cavity with H/d_f equal to 0.59, and as a function of mainstream velocity. This is the "optimized cavity" for minimum drag⁶. Combustion was taking place. Some of the appropriate CO minima and NO_x maxima, and LBO points, are given in Figures 9 and 6 respectively of Reference 1. Additional data were gathered but were not reported in that reference. For information, these emissions maxima and minima occurred at primary jet equivalence ratios around 2 to 3.

Two curves are presented: one for zero primary air, obtained from LBO measurements, and, a second for a constant primary air velocity of 42m/s. The second curve includes estimates obtained by all three approaches described above. In addition, a single point is compared to the first curve (zero primary air) at 30m/s mainstream air velocity. This is obtained in non-reacting flow for this cavity from the CFD (computational fluid dynamics) results (based on the

behavior of injected zero mass, infinite drag tracer particles that represents the computational analogue of the experiment described in the previous section) of Reference 16.

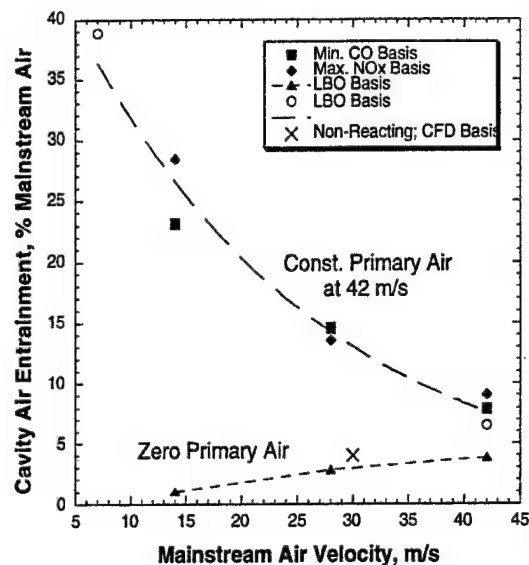


Figure 2: Estimated Entrainment Inferred from Three Measurements and CFD Calculation

For the first curve the non-reacting flow point from the CFD is in good general agreement with the reacting flow points from LBO 's. For the second curve there is no systematic dependence of entrainment on the method of making the estimates; further, the values obtained by the different approaches are in good agreement with each other. These agreements give confidence that the estimated values for entrainment are reasonable and, that reliance can be placed on the more extensive and easier to obtain LBO data. Finally, since the set of estimates for the second curve are based on data at both 0.5 and 1.0 nominal equivalence ratios, it may be provisionally argued that the entrainment is independent of cavity heat release rate to first order.

It can be seen that for zero primary air the entrained mass flow rate increases slowly with increasing mainstream velocity. However, it is a small fraction of the mainstream, being less than 4% at 42m/s. The powerful effect of primary air on "pumping" the cavity is well-illustrated with the entrained air being approximately doubled to about

7.5% when the primary air velocity is also 42m/s. For lower mainstream velocities at the constant primary air velocity the entrained air increases dramatically to over 38% at 7m/s. For these latter conditions it should be remembered that the mainstream is not infinite. Eventually, continuing entrainment will cause the mainstream to be separated off the combustor wall. Finally, mainstream entrainment would reach a saturation value. The increased entrainment "appetite" of additional pumping would result in self-entrainment of the cavity flow.

The change in slope taking place between zero and 42m/s primary air jet velocities indicates that a competition exists between the two mechanisms (natural and pumped) for entrainment.

The effect of primary air jet pumping on cavity entrainment of mainstream flow is explored in Figure 2 by means of *LBO* data from the original experiment. For these data the mainstream velocity was fixed at 42m/s; primary air jet velocity was varied between zero and 51m/s.

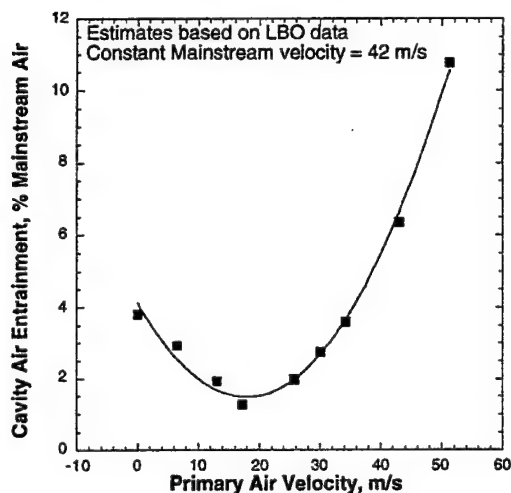


Figure 3: Effect of Primary Air Jet Velocity on Mainstream Entrainment at Fixed Mainstream Velocity

The figure shows that as the primary air jets come on entrainment first decreases from the natural-entrainment value of almost 4% down to a minimum of about 1.3% at about 18m/s primary air jet velocity. At higher values of primary air jet velocity the entrainment

steadily increases to around 11% at 51m/s jet velocity. The existence of a minimum entrainment implies a balance condition between the two entrainment mechanisms.

Correlation of Entrainment Data From Ref. 1

It is well-known that entrainment into shear layers and jets is momentum driven, e.g. References 20 and 21. Entrainment into the trapped vortex cavity involves the fluid dynamics of both shear layers and jets. It has been demonstrated²² that the effects of entrainment for non-reacting and reacting complex jet systems involving streamline curvature and recirculation could be successfully correlated by the square root of jet momentum ratio. For these reasons correlation of the cavity entrainment was attempted for the present data based on the square root of the ratio of cavity momentum to mainstream momentum.

Figure 4 shows the collected data for the 0.59 H/d_j cavity, derived from the original series of measurements, expressed in terms of the square root of the ratio of cavity momentum to mainstream momentum.

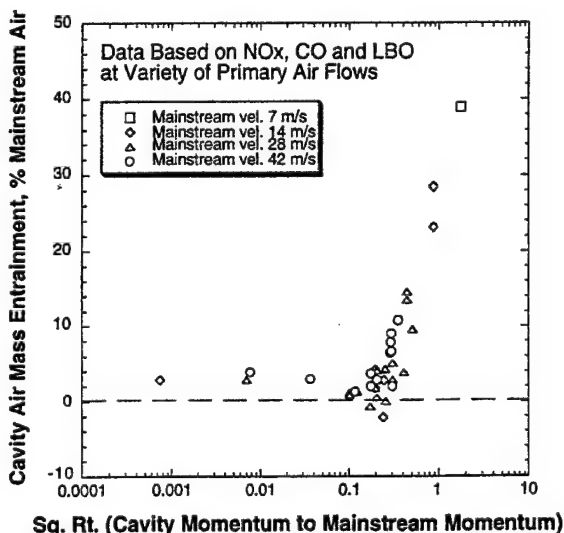


Figure 4: Correlation of Cavity Entrainment (Original Experiments)

The data in Figure 4 are based on values derived by the *NOx*, *CO* and *LBO* methods, and cover mainstream velocities from 7m/s to 42m/s with a wide

variety of primary jet velocities from 0m/s to 51m/s; fuel flow rates of gaseous propane ranged from 2 to 20slpm. The cavity momentum is defined as being the sum of the separate primary air jet and the fuel jet momenta. Note that the abscissa covers a range of five orders of magnitude in the correlating parameter. Considering the wide ranges of operating variables covered and the different approaches used for estimating cavity entrainment, the correlation achieved is remarkably good.

Three regions in the correlated data can be observed: First, a region on the left of the plot for values of the correlating parameter less than 0.1, where entrainment is very low, not exceeding 4% of the mainstream air. Second, a small region central in the plot between 0.1 and 0.25 for the correlating parameter, where entrainment into the cavity is zero or actually negative (-2% maximum), i.e. a net outflow. Third, a region on the right of the plot for values of the correlating parameter greater than 0.25 where entrainment increases rapidly in linear fashion to almost 40% at a value of 2.0 for the correlating parameter.

The left-hand region represents dominance of natural entrainment into the cavity. The right-hand region represents dominance of primary air jet pumping of the cavity. The central region represents a region of neutrality where the two mechanisms are in balance. Clearly, this central region is one of maximum vortex stability and minimum base drag.

Effect of Cavity Length - The Second Test Series

With reference to Figure 1 it can be seen that movement of the combustor central shaft assembly and the integral afterbody, through the forebody (sliding fit), varies the length H of the vortex cavity. This changes the ratio H/d_f , with consequent effects on the vortex system, and hence, on entrainment.

For natural entrainment, (no primary air jets), the optimum (minimum base drag) cavity configuration of H/d_f equal to 0.59 has an instantaneous vortex system¹⁶ that consists of a large and well-organized axially-symmetrical toroidal vortex with two quite small corner toroidal vortices located in the corners between the shaft and forebody and, the shaft and afterbody, respectively. Smaller values of H/d_f result in growth of the smaller upstream corner vortex to essentially fill the cavity, while the original, large symmetrical vortex is shrunk and displaced to the outer

rear-most region of the cavity where it is periodically shed over the afterbody due to communication with the vortex on the downstream face of the afterbody. Smaller still values of H/d_f with d_f fixed, produce three major vortices of similar size, with one in the body of the cavity near the shaft, one at the top of the cavity, and one precariously located on the thickness of the afterbody, over which the dividing stream surface-contour passes. This system has very strong coupling with the comparatively larger vortex on the afterbody downstream face. For an increase in H from the optimum value, the large symmetric vortex dominating the cavity weakens and becomes disorganized.

The dynamic behavior of the various instantaneous vortex systems described above governs the cavity entrainment, flame stability and emissions generated in the cavity. Each vortex pattern is affected in its own way by the presence of primary air jets pumping the cavity through strengthening, disrupting or displacing vortices. A second test series was undertaken to explore the effect of these behaviors on mainstream entrainment.

The cavity dimension H was varied to give cavity length to depth ratios H/d_f of 0.36, 0.45, 0.54 and 0.64. The mainstream velocities were 28, 35 and 42m/s, and for each mainstream velocity the primary jet air velocity was varied from 4m/s to 34m/s in 8 steps. These velocities were selected, based on the earlier experiences, to avoid any potential unmixedness uncertainties in the LBO's. As before, the fuel was gaseous propane, and the inlet air was at atmospheric pressure and temperature. LBO's were conducted at each condition.

The effect of primary air jet velocity at constant mainstream velocity for all cavities is very similar to that given in Figure 3 for the original data at 42m/s mainstream velocity and with H/d_f equal to 0.59. Figure 5 shows a plot of the entrainment versus primary air jet velocity at the three mainstream velocities for the 0.36 H/d_f cavity. Figure 5 is to the same scale as Figure 3, and so may be compared directly.

It is noteworthy that for the data-points indicated in Figure 5, around 24m/s primary air jet velocity for the 35m/s mainstream velocity, an acoustic resonance was encountered. The flame moved partially out of the cavity and was stabilised on the upstream edge of the afterbody. A loud "buzz" was generated. This resonance condition was extremely repeatable, and was

encountered for all of the cavities in this second test-series. It only appeared for the higher mainstream velocities of 35 and 42m/s. Depending on the cavity, the resonance appeared locally over the entire range of primary air jet velocities, moving from high values of jet velocity for the 0.36 cavity to both high and low values for the 0.54 and 0.64 cavities. The appearance of the resonance resulted in an increase in the blowout fuel flow rate, as can be readily deduced from Figure 5.

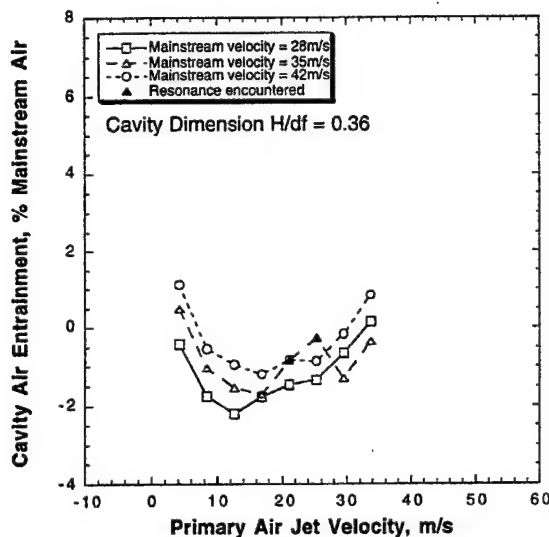


Figure 5: Entrainment Characteristics for the Smallest Cavity Length

When compared to Figure 3, it can be seen from Figure 5 that the 0.36 H/d_f cavity is too small should there be any significant amount of primary jet air introduced into it, in addition to the natural entrainment. For all three mainstream velocities the entrainment is negative, i.e. an overflow, for primary air jet velocities above about 7m/s. Entrainment does not become positive again until a strong jet pumping is established. This occurs for mainstream velocities above 35m/s when the jet velocities are greater than about 33m/s. Even so, there is not a great deal of entrainment.

As the cavity length is increased the negative entrainment is reduced. Entrainment becomes entirely positive for the entire range of primary air jet velocities and the three mainstream velocities when H/d_f is increased to 0.54. For all cavities at 42 and 35m/s mainstream velocities the primary air jet velocity at

which minimum entrainment occurs is 17m/s. However, for all cavities at 28m/s mainstream velocity the minimum entrainment occurs at 12.6m/s primary air jet velocity.

Figure 6 illustrates the effect of cavity geometry on the minimum entrainment condition for the 42m/s mainstream velocity and 17m/s jet velocity. It can be seen that around the optimum cavity dimensions of 0.59 H/d_f , entrainment is positive but low, at about 1 percent. There is little change in entrainment with small reductions in H/d_f until a value of about 0.45. For values of H/d_f less than 0.4 entrainment quickly becomes negative, being -1.2 percent for a cavity of 0.36. For cavities with H/d_f greater than 0.59 entrainment increases sharply, being 3.22 percent at 0.64 H/d_f .

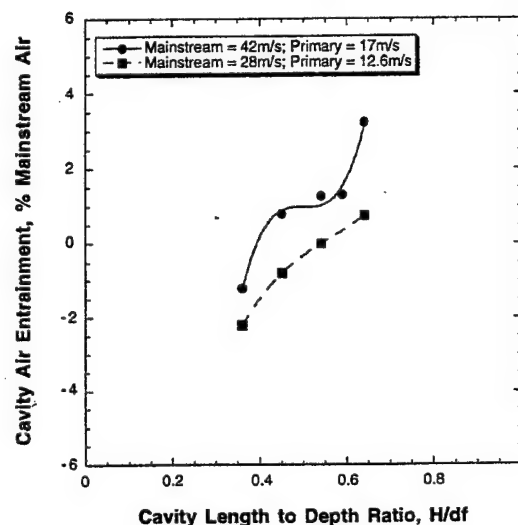


Figure 6: Effect of Cavity Dimensions on Minimum Entrainment

Also shown on Figure 6 are the minimum entrainment data for the 28m/s mainstream velocity at 12.6m/s primary air jet velocity. The minimum entrainment at the lower mainstream velocity is reduced, and the sensitivity to cavity dimensions near the optimum value of 0.59 appears to be increased slightly.

In a gas turbine combustor application of a TV combustor the primary air jets would be fed by the

pressure drop across the liner wall. In typical such applications the velocities of the primary air jets would then be greater than the range covered in the present experiments. Therefore, the effect of cavity dimensions on entrainment at one of the higher values of primary air jet velocity of around 30m/s is examined in Figure 7 for the three mainstream velocities of 28, 35 and 42m/s.

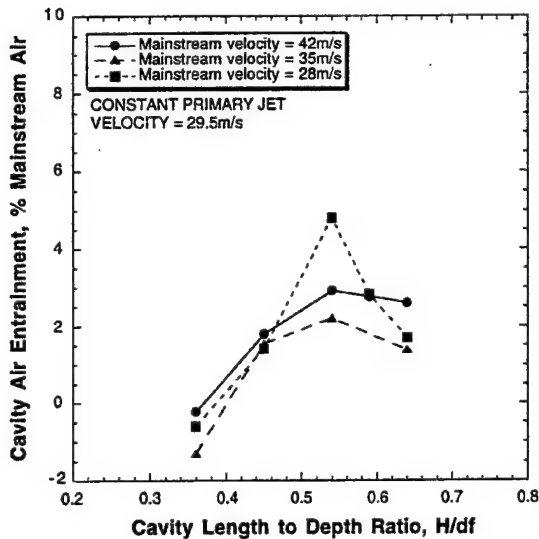


Figure 7: Effect of Cavity Dimensions on Entrainment at Higher Primary Jet Velocities

It can be seen from Figure 7 under these conditions where jet pumping dominates entrainment into the cavity, that for all of the mainstream velocities entrainment reaches a maximum at a cavity length to depth ratio of about 0.54. Once again, for H/d_f less than about 0.4, the entrainment is negative for all velocities. For a cavity H/d_f above 0.54 the entrainment decreases slightly for this jet velocity.

With the aid of correlation plots like Figure 4, constructed for each of the cavities, an entrainment map can be prepared. From the correlated entrainment data for each cavity the maximum and minimum values of the square root of the ratio of cavity to mainstream momenta, $(M_c/M_m)^{1/2}$, for zero entrainment can be established. Plots of these maximum and minimum zero entrainment values against cavity length to depth ratio identify regions of positive and negative entrainment.

Figure 8 shows the resulting entrainment map. It can be seen that for all values of $(M_c/M_m)^{1/2}$ entrainment is positive with H/d_f greater than 0.64. For cavities with H/d_f less than 0.64, the range of $(M_c/M_m)^{1/2}$ for which entrainment is negative increases rapidly with decreasing H/d_f .

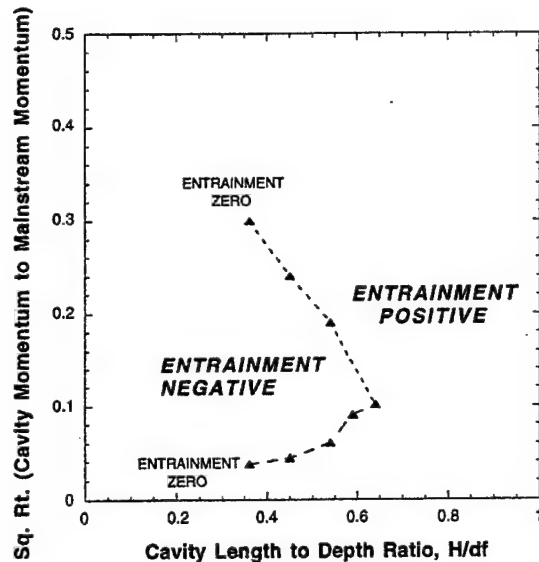


Figure 8: Cavity Entrainment Map

Discussion

The most likely use of a TV combustor in a gas turbine engine is for the pilot-stage in a fuel-staged combustor designed to operate with either low gaseous emissions production, or with a high engine turn-down ratio. The potential high flame stability offered by mechanically trapping the vortex that provides flame-holding, is an attractive feature for a pilot. The combustion efficiency of such a pilot at low engine power conditions must be high. Conversely, at high power conditions it would be desirable to minimize the production of oxides of nitrogen, an atmospheric pollutant. These conflicting design requirements demand a careful control of actual equivalence ratios within the pilot stage over the entire range of engine operating conditions. For these reasons a precise knowledge of the amount of air actively involved in chemical reaction in a TV combustor is essential. Therefore, an understanding and quantification of air entrained into a vortex cavity are desirable.

The use of indirect methods to assess entrainment in a TV combustor conveniently avoids the considerable difficulties associated with direct methods. Indirect methods, especially based on LBO's, are usually relatively fast, and allow wide ranges of operating conditions and cavity geometries to be assessed at reasonable cost. Care must be taken however, not to seriously violate the assumptions involved with indirect methods. In the present instance, the key assumption was good mixing of fuel and air in the cavity. In order not to violate this assumption, low values of mainstream velocity could not be used **unless** the entrainment was strongly jet-dominated, i.e. for simultaneously high values of primary air jet velocity.

An "optimum cavity" length to height ratio of 0.59 was carried over from the external aerodynamics drag-minimization work on long aspect ratio bodies of revolution. The minimum drag condition implies that vortex shedding from the cavity, and hence, entrainment into the cavity, is at a minimum for this optimum.

Preliminary work with the optimum cavity resulted in behavior (Figures 2 and 3) which indicated that entrainment was governed by two processes. These were described as "natural entrainment" and "jet pumping" effects. The inferred entrainment data for mainstream velocities from 7 to 42m/s with wide ranges of jet velocity (both subject to the caveats given above), when expressed as a percentage of the mainstream air mass flow rate, were correlated acceptably by the square root of the ratio of cavity momentum to mainstream momentum (Figure 4). This correlation showed that for low values of $(M_c / M_m)^{1/2}$ less than about 0.1, entrainment was fairly low at under 5 percent. This region was attributed to "natural entrainment" due to the presence of the cavity in a cross-flow. For values of $(M_c / M_m)^{1/2}$ above about 0.3, entrainment increased very rapidly to substantial values. This region was attributed to the ejector-like effect of "jet pumping" of the cavity by the metered flows of fuel and combustion air directly introduced into the cavity. Between these two dominant regimes falls a small range of $(M_c / M_m)^{1/2}$ where the two competing entrainment processes are more or less in balance. Within this range negative entrainment can take place. The outflow of mass arises because the cavity is too small for the entering flows.

Entrainment into the cavity is governed by the dynamic behavior of the vortex system established by the cavity length to depth ratio, and how this vortex

system is changed by the presence of the jets. Some understanding of the former effects is being gathered, e.g. Reference 16, but detailed knowledge of the effects of direct injection into the cavity remains to be explored.

The range of H/d_f values presently explored with direct injection into the cavity covered values both less than and greater than, the "optimum" of 0.59 obtained without direct injection or combustion, and based on minimum drag considerations.

The presence of direct injection, even at moderate values of cavity momentum, apparently modifies the flow behavior within and into and out of, the cavity. In the momentum region of balanced natural and jet pumping entrainment, where entrainment is at a minimum (Figure 5), entrainment changes from positive to negative for cavity dimensions H/d_f of 0.5-0.6 (Figure 6). This is in accord with the finding from external aerodynamics. However, in the momentum range where jet pumping is **beginning** to govern the entrainment process, entrainment reaches a (positive - i.e. inflow) maximum at an H/d_f about 0.55 (Figure 7). This is in conflict with the minimum drag assumptions, but does indeed represent an optimum for the TV combustor.

If a positive entrainment into the vortex cavity is desired for wide ranges of $(M_c / M_m)^{1/2}$ that include both natural and jet-pumping driven entrainment, it is necessary to use a cavity H/d_f greater than 0.65 (Figure 8). For control of the cavity combustion processes positive entrainment is generally desirable.

Conclusions

1. Provided that reasonable care is taken, indirect methods can be conveniently used to assess mainstream mass entrainment into the cavity of a trapped vortex combustor.
2. When the vortex cavity has direct injection of fuel and air, natural mainstream entrainment into the cavity can be supplemented by jet-pumping effects.
3. Entrainment is controlled by the ratio of cavity momentum to that of the mainstream.
4. Depending on the magnitude of cavity momentum to that of the mainstream, the entrainment can be either negative (outflow) or positive (inflow).

5. When the momentum of the jets directly injected into the cavity is low, minimum net entrainment is obtained at a cavity length to depth ratio of 0.55-0.90.
6. When the momentum of the directly-injected jets is high, a maximum positive entrainment is obtained for a cavity length to depth ratio of 0.55.
7. For positive entrainment over wide ranges of the ratio of cavity momentum to mainstream momentum, the cavity length to depth ratio should be greater than 0.65.

Acknowledgements

The enthusiasm, motivation and support of Dr. W.M. Roquemore of Wright Laboratory are greatly appreciated. Dr. Roquemore conceived applying the TV combustor to gas turbine engines. This on-going research is sponsored by the U.S. Air Force, Wright Laboratory, Aero Propulsion and Power Directorate.

References

1. Hsu, K-Y, Goss, L.P. and Roquemore, W.M., "Performance of a Trapped-Vortex Combustor," Paper No. 95-0810, AIAA 33rd. *Aerospace Sciences Meeting & Exhibit*, Reno, Nevada, January 9-12, 1995.
2. Valenti, M., "Upgrading Jet Turbine Technology," *Mechanical Engineering*, Vol. 117, No.12, December 1995, pp. 56-60.
3. Sturgess, G.J., "Combustor Design Trends for Aircraft Gas Turbine Engines," Paper No. 96-TA-029, *ASME TurboAsia '96 Congress & Exposition*, Jakarta, Indonesia, November 5-7, 1996.
4. Schlichting, H. *Boundary Layer Theory*, 4th. edit., McGraw-Hill Book Co., New York, New York, 1960.
5. Mair, W.A., "The Effect of a Rear-Mounted Disc on the Drag of a Blunt-Based Body of Revolution," proc. Royal Aeronautical Society, *The Aeronautical Quarterly*, November 1965, pp. 350-360.
6. Little, Jr., B.H. and Whipkey, R.R., "Locked Vortex Afterbodies," proc. AIAA, *Journal of Aircraft*, Vol. 16, No. 5, May 1979, pp. 296-302.
7. Miner, I.O., "The Dall Flow Tube," Publication TP5018/958, George Kent Ltd., Luton, England, 1958.
8. Sturgess, G.J., unpublished work, Bristol-Siddeley Engines, England, 1961.
9. Hubble, P.E., unpublished work, Bristol-Siddeley Engines, England, 1961-62.
10. Collection of author (GJS)
11. Oates, G.C., (editor), *Aerothermodynamics of Aircraft Engine Components*, AIAA Education Series, AIAA, Chap.2, "Afterburners."
12. Vinogradov, V., "Russian Hydrogen Fueled Scramjet Engine Technology," Central Institute of Aviation Motors, (CIAM), Moscow, 1994.
13. Niioka, T., Terada, K., Kobayashi, H. and Hasegawa, S., "Flame Stabilization of Strut Divided into Two Parts by Supersonic Airflows," *AIAA J. Prop. Power*, Vol. 11, No.1, January-February 1995, pp. 112-116.
14. Uchiumi, M., Kobayashi, H., Hasegawa, S. and Niioka, T., "Flame-Holding Mechanism of a Newly Devised Strut for the Scramjet Engine," Paper No. ISTS 94-a-09, *19th. International Symposium on Space Technology and Science*, Yokohama, Japan, May 15-24, 1994.
15. Gharib, M. and Roshko, A., "The Effects of Flow Oscillations on Cavity Drag," *J. Fluid Mech.*, Vol. 177, 1987, pp. 501-530.
16. Katta, V.R. and Roquemore, W.M., "Numerical Studies on Trapped-Vortex Concepts for Stable Combustion," Paper No. 96-TA-019, *ASME Turbo Asia '96 Congress & Exposition*, Jakarta, Indonesia, November 5-7, 1996.
17. Heneghan, S.P., Vangsness, M.D., Ballal, D.R., Lesmerises, A.L., and Sturgess, G.J., "Acoustic Characteristics of a Research Step Combustor, AIAA Paper No. 90-1851, AIAA/SAE/ASME/ASME 26th. *Joint Propulsion Conference*, Orlando, Florida, July 16-18, 1990.
18. Lewis, B. and von Elbe, G., *Combustion, Flames and Explosion of Gases*, 2nd. Edition, Academic Press, 1961.
19. Heywood, J.B. and Mikus, T., "Parameters Controlling Nitric Oxide Emissions from Gas Turbine Combustors," AGARD Propulsion & Energetics Panel

41st. Meeting on *Atmospheric Pollution by Aircraft Engines*, London, England, 1973.

20. Abramovich, G.N., *The Theory of Turbulent Jets*, M.I.T. Press, Cambridge, MA, 1963.

21. Hinze, J.O., *Turbulence*, 9th. edition, McGraw-Hill Book Co., New York, New York, 1975.

22. Sturgess, G.J., Heneghan, S.P., Vangsness, M.D., Ballal, D.R. and Lesmerises, A.L., "Isothermal Flow Fields in a Research Combustor for Lean Blowout Studies," Trans. ASME *Journal of Engineering for Gas Turbines and Power*, Vol. 114, No.2, April 1992, pp. 435-444.

Characteristics of a Trapped-Vortex Combustor

K.-Y. Hsu* and L. P. Goss†

Innovative Scientific Solutions, Inc., Dayton, Ohio 45440-3638

and

W. M. Roquemore‡

U.S. Air Force Wright Laboratory, Wright–Patterson Air Force Base, Ohio 45433-7103

Combustion characteristics are described for a conceptual combustor that utilizes a trapped vortex (TV) in a cavity to provide flame stability. The cavity is formed between two axisymmetric disks mounted in tandem. The upstream disk is referred to as the forebody, and the downstream disk is referred to as the afterbody. With coflowing annular air, a vortex is trapped in the cavity for certain geometries. Primary air and gaseous propane are injected directly into the cavity through multiple jets located on the upstream face of the afterbody. Particle-imaging-velocimetry measurements reveal that when the cavity length is 0.59 of the forebody diameter, a vortex is trapped in the cavity. Very low overall lean-blow-out equivalence ratios are obtained for the TV combustor over a wide range of annular- and primary-airflow rates. Temperature profiles obtained with a coherent-anti-Stokes-Raman-spectroscopy system show that as the primary-airflow rate increases (equivalence ratio approaches unity), the temperature in the vortex increases for a fixed fuel flow. An increase in the primary-airflow rate also results in a decrease in the flame length. Peak combustion efficiency increases from 96.7 and 99% as the annular air is decreased, and to 98.8 and 99.8% when a second trapped vortex is added to the combustor via a second afterbody just downstream of the first afterbody.

Introduction

COMBUSTION stability is often achieved using recirculation zones to provide continuous sources of ignition by mixing hot products and burning gases with the incoming fuel and air. Swirl vanes, bluff-bodies, and rearward-facing steps are commonly used methods of establishing recirculation zones for flame stabilization. This paper investigates the use of cavities as a means of stabilizing flames. In 1957, Huellmantel et al.¹ investigated recesses in a wall as a means of improving flame stability and reducing the pressure drop across a combustor. They evaluated 12 recess or cavity configurations in a small 2.5 cm by 4.5 cm tunnel and found the blow-out velocities of premixed propane/air flames to be considerably higher for recessed flameholders and to have lower pressure drops than a V-gutter flameholder. They also found that flame stability was not sensitive to the shape of the recess as long as separation was present at the leading edge of the recess. Morrison et al.² investigated the blowout limit of a cavity with fuel injected directly into the recirculation zone. Although their results did not fully characterize the performance of the cavity, they did support the idea that cavity flameholders could result in a compact ramjet/scramjet combustor design. Niioka et al.³ investigated the flame-stabilization characteristics of a cavity between two struts. Hydrogen fuel was injected along the centerline of the cavity. They found that flame stability could be achieved in a flow with a freestream Mach number of 1.5, but that the stability was strongly dependent on the separation of the two struts. Willis et al.⁴ investigated the use of a dump-cavity combustor as a means of

waste destruction. The waste was injected directly into the cavity. The waste was completely destroyed when the combustor operated in a quiet mode in which the recirculation zone in the cavity was stable. They identified the cavity lengths and premixed fuel-to-air ratios that yielded stable and unstable combustion.

Cavities have been extensively investigated by the aerodynamic community as a means of recovering pressure or reducing drag. Indeed, the term trapped vortex was applied to devices discussed by Ringleb⁵ for controlling flow separation as applied to diffusers. The rules for sizing cavities to reduce the drag of bluff-bodies was investigated by Mair⁶ and Little and Whipkey,⁷ who investigated cavities formed between two axisymmetric disks spaced along a central spindle. Mair⁶ showed that for the ratio of afterbody-to-forebody disk diameters of <1, an optimal separation distance existed where the drag was a minimum. Furthermore, the minimum drag was considerably lower than that of the forebody disk alone. Mair⁶ also found that for a given afterbody diameter, there were separation distances where the drag increased dramatically above that of the forebody alone. Little and Whipkey⁷ showed that the minimum drag corresponds to the condition where the recirculation zone is stable. They established a correlation between the disk separation distance and afterbody disk diameter, both being normalized by the forebody disk diameter, which yielded a stable or locked vortex. Gharib and Roshko⁸ reviewed other studies in which low- and high-drag conditions were achieved by changing the cavity size. They also performed a systematic investigation of the process and concluded that low drag occurs when the cavity shear layer stagnates at the downstream corner of the cavity. When this happens, the vortex motion in the cavity is stable.⁷ Gharib and Roshko⁸ associated the low-drag condition with self-sustained cavity flow oscillations through a feedback mechanism that maintains the locked-on position of the stagnation zone to the downstream corner of the cavity. Thus, the feedback mechanism helps maintain a stable vortex in the cavity, even when external fluid is injected directly into the cavity.⁹ Katta and Roquemore¹⁰ used a time-dependent, axisymmetric mathematical model to predict the results of Mair⁶ and Little and Whipkey,⁷ and the combustor results of Hsu et al.¹¹ The simulations showed that a vortex

Presented as Paper 95-0810 at the AIAA 33rd Aerospace Sciences Meeting, Reno, NV, Jan. 9–12, 1995; received July 5, 1996; revision received Aug. 20, 1997; accepted for publication Aug. 29, 1997. This paper is declared a work of the U.S. Government and is not subject to copyright protection in the United States.

*Senior Engineer, 2786 Indian Ripple Road. Member AIAA.

†President and Director of Research, 2786 Indian Ripple Road. Member AIAA.

‡Senior Scientist, Aero Propulsion and Power Directorate, Fuels and Lubrication Division. Member AIAA.

was trapped in the cavity when the afterbody diameter and disk separation were consistent with the rules established by Little and Whipkey.⁷ The simulations also showed that a vortex would be trapped in the cavity when the stagnation point was located at the downstream corner of the cavity.⁸ Furthermore, when a vortex was trapped in the cavity, very little fluid was entrained into the cavity. The cavity entrainment was estimated using lean-blow-out (LBO) data under various cavity lengths and flow conditions by Sturgess and Hsu.¹²

To our knowledge, the flame-stability characteristics of cavities that are aerodynamically designed to trap a vortex have not been investigated. One reason for this may be that when a vortex is trapped in a cavity, very little exchange of main flow and cavity fluid occurs. This constitutes a problem because flame stability requires a continuous exchange of mass and heat between the cavity and main flow. This problem can be solved by directly injecting both fuel and air into the cavity in a manner that reinforces the vortex. The goal of the present study was to investigate the flame-stability characteristics of a trapped vortex (TV) combustor in which fuel and air are injected directly into the cavity from the face of the afterbody. This back-face fuel-injection scheme is similar in appearance to the T and mushroom vaporizers used in prevaporizing combustion chambers.¹³ However, in vaporizer combustion systems, the flame is not stabilized by a vortex trapped in a cavity. In a TV combustor, the flame in the cavity is not directly exposed to the high inlet velocities of a main airflow; therefore, a TV combustor has the potential of providing stable operation over a wide range of inlet airflow rates and fuel-to-air ratios while maintaining high combustion efficiencies, low lean-blow-out-limits, and a low-pressure drop. Low nitric oxide (NO_x) emissions might also be achievable by controlling fuel-to-air ratio, mixing, and residence time in a cavity pilot burner and a main burner. As noted in the studies of Huellmantel et al.,¹ wall heating and the influence of cooling air on the combustion process are concerns with this method of flame stabilization. This paper describes preliminary investigations of the influence of cavity size on the pressure drop across the combustor and on the LBO limits. Combustion efficiency and emissions are also investigated as a function of fuel-to-air ratio in the cavity and inlet-air velocity.

Experimental Descriptions

The combustor used in this study consists of a forebody and an afterbody (Fig. 1a). Stainless steel was used in fabricating the combustor assembly. The afterbody is connected to two concentric tubes along the centerline of the forebody. Fuel and primary air are delivered through these concentric tubes to two separate chambers in the afterbody that is 50.8 mm in diameter. The forebody, having a diameter d_f of 70 mm, is located at the exit plane of the vertically mounted annular-air duct that has a diameter of 80 mm. The blockage ratio, defined as the ratio of the area of the forebody to that of the air duct, is 76%. A maximum averaged annular-air velocity of 42 m/s can be achieved with this configuration. An axisymmetric cavity, defined as the void region between the forebody and the afterbody, is used. The cavity length H is defined as the axial distance between the forebody and afterbody, as noted in Fig. 1a. The cavity length is adjustable and is an important parameter in this study. The unheated annular- and primary-air flows originate from two air supplies that are controlled and metered separately. The experiment was conducted under atmospheric conditions.

The arrangement of fuel and primary-air injection on the afterbody is shown in Fig. 1b. Gaseous-propane fuel is injected through eight orifices (1.75 mm in diameter), and the primary air is supplied through 24 orifices (2.29 mm in diameter) surrounding the fuel jets. The fuel and primary air are injected near the centerline to follow the natural recirculation flow pattern created in the cavity. Direct injection of primary air serves several purposes: 1) it provides direct control of the local

equivalence ratio inside the recirculation zone, 2) it enhances mixing by increasing the mixing region through distributed fuel and air jets, and 3) it provides some cooling for the injector assembly. A water manometer is used to measure the static pressure drop across the combustor over a range of cavity-length and inlet-flow conditions. The LBO limits of this combustor were tested over a range of primary- and annular-airflow conditions.

A 35-mm camera and a video recorder were used to record the flame images under various flow conditions. The instantaneous velocity field was obtained using the two-color particle-imaging-velocimetry (PIV) technique.^{14,15} A pulsed Nd:YAG laser and a Nd:YAG-pumped dye laser were used for generating two different wavelengths to eliminate ambiguity in determining the flow direction. Cylindrical lenses were employed to form a laser sheet vertically across the centerline of the burner. Monospherical particles of Al_2O_3 (5 μm in diameter) were seeded through the primary airjets. A 35-mm camera mounted at a right angle to the laser sheet was used to record the images of the particles illuminated by the laser. A synchronization circuit was employed to control the time separation between the two laser pulses. The typical time separation was set to $\sim 30 \mu\text{s}$ for the flow conditions studied. A color scanner was used to digitize the images, and the data were stored in a computer for further analysis. The data analysis and experimental setup of the two-color PIV technique are treated in detail in Refs. 14 and 15.

The radial temperature was profiled at different axial locations inside the recirculation zone using the coherent-anti-Stokes-Raman-spectroscopy (CARS) technique. The CARS system employed in this study was based on a Nd:YAG/broadband dye-laser combination tuned for N_2 excitation. An intensified charge-coupled device (CCD) camera mounted at the exit plane of the monochromator was interfaced with a com-

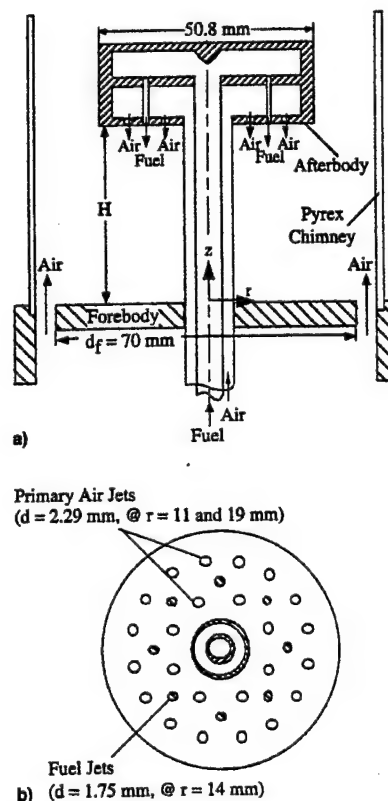


Fig. 1 Schematic diagrams of a) trapped-vortex combustor and b) injection plane of afterbody.

puter for single-shot broadband spectrum detection. Temperature information was obtained using a nonlinear least-squares routine to fit the measured spectra. The shot-to-shot and mean errors of the temperature measurements resulting from this CARS system were estimated to be about 5 and 1%, respectively. At each spatial location, 1000 spectra were collected at a rate of 10 Hz, and the mean and rms temperatures at each spatial location were plotted.

Emission measurements were made under various flow conditions to further characterize the performance of the combustor. A portable emission-sampling/analyzer unit was used to measure the concentrations of CO, NO_x, O₂, and unburned hydrocarbon (UHC) at the exit of the combustor. The equilibrium CO₂ concentration was calculated from the measured O₂ concentration. A routine was then used to calculate the exhaust equivalence ratio and combustion efficiency based on the gas sample collected. The flow was confined by a Pyrex tube (80 mm i.d.), 910 mm in length, to eliminate the uncertainty in the measurement resulting from entrained ambient air. The gas samples were collected at an axial location $z = 860$ mm downstream from the face of the forebody. The preliminary single-point measurements were made using stainless-steel tubing (3-mm i.d.) as the sampling probe. The radial profiles of emission concentration were generally uniform, except under certain flow conditions. For obtaining the overall emission characteristics of the combustor for comparison purposes, a probe with multiple holes was used to measure the averaged emission concentrations. The probe was placed inside the glass chimney and intersected the centerline of the flow. Five holes (0.4 mm in diameter), located at the same axial location, were placed at specific radial locations to collect area-weighted samples. The uncertainty between the measured equivalence ratios and the metered overall equivalence ratios was found to be within 10% under the flow conditions studied. The analyzer was calibrated with calibration gases; however, the absolute values of the concentrations may be biased because of the noncooled sampling probe. Because only the trends of the emission characteristics of the combustor were of interest in this study, the quenching of reactions from the sampling were not investigated. During the emission measurements, flame lengths were also measured visually under various flow conditions.

Results

Preliminary experiments were conducted to determine the impact of afterbody diameter and cavity length on the flame structure. The diameter of the forebody was fixed at 70 mm for this study. Three afterbodies having different diameters were investigated, and the cavity length for each was systematically varied under combustor conditions. Although this was a preliminary investigation, it did show that the visual flame structure is strongly dependent on afterbody diameter and cavity length. An afterbody having a diameter of $0.73d_f$ was used because it was observed to produce the most stable flame. The results will be presented in the following sequence: 1) choice of optimal cavity length based on the criteria of low-pressure drop and low LBO limits; 2) impact of primary air on LBO, velocity and temperature fields, emissions and combustion efficiency, and flame length; and 3) impact of adding a second afterbody on emissions and combustion efficiency.

Cavity Length

Figure 2 shows the impact of cavity length on pressure drop across the combustor for different annular-air flows under non-reacting flow conditions. The primary air was turned off for this test, and the flow was confined by an 80-mm-diam, 150-mm-long Pyrex tube. The pressure drop dp is defined as the pressure difference between duct and ambient P . The normalized pressure drop dp/P for the cold flow is plotted in Fig. 2 at annular-air velocities of 14, 28, and 42 m/s. As the cavity length is varied, dp/P is observed to pass through a minimum at a cavity length of $\sim 0.6d_f$, which is more noticeable for the

high annular-air flow. An increase in dp/P from 0.1 to 1.2% was measured as the annular-air velocity was increased. The results of Mair⁶ and Little and Whipkey,⁷ who conducted systematic studies of drag reduction for disks mounted in tandem, showed that minimum drag is achieved with an afterbody diameter of $0.75d_f$ and a cavity length of $0.6d_f$. The cold-flow data plotted in Fig. 2 are in very good agreement with their findings.

For a combustor flow at an annular air velocity U_a of 28 m/s and an overall equivalence Φ_o of 0.12, dp/P increases to about 0.65% as compared to 0.4–0.55% for nonreacting flows. This suggests that the cavity injection and heat addition increase the pressure drop across the combustor. In the reacting flow, the pressure drop increased to around 1.5% at an annular-air velocity of 42 m/s when the combustor was operated under higher fuel loading. For combustor flow, the maximum pressure drop occurred as the cavity reached stoichiometric conditions. Although the combustor flow exhibited very little change in dp/P with cavity length at a fixed fuel flow (Fig. 2), the change in flame stability was noticeable. A stable flame with a well-defined vortex was observed visually for the cavity-length range of 0.45 – $0.65d_f$. Multiple vortices and vortex shedding were observed at cavity lengths $>0.65d_f$; and a quasi-steady flame existed for $<0.45d_f$. These results are consistent with the cold-flow results of Little and Whipkey,⁷ who observed a stable vortex in the cavity when the cavity length corresponded to that of minimum drag. Katta¹⁰ has studied the dynamics of the vortex structures under reacting and nonreacting flows using a time-dependent computational fluid dynamics (CFD) code. For nonreacting flows, a stable cavity flow was observed at an optimal cavity dimension that produces minimum drag. For a nonoptimal cavity dimension, vortex shedding was revealed through time-dependent calculations. The fluid injection inside the cavity also had a strong impact on the stability of the vortex in the cavity.

For achieving good combustion stability, a stable vortex in the cavity region is very desirable. The impact of cavity length on LBO limits was investigated under three annular-airflow conditions with zero primary air, and the results are shown in Fig. 3. The overall LBO equivalence ratio is <0.05 for all conditions studied. However, this ratio increases dramatically for cavity lengths $>0.65d_f$. Visual observation of the flame indicated that this increase in LBO limit is probably the result of vortex shedding at a cavity length greater than the optimum. Because the most stable flame and minimum pressure drop occurred at $0.59d_f$, this optimal cavity length was chosen for the experiments described in the following sections.

Flowfield and Flame Characteristics

Flame photographs and PIV were used to determine whether a stable vortex had formed in the TV combustor. For these experiments, the Pyrex tube was removed for optical access and, thus, the flame was unconfined. Unconfined flames are

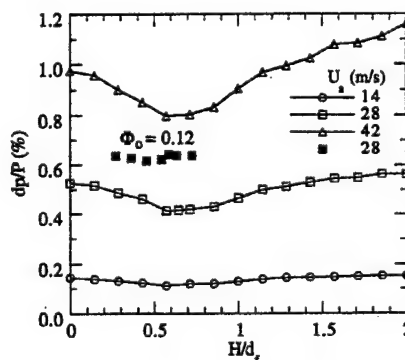


Fig. 2 Impact of cavity length H/d_f on pressure drop under cold (open) and combustor (solid) flows.

shorter and have a larger diameter near the vortex center, but have the same general features as confined flames.

The flame is visually stabilized inside the cavity; this region will be referred to as the primary zone of the combustor. The overall equivalence ratio is ~ 0.06 at an annular-air velocity of 28 m/s. The equivalence ratio in the primary zone Φ_p , as calculated from the fuel and primary air only, is ~ 1.2 . The instantaneous velocity field obtained using the PIV technique is shown in Fig. 4. Repeated measurements showed that the velocity field of the large vortical structure does not change significantly from shot-to-shot, i.e., the vortex is essentially stationary. The velocity field exhibits a strong recirculating flow similar to that of a toroidal vortex. The center of the vortex is located at a radius slightly less than that of the afterbody. The

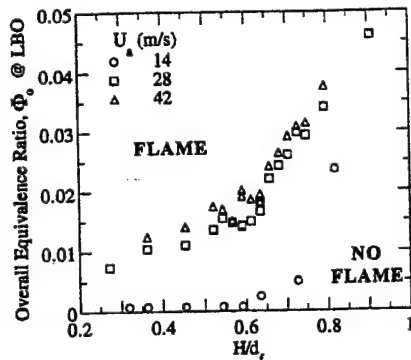


Fig. 3 Effect of cavity length H/d_f on LBO under various annular-airflows.

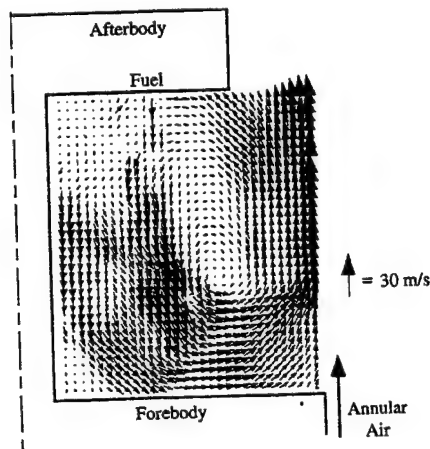


Fig. 4 Instantaneous velocity field obtained by PIV with combustor flow at $U_{air} = 28$ m/s.

radial location of the vortex center did not change significantly under different primary-air, annular-air, and fuel-flow conditions.

The primary-air and fuel jets control the local equivalence ratio, mixing, residence time, and stability in the primary zone. For enhancing combustor performance, these jets should be injected in such a way that they reinforce the vortex, causing it to remain stable for a wide range of flow conditions. The velocity field in Fig. 4 includes flow from the fuel and primary-air jets, as denoted by the large velocity vectors near the afterbody face. The jets appear to dissipate before reaching the face of the forebody and be mixed into the recirculation zone and convected around the vortex center. The flow around the vortex center has a large velocity component well inside the forebody radius. Most of this fluid seems to mix with the annular air and be convected past the afterbody. However, the flow around the vortex center appears to re-enter the primary zone. The fluid contains mainly hot products and radicals that will ignite the incoming fuel and air mixtures. This process of recirculated hot products is the key to the stability of a TV combustor.

The general structure of the cavity flow appeared to be the same as that shown in Fig. 4 for a wide range of fuel and airflow conditions; this is illustrated by the flame images in Fig. 5. The annular-airflow rate was fixed at 3000 slpm and had an average velocity of 42 m/s. The fuel-flow rate was fixed at 25 slpm and had a mean fuel-jet velocity of 22 m/s. The primary air was adjusted to 56, 140, and 280 slpm, corresponding to a primary air velocity of 10, 24, and 48 m/s, respectively. The Φ_p were 11, 4.4, and 2.2, respectively, as indicated in the three flame images. The actual equivalence ratio in the cavity may be leaner because of fuel transport and additional entrainment of annular air. The overall equivalence ratio of 0.21 was not altered significantly as a result of the relatively small changes in the primary-air flows as compared with the annular-air flow. The appearance of the flame indicates that a stable vortex has formed in the cavity under these conditions. The soot concentration in the cavity region decreases with Φ_p , as shown in Fig. 5. A blue flame established in the shear layer between the cavity and the annular air and anchored around the circumference of the forebody is also evident. Although the color and length of the flame varied with Φ_p , the shape of the flame in the cavity was approximately the same under all flow conditions, furnishing additional evidence that the primary zone has been stabilized by correctly sizing the cavity to trap a vortex.

The temperature fields represented by radial temperature profiles for these three conditions are shown in Fig. 6; the data were obtained with the CARS technique. Radial profiles of mean temperature are shown for axial locations of $z = 5$ and 40 mm, as measured from the forebody face. As the primary air increases, the axial location of the vortex center moves downstream as illustrated in Fig. 5. The third axial-temperature measurements were made intercepting the vortex center that

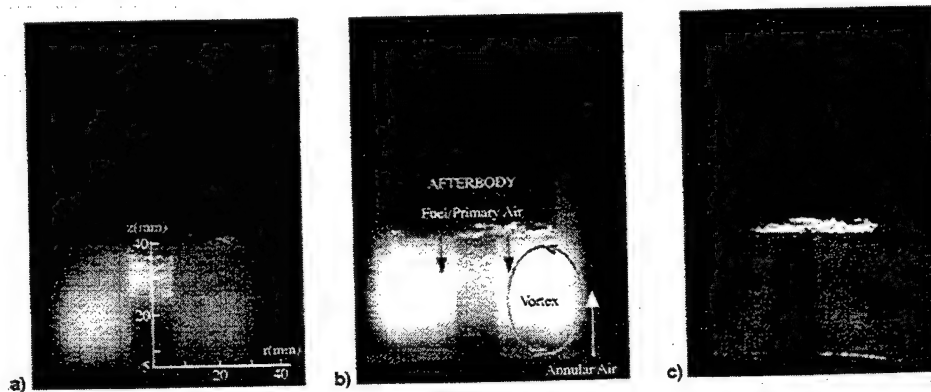


Fig. 5 Effect of primary air on flame structures at $U_{air} = 42$ m/s and $\Phi_0 = 0.21$. Φ_p = a) 11, b) 4.4, and c) 2.2.

changed from $z = 23$ to 28 mm as the primary air was increased. The unconnected symbols denote the spatial distributions of the rms of temperature.

The locations of the primary-air and fuel jets are evident in the temperature profiles in Fig. 6. The former are located at $r = 11$ and 19 mm, and the latter at $r = 15$ mm, as shown in Fig. 1b. For the weaker primary-airflow, $\Phi_p = 11.1$, the air-jet trajectories are affected by the annular air, as evidenced by the cold-temperature zone being shifted from $r = 11$ to 8 mm. At higher primary-airflow rates (lower Φ_p), the stronger air jets are not disturbed by the annular air. However, the colder jet temperatures are not observed near the forebody, which suggests that the jet flows mix and react before reaching the face of the forebody.

The flame length and soot concentration decrease as the primary-airflow rate increases. The increase in temperature with a decrease in Φ_p is evident in the flat temperature region ($20 \text{ mm} < r < 30 \text{ mm}$) in Fig. 6 at $z = 40$ mm. The temperature increases by ~ 700 K as the primary air is increased. A maximum temperature of 2150 K (near-stoichiometric flame temperature) was measured at the highest primary-airflow; how-

ever, the fluctuation in temperature is only ~ 200 K, as compared to 400 K for the lower primary-airflow. This suggests that mixing improves with increased velocity of the air jets. The higher temperature occurs near the face of the afterbody for the higher primary-airflow and at the vortex center for the lower flow. This is thought to result from different jet mixing and residence times, local equivalence ratios, and recirculation of hot products in the cavity region as the primary-air velocity is increased.

Lean Blow-Out

LBO is an important design parameter for aircraft gas-turbine engines because it can impact the lower operating limits of the combustor. In gas-turbine combustors, LBO is often preceded by an unstable flame resulting from instability in the primary zone. Combustion in the primary zone then becomes intermittent, and the flame is quenched spatially and temporally. This intermittence in combustion has a direct impact on the ignition source and, as a result, the unsteadiness tends to grow until the flame blows out. In the TV combustor, the flame in the primary zone is shielded from high annular-airflow. The vortex in the cavity provides a stable ignition source through re-injection of hot products and radicals. Because the vortex is stable over a wide range of flow conditions, a TV combustor should have good LBO characteristics. The data in Fig. 3 indicate that this is the case when the primary-airflow rate is zero. The question then arises as to the influence of the primary air on the LBO limits.

The fuel and primary-airflow rates under LBO conditions are shown in Fig. 7 to illustrate the influence of primary air. The LBO experiments were conducted by fixing the primary-airflow rates and decreasing the fuel flow rate until the flame was extinguished. The LBO test was conducted with various primary-airflows and two annular-airflows. The data in Fig. 7 show that the greatest difference between the LBO for low and high annular-airflows occurs at low primary-airflows. To examine this point in more detail, it is useful to consider annular-air entrainment into the vortex when the primary air is zero.

The air involved in the LBO process must be entrained into the vortex from the annular flow when no primary air is introduced. The amount of entrainment can be estimated using LBO data in Fig. 3 for a cavity length of $0.59d_f$. If one assumes that the cavity is well mixed (which is only correct to a first-order approximation), then with zero primary air, the Φ_p at LBO would correspond to the lower flammability limit of premixed propane-air flames. Through the use of $\Phi_p = 0.5$ (lean flammability limit) and the LBO data for high annular-airflow rates in Fig. 3, it is estimated that only $\sim 3\%$ of the annular air is entrained into the cavity. For the low annular-airflow ($U_a = 7$ m/s), the estimate of entrainment is inadequate because mixing in the trapped vortex is poor. Values for air entrainment between 2.5 and 3.5% were obtained for different annular-airflow rates, which implies that the percentage of air entrained into

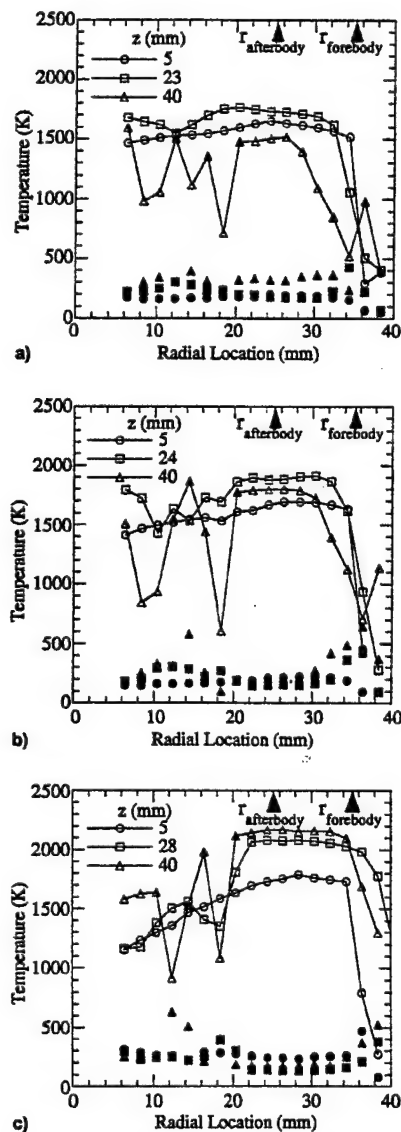


Fig. 6 Effect of primary air on temperature distributions inside cavity at $U_{ar} = 42$ m/s and $\Phi_0 = 0.21$. Φ_p = a) 11, b) 4.4, and c) 2.2.

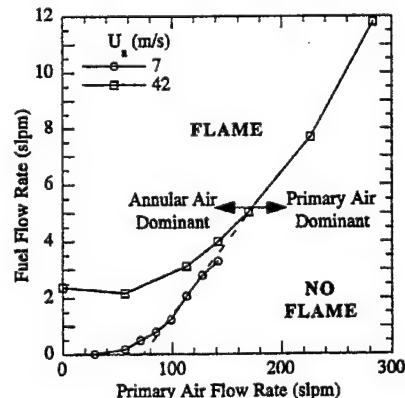


Fig. 7 Effect of primary-airflow on LBO.

the trapped vortex is relatively constant at the higher annular-airflow rates when no primary air is introduced.

As shown in Fig. 7, the fuel flow rate at LBO does not change significantly until the primary-airflow rate exceeds 60 slpm. A linear relationship between the fuel and primary-airflow rates begins to develop when primary-airflow rates are ~ 75 and 150 slpm for annular-air velocities of 7 and 42 m/s, respectively. At a primary-airflow rate of 175 slpm, the two curves in Fig. 7 should merge, as denoted by the dashed line. Beyond this point, the LBO depends only on the primary-airflow rate and, thus, is independent of the annular-airflow rate. The percentage of estimated air entrained into the trapped vortex increases with the primary-airflow. The assessment of entrainment using LBO data under various cavity-length and flow conditions is discussed in detail by Sturgess and Hsu.¹²

Flame Length

Flame length is important in practical combustors. Aircraft gas-turbine combustors are typically designed to be short to increase the thrust-to-weight ratio. State-of-the-art combustors are 15–25 cm long; therefore, the flame must be confined to this length to protect the turbine section. Advanced gas-turbine combustors operate at a maximum pressure of ~ 40 atm, with combustor inlet temperatures of ~ 1000 K. These high-pressure and -temperature conditions result in fast reaction rates and, thus, give rise to shorter flames. Typically, the flame length increases when the combustor is operated at room temperature and atmospheric pressure. Although studies of flame characteristics under ambient conditions deviate from those under practical operating conditions, such fundamental studies are often conducted in attempts to understand flame behavior as flow parameters are changed. For the present study, the flame length was examined as a function of fuel, primary air, and annular airflows.

Figure 8a shows how the visible flame length changes with fuel and annular-airflow rates at a constant primary-airflow rate of 140 slpm. The annular-airflow rates were fixed at 1000, 2000, and 3000 slpm, corresponding to annular-air velocities of 14, 28, and 42 m/s, respectively. In Fig. 8a, the data under the higher annular-airflow conditions collapsed on a single curve when the flame length was plotted as a function of the

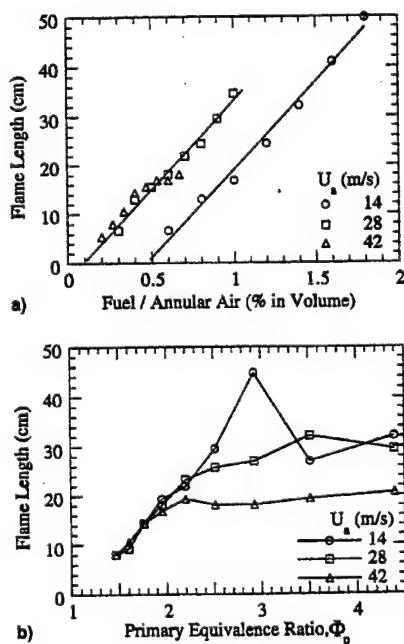


Fig. 8 Impact of flame length resulting from variations in a) fuel flow with constant primary air of 140 slpm, and b) primary equivalence ratio with constant fuel flow of 20 slpm.

ratio of fuel to annular air (proportional to overall equivalence ratio). With a constant cavity volume and fixed primary air, the fuel is consumed at a certain rate. As the fuel flow increases, the flame length increases as a result of the excess fuel being transported and reacting in the shear layer between the cavity and annular air. A linear relationship between flame length and overall fuel-to-air ratio is observed; the slope remains constant for different annular airflows, but the y-intercept changes. An increase in annular-airflow rate with the fuel flow fixed results in a shorter flame because of enhanced turbulent mixing. However, the flame can also be quenched locally thorough vortex-flame interactions, as observed in turbulent diffusion flames. This implies that the combustion efficiency (percent of fuel consumed) decreases with increasing annular-airflow.

Figure 8b shows the variation in flame length with Φ_p as the primary air is varied. The experiments were conducted at a fixed fuel flow rate of 20 slpm and at three fixed annular-airflow rates (1000, 2000, and 3000 slpm). In the range $\Phi_p < 2$, the flame length increased with Φ_p as the primary-airflow decreased. It is thought that the better mixing and higher temperature caused by higher primary air resulted in a shorter flame. In this flow range, the average velocity of the primary air is higher than that of the annular air. Therefore, the flame length is dominated by the primary air and is independent of the annular air, as indicated in Fig. 8b. The curves in Fig. 8b intercept at a flame length of 17 cm, which corresponds to the end of the recirculation zone established downstream of the afterbody. The wake region behind the afterbody provides another low-speed region for consumption of excess fuel. Although the length of the wake fluctuates with time, in a time-averaged view, it occurs at $2.4d$ downstream of the afterbody (about 17 cm from the face of the forebody).

The flame length is strongly influenced by annular-airflow in the region $\Phi_p > 2$, as shown in Fig. 8b. It is evident that the flame length remains relatively constant for a fixed annular-airflow and is reduced as the annular air is increased. In the range $\Phi_p > 2$, the primary-airflow is weak and the cavity temperature is low. The consumption of excess fuel in the annular-airstream relies mainly on mixing controlled by the annular air. Therefore, the higher annular-airflow provides better mixing, which results in a shorter flame, and the flame length remains constant at a fixed annular-airflow. Note that the shorter flame does not guarantee higher combustion efficiency, as discussed in the next section. At the lower annular-airflow (14 m/s), the flame length differs from that at higher airflows. The higher fuel-jet velocity (~ 17 m/s) may cause the fuel jet to become dominant.

Two-Cavity TV Combustor

The wake region behind the afterbody provides a low-speed region for further consumption of excess fuel; however, vortex shedding can cause local quenching, which can lead to reduced combustion efficiency. Little and Whipkey⁷ showed that adding a second afterbody results in a significant reduction in drag. The second cavity seems to reduce the unsteady wake motion created behind the first afterbody in a one-cavity configuration. In a combustor flow, the second cavity should also improve the combustion efficiency by eliminating some of the unsteady combustion in the wake region.

Combustion Efficiency and Emissions

Figure 9 presents data on combustion efficiency and emission indices of unburned hydrocarbons (EI_{UHC}), carbon monoxide (EI_{CO}), and oxides of nitrogen (EI_{NO_x}) for one-cavity (open symbols) and two-cavity (solid symbols) configurations. The test conditions were the same as those described for collection of the flame-length data in Fig. 8b. The fuel flow rate was fixed at 20 slpm (corresponding to a velocity of 17 m/s), and the annular-airflow rate was fixed at 1000, 2000, and 3000 slpm (corresponding to velocities of 14, 28, and 42 m/s, re-

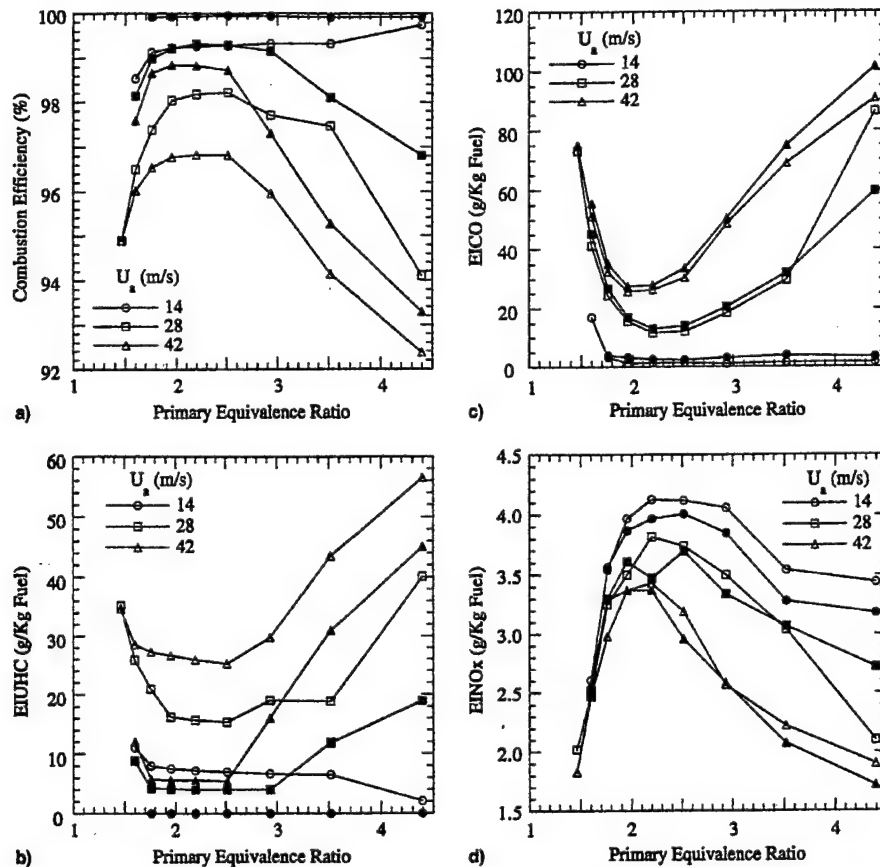


Fig. 9 Impact of primary- and annular-airflows on a) combustion efficiency and on emission indices of b) unburned hydrocarbon, c) carbon monoxide, and d) oxides of nitrogen at a fixed fuel flow. The open and solid symbols denote results from one- and two-cavity configurations, respectively.

spectively). Emissions data were collected at different primary-airflow rates. To illustrate the impact of primary air on emissions and combustion efficiency, the results are plotted as a function of Φ_p .

The characteristics of emission for the one- and two-cavity combustors showed similar trends for all of the data in Fig. 9. In general, the combustion efficiency decreases as the annular air is increased, as shown in Fig. 9a. Comparing these results and the flame-length data shown in Fig. 8b, it is clear that the shorter flame observed at high annular air is partially caused by incomplete combustion. The efficiency for the lowest annular-airflow rate is higher and flat over a wide range of Φ_p . As the annular-airflow increases, the emission and combustion efficiency become more sensitive to the primary-airflow. At the highest annular-airflow rate, the efficiency peaks at a narrower region of Φ_p between 1.8 and 2.6. A very rapid decay in efficiency takes place at low values of Φ_p (higher primary-airflow rates), and a more gradual decay occurs at higher Φ_p . It is also evident that the addition of a second afterbody (noted by the solid symbols) substantially improves the efficiency, but does not change the location of the peaks or the decay regions of the curves. Figures 9b and 9c show that inefficiency in the combustion process is the result of both UHC and CO. Even more interesting is the fact that the improvements in efficiency obtained by adding the second afterbody are mainly the result of the reduction of UHC emissions. It was also observed that CO increases slightly with the two-cavity configuration, which is a result of the additional consumption of UHC. It is also evident in comparing Figs. 9a and 9d that the NO_x and combustion efficiency peak and decay at the same values of Φ_p . The lowest NO_x and combustion efficiency occur at the highest annular-airflow rate because of the short residence time. The

addition of the second cavity produces only a small difference in NO_x . Therefore, it is thought that the CO and NO_x are produced mainly in the first cavity.

Discussion

The emission characteristics are shown to be influenced by the primary- and annular-airflows when the fuel flow is maintained constant. The rapid decay that occurs in combustion efficiency, NO_x , and the flame lengths are shown in Figs. 9 and 8b for $\Phi_p < 2$. In this region, the decrease of Φ_p corresponds to increasing primary-air velocities from 40 to 52 m/s. The reduced residence times of the reacting mixture in the cavity (estimated to be 1–0.8 ms) increase the UHC and CO, as shown in Figs. 9b and 9c. The low consumption of fuel means that the heat-release rate—and, thus, the temperature in the primary zone—decreases as the primary-airflow rate increases. Both the low temperature and the reduced residence time of the reacting fuel in the primary zone are responsible for the rapid decay in combustion efficiency and NO_x in the region of $\Phi_p < 2$. Most of the NO_x is thought to be formed in the primary zone; this is supported by the temperature data in Fig. 6c. Note that temperatures are near-stoichiometric in the vicinity of the face of the first afterbody at $\Phi_p = 2.2$, which, of course, results in very high NO_x production rates. As discussed earlier, Φ_p is defined by the metered fuel and primary-airflows and does not represent the actual cavity equivalence ratio. If most of the NO_x is formed in the primary zone, then adding a second cavity should have little impact on NO_x emissions. Figure 9d shows a slight reduction of NO_x with the addition of the second cavity.

When the mixture has a short residence time in the cavity, the excess fuel will be convected downstream. Under high

primary-air conditions, a flame bulge is formed, as illustrated in Fig. 5c. The bulge extends into the annular-airstream, causing a turbulent wake to be formed downstream. The increase in turbulence in the wake region of the shear layer results in the formation of a large number of unsteady vortex structures. From the time-dependent CFD calculations reported by Katta and Roquemore,¹⁰ unsteady flow structures are observed around the circumference of the afterbody, which causes an increase in drag. Some of the interactions in the unsteady wake regions can result in local quenching of the flame and contribute to combustion inefficiency. The intensity and frequency of the vortices generated in the shear layer and wake region increase with annular-airflow. The flow residence time also decreases as the annular air is increased. The combination of shorter fuel residence time and intensified vortex-flame interactions as the annular air is increased causes a reduction in combustion efficiency and flame length, as shown in Figs. 9a and 8b.

The improvement associated with the addition of the second cavity is an approximate measure of the combustion inefficiency resulting from the wake of the first afterbody in the one-cavity configuration. It can be noted in Fig. 9a that the improvements in combustion efficiency resulting from addition of the second cavity are greater for the higher annular-airflow rates. The frequency of vortex-flame quenching interactions, occurring in the wake and shear layer behind the first afterbody, increases with annular-air velocity. Therefore, the recirculation zone created by the second cavity significantly improves the combustion efficiency for higher annular-air conditions.

It was noted previously that the improvements in combustion efficiency resulting from the addition of the second cavity are solely a result of reductions of UHCs. In fact, the CO concentration increases slightly (see Figs. 9b and 9c). The secondary cavity provides an additional recirculation zone for fuel consumption. It is thought that the mixture is locally fuel-rich in the second cavity as a result of limited entrainment of air. Combustion in the fuel-rich second cavity favors the formation of CO rather than CO₂, as noted in Fig. 9c.

The decay in combustion efficiency at larger Φ_p is evident in Fig. 9a. The primary air directly controls the mixing and local fuel and air ratio and, as a result, influences the combustion characteristics. The entrainment and mixing of fuel into the air jets increases as the air velocity becomes much higher than the fuel velocity. On the other hand, the entrainment—and, hence, mixing—decreases as the velocity of the primary air approaches that of the fuel, as occurs for $\Phi_p > 2.6$. For example, the velocity ratios of primary air to fuel at $\Phi_p = 2.6$ and 4.4 are 1.8 and 1.2, respectively. Under higher Φ_p conditions, the primary-zone velocity is lower than the annular-air velocity. Therefore, the excess fuel, resulting from a richer cavity, entering the shear layer is more likely to be entrained into the annular-airstream. Once the fuel is transported to the annular-air side, which is away from the ignition source, the combustion efficiency decreases as a result of increasing UHC, as shown in Figs. 9a and 9b. The increase of annular air results in higher UHC and lower efficiency. The second cavity significantly improves efficiency for the low- Φ_p condition; however, it is less effective for the high- Φ_p condition because of fuel being transported away from the wake region. The temperature in the first cavity is also related to the combustion efficiency. High reaction temperatures normally result in high efficiencies; this trend can be observed by comparing the temperatures in Figs. 6a and 6b with the combustion efficiencies in Fig. 9a for Φ_p of 4.4 and 2.2, respectively. The peak temperatures of 1800 and 2150 K correspond to efficiencies of 92 and 97%, respectively.

Conclusions

A TV concept has been investigated for flame stabilization. Fuel and primary air are injected directly into the vortex from

multiple jets on the afterbody. Combustion parameters such as LBO, pressure drop, flame length, combustion efficiency, and NO_x emissions were examined for a wide range of cavity lengths and flow conditions.

It was found that the TV combustor has a low LBO limit over a wide operating range because of the cavity being shielded from the annular air. Cavity length has a strong impact on the LBO limit. A cavity length of $\sim 0.6d_f$ was found to be optimal under various annular-airflows when no primary air is used. The primary air has a direct impact on the LBO limit as a result of mixing and residence time. The lowest LBO limits were achieved at low primary-airflow rates. At higher primary-airflows, the fuel flow rate at the LBO limit was found to increase linearly with the primary-airflow rate.

Another feature of the TV combustor is its low-pressure drop. This feature may provide significant reductions in specific fuel consumption.

Combustion efficiencies of $\sim 99\%$ were recorded at a low annular-air velocity of 14 m/s over a wide range of primary airflows. At a higher annular-air velocity of 42 m/s, the peak efficiency was $\sim 97\%$ and increased to $\sim 99\%$ when a second cavity was added to the combustor. Combustion is sensitive to the primary air and has a narrower high-efficiency range at higher annular-airflows. The majority of the NO_x is thought to be formed in the primary zone.

In conclusion, this paper has presented the preliminary results on the evaluation of a simple, compact, low-pressure-drop combustor utilizing the TV concept. This TV combustor exhibited good stability limits and reasonable combustion efficiencies under high-flow conditions. However, considerable work is required before the practical aspects of a TV combustor can be demonstrated. Recently, the TV concept was used for flame stabilization in developing an advanced gas-turbine combustor. In optimizing cavity performance, it was found that the combustion efficiency and LBO limits were significantly improved over a wide range of operating conditions. The aspect ratio of the cavity and the fuel and air injection scheme in the cavity have a strong impact on cavity performance. Future investigations will continue to focus on methods of improving the performance characteristics while substantially reducing NO_x. The fuel residence time and cavity entrainment that can impact practical designs will be investigated. The impact of using air to cool the cavity walls on combustion characteristics will be evaluated.

Acknowledgments

This work was supported by U.S. Air Force Contracts F33615-90-C-2033 and F33615-95-C-2507, and the Air Force Office of Scientific Research Aerospace Sciences Division. The authors would like to thank G. Sturgess and D. Burrus for helpful discussions, E. Jumper and C. Lyon for providing references and insightful discussions, and B. Sarka for assistance with the experimental work.

References

- Huellmantel, I. W., Ziemer, R. W., and Cambell, A. B., "Stabilization of Premixed Propane-Air Flames in Recessed Ducts," *Jet Propulsion*, Vol. 27, Jan. 1957, pp. 31–43.
- Morrison, C. Q., Campbell, R. L., Edelman, R. B., and Jaul, W. K., "Hydrocarbon Fueled Dual-Mode Ramjet/Scramjet Concept Evaluation," JANNAP Propulsion and Joint Subcommittee Meeting, Dec. 1996.
- Nioka, T., Terada, K., Hideaki, K., and Hasegawa, S., "Flame Stabilization Characteristics of Strut Divided into Two Parts in Supersonic Airflow," *Journal of Propulsion and Power*, Vol. 11, No. 1, 1995, pp. 112–116.
- Willis, J. W., Cadou, C., Mitchell, M., Karagozian, A. R., and Smith, O. I., "Destruction of Liquid and Gaseous Waste Surrogates in an Acoustically Excited Dump Combustor," *Combustion and Flame*, Vol. 99, No. 2, 1994, pp. 280–287.
- Ringleb, F. O., "Separation Control by Trapped Vortices," *Boundary Layer and Flow Control*, edited by G. V. Lachmann, Pergamon, New York, 1961, pp. 265–294.

⁶Mair, W. A., "The Effect of a Rear-Mounted Disc on the Drag of a Blunt-Based Body of Revolution," *Aeronautical Quarterly*, Vol. 10, Pt. 4, Nov. 1965, pp. 350-360.

⁷Little, B. H., Jr., and Whipkey, R. R., "Locked Vortex Afterbodies," *Journal of Aircraft*, Vol. 16, No. 5, 1979, pp. 296-302.

⁸Gharib, M., and Roshko, A., "The Effect of Flow Oscillations on Cavity Drag," *Journal of Fluid Mechanics*, Vol. 177, April 1987, pp. 501-530.

⁹Sarohia, V., and Massier, P. E., "Control of Cavity Noise," AIAA Paper 76-528, July 1976.

¹⁰Katta, V. R., and Roquemore, W. M., "Numerical Studies on Trapped-Vortex Concepts for Stable Combustion," *Journal of Engineering for Gas Turbines and Power* (to be published).

¹¹Hsu, K.-Y., Goss, L. P., Trump, D. D., and Roquemore, W. M., "Performance of a Trapped Vortex Combustor," AIAA Paper 95-0810, Jan. 1995.

¹²Sturgess, G. J., and Hsu, K.-Y., "Entrainment of Mainstream Flow in a Trapped-Vortex Combustor," AIAA Paper 97-0261, Jan. 1997.

¹³Lefebvre, A. H., *Gas Turbine Combustion*, Taylor and Francis, Washington, DC, 1983, pp. 448-451.

¹⁴Goss, L. P., Post, M. E., Trump, D. D., and Sarka, B., "Two-Color Particle Imaging Velocimetry," *Journal of Laser Applications*, Vol. 3, No. 1, 1991, pp. 36-42.

¹⁵Post, M. E., and Goss, L. P., "Two-Color Particle-Imaging Velocimetry in Vortex Structures," AIAA Paper 93-0412, Jan. 1993.

COMBUSTION CHARACTERISTICS OF A TRAPPED VORTEX COMBUSTOR

G.J. Sturgess
K-Y Hsu

*Innovative Scientific Solutions, Inc.,
Beavercreek, Ohio*

Abstract

The lean blowout stability of a laboratory-scale version of a trapped-vortex combustor is described. Three cavity axial lengths were tested at atmospheric pressure and ambient temperature over a range of mainstream velocities from 15 to 95 m/s. For each geometry and mainstream velocity, three values of cavity jet airflow were used; 5, 10 and 15 percent of the mainstream mass flow rate respectively. Pressure transducer and microphone measurements were used to assess noise levels and acoustic coupling of heat release with cavity dynamics. Planar laser-induced fluorescence of OH was used to obtain qualitative understanding of the flame structures. It was found that at very low cavity air-jet momentum, the flow in the cavity is poorly organized and is highly subject to mainstream influences. A range of operating conditions exists where the flame at blowout is contained within the cavity, and blowout stability is high. At higher cavity mass loadings burning in the cavity is not contained and is supplemented by burning in the interfacial shear layer between mainstream and cavity flows. Blowout then is from this shear layer, and depends on the ratio of mainstream to cavity momentum and the cavity axial length, as well as cavity loading. Comparison of lean blowouts with those for a swirl-stabilized combustor indicates that a well-designed trapped vortex combustor can have superior operability characteristics.

Introduction

In an introductory paper¹ a laboratory-scale combustor of unique form was described. The combustor uses a vortex mechanically trapped in a cavity (TV) for flame stabilization. The arrangement was such as to expose an axisymmetric annular cavity formed in a centerbody, to a by-passing co-axial mainflow of air that was confined by an enclosing circular cross-section duct. Primary air was injected into the cavity to strengthen the naturally occurring vortex. In addition, a gaseous propane fuel supply was directly

injected into the cavity, in close association with the primary air. A quantity of mainstream air is entrained into the cavity by the action of the cavity vortex and by the additional pumping action of the primary air and the fuel jets. This was determined indirectly by empirical means². Combustion took place within the cavity, to a degree determined by the cavity mass loading and equivalence ratio. The combustion efficiency achieved and the gaseous emissions generated both depended strongly on these quantities.

Subsequent computational fluid dynamic (CFD) studies were made of the stationary-state and time-dependent flow behavior^{3,4}. These studies revealed the important general flow structures, and provided insights into the complex dynamic behavior of the cavity and its interactions with the mainstream.

Background

Performance trends for future advanced aircraft gas turbine engines such as are being developed for the commercial market place, and especially for the IHPTET (*Integrated High Performance Turbine Engine Technology*) technology demonstrator program of the United States Air Force⁵, will demand the design and use of lightweight combustion systems that are also compact and which have high combustion intensities of the order³ of $(10-16) \times 10^6$ BTU/hr.ft³atm. [$(10-16) \times 10^4$ kW/m³bar]. Furthermore, engines for military application will be expected to have much-expanded operating envelopes. Therefore, combustion stability, always important, will become a key design concern.

The trapped vortex combustor concept, with its great potential for enhanced stability, appears to be a natural choice for providing the stabilization capability of such future combustion systems. A TV combustor module arranged in parallel with a main combustion module could form the pilot for a fuel-staged combustor, the main stage of which could be operated

Original version published in 1999 by Research and Technology Organization, North Atlantic Treaty Organization (RTO/NATO) in Meeting Proceedings MP-14, Gas Turbine Engine Combustion, Emissions, and Alternative Fuels. PUBLISHED WITH PERMISSION

lean and with short residence time in order to minimize the formation of thermal nitric oxide, an atmospheric pollutant.

Present Contribution

Additional lean blowout (LBO) studies have been made using the original, axisymmetric centerbody combustor, over an extended range of mainstream velocities and for three cavity axial lengths. The blowout data have been analyzed to determine stable operating conditions for a vortex to be trapped within the cavity. Planar imaging of the hydroxyl radical at near-blowout conditions, together with combustor noise measurements, have been used to assist with interpreting the analyses. By comparison with LBO data for a swirl-stabilized combustor, it is demonstrated that the TV combustor does have superior flame stability.

Combustor Arrangement

The original laboratory-scale TV combustor was described in Reference 1. The combustor consists of two major portions: a centerbody assembly and, a housing assembly.

The centerbody assembly is formed from a long central shaft of stainless steel that is made up of an inner fuel tube surrounded by a concentric air passage with outer diameter d_i , of 12.7mm, and which passes with a sliding fit through a solid disk of 70mm diameter, d_f , that forms a forebody. On the downstream end of the shaft is permanently mounted a short, hollow drum of 50.8 mm diameter, d_a , that forms an afterbody.

The drum contains two inner compartments that form respectively, primary air and fuel manifolds. These manifolds are supplied through the supporting double-tube shaft. The adjustable spacing H , between the forebody, the afterbody and the shaft forms an annular cavity within which a vortex may be trapped.

Fuel is discharged upstream into the vortex cavity from the upstream face of the drum via a ring of 8 circular jets each of 1.75mm diameter; tubes from the fuel manifold pass through the air manifold to feed these into the vortex cavity from the upstream face of the

drum via two concentric rings of circular jets each of 2.286mm diameter. There are 8 air jets in the inner ring and 16 air jets in the outer. The ring of fuel jets is concentric with and between, the rings of air jets. The fuel jets are circumferentially oriented to place a fuel jet midway between adjacent pairs of inner and outer air jets.

The forebody is supported concentric in a duct of 80 mm internal diameter, d_c , that supplies main air to the combustor from an air conditioning unit similar to that described in Reference 6. The combustor main body is a length of 80mm internal diameter Pyrex tubing. The length of the combustor in the original experiment was 910mm; for an earlier set of LBO experiments reported here as a repeatability check, a replacement (due to breakage) length was 780mm. For the LBO data of the present experiments the combustor body was a metal cylinder of 80 mm internal diameter and length of 305 mm. The change in material was due to continuing breakages: no effect of main combustor length of material on cavity blowout was discernible. For the optical measurements the Pyrex tube was used.

The complete centerbody assembly is cooled by the flows of air and fuel internally through it. The combustor main wall is protected initially from direct exposure to flame temperatures by the cool annular jet of main air that is in contact with it. No downstream external cooling of the main wall was provided. The forebody has no direct cooling, other than that provided by the annular flow of main air passing its outer edge.

The combustor and its conditioning unit for main air were mounted vertically in a test cell at the Air Force Research Laboratory, Wright-Patterson Air Force Base. The main air and cavity air originated from two air supplies, and were metered and controlled separately. The gaseous propane fuel was supplied from bottles. Exhaust from the combustor was collected and removed through a conventional exhaust hood.

A schematic view of the combustor is given in Figure 1. The sketch shows fuel and air paths, and suggests the modes of burning.

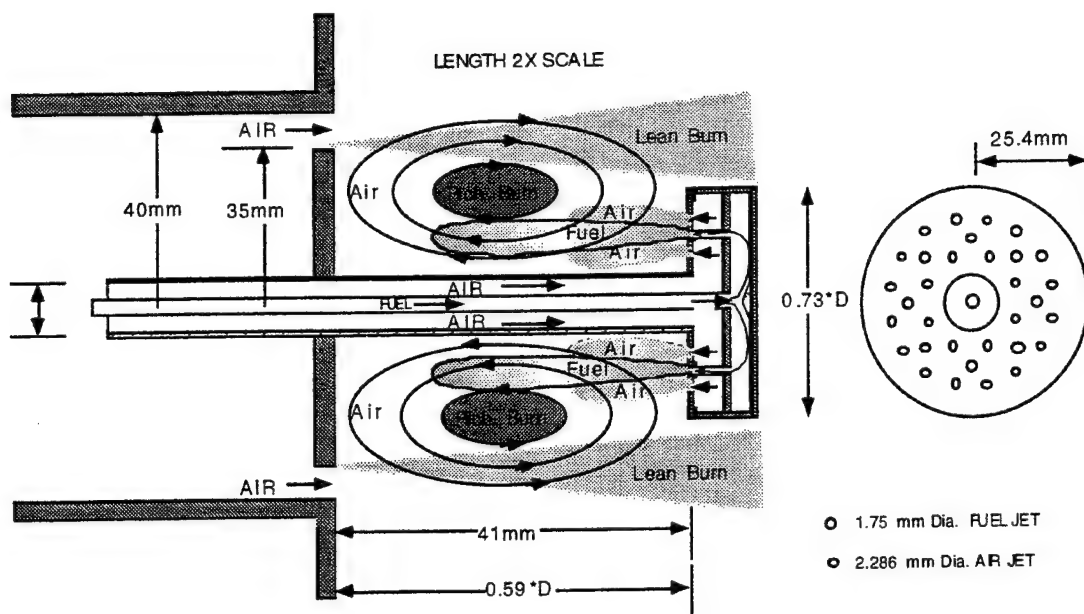


Figure 1: Schematic of Combustor Centerbody Assembly. Showing Operation

Test Conditions

The cavity axial length, H , was successively changed from 25.4 mm. to 38.1 mm, and finally, to 44.5 mm, giving variation in the cavity length to depth ratio H/d_f of 0.36, 0.54 and 0.635. The forebody diameter d_f is 70 mm. This form of geometric variation is extremely convenient. It would also have been useful to preserve the cavity aspect ratio as H was changed. However, this would have necessitated new centerbody assemblies, and would have been rather costly.

Lean blowouts were performed at atmospheric pressure and ambient temperature. Each cavity geometry was tested over a range of mainstream velocities from 15 m/s to 95 m/s. Over the range of mainstream velocities, the cavity jet air mass flow rate was set at 5 percent, 10 percent and 15 percent of the mainstream air mass flow rate.

LBO Tests

LBO's were performed by establishing burning at the desired airflows. Fuel flow was progressively reduced in a series of steps with pauses between steps to allow for thermal equilibrium to be established in the rig components. Airflows were checked and adjusted as necessary. As the blowout condition was approached,

the fuel decrements of the steps was progressively reduced to avoid overshooting the true blowout value.

OH Imaging

Planar laser-induced fluorescence (PLIF) was used to obtain a feel for the flame behavior at near-blowout conditions. A pulsed Nd:YAG - pumped dye laser was used to excite OH radicals in the cavity region. Although OH is long-lived and is therefore subject to convection effects, it does provide a simple qualitative way to capture impressions of the instantaneous flame structures.

Acoustic Measurements

The acoustic signature of the combustor was assessed by a dynamic pressure transducer that was mounted in the air duct feeding the mainstream past the combustor forebody. In addition, a microphone was mounted outside of the combustor, close to the exit from the main body duct.

Entrainment Estimates

The total mass flow rate in the cavity on a stationary state basis is the sum of the injected fuel, cavity jet air, and air entrained from the mainstream.

Entrainment measurements were not made in the present testing; information contained in Reference

2 was used for this purpose. Direct measurements of entrainment are exceedingly difficult. Therefore, the technique used was to infer entrainment from three other measurements made for cavity-contained flames. Figure 2 presents an example of correlated inferred entrainment data, taken from the reference; note both positive and negative values.

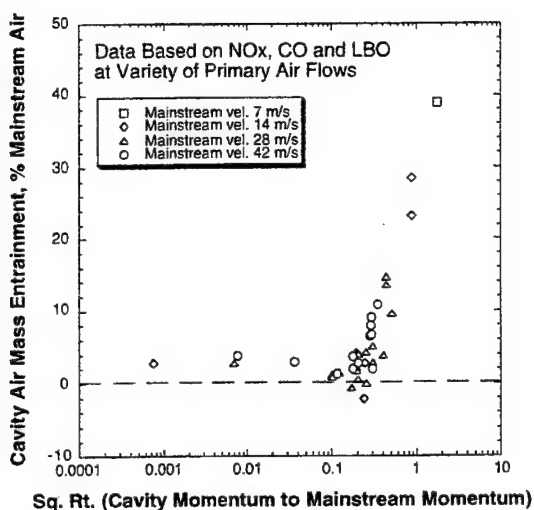


Figure 2: Example of Estimated Entrainment for the 0.54 H/d_f Cavity

Basic Blowout Data

An example of the basic blowout data is presented in Figure 3, in terms of the LBO fuel mass flow rate versus main air flow rate for the 38.1 mm cavity length, as a function of cavity air jet flow, which is expressed as a percent of mainstream mass flow rate.

The blowout fuel flow rate increases as main air flow is increased for each cavity jet air flow rate; it also increases as cavity jet air flow is increased at fixed main air flow. For the 5 percent jet flow, the blowout fuel flow appears to increase smoothly with main air flowrate, following a concave-upwards curve. However, for the 10 and 15 percent jet flows there are sharp gradient changes at a main air flow rate of about 0.0635 kg/s, with subsequent behavior following a concave-downwards characteristic. The discontinuous nature of the curves for the higher jet flows at high main air flows is indicative of a change in the blowout behavior.

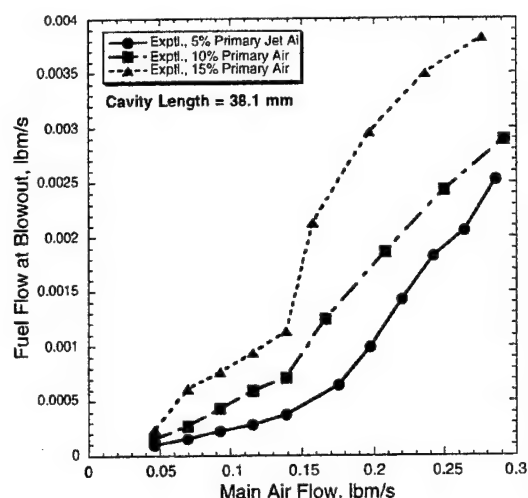


Figure 3: Basic LBO Data for the 0.54 H/d_f Cavity

Correlation of Blowout Data

Finite rate chemistry is important at LBO conditions. Reaction rate theory then leads to the loading parameter group LP, together with equivalence ratio, as controlling blowout, and experimental data can be correlated on this basis. LP is defined as follows:

$$LP = \frac{\dot{m}}{VP^n F} \quad (1.)$$

where, in the context of the cavity,

$$\dot{m} = \dot{m}_f + (\dot{m}_a)_{jets} + (\dot{m}_a)_{ent} \quad (2.)$$

$$V = V_{cav} \quad (3.)$$

$$F = \frac{10^{(0.00154 T_m)}}{3.72} \quad (4.)$$

\dot{m} signifies mass flow rate and subscripts f and a denote fuel and air respectively; subscript 'jets' refers to the cavity air jets and subscript 'ent' indicates entrainment. The fuel is included here because, being gaseous propane, it occupies significant volume. P is the combustion pressure; exponent 'n' an apparent reaction order, and is a constant if combustion proceeds in a single step reaction, with a value of 2.0 if this reaction is second-order. In reality 'n' is a variable less than 2.0, and its actual value is determined empirically. Since the present tests were made at atmospheric pressure and P is in atmospheres, 'n' does

not have to be determined. F is an exponential temperature correction factor⁷ that corrects to an inlet temperature of 400°K.

The loading parameter has been successfully in use for correlating LBO's and combustion efficiency for many years, e.g. Kretschmer & Odgers⁸.

Figure 4 shows the data from Figure 3 plotted in loading parameter form, using Equation (1.). Also shown on the plot are some data obtained

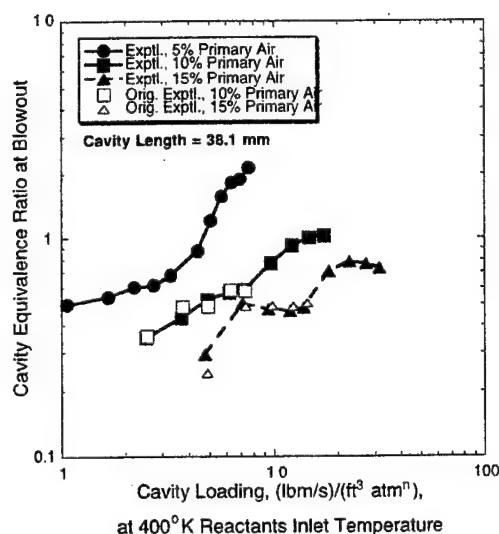


Figure 4: LBO Data for 0.54 H/d_r Cavity

earlier using the same combustor in a different test facility. The cavity equivalence ratio is defined as,

$$(\phi_{cavity})_{LBO} = \frac{(\dot{m}_f)_{LBO}}{0.06377(\dot{m}_a)_{cav}} \quad (5.)$$

where,

$$(\dot{m}_a)_{cav} = (\dot{m}_a)_{jet} + (\dot{m}_a)_{ent} \quad (6.)$$

and 0.06377 is the stoichiometric fuel/air mass ratio for propane.

The most obvious feature of Figure 4 is that, despite containing all necessary flow information, the LP group does **not** correlate this data. The plot shows that increasing cavity jet air flow improves the stability. This apparent failure of loading parameter is because cavity jet air not only affects cavity equivalence ratio and cavity loading, it also drives and strengthens

the large natural vortex that is trapped in the cavity. Therefore, change in cavity jet air may also be considered as a geometry change, analogous to a swirler vane angle change in a conventional swirl-stabilized combustor.

The earlier data at 10 and 15 percent cavity jet air flow rates agrees extremely well with the present LBO data. This confirms the repeatability of the observed behavior.

Note that the shapes of the curves change dramatically as cavity jet air flow is increased. At 15 percent jet air flow the observed behavior is that normally associated with blowout from multiple flame positions, i.e. the overall characteristic is apparently composed of components from several individual blowout characteristics; e.g. Reference 9.

A more appropriate comparison of data would be on a constant cavity jet air flow basis for all of the cavity lengths. All of the features and flows present should then be accounted for in the LP group and cavity equivalence ratio. Figures 5 and 6 show such plots at the 5 percent and 10 percent cavity jet flows respectively, and in each case for all three of the cavity lengths.

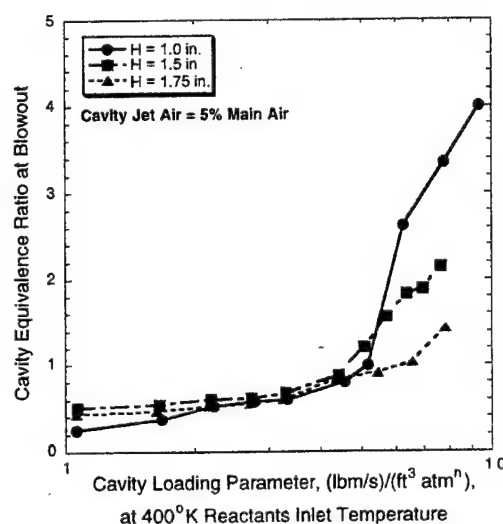


Figure 5: LBO's for All Cavities at 5% Jet Air

It can be seen that for each cavity jet airflow, a satisfactory correlation of data is obtained for a limited range of cavity loading parameter. Once a critical value

of cavity loading is exceeded, the correlation fails. After this critical loading, blowouts for all of the cavities exhibit a sharp change in slope, with the smallest cavity having the worst stability

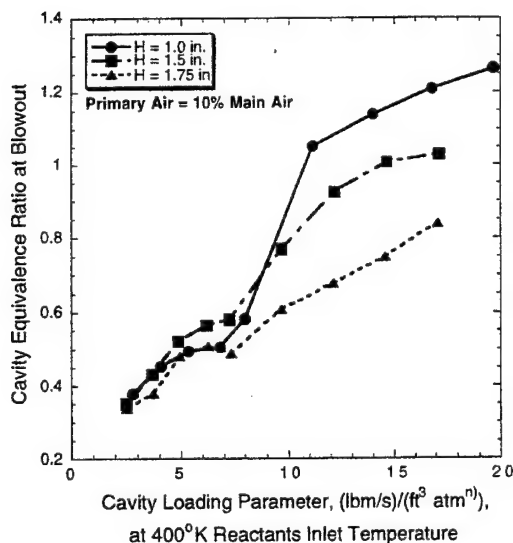


Figure 6: LBO's for All Cavities at 10% Jet Air

The cavity loading at correlation breakdown for all cavity lengths is plotted against cavity jet air mass flow rate, expressed as a percentage of main air flow, in Figure 7.

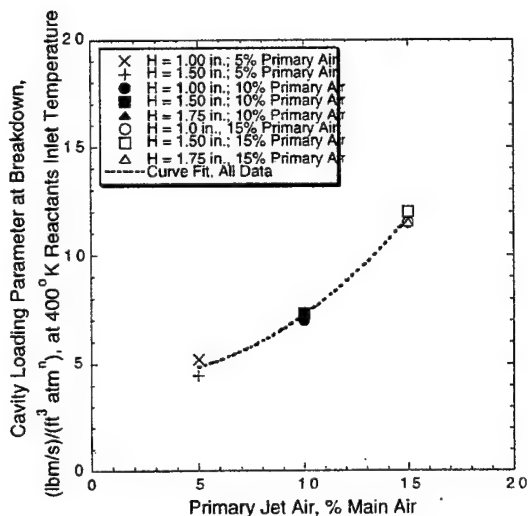


Figure 7: Cavity Loadings at Burning Mode Change

The correlation breakdown data for all three cavities agree well in this form, and the cavity loading at breakdown increases with cavity jet air. This behavior would be expected if the cavity jet air does indeed drive and strengthen the trapped vortex. The jet air, at higher flow rates, also increases the entrainment of mainstream air into the cavity, as Figure 2 indicates. Together, these increase the cavity loading. Eventually, the cavity becomes overloaded, and burning at blowout can no longer be contained within the cavity.

Figure 8 records the cavity equivalence ratio at correlation breakdown, also as a function of cavity jet air. Again, there is good agreement for all of the cavities at all of the jet flows. Note that the bulk equivalence ratios where breakdown occurs are all below unity. If burning at blowout is not contained in the cavity, then it is not due to there being insufficient air in the cavity to complete combustion.

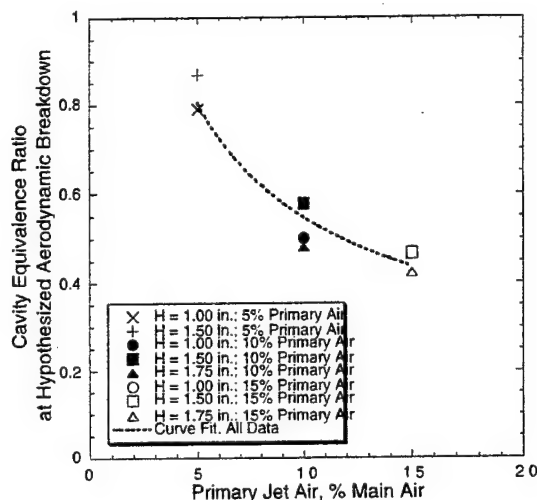


Figure 8: Equivalence Ratio at Mode Change

Cavity equivalence ratios at LBO are plotted in Figure 9 against cavity loading parameter for all flows that are contained clearly within the cavity at blowout; data falling at higher loadings than the correlation breakdown are excluded. The data correlate well and fall into two distinct groups: one group for all cavities at cavity jet flows of 5 percent of mainstream air mass flow rate, and another group for all cavities at 10 and 15 percent of mainstream air flow rate. All the cavities at 5 percent cavity jet flow have worse stability than all the cavities at 10 and 15 percent jet flows.

Referring back to Figure 4 and the discussion of it, the explanation of the two groupings of correlated data in Figure 9 would appear to be that a 5 percent cavity jet flow has insufficient momentum to organize and adequately stabilize, a lazy and inherently unstable naturally-trapped vortex.

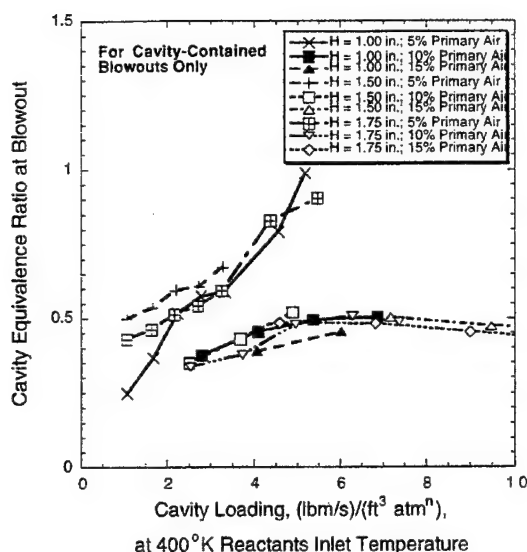


Figure 9: Blowout Correlation for Cavity-Contained Flames Only

Noise Measurements

The observed noise under non-reacting flow conditions is broad-band, and the level increases with increase in mainstream flow velocity. The presence of combustion increases the noise level at given flow conditions. Under certain reacting flow conditions for the different cavity lengths, a strong increase in combustion noise was observed. Blowout would occur abruptly with such noisy operation.

To illustrate the noise measurements, two test conditions for the 38.1 mm cavity length are presented; these are delineated as Cases A and B. The test conditions for Case A are as follows: mainstream velocity 38 m/s, cavity equivalence ratio 1.05, cavity air jet mass flow rate 1.9 percent mainstream mass flow rate, and, cavity loading of 1.31 (lbm/s)/(ft³ atmⁿ) at 400°K. For Case B: mainstream velocity 38 m/s, cavity equivalence ratio 0.7282, cavity air jet mass flow rate 3.15 percent mainstream mass flow rate, and, cavity

loading of 1.83 (lbm/s)/(ft³ atmⁿ) at 400°K. The fuel flow rate was constant for both cases. The major variable therefore, was cavity jet air flow, with mainstream entrainment following.

With respect to Figure 9, the cavity loadings place both cases in the category of cavity-contained blowouts, but following the poorer stability grouping. Of course, the equivalence ratios for both cases are considerably above LBO.

Figure 10 shows noise time traces, as a signal voltage from the microphone, for non-reacting flow at Case A conditions, and for reacting flow at Cases A and B conditions.

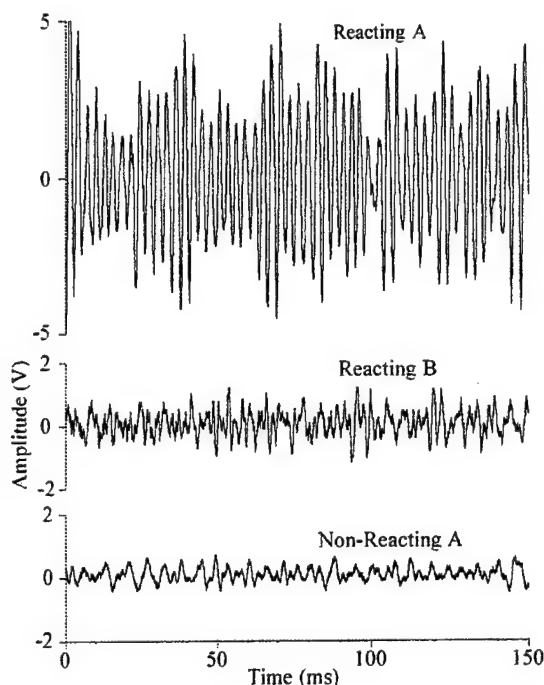


Figure 10: Noise Time Traces From Microphone

The noise level for Case A with a near-stoichiometric equivalence ratio, was considerably above that for Case B, which is fuel-lean. The corresponding power spectra for the three traces is given in Figure 11. For Case A there is a distinct peak frequency at 280 Hz. No distinct frequency was observed for Case B at the lower equivalence ratio.

It appears as though coupling exists between heat release and flow structure for the higher equivalence ratio. The apparent absence of such coupling for the

lower equivalence ratio might be due to damping effects arising from higher viscosities associated with the lower cavity temperatures at this condition.

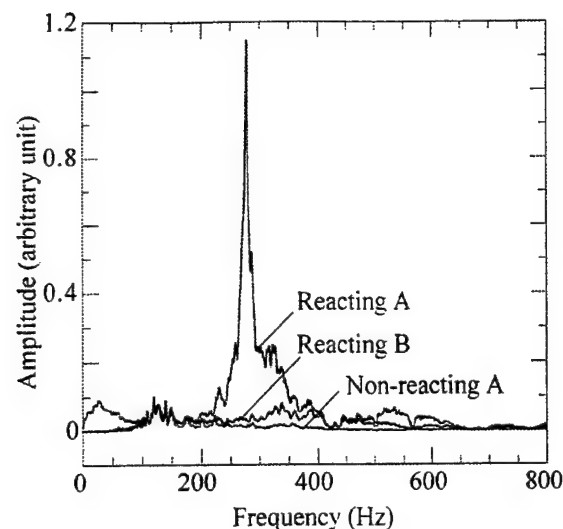


Figure 11: Noise Averaged Power Spectra

OH Imaging

The flame structures in the cavity are highly three-dimensional and the mean flow field is extremely non-stationary. Therefore, the individual, near-instantaneous, planar images of OH captured are rather difficult to interpret. Phase-locking was not attempted in this initial investigation, and structure detail was lost in ensemble-averaging many images. Careful review, sorting and sequence-animation of a large number of randomly-collected images was necessary in order to gather reasonable qualitative interpretations of the flame behavior at near-blowout conditions. Based on this process the following general observations were possible.

In general, at low mainstream and low cavity air jet mass flow rate combinations, flame is fully contained within the cavity and LBO occurs from the shear layers associated with the fuel jet. This is consistent with Figure 9 where the two sets of correlated LBO data for cavity-contained converge for small cavity loadings. For no cavity length H , is the whole cavity volume effectively utilized at LBO. As the mainstream velocity is increased while cavity air jet mass flow rate remains low, (for example, Case B conditions above), the mainstream momentum

influences the cavity flow and results in unburned fuel getting into the shear layer formed between the mainstream and the cavity flows at the outer diameter of the combustor forebody (see Figure 1). This is also consistent with Reference 2, see Figure 2, where negative entrainment was found. The fuel reacts in this shear layer, as is illustrated by two images in Figure 12 for Case B conditions with the 38.1 mm cavity length. Figure 13 shows an example of jet shear burning contained within the cavity at 0.50 cavity equivalence ratio.

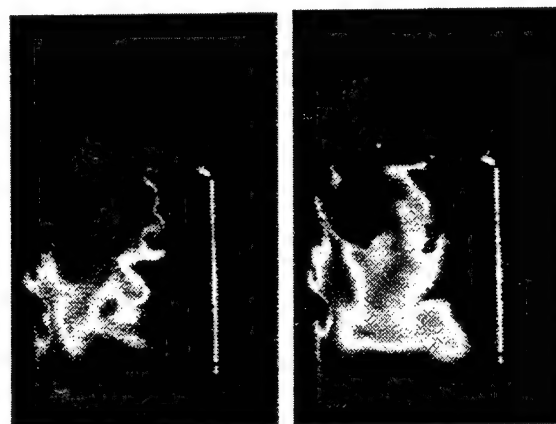


Figure 12: OH Images for Case B

In Figure 12 the combustor is mounted vertically, with mainstream flow from bottom to top and cavity jet and fuel flows from top to bottom. The central shaft that supports, and supplies fuel and cavity jet air to, the drum, is visible to the right of each image. Mainstream air is flowing to the left of each image. The origin of the fuel entering the cavity from the drum is visible as the origin of the OH emission. Jet shear layer burning in the cavity can be seen, and these jet shears oscillate left to right about the fuel origin, rather like a pendulum. Fuel enters the mainstream/cavity interfacial shear layer to the left of the images, and burns there; classical shear layer vortex roll-up is visible. The direction of the visible roll-up in this shear layer indicates that the mainstream velocity is greater than that of the cavity flow. This observation is consistent with the conditions stated above for Case B, where mainstream velocity was 38 m/s and cavity jet injection velocity was 15 m/s. Due to the high mainstream momentum, the interfacial shear layer seldom interacts with the cavity rear wall to be recirculated back into the cavity.

In Figure 13 a fuel jet is visible as a dark region of quasi-potential core, with bright OH emission

indicating burning in the jet shear layers around the fuel potential core. Flame impinges on the support shaft to the right of each image. It also is picked up by the outer layers of the large vortex trapped within the cavity and recirculated around the cavity. The indicated vortex center is not fixed in space but moves both axially and radially. In the lower left region of the left-hand image, a darker grey region is evident. This is convected OH, and does not represent a flame.

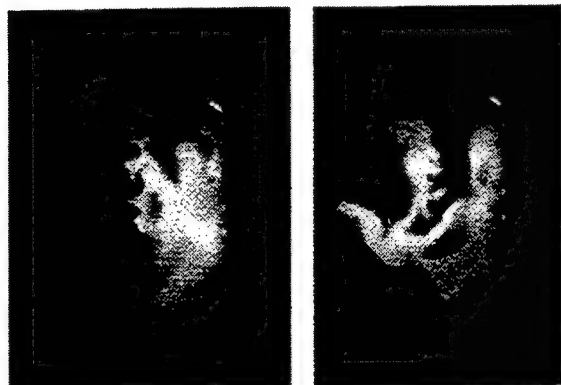


Figure 13: Example of Cavity-Burning with 0.50 Cavity Equivalence Ratio

As cavity jet flow is increased for fixed mainstream conditions in this cavity length, mixing in the cavity appears to improve. OH generation is pushed towards the cavity front wall formed by the forebody, and more, but not all, of the cavity volume is utilized by the large trapped vortex; OH is largely concentrated in the surface layers of this vortex, and there is no burning of significance taking place in the interfacial shear layer.

For increases in cavity jet air in the 25.4 mm cavity length, the jet flow reaches, and is turned radially-outwards by, the cavity front wall. The turned flow can impact the interfacial shear layer off the outer diameter of the forebody, moving it radially outwards to prevent recirculation of this layer back into the cavity by interaction with the cavity rear wall formed by the drum. Some flame spillage is observed prior to the cavity jet flow reaching the cavity forward wall, even when the cavity equivalence ratio is low. Blowout occurs suddenly from the interfacial shear layer.

For the 44.5 mm cavity length the whole cavity flow relatively disorganized and there is a notable increase in noise level compared to the other cavities.

The large trapped vortex remains at almost the size size as that for the 25.4 mm cavity length because the fuel/air jet system is turned radially outwards before it reaches the cavity front wall by the excess mainstream momentum.

Blowouts From Shear Layer Burning

From the OH imaging, it is obvious that the LBO correlation breakdown noted in Figures 5 and 6 can be associated with the excess of mainstream momentum over cavity flow momentum entraining unburned fuel from the cavity into the interfacial shear layer off the forebody outer diameter. If this occurs when the cavity jet system itself also has high momentum, the enhanced radial outflow from the cavity moves radially and prevents, the interfacial shear layer from being recirculated into the cavity by the cavity rear wall. Blowouts would then be controlled by the interfacial shear and not solely by the cavity. Cavity loading alone would not be sufficient to correlate all of the blowout data, as was noted.

For the situations with LBO from significant shear layer burning, the total fuel burned at blowout is split in undetermined fashion between cavity burning and shear layer burning. Also undetermined is the amount of air involved in the shear layer. The shear layer air can be written.

$$(\dot{m}_a)_{\text{shear layer}} = (\dot{m}_a'')_{\text{ent}} \times A_{\text{layer}} \quad (7.)$$

where,

A_{layer} = interfacial area between cavity flow
and mainstream flow

$(\dot{m}_a'')_{\text{ent}}$ = entrainment mass flux across A_{layer}

For the fixed diameters forming cavity forward and rearward walls, A_{layer} will be proportional to the cavity length H . Neglecting density differences across the shear layer, which can modify entrainment rates but are presently unknown, the entrainment mass flux will be proportional to the mainstream to cavity flow momentum ratio.

These additional controlling LBO parameters were incorporated as follows: First, the volume term in the cavity loading parameter was increased to allow for the shear layer presence. For this purpose the increase in shear layer radial width over cavity length was estimated from the OH images. This gave $(LP)_{\text{SLB}}$. Second, the resulting loadings were multiplied by the mainstream to cavity flow momentum ratios. Finally, the cavity

equivalence ratios at blowout were multiplied by the cavity length, H .

The modified terms were applied to the blowout data for blowouts just from shear layer burning, i.e. the data beyond the cavity breakdown loading. Figure 14 shows that these additional terms correlate the shear layer blowout data for all cavity jet mass flow rates and for all of the cavity lengths.

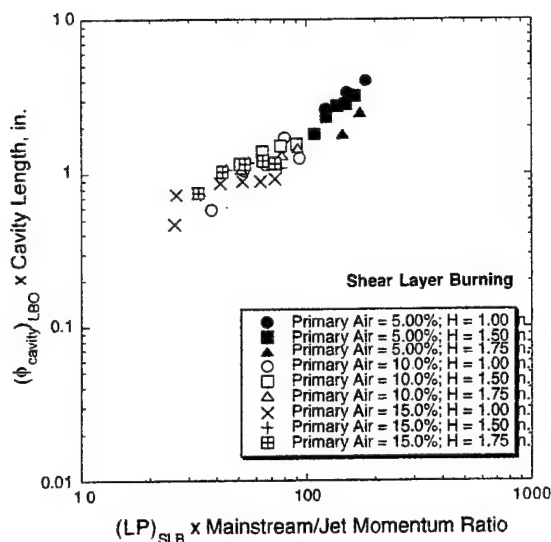


Figure 14: Correlation of LBO Data for Shear Layer Burning

Comparison with Swirl-Stabilized Combustors

The trapped vortex combustor has been promoted as a means towards achieving enhanced lean blowout stability for high altitude operations because the recirculation zone is mechanically held in place. By being trapped in a cavity it is not subject to, or is less sensitive to, variations in flow due to engine operating conditions or inlet flow distortions. To substantiate these claims the present LBO data can be compared to LBO data from a conventional swirl-stabilized combustor. A comparison of the present data is therefore made against the LBO data contained in Reference 10.

The data in Reference 10 were for a four-injector, planar sector combustor, modeled extremely closely on a full annular combustor from a real aircraft

gas turbine engine. The engine had demonstrated good LBO stability (and windmilling relights) with liquid Jet-A fuel to flight altitudes in excess of 10,700 m. The sector combustor, like the engine combustor, utilized swirling air in an airblast atomizer and a dome-swirler, together with sudden expansion into the combustor dome, to generate a recirculation zone; however, gaseous propane, as with the TV combustor tests, was used as a fuel. The dome and atomizer air swirlers generated toroidal recirculation zones around the axial centerline of each fuel injector. The sector tests were made at atmospheric pressure with ambient temperature inlet air; low pressures were simulated using an excess gaseous nitrogen dilution technique¹¹. With this approach, LBO's down to 0.25 atm. equivalent pressure were measured.

Comparisons have been made for the TV combustor operating with cavity-controlled LBO's since these operational conditions fulfill the design intent. For consistency with the swirl-stabilized combustor results the equivalence ratio used was an overall one based on the total mass flow rate exiting the combustor.

Figure 15 shows the sensitivities of the two recirculations to the amount of air directly injected into the vortices, expressed as a percentage of the total airflow to follow conventional practice.

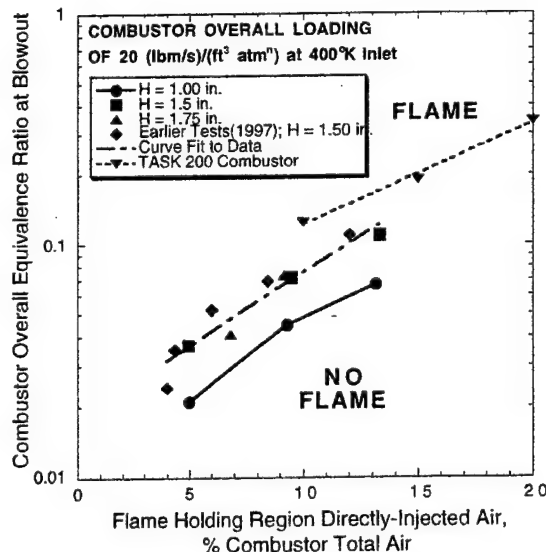


Figure 15: Comparison of TV Combustor With Swirl Combustor - Sensitivity to Directly-Injected Air

For the TV combustor the directly-injected air corresponds to the cavity jet air; for the swirl-stabilized combustor it corresponds to the air introduced through the combustor dome. The sensitivity is indicated by the overall equivalence ratio at blowout. For both combustors the combustor loading was constant at 20 (lbm/s)/(ft³ atmⁿ) at 400°K.

Setting aside the 25.4 mm length cavity, the data for the 38.1 and 44.5 mm cavities correlate well for all cavity flows. The sensitivity of the TV combustor to directly injected air **for cavity-contained blowouts** is about the same as that generated by swirl (gradients virtually the same). This is not surprising since a recirculation is a recirculation, regardless of how it is generated. The TV combustor over the range 5 to 15 percent directly-injected air has better stability than does the swirl-stabilized combustor; however, because of the slight gradient difference, this advantage is lost at higher airflows.

In Figure 16 LBO's for a "well-designed", i.e. the right amount of cavity jet air to drive the vortex but to avoid interfacial shear layer burning, are compared with the LBO's from the swirl-stabilized combustor¹⁰.

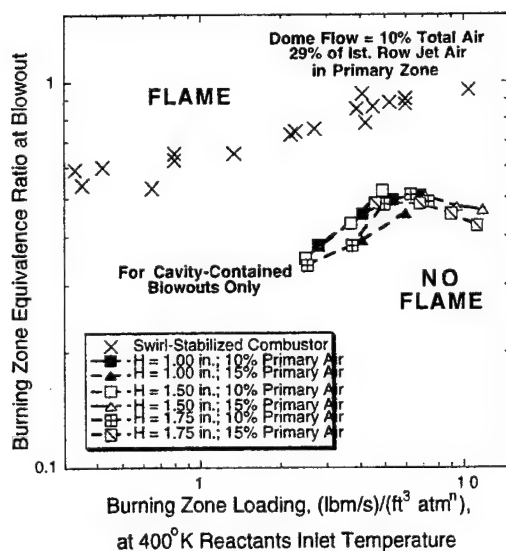


Figure 16: Comparison of Cavity-Contained TV Combustor with Swirl-Stabilized Combustor

The trapped vortex combustor data are taken directly from Figure 9. The data for the swirl-stabilized combustor were selected for a dome flow equal to 10

percent of the combustor total so that it is directly comparable to the TV combustor data. The "Burning Zone" is the cavity for the TV combustor, and the primary zone for the swirl-stabilized combustor. The primary zone length was taken as the downstream distance from the dome to the first row of transverse primary air jets in the liners. The amount of first row jet air recirculated back into the primary zone was taken as 29 percent of the jet total¹¹. This amounts to less than 2.0 percent of the combustor total.

It can be seen that within its constraints, the TV combustor has a significantly better LBO stability than does the example of swirl-stabilized combustors.

Discussion

The trapped vortex combustor is a complex device. However, it generates a recirculation zone, and that recirculation zone in general, appears to behave just like any other recirculation zone. Without direct injection of air into the cavity the natural trapped vortex generated by flow over the cavity is very lazy and is poorly organized for combustion purposes. There has to be sufficient cavity air injected in jet form, to drive the natural vortex. Present indications are that this amount is greater than 5 percent of the mainstream air. Cavity jet air equal to 10 percent of the mainstream is more than adequate, and, as Figure 9 shows, increasing the cavity jet air to 15 percent of the mainstream results in no further improvement in stability with this method of introduction.

Cavity jet air acts in three ways: 1.) it changes the cavity equivalence ratio; 2.) it drives the vortex by determining the circulation developed, and has a similar result to swirler vanes, and, 3.) it influences the cavity residence time through mass loading.

A cavity mass loading can be reached where flame is not contained within the cavity, but is supplemented by shear burning in the interface between the cavity flow and the mainstream moving by the cavity. Burning in the interfacial shear layer is very sensitive to the mainstream, and a blowout in the shear layer also results in a simultaneous blowout in the cavity. Cavity axial length only plays a role in influencing the cavity loading, and in determining the shear layer extent.

Flow behavior in the cavity, the interfacial shear layer and, in the interactions of the interfacial shear layer with the mainstream and with the cavity, is

highly dynamic. This dynamic behavior depends, in general, on cavity geometry beyond the simple axial length variation examined presently. Like many other combustion systems, despite its good LBO performance, the TV combustor can be subject to acoustic coupling of heat release with flow structure dynamic behavior, (Figure 11).

Conclusions

1. A trapped-vortex combustor requires greater than 5 percent mainstream air to be directly-injected into the cavity in order to drive the vortex, for successful combustion.
2. A critical cavity loading exists beyond which flame is not contained within the cavity at lean blowout.
3. When the critical cavity loading is exceeded, cavity burning is supplemented by classical shear layer burning at the interface between cavity and mainstream flows. Blowout occurs from the interfacial shear layer.
4. Dynamic flow interactions are extremely important to cavity flame stability, and the trapped vortex can be subject to acoustic coupling of heat release and flow structures.
5. Compared to a generic, conventional, swirl-stabilized combustor, the trapped vortex combustor exhibits superior lean blowout capability when burning is maintained within the cavity.

Acknowledgements

The enthusiasm, motivation and support of Dr. W.M. Roquemore of AFRL are greatly appreciated. Dr. Roquemore conceived applying the TV combustor to gas turbine engines. This on-going research is sponsored by the U.S. Air Force Research Laboratory, Propulsion Directorate, Wright-Patterson Air Force Base, through Contract No. F33615-95-C-2507.

References

1. Hsu, K-Y, Goss, L.P. and Roquemore, W.M., "Performance of a Trapped-Vortex Combustor," *Journal of Propulsion & Power*, Vol. 14, No.1, 1998
2. Sturgess, G.J. and Hsu, K-Y., "Entrainment of Mainstream Flow in a Trapped-Vortex Combustor," Paper No. 97-0261, *AIAA 35th. Aerospace Sciences Meeting & Exhibit*, Reno, Nevada, January 6-10, 1997.
3. Katta, V.R. and Roquemore, W.M., "Numerical Studies on Trapped-Vortex Concepts for Stable Combustion," *Trans. ASME, J. Engineering for Gas Turbines and Power*, Vol. 20, January 1998, pp. 60-68.
4. Katta, V. R. and Roquemore, W.M., "Simulation of Unsteady Flows in an Axisymmetric Research Combustor Using Detailed Chemical Kinetics," Paper No. 98-3766, *34th. AIAA/ASME/SAE/ASEE Joint Propulsion Conference & Exhibit*, Cleveland, Ohio, July 13-15, 1998.
5. Valenti, M., "Upgrading Jet Turbine Technology," *Mechanical Engineering*, Vol. 117, No.12, December 1995, pp. 56-60.
6. Heneghan, S.P., Vangsness, M.D., Ballal, D.R., Lesmerises, A.L., and Sturgess, G.J., "Acoustic Characteristics of a Research Step Combustor," *AIAA Paper No. 90-1851, AIAA/SAE/ASME/ASEE 26th. Joint Propulsion Conference, Orlando, Florida*, July 16-18, 1990.
7. Parnell, E.C. and Williams, M.R., "A Survey of Annular Vaporizing Combustion Chambers," *proc. Intl. Symp. Combustion and Heat Transfer in Gas Turbine Systems*, Vol. II, Pergamon Press, 1971, pp. 91-103.
8. Kretschmer, D. and Odgers, J., "Modeling of Gas Turbine Combustors - A Convenient Reaction Rate Expression," *Trans. ASME, J. Energy & Power*, 1972, pp. 173-180.
9. Sturgess, G.J., Gogineni, S. and Shouse, D.T., "Influences of Airblast-Atomizing Fuel Injector Design on Primary Zone Characteristics at Blowout," Paper No. 97-0269, *AIAA 35th. Aerospace Sciences Meeting & Exhibit*, Reno, Nevada, January 6-10, 1997.
10. Sturgess, G.J. and Shouse, D., "Lean Blowout Research in a Gaseous Gas Turbine Combustor with High Optical Access," *Trans. ASME, J. Engineering Gas Turbines & Power*, Vol. 119, January 1997, pp. 108-118.
11. Sturgess, G.J., Heneghan, S.P., Vangsness, M.D., Ballal, D.R. and Lesmerises, A.L., "Lean Blowout in a Research Combustor at Simulated Low Pressures," *Trans. ASME, J. Engineering Gas Turbines & Power*, Vol. 119(4), October 1996, pp.773-781.

12. Sturgess, G.J., McKinney, R. and Morford, S., "Modification of Combustor Stoichiometry Distribution for Reduced NO_x Emissions from Aircraft Engines," Trans. ASME, *J. Engineering Gas Turbines & Power*, Vol. 115, No. 3, July 1993, pp. 570-580.

PAPER No. 44
Sturgess
 (presenter: G.J. Sturgess)

Question 1: N. Selcuk, Middle East Technical University, Turkey

Could you please elaborate a little bit on the CFD code that you have used.

Answer:

Although detailed reference to the CFD code and work is not given in the paper, which concentrated on the experimental results, I used some of the calculations obtained with it in the presentation to illustrate the flowfield in the trapped vortex combustor. The code is called UNICORN (Unsteady Ignition and Combustion with Reactions), and it was developed by my colleague at ISSI, Dr. Vish Katta; it is the same code that was referred to in Paper 17 by Grish et. al, presented at this meeting. The code is two-dimensional, and offers time-accurate direct numerical simulations (DNS) or time-averaged simulations with turbulence models. Global, reduced and detailed chemical reaction mechanisms are available for combustion in air of hydrogen, methane, propane, methanol, ethylene and acetylene as fuels; the fuel can be in gaseous or liquid phase if appropriate, for droplet burning and spray flames calculations. Detailed simultaneous calculations for NO_x are also provided. Post-processing software called IGAS (Integrated Graphics and Animation Software) also developed by ISSI allows for complex data presentation.

Question 2: M. Razdan, RR-Allison, U.S.

Concerning the estimation of mainstream mass entrainment into the cavity, how big an impact does such entrainment have on the cavity loading parameter, and hence, on the lean blowout in an engine situation?

Answer:

Mainstream entrainment into the cavity can vary widely, depending for a given cavity on the momentum ratio of the cavity directly-injected flow to that of the mainstream, and can be either positive or negative according to this ratio. It also depends on the cavity dimensions; the curve shown was for a near-optimum, i.e. maximum vortex stability with minimum entrainment. cavity size. Non-optimum cavities can have quite different entrainment characteristics while still showing, in general, both positive and negative entrainment (see Sturgess & Hsu, Paper No. AIAA-97-0261). Entrainment, of course, is extremely difficult to measure directly. In general, including the entrainment into the cavity loading parameter becomes particularly important at high values of cavity loading, where the "nose" of the blowout stability loop is approached.



AIAA 99-0488

**CHARACTERISTICS OF COMBUSTION INSTABILITY
ASSOCIATED WITH TRAPPED-VORTEX BURNER**

K. Y. Hsu, C. D. Carter, V. R. Katta, and, W. M. Roquemore
Air Force Research Laboratory
Wright-Patterson AFB, OH

**37th AIAA Aerospace Sciences
Meeting and Exhibit
January 11-14, 1999 / Reno, NV**

CHARACTERISTICS OF COMBUSTION INSTABILITY ASSOCIATED WITH TRAPPED-VORTEX BURNER

K. Y. Hsu*, C. D. Carter*, V. R. Katta* and, W. M. Roquemore†
Air Force Research Laboratory, Wright-Patterson Air Force Base, OH

Introduction

The performance of a trapped-vortex (TV) combustor operated under atmospheric conditions has been documented in previous studies¹⁻³. The previous results showed that low lean blowout limits were achieved over a range of flow conditions. Proper sizing of the cavity and proper injection in the cavity were found to be critical in providing combustion stability. The design rules for trapping a vortex were established by several investigators^{4,5} who were interested in reducing the drag behind a disk. They demonstrated that the drag that normally results from the unsteady vortex motion behind disks could be reduced by trapping a vortex in a cavity formed between two disks mounted in tandem. The flow oscillation associated with different cavity geometry has been studied in great length⁶⁻⁹. A self-sustained oscillation was found to be established under certain geometric aspect ratio that resulted in low drag¹⁰. The oscillations resulted from flow impingement associated with shear layer and cavity corner have also been identified¹¹⁻¹³. To reduce cavity noise, the mass addition into the cavity was studied over a range of cavity aspect ratios¹⁴. The mass transport and its interaction with shear layer complicate the phenomena, and the prediction of the resonant frequency becomes difficult. Combustion instabilities are a result of the resonant interaction between two or more physical mechanisms, which the coupling between unsteady heat release and pressure fluctuations is believed to follow the Rayleigh's criterion for most cases. A driving process generates the perturbations of the flow; a feedback process couples the perturbation to the driving mechanism and produces the resonant interaction that may lead to oscillatory combustion. The heat release can amplify and modify certain flow frequencies.

This paper presents the lean blowout limits over an extended range of flow conditions. It was found that the flame blows out differently under different conditions, and there exist acoustic noise that could affect the stability of the cavity combustion under certain conditions. This acoustic phenomena may not appear in a practical system, but, it deserves attention to better understand the fundamental processes. The

objectives of this study are to identify and to understand the dynamic behavior and acoustic noise associated with these conditions and study the effect of cavity size and flow condition on noise level.

Experimental Descriptions

The burner used in this study consists of a forebody and an afterbody, as shown in Fig. 1(a). The afterbody connects to two concentric tubes along the centerline of the forebody. Fuel and primary air are delivered through these concentric tubes to two separate chambers in the afterbody that is 50.8 mm in diameter. The forebody, having a diameter (d_f) of 70 mm, is located at the exit plane of the vertically mounted annular-air duct that is 80 mm in diameter. The blockage ratio, defined as the ratio of the area of the forebody to that of the air duct, is 76%. An axisymmetric cavity is created in the region between the forebody and the afterbody. The cavity length, H , which is adjustable and defined as the axial distance between the forebody and afterbody, as noted in Fig. 1(a). The annular- and primary-air flows originate from two air supplies and are controlled and metered separately. To eliminate the entrainment and room air disturbances, a quartz tube of 80 mm in inside diameter and 305 mm in length is used to confine the flow.

A schematic diagram of the fuel and primary-air injection plane is shown in Fig. 1(b). Gaseous-propane fuel is injected through eight orifices (each 1.75 mm in diameter), and the primary air is supplied through 24 orifices (each 2.29 mm in diameter) surrounding the fuel jets. Direct injection of primary air serves several purposes: 1) provides direct control of the local equivalence ratio in the cavity zone; 2) enhances mixing by increasing the mixing region through distributed multiple fuel and air jets; and 3) provides cooling for the injector assembly. All the tests were conducted under atmospheric pressure and the gases injected at temperature of 300 K.

The planar laser-induced fluorescence (PLIF) technique is used to image the OH radical. The frequency-doubled output of a Nd:YAG-pumped dye laser was tuned to the $R_1(8.5)$ transition of the $A^2\Sigma^+ - X^2\Pi$ ($v'=1, v''=0$) band of OH ($\lambda = 281.34$ nm). The

15-mJ UV beam was expanded into a 70-mm-high sheet and focused in the probe region (the cavity). Fluorescence from the A-X (1,1) and (0,0) bands ($\lambda = 306\text{--}320\text{ nm}$) was imaged onto the intensified CCD array (576×384 pixels) using a UV Nikkor 105-mm, f/4.5 lens. The field of view was 64 mm (height) \times 42.7 mm (width), and pixels in the array were binned 2×2 prior to the read-out process; thus, the effective pixel size, 0.22 mm, matched roughly the sheet thickness. Schott glass, UG-11 and WG-295, were employed as short-wave- and long-wave-pass filters. The WG-295 filter was particularly important for blocking the strong surface scattering from the UV beam, since the beam impinged on the burner surface. Furthermore, flame emission was minimized using a 200-ns intensifier gate. The laser sheet was oriented vertically along the burner axis and intercepts one of the fuel jets originated from the afterbody. Although the OH images do not necessarily represent the instantaneous reaction zone, they provide a simple qualitative way to capture the instantaneous structures.

A microphone located 30 cm outside the burner was used in conjunction with OH imaging to measure the acoustic noise generated from the burner. Two dynamic pressure transducers were used to record the pressure fluctuations in the reactant supply lines. One transducer was mounted on the outer wall of the annular air stream located 2 cm upstream of the forebody, and another transducer was located upstream of the fuel supply line. Due to the limitation of accessibility, the pressure fluctuation of the fuel supply line was measured about 1 m upstream from the injection point. The signal from the microphone and pressure transducers were recorded with a digital oscilloscope and a spectrum analyzer. The resulting power spectrum at each condition was linearly averaged over 50 spectra with frequency resolution of 2 Hz. To correlate the acoustic frequency with combustion, a combination of a He-Ne diode-laser and a photodiode was set up to record the beam steering frequency resulting from the temperature fluctuations created by the dynamic flame structures at locations of interest.

Results and Discussion

Lean Blowout

The lean blowout test¹ over a range of H/d_f with three fixed annular air flows and without primary air injection is shown in Fig. 2. Excellent combustion stability is obtained for $H/d_f < 0.6$. For cavity $H/d_f > 0.6$, a dramatic increase of equivalence ratio at blowout indicates that the cavity has lost its natural stability. Clearly shown in the figure is the break point at $H/d_f =$

0.6 which agrees with the conclusion in trapping the vortex⁴. Without primary air injected directly into the cavity, the air that participates in the cavity combustion is from the entrainment of the annular air. The flame stability of the cavity is directly related to annular air and its interaction with the cavity. This interaction occurs at two regions; one is the shear layer along the interface between the annular and cavity regions, and the other is the possible impingement region near the afterbody. The shear layer disturbance increases with annular air velocity, and this can affect flame stability in the cavity. For a small cavity, the disturbance in the shear layer is less likely to have impact on the cavity. The increase of cavity length beyond $H/d_f = 0.6$ increases the possibility of disturbance from shear layer and flow impingement at the upstream face of the afterbody through unsteady interactions. The impingement of annular air results in high pressure fluctuations and high drag, and reduces the stability of the cavity combustion.

The natural entrainment of annular air into cavity region is very limited². For practical applications, it is required to inject air into the cavity to cool the liner and to control the cavity equivalence ratio for better combustor performance. The blowout test was conducted with annular air velocity ranging from 15 m/s to 100 m/s. Three fixed ratios between primary air and annular air (A_p / A_a) of 5%, 10%, and 15 % were tested over the entire range of annular air flow. Three cavity heights of $H/d_f = 0.36, 0.54$, and 0.64 were selected for the lean blowout test. In Fig. 3, the primary equivalence ratios, based on fuel and primary air at blowout were plotted against the annular air velocity. For the case of 5% primary air injection, the primary equivalence ratio at blowout increases dramatically when $U_a > 60\text{ m/s}$, and presents the same trend for three different cavity heights. It is noticed that the smaller cavity has better stability for $U_a < 60\text{ m/s}$; for $U_a > 60\text{ m/s}$, however, the stability of the small cavity becomes worse than that of the larger cavity. Blowout is sensitive to the annular air and the cavity aspect ratio under low primary air loading.

For cases of higher primary air injection of 10 and 15% of annular air flow, the equivalence ratio at blowout increases slowly with annular air flow and reaches a plateau for all three cavity heights. The annular air has less impact on blowout for higher primary air loading such as 10% and 15% cases due to increase mass injection, heat release, and enhanced mixing. It was also found that the increased primary air loading greatly enhances the combustion efficiency for a wide range of equivalence ratios.

During blowout tests, two types of blowout were observed. When the flame is near extinction under most

cases, the flame length is reduced as the fuel is reduced and finally blowout smoothly. Typically, several jet flames anchored from the injection plane located at the afterbody were observed. This type of smooth blowout generally represents a better stability with lower blowout limit. Occasionally, another type of blowout was observed which is completely abrupt during the blowout process. Instead of gradual disappearance of the shear layer flame, as observed in the smooth blowout case, the flame becomes intermittent and blows out abruptly even when the whole cavity is visually burning. This type of abrupt blowout is generally preceded by the higher level of audible noise and intermittent combustion. It is believed that the dynamic flame structure under various flow conditions and different cavity heights is critical to the understanding of combustion stability. It should be noted that the burner noise is reduced when the chimney is removed. The confinement of the burner may contribute to the noise through some acoustic coupling that may be very different in a practical system.

OH Imaging and Burner Noise

To illustrate the flame structure under low primary air flow, figure 4 shows the instantaneous OH images obtained at the fixed-flow condition of $U_a = 38$ m/s with $A_p/A_a = 1.2\%$, and a primary equivalence ratio of 1.49. Randomly selected OH images correspond to $H/d_f = 0.36, 0.54$, and 0.64 are shown in Fig. 4. a, b, and c, respectively. The OH images reveal complicated structures in the cavity region. The unburned fuel jet and the surrounding jet-mixing region originating from the afterbody are clearly identified. It should be emphasized that the flow is three-dimensional. It is evident that the fuel-jet reaches to the forebody with the smaller cavity and establishes an anchored shear-layer flame as shown in Fig. 4.a. The shear-layer flame becomes less obvious as the cavity becomes larger. For $H/d_f = 0.64$ (Fig. 4 c), the fuel jets do not have sufficient momentum to transport the fuel to the forebody. The OH images obtained at $\Phi_p = 3.0$ and 6.1 by increasing fuel flow are shown in Figs. 5 and 6, respectively. The cavity with $H/d_f = 0.36$, the excess fuel cannot be consumed inside the cavity, resulting in burning in the shear layer as shown in the Figs. 5.a and 6.a. The shear layer structures are very evident in the images with increased fuel flow. For $H/d_f = 0.54$, the increased fuel helps established the anchored shear-layer flame without obvious structures in the shear layer. The shear layer flame seems to shield the cavity from the annular air. For $H/d_f = 0.64$, shear-layer flame becomes evident with distinct structures when the fuel is increased. The shear-layer flame is still not anchored

around the forebody. The high dynamic OH structures near the afterbody are speculated to be related the dynamic flow impingement process. As the cavity height is increased, the fuel jet is pushed further toward the centerline of the burner, increasing the possibility of the flow impingement. The combination of the increase level of flow impingement and the lack of fuel transport toward the edge of the forebody is believed to be the reason of reduced flame stability. This result is consistent with the blowout data showing reduced flame stability at larger cavity height under low primary-air flow (Fig. 3).

Under the same air flows described in Figs. 4, 5, and 6, the level of burner noise measured by a microphone mounted outside the burner is shown in Fig. 7. For the low fuel flow ($\Phi_p < 3$), the noise level increases with cavity height. For $\Phi_p > 3$, the noise level is lowest at $H/d_f = 0.54$ and increases slightly at $H/d_f = 0.36$, and becomes much higher for $H/d_f = 0.64$. Comparing the noise level and the corresponding OH images in Figs. 4, 5, and 6, the noise level increases with the length-scale in the shear layer. The appearance of the chaotic OH structures, in the flow impingement region, is also related to the increase level of noise. The noise level typically increases with fuel flow for all three cavity height due to increase heat release, except at conditions of $\Phi_p = 1.5$ and 2.2 for $H/d_f = 0.54$, and 0.64 where unusual resonant noise was encountered. The power spectra at $\Phi_p = 1.5$ for three cavity heights are shown in Fig. 8. The dominant frequency bands centered about 245 and 277 Hz are observed for $H/d_f = 0.64$ and 0.54 , respectively, which are responsible for the higher noise level observed in Fig. 7. A weaker higher-frequency band around 472 Hz is observed for $H/d_f = 0.64$. For $\Phi_p > 3$, the burner noise results mainly from three frequency bands peaked around 340, 390, and 470 Hz for all three cavity heights. The system generates noise with multiple frequency, and mode switching occurred at different flow conditions. A combination of He-Ne diode-laser and photodiode was used to measure the temporal temperature fluctuation in the shear layer region also identified the same dominant frequencies as shown in Fig. 8. Therefore, it is believed that the dominant frequency is related to the structures in the shear layer. When the noise level is high, the fuel stream also records the same dominant burner frequency. The possible modulation of the fuel flow (heat release) could coupled to the system and amplify the burner noise. In a practical system, the pressure feedback into the fuel system could be eliminated with choked injection orifices.

The impact of primary air on noise level, under the flow condition of $U_a = 38$ m/s and fuel jet velocity of 3.6 m/s, is shown in Fig. 9. For a fixed fuel flow,

the noise level is reduced with increased primary air (reduce primary equivalence ratio) for $H/d_i = 0.36$ and 0.64 . The reduction of noise with increase primary air is more effective for larger cavity. The noise level for $H/d_i = 0.54$ remained relatively low and independent of the primary air flow. The mass addition of primary air, the enhancement of jet mixing inside the cavity, and reduction of large structure shear-layer burning seems to reduce to noise level to a certain degree.

Modeling using UNICORN

To better understand the noise characteristics of trapped-vortex burner, simulations were made using an axisymmetric code known as UNICORN (Unsteady Ignition and Combustion using ReactionNs)^{15,16}. It uses time-dependent axial-momentum, radial-momentum, continuity, enthalpy and species-conservation equations. Density is obtained by solving the state equation, while the pressure field at every time step is determined from pressure Poisson equations. Even though the governing equations are solved in an uncoupled manner, the species-conservation equations are coupled through the source terms during the solution process to improve the stability of the algorithm. Temperature- and species-dependent thermodynamic and transport properties are used. The enthalpy of each species is calculated from polynomial curve fits, while the viscosity, thermal conductivity, and diffusion coefficients of the species are estimated from the Lennard-Jones potentials. A simple global-chemical-kinetics model involving propane, oxygen, water, carbon dioxide and nitrogen is used. The specific reaction rate for this global reaction is written in Arrhenius form with a very large pre-exponential factor.

An orthogonal, staggered grid system with rapidly varying cell sizes in both the axial (z) and radial (r) directions is utilized for discretizing the governing equations. The momentum equations are integrated using an implicit QUICKEST (Quadratic Upstream Interpolation for Convective Kinematics with Estimated Streaming Terms) numerical scheme^{17,18} which is third-order accurate in both space and time and has a very low numerical-diffusion error. The enthalpy and species equations are integrated using a hybrid scheme of central and upwind differencing¹⁹. The resulting algebraic equations are solved individually using an iterative ADI (Alternative Direction Implicit) technique. The pressure field at every time step is accurately calculated by simultaneously solving the system of algebraic pressure Poisson equations at all grid points using the LU (Lower-Upper) decomposition technique.

In the experiments fuel and primary air were introduced into the cavity from distributed holes on the

afterbody. However, in the present axisymmetric simulations, these injection holes are grouped into three annular ring jets with the fuel jet sandwiched between the air jets. Based on the hole size and mean distance from the centerline, reconstructed annular jets of 1-mm thickness are used with the mid sections located at 11, 14, and 19 mm from the axis of symmetry on the afterbody. The annular air was issued into the burner through the annular gap formed between the forebody and the chimney. Flat velocity profiles are used at the annular and primary inflow boundaries. A simple extrapolation procedure with weighted zero- and first-order terms is used to estimate the flow variables at the outflow boundary. The usual no-slip, adiabatic, and chemically inert boundary conditions are applied at the walls.

A flow rate of 2686 slpm (corresponding to 38 m/s velocity) is used for the annular air. Three cases were studied in the present investigation. In the first, the fuel and primary-air flow rates were chosen such that the primary equivalence ratio (Φ_p) is equal to 1.5. The corresponding ratio between the primary and annular air flows (A_p/A_a) is 1.9%. The primary air flow was increased for the second case such that $A_p/A_a = 3.0\%$ and $\Phi_p = 1.0$. For the third case, the fuel flow was increased by keeping the annular and primary air flows same as those used for the first case. This gave $A_p/A_a = 1.9\%$ and $\Phi_p = 4.5$ for the third case. The cavity aspect ratio, H/d_i , is fixed at 0.54 for all the cases.

A grid system having 301 and 121 points in z and r directions, respectively is used in these simulations. The grid spacings in the cavity region are 0.3 and 0.25 mm in the z and r directions, respectively. Starting from a uniform initial flowfield in the burner, direct numerical simulations are made for the three cases described earlier. For obtaining results not biased by the initial uniform flow field, initial calculations for 20,000 time steps (corresponding to 0.08 s of real time) were discarded prior to recording the dynamic solutions. Calculations were then continued for another 20,000 time steps for data-analysis purposes.

The instantaneous temperature fields computed with a fast-chemistry assumption are shown in Figs. 10, 11, and 12 for the cases 1, 2, and 3, respectively. In each figure, three instantaneous plots are shown. Iso temperature contours are plotted in these figures using a gray-scale color table with dark black color representing either the maximum (2100 K) or the minimum (300 K) temperature and bright white color representing the median (1200 K) temperature. All three cases resulted in highly dynamic flows inside and outside the cavity region. For lower equivalence ratios (1.5 and 1.0), the combustion seems to be completed inside the cavity region. In contrast, the excess fuel in Case 3 is burning

in the shear layer formed between the annular and cavity flows and in the wake region of the afterbody. Note that the changes in the amount of mass injected into the cavity for the three cases (either fuel or primary air) are quite small compared to the amount of fluid that is being trapped in the cavity by the annular flow. Therefore, the differences in the dynamic characteristics noted in Figs. 10-12 are believed to be resulting from the heat release rather than the changes in mass injection. When all the injected fuel is burnt in the cavity region (Cases 1 and 2), the volumetric expansion is resulting in periodic ejection of packets of burnt gases from the cavity region yielding more unsteadiness to the cavity flow. As the heat release in the cavity decreases with the equivalence ratio, the cavity flow is being less disturbed. For Case 3, the fluid in the cavity is nearly trapped and the injected fuel is escaping along the shear layer. This isolation between the cavity flow and the annular flow allowed the instabilities to develop along the shear layer associated with the annular and primary flows.

Fast Fourier Transforms (FFT) of the temperature data collected at three locations inside the cavity for the three cases are shown in Figs. 13 a, b, and c, respectively. The locations at which the data are collected are marked with symbols x, 0, and * in Figs. 10-12. As expected, Cases 1 and 2 yielded frequency spectra that have peaks in the lower frequency range (< 500 Hz). Interestingly, the dominant frequency for Case 1 is occurring at 272 Hz which is very close to the noise frequency measured in the experiments for the similar conditions (see Fig. 8). In fact, the three instantaneous temperature plots shown in Fig. 10 are plotted with a phase difference of 3.67 ms, which represents a frequency of 272 Hz. From these temperature plots it may be noted that only the vortex near the corner of the afterbody but inside the cavity is repeated; suggesting that shedding of that corner vortex is causing the 272 Hz noise in the frequency spectra. It is also noted from the animation of several sequentially taken temperature plots that annular air is periodically entering the cavity from the afterbody corner and hot products are leaving the cavity periodically from a location closer to the forebody.

The higher-equivalence-ratio case (Case 3) yielded FFT spectra having peaks in the low frequency range (< 500 Hz) and high frequency range (> 2500 Hz). Interestingly, the distinctive peak appearing at ~ 480 Hz for this case is also resulting from the corner vortex close to the afterbody. However, the magnitude associated with this frequency is less compared to that predicted for lower-equivalence-ratio cases. This shift in frequency from 272 to 480 Hz and the reduction in noise

level with equivalence ratio are also observed in the experiments.

Finally, the time averaged temperature plots for the three cases are shown in Figs. 14 a, b, and c, respectively. Data collected over 20,000 time steps are used for generating these plots. The time-averaged temperature for all three cases is quite smooth and all the instantaneous vortical structures have disappeared. Figure 14 clearly indicates that all the injected fuel is burning in the cavity region for Cases 1 and 2 and only a fraction of it is burning in the cavity region for Case 3.

Conclusions

For low primary air injected into the cavity, the blowout and burner noise are sensitive to the cavity size. The larger cavity is more susceptible to the disturbances from the shear layer and the flow impingement on afterbody. Burner noise is reduced by increasing primary air flow, and the effect is more pronounced for cavity $H/d_f > 0.6$. The burner noise frequency is related to the dynamic structures in shear layer and flow impingement regions near the afterbody from both experimental and numerical observations. Cavity size of $H/d_f = 0.54$ generates less noise level for fuel-rich case. It is believed that for a given cavity size, there is a threshold cavity mass-loading which generate minimum noise. Deviation from that threshold cavity-loading will probably increase noise level resulted either from the shear layer or from the flow impingement regions. For future study, finite-rate chemistry model will be utilized in the numerical code to predict the dynamic heat release. More conditions should be examined to further understand the dynamic behavior of trapped-vortex burner.

Acknowledgments

This work was supported by Air Force Contract F33615-95-C-2507 and the AFOSR Aerospace Sciences Division. The authors would like to thank G. J. Sturgess for helpful discussions, and D. D. Trump and K. Grinstead for experimental support.

References

- ¹Hsu, K. Y., "Characteristics of a Trapped-Vortex Combustor," *AIAA Journal of Propulsion and Power*, Vol. 14, No. 1, 1998, pp. 57-65.
- ²Sturgess, G. J. and Hsu, K. Y., "Entrainment of Mainstream Flow in a Trapped-Vortex Combustor," AIAA Paper 97-0261, Reno, NV, 1997.

- ³Sturgess, G. J., and Hsu, K. Y., "Combustion Characteristics of a Trapped Vortex Combustor," *Symposium of Gas Turbine Combustion, Emissions and Alternative Fuels, North Atlantic Treaty Organization*, Lisbon, Portugal, 1998, pp. 44.1-44.13.
- ⁴Little Jr., B. H., and Whipkey, R. R., "Locked Vortex Afterbody," *J. Aircraft*, Vol. 16, No. 5, 1979, pp. 296-302.
- ⁵Mair, W. A., "The Effect of a Rear-Mounted Disc on the Drag of a Blunt-Based Body of Revolution," *The Aeronautical Quarterly*, Vol. No. 1965, pp. 350-360.
- ⁶Gharib, M., and Roshko, A., "The Effect of Flow Oscillation on Cavity Drag," *J. Fluid Mech.*, Vol. 177, 1987, pp. 501-530.
- ⁷Yu, Y. H., "Measurements of Sound Radiation from Cavities at Subsonic Speeds," AIAA Paper 76-529, Palo Alto, CA, 1976.
- ⁸Komerath, N. M., Ahuja, K. K., and Chambers, F. W., "Prediction and Measurement of Flow over Cavities - A Survey," AIAA paper 87-0166, Reno, NV, 1987.
- ⁹Sarohia, V., and Massier, P. F., "Investigation of Pressure Oscillations in Axi-symmetric Cavity Flows," Jet Propulsion Laboratory, HDL-CR-77-025-1, 1977.
- ¹⁰Rockwell, D., and Naudascher, E., "Review - Self-sustaining Oscillations of Flow Past Cavities," *Transaction of ASME*, Vol. 100, 1978, pp. 152-165.
- ¹¹Knisely, C., and Rockwell, D., "Self-Sustained Low Frequency Components in an Impinging Shear Layer," *J. Fluid Mech.*, Vol. 116, 1982, pp. 157-186.
- ¹²Rockwell, D., and Knisely, C., "The Organized Nature of Flow Impingement upon a Corner," *J. Fluid Mech.*, Vol. 93, No. 3, 1979, pp. 413-432.
- ¹³Rockwell, D., "Oscillation of Impinging Shear Layers," *AIAA Journal*, Vol. 21, No. 5, 1983, pp. 645-664.
- ¹⁴Sarohia, V., and Massier, P. F., "Control of Cavity Noise," AIAA Paper 76-528, Palo Alto, CA, 1976.
- ¹⁵Roquemore, W. M., and Katta, V. R., "Role of Flow Visualization in the Development of UNICORN Computational Fluid Dynamics Model," Proceedings of Visual Society of Japan, SPIE 98, Yokohama, Japan, Dec. 6-9, 1998.
- ¹⁶Katta, V. R., and Roquemore, W. M., "Study of Trapped-Vortex Combustor Using Detailed Chemical Kinetics," *AIAA J. of Propul. Power*, Vol. 14, No. 3, pp. 273-281, (May-June 1998).
- ¹⁷Leonard, B. P., "A Stable and Accurate Convective Modeling Procedure Based on Quadratic Upstream Interpolation," *Computer Methods in Applied Mech. and Engineering*, Vol. 19, 1979, p. 59.
- ¹⁸Katta, V. R., Goss, L. P., and Roquemore, W. M., "Numerical Investigations of Transitional H₂/N₂ Jet Diffusion Flames," *AIAA Journal*, Vol. 32, 1994, pp. 84-94.
- ¹⁹Spalding, D. B., "A Novel Finite Difference Formulation for Difference Expressions Involving Both First and Second Derivatives," *International Journal of Numerical Methods in Engineering*, Vol. 4, 1972, p. 551.

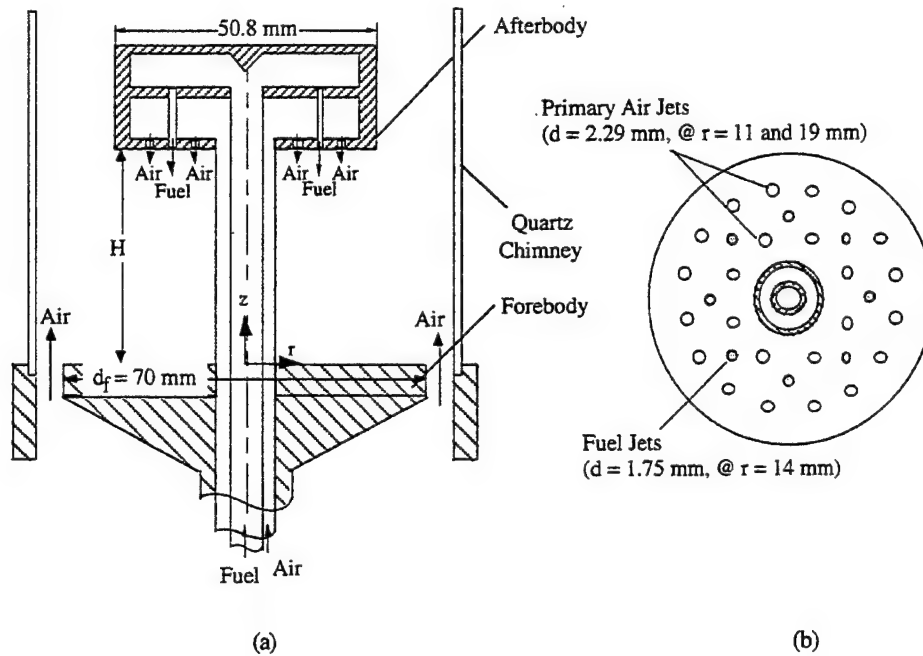


Figure 1. Schematics of (a) Trapped-Vortex Combustor, and (b) Injection Face of Afterbody

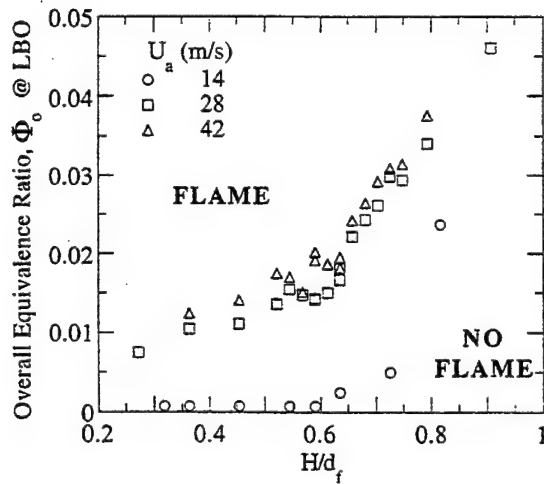


Figure 2. Lean Blowout without Primary Air

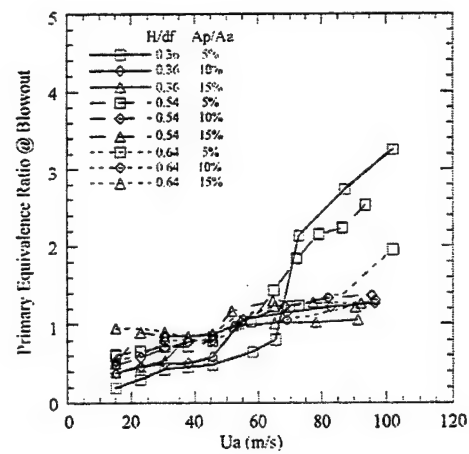


Figure 3. Lean Blowout with Primary Air

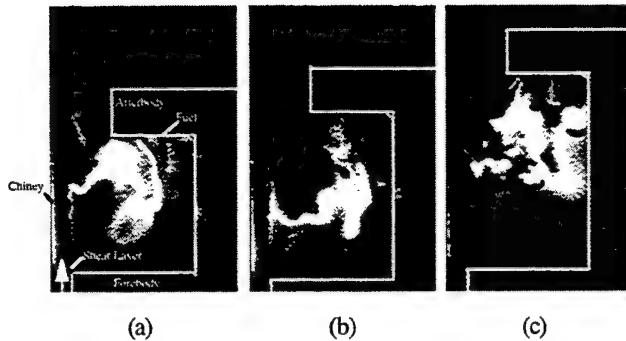


Figure 4. OH Images of $H/df =$ a) 0.36, b) 0.54, and c) 0.64. $U_a = 38$ m/s, $Ap/Aa = 1.2\%$, and $\Phi_p = 1.5$.

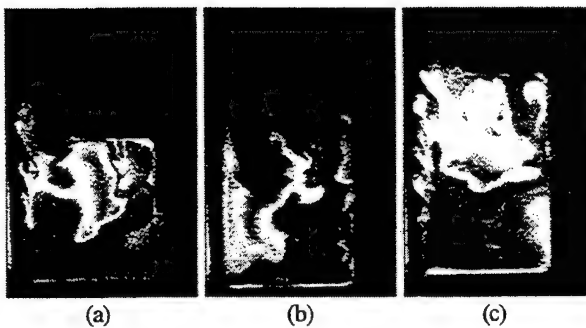


Figure 5. OH Images of $H/df =$ a) 0.36, b) 0.54, and c) 0.64. $U_a = 38$ m/s, $Ap/Aa = 1.2\%$, and $\Phi_p = 3.0$.

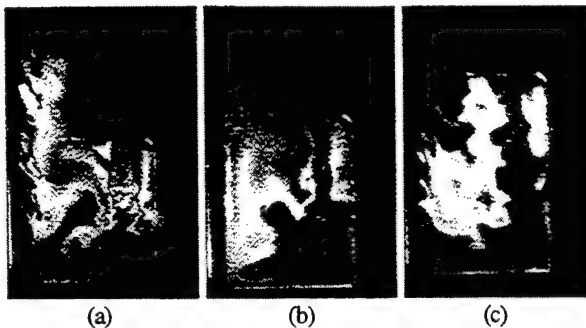


Figure 6. OH Images of $H/df =$ a) 0.36, b) 0.54, and c) 0.64. $U_a = 38$ m/s, $Ap/Aa = 1.2\%$, and $\Phi_p = 6.1$.

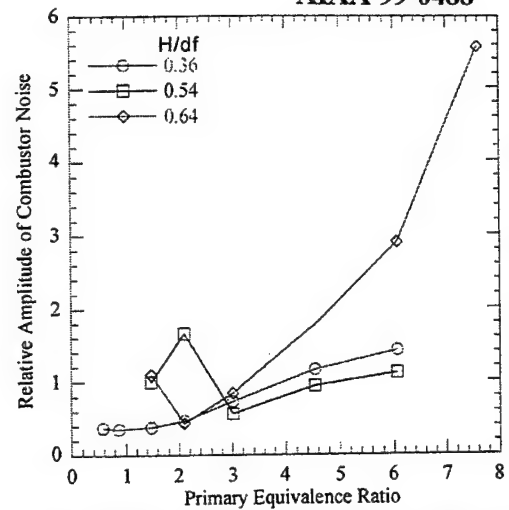


Figure 7. Combustor Noise Measured at $U_a = 38$ m/s and $Ap/Aa = 1.2\%$

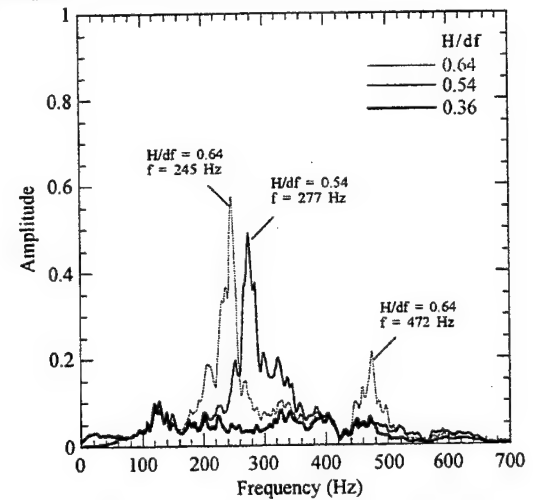


Figure 8. Power Spectrum of Combustor Noise at $U_a = 38$ m/s, $Ap/Aa = 1.2\%$, and $\Phi_p = 1.5$

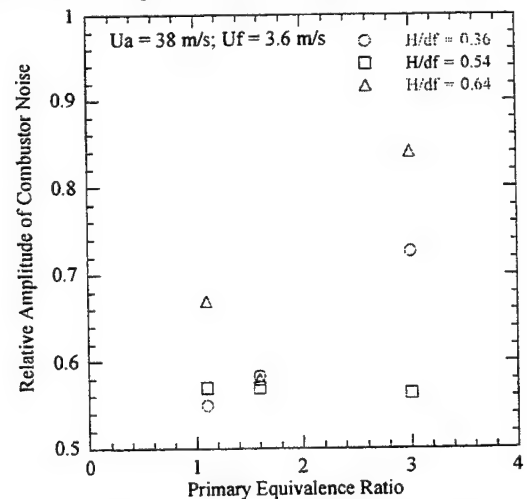


Figure 9. Effect of Primary Air on Combustor Noise at $U_a = 38$ m/s, $U_f = 3.6$ m/s.

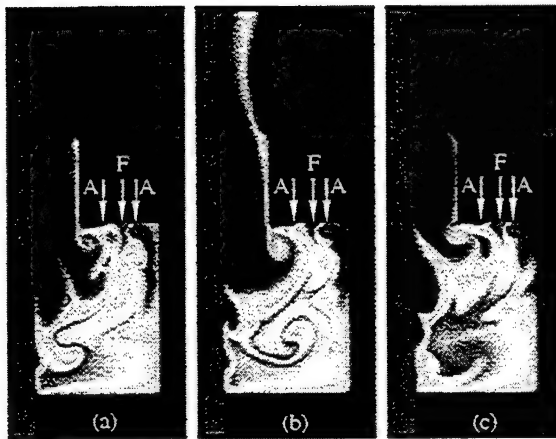


Fig. 10. Instantaneous temperature plots for the case $A_p/A_a = 1.9\%$ and $\Phi_p = 1.5$. (a) t_0 ms, (b) $t_0 + 3.7$ ms, (c) $t_0 + 7.4$ ms.

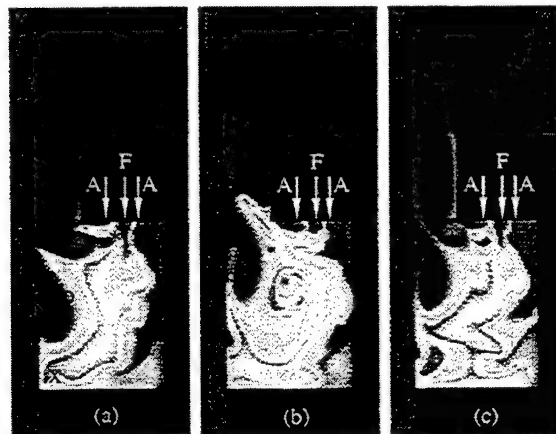


Fig. 11. Instantaneous temperature plots for the case $A_p/A_a = 3.0\%$ and $\Phi_p = 1.0$. (a) t_0 ms, (b) $t_0 + 3.7$ ms, (c) $t_0 + 7.4$ ms.

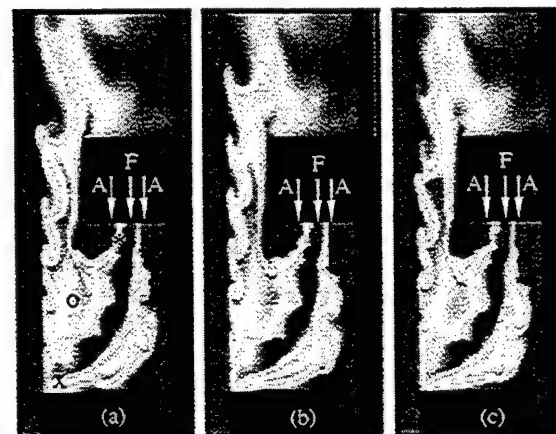
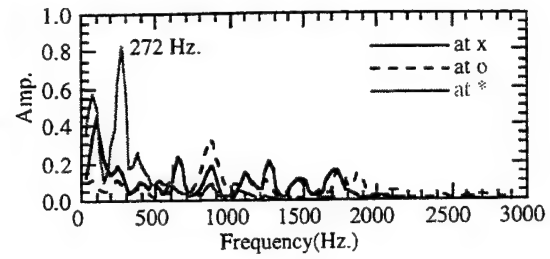
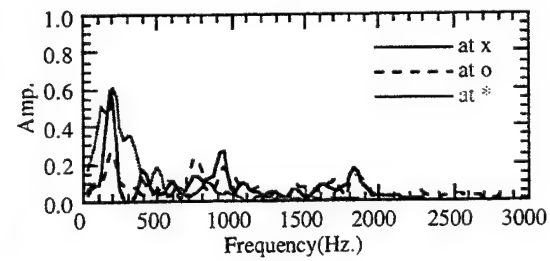


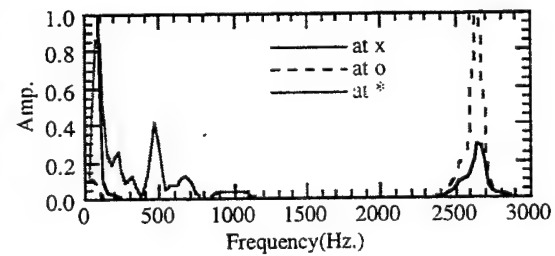
Fig. 12. Instantaneous temperature plots for the case $A_p/A_a = 1.9\%$ and $\Phi_p = 4.8$. (a) t_0 ms, (b) $t_0 + 0.8$ ms, (c) $t_0 + 1.6$ ms.



(a)



(b)



(c)

Fig. 13. Frequency spectra obtained at different locations in the cavity for the cases (a) $A_p/A_a = 1.9\%$, $\Phi_p = 1.5$, (b) $A_p/A_a = 3.0\%$, $\Phi_p = 1.0$, (c) $A_p/A_a = 1.9\%$, $\Phi_p = 4.8$.

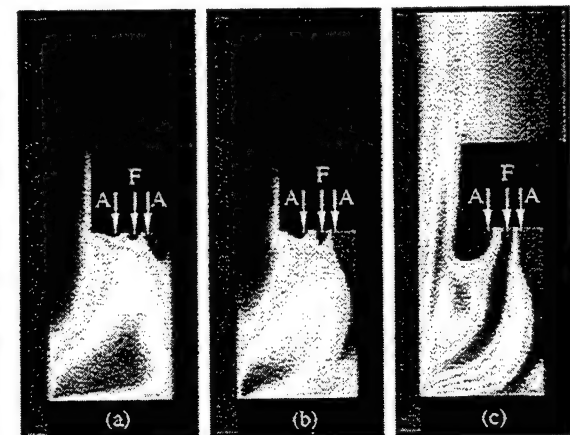


Fig. 14. Time-averaged temperature for the cases (a) $A_p/A_a = 1.9\%$, $\Phi_p = 1.5$, (b) $A_p/A_a = 3.0\%$, $\Phi_p = 1.0$, and (c) $A_p/A_a = 1.9\%$, $\Phi_p = 4.8$.

3.1.3.2 Lean Blowout and Emission

3.1.3.2.1 Generic Combustor. In the paper entitled "The Role of Transverse Air Jets in the Formation of Gas Turbine Emissions" (see pp. 417-428), results are presented for emission and lean blowout measurements in the primary zone of a generic combustor to determine the effects of circular combustion air jets in a range of sizes. In the companion paper entitled "Emissions and Operability Trades in the Primary Zones of Gas Turbine Combustors" (see pp. 429-441), the measured indices of NO_x and CO generated in the primary zone of the generic combustor at simulated high-power conditions are reported. A subsequent publication entitled "Study of Flame Stability in a Step Swirl Combustor" (see pp. 442-449) discusses the significance and application of anchored and lifted flames to combustor stability and LBO in practical gas turbine combustors. Extensive parametric investigations of experimental lean blowout in a generic primary zone for two major combustion air-jet patterns are reported in the paper entitled "Influences of Airblast-Atomizing Fuel Injector Design on Primary Zone Flame Characteristics at Blowout" (see pp. 450-465). The basis for a stochastic method for correcting the combustion reaction chemistry of Jet-A fuels to account of fuel/air unmixedness in liquid-fueled turbine combustors is discussed in the paper entitled "An Account of Fuel/Air Unmixedness Effects on NO_x Generation in Gas Turbine Combustors" (see pp. 466-480).



AIAA 96-0705
The Role of Transverse Air Jets
in the Formation of
Gas Turbine Emissions

D.T. Shouse, C. Frayne, J. Stutrud
Aero Propulsion and Power Directorate
Wright-Patterson AFB, Ohio

S. Gogineni
Systems Research Laboratories
Dayton, Ohio

G.J. Sturgess
Innovative Scientific Solutions Inc.
Beavercreek, Ohio

34th Aerospace Sciences
Meeting & Exhibit
January 15-18, 1996 / Reno, NV

THE ROLE OF TRANSVERSE AIR JETS IN THE FORMATION OF GAS TURBINE EMISSIONS

D. Shouse, C. Frayne, J. Stutrud
Aero Propulsion and Power Directorate
Wright-Patterson AFB, Ohio

S. Gogineni
Systems Research Laboratories
2800 Indian Ripple Road
Dayton, Ohio

G.J. Sturgess
Innovative Scientific Solutions Inc.
3845, Woodhurst Court,
Beavercreek, Ohio

Abstract

Results are presented of emissions and lean blowout measurements in a generic combustor primary zone for the effects of opposed, circular combustion air jets of a range of sizes, positioned half a dome height downstream from the dome. The primary zone was operated at simulated engine high power conditions, and representative dome and liner pressure drops. It is shown that most of the NO_x is generated in the jets. Although an optimum jet size is identified, the lowest overall emissions resulted from a no combustion air jet configuration: air jets are necessary however, to confer lean blowout stability and short flame length.

Introduction

In 1987 the U.S. Air Force Wright Laboratory, Aero Propulsion and Power Directorate (WL/PO), Wright-Patterson Air Force Base, Ohio, established the *Combustor Design Model Evaluation (CDME) Program*. This effort is a comprehensive joint Government, Industry and University research program aimed at improving the design and analysis capabilities for the combustors of aircraft gas turbine engines. The CDME program is addressing many important aspects of combustor design.

One study that is currently in progress is an investigation into the minimization of engine exhaust emissions, and the relationships between generation of these emissions and combustor operability characteristics. As part of this study a broad-ranging

investigation of combustor primary zone behavior is being conducted.

Program Objectives

The overall intent of this part of the CDME program is to understand the detailed behavior of the major flame holding of a modern generic combustor for aircraft gas turbine engines, and to establish an appropriate database suitable for design purposes.

Test Vehicle

A relatively simple combustor developed under an earlier program¹ has been adapted for the experimental study of the influence of simulated engine primary zone flow structures on the emissions generation and lean stability characteristics.

The combustor consists of a single representative fuel injector and its associated dome interface, mounted in a plain bulkhead. The injector is a high-swirl airblast atomizer², and the dome interface consists of a small, discrete-jet swirler co-annular with the injector, together with a dome heat shield fed with cooling air that is discharged radially across the bulkhead face. The cross-section of the combustor is square for optical access by laser diagnostics, but generous fillets are provided in the corners to suppress vorticity generation that might result in spurious flameholding. The hydraulic diameter is 153 mm and the length is 490 mm. The combustor outlet is restricted by a 45 percent geometric blockage orifice plate to provide representative back pressure of the unsimulated portion of a real combustor.

The combustor is mounted horizontally, and the top and bottom walls are removable, uncooled metal plates that accommodate appropriate arrays of combustion air jets. One combustor side-plate (at 90 degrees to the liner plates containing the air jets) contains a fitting for application of a torch ignitor; the other side contains a full-length quartz window for visual access.

Figure 1 shows the combustor with its air entrance conditioning unit. Air supplies to the dome and the combustion air jets are separately metered, and may be electrically preheated to a maximum temperature of about 500F (533K).

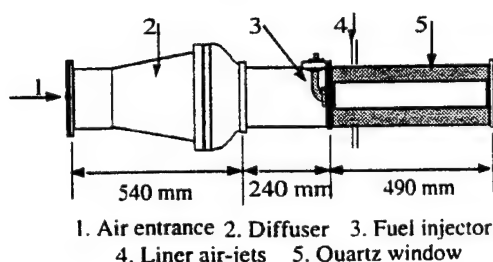


Figure 1a): Laboratory-Scale Gas Turbine Combustor

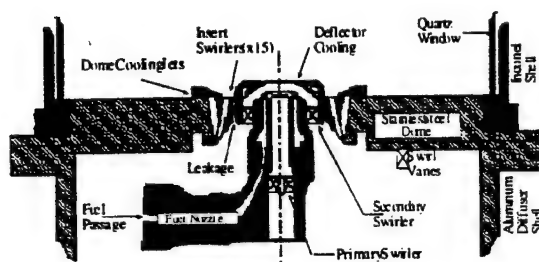


Figure 1b): Combustor Fuel Injector and Dome

Engine Power Simulation

The efficacy of the combustor for its intended purpose is discussed in detail in Reference 2. The combustor represents a "single-cup" planar segment of an annular combustor, and simulates the primary zone only.

It is operated at atmospheric pressure for convenience and cost reasons. Engine high power conditions are simulated by closely matching Spalding's partial modeling flow criterion K_f ,

reasonably approximating the temperature rise term $\Delta T/T_{in}$, and by substituting gaseous propane for liquid JP/Jet fuel. Together, these ensure that engine flow patterns are closely approximated and that liquid evaporation is not a problem. It was concluded that the combustor can reproduce reasonably well and to an acceptable degree the flow patterns of an engine combustor.

Description of the Rig

The test combustor is installed horizontally in a test cell at Wright Patterson Air Force Base, Ohio. Reference 2 gives a detailed description of the rig and facility in which the combustor is installed. Of relevance here is the fact that inlet air was dried to very low dew points prior to entering the compressors.

Experimental Variables

The array of combustion air ports presently to be described is confined to an opposed pair of circular flush holes (in upper and lower liners) placed inline with the fuel injector centerline. Diameters of 0.25 in. (6.35 mm), 0.375 in. (9.53 mm), 0.50 in. (12.70 mm) and 0.75 in. (19.05 mm) are reported. Although these pairs of jets could be situated 1.0, 0.75 and 0.5 dome heights (H_d) downstream from the dome, only the latter position is used in the results to be presented.

The inlet air temperature was held constant at a nominal 500F (533K). This value was selected in order to first, satisfy the simulation criteria, and second, to ensure the generation of sufficient NOx without a large burnup of CO; thus, trends and effects in these two pollutants could be detected easily and measured accurately.

Pressure drop across a combustor is in practice, not a free variable but is set by engine performance considerations. Generally, the allowable pressure drop across a dome is a little higher than that across liners due to the recovery of some dynamic head from the compressor. For the majority of the work to be presented the dome pressure drop was held fixed at a nominal value of 4.3 percent of the upstream pressure, and the liner pressure drop was 3.0 percent. These values are representative of typical engine conditions. Under these conditions all of the transverse jets with different initial diameters penetrated to the combustor centerline.

To extend the generality of the results the normal range of liner air pressure drops for each hole size was 1-5 percent of the upstream pressure. To explore the effects of jet turbulence this range was extended to as high as 12 percent for the 0.5 in. (12.70 mm) hole.

Emissions Measurements

The emissions sampling probe is a water-cooled, quick-quench, single-point type, and is made of stainless steel with an Inconel tip. The sample enters a converging nozzle of orifice diameter 0.059 in. (1.5 mm), which then diverges to the 0.180 in. (4.6 mm) I.D. of the stainless tube. This arrangement results in a supersonic expansion which reduces the gas stream temperature. Together with the water cooling of the probe, this achieves quenching of chemical reactions.

The sample is transferred from the probe by heated lines that avoid condensation, to the emissions measuring equipment, which is fairly standard. Again, detailed descriptions are given in Reference 2.

The axial measurement plane for gaseous emissions was 14 in. (356 mm) downstream from the face of the dome. Kinetics calculations indicated that at this position the bulk NOx was not changing too rapidly, and CO consumption rates were reasonably slow. Furthermore, at this axial station the profiles of measured emissions were flat enough over the entire range of equivalence ratios (for all jet sizes at the $H_d/2$ position) for centerpoint and area-weighted mean values to be in exceptionally close agreement, thus permitting centerpoint values to be used for economy, (errors less than ± 10 percent). Since the emissions probe was introduced into the combustor from the rear through the exit orifice plate, the extent of the radial traverses was determined by the size of this orifice plate. The extent of the radial profile traverses was ± 1.75 in. (± 44 mm) from the combustor centerline. Traverses were made both horizontally and vertically.

Comparisons were made of the metered fuel/air ratios to the measured exhaust fuel/air ratios based on the carbon balance. The agreements were better than 10 percent for metered equivalence ratios of 1.0 and less.

As the inlet air was dried in the facility prior to entering the rig the NOx levels to be quoted are all dry values.

Test Procedure

For each air-port size, axial position and pressure drop, the fuel flow rate was varied to cover a range of overall equivalence ratios such that the anticipated minimum in the CO-curve and the maximum in the NOx-curve could be fully established.

It is usual to present emissions measurements as a function of an appropriate equivalence ratio. The presumption is that the flow patterns in the combustor are established by the geometry and remain unchanged with this method (varying fuel flow rate) of operating, thus making equivalence ratio a good single descriptor of the emissions. Since the combustion air jets established by the different liner hole sizes all penetrated to the combustor centerline, this is a reasonable supposition. However, the high engine power simulation assumed that flow patterns were not affected to first order by the fuel flow. With a gaseous fuel having flow rate as a prime operational variable, this assumption must be verified due to fuel momentum considerations.

It is difficult to establish a true uniqueness test of the data due to the large number of variables involved. However, at fixed dome and liner pressure drops turbulence generated will be fixed, and variations in NOx with overall equivalence ratio for fixed jet size can be compared against variations in NOx with overall equivalence ratio for fixed fuel flow rate but with a range of combustion air jet initial diameters, i.e. variable airflow.

Such a comparison is complicated by the postulated mechanism for jet NOx formation² (see below also), which is proportional to jet size. However, provided that jet NOx is not a large proportion of the total NOx (small jets and/or low equivalence ratios), and, provided that the comparison is restricted to jet sizes equal to or less than the fixed jet size of the comparison, and that the range of constant fuel flows examined is selected to be within the range of flows for the fixed jet data, such comparisons may be made.

Figure 2 compares NO_x emission indices (EI's in gm NO_x as NO₂/kg fuel burned) data for the 0.5 in. (12.7 mm) jet case over a range of equivalence ratios obtained by varying fuel flow, with NO_x data for 0.5 in. (12.7 mm), 0.375 in. (9.5 mm) and 0.25 in. (6.35 mm) at fixed fuel flow rates of 0.075, 0.100, 0.125 and 0.150 lbm/min. (0.034, 0.045, 0.057 and 0.068 kg/min. respectively). Rich and lean points are included.

The plotted data in Figure 2 on both lean and rich sides correlate within the measurement accuracy and repeatability of the single-test data scatter².

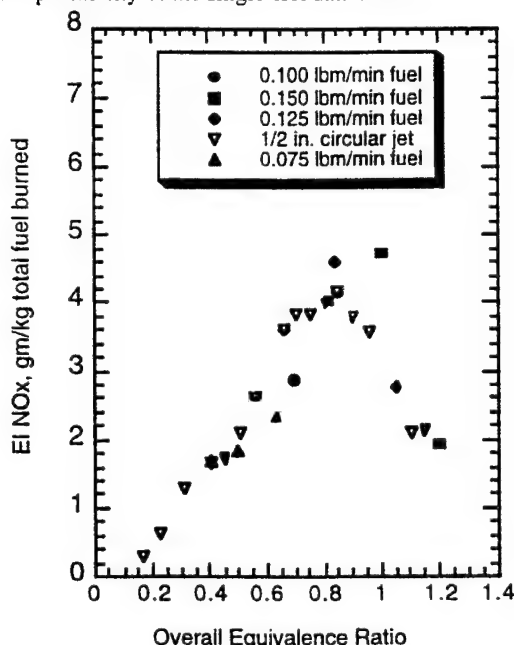


Figure 2: Uniqueness Plot Based on NO_x, to Evaluate Fuel Momentum Effects

The conclusion can therefore be drawn that fuel momentum does not affect the flow field, and as a consequence, that for fixed pressure drop, equivalence ratio is a unique parameter describing NO_x.

Dome Characteristics

The combustor can be operated with zero combustion air jets to obtain the characteristics of the dome alone.

Figure 3 is a plot of the emission index (EI) of NO_x for the dome alone, as a function of dome equivalence ratio (metered). As expected, the measured NO_x reaches a peak of about 3.6 at a dome equivalence ratio of 0.82. As the dome equivalence

ratio exceeds unity NO_x falls due to decreasing bulk flame temperatures, but unburned fuel leaves the combustor.

Also shown on Figure 3 are calculated NO_x curves using two approaches. First, assuming "experimentally-perfect premixing" of fuel and air, and second, representing the dome flow field as a reactor network having a degree of partial stirring. For the "experimentally-perfect premixing" case the empirical correlation of Roffe & Venkataramani³ for lean propane and air systems was used. In this correlation the residence times were estimated for volumes based on observed flame dimensions. The reactor network was based on computational fluid dynamic calculations for this injector and hole pattern¹, with reactor dimensions based on observed flame dimensions and having fuel heating value reduced to account for estimated heat losses from the combustor. The network consisted of a well-stirred reactor with a parallel plug-flow reactor that processed 13 percent of the total flow that was recirculated back into the dome.

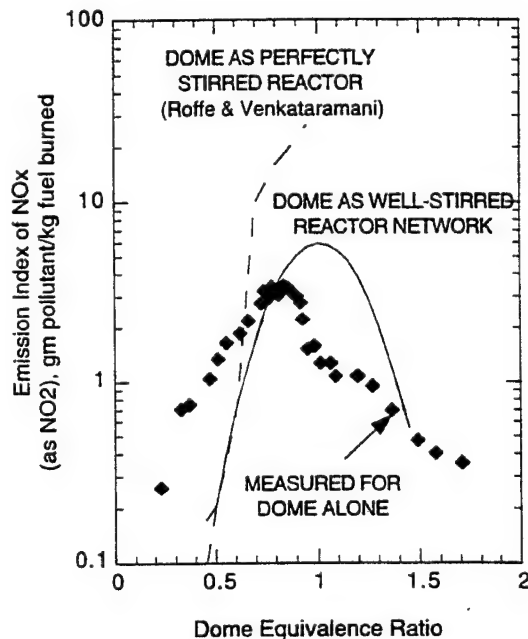


Figure 3: Assessment of Dome NO_x Characteristics

The effect of improved mixing as represented in the two calculations, is to increase the peak NO_x and to narrow the NO_x curve across equivalence ratio; furthermore, the peak NO_x occurs at dome equivalence ratios around unity.

Comparing the measured dome NOx against the two calculations demonstrates that despite the use of a gaseous fuel and the intimate association of fuel and air in the fuel injector, the fuel is burned in the dome in far from premixed form, and consequently, exhibits some degree of diffusion flame burning.

Overall Burning Characteristics

In Reference 2 the NOx data were analyzed in terms of a rich/lean burning system, where excess fuel from a fuel-rich dome was assumed to burn fuel-lean in the combustion air jet system, as was described in Reference 4. If this is so, the question concerning the nature of the flame in these two burning zones arises. It was assumed in Reference 2 that it was the same in both zones, i.e. based on the previous section, flames exhibiting some degree of diffusion burning.

Figure 4 is a plot of overall NOx EI's for several jet systems at $H_d/2$ from the dome, including the dome alone, plotted against dome equivalence ratio, at fixed pressure drops.

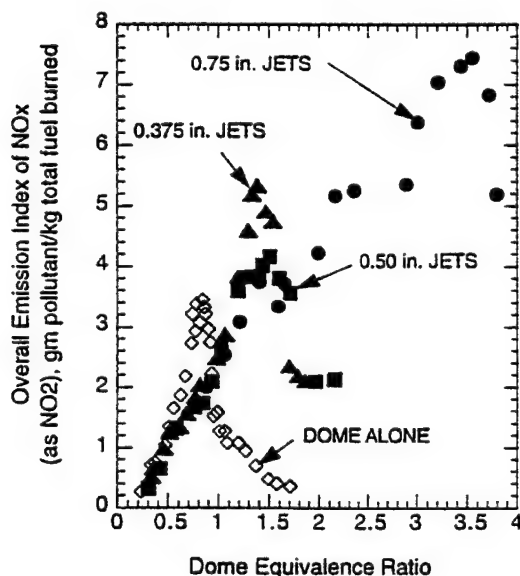


Figure 4: Overall Burning Characteristics for NOx

The characteristic of the dome-alone NOx is that from Figure 3. The characteristics for the individual combustion air jet cases collapse onto a common curve for dome equivalence ratios up to about 1.15. For dome equivalence ratios of 0.55 and less, this collapsed data is co-incident with the dome

alone data. This behavior indicates that basic flame characteristics in the dome are unaffected by the presence of the jets.

The NOx peak for jets being present is shifted to higher dome equivalence ratios, in the range 1.3 - 1.55, from the nominal 0.82 equivalence ratio for the dome alone. The levels of NOx at the peak, and the subsequent behavior on the dome rich-side of the peak, are dependent on the individual jet size.

The shifted NOx peak from 0.82 with no jets to 1.3 - 1.55 dome equivalence ratio with jets, indicates that in addition to peak temperatures being reached at lower equivalence ratios (0.82 rather than about 0.92-1.0) due to unmixedness effects, some of the combustion jet air is actually active in the dome. The co-incidence of the data for individual jets at equivalence ratios less than 1.15 suggests that the dome aerodynamics are not strongly influenced, or least modified, by the details of the air jets, i.e. that any additional air introduced into the dome takes part in chemical reactions in a region somewhat separate from the jets themselves, and, that this region is not far upstream in the dome itself. Flame photographs identify a small luminous region on the injector centerline, just upstream of the confluence of the transverse combustion air jets. CFD analysis of this type of combustion system¹, identifies a well-mixed recirculation bubble in this position. This bubble could be where the small quantity of jet air is utilized in the dome. The centerline penetration of all jets at 3 percent liner pressure drop ensures that this bubble is present whenever the jets are present.

It will be noted that for the 0.75 in. (19.05 mm) jets, where, as was shown in Reference 2, most of the total NOx produced originates in the jets, high levels of NOx are eventually produced after the initial NOx-peak that denotes a stoichiometric dome. This is mainly due to jet NOx as the equivalence ratio increases. These high levels of NOx fall onto the same general curve as for the other jets, and for the dome alone at dome equivalence ratios less than 0.55. The existence of this "common curve" indicates that that there is no substantial difference in the flame characteristics of dome and jets, and, that the NOx produced in both regions is produced by the same kinetic mechanism.

Jet System Behavior

In Reference 2 the adopted analysis strategy for emissions data reduction was one of

treating the generic primary zone as being a quasi-staging¹, rich/lean burning combustor. The dome region was generally fuel-rich, and the importance of NOx generation in the "lean burning" combustion air jet system itself was highlighted.

This aspect is illustrated here in Figure 5 where the percentage of total NOx that is generated in the jets for each initial jet size is plotted in terms of overall equivalence ratio. The jet NOx was obtained from the total NOx at given overall equivalence ratio by subtracting from it the dome-alone NOx at an appropriate dome equivalence ratio. Such a procedure is only valid if the predominant mechanism for NOx generation is the same in both regions of the combustor. As was demonstrated above, this appears to be the case. The percent NOx was obtained by multiplying the calculated emission indices for the jets by the mass flow rate of fuel burned in the jets, and dividing by the measured overall emission index for the primary zone at the same equivalence ratio, multiplied by the total fuel flow rate.

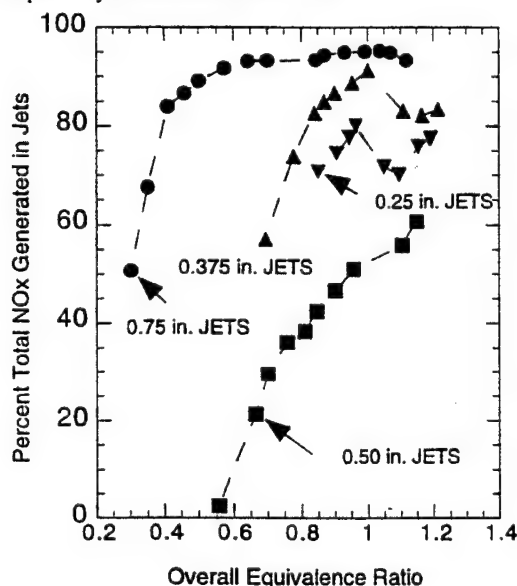


Figure 5: Contribution of Jet-Generated NOx

Figure 5 shows that for the 0.75 in. (19.05 mm) initial jet size more than half of the NOx originates in the jets for all operating equivalence ratios; for the 0.50 in. (12.7 mm) jet the jet NOx only reaches 50 percent of the total for a stoichiometric primary zone. The general behavior is for the percent jet NOx to increase with overall equivalence ratio, and to do so rather steeply initially until a plateau level is reached. This behavior is

repeated for each jet system, and the plateau level is lower for smaller jets than for the larger jets. For the 0.75 in. (19.05 mm) jets the plateau is for about 95 percent jet NOx; for the 0.375 in. (9.53 mm) jets it is about 85 percent, and for the 0.25 in. (6.35 mm) jets it is about 75 percent. The 0.5 in. (12.70 mm) jet system has not yet reached its plateau level in the range of overall equivalence ratios covered. This jet system is the exception to the general behavior. If overall equivalence ratio is increased above unity, percent combustion air jet NOx contribution to overall NOx would eventually start to fall as the jet system became over-rich. This is clearly evident for the two smaller jets.

The 50 percent jet NOx condition is reached at overall equivalence ratios that increase with decreasing jet size, and that corresponds to the condition where the dome equivalence ratio exceeds unity in each case. For the 0.50 in. (12.70 mm) jet system the 50 percent jet NOx condition is reached at an overall equivalence ratio of 0.96. From stoichiometry plots this corresponds to a dome equivalence ratio of 1.7. This jet system generates lower jet NOx levels at all overall equivalence ratios than either larger or smaller jets. Clearly, the 0.5 in. (12.70 mm) jet system behaves differently to all of the others.

Figure 6 is a plot from Reference 2 with additional information added for the smaller jets. The plot shows the EI's of jet NOx for each jet as a function of jet equivalence ratio.

For jet equivalence ratios less than 0.8-0.9 (where a NOx peak is expected) the NOx for the 0.375 (9.53 mm), 0.50 in. (12.7 mm) and 0.75 in. (19.05 mm) jets is essentially independent of jet equivalence ratio. This suggests that the fuel burned in the jets at these lower equivalence ratios is reacted in stoichiometric interfaces associated with the fresh air entering through the jets. The jet NOx EI's consistently begin to decrease at higher jet equivalence ratios. This is because unburned fuel is now exiting the combustor. The jet NOx EI plateau levels for the lower jet equivalence ratios decrease with increasing jet initial diameter, with the exception of the 0.50 in. (12.7 mm) jet system, which again has the lowest values. For the 0.25 in. (6.35 mm) jets the jet NOx EI's continuously decrease with increasing jet equivalence ratio over the entire range covered. This suggests that there is something different about this jet system.

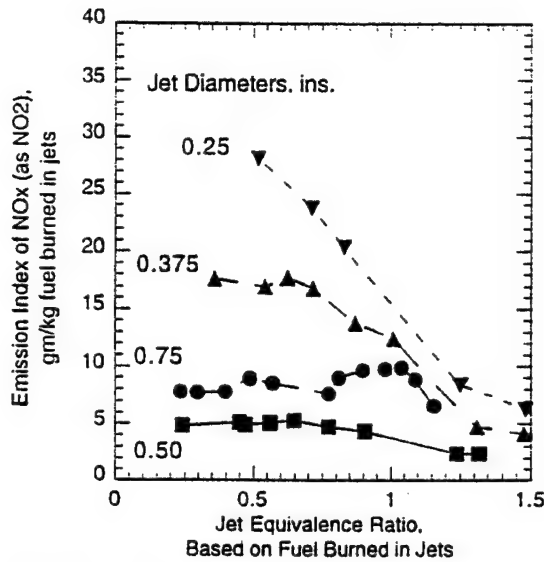


Figure 6: Demonstration of Stoichiometric Burning in Jet Systems

When the absolute jet NOx in gm/min. is plotted against jet equivalence ratio, Figure 7, the behavior exhibits the characteristic equivalence ratio dependency, with NOx peaks occurring in the jet equivalence ratio range of 0.8-1.0. The absolute NOx levels decrease with decreasing jet size, which is the opposite behavior to that of the EI's. This is accounted for by the different amounts of the total fuel actually burned in the jets, where the 0.75 in. (19.05 mm) jet burns the most fuel and the 0.25 in. (6.36 mm) the least, and where, for a given jet size, the amount of jet fuel decreases with decreasing overall equivalence ratio. Once again, the 0.50 in. (12.7 mm) jet system shows as the optimum, having the lowest absolute jet NOx.

The optimum behavior of the 0.50 in. (12.7 mm) jet system is demonstrated in Figure 8 where the EI's of jet NOx are plotted against jet diameter for three primary zone (overall) equivalence ratios in the range of peak bulk-flame temperatures. Note that for all jet sizes, the jet NOx EI's decrease with increasing primary zone equivalence ratio, and the sensitivity to jet size decreases also.

Behavior in Relation to Primary Zones

From individual plots of overall NOx emissions against overall equivalence ratio for each jet size, values of NOx EI's at specific primary zone equivalence ratios can be extracted. From such values

plots of overall NOx emissions as a function of jet size can be produced.

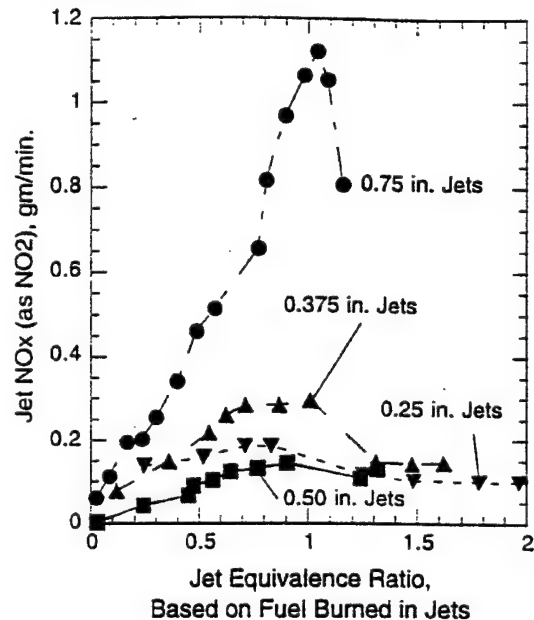


Figure 7: Absolute Values of Jet NOx

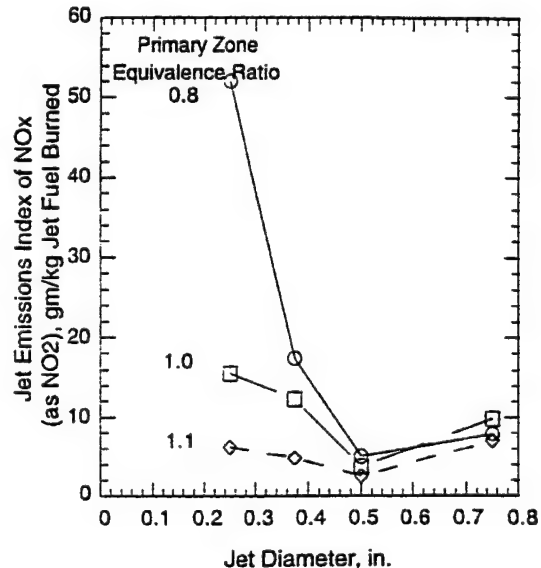


Figure 8: Indication of Optimum Jet Diameter

Figure 9 shows such a plot for primary zone equivalence ratios of 0.5, 0.8, 1.0 and 1.1. Since a particular primary zone equivalence ratio represents a specific bulk temperature, thermal NOx should be independent of jet size. That it is not, implies that the different jet sizes do result in some changes to flame

structure in the jets, (since most of the NOx is generally generated in the jets) as was suggested, and that these changes are responsible for the observed increase in NOx.

Remembering that the overall NOx consists of NOx produced in the dome and NOx produced in the jets, the NOx EI for total fuel burned characteristics with jet diameter are similar at each primary zone equivalence ratio. NOx EI increases from the dome-alone value with the addition of combustion air jets. This is due to participation of some jet air in dome burning, as discussed above, and this increases with jet size for the 0.25 in. (6.35 mm) and 0.375 in. (9.53 mm) jets, together with a growing, and eventually dominating, contribution of jet NOx. At unity primary zone equivalence ratio and above, there appears to be an optimum jet size at 0.50 in. (12.7 mm) diameter. There is a sharp increase in overall NOx EI at all primary zone equivalence ratios, that is associated with the use of 0.75 in. (19.05 mm) diameter jets. The lowest NOx at each of the primary zone equivalence ratios is achieved by the dome alone configuration.

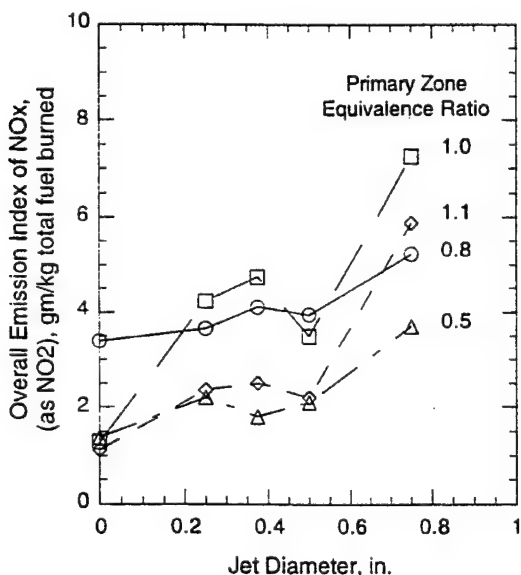


Figure 9: Optimum Jet Size for Overall Primary Zone

Figure 10 is a similar plot, but where the overall NOx is expressed as an absolute value, in gm/min., and is plotted against the mass flow rate ratio of jet air to dome air. In this plot at given primary zone equivalence ratio, the mass flow ratio

varies as the jets are changed, and fuel flow rate increases with air mass flow ratio. Thus, as air mass flow rate ratio increases the dome gets progressively richer since its air flow is fixed.

The stoichiometry breakdowns for the combustor² show that for all but the highest air mass flow ratio shown on Figure 10, the dome is fuel-lean at 0.5 primary zone equivalence ratio, and is around stoichiometric or less at 0.8 primary zone equivalence ratio; the jet systems are always fuel-lean. Thus, primary zone equivalence ratios less than 0.8 generally represent overall lean burning in this combustor. For higher primary zone equivalence ratios, the dome is always very fuel-rich, and jet equivalence ratio becomes stoichiometric at unity primary zone equivalence ratio. Thus, primary zone equivalence ratios of unity or greater generally represent overall rich burning.

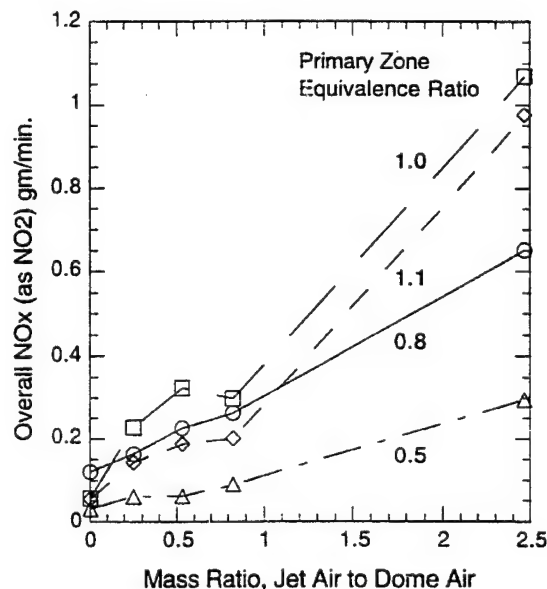


Figure 10: Dependence of Absolute NOx Emissions on Jet to Dome Mass Flow Ratio

Figure 10 shows a clear difference in NOx characteristics between these two primary zone equivalence ratio regimes. For 0.5 and 0.8 primary zone equivalence ratios the absolute NOx level increases essentially linearly with increasing air mass flow rate ratio. As the primary zone equivalence ratio is increased the NOx levels increase due to the increased bulk temperature, and the sensitivity to air mass flow rate ratio is increased. At any primary zone equivalence ratio the increase in overall NOx with

increase in air mass flow rate ratio is due to the growing contribution of jet NO_x.

It is not sufficient to confine consideration to NO_x alone as the indicator of low emissions; the inefficiency emissions must also taken into account.

Figure 11 is a plot of overall NO_x emissions indices against overall CO emissions indices for each of the jet sizes, including the dome alone: the data for each jet size is limited on the left-hand-side by 0.5 primary zone equivalence ratio and on the right-hand-side by 1.1 primary zone equivalence ratio. Such a plot represents the emissions trades between NO_x and CO that might be made. If a box is placed around the data for any particular jet size in the plot, bounded on one side by the maximum CO, on the top by maximum NO_x, and, on the remaining side and the bottom by the respective axes, then that box is a qualitative measure of the total emissions production of the particular configuration. Data for any other configuration over the same equivalence ratio range that falls wholly *inside* the box, represents a **truly lower emissions configuration**.

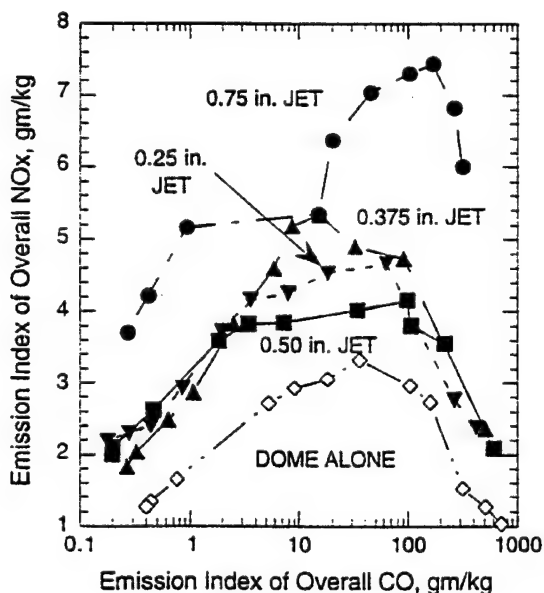


Figure 11: Overall Emissions Assessment for Range of Jet Sizes

Review of the figure reveals several interesting facts. First, the dome-alone configuration does truly represent the lowest emissions configuration, since it has the smallest box. Second,

the 0.50 in. (12.70 mm) jet does indeed represent some kind of optimum jet configuration for this primary zone since its box is smaller than the boxes for the other jets, i.e. it does not achieve its low NO_x by producing large amounts of CO. Third, the 0.75 in. (19.05 mm) jet is the worst emissions producer, and this is through its jet NO_x generation.

The levels of CO over the equivalence ratio range in Figure 11 are all at or very close to, the appropriate equilibrium levels for the test conditions. For lower equivalence levels outside the range there is an upwards departure from equilibrium CO as a lean blowout condition is approached; similarly, at higher equivalence ratios there is also an upwards departure from equilibrium CO due to a lack of oxygen. Combustion efficiencies for the dome alone and for the 0.5 in. (12.70 mm) jet, for example, are essentially 100 percent to an overall equivalence ratio of about 0.8, and then fall off more or less together.

The finding that the dome alone configuration, i.e. no traverse air jets whatsoever, gives the lowest emissions, raises the valid question as to the need for the separate combustion air jets.

The combustion air jets are needed to reduce flame length and to enhance lean stability. Figure 12 shows some limited stability data for the dome alone and for the dome with the 0.50 in. (12.70 mm) jets, in the form of blowout overall equivalence ratio against the air loading parameter, ALP. The ALP is as defined in Reference 5. The blowouts were conducted at atmospheric pressure, with variation of dome pressure drop for the dome alone, and liner pressure drop at fixed dome pressure drop for the with-jet case. In addition for the dome alone case, two inlet air temperatures were used - ambient and 500F (533K). The plot shows that for given ALP the with-jets case blows out at lower equivalence ratio than does the dome alone. For the dome alone situation there were several flame modes observed¹. Blowouts for the range of ALP's in Figure 12 were governed by lifted and attached flame conditions⁶; the presence of the combustion air jets exerts a back-pressure on the flame that modifies the flame behavior.

Figure 13 presents the dependency of overall equivalence ratio at blowout on jet size at fixed dome and liner pressure drops. It can be seen that the 0.50 in. jet size again represents an optimum for this dome.

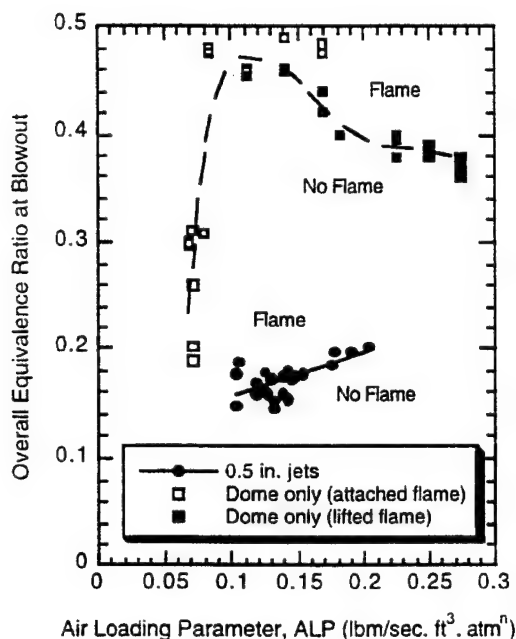


Figure 12: Stability Plot for Dome Alone and Dome with 0.5 in. Jets

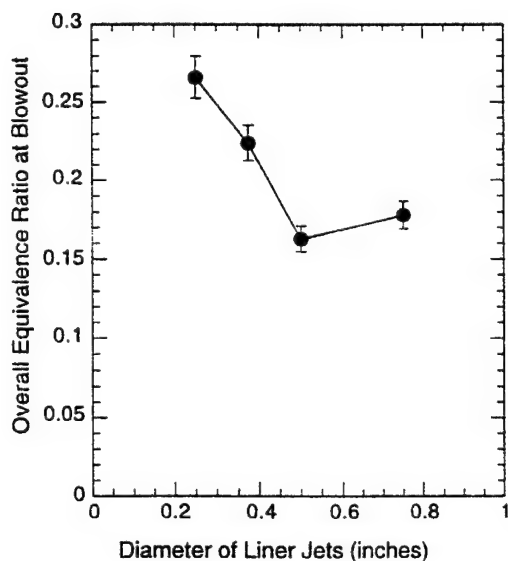


Figure 13: Blowout Equivalence Ratio as a Function of Jet Size

Discussion

Initial results, consisting of emissions measurements and lean blowout data, have been presented for a number of circular, single hole,

opposed, combustion air jet sizes at a fixed liner position close to the dome, and at fixed dome and combustor liner pressure drops that are representative of engine design values. The absolute levels of emissions are dependent on the way that the simulations were conducted, and therefore the present results ideally should not be used for predictive purposes by scaling. However, the trends that are produced are valid, and will eventually (when complete) be useful for design purposes.

The series of emissions measurements gathered over wide ranges of test conditions for the different geometric configurations investigated, could form a useful data-set for evaluating the response of CFD modeling to realistic combustor geometries.

It was established that equivalence ratio was a suitable and unique parameter with which to consider the emissions measurements in this combustor and with the manner in which it was operated. The data have been analyzed in terms of a rich dome/lean jet burning behavior. This approach appeared to account nicely for the effects observed.

The combustor dome behaves as a partially stirred reactor, and shows significant unmixedness effects in its NO_x characteristic. The partial set of results demonstrates that the jets play a significant role in generating the total NO_x measured over equivalence ratio ranges that are typical of many primary zones. The jet contribution appears to arise from stoichiometric burning in the jets system. This stoichiometric jet burning is clearly identifiable for all but the smallest of the jets (0.125 in. dia.). As a consequence of the jet contributions to total NO_x, the dome alone configuration emerges as the lowest producer of NO_x and CO emissions. The jets are needed to shorten flame length, and to enhance lean blowout stability of the primary zone. Of the jet systems examined, that for the 0.5 in. (12.70 mm) diameter jet shows distinct optimum behavior in terms of minimum NO_x emissions and maximum lean blowout stability.

The results to date indicate the need to use advanced optical diagnostic techniques to determine the exact flame structures existing in the jet systems, and how these are affected by the flow interactions between the dome and the jets. Detailed flow visualization is clearly most desirable. In particular, quantitative information on recirculation zone mass flow rates is essential. The parametric variations in liner pressure drop and combustion air jet axial

position will also be of assistance in this respect. An explanation for the optimum behavior of the 0.50 in. (12.70 mm) jet must be obtained.

Although there was no attempt in this combustor to achieve a true rich burn/quick quench/lean burn low emissions design, the present primary zone does function somewhat in this fashion. The findings here indicate how difficult it will be in such low emissions designs to achieve the quick quench portion and hence, to get a true lean burn.

The limited stability characteristics presented demonstrate that low emissions characteristics in a combustor cannot be pursued without regard to the other design criteria that must be satisfied for successful practical combustor designs.

Conclusions

1. Most of the NO_x generated in the generic primary zone appears to originate from stoichiometric burning in the combustion air jet system.
2. Minimum total emissions are produced when all of the reactants are introduced through the combustor dome.
3. Combustion air jets are necessary to reduce flame length and confer lean blowout stability.
4. For at present undefined reasons, the 0.50 in. (12.70 mm) dia. opposed circular jets exhibit a clear optimum for the dome when the jets are positioned half a dome height downstream. This optimum is for minimum NO_x and lean blowout stability.

Acknowledgments

The enthusiasm, motivation, support and contributions of Dr. W.M. Roquemore are greatly appreciated. The authors wish to thank Ron Britton, Mike Burns and Melvin Russell for their help in operating the test facility and in making the emissions measurements. This on-going research was sponsored by the U.S. Air Force, Wright Laboratory, Aero Propulsion and Power Directorate.

References

1. Sturgess, G.J., *Combustor LBO Design Model Evaluation, Final Report*, (Draft) Pratt & Whitney Doc. No. FR-23400, 1 May, 1995
2. Gogeneni, S., Shouse, D., Frayne, C., Stutrud, J., and Sturgess, G., "Influence of Combustion Air Jets on Primary Zone Characteristics for Gas Turbine Combustors," *proc. ISABE 12.th. Intl. Symp. on Air Breathing Engines*, editor F. Billig, Vol. 1, Melbourne, Australia, Sept. 10-15, 1995, pp. 475-487.
3. Roffe, G. and Venkataramani, K.S., "Emissions Measurements for Lean Premixed Propane/Air Systems at Pressures up to 30 Atmospheres," NASA Rept CR-159421, 1978.
4. Sturgess, G.J., McKinney, R.G. and Morford, S.A., "Modifications of Combustor Stoichiometry for Reduced NO_x Emissions from Aircraft Engines," *Trans. ASME, J. Engrg. Gas Turbines and Power*, Vol. 115, No. 3, 1993, pp. 570-580.
5. Sturgess, G.J. and Shouse, D., "Lean Blowout in a Generic Gas Turbine Combustor with High Optical Access," ASME Paper No. 93-GT-332, May 1993, to appear in ASME *Trans. J. Engrg. for Gas Turbines and Power*.
6. Hedman, P.O., Sturgess, G.J., Warren, D.L., Goss, L.P. and Shouse, D.T., "Observations of Flame Behavior From a Practical Fuel Injector Using Gaseous Fuel in a Technology Combustor," *Trans. ASME, J. Engrg. for Gas Turbines and Power*, Vol. 117, No. 3, July 1995, pp. 441-452.



AIAA 96-2758
Emissions and Operability Trades
in the Primary Zones of
Gas Turbine Combustors

G.J. Sturgess
Innovative Scientific Solutions Inc.
Beavercreek, Ohio

S. Gogineni
Systems Research Laboratories, Inc.
Dayton, Ohio

D.T. Shouse, C. Frayne, and J. Stutrud
Aero Propulsion and Power Directorate
Wright-Patterson AFB, Ohio

32nd AIAA/ASME/SAE/ASEE
Joint Propulsion Conference
July 1-3, 1996 / Lake Buena Vista, FL

EMISSIONS AND OPERABILITY TRADES IN THE PRIMARY ZONES OF GAS TURBINE COMBUSTORS

G.J. Sturgess*

*Innovative Scientific Solutions, Inc.,
Beavercreek, Ohio*

S. Gogineni

*Systems Research Laboratories, Inc.,
Dayton, Ohio*

D.T. Shouse, C. Frayne and J. Stutrud,

*Aero Propulsion and Power Directorate, Wright Laboratory,
WPAFB, Ohio*

Abstract

Measured emissions indices of NO_x and CO generated in the primary zone of a generic combustor for aircraft gas turbine engines are examined at simulated high power conditions as a function of primary zone geometry. For a stoichiometric primary zone the emissions can vary by a factor greater than 3, solely due to combustion air jet size and primary zone length. The trade between NO_x and CO shows that between 0.5 and 1.1 primary zone equivalence ratios, a primary zone length of 0.5 dome heights is the lowest overall pollution generator. The stability behavior is complex and depends on how the particular geometry, operating conditions and fuel injector design together influence the flame shape. The stability loop for a complete combustor is actually a composite made up of a number of individual stability loops for particular flames. For a non-variable geometry, non-fuel staged combustor the emissions and stability are fixed via local stoichiometry; optimization is therefore worthwhile.

Background

Levels of gaseous emissions from aircraft gas turbine engines for commercial operations are regulated by ICAO standards¹. These standards are presently becoming more stringent, and this trend is likely to continue due to environmental pressures. Engines for subsonic commercial service might be forced to adopt complex and expensive combustors and fuel systems in

order to comply with future regulations governing emissions. The design characteristics of possible future high-speed (supersonic) commercial transport systems will be determined in part, by the emissions level potentials achieved in on-going NASA research programs. Military operations are currently not regulated. However, U.S. Air Force "good neighbors" policies demand that the emissions issues be fully understood. In this vein good faith efforts are made to contain engine emissions levels where this is consistent with meeting operational requirements^{2,3}.

The design of gas turbine engine combustors for aircraft applications must address a wide range of goals in addition to those associated with low emissions. These operability goals, including flame stability, altitude relight capability and turndown ratio capacity, cannot be compromised. Therefore, low emissions design approaches must always be considered in relation to their effects on operability. Many of the design goals can represent conflicting requirements. Furthermore, the weighting of specific goals can change according to the intended application. For these reasons parametric studies of emissions in conjunction with operability characteristics are needed.

Introduction

One study that is currently in progress is an investigation into the minimization of engine exhaust emissions, and the relationship between generation of

* AIAA Senior Member

these emissions and combustor stability characteristics. This effort is part of the U.S. Air Force's *Combustor Design Model Evaluation (CDME) Program* conducted by the Aero Propulsion and Power Directorate of Wright Laboratory (WL/PO), Wright-Patterson Air Force Base, Ohio.

As a part of this Air Force work a broad-ranging investigation of combustor primary zone behavior is being conducted. The primary zone configuration is a generic one that has demonstrated extremely low emissions of unburned hydrocarbons (UHC's) and carbon monoxide (CO) at low engine powers, together with moderate reductions in oxides of nitrogen (NOx) at high engine powers⁴. It also has acceptable flame stability and altitude relight capability for routine engine service. The generic low emissions combustion concept is one that is used in Pratt & Whitney's PW4000 series of engines, International Aero Engine's V2500-A5 engine, and in versions of General Electric's CF6-80 engine⁵. To achieve the emissions goals it relies on a fuel-rich primary zone at take-off power for low-NOx, followed by an oxygen-rich intermediate zone to complete CO-burnout.

Previous Work

A complete description of the research combustor, rig, test facilities, and emissions instrumentation and measurement techniques, as well as of the high-power simulation justification, are given in Reference 6, where the stoichiometry relations for the various combustion air port geometries are also provided.

Initial emissions information is presented in References 6 and 7, for a primary zone of fixed length equal to one-half of the combustor dome height. The results given were for a primary zone operated at a fixed dome pressure drop of 4.3 percent, and a fixed liner pressure drop of 3.0 percent, these values being representative of engine practice.

It was shown that for a given primary zone equivalence ratio the combustor dome alone (no combustion air jets) gave the lowest emissions, but had poor stability. When combustion air jets were present the lowest emissions and lowest overall equivalence ratio at lean blowout (LBO) were achieved when 0.50 inch diameter combustion air jets were used. These jets were opposed to each other, and were inline with a fuel injector. Most of the total primary zone NOx was generated in the jet system.

Present Contribution

The work of the earlier studies is continued by examining the effects on emissions and LBO of the primary zone length with the 0.50 inch diameter combustion air jets. The dome and liner pressure drops are maintained at 4.3 and 3.0 percent respectively, and the jet arrangement is opposed, inline with the fuel injector. Two jet configurations are used: single, circular-section, plain jets, and jets with the same total effective area as the plain jets, but divided into 4 smaller individual jets arranged at the same distance downstream. The individual jets are oriented in diamond-fashion to the general direction of flow. The intent of this latter configuration is to attempt to alter the combustion air local mixing while maintaining the general primary zone flowfield and overall stoichiometry.

Primary zone lengths equal to 0.50, 0.75 and 1.00 dome heights are used for each jet configuration. The emissions measurement plane is fixed at the original 2.32 dome heights downstream from the dome for each jet/length combination.

Test Vehicle and Power Simulation

The combustor consists of a single representative fuel injector and its associated dome interface, mounted in a plain bulkhead. The injector is a high-swirl airblast atomizer, and the dome interface consists of a small, discrete-jet air swirler that is co-annular with the injector, together with a dome heat shield fed with cooling air which is discharged radially outwards across the bulkhead face. The cross-section of the combustor is square to provide good optical access for laser diagnostics; however, generous corner-fillets are provided to suppress secondary flow vorticity generation that might result in spurious flameholding⁸. The hydraulic diameter is 153 mm and the length is 490 mm. The outlet is restricted by a 45 percent geometric blockage orifice plate to provide representative back-pressure of the dilution zone from a real combustor⁹.

The combustor is mounted horizontally in a test cell at Wright Patterson Air Force Base. The combustor top and bottom walls are removeable, uncooled metal plates that accommodate appropriate arrays of combustion air jets supplied using a separately metered air supply. One combustor side-plate contains a fitting for application of a torch ignitor; the opposite side contains a full-length quartz window for visual access.

Figure 1 shows the combustor with its entrance air conditioning unit, and also, details of the dome region. More complete details are given in References 6 and 7.

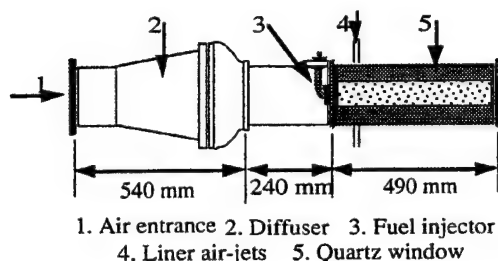


Figure 1a): Diagram of Rig

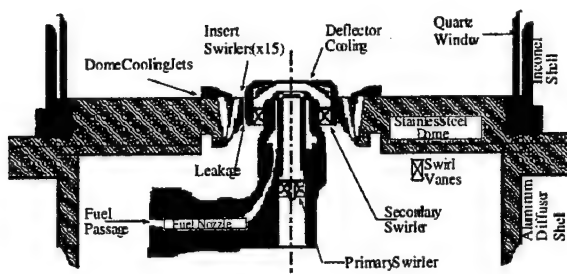


Figure 1b): Dome Region of Combustor

As modeled in the experiment the combustor represents a "single-cup" planar segment of an annular combustor, and covers only the primary zone. Although the side boundary conditions are incorrect, it is argued in Reference 6 that this only introduces a second order effect.

To simulate engine high power operation Spalding's flow criterion and non-dimensional temperature¹⁰ were matched in the experiment, together with the liner and dome pressure drops. Gaseous propane was substituted for liquid JetA/JP8 to eliminate spray scaling and droplet evaporation problems. Therefore, the primary zone flow patterns should be closely matched.

To establish the desired similarity criteria the combustor was operated at atmospheric pressure with the separately metered dome and combustion air jet flows electrically heated to about 500F (533K).

Emissions Measurements

The axial plane for the emissions measurements was fixed for all dome/jet combinations at 14 ins. (356 mm) or, 2.32 dome heights, downstream from the combustor dome. Details of the emissions probe, sampling protocol and measuring equipment are described in Reference 6. Procedures and data reduction followed recommended ICAO practices, with the exception noted below.

The inlet air was dried to extremely low dew points prior to entering the electrical heaters. The measured NOx values quoted are therefore all dry values.

With simulation used for engine high power conditions, the general measured emissions trends are believed to be valid, although the absolute values should not be considered representative of engine levels.

Since combustion inefficiency for propane/air systems results in mainly carbon monoxide (CO) and negligible unburned hydrocarbons (UHC), measured CO/UHC ratios are not representative of engines. However, UHC in actual engines normally results from the reaction-freezing effects of combustor liner film cooling at low power levels, which is not included in the present simulation.

This is illustrated in Figure 2 where collected CO and UHC engine data from Reference 11 are compared with present results over a range of equivalence ratios for cases with no combustion air jets and with a variety of air jets all positioned at one-half a dome height, H_d , downstream from the dome. The CO and UHC levels for the engines and the simulation are in good agreement at high-power conditions, but diverge sharply at low power conditions due to a) the burning characteristic of propane versus JP8, and, b) the lack of film cooling in the simulation.

The figure illustrates that the measured CO is due to a failure to burnup CO, and that it is not due to any chilling of the normally fast hydrocarbon consumption reactions.

Test Procedure

Results are presented for two types of combustion air jet: 1.) jets generated by individual plain circular ports of 0.50 in. (12.7 mm) diameter that are flush with the combustor liner, and, 2.) jets generated by a square array of four, plain circular ports of 0.25 in.

(6.35 mm) diameter equally-spaced on a pitch circle of 0.575 in. (14.605 mm) diameter. The square array of the second type is oriented with one individual hole in the upstream position. The effective area of the second type of port was intended to be equal to that of the first type. However, the individual jetlets acted together to increase the net discharge coefficient of the array so that at 3 percent liner pressure drop, the multi-hole array flowed about 10 percent greater jet mass flow rate than did the single 0.50 (12.7 mm) ports.

The purpose of the multi-hole array was to present an increased initial perimeter (by 50 percent) for enhanced mixing of the combustion jet air with the primary zone flow.

For each air-port size, axial position and pressure drop examined, the fuel flow rate was varied to cover a wide range of overall equivalence ratios. The assumption of constancy of flow-field with this method of operating was verified in Reference 7. More complete details of the test procedure are given in this reference.

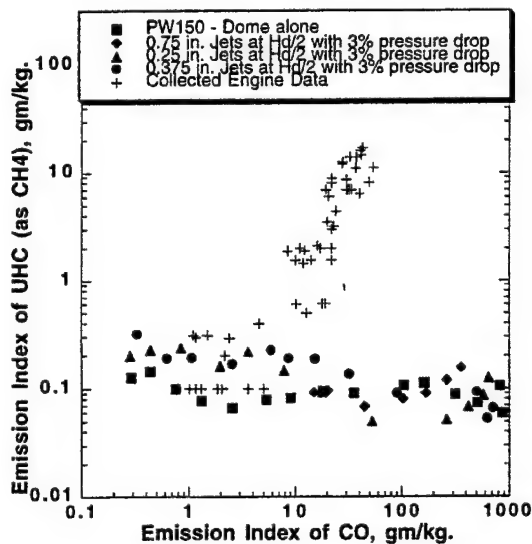


Figure 2: Comparison of Low Power Emissions for Engines and Test Vehicle

Effect on Emissions of Primary Zone Length

The majority of the work was conducted on the 0.50 inch (12.70 mm) initial diameter plain, circular jets, placed opposed to one another on the fuel injector

centerline. These jets had shown the lowest values of jet NOx and overall pollution at the 0.50 H_d position.

For overall equivalence ratios greater than about 0.5 the CO produced was only weakly dependent on the axial position of the 0.50 inch (12.7 mm) jets. This is demonstrated in Figure 3 for overall equivalence ratios between 0.5 and 1.1. The general levels of CO at each equivalence ratio increased, of course, with increasing overall equivalence ratio.

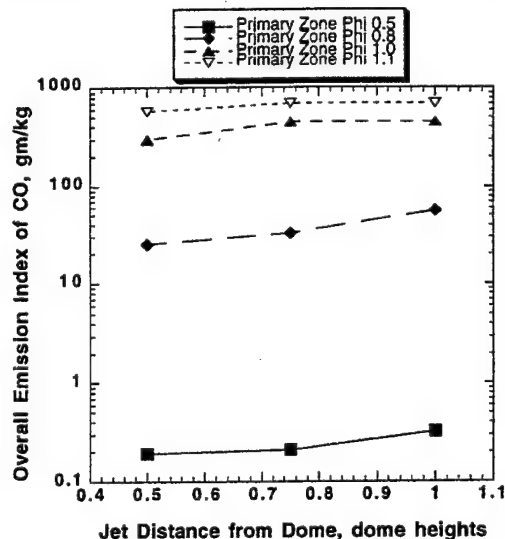


Figure 3: Dependence of Overall CO on Jet Position for 0.50 in. Jets at 3% Liner Pressure Drop

In Figure 4 it can be seen that the CO reaches equilibrium levels at about 0.5 overall equivalence ratio. The weak dependence on axial position of the jets at the equilibrium levels is almost certainly due to the slightly different heat losses for each primary zone length. The estimated effect of a typical level of heat loss on the equilibrium line is shown on the figure. For overall equivalence ratios greater than about 0.80 the measured CO is at super-equilibrium levels. This suggests that heat losses in the post-flame region of the primary zone are also increasing with overall equivalence ratio. This is reasonable due to the increasing bulk flame temperatures.

It will be noted in Figure 4 that for low values of overall equivalence ratio the axial position of the jets does exert a fairly strong influence on the CO curve in terms of the amount of CO at the minimum and the position at which the CO minimum occurs. This is indicative of the likely importance of jet position to the

blowout characteristics. Figure 5 illustrates this aspect by showing the CO at an overall equivalence ratio of 0.2. At this low value of equivalence ratio the CO increases sharply with increasing jet distance from the dome, with the implication that better stability exists with the jets closer to the dome.

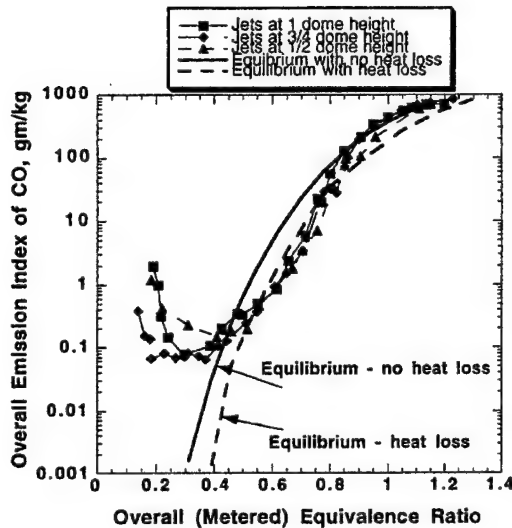


Figure 4: CO Characteristics for 0.50 in. Jets at 3% Liner Pressure Drop

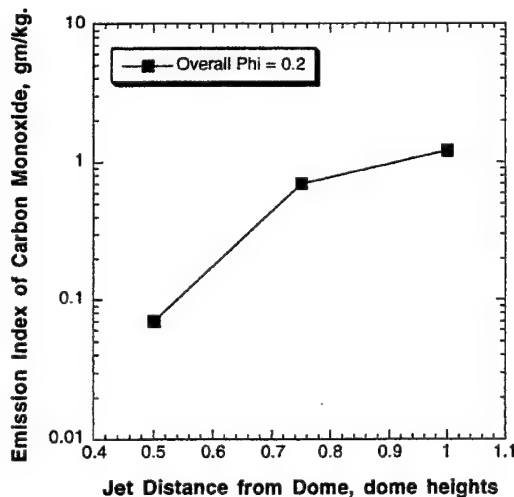


Figure 5: Effect of Jet Position on CO at Low Overall Equivalence Ratio Approaching Lean Blowout

Figure 6 displays the position-sensitivity of overall NOx emissions for the 0.50 in. (12.7 mm) jets

at 3 percent liner pressure drop. The primary zone equivalence ratio is here directly equivalent to the overall equivalence ratio.

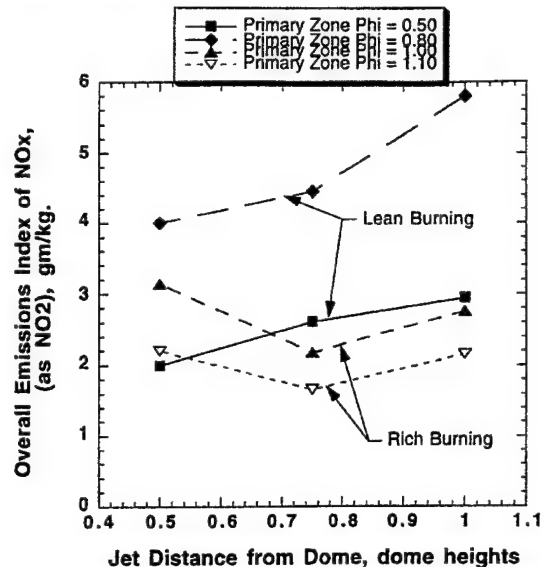


Figure 6: Dependence of Overall NOx on Jet Position for 0.50 in. Jets at 3% Liner Pressure Drop

It can be seen from the figure that when the primary zone is overall fuel-lean, the overall emission indices (E.I.'s) of NOx increase with increasing distance from the dome, while the level increases with primary zone equivalence ratio. When the primary zone is stoichiometric or overall fuel-rich, the E.I.'s of NOx show a minimum at $0.75 H_d$. The NOx levels decrease with increasing equivalence ratio for this fuel-rich condition. For jets positioned at $0.75 H_d$ or greater from the dome, stoichiometric or rich burning produces less NOx than does lean burning at all jet positions.

For fuel-lean bulk combustion the primary mechanism for NOx generation is thermal via the Zeldovich mechanism, and this takes place in the post-flame region, i.e. it is a "time at temperature" process. The observed increase in NOx with increasing distance of the combustion air jets from the dome is therefore probably due to increased primary zone residence time, provided that adequate jet air is always recirculated forwards into the dome to take part in the combustion process. The strong gradient change taking place at $0.75 H_d$ for 0.50 bulk equivalence ratio probably represents at condition where the jets are far enough downstream for the amount of jet air recirculated forwards into the dome to be reduced, thereby resulting in local

combustion at significantly higher equivalence ratios than the bulk value. This hypothesis is supported by the curve for 0.80 bulk equivalence ratio, where for jet distances greater than $0.75 H_d$ the NOx gradient is reduced slightly. Since peak NOx is generated at equivalence ratios about 0.80⁷, the implication here is that the reduced quantity of recirculated air causes most of the NOx to be generated at higher than the bulk equivalence ratio.

For fuel-rich bulk combustion the thermally generated NOx is reduced due to the lower bulk flame temperatures and the unavailability of O-atoms. Under very high temperatures in an oxygen-deficient region, atmospheric nitrogen reacts preferentially with lower hydrocarbon fragments produced by fuel cracking, to produce nitric oxide, NO, via the amine-group. This is the so-called "prompt NO" process, and takes place very quickly within the flame structures themselves, rather than in the post-flame region.

Pursuing the argument above for lean bulk combustion, the jet air recirculated for jet distances greatly the $0.75 H_d$ from the dome is perhaps so reduced for bulk equivalence ratios greater than unity, that the initial reactions in the dome take place extremely fuel-rich. This effectively eliminates any thermal NOx generation in the dome. Only prompt NOx is produced. However, large quantities of CO ensue. A significant amount of this CO is then reacted downstream by combustion taking place around the jets. This jet-supported combustion takes place at stoichiometric conditions, and results in thermal-NOx production. It has been previously demonstrated that jet NOx generated in this fashion can form the bulk of the total primary zone NOx⁷.

Figure 6 indicates that for minimum NOx production in fuel-rich systems an optimum jet position for 0.50 in. (12.70 mm) combustion air jets is $0.75 H_d$ downstream from the dome. It is not sufficient however, to confine consideration to NOx alone as the indicator of low emissions. Also to be taken into account is CO.

In Reference 7 the total pollution of a configuration was quantitatively described in terms of the area of a box set by the maximum NOx and the maximum CO values for a given range of bulk equivalence ratios. This procedure is adopted here in Figure 7 for the 0.50 in. (12.70 mm) diameter combustion air jets. The range of equivalence ratios at each jet position is 0.5 to 1.1.

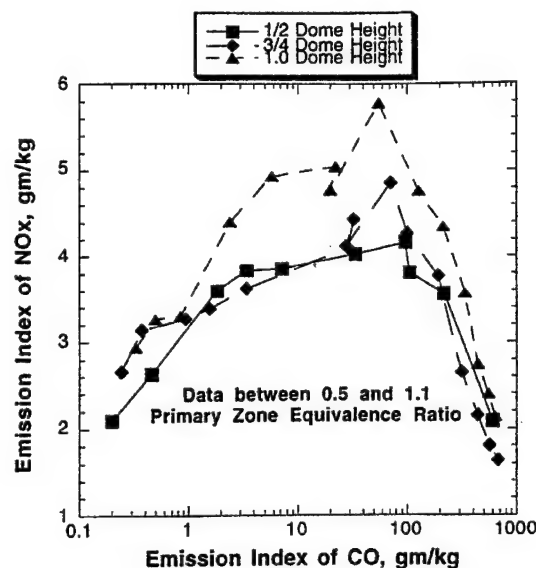


Figure 7: Overall Emissions Assessment for the 0.50 in. Jets at Several Axial Positions

Figure 7 shows that the greatest net pollution generator is the configuration with the 0.50 in. (12.70 mm) jets placed axially from the dome at one dome height downstream. With these jets placed at $0.5 H_d$ downstream from the dome, the minimum net pollution results; however, there is little increase in net pollution for jet positions up to $0.75 H_d$ downstream.

Effect on Emissions of Jet Type

The emissions trades for the two jet types at a downstream location of $H_d/2$ is given in Figure 8. Again, the range of equivalence ratios represented by the data is from 0.5 to 1.1.

Unfortunately, no data were taken at exactly 3.0 percent liner pressure drop for the multi-jet air ports. Data are therefore given in the figure for 3.1 and 3.2 percent conditions. It can be seen that these results can be considered as being representative for the 3.0 percent case for the multi-jet ports.

It is obvious from Figure 8 that the multi-jet combustion air ports result in greater net pollution than do the 0.50 in. (12.7 mm) plain ports. The increase is due to much greater production of NOx. The increased NOx is generated at overall equivalence ratios in the range 0.7 to 1.0. Based on the findings in Reference 7,

it appears reasonable to believe that this increased NOx resulted from stoichiometric burning at the enhanced jet interfacial area offered by the multi-jet port configuration.

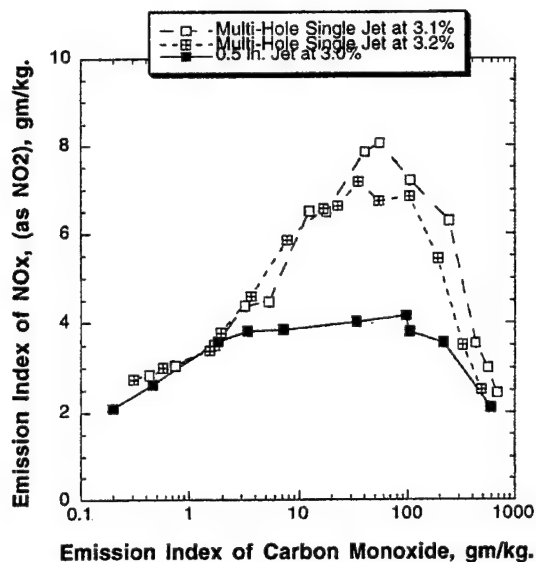


Figure 8: Overall Emissions Assessment for the Jet Configurations at Half-Dome Height Axial Position

Stability Measurements

Stability was defined through lean blowout (LBO). Occasionally, non-stationary behavior of the flame and/or a noticeable acoustic signature would be noted as an LBO was approached, depending on the jet size and axial position, and, combinations of operating conditions. Although it is recognized that such phenomena are an integral part of combustor stability, no pressure transducer or microphone data were taken, unfortunately.

LBO's for the various jet configurations were gathered at atmospheric pressure with 80, 150, 250, 300, 400 and 500 F (300 - 533K) nominal air inlet temperatures, and dome pressure drops from 2.5 to 6.5 percent; at each dome pressure drop the liner pressure drop was varied from 0.5 to 5.5 percent. These test conditions enabled a significant variation in combustor loading to be obtained without resorting to either sub-atmospheric pressures or simulation of such reduced pressures¹². However, the complete lean stability characteristics could not be obtained for any

configuration without resort to the low pressure effect on combustion reaction rates.

The procedure was to set the assigned air temperature and pressure drops, and then to progressively reduce the fuel flow until a blowout was obtained. As a blowout point was approached the fuel decrements were made successively smaller. Time was allowed for the rig to attain thermal stability between fuel decrements, until the flame reached a non-stationary condition. Blowouts were detected visually through the quartz viewing window (Figure 1), using a sensitive video camera.

Effect on LBO of Primary Zone Length

It is desirable if the variety of boundary conditions at which LBO's were obtained could be combined in some form to represent the reaction conditions under which the flame is extinguished. A traditional approach that is commonly used for correlating experimental LBO data derives from reaction rate theory¹⁰ and is expressed as the combustor loading parameter, LP, where,

$$LP = \frac{\dot{m}}{VP^n F}$$

and,

\dot{m} = mass flow rate in combustor
 V = combustor volume
 P = combustion pressure
 n = apparent reaction order
 F = exponential inlet air temperature correction factor

With a gaseous fuel \dot{m} is taken as the sum of the air and fuel mass flow rates in lbm/sec., V is the volume of the primary zone in ft³ and is defined by the position of the combustion air jets, P is 1 atmos. and F is given by,

$$F = \frac{10^{0.00143T}}{3.72}$$

where T is the reactants inlet temperature in K. In this form F corrects the data to a constant temperature of 400K.

The equivalence ratio, based here on the loading airflow, at LBO is plotted against the global LP to form the lean-portion of the combustor blowout curve.

There are a number of difficulties with plotting stability results in the global manner described. One of direct interest applies when the combustor uses a fuel injector of the airblast atomizing type, as in the present case.

An airblast atomizer uses a small quantity of air to achieve atomization of the liquid fuel. Generally, the atomization quality achieved is high, and the resulting very small fuel droplets in the spray have little or no momentum of their own. The atomized fuel is initially distributed according to the flow patterns produced by the injector air. The atomizing air used in the fuel injector also forms part of the total combustion air introduced in a primary zone. Together with injector-induced local flow patterns, it therefore determines to first order, the local fuel/air ratios in the flame stabilization region¹³. Hence, when an airblast atomizer is used, the combustor LBO characteristics depend not only on the global combustor loading LP, but also upon the detailed design characteristics of the fuel injector.

As a result of this behavior that is peculiar to airblast atomizing fuel injectors, a combustor approaching LBO can exhibit a variety of flame types, depending on how a given value of LP is obtained¹⁴. In the present instance, the injector integral swirl number and overall momentum ratio¹⁵ remain fixed so that the effect on flame characteristics is confined to one local equivalence ratio. In the added presence of combustion air jets, a total of six distinct flame types have been observed in the combustor.

Figure 9 displays a portion of the LBO curve for the combustor with the 0.50 in. (12.7 mm) combustion air jets placed at $0.5 H_d$ downstream from the dome. The data points are delineated by flame-type, and only the three major flame categories are identified (each major category contains two sub-types of flame). The air jet mass flow considered active in the primary zone, and hence included in the calculation of LP and blowout equivalence ratio, was taken as 27.9 percent of the total jet mass flow¹⁶. High values of LP correspond to high altitude, low ambient temperature, high-speed flight conditions, and therefore represent difficult combustion conditions.

Shown also on the plot is a line along which the emissions measurements for this configuration were made at fixed pressure drops. The track is well-inside the burning region and is removed from the peak heat release rate condition. The line corresponds to low

values of LP, and therefore represent relatively easy combustion conditions.

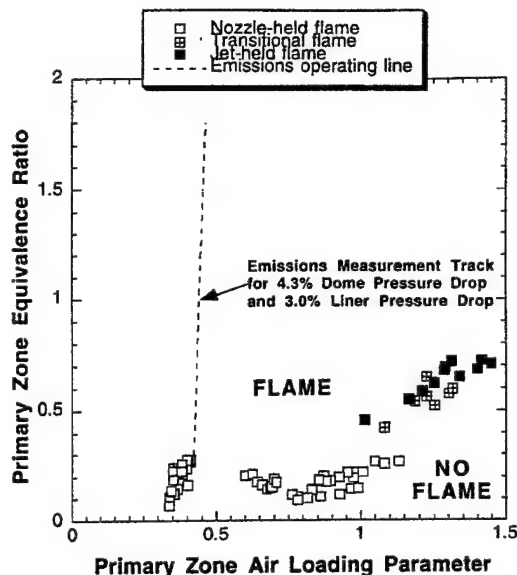


Figure 9: Portion of LBO Curve for 0.50 in. Jets at Half Dome Height Downstream

The figure reveals that as the primary zone loading is increased the combustor blows out initially with an attached flame, moves to a transitional flame, and finally, to a lifted flame. The attached flame category is similar to that illustrated in Reference 14, Figure 3, at injector equivalence ratios from 0.85 to 0.46. The sub-category is attached like these flames, but with the addition of a lower intensity, wedge-shaped or conical tail extending downstream to the liner origins of the combustion air jets. The lifted flame category is completely detached from the fuel injector and is held on the combustion air jets; the sub-category is where the flame has low intensity and is held entirely in the jet wakes, outside the primary zone. The transition flame category generally has a large, poorly-organized flame occupying the volume between the dome and the jets; in appearance it falls between the attached and lifted states. The sub-category is where the transition flame randomly jumps alternatively in oscillating fashion between the well-organized attached and lifted states.

The discontinuities in the blowout curve are solely due to the lack of data gathering in the missing regions. It can also be seen that the region of loadings which produces the attached flame category yields an LBO curve that turns back on itself twice. It is believed that this lobed feature is associated with the

recirculation zones and their relation with the attached flame sub-category, but the details remain to be investigated.

It should be noted in Figure 9 that at a loading parameter of about $1.05 \text{ lbm}/(\text{sec.ft.}^3 \text{ atm.}^n)$ there are conditions where the flame can be either attached or transitional/lifted, with a loss in stability (increase in blowout equivalence ratio) for the latter flames.

Figure 10 shows the LBO characteristic for the 0.50 in. (12.7 mm) jets positioned at $0.75 H_d$; data-point delineation is again by flame-type. In this plot the percentage of jet air considered active in the primary zone remains fixed at 27.9 percent. The reason for this is based on the gradients of the fuel-lean NOx data in Figure 6.

The form of the stability curve is very similar to that shown in Figure 9 for the $0.5 H_d$ jet position. However, there are some significant differences, the most obvious of which is the absence of the lobe region. The second is that attached flames do not appear for values of LP greater than $0.83 \text{ lbm}/(\text{sec.ft.}^3 \text{ atm.}^n)$, and at this loading there is an abrupt change to the less stable transition and lifted flames. For the $0.5 H_d$ jet position attached flames are observed out to loadings of $1.15 \text{ lbm}/(\text{sec.ft.}^3 \text{ atm.}^n)$. The initial gradient of the lifted flame portion of the characteristic in Figure 10 is the same as that in Figure 9; however, because of the absence of the lobed region and the abrupt change in flame type, it begins at much lower values of LP. The implication of this is that the primary zone with combustion air jets at $0.75 H_d$ downstream from the dome will achieve its peak heat release rate condition at a smaller loading parameter than does the primary zone with its jets at $0.5 H_d$. The peak heat release rate condition is achieved when the primary zone equivalence ratio at blowout reaches a value of unity.

If Figures 9 and 10 to the same scale are overlaid, the area above the curve (on the flame-side) is greater for the primary zone with the combustion air jets at $0.5 H_d$ downstream from the dome. In other words, this primary zone has better stability over a wider range of operating conditions than does the other primary zone. This finding is consistent with the CO data contained in Figure 5 at low values of overall equivalence ratio approaching a blowout condition, which suggested that the $0.5 H_d$ jet position might have the best stability.

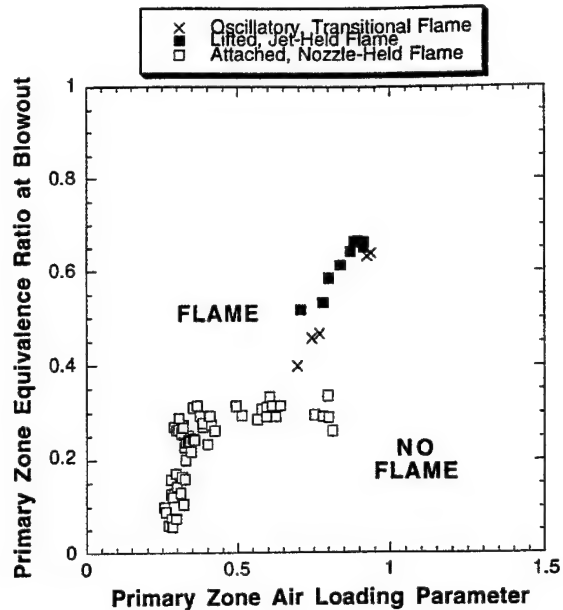


Figure 10: Portion of LBO Curve for 0.50 in. Jets at Three-Quarters Dome Height Downstream

Effect on LBO of Jet Type

The partial stability curve for the multi-jet ports at the position of half a dome height downstream from the dome is presented in Figure 11. Again, the data are delineated by the major category of flame-type observed. The amount of jet air recirculated is again taken as 27.9 percent, although this is somewhat tentative for this jet configuration.

Although the data are rather sparse, it can be seen that the shape of the curve is somewhat similar to that for the 0.50 in. (12.7 mm) jets at $H_d/2$, as displayed in Figure 9, to which Figure 11 should be compared, i.e. there is a lobe, although it is an abbreviated one. Note also that for loading parameters greater than about $0.95 \text{ lbm}/(\text{sec.ft.}^3 \text{ atm.}^n)$ there is a sudden change in the flameholding from the attached category alone to flames of either attached, transition, or, lifted categories. In this region the correlation of data is poor. It is probable that the characteristics of the lifted, jet-held, flames are strongly influenced by the individual jetlet origin of the air making up the gross combustion air jets.

When Figure 11 is overlaid with Figure 9 to the same scale, it is apparent that there is a serious loss of area in the flame region above the curve obtained for

the 0.50 in. plain jets at this axial position, i.e the use of the multi-jet port configuration results in a loss in stability.

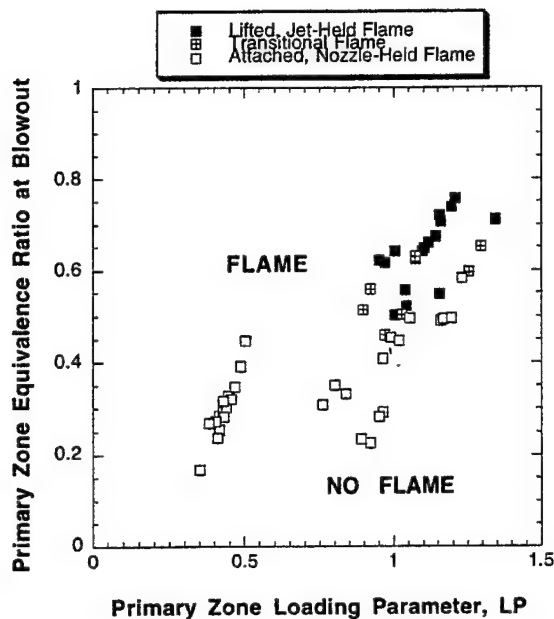


Figure 11: Portion of LBO Curve for Multi-Jets at One-Half Dome Height Downstream

Discussion

With respect to UHC and CO at least, Figure 2 suggests that the simulation of engine conditions at higher power levels used in operating the test vehicle, is satisfactory. Other, similar, comparisons not presented here, for NOx, tend to confirm this.

Previous work presented in Reference 7 had shown that for combustion air jets positioned at $0.5 H_d$ downstream from the dome, the 0.5 in. (12.7 mm) circular jets had the lowest total emissions for a given primary zone equivalence ratio. For this reason the present work was centered on these jets.

For the 0.5 in. (12.7 mm) jets the CO is at equilibrium for overall equivalence ratios equal to and greater than 0.5 at all jet distances from the dome (Figure 4). Therefore, there is almost no sensitivity of CO to jet distance. The very slight increases in CO with increasing jet distance shown in Figure 3 are most likely associated with heat losses from the primary zone. The existence of the CO minima seen in Figure 4

arises as the gas temperatures due to local heat release fall with reducing equivalence ratio, and the bulk residence time consequently becomes inadequate to reduce CO to the equilibrium levels. CO then eventually increases as combustion efficiency falls further on the approach to an LBO. Figure 5 indicates, from the sharp increases in CO at low equivalence ratios beyond the CO-minima, that increasing the jet distance from the dome progressively reduces the stability of the primary zone.

Figure 6 shows that the variation of NOx with jet distance depends on whether the primary zone is operated rich or lean. For a lean primary zone the lowest primary zone equivalence ratio gives the lowest NOx, and the NOx increases with jet distance. This behavior is characteristic of thermal NO. For a stoichiometric or rich primary zone the NOx reaches a minimum at $0.75 H_d$ jet distance from the dome. This is most probably due to a changing balance in the combined NOx due to the prompt mechanism in the dome and the thermal mechanism around the jets. The variation in Figure 6 for a stoichiometric primary zone is like that for a rich primary zone, and for jet distances greater than $0.75 H_d$, gives lower NOx than does the 0.5 equivalence ratio primary zone at these distances. This is undoubtedly due to fuel/air unmixedness effects that result in the actual burning taking place over a wide range of equivalence ratios on either side of the bulk value.

The overall emissions assessment made in Figure 7 identifies the $0.5 H_d$ jet location as yielding the lowest net pollution for primary zone bulk equivalence ratios in the range 0.5 to 1.1.

Figure 8 gives the surprising result that the same quantity of air introduced at the same axial position in the combustor can result in quite different emissions levels, and that these depend on the initial jet shape. In this instance, the design intent of the multi-jet holes was to improve the mixing of combustion jet air with the gases exiting the primary zone. In practice, the increased perimeter of the multi-jets merely increased the stoichiometric burning interface around the jets. This did not change CO, but did increase thermal NO dramatically, by a peak factor essentially equal to the perimeter increase, i.e. by a factor of about 2.

The indications from Figure 5 that increasing the distance of the 0.5 in. (12.7 mm) combustion air jets from the dome would decrease the primary zone stability, were confirmed by the stability characteristics

measured and presented in Figures 9 and 10. The details of the effects seen remain to be explored using laser diagnostics, but the blowout tests did reveal the complex flame behavior that was governed not only by the primary zone loading, but also by the details of the airblast-atomizing fuel injector.

Somewhat surprisingly, the multi-jet configuration with its increased burning perimeter around the individual jets, had the worst stability at the 0.5 H_d position compared to the 0.5 in. (12.7 mm) plain circular jets. It is not immediately clear why this should be so. The indications from the lifted-jet flame-holding region suggest that the individual jets offered a variety of "choices" as to local flame type. Again, resolution of what determines a "choice" will require application of laser diagnostics.

If common-scale versions of Figures 9, 10 and 11 are overlaid, the attached-flame region at primary zone loadings less than 0.5 lbm/(sec.ft.³atm.ⁿ) are identical. This indicates that stability is entirely determined by events in the dome, although the jets do exert some back-pressure effects.

Conclusions

1. Combustion air admitted to the combustor primary zone by opposed 0.5 in. (12.7 mm) circular ports placed inline with the fuel injector and positioned at 0.75 dome heights downstream from the dome, results in minimum NOx.
2. Minimum overall pollution is generated when these jets are positioned 0.5 dome heights downstream from the dome.
3. For stoichiometric and slightly rich primary zones having the same quantity of combustion air introduced at the same axial location, the resulting NOx is affected by the initial jet shape, with the quantity of NOx apparently being proportional to the jet perimeter.
4. For circular 0.5 in. (12.7 mm) diameter combustion air jets, the combustor stability is reduced when the jets are moved downstream from the 0.5 dome height axial position.
5. For combustion air jets at the same axial position of 0.5 dome heights from the dome, and passing the same quantity of air, the combustor stability is worsened when the jet initial perimeter is increased by use of multi-jets rather than a single, circular jet.

6. When an airblast-atomizing fuel injector is used in a combustor, the stability characteristic depends not only on the primary zone bulk loading parameter and the combustion air jet configuration, but also on the local stoichiometries in the initial flame-holding region and, how these are influenced by the details of the injector design.

7. For an attached flame condition combustor stability is determined by events in the dome, regardless of jet configuration and position.

8. Optimizing a primary zone design for low emissions should not be done independently of combustor stability.

Acknowledgements

The enthusiasm, motivation and support of Dr. W.M. Roquemore of Wright Laboratory are greatly appreciated. The authors wish to thank Ron Britton, Melvin Russell (WL) and Charlie Smith (ISSI) for their patience and assistance in operating the test facility and in making the emissions measurements. This on-going research is sponsored by the U.S. Air Force, Wright Laboratory, Aero Propulsion and Power Directorate.

References

1. International Civil Aviation Organization (ICAO) Annex 16, Vol. II, 1981; ICAO Annex 16, Vol. II, 2nd. Edition, 1993.
2. AFR 19-1: "Protection and Enhancement of Environmental Quality," 18 February, 1972.
3. AFR 19-2: "Air Force Guidance on Major Actions Significantly Affecting the Quality of the Human Environment," 20 January, 1972.
4. Sturgess, G.J., McKinney, R.G. and Morford, S.A., "Modifications of Combustor Stoichiometry for Reduced NOx Emissions from Aircraft Engines," Trans. ASME, *J. Engrg. Gas Turbines and Power*, Vol. 115, No.3, 1993, pp. 570-580.
- 5.
6. Gogineni, S., Shouse, D., Frayne, C., Stutrud, J. and Sturgess, G.J., "Influence of Combustion Air Jets on Primary Zone Characteristics for Gas Turbine Combustors," proc. ISABE 12th. Intl. Symp. on Air

Breathing Engines, editor F. Billig, Vol.1, Melbourne, Australia, September 10-15, 1995, pp. 475-487.

7. Shouse, D.T., Frayne, C., Stutrud, J., Gogineni, S. and Sturgess, G.J., "The Role of Transverse Air Jets in the Formation of Gas Turbine Emissions," Paper No. 96-0705, pres. AIAA 34th. *Aerospace Sciences Meeting & Exhibit*, Reno, Nevada, January 15-18, 1996.

8. Sturgess, G.J., Sloan, D.G., Lesmerises, A.L., Heneghan, S.P. and Ballal, D.R., "Design and Development of a Research Combustor for Lean Blowout Studies," Trans. ASME, *J. Engrg. Gas Turbines and Power*, Vol.114, No.1, January 1992, pp. 13-19.

9. Sturgess, G.J., Heneghan, S.P., Vangsness, M.D., Ballal, D.R., Lesmerises, A.L. and Shouse, D.T., "Effects of Back-Pressure in a Lean Blowout Research Combustor," Trans. ASME, *J. Engrg. Gas Turbines and Power*, Vol.115, Vol.3, July, 1993, pp. 486-498.

10. Spalding, D.B., "Performance Criteria of Gas Turbine Combustion Chambers - A Method of Comparison and Selection for the Designer," *Aircraft Engineering Monograph*, Bunhill Publications Ltd., London, England, August 1956.

11. Sturgess, G.J., "Pollution Aspects of Aircraft Gas Turbine Engines," Workshop Lecture Notes on *Advanced Aircraft Engine Design, Vol.II*, given at National Cheng Kung University, Tainan, Taiwan, R.O.C., May 24-26, 1994.

12. Sturgess, G.J., Heneghan, S.P., Vangsness, M.D., Ballal, D.R. and Lesmerises, A.L., "Lean Blowout in a Research Combustor at Simulated Low Pressures," Paper No. 91-GT-359, pres. ASME *Intl. Gas Turbine and Aeroengine Congress and Exposition*, Orlando, Florida, June 3-6, 1991.

13. Marshall, A.W. and Gupta, A.K., "Effects of Jet Momentum Distribution on Thermal Characteristics of Co-Swirling Flames," Paper No. 96-0404, pres. AIAA 34th. *Aerospace Sciences Meeting & Exhibit*, Reno, Nevada, January 15-18, 1996.

14. Hedman, P.O., Sturgess, G.J., Warren, D.L., Goss, L.P. and Shouse, D.T., "Observations of Flame Behavior from a Practical Fuel Injector Using Gaseous Fuel in a Technology Combustor," Trans. ASME, *J. Engrg. Gas Turbines and Power*, Vol.117, No.3, July 1995, pp. 441-452.

15. Gupta, A.K., Lilley, D.G. and Syred, N., *Swirl Flows*, Abacus Press, London, England, 1984.

16. Sturgess, G.J. and Shouse, D.T., "Lean Blowout Research in a Generic Gas Turbine Combustor with High Optical Access," Paper No. 93-GT-332, pres. ASME *Intl. Gas Turbine and Aeroengine Congress and Exposition*, Cincinnati, Ohio, May 24-27, 1993, (to appear in ASME Trans.).

Study of Flame Stability in a Step Swirl Combustor

M. D. Durbin

M. D. Vangsness

D. R. Ballal

Fellow ASME

University of Dayton,
Dayton, OH 45469

V. R. Katta

Innovative Scientific Solutions, Inc.,
Dayton, OH 45430

A prime requirement in the design of a modern gas turbine combustor is good combustion stability, especially near lean blowout (LBO), to ensure an adequate stability margin. For an aeroengine, combustor blow-off limits are encountered during low engine speeds at high altitudes over a range of flight Mach numbers. For an industrial combustor, requirements of ultralow NO_x emissions coupled with high combustion efficiency demand operation at or close to LBO. In this investigation, a step swirl combustor (SSC) was designed to reproduce the swirling flow pattern present in the vicinity of the fuel injector located in the primary zone of a gas turbine combustor. Different flame shapes, structure, and location were observed and detailed experimental measurements and numerical computations were performed. It was found that certain combinations of outer and inner swirling air flows produce multiple attached flames, a flame with a single attached structure just above the fuel injection tube, and finally for higher inner swirl velocity, the flame lifts from the fuel tube and is stabilized by the inner recirculation zone. The observed difference in LBO between co- and counterswirl configurations is primarily a function of how the flame stabilizes, i.e., attached versus lifted. A turbulent combustion model correctly predicts the attached flame location(s), development of inner recirculation zone, a dimple-shaped flame structure, the flame lift-off height, and radial profiles of mean temperature, axial velocity, and tangential velocity at different axial locations. Finally, the significance and applications of anchored and lifted flames to combustor stability and LBO in practical gas turbine combustors are discussed.

Introduction

A prime requirement in the design of a modern gas turbine combustor is good combustion stability, especially near lean blowout (LBO), to ensure an adequate stability margin. For an aircraft engine, combustor blow-off limits are encountered during low engine speeds at high altitudes over a range of flight Mach numbers and a good design ensures that the combustor steady-state burning remains within the operating envelope. This envelope should be extensive enough to encompass the under- and overshoots associated with the different response rates to the throttle movements of the fuel system and the rotating machinery. For an industrial combustor, requirements of ultralow NO_x emissions coupled with high combustion efficiency demand operation at or close to LBO, thereby eroding the safety margins. Therefore, a fundamental study of flame stability in a model step swirl combustor (SSC) has important practical applications, and this provided a strong motivation to undertake the present investigation.

The physical mechanisms responsible for the stabilization of a flame on the fuel injector lip (in the near-field region) are not fully understood. In the past, the stabilization mechanism of free jet diffusion flames has been investigated by Vanquickenborne and van Tiggelen (1966), Gollahalli et al. (1985), Pitts (1988, 1990), Bradley et al. (1990), Takahashi et al. (1984, 1990), and Takahashi and Goss (1992). A prime goal of these investigations was to predict flame blowout accurately. For example, Vanquickenborne and van Tiggelen (1966) developed the stabilization criterion that the total approach velocity should be balanced by the turbulent burning velocity of the mixture. Takahashi et al. (1984) found that the local velocities in the vicinity of an attached flame are laminar, and the flame stability mechanism is the balance of the total approach velocity

in the attached flame zone with the laminar burning velocity of the mixture. However, in a modern annular gas turbine combustor, the flame is stabilized by producing a swirl-induced recirculation zone in the flow field. This zone is generated by a combination of three mechanisms: an axial swirling air jet associated with each fuel introduction, sudden expansion of the axial swirling jets as they enter the primary zone, and back pressure provided by an array of radial air jets at the end of the primary zone. An SSC was designed to reproduce this type of complicated recirculation flow pattern. This paper discusses the different shapes, structure, and location of the stabilized flame in the SSC and how these various factors affect LBO.

Test Facility

The SSC. Figure 1 shows a schematic diagram of the SSC, which has a 150 × 150-mm cross section with rounded corners, length of 754 mm, and a step height of 55 mm. The SSC provides a geometrically simple, optically accessible research combustor capable of reproducing the fuel-air mixing pattern downstream of the airblast atomizer located in the dome region of a modern annular gas turbine combustor. The SSC also offers independent control over inner and outer airstreams. The SSC was mounted on a vertical combustion tunnel with a three-axis traversing mechanism.

Fuel was supplied to the combustor by the annular fuel tube (20 mm i.d. and 29 mm o.d.), which is coaxially sandwiched between swirling airstreams: the inner air jet (20-mm-dia) and the outer annular air jet (29 mm i.d. and 40 mm o.d.). The combustor exit has a 45 percent blockage orifice plate on top, which simulates the back pressure exerted by the dilution jets in a practical gas turbine combustor (see Sturgess et al., 1990). The SSC has quartz windows on all four sides to permit visual observations and laser diagnostics measurements. The stationary helical vane swirlers were located 25 mm upstream from the burner tube exit in each of the air passages. The inner swirler has six vanes with a central 1.4-mm-dia hole to prevent the flame from anchoring to the swirler. The outer swirler has

Contributed by the International Gas Turbine Institute and presented at the 40th International Gas Turbine and Aeroengine Congress and Exhibition, Houston, Texas, June 5-8, 1995. Manuscript received by the International Gas Turbine Institute February 10, 1995. Paper No. 95-GT-111. Associate Technical Editor: C. J. Russo.

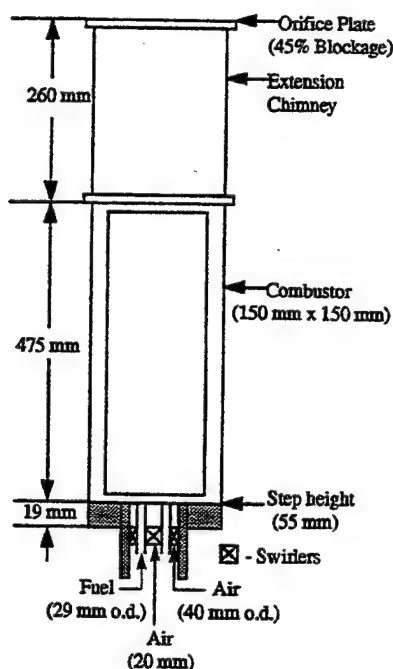


Fig. 1 Schematic diagram of a step swirl combustor

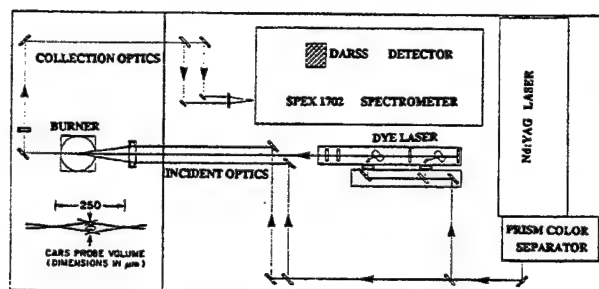


Fig. 2 Schematic of the CARS system optics

twelve vanes. Inner swirler lengths are 25 and 19 mm, respectively, for 30 and 45 deg swirlers; outer swirler length was 32 mm for the 30 deg swirler. Swirler lengths and number of vanes were adequate to ensure that the air closely follows the swirl vane angle. The swirlers were precision-fabricated in a rapid prototype manufacturing process known as stereolithography. These swirlers performed satisfactorily at the level of high temperatures present in the SSC.

Instrumentation

CARS System. Figure 2 shows a schematic of a Coherent Anti-Stokes Raman Spectroscopy (CARS) optics system, which was used for nonintrusive flame temperature measurements. Pan et al. (1991) have provided detailed information on

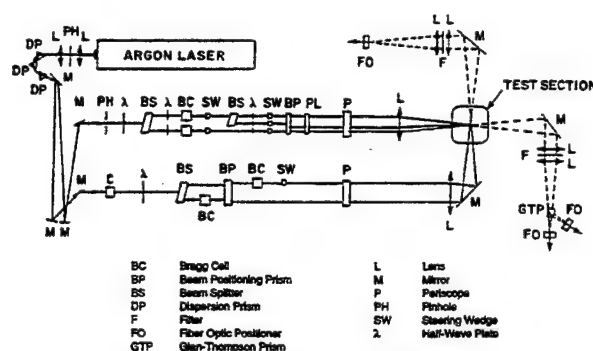


Fig. 3 Schematic of the LDA system optics

CARS measurements. Briefly, the CARS signal was generated by combining two 30 mJ doubled Nd:Yag beams at 532 nm and one 25 mJ broad band dye laser beam centered at 607 nm and pumped by the same Nd:Yag laser. The pulse laser and detector camera run at 10 Hz. A Boxcars configuration with an ellipsoidal probe volume approximately $25 \mu\text{m}$ (dia) \times $250 \mu\text{m}$ (length) was used for collecting the signal. The detector is a Princeton Instruments intensified 576×384 charge coupled device (CCD). The intensifier is triggered by a Princeton PG-10 pulser. A Princeton ST-130 controller operates the camera and the detector cooler. The collection process is controlled by Princeton's ST-130 CSMA software package running on a personal computer. Spectra are fit to a library of spectra by a nonlinear fitting routine running on a personal computer. A total of 250 samples were taken for each CARS temperature measurement.

LDA System. Figure 3 illustrated the optical setup of the LDA system. Nonintrusive velocity measurements were made using a Dantec Fiber-Flow LDA system. Essentially, this LDA system is an upgraded version of the system used by Durbin and Ballal (1996). The two-dimensional LDA system uses the 514 nm and 488 nm lines from an argon-ion laser. The laser output is directed into a Dantec Fiber flow transmitter where the colors are separated and directed to optical fiber couplers by a Bragg cell operating at 40 MHz. The four beams are guided to the probe via polarization preserving fibers. The recollimated and focused laser beams cross to produce an ellipsoidal probe volume approximately $100 \mu\text{m}$ (dia) \times $1000 \mu\text{m}$ (length). A fluidized-bed seeder was used to inject submicron-sized (97 percent $< 1 \mu\text{m}$) ZrO_2 particles into each burner tube passage. Velocity biasing was resolved by seeding one passage at a time in a manner similar to Takahashi et al. (1992). The forward scattered signal is collected and separated by dichroic mirrors before it is detected by photomultiplier tubes and processed by individual TSI burst counters. Typical coincident sampling rates exceeded 1 kHz in flames. A total of 2048 coincident samples were collected for each velocity measurement. Custom-designed software was used to reduce the data on a personal computer. Three-component noncoincident velocity measurements were made with the two-dimensional LDA system by scanning in the transverse and radial directions to get axial and

Nomenclature

k = turbulent kinetic energy
 Re = Reynolds number
 T = mean temperature
 U, W = mean axial and tangential velocities, respectively

X, Y, Z = transverse, radial, and axial directions, respectively
 ϵ = turbulent-energy dissipation rate
 θ = swirl vane angle
 ϕ = overall equivalence ratio

Subscripts

f = fuel
 i = inner
 o = outer

Table 1 Test matrix for the step swirl combustor experiments (all tests at room temperature and atmospheric pressure)

Variable	Range
Inner vane angle, θ_i , degrees	0, 30 and 45
Outer vane angle, θ_o , degrees	30
Vane configuration	co and counter-swirl
Inner air velocity, U_i , m/s	14.4
Re	18.0×10^3
Outer air velocity, U_o , m/s	8.6
Re	14.8×10^3
Fuel velocity, U_f , m/s	2.5
Re	3.2×10^3
Equivalence ratio, ϕ	0.9
Fuel	methane

tangential velocities, and axial and radial velocities, respectively.

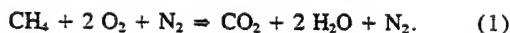
Test Conditions. Table 1 lists all the test conditions. Durbin and Ballal (1996) have shown that increasing the inner vane angle increases turbulent mixing and strengthens the inner recirculation zone; these changes dramatically affect the flame structure and the stability characteristics. Therefore, experiments were performed to reveal the differences in flame structure by changing the inner vane angle. Test conditions were also chosen to compare: (i) attached versus lifted flames and (ii) co-versus counterswirl configurations.

Experimental measurements included flame photography, three-component mean and rms velocities, mean and rms temperatures, and LBO. The LBO data were collected by maintaining a constant airflow rate, heating the combustor to a near steady-state temperature at stoichiometric fuel-air ratio, and then gradually decreasing the fuel flow rate until blowout occurred. This is a standard procedure that has been adopted in our laboratory since the work of Sturgess et al. (1991).

Turbulent Combustion Model

A time-dependent axisymmetric model, which solves axial- and radial-momentum equations, continuity, swirl, turbulent energy (k), turbulent-energy dissipation (ϵ), and enthalpy and species conservation equations was used to simulate the flow-field in the SSC. The standard isotropic $k-\epsilon$ turbulence model was incorporated into this code. Details are described by Katta and Roquemore (1993) and Katta et al. (1994). Briefly, in this turbulence model, density (ρ) was obtained by solving the state equation while pressure field at every time step is determined from pressure Poisson equations. Even though all the governing equations were solved in an uncoupled manner, the turbulence and species conservation equations are coupled through the source terms during the solution process to improve the stability of the algorithm.

In the present analysis of reacting flows, a simple global-chemical-kinetics model involving methane, oxygen, water, carbon dioxide, and nitrogen was used as follows:



The specific reaction rate for Eq. (1) was written in Arrhenius form with an activation energy of 20 kcal/mole and pre-exponential of $2.0 \times 10^{19} \text{ m}^6/\text{mole}^2/\text{s}$. These rate constants were determined by predicting the lift-off of a 8 m/s laminar methane jet flame (Katta, 1995).

An orthogonal, staggered grid system with varying cell sizes in both the z and y directions was utilized. The momentum and swirl equations were integrated using an implicit Quadratic Upstream Interpolation for Convective Kinematics with Estimated Streaming Terms (QUICKEST) numerical scheme

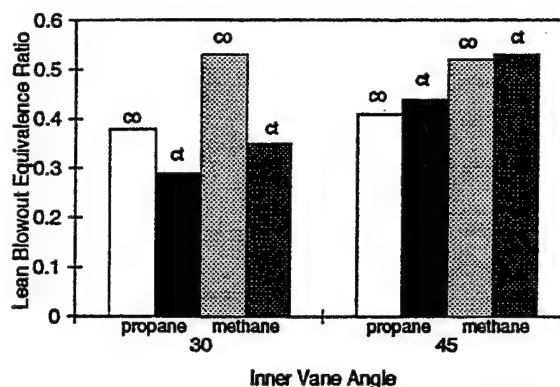


Fig. 4 Lean blowout data comparing inner vane angle, co-swirl (co) and counter-swirl (ct), and methane with propane. Test conditions were $\theta_o = 30^\circ$, $\phi = 0.9$, $U_i = 14.4 \text{ m/s}$, $U_o = 8.6 \text{ m/s}$, $U_f = 2.5 \text{ m/s}$.

(Katta et al., 1994; Leonard 1979), which is third-order accurate in both space and time and has a very low numerical diffusion error. On the other hand, the species, enthalpy, and turbulence-energy conservation equations, which have relatively large source terms, were integrated using the hybrid scheme of Spalding (1972). By rearranging the terms, the finite-difference form of each governing equation at all grid points was written as a system of algebraic equations, which was then solved by using Alternative Direction Implicit (ADI) technique. The time increment, Δt , was determined from the stability constraint and maintained as a constant during the entire calculation. The pressure field at every time step was accurately calculated by simultaneously solving the system of algebraic pressure Poisson equations at all grid points using the LU (Lower-Upper) decomposition technique.

Temperature- and species-dependent thermodynamic and transport properties were used in this formulation. The enthalpy of each species was calculated from polynomial curve-fits, while the viscosity, thermal conductivity, and diffusion coefficients of the species were estimated from the Leonard-Jones potentials. Measured velocity profiles were used at the fuel and air inflow boundaries. All other flow variables (k , ϵ , mass fractions, and T) along these boundaries were assumed to be distributed uniformly. A simple extrapolation procedure (Katta et al., 1994) with weighted zero- and first-order terms was used to estimate the flow variables on the outflow boundary. The usual no-slip, adiabatic, and chemically inert boundary conditions were applied at the walls. Wall functions were used for determining the gradients of the flow variables near the walls.

Results and Discussion

Experimental Observations

Flame Stability. LBO data were collected for all test conditions. In addition, some propane LBO data were collected to examine fuel effects on flame stability. Figure 4 shows LBO data comparing co- and counterswirl and propane with methane. These differences will be discussed after examining flame characteristics utilizing long exposure flame photographs taken with a 35-mm camera. Figure 5(a-e) reveal dramatic flame structure differences in the five test configurations. The only two variables in test conditions for the five cases were inner vane angle and co- or counterswirl configuration. Test conditions were $\theta_o = 30 \text{ deg}$, $\phi = 0.9$, $U_i = 14.4 \text{ m/s}$, $U_o = 8.6 \text{ m/s}$, $U_f = 2.5 \text{ m/s}$, using methane fuel.

Figure 5(a) shows that no swirl in the inner air stream produces a long tubelike central flame structure. The 30 deg outer swirl produces an outer flame structure, which approximates the 30 deg pattern. The attached flame appears to be stabilized

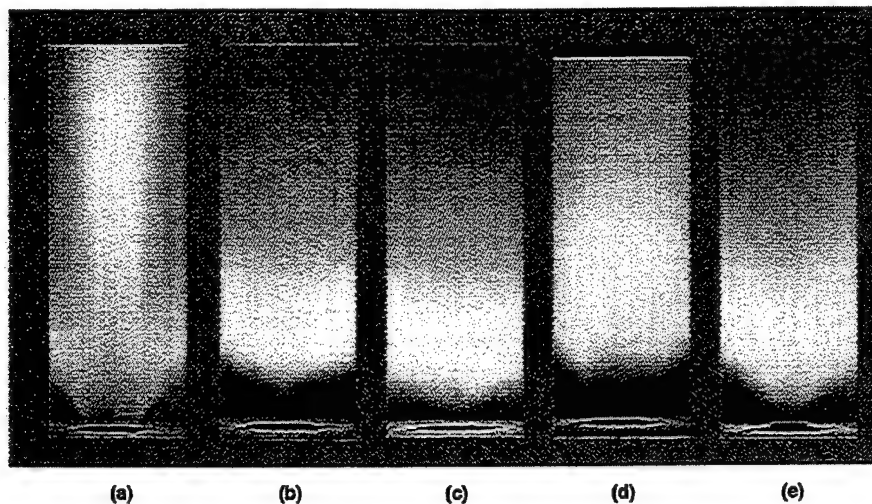


Fig. 5 Photographs illustrating the flame structure for (a) $\theta_i = 0$ deg, (b) $\theta_i = 30$ deg coswirl, (c) $\theta_i = 45$ deg coswirl, (d) $\theta_i = 30$ deg counterswirl, and (e) $\theta_i = 45$ deg counterswirl. Test conditions were $\theta_o = 30$ deg, $\phi = 0.9$, $U_i = 14.4$ m/s, $U_o = 8.6$ m/s, $U_f = 2.5$ m/s, methane.

at the inner air side of the fuel tube and also at the outer air side of the fuel tube. Small traces of flame structure outside the outer air stream are also visible and this can only occur if the fuel penetrates the fast-moving outer air stream or if the fuel recirculates in the outer recirculation zone before burning. It is suspected that the dynamic characteristics of the turbulent flow bring packets of fuel into the recirculation zone and these packets, in turn, burn in the mixing layer of the outer air and the recirculation zone. Sturgess et al. (1991) have observed similar results for a flame stabilized in the outer recirculation zone. This dynamic turbulent exchange phenomenon is more dramatic for an outer vane angle of 60 deg, which produces a stronger outer recirculation zone.

Figure 5(b) shows a flame photograph with coswirl configuration and 30 deg inner vane angle. The flame is lifted, there is premixing at its base, and it stabilizes with a dimple shape within the inner recirculation zone. The flame lifts because the

inner air stream penetrates the fuel stream with a velocity too high for an attached flame to stabilize and the flame is blown downstream. Also, the inner recirculation is caused by the inner air stream pushing out toward the wall, leaving a low-pressure region in the central portion of the combustor. Chen and Driscoll (1988) have made similar observations on the formation and structure of an inner recirculating vortex. Figure 5(c) shows that increasing the inner vane angle from 30 deg coswirl to 45 deg coswirl widens the flame shape and decreases the lift height. This occurs because an increase in vane angle increases the size and strength of the inner recirculation zone but it does not change the stability mechanism; i.e., flame is still stabilized within the inner recirculation zone.

Figure 5(d) shows the flame structure for 30 deg inner vane angle counterswirl. The flame has a bulbish shape above the fuel tube. Decreasing the fuel flow velocity causes the flame attachment just above the fuel tube. Figure 5(e) shows that

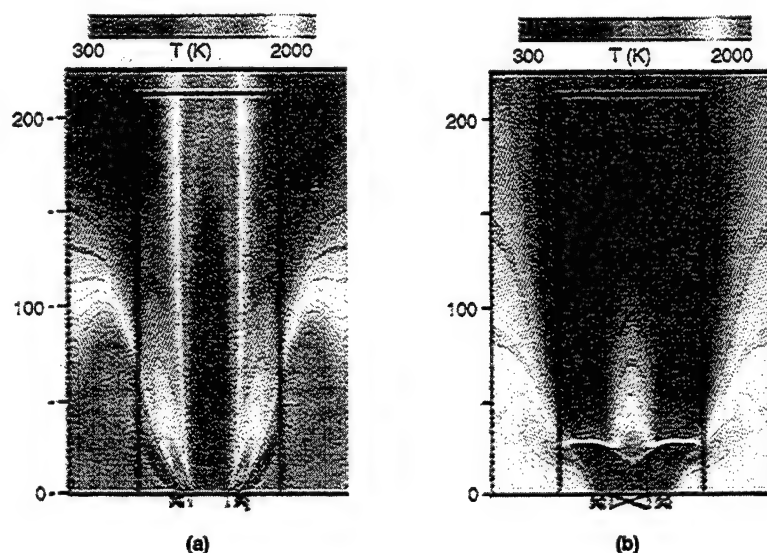


Fig. 6 Computed temperature distribution in SSC for (a) $\theta_i = 0$ deg and (b) $\theta_i = 30$ deg coswirl. Test conditions are identical to Figs. 5(a) and 5(b), respectively.

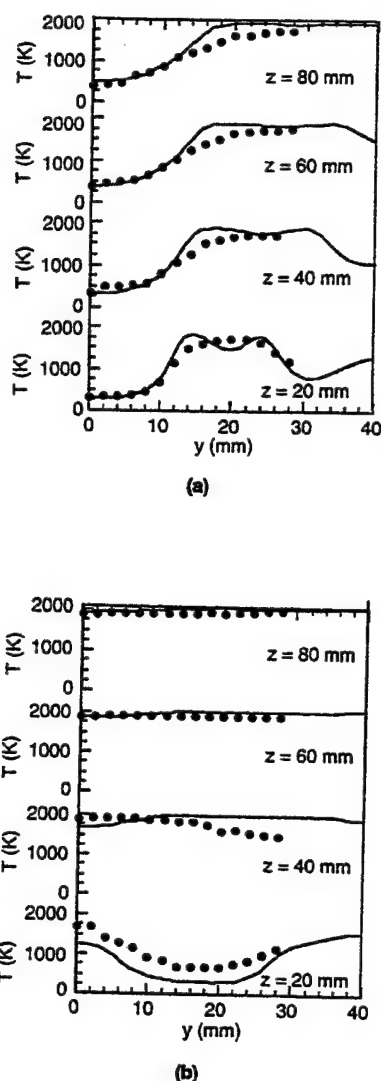


Fig. 7 Radial temperature profiles at different axial locations for (a) $\theta = 0$ deg, and (b) $\theta = 30$ deg. Test conditions correspond with Figs. 5(a) and 5(b), respectively. • Experimental, — computational.

increasing the inner vane angle from 30 deg counterswirl to 45 deg counterswirl causes too much penetration of the inner air into the fuel zone and this causes the flame to lift and stabilize within the inner recirculation zone.

Lean Blowout. Figure 4 shows LBO data comparing co- and counterswirl for two values of the inner vane angle, namely 30 and 45 deg, for both methane and propane gaseous fuels. The propane data were taken at identical test conditions for comparison purposes. Three observations can be made:

1 LBO values were found to be lower with propane fuel than with methane fuel for all the conditions of the tests. A plausible explanation is that the air/methane mass velocity ratio $(\rho U)_a/(\rho U)_m$ is higher than the corresponding air/propane ratio; this produces enhanced methane-air mixing (as compared to propane-air mixing) and hence a higher value of LBO. Figures 5(b), 5(c), and 5(e) for methane flames clearly show an evidence of premixing at the flame base followed by a lifted flame structure stabilized in the inner recirculation zone.

2 For a 30 deg inner vane angle, LBO values were lower for counterswirl as opposed to coswirl flow direction. This result

arises because for the counterswirl flow, shearing braids cause lower air velocities just above the fuel tube leading to an attached flame (which has a lower value of LBO); in contrast the coswirl flow gives higher axial mean velocity directly above the fuel tube, causing the flame to lift from the fuel tube thereby compromising flame stability; i.e., higher values of LBO are obtained.

3 As the inner vane angle is increased from 30 to 45 deg, LBO values increase correspondingly and also LBO becomes less sensitive to swirl flow direction. This happens because the higher (45 deg) inner swirl angle directs more inner airflow toward the fuel tube, causing the flame to lift. This lifted flame produces higher values of LBO.

Analysis

Flame Stability—Computed Results. Predictions were made for different flow conditions using the turbulent combustion model described earlier. Results in the form of temperature distributions for zero- and 30 deg inner coswirl cases (corresponding to Figs. 5(a) and 5(b) are shown in Figs. 6(a) and 6(b), respectively. Measured axial, radial, and tangential velocity profiles at the exits of the inner-air and fuel tubes and turbulent mass-averaged outer air velocity obtained from the volu-

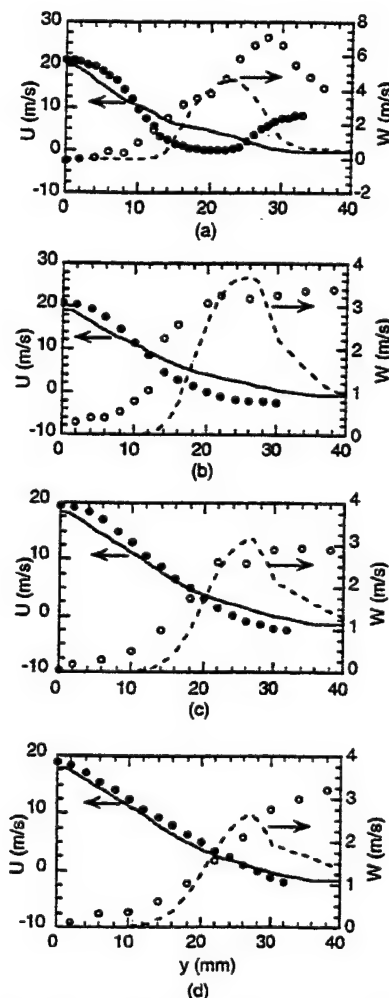


Fig. 8 Calculated and measured velocities for $\theta = 0$ deg case at axial locations (a) 20 mm, (b) 40 mm, (c) 60 mm, and (d) 80 mm. Circles and lines represent measured and computed velocities, respectively.

metric flow rate provided the inlet boundary conditions for these predictions. Figures 6(a) and 6(b) show the predicted flame images, i.e., temperature distributions corresponding to flame photographs shown in Figs. 5(a) and 5(b). Note, the inner box marked on the computed-flame images corresponds with the dimensions of the flame photographs. The following observations were made from the calculated temperature fields: (i) In Fig. 6(a) (zero inner swirl), the computations correctly predicted the locations of flames on either side of the fuel jet. (ii) In Fig. 6(b) (30 deg coswirl), a recirculation bubble develops inside the inner air jet and it produces the dimple-shaped flame, and (iii) the lift-off height for case (ii) predicted by the model matches well with the experimental data. These computations support the qualitative observations on flame photographs described above.

The calculated radial temperature profiles at different axial locations are compared with the measured data in Figs. 7(a) and 7(b) for zero swirl and 30 deg swirl cases, respectively. In Fig. 7(a), in the absence of swirl, the inner air jet spreads gradually, leading to a long tubelike inner flame. Both the calculations and measurements show that the temperature at the center of the SSC over the measurement range ($z = 0$ to 80 mm) is nearly the same as that of the room temperature air.

Figures 8 and 9 illustrate a comparison between predicted and measured velocities for the zero and 30 deg swirl cases, respectively. Axial (U) and swirl (W) velocity components were compared at different axial locations. For the no-swirl case, calculated velocity profiles agreed well with the experimental data. With 30 deg inner swirl, the measured swirl velocity was generally higher than the predictions, especially in the regions $Y > 22$ mm. Since the outer air was not seeded and the outer velocity profile was approximated, there are discrepancies at locations radially away from the outer jet.

In summary, our simple turbulence model with a single-step global-chemical-kinetics provides a reasonable prediction of flame shape and location, flame temperatures, and axial and swirl velocities. Wherever differences exist between predictions and measurements, an explanation is offered and further investigations along those lines are proceeding.

Flame Shape, Structure, and Location. From the examination of numerous flame photographs and the detailed numerical computations, flame stability in the SSC at the tested flow conditions primarily depends upon the attached flame and the lifted flame processes as sketched in Fig. 10 and described below. Sturgess et al. (1991) and Sturgess and Shouse (1993) have found that studies of such fundamental flame stability processes have great relevance to flame stability in modern annular gas turbine combustors.

1 Multi-attached flame. This type of attached flame is sketched in Figs. 10(a, b). As shown in Fig. 10(a), for the combination of strong outer swirl (60 deg) and zero inner swirl, the flame is simultaneously attached at three locations: (i) inner air side of the fuel stream, (ii) outer air side of the fuel stream, and (iii) outside of the outer air stream. It may be postulated that the dynamic characteristics of the flow bring packets of fuel into the outer recirculation zone, then burn in the mixing layer of the outer air and the recirculation zone. As the strength of the outer air swirl is decreased (30 deg) the attached flame structure shifts to that sketched in Fig. 10(b) where the flame no longer has an attachment on the outer air side of the fuel stream.

2 Single-attached flame. Figure 10(c) illustrates this single attached flame structure. This type of attached flame is observed for low inner (30 deg) and outer (30 deg) countercircling air flows. Such flow conditions cause the collapse of the twin attached flame structure sketched in Fig. 10(b) to a

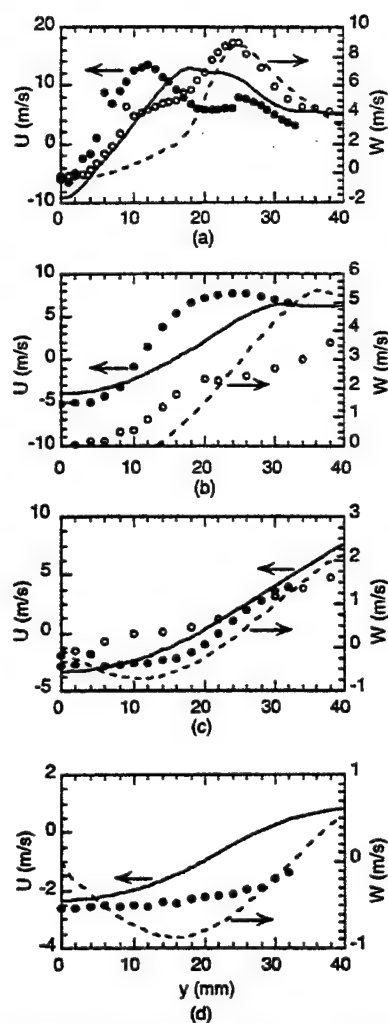


Fig. 9 Calculated and measured velocities for $\theta = 30$ deg case at axial locations (a) 20 mm, (b) 40 mm, (c) 60 mm, and (d) 80 mm. Circles and lines represent measured and computed velocities, respectively.

single attachment just above the fuel tube. This type of attached flame was also observed for the coswirl configuration but at a lower combustor loading.

3 Lifted flame. Figure 10(d) illustrates this type of flame; also it is observed in the photographs of Figs. 5(b), 5(c), and 5(e). The flame lifts from the fuel tube lip because of the high mean axial velocity in the near-field region above the fuel tube. The lifted flame is stabilized by the inner recirculation zone. However, increasing the swirl intensity and/or combustor loading only slightly changes flame stability, i.e., LBO values remain fairly constant for lifted flames. This is because the lifting of a flame is usually accompanied by a premixing of fuel and air at the base of the flame. This premixing compromises the stability of the lifted flame over that of an attached flame, i.e., LBO values are higher for a lifted flame than for an attached flame.

Now, it is also clear that the observed difference in LBO between co- and countercircling configurations, as shown in Fig. 4, is primarily a function of how the flame stabilizes. Counterswirl conditions readily produce an attached flame for moderate inner swirl intensity (30 deg); however, both configurations produce lifted flames for higher swirl intensity (45 deg) and for this

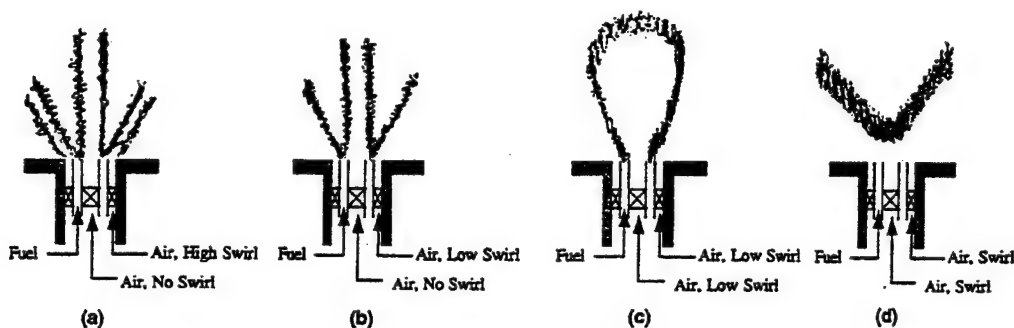


Fig. 10 Sketches illustrating the flame shape, structure, and location in the SSC

latter condition the LBO values are very similar. Finally, Sturgess et al. (1991) and Sturgess and Shouse (1993) have elucidated the significance and applications of anchored and lifted flames to practical gas turbine combustor stability and LBO. They observe three basic flame conditions: a thin sheathlike pilot anchored flame, a shear layer flame associated with the inner and outer recirculation zones, and a lifted main flame, which allows considerable premixing of reactants to take place prior to combustion. These observations further confirm the relevance and importance of the present work to practical gas turbine combustors.

Conclusions

An SSC was designed to reproduce the swirling flow pattern present in the vicinity of the fuel injector located in the primary zone of a gas turbine combustor. Different flame shapes, structure, and location were observed and detailed experimental measurements and numerical computations were performed.

1 For the combination of strong outer swirl and zero inner swirl, a multiple attached flame exists simultaneously over the fuel and air injection tubes. As the strength of the outer air swirl is decreased and that of the inner swirl increased, the flame structure gradually shifts to a single attachment above the fuel injection tube.

2 For higher inner swirl velocity, the flame lifts from the fuel tube and is stabilized by the inner recirculation zone. Premixing of fuel and air at the base of the flame compromises the stability of the lifted flame over that of an attached flame, i.e., LBO values are higher for a lifted flame than for an attached flame.

3 The observed difference in LBO between co- and counterswirl configurations is primarily a function of how the flame stabilizes. Counterswirl conditions readily produce an attached flame for moderate inner swirl intensity; however, both configurations produce lifted flames for higher inner swirl intensity and for this latter condition the LBO values are very similar.

4 Computations based upon a turbulent combustion model correctly predict the attached flame locations, the development of an inner recirculation zone, which produces a dimple-shaped flame structure, and finally the flame lift-off height. The calculated radial mean temperature profiles at different axial locations agreed well with the measured CARS temperature. Also, the calculated velocity profiles agree reasonably well with the LDA measurements of mean axial and mean tangential velocities. These computations show the presence of a strong inner recirculation zone in the SSC, provide the location of the reattachment point of this recirculation bubble, and confirm the transport of combustion products upstream.

Finally, Sturgess et al. (1991) and Sturgess and Shouse (1993) have elucidated the significance and applications of an-

chored and lifted flames to practical gas turbine combustor stability and LBO. This confirms the importance and relevance of the present work to gas turbine combustors.

Acknowledgments

This work was supported by the U.S. Air Force, Wright Laboratory, Fuels and Lubrications Division, Aero-Propulsion and Power Directorate, Wright Patterson Air Force Base, Dayton, OH, under contract No. F33615-92-C-2207, with Mr. Charles W. Frayne serving as the Air Force Technical Monitor. The authors wish to thank Mr. W. John Schmoll for the custom LDA processing software.

References

- Bradley, D., Gaskell, P. H., and Lau, A. K. C., 1990, "A Mixedness-Reactedness Flamelet Model for Turbulent Diffusion Flames," *Twenty-Third Symposium (International) on Combustion*, The Combustion Institute, p. 685.
- Chen, R. H., and Driscoll, J. F., 1988, "The Role of the Recirculation Vortex in Improving Fuel-Air Mixing Within Swirling Flames," *Twenty-Second Symposium (International) on Combustion*, The Combustion Institute, p. 281.
- Durbin, M. D., and Ballal, D. R., 1996, "Studies of Lean Blowout in a Step Swirl Combustor," *ASME JOURNAL OF ENGINEERING FOR GAS TURBINES AND POWER*, Vol. 118, pp. 72-78.
- Gollahalli, S. R., Savas, O., Huang, R. F., and Rodriguez Azara, J. L., 1985, "Structure of Attached and Lifted Gas Jet Flames in Hysteresis Region," *Twenty-First Symposium (International) on Combustion*, The Combustion Institute, p. 295.
- Katta, V. R., and Roquemore, W. M., 1993, "Numerical Method for Simulating Fluid-Dynamic and Heat-Transfer Changes in Jet Engine Injector Feed-Arm Due to Fouling," *Journal of Thermophysics and Heat Transfer*, p. 651.
- Katta, V. R., Goss, L. P., and Roquemore, W. M., 1994, "Numerical Investigations of Transitional H₂/N₂ Jet Diffusion Flames," *AIAA Journal*, Vol. 32, p. 84.
- Katta, V. R., 1995, internal report in preparation.
- Leonard, B. P., 1979, "A Stable and Accurate Convective Modeling Procedure Based on Quadratic Upstream Interpolation," *Computational Methods in Applied Mechanics and Engineering*, Vol. 19, p. 51.
- Pan, J. C., Vangsness, M. D., Heneghan, S., and Ballal, D. R., 1991, "Scalar Measurements of Bluff Body Stabilized Flames Using CARS Diagnostics," *ASME Paper No. 91-GT-302*.
- Pitts, W. P., 1988, "Assessment of Theories for the Behavior and Blowout of Lifted Turbulent Jet Diffusion Flames," *Twenty-Second Symposium (International) on Combustion*, The Combustion Institute, p. 809.
- Pitts, W. P., 1990, "Large-Scale Turbulent Structures and the Stabilization of Lifted Turbulent Jet Diffusion Flames," *Twenty-Third Symposium (International) on Combustion*, The Combustion Institute, p. 661.
- Spalding, D. B., 1972, "A Novel Finite Difference Formulation for Difference Expressions Involving Both First and Second Derivatives," *International Journal for Numerical Methods in Engineering*, Vol. 4, p. 551.
- Sturgess, G. J., Lesmerises, A. L., Heneghan, S. P., and Ballal, D. R., 1990, "Design and Development of a Research Combustor for Lean Blowout Research," *ASME JOURNAL OF ENGINEERING FOR GAS TURBINES AND POWER*, Vol. 114, p. 13.
- Sturgess, G. J., Sloan, D. G., Roquemore, W. M., Shouse, D., Lesmerises, A. L., Ballal, D. R., Heneghan, S. P., Vangsness, M. D., and Hedman, P. O., 1991, "Flame Stability and Lean Blowout—A Research Program Progress Report," Paper No. 91-7037, *Proceedings of Tenth ISABE*, Nottingham, United Kingdom.
- Sturgess, G. J., and Shouse, D., 1993, "Lean Blowout Research in a Generic Gas Turbine Combustor With High Optical Access," Paper No. 93-GT-332, to appear in the *Transactions of the ASME*.

Takahashi, F., Mizomoto, M., Ikai, S., and Fukati, N., 1984, "Lifting Mechanism of Free Jet Diffusion Flames," *Twentieth Symposium (International) on Combustion*, The Combustion Institute, p. 295.

Takahashi, F., Schmoll, W. J., and Vangsness, M. D., 1990, "Effects of Swirl on the Stability and Turbulent Structure of Jet Diffusion Flames," Paper No. AIAA-90-0036.

Takahashi, F., and Goss, L. P., 1992, "Near-Field Turbulent Structures and

the Local Extinction of Jet Diffusion Flames," *Twenty-Fourth Symposium (International) on Combustion*, The Combustion Institute, p. 351.

Takahashi, F., Vangsness, M. D., and Belovich, V. M., 1992, "Conditional LDV Measurements in Swirling and Non-swirling Coaxial Turbulent Air Jets for Model Validation," Paper No. AIAA-92-0580.

Vanquickenborne, L., and van Tiggelen, 1966, "The Stabilization Mechanism of Lifted Diffusion Flames," *Combustion and Flame*, Vol. 10, p. 59.



AIAA 97-0269

**Influences of Airblast-Atomizing Fuel Injector
Design on Primary Zone Characteristics at
Blowout**

G.J. Sturgess and S. Gogineni
Innovative Scientific Solutions, Inc.
Beavercreek, OH

D.T. Shouse
Aero Propulsion and Power Directorate
Wright Laboratory
Wright-Patterson Air Force Base, OH

35th Aerospace Sciences
Meeting & Exhibit
January 6-10, 1997 / Reno, NV

INFLUENCES OF AIRBLAST-ATOMIZING FUEL INJECTOR DESIGN ON PRIMARY ZONE FLAME CHARACTERISTICS AT BLOWOUT

G.J. Sturgess*

S. Gogineni*

*Innovative Scientific Solutions, Inc.,
Beavercreek, Ohio*

D.T. Shouse

*Aero Propulsion and Power Directorate,
Wright Laboratory,
Wright Patterson Air Force Base, Ohio*

Abstract

Extensive parametric investigations of experimental lean blowout data in a generic primary zone for two major combustion air jet patterns are presented. The data are delineated by flame shape, of which three basic categories are identified, with two sub-configurations being found within each category. It is shown that for a given aerodynamic flow pattern the flame type is determined by competing considerations of local equivalence ratio and residence time. For these reasons correlation of blowout data by means of a simple combustor loading parameter can breakdown, since a given loading parameter can be established by different combinations of operating conditions. Modeling of lean blowout therefore appears to be essential for a complete description of flame stability.

Background

The design of gas turbine engine combustors for aircraft application must address a wide range of goals that include gaseous emissions and operability. In seeking low gaseous emissions the operability goals, which include flame stability, altitude relight capability, turndown ratio capacity and combustion dynamics, cannot be compromised. Therefore, low emissions design approaches must always be considered in relation to their effects on operability.

Although military operations are currently not regulated for emissions, this situation is apparently

under review. In any case, U.S. Air Force "good neighbors" policies, as well as low observables considerations (smoke [particulates] and visible oxides of nitrogen ["brown smoke"]), demand that the emissions issues, and trades with operability, be fully understood.

Introduction

A study that is presently in progress is an investigation into the minimization of engine exhaust emissions, and into the relationship existing between generation of these emissions and combustor stability characteristics. This effort is part of the U.S. Air Force's *Combustor Design Model Evaluation (CDME) Program* being conducted by the **Aero Propulsion and Power Directorate** of Wright Laboratory, (WL/PO), Wright-Patterson Air Force Base, Ohio.

As a part of this Air Force work a broad-ranging investigation of combustor primary zone behavior is being conducted. The primary zone configuration selected for the initial portion of the study is a generic one that has demonstrated extremely low emissions of unburned hydrocarbons (UHC's) and carbon monoxide (CO) at low engine power conditions, together with moderate reductions in oxides of nitrogen (NOx) and acceptable exhaust smoke at high power conditions. It also has acceptable flame stability and altitude relight capability for routine engine service.

* AIAA Senior Member

+ AIAA Member

The combustor design approach is very simple¹, and is in use in several applications. To achieve the emissions goals it relies on a fuel-rich primary zone at take-off power levels for low NO_x, followed by an oxygen-rich intermediate zone to complete CO-burnout. The richness of the initial burning zone is constrained by considerations of smoke. At low power levels a concentrated local flame zone is established that has an equivalence ratio sufficient to result in very high combustion efficiencies. This zone also confers the requisite flame stability.

An important feature of the combustor primary zone is the use of an airblast-atomizing fuel injector. This injector, together with its associated "insert swirler," is responsible for establishing the detailed aerodynamic flow patterns that provide the low emissions and flame stability characteristics.

Previous Work

A complete description of the research combustor, rig, test facilities and, emissions instrumentation and measurement techniques, as well as of the high-power simulation and its justification, are given in Reference 2. Initial emissions information is presented in References 2 and 3, for a primary zone of fixed length equal to one-half of the combustor dome height. The results given were for a primary zone operated at a fixed dome pressure drop of 4.3 percent of inlet total pressure, and a fixed liner pressure drop of 3.0 percent, these values being representative of engine practice. The data presented are for gaseous propane as a fuel. Propane is a good simulant for jet fuels (Jet-A and JP8) and allows the effects of fuel atomization and evaporation to be separated from those of aerothermochemistry.

It was shown that for a given primary zone equivalence ratio the combustor dome alone (no combustion air jets) gave the lowest emissions, but that the dome alone had poor stability. When combustion air jets were present the lowest emissions and lowest overall equivalence ratio at lean blowout (LBO) were achieved when 0.50in. (12.7mm) diameter combustion air jets were used. These jets were opposed to each other, and were inline with a fuel injector.

Continuation of the work is presented in Reference 4 where the effects on emissions and LBO of primary zone length with the 0.50in (12.7mm) diameter combustion air jets are examined. For the emissions measurements the dome and liner pressure drops were

maintained at 4.3 and 3.0 percent respectively. The combustion air jet configuration remained unchanged (opposed and inline), but two jet configurations were used: single, circular-section, plain jets, and jets with the same total effective area as the plain jets but divided into four smaller individual jets arranged in diamond-fashion at the same distance downstream. Primary zone lengths of 0.50, 0.75 and 1.00 dome heights were used for each jet configuration.

For the gaseous emissions it is shown that the 0.50in. (12.7mm) diameter plain jets, opposed and inline with the injector, positioned at 0.75 dome heights downstream from the dome, gave the lowest NO_x. However, minimum overall pollution (CO, UHC and NO_x) was obtained with these jets at the 0.50 dome-height downstream position. For stoichiometric and slightly fuel-rich primary zones having the same amount of combustion air introduced at the same location, minimum NO_x was obtained for a jet configuration with the minimum net perimeter. This was indicative of a stoichiometric reaction zone surrounding the jets.

For combustion stability a complex picture emerged. Primary zone length exerted a strong influence on LBO, where for 0.50 primary zone equivalence ratio at blowout, the allowable combustor loading for the 0.50in. (12.7mm) jets was increased linearly with the inverse of length by an order of magnitude over the dome-alone stability. The best overall stability was obtained at the best overall emissions configuration, i.e. the 0.50in (12.7mm) jets at one-half dome height downstream. The worst stability (with the exception of the dome-alone) was obtained for the highest NO_x configuration, i.e. the diamond-array multi-jets at one-half dome height downstream from the dome.

Correlation of the blowout data at all primary zone lengths using a familiar combustor loading parameter⁵ revealed complex characteristics indicative of multiple flame zones. Data correlation using this approach with conventional application broke down for the diamond-array multi-jet combustion air jet configuration.

Depending on the operating conditions and the combustion air jet configuration, several different flame types at LBO were observed. There were three major such types clearly identified: attached, lifted and transitional; each major category itself contained two sub-types of flame. It was concluded that the flame behavior, and hence the LBO behavior, resulted from the interaction of the flowfield from the airblast-atomizing

fuel injector with that established by the combustion air jets.

Fuel Injector and Flame Characterization

Figure 1 provides a cross-section of the dome region in the present combustor⁶. It consists of a removeable airblast-atomizing fuel injector, injector/dome interfacing, and the dome.

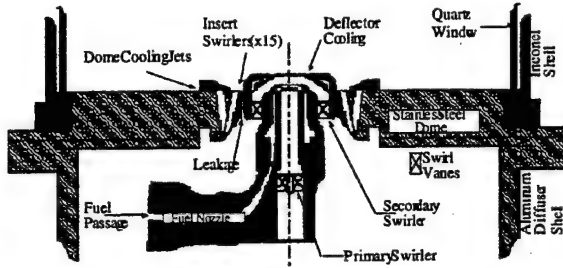


Figure 1: Cross-Section of Combustor Dome Region

The interfacing in the dome is a floating assembly semi-permanently mounted in the dome. It accommodates axial and radial thermal growths, and provides a radially-discharged film of dome cooling air. Integral with the interface assembly is an insert swirler providing 15 individual circular air jets. These jets can have a compound angle made up of an angle to the injector centerline, as well as a swirl angle. In the present instance the angle to the centerline was 12.5 degrees while the swirl angle was zero. The purpose of the insert swirler is primarily one of smoke control.

The fuel injector has air passages consisting of a central (primary) swirling air jet and a concentric outer (secondary) swirling air jet. Between the primary and secondary air jets is an annular fuel jet. The secondary air jet and the annular fuel jet are discharged to converge on the injector centerline. Two injectors have been used in this study, designated by LS and HS signifying low and high swirl components respectively. The work presented is for the HS injector.

For the HS injector the primary air jet had a measured effective area of 0.02456in², (15.85mm²) and the secondary air jet had an effective area of 0.10685in² (68.94mm²). The insert swirler effective area was 0.0539in² (34.77mm²), and the dome cooling metering area was 0.0770in² (49.68mm²). Leakage between the injector and the interface assembly was 0.00153in² (0.99mm²). The measured dome effective area was 0.2627in² (169.48mm²) compared to 0.2623in² (169.23 mm²) obtained from summation of the individual

contributions. Therefore, the injector contributed 49.3 percent of the total dome airflow, and the insert swirler contributed 20.2 percent of the dome total.

The outer air jet had a swirl angle of 55 degrees, while the inner jet had a swirl angle of 70 degrees. The annular fuel jet was also provided with swirl. The flow from all three passages co-rotated. The nominal swirl number (for the air passages) was 1.41. The discharge diameter for the outer jet was 0.590in. (14.986mm), and the insert swirler was on a pitch-circle diameter of 1.375in. (34.925mm).

Marshall & Gupta⁷ had observed similar flames and blowout behavior to that described in Reference 4. Their model burner/combustor was unconfined and had no combustion air jets, but it did allow the heat loading, Reynolds number and overall equivalence ratio to be held constant while swirl and flow distribution were systematically varied between two concentric airstreams arranged about a central, circular gaseous fuel source. The Marshall & Gupta burner was similar in many respects to that used presently. They observed seven strikingly different flames as the burner aerodynamics manipulated the combustion characteristics.

It is well-known⁸ for swirl flames produced by injector/swirler packages of the types described in References 2 and 7, that the thermal behavior is determined by some suitable injector equivalence ratio ϕ_{inj} , the injector passage momentum ratio MR , where

$$MR = \frac{\oint_{outer} \rho u^2 r dr}{\oint_{inner} \rho u^2 r dr} \quad (1.)$$

the overall swirl number S , where

$$S = \frac{2 \oint \rho w u r^2 dr}{D \oint \rho u^2 r dr} \quad (2.)$$

and,

u = axial velocity

w = tangential velocity

ρ = density

r = radius

D = overall diameter

and, individual passage swirl ratios.

Marshall & Gupta were able to characterize their observed flame behavior in terms of these four basic parameters.

On a one-dimensional flow basis Equation 1 can be reduced to,

$$MR = \left(\frac{\dot{m}_{a,outer}}{\dot{m}_{a,inner}} \right)^2 \frac{r_I^2}{(r_O^2 - r_I^2)} \quad (3.)$$

and Equation 2 to,

$$S = \frac{2r_{mean} \tan \theta}{D} \quad (4.)$$

where,

\dot{m}_a = air mass flow rate

θ = net swirl angle

and subscripts *O* and *I* refer to the outer and inner passage dimensions respectively. In obtaining Equation 4 from Equation 2 the effects of the fuel-swirl have been neglected.

Consideration now of Equations 3 and 4 for the present experiments reveals that as dome pressure drop, air inlet temperature and fuel flow rate are independently varied, *MR* and *S* will remain fixed to first order; only ϕ_{inj} will change. The passage swirl ratios also remain fixed.

Therefore, the presently observed flame shapes (six of them) are due only to the effects of injector equivalence ratio and, the interaction of a fixed nominal injector flow pattern with the combustion air jets.

Present Contribution

The interaction of fuel injector flows with combustion airjets through effects on the combustor stability in terms of LBO and flame type are described for 0.50in. (12.7mm) and 0.75in. (19.05mm) opposed plain jets at axial positions of 0.50 and 0.75 dome heights downstream. The combustor loading is varied through independent changes in dome and liner pressure drops, over a range of air inlet temperatures.

Test Vehicle

The combustor models a "single-cup" planar segment of an annular combustor², and consists of a single fuel injector and its associated dome interface, mounted in a plain bulkhead. The cross-section of the

combustor is square to provide good optical access for laser diagnostics; however, generous corner fillets are provided to suppress corner vorticity due to secondary flow development. The hydraulic diameter is 6.02in. (153mm) and the overall length is 19.29in. (490mm). The outlet is restricted by a 45 percent geometric blockage orifice plate to provide representative back-pressure for a dilution zone from a real combustor.

The combustor is mounted horizontally in a test-cell at Wright-Patterson Air Force Base, as Figure 2 shows. The combustor top and bottom walls are removeable, uncooled metal plates that accommodate appropriate arrays of combustion air jets supplied via suitable manifolds using a separately-metered air supply. One combustor side-plate contains a fitting for application of a removeable torch ignitor; the opposite side contains a full-length quartz window for visual access. Air for the dome is provided from a plenum chamber fed with flow-conditioned air. The fuel is gaseous propane.

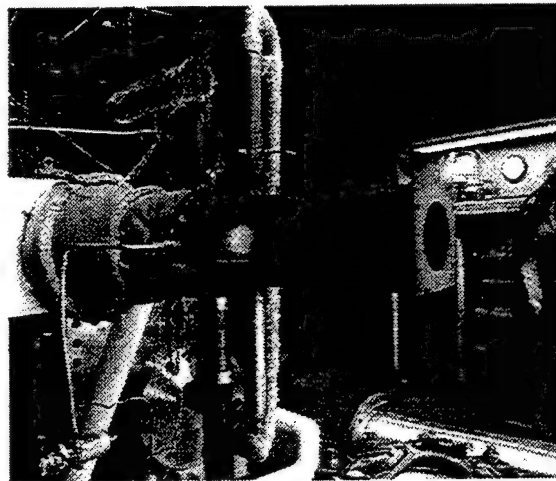


Figure 2: Combustor Rig

Range of Variables and Test Procedure

All LBO's presently reported were conducted at atmospheric pressure. The jet and dome air supplies were electrically heated to give inlet temperatures over the range 75 - 500F (297 - 533K). At each set temperature, liner and dome pressure drops were independently varied over the respective ranges of 0.50 - 6.0 percent inlet total pressure and 2.5 - 6.0 percent.

The matrix of test conditions was applied for 0.50in. (12.7mm) and 0.75in. (19.0mm) diameter opposed plain jets inline with the fuel injector and

placed at 0.50 and 0.75 dome heights downstream. Additional data were taken at 1.00 dome height downstream for these jets and for all these axial positions for the multi-jet configuration. However, for reasons of brevity these additional experiments are not presently described in great detail.

Stability was defined through LBO. Occasionally, non-stationary behavior of the flame and/or a noticeable acoustic signature would be noted as an LBO was approached, depending on the jet size and position, and, combinations of operating conditions. Unfortunately, no pressure transducer or microphone data were taken.

The procedure was to set the assigned air temperature and pressure drops with a primary zone equivalence ratio of about unity. When thermal stability was attained the fuel flow was progressively reduced until a blowout was obtained. As a blowout point was approached the fuel decrements were made progressively smaller. Time was allowed for the rig to attain thermal stability between fuel decrements, until the flame reached a non-stationary condition. Blowouts were detected visually through the quartz viewing window using a sensitive video camera with a relatively high framing rate to somewhat enhance the discrete nature of the flames.

Observed Flames

The range of different flames observed is illustrated photographically in Figure 3. Still photographs were not taken for all geometries/operating conditions, and two of the flame types were difficult to photograph: The lifted flame burning downstream in the combustion air jet wakes did not have sufficient luminosity for conventional film, and the oscillatory transitional flame by its very nature could not be statically recorded.

Although the photographs shown in Figure 3 were not made at blowout conditions, LBO could occur under appropriate conditions from any of the flame types illustrated. All of the combustion air jet geometries investigated (0.25in., 0.375in., 0.50in. and 0.75in. diameter plain jets and the multi-jet array) at each of the axial positions where they were installed exhibited similar behavior. It should be noted that the jets for all of the port configurations over the liner pressure drop range 1 - 5 percent, entered normal to the liner surface and appeared to penetrate eventually to the combustor centerline.

The important *attached flame* shown in Figure 3a), was very similar in appearance to that described in Reference 6 for the dome alone.

Parametric Investigations

The flexibility of the rig allowed parametric studies of the independent effects of dome and liner pressure drops, and air inlet temperature, for a given geometry, to be conducted.

Figure 4 shows the effects of liner pressure drop at various dome pressure drops with an air inlet temperature of 75F (297K) for the 0.75in. (19.05mm) jets at one-half a dome height downstream. The data points are delineated by major flame category. Note the non-smooth nature of the curves. This behavior is inherent in LBO data since a blowout represents a singularity.

The figure shows that at low air inlet temperatures and at low dome pressure drops less than 4.3 percent, the primary zone equivalence ratio at blowout $(\phi_{PZ})_{LBO}$ increases with increasing liner pressure drop. For dome pressure drops less than 4.3 percent with liner pressure drops less than 1.5 percent, the flame is transitional or attached; for all other conditions it is lifted.

The primary zone equivalence ratio is defined as follows:

$$\phi_{PZ} = \frac{\dot{m}_f}{0.0638 \dot{m}_{a,PZ}} \quad (5.)$$

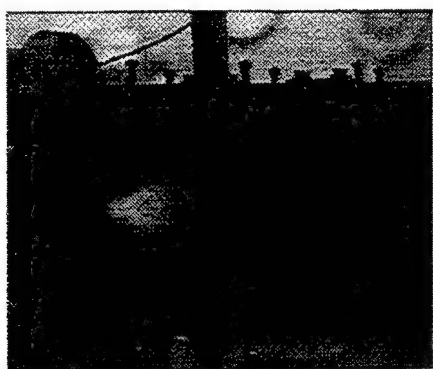
where,

\dot{m}_f = total fuel mass flow rate

$\dot{m}_{a,PZ}$ = primary zone active airflow
 $= \dot{m}_{a,dome} + \dot{m}_{a,recirc}$

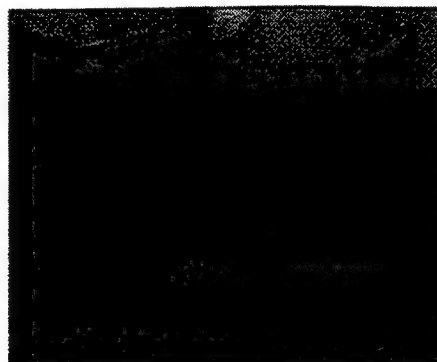
$\dot{m}_{a,recirc}$ = jet mass flow rate recirculated into the dome
 $= 0.279 \dot{m}_{a,jets}$

The constant 0.0638 in Equation 5 is the stoichiometric fuel/air mass ratio for propane/air mixtures. The jet and dome airflows were metered quantities. The amount of combustion jet air recirculated into the dome was obtained separately¹ for systems of this general type. This fraction (27.9 percent) was maintained constant for all of the jet sizes since all of the jets penetrated to the combustor centerline.

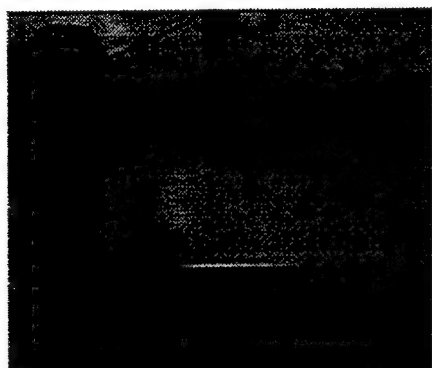


i) Attached

a) Multijets
Liner drop = 5%
Equivalence ratios
Overall = 0.2
Dome = 0.7

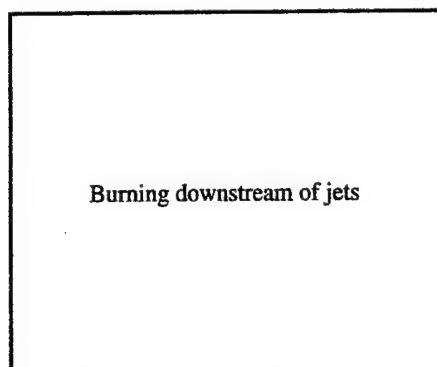


b) Multijets
Liner drop = 1%
Equivalence ratios
Overall = 0.5
Dome = 0.6

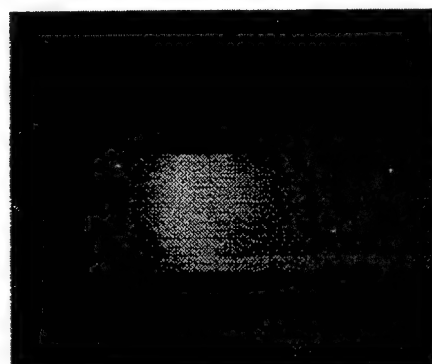


c) Multijets
Liner drop = 1%
Equivalence ratios
Overall = 0.52
Dome = 1.05

ii) Lifted

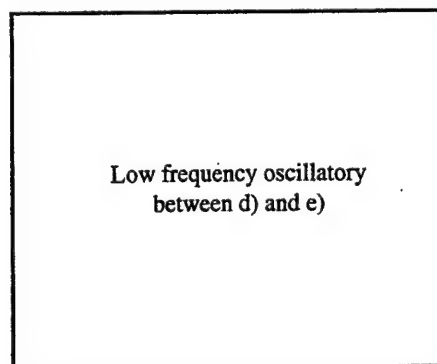


d)



e) 0.5in. jets
Liner drop = 5%
Equivalence ratios
Overall = 0.63
Dome = 2.33

iii) Transitional



f)

Jet position = $H_d/2$
Dome pressure drop = 4.3%
Air inlet temperature = 500 F (533K)

Figure 3. Illustrations of the Observed Flame Configurations

For these relatively low air temperatures (75F, [297K]) and dome pressure drops above 4.3 percent, $(\phi_{PZ})_{LBO}$ is relatively insensitive to liner pressure drop for values above 2 percent, and to dome pressure drop. All flames for these conditions are lifted.

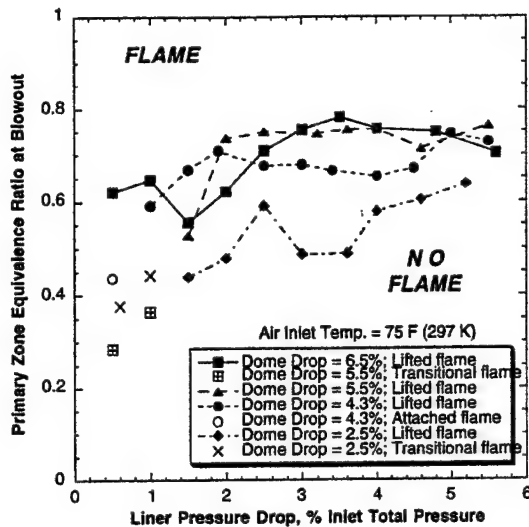


Figure 4: Effect of Liner Pressure Drop for 0.75in. Jets

Figure 5 shows the effects of dome pressure drop for a fixed liner pressure drop of 3.0 percent.

For dome pressure drops above 2.5 percent all the flames are lifted, and $(\phi_{PZ})_{LBO}$ increases with dome pressure drop for values less than 5 percent. For values above 5 percent, it is insensitive to dome pressure drop.

The effects of air inlet temperature on $(\phi_{PZ})_{LBO}$ are given in Figure 6 for a fixed liner pressure drop of 3 percent and dome pressure drops of 2.5 and 5.5 percent. Again, flame types are delineated. The curve fits shown are exponentials, based on the Arrhenius expression for reaction rate.

For given pressure drops air inlet temperature exerts a strong influence on blowout. The data points for 4.3 percent dome pressure point (not shown) fall exactly on the exponential curve fit. For temperatures above 150F (339K) at all dome pressure drops, the flames are either transitional or attached at blowout; for air inlet temperatures above 300F (422K) the flames at blowout are attached.

Figure 7 should be compared to Figure 5, and gives the effect of dome pressure drop at 500F (533K) air inlet temperature and 3 percent liner pressure drop.

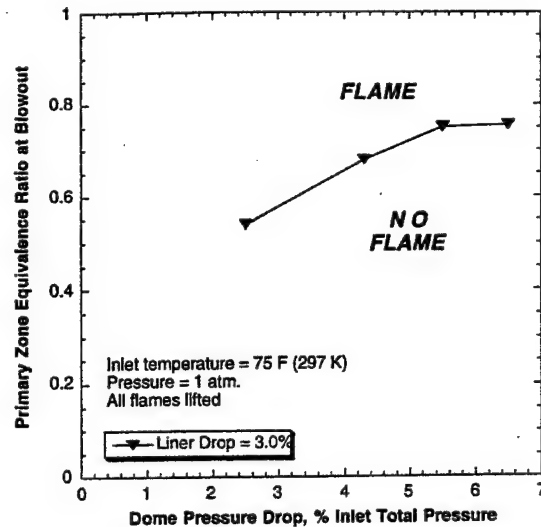


Figure 5: Effect of Dome Pressure Drop for 0.75in. Jets

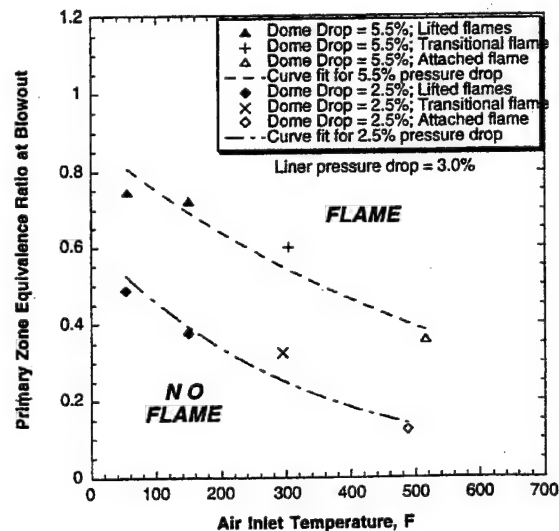


Figure 6: Effect of Air Inlet Temperature for 0.75in. Jets at Low and High Dome Pressure Drops

Although all flames are attached in this case, the behavior is almost the same as for the lower temperature, with relative insensitivity to dome pressure drop for values above 5 percent, or even a slight recovery of stability for greater than 5.5 percent. Blowout is more strongly influenced for lower values of dome pressure drop, as it is at the lower temperatures also.

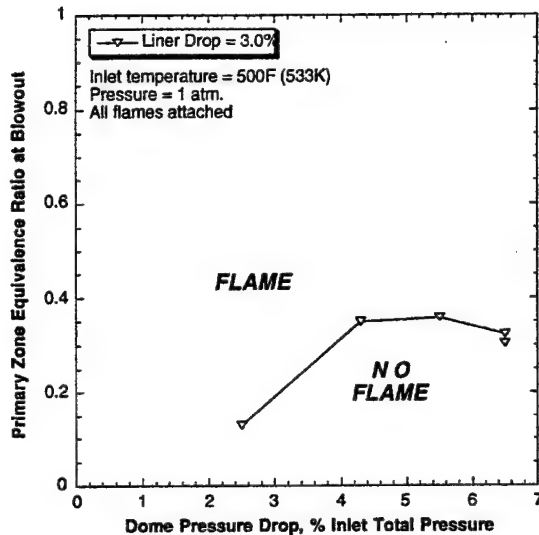


Figure 7: Effect of Dome Pressure Drop at Higher Air Temperatures

Figure 8 shows the effect of liner pressure drop at low dome pressure drops (2.5 percent) with high and low air inlet temperatures. At 486F (526K) air temperature all flames are attached, and there is little sensitivity to liner pressure drop. At 75F (297K) air temperature the flames are lifted for liner pressure drops above 1.0 percent, and are transitional for lower values. The sensitivity to liner pressure drop is increased compared to the higher temperature case.

A similar plot is given in Figure 9 but for a dome pressure drop of 5.5 percent. The general behavior is like that of Figure 8 for the 2.5 percent pressure drop. However, here the blowout sensitivity of the lifted flame at 75F (297K) to liner drop is about the same as for the attached flame at 520F (544K). What is particularly interesting are the blowouts for the transitional and attached flames at the lower temperature when the liner pressure drop is below 2 percent. The

attached flames for the 75F (297K) and 520F (544K) cases at 0.5 percent liner pressure drop have the same blowouts.

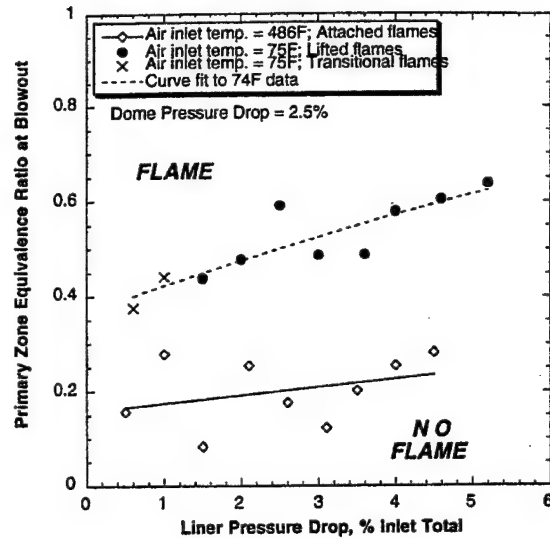


Figure 8: Effects of Temperature and Liner Drop at Low Dome Pressure Drop

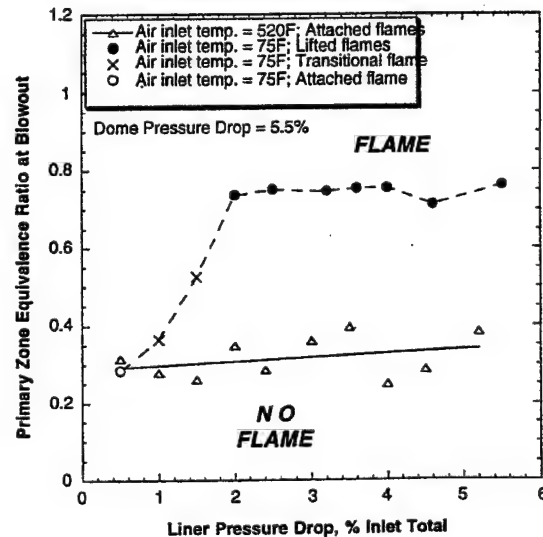


Figure 9: Effects of Temperature and Liner Drop at High Dome Pressure Drop

The general characteristics of the 0.50in. (12.7mm) jets at one-half dome height downstream are broadly similar to those described above for the 0.75in. (19.05mm) jets. The changes of flame type take place at different conditions of course, due to the differences in overall stoichiometry at the same liner pressure drops.

Figure 10 compares the effects of liner pressure drop on blowout for the 0.75in. (19.05mm) and 0.50in. (12.7mm) combustion air jets at the one-half dome height position; the dome pressure drops are 5.5 percent at the air inlet temperature of 75F (297K).

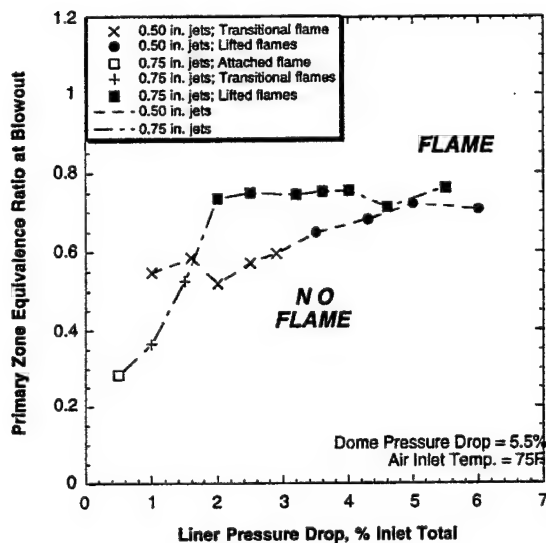


Figure 10: Comparison of Pressure Drop Sensitivity for Two Jet Sizes at One-Half Dome Height Position

It can be seen that the lifted flames for both jet sizes blowout at about the same equivalence ratio for liner pressure drops of 3.5 percent and above, and are insensitive to liner pressure drop above about 4.0 percent. The transitional flames for both jets also blowout at about the same values, and are more sensitive to liner pressure drop. For the 0.50in. (12.7mm) jets the transitional flames appear at liner pressure drops less than 3.5 percent, as opposed to less than 2 percent for the 0.75in. (19.05mm) jets.

The effects of primary zone length on stability and flame type are explored in Figure 11 for the 0.50in. (12.7mm) combustion air jets. The air inlet temperature

is 75F (297K) and the dome pressure drops are 5.5 percent. Under these circumstances attached flames are not likely to be seen.

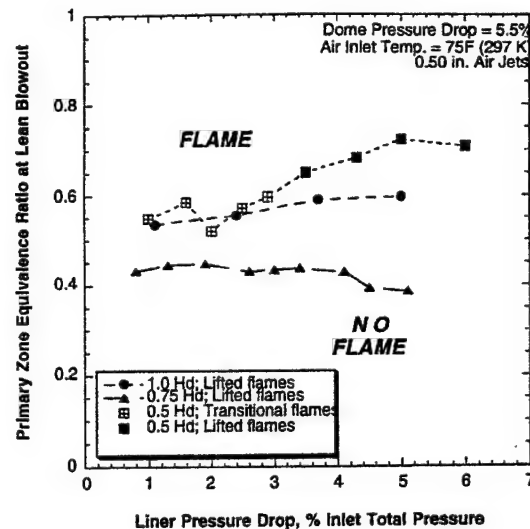


Figure 11: Effect of Primary Zone Length for 0.50in. Jets at High Dome Pressure Drop and Low Temperature

The figure shows that for the closest jet position and up to 2.5 percent liner pressure drop, the flames are transitional, as seen in Figure 10, and for higher liner pressure drops they are lifted. The flames are lifted over the entire range of liner pressure drops for the 0.75 and 1.0 dome height jet positions. At all jet positions and for all liner pressure drops there is little or no strong sensitivity of blowout to liner pressure drop. The values of $(\phi_{PZ})_{LBO}$ for the 0.50 H_d and 1.0 H_d jet positions are essentially the same; however, the stability for the 0.75 H_d jet position is noticeably improved over that for the other two positions. The 0.75 H_d jet position with plain jets of this size was the one that had given minimum NO_x^4 when the air temperature was 500F (533K). Note that for given pressure drops and air temperature, (i.e. given airflow) increasing the primary zone length reduces the combustor loading (essentially a residence time effect) as well as changing the level of interaction of the dome flow with the jet flow. The trends shown apparently represent some kind of optimum trade between these two influences.

In contrast to Figure 11 is Figure 12, which shows the effect of primary zone length for the 0.50in. (12.7mm) jets when all of the flames are attached. The operating conditions for this flame behavior are 4.3 percent dome pressure drop with an air inlet temperature of 300F (422K).

It can be seen from Figure 12 that when the flames are all attached, there is essentially no sensitivity to liner pressure drop at any primary zone length and that stability decreases with increasing distance of the jets from the dome.

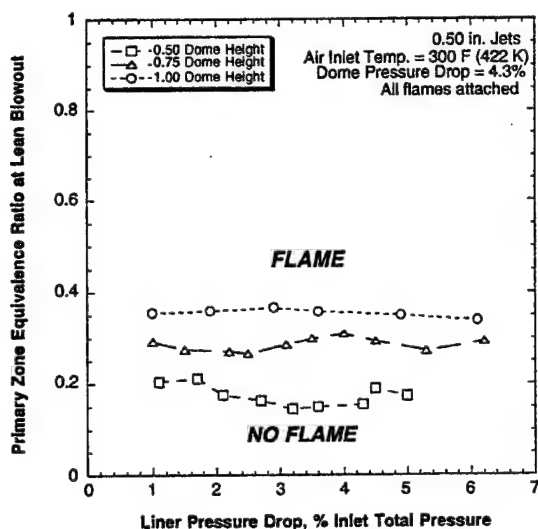


Figure 12: Effect of Primary Zone Length with Attached Flames

Correlation of Blowout Data

The changing flame types and the parametric behavior described above is complex, and does not suggest that any simple correlation group for LBO would have likely universal utility. However, it is instructive to attempt correlation and to compare the results for the different jet sizes and positions.

Correlation of the earlier data⁴ was attempted in that reference on the basis of a loading parameter LP , based on reaction rate theory⁵, expressed as

$$LP = \frac{\dot{m}}{VP^n F} \quad (6.)$$

where

\dot{m} = sum of active air and fuel (gaseous) mass flow rates, (lbm/s)

V = reactor volume, (ft³)

P = combustion pressure (atm)

F = exponential inlet air temperature

correction factor to 400K

$$= \frac{10^{0.00143 T_{in}}}{3.72}$$

T_{in} = air inlet temperature, (K)

n = apparent reaction order

When LP is concerned with the primary zone the air mass flow rate for \dot{m} is as defined in association with Equation 5, and V is based on a length equal to the distance downstream from the dome of the combustion air jets. For the present tests P^n is unity.

Figure 13 contains information reproduced from Reference 4 and shows the correlated LBO data for the 0.50in. (12.7mm) combustion air jets at the 0.5 and 0.75 H_d positions in terms of the global loading parameter and primary zone equivalence ratio. The major flame categories are shown. Figure 14 is a similar plot for the 0.75in. (19.05mm) jets at the 0.5 H_d position. High values of LP correspond in real engines to high altitude, low temperature, high-speed flight operations, and therefore represent difficult combustion conditions.

Remarkably good correlations of blowouts are obtained for the data from the 0.50in. (12.7mm) jets at both jet positions. The resulting stability characteristics are not the simple curves commonly given in textbooks, e.g. Reference 9. They exhibit the complex behavior frequently found in real systems. Such behavior is commonly attributed to the existence of multiple flame zones each having its own individual stability characteristic¹⁰ that together make up the overall characteristic. At the closest jet position in particular the attached flame yields a lobate LBO curve that turns back on itself twice. The discontinuities in the individual curves are solely due to the lack of data gathering. At both jet positions as the primary zone loading is progressively increased the combustor blows out initially with attached flames, moves to transition flames and finally, blows out from lifted flames. On each blowout characteristic there are regions of flame-type overlap where for a given loading blowouts can be either from a transitional flame or from a lifted flame.

At both jet positions the initial portions of individual blowout characteristics from an attached

flame condition, are very nearly common, although the $0.5 H_d$ position does exhibit the slightly better stability. When the loadings are increased this attached flame near-commonality breaks down as the lobate region at the $0.5 H_d$ jet position is lost for the $0.75 H_d$ jet position. The rate of increase in $(\phi_{PZ})_{LBO}$ with increasing loading parameter at the $0.75 H_d$ jet position with lifted flames is about the same as that for lifted flames at the $0.5 H_d$ jet position. However, the loss of the lobate region for the further jet position gives an overall reduction in stability compared to the jet position closest to the dome.

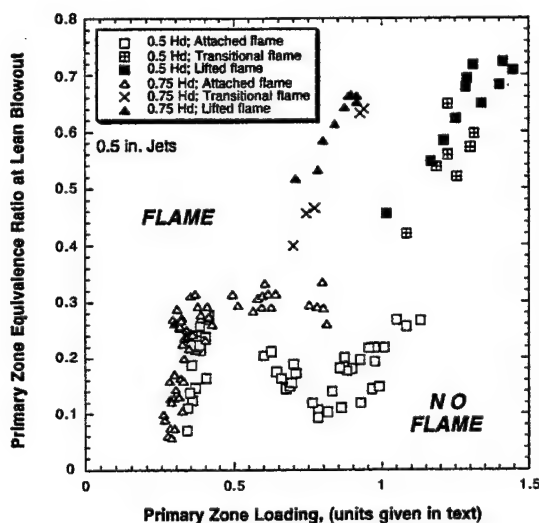


Figure 13: Correlation of Blowouts for 0.5in. Jets at Two Jet Positions

It would be difficult to interpret the lean stability curve for the 0.75in. (19.0mm) jets at $0.5 H_d$ (Figure 14) without reference to the similar curves shown for the 0.5in. (12.7mm) jets in Figure 13. The 0.75in. (19.05mm) jets have the same blowout behavior as do the 0.5in. (12.7mm) jets at this axial position from the dome. However, the attached flame lobate region is reduced in extent. Also, the blowouts over the range of loadings where attached, transitional and lifted flames can co-exist extends over a wider range of primary zone equivalence ratios. Generally, the data for the 0.75in. (19.05mm) jets are not as tightly correlated as are the data for the 0.5in. (12.7mm) jets.

Also shown in Figure 14, using smaller size symbols for clarity, is the 0.5in. (12.7mm) stability curve at $0.5 H_d$ from Figure 12. By comparing the two data-sets it can be seen that at very low loadings the attached flame for the 0.75in. (19.05mm) jets have better stability than do the attached flames for the 0.5in. (12.7mm) jets. Due to the more extensive lobate region of the 0.5in. (12.7mm) jets, the stability curves cross at loadings of about $0.55 \text{ lbm/s/(ft}^3\text{atm}^n)$ [$8.813 \text{ kg/s/(m}^3\text{atm}^n)$] so that the 0.5in. (12.7mm) jets now have better stability with attached flames. The stability curves cross yet again at loadings around $1.1 \text{ lbm/s/(ft}^3\text{atm}^n)$ [$17.625 \text{ kg/s/(m}^3\text{atm}^n)$] so that the 0.75in. (19.05mm) jets have the better stability when the flames are lifted. These crossing and recrossings of the respective stability curves explain some of the apparent anomalous behavior described in the previous sections.

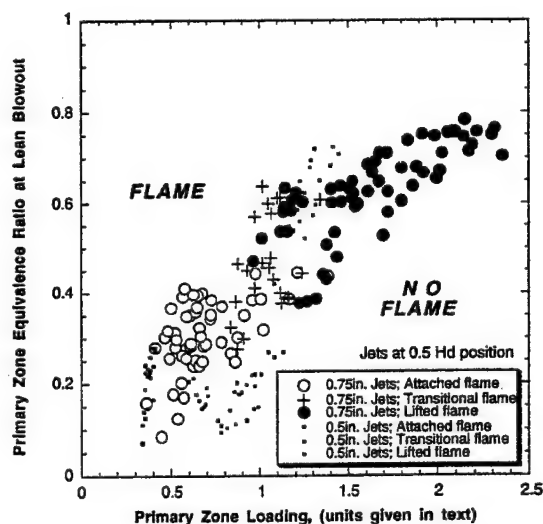


Figure 14: Correlation of Blowouts for 0.75in. Jets at One-Half Dome Height Position Downstream

Cause of Flame-Lift

As indicated above the observed movement of the flame zone from attached to lifted conditions should be solely attributable to the effects of variations in the airblast fuel injector equivalence ratio with operating conditions. This should be true provided that a) the attached flames are always anchored on the injector outlet so that recirculated jet air is not relevant, and b) that the chemical reaction rates remain fast enough to

accommodate any adverse changes in local residence times that might take place. For the closely coupled injector and insert swirler airflows of the present arrangement (Figure 1) the "injector" should be taken to include the insert swirler.

The flame photographs of Figure 3 a) and b) show that the attached flames are indeed anchored on the fuel injector outlet. They also indicate, Figure 3 a), c) and e), that the insert swirler jets play a significant part in the near-field flame as the transitional flame mode is entered.

The blowout data for each jet size and jet axial position were replotted in terms of primary zone loading parameter versus actual injector equivalence ratio. Attached flames only existed up to about 1.5 injector equivalence ratio. Then, the insert swirler air was included in the equivalence ratio. It was found that for no combination of jet size or position were attached flames present at combined injector and insert swirler equivalence ratios greater than unity. This is illustrated for the 0.75in. (19.05mm) jets at the $0.5 H_d$ position in Figure 15.

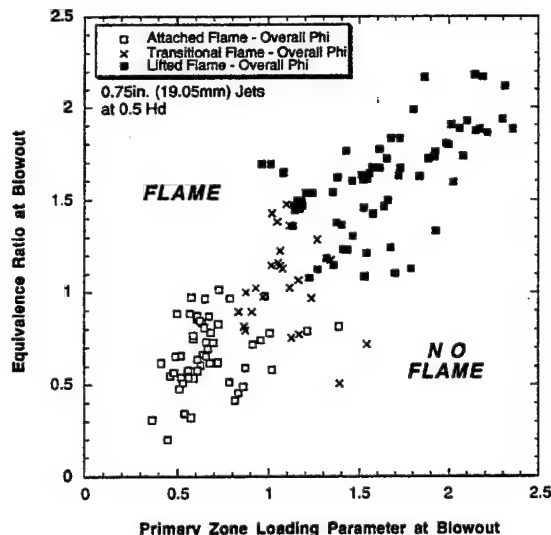


Figure 15: Effect of Local Equivalence Ratio on Flame Lift

The figure implies that the unity equivalence ratio is a limiting condition for the attached flame. Figure 15 also shows that transitional flames could be

encountered for combined equivalence ratios both less and greater than unity, but only when the primary zone loading parameter became high enough. This, together with the equivalence ratio finding, indicates that transitional flames could be produced by reaching or exceeding the limiting equivalence ratio, inadequate residence time, or, combinations of local equivalence ratio and residence time that exceeded the local flameholding capability.

A more conventional flame map for the 0.75in (19.05mm) jets at the $0.5 H_d$ position is shown in Figure 16. The blowout data are treated as if the flames were simple jet-flames, so that injector equivalence ratio at blowout is plotted against the mixture mean axial velocity at the injector exit. Demarcation lines are shown between the three major flame categories.

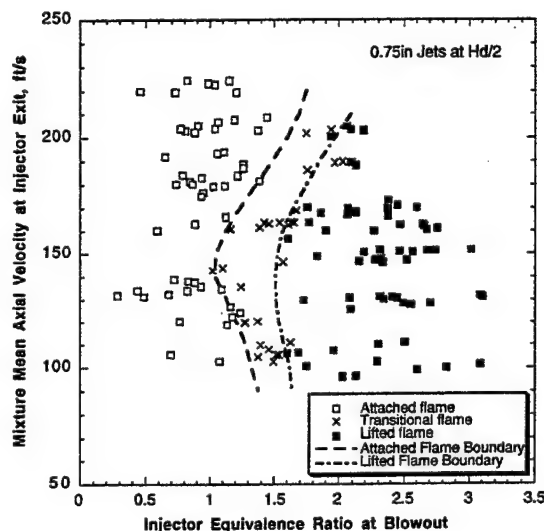


Figure 16: Flame Map for Largest Jets at Closest Position to Dome

It can be seen that equivalence ratio is the strongest factor determining flame type. All flame types can exist over the entire velocity range covered, from 90ft/s (27.4m/s) to 225ft/s (68.6m/s). Noteworthy is the "necking" in the flame boundaries (especially for the attached flames), at about 150ft/s (45.7m/s). For simple jet flames a limiting blowoff velocity over all equivalence ratios would be expected. Presently, the attached flame region is extended in equivalence ratio

range after the neck velocity. For this enclosed jet system at the higher velocities the reaction zone tends to be driven further downstream towards the transverse combustion air jets. The blockage presented by these penetrating jets locally slows the axial velocities in the reaction zone. Furthermore, the increase in injection axial velocity is accompanied by an increase in tangential velocity. The increased tangential velocity broadens the recirculation zone as the blockage reduces the axial velocity; internal recirculation can be produced.

Discussion

The described parametric behavior carries Marshall & Gupta's swirl-flame quantitative description one step further. It demonstrates that the behavior of a basic fuel/air module, when integrated into a gas turbine combustor, is further modified by the air jet configuration used in that combustor.

In terms of perceived stability it is intuitively better to have an attached flame than a lifted flame. Swirling air is introduced in association with part of the combustion air for the express purpose of improving flame holding⁸. Flame holding in the downstream jet system providing the remainder of the combustion air is blockage-based, and is inherently less certain. These perceptions are borne out in the parametric results presented, where for given pressure drops the attached flames are almost always seen to have lower values of $(\phi_{PZ})_{LBO}$, i.e. better stability, than for the lifted flames.

The circumstances determining the existence of an attached flame for 0.75in. (19.05mm) combustion air jets at the closest ($0.5 H_d$) position to the combustor dome are seen (Figure 4) to be low values of liner and dome pressure drops (less than 1.5 percent and 4.3 percent respectively) when the air inlet temperatures are modest (75F [297K]). This is also the case for the 0.5in. (12.7mm) jets, as in Figure 10. This behavior is indicative of the local reaction rates not being fast enough for the available residence times produced at the higher pressure drops. Increasing the air temperature at fixed and moderate (3 percent) liner pressure drops can change a lifted flame into an attached flame, regardless of whether the dome pressure drop is high or low, (Figure 6). The effect of changing temperature, which has only a small effect on local equivalence ratio, has an exponential effect on chemical reaction rates. This also indicates the importance of reaction zone residence times. The implied residence time effects suggest that primary zone loading, as defined by Equation 6, might

be an appropriate parameter for correlating blowout data since it can be related to a residence time.

For the 0.5in. (12.7mm) jets at relatively low air temperatures (75F [297K]) and for high dome pressure drops (5.5 percent) moving the jets closer to the dome can result in transitional flames for liner pressure drops of 3 percent and less (Figure 11). However, the stability is **not improved** for this jet size. The optimum stability for these jets and conditions is achieved at the $0.75 H_d$ position with lifted flames. Conversely, for the same jets at high air temperatures and with attached flames, Figure 12, moving the jets closer to the dome continuously improves stability. This type of behavior could be due to the beneficial effects of the back-pressure exerted on the attached flames by the jets¹¹.

For a given gas turbine combustor design the dome and liner pressure drops are not independent variables. They will have a fixed ratio, dome to liner, that is determined by the geometric layout and the air flow splits selected. Generally, the ratio is greater than unity. The combustor overall pressure drop, air inlet temperature and air mass flow rate are linked through the flow function, $\dot{m}_a \sqrt{T_{in}} / P_{in}$. In flight operations the flow function is established by the engine power setting and, aircraft altitude and Mach number. For these reasons it is essential to also consider a correlated form of the blowout data. The parametric results indicated the importance of equivalence ratio and residence time. Therefore, the loading parameter approach appears as a reasonable approach.

The LBO data for the 0.5in. (12.7mm) jets at the 0.5 and $0.75 H_d$ positions are correlated well using the loading parameter approach (Figure 13). The range of operating conditions used in the parametric tests results in primary zone loadings that extend from close to the "flammability limit" at very low values, to close to the peak heat release rate condition for the primary zone, $[(\phi_{PZ})_{LBO} = 1.0]$. To actually reach the peak heat release rate point would have required a combination of sub-atmospheric temperatures and pressures as operating conditions.

At both jet positions the resulting lean stability curves are complex and exhibit similar behavior that shows the existence of "lobes" where there is a local recovery of stability as loading is continuously increased. Such behavior has been previously observed over the years in several practical combustors using swirl flames. It was argued that the

lobate behavior resulted from changes in flame holding. However, this had never been directly observed due to lack of suitable optical access. The present data confirm that the different parts of the stability curves are indeed due to flame shifts as the combustion conditions become more arduous.

Figure 13 shows that where the primary zone loading results in attached flames, only attached flames exist. Where the primary zone loadings are high enough that attached flames cannot exist, then there are regions of loading where the flames can be either transitional or lifted. Whether a flame in this region of loadings is transitional or lifted depends on exactly how the combustor loading is achieved. Eventually, the loadings become high enough that only lifted flames can occur, regardless of how the loading is achieved.

The figure shows that for all values of primary zone loading the lean stability curve for the 0.5in. (12.7mm) jets in the $0.5 H_d$ position is to the right of the lean stability curve for these jets in the $0.75 H_d$ position. Therefore, moving these jets downstream reduces the lean stability. However, the loss in stability by the downstream movement of the jets is greater for the lifted flame condition than it is for the attached flame condition. The better lifted stability for the $0.75 H_d$ position seen in Figure 11 is explainable due to the lower primary zone loading associated with the increased length of the primary zone.

The LBO data for the 0.75in. (19.05mm) jets in the $0.5 H_d$ position are not so well correlated (Figure 14) as are the data for the 0.5in. (12.7mm) jets in this position. The features of the resulting lean stability curve however, are very similar to those for the smaller jets. However, it is doubtful if these features could be interpreted without reference to Figure 13. The reasons for this are associated with the increased data-scatter and, the marked reduction in the attached flame lobate stability region for this larger jet size. Furthermore, the overlap region where the flame type depends on exactly how the loading was achieved, now includes attached flames.

It will be noted from Figures 13 and 14 that for both jet sizes and both jet axial positions, the LBO behavior of the attached flames near "flammability limit" loadings [$\text{less than } 0.6 \text{ lbm/s(ft}^2\text{atm)}; \{9.6 \text{ kg/s/(m}^2\text{atm)}\}$] is very similar. This again is where the influence of the combustion air jets on the flame is at a minimum since most if not all of the combustion is completed before the flow reaches the jets. This is the

closest that a practical combustor with jets ever gets to the conditions that Marshall & Gupta investigated. Even so, the presence of the combustion air jets is still detectable in the attached flame.

Figures 13 and 14 demonstrate the limitations of the loading parameter to describe lean stability. Due to the flame changes, the loading parameter is a necessary but not sufficient parameter for describing the stability for even a specific combustor geometry. The dramatic shifts in stability that have been demonstrated for relatively minor geometric changes in the combustor preclude any form of "universal" correlation for stability. This is so even for the initial attached flame region, where the flame is held on the injector and is confined in extent to the dome of the combustor.

The difficulty with the loading parameter is in the manner with which it is usually applied to gas turbine combustors. The application, as here for the primary zone, is made on a **global basis**. However, the real flame behavior within a primary zone, and hence the combustor stability, is established entirely on a **local basis**. A global application completely neglects the essential local details. To be successful an approach to LBO must account for the detailed aerodynamics of the primary zone on at least one higher level than global, together with sufficient chemistry to acknowledge local changes in reaction rates.

Conclusions

1. The free-flame characteristics of co-swirling fuel/air injector modules are strongly modified when the modules are introduced into gas turbine combustor containing transverse air jets.
2. Relatively minor geometric changes in a combustor liner with a fixed geometry swirl generator module can result in very significant shifts in primary zone global LBO stability.
3. The flame changes and shifts in global LBO stability are due to complex local flameholding behavior associated with the detailed interactions of the swirling and transverse jet systems.
4. A necessary condition for a desirable attached flame at blowout is that the injector equivalence ratio for the injector module (including any closely-associated auxiliary air swirler) not exceed unity at any primary zone loading. However, this is not a sufficient condition.

5. An additional condition necessary for an attached flame is that the local residence time in the initial flame region be equal to or greater than the required reaction time.

6. Simple characterization of the detailed primary zone behavior with large changes in combustor operating conditions, or with small changes in combustor geometry, is not possible.

7. The inability to characterize primary zone behavior in simple fashion introduces the need for some appropriate modeling procedure to establish stability.

Acknowledgements

The enthusiasm, motivation and support of Dr. W.M. Roquemore of Wright Laboratory are greatly appreciated. The authors wish to thank Melvin Russell (WL) and Charlie Smith (ISSI) for their patience and assistance in operating the test facility and in making the tedious blowout measurements. This on-going research is sponsored by the U.S. Air Force, Wright Laboratory, Aero Propulsion and Power Directorate.

References

1. Sturgess, G.J., McKinney, R.G. and Morford, S.A., "Modifications of Combustor Stoichiometry for Reduced NOx Emissions from Aircraft Engines," Trans. ASME, *J. Engrg. Gas Turbines and Power*, Vol. 115, No. 3, 1993, pp. 570-580.
2. Gogineni, S., Shouse, D., Frayne, C., Stutrud, J. and Sturgess, G.J., "Influence of Combustion Air Jets on Primary Zone Characteristics for Gas Turbine Combustors," proc. ISABE 12th. Symp. on Air Breathing Engines, editor F. Billig, Vol. 1, Melbourne, Australia, September 10-15, 1995, pp. 475-487.
3. Shouse, D.T., Frayne, C., Stutrud, J., Gogineni, S. and Sturgess, G.J., "The Role of Transverse Air Jets in the Formation of Gas Turbine Emissions," Paper No. 96-0705, pres. AIAA 34th. Aerospace Sciences Meeting & Exhibit, Reno, Nevada, January 15-18, 1996.
4. Sturgess, G.J., Gogineni, S., Shouse, D.T., Frayne, C. and Stutrud, J., "Emissions and Operability Trades in the Primary Zones of Gas Turbine Combustors," Paper No. 96-2758, pres. 32nd. AIAA/ASME/SAE/

ASEE Joint Propulsion Conference, Lake Buena Vista, Florida, July 1-3, 1996.

5. Spalding, D.B., "Performance Criteria of Gas Turbine Combustion Chambers - A Method of Comparison and Selection for the Designer," *Aircraft Engineering Monograph*, Bunhill Publications Ltd., London, England, August 1956.

6. Hedman, P.O., Sturgess, G.J., Warren, D.L., Goss, L.P. and Shouse, D.T., "Observations of Flame Behavior from a Practical Fuel Injector Using Gaseous Fuel in a Technology Combustor," Trans. ASME, *J. Engrg. Gas Turbines and Power*, Vol. 117, No.3 July 1995, pp.441-452.

7. Marshall, A.W. and Gupta, A.K., "Effects of Jet Momentum Distribution on Thermal Characteristics of Co-Swirling Flames," Paper No. 96-0404, pres. AIAA 34th. Aerospace Sciences Meeting & Exhibit, Reno, Nevada, January 15-18, 1996.

8. Gupta, A.K., Lilley, D.G. and Syred, N., *Swirl Flows*, Abacus Press, Tunbridge Wells, England, 1984.

9. Lefebvre, A.H., *Gas Turbine Combustion*, Hemisphere Publishing, McGraw-Hill Books, 1983.

10. Sturgess, G.J., *Combustor LBO Design Model Evaluation: Final Report*, (Draft), Pratt & Whitney Rept. FR-23400, May 1995.

11. Sturgess, G.J., Heneghan, S.P., Vangsness, M.D., Ballal, D.R., Lesmerises, A.L. and Shouse, D.T., "Effects of Back-Pressure in a Lean Blowout Research Combustor," Trans. ASME, *J. Engrg. Gas Turbines and Power*, Vol. 115, No.3, July 1993, pp. 486-498.

AN ACCOUNT OF FUEL/AIR UNMIXEDNESS EFFECTS ON NO_x GENERATION IN GAS TURBINE COMBUSTORS

G.J. Sturgess
Innovative Scientific Solutions, Inc.,
2786, Indian Ripple Road,
Dayton, Ohio 45440-3638
Phone: (937) 252-2706
Fax: (937) 656-4652
Email: gsturgess@aol.com

ABSTRACT

The basis of a stochastic method is presented for correcting the combustion reaction chemistry of Jet-A fuels to account for fuel/air unmixedness in liquid-fueled aircraft gas turbine combustors. Details of a correction factor for oxides of nitrogen are given in terms of two reduced reaction mechanisms for jet fuel.

I INTRODUCTION

Levels of gaseous emissions generated by aircraft gas turbine engines for commercial operations are regulated by international (International Civil Aviation Organization) pollution standards. In addition, certain nations apply tariffs on highly polluting aircraft. Military aircraft operations are currently not regulated for emissions; however, the U.S. Air Force pursues a "good neighbors" policy with respect to emissions, contingent on operational requirements. Ground-based electrical power generation is subject to extremely severe local regulation. The regulated gaseous pollutants of current concern are carbon monoxide (CO), total unburned hydrocarbons (UHC) expressed as equivalent methane (CH₄), and total oxides of nitrogen (NO_x), expressed as equivalent nitrogen dioxide (NO₂).

Gas turbine engine manufacturers must therefore possess the ability to make accurate calculations of the gaseous emissions produced by their equipment. For the aircraft application the scope of these calculations can cover such items as assessment of new combustion concepts, evaluation of the effects of changing operating conditions due to engine power

growth, and, simulation of engine operation in customer airplanes and route structures. Many state-points are implied and a considerable computational effort can be involved; in addition, such calculations must be timely. Appropriate balances between physical realism and computational accuracy on one hand, and engineering utility and turn-around time on the other, must be found. As a consequence, this results in the employment of a range of related calculation approaches, each suited to its particular purpose.

Figure 1 gives a view of the interior of an annular combustor and reveals the entries for the numerous inflows, as well as the outflow into the turbine section. Flow is from left to right, and the engine centerline is to the top of the upper illustration. Below is a sketch of the typical time-averaged flow field that indicates the major features; note the local toroidal recirculations associated with each fuel injector and the resulting stagnation plane, and the rapid acceleration region into the turbine. The engine centerline is to the bottom of the sketch. Calculation of gaseous pollutant formation within gas turbine combustors involves several quite serious difficulties.

First, the basic flow structures present must be determined. These structures will govern where flame is held within the combustor and the positions where substantial heat release can take place. In turn, these establish the temperature field and local residence times. Together with fuel distribution, local temperature and residence times determine, via non-equilibrium chemistry, the generation of CO, UHC and NO_x. The calculation tool most successfully used for establishing the flow structures and associated

information is stationary-state (a presumed condition) computational fluid dynamics, CFD.

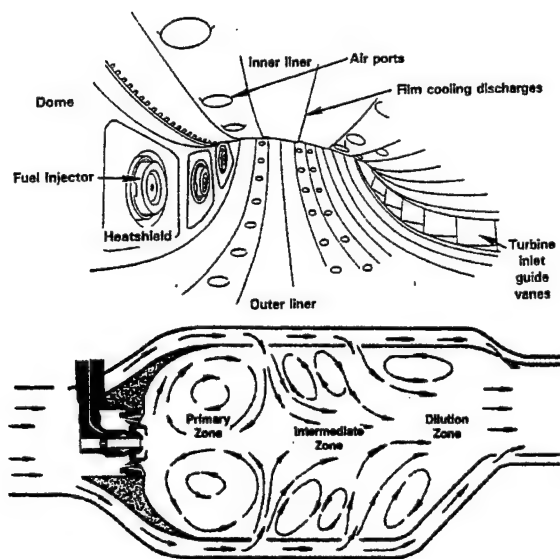


Fig.1: Interior View of Annular Combustor and Time-Averaged Major Flow Structures

Second, local residence time in a local temperature determines the pollutant formations through the fuel/air chemistry. "Full" chemical reaction mechanisms can be rather extensive. The commonly used aviation fuel Jet-A is not a pure substance but consists of a mixture of hundreds of individual hydrocarbons. It is therefore necessary to assume either a generic "fuel molecule," or to represent the real fuel by just a few dominating hydrocarbons. Detailed mechanisms comprising around 200 species and 1100 elementary reactions exist, but are generally considered to be computationally prohibitive even for extensive stand-alone kinetic studies. A more palatable detailed mechanism based on only 25 major, stable intermediate and radical species^{1, 2} is still too complex for direct engineering application. Simplified reaction mechanisms, based on reasonable detailed mechanisms³, must be used for practical calculations in engine combustors. Unfortunately, there is a fairly significant discrepancy between a chemical kineticist's view of a "simplified" mechanism and a "simplified" mechanism that can be used within a CFD code. Typically, a 5-10 step mechanism involving a single generic fuel molecule and only a very, very few species, is the current limit for CFD to be used in engineering calculations. The reasons for this are several: not only are the kinetic equations to be solved mathematically "stiff," but a transport equation also has to be solved

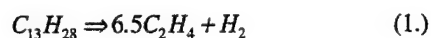
for each of the chemical species present. Together, these translate into significant increases in solution times. A kinetically-acceptable reaction mechanism for Jet-A would fall somewhere between this level and that represented by the Maurice² mechanism. However, when applied to a three-dimensional, recirculating flow calculation domain containing the 300,00-500,000 nodes necessary to define the geometry and achieve acceptable flow resolution, the resulting computational task is immense. The possible need to include a liquid fuel spray model in the CFD calculation compounds the problem. Despite continuing progress in computer capabilities and solution algorithms⁴, the strain of such an immense computational burden on the networks of work-stations used by industry, is insupportable. This is certainly so for making multiple state-point calculations and is probably presently so for even single state-point calculation. As an example of the task magnitude, a typical single state-point calculation for a gas turbine combustor might easily occupy a network of 10-20 moderately powerful workstations for an elapsed time of 3-5 working days, using non-peak computing time.

Third, the reaction rate constants available to apply to reaction mechanisms are appropriate for premixed fuel and air situations, and are sometimes obtained in non-flowing systems. Chemical reaction rates involve these rate constants and local concentrations of reactants. In aircraft gas turbines air and liquid fuel are introduced into the combustor separately. Therefore, chemical reaction in such gas turbine combustors proceeds concurrently with fuel droplet evaporation and turbulent mixing of air and fuel vapor. Reaction will take place as turbulent eddies of pure fuel vapor, pure air, partially-mixed fuel and air, and hot products of combustion, all come together in random fashion. The net reaction rates achieved will depend on the ensemble of these local processes. Global reaction rates can therefore be rather different from those to be expected from bulk flow conditions. This is also true for premixed systems typical of industrial gas turbines, where turbulent eddies of fuel/air mixture have to interact with eddies of hot products for ignition. To account for such effects directly in a CFD calculation would necessitate provision of a grid-resolution down to the Kolmogorov eddy scales where mixing is complete on the molecular level. Turbulent mixing time and length scales are two to three orders of magnitude smaller than global time and length scales; flame time and length scales are three to four orders of magnitude smaller than the global. It is therefore not possible to do this directly for engineering flow fields at realistic Reynolds numbers.

Calculation of pollutant formation in gas turbine combustors is seen to be extremely tasking. The present work is concerned with only a small part of the problem. It addresses an approach to the third of the difficulties described, that of fuel/air unmixedness effects on pollutant formation, specifically, on NOx levels. For absolute realism and accuracy, it is necessary to model the correct physics on the correct scale. Since correct scales cannot be resolved due to cost/time considerations, a reasonable approach is to use chemistry models that are appropriate to what can be resolved. With such an approach, it is the *effects of the chemistry* on the resolved scale length that are accounted for, not the details of the chemistry *per se*.

II BACKGROUND

In a numerical study to assess the impacts of turbulence fluctuations on reaction chemistry, Brankovic⁵ of Pratt & Whitney, considered the effects of turbulent fluctuations in temperature on the forward rate constant for the pyrolysis reaction,



It was shown that such fluctuations can have a significant effect on reaction rates. It was concluded that the fluctuations at higher temperatures could be large enough to result in local flame extinction.

The state-of-the-art (defined as being in daily use making multiple engineering calculations in commercial engine companies) in gas turbine pollutant calculation is to perform a CFD calculation using a probability distribution function (pdf) combustion model.

A number of pdf models could be employed. With increasing information content, these would be,

- 1.) joint pdf of composition
- 2.) joint pdf of velocity and composition
- 3.) joint pdf of velocity, dissipation and composition

Use of joint pdf of composition models is now common. A joint pdf of velocity and composition with a 4-step, 5-variable CH₄/air chemistry was explored by Correa *et. al*⁶. The results compared favorably with Raman data for mixture fraction, major species and temperature; however, some shortcomings were noted. Unfortunately, since the solution costs increase with

the amount of contained information, current gas turbine routine use is generally at the lowest level possible, with a joint pdf of composition.

A pdf transport equation can be solved directly (using a separate Monte-Carlo code that interacts with the CFD code⁷), or, the shape of the pdf can be presumed, with clipped Gaussian⁸ or β - functions⁹ being popular choices that are close to the measured form. Since the results are not especially sensitive to the shape of the pdf and since, despite recent algorithm progress, Monte Carlo procedures remain inherently expensive, most approaches use the presumed shape.

As always, the pragmatic engineer must consider the cost/benefit equation when performing work. So, the scalar is usually taken as the mixture fraction f , where

$$f = \frac{\dot{m}_{fuel}}{\dot{m}_{fuel} + \dot{m}_{air}} \quad (2.)$$

and \dot{m} signifies mass flow rate. Then, equilibrium chemistry is adopted so all thermochemical statistics are obtained from the pdf of mixture fraction. These are calculated during case initialization, and are accessed from the instantaneous f values through tabular lookup.

It is possible to extend the presumed pdf model to non-equilibrium chemistry. If there are significant departures from equilibrium, an additional scalar can be introduced, the Reaction Progress Variable ζ , where

$$\zeta = \frac{m_i - m_i^u}{m_i^b - m_i^u} \quad (3.)$$

and m_i is the mass fraction of some suitable chemical species i , from the reaction mechanism, having limits u and b so that $\zeta=1$ represents fully reacted to equilibrium at given mixture fraction f , and $\zeta=0$ represents unreacted mixture at the given f . f and ζ are taken as being uncorrelated, and assumptions are made for the functional dependence of $P(f, \zeta)$ on the respective moments. Additional transport equations are solved for the first and second moments of ζ from the assumed shape. The time-mean properties are obtained from,

$$\bar{\theta} = \text{int errmittency terms} + \int \int \theta(f, \zeta) P(f, \zeta) df d\zeta \quad (4.)$$

Unfortunately, although the pdf approaches presented above do result in improved descriptions of the hot gas temperature fields throughout gas turbine combustors at an acceptable cost for a single solution, they presently are limited to either equilibrium chemistry (the usual choice), or to extremely simple non-equilibrium chemistry. The maximum reduced mechanism considered reasonable is of the order of 10 reaction steps involving 12 chemical species; frequently, less steps and species are used. Pollutant calculations require more extensive reaction mechanisms and more species. Therefore, emissions calculations of NO_x for example, are made in uncoupled fashion by post-processing the CFD solution. Where required, multiple state-point calculations can then be made by scaling the post-processed emissions values using either empirical data correlations or data-correction procedures¹⁰. Although extrapolation is involved in such extensions, the values so-obtained are probably adequate for their intended purpose (normally route structure analyses). Unfortunately, apart from the original CFD calculation and only then by inference from the temperature fields, they do not offer much insight into how to improve a given design for lower emissions.

III PRESENT CONTRIBUTION

A simple statistical method of accounting for fuel/air unmixedness effects on the reaction rates of NO_x chemistry is presented. The effects of the chemistry on the currently resolved lengths scales are covered, not the details of the chemistry/turbulent mixing process. The method is useful for post-processing CFD solutions that are based on equilibrium chemistry or extremely simplified non-equilibrium chemistry. The philosophy used is pragmatic, and is consistent with that of (industrial) state-of-the-art combustion models presently used in CFD calculations.

IV POLLUTION CHEMISTRY AND TURBULENCE

As described above, air and liquid fuel are introduced separately in the aircraft gas turbine combustor. Liquid fuel is injected into the combustor as a spray; air is introduced through a system of jets. The fuel droplets of various sizes evaporate as they travel, at a rate depending on relative droplet/air velocities, droplet sizes and number density, and ambient temperature. The fuel vapor resulting mixes with fresh air and burnt hot products of combustion. Combustion is therefore non-premixed, with droplet

evaporation and turbulent mixing of air and fuel vapor all taking place concurrently with chemical reaction and heat release. Under these conditions, the local turbulence structure of the flow controls the times that each of the reactants and hot products can mix with each other and react.

Two time scales are of relevance:

1.) **Turbulence Time Scale, τ_T** , which is the mixing time for eddy length scale reduction by breakup of large eddies to fine-scale eddies. The fine-scale eddies are on the Kolmogorov length scale where molecular mixing is complete. Chemical reactions take place on the molecular level.

2.) **Reaction Time Scale, τ_R** , is the chemical reaction time for the mixed and ignited reactants to reach their local equilibrium product values. These two time scales can be combined into a Damkohler Number. The Damkohler Number determines the type of chemistry appropriate. Figure 2 provides a diagrammatic representation of the physical significance of these times. For the mixing-limited regime, the reaction time is very small compared to the turbulence time, so that reaction takes place at the local instantaneous conditions. Under these circumstances combustion is mixing-limited, and equilibrium chemistry is appropriate. For the kinetically-limited regime, the reaction time is much greater than the turbulence time, so that reaction takes place at mean conditions. Under these circumstances non-equilibrium chemistry is necessary. When the two times are comparable, i.e. around unity Damkohler Number, the turbulence - chemistry interactions are greatest.

It is important to estimate for the emissions reactions what the Damkohler Numbers are in gas turbine combustors. This has been done as functions of engine power level and combustor design equivalence ratio; as well as for different regions within a typical combustor. To make these estimates the "characteristic time" approach of Mellor and co-workers¹¹ was used. The following expressions were used for the τ_R 's, in milliseconds:

$$[\tau_R]_{HC} = \frac{10^{-4}}{\phi_{BZ}} \exp\left(\frac{21,000}{RT_{stoch}}\right) \quad (5.)$$

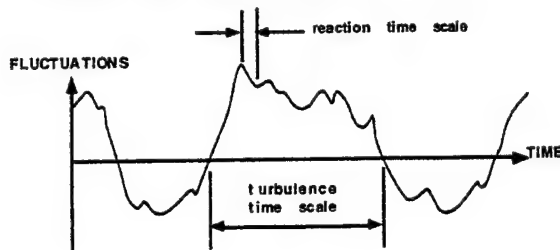
$$[\tau_R]_{CO} = 10^{-1} \exp\left(\frac{3,100}{RT_{CO}}\right) \quad (6.)$$

$$T_{CO} = 0.85T_{in} + 0.15T_B \quad (7.)$$

$$[\tau_R]_{NO} \propto \exp\left(\frac{135}{RT_{stoich}}\right) \quad (8.)$$

where ϕ is equivalence ratio, T is temperature °K, and R is the universal gas constant; the subscripts signify as follows - *HC* hydrocarbons, *CO* carbon monoxide, *NO* nitric oxide, *stoich* stoichiometric equivalence ratio, *in* compressor delivery temperature, *B* burnt, and *BZ* burning zone.

- Mixing-limited Regime - fast/equilibrium chemistry



- Kinetically-limited Regime - slow/non-equilibrium chemistry

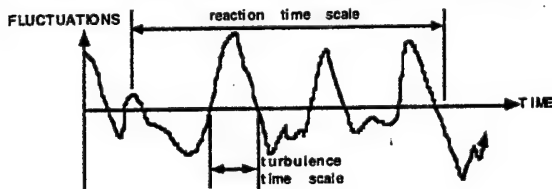


Fig. 2: Representation of Turbulence Influence on Chemistry

Figure 3 shows the ratio of CO to HC consumption times, and the ratio of NO generation to HC consumption times, at an engine idle power condition over a range of primary zone equivalence ratios. From Figure 1 the primary zone may be defined as consisting of the circumferential array of large toroidal recirculation zones associated with each fuel injector, and part of the first row of transverse air jets. At idle power, flame is generally confined to this region. For modern, high-thrust aircraft gas turbines the pressure in the combustor at idle power is in the range of 3-5 atmospheres. This represents a quite favorable combustion condition. It can be seen that the hydrocarbon consumption is much faster than carbon monoxide consumption; nitric oxide generation is much slower than hydrocarbon consumption. In addition, NO generation is much faster than CO consumption.

Turbulent mixing times were estimated from the time scale of the large eddies, which is given by,

$$\tau_T = \ell_e / u_e \quad (9.)$$

where ℓ_e is the eddy characteristic dimension and u_e is its characteristic velocity. The large eddy characteristic dimension is usually taken as being equal to 3% of the characteristic dimension of the flow passage. The characteristic dimension for the primary zone is the combustor dome height. The eddy velocity is obtained from the turbulence intensity.

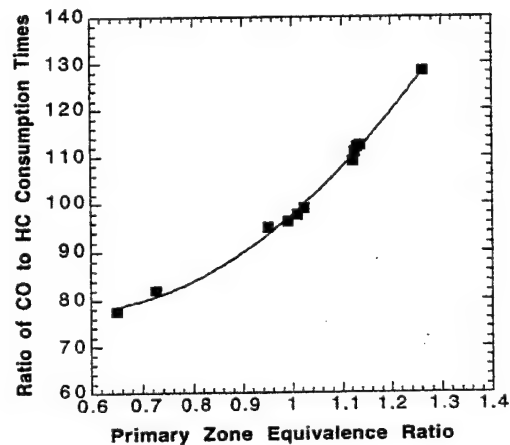
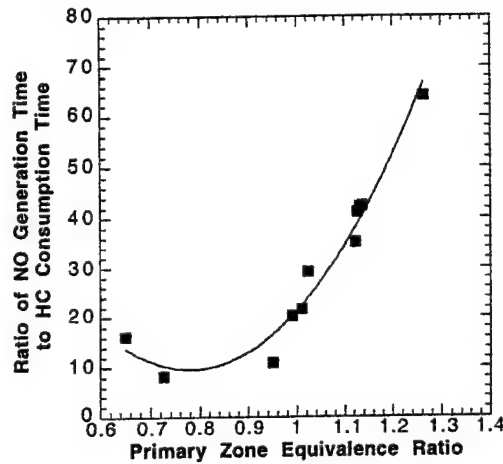


Fig. 3: Ratios of Pollution Consumption/Formation Times in a Gas Turbine Combustor Primary Zone at Idle Power Conditions

The mixing time was estimated to be a factor of 5-15 greater than that for hydrocarbon consumption. Therefore, hydrocarbon consumption at idle power is mixing limited and fast chemistry is appropriate. [Note that significant UHC emissions can be measured from engines at idle power. The source of these emissions is almost invariably partially reacted or unreacted liquid fuel becoming trapped in the liner film cooling air, where chemical reactions are frozen at these operating conditions. This is not the same situation as the bulk conditions considered above.] Conversely, the mixing time is .02-0.1 that of the CO consumption time. Therefore, CO burnout is kinetically limited, and non-equilibrium chemistry is appropriate. However, the mixing time is only 0.3-1.5 that for significant NO generation. Therefore, non-equilibrium chemistry is appropriate for NOx generation.

Consideration of this study reveals that appropriate kinetic calculations are necessary in order to estimate both CO and NO derived from bulk flow conditions in the combustor. The CO is consumed at mean conditions, so that "laminar" kinetic rate constants are acceptable. However, NO formation rates will be strongly influenced by local fluctuations in the flow, so that "laminar" kinetic rate constants will not be appropriate.

Although the characteristic time ratios can vary considerably up an engine power curve, the conclusions given above are not changed. It is seen that some corrections to kinetic rate constants for turbulent mixing effects are necessary for the NOx reactions.

V FUEL/AIR UNMIXEDNESS

As Brankovic⁵ demonstrated, chemical reaction rate constants can be modified from the accepted "laminar" values by fluctuations in temperature due to turbulence. Such fluctuations in temperature are the dominant mode for reaction rate "enhancement" with premixed combustion. For non-premixed combustion, especially with liquid fueled systems such as in the aircraft gas turbine, the dominant influence on reaction rates becomes spatial and temporal fluctuations in local equivalence ratios.

Enhancement of fuel/air/hot products mixing in the gas turbine conventional combustor is achieved by the introduction of transverse air jets penetrating across the reaction zone from the liner walls. Since the air jet dimensions are smaller than the combustor dimensions, discrete eddies of a size much smaller than

that of the combustor are formed. A distribution of eddies is formed, and within each eddy a roughly homogeneous local fuel/air mixture exists. The mixture composition of all of these eddies will not be identical; some eddies will be richer and some will be leaner than the average fuel/air ratio. Eddies with a mixture composition that falls inside the flammability limits will be ignited by merging with eddies of hot products, provided that the rate of eddy mixing is slow enough that the products ignite the reactants before dilution and cooling takes place¹². If the eddy lifetimes are long compared with burnout time within the eddy, then burning will take place over a range of equivalence ratios. The consumed reactants eddy, now another hot products eddy, can then serve as a new ignition source for another reactants eddy.

Many of the statistical characteristics of turbulence follow Gaussian distributions. Therefore, it can be taken that in any non-premixed (but not pure diffusion-burning) system the fuel burns with a Gaussian distribution of equivalence ratios about the mean equivalence ratio¹³. With this view, the pdf of fuel burned at temperature T will be a high-sigma (broad) Gaussian of burning temperatures for poorly mixed systems, and a low-sigma (narrow) Gaussian for better mixed systems. Since at the initial introduction of fuel into the combustor the distribution cannot be Gaussian, (being two separate streams - pure fuel and pure air) the validity of the Gaussian distribution in equivalence ratios for the burning zone downstream of the immediate initial region has been successfully examined by Flagan & Appleton¹⁴. With the assumptions that the mixture eddies described above are uniformly distributed throughout the burning zone and that the burnt eddies remain coherent during their residence time in the burning zone, Fletcher & Heywood¹⁵ introduced a mixing parameter S defined,

$$S = \frac{\sigma}{\bar{\phi}} \quad (10.)$$

where $\bar{\phi}$ is the bulk equivalence ratio, and σ is the standard deviation for a Gaussian distribution of equivalence ratios about the mean value. Following fuel injection and once a Gaussian distribution is formed in the burning zone, continuing turbulent mixing will result in a decay of S with time along a given eddy trajectory in the burning zone. For the work to follow, S is the time-averaged value in a given burning zone. With the above definition, a value of S equal to zero represents perfect mixing.

A given value of S will be achieved from two contributions to mixing: one associated with the way that the fuel is introduced into the combustor, and one associated with the total energy available to the system for mixing and how effectively it is utilized. The details of the fuel injection process will determine the liquid droplet sizes and distribution of droplets within the primary zone. The system energy for mixing is derived from the air pressure drop across the combustor walls, and determines the turbulence intensity generated¹⁷ together with air jet penetrations into the reacting flow. The design of the air jet patterns and their matching to the fuel distribution produced by the fuel injection system determines how effectively this energy is utilized in the mixing process. Together, these influence the spread of eddy equivalence ratios (σ), and how they change with time in the burning zone, thereby modifying the time-averaged S . It might be anticipated therefore, that different combustor designs would have different values of unmixedness.

The mixing parameter can be established empirically by matching modeling predictions to measured emissions data. As suggested above, the values of S would be expected to differ combustor to combustor, depending on primary zone design details, and to change along a given combustor as the bulk equivalence ratio is changed by downstream air addition. However, the functions of the primary zone are the same in any combustor for a given engine application, e.g. aircraft use. Furthermore, the design goals will also be similar. Additionally, the pressure drops across different combustor walls will not vary too much since on one hand, engine cycle performance demands that it be as low as possible, while on the other hand, experience teaches that there is a minimum value below which it is difficult to control the combustion process and so develop a successful combustor, i.e. there is a rather narrow window of pressure drops available to the designer. Therefore, it could be anticipated that combustors belonging to the same class, e.g. swirl-stabilized annular combustors for aircraft gas turbines, might have similar values of S .

Heywood & Mikus¹⁷ estimated the appropriate S values for a swirl-stabilized can-combustor using an air-atomizing fuel injection system in a fuel-lean primary zone. Sturgess *et al.*¹⁸ conducted a similar study for a non-swirl stabilized, annular combustor using a tee-vaporizer tube in a fuel-lean primary zone. Morford¹⁹ extended the study to include swirl-stabilized annular combustors using air-atomizing fuel injection systems in fuel-rich primary zones. These collected data

are presented in Figure 4, together with some additional data from this study for swirl-stabilized annular combustors using hybrid (pressure-atomizing primary injection/air-atomizing secondary injection) fuel injection systems with rich and lean primary zones. The resulting data contain considerable scatter, and the uncertainty associated with the modeling in each case is high. However, the different combustors agree with each another tolerably well, and the dependency on mean equivalence ratio is fairly well established. The behavior with mean equivalence ratio is not unexpected. For fuel-lean cases fuel is mixing in air, while for the fuel-rich cases air is mixing in fuel. Note that apart from equivalence ratio, the values of S did not appear to depend on combustor operating conditions, which varied considerably for the combustors considered.

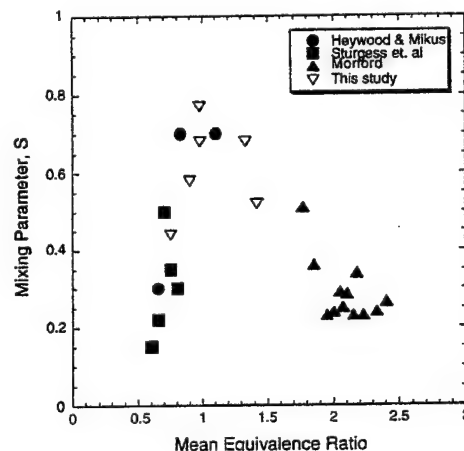


Fig. 4: Estimated Mixing Parameter Values

VI NO_x CORRECTION FACTOR

A NO_x correction factor CF , may be defined as ,

$$CF = \frac{[NO_x]_{unmixedness}}{[NO_x]_{\bar{\phi}}} \quad (11.)$$

where $[NO_x]_{unmixedness}$ = actual emission index of NO_x (g pollutant/kg fuel burned)

$[NO_x]_{\bar{\phi}}$ = theoretical emission index of NO_x at mean equivalence ratio

$[NOx]_{\phi}$ can be found by solving at a given mean equivalence ratio and operating condition, a chemical reaction mechanism using standard "laminar" rate constant information from the literature. $[NOx]_{unmixedness}$ can be found by solving the same reaction mechanism at the same operating conditions with a suitable distribution of equivalence ratios about the mean equivalence ratio. The distribution of equivalence ratios can be found from an appropriate value of S obtained from Figure 4 at the selected ϕ .

The NOx correction factor may be applied to a calculation as follows: Consider two adjacent elements A, B of a three-dimensional array representing a reacting flow field. A and B might be cells in a CFD calculation or individual reactors in a stirred reactor network. Let A and B be arranged in series. Specie i in B is the net of i convected into the element and any sources or sinks of i present in B, e.g.

$$i_B = \alpha i_A + S_{i,B} \quad (12.)$$

where α is the fraction of i in A that enters B, and $S_{i,B}$ is the source term for i within B. i_A and i_B result from "laminar" chemistry. Then,

$$S_{i,B} = i_B - \alpha i_A \quad (13.)$$

giving with unmixedness,

$$[i_B]_{unmix} = (S_{i,B})CF_B + \alpha[i_A CF_A]_{unmix} \quad (14.)$$

VI REACTION MECHANISM

The original chemical reaction mechanism selected for Jet-A fuel was that of Kollrack²⁰. The mechanism is a reduced scheme containing 30 steps involving 21 species, and it begins with a generic fuel molecule $C_{12}H_{23}$. It contains the extended Zeldovich reactions for thermal NO and any prompt-NO formed by super-equilibrium O-atoms. Although not perfect, this reaction mechanism has been verified for NOx²¹ using prevaporized, premixed Jet-A experimental data from several simple combustion experiments in the literature. This verification extended over a range of equivalence ratios from 0.5 to 0.8, inlet mixture temperatures from 600-833K, and combustion pressures from 1-5.3 atmospheres. Although these conditions do not extend too far into the gas turbine engine operating range, they do represent the best of the limited data available.

Experience (not given here) in applying the Kollrack mechanism to real gas turbine combustors operating from idle to take-off power conditions, indicated that at intermediate power levels and independent of the flow modeling used, NOx was underestimated. Intermediate engine power levels involve pressures in excess of 10 atm. and primary zone bulk equivalence ratios greater than unity. For this reason changes to the Kollrack mechanism were introduced. The changes were two-fold:

1. Rate constants for the extended Zeldovich reactions were updated to commonly accepted values, e.g. those of Bittker & Wolfbrandt²².

2. A prompt-NO mechanism involving hydrocarbon fragments was added, following Glarborg, Miller & Kee²³.

This latter inclusion increased the total mechanism to 71 reactions involving a total of 31 species. The modified reaction mechanism is presently referred to as Modified Kollrack+ scheme, and the additional steps are given in Table I. The production of CH is rate controlling for NO produced via hydrocarbon fragments, and it is important to get this correct.

The Modified Kollrack+ mechanism was given the same validation tests as the original Kollrack mechanism²¹. Figure 5 presents an example of the NOx performance of the two kinetic mechanisms for premixed Jet-A combustion. The experiment is that of Semerjian & Ball²⁴ with a perforated-plate flameholder at atmospheric pressure. It can be seen that the Modified Kollrack+ scheme represents the form of the measured data better than does the original Kollrack scheme. The small displacement discrepancy is believed due to the relatively crude flow modeling used. On an overall basis there is little to choose between the two mechanisms; however, the available benchmark experiments for comparison are extremely limited in operating conditions.

VII ASSESSMENT OF CORRECTION FACTORS

The procedure used to assess $[NOx]_{\phi}$ and $[NOx]_{unmixedness}$ was based on a perfectly-stirred reactor (PSR) code²⁵. For $[NOx]_{unmixedness}$ a parallel array of n - PSR's was established. Each reactor in the array had identical dimensions and airflows. The fuel flow rate to each reactor was adjusted to satisfy a Gaussian distribution of local equivalence ratios, with a width

determined from the S - value appropriate to the mean equivalence ratio. A curve was fit to the data of Figure 6 for this purpose. The individual outputs from the PSR array led into a **non-reacting** mixer of volume equal to the sum of that for the individual array reactors. $[NO_x]_{unmixedness}$ was obtained from the output of the mixer. The number of reactors in the parallel array was increased until the output from the mixer

$k_f = 10^{B_f} T^{N_f} \exp\left\{-\frac{T_f}{T}\right\}$ SI Units				
STEP	REACTION	B_f	N_f	T_f
31.	$CH_3 + OH \leftrightarrow CH_2 + H_2O$	10.48	0.0	1510
32.	$CH_3 + O \leftrightarrow CH_2 + OH$	10.70	0.0	6042
33.	$CH_3 + H \leftrightarrow CH_2 + H_2$	10.95	0.0	7693
34.	$CH_3 + H \leftrightarrow CH + H_2$	16.15	-2.0	0.0
35.	$CH_2 + O \leftrightarrow CO + H + H$	10.48	0.0	0.0
36.	$CH_2 + O \leftrightarrow CO + H_2$	10.70	0.0	0.0
37.	$CH_2 + OH \leftrightarrow CH_2O + H$	10.30	0.0	0.0
38.	$CH_2 + CO_2 \leftrightarrow CO + CH_2O$	8.04	0.0	503.0
39.	$CH + OH \leftrightarrow HCO + H$	10.48	0.0	0.0
40.	$CH + CO_2 \leftrightarrow HCO + CO$	9.53	0.0	347.4
41.	$CH + O_2 \leftrightarrow HCO + O$	10.52	0.0	0.0
42.	$CH + O \leftrightarrow CO + H$	10.76	0.0	0.0
43.	$CH + N_2 \leftrightarrow HCN + N$	8.00	0.0	6847.9
44.	$CH_2 + N_2 \leftrightarrow HCN + NH$	11.00	0.0	30211.5
45.	$HCN + O \leftrightarrow NCO + H$	1.08	2.6	2507.6
46.	$HCN + O \leftrightarrow NH + CO$	0.72	2.64	2507.6
47.	$HCN + OH \leftrightarrow CN + H_2O$	9.64	0.0	4531.7
48.	$HCN + OH \leftrightarrow HCNO + H$	8.60	0.0	2800.0
49.	$CN + OH \leftrightarrow NCO + H$	10.70	0.0	0.0
50.	$CN + O \leftrightarrow CO + N$	10.26	0.0	0.0
51.	$HCNO + H \leftrightarrow NH_2 + CO$	10.30	0.0	1510.6
52.	$NCO + H \leftrightarrow NH + CO$	10.70	0.0	0.0
53.	$NH + OH \leftrightarrow HNO + H$	10.30	0.0	0.0
54.	$NH + O_2 \leftrightarrow HNO + O$	11.00	0.0	6042.3
55.	$NH + OH \leftrightarrow NO + H_2O$	8.70	0.5	1006.0
56.	$NH + NO \leftrightarrow N_2O + H$	11.63	-0.5	0.0
57.	$HNO + OH \leftrightarrow NO + H_2O$	10.56	0.0	0.0
58.	$HNO + H \leftrightarrow NO + H_2$	9.60	0.0	0.0
59.	$CH + NO \leftrightarrow HCN + O$	11.04	0.0	0.0
60.	$CH_2 + NO \leftrightarrow HCNO + H$	9.46	0.0	-3021.0
61.	$HCNO + H \leftrightarrow HCN + OH$	10.70	0.0	6042.3
62.	$NCO + N \leftrightarrow N_2 + CO$	10.30	0.0	0.0
63.	$NH + NO \leftrightarrow N_2 + OH$	10.00	0.0	0.0
64.	$NH_2 + NO \leftrightarrow N_2 + H_2O$	12.58	-1.25	0.0
65.	$N_2O + H \leftrightarrow N_2 + OH$	10.88	0.0	7653.6
66.	$N_2O + O \leftrightarrow N_2 + O_2$	11.00	0.0	14199.0
67.	$CH_2 + CH_2 \leftrightarrow C_2H_2 + H_2$	10.50	0.0	0.0
68.	$CH_2 + CH_3 \leftrightarrow C_2H_4 + H$	10.30	0.0	0.0
69.	$CH + CH_4 \leftrightarrow C_2H_4 + H$	10.78	0.0	0.0
70.	$CH_2 + CH \leftrightarrow C_2H_2 + H$	10.60	0.0	0.0
71.	$CH + CH_3 \leftrightarrow C_2H_2 + H$	10.48	0.0	0.0

Table I: Additions to Kollrack Mechanism

became insensitive to the number of reactors, n . This condition was satisfied with 13 reactors for equivalence ratios less than unity. $[NO_x]_{\bar{\phi}}$ was obtained from a single PSR of volume equal to the sum of that for the

reactors in the parallel array. This single PSR was operated at the mean equivalence ratio with an airflow equal to the sum of that of the parallel array.

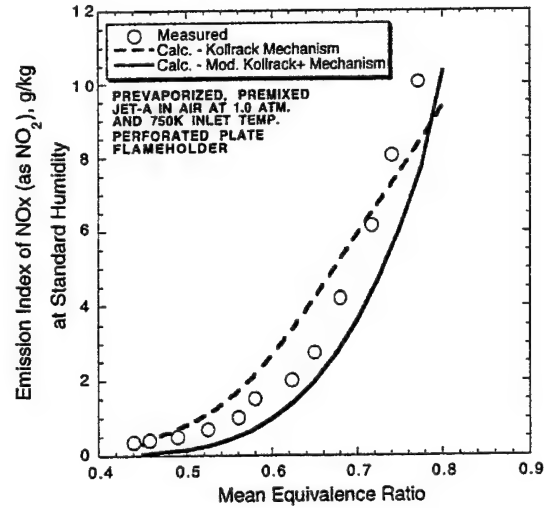


Fig. 5: Comparison of NOx by Reaction Mechanism

As an example, Figure 6a) shows the Gaussian distribution of cumulative fuel burned as a function of equivalence ratio in each of the array reactors, for a mean equivalence ratio of 0.6. Figure 6b) and Figure 6c) respectively, give the resulting individual reactor flame temperatures and NO generated at the local equivalence ratios. The calculations were made at a combustion pressure of 20 atmospheres with an air inlet temperature commensurate with the pressure. It can be seen that only a small amount of fuel is actually burned near the mean equivalence ratio, and that a wide range of flame temperatures result, increasing with local equivalence ratio. The bulk of the nitric oxide generated comes from burning only a small fraction of the total fuel that is reacted at the maximum temperatures present in the array. However, the total nitric oxide resulting is considerably more than that generated by any single PSR in the array.

The total NOx generated by the array at this condition using the Kollrack mechanism was 42.450 g/kg (as NO₂). The NOx produced by the single large PSR operating at the 0.6 mean equivalence ratio was 17.1167 g/kg (as NO₂). Therefore, the NOx correction factor CF , is the ratio of these two numbers, i.e. 2.4802. In other words, fuel/air unmixedness typical of

a certain class of gas turbine combustors (swirl-stabilized, annular combustors with air-atomizing fuel injection systems) at these operating conditions, would increase the NO_x generated by a factor of 2.4802 compared to a perfectly premixed system operating at the same conditions.

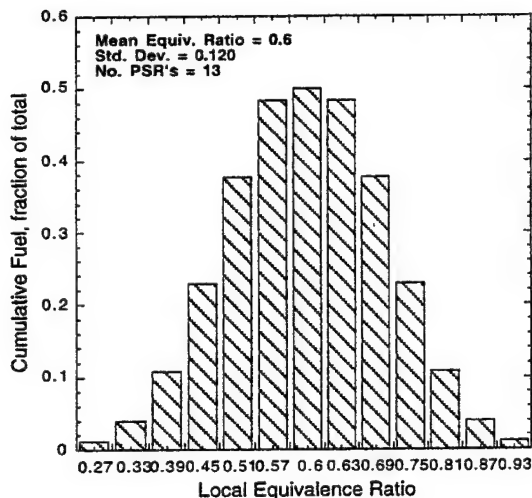


Fig. 6a): 13-Reactor Array Fuel Distribution

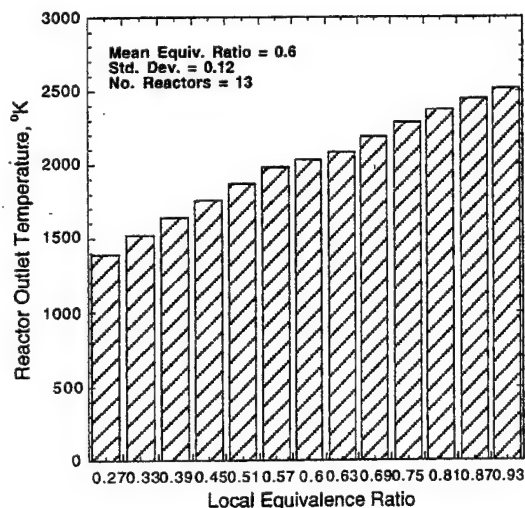


Fig. 6b): Outlet Temperatures for Array

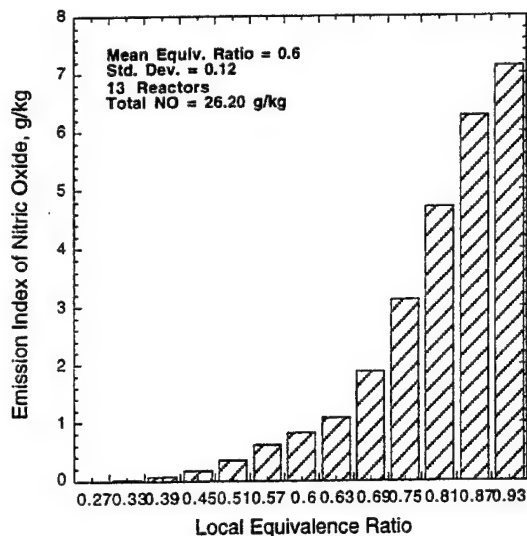


Fig. 6c): Nitric Oxide from Array

It can be appreciated that as the mean equivalence ratio is increased, and unmixedness increases also (Figure 4), the upper spread of local equivalence ratios in the array will eventually exceed unity equivalence ratio. The temperature distribution will change accordingly, as will the local condition that results in maximum individual reactor nitric oxide. The possibility therefore exists that unmixedness, under certain conditions, can suppress NO_x formation, and that *CF* will have a value less than unity.

Figure 7a) shows for the 13-reactor array, a problem at mean equivalence ratios greater than unity, where a waviness develops in the integrated array-NO_x. Figure 7b) shows the NO_x obtained from the equivalent single PSR reactor. Since *CF* is the ratio of these two curves and NO_x values from the single reactor are 2-3 orders of magnitude smaller than the reactor-array values at high mean equivalence ratios, the waviness results in an unacceptable large variation in *CF*.

Figure 7 was made for the Modified Kollrack+ reaction mechanism, but similar behavior was apparent with the Kollrack mechanism. The waviness is associated with the discrete representation of the Gaussian distribution of eddy equivalence ratios. The number of parallel reactors in the array was arbitrarily

increased to 25, and the problem was eliminated, as the second curve in Figure 7a) indicates.

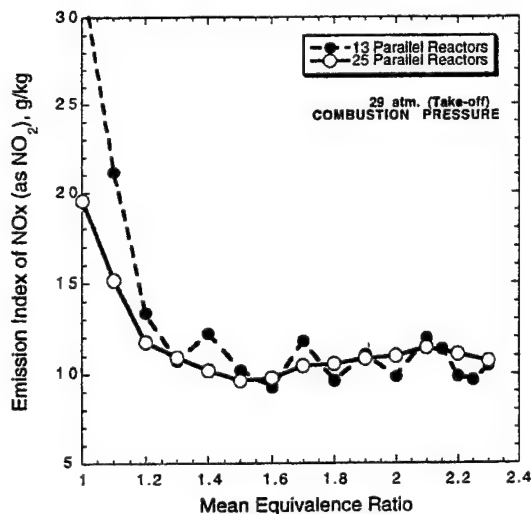


Fig. 7a): Effect of Array Size at High Equivalence Ratio

cross at a mean equivalence ratio of 1.2. For mean equivalence ratios below 0.5 the effect of pressure becomes more pronounced, with increasing pressure reducing CF .

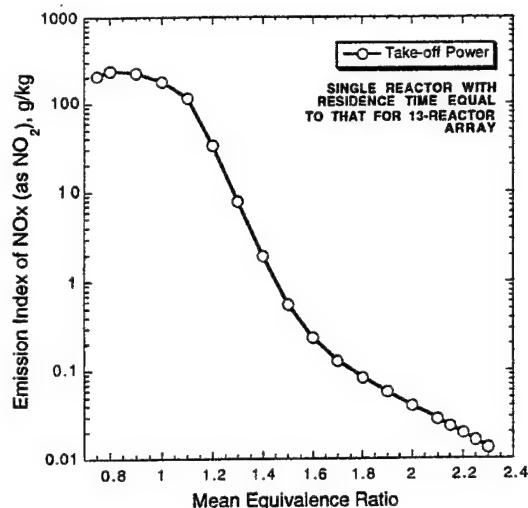


Fig. 7b): Single Reactor (Premixed) NOx

VIII NOx CORRECTION FACTOR IN AN ENGINE

To assess the likely importance to gas turbine engines, the NOx correction factor CF , has been calculated over a range of mean equivalence ratios from 0.2 to 2.3 at combustion pressures from 4 to 29 atmospheres. The air inlet temperature was commensurate with pressure to represent a typical engine compression characteristic. The fuel was liquid Jet-A, and had a temperature of 339°K (150°F) at 5 atm. combustion pressure, increasing to 436°K (325°F) at 25 atm., thereafter remaining constant at 436°K. The Kollrack and Modified Kollrack+ chemical reaction mechanisms were used. Values of fuel/air unmixedness were taken from Figure 4.

Figure 8 presents the results of the study for the Kollrack mechanism over the mean equivalence ratio range 0.2-1.4. For higher mean equivalence ratios, CF -values rise significantly, and are not shown for convenience. It can be seen from the figure that, except for mean equivalence ratios less than 0.5 and greater than 1.3, there is little effect of combustion pressure (and air inlet temperature) on CF ; there is however, a systematic variation with pressure, and the curves do

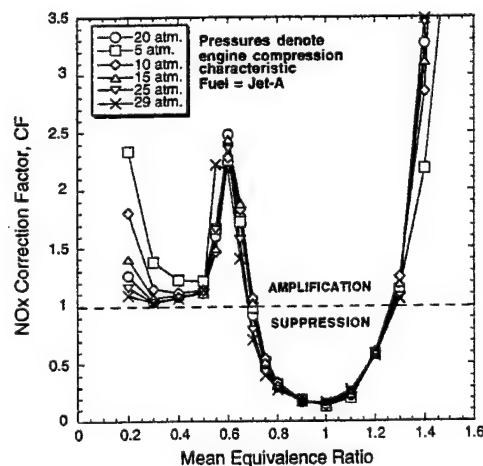


Fig. 8: NOx Correction Factor Variation with Mean Equivalence Ratio up an Engine Compression Curve for the Kollrack Mechanism

For mean equivalence ratios greater than 0.7 and less than 1.27, unmixedness suppresses NOx formation, with CF falling below unity. This can be explained as a temperature effect on NO formation. For gas temperatures above about 2050°K, thermal NO is well-known to be generated rapidly and is the dominant contributor to NOx. This is through the reversible reactions,



The mean exhaust temperature from the reactor array (with a variable and non-zero value of S) becomes less than that from the single reactor, for which $S=0$, at a mean equivalence ratio of 0.65, and falls below the critical 2050°K for mean equivalence ratios greater than 0.7. This is in good agreement with the lower mean equivalence ratio limit for $CF < 1.0$ in Figure 8. For equivalence ratios greater than 1.27 the single reactor exhaust temperature falls off rapidly from its higher values, while that from the array of reactors does not due to the distribution of higher local temperatures always present. The reversible reaction,



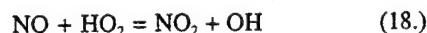
continues to hold up NO production in the array, while it drops off in the single reactor.

For mean equivalence ratios around 0.6, CF increases sharply to values in the range 2.2 to 2.5. Consideration of Figure 6 shows that just over half of the fuel is burned at temperatures exceeding 2000°K, and most of that half at temperatures above the critical 2050°K. Between mean equivalence ratios of 0.6 and 0.4, CF falls off dramatically and remains relatively flat at values just over unity. This is because the mean temperature levels are down below the critical for excess NOx generation, and the spread of temperatures around the mean is becoming extremely narrow.

The behavior described can be appreciated clearly from Figure 9 which, for several values of mean equivalence ratio, shows the temperature spread around the mean depending on the individual equivalence ratios in the reactor array. It can be seen that as mean equivalence ratio increases, the width of the individual reactor equivalence ratios increases (following Figure 4). The magnitude of the deviation of temperatures from the means also increases with mean equivalence ratio, and changes from being both positive and

negative at low mean equivalence ratios to being wholly negative for mean equivalence ratios greater than unity.

It is also well-known that for gas temperatures below about 1500°K, NO_2 and N_2O become the dominant components of the total NOx generated, not thermal NO. While the basic Kollrack mechanism does not presently allow for N_2O , it does permit formation of NO_2 from the reversible reaction,



At 20 atm. combustion pressure the critical 1500°K gas temperature corresponds to a mean equivalence ratio of 0.32. At the same pressure, the ratio of NO/NO_2 for the array exceeds that from the single reactor at all combustion pressures. Thus, the single reactor always produces a greater percentage of NO_2 than does the array for mean equivalence ratios less than 0.5. However, for the same conditions, the array produces more NO and NO_2 in absolute terms than does the single reactor. This is a consequence of the spread of equivalence ratios about the mean for the array, and the resulting higher and lower reaction temperatures experienced.

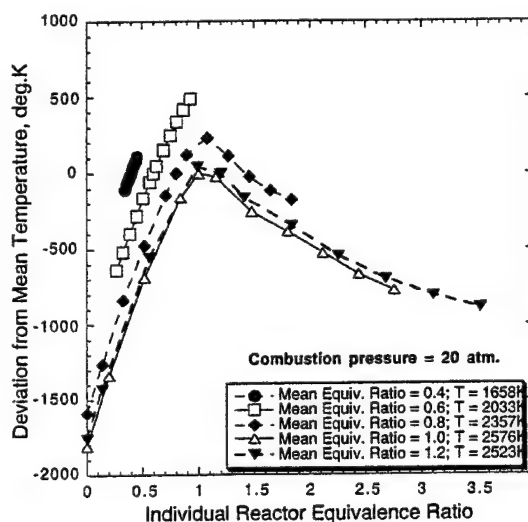


Fig. 9: Effect of Unmixedness on Burning Temperature Deviations from Mean Values (Kollrack Mechanism)

Figures 10 and 11 give similar results for NOx correction factor dependency on mean equivalence ratio and engine operating conditions, but for the Mod. Kollrack+ reaction mechanism and a 25 reactor parallel array for all mean equivalence ratios.

The overall behavior of CF is similar to that given in Figure 8 for the Kollrack mechanism. However, there are some significant differences in sensitivities. For the Mod. Kollrack+ mechanism at high engine power levels (29 atm.) for mean equivalence ratios greater than 1.5, there is a strong effect of unmixedness on CF . The effect of fuel/air unmixedness on CF at idle engine conditions (4 atm.) for mean equivalence ratios greater than 1.5 is much less than at the higher pressure, but is still important. These characteristics are similar to those for the Kollrack mechanism, but exhibit much greater sensitivity to operating condition. At mean equivalence ratios around 0.6, the effects of unmixedness on CF are much greater at idle power than at take-off power. For Kollrack, the peak in CF at 0.6 mean equivalence ratio has insignificant variation between idle and take-off; for Mod. Kollrack+ CF decreases from 18 at idle to about 4 at take-off. Also, at 0.2 mean equivalence ratio the Kollrack mechanism gives a systematic and significant decrease in CF from idle to take-off power levels, i.e. from 2.33 to 1.1; the Mod. Kollrack+ shows negligible difference in CF between the two conditions, and no increase in CF with decreasing mean equivalence ratio.

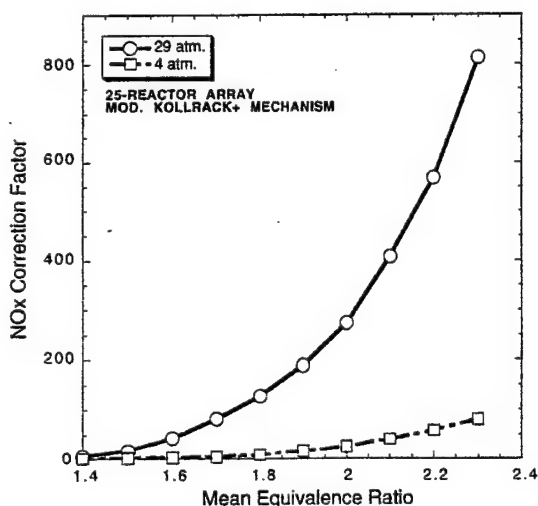


Fig. 10: NOx Correction Factors for Modified Kollrack Reaction Mechanism+

To assess the effects of discretization of the Gaussian distribution, the Mod. Kollrack+ mechanism was also applied to the 13-reactor parallel array. At idle power, 13 versus 25 parallel reactors reduces the peak CF value at 0.6 mean equivalence ratio from 18 with 25 down to 15.4 with 13. At very rich mean equivalence ratios increasing the number of parallel reactors from 13 to 25 increases CF slightly, from 36.7 to 39.1 at 2.1 mean equivalence ratio.

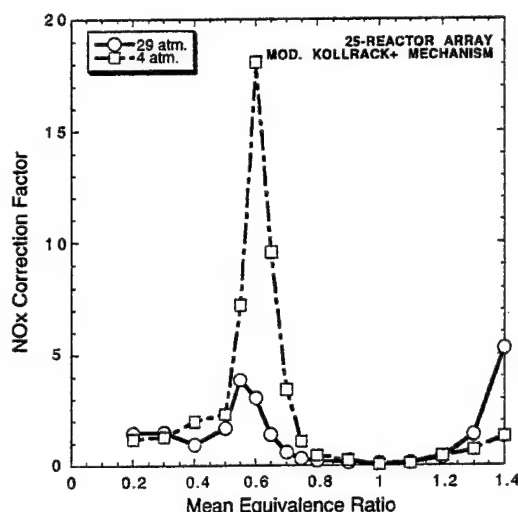


Fig. 11: NOx Correction Factors at Lower Equivalence Ratios; Modified Kollrack Mechanism Plus Additional CH-Steps, Based On 25-Reactor Array

IX SUMMARY AND CONCLUSIONS

It was stated that detailed reaction chemistry is necessary for calculation of the major pollution species currently subject to regulation. A brief review of the current state-of-the-art of CFD typical at the gas turbine engine companies showed that incorporation of such chemistry directly was not presently cost-effective. Arguments were presented that turbulent fluctuations in reacting flow situations can have significant effects on reaction chemistry. An order of magnitude analysis of Damkohler Numbers in gas turbines suggested that the NOx chemistry was the most seriously affected.

For non-premixed combustors, especially those using liquid fuel, it was postulated that fluctuations in local fuel/air ratio produced the dominant effects on the NO_x chemical reaction rates. Spatial and temporal fluctuations in local equivalence ratio were combined into an average fluctuation, and the statistical mixing parameter of Fletcher & Heywood¹⁶ was invoked, together with the reasonable assumption of a Gaussian distribution of local equivalence ratios about the mean value. Collected empirical information from the literature was used to relate the mixing parameter to mean equivalence ratio. A NO_x correction factor was introduced to relate the NO_x produced with fuel/air unmixedness to NO_x produced at the mean equivalence ratio. Values of the NO_x correction factor were derived over a wide range of gas turbine engine operating conditions. This was done using the correlated empirical mixing parameter information, together with calculation for parallel arrays of PSR reactors upon which chemical reaction mechanisms for Jet-A fuel were solved. Significant effects were revealed with both NO_x amplification and suppression being seen over the range of mean equivalence ratios. The detailed behavior of NO_x correction factors is governed by the details of the chemical reaction mechanism used. Two such mechanisms were presented. Both rely on a reduced mechanism for jet fuel, but have differing degrees of complexity. It is not presently possible to make a definitive decision between these two mechanisms.

ACKNOWLEDGEMENTS

The continuing enthusiasm, motivation and support of Dr. W.M. Roquemore of the Air Force Research Laboratory are greatly appreciated. This ongoing research is sponsored by the U.S. Air Force Research Laboratory, Propulsion Sciences & Advanced Concepts Division, Wright-Patterson Air Force Base, through Contract No. F33615-95-C-2507. In particular, the support and patience of Carlos A. Arana, WL/POTC, is acknowledged.

REFERENCES

1. R.P. Lindstedt, and L.Q. Maurice, "A Detailed Chemical Kinetic Model for Practical Aviation Fuels," Paper No. AIAA-97-2836, presented at 33rd. AIAA/ASME/SAE/ASEE Joint Propulsion Conference & Exhibit, Seattle, WA, July 6-9, 1997.
2. L.Q. Maurice, "Detailed Chemical Kinetic Models for Aviation Fuels," Ph.D. Thesis, Imperial College, University of London, October 1996.
3. R.P. Lindstedt, "Systematically Reduced Kinetic Models: A European Perspective," Paper No. AIAA-97-3368, presented at the 33rd. AIAA/ASME/SAE/ASEE Joint Propulsion Conference & Exhibit, Seattle, WA, July 6-9, 1997.
4. S.B. Pope, "Computationally Efficient Implementation of Combustion Chemistry using *In Situ* Adaptive Tabulation," *Combustion Theory and Modelling*, Vol. 1, 1997, pp. 41-63.
5. A. Brankovic, Pratt & Whitney, private communication, 1995.
6. S.M. Correa, A. Gulati, and S.B. Pope, *Twenty-Fifth Symposium (International) on Combustion*, The Combustion Institute, Pittsburgh, PA, 1994, pp.1167-1173.
7. A.D. Leonard, and F. Dai, "Applications of a Coupled Monte Carlo PDF/Finite Volume CFD Method for Turbulent Combustion," Paper No. AIAA-94-2904, presented at 30th. AIAA/ASME/SAE/ASEE Joint Propulsion Conference, Indianapolis, IN, June 27-29, 1994.
8. A.D. Gosman, F.C. Lockwood, and S.A. Syed, "Prediction of a Horizontal Free Turbulent Diffusion Flame," *16th. Symposium (International) on Combustion*, The Combustion Institute, Pittsburgh, PA, 1976, pp. 1543-1555.
9. M. J. Kenworthy, S.M. Correa, S.M. and D.L. Burrus, *Aerothermal Modeling Phase 1 - Final Report*, Volumes I and II, NASA Report CR-168296, November 1983.
10. V.J. Sarli, D.C. Eiler and R.J. Marshall, "Effects of Operating Variables on Gaseous Emissions," presented at Air Pollution Control Association (APCA) Specialty Conference on *Air Pollution Measurement Accuracy as It Relates to Regulation Compliance*, New Orleans, LA, October 26-28, 1975.
11. J.H. Tuttle, M.B. Colket, and A.M. Mellor, "Characteristic Time Correlation of Emissions from Conventional Aircraft Type Flames," Rept. No. PURDU CL 96-05, Purdue University, West Lafayette, IN, May 1976.

12. F.C. Lockwood, and I.A.E. Megahed "Extinction in Turbulent Reacting Flows," *Combustion Science and Technology*, Vol. 19, 1978, pp. 77-80.
13. H.L. Morton, and R.L. Marshall, "Impact of Emission Regulations on Gas Turbine Combustor Design," *Canadian Aeronautics and Space Journal*, Vol. 20, No.3, 1974, pp. 101-109.
14. R.C. Flagan, R.C. and J.P. Appleton, "A Stochastic Model of Turbulent Mixing with Chemical Reaction: Nitric Oxide Formation in a Plug-Flow Burner," *Combustion and Flame*, Vol. 23, 1974, pp. 249-267.
15. R.S. Fletcher, and J.B. Heywood, "A Model for Nitric Oxide Emissions from Aircraft Gas Turbine Engines," AIAA Paper No. 71-123, presented at AIAA 9th. Aerospace Sciences Meeting, New York, NY, January 25-27, 1971.
16. A.H. Lefebvre, and G.A. Halls, "Some Experiences in Combustor Scaling," AGARDograph 37, *Advanced Aero Engine Testing*, Eds. A.W Morley and J. Fabri, Pergamon Press, London, 1959, pp.177-204.
17. J.B. Heywood, and T. Mikus, "Parameters Controlling Nitric Oxide Emissions from Gas Turbine Combustors," presented at AGARD Propulsion and Energetics Panel 41st Meeting on *Atmospheric Pollution by Aircraft Engines*, London, England, April 9-13, 1973.
18. G.J. Sturgess, R.G. McKinney, and S.A. Morford, "Modification of Combustor Stoichiometry Distribution for Reduced NOx Emission from Aircraft Engines," Trans. ASME *J. Engineering for Gas Turbines and Power*, Vol. 115, No. 3, July 1993, pp. 570-580.
19. S.A. Morford, Pratt & Whitney, 1993.
20. R. Roberts, L.D. Aceto, R. Kollrack, D.P. Teixeira, and J.M. Bonnell, "An Analytical Model for Nitric Oxide Formation in a Gas Turbine combustor," *AIAA Journal*, Vol. 19, No.6, 1972, pp. 820-826.
21. G.J. Sturgess, "Assessment of an Abbreviated Jet-A/JP-5/JP-8 Reaction Mechanism for Modeling Gas Turbine Engine Gaseous Emissions," Paper No. AIAA-97-2709, presented at 33rd. AIAA/ASME/SAE/ASEE Joint Propulsion Conference & Exhibit, Seattle, WA, July 6-9, 1997.
22. D.A. Bittker, and G. Wolfbrandt, "Effect of Fuel Nitrogen and Hydrogen Content on Emissions in Hydrocarbon Combustion," Paper No. 81-GT-63, presented at the ASME Gas Turbine Conference & Products Show, Houston, TX, 9-12 March, 1981.
23. P. Glarborg, J.A. Miller, and R.J. Kee, "Kinetic Modeling and Sensitivity Analysis of Nitrogen Oxide Formation in Well-Stirred Reactors," Paper WSS/CL 1-5B, presented at the Western States Section/Combustion Institute, Joint Technical Meeting, San Antonio, TX, 22-23 April, 1985.
24. H. Semerjian, and I.C. Ball, "Potential Reduction in NOx Emissions with Premixed Combustors," presented at Central States Section/Combustion Institute, Spring Technical Meeting, NASA Lewis Research Center, Cleveland, OH, 28-30 March, 1977.
25. B.S. Pratt, and D.T. Pratt, "MARK2X Computer Code, private communication, 1990; D.T. Pratt, MARK3GY Computer Code, private communication, 1998.

3.1.3.2.2 Hybrid Model. The paper entitled "A Hybrid Model for Calculating Lean Blow-Outs in Practical Combustors" (see pp. 482-497) discusses a hybrid approach used to address the immense computational burden associated with the calculation of singularities, such as blowout, and complete-cycle chemistry-dominated processes, such as emissions, in geometrically complex practical gas turbine combustion chambers. A later publication entitled "Assessment of an Abbreviated Jet-A/JP-5/JP-8 Reaction Mechanism for Modeling Gas Turbine Engine Gaseous Emissions" (see pp. 498-513) documents extension of the concept of hybrid modeling from its original application in calculating the singularity of lean blowout for practical combustors to calculating gaseous emissions.



AIAA 96-3125
A Hybrid Model for Calculating
Lean Blow-outs in
Practical Combustors

G.J. Sturgess
Innovative Scientific Solutions Inc.
Beavercreek, Ohio

D.T. Shouse
Aero Propulsion and Power Directorate
Wright-Patterson AFB, Ohio

32nd AIAA/ASME/SAE/ASEE
Joint Propulsion Conference
July 1-3, 1996 / Lake Buena Vista, FL

A HYBRID MODEL FOR CALCULATING LEAN BLOWOUTS IN PRACTICAL COMBUSTORS

G.J. Sturgess*

*Innovative Scientific Solutions, Inc.,
Beavercreek, Ohio*

D.T. Shouse

*Aero Propulsion and Power Directorate, Wright Laboratory,
WPAFB, Ohio*

Abstract

To address the immense computational burden associated with the calculation of singularities, such as blowout, and complete-cycle, chemistry dominated processes, such as emissions, in geometrically complex practical gas turbine combustion chambers, a hybrid modeling approach is presented. The procedure begins with a computational fluid dynamics (CFD) calculation at representative operating conditions of interest. Partial-modeling assumptions are invoked to justify reliance on this single solution as the basis for the hybrid procedure. The field solutions resulting from the CFD calculation are post-processed using a dissipation-gradient analysis and topology methods to represent the fluid dynamics by means of a connected network of fuel/air mixers, well-stirred reactors and plug-flow reactors. Detailed chemistry is solved on the network over the required range of operating conditions to yield the desired matrix of solutions. The efficacy of this uncoupled approach is successfully demonstrated by comparison of calculations with measured blowout data for a variety of conditions, including flow-split variation, in a planar sector of a simplified annular gas turbine combustor.

Background

Levels of gaseous emissions generated by aircraft gas turbine engines for commercial operations are regulated by international standards that are becoming progressively more stringent. Military aircraft operations are currently not regulated for emissions, but the U.S. Air Force pursues a "good neighbors" policy with respect to emissions. Therefore, it is desirable that

engine manufacturers have available a tool for assessing the low emissions potentials of new, standard designs and for evaluation of new combustor concepts, prior to any experimental evaluation.

For reasons of safety in commercial aircraft operations, engine systems are required to satisfy a number of aircraft-determined stability criteria. Military operations, especially for fighter-type aircraft, require engine stability over much-expanded operating envelopes. The blowout characteristics of the combustor itself form a critical part of overall engine stability, and establish an absolute limit on what can be achieved. Means of calculating this limit prior to coupling with an engine system are essential.

The combustion processes involved in both emissions generation and combustor blowout are chemistry-dominated. Furthermore, as design goals, emissions and blowout are strongly linked in that combustor design changes which are good for one are often bad for the other. For these reasons a common evaluation tool suitable for both phenomena would be convenient.

The nature of such a common evaluation tool is established by how the tool is used. Complete emissions and blowout mapping for a particular combustor configuration requires many related applications of the tool over a matrix of operating conditions. Changes to the configuration require repetition of the complete process. Therefore, a large computational effort is implied. Timeliness and economic considerations imply that the tool be as simple as possible.

* AIAA Senior Member
Copyright (c) 1996 by authors.
Published by the American Institute of Aeronautics
and Astronautics, Inc., with permission.

Introduction

One study that is relevant to the background given above and which is currently in progress, is an investigation into the minimization of engine exhaust emissions, the exploration of the relationship between generation of these emissions and combustor stability characteristics¹, and the understanding of lean blowout in particular. This effort is part of the U.S. Air Force's *Combustor Design Model Evaluation (CDME) Program* conducted by the Aero Propulsion and Power Directorate of Wright Laboratory (WL/PO), Wright-Patterson Air Force Base, Ohio. The goal of the program is an improvement in modeling used to facilitate design work.

As a part of this Air Force work a broad-ranging investigation of combustor primary zone behavior is being conducted. For the lean blowout (LBO) portion, a two-part, modeling/experimental, approach was pursued. The experimental section progressively moved in three steps through a simple research combustor to a planar sector of a simplified generic gas turbine engine combustor, e.g. Reference 2.

Modeling of the LBO process followed several complimentary approaches³, and fell into four parts concerned with 1.) correlation, for experimental data, 2.) phenomenological, for quick status assessment, 3.) mathematical, for *a priori* calculation of detailed flame characteristics, and 4.) hybrid, as a design analysis tool.

Summary of Program Modeling Considerations

The common theme between the four modeling parts was the well-stirred reactor. This well-stirred reactor concept figured prominently from the experimental observation that under most circumstances of interest, flame lift always took place prior to blowout. Therefore, a key modeling postulate was made that LBO always took place from a partially-mixed condition, even though the fuel and air might be introduced separately to give a nominal diffusion flame.

The experimental data correlation used well-stirred reactor theory directly, by treating the heat release zone of a combustor as a single reactor that could be sized by methodical procedures. The resulting loading parameter approach proved to be very successful⁴, but only for simple combustors that had a single and well-defined reaction zone.

The phenomenological model for stability assessment compared the ratio of a mixing time scale and a chemical reaction time scale to a critical value determining flame extinction. Pertinent empirical data were incorporated into these times, and constants were established by means of a limit analysis. The ratio of these times was also related to a critical Karlovitz Number (flame stretch criterion) for flame extinction in the case of weak turbulence. The drawback of this approach was that it involved local turbulence characteristics and flame speed, and therefore needed to be applied on a point-by-point basis throughout the combustor. Therefore, it was best applied fully-coupled through a CFD solution; this eliminated its utility as a quick assessment tool.

The mathematical modeling approach selected was the Eddy Dissipation Concept combustion model of Magnussen⁵. The EDC model concentrates on the physics of the fine-scale turbulence where most of the dissipation of turbulence kinetic energy into heat takes place and where molecular mixing is achieved. In this it follows the same approach as the phenomenological model. However, it makes the assumption that reactants are homogeneously mixed within the fine-scale eddy structures, and therefore treats these as being well-stirred reactors. Since the physical scale of these structures is normally well below resolution by any reasonable CFD computational grid, the EDC model is a sub-grid scale combustion model.

The EDC model involves two parts, 1.) establishing the sub-grid scale reactors and the surrounding fluid feed-stream conditions, and, 2.) establishing the chemical reaction rates within the sub-grid scale reactors. The first part can be reduced to a series of residence time scales, and is provided by the turbulence model in the CFD code. The second part can be reduced to chemical kinetic time scales. Comparison of the sets of time scales establishes flame extinction criteria. The similarities to the phenomenological model are obvious.

Incorporation of a classical reaction kinetics mechanism into a CFD codes involves a number of difficulties. A major one is that a transport equation must be solved for each individual chemical species involved in the mechanism.

For example, taking propane/air combustion, a reasonably complete mechanism that incorporates the coupling between hydrocarbon combustion and nitrogen chemistry, with capability of delineating the relative

importance of thermal and prompt NO formation mechanisms, could contain well over 300 steps and nearly 70 intermediate and stable species. A simplified propane/air mechanism, for which the NO_x formation chemistry is completely uncoupled and would have to be obtained by post-processing, might reduce to 5 reaction steps and 8 species. Unfortunately, a reasonably complete reaction mechanism for propane/air combustion, consisting of 249 reactions and 51 species, was unable to reproduce a classic well-stirred reactor experimental blowout curve⁶.

Patraik & Kailasanath have demonstrated that CPU time increases with the number of chemical species to the sixth power. The additional computational burden so-arising may be manageable for very simple reacting flowfields and for reduced reaction mechanisms, but it rapidly becomes unacceptable as flowfield complexity increases.

The EDC model was therefore implemented in the limit of fast chemistry. In this limit an extinction criterion has to be established, just as with the phenomenological stability parameter model. However, unlike the stability parameter model, the EDC model does account directly for intermittency effects.

The fast chemistry version of the EDC model in a TEACH-type CFD code, was able to successfully calculate flame lift for both classical jet diffusion flames from the literature, and in the simple research combustor of this study⁶. However, it was not able to calculate the observed flame behavior at the onset of a complete lean blowout sequence, beginning with flame-lift. Furthermore, when calculating the relatively simple flow field of the research combustor on a reasonably fast work-station, even the fast chemistry version of the model required excessive computational times. These times precluded serious consideration for application in calculating the stability loop of a practical engine-combustor.

Present Contribution

The promising concepts at the hearts of the earlier methods above, which had drawbacks or limited successes when working at the micro-scale level, have been applied at the macro-scale level. This macro-scale approach sacrifices some of the detail of the micro-scale level, but permits rapid calculation of global stability characteristics.

A careful mixture of the best features of CFD and stirred reactor network methods, hybrid modeling uncouples the reaction kinetics from the flowfield calculation, but is much more than the post-processing of a CFD solution. The calculation times for hybrid modeling are such that it is a pragmatic engineering tool which allows investigation of a wide range of operating conditions and/or flow splits in a combustor in a timely and cost-effective fashion. It is flexible enough to be used for either LBO or emissions calculations. When used for emissions calculations it can be extended to permit allowance for unmixedness effects on reaction rates.

Basics of Hybrid Modeling

The basis of the hybrid modeling approach is to separate the fluid dynamic processes in the combustor from the chemical processes, and to solve them separately. Such separation implies that mixing and chemical time scales can be treated as being very different. This is not such a bad approximation in conventional combustors for aircraft gas turbines, which are always mixing-limited. However, this is only true in a global sense, and not in an eddy sense. Therefore, where they are important, unity Damkohler Number effects of turbulence/chemistry interactions on reaction rates are implicitly ignored. (They can, however, be explicitly addressed later to some degree, in the detailed development.)

The hybrid procedure solves the detailed chemistry on an environment that is established by the fluid dynamics. The fluid dynamics is obtained from a stationary-state CFD solution using a simple combustion model. Consistent with this stationary-state fluid dynamics assumption, stability is here defined through blowout, specifically, LBO. Occasionally, non-stationary behavior of the flame and/or a noticeable acoustic signature can be noted as an LBO is approached in a gas turbine combustor. Although it is recognized that such dynamic phenomena are an integral part of combustor stability, they are not directly accounted for in the hybrid approach.

It is further assumed that the fundamental (stationary) flow field within the combustor, once calculated by CFD at representative operating conditions, does not change substantially as a blowout is approached, and as the operating conditions (e.g. air inlet temperature, pressure, overall fuel/air ratio, etc.) are varied. This constancy of the major features of the flow field is also taken to hold for modest re-

distributions of airflow into the combustor, provided that the positions of the various air ports in the liners are not changed. The value of this is that only a single CFD solution is required. Justification for the assumption arises through Spalding's partial modeling criteria⁷, which demonstrated that, to first order, flow patterns depend only on the geometry of the combustor, provided fuel momentum is low. This latter condition is satisfied for airblast-atomizing fuel injectors, where fuel distribution is achieved through the fuel injector airflow.

Generalization of the Stirred Reactor Concept

The calculated flow field forms the (fixed) background upon which the chemistry is calculated. The vehicle for making the kinetic calculations is the stirred reactor.

Bragg⁸ proposed that a gas turbine combustor could be modeled as a perfectly-stirred reactor (PSR) and later, as a well-stirred reactor (WSR) representing the primary zone where flame is held, followed by a plug-flow reactor (PFR) representing the secondary burn-up zone; the dilution zone was taken as a non-reacting mixer. A WSR is a reacting volume within which the time-scales of turbulent mixing are assumed to be finite but are less than the chemical time-scales. For a PSR, the ratio of mixing to chemical times is zero. A PFR is a PSR transversely across the flow direction, but not longitudinally where concentration and temperature gradients exist. Thus, a PSR is zero-dimensional, but a PFR is one-dimensional.

Experimental realizations of (near) PSR's, e.g. Longwell et al.⁹ and Longwell & Weiss¹⁰, when operated at near-blowout conditions have indicated that blowout occurs locally while global stability still exists¹¹. This implies development of three-dimensionality, and it follows from this that representation of a combustor primary zone by a single reactor is an inappropriate over-simplification. This was also the experience with data-correlation for the more complex experimental combustors of this program².

With this realization, Bragg's basic idea can be generalized, where the total fluid in the combustor is partitioned into a number of flow structures that define "reactors" and "surrounding fluid." The "surrounding fluid" includes all of the remaining fluid in the combustor outside of the reactors, regardless of turbulence scale. The composition and temperature of

the "surrounding fluid" constitute the feed-stream conditions to the reactors. These ideas are common to the Magnussen EDC on the microscale level⁵, but are used here in a supra-grid approach. The "surrounding fluid" providing the feed streams for a given "reactor" could in fact, be the products stream from other reactors, or, fresh reactants entering the combustor, or, any combination of these.

The resulting network of interconnected reactors of various types and sizes, represents the globally active regions of the complete combustor. With such a network, portions of the network can undergo blowout while overall combustion continues via other portions of the network.

Determination of Reactor Network

Such reactor representations of the combustor as described above have been used previously, e.g. Correa & Overton¹², with somewhat simple and intuitively-derived networks. However, to be able to include the chemistry realistically, it is necessary to accurately know the reactor volumes and types, as well as the mass exchange rates between the reactors and the surrounding fluid, and, the connectivity linking the individual reactors into a network. In other words, to reflect in the network, the major aerodynamic features of the complete combustor as revealed by the CFD solution that forms the starting point of hybrid modeling.

The CFD solution can be post-processed to provide the needed information. The first information required is a definition of the major features in the flow.

Although great progress is being made, e.g. Globus et al.¹³, direct computation of fluid flow topology in three-dimensional, multi-specie, non-isothermal, chemically-reacting flow fields has not yet been derived in sufficient generality for many of the complex features present in gas turbine combustors. Indirect and piecemeal methods have to be resorted to therefore.

For a recirculation zone, for example, the following information is required:

- (i) volume
- (ii) recirculated mass flow rate
- (iii) mean residence time
- (iv) temperature or mean equivalence ratio
- (v) information on the degree of mixing present

(i) Lagrangian particle tracking techniques, used in the otherwise Eulerian CFD solution for fuel droplet tracking and to reveal flow patterns via streaklines (trajectories of zero mass, infinite drag particles introduced into the flow), can be used to define recirculation zones. Together with streaklines, an algorithm can be used based on the elapsed time interval since a particle at a point of interest was introduced into the computational domain. Neighboring particles residing in other topological features will have different elapsed times, e.g. a stagnation surface for *closed* recirculation zones may be defined as the boundary between a region within which particles have effectively infinite residence times and adjacent regions where the residence time is finite. Boundaries of the zone can then be displayed using tangent surfaces and conventional contour plotting.

(ii) The recirculated mass flowrate can be computed by summing the mass flowrate of each computational particle along its trajectories, i.e.

$$\dot{m}_{\text{recirc.}} = \sum_{i=1}^N \left(\frac{\bar{\rho}_i V_i}{t_i} \right) \quad (1.)$$

where,

V = region volume
 $\bar{\rho}$ = region density (to which particle density is made equal)
 t = total elapsed time particle in recirculation
 N = number of particles introduced in recirculation

(iii) The residence time can be computed by tracking a particle backwards, forwards and sideways to the tangent surfaces (zero-velocity boundaries) of the region.

(iv) To determine whether or not a region is designated as a "reactor," the calculated local fuel/air ratios in the region must be within established flammability limits (empirical data with account of broadening due to temperature and pressure). When a reacting-flow CFD solution is used, reaction in the solution must be "undone" to estimate these fuel/air ratios. If the calculated local fuel/air ratios are outside the flammability limits, the region must be designated as a non-reacting "mixer."

(v) To ascertain if a designated reactor region is qualified as being a PSR, the dissipation gradient method of Swithenbank¹⁴ can be used.

The dissipation gradient method shows that for mechanical generation of turbulence, the minimum condition for a PSR can be represented by the resulting pressure loss factor. Swithenbank shows that the condition is given by,

$$\frac{\Delta P}{q_{\text{in}}} \geq 3.0 \quad (2.)$$

However, perfectly-stirred conditions are not achieved immediately. At any point, an energy balance can be expressed in terms of mean velocity profile distortion, the (isotropic) turbulence generated, and the total dissipation of turbulence energy, i.e.

$$\frac{\Delta P}{q_{\text{in}}} = \frac{KE_{\text{mean}}}{q_{\text{in}}} + 3 \left(\frac{u'}{\bar{u}_{\text{in}}} \right)^2 + \frac{D}{q_{\text{in}}} \quad (3.)$$

For long times, the velocity profile distortions will have mixed out and the generated turbulence will have been dissipated, but total dissipation will reach a finite number. Hence, in the limit Equation 3 becomes,

$$\frac{\Delta P}{q_{\text{in}}} = \frac{D}{q_{\text{in}}} \quad (4.)$$

Now, in a given co-ordinate direction x , the total dissipation per unit volume can be expressed in terms of the familiar rate of dissipation per unit volume ($\bar{\rho}\epsilon$), and a time scale, and can be written in integral form,

$$D = \int_0^x \frac{\bar{\rho}\epsilon}{\bar{u}_{\text{in}}} dx \quad (5.)$$

where,

$$\epsilon = \epsilon(x, y, z)$$

The dissipation rate can then be expressed in appropriate eddy dimensions, which yields a cubic expression. Since mixing is proportional to dissipation, this expression constitutes an appropriate and precise basis for determining the perfectly stirred regions of a flow. After some manipulation, the final conditional equation is,

$$\frac{d(D/q_{\text{in}})}{d(x/y_{\text{max}})} \leq 0.1 \quad (6.)$$

where y_{max} is related to the size of the energy-containing eddies, and 0.1 is Swithenbank's recommended value. Investigation of this analysis in the

simple research combustor⁴ suggested that the limit value of the gradient could be as high as 10.0 without serious difficulties.

For use in a real combustor, the co-ordinate direction x , takes the value x , y , z in turn. Thus, application becomes very tedious. Fortunately, it proved conveniently possible to associate the relaxed limiting dissipation gradient to an appropriate value of non-dimensionalized kinetic energy of turbulence, field values of which are a normal output of any CFD code.

The local x, y, z co-ordinate directions for a flow structure can be determined from the streaklines of the CFD solution. Together with the definitions of PSR's and PFR's given above, the types of reactor appropriate to a flow structure can then be determined from the kinetic energy of turbulence fields of the CFD solution. Tangent surfaces can be used to establish local volumes that are PSR's; plane-surfaces normal to flow trajectories can be used to define local volumes that are PFR's.

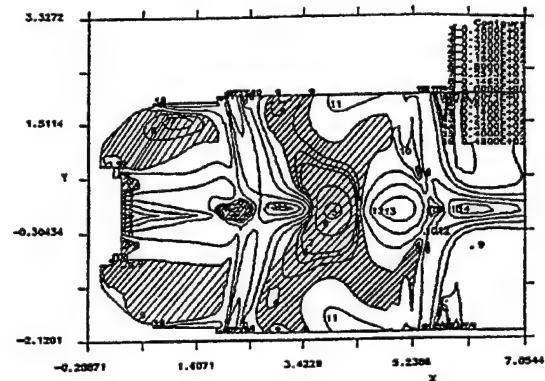
The combustor fields, when post-processed in the manner outlined, will contain a large number of identified, sized and classified flow structures, the connectivity of which is established by the streaklines. This information now has to be reduced to a suitable reactor network. Some simplification is desirable, and this should be based on structure functionality. This is best illustrated by a simple example.

Figure 1 displays the recirculation zones (shaded) identified in the primary zone of an annular combustor at planes inline (1a) and between (1b)) airblast-atomizing fuel injectors; super-imposed are contours of mean axial velocities to give an indication of the flowfield. Inline with the fuel injector can be seen an opposed pair of combustion air jets that collide at mid-combustor height; a third row of transverse air jets can also be seen downstream from the first. For the first row of air jets, there is no first-row jet midway between fuel injectors (1b)), but a pair of jets from the second row of ports can be seen. The flow from the fuel injector is essentially axial (Fig. 1a)) until it divides to move around the blockage of the combustion air jets. More details on the CFD solution can be obtained from Reference 2.

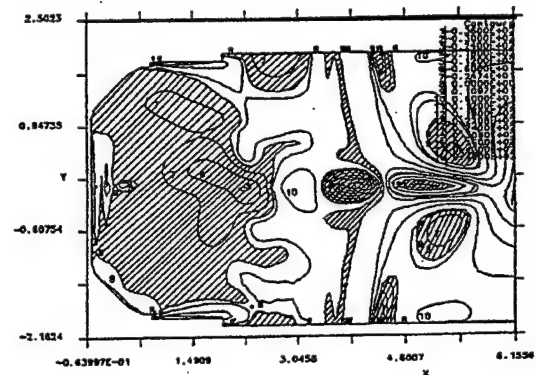
For the simplification illustration, concentrate on the recirculation zones shown upstream of the first row of combustion air jets.

The large, main recirculation zone is actually continuous circumferentially around the combustor

dome, but has local holes punched through it by the coherent fuel/air jets issuing axially from the fuel injectors. There are small spherical recirculations where the combustion air jets and each injector flow collide. Finally, there are discontinuous recirculations on the liners between the first row air jets; these link to the main recirculation region locally between fuel injectors. The mass flows within these recirculations are derived from both the fuel injector and the first row of combustion air jets. Local stoichiometry is such that chemical reactions and heat release take place within these regions. Functionally, all of the zones feed mass from downstream back into the flow from the fuel injector.



1a): Section Through Fuel Injector



1b): Section Between Fuel Injectors

Figure 1: Identified Recirculation Zones in a Primary Zone

Figure 2 shows how the recirculation zone information contained in Figure 1 might be simplified

and represented as part of a reactor network. Details making up the modeling of the injector flow and the downstream portion of the combustor are not given.

In this instance the turbulence information indicated that the recirculation reactor was a PSR. In the figure, 'a' is the percentage of first row jet air interacting directly with the injector flow (via the spherical zones), 'b' is the percentage of jet air not entering directly into the primary zone and flowing on downstream, and 'c' is the percentage of combined injector flow, jet air and recirculated mass in the injector reactors, that is recirculated back to the dome.

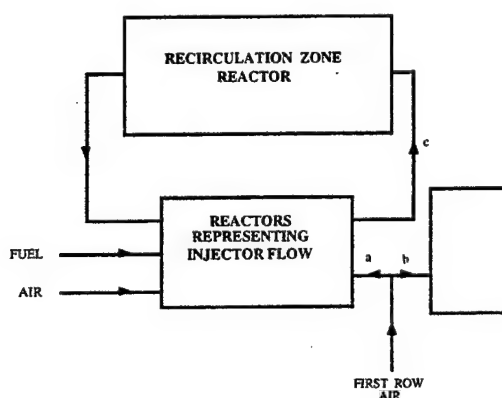


Figure 2: Reduction of Primary Zone Recirculation Zones to Simple Reactor

The procedure described above is repeated throughout the combustor for all of the flow features identified in the post-processing of the CFD solution. In making the necessary decisions on functional simplicity, it is inevitable that the "lumping" of individual regions to fit the connectivity given by streaklines can result in some drastic simplifications of local behavior. Furthermore, with the simplifications being conducted manually, any resulting network is not necessarily the only interpretation that is possible.

Note also, that the sum of the volumes of all the reactors in the derived network is not necessarily equal to the total volume of the physical combustor. Similarly, if reactors are arranged in series, the sum of their lengths is not necessarily equal to the total length of the combustor.

As a guide, most combustors can be adequately represented by about ten reactors.

Unmixedness Effects

For any reactor network the effects of fuel/air unmixedness on chemistry can be accounted for by replacing each individual reactor with a parallel array of like-reactors, over which the total inlet flow is distributed according to a Gaussian equivalence ratio distribution. The width of the Gaussian describes the degree of mixing. Experience has shown that 10 - 13 parallel reactors/reactor are adequate for this purpose.

The number of reactors then representing the combustor could be in the range 100 - 120, compared to Bragg's original proposals of one or two. This large number of reactors does increase solution time considerably, and should not be used unless necessary, i.e. for emissions calculations. Even for emissions calculations some further reasonable assumptions and simplifications can be made that can reduce correction for unmixedness to a 3-D look-up table.

Chemical Reaction Mechanism

When a satisfactory reactor network has been assembled, the detailed chemistry is then solved on this network. Any appropriate reaction mechanism may be used for the chemistry, although the more steps it contains the longer the solution times.

For LBO purposes a reduced, quasi-global mechanism by Kollrack^{15,16} for JP5/JP8/Jet-A has proved useful. When formulating the mechanism, Kollrack represented the multi-component real fuel by the generic molecule $C_{12}H_{23}$. The mechanism includes a two-stage fuel pyrolysis, and then gives emphasis to the more stable intermediate species via a second stage in which simpler hydrocarbons are reacted; a third stage is dominated by recombination reactions and the conversion of CO to CO_2 . Included in the reactions is the extended Zeldovich mechanism for thermal NO, but there is no account of "prompt NO." There are 30 steps involving 21 species.

The reaction chemistry of vaporized Jet A resembles that of propane. It was found⁶ that Kollrack's mechanism, when used with propane thermodynamic properties and modification of the global steps for the appropriate C:H ratio, gave the best description of LBO of several competing mechanisms for propane/air combustion when compared to the experimental blowout curve obtained by Clarke et al.¹⁷ in a well-stirred reactor. It also gave good agreement with the

experimental LBO curve for the simple research combustor used in the CDME program⁴.

The Kollrack reduced mechanism is recommended for LBO calculations with JP5/JP8/Jet-A/propane fuels in air.

Heat Losses

Heat losses from the flame can be important at LBO conditions. Such losses may have been accounted for in the CFD calculation, but most codes presently do not include conjugate heat transfer. However, heat losses can be accounted for at the reactor stage.

At LBO the flame is usually confined to the primary zone of the combustor. Therefore, heat lost through the liner walls to the shroud flows is essentially lost to the combustion process. Estimated heat losses, provided that they are not excessive, can be accounted for on the reactor network by an appropriate downwards adjustment of the fuel lower heating value.

Definition of Blowout

Determination of any singularity, such as LBO, usually presents some difficulties. This is so whether the determination is by experiment or by calculation.

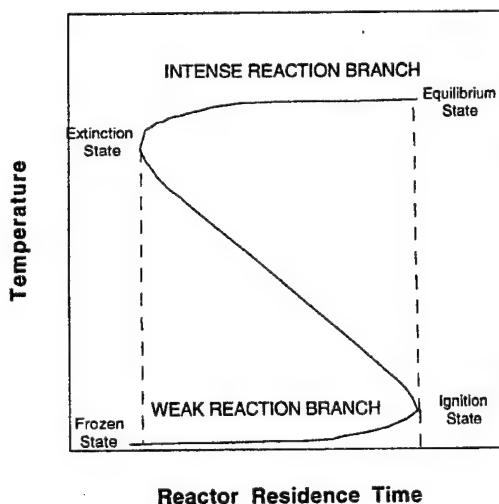


Figure 3: Characteristic Reaction Curve Showing All Possible Modes of Operation

The reaction behavior of a premixed fuel and oxidant can be conveniently characterized by a plot of reaction temperature versus reactor residence time. In this form, an S-shaped curve is followed, as illustrated in Figure 3. From the **chemically frozen state** an increase in residence time allows weak and slow chemical reactions to occur. Eventually, an **ignition state** is reached where the rate of heat release is greater than heat transport out of the reactor. This allows a rapid increase in temperature, via Arrhenius kinetics, that induces a coupled increase in reaction rate, and the **equilibrium state** is approached. The **extinction state** represents a condition where intense burning is not possible, such that the rate of heat release is no longer sufficient for an appreciable amount of reaction in the available residence time. Between the extinction and ignition states is a region of *non-physical solutions*. Transition between upper and lower branches of the reaction curve occurs precipitously.

Stirred reactor codes, such as the PSR/CHEMKIN code¹⁷, solve the system of non-linear equations of the kinetics by a modified Newton algorithm. If the Newton algorithm fails to converge, a continuation method is used whereby the solution estimate is conditioned through a time-integration procedure that provides initial estimates within the convergence domain of Newton's method. This "predictor-solver" strategy is generally robust, except for use in the limit of extinction. The determinant of the Jacobian matrix is positive on the upper branch of the reaction curve, and negative on the intermediate branch. The extinction point is therefore singular, i.e. the determinant of the Jacobian is zero. This causes the Newton algorithm to become progressively even more ill-conditioned as extinction is approached, and precludes successful convergence.

Near the extinction point alternative methods, such as arc-length parameterization¹⁸⁻²², must be employed. The robustness and efficiency of the combined arc-length/continuation method are largely functions of step-length control. The step-length control has to be adaptive to achieve a stable solution.

Implementation of the combined arc-length/continuation method with adaptive step-control in CHEMKIN was successful in computing the reaction curve to the extinction point⁶ for a single reactor. However, a substantial number of steady-state solutions were required to reach the extinction point. This could constitute a severe CPU problem when used with a network of reactors.

Since it was computationally too costly to make precise determinations of the extinction points for the multiple reactors of a reactor network, a pragmatic but careful protocol was established to ensure that the correct LBO solution was achieved, without recourse to complex additional solution algorithms.

The procedure adopted was as follows: Combustion was established on the network at or near stoichiometric primary zone bulk equivalence ratio with atmospheric or greater inlet air pressure and temperature, and the desired airflow. Pressure was then reduced in several coarse (4 or 5) steps to the desired level for the blowout while maintaining high primary zone flame temperatures. Holding pressure at the desired level, inlet air temperature was then reduced in several coarse steps (3 or 4) to the desired value while maintaining primary zone bulk equivalence ratio. Finally, the fuel flow was progressively reduced in ever-smaller decrements while holding the desired airflow, pressure and inlet temperature values. The fuel decrement step size was decided based on the rate of change of the critical reactor (the one in the network sustaining combustion) outlet temperature. The combustor was taken as being blown out when the critical reactor outlet temperature dropped to or below a critical value.

For the purposes of establishing a suitable value for the blowout critical temperature, no explicit distinction was made between the extinction and ignition states. At the ignition state, an increase in reaction temperature induces a coupled increase in reaction rate in a runaway process. The reaction temperature for this runaway state was taken as the critical temperature. Based on a suggestion of Appleton & Heywood²³, for hydrocarbon fuels in air, the critical temperature was 2200F (1480K). It is felt that this value is a little on the conservative side, but the conservatism could allow some implicit account of the adverse effects of non-stationary flow behavior known to precede and influence a blowout event.

Reactor Network Code

The reaction mechanism chosen was solved on a reactor network code that used the CREK chemical kinetic package of Pratt & Wormeck²⁴.

Test Case

To evaluate the efficacy of the hybrid modeling approach in the calculation of LBO, experimental data from a 4-injector, planar reactor of a simplified gas

turbine combustor were used. The combustor, test procedure and measurements are described in Reference 25; additional LBO and temperature field data for this combustor are given in Reference 2.

The experimental data available included detailed CARS temperature measurements² on a horizontal plane at mid-combustor height, together with measurements on a vertical cross-plane normal to this plane at 5 cm downstream from the dome. The LBO data included the following:

- a) effect of primary zone airflow at atmospheric pressure and temperature,
- b) effect of combustion pressure at atmospheric temperature for a range of primary zone airflows,
- c) effect of combustor loading at 10%, 15% and 20% dome flows.

The CFD calculations for the test combustor were made at representative flow conditions for the blowout testing, and they are described very briefly in Reference 2; more detail is given in Reference 26.

Post-processing of the CFD solution to establish the reactor network is given in Reference 26. Figure 1 above is taken from Reference 2, and shows some of the recirculation zones. The resulting reactor network is illustrated in Figure 4. It consists of seven reactors in series, and one reactor in parallel with the first three series reactors. In this instance all of the reactors are either PFR's or PSR's. A detailed relation of the derived network to the CFD solution upon which it is based, is given in Reference 26. The network shown is not the only one possible. It represents a greatly simplified flowfield. Until the efficacy of the hybrid modeling approach was established, it did not appear that excessive refinement could be justified.

Primary Zone Mean Temperatures

From the test case measured distributions of mean temperature², data were extracted in a horizontal axial band of width 2 cm, inline with a fuel injector at the combustor mid-height. The measured axial distributions, in terms of maximum and minimum temperatures, were compared against the calculated temperatures at the exits from each of the seven inline reactors of the network. The network was run with the actual inlet conditions appropriate to the measurements. Similarly the maximum and minimum temperatures for

L = reactor length, inches A = reactor cross-sectional area, sq. inches

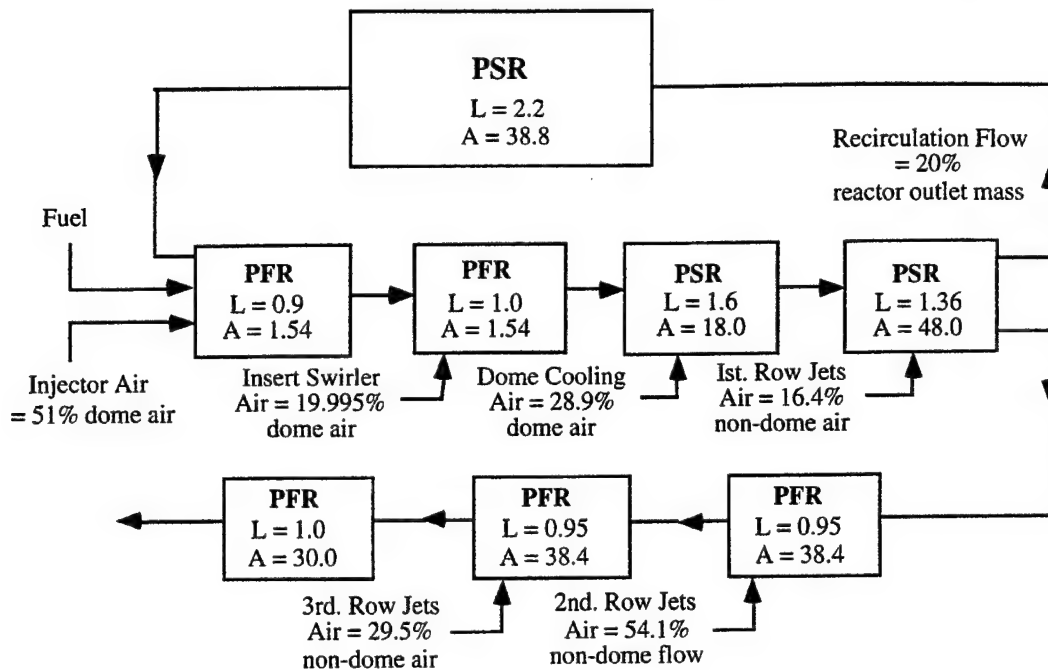


Figure 4: Network of Reactors Representing Test Combustor at Near-LBO Conditions

a horizontal band of 2 cm width, midway between fuel injectors, was compared with the outlet temperature from the recirculation reactor of the network. propane and with allowance for estimated heat losses.

The reaction mechanism used for the calculations was that above of Kollrack, modified for

Figure 5 shows the comparison of measurements and calculations inline with the fuel injectors. The reactors are marked by number, with No. 1 being the first PFR; Reactor No. 7 is not shown since it extends beyond the range of the measured data. The length of the bar indicates the downstream extent of each reactor.

It can be seen that the calculated temperatures reproduce well the axial distribution of measured temperatures, and also agree well as to the temperature levels. The agreements are particularly good for distances of 0 - 70 mm, the important region of the combustor that determines flame stability. For distances greater than 100 mm from the combustor dome the calculated temperatures are 50 - 100 deg.K higher than the measured values. It should be remembered that the

measurements are on a *plane* while the calculations represent *volumes*.

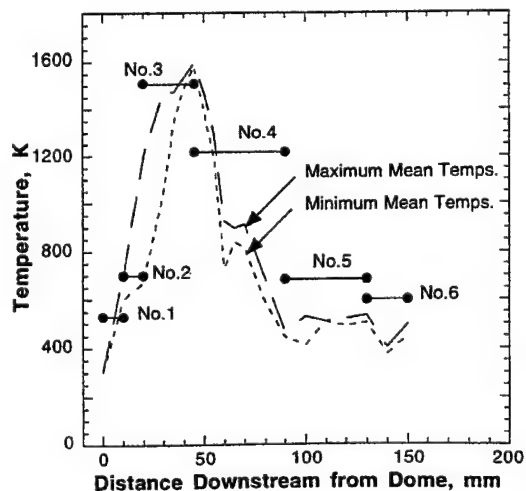


Figure 5: Comparison of Mean Temperatures Inline with a Fuel Injector

Figure 6 contains similar information for the recirculation region between injectors. Here, the agreement is not so good, except at 40 mm downstream. However, it should be remembered that the recirculation reactor represents not only the recirculation

between fuel injectors, where the measurements are made, but also the recirculation volumes above and below the injector discharge flow (Figures 1 and 2). It would therefore, be expected that the calculation might yield higher temperatures than those measured. A further reason is that the three-dimensional nature of the temperature field might imply the single-plane measurements are not sufficiently representative. However, it could also be that the accuracy of the calculation could be improved by representing the between-injector recirculation separately from around-injector recirculation.

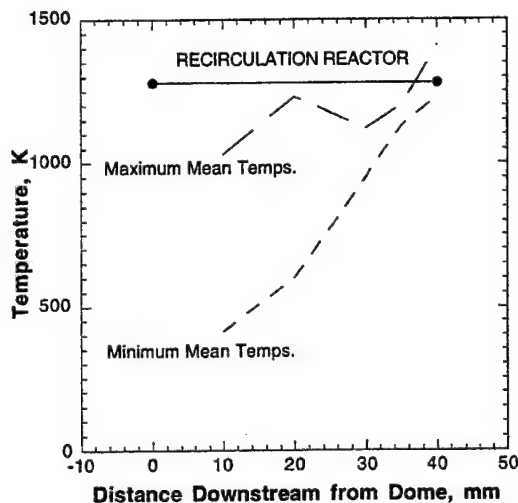


Figure 6: Comparison of Mean Temperatures Between Fuel Injectors

Primary Zone Airflow

For a fixed dome flow equal to 15 percent of total combustor airflow it had been observed²⁵ that the effect of increased primary zone airflow (by increasing pressure drop) at atmospheric pressure produced a change in flame condition between lifted and attached flames at blowout. This was a result of local equivalence ratio changes and flow unsteadiness¹. Primary zone airflow, on the basis of previous experience was defined²⁵ as,

$$W_{PZ} = W_{dome} + 0.279W_{1st. jets} \quad (7.)$$

Figure 7 compares the experimental LBO data with the calculated behavior. The agreement is excellent up to a primary zone airflow of about 0.135 lbm/sec. (0.0613 kg/sec.). Above this airflow LBO is from an observed attached flame condition. The calculations reproduce this behavior extremely well through changes in the outlet temperature of the Recirculation Reactor, that act to "bootstrap" reactions and increase the temperatures in the first three series reactors. The third of the series reactors, a PSR which represents the condition immediately prior to introduction of the first row combustion air jets, controls the LBO's.

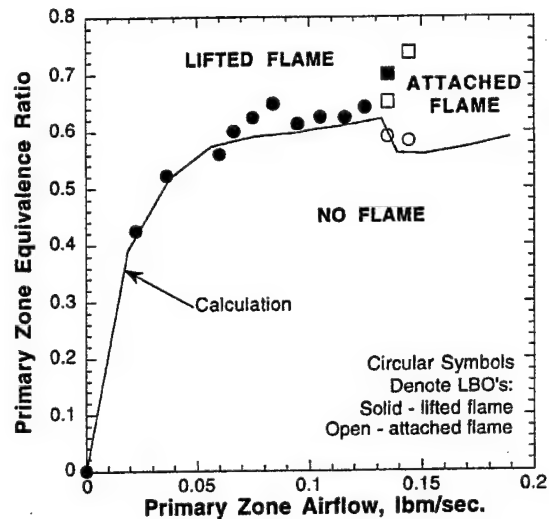


Figure 7: Comparison of Calculated Blowouts with Measurements for Primary Zone Airflow Variation

Operating Pressure

The effects of pressure on LBO were simulated experimentally at atmospheric pressure and temperature by means of the calibrated excess nitrogen diluent technique, and an appropriate residence time correction was applied to account for the physical presence of the excess nitrogen²⁹. Calculations were made at true low pressures. The dome flow was again 15 percent of the total combustor airflow.

Figure 8 shows a comparison of the calculated and the measured effect of operating pressure on LBO

for several constant primary zone airflows (varying pressure drops).

The agreement of the calculations with the measurements is good for the 0.023 lbm/sec. (0.0104 kg/sec.) primary zone airflow from 1.0 down to about 0.2 atmospheres pressure. The absolute agreements are not so good for the 0.037 and 0.066 lbm/sec. (0.0168 and 0.0299 kg/sec.) airflows; however, the trends are correct. Also, crossplots of the effect of primary zone airflow at a specified operating pressure, (i.e. the equivalent of Figure 7 at say, 0.4 atms.) are in very good agreement with the measured effect. Generally, given the somewhat imprecise character of LBO measurements, the agreements can be considered as satisfactory.

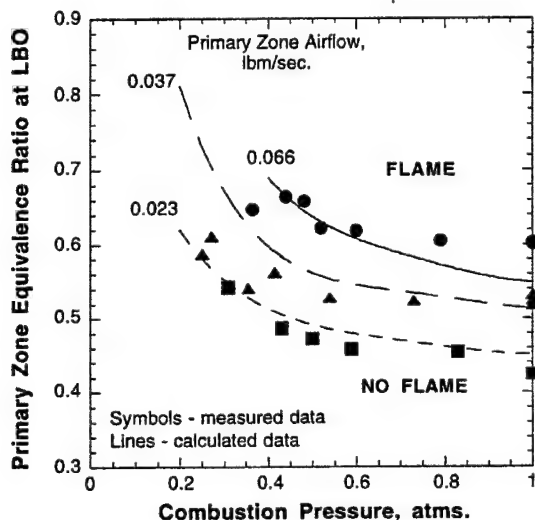


Figure 8: Comparison of Calculated and Measured LBO's as a Function of Pressure for Several Primary Zone Airflows

Dome Flow

An important combustor design variable is the quantity of total airflow that is introduced into the dome. It has been shown experimentally²⁵ that the percent dome airflow exerted a strong influence on stability, with more dome flow reducing stability at all combustor loadings. Dome airflow is also limiting to the peak heat release rate achieved.

Figures 7 and 8 had primary zone airflow (which includes dome flow - Equation 7) as a variable, but this variation was achieved through overall pressure drop. As a percentage of total combustor air the dome air for these figures was fixed at 15 percent. Fortunately, the test vehicle had separately-metered and controlled dome and liner airflows²⁵, so that dome airflow as a percentage of the combustor total was easily varied without recourse to either pressure drop or combustor air port changes.

Figures 9 and 10 respectively compare the calculated and measured LBO's at 10 and 20 percent dome flow splits. The blowouts are described in terms of the combustor overall equivalence ratio against an overall combustor loading group. The axes are given in overall terms to avoid having to definitively identify where the flame terminates as loading is varied. However, it is recognized that the flame stability is determined in the primary zone, and therefore, the apparent reaction order is based on primary zone conditions.

Loading is defined by,

$$LP = \frac{\dot{m}_{Tot}}{VP^n F} \quad (8.)$$

where,

\dot{m} = mass flow rate in combustor
 V = combustor volume
 P = combustor pressure
 n = apparent reaction order
 F = exponential inlet air temperature correction factor

With a gaseous fuel \dot{m} is taken as the sum of the air and fuel mass flow rates in lbm/sec., V is in ft³, P is in atms., n is given by,

$$\begin{aligned} (\phi_{PZ})_{LBO} &< 1.0; \quad n = 2(\phi_{PZ})_{LBO} \\ (\phi_{PZ})_{LBO} &\leq 1.0; \quad n = 2.0 \end{aligned}$$

and F is given by,

$$F = \frac{10^{0.00143T}}{3.72} \quad (9.)$$

where T is the reactants inlet temperature in K. In this form F corrects the data to a constant temperature of 400K.

In Figures 9 and 10 it will be noted that the experimental data fall into two distinct groupings, one placed at the left and center of each plot, and the other to the right of the plots. Those data-points falling into the respective right-hand groupings exhibit poorer correlation, and represent tests for which the calculated primary zone equivalence ratio was actually greater than unity, but for which reaction order n was taken as 2.0. Flames for the data in these groupings had burning extending beyond the conventional primary zone.

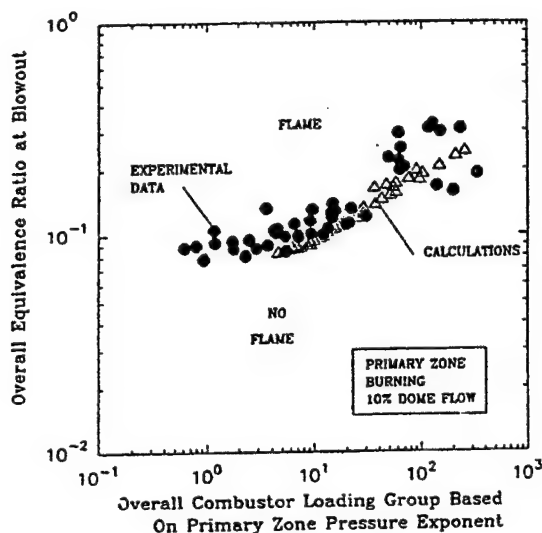


Figure 9. Comparison of Measured and Calculated Stability for 10% Dome Flow

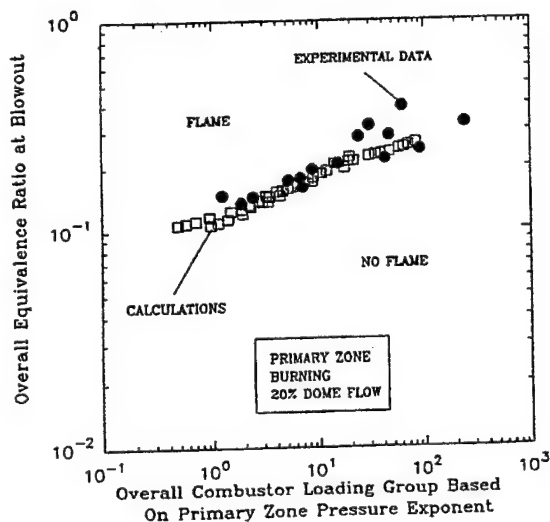


Figure 10. Comparison of Measured and Calculated Stability for 20% Dome Flow

In Figure 9 the calculated LBO's were again controlled by the third of the series reactors of the network (Figure 4) for values of combustor loading up to about 34.0 (appropriate units). For higher values of overall loading the third series reactor exceeded its peak heat release rate, and control of stability was passed from it to first, the Recirculation Reactor, and then, to the fourth series reactor. This kind of behavior was observed physically in the experiments²⁵. For loadings where control is passing from one network reactor to another, the solution procedure slows down as the size of the fuel decrement is cut to avoid provoking premature blowout.

Given the *caveats* on the correlation of the experimental data, the agreement of the calculations with the measurements over 4 orders of magnitude variation in loading can be considered to be remarkably good.

Calculations for the 20 percent dome flow case in Figure 10 behave very much like those for the 10 percent case, except that control passes from the third series reactor at a combustor loading of about 10.0 (appropriate units). It is evident that the increase in dome airflow reduces the overall stability.

Although there are less experimental data at 20 percent dome flow, the agreements of calculations and measurements is again extremely good over the complete range of loadings.

The figures reveal the large number of calculations that were carried out to establish the blowout characteristic at each dome flow. This is indicative of the relative ease of making these calculations. Note also that the calculations do not fall on a smooth curve. The (limited) scatter is a reflection of the singular nature of blowout.

Discussion

A hybrid modeling procedure for calculating LBO has been presented in outline. It combines CFD modeling with reactor network modeling to solve combustion processes that are chemistry-dominated within a complex flowfield. The calculation is done in uncoupled fashion using complex chemistry; however, aerodynamic information is incorporated via the formulation of the reactor network. For application at different operating conditions etc., it relies on the partial modeling postulate that for gas turbines the flowfield is determined to first order by the combustor geometry.

Therefore, repeat CFD calculations are only necessary for extensive geometric changes in combustor geometry.

The procedure successfully calculated the effects of airflow rate, combustion pressure, airflow distribution, and (not illustrated) inlet temperature, on stability, as represented by LBO, in a simplified, generic gas turbine combustor. It was also able to account for flame lift, when this was stoichiometry-driven. Computational times were very reasonable, and permit the calculation of blowout curves for practical combustors.

The methodology is also suitable for calculating gas turbine emissions. In this role, extensions can be made to account for the effects of fuel/air unmixedness on chemical reaction rates.

Hybrid modeling is a pragmatic procedure that has a useful role as an engineering design and development tool for practical gas turbine engine combustors, where extensive performance envelopes and the effects of geometric changes have to be explored. Although hybrid modeling makes these kind of calculations feasible, it should be recognized that the amount of work involved is not negligible.

Conclusions

1. Hybrid modeling does allow for account of the complexities of both aerodynamics and chemistry, in a related but uncoupled fashion.
2. The procedure involves three distinct steps - a CFD solution, post-processing of the CFD solution to establish a reactor network, and, solving complex chemistry on the network. The overall computational time is very reasonable, with the CFD solution being the "rate-determining" step.
3. To avoid solution difficulties on the reactor network as LBO is approached, a blowout protocol based on a minimum enthalpy, expressed through a critical flame temperature, is used.
4. Interrogation of the reactor network enables the details of the LBO with respect to location, local equivalence ratio, residence time, etc., to be established.
5. The efficacy of the method for calculating LBO's in a generic gas turbine combustor has been successfully demonstrated.

Acknowledgements

As always, the enthusiasm, motivation and support of Dr. W.M. Roquemore of Wright Laboratory are greatly appreciated. The contributions of Dr. David G. Sloan, currently of Asea Brown Boveri, are gratefully acknowledged. The authors wish to thank Melvin Russell for assisting with the experiments. This research was sponsored by the U.S. Air Force, Wright Laboratory, Aero Propulsion and Power Directorate. G.J.S. wishes to thank Prof. Dave Pratt of University of Washington, for a discussion many years ago that contributed so much to this work.

References

1. Sturgess, G.J., Gogineni, S., Shouse, D.T., Frayne, C. and Stutrud, J., "Emissions and Operability Trades in the Primary Zones of Gas Turbine Combustors," Paper No. 96-3125, pres. AIAA 32nd AIAA/ASME/SAE/ASEE Joint Propulsion Conference, Lake Buena Vista, Florida, July 1-3, 1996.
2. Switzer, G., Sturgess, G.J., Sloan, D., and Shouse, D., "Relation of CARS Temperature Fields to Lean Blowout Performance in an Aircraft Gas Turbine Generic Combustor," Paper No. 94-3271, pres. AIAA 30th AIAA/ASME/SAE/ASEE Joint Propulsion Conference, Indianapolis, IN., June 27-29, 1994.
3. Gogineni, S., Shouse, D.T., Frayne, C., Stutrud, J. and Sturgess, G.J., "Influence of Combustion Air Jets on Primary Zone Characteristics for Gas Turbine Combustors," proc. ISABE 12th. Intl. Symp. on Air Breathing Engines, editor F. Billig, Vol. 1, Melbourne, Australia, September 10-15, 1995, pp. 475-487.
4. Sturgess, G.J., Hedman, P.O., Sloan, D.G. and Shouse, D., "Aspects of Flame Stability in a Research Dump Combustor," Paper No. 94-GT-496, pres. ASME Intl. Gas Turbine and Aeroengine Congress and Exposition, The Hague, Netherlands, June 13-16, 1994.
5. Magnussen, B.F., "Heat Transfer in Gas Turbine Combustors - A Discussion of Mathematical Modeling of Combustion, Heat and Mass Transfer with Emphasis on Heat Transfer in Gas Turbine Combustors," AGARD Conference Preprint No. 390, *Heat Transfer and Cooling in Gas Turbines*, Paper No. 23, 1985.
6. Sloan, D.G. and Sturgess, G.J., "Modeling of Local Extinction in Turbulent Flames," Paper No. 94-GT-433, pres. Intl. Gas Turbine and Aeroengine

Congress and Exposition, The Hague, Netherlands, June 13-16, 1994, (to appear in ASME Trans.).

7. Spalding, D.B., "Performance Criteria of Gas Turbine Combustion Chambers - A Method of Comparison and Selection for the Designer," *Aircraft Engineering Monograph*, Bunhill Publications Ltd., London, England, August 1956.

8. Bragg, S.L., "Application of Reaction Rate Theory to Combustion Chamber Analysis," Aeronautical Research Council Pub. ARC 16170, Ministry of Defence, London, England, 1953.

9. Longwell, J.P., Frost, E.E. and Weiss, M.A., "Flame Stability in Bluff-Body Recirculation Zones," *Ind. Engrg. Chem.*, Vol. 45, No. 8, 1953, pp. 1629-1633.

10. Longwell, J.P. and Weiss, M.A., "High Temperature Reaction Rates in Hydrocarbon Combustion," *Ind. Engrg. Chem.*, Vol. 47, No. 8, 1955, p.1634.

11. Barat, R.B., "Behavior of Jet-Stirred Combustors Near Blow-Out," *Chemical and Physical Processes in Combustion*, Fall Technical Meeting of the Eastern States Section of the Combustion Institute, Ithaca, New York, October 14-16, 1991.

12. Correa, S.M. and Overton, K.S., "A Model for Optimizing Emissions and Stability of a Gas Turbine Combustor," Paper No. 88-2858, pres. 24th. AIAA/ASME/SAE/ASEE Joint Propulsion Conference, Boston, MA., July 11-13, 1988.

13. Globus, A., Levit, C. and Lasinski, T., "A Tool for Visualizing the Topology of Three-Dimensional Vector Fields," Rept. No. RNR-91-017, NASA Ames Research Center, Moffet Field, California, April 1991.

14. Swithenbank, J., "Flame Stabilization in High Velocity Flow," *Combustion Technology - Some Modern Developments*, editors H.B. Palmer and J.M. Beer, Academic Press, 1974, pp. 91-125.

15. Roberts, R., Aceto, L.D., Kollrack, R., Teixeira, D.P. and Bonnell, J.M., "An Analytical Model for Nitric Oxide Formation in a Gas Turbine Combustor," *AIAA Journal*, Vol. 19, No. 6, 1972, pp. 820-826.

16. Kollrack, R., "Model Calculations of the Combustion Product Distributions in the Primary Zone of a Gas Turbine Combustor," Paper No. 76-WA/GT,

pres. ASME Winter Annual Meeting, New York City, 1976.

17. Glarborg, P., Kee, R.J., Grcar, J.F. and Miller, J.A., "PSR: A Fortran Program for Modeling Well-Stirred Reactors," Sandia National Laboratories Rept. SAND 86-8209, VC-4 (reprint), October 1988.

18. Seydel, R., *From Equilibrium to Chaos*, Elsevier Science Publishing Company, New York City, New York, 1988.

19. Keller, H.B., "Numerical Solution of Bifurcation on Non-Linear Eigenvalue Problems," *Applications of Bifurcation Theory*, Editor P. Rabinowitz, Academic Press, New York City, New York, 1977, pp. 359-384.

20. Keller, H.B., *Lectures on Numerical Methods in Bifurcation Problems*, Springer-Verlag, New York City, New York, 1987.

21. Kee, R.J., Miller, J.A. and Evans, G.H., "A Computational Model of the Structure and Extinction of Strained Opposed Flow, Premixed Methane-Air Flames," proc. 22nd. Symposium (International) on Combustion, The Combustion Institute, Pittsburgh, PA., 1988, pp. 1479-1494.

22. Giovangigli, V. and Smooke, M.D., "Calculation of Extinction Limits for Premixed Laminar Flames in a Stagnation Point Flow," *Journal of Computational Physics*, Vol. 68, 1987, pp.327-345.

23. Appleton, J.P. and Heywood, J.B., "The Effects of Imperfect Fuel-Air Mixing in a Burner on NO Formation from Nitrogen in the Air and the Fuel," proc. 14th. Symposium (International) on Combustion, The Combustion Institute, 1973, pp. 777-786.

24. Pratt, D.T. and Wormeck, J.J. "CREK - A Computer Program for Calculation of Combustion Reaction Equilibrium and Kinetics in Laminar or Turbulent Flow," Rept. No. WSU-ME-TEL-76, Dept. Mech. Engrg., Washington State University, 1976.

25. Sturgess, G.J. and Shouse, D.T., "Lean Blowout Research in a Generic Gas Turbine Combustor with High Optical Access," Paper No. 93-GT-332, pres. Intl. Gas Turbine and Aeroengine Congress and Exposition, Cincinnati, Ohio, May 24-27, 1993.

26. Sturgess, G.J., *Combustor LBO Design Model Evaluation: Final Report*, (Draft) Pratt & Whitney Rept. FR-23400, May, 1995.



AIAA 97-2709

**ASSESSMENT OF AN ABBREVIATED
JET-A/JP-5/JP-8 REACTION MECHANISM
FOR MODELING GAS TURBINE ENGINE
GASEOUS EMISSIONS**

**G.J. Sturgess
Innovative Scientific Solutions, Inc.
Beavercreek, OH**

**33rd AIAA/ASME/SAE/ASEE Joint Propulsion
Conference & Exhibit
July 6 - 9, 1997 / Seattle, WA**

**For permission to copy or republish, contact the American Institute of Aeronautics and Astronautics
1801 Alexander Bell Drive, Suite 500, Reston, VA 22091**

ASSESSMENT OF AN ABBREVIATED JET-A/JP-5/JP-8 REACTION MECHANISM FOR MODELING GAS TURBINE ENGINE GASEOUS EMISSIONS

G.J. Sturgess*

*Innovative Scientific Solutions, Inc.,
Beavercreek, Ohio*

Abstract

The concept of hybrid modeling is extended from its original application in calculating the singularity of lean blowout for practical combustors, to calculating gaseous emissions. As part of this extension a baseline chemical reaction mechanism is explored in relatively simple flow, fuel-lean combustion systems. The experiments from the literature all used perforated plate flameholders that necessitate some flowfield modeling. Bulk and axial profile measurements of NO_x , CO , CO_2 and gas temperature over relatively extensive operating conditions are compared against hybrid model calculations. It is concluded that although additional work is needed, the approach is viable for emissions calculations, and that the baseline reaction mechanism represents a reasonable starting point.

Background

Levels of gaseous emissions generated by aircraft gas turbine engines for commercial operations are regulated by international standards. Military aircraft operations are currently not regulated for emissions; however, the U.S. Air Force pursues a "good neighbors" policy with respect to emissions. Therefore, it is essential that engine manufacturers have available suitable analysis tools for assessing the low emissions potentials of new conventional combustor designs, and for evaluation of new combustor concepts. Answers to emissions issues are generally required before any experimental evaluations of the new designs can be conducted.

The levels of gaseous oxides of nitrogen (NO_x), carbon monoxide (CO) and unburned hydrocarbon (UHC) emissions exiting a gas turbine combustor are determined by the engine operating

conditions, the aerodynamic flow field, the stoichiometry distribution, and the fuel/air mixing established by the combustor geometry, together with the resulting chemical reactions taking place in the combustor. *A priori* calculation of these concurrent processes is extremely difficult. Furthermore, the number of emissions calculations required can be very large. This number will involve much more than those calculations for evaluating candidate designs for their emissions potential, and/or optimizing a given design for minimum emissions while retaining maximum performance. For example, in the marketing of a new engine for commercial use, customer airlines will expect complete emissions mission-profiles for the engine, in one or more candidate airplanes, over their entire route structure.

The suite of emissions analysis tools to be used must therefore be selected with great care. Generally, appropriate balances between physical realism and computational accuracy on one hand, and engineering utility and turn-around time on the other, must be found.

Introduction

The leading edge of physical realism for gas turbine combustor modeling is contained in computational fluid dynamics (CFD) modeling.

The state of the art in CFD for this purpose in the engineering community may be described as follows: The procedure normally involves calculation on either body-fitted grids or unstructured grids with of the order of 100,000 – 300,000 nodes, where the calculation domain is a repeating sector (for the annular configuration) with periodic boundary conditions, of either the combustor, or the complete combustion

* AIAA Senior Member

section from compressor delivery to turbine entry. Grid-independence is not claimed for solutions on these grids.

For turbulence the familiar $K-\epsilon$ is frequently used. Although this model is known to be incorrect in many flow situations, its shortcomings are well-understood and can be allowed for in assessing results.

A "presumed p.d.f." combustion model accounts for the effects of turbulence on reaction rates, and is commonly used with equilibrium chemistry in mixture fraction form. This is a choice of economy, but represents a worthwhile improvement over the less computationally expensive but much less realistic, eddy break-up model. Where finite-rate chemistry is used, the reaction mechanism is restricted to four or five steps because of the additional solution costs that arise. These costs accrue not only from the mathematically-stiff chemical equations, but also from the additional transport equations that must be solved for each of the chemical species in the mechanism.

At high power operating conditions the liquid fuel is normally approximated by its gaseous equivalent without serious error. At low powers, a liquid spray model, typically involving Lagrangian tracking together with the particle-source-in-cell (PSIC) techniques for local heat release, may be used. Such models are only suited for dilute sprays, and are not strictly appropriate in most gas turbine combustors.

The solutions obtained presume a stationary-state flow exists in the combustor. While this is a reasonable presumption for many purposes, it is not so in all instances.

Post-processing of the solution to obtain NO_x can be conducted assuming that nitric oxide (NO) originates with the Zeldovich mechanism, and that Zeldovich NO is just "time-at-temperature" driven, i.e. prompt NO from super-equilibrium O -atoms, or from interaction with fuel fragments, is ignored.

In industry CFD is generally carried out on work-station platforms, operating either individually with multiple processors or as part of a local network (LAN). For the approach described above, typical run-times are of the order of five working days, depending on the comprehensiveness of the physical modeling included, number of grid-nodes, and the details of the workstation/LAN. Case set-up time will depend on the extent of the computational domain and the type of grid

used. Provision of suitable boundary conditions will depend on the extent of the computational domain, but can also be time consuming. Altogether, a turn-around time of two to three working weeks per case is not an unreasonable estimate. Post-processing a solution to extract engineeringly-useful information can take up to an additional working week.

Tremendous progress has been made in developing and applying CFD to gas turbine combustors. This progress, together with advancing workstation capabilities, will continue. Useful contributions to the design and development processes are being made. However, three clear points emerge for the present:

1. CFD is currently a better analysis tool than it is a design tool.
2. It is not presently suitable for providing answers to cases where reaction chemistry dominates.
3. At this time it cannot provide the quick turn-around necessary for multiple state-point problems.

If CFD is not a suitable tool for addressing the emissions issues, then what is?

Hybrid Modeling

Hybrid modeling¹ was introduced to address chemistry-controlled and singular problems in gas turbine combustion, such as calculating lean blowouts (LBO's), which is both singular and chemistry controlled, and was successful for this purpose.

Hybrid modeling commences with a CFD solution to establish the basic flowfield set up by the combustor at operating conditions near to those of interest. Partial modeling concepts² are then invoked to freeze this flowfield over a wide range of operating conditions.

Post-processing of the frozen flowfield using three-dimensional fluid flow topology³, together with dissipation gradient analysis⁴ and streak-line tracking, are used to represent the flowfield by its equivalent network of connected non-reacting mixers (NRM), plug-flow reactors (PFR), and perfectly-stirred reactors (PSR). By these means the three-dimensionality of the real flowfield is reduced to a low resolution, quasi-two-dimensional network that is made up of one-

dimensional (PFR) and zero-dimensional (PSR) elements.

Detailed chemistry can then be solved on the established network in uncoupled fashion, for a wide variety of operating conditions.

Although hybrid modeling can be viewed as being an elaborate form of post-processing, the capability to then conduct calculations at many state-points on a given network, means it is in fact, much more. Since it addresses the chemistry issues, in principle, it is potentially equally-well suited to address the emissions issues as well as the singularities.

The elapsed time for hybrid modeling includes the initial large cost of the CFD calculation, but this is a once-only cost for a given combustor. There is a 50% increase in the post-processing effort in order to establish the reactor network. Then however, multiple calculations may be run with the network on a PC platform at 2 - 5 minutes per state-point, depending on the extent of the reactor network, the chemical reaction mechanism used, and the operating conditions of the state-point.

Motivation

The chemistry to be solved on the reactor network established via hybrid modeling to represent the combustor flowfield, in principle, can consist of as many steps as are necessary. There are no time-penalties associated with the number of species used, as there are with a CFD approach. The reaction mechanism requirements for making emissions calculations however, are more severe than those for making LBO calculations where it is only really necessary to get the heat release correct.

For hydrocarbon fuels the chemical mechanisms necessary contain breakdown of a fuel molecule into the relatively stable species of the olefine, alkane, acetylene and aldehyde families, and involve little heat release. A sequence of reactions breaking down hydrocarbon intermediates with two or more carbon atoms into formaldehyde and then formyl (HCO) follow. The steep rise to equilibrium temperature comes from the major production of H_2O , CO_2 , H_2 and CO . For generality, a complete set of reaction steps for gaseous emissions purposes would also include the Zeldovich NO , Fenimore-type prompt- NO , N_2O production, and conversion of NO

to NO_2 . Steps for the production of free-carbon as soot (particulates) could even be included⁵.

The combination of a large number of steps in the reaction mechanism with a large number of reactors (especially involving recirculation and/or parallel arrays to account for fuel/air unmixedness effects) in a network to represent the flowfield, together with state points at high operating pressures, can drive up solution times, even with hybrid modeling. For example, a case with 25 reactors in the network and 345 reaction steps, at 70 atmospheres operating pressure, required an overnight run on a 166 MHertz PC. Therefore, it is always desirable to operate with the minimum number of reaction steps possible. The term "abbreviated mechanism" is used here to distinguish between a "full mechanism" that a chemist would feel comfortable with, and a "reduced mechanism" that might be allowable in a current CFD code for engineering use.

Jet fuels, such as Jet-A/JP-5/JP-8, which for the present purposes, differ only in trace additives to control physical properties, are not pure substances but consist of a blend of several thousand different hydrocarbons. Therefore, the "fuel molecule" to be used is any reaction mechanism for such a fuel, is an idealized representation.

This being so, the combination of an idealized molecular representation for a jet-fuel in an abbreviated reaction mechanism, requires that before such a mechanism can be reliably used as the basis for extensive emissions calculations in a complicated engine combustor flowfield, the mechanism be validated in some appropriate fashion. This is the motivation of the present work.

Requirements

For the purposes of making gaseous emissions estimates, it is necessary to be able to calculate the emission indices (g pollutant/kg fuel burned) of NO_x expressed as NO_2 and corrected to a standard humidity, CO , and UHC expressed as CH_4 . The state-point values of these exhaust products for a particular engine cycle are integrated around a standardized landing and take-off cycle to yield g pollutant/kN engine thrust.

The minimum accuracy demanded for the present purpose is within that with which engine measurements of emissions can be made. Such engine measurements at defined state-points will normally include the influence of uncertainties in thrust

measurement as well as sampling error; the net uncertainty also includes engine-to-engine performance variations. For *CO* and *UHC* respectively (dominant at low power levels) ± 8 g/kg and ± 6 g/kg, while for *NOx* (dominant at higher power levels) ± 1.5 g/kg, are not untypical⁶, where the thrust uncertainty constitutes a significant portion of the overall uncertainty. For routine tests of isolated combustors, where better control of operating conditions can be exercised, ± 1.0 g/kg can be expected. In this instance the majority of the uncertainty is associated with sampling error.

Present Contribution

A promising abbreviated reaction mechanism^{7,8} for Jet-A/JP-5/JP-8 jet fuels is given a preliminary evaluation by comparing calculations made using it and measurements reported in the literature of *CO/CO₂*, *NOx* and temperature from premixed, prevaporized Jet-A fuel in air burning on perforated-plate flameholders from 1 to 5 atmospheres pressure.^{9, 10, 11, 12}

Reaction Mechanism

The abbreviated reaction mechanism selected was that of Kollrack^{7,8} for Jet-A, where the fuel is represented by the simulated generic molecule *C₁₂H₂₃*. This mechanism was selected as a starting set because of its previous successes in the calculation of LBO's,¹ and because of its simplicity.

The Kollrack mechanism includes a two-stage fuel pyrolysis, and then gives emphasis to the more stable intermediate species via a second-stage in which simpler hydrocarbons are reacted; a third-stage is dominated by recombination reactions and the conversion of *CO* to *CO₂*. In its original form used here the extended Zeldovich reactions are included for thermal *NO* and any prompt-*NO* formed via super-equilibrium *O*-atoms. There are 30 steps involving 21 species in the reaction, which is contained in Table 1.

Reactor Network Code

The algorithm used for the solution of a system of non-linear, stiff, ordinary differential kinetics equations is CREK^{13, 14} (Combustion Reaction Kinetics). This algorithm is incorporated in a development, (MARK3) by Pratt (1991) of the reactor network code MARK2 by Pratt & Pratt¹⁵. MARK3 in its various versions is an interactive code that allows a number (up to 25) of NRM, PFR and PSR elements to

be connected in series, parallel and recycle arrangements; fuel and air inflows are allowed at each element. The reaction mechanism (up to 450 steps), species thermodynamic properties and the network geometry are read from a specified data file. The fuel can be in either liquid or gaseous phase.

$$k_j = 10^{B_j} T^{N_j} \exp\left\{-\frac{T_j}{T}\right\}$$

STEP	REACTION	B _j	N _j	T _j
1.	<i>C₁₂H₂₃</i> + <i>O₂</i> → 5 <i>C₂H₄</i> + <i>C₂H₃</i> + <i>O₂</i>	4.48	1.5	7900
2.	<i>C₁₂H₂₃</i> + <i>OH</i> → 6 <i>C₂H₄</i> + <i>O</i>	7.3	1.0	4500
3.	<i>C₂H₄</i> + <i>H</i> ↔ <i>C₂H₃</i> + <i>H₂</i>	10.48	0.0	9500
4.	<i>H</i> + <i>H</i> + <i>M</i> ↔ <i>H₂</i> + <i>M</i>	12.3	-1.0	0
5.	<i>O</i> + <i>O</i> + <i>M</i> ↔ <i>O₂</i> + <i>M</i>	11.0	-1.0	0
6.	<i>H</i> + <i>OH</i> + <i>M</i> ↔ <i>H₂O</i> + <i>M</i>	13.85	-1.0	0
7.	<i>H</i> + <i>O₂</i> ↔ <i>OH</i> + <i>O</i>	11.35	0.0	8400
8.	<i>O</i> + <i>H₂</i> ↔ <i>OH</i> + <i>H</i>	10.24	0.0	4730
9.	<i>CO</i> + <i>OH</i> ↔ <i>CO₂</i> + <i>H</i>	-14.75	7.0	-7000
10.	<i>H</i> + <i>H₂O</i> ↔ <i>OH</i> + <i>H₂</i>	10.92	0.0	10050
11.	<i>CH₃</i> + <i>O₂</i> ↔ <i>CH₂O</i> + <i>OH</i>	9.0	0.0	4000
12.	<i>HO₂</i> + <i>M</i> ↔ <i>H</i> + <i>O₂</i> + <i>M</i>	12.32	0.0	2300
13.	<i>HO₂</i> + <i>H</i> ↔ 2 <i>OH</i>	9.89	0.0	950
14.	<i>CH₂O</i> + <i>OH</i> ↔ <i>H₂O</i> + <i>HCO</i>	10.90	0.0	2120
15.	<i>O</i> + <i>H₂O</i> ↔ 2 <i>OH</i>	10.76	0.0	9000
16.	<i>N₂</i> + <i>O</i> ↔ <i>NO</i> + <i>N</i>	9.0	0.0	25000
17.	<i>N</i> + <i>O₂</i> ↔ <i>NO</i> + <i>O</i>	5.0	1.0	2000
18.	<i>N</i> + <i>OH</i> ↔ <i>NO</i> + <i>H</i>	9.0	0.0	0
19.	<i>HCO</i> + <i>O₂</i> ↔ <i>HO₂</i> + <i>CO</i>	10.48	0.0	7000
20.	<i>HCO</i> + <i>OH</i> ↔ <i>H₂O</i> + <i>CO</i>	10.30	0.0	0
21.	<i>C₂H₄</i> + <i>OH</i> ↔ <i>C₂H₃</i> + <i>H₂O</i>	9.78	0.0	1750
22.	<i>CH₂O</i> + <i>HO₂</i> ↔ <i>HCO</i> + 2 <i>OH</i>	9.0	0.0	4500
23.	<i>C₂H₂</i> + <i>HO₂</i> ↔ <i>HCO</i> + <i>CH₂O</i>	9.3	0.0	5500
24.	<i>C₂H₃</i> + <i>O₂</i> ↔ <i>C₂H₂</i> + <i>HO₂</i>	9.23	0.0	5000
25.	<i>NO</i> + <i>HO₂</i> ↔ <i>NO₂</i> + <i>OH</i>	3.0	1.0	0
26.	<i>C₂H₄</i> + <i>O</i> ↔ <i>CH₃</i> + <i>HCO</i>	9.93	0.0	1500
27.	<i>C₂H₄</i> + <i>HO₂</i> ↔ <i>CH₃</i> + <i>HCO</i> + <i>OH</i>	9.9	0.0	5000
28.	<i>H₂</i> + <i>CH₃</i> ↔ <i>CH₄</i> + <i>H</i>	7.0	-1.5	7140
29.	<i>C₂H₂</i> + <i>OH</i> ↔ <i>CH₃</i> + <i>CO</i>	8.2	0.0	2500
30.	<i>CH₃</i> + <i>O</i> ↔ <i>CH₂O</i> + <i>H</i>	11.11	0.0	1000

Table 1: Reaction Mechanism and Rate Constants

Data Sets

To evaluate a reaction mechanism it is desirable to separate completely any fluid dynamics modeling from the chemistry modeling. Ideally therefore, experiments for comparison should have zero dimensions, i.e. no gradients of temperature, species concentration or velocity whatsoever. The closest approach to this ideal is a WSR, which in theory, has

zero gradients of temperature and species concentration, and is one-dimensional in through-put velocity. It is desirable that the operating conditions for such WSR experiments cover wide ranges of residence time, equivalence ratio, inlet temperature and combustion pressure. Measurements from these experiments should include, in addition to reaction temperature and heat losses, not only conventional gas-sampling measurements, but also quantitative differentiation between hydrocarbon species.

Unfortunately, extensive and reliable measurements of the desired type from WSR experiments with jet fuels are only just becoming available.

Considerable work with vaporized Jet-A premixed in air is reported in the literature for perforated-plate flameholders. The experiments are one-dimensional in bulk throughput velocity, but are locally highly three-dimensional in the immediate wake-region just downstream from the perforated-plate. Furthermore, the scope of the measurements for these experiments is rather limited for the present purposes. However, they can serve as a starting point for reaction mechanism preliminary evaluation.

Semerjian & Ball⁹ premixed vaporized Jet-A with air preheated to an inlet temperature of 756K at atmospheric pressure, and stabilized flame on uncooled flameholders of 80 percent blockage in an uninsulated rectangular-section duct of 7.6 cm x 3.8 cm dimensions. Comparisons of NO_x as a function of equivalence ratio for calculations made using MARK3 with the Kollback mechanism and these measurements are made at 4 ms hot residence time for a 32-hole flameholder.

Cooper¹⁰ premixed liquid Jet-A with air to give mixture inlet temperatures of 600 and 700K at 2.96 atm pressure; flame was stabilized on a water-cooled flameholder of 75 percent blockage in an insulated circular duct of 10.2 cm diameter. Comparisons of NO_x as function of equivalence ratio are made for 35 m/s reference velocity at 79 cm downstream from a 61-tube flameholder.

Marek & Papathakos¹¹ used a similar arrangement to Cooper except that measurements were made 31 cm downstream from the flameholder, with mixture inlet temperatures of 640, 800 and 833K at a combustion pressure of 5.3 atm. Comparisons of calculated and measured NO_x , combustion inefficiency and CO are made as a function of equivalence ratio.

Semerjian & Vranos¹², using the apparatus of Semerjian & Ball, made local axial traverses of CO_2 , CO , NO_x and gas temperature inline with jets from 18 and 8 hole uncooled flameholders of 80 percent blockage. The mixture inlet temperature was 750K, the combustion pressure was atmospheric, the reference velocity was 20 m/s, and equivalence ratios of 0.45, 0.60 and 0.74 were used. Comparisons are made with present calculations for these data. Some limited axial traverses of NO_x were also made between jets.

Flow Field

The flowfield in the region where flame stabilization takes place for a perforated-plate flameholder is relatively simple, and consists of an array of potential cores for the individual jets submerged in an array of wake regions anchored on the flameholder rear-face between jets. The bulk of the initial heat release takes place in the shear layers between jet and wake regions. The wakes serve as a source of hot combustion gases and active radicals for the shear layers. This is illustrated diagrammatically in Figure 1. Downstream of this initial flame zone is a burnout region of turbulent, axial flow.

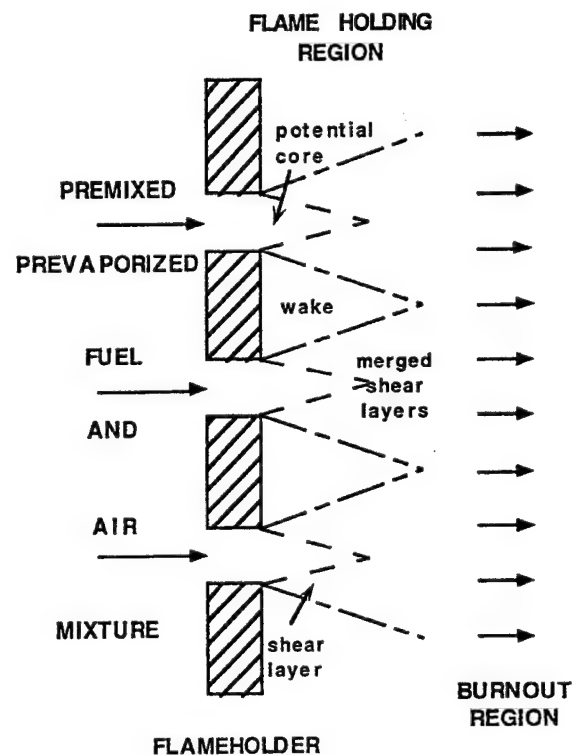


Figure 1: Flowfield for Data-Sets

The flowfield described is identical for each of the experiments in the data set. The relative dimensions of the flow features and the recirculated mass flow rates, scale with the jet initial diameters and the flameholder blockage¹⁶.

Modeling of Flowfield

The flame-holding region of the combustor, together with the subsequent burnout region and the upstream fuel/air mixture preparation section of each rig, have to be represented by an appropriate network of reactors, each sized for the particular data-set being calculated and modeling the appropriate local flow conditions. Given the discrete nature of these reactors, complex flow features, such as the shear layers and their interactions with the wakes, etc., have to be represented in piece-wise fashion.

The upstream fuel/air mixture preparation section of all the experiments was modeled as a non-reacting mixer (NRM) of appropriate dimensions. Liquid fuel was introduced into the NRM (1), together with the appropriate air quantity at a temperature iteratively adjusted to give the stated mixture temperature entering the combustor.

For the flame-holding region displayed in Figure 1, the potential core and the shear layers with subsequent wake and wake/shear layer exchanges, were modeled by parallel reactor arrangements. The potential core was represented by a plug-flow reactor (PFR). In parallel with the potential core PFR (2), the initial region of the shear layers was also represented by a small PFR (3). The wake region was treated as being equivalent to a well-stirred reactor (WSR). Entrainment of shear layer flow into the wakes and interaction of the wakes with the shear layers were addressed through another PFR (4) for the shear layers in series with the initial shear layer PFR, but in parallel with the wake WSR (5), and having mass exchange between this PFR and the WSR. The (usually temporally disorganized) end of the discrete shear layer region was represented by a series-WSR (6). The merged shear layer region brings together the potential core PFR with the discrete shear layer reactors. The merged shear layers were modeled as a PFR (7) with a parallel WSR (8), having some mass-exchange between the two to represent the very turbulent behavior characteristic of this region.

The burnout region of the combustor was represented by a simple PFR (9). For the experiment of

Semerjian & Vranos¹² the axial traverses were simulated by varying the length of the burnout PFR.

The network described was used for each of the data-sets studied. Figure 2 shows the network with dimensions and flow splits appropriate for Cooper's experiment¹⁰. The procedures for determining such networks are described in Reference 1.

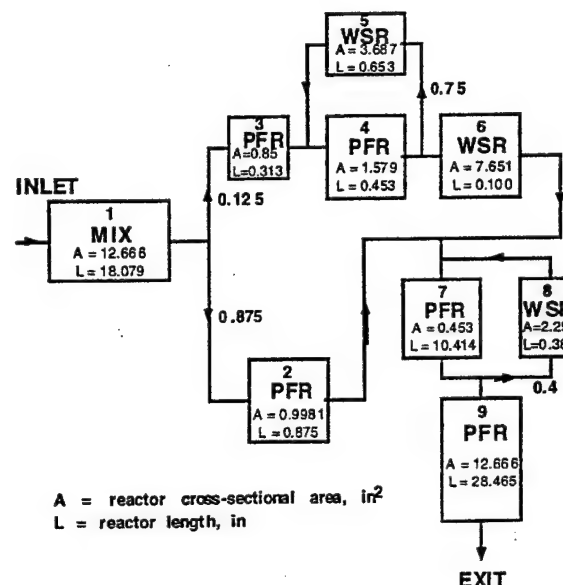


Figure 2: Reactor Network

Results

The bulk measurements allow the effects of equivalence ratio, combustion pressure and, to a limited extent, mixture inlet temperature, to be examined for some of the pollutants of interest.

The effect of equivalence ratio at 756K inlet temperature and atmospheric pressure on NO_x are given in Figure 3 for 4 ms overall residence time, from the data of Semerjian & Ball⁹ with a 32-hole flameholder at 80 percent blockage. The emission indices (EI) of NO_x (as NO_2 and corrected to standard humidity) are very low at equivalence ratios near to lean blowout (LBO) being less than 1.0 g NO_x /kg fuel burned. They increase rapidly with equivalence ratio to an EI of slightly greater than 10.0 at 0.75 equivalence ratio. The calculations agree with the measurements near to LBO, and show a similar increase to the measurements; however, the gradient is not quite correct. The maximum differences between calculations and measurements are ± 1.0 g/kg.

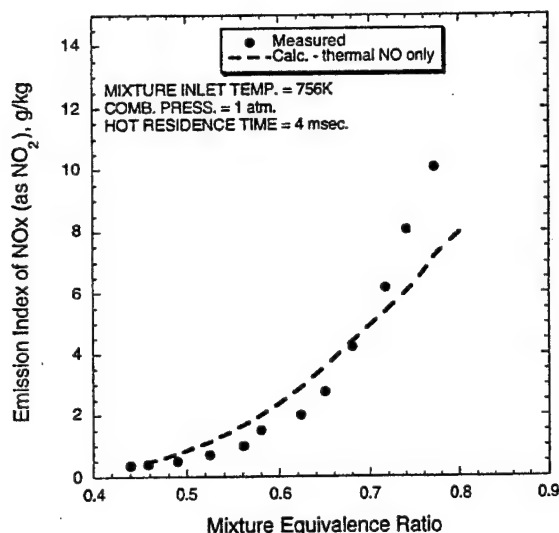


Figure 3: Oxides of Nitrogen at Atmospheric Pressure (Semerjian & Ball)

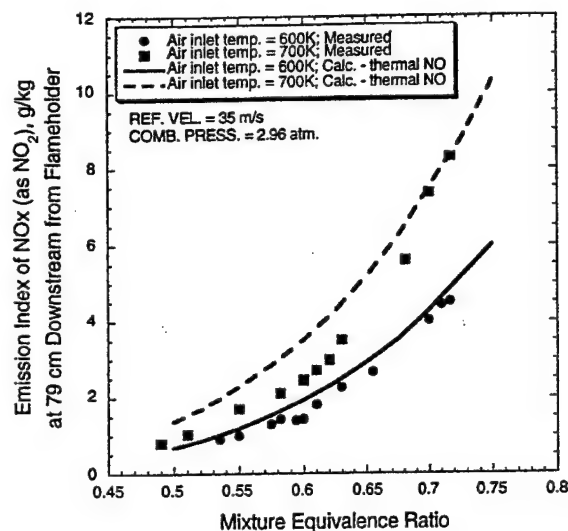


Figure 4: Oxides of Nitrogen at 2.96 atm (Cooper)

Cooper's experimental data at inlet temperatures of 600 and 700K show similar NO_x trends at 2.96 atm combustion pressure for a 61-hole flameholder with 75 percent blockage. The effect of increased inlet temperature is to elevate the level of NO_x and also its sensitivity to equivalence ratio. Figure 4 compares the measurements with the calculations. At 600K inlet temperature the agreement between calculations and measurement are excellent, with differences within the order of accuracy of the measurement. At the 700K inlet temperature condition the calculations over-estimate the measurements by a maximum of 1.0 g/kg at about 0.6 equivalence ratio, but agree with the measurements for equivalence ratios of 0.70 and 0.72.

At 5.3 atm the NO_x data of Marek & Papathakos¹¹ for 640 and 800/833K inlet temperatures show excellent agreement over the respective ranges of equivalence ratio with the calculations, as Figure 5 indicates. It does appear as though the gradient calculated for the 640K inlet temperature is not quite correct.

The combustion inefficiency at 833K is over-calculated for equivalence ratios greater than 0.4, although the calculated LBO is in good agreement with the experimental value. Figure 6 illustrates this.

Figure 7 shows that too much CO is calculated at the 800/833K temperature, and this is the

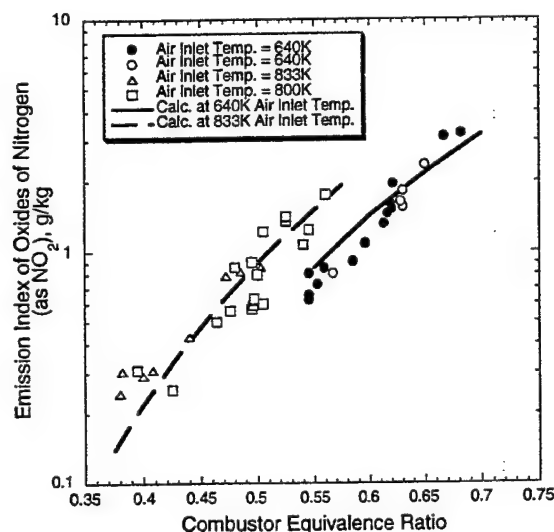


Figure 5: Oxides of Nitrogen at 5.3 atm (Marek & Papathakos)

reason for the high inefficiency calculation noted in Figure 6. The data indicate that at 640K inlet temperature the CO is at equilibrium levels for equivalence ratios above 0.55, whereas super-equilibrium values are calculated up to 0.7 equivalence ratio. Note that the experimental increase in CO as LBO is approached for 800/833K inlet temperatures is not duplicated in the calculations.

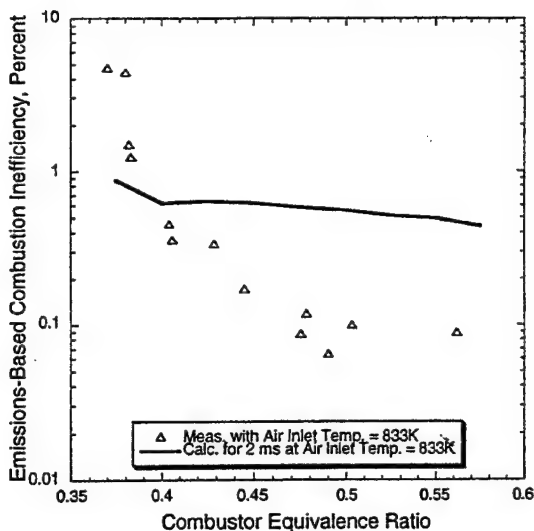


Figure 6: Combustion Inefficiency at 5.3 atm and 833K Inlet (Marek & Papathakos)

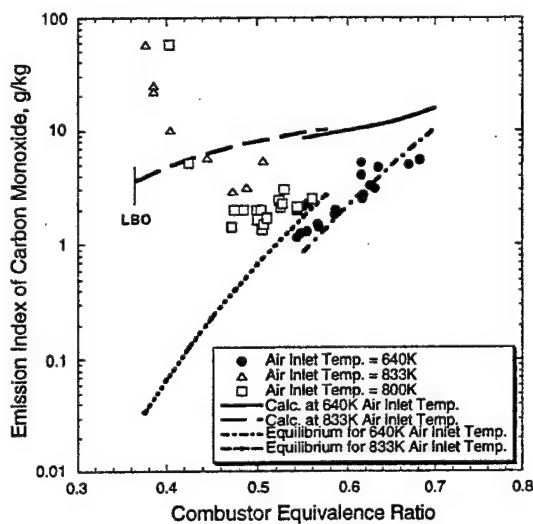


Figure 7: Carbon Monoxide at 5.3 atm and 833K Inlet (Marek & Papathakos)

The experiments of Semerjian & Vranos¹² used the same general apparatus of Semerjian & Ball, but changed the length-scale of the experiment by using flameholders of 18-holes and 8-holes respectively, while maintaining an 80 percent blockage. The measurements, rather than being for a fixed residence time as in the previous experiments, consisted of axial traverses, predominantly along individual jet-axes. The

combustion pressure was atmospheric, and the mixture inlet temperature was 750K.

The most apparent effect of the length-scale change was clear indication of chemical reaction and heat release taking place **upstream** of the flameholder. The large stagnation regions between holes on the upstream face of the flameholder provided long residence times in excess of the ignition delay time for the mixture. Furthermore, the uncooled flameholder was heated by conduction from the combustion taking place in the wake regions on its downstream face. The upstream combustion was evidenced by measured local temperatures in the jets at the flameholder exit plane that were in excess of the measured bulk mixture inlet temperature. In addition, non-zero values of NO_x and CO at this position were measured. Upstream combustion effects were **not** included in the calculations.

Figure 8 compares calculated and measured NO_x (as ppm NO_2 at standard humidity) along a jet axis downstream from the flameholder, at equivalence ratios of 0.45, 0.60 and 0.74. The data are for the 18-hole flameholder.

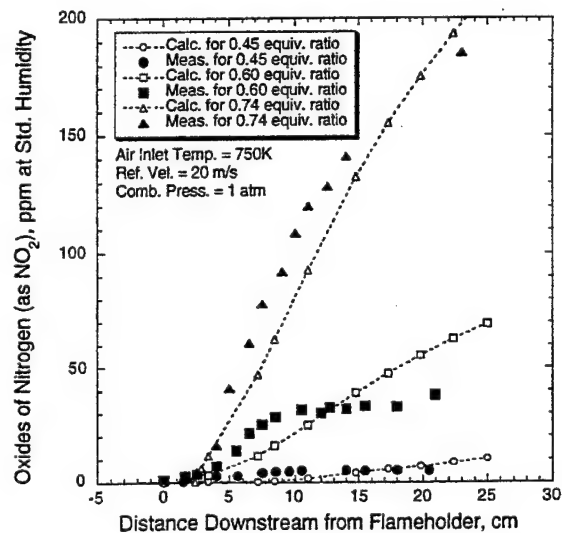


Figure 8: NO_x Profiles Along Jet Axis for 18-Hole Flameholder (Semerjian & Vranos)

In general, the agreements in the figure are good. However, a more detailed inspection reveals some important discrepancies. At 0.45 equivalence ratio an LBO is being approached in the calculations as shear layer/wake flameholding is weakened. This results in a

partial flame-lift. Flame-lift is not evident in the measurements, and this may be due to heat conduction from upstream combustion through the flameholder to the downstream wake regions. For 0.60 equivalence ratio the measured initial rise in NO_x is greater than calculated, and the measured final increase in NO_x with distance is much less than calculated. The details of these particular discrepancies are discussed below. The agreement of NO_x - profiles at 0.74 equivalence ratios is reasonably satisfactory.

Measured and calculated profiles of carbon monoxide inline with jets for the 18-hole flameholder are given in Figure 9 at the three equivalence ratios.

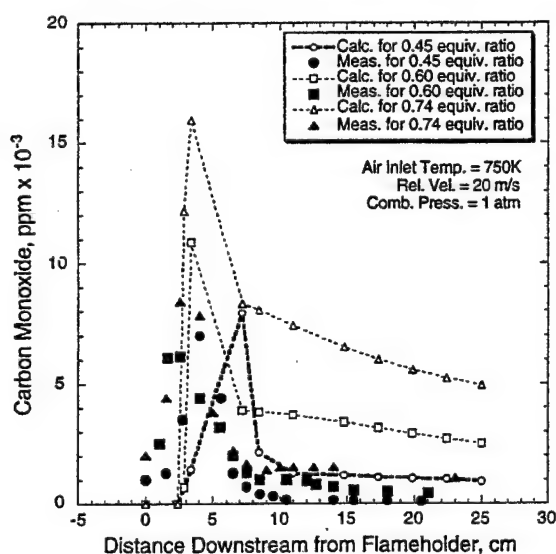


Figure 9: Profiles of Carbon Monoxide for the 18-Hole Flameholder (Semerjian & Vranos)

It is seen in Figure 9 for the measured data that in the exit plane of the flameholder, CO is non-zero, and that the amount of CO at inlet increases with increasing equivalence ratio. The measurements indicate that CO reaches a peak in the flameholding region and then tapers off to very low values in the burnout region of the combustor. The position of this CO - peak moves downstream slightly as the equivalence ratio is reduced.

The calculations have the same general form as the measurements. However, CO at the inlet plane is (constrained to be) zero, and remains zero through the potential core regions (see Figure 1). At the end of the potential core the calculated CO increases rapidly in the

merged shear layer region, and reaches peaks before the burnout region is approached. The magnitudes of the measured peaks are over-estimated in the calculations, except for the 0.45 equivalence ratio. The position of the CO - peak moves downstream with decreasing equivalence ratio; for the 0.45 equivalence ratio this downstream movement is significant as the calculated flame undergoes partial flame-lift. This movement at 0.45 equivalence ratio is much greater than for the measurements; the positions of the peaks for the higher equivalence ratios are reasonably well calculated. The levels of CO in the burnout region are much higher than the measured values. This discrepancy may be due to the beneficial upstream combustion taking place in the experiment, and unaccounted for in the calculations.

The carbon dioxide profile comparisons for the 18-hole flameholder are presented in Figure 10.

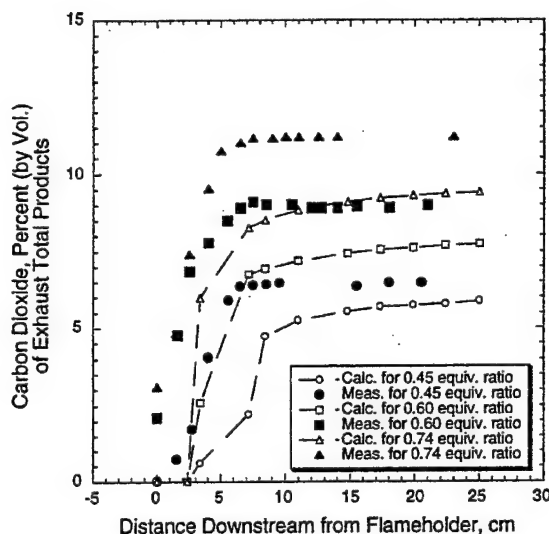


Figure 10: Carbon Dioxide Profiles for the 18-Hole Flameholder (Semerjian & Vranos)

Again, the presence of upstream reaction is evidenced by the measured non-zero values of CO_2 at the discharge plane from the flameholder; the initial values of CO_2 also increase with increasing equivalence ratio. CO_2 increases very rapidly with downstream distance through the flame-holding region of the combustor for the two higher equivalence ratios; for the 0.45 equivalence ratio this increase is much less rapid. Levels plateau quickly in the burnout region as combustion is completed.

The calculations mirror the form of the measurements, except for zero initial CO_2 that is maintained through the potential core region. The calculated flame-lift effect is evident for 0.45 equivalence ratio.

The effects of length-scale are examined directly by comparing measurements and calculations for 18-hole and 8-hole flameholders at the constant blockage of 80 percent. For these comparisons the mixture inlet temperature was 750K, the combustion pressure was atmospheric, and the equivalence ratio was 0.60 with 20 m/s reference velocity. Again, axial profiles along jet centerlines are used.

Figure 11 compares calculated and measured profiles of CO for the two flameholder hole sizes.

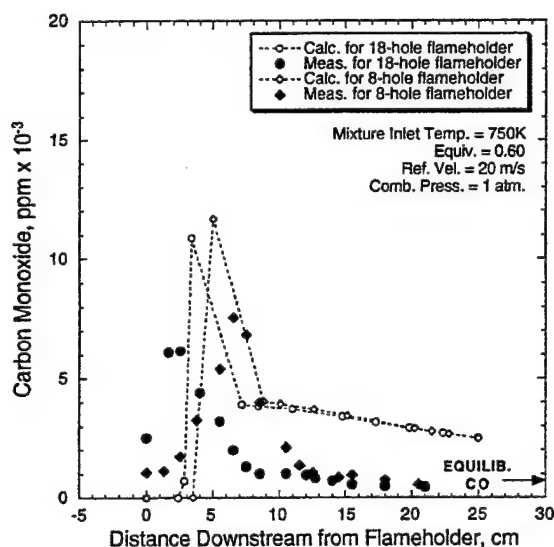


Figure 11: Comparison of CO - Profiles for 18-Hole and 8-Hole Flameholders at 0.6 Equivalence Ratio (Semerjian & Vranos)

The measurements show non-zero CO at the combustor entry, and the quantity of CO increases with the number of holes. The general form of the measured CO profiles is similar to that seen in Figure 9. However, the 8-hole configuration evidences the existence of a potential core, albeit at non-zero values for CO . The increase in length-scale, i.e. the hole diameter for the 8-hole flameholder, results in the flameholding region of the flowfield extending further downstream than for the 18-hole flameholder. Therefore, the measured CO -peak is moved downstream compared to that for the smaller length-scale, and the peak CO

level is increased. In the burnout region both flameholders give essentially the same CO levels, which are about half the equilibrium value at combustor exit. Heat losses from the uninsulated combustor could account for these sub-equilibrium levels.

The calculations mirror the measured behavior extremely well. They show increased potential core length, downstream shift of the CO - maximum, and increased peak- CO for the 8-hole flameholder, as well as common CO - levels for both flameholders in the burnout region of the combustor. Levels in the burnout region exceed the equilibrium value, and of course, the measured values. This again could result from the unaccounted-for upstream combustion.

Temperature profiles for the two flameholder configurations at the same operating conditions as previously are displayed in Figure 12.

The effects of the upstream combustion can really be appreciated from these measurements, where the inlet temperature for the 18-hole flameholder was 1180K, and for the 8-hole flameholder it was 1050K, compared to the nominal inlet temperature of 750K. The measurements also reveal the effects of heat losses from the uninsulated combustor body. The gas temperatures for both flameholders are essentially equal in the burnout region of the combustor, but show small declines from their peak value close to the adiabatic

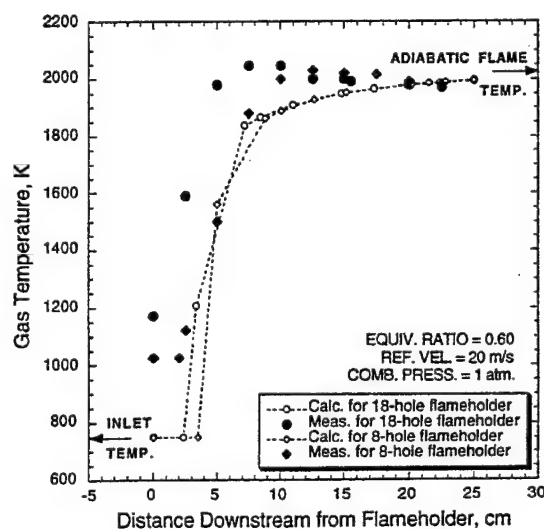


Figure 12: Temperature Profiles for 18-Hole and 8-Hole Flameholders at 0.60 Equivalence Ratio (Semerjian & Vranos)

flame temperature, to exit-levels just below this temperature. The temperatures for the increased length-scale flameholder (8-hole) show a distinct thermal potential core.

The calculations give a thermal potential core for both flameholders, with a small increase in this length for the increased length-scale flameholder. The calculated thermal potential core lengths are greater than the measured potential core lengths. In the merged shear layer region the gas temperatures increase sharply, in line with the measurements. In the burnout region calculated gas temperatures climb slowly towards the adiabatic flame temperature. The calculation does not include heat losses.

Figure 13 makes the comparisons of NO_x , between calculations and measurements for the two flameholders at the 0.60 equivalence ratio.

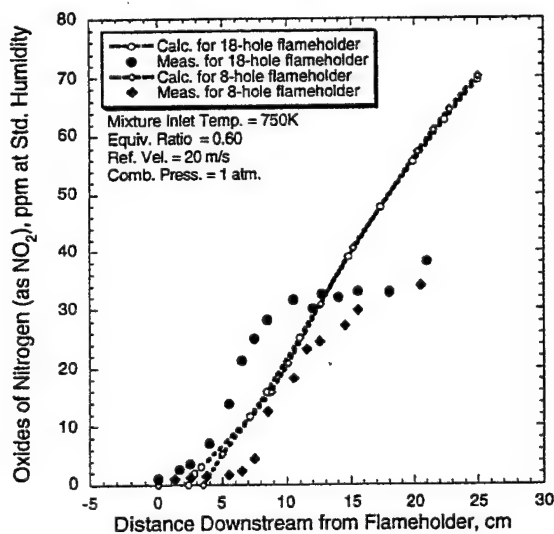


Figure 13: NO_x Profiles for 18-Hole and 8-Hole Flameholders at 0.60 Equivalence Ratio (Semerjian & Vranos)

The measured NO_x data show the existence of a significant concentration potential core for the 8-hole flameholder. For the 18-hole flameholder no potential core is in evidence. The potential core for the 8-hole flameholder shifts the increase in NO_x for this flameholder further downstream, although the rate of NO_x - increase with distance for the two flameholders is about the same. The curves for both flameholders indicate a NO_x - plateau is reached about mid-distance into the burnout region of the combustor. It appears as

though after the plateau is reached, NO_x does increase with distance, but at a much reduced rate.

The calculations show concentration potential cores for both flameholders, with the increased length-scale flameholder having the longer core. This is in line with the measurements, but the calculated core for the 8-hole flameholder is much less than the measurements indicate. Conversely, the measurements indicate that the core length for the 18-hole flameholder is much more than that calculated. The initial gradient calculated for NO_x is about correct, but in the merged shear layer region of the combustor there are no differences in level at a given axial station, such as the measurements show. For distances between the NO_x - plateau region of the measurements and the exit from the combustor, the calculated NO_x continues to increase at about the same rate. A slight reduction in the calculated gradient is observed towards the end of the combustor, but it is not significant.

The experimental behavior described in Figure 13 is suggestive of the action and relative dominance of two concurrent but different chemical processes. In this instance, the relevant mechanisms could be a) the formation of "prompt NO " via super-equilibrium O - atoms, and b) thermal NO , both acting through the Zeldovich equations (Equations 16-18 in Table 1).

To explore this issue with a view to explaining the apparent failure of the NO_x calculation in Figure 13, the calculated portion of this figure for the 18-hole flameholder is repeated in Figure 14 for reference purposes. To it, the O - atom and OH - radical concentrations from the calculation, referenced to their equilibrium values, have been added. The OH - radical also serves as an indicator of the flame location.

It can be seen from Figure 14 that at the end of the potential core the OH - radical concentration jumps to about 2.5 times its equilibrium value, indicating the presence of flame in the merged shear layer region. It then decays almost linearly through the burnout region of the combustor, but remains always above its equilibrium value. Simultaneously, the O - atom concentration shoots up dramatically at the end of the potential core, so that within 1.0 cm its concentration is almost 14.5 times its equilibrium value. Thereafter, the O - atom concentration decays exponentially, but is still over 5.0 times its equilibrium level at the end of the combustor. The gradient of NO_x concentration decreases as the O - atom pool is depleted.

It is clear that the bulk of the calculated NO_x downstream of the potential core in this fuel-lean combustion is derived through the prompt- NO mechanism in the Zeldovich equations due to the presence of massive quantities of O -atoms¹⁷.

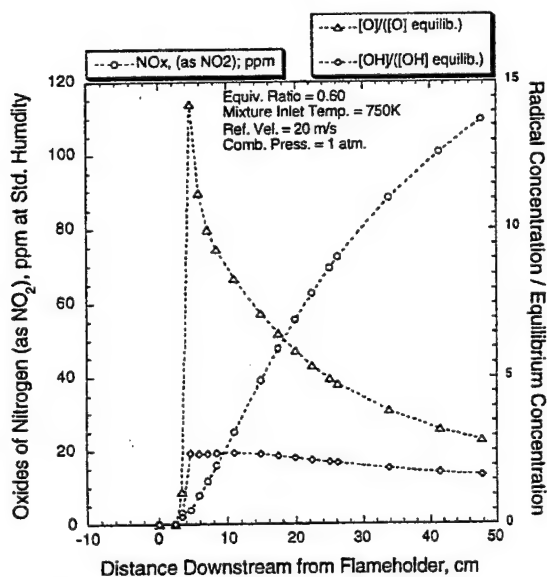


Figure 14: Calculated Radical Pool for 18-Hole Flameholder at 0.6 Equivalence Ratio

From the foregoing it is obvious that to obtain the correct NO_x profiles, the atom/radical pool must be correctly accounted for.

Heat losses from the combustion section will further deplete the atom/radical pool, as illustrated in Figure 15, which should be related to Figure 12 for the burnout region. However, a major influence on the radical pool would be the upstream combustion demonstrated to exist for this experiment, and illustrated in Figure 12 via the mixture inlet temperatures. Together, these processes, heat losses and upstream combustion, would give an atom/radical pool significantly different from that calculated. Hence, the calculated NO_x profiles in the burnout region, given the caveats on the calculation (no heat losses and no upstream combustion), could not be expected to be correct.

Discussion

Hybrid modeling attempts to address a real need in industry. That is, the ability to make timely, relatively rapid and inexpensive but engineeringly-accurate, repetitive calculations of LBO and gaseous emissions in practical combustors of complex

geometry. The methodology is physics-based, and does not rely directly on any empiricism. Initial development of the method is extremely promising.

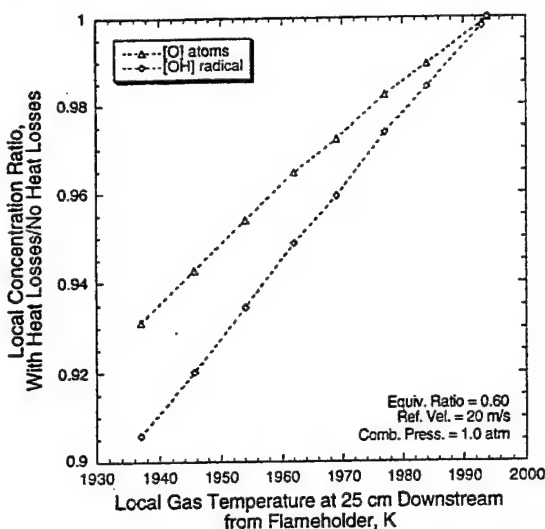


Figure 15: Effect of Burnout Region Heat Losses on the Atom/Radical Pool

Evaluation of hybrid modeling for emissions calculations is in its early stages. Such assessment is not an easy procedure since there are two linked components to be explored: flowfield modeling and chemistry modeling. Comparison with data from simple experiments that uncouple these components is desirable. Such experiments ideally should use real jet fuels, and the operating parameters should cover wide ranges of residence time, inlet temperatures, combustion pressure and stoichiometry. Measurement of major species such as $NO/N_2O/NO_2$, CO , CO_2 , H_2O and total UHC are essential; differentiation between individual hydrocarbon species making up the total UHC is extremely desirable. Such experiments are very difficult to conduct.

The experiments currently selected from the literature as part of this investigation were not originally intended for the present purpose. Consequently, they do not fulfill all of the desired requirements listed above. The most serious deficiency is in the limited measured data taken. This was the case for all of the experiments considered. Although geometrically simple, they do necessitate flowfield modeling concurrent with the chemistry modeling. The required flow modeling is conveniently the same for each of these experiments.

The perforated plate flameholder that forms the essence of the selected experiments was earlier used to establish baselines for low emissions of NO_x . This configuration has also been considered for practical application in natural gas fueled, dry low- NO_x combustors for industrial gas turbines. It has not yet found application due to poor LBO stability and excessive combustion dynamics (e.g. noise).

Ensuring that chemical reactions are fully quenched in any gas sampling probe is always a difficult task. For Cooper's experiment¹⁰ it was found that for some operating conditions the measured CO was below that for equilibrium. The combustor was insulated, so part of the problem may have been in the emissions sampling probe. For this reason CO comparisons are not presented for this experiment.

It was found that the data from the most useful of the selected experiments, that of Semerjian & Vranos¹², was compromised by upstream burning. This upstream burning was most apparent for the larger length-scale flameholders used (e.g. 18-hole and less for constant blockage) and at higher equivalence ratios (0.60 and above). The "optimum configuration" for such upstream burning appeared to be the 18-hole flameholder. The upstream burning was undoubtedly associated with the size and stability of the stagnation regions formed on the upstream face of the flameholder.

Upstream burning was seemingly avoided in the experiments of Cooper¹⁰ and Marek & Papathakos¹¹ by use of a water-cooled flameholder and smaller length-scales (61-hole flameholder with 75 percent blockage). Although the flameholder used by Semerjian & Ball⁹ was uncooled, it had a 32-hole flameholder with 80 percent blockage.

The dependency of bulk NO_x on equivalence ratio, for ratios in the range 0.45 to 0.75, and at pressures from 1.0 to 5.3 atm, was well-calculated, (Figures 3 - 5). The mixture inlet temperature range covered was rather limited, being 600 - 833K, but appeared to be adequately accounted for in the calculations.

Bulk CO was generally over-estimated, Figure 7, except near LBO where it was under-estimated. LBO itself was well-calculated, an ability that had been previously established, Reference 1. It is not known what effect the water-cooled flameholder for some of the experiments had on the CO measurement. Since the flame-holding is strongly associated with the wake-regions (Figure 1), heat losses might have exerted a

powerful effect on measured CO . Since the inefficiency, Figure 6, was largely due to CO , this behavior was reflected in the inefficiency comparison.

Although the measurements from the experiment of Semerjian & Vranos¹² are compromised, it is instructive to retain them for a variety of reasons. They provide local streamwise profiles of emissions, as opposed to bulk values, thereby adding dimensionality to the comparisons. They also cover a wider range of quantities than the other experiments, by including CO_2 and gas temperature. Furthermore, they represent an example of lean-burn NO_x , where the "prompt NO " mechanism can be clearly seen, together with the thermal NO mechanism.

For the 18-hole flameholder of Semerjian & Vranos the general profile shapes for NO_x with axial distance at 0.45, 0.60 and 0.74 equivalence ratios, Figure 8, are reasonably well calculated. Detailed examination reveals that at 0.45 equivalence ratio a lifted flame is apparent in the calculations, while this is not the case in the measurements. It is possible the upstream combustion in the experiment, by means of heat conduction through the flameholder, provided assistance to flame-holding in the wake regions on the downstream face of the flameholder. The problems with "prompt NO " and decay of the O -atom pool for 0.6 equivalence ratio have been explored above. Although similar problems can be observed for the 0.74 equivalence ratio comparison, the super-equilibrium O -atom pool is much reduced at this higher equivalence ratio, and thermal NO plays a bigger role in the total NO_x . The effects of upstream combustion giving early depletion of O -atoms in the experiment, although still present, are therefore of reduced significance.

Upstream burning in the experiment can also be used to account for the quantitative differences in measured and calculated CO and CO_2 profiles for the 18-hole flameholder, Figures 9 and 10, and for the 8-hole flameholder, Figure 11. The quantitative behavior of the calculations is quite correct in each case.

The differences between measured and calculated temperature profiles in Figure 12 can be attributed to upstream burning, and to heat losses in the burnout region of the uninsulated combustor.

The Semerjian & Vranos experiment represents a test of the flowfield modeling as well as of the chemistry modeling. All-in-all, given the caveats mentioned above for quantitative agreements, the calculations represent the observed behavior rather well.

Conclusions

Although the present study is far from a definitive evaluation of either hybrid modeling for calculation of gaseous emissions from practical combustors or of the abbreviated reaction mechanism for Jet-A/JP-5/JP-8 fuels, the following conclusions can be made:

1. The Kollrack mechanism for Jet-A represents an acceptable **starting point** for an abbreviated reaction mechanism for jet fuels, for the stated purpose.
2. For the simple flowfield that a perforated-plate flameholder represents, hybrid modeling looks like a promising approach that might be developed for calculating gas turbine combustor gaseous emissions.
3. Good experiments, of the kind described above, are needed to truly evaluate chemical reaction mechanisms for real fuels.
4. Additional evaluations of both hybrid modeling with more complex flowfields, and the Kollrack reaction mechanism with fuel-rich mixtures in particular, are needed.

Acknowledgements

The continuing enthusiasm, motivation and support of Dr. W.M. Roquemore of Wright Laboratory are greatly appreciated. This on-going research is sponsored by the U.S. Air Force, Wright Laboratory, Aero Propulsion and Power Directorate, through Contract No. F33615-95-C-2507. In particular, the support of Carlos A. Arana, WL/POTC is acknowledged. Thanks also to Dr. David Pratt, a friend of many years, for conceiving of the MARK-family of reactor network codes. The original work and thinking of Dr. Reiner Kollrack are gratefully acknowledged. "Was nun, Reiner?"

References

1. Sturgess, G.J. and Shouse, D.T., "A Hybrid Model for Calculating Lean Blow-outs in Practical Combustors," AIAA Paper No. 96-3125, presented at 32nd. AIAA/ASME/SAE/ASEE Joint Propulsion Conference, Lake Buena Vista, Florida, July 1-3, 1996.
2. Spalding, D.B., "Performance Criteria of Gas Turbine Combustion Chambers - A Method of

Comparison and Selection for the Designer," *Aircraft Engineering Monograph*, Bunhill Publications Ltd., England, August 1956.

3. Globus, A., Levit, C. and Lasinski, T., "A Tool for Visualizing the Topology of Three-Dimensional Vector Fields," Rept. No. RNR-91-017, NASA Ames Research Center, Moffet Field, California, April 1991.

4. Swithenbank, J., "Flame Stabilization in High Velocity Flow," *Combustion Technology - Some Modern Developments*, editors H.B. Palmer and J.M. Beer, Academic Press, 1974, pp. 91-125.

5. Colket, M.D., UTRC, private conversation, March 1997.

6. Dieck, R.H., "Gas Turbine Emission Measurement Uncertainty," undated and unnumbered Pratt & Whitney report.

7. Roberts, R., Aceto, L.D., Kollrack, R., Teixeira, D.P. and Bonnell, J.M., "An Analytical Model for Nitric Oxide formation in a Gas Turbine Combustor," *AIAA Journal*, Vol. 19, No. 6, 1972, pp. 820-826.

8. Kollrack, R., "Model Calculations of the Combustion Product Distributions in the Primary Zone of a Gas Turbine Combustor," Paper No. 76-WA/GT, presented at ASME Winter Annual Meeting, New York City, 1976.

9. Semerjian, H.G. and Ball, I.C., "Potential Reduction in NO_x Emissions with Premixed Combustors," presented at Spring Technical Meeting of The Combustion Institute - Central States Section, NASA Lewis Research Center, Cleveland, Ohio, March 28-30, 1977.

10. Cooper, L.P., "Effect of Degree of Fuel Vaporization Upon Emissions for a Premixed Partially Vaporized Combustion System," NASA Technical Paper 1582, January 1980.

11. Marek, C.J. and Papathakos, L.C., "Exhaust Emissions from a Premixing, Prevaporizing Flame Tube Using Liquid Jet-A Fuel," NASA Rept. TM X-3383, April, 1976.

12. Semerjian, H. and Vranos, A., "NO_x Formation in Premixed Turbulent Flames," proc. *Sixteenth Symposium (International) on Combustion*, The Combustion Institute, Pittsburgh, Pennsylvania, 1976, pp. 169-179.

13. Pratt, D.T. and Wormeck, J.J., "CREK - A Computer Program for Calculation of Combustion Reaction Equilibrium and Kinetics in Laminar or Turbulent Flow," Rept. No. WSU-ME-TEL-76, Dept. Mech. Engrg., Washington State University, 1976.
14. Pratt, D.T. and Radhakrishnan, K., "CREK1D: A Computer Code for Transient, Gas-Phase Combustion Kinetics," NASA Rept. TM-83806, October 1984.
15. Pratt, B.S. and Pratt, D.T., "MARK2X Computer Code," private communication, 1990.
16. Abramovich, G.N., *The Theory of Turbulent Jets*, M.I.T. Press, 1963.
17. Bowman, C.T. and Kestin, A.S., "Kinetic Modeling of Nitric Oxide Formation in Combustion Processes," presented at Fall Technical Meeting of The Combustion Institute - Western States Section, University of California - Irvine, California, October 1971.

3.1.3.2.3 Well-Stirred Reactor. The well-stirred reactor was used to study lean blowout limits and emissions from a variety of pure hydrocarbons. Results presented in the paper entitled "Emissions Characteristics of Liquid Hydrocarbons in a Well Stirred Reactor" (see pp. 515-533) showed that hydrocarbon structure plays a pivotal role in the production of emissions and in determining lean blowout limits. In a subsequent publication entitled "Fuel Effects on Lean Blowout and Emissions from a Well Stirred Reactor" (see pp. 534-541), it is shown that fuel type affects lean blowout limits, combustion efficiency, and pollutant emissions. These observations have important practical implications with regard to the design of gas turbine combustors.



AIAA 97-2710

Emissions Characteristics of Liquid Hydrocarbons in a Well Stirred Reactor

J. W. Blust, D. R. Ballal

University of Dayton

Dayton, OH

G. J. Sturgess

Innovative Scientific Solutions, Inc.

Beavercreek, OH

**33rd AIAA/ASME/SAE/ASEE Joint Propulsion
Conference & Exhibit
July 6 - 9, 1997 / Seattle, WA**

For permission to copy or republish, contact the American Institute of Aeronautics and Astronautics
1801 Alexander Bell Drive, Suite 500, Reston, VA 22091

EMISSIONS CHARACTERISTICS OF LIQUID HYDROCARBONS IN A WELL STIRRED REACTOR

J. W. Blust*, and D. R. Ballal†
University of Dayton, Dayton OH

G. J. Sturgess‡
Innovative Scientific Solutions, Inc., Beavercreek OH

Abstract

The design and development of low-emissions, lean direct injection aero and lean premixed industrial gas turbine combustors is challenging because of a need to satisfy conflicting requirements of operability, combustion performance and low emissions. A toroidal well stirred reactor (WSR) provides a laboratory idealization of an efficient, highly compact primary zone of a gas turbine combustor, and facilitates the study of combustion and emissions. The WSR was used to study lean blow-out limits and emissions from a variety of pure hydrocarbons. In particular, effects of residence time and flame temperature on lean blow-out limits, NO_x , CO and unburned hydrocarbon emissions were measured from normal and cyclic alkanes, aromatics and a blend of hydrocarbons. Results showed that hydrocarbon structure plays a pivotal role in the production of emissions, and in determining lean blow-out limits.

Nomenclature

A	= Avagadro's number
AFT	= adiabatic flame temperature
C	= molecular collision factor
$(\text{C/H})_{\text{mole}}$	= carbon to hydrogen mole ratio
CN	= carbon number
E	= activation energy
EI	= emissions index (g emission/kg hydrocarbon)
H	= enthalpy
h	= Planck's constant
LBO	= lean blow-out
LHV	= lower heating value of hydrocarbon (J/kg)
LP	= loading parameter ($\text{g-mol/s} \cdot \text{l} \cdot \text{atm}^n$)
M	= molecular weight of gas mixture
Me	= Mach number at exit of reactor jet

* Ph.D. Student, AIAA Student Member.

† AIAA Fellow.

‡ AIAA Senior Member.

Copyright ©1997 by Authors. Published by the American Institute of Aeronautics and Astronautics, Inc. with permission.

P	= pressure
PSR	= perfectly stirred reactor
ppmw	= parts per million by weight
ppmV	= parts per million by volume
Q	= mass flow rate (g/sec)
R	= universal gas constant
RTD	= residence time distribution
S	= thermocouple surface area
Δs^*	= entropy change between states of activated complex and initial reactants
T	= temperature
UHC	= unburned hydrocarbons
V	= reactor volume
WSR	= well stirred reactor
x	= mole fraction of specie
ϕ	= equivalence ratio
η	= efficiency
ρ	= density
τ	= residence time

Subscripts

cat	= catalysis
comb	= combustion
eb	= eddy breakup
f	= flame, fuel
in	= inlet
jr	= jet ring
o	= oxygen
tm	= turbulent mixing

Superscripts

n	= apparent reaction order
---	---------------------------

Introduction

As recommended by the 1990 Federal Clean Air Act, reduction of emissions of carbon monoxide (CO), unburned hydrocarbons (UHC), and oxides of nitrogen (NO_x) is necessary for aero- and land based gas turbine engines. Reduction of emissions is challenging, as such reductions often conflict with concurrent performance requirements, such as efficiency, pattern factor, relight, part-load capability (for industrial combustors), and operability requirements such as combustion stability and altitude relight (for aero combustors). Thus, it becomes necessary to examine closely the fuels used by gas turbine engines to see what limitations these present to

the designers of cleaner burning, high performance engines. In particular, it is desirable to investigate the effects of individual hydrocarbon components in a gas turbine fuel, as well as the fuel *in toto* (i.e. jet fuel for aero engines), on the emissions and performance characteristics of the engine under realistic combustion conditions. Additionally, it is important to study the effects of cracked heavy hydrocarbons on combustion performance and emissions. As a result, a need exists to determine the mechanisms responsible for the formation of pollutants in a gas turbine combustor as well as to determine the lean combustion limits of jet fuels and jet fuel components under these conditions. The well stirred reactor (WSR) provides a means to study these phenomena in a well-controlled laboratory combustor configuration.

A promising strategy to reduce NO_x , CO and UHC from gas turbine combustors is to fully vaporize the fuel, premix it with air and then burn this mixture fuel-lean. In support of this approach, experiments have been conducted in the past to establish the limits that might be achieved. These efforts have produced lean, premixed, prevaporized (LPP) combustors (e.g. Marek and Papathakos¹; Mularz²), using geometrically simple hardware. In an LPP combustor, complete fuel vaporization and fuel-air mixing takes place prior to chemical reaction; reaction of this mixture at a very lean fuel-air ratio decreases combustion temperatures and hence reduces the formation of thermal NO .

The referenced experiments were geometrically axisymmetric, and were aerodynamically one-dimensional in a global sense while being three-dimensional locally at the perforated-plate flameholders used. While aerodynamic effects are minimized in such combustor configurations, nonetheless, they are present to a degree (Sturgess³). A perfectly stirred reactor (PSR), however, is a theoretical reactor that is zero-dimensional with respect to reactant concentration and temperature gradients. This homogeneity allows the combustion behavior to be uncoupled from any aerodynamic effects. Therefore, in the present investigation, we have supplied a toroidal WSR with premixed, prevaporized liquid hydrocarbons. The WSR is a laboratory reactor that emulates as much as possible the PSR condition. Thus, we have gained an understanding of the CO, UHC and NO_x emissions from just the combustion chemistry of these fuels.

It should be noted that similar research using liquid hydrocarbons has been performed previously in

various stirred reactor configurations (Brezinsky et al.⁴; Capehart et al.⁵; Dagaut et al.⁶; Vaughn, et al.⁷; Zelina et al.⁸). The present WSR benefits from previous work, and offers a refined test vehicle for this purpose.

Experimental Setup

WSR Test Facility and Instrumentation

A 250-ml toroidal WSR of Nenniger et al.⁹, as modified by Zelina and Ballal¹⁰, was used for this experiment. The reactor was constructed of alumina cement, and featured a jet ring with 32 stainless steel jets, 1 mm I.D., to inject the fuel-air mixture at high subsonic velocity. A schematic of the test facility and instrumentation for gaseous fuels is shown in Fig. 1.

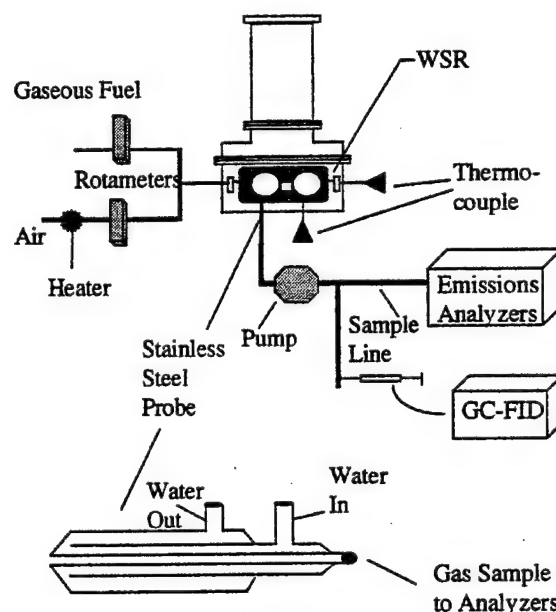


Fig. 1: WSR test facility and associated instrumentation.

The Horiba Emissions Analyzers comprised the following units: Model MPA-510 oxygen analyzer (0 to 50 percent), Model FIA-510 total hydrocarbon analyzer (0 to 10,000 ppm carbon), Model VIA-510 CO (0 to 20 percent) and CO_2 (0 to 100 percent) analyzer, and Model CLA-510 SS NO and NO_x analyzer (0 to 2000 ppmV). These units were calibrated with gases of the following concentrations: hydrocarbon = 404 ppmV propane, NO = 92 ppmV, NO_2 = 1.6 ppmV, CO = 0.4 percent, O_2 = 4.03 or 5.02

percent and $\text{CO}_2 = 11.06$ percent. Emissions readings were delivered on a dry basis, with water scrubbed from the sample gas to a maximum dew point of 5C. The units required a total of 4 slpm gas sample, with a pressure within ± 10 cm of water of ambient.

A gas sample was drawn from the WSR by a water-cooled stainless steel probe (Blust et al.¹¹) and pumped into each unit through a heated sampling line to be analyzed for the various product species. The stainless steel probe used in this experiment featured a small inside diameter, which resulted in a pressure drop when hot sample was drawn from the reactor. The subsequent vacuum necessitated connecting a single speed corrosion resistant pump rated 12 slpm to the sampling line.

Hydrocarbon speciation at LBO conditions was performed by collecting sample gas in a Tedlar bag and directly injecting sample into a gas chromatograph-flame ionization detector (GC-FID, Hewlett-Packard HP 5890 A). Qualitative identifications of products were performed by comparing retention times of unknown analytes to those of pure compounds. Relative quantitation was performed by analyzing selected standards. Overall quantitation was estimated by comparing total response from the GC-FID to the values measured from the FIA-510 total hydrocarbon analyzer.

Combustion temperature, T_f , was measured by insertion of a Type B thermocouple (platinum-6% rhodium, platinum-30% rhodium) into the toroidal volume. This thermocouple was coated with alumina ceramic to protect the thermocouple from its environment, because platinum-rhodium alloys are subject to high-temperature contamination that can embrittle the alloy.

Temperature measurements were corrected for heat loss by radiation and conduction, and heat gain by convection and catalysis. It has been suggested that reactions, particularly those involving a third body such as H, OH and O-recombination, occur at the hot ceramic surface. The exact form of the catalysis equation needed to make temperature corrections was unknown, so thermocouples were first calibrated by comparing measurements from thermocouples to T_f measured via the calorimetric method, which utilized combustion efficiency, η_{comb} , (ARP 1533¹²) and adiabatic flame temperature, AFT, to calculate the temperature of a combustion process. Combustion efficiency was calculated as follows:

$$\eta_{\text{comb}} = 1 - \frac{10109EI_{\text{CO}} - EI_{\text{UHC}}}{\text{LHV } 1000} \quad (1)$$

Combustion temperature, then, was as follows:

$$T_f = \eta_{\text{comb}}(\text{AFT} - T_{\text{in}}) + T_{\text{in}} \quad (2)$$

This method was modified to account for measured reactor heat loss. In particular, the AFT term was corrected for heat loss using a curve-fit of heat loss as a function methane-air ϕ . In turn, a relation of heat loss as a function of T_f of any fuel was created. Finding the proper flame temperature to substitute for AFT in Eq. 2 required iteration, but these formulae converged quickly to yield final T_f .

Once the temperature of the flame was calculated via the calorimetric method, a form of the catalysis equation evolved that forced the uncorrected measured temperature to match that calculated above. For thermocouples coated with alumina ceramic, this was:

$$H_{\text{cat}} = 928,000S \exp\left(\frac{-11,000}{RT_{\text{measured}}}\right) \quad (3)$$

where S is thermocouple surface area. Recombination reactions have low (~ zero) activation energies. That a non-zero E was calculated suggests that a barrier to surface catalysis is provided by the ceramic. Fig. 2 shows temperature measurements taken via the calorimetric method and by corrected thermocouple measurements for several fuels at $\tau = 7.3$ msec.

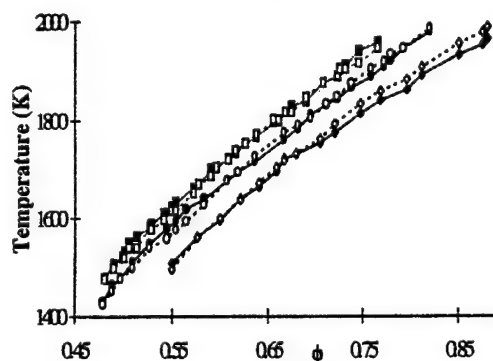


Fig. 2: Reactor temperature versus equivalence ratio for methane (diamond), ethylbenzene (square), and cyclohexane (circle). Solid symbol indicates measurement by corrected thermocouple, hollow symbol by calorimetric method.

The WSR was operated at atmospheric pressure. Air and gaseous flow rates to the WSR were measured via rotameters. In this facility, the air rotameter was rated at 0 to 600 slpm and fuel rotameter at 0 to 58 slpm range. Additionally, a rotameter was installed to meter nozzle air for delivery to an air-blast atomizer (see below), rated at 0 to 180 slpm.

A vaporizer was built to prevaporize liquid hydrocarbons, mix the vaporized hydrocarbon with air, and then supply this mixture to the WSR. A schematic of the vaporizer is shown in Fig. 3. The vaporizer design consisted of a 3 kW air heater (Hotwatt), pressurized fuel tank, vaporization chamber, various flowmeters, nozzle air line, safety devices, and a fuel atomization nozzle. Combustion air was metered through a rotameter and passed through a heater. This air was heated to a temperature sufficient to vaporize a hydrocarbon, but below autoignition temperature, measured by a Type K (chromel-alumel) thermocouple. This hot air was then injected into the vaporization chamber perpendicular to the hydrocarbon mist stream. This established a recirculation zone in the vaporizer to provide additional time for fuel vaporization.

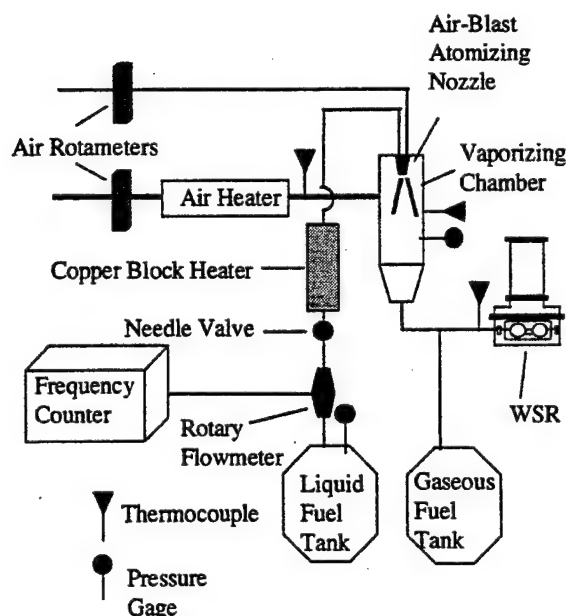


Fig. 3: Vaporizer system for study of liquid hydrocarbons.

Liquid hydrocarbons were contained in a five-gallon pressure tank charged to 60 psig with nitrogen.

Liquids were metered by a rotary flowmeter (Model E-15, Miniflow Systems, Inc.) and flowrate was varied by adjusting a needle valve. Liquid hydrocarbons were injected through an air-blast atomizing nozzle (Delavan Model 30609-2) into the high-temperature air stream in the vaporizer chamber. Vaporized hydrocarbons and air were transported through an insulated, heated line to the WSR. Also, a Type K thermocouple was inserted in the fuel/air mixture to monitor inlet temperature, and a second thermocouple was placed adjacent to the WSR jet ring to monitor fuel/air temperature just prior to injection into the reactor.

Residence time in the vaporizer was greater than 1.2 sec and was significantly greater than the vaporization time predicted for pure hydrocarbons (e.g. n-heptane 0.36 sec, Ballal and Lefebvre¹³). Additionally, this residence time provided insufficient time for cracking of hydrocarbons in the vaporizer (Stoffel and Reh¹⁴). When necessary, liquids were preheated prior to atomization via a copper block heater sandwiched on the fuel delivery tube.

Nominal reactor residence time, τ , was obtained via the following formula:

$$\tau = \frac{PV}{(R/M)T_r Q} \quad (4)$$

The above flow conditions permitted the operation of the reactor over the range of equivalence ratios $\phi = 0.43$ to 0.88, loading parameter $LP \sim 1$ g-mol/s*1*atm^{1.75}, residence times $\tau \sim 5$ to 8 ms and reactor temperatures $T_r = 1350$ to 2000 K. Hydrocarbons available for study in the WSR included: methane, ethane, cyclohexane, n-heptane, n-dodecane, toluene, ethylbenzene and a gaseous mix of 15 percent methane, 25 percent ethane, 60 percent ethylene by volume. Gaseous fuels were commercially pure grade, pure hydrocarbon liquids were spectroscopic grade (99+ percent).

Error Analysis

Gaseous fuel flow was monitored to within ± 2 percent of reading using a Gilmont rotameter. Air flow was monitored to within ± 2 percent of full scale using a Brooks rotameter. The combined error produced an uncertainty of ± 3.5 percent in ϕ during combustion of methane in air. Nozzle air was monitored to within ± 2 percent of full scale using a Gilmont rotameter. Liquid hydrocarbons were controlled to within ± 0.3 g/min by the liquid fuel

delivery system. The combined error produced an uncertainty of ± 3.5 percent during combustion of a liquid fuel in air. The T_f measurements were accurate to within ± 30 K. The Horiba emissions analyzers quote an accuracy to within 1 percent of full scale. For these WSR experiments, this represented an error of: 2 ppmV NO_x , 50 ppmV CO, 10 ppmV carbon for UHC, 0.25 percent O_2 , and 0.5 percent CO_2 . Residence time, τ , was typically controllable to within ± 0.6 ms. Additionally, CO measurements were repeatable from day to day within ± 100 ppmV, and NO_x within ± 1.5 ppmV. UHC measurements at very lean conditions suffered from poor repeatability due to variance in the LBO condition. This is discussed in detail in the CO and UHC measurements subsection.

Previous work (Blust et al.¹¹) has shown that the sampling system was capable of retaining approximately 99 percent of the CO concentration simulated to be the WSR product concentration at $\phi = 0.6$, $\tau = 7.0$ ms.

Test Conditions

The test matrix shown in Table 1 was conducted with the WSR. Emissions measurements were performed for all test conditions shown. A mix of 13 vol% CH_4 , 22 vol% C_2H_6 , 52 vol% C_2H_4 , 13 vol% C_7H_8 , $\text{CN} = 2.52$, $(\text{C}/\text{H})_{\text{mole}} = 0.5081$ was selected as simulant for heavy, aromatic-containing fuels that are

cracked using thermal or catalytic processes into light fractions with residual light aromatics. Additionally, several of the leanest conditions shown represented LBO, at which point bag sample emissions data were collected. This will be discussed in detail in later sections.

The Well Stirred Condition

In order for the WSR to be well mixed, the reactor must be both micromixed and macromixed. For micromixing to be successful, the turbulent mixing time of the combustion gas, t_m , must be less than the order of the fastest reactions occurring in the process. The turbulent mixing time in the reactor was calculated via turbulent theory (Nenniger¹⁵, Zelina and Ballal¹⁶) and compared to the reaction rate orders for methane at 1 atm estimated by Getz and Zabarnick¹⁷. Methane-air combustion at $\tau = 6.0$ msec, $T_f = 1747$ K, $\phi = 0.7$, $P = 1$ atm represents typical combustion conditions, during which $\tau_m = 19$ μsec . At similar conditions hydrocarbon reduction time is ~ 10 μsec , CO oxidation time is ~ 500 μsec , and NO_x formation time is ~ 20 msec. Accordingly, the WSR was perhaps not well mixed with respect to the initial reduction reactions of hydrocarbons, but was sufficiently well mixed for the oxidation reactions that subsequently occurred in the reactor.

Table 1: WSR Test Matrix

Hydrocarbon	τ (msec)	ϕ_{\min}	ϕ_{\max}	$T_{f\min}$ (K)	$T_{f\max}$ (K)
Methane	7.3	0.55	0.88	1507	1967
	6.32	0.59	0.83	1517	1918
Ethane	7.26	0.48	0.84	1407	1996
	7.47	0.48	0.82	1429	1981
Cyclohexane	5.22	0.51	0.78	1536	1922
	7.19	0.53	0.84	1517	1975
n-Heptane	5.49	0.54	0.81	1595	1974
	7.32	0.46	0.79	1499	1946
Toluene	5.35	0.5	0.78	1552	1936
	7.43	0.48	0.76	1478	1958
Ethylbenzene	5.33	0.49	0.67	1546	1839
	6.75	0.49	0.77	1530	2007
13 vol% Methane, 22 vol% Ethane, 52 vol% Ethylene, 13 vol% Toluene	5.17	0.46	0.76	1391	1969
n-Dodecane	7.39	0.46	0.8	1357	1979
	5.2	0.55	0.79	1581	1983

Successful macromixing necessitates the WSR having the proper residence time distribution (RTD), and spatial homogeneity of species and temperature. To test RTD, Calo, et al.¹⁸ injected various pulse times and concentrations of krypton tracer into the WSR jet ring during methane-air combustion ($\tau = 11.6$ msec, $T_f = 1754$ K, $\phi = 0.7$, $P = 1$ atm). Krypton concentration versus time for each pulse was monitored by a free-jet, molecular beam mass spectrometer (Ballenthin, et al.¹⁹) pulling sample from the WSR through an air-cooled quartz probe. A significant amount of pulse dispersion occurred in the jet ring, and this had to be accounted for prior to examining the reactor RTD. Ultimately, it was found that the measured RTD, adjusted for jet ring dispersion, exhibited the exponential growth and decay patterns typical of an inert pulse tracer in a stirred reactor. Spatial homogeneity was previously demonstrated by Zelina²⁰. Maximum detected variabilities were: $T_f = \pm 25$ K, $\text{NO}_x = \pm 2.5$ ppmV, $\text{CO} = \pm 90$ ppmV. These variabilities were approximately the same as the day to day repeatability in the WSR system, and may account for the repeatability limits. Thus, the WSR was successfully macromixed.

Calculations

To anchor the present results the methane experimental data were compared to calculations for a PSR using the GRI. 2.1 reaction mechanism. The algorithm used for the solution of a system of non-linear, stiff, ordinary differential kinetics equations is CREK (Pratt and Wormeck²¹). This algorithm is incorporated in a reactor network code (Pratt and Pratt²²). The calculations and measurements for NO_x , CO , CO_2 , O_2 , and H_2O vapor were in close agreement. This agreement commented favorably on the high degree of mixing attained in the WSR, and successful operation of the sampling and temperature measurement systems.

Results and Discussion

Often, emissions concentrations are expressed by emissions index, EI. For EI calculation, all UHC is treated as methane, and NO_x as NO_2 . All emissions are stated on dry basis.

Temperature Measurements

Measured T_f (via thermocouple) is plotted against ϕ for several hydrocarbons at $\tau \sim 7.3$ ms in Fig. 4. Also plotted are the equilibrium flame temperatures

versus ϕ (Gordon and McBride²³). Two observations were made with respect to this figure.

(i) Measured temperatures for a specific hydrocarbon never reach the corresponding equilibrium flame temperature because the reactor residence time was short enough that the products did not reach their equilibrium concentrations. Observed η_{comb} was less than equilibrium η_{comb} and measured T_f was lower than equilibrium flame temperature. Additionally, the WSR was not adiabatic. Heat loss of 3 to 5 percent was typical.

(ii) The measured temperature curves were concave down, with the measured temperature departing the equilibrium line more at low and high ϕ than in the middle. This reflected changes in η_{comb} for each hydrocarbon with respect to ϕ .

Lean Blow-Out

In aero and industrial combustors, flame stabilization is essential to combustor performance and safety. Combustion must be sustained over a wide range of operating conditions, and so it is essential to designers to know the stability limits of a fuel under realistic conditions. In practical combustors stability is provided by the primary zone. It has been proposed (Avery and Hart²⁴; Bragg²⁵; Childs²⁶) that the primary zone of a gas turbine combustor could be modeled as a stirred reactor. To this end the WSR was used as a flameholder to maintain lean combustion and measure the LBO limits of fuels.

Defining unstable combustion and LBO limit in the WSR was difficult. No optical access was provided by the toroidal design, so temperature was used as the primary method of detecting LBO. In particular for this experiment, LBO was defined as the condition characterized by a rapid, large magnitude drop in temperature, and preceded by substantial increase in UHC and noise, as ϕ was decreased while maintaining constant τ .

At LBO, it was of interest to measure T_f , ϕ , EI of CO and UHC, and flow rates of reactants and thus to calculate η_{comb} and loading parameter (LP). Loading parameter is an expression of the maximum heat release capability of a fuel per volume of reactor and pressure to the n-th power. LBO ϕ from several hydrocarbons are plotted against LP in Fig. 5.

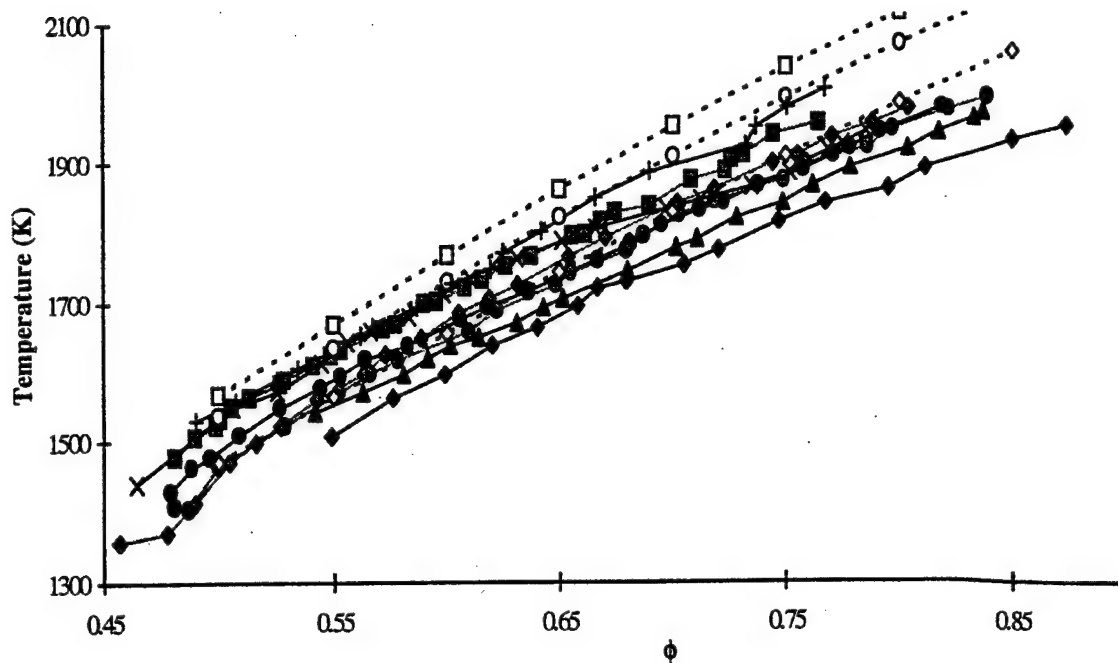


Fig. 4: Reactor temperature versus equivalence ratio for several hydrocarbons at nominal residence time 7.3 msec: methane (black diamond), ethane (gray circle), cyclohexane (black circle), n-heptane (black triangle), n-dodecane (gray diamond), toluene (X), ethylbenzene (gray square), cracked fuel simulant (+). Also shown (hollow symbols) are equilibrium methane, cyclohexane, and ethylbenzene (Gordon and McBride²³).

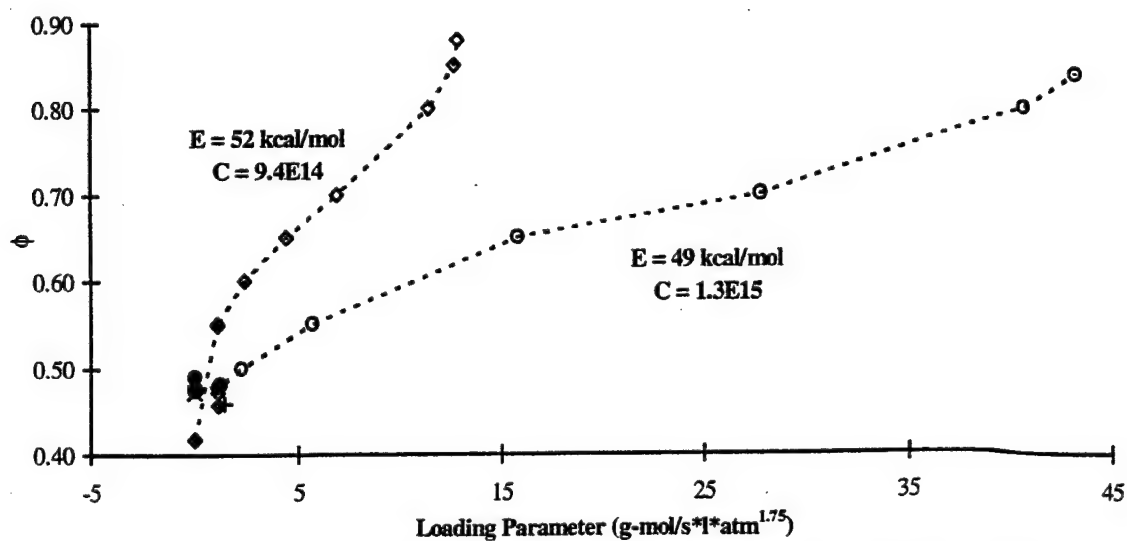


Fig. 5: Equivalence ratio versus loading parameter at LBO for several hydrocarbons: methane (black diamond), ethane (gray circle), cyclohexane (black circle), n-dodecane (gray diamond), toluene (X), cracked fuel simulant (+). Also shown (dotted lines) are calculated methane and ethane stability loops.

When available, LBO limits for each hydrocarbon as measured in a vertical glass tube experiment (Lefebvre²⁷, except cyclohexane from Lewis and von Elbe²⁸) are included in this figure, with these lean limits modified for T_{in} by the Burgess-Wheeler law (Lefebvre²⁷). In this formula, measured jet ring temperature T_{jr} was substituted for T_{in} to give the following form:

$$\begin{aligned} \text{LBO (percent V in air)} \\ = \text{LBO}_{298K} \left[1 - \frac{0.75(T_{jr} - 298)}{\text{LBO}_{298K} \text{LHV (kcal/mol)}} \right] \end{aligned} \quad (5)$$

Flow of reactants in the glass tube was zero, so the LP of these LBO limits was zero.

LBO equivalence ratios from the vertical tube experiment were comparable to LBO equivalence ratios as measured in the WSR for most hydrocarbons, methane being an exception. This indicated that methane, for instance, possesses a significantly different stability loop from ethane, cyclohexane and toluene. To demonstrate this, the calculated stability loops of methane and ethane are also plotted on Fig. 5.

Stability theory has been described in detail elsewhere (Lefebvre²⁷; Zelina²⁰). In this theory, the rate of reaction between fuel and air is expressed by the material balance equation:

$$\eta_{\text{comb}} \phi Q = C V T_f^{1/2} \exp(-E/RT_f) \rho^n x_f^m x_o^{n-m} \quad (6a)$$

where $n = 1.75$, $m = 0.75$, x is the mole fraction of fuel or air and C is the molecular collision factor calculated as follows (Kanury²⁹):

$$C = \frac{RT_f^{1/2}}{hA} \exp\left(\frac{\Delta s^*}{R}\right) \quad (6b)$$

where h is Planck's constant, A is Avagadro's number, and Δs^* is the entropy change between the states of activated complex and initial reactants. For lean mixtures, Eq. (6a) is written as:

$$LP = \frac{Q}{VP^n} = \exp\left(\frac{E}{RT_f}\right) \frac{C x_f^{0.75} x_o}{T_f^{1.25} \eta_{\text{comb}} \phi R^{1.75}} \quad (6c)$$

Thus,

$$E = RT_f \ln\left(\frac{C x_f^{0.75} x_o}{LP T_f^{1.25} \eta_{\text{comb}} \phi R^{1.75}}\right) \quad (6d)$$

Entropy of the activated complex in Eq. (6b) was found by applying a quantity of energy equal to E to the energy of reactants and evaluating entropy at this condition. Thus, to calculate C and E required iteration between Eqs. (6b) and (6d). The stability curves in Fig. 5, then, were generated by varying ϕ in Eq. (6c), using the measured T_f for each ϕ , including non blow-out conditions, but using η_{comb} corresponding to that measured at LBO.

Using the above analysis, for methane $E = 52$ kcal/mole and $C = 9.4 \times 10^{14} \text{ K}^{1/2} \text{ sec}^{-1}$; for ethane $E = 49$ kcal/mole and $C = 1.3 \times 10^{15} \text{ K}^{1/2} \text{ sec}^{-1}$. Note that the activation energy calculated for methane is much greater than that calculated for surface catalysis, Eq. (3).

It is important to note, however, that LBO is a "soft" limit; that is, a great amount of hysteresis exists in the limit. If LBO is attempted after the reactor has been burned very hot, the mixture is capable of burning at leaner conditions than if the limit is approached from a cooler operating condition. A variance in T_{jr} of ± 50 K has been measured, depending on the temperature at which the reactor is run, and for how long that condition is sustained. Using Eq. (4), this corresponds to an uncertainty in the LBO ϕ of ± 0.02 .

CO₂ and O₂ Measurements

In a WSR operating in the stable mode, CO₂ concentration should peak and oxygen concentration should drop to near zero at stoichiometric equivalence ratio. Fig. 6 shows measured CO₂ and O₂ concentrations (vol%) as a function of equivalence ratio from several hydrocarbons. Also plotted are calculated equilibrium values for cyclohexane-air combustion. As expected, CO₂ increased and O₂ decreased as ϕ approached unity.

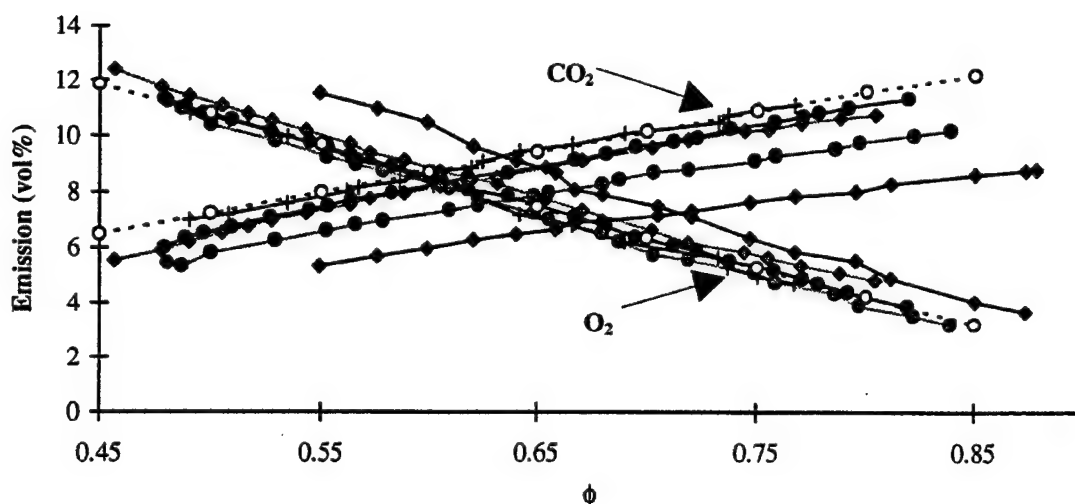


Fig. 6: CO_2 and O_2 concentration versus equivalence ratio for several hydrocarbons at nominal residence time 7.3 msec: methane (black diamond), ethane (gray circle), cyclohexane (black circle), n-dodecane (gray diamond), toluene (X), cracked fuel simulant (+). Also shown (hollow circle) is equilibrium cyclohexane (Gordon and McBride²³).

CO and UHC Measurements

CO and UHC emissions are important because they also represent a direct measure of combustion inefficiency (see Eq. (1)). If the combustion zone operates fuel-rich, has inadequate mixing, or is quenched by cold air, large quantities of CO (which is relatively resistant to oxidation) will be emitted due to the lack of oxygen needed to complete the reaction to CO_2 , or insufficient time being provided for CO to be oxidized. UHC emissions include fuel which emerges from the combustor exit in the form of condensate or vapor, and the products of the thermal degradation of the parent fuel into species of lower molecular weight, such as methane, acetylene, ethylene and propylene. UHC emissions are associated with poor atomization, inadequate burning rates, insufficient residence time and premature quenching. Thus, it is desirable to find combustor operating conditions that minimize the emission of CO and UHC, and therefore maximize combustion efficiency.

Clearly, operating the WSR fuel-rich will produce great amounts of CO and UHC. Although rich combustion is interesting for studying reaction chemistry, it is not interesting from an engine standpoint unless a lean afterburning approach is taken (as in a Rich, Quench, Lean combustor). This paper will focus, then, on lean combustion, and locating operating conditions that minimize CO and UHC production.

Fig. 7 shows emissions index of CO from several hydrocarbons at several T_f plotted as a function of carbon number at residence time of 7.3 ms. Alkanes and aromatics are plotted separately, and cracked fuel simulant is treated as an alkane. All hydrocarbons in general exhibited a U-shaped trend in CO production. As temperature increased, CO concentration first decreased as reaction rate of CO consumption increased. A minimum of CO was reached, then CO increased as temperature increased. This increase was due to an increased rate of CO_2 dissociation.

As shown in Fig. 7, alkanes, *sans* methane, displayed a slight increase in CO as carbon number increased. This increase was modest, and discontinued for $\text{CN} > 7$ (depending on the temperature this trend was occasionally reversed for $\text{CN} > 7$). Increasing molecular weight from one heavy alkane to another (i.e. from n-heptane to n-dodecane) did not result in increase in CO. Aromatics showed a reverse trend from alkanes, with a decrease in CO being observed in general as CN increased from 7 to 8. Finally, methane produced more CO than all other hydrocarbons investigated. This distinction for methane is somewhat artificial due to the definition of emissions index. By ppmV, CO in the sample from methane is not so high. However, the low molecular weight of methane biases the EI high.

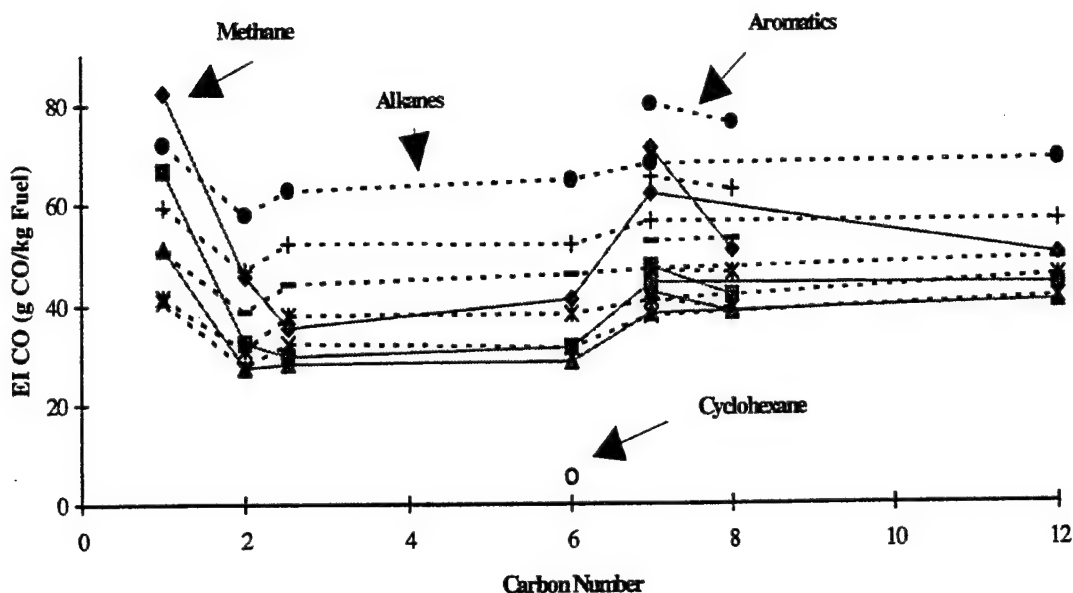


Fig. 7: Emissions indices of CO versus carbon number for several hydrocarbons at nominal residence time 7.3 msec at several temperatures: 1550 K (diamond), 1600 K (square), 1650 K (triangle), 1700 K (X), 1750 K (star), 1800 K (dash), 1850 K (+), 1900 K (black circle). Also shown (hollow circle) is equilibrium cyclohexane at 1900 K (Gordon and McBride²³).

Also shown in Fig. 7 is the corresponding equilibrium concentration of CO from cyclohexane at 1900 K. As shown, measured CO values were much higher than equilibrium because reactor residence time was less than the time required for oxidation of CO. The CO concentration from equilibrium calculations increased at high temperatures due to CO₂ dissociation, and this was also observed in the measured CO concentrations.

The slow oxidation of CO suggests that changing residence time in the reactor will affect the measured CO. Fig. 8 shows profiles of CO (ppmV) versus T_f from several hydrocarbons at 7.3 and 5.3 msec residence times (methane $\tau = 7.3$ or 6.3 msec). As shown, decreasing residence time increased CO. Also, at higher temperatures the longer and shorter residence time CO profiles tended to converge, indicating that the CO₂ dissociation rate proceeded faster than the CO oxidation under these conditions. A similar trend of decreasing CO with increased residence time was found by Steele³⁰.

However, it must be noted that temperature produces the greatest effect on CO production from fuels. Thus, it is important to find at what temperature the minimum amount of CO is produced from each

hydrocarbon, and to find a predictive method to finding the temperature for minimal CO production from any fuel. Because liquid hydrocarbons are preheated more than gaseous fuels, Fig. 9 shows the temperature at which CO minima occur corrected for preheat versus carbon number of each hydrocarbon. This correction was made as follows:

$$T_{\text{correct}} = T_f - (T_{\text{in}} - 296) \quad (7)$$

This figure shows that as the carbon number of the fuel was increased the temperature at which CO minima occur decreased. Also, the figure shows that the rule applied to alkanes and aromatics, with cracked fuel simulant classified as an alkane. Within the uncertainty of T_f , all the data points in Fig. 9 can be approximated together as a line of the following form:

$$T_{\text{CO min correct}} = -11.35 \cdot \text{CN} + 1713 \quad (8)$$

Caution should be exercised in generalizing results of Eq. (8) to all combustors. The WSR represents a system with excellent mixing and minimal wall quenching and heat loss. A system with cold walls, for instance, would display a CO minimum at higher temperature than when the walls are hot. Also, Eq. (8) was derived from $\tau \sim 7.3$ msec data. Reducing

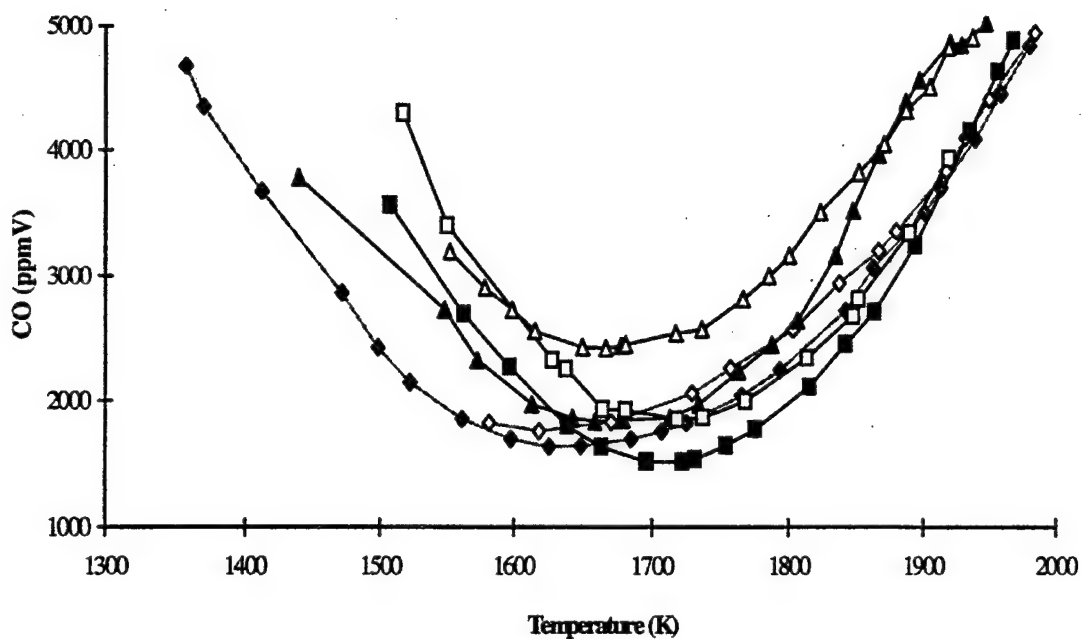


Fig. 8: CO versus reactor temperature. For methane (square), nominal residence time is 7.3 msec (solid symbol) or 6.3 msec (hollow symbol). For n-dodecane (diamond), and toluene (triangle), nominal residence time is 7.3 msec (solid symbol) or 5.3 msec (hollow symbol).

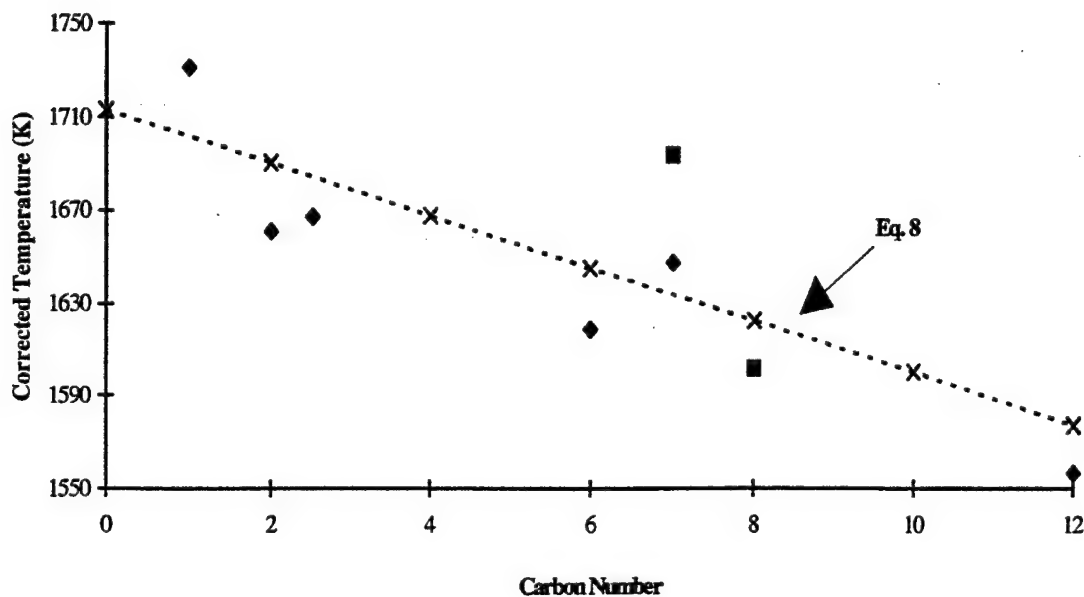


Fig. 9: Corrected temperatures of CO emissions index minima versus carbon number of hydrocarbon for alkanes (diamond) and aromatics (square). Also included (dotted line) is calculated relation of CO minima to carbon number, Eq. (8).

residence time tends to increase the temperature at which minima occur.

Fig. 10 shows emissions index of UHC from several hydrocarbons at several T_f plotted as a function of carbon number at residence time of 7.3 msec. All hydrocarbons in general produced only trace quantities of UHC at temperatures above 1600 K (for $\phi < 1$). At $T_f < 1600$ K, however, a rapid increase in UHC occurred, suggesting the reactants were approaching LBO, and insufficient residence time existed for complete oxidation at these lower temperatures.

As shown in Fig. 10, alkanes showed a rapid decrease, then modest increase in UHC as carbon number increased. High UHC of methane reflected the hydrocarbons's narrow stability loop (see Lean Blow-Out), with ethane behaving more like other alkanes. Toluene produced more UHC at a given temperature than other hydrocarbons besides methane, suggesting that this hydrocarbon did not oxidize rapidly at low temperature. Conversely, ethylbenzene produced UHC more equivalent to alkanes of the same carbon number.

Equilibrium calculations predicted no UHC in the sample, and for $T_f > 1600$ K, this was also observed in the WSR. However, at lower temperatures complete oxidation proceeded slowly, and the residence time was

less than required to approach equilibrium. The slow oxidation of fuel at low temperatures suggests that change in residence time while $T_f < 1600$ K will affect measured UHC. Fig. 11 shows profiles of UHC (ppmC) versus T_f from methane at 7.3 and 6.3 msec residence times, and cyclohexane at 7.5 and 5.2 msec residence times. As with CO, decreasing residence time increased UHC.

Composition of UHC at LBO from several hydrocarbons is compared in Table 2. That ethylene was the major component of UHC from lean alkane combustion is not surprising. Literature has suggested that ethylene is the most abundant intermediate hydrocarbon product from n-heptane (Maurice³¹), and the mechanisms for combustion of other alkanes are similar. Conversely, acetylene was the most abundant UHC component from toluene. Acetylene is a product of the decomposition of benzene, which itself is a common product of the decomposition of toluene. As a result, trace amounts of C6 were also identified in the UHC mixture from toluene. The cracked fuel simulant behaved more like an alkane than aromatic with regard to components in the UHC mixture. Also, the UHC species from all hydrocarbons in general were less saturated and of lower molecular weight than the parent fuel.

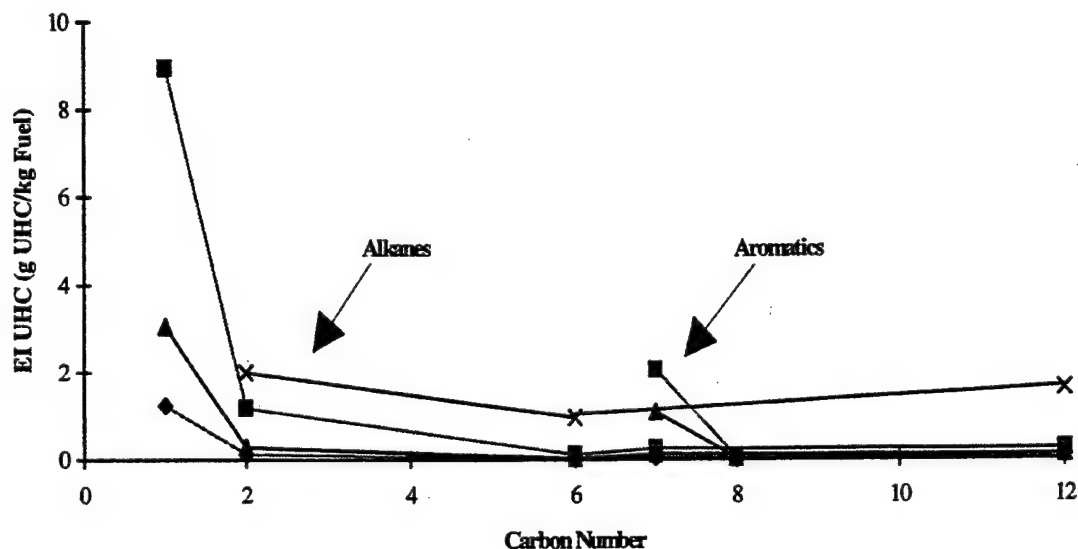


Fig. 10: Emissions indices of UHC versus carbon number for several hydrocarbons at nominal residence time of 7.3 msec at several temperatures: 1450 K (X), 1500 K (square), 1550 K (triangle), 1600 K (diamond).

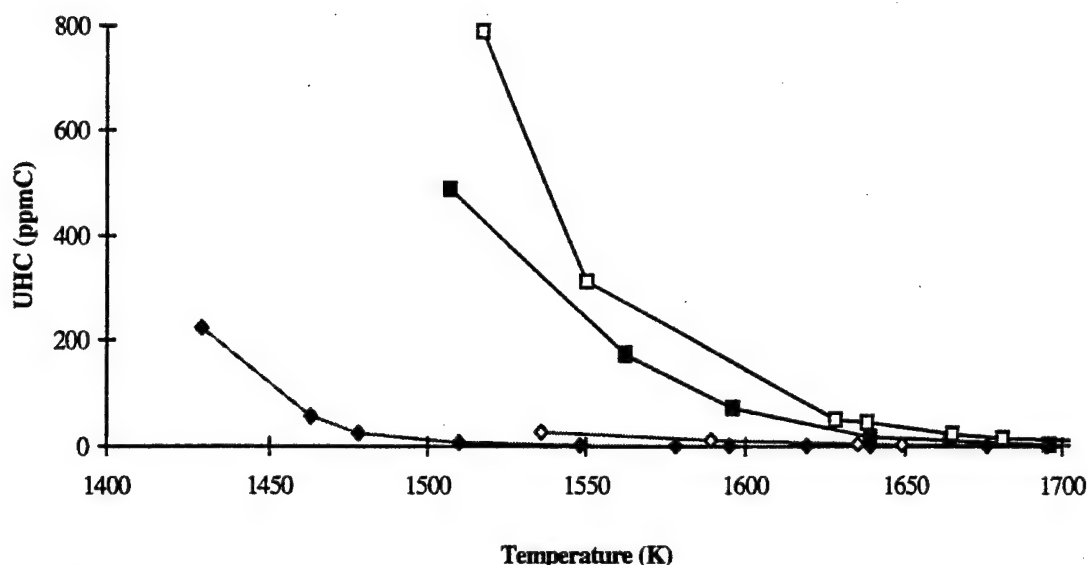


Fig. 11: UHC versus reactor temperature. For methane (square), nominal residence time is 7.3 msec (solid symbol) or 6.3 msec (hollow symbol). For cyclohexane (diamond), nominal residence time is 7.5 msec (solid symbol) or 5.2 msec (hollow symbol).

Table 2: Effluent Hydrocarbon Species by Percent Volume of UHC

Hydro-carbon	CH ₄	C ₂ H ₄	C ₂ H ₆	C ₂ H ₂	C ₃ H ₆	C ₄	C ₅	C ₆	τ (msec)	ϕ	T _f (K)
Toluene	27	15	0	56	0	0	0	3	7.56	0.46	1439
Cyclohexane	30	49	12	9	0	0	0	0	6.83	0.51	1513
Ethane	20	40	40	0	0	0	0	0	6.95	0.48	1407
13 vol% Methane, 22 vol% Ethane, 52 vol% Ethylene, 13 vol% Toluene	23	58	16	3	0	0	0	0	5.96	0.46	1391
n-Dodecane	19	60	6	2	6	3	2	2	7.71	0.46	1357

As previously mentioned, hysteresis occurred in LBO ϕ in the reactor. As a consequence of this, UHC measurements suffer from a great amount of uncertainty at LBO. A difference in ϕ of ± 0.02 near blow-out can result in an order of magnitude difference in UHC concentration.

NO_x Measurements

In the study of NO_x emissions, the formation of species such as NO and NO₂ is a complex function of temperature, residence time, equivalence ratio, and detailed chemical kinetics, a better understanding of which would help designers of combustion devices to

limit NO_x production without compromising combustion efficiency. An understanding of the chemical pathways responsible for NO_x production in a combustion environment with heavy hydrocarbons is becoming possible. The relative roles of the thermal NO (Zeldovich) mechanism, super-equilibrium effects, prompt NO mechanism, N₂O mechanism, and fuel nitrogen mechanisms are suggested by other researchers for some fuels (Capehart et al.⁵; Nicol³²; Steele³⁰). The present work is an extension and verification of these earlier efforts.

Emissions indices of NO_x versus T_f from several hydrocarbons at nominal residence time of 7.3 msec are plotted in Fig. 12. Equilibrium NO_x concentrations were not shown because NO_x chemistry is slow and insufficient residence time is generally available in the WSR to allow NO_x concentration to approach equilibrium values. NO_x emissions from all hydrocarbons exhibited the same basic trend. As temperature increased, a slight decrease in NO_x emissions was detected. Elevated NO_x at near blow-out conditions was in general attributed to the N_2O mechanism. Then, NO_x increased as temperature increased, first gradually, then rapidly for $T_f > 1800$ K. This response was generally attributed to the Extended Zeldovich NO mechanism.

Below 1800 K, the curves overlapped enough to be indistinguishable from one another. For $T_f > 1800$ K, though, the NO_x emissions rapidly increase with increasing T_f . At the high T_f regime, normal paraffins in general produced less NO_x than aromatics and cyclohexane. Cracked fuel simulant produced more NO_x than other hydrocarbons.

The slow formation rate of NO_x suggests that changing residence time in the reactor will affect the

measured NO_x . Fig. 13 shows profiles of NO_x (ppmV) versus T_f from several hydrocarbons at 7.3 and 5.3 msec residence times. As shown, increasing residence time increased NO_x . Capehart³³ has suggested a linear increase in NO_x with time. For n-dodecane, this formula is shown in Eq. (9)

$$\text{NO}_x = \left(\frac{20.95 - [\text{O}_2]}{20.95 - 15} \right) 63,523\tau \exp\left(\frac{-18,776}{T}\right) \quad (9)$$

Data to suggest E and k of Eq. (9) were acquired in a jet-stirred reactor of $\tau \sim 3.3$ msec, and extrapolation of this work to 5.3 msec proved satisfactory, as shown in Fig. 13. However, Eq. (9) estimated high compared to measured NO_x at $\tau = 7.3$ msec. The present work suggests the following equation for n-dodecane:

$$\text{NO}_x = \left(\frac{20.95 - [\text{O}_2]}{20.95 - 15} \right) 690,000\tau^{1/2} \exp\left(\frac{-22,100}{T}\right) \quad (10)$$

A $\tau^{1/2}$ relation of residence time to NO_x emissions is suggested in Eq. (10) for n-dodecane, the results of which are shown in Fig. 13.

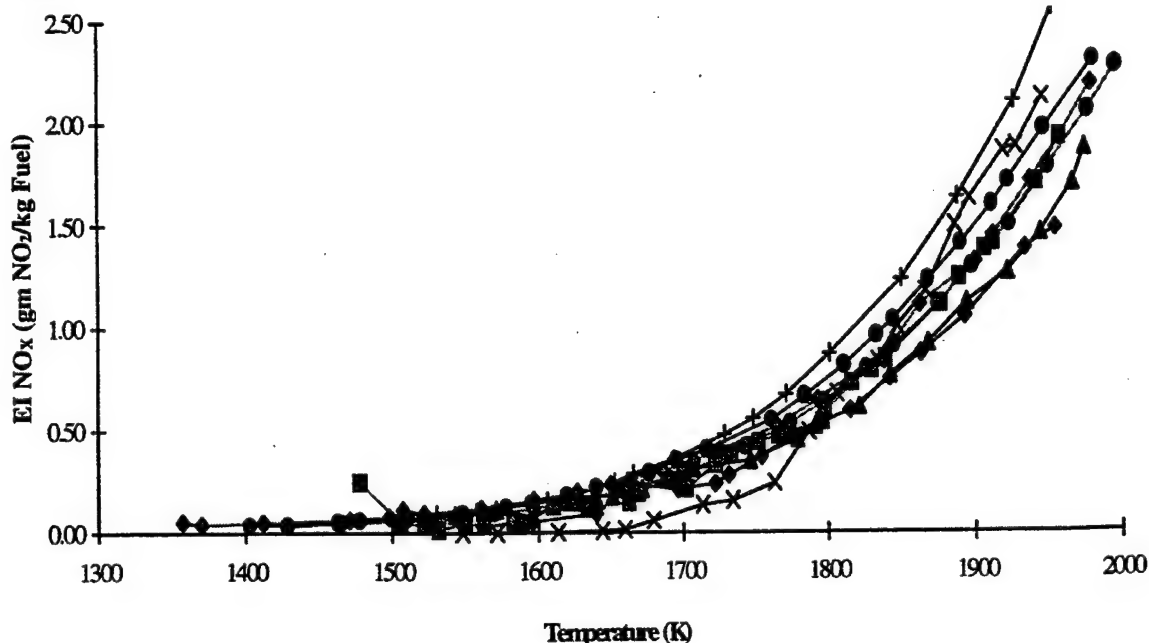


Fig. 12: Emissions indices of NO_x versus reactor temperature for several hydrocarbons at nominal residence time 7.3 msec: methane (black diamond), ethane (gray circle), cyclohexane (black circle), n-heptane (black triangle), n-dodecane (gray diamond), toluene (X), ethylbenzene (gray square), cracked fuel simulant (+).

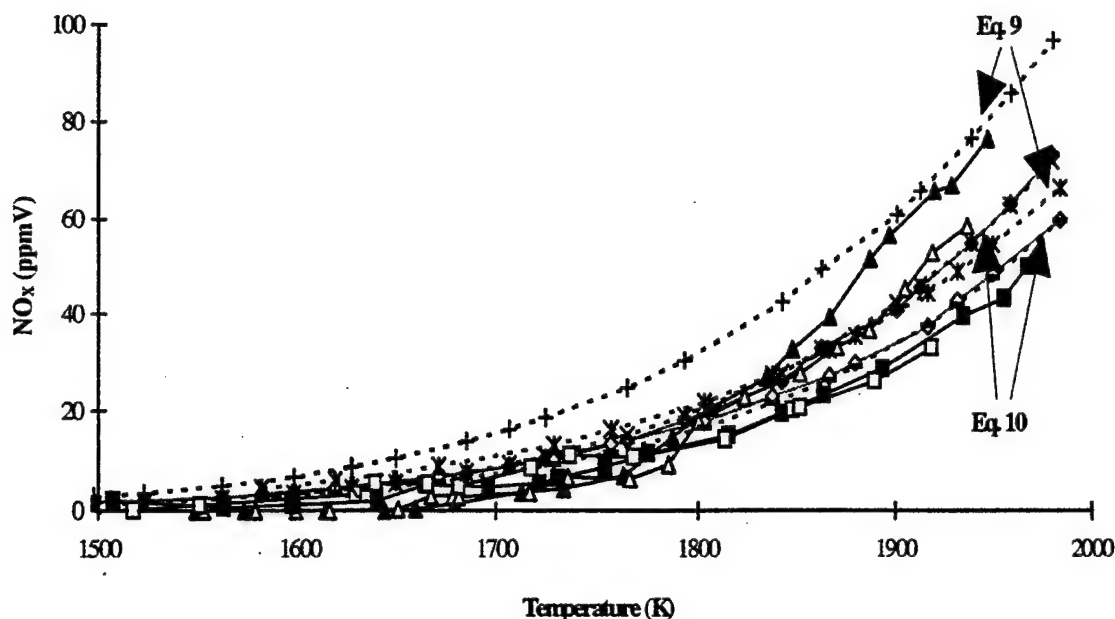


Fig. 13: NO_x versus reactor temperature. For methane (square), nominal residence time is 7.3 msec (solid symbol) or 6.3 msec (hollow symbol). For n-dodecane (diamond), and toluene (triangle), nominal residence time is 7.3 msec (solid symbol) or 5.3 msec (hollow symbol). Also included (dotted line) are estimates for n-dodecane by Capehart³⁵ for 7.3 msec (+), 5.3 msec (star) and estimates (Eq. (10)) for 7.3 msec (X) and 5.3 msec (dash).

Researchers (Bahr³⁴; Zelina et al.⁸) have previously suggested that NO_x increases with increase in (C/H) mole ratio. In the present work, EI NO_x from several hydrocarbons at $T_f = 1800$ K and 1950 K were plotted vs. (C/H) mole ratio, with alkanes and aromatics plotted separately. Fig. 14 shows the result. Scatter existed in the trends, but the hydrocarbons exhibit a general increase in EI NO_x as (C/H) mole ratio increased. Further, the trend became more apparent at higher temperature. This evidence suggests that designers should be concerned about the effect decreasing hydrogen content in a fuel could have on NO_x emissions from combustors.

Conclusions

A toroidal WSR which represents a laboratory idealization of an efficient, highly compact primary zone of a gas turbine combustor was used to study lean blow-out limits and emissions from several pure hydrocarbons. A number of conclusions were drawn from the present work:

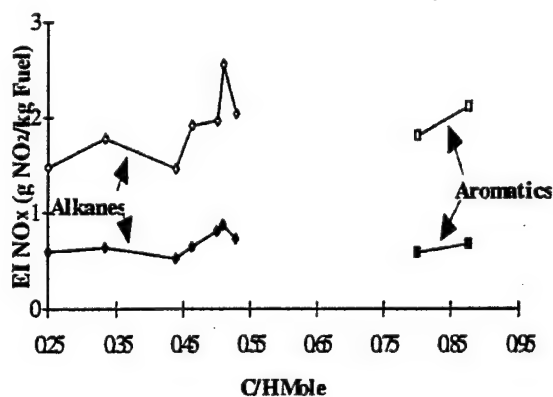


Fig. 14: Emissions indices of NO_x versus (C/H) mole ratio of hydrocarbon for alkanes (diamond) and aromatics (square) at 1800 K (solid symbol) and 1950 K (hollow symbol).

1. All hydrocarbons except methane showed lean limits of $\phi \sim 0.47$ with $\text{LP} \sim 1 \text{ g-mol/s} \cdot \text{atm}^{1.75}$ (methane LBO was $\phi \sim 0.55$ at similar LP). Global activation energies and collision factors were calculated via stability theory to be $E = 52 \text{ kcal/mole}$

and $C = 9.4 \cdot 10^{14} \text{ K}^{1/2} \text{ sec}^{-1}$ for methane; $E = 49 \text{ kcal/mole}$ and $C = 1.3 \cdot 10^{15} \text{ K}^{1/2} \text{ sec}^{-1}$ for ethane.

2. Hydrocarbons of different structure and carbon number produced different amounts of CO at the same temperature and residence time. To a limited degree, alkanes produced more CO as carbon number increased. This ceased to be true for $CN > 7$, nor was this true for methane, which produced high EI of CO due to the hydrocarbon's low molecular weight. Toluene produced more CO than ethylbenzene; the latter behaved more as an alkane than as toluene.

3. Reactor residence time affected CO production. In general, increasing residence time decreased the production of CO. Additional time enabled CO to be more completely oxidized. At $T_f > 1850 \text{ K}$, CO from longer and shorter residence time experiments tended to converge, indicating that CO_2 dissociation reactions were competing with the oxidation of CO.

4. A linear relationship was found for the temperature at which CO approaches minimum production versus the carbon number of the fuel. This relationship was consistent for alkanes and aromatics.

5. UHC production from alkanes at a given temperature decreased greatly from methane to ethane, but increased slightly for high carbon number hydrocarbons (i.e. n-dodecane). Toluene produced more UHC than alkanes at the same temperature (including n-heptane with the same carbon number) indicating that toluene oxidized poorly at low temperature. Ethylbenzene behaved as an alkane with respect to UHC production.

6. For $T_f < 1600 \text{ K}$, residence time affected UHC production. In general, increasing residence time decreased the production of UHC. Additional time enabled UHC to be more completely oxidized.

7. Governing mechanisms of NO_x production changed as temperature increased. At $T_f < 1500 \text{ K}$, the N_2O mechanism was suggested to account for measured NO_x . At $T_f > 1800 \text{ K}$, the Extended Zeldovich mechanism accounted for most NO_x produced. For $T_f > 1800 \text{ K}$, hydrocarbons of different structure and carbon number produced different amounts of NO_x at the same residence time. Under these conditions, normal paraffins produced less NO_x than cyclohexane and aromatics.

8. Increasing residence time increased NO_x production. A square root relationship of NO_x production versus residence time was suggested for n-dodecane. Additionally, a modest increase in NO_x with an increase in the (C/H) mole ratio was detected for several hydrocarbons.

Acknowledgment

This work is supported by the Air Force Wright Laboratory, Aeropropulsion and Power Directorate, Wright Patterson Air Force Base, OH, under contract F33615-92-C-2207, with Mr. Charles W. Frayne serving as technical monitor. The authors are grateful to Mr. Rich Striebich for providing assistance with the GC-FID analysis, and Mr. Matthew Getz for providing technical assistance.

References

1. Marek, C. J., and Papathakos, L. C., "Exhaust Emissions from a Premixing, Prevaporizing Flame Tube Using Liquid Jet A Fuel," *NASA TM X-3383*, 1976.
2. Mularz, E. J., "Lean, Premixed, Prevaporized Combustion for Aircraft Gas Turbine Engines," *NASA TM-79148*, 1979.
3. Sturgess, G. J., "Assessment of an Abbreviated Jet A/IP-5/IP-8 Reaction Mechanism for Modeling Gas Turbine Engine Gaseous Emissions," *AIAA Paper No. 97-2709*, 1997.
4. Brezinsky, K., Litzinger, T. A., and Glassman, I., "The High Temperature Oxidation of the Methyl Side Chain of Toluene," *International Journal of Chemical Kinetics*, Vol. 16, pp. 1053-1074, 1984.
5. Capehart, S. A., Lee, J. C. Y., Williams, J. T. and Malte, P. C., "Effect of Fuel Composition on NO_x Formation in Lean Premixed Prevaporized Combustion," *ASME Paper No. 97-GT-336*, 1997.
6. Dagaut, P., Reuillon, M., and Cathonnet, M., "Experimental Study of the Oxidation of n-Heptane in a Jet Stirred Reactor from Low to High Temperature and Pressures up to 40 Atm," *Combustion and Flame*, Vol. 101, pp. 132-140, 1995.
7. Vaughn, C. B., Howard, J. B., and Longwell, J. P., "Benzene Destruction in Fuel Rich Jet-Stirred Combustion," *Combustion and Flame*, Vol. 87, pp. 278-288, 1991.

8. Zelina, J., Blust, J. W., and Ballal, D. R., "Combustion of Liquid Fuels in the Well Stirred Reactor," *ASME Paper No. 96-GT-047*, 1996.
9. Nenniger, J. E., Kridiotis, A. C., Chomiak, J., Longwell, J. P., Sarofim, A. F., "Characterization of a Toroidal Well-Stirred Reactor," *Twentieth Symposium (International) on Combustion, The Combustion Institute*, pp. 473-479, 1984.
10. Zelina, J., and Ballal, D. R., "Combustion Studies in a Well Stirred Reactor", *AIAA Paper No. 94-0114*, 1994,
11. Blust, J. W., Getz, M. G., and Zabarnick, S., "Probe Design Optimization for the Well Stirred Reactor," *AIAA Paper No. 97-0907*, 1997.
12. Aerospace Recommended Practice 1533, "Procedure for the Calculation of Gaseous Emissions from Aircraft Turbine Engines," *Society of Automotive Engineers, Inc.*, Warrendale, PA, pp. 1-36, 1994.
13. Ballal, D. R. and Lefebvre, A. H., "Ignition and Flame Quenching of Flowing Heterogeneous Fuel-Air Mixtures," *Combustion and Flame*, Vol. 35, pp. 155-168, 1979.
14. Stoffel, B., and Reh, L., "Conversion of Liquid to Gaseous Fuels for Lean Premixed Combustion," *ASME Paper No. 95-GT-412*, 1995.
15. Nenniger, J. E., "Polycyclic Aromatic Hydrocarbon Production in a Jet-Stirred Combustor," *Doctor of Science Thesis*, Massachusetts Institute of Technology, 1983.
16. Zelina, J., and Ballal, D. R., "Emissions Studies in a Well-Stirred Reactor and Applications to Combustion Modeling," *Proceeding of FACT, Vol. 21, ASME (Int.) Joint Power Generation Conference*, pp. 255-263, 1996.
17. Getz, M. G., and Zabarnick, S., internal communication, 1997.
18. Calo, J. M., Miller, T., Ballenthin, J. O., Striebich, R., Blust, J., and Getz, M., "The Residence Time Distribution (RTD) of the Well-Stirred Reactor (WSR)," to be published as USAF technical report, 1997.
19. Ballenthin, J. O., Miller, T., Calo, J. M., Striebich, R., Blust, J., and Getz, M., "Free-Jet, Molecular Beam Mass Spectrometer System for Monitoring the Gas-Phase Composition in a Well-Stirred Combustor," *Fifth International Congress on Toxic Combustion Byproducts.*, 1997.
20. Zelina, J., "Combustion Studies in a Well-Stirred Reactor," *Doctor of Science Thesis*, University of Dayton, 1995.
21. Pratt, D. T., and Wormeck, J. J., *CREK*, a computer program for calculation of combustion reaction equilibrium and kinetics in laminar or turbulent flow, 1976.
22. Pratt, B. S., and Pratt, D. T., *MARK2X* Computer Code, private communication, 1990.
23. Gordon S., and McBride, B. J., "Computer Program for Calculation of Complex Chemical Equilibrium Compositions, Rocket Performance, Incident and Reflected Shocks, and Chapman-Jouget Detonations" (NASA, Washington D. C.), *SP-273 Interim Revision*, 1976.
24. Avery, W. H., and Hart, R. W., "Combustor Performance with Instantaneous Mixing," *Ind. End. Chem.*, Vol. 45, No. 8, pp. 1634-1637, 1953.
25. Bragg, S. L., "Application of Reaction Rate Theory to Combustion Chamber Analysis" *ARC 16170*, Aeronautical Research Council, England, 1953.
26. Childs, J. H., "Preliminary Correlation to Efficiency of Aircraft Gas-Turbine Combustors for Different Operating Conditions," *NACA RM E50F15*, 1950.
27. Lefebvre, A. H., *Gas Turbine Combustion*, Hemisphere Publishing Corp., McGraw-Hill, NY, 1983.
28. Lewis, B., and von Elbe, G., *Combustion, Flames and Explosions of Gases*, 2nd Ed., Academic Press, 1961.
29. Kanury, A. M., *Introduction to Combustion Phenomena*, Vol. 2, Gordon and Breach Science Publishers, NY, pp. 30-42, 1984.
30. Steele, R. C., "NO_x and N₂O Formation in Lean-Premixed Jet-Stirred Reactors Operated From 1 to 7 atm," *Doctor of Science Thesis*, University of Washington, 1995.

31. Maurice, L. Q., "Detailed Chemical Kinetic Models for Aviation Fuels," *Doctor of Science Thesis*, Imperial College, 1996.
32. Nicol, D. G., Steele, R. C., Marinov, N. M., and Malte, P. C., "The Importance of the Nitrous Oxide Pathway to NO_x in Lean-Premixed Combustion," *Transactions of the ASME: Journal of Engineering for Gas Turbines and Power*, Vol. 117, pp. 100-111, 1995.
33. Capehart, S. A., " NO_x Formation in Lean-Premixed Combustion of Liquid Hydrocarbons," *Master of Science Thesis*, University of Washington, 1995.
34. Bahr, D. W., "Control and Reduction of Aircraft Turbine Engine Exhaust Emissions," in W. Cornelius and W. G. Agnew (eds.), *Emissions from Continuous Combustion Systems*, pp. 345-372, Plenum, NY, 1972.

Fuel Effects on Lean Blowout and Emissions from a Well-Stirred Reactor

J. W. Blust* and D. R. Ballal†

University of Dayton, Dayton, Ohio 45469-0151

and

G. J. Sturgess‡

Innovative Scientific Solutions, Inc., Dayton, Ohio 45440-3638

The design and development of low-emission, lean premixed aero- and industrial gas-turbine combustors is challenging because of a need to satisfy conflicting requirements of operability, combustion performance, and low emissions. A toroidal well-stirred reactor (WSR) is a laboratory idealization of a compact primary zone of a gas-turbine combustor. Such a WSR was designed, built, and operated at atmospheric pressure to study lean blowout and emissions of CO, unburned hydrocarbons, and NO_x over a range of residence time and fuel–air ratios. A variety of normal and cyclic alkanes, aromatics, and a blend of pure hydrocarbon fuels were tested. Results showed that fuel type affects lean blowout limits, combustion efficiency, and pollutant emissions. These observations have important practical implications to the design of gas-turbine combustors.

Nomenclature

A	= Avagadro's number
C	= molecular collision factor
(C/H)	= carbon to hydrogen mole ratio
E	= activation energy
EI	= emissions index, g/kg fuel
F	= concentration of fuel (percent volume in air)
h	= Planck's constant
k	= reaction rate
LHV	= lower heating value of hydrocarbon, J/kg
LP	= loading parameter, g mole/s L atm"
M	= molecular weight of gas mixture
Ma	= Mach number at exit to reactor jet
m	= mass flow rate, kg/s, or molar flow rate, g mole/s
n	= global reaction order
P	= pressure
Q	= reactor heat loss
R	= universal gas constant
T	= temperature
t	= time
V	= reactor volume
x_i	= mole fraction of species i
Δs^*	= entropy change between states of activated complex and initial reactants
η	= efficiency
ρ	= density
τ	= residence time
ϕ	= equivalence ratio

Subscripts

calc	= calculated
comb	= combustion
eb	= eddy breakup
f	= flame, fuel
in	= inlet
jr	= jet ring
min	= minimum
o	= oxygen
η	= Kolmogoroff microscale

Introduction

THE performance requirements of military and civilian aircraft and industrial gas turbines for the next century pose many challenges to designers. The amendments to the 1990 Federal Clean Air Act mandate significant reduction of CO, unburned hydrocarbons (UHC), and NO_x from aero- and land-based gas-turbine engines currently under development. Unfortunately, any solution designed to decrease emissions leads to concurrent penalties in performance, such as poor low-power (idle) efficiency, poor pattern factor, difficult altitude relight, and poor part-load combustion stability. Further, the burning of residual fuels, aromatics, or naphtha in industrial gas-turbine combustors and low-volatility JP-8 fuel in aeroengines makes it imperative to study the effects of fuel type on lean blowout (LBO) and emissions from combustors. A well-stirred reactor (WSR) provides a controlled laboratory combustor configuration to study these effects.

A well-known strategy to reduce NO_x from a gas-turbine engine is to design a lean, premixed, prevaporized (LPP) combustor. Experiments to minimize emission levels in an LPP system have been performed by Anderson,¹ Marek and Papatrakos,² and Mularz.³ A well-stirred reactor is simply a laboratory idealization of a gas-turbine combustor. In the present investigation, we have supplied a toroidal WSR with premixed, prevaporized fuel–air mixtures and studied the effects of fuel type on lean blowout, combustion efficiency, and emissions. It should be noted that research using vaporized fuels has been performed in various combustors and reactor configurations.^{4–9} Our studies benefit from this previous research work and provide new insights into the effects of fuel type on blowout, efficiency, and emissions.

Presented as Paper 97-2710 at the AIAA/ASME/SAE/ASEE 33rd Joint Propulsion Conference, Seattle, WA, July 6–9, 1997; received Oct. 9, 1997; revision received Nov. 3, 1998; accepted for publication Nov. 3, 1998. Copyright © 1998 by the authors. Published by the American Institute of Aeronautics and Astronautics, Inc., with permission.

*Ph.D. Student, Department of Mechanical and Aerospace Engineering, 300 College Park; currently Senior Engineer, Combustion Engineering Department, Solar Turbine, Inc., San Diego, CA 92186.

†Professor, Department of Mechanical and Aerospace Engineering, 300 College Park. E-mail: ballal@udri.udayton.edu. Fellow AIAA.

‡Vice President, 2766 Indian Ripple Road. Associate Fellow AIAA.

Experimental Work

WSR Test Facility and Instrumentation

A 250-ml toroidal WSR, as designed by Nenniger et al.¹⁰ and modified by Zelina and Ballal,¹¹ was used for this experiment. The reactor was constructed of alumina cement, featured a jet ring with 32 stainless-steel jets, each 1-mm i.d., and injected premixed fuel-air mixture at high subsonic velocity ($Ma = 0.42-0.85$). Figure 1 shows the test facility and instrumentation.

The Horiba emissions analyzers comprised the following units: model MPA-510 oxygen analyzer (0–50 vol %), model FIA-510 total hydrocarbon analyzer (0–10,000 ppm carbon), model VIA-510 CO (0–20 vol %) and CO₂ (0–100 vol %) analyzers, and model CLA-510 SS NO and NO_x analyzers [0–2000 parts per million by volume (ppmV)]. These units were calibrated with gases of the following concentrations: hydrocarbon = 404-ppmV propane, NO = 92 ppmV, NO₂ = 1.6 ppmV, CO = 0.4 vol %, O₂ = 4.03 or 5.02 vol %, and CO₂ = 11.06 vol %. The analyzers used 4 slpm of gas sample with a pressure of ± 10 cm of water at ambient. Water was scrubbed from the sample gas to a maximum dew point of 5 C. All emissions are quoted on a dry standard air basis.

A combustion gas sample was drawn from the center of the WSR torus by a water-cooled stainless-steel probe designed by Blust et al.¹² The probe created a pressure drop, and to compensate for it, a pump rated to 12 slpm elevated the sample

line pressure. This sample was pumped into each analyzer unit through a heated sampling line. Hydrocarbon speciation at an LBO condition was performed using a gas chromatograph-flame ionization detector (GC-FID, Hewlett-Packard HP 5890A), and the qualitative identification of combustion products was performed by comparing retention times of unknown analytes to those of pure compounds.

Combustion temperature, T_p , was measured by inserting a type B thermocouple (platinum-6% rhodium, platinum-30% rhodium) into the torus. This thermocouple was coated with alumina ceramic to protect the thermocouple from the reactor environment. All thermocouples were calibrated, and temperature measurements were corrected for heat loss by conduction and radiation and heat gain by convection and catalysis as described by Blust.¹³ Figure 2 shows the close agreement obtained between temperatures measured using two different methods. Such a procedure ensured the accuracy of combustion temperature measurements.

A vaporizer was built to evaporate liquid fuels, mix the vaporized fuel with air, and then supply this combustible mixture to the WSR. The vaporizer used a 3-kW air heater (Hotwatt), pressurized fuel tank, vaporization chamber, various flow meters, nozzle air line, safety devices, and a fuel atomization nozzle. Heated air was injected to establish a recirculation zone in the vaporizer. This recirculation provided a residence time as high as 1.2 s to fully vaporize the liquid fuel (Ballal and Lefebvre¹⁴ have estimated a vaporization time of 0.36 s for n -

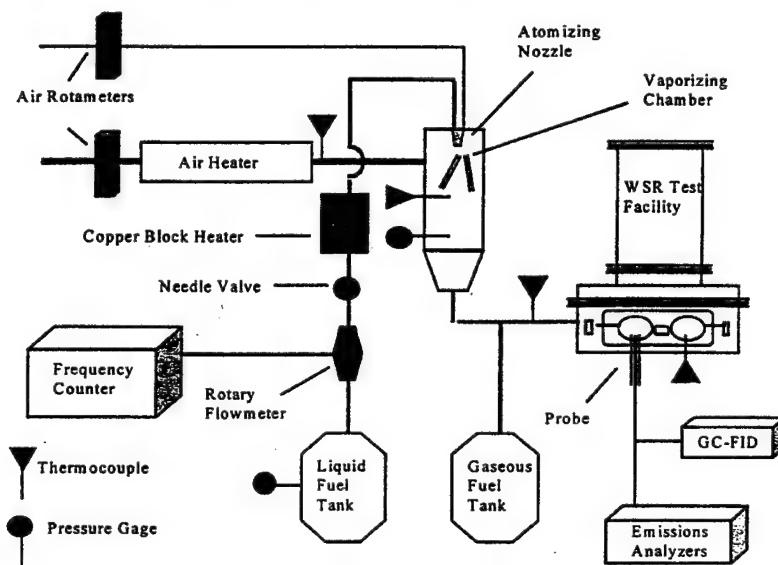


Fig. 1 WSR test facility and associated instrumentation.

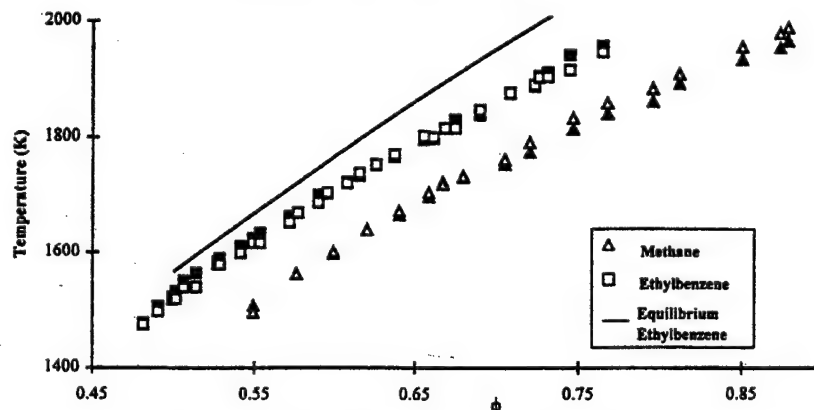


Fig. 2 Reaction temperature vs. equivalence ratio at 7.3 ms residence time. Solid, thermocouple; hollow, calorimeter; and —, Gordon and McBride²¹.

Table 1 WSR test matrix

Hydrocarbon	CN	(C/H)	τ , ms	ϕ_{\min}	ϕ_{\max}	$T_{f\min}$, K	$T_{f\max}$, K
Methane	1	0.25	7.3	0.55	0.88	1507	1967
			6.32	0.59	0.83	1517	1918
Ethane	2	0.333	7.26	0.48	0.84	1407	1996
Cyclohexane	6	0.5	7.47	0.48	0.82	1429	1981
			5.22	0.51	0.78	1536	1922
<i>n</i> -heptane	7	0.4375	7.19	0.53	0.84	1517	1975
			5.49	0.54	0.81	1595	1974
Toluene	7	0.875	7.32	0.46	0.79	1499	1946
			5.35	0.5	0.78	1552	1936
Ethylbenzene	8	0.8	7.43	0.48	0.76	1478	1958
			5.33	0.49	0.67	1546	1839
Cracked fuel simulant	2.52	0.5081	6.75	0.49	0.77	1530	2007
			5.17	0.46	0.76	1391	1969
<i>n</i> -dodecane	12	0.4615	7.39	0.46	0.8	1357	1979
			5.2	0.55	0.79	1581	1983

heptane). Nominal reactor residence time, τ , was computed by $\tau = PVI(RT_f/mM)$.

The WSR was operated over the range of equivalence ratios $\phi = 0.43$ – 0.88 , loading parameter¹⁵ $LP \sim 1.3$ g mol/s L atm^{1.75}, residence times $\tau \sim 5$ – 8 ms, and reactor temperatures $T_f = 1350$ – 2000 K. Fuels studied in the WSR were: methane, ethane, cyclohexane, *n*-heptane, *n*-dodecane, toluene, ethylbenzene, and a cracked fuel simulant comprising 15% methane, 25% ethane, and 60% ethylene by volume.

Error Analysis

Gaseous fuel flow was monitored to within $\pm 2\%$ of reading using a Gilmont rotameter, and air flow was monitored to within $\pm 2\%$ of full scale using a Brooks rotameter. The combined error produced an uncertainty of $\pm 3.5\%$ in ϕ during the combustion of methane in air. Nozzle air was monitored to within $\pm 2\%$ of full scale using a Gilmont rotameter. Liquid hydrocarbons were controlled to within ± 0.3 g/min by the liquid fuel delivery system. The combined error produced an uncertainty of $\pm 3.5\%$ in ϕ during combustion of a liquid fuel in air. The measurement of combustion temperature T_f was repeatable to within ± 30 K. The Horiba emissions analyzers have an accuracy to within 1% of full scale. This represented an error of 2-ppmV NO_x, 50-ppmV CO, 10-ppmV carbon for UHC, 0.25 vol % O₂, and 0.5 vol % CO₂. Residence time was typically controllable to within ± 0.6 ms. Additionally, CO measurements were repeatable from day-to-day within ± 100 ppmV, and NO_x within ± 1.5 ppmV. UHC measurements close to lean blowout suffered from poor repeatability. The preceding uncertainties in temperature and emissions translate into uncertainty in ϕ_{LBO} of ± 0.02 . Finally, Blust et al.¹² demonstrated minimum oxidation reactions in the water-cooled stainless-steel probe.

Test Conditions

Table 1 shows matrix of tests performed at atmospheric pressure. A volumetric mix of 13% CH₄, 22% C₂H₆, 52% C₃H₈, 13% C₇H₈ by volume produced a fuel with carbon number (CN) = 2.52 and carbon to hydrogen mole ratio, (C/H) = 0.5081. This fuel was selected as a simulant for heavy, aromatic-containing fuels that are cracked using thermal or catalytic processes into light fractions with residual light aromatics.

Well-Stirred Condition

To obtain unambiguous results, the WSR must be both micromixed and macromixed. For micromixing, the Kolmogoroff microscale time of the combustion gas, t_{η} , must be less than the chemical reaction time of the process. Now, a typical value of Kolmogoroff microscale time in the reactor was $t_{\eta} = 19$ μ s, as calculated by Zelina and Ballal,¹⁶ using the turbulent flow theory. For methane–air combustion at $\tau = 6.0$ ms, $T_f = 1747$ K, $\phi = 0.7$, $P = 1$ atm, chemical reaction time was $= 25$ μ s,

CO oxidation time = 500 μ s, and NO_x formation time = 20 μ s as calculated by Getz¹⁷ using the Miller and Bowman¹⁸ mechanism and perfectly stirred reactor (PSR) code,¹⁹ with CHEMKIN-II formalism.²⁰ This analysis suggests that the WSR was sufficiently well mixed at the microscale level.

Successful macromixing necessitates the WSR having the proper residence time distribution (RTD) and spatial homogeneity of species and temperature. In an earlier investigation, Zelina and Ballal¹⁶ verified the RTD and demonstrated the spatial homogeneity of the WSR. Maximum detected variabilities were found to be $T_f = \pm 25$ K, NO_x = ± 2.5 ppmV, and CO = ± 90 ppmV. These tests suggested that the WSR was successfully macromixed.

Results and Discussion

Flame Temperature Measurement

Figure 2 shows a plot of measured T_f against ϕ for the combustion of methane and ethylbenzene fuels at $\tau = 7.3$ ms. Also plotted is the calculated equilibrium flame temperature vs ϕ for ethylbenzene using the Gordon and McBride²¹ code. It is observed that the measured temperature is always lower than the corresponding equilibrium flame temperature because of heat loss and also because of a finite reactor residence time. Also, the thermocouples measure flame temperatures that are in close agreement with calorimeter measurements.

LBO Measurement

Figure 3 shows a plot of LBO equivalence ratio vs WSR loading parameter for several hydrocarbons. The LBO condition was characterized by a rapid, large temperature drop, and preceded by a substantial increase in UHC and noise leading to complete extinction. Also, at the threshold of extinction, we measured T_f , ϕ , reactant flow rates, and the emission index (EI) of CO and UHC. Finally, the static flammability limits (for $LP = 0$) of these fuels as quoted by Lewis and Von Elbe²² are also included here. These results can be explained by the WSR stability theory.

Briefly, the rate of fuel and air reaction is expressed by the material balance equation:

$$\eta_{\text{comb}} \phi m = CVT_f^{1/2} \exp(-E/RT_f) \rho^n x_f^r x_o^{n-r} \quad (1)$$

where m is the molar flow rate of reactants; ρ is the density of reactants; E is activation energy; x_i is the mole fraction of fuel, f , or oxygen, o ; and the global reaction order of methane and ethane is $n = 1.75$ (Lefebvre²³), and $r = n - 1$. Now, from Kanury,²⁴ the molecular collision factor C may be calculated as

$$C = \frac{RT_f^{1/2}}{hA} \exp\left(\frac{\Delta s^*}{R}\right) \quad (2)$$

For lean mixtures, Eq. (1) may be rewritten to yield LP or E as

$$LP = \frac{m}{VP^n} = \exp\left(\frac{-E}{RT_f}\right) \frac{Cx_f^{0.75} x_o}{T_f^{1.25} \eta_{comb} \phi (R/M)^{1.75}} \quad (3)$$

$$E = RT_f \ln \left[\frac{Cx_f^{0.75} x_o}{LP \cdot T_f^{1.25} \eta_{comb} \phi (R/M)^{1.75}} \right] \quad (4)$$

In Eq. (2), the entropy of the activated complex was found by applying a quantity of energy equal to E to the energy of reactants and evaluating entropy at this condition. Next, an iterative calculation provides values of C and E ; for methane $E = 52$ kcal/mol and $C = 9.4 \times 10^{14} \text{ K}^{-1/2} \text{ s}^{-1} \text{ m}^{3n-3} \text{ mol}^{1-n}$, and for ethane $E = 49$ kcal/mol and $C = 1.3 \times 10^{15} \text{ K}^{-1/2} \text{ s}^{-1} \text{ m}^{3n-3} \text{ mol}^{1-n}$. Substitution of these values in Eq. (3) together with the measured values of other parameters (LBO, T_f , and η_{comb}) provides a relationship between LP vs ϕ that is shown plotted in Fig. 3. It is observed that the predictions are in good agreement with the measurements.

Combustion Efficiency Measurement

Figure 4 shows the combustion efficiency η_{comb} plotted against CN for several fuels at LP = 1.3 g mol/s L atm^{1.75}. The combustion efficiency was calculated from the measured values of emissions indices of CO and UHC using the Aerospace Recommended Practice (ARP 1533²⁵) relationship:

$$\eta_{comb} = 1 - (10109EI_{CO}/LHV) - (EI_{UHC}/1000) \quad (5)$$

The results clearly demonstrate that, in general, as CN increases, η_{comb} decreases gradually from 99 to 94%, i.e., fuel type affects combustion efficiency. These results were found to be relatively independent of ϕ or T_f within the uncertainty limits of these experiments. To test the sensitivity of measured

η_{comb} to UHC and CO species, two curves of η_{comb} , one taking into account only CO, the other only UHC species, are also plotted in Fig. 4. The curve of η_{comb} with only UHC shows that, for CN < 7, η_{comb} was constant for all fuels and slightly decreased for toluene and *n*-dodecane. The curve of η_{comb} with only CO shows that methane has the highest combustion efficiency. Thus, decreasing η_{comb} at higher CN was attributable to incomplete combustion of UHC products for most fuels.

It should be noted that the LBO combustion efficiencies in these WSR experiments are higher than those found in practical gas-turbine combustors. This is because of a high degree of uniform mixing in a WSR and the use of single as opposed to multicomponent (wide-cut) hydrocarbon fuels studied herein. The LBO limit of a gas-turbine combustor is wider than that of a WSR because incomplete mixing in the former produces pockets of locally flammable (usually lighter fuel components) mixture that sustains combustion. However, this combustion process also produces a large amount of CO and UHC, thereby lowering the combustion efficiency. For example, Fig. 4 shows that η_{comb} is lower for a cracked fuel simulant (CN = 2.52) than for pure fuels such as ethane or cyclohexane.

CO₂ and O₂ Measurements

In a WSR operating in the stable mode, CO₂ concentration should peak and oxygen concentration should drop to near-zero at stoichiometric equivalence ratios. Figure 5 shows typical measured CO₂ and O₂ concentrations (vol %) and calculated equilibrium values as a function of equivalence ratio. As expected, CO₂ increased and O₂ decreased as ϕ approached unity. Also, there is excellent correlation between predictions and measurements that demonstrates a close to ideal behavior of the WSR.

CO and UHC Measurements

The CO and UHC emissions are important because they represent a direct measure of combustion inefficiency. If the

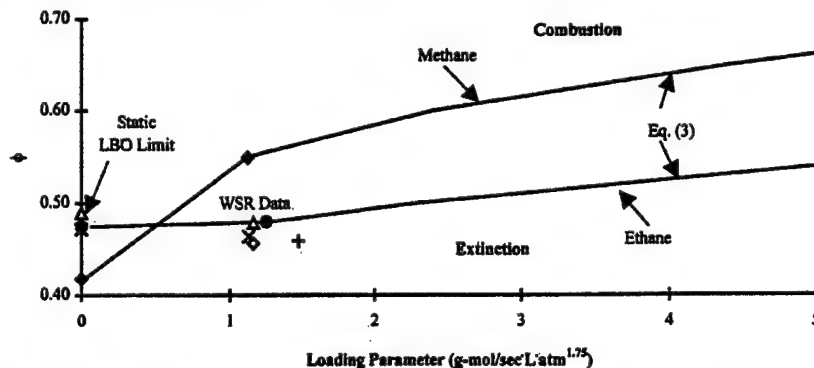


Fig. 3 LBO equivalence ratio vs loading parameter for several fuels: ♦, methane; ●, ethane; △, cyclohexane; ◇, *n*-dodecane; ×, toluene; +, cracked fuel simulant; and —, Eq. (3).

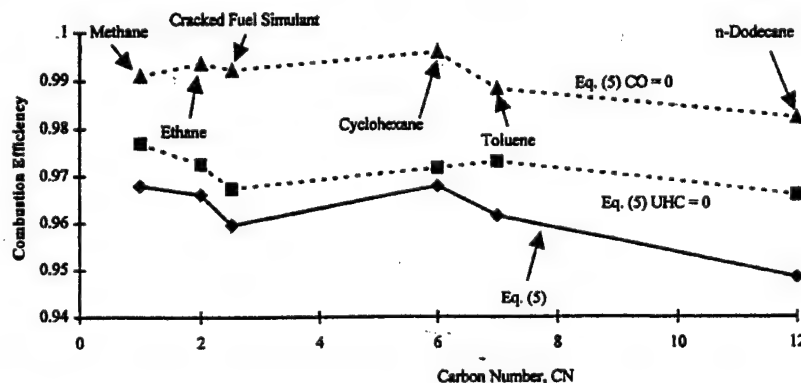


Fig. 4 Combustion efficiency [Eq. (5)] vs CN for several fuels. Also, the two curves (---) show the relative effects of CO and UHC on combustion efficiency.

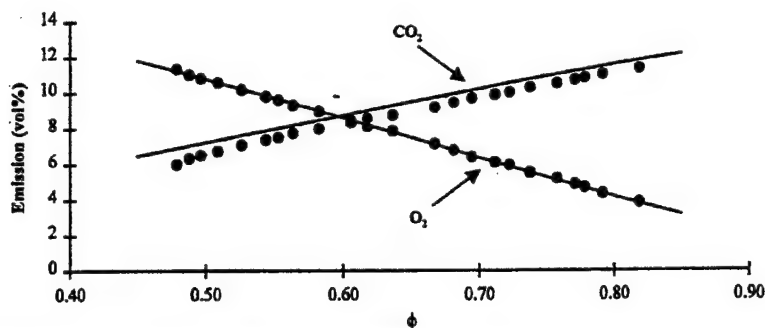


Fig. 5 CO_2 and O_2 concentration vs equivalence ratio for cyclohexane at residence time 7.5 ms. —, equilibrium calculations using Gordon and McBride²¹ code.

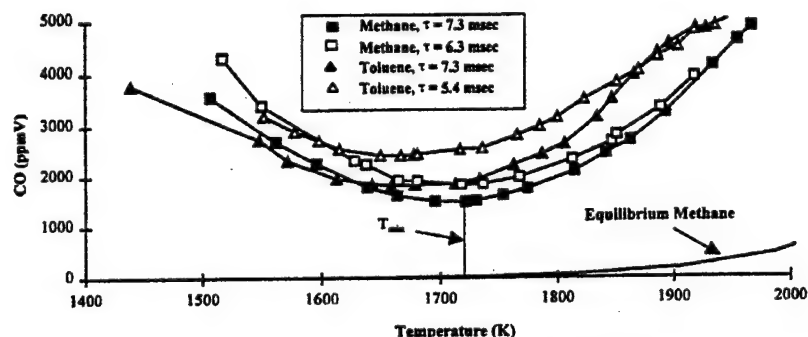


Fig. 6 CO emissions vs reaction temperature. Temperature at minimum CO emission and equilibrium methane calculation are shown (Gordon and McBride²¹).

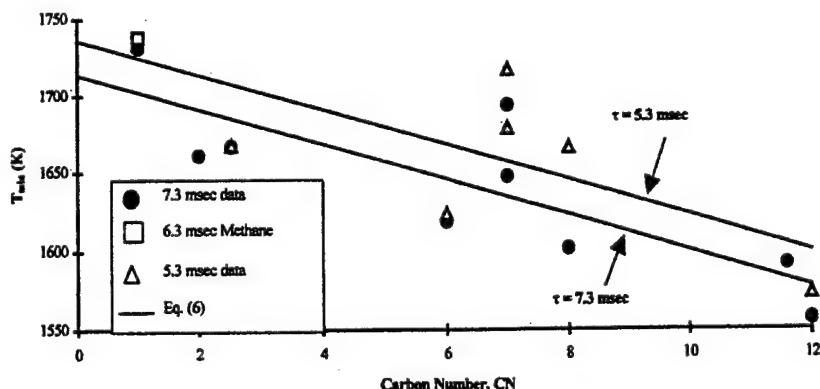


Fig. 7 Temperature at minimum CO emission vs CN. Also predictions using Eq. (6) are shown.

combustor operates fuel-rich, has inadequate mixing, or is quenched by cold air, large quantities of CO (which is relatively resistant to oxidation), will be emitted as a result of the lack of oxygen needed to complete the reaction to CO_2 , or insufficient residence time provided for CO to be oxidized. UHC emissions are associated with poor atomization, inadequate burning rates, insufficient residence time, and premature quenching.

Figure 6 shows profiles of CO (ppmV) vs T_r from methane and toluene fuels at residence times of 7.3, 6.3, and 5.4 ms. In general, all hydrocarbons exhibited a U-shaped trend in CO concentration. As temperature increased, CO concentration first decreased as reaction rate of CO consumption increased, next a minimum was reached, and finally, the CO concentration increased as a result of an increased rate of CO_2 dissociation. Also, it is observed that decreasing residence time increased CO, and these CO concentrations are significantly

higher than, for example, the computed equilibrium CO concentration (assuming infinite residence time) for methane.

Figure 7 shows plots of temperature, T_{\min} at which CO minima occurs vs carbon number CN at 7.3 and 5.3 ms residence times (methane $\tau = 7.3$ or 6.3 ms), corrected to the standard inlet temperature 296 K by using $T_{\min} = T_r - (T_{\text{in}} - 296)$ K. These results show that as the carbon number of the fuel is increased, T_{\min} decreases. This rule applied to alkanes and aromatics, with the cracked fuel simulant classified as an alkane. Also, the effect of decreasing residence time was to increase T_{\min} presumably, because of a reduction of CO oxidation at short residence time, whereas the CO_2 dissociation rate proceeded quickly regardless of residence time. All of the data plotted in Fig. 7 can be approximated by a relationship:

$$T_{\min} = -11.35\text{CN} - 11.27\tau(\text{ms}) + 1796 \quad (6)$$

Figure 8 shows emissions index of CO from several hydrocarbons, at several values of T_f , plotted as a function of CN at a residence time of 7.3 ms; cracked fuel simulant is treated as an alkane. As shown, alkanes, sans methane, displayed a slight increase in CO as CN increased. Methane produced more CO than any other fuel, presumably because the stable methane molecule resists quick oxidation. In contrast to alkanes, the two aromatic fuels showed a decrease in CO as CN increased from 7 to 8. The primary path of toluene consumption at high temperature is C-C rupture, resulting in $C_7H_8 \rightarrow C_6H_6 + CH_3$. The C-H rupture of the methyl chain occurs quickly, but the $C_7H_7 + H$ reaction is rapidly equilibrated, and as suggested by Lindstedt and Maurice,²⁶ toluene is recycled. Because of this recycling, toluene is resistant to oxidation, resulting in considerable UHC and CO in the products.

Figure 9 shows the emissions indices of UHC from several hydrocarbons at several T_f , plotted as a function of CN at residence time of 7.3 ms. As shown, alkanes showed a rapid decrease, then a modest increase in UHC as CN increased. The high UHC for methane at 1500 K is a result of the WSR operation at LBO. Ethane behaved more like other alkanes. Toluene produced more UHC at a given temperature than other

hydrocarbons besides methane, whereas ethylbenzene produced a quantity of UHC more akin to alkanes of the same CN. As with CO, similarity between methane and ethane, toluene and ethylbenzene is observed.

Table 2 summarizes the composition of UHC at LBO from several hydrocarbons. Ethylene is the most abundant intermediate hydrocarbon product from *n*-heptane, and the mechanisms for combustion of other alkanes are similar. Thus, ethylene is the major component of UHC from lean alkane combustion. Conversely, acetylene was the most abundant UHC component from toluene because it is a product of the decomposition of benzene, which itself is a common product of the decomposition of toluene. As a result, trace amounts of C6 were also identified in the UHC mixture from toluene. The cracked fuel simulant behaved more like an alkane than an aromatic.

NO_x Measurements

NO_x emission from gas-turbine combustors is typically associated with primary zone combustion at near-stoichiometric conditions and high-power settings. To reduce NO_x, advanced combustor designs employ uniform/pre mixing, fuel-lean com-

Table 2 Effluent hydrocarbon species by volume percent of UHC

Hydrocarbon	CH ₄	C ₂ H ₄	C ₂ H ₆	C ₂ H ₂	C ₃ H ₆	C ₄	C ₅	C ₆	τ , ms	ϕ	T_f , K
Toluene	27	14.5	0	55.5	0	0	0	3	7.56	0.46	1439
Cyclohexane	30	49	12	9	0	0	0	0	6.83	0.51	1513
Ethane	20	40	40	0	0	0	0	0	6.95	0.48	1407
Cracked fuel simulant	23	58	16	3	0	0	0	0	5.96	0.46	1391
<i>n</i> -dodecane	19	60	6	2	6	3	2	2	7.71	0.46	1357

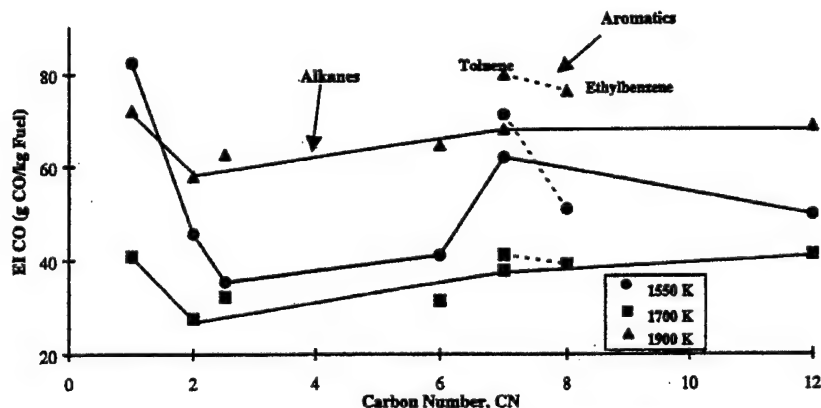


Fig. 8 Emissions index of CO vs CN for several fuels at a nominal residence time of 7.3 ms.

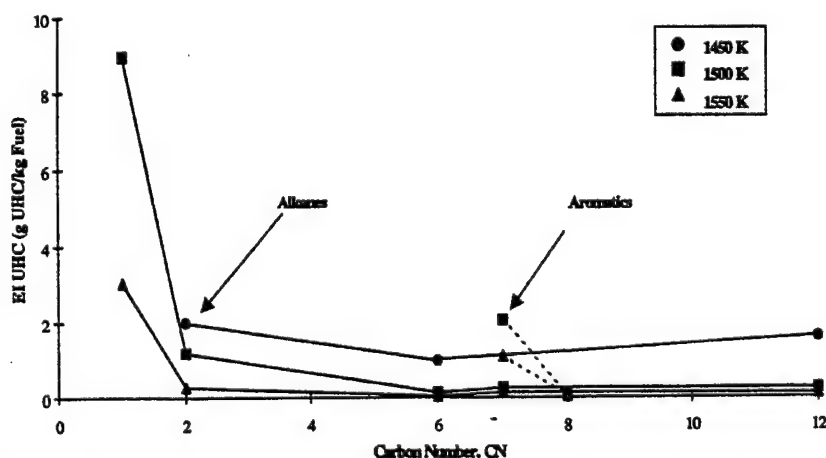


Fig. 9 Emissions indices of UHC vs CN for several fuels at a nominal residence time of 7.3 ms.

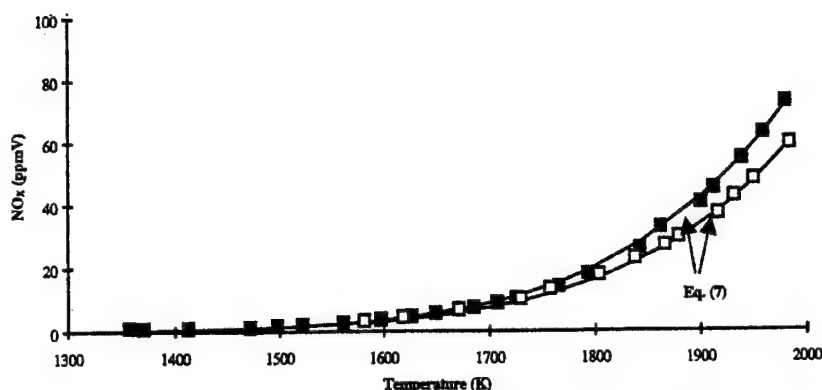


Fig. 10 NO_x emissions vs reaction temperature for n -dodecane (square) at residence time 7.3 ms (solid symbol) and 5.3 ms (hollow symbol). —, predictions for n -dodecane using Eq. (7).

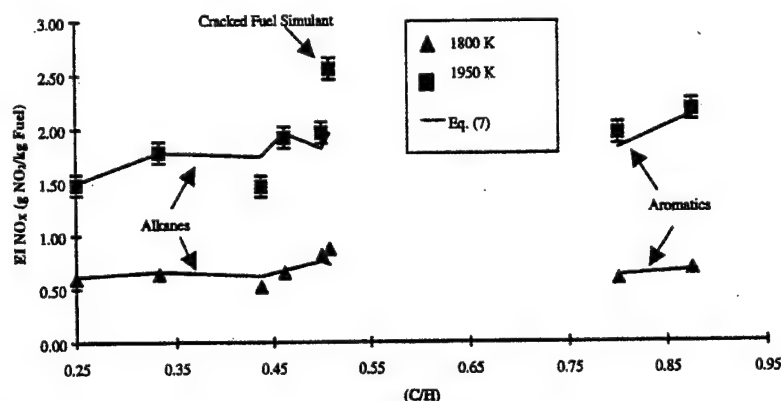


Fig. 11 Emissions indices of NO_x vs (C/H) ratio of fuels at a nominal residence time of 7.3 ms.

bustion, and/or even water/steam injection to decrease reaction temperature. The formation of species such as NO and NO_2 is a complex function of temperature, residence time, equivalence ratio, and detailed chemical kinetics. Recently, Capehart et al.⁶ and Nicol et al.²⁷ discussed fuel nitrogen mechanisms, the thermal NO (Zeldovich) mechanism, super-equilibrium effects, prompt NO mechanism, and N_2O mechanism. Figure 10 shows profiles of NO_x (ppmV) vs T_f from n -dodecane. As equivalence ratio (and hence, also reaction temperature) increased above its LBO value, NO_x emissions increased gradually, then rapidly for $T_f > 1800$ K, because of the extended Zeldovich NO_x mechanism. Also, increasing residence time increased NO_x . The present work suggests the following equation for n -dodecane:

$$\text{NO}_x = k\tau^{1/2} \exp(-E/RT_f) \quad (\text{ppmV}) \quad (7)$$

where $k = 9,229,000 \text{ ppmV NO}_x/\text{ms}^{1/2}$, and $E = 50,240 \text{ kcal/g mol}$. Equation (7) was plotted in Fig. 10 and yields a satisfactory prediction of experimental results in the range of residence time 5–8 ms. The relationship, $\text{NO}_x \propto \tau^{1/2}$ was also observed for other fuels such as methane, n -heptane, cracked fuel simulant, toluene, and ethylbenzene. This effect of residence time implies that the rate of change of formation $d(\text{NO}_x)/dt \propto \tau^{-1/2}$, i.e., formation rate is greater at shorter residence time.

Because all tested fuels exhibited $\text{NO}_x \propto \tau^{1/2}$ trend, values of E and k were calculated for all fuels using the iterative procedure described by Nicol et al.²⁷ A range of these calculated results over (C/H) ratio of 0.25–0.9 were $E = 52$ –71 kcal/g mol and $k = 11$ –922 K ppmV $\text{NO}_x/1000 \text{ ms}^{1/2}$. These results suggest that NO_x increases with an increase in the (C/H) ratio because of the propensity of the hydrocarbon to produce CH_x radicals. The calculated values of E and k together

with other test parameters were substituted in Eq. (7) and predictions of emissions index EI_{NO_x} were obtained. For the EI_{NO_x} calculations, all NO_x was treated as NO_2 .

Figure 11 shows measured and calculated emissions indices of NO_x vs (C/H) ratio of the various fuels tested. These measurements were made at a nominal residence time of 7.3 ms and at $T_f = 1800$ K and 1950 K, with alkanes and aromatics plotted separately, and with cracked fuel simulant plotted with the alkanes. A gradual increase in NO_x emissions is observed as (C/H) ratio is increased from 0.25 (methane) to 0.875 (toluene). Further, this increase is even more pronounced at a higher temperature, $T_f = 1950$ K. Also, the two aromatic fuels showed a similar increase in NO_x with (C/H) ratio, with toluene producing more NO_x than ethylbenzene. Finally, the NO_x calculations accurately predict increase in NO_x as (C/H) ratio is increased. Lindstedt and Maurice²⁶ suggested that branched aromatic molecules at high temperature (>1850 K) form a greater quantity of prompt NO_x precursor such as CH_x than alkanes do. Presumably, this mechanism increases prompt NO_x formation, and hence, also the total NO_x . These observations suggest an increase in pollutant emissions from gas turbines burning crude or residual fuels with high (C/H) ratio.

Conclusions

A toroidal WSR, which represents a laboratory idealization of a primary zone of a gas-turbine combustor, was used to study lean blowout, combustion efficiency, and gaseous emissions from several fuels. The following conclusions resulted from this research.

- 1) All fuels, except methane, showed a lean blowout limit at $\phi = 0.47$ with $\text{LP} = 1.3 \text{ g mol/s L atm}^{1.75}$ (methane LBO was $\phi = 0.55$). These measurements and combustion stability theory yielded global activation energies and collision factors for many fuels; e.g., $E = 52 \text{ kcal/mol}$ and $C = 9.4 \times 10^{14} \text{ K}^{-1/2}$

$s^{-1} m^{3n-3} mol^{1-n}$ for methane, and $E = 49$ kcal/mol and $C = 1.3 \times 10^{15} K^{-1/2} s^{-1} m^{3n-3} mol^{1-n}$ for ethane.

2) Combustion efficiency η_{comb} decreased as fuel CN increased. This relation was observed for alkanes, aromatics, and cracked fuel simulant.

3) Both fuel type (alkanes, aromatics, etc.) and CN affect CO emissions at the same temperature and residence time. In general, alkanes produced more CO as CN increased (except methane), and toluene produced more CO than ethylbenzene. Also, increasing residence time decreased CO emissions. Finally, Eq. (6) provides a relationship between the reaction temperature at which CO emission approaches a minimum vs the CN of the fuel.

4) UHC emissions from alkanes decreased greatly from methane to ethane and remained unchanged for higher CN fuels. Toluene produced more UHC emissions than alkanes at the same temperature. At a low reaction temperature ($T_f < 1600$ K), increasing residence time decreased UHC emissions.

5) Fuel type (C/H ratio) influenced NO_x emissions. As (C/H) ratio increased, NO_x increased, for both alkanes and aromatics. Increasing residence time increased NO_x emissions. Equation (7) provided a good prediction of NO_x emissions in the range of residence times of 5–8 ms.

Acknowledgments

This work was supported by the U.S. Air Force Wright Laboratory, Aero Propulsion and Power Directorate, Wright-Patterson Air Force Base, Ohio, under Contract F33615-92-C-2207, with Charles W. Frayne serving as the Technical Monitor. The authors are grateful to Rich Striebich and Matthew Getz for providing technical assistance.

References

- ¹Anderson, D. N., "Effects of Equivalence Ratio and Dwell Time on Exhaust Emissions from an Experimental Premixing Prevaporizing Burner," American Society of Mechanical Engineers, Paper 75-GT-69, June 1975.
- ²Marek, C. J., and Papathakos, L. C., "Exhaust Emissions from a Premixing, Prevaporizing Flame Tube Using Liquid Jet A Fuel," NASA TM X-3383, April 1976.
- ³Mularz, E. J., "Lean, Premixed, Prevaporized Combustion for Aircraft Gas Turbine Engines," NASA TM-79148, June 1979.
- ⁴Sturgess, G. J., "Assessment of an Abbreviated Jet A/JP-8 Reaction Mechanism for Modeling Gas Turbine Engine Gaseous Emissions," AIAA Paper 97-2709, July 1997.
- ⁵Brezinsky, K., Litzinger, T. A., and Glassman, I., "The High Temperature Oxidation of the Methyl Side Chain of Toluene," *International Journal of Chemical Kinetics*, Vol. 16, 1984, pp. 1053–1074.
- ⁶Capehart, S. A., Lee, J. C. Y., Williams, J. T., and Malte, P. C., "Effect of Fuel Composition on NO_x Formation in Lean Premixed Prevaporized Combustion," American Society of Mechanical Engineers, Paper 97-GT-336, June 1997.
- ⁷Dagaut, P., Reuillon, M., and Cathonnet, M., "Experimental Study of the Oxidation of *n*-Heptane in a Jet Stirred Reactor from Low to High Temperature and Pressures up to 40 Atm," *Combustion and Flame*, Vol. 101, 1995, pp. 132–140.
- ⁸Vaughn, C. B., Howard, J. B., and Longwell, J. P., "Benzene Destruction in Fuel Rich Jet-Stirred Combustion," *Combustion and Flame*, Vol. 87, 1991, pp. 278–288.
- ⁹Zelina, J., Blust, J. W., and Ballal, D. R., "Combustion of Liquid Fuels in the Well Stirred Reactor," American Society of Mechanical Engineers, Paper 96-GT-047, June 1996.
- ¹⁰Nenniger, J. E., Kridiotis, A. C., Chomiak, J., Longwell, J. P., and Sarofim, A. F., "Characterization of a Toroidal Well-Stirred Reactor," 20th Symposium (International) on Combustion, The Combustion Inst., Pittsburgh, PA, 1984, pp. 473–479.
- ¹¹Zelina, J., and Ballal, D. R., "Combustion Studies in a Well Stirred Reactor," AIAA Paper 94-0114, Jan. 1994.
- ¹²Blust, J. W., Getz, M. G., and Zabarnick, S., "Probe Design Optimization for the Well Stirred Reactor," AIAA Paper 97-0907, Jan. 1997.
- ¹³Blust, J. W., "Effects of Fuel Structure on Emissions and Stability in the Well Stirred Reactor," Ph.D. Dissertation, Univ. of Dayton, Dayton, OH, 1998.
- ¹⁴Ballal, D. R., and Lefebvre, A. H., "Ignition and Flame Quenching of Flowing Heterogeneous Fuel-Air Mixtures," *Combustion and Flame*, Vol. 35, 1979, pp. 155–168.
- ¹⁵Longwell, J. P., and Weiss, M. A., "High Temperature Reaction Rates in Hydrocarbon Combustion," *Industrial and Engineering Chemistry*, Vol. 47, 1955.
- ¹⁶Zelina, J., and Ballal, D. R., "Emissions Studies in a Well-Stirred Reactor and Applications to Combustion Modeling," *Proceedings of FACT*, Vol. 21, American Society of Mechanical Engineers, New York, 1996, pp. 255–263.
- ¹⁷Getz, M. G., "Investigation of Halon 1301 Interactions in Methane Combustion," M.S. Thesis, Univ. of Dayton, Dayton, OH, 1997.
- ¹⁸Miller, J. A., and Bowman, C. T., "Mechanism and Modeling of Nitrogen Chemistry in Combustion," *Progress in Energy and Combustion Science*, Vol. 15, No. 3, 1989, pp. 287–338.
- ¹⁹Glarborg, P., Kee, R. J., Grcar, J. F., and Miller, J. A., "PSR: A Fortran Program for Modeling Well-Stirred Reactors," Sandia National Lab., SAND86-8209 UC-4, Livermore, CA, 1988.
- ²⁰Kee, R. J., Miller, J. A., and Jefferson, T. H., "CHEMKIN: A General-Purpose, Problem-Independent, Transportable, FORTRAN Chemical Kinetics Code Package," Sandia National Lab., SAND80-8003, Livermore, CA, 1980.
- ²¹Gordon, S., and McBride, B. J., "Computer Program for Calculation of Complex Chemical Equilibrium Compositions, Rocket Performance, Incident and Reflected Shocks, and Chapman-Jouget Detonations," NASA, SP-273 Interim Revision, 1976.
- ²²Lewis, B., and Von Elbe, G., *Combustion, Flames and Explosions of Gases*, 2nd ed., Academic, New York, 1961.
- ²³Lefebvre, A. H., *Gas Turbine Combustion*, Hemisphere, New York, 1983.
- ²⁴Kanury, A. M., *Introduction to Combustion Phenomena*, Vol. 2, Gordon and Breach, New York, 1984, pp. 30–42.
- ²⁵Anon., *Procedure for the Calculation of Gaseous Emissions from Aircraft Turbine Engines*, Aerospace Recommended Practice 1533, Society of Automotive Engineers, Warrendale, PA, 1994, pp. 1–36.
- ²⁶Lindstedt, R. P., and Maurice, L. Q., "Detailed Kinetic Modeling of Toluene Combustion," *Combustion Science and Technology*, Vol. 120, No. 2, 1996, pp. 119–167.
- ²⁷Nicol, D. G., Steele, R. C., Marinov, N. M., and Malte, P. C., "The Importance of the Nitrous Oxide Pathway to NO_x in Lean-Premixed Combustion," *Journal of Engineering for Gas Turbines and Power*, Vol. 117, No. 1, 1995, pp. 100–111.

3.1.3.3 Combustor Design Trends. In the invited paper entitled "Combustor Design Trends for Aircraft Gas Turbine Engines" (see pp. 543-559), advanced performance trends are surveyed for possible future gas turbine engines for powering classes of military and commercial aircraft. The resulting combustor trends are enumerated and examples of enabling technology given. Recent advances in manufacturing and materials technology have sparked interest in the development of ultracompact aircraft engines for delivering high thrust for future air vehicles. These engines are expected to utilize a constant-temperature cycle to gain extra thrust by burning fuel in the turbine section. The paper entitled "Influence of Ceramic-Matrix-Composite Wall Plates on Combustor Performance" (see pp. 560-570) describes preliminary studies conducted on an Inner Turbine Burner (ITB) that uses ceramic-matrix-composite (CMC) materials on the cavity walls.



The Society shall not be responsible for statements or opinions advanced in papers or discussion at meetings of the Society or of its Divisions or Sections, or printed in its publications. Discussion is printed only if the paper is published in an ASME Journal. Authorization to photocopy material for internal or personal use under circumstance not falling within the fair use provisions of the Copyright Act is granted by ASME to libraries and other users registered with the Copyright Clearance Center (CCC) Transactional Reporting Service provided that the base fee of \$0.30 per page is paid directly to the CCC, 27 Congress Street, Salem MA 01970. Requests for special permission or bulk reproduction should be addressed to the ASME Technical Publishing Department.

Copyright © 1996 by ASME

All Rights Reserved

Printed in U.S.A.

PUBLISHED WITH PERMISSION

Combustor Design Trends For Aircraft Gas Turbine Engines

G.J. STURGESS

Innovative Scientific Solutions Inc.,
Beavercreek, Ohio

Abstract

Advanced performance trends are surveyed for possible future gas turbine engines to power several classes of military and commercial aircraft. The resulting combustor trends are enumerated. Examples of enabling technology are given. Combustion considerations are discussed, and many commonalities between applications are discovered; fuel/air mixing and combustion dynamics emerge as topics of considerable importance.

Introduction

Technology forecasting in the aerospace field can be a hazardous past-time. For the years 1945-65, experience taught that such forecasts were generally substantially incorrect within three years of their origin, and could be seriously wrong after five years. However, these were years of rapid change involving a young product - the gas turbine engine (Hooker, 1959).

An earlier attempt at forecasting combustor technology (Sturgess, 1980), highlighted three areas that were felt likely to present a major challenge. These were combustor durability, alternative fuels, and design system changes through the introduction of computational fluid dynamics (CFD) as a tool. Some sixteen years later, actual developments in combustor durability and CFD have followed closely to the forecast; alternative fuels did not become an issue. The forecast missed the return of exhaust emissions as a serious challenge, except for smoke (in relation to alternative fuels). At a 50-50 score, this kind of performance

in technology forecasting perhaps is as good as can be expected.

The nature of technology forecasting itself is subject to change, and whereas in the past technology alone was sufficient, nowadays a thorough understanding of the financial side of aerospace and its influence on technical innovation, is now a desirable attribute. In the post-Vietnam years the pace of introduction for new technology was slowed by economic considerations, and in the 1970's the aircraft gas turbine engine was being described as a "mature product" with the implication that little new could be accomplished. While this was an exaggeration, nevertheless by the 1980's an era of "incremental change" had come about. In recent years therefore, there have been more changes in the engineering process by which the engine is produced, (Gillette, 1996), than there have been in the engine. These changes have been directed towards reducing the cost and time to design and develop an engine, and towards reducing the staggering financial risk associated with a new centerline engine. Technology now has to "buy" its acceptance on an engine by offering the customer a substantial benefit of some tangible form.

Despite any inherent shortcomings, technology forecasting remains necessary and has two major functions. First, it is necessary to identify those pieces of technology that are essential to achieving further steady progress, the so-called "enabling technologies." These must be identified well in advance of their likely application, in order that they are ready for incorporation on an engine when needed. For commercial aviation the advent of full extended range (ETOPS certification) put an end to the days when a customer would

accept "development in service." The second need for technology forecasting is to avoid being caught unprepared by paradigm-breaking events. Such an event could originate from competitive breakthroughs elsewhere, or, through the introduction of restrictive legislation, such as excessively tough noise or emissions regulations.

Present Contribution

The procedure for establishing goals and identifying enabling technologies is described in outline, and some of these technologies are described by means of current performance trends and Air Force initiatives. A probable paradigm-breaking event is also identified.

Categorization of Applications

Any engine study begins with an application. The application originates with a customer, who can be either an airline or the military. Therefore, engines for customer applications can be classified by **duty-function** as being either "commercial" or "military." This is illustrated in Figure 1.

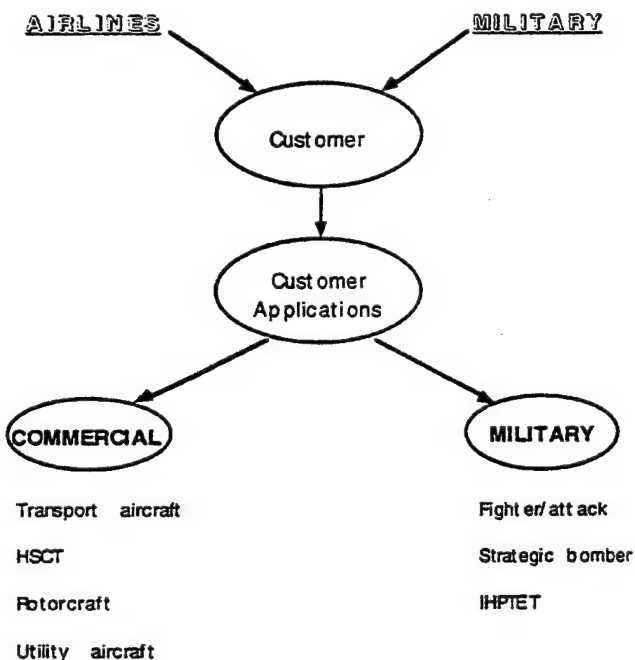


Fig.1: Categorization of Applications by Duty-Function

In Figure 1, engines for "transport aircraft" could see either airline or military service, since the engine design criteria will be similar. An example of this would be the Pratt & Whitney PW2037 engines in the Boeing 757 airliner, and its military counterpart the Pratt & Whitney F-117 in the

McDonald-Douglas C-17 military transport. Conversely, engines for a fighter/attack aircraft clearly would be classified as only military. There are few differences in use between the commercial and military classifications of engines for rotorcraft, so these have been placed under military applications, where most of them originate. Utility aircraft are used by both commercial and military operators, and in similar fashion, but the engines originate on the commercial side, where they have been placed.

Aircraft using sustained supersonic cruise, such as the proposed high speed commercial transport (HSCT) and a possible new strategic bomber for the Air Force, are specialized applications with many similarities. They have been placed separately since the engines for the HSCT are constrained by considerations of low emissions, which the engines for the bomber are not, at present.

The Air Force integrated high performance turbine engine technology (IHPTET) program is in a special category that is uniquely military. It is an engine technology demonstrator program that is intended to push the limits in every direction. As such, it represents a possible paradigm-breaking event that is perhaps only limited by costs.

Relation Between Application and Engine Goals

Engine goals are important since they embody the philosophy that should prevail in the design of the combustor. For example, it would not make much sense to use expensive advanced combustor liner materials, together with an elaborate cooling scheme, in an expendable engine intended for a short-range attack missile.

Most engines will have a similar list of design goals. It is the emphasis given to individual design goals that will change according to the intended application. Figure 2 illustrates this, and shows the major goals that might be applied for the different classes. For example, an engine intended for a long-range, subsonic cruise transport aircraft would have a low cruise specific fuel consumption very high on its list of goals, together with retention of this performance over long "time-on-the-wing" periods. In contrast, the engine for a utility aircraft would have reliability at the top of its list of goals. In the operating and financial circumstances that utility aircraft are used, these engines must start every time the key is turned.

Procedure for Establishing Enabling Technologies

Once an application is identified and the engine design goals (and philosophy) established, the enabling technologies must be determined at the component level. To

complete this step, an engine configuration and performance information are needed. Figure 3 illustrates the complete procedure.

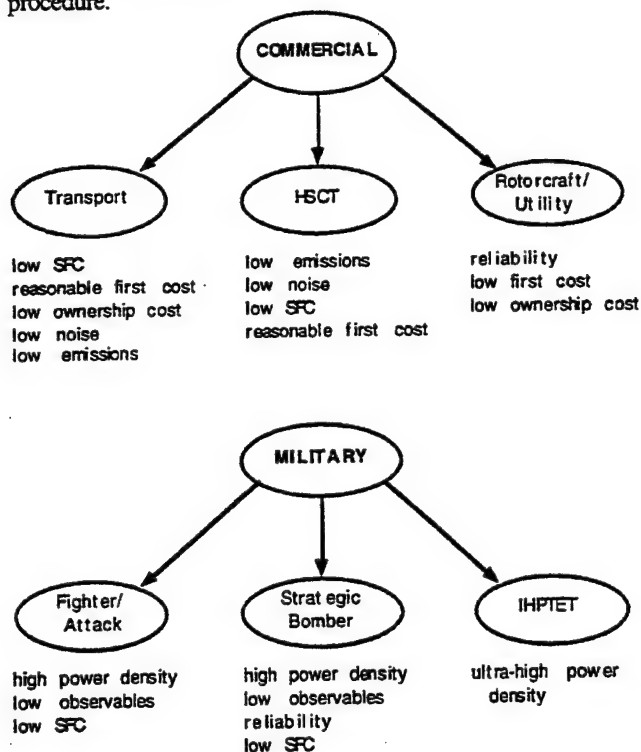


Fig. 2: Determination of Emphasis Given to Engine Goals by Application

It will be seen in Figure 3 that considerable iteration usually takes place, and that this occurs on several levels, both internally at company level, and externally with the customer and the National Laboratories (with a role as repositories of technology). The company-internal iterations involve the rotating machinery component groups in determining the final details of the engine layout. The combustor group is not normally explicitly involved at this stage. Combustor involvement is implicit through the use of **rules-based design (RBD)** programs used to establish the engine configuration.

With the engine layout established and the preliminary performance (SOAP: state-of-the-art performance) table information provided, the component groups can then establish a prioritized list of design goals, consistent with the engine design goals, for the major components of the engine. This will involve some negotiation for interfacing with adjacent components. They can also commence studies to ascertain if their current design base can produce configurations that fit into the envelope allowed in the engine layout, and which satisfy the component design goals. These

studies will identify any limiting technologies. Hopefully, **prior use of technology forecasting** should have identified these as **enabling technologies**, and the research and development (R&D) organizations will have appropriate solutions readily available. Figure 4 represents the acquisition time line for an advanced technology engine.

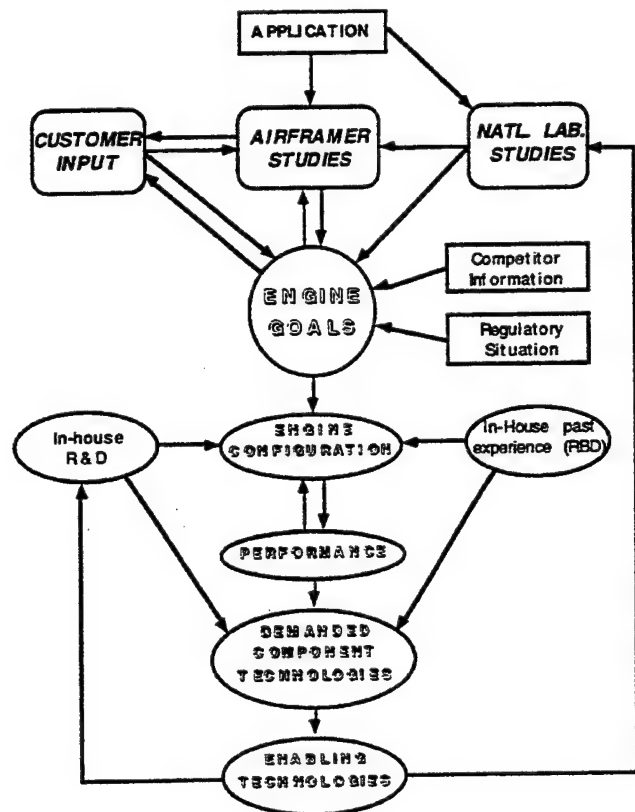


Fig. 3: Procedure for Establishing Enabling Technologies

Performance Trends

To illustrate identification of likely relevant enabling technologies for future combustors, the procedure of Figure 3 is entered at the level of engine performance.

Engine cycle performance trends for real engines at on-design conditions are complex, and depend strongly on the component losses, the amount of cooling air used in the turbines, flight conditions, and the particular design choices made, i.e. design for minimum specific fuel consumption, or, design for maximum power density. At off-design conditions, trends can be opposite to those at on-design conditions. For turbofan engines the two streams - fan and core engine - result in added complication in reaching a matched balance between the fan and core engine to achieve overall engine optimum performance aspects in a succinct manner. Actual examples

can be helpful, but such curves are invariably considered to be proprietary by the respective manufacturers.

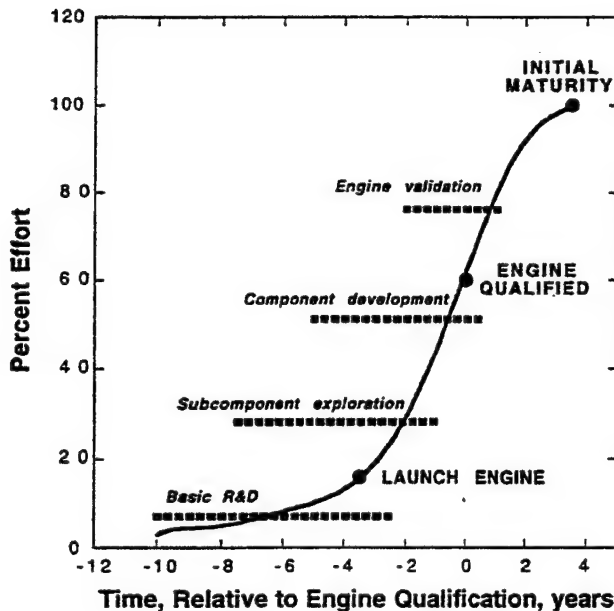


Fig. 4: Acquisition of Advanced Technology for a New Engine

The general performance trends are as follows: An increase in turbine inlet temperature (TIT) always results in more thrust per unit mass of air entering the engine (specific thrust, F_n / \dot{m}_a). For a given thrust, this gives a reduction in engine weight (increase in thrust to weight ratio, F_n / W), and in frontal area, and hence, in installed drag. However, if really high temperatures are contemplated, the improved F_n / W ratio is obtained at the expense of increased fuel consumption, i.e. an increase in specific fuel consumption, SFC. At a given operating temperature, increasing the engine pressure ratio, OPR, decreases the SFC, and also specific thrust, but only slightly, as well as reducing thrust/weight ratio somewhat (through a heavier compressor). Increasing the bypass ratio (BPR) of a turbofan engine enables the entire high-pressure section (core engine) to be smaller and lighter for a given installed thrust, and gives a lower SFC. However, it increases drag through the higher frontal area of the big fan, and increases the weight through the large diameter cowl.

From the basic behavior above, it can be seen that if low SFC is an important engine design goal, (transport application), then to take advantage of all possible

performance improvements, OPR, TIT and BPR should all be high. If high power density is an important engine design goal, (fighter/attack application), then OPR and TIT, should high, together with minimum frontal area and engine weight.

Company-conducted explorations of performance trends are usually confidential. However, results from a Pratt & Whitney study (Koff, 1989, 1991) provide interesting insights into some of the barriers to be overcome. For the turbo-fan engine the core is key to achieving higher performance. There are three parts to this: First, in increasing TIT as indicated above. Second, in improving rotating machinery already-high efficiencies through application of computer-designed blading to minimize secondary flow tip losses. Third, in improving the specific thrust at given TIT by minimizing wasted energy in the core engine, e.g. reducing windage losses in bearing compartments, and, in reducing air lost from the thermodynamic cycle by acting as buffer air for bearings, and as cooling air in the turbine. The power saved in this fashion can further increase propulsive efficiency by providing the energy needed to drive higher BPR fans, such as the ADP, advanced ducted propulsor (Meece, 1995).

In a study for future engines trends NASA has extrapolated existing commercial engine historical design trends to beyond the year 2,000 A.D. (Taccina, 1990). For large, subsonic turbofans, these studies indicated combustor inlet pressures at cruise of 300 psia (24 atm.) with corresponding combustor inlet temperatures of 1220 F (933 K). Trends for TIT's were to values over 2540 F (1667 K). Operation at these temperature and pressure levels would confer on the engine the benefits of high thermal efficiency and low SFC. The values quoted have already been surpassed, by substantial margins, in engines presently entering service.

For commercial applications therefore, the industry (Meece, 1995) sees continued gains in performance by the year 2015 A.D., to the order of a further 25 percent reduction in SFC relative to today's levels, achieved by all the means described above, and with OPR's of 75 at BPR's up to 25, together with 100 percent increase in F_n / W . The use of composite materials will play a significant and increasing role in the weight reduction, and indeed, will make the large diameter fans of the ultra-high BPR's feasible.

The U.S. Government's IHPTET initiative is aimed at taking engine technology well beyond that seen in the AFT Advanced Tactical Fighter (the F-119 engine in the F-22 aircraft). These engines experience temperatures up to 3500 F (2200 K) and pressures in excess of 40 atm. (Valenti, 1995). The IHPTET program has defined far-term goals for a variety of engines that advance in several phases. Actual performance figures are classified, but for each phase the delta's (relative to

the F-119) applied to TIT, etc., increase. Each engine component has been assigned its own goals that increase in similar fashion. Typically, for the fighter/attack application the overall engine goals, relative to the F-119/F-22 combination, are to double F_n/W , together with a halving of SFC. For subsonic transport applications the goal is a 30 percent decrease in SFC. The payoffs resulting from satisfaction of the initial goals are seen as:

- * sustained Mach 3+ cruise capability in an F-15 size aircraft
- * 100 percent range/loiter/payload increase in an F-14 size aircraft
- * 100 percent range/payload increase in a CH-47 size helicopter.

For the fighter/attack application OPR's up to 100 and TIT's up to near the stoichiometric limit for hydrocarbon fuels are being considered. Since the engine goal is a high power density and low drag, BPR's remain modest. Therefore, the weight side of the F_n/W balance is being forcefully addressed.

For the small engine utility/rotorcraft application, typical OPR's in the range of 25 to 50 with combustor inlet temperatures of 900 to 1450 F (756 to 1061 K), and TIT's of 2800 to 3600 (1811 to 2256 K), are being considered. These values are very aggressive compared to current performance in engines of this type.

For supersonic cruise applications studies (Smith, Jr., 1988) have generally narrowed down airliner application to Mach 2-3 cruise at 65,000 ft. (19.8 km) using kersene-type fuel with increased thermal stability to absorb the elevated levels of fuel thermal prestressing associated with sustained supersonic cruise. The engine would be of conventional layout, and thermodynamic cycle studies have shown that raising the allowable compressor discharge temperature increases the OPR possible, and provides incentive to go up to a higher TIT. As flight Mach number is increased the thermal efficiency increases, but the maximum occurs at a lower TIT due to ram effects in the engine inlet. For Mach 2.0 cruise with 1400 F (1033 K) compressor delivery temperature, the TIT might be 2950 F (1894 K) for maximum thermal efficiency. Of course, selection of actual temperatures will represent a suitable compromise choice between the effects on efficiency, jet noise, weight, drag and exhaust emissions.

Mission requirements for a strategic bomber utilizing sustained supersonic cruise are such that novel engine configurations become necessary, with thermodynamic performance that results in engine operating conditions that

are more severe than for commercial applications with supersonic cruise.

Summary of Combustor Trends

For the different categories of application for engines in Figure 1, regardless of mission or size, the trends for the operating conditions likely to be experienced by future combustors are the same: increased combustion pressure and increased TIT's. Table 1 summarizes likely ranges of the leading variables associated with the combustor.

Table 1: Possible Ranges of Future Combustor Variables

Compressor exit Mach Number:	0.25 - 0.35
Inlet pressure:	25 - 80 atm. (SLTO)
Inlet temperature:	1100 - 1600 F (867 - 1144 K)
Combustor configuration:	annular
Overall section pressure loss:	< 3.5 % inlet total pressure
Combustor L_c/H_d :	1.5
Overall equivalence ratio:	0.4 - 0.7
Mean radius:	216 - 250 mm (regardless of core airflow)
Dome height:	50 - 150 mm (dependent on airflow)
Combustion intensity:	(10 - 16) $\times 10^6$ BTU/hr.ft ³ atm. (10 - 16) $\times 10^4$ kW/m ³ bar

In Table 1 the ranges of combustor dimensions were arrived at as follows: Most current combustors have a burning length L_c , divided by the dome height H_d , of 2.0-2.5. With the imperative to reduce engine weight, there is a tendency to reduce L_c ; and, in order to reduce pressure losses due to heat addition and to achieve good altitude stability, there is a tendency to increase dome height. Together, these give a reducing length to dome height ratio for future combustors.

Dome height is usually selected on the basis of combustion section airflow and minimum operating pressure. However, regardless of airflow, few combustors have achieved adequate altitude stability with $H_d < 50$ mm, due to excessive heat losses to radiation at low pressures. Thus, there is a practical minimum on dome height.

The remarkably similar values for combustor mean radius, regardless of airflow and application, arise from the obvious fact that annular combustors have the engine mainshaft passing through them, and this gives an absolute

minimum on combustor size. For large turbofans, the trend of increasing BPR results in smaller cores for a given thrust, and these cores are becoming of similar size to military engines with lower bypass ratios. For small utility and rotorcraft engines, the layout frequently involves a reverse-flow combustor that is outboard of the turbine section. Therefore, most combustors will fall in the mean radius range quoted.

It can be realized from the above that combustor designers in the near-future, are going to be faced with very similar problems regardless of the engine applications with which they are concerned.

Examples of Some Enabling Technologies

Some of the consequences of the performance trends and likely combustor operating conditions described will fall outside of direct combustor effects, but nevertheless will exert a considerable influence on the options available to the designer.

Fuel pump:

An example of this is the fuel pump. Figure 5 illustrates how the fuel pump emerges as an enabling technology. Not only is the life of the pump itself an issue, it may force a choice of fuel injector flow number on the designer. This could influence the choice of injector type and number, and hence, determine liquid fuel atomization quality and distribution within the combustor, at important engine operating points. This would be quite independent of any combustion considerations. Injector flow number is defined as follows:

$$FN = \frac{\dot{m}_f}{\sqrt{\Delta P_{inj}}}$$

where the fuel flow rate \dot{m}_f is usually given in $lbm/hr.$, and the fuel pressure drop across the fuel injector ΔP_{inj} , is given in $p.s.i.$

Super-critical fuel:

A further example of an enabling technology is the ability to handle super-critical fuel.

JP8 fuel has a critical pressure of 42 atm., with a critical temperature of 710 F (650 K); Jet A has a critical pressure of about 21 atm. with a critical temperature of about 800 F (700 K). At sea level take-off (SLTO), current large turbofans already introduce Jet A above its critical pressure;

however, the fuel maximum temperature does not normally exceed 250 F (394 K) continuous, or 350 F (450 K) with a 5-minute maximum. Evaporation of liquid fuel droplets sprayed into the combustor therefore takes place normally at the "wet-bulb" temperature of, at about 30 atm., about 563 F (568 K). This condition is sometimes referred to as "transcritical injection."

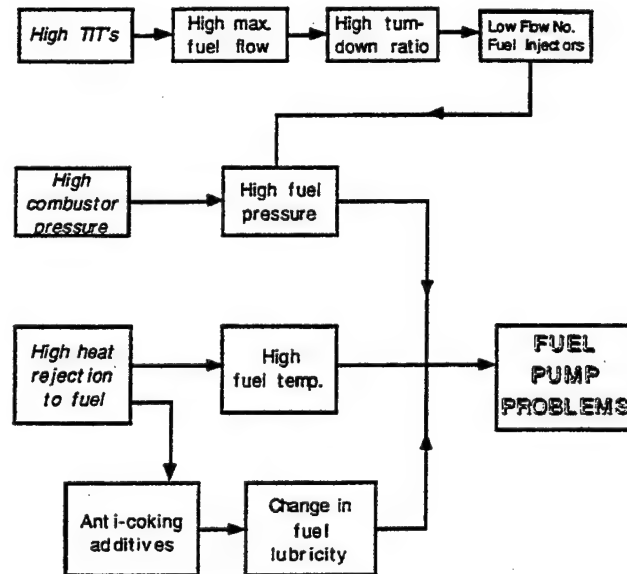


Fig. 5: Illustration of the Fuel Pump as an Enabling Technology

This may not be so in the future. An advanced, high-thrust ADP application having an ultra-high BPR achieved with a gear-driven fan (Meece, 1995) might reject as much as 1,000 HP (745.7 kW) as heat to the oil in the gear-box (Wilde, 1995). Since oil/air heat exchangers result in too much drag, the heat in the oil would be rejected to the fuel, with a resulting increase in fuel temperature.

In a military aircraft, the ever-growing heat load generated by the electronics suite is now also rejected to the fuel. As examples, the F-4 aircraft had a total heat sink requirement from engine, electrical, hydraulic and crew environmental system of 6,500 BTU/min. (114.2 kW), and this was accommodated through aerodynamic cooling; however, the F-15 aircraft has a requirement of 8,000 BTU/min. (140.6 kW) and is forced to use fuel cooling. For the upcoming F-22 aircraft the heat sink requirement from all sources has risen to 18,000 BTU/min. (316.3 kW). Should this system heat rejection be combined with a sustained supersonic cruise capability, the fuel in the tanks, the heat sink, would already be quite hot, particularly towards the end of a mission when most of the fuel would have been consumed.

If the engines of the future operate at higher pressures and temperatures, the "normal" heat pick-up from the engine in delivering fuel into the combustor will increase substantially. The problem can be compounded if some of the high pressure turbine, say the inlet guide vanes, is fuel-cooled in order to enhance turbine and cycle efficiencies by reducing cooling air.

For the above, and other reasons, the ability to handle fuel supplied to the combustor in the supercritical state, will be important.

While the existence of fuel at super-critical conditions within the fuel system introduces problems of its own, such as possible flow instabilities, super-critical fuel introduced into the combustor raises the issues of achieving the required distribution of the super-critical fluid across the burning zone, fuel/air mixing, and the (unknown) combustion characteristics of fuel in this state. It does appear as though some of the physical transport properties might be continuous across the critical point, but much uncertainty remains.

Paradoxically, there may be a fuel atomization difficulty at just prior to super-critical conditions, during transcritical conditions.

The break-up processes of liquid jets and sheets in a co-flowing air-stream are similar, and that for a sheet is illustrated diagrammatically in Figure 6. The concern is with the normally fast ligament formation and breakup phase.

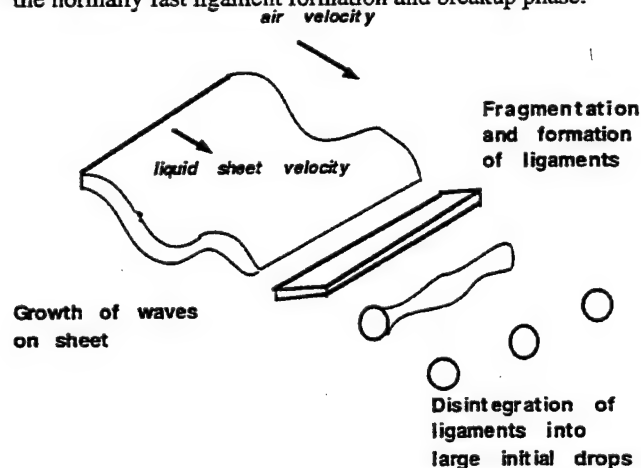


Fig. 6: Diagrammatic Representation of Liquid Sheet Breakup in Air

For the breakup of liquid jets and sheets the fuel properties are generally characterized by the Ohnesorge Number Z , where

$$Z = \frac{\mu_f}{\sqrt{\rho_f \sigma_f d_j}}$$

and the jet/sheet Reynolds Number Re_j , where

$$Re_j = \frac{\rho_f (\bar{u}_j - \bar{u}_a) d_j}{\mu_f}$$

and subscripts 'f' and 'a' refer to liquid and air respectively; ρ , μ , d , \bar{u} signifying density, viscosity, diameter/thickness and velocity. Surface tension is σ . For a given value of Z the Reynolds number has to be large enough for a particular fuel and jet/sheet to undergo immediate ($< 10^{-5}$ sec.) breakup.

For spherical droplets in flight, formed in the initial ligament phase, further breakup then occurs due to surface area to volume ratio effects if the Weber Number, We , where

$$We = \frac{\rho_a (\bar{u}_d - \bar{u}_a)^2 r_d}{\sigma_f}$$

and r_d is the droplet radius, exceeds a critical value of about 10-15. Such secondary breakups do not occur instantaneously, but after a specific time interval that is 1 - 5.5 times the characteristic time for spherical droplets (Faeth, 1996). The characteristic breakup time is proportional to the square root of fuel to air density ratio, the reciprocal of droplet relative velocity, and the droplet diameter, (Wu et al., 1995). During the initial phases of secondary breakup the originally spherical droplet undergoes flattening into a disk-like shape. This is due to low peripheral pressures caused by acceleration of gas over the surface. Drag coefficients for flattened droplets can be 10 - 15 times those for spherical droplets, with consequent increases in droplet velocity changes. Faeth has recognized that this secondary breakup can be rate-limiting for the atomization process.

For the limiting case of a supercritical fluid, the surface tension is zero, and both Z and We are infinite; atomization is therefore apparently a non-issue. An obvious difficulty arises through the relative velocity term in Re_j and We at sub-critical conditions but when the density ratio ρ_a/ρ_f tends to unity. Under such circumstances the terminal velocity of the liquid is reached extremely quickly due to very high drag forces, and the relative velocity tends to zero before the ligament breakup process is completed (Tishkoff, 1996).

Since the critical point represents a singularity with respect to compressibility and specific heat which become infinite, and the heat of vaporization which vanishes, it is better to operate well away from this region. If the critical point has to be passed through, then this should be accomplished quickly and not near any engine steady-state operating point. Engine operation at super-critical conditions should ideally be well into the super-critical regime to avoid problems associated with the singularity. Careful engine system design will be needed to achieve this.

There is reason for concerns over atomization quality even at nominal super-critical conditions. In a super-critical combustor environment the greatly increased solubility of the gas-phase into the liquid phase can bring combustion products into the transcritical liquid phase. In addition, the droplet flattening the preceeds secondary breakup results in a vortex ring formation around the periphery of the flattened droplet. The vorticity enhances entrainment of ambient fluid into the near-supercritical droplet (Mitts *et al.*, 1996). By these means the effective critical point conditions are raised way above the nominal critical point conditions for the pure fuel. Under such circumstances surface tension does not vanish. Large droplets, as described above, could thus be left. Furthermore, the vorticity ring has high coherence, and therefore tends to persist, resisting liquid-phase breakup.

These are not the end of the problems of super-critical fuel. Since the engine has to be started, accelerated and operated at low power levels where the pressures and temperatures experienced by the fuel will be below super-critical conditions, a form of "dual-fuel" injection capability will perhaps be needed.

Combustor material:

The combination of high air inlet temperatures and high combustion pressures with high TIT's, means that extremely high heat release rates will occur in future combustors. High heat release rates will result in high heat fluxes to the combustor liners and dome. The cooling capacity of the air flowing round the combustor and used to provide liner cooling, will be reduced owing to its higher temperatures. Therefore, for a given liner material and cooling technology, an increase in coolant flux will be demanded.

If the overall bulk equivalence ratio for the combustor is high, the equilibrium levels of carbon monoxide will also be high. Any air not fully taking part in the combustion process will result in an increase in the actual burning equivalence ratio. Therefore, use of air for combustor liner and turbine inlet guide vane (IGV) platform cooling (some of which is supplied in the combustor) leads to an increase in the equilibrium carbon monoxide, and so reduces

the chemical combustion efficiency. The additional large quantities of CO so-produced could emerge from the engine exhaust as a pollutant, when its heat of combustion is lost to the engine cycle. At stoichiometric conditions and relatively low operating pressures, this could amount to as much as 20 percent of the heating value of the fuel. Alternatively, if the gas temperatures remain high enough [above 2800 F (1800 K)], some of the CO could burn in the turbine and so add to its cooling air requirement.

For commercial applications, where exhaust emissions are regulated and production of oxides of nitrogen are a special concern, precise control of fuel/air mixing to desired burning equivalence ratios is demanded. Removal from the combustion process of any air for cooling, will adversely influence the level of mixing attained and hence, will have a deleterious effect on exhaust emissions. Similarly, for low emissions designs the existence of excessive wall cooling air can result in local quenching of the fuel chemical reactions and consequently, high emissions of CO and unburned hydrocarbons (UHC's) at low power levels.

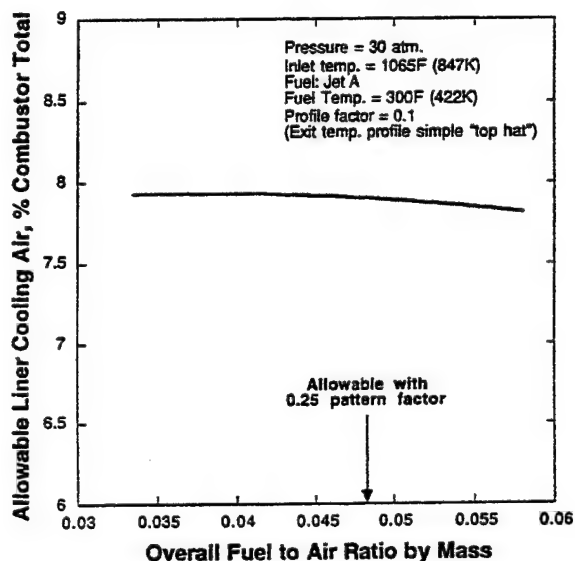


Fig. 7: Effect of Desired Exit Temperature Distribution on Allowable Liner Cooling Air for High Temperature Rise Combustion

Although reduction in future combustor size to save engine weight will help reduce the total amount of cooling air needed, almost any cooling air is too much to meet the advanced goals. Therefore, not only will more efficient liner cooling schemes have to emerge, the availability of a suitable

advanced high-temperature liner material becomes an enabling technology.

Figure 7 is indicative of the level of material technology that will be needed. The combustor operating conditions in the illustration are modest. The calculations were made for a constant 0.1 profile factor, and the limiting overall fuel/air ratio for a 0.25 pattern factor is shown.

Combustion Considerations

The major enabling technologies described above establish the broad background against which the fine details of the combustion processes for future combustors have to be evolved. The details of the combustion process will be centered on two important aspects: fuel-staging, and fuel/air mixing.

Fuel-staging:

Fuel-staging is inconvenient, and represents increased complexity, weight and cost, together with introducing severe concerns over reliability. These problems will have to be solved since fuel-staging is necessary due to the increased range of overall fuel/air ratios (OFAR's) that will be experienced in high TIT combustor designs. Fuel-staging does have two advantages going for it: First, it is a logical extension of existing systems technology. Second, the advent of the full authority digital engine control (FADEC) makes control of staging around a complete flight envelope feasible.

If the expanded range of OFAR's is attempted in a fixed geometry combustor, either a visible exhaust smoke problem at high powers, or a loss in stability at altitude relight conditions, ensues (Bahr, 1987). Fuel-staging breaks the linear relationship between OFAR and burning zone equivalence ratio. This allows operation at the low end of the OFAR range to be designed for stability and altitude relight, and high combustion efficiency; conversely, operation at the high power end of the OFAR range can be designed for a burning zone equivalence ratio below the threshold for the onset of visible smoke. Of course, two burning zones have to be provided in some way, one for each fuel-stage.

Perfectly premixed combustion systems have very narrow stability limits that are not suitable for the wide-ranging requirements of aircraft engines. Therefore, if well-mixed systems are desired, it is necessary to provide some kind of pilot to ensure continuous and efficient burning at all operating conditions. Fuel-staging is one method of providing this. It will be shown below that such improved fuel/air mixing is necessary.

Fuel/air mixing:

The major drivers for commercial and military combustors are respectively, low exhaust emissions and high temperature rise. In the future these drivers may, and probably will, converge. Both will depend on improved mixing.

Exhaust emissions of oxides of nitrogen (NO_x), which are regulated for commercial operations, are made up of about 90 percent by volume of nitric oxide (NO), less than 10 percent by volume of nitrogen dioxide (NO_2), and 1 - 3 percent by volume of higher oxides with nitrogen tetroxide (N_2O_4) being in equilibrium with NO_2 . The "brown tinge" sometimes presently observed in engine exhaust plumes on hot, dry days is not smoke (free carbon particles) but visible nitrous oxide (N_2O) and N_2O_4 , which have a strong reddish-brown color. In the far exhaust plume, further quantities of N_2O , N_2O_4 and nitrogen pentoxide (N_2O_5), which is also brown in color, can be produced from the NO and radicals present in the plume.

If very large quantities of NO_x are produced by a combustor, the engine exhaust can become readily visible due to the proportionately larger quantities of the brownish gases in the plume. From a military low observables point of view, this could be a matter of growing concern.

For aviation fuels, which contain negligible chemically-bound nitrogen, NO_x is produced by two mechanisms in the combustor. First, there is thermal NO via the well-known Zeldovich mechanism, which is a "time-at-temperature" process. Second, there is the so-called prompt NO (Fenimore, 1971) where in a hot, oxygen-deficient atmosphere nitrogen reacts preferentially with lower hydrocarbon fragments produced by fuel cracking, to yield NO via the amine group. In both instances the nitrogen is atmospheric. Thermal NO is generated therefore in the post-flame region, and prompt NO is generated locally in (especially stoichiometric) flame regions.

Frequently, estimates of thermal NO are made using the partial-equilibrium approximation for atomic oxygen with the Zeldovich mechanism. Justification for this is that the overall formation rate of NO is generally slow compared to hydrocarbon oxidation reactions, and therefore, NO can be uncoupled from the fuel oxidation process and that use of equilibrium radical concentrations is appropriate.

The above approximation alone cannot account for the large rates of measured NO production. Empirical models for prompt NO , e.g. that of Moore, (Moore, 1971), often make up for most of this observed discrepancy. (Sloan, 1991) Remaining differences could be attributed to fuel/air

unmixedness effects, e.g. as in Figure 8 below, where fuel is actually reacted over a range of equivalence ratios distributed about the bulk value.

The impact on the Zeldovich mechanism of super-equilibrium radical concentrations that are present when the reacting mixture is far from equilibrium, as it is in and near flame fronts, has yet to be definitively addressed. Certainly the magnitude of the radical O concentration decreases with increasing temperature, at given equivalence ratio (Miller & Bowman, 1989, and Fenimore, 1971). Also, even though super-equilibrium effects on NO formation rates may be present over a wide temperature range, the activation energy for NO formation is so large [76 kcal/gmol - (Monat et al., 1979)] in the Zeldovich mechanism that such accelerated rates still remain low.

Support for the prompt NO mechanism as the major explanation can be provided as follows. If an overall fit of total NO data resulting from lean burning, premixed, prevaporized jet fuel, regardless of the NO source, is made with a rate expression that has the concentration dependency of a thermal NO expression, then a strong similarity exists between the resulting temperature dependency and that of the prompt NO rate expression. For example, the overall fit (Sturgess, 1991),

$$\frac{d[NO]}{dt} = 1.2 \times 10^8 \exp(-64,000/RT) [O_2]^{1/2} [N_2]$$

g mole / cm³ sec.

compared to the prompt NO expression of De Soete (De Soete, 1975)

$$\frac{d[NO]_{prompt}}{dt} = 1.2 \times 10^7 \exp(-60,000/RT) [O_2]^b [N_2] [fuel]$$

where exponent b varies between zero and unity.

Contributions to total NO_x via the N_2O route are only significant for flame temperatures of 1500K and less, e.g. lean premixed combustors burning natural gas at modest engine operating conditions.

Therefore, for the aircraft application, it appears as though only issues associated with thermal and prompt NO_x need be considered. Leaving the combustor, the balance between prompt and thermal NO depends on details of particular designs.

When the fuel and air are separately introduced into the combustor the control strategies for NO are to mix the reactants as rapidly as possible to the selected bulk

equivalence ratios to avoid reaction at stoichiometric interfaces which generate large quantities of NO (Shouse et al., 1996), and to minimize the post-flame residence time (commensurate with accomplishing CO burn-up) (Sturgess et al., 1996). Most low- NO_x designs involve staging of some form, and the bulk equivalence ratios may be either fuel-lean (with a pilot for stability), or, rich-then-lean. At the cost of little added complication, the pilot may be modulated to low equivalence ratios at high power to minimize its contribution to NO_x . The rich-then-lean choice has to deal with the difficult problem of a rapid quench between rich and lean zones to avoid the stoichiometric interface problem.

Figure 8 illustrates the realities of fuel/air mixing for a 1970's era low-emissions combustor designed to have a fuel-lean primary zone on a bulk basis, and using conventional liner pressure drops and airblast-atomizer technology.

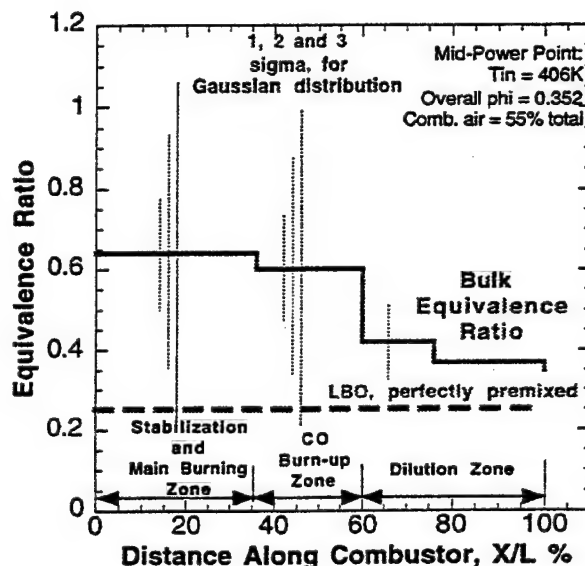


Fig. 8: Effect of Imperfect Mixing on Local Stoichiometry for a Low-Emissions Combustor

Mixing in the analysis is represented via a Gaussian distribution of local equivalence ratio, where the width of the Gaussian is determined by a data-survey of actual combustors (Heywood & Mikus, 1973, Sturgess & Morford, 1994). Although the primary zone had a bulk equivalence ratio of 0.63, i.e. rather lean, fuel was actually burned over a range of equivalence ratios from about 0.2 to about 1.1. Local flame temperatures ranged far from the bulk value, and had values low enough to slow the CO consumption reactions and high

enough to accelerate the NO_x reactions. "Stirring" downstream of the primary zone cannot be guaranteed to take care of such stratification. As a consequence, measured CO levels for this combustor were very much higher than expected and measured NO_x , while relatively low, was also higher than anticipated for the design equivalence ratio. The conclusion was reached that this combustor achieved its relatively low NO_x at the expense of increased CO at all power levels, i.e. the combustor did not represent a true low emissions design, and was mixing-limited.

For high TTT's at high heat release rates (i.e. with smaller, weight-saving combustors), and attempted with similar mixing technology, plots like Figure 8 would exist, but at higher bulk equivalence ratios. In this case, the spread of achieved equivalence ratios would cause proportionally more of the fuel to experience local equivalence ratios greater than unity. As a consequence, CO and UHC (unburned hydrocarbons) emissions from the combustor would be high at high power conditions, and temperature rise could become mixing-limited.

It has been demonstrated (Swithenbank, 1974) that, given sufficient time, and using mechanically-generated turbulence, perfectly-stirred conditions (zero gradients of concentration and temperature) can be achieved by using a combustor pressure loss factor,

$$\frac{\Delta P}{q} \geq 3.0$$

where the dynamic head q is based on mean axial velocity upstream of the turbulence-generating device.

The combustor can be viewed as a high solidity turbulence grid enclosing the reacting flow contained within it. Therefore, Swithenbank's critical pressure loss factor should be applicable. However, experience teaches that few practical combustors are successful if the pressure loss factor is less than about 25 inlet dynamic heads, (e.g. Lefebvre, 1983). Why is there such a large discrepancy between fundamentals and practice?

Chemical reactions take place between molecules; therefore, fuel and air must be mixed on the molecular level. The length scale of turbulent eddies for molecular mixing, where introduced energy is finally produced as heat, is given by the Kolmogorov eddy length scale η , where,

$$\eta = (\nu^3 / \epsilon)^{1/4}$$

where ν is the kinematic viscosity and ϵ is the dissipation rate of turbulence kinetic energy. For fully developed

turbulence a Reynolds number-independent wave number k_d , can be identified where dissipation reaches a maximum. Experimentally, it has been shown by Townsend and, Stewart & Townsend (Hinze, 1975) that at high Reynolds numbers most viscous dissipation occurs at a condition given by,

$$k_d \eta = 0.2$$

Hence, if mixing is (reasonably) equated with dissipation, the length scale for mixing ℓ_d , is about,

$$\ell_d = 5\eta$$

By these means the mixing length scales at standard atmospheric conditions can be estimated as about 0.4 mm, and at 100 atm. pressure with 1800 F (1256 K) as about 0.4×10^{-3} mm.

In order to make these estimates information concerning the dissipation rates of turbulence kinetic energy was needed. Direct measurement of dissipation is not easy, and certainly no measurements at 100 atm. are known to this author. Furthermore, dissipation will vary spatially throughout a combustor. To obtain the length scale estimates given above, "typical combustor values" at lower pressures were used and were extrapolated via a suitable model, to the 100 atm. condition. From atmospheric pressure to the 100 atm. condition the dissipation estimated in this fashion varied by some orders of magnitude. Therefore, the length scale values given should be treated with caution until actual measurements become available, and should be viewed as only representing the likely ranges to be encountered. However, the turbulence assumptions made at the 100 atm. condition place such a combustor on a Borghi plot consistent with other combustors of Sattelmayer and of Correa at pressures from 1 to 15 atm., Sturgess, 1996.

Consider now the typical conventional combustor of annular form. The circumferential spacing between fuel injectors is about 1.0 dome height, the first row of air addition ports are placed between 0.5 and 1.0 dome heights downstream from the dome, with about half-a-dome height spacing between jets, and, the combustor length is 2-3 dome heights, of which the intermediate zone is about half-a-dome height in length, as is the dilution zone. Partial modeling has demonstrated that to first order, the gross flow field in a combustor is determined by the confining geometry (Spalding, 1956). The characteristic length for a conventional combustor can therefore be taken as the dome height, H_d . From Table 1, dependent on airflow,

$$50 < H_d < 150 \text{ mm}$$

Given the vertical cross-sectional symmetry, the major flow structures established in the combustor will hence have a linear dimension on the order of 25 - 75 mm.

When the typical flow structure dimension in a conventional combustor is compared to the length scale of the eddies for turbulent mixing, the dynamic range is from about 60 at low pressures to about 190×10^3 at high pressures. Therefore, although gross Reynolds numbers might suggest otherwise, the turbulence, on a bulk basis, is not fully developed throughout the combustor. Intense mixing thus only occurs in a relatively few shear layers of limited extent, that exist around the peripheries of the major flow structures present in the combustor. For example, the shear layers between the liquid fuel sheet and the air jets associated with it in airblast atomizing fuel injectors, the shear layers between the fuel/air spray from the injectors and the dome recirculation zones, and, the shear layers between the transverse air jets and combustion gases moving around them. The majority of the energy introduced into the combustor by the pressure drop across the liners goes, not into direct mixing, but into bulk mass transport over the relatively large distances between flow features. This explains the difference between theory and experience with respect to combustor pressure loss factor.

With the present uncertainties described above with respect to dissipation rate at very high pressures, the absolute magnitude of the mixing length scales may be inaccurate. However, the relative magnitudes with respect to the combustor flow structure sizes certainly are in the correct range. Therefore the conclusions drawn are valid.

If improved fuel/air mixing is required due to the needs to control emissions and to achieve high heat release rates, then combustion section pressure loss must be utilized much more effectively. For cycle performance reasons it cannot be increased. More effective use of pressure loss implies, 1.) a reduction in the combustor characteristic length scale by at least an order of magnitude, and, 2.) an increase by a factor of at least two, in the number of shear layers existing and active in the combustor.

The inference from these two changes, and the implication from partial modeling (Spalding, 1956), is that fairly radical changes in combustor geometry will be needed. The geometric layout of gas turbine combustors has existed essentially unchanged since the days of Whittle and von Ohain. Therefore, the changes suggested may fairly be described as "paradigm-breaking." However, if mixing is made more effective, it might be possible to contribute towards achieving two additional important engine goals: 1.) a reduction in combustor pressure loss, and, 2.) a reduction in

section length. Such reductions would help SFC and F_n/W respectively.

Emissions:

The well-known adverse atmospheric and environmental effects of gas turbine emissions, and especially NO_x , have led to increasingly severe regulatory action for commercial aircraft operations (Segalman et al, 1994). The direct concern over NO_x - emissions for military visibility reasons is described above. There is an additional cause for concern. NO_2 has lethal toxic potency, as does NO but only at one-fifth the potency of NO_2 (Lilley, 1996). Fatality with NO_2 occurs within 10 minutes at exposure levels of 200 ppm. As a pulmonary irritant, prolonged exposure to NO_x at low concentrations has also been identified as a cause of emphysema. Now, in addition to normal airfield taxi-take-off-landing operations, a modern military warplane usually spends some 30-45 minutes on the ground, prior to a mission, at engine idle power while the electronics suite is aligned and calibrated. Therefore, the potential hazard to flight-line crews during both routine and extended operations can be appreciated.

Improved fuel/air mixing has been identified as a necessary control parameter for emissions. However, it appears that fairly drastic design changes will be necessary to achieve significant improvements in the direct, *in situ*, mixing required to avoid the twin dangers of auto-ignition and flash-back associated with premixing. Therefore, it is desirable to assess the impact of advanced engine performance (as typified by the IHPTET effort) on NO_x emissions.

Figure 9 displays projections of the emission indices of NO_x (as NO_2) as a function of pressure up to 100 atm., at a fixed overall equivalence ratio of 0.5, for a number of different combustors. Combustor inlet temperature was varied with the pressure along an assumed compression characteristic. The combustors shown represent, from top to bottom, a single-stage conventional combustor, an axially-staged combustor utilizing otherwise conventional technology (Segalman et al, 1994), a fuel-staged, increased-mixing combustor, and a single-stage, ideal, prevaporized, premixed combustor with all of the combustion air introduced through the dome. The "ideal" combustor is of course, impractical, but serves as a limit on what is attainable. All of the combustors assumed use of an advanced liner material/cooling scheme that utilized a maximum of 15.5 percent of the total combustor air for cooling and profile-trim purposes; this air was taken as not being available for combustion purposes. The (hot) residence time in all combustors was fixed at 2.7 ms. All NO_x values are corrected to standard humidity.

In each case considered, except for the "ideal," a calibrated "flow model" for that combustor configuration was exercised over the range of operating conditions, and involved solving the same detailed chemical kinetic reaction mechanism on the appropriate flowfield. Both thermal and prompt NO_x were included. This procedure is considered to be more accurate than just extrapolating a simple NO_x correlation. It is important to note that a completely independent assessment (by methods unknown to the present author) of the fuel-staged, increased-mixing combustor over this pressure range produced results virtually identical in slope and almost equal in magnitude to the present calculations. However, it is naive not to accept that some level of uncertainty is involved over the wide range of pressures covered.

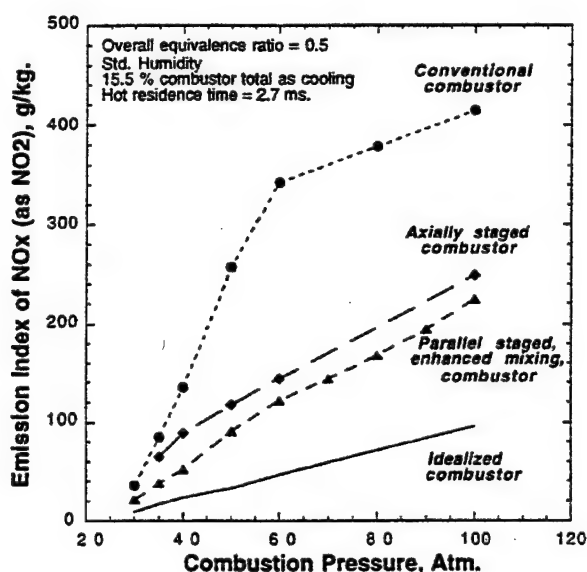


Fig. 9: Effect of High Pressure Combustion on NO_x Emissions for Several Combustor Designs

For the ideal combustor, the calibrated lean, premixed, prevaporized, jet-fuel NO_x rate equation given above (Sturgess, 1991) was integrated directly.

The calculated NO_x from the conventional combustor was found to increase rapidly to very high levels with increasing pressure. These levels reached equilibrium values about 60 atmospheres. Quite clearly, the environmental impacts, visibility issues and potential health effects will most likely preclude the use of conventional combustor technology in advanced engines of the future.

The curve for the "ideal" low- NO_x combustor shows quite high levels of NO_x being produced at 100 atm. relative to levels produced in current engines. Therefore the term "low- NO_x " as applied to combustors for future engines is a misnomer; perhaps "minimized NO_x " or "contained NO_x " might be better. It should be remembered that Figure 9 is expressed in g NO_x per kg fuel burned. Use of increased pressure would reduce the amount of fuel burned for a given mission. This might, in turn, give a reduction in the absolute mass of NO_x from integration over an operating envelope. Therefore, not only are the absolute values of NO_x in Figure 9 important, but also the gradients.

It can be seen that the fuel-staged, but otherwise conventional, ASC combustor (Segalman et al., 1994), does very well on containing NO_x production compared to the conventional combustor. Figure 10 illustrates the NO_x reduction that is achievable just due to staging, (Segalman et al., 1993).

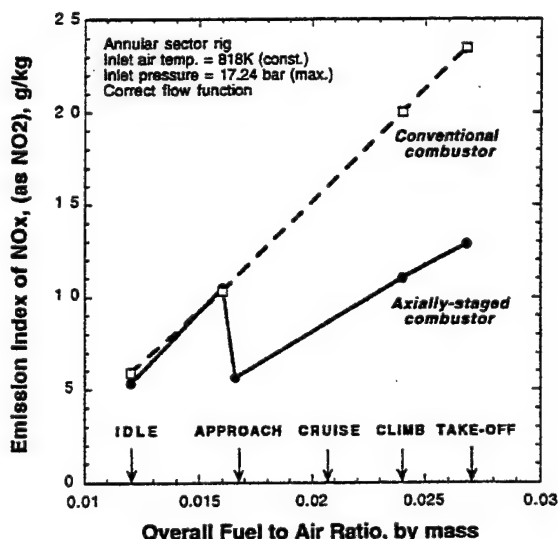


Fig. 10: Illustration of Reduced NO_x Due to Fuel-Staging

The gradient of NO_x with pressure for the axially-staged combustor in Figure 9 is also reduced relative to the conventional combustor. However, the absolute levels of NO_x are still rather high, being over 250 g/kg at 100 atm. Relative to the ideal but impractical combustor, it shows the progress that is theoretically still to be achieved. The curve for this combustor was produced using a model that did very well at calculating the ASC engine test results to about 32

atm. Therefore, there is a fairly high degree of confidence that the results are reasonably realistic.

The NO_x characteristic for the fuel-staged, increased-mixing combustor falls between the ASC and the ideal cases, being closer to the former than the latter. However, it does represent an improvement over existing technology. The improvement over the ASC is primarily attributable to the improved fuel/air mixing associated with a reduced length-scale in the main stage. It represents the first step in what might be possible if the design paradigm is broken, as described above.

The curve is constructed with an extrapolation (a very large extrapolation, admittedly) using modeling, of experimental results obtained in a rig demonstrator at atmospheric pressure. Whether it is possible to develop such a combustor into an "engine-worthy" design, and while doing so retain the reduced emissions or even improve on them, remains to be seen. Note also that the residence time is the same as that for all of the combustors. With improved mixing it might be possible to reduce the residence time. Such a reduction would further lower the thermal NO_x produced.

Extending the analysis in parametric form for overall equivalence ratio revealed quite severe increases in NO_x levels, with even the "ideal" combustor producing 200 g/kg at 100 atm. for 0.7 equivalence ratio. To restore the NO_x of the "ideal" combustor at 100 atm. and 0.7 equivalence ratio to the previous 100 g/kg. for 0.5 equivalence ratio at this pressure, it was necessary to reduce the residence time from 2.7 ms to under 1.5 ms.

It will be observed in Figure 9 that the calculated gradients of NO_x with increasing pressure for the two fuel-staged combustors and the "ideal" combustor do not vary very much over the pressure range, and agree reasonably closely with each other.

In general, the pressure exponent for NO_x depends on which of the NO_x generation mechanisms dominates in a combustor, and, for each mechanism, can vary significantly with local equivalence ratio, i.e. the dependency is determined by both equivalence ratio and adiabatic flame temperature. The behavior is therefore complex. An example of this complexity is illustrated in Figure 11 for experimental lean methane/air mixtures at 322K inlet temperature, burning on a perforated plate flameholder at 3 - 10 atmospheres, and calculations made over a wider range of conditions up to inlet temperatures of 728K and pressures of 14.6 atmospheres (Sturgess, 1992). In the figure, the pressure exponent is plotted against adiabatic flame temperature. The generality of such calculations will depend, of course, on the accuracy of the reaction mechanisms used and the reliability of the associated rate constants.

While the experimental data in Fig. 11 is very limited, the close agreement with the calculations in this region can be noted. It is also well-known that for adiabatic flame temperatures of 1500K and less for methane/air systems, N_2O is the dominant pathway to NO_x .

Accurate representation of the the pressure dependency of NO_x is clearly important when making calculations at greatly elevated pressures, as in Fig. 9.

The pressure dependencies of the fuel-staged combustors shown in Figure 9, when these combustors are operated over the same range of conditions, therefore depends on the details of the emissions-control strategy used, and also, on the degree of fuel/air mixing achieved in each design. Clearly, these may be judged to be somewhat similar for the cases shown in the study.

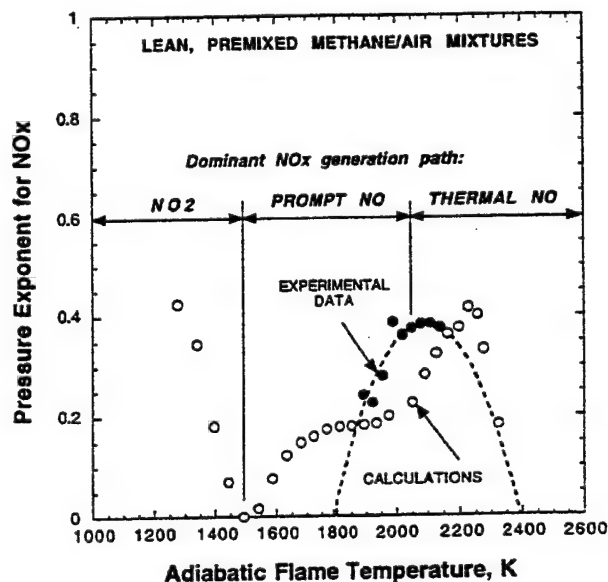


Fig. 11: Provisional Pressure Dependency for NO_x

Figure 12 illustrates why the "ideal" combustor will remain an ideal, and why it will be difficult to achieve the pre-combustion improved fuel/air mixing essential to lower NO_x generation. The figure presents the variation of estimated ignition delay times along the compression characteristic for perfect premixing and for the relatively poor mixing rates typical of current systems. The estimated mixing and ignition delays are for vaporized JP8/Jet A to simulate fuel injected in the super-critical state. The ignition delays were found from a

data correlation of JP5/Jet A/JP4/Avtur etc., and that included data up to 60 atm. pressure (Sturgess, 1979).

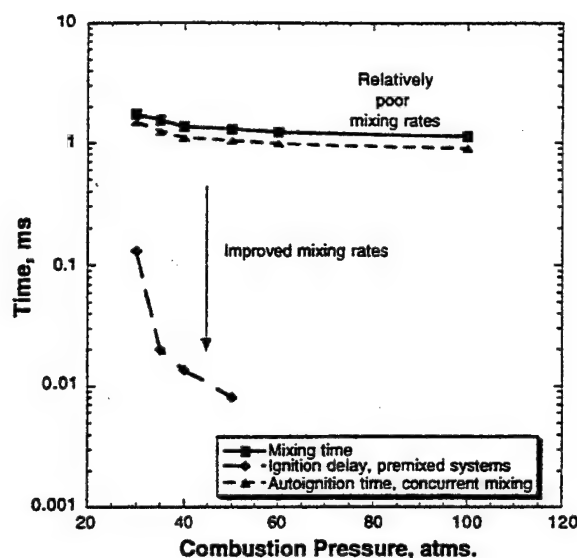


Fig. 12: Influence of Compression Characteristic on Autoignition Behavior for Current and Perfect Mixing Systems

Ignition delay times for perfect premixing are less than 0.1 ms for pressures above 30 atm. For current systems it can be seen that the estimated autoignition occurs before the estimated mixing is complete, and this concurrent behavior is to be expected. Ignition delays are less than 1 ms.

The implications of the calculations are as follows: 1.) perfect premixing will be impossible at elevated pressures and the temperatures that go with them, 2.) design of any kind of practical fuel/air mixer to achieve some, but less than perfect, mixing prior to combustion will be exceedingly difficult, since flow wakes and separations must be avoided under all circumstances, and, 3.) direct injection of fuel, but with wide dispersion to improve presentation to combustion air, appears as a lower-risk approach.

Combustion dynamics:

The trend for the future would appear to be towards improved mixing. It is well-known that well-mixed combustion systems can be notoriously susceptible to nonstationary behavior of the mean flow field, with the possibility of acoustic coupling. The term "combustion

dynamics" is coming into use to describe this type of behavior. The nonstationary behavior situation is exacerbated when the well-mixed combustor is operated lean as an emissions control strategy. High combustion pressures further increase the tendency towards mean flow instability.

If an engine is designed with high turndown ratios and ultra-high combustion pressures, and the fuel pump enabling technology is not adequate, use of high flow number fuel injectors may be forced on the designer. One implication of high flow number fuel injectors is that at low engine power levels, the fuel system at the combustor does not "run full." This means that the fuel supply is "acoustically open" to the combustor. In a well-mixed, fuel-lean combustor that is dynamically active, a driven oscillation can then be established, especially during low power level engine transients.

The consequences of such combustion dynamics can range from increased engine noise (passenger annoyance, regulation violations), increased heat transfer in the combustor, ingestion of hot partial-combustion products into fuel injectors (coking problem), and, engine component (pipework usually) resonances.

This is a phenomenon that is present to some degree in many of today's conventional combustors, and is commonly referred to as "rumble." Frequencies range from about 50 to 500 hertz, and peak-to-peak amplitudes can be rather high. In these cases it is either ignored or "engineered around." Neither of these treatments are expected to be adequate if the combustor changes described above come into production. It is an area that is expected to assume increasing importance in these future combustors. Unfortunately, our understanding of, and our ability to calculate, combustion dynamics is rudimentary at best. The possibility of solving these difficulties, or even exploiting them to advantage, by means of active combustion control (ACC) is an intriguing possibility.

Conclusions

Many important issues that are relevant to combustion systems for future aircraft gas turbine engines have been touched upon. In such a presentation as this the treatment of individual issues can only be cursory. Much is still unknown in many of the topics highlighted, and research work is proceeding in these areas. It is most likely that some of the issues presented will turn out not to be major blockages to progress, while others will surface that are not presently mentioned. Variable geometry, active combustion control, endothermic fuels, and the use of micro-electronic and mechanical systems (MEMS) technology are not discussed.

Their omission is deliberate. These are dynamic areas of great potential, subject to on-going research and development, and as such, the associated technology is sensitive.

From the areas discussed the following general conclusions can be drawn:

1. Future engine layouts and performance will cause combustors for many applications to become similar in general size. Common design problems and solutions will come about.
2. Combustor operating conditions will continue to increase in severity through increased operating pressure, air inlet temperature and temperature rise.
3. Major enabling technologies have been identified as:
 - a) an ultra-high pressure fuel pump capable of handling hot fuel,
 - b) the ability to deliver and burn super-critical fuel,
 - c) high temperature liner materials.
4. Major design challenges for the combustor are:
 - a) increased space heating rates with no increase in pressure drop,
 - b) containing exhaust emissions as operating conditions increase.
5. Significant changes to the combustor will include:
 - a) certainly, fuel staging for high turndown ratios,
 - b) probably, geometry changes for enhanced fuel/air mixing,
 - c) possibly, active combustion control for engine health maintenance, reduced noise, and perhaps, enhanced fuel/air mixing.

Acknowledgement

The author would like to acknowledge support of this work through the U.S. Air Force, Wright Laboratory, Aero Propulsion and Power Directorate, Contract Number F33615-95-C-2507. Special thanks are due to Mr. Carlos Arana of the Air Force, who asked some of the questions that have been addressed. The encouragement of Dr. W.M. Roquemore is gratefully acknowledged.

References

Bahr, D.W., 1987, "Technology for the Design of High Temperature Rise Combustors," *AIAA Journal of Propulsion*, Vol.3, No.2, March-April, pp. 179-186.

De Soete, G.G., 1975, "Overall Reaction Rates of NO and N₂ Formation from Fuel Nitrogen," proc. *15th. Symposium (International) on Combustion*, The Combustion Institute, Pittsburgh, Pennsylvania, pp. 1093-1102.

Faeth, G.M., 1996, "Secondary Breakup and Turbulence Interactions of Drops, proc. *ARO & AFOSR Contractor's Meeting in Chemical Propulsion*, Virginia Beach, Virginia, June 3-6, p.140.

Fenimore, C.P., 1971, "Formation of Nitric Oxide in Premixed Hydrocarbon Flames," proc. *13th. Symposium (International) on Combustion*, The Combustion Institute, Pittsburgh, Pennsylvania, pp. 373-380.

Gillette, Jr., F.C., 1996, "Designing Gas Turbine Engines for 21st. Century Mechanics," *Global Gas Turbine News*, pub. IGTI, Vol.36, No.1, pp. 4-8.

Heywood, J.B. and Mikus, T., 1973, "Parameters Controlling Nitric Oxide Emissions from Gas Turbine Combustors," presented at AGARD Propulsion & Energetics Panel's 41st. Meeting on *Atmospheric Pollution by Aircraft Engines*, London, England.

Hinze, J.O., 1975, *Turbulence*, 2nd. edition, McGraw-Hill, Inc., New York, New York, pgs. 223, 224.

Hooker, S.G., 1959, "Future of Air-Breathing Engines in Aviation," Inst. Mech. Engrs., James Clayton Lecture, London, England.

Koff, B.L., 1989, "The Next 50 Years in Jet Propulsion," presented at 50th. Anniversary of Jet Powered Flight, Dayton, Ohio, 23 August.

Koff, B.L., 1991, "Spanning the Globe with Jet Propulsion," Paper No. 91-2987, William Littlewood Memorial Lecture, *AIAA 1991 Annual Meeting & Exhibit*, Arlington, Virginia, April 30-May 2.

Lefebvre, A.H., 1983, *Gas Turbine Combustion*, Hemisphere Publishing Corp.

Lilley, D.G., 1996, "Fire Hazards of Flammable Fuel Release," Paper No. 96-0405, *AIAA 34th. Aerospace Sciences Meeting & Exhibit*, Reno, Nevada, January 15-18.

Meece, C.E., 1995, "Gas Turbine Technologies of the Future," Paper ISABE 95-7006, proc. *International Air Breathing Engines 12th. Intl. Symp. on Air Breathing Engines*, editor F. Billig, Vol.1, Melbourne, Australia, Sept. 10-15, pp. 79-88.

- Miller, J.A. and Bowman, C.T., 1989, "Mechanism and Modeling of Nitrogen Chemistry in Combustion," *Progress in Energy and Combustion Science*, Vol. 15, pp.287-338.
- Mitts, C., Talley, D. and Poulidakos, D., 1996, "A Fundamental Study of Supercritical Droplet Deformation and Breakup Through a Miscible Fluid Analog," Paper No. AIAA-96-2858, proc. 32nd. AIAA/ASME/SAE/ASEE Joint Propulsion Conference, Lake Buena Vista, Florida, July 1-3.
- Monat, J.P., Hanson, R.K. and Kruger, C.H., 1979, "Shock Tube Determination of the Rate Coefficient for the Reaction $N_2 + O = NO + N$, proc. 17th. Symposium (International) on Combustion, The Combustion Institute, Pittsburgh, Pennsylvania, pp. 543-552.
- Moore, J., 1971, "The Effects of Atmospheric Moisture on Nitric Oxide Production," *Combustion and Flame*, Vol. 17, pp. 265-267.
- Segalman, I., McKinney, Sturgess, G.J., and Huang, L-M, 1993, "Reduction of NO_x by Fuel-Staging in Gas Turbine Engines - A Commitment to the Future," AGARD Conference Proceedings 536, *Fuels and Combustion Technology for Advanced Aircraft Engines*, proc. Propulsion and Energetics Panel 81st. Symposium, Fiuggi, Italy, 10-14 May, pp. 29-1 - 29-17.
- Segalman, I., Smith, R., Sturgess, G., Morford, S. and Hoke, J., 1994, "Engine Demonstration of NO_x Reductions with a Fuel-Staged Gas Turbine Combustor," Paper No. 94-2712, proc. 30th. AIAA/ASME/SAE/ASEE Joint Propulsion Conference, Indianapolis, IN, June 27-29.
- Shouse, D.T., Frayne, C., Stutrud, J., Gogineni, S. and Sturgess, G.J., 1996, "The Role of Transverse Air Jets in the Formation of Gas Turbine Emissions," Paper No. 96-0705, 34th. Aerospace Sciences Meeting & Exhibit, Reno, Nevada, January 15-18.
- Sloan, D.G., 1991, "Calculation of NO_x in a Premixed Flame, Pratt & Whitney internal memorandum.
- Smith, Jr., M.G., 1988, "21st. Century High Speed Transport Propulsion," Paper No. 88-2987, proc. AIAA/ASME/SAE/ASEE 24th. Joint Propulsion Conference, Boston, MA., July 11-13.
- Sturgess, G.J., 1979, "Advanced Low Emissions Catalytic Combustor - Phase I," Pratt & Whitney Report PWA-5589-19, prepared under NASA Lewis Research Center Contract NAS3-20821.
- Sturgess, G.J., 1980, "Gas Turbine Combustor Design Challenges for 1980's," Paper No. 80-1285, AIAA/SAE/ASME 16th. Joint Propulsion Conference, Hartford, Connecticut, June 30 - July 2.
- Sturgess, G.J., 1991, "Calculation of NO_x in Combustors," Pratt & Whitney internal memorandum.
- Sturgess, G.J., 1996, "Combustion/Turbulence Interaction: - A Bridge Between Theory and Application," invited talk, Workshop on Combustion Modeling, ARO & AFOSR Contractor's Meeting in Chemical Propulsion, Virginia Beach, Virginia, June 3-6.
- Sturgess, G.J. and Morford, S., 1994, Pratt & Whitney internal presentation.
- Sturgess, G.J., Gogineni, S., Shouse, D.T., Frayne, C., and Stutrud, J., 1996, "Emissions and Operability Trades in the Primary Zones of Gas Turbine Combustors," Paper No. 96-2758, 32nd. AIAA/ASME/SAE/ASEE Joint Propulsion Conference, Lake Buena Vista, Florida, July 1-3.
- Swithenbank, J., 1974, "Flame Stabilization in High Velocity Flow," *Combustion Technology - Some Modern Developments*, editors, H.B. Palmer and J.M. Beer, Academic Press, pp. 91-125.
- Tacina, R.R., 1990, "Combustor Technology for Future Aircraft," Paper No. 90-2400, proc. AIAA/SAE/ASME/ASEE 26th. Joint Propulsion Conference, Orlando, Florida, July 16-18.
- Tishkoff, J., 1996, after-dinner talk on AFOSR Programs, DoE Advanced Gas Turbine Systems Research *Combustion Workshop III*, UCLA Conference Center, Lake Arrowhead, CA., March 19-122.
- Valenti, M., 1995, "Upgrading Jet Turbine Technology," *Mechanical Engineering*, Vol. 117, No.12, December. pp. 56-60.
- Wilde, G.L., 1995, interview given in *Global Gas Turbine News*, published by IGTL, Vol. 35, No. 4, pp. 4-7.
- Wu, P-K., Hsiang, L-P. and Faeth, G.M., 1995, *Liquid Rocket Engine Combustion Instability*, ed. V. Yang and W. Anderson, AIAA, Washington DC, p. 247.



AIAA 2000-3351

**Influence of Ceramic-Matrix-Composite
Wall Plates on Combustor Performance**

V. R. Katta, R. Anthenien, R. Mantz,
W. M. Roquemore, R. A. Brockman, R. John,
L. P. Zawada, T. A. Parthasarathy and R. Kerans
Air Force Research Laboratory
Wright-Patterson AFB, OH

**36th AIAA/ASME/SAE/ASEE
Joint Propulsion Conference & Exhibit
July 17-19, 2000 / Huntsville, AL**

For permission to copy or to republish, contact the American Institute of Aeronautics and Astronautics,
1801 Alexander Bell Drive, Suite 500, Reston, VA, 20191-4344.

Influence of Ceramic-Matrix-Composite Wall Plates on Combustor Performance

V. R. Katta¹, R. Anthenien², R. Mantz², W. M. Roquemore², R. A. Brockman³, R. John⁴,
L. P. Zawada⁴, T. A. Parthasarathy⁵ and R. Kerans⁴

Air Force Research Laboratory
Wright-Patterson Air Force Base, OH 45433-7103

Abstract

Recent advances in manufacturing and materials technologies have driven interest into the development of ultra compact aircraft engines for delivering high thrust for the future air vehicles. These engines are expected to utilize the advantages of constant-temperature cycle to gain extra thrust by burning fuel in the turbine sections. However, the high-velocity and high-g conditions prevail in the turbine section pose a formidable task for achieving sustained combustion. Air Force has recently proposed a trapped-vortex strategy to circumvent these difficulties and a series of experimental and numerical studies were initiated to study various concepts associated with turbine burners. This paper describes preliminary studies conducted on a Inner Turbine Burner (ITB) that uses Ceramics-Matrix-Composite (CMC) materials on the cavity walls. A well tested two-dimensional CFD code was used for the simultaneous simulation of reacting flow in the combustor and heat transfer in the metal parts. Calculations made with stainless steel and CMC back plates showed that a reduction in wall temperature can be achieved with the latter. Numerical experiments were performed by using fictitious metals with different material properties as back plates in the cavity to understand the role of individual material properties on combustor performance.

Introduction

Utilization of vortex motion to the aerodynamic advantage has been studied for many years. Experiments of Rohsenow et al.¹ have shown that when two circular orifices are placed in series in a pipe, a large recovery of pressure occurs across the second orifice in certain circumstances; hence, the overall pressure drop is considerably less for the two orifices than for a single one having the same flow. In ribbed diffusers, Migay² found

that balancing the fluid removed by entrainment and the fluid entering the cavity by reversed flow ensures that the flow outside the cavities will follow the ribs fairly closely, and a good pressure recovery will be obtained. Mair³ and Little and Whipkey⁴ showed that on mounting a disk behind the base of a blunt body the drag of the blunt object can be reduced. Using similar concepts, Roshko and Koenig⁵ reported a reduction in drag of blunt forebodies when disks are placed on spindles ahead of the body.

Using trapped-vortex (TV) concepts Hsu et al.⁶ proposed a revolutionary advancement in the development of a simple, compact, and efficient method of combustion. It employed a vortex that is trapped in a cavity formed within the combustor to stabilize the flame. Experiments conducted on the center-body TV combustor suggested that the lean blowout characteristics of the combustor indeed improved significantly when the cavity size is kept at optimum value for trapping a vortex. These experiments also demonstrated that when the cavity has an optimum size, the combustion efficiency increased and the concentrations of the pollutants such as NO_x and soot decreased. Following their successful incorporation of the Trapped-Vortex concept for the main combustors, researchers at Wright Patterson Air Force Base came up with a novel idea of using such a concept in obtaining a stable combustion in the vicinity of the turbine section.

In traditional jet engines as the combustion products pass through the turbine section their temperature decreases. This leads to under utilization of thrust extraction through the exhaust nozzles. For increasing the overall thrust of the engine, afterburners are added between the turbine and exhaust nozzle in which additional fuel is burnt to increase the gas temperature. The disadvantage with the afterburners comes from the increased weight of the engine. Typically, afterburners are quite long and heavy. Recently, Sirignano et al.⁷ and Schauer⁸ have proposed independently the idea of turbine burner by making the turbine operation at constant temperature. This may be achieved by burning additional fuel in the turbine section. However, because of the high-velocity and high-g conditions prevail in the turbine section, sustained combustion in the turbine passages formulates a formidable task.

To circumvent the problems associated with stabilizing combustion in turbine passages, Air Force has proposed a trapped-vortex strategy for the development of

¹Innovative Scientific Solutions, Inc.
2766 Indian Ripple Road, Dayton, OH 45458
vrkatta@erinet.com

²Propulsion Directorate

³University of Dayton Research Institute

⁴Materials Directorate

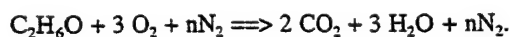
⁵Universal Energies System, Inc.

a inner turbine burner. In this design, turbine vans are provided with cavities into which fuel and air are injected from separate ports. As the fluid inside these cavities is somewhat shielded from the high-velocity main flow over the vanes, one might expect a stable combustion within the cavities. However, for optimizing the performance of the cavity supported turbine burner, one must properly size the cavities^{9,10} for the high-velocity and high-g main flow. And also, to protect the turbine vanes from the high-temperature gasses, plates made with special materials such as Ceramic matrix Composites (CMC)¹¹ need to be used. On the other hand, use of such low-thermal-conductivity plates could alter the combustion process within the cavity. Therefore, for the successful design of a turbine burner, one must understand the effects of cavity size and CMC wall plates on combustion processes. In this paper, the effects of CMC wall plates are investigated by conducting experiments using a laboratory turbine burner and performing numerical calculations using a two-dimensional CFD model developed at Wright Laboratory known as UNICORN.¹²

Mathematical Model

A time-dependent, axisymmetric mathematical model that solves for axial- and radial-momentum, continuity, and enthalpy- and species-conservation equations is used to simulate the flowfields in the annular combustion chamber. Density is obtained by solving the state equation, while the pressure field at every time step is determined from pressure Poisson equations. Even though the governing equations are solved in an uncoupled manner, the species-conservation equations are coupled through the source terms during the solution process to improve the stability of the algorithm. Temperature- and species-dependent thermodynamic and transport properties are used in this formulation. The enthalpy of each species is calculated from polynomial curve fits, while the viscosity, thermal conductivity, and diffusion coefficients of the species are estimated from the Lennard-Jones potentials.

In the present work reacting flows were simulated using a simple global-chemical-kinetics model involving ethanol, oxygen, water, carbon dioxide and nitrogen which is expressed as follows;



The specific reaction rate for the above equation is written in Arrhenius form with a very large pre-exponential factor.

The governing equations are integrated using an implicit QUICKEST (Quadratic Upstream Interpolation for Convective Kinematics with Estimated Streaming

Terms) numerical scheme^{13,14} which is third-order accurate in both space and time and has a very low numerical-diffusion error. An orthogonal, staggered grid system with rapidly expanding cell sizes in both the z and r directions is utilized for discretizing the governing equations. After rearrangement of terms, the finite-difference form of the governing equation for the variable Φ at a grid point P can be written as an algebraic equation as follows:

$$\begin{aligned} A_P \Phi_P^{N+1} + A_{z^{++}} \Phi_{z^{++}}^{N+1} + A_{z^+} \Phi_{z^+}^{N+1} + A_{z^-} \Phi_{z^-}^{N+1} \\ + A_{z^{--}} \Phi_{z^{--}}^{N+1} + A_{r^+} \Phi_{r^+}^{N+1} + A_{r^-} \Phi_{r^-}^{N+1} + A_{r^+} \Phi_{r^+}^{N+1} \\ + A_{r^-} \Phi_{r^-}^{N+1} = S_P^\Phi + \Delta t \rho_P \Phi_P^N \end{aligned}$$

The time increment, t , is determined from the stability constraint and maintained as a constant during the entire calculation. The superscripts N and N+1 represent the known variables at the N-th time step and the unknown variables at the (N+1)-th time step, respectively; the subscripts z^+ and z^- indicate the values at the grid points immediately adjacent to point P in the positive and negative z-directions, respectively. Similarly, the subscripts z^{++} and z^{--} represent the values at two grid points from P in the respective directions. The coefficients A and the terms on the right-hand side of the above equations are calculated from the known flow variables at the N-th time step. The above equations for N_z+2 variables are solved individually using an iterative ADI (Alternative Direction Implicit) technique. The pressure field at every time step is accurately calculated by simultaneously solving the system of algebraic pressure Poisson equations at all grid points using the LU (Lower-Upper) decomposition technique.

Temperature distributions inside the metal parts are obtained by solving enthalpy equations with appropriate thermal properties of the materials. However, metal density, heat capacity and thermal conductivity are assumed to be independent of temperature in the present study.

Flat velocity profiles are used at the main and primary inflow boundaries. A simple extrapolation procedure with weighted zero- and first-order terms is used to estimate the flow variables at the outflow boundary¹⁵. The usual no-slip and chemically inert boundary conditions are applied at the walls. While solving the gas-flow equations, temperature along the wall-fluid interface is obtained by extrapolating the values at the grid points inside the walls. Similarly, extrapolation from the grid points in the gaseous flow is used for determining wall temperatures while solving for the temperature distribution inside the metals.

Experimental Facility

The experimental facility allows testing of research combustor sectors, typically in the 152-mm size range, at atmospheric pressure. The facility can supply a total of up to 20 kg of heated air per minute, with three independently controlled air systems available to allow for different air splits supplied to the combustor (*i.e.* a main air supply and two smaller control systems for controlling pilot and cooling air supplies). The air can be supplied at temperatures ranging from room temperature to 533 K. Two independently controlled fuel systems are available, each supplying flow at up to 24×10^5 N/m² and 3.8×10^{-3} m³ per minute. The facility is well equipped with instruments for measuring pressure, temperature and flow rates. Emissions analyzing equipment is also available to detect CO, CO₂, NO_x, O₂, and total unburned hydrocarbons.

Burner Configuration

The combustor is constructed of stainless steel, with a quartz tube exhaust section to allow for viewing of the flame (Fig. 1). The main air flow enters the combustor from a settling chamber, flows through a honeycomb flow straightener and around the bullet nose of the center body [see Fig. 2(a)]. The centerbody has a radius of 31.75 mm, the annulus has a radius of 38.1 mm for a total annulus entry height of 9.5 mm. The cavity has a radius of 45.7 mm and is 25.4 mm long. Air enters the cavity in a direction 15° off axis from both the fore and aft faces of the cavity. This air supply is controlled independently of both the main air flow and a third air supply which enters around the circumference of the cavity. The circumferential air supply enters the cavity at a 45° angle to the radial direction (in the same direction as the face jets) in 12 paired jets around the circumference. Fuel is sprayed into the cavity at 6 equally spaced points around the circumference of the cavity. Simplex pressure atomizing nozzles are used. Ethanol is used as the fuel. A ceramic-matrix-composite (CMC) is window-frame mounted to the entire aft face of the cavity.

The combustor rig is connected to instruments for measuring pressure and temperature. The exhaust products are monitored for CO, CO₂, O₂, NO_x, and unburned hydrocarbons. Combustion efficiency is calculated from these emissions.

Main air flow rates are typically 3.4 to 6.8 kg/min at 533 K. This gives inlet annulus velocities in the range of 0.15 Mach. Circumferentially supplied air is typically between 0.68 and 2.27 kg/min, and air supplied through the faces of the cavity is typically 1.14–1.81 kg/min, both at 533 K. Fuel is supplied to give cavity equivalence ratios in the range of 0.5 to 3.

The discrete injection jets used in the combustor shown in Fig. 2(a) found to yield not only highly efficient burning but also significantly three-dimensional flowfields. For simulating these flows one needs to resort to three-dimensional mathematical models. While efforts are being placed for the development of three-dimensional models, preliminary investigations are made using the previously described two-dimensional CFD model, known as UNICORN, to understand the effects of insulating liners on combustion. The burner geometry has been simplified as shown in Fig. 2(b) for the application of a two-dimensional code. The geometrical changes made to the centerbody are not expected to alter the combustion characteristics significantly. On the other hand, the injection pattern used in the 2-D version may cause significant differences when compared to the 3-D flow associated with the geometry shown in Fig. 2(a). Nevertheless, the distributed fuel and air slot jets seem to result reasonable overall combustion characteristics—such as, flame spread and length—that were noted in the experiment. Therefore, for the investigation of role of ceramic materials on combustion, the 2-D geometry shown in Fig. 2(b) was adopted and numerical studies were performed using the two-dimensional CFD code described earlier.

Results and Discussion

The flow conditions selected for this study represent those used in an experiment conducted on the combustor shown in Figs. 1 and 2(a). The main air was flowing at 30 m/s (3.8 kg/min) through the annular gap while the cavity air was injected at 2.83 and 1.41 m/s through the top and side air-jet slots, respectively. All these cavity-air jets were set at 45° angle with respect to the radius. Finally, fuel was injected into the cavity at 0.12 m/s (0.21 kg/min). These flow rates yielded a cavity equivalence ratio of 0.9 and overall equivalence ratio of 0.066.

Calculations were initially made by assuming the material properties of the back plate identical to the other parts of the combustor and to that of stainless steel. The density, thermal conductivity and enthalpy are 53 J/m-s-K, 7800 kg/m³, and 0.465 J/kg-mole/K, respectively. Calculations were started with uniform cold flow distribution inside the cavity and ignition was provided at time $t = 0$. Each calculation was performed for 50,000 time steps with $t = 1 \mu$ s. The last 10,000-step results were stored and used later for data analysis purpose. Time-averaged quantities were obtained from these 10,000 data sets.

Results obtained with stainless steel (SS) back plate are shown in Fig. 3. The instantaneous temperature distributions in the gas medium as well as solid metal are shown in Fig. 3(a). It is apparent that the 4 fuel and 5 air

jets are generating long flame tongues in the cavity. These flame tongues fluctuate as the shear layer between the main air and the cavity fluid becomes unstable. Fig. 3(a) further suggests that within the solid material of the combustor, the tip of the back plate is at highest temperature. In order to establish that the results shown in Fig. 3(a) are reasonably grid independent, calculations were repeated using a finer grid system having 550 X 281 points. This grid system decreased grid spacing by half in both the z and r directions. The instantaneous temperature distribution obtained with this fine mesh is shown in Fig. 3(b).

A comparison between the reacting flows shown in Figs. 3(a) and 3(b) suggests that, in general, the unsteady characteristics of the flow are reasonably well simulated by the standard mesh which has a grid spacing of 0.1 mm in both the z and r directions. The time-averaged temperature and swirl velocity for the standard mesh are shown in Fig. 3(c) and 3(e), respectively, and those for the fine mesh are shown in Figs. 3(d) and 3(f), respectively. In general, the fine mesh yielded slightly longer flames and as a result the back plate and the solid metal behind it are at slightly lower temperature in this case [Fig. 3(d)] compared to those seen in Fig. 3(c). The swirl component of the velocity computed using standard grid [Fig. 3(e)] matches well with that obtained with the fine mesh [Fig. 3(f)].

Further calculations were made using the standard mesh (251X141) for the same flow conditions but with different back plates. The thickness of the back plate used is 2.0 mm. Results obtained for a Ceramics-Matrix-Composite (CMC) back plate are shown in Fig. 4. The thermal conductivity, specific heat and density used are 2.5 J/m/s/K, 0.465 J/kg-mole/K, and 800 kg/m³, respectively. Instantaneous velocity and temperature fields are shown in Figs. 4(a) and 4(b), respectively. The strong vortex generated at the back-plate is evident in the velocity plot. This figure also shows that very little main air from the annular gap is entering the cavity as the fluid injected into the cavity is sufficient in filling it up. As a result, the flames inside the cavity appear to be quite stable. The time-averaged temperature distributions in the gas and solid are shown in Fig. 4(c). The flame structures in the cavity are similar in shape and size to the instantaneous ones indicating that the flow inside the cavity is nearly in steady state.

A comparison between the time-averaged temperatures obtained with SS back plate [Fig. 3(c)] and CMC back plate [Fig. 4(c)] reveals the following features;

- 1) the temperature distribution inside the solid did not change with the use of CMC material where the surrounding flow is in steady state and 2) when the flow is unsteady (near the back-plate tip and over the aft body) CMC back plate reduced the solid temperature. Enlarged

view of the temperatures within the back plate is shown in Fig. 4(d).

The swirl velocity also seems to decrease with the use of CMC material near the back plate tip and over the aft body [compare Figs. 3(e) and 4(e)]. This may be due to the decrease in temperature, and hence, the viscosity. The wall temperature and heat transfer into the solid are plotted for the SS and CMC back-plate cases in Fig. 4(f). Here, distance, d , is measured along the back plate and aft body starting from the air-hole location ($r = 55$ mm). Solid lines represent the values obtained with SS back plate. Locations of the back plate and aft bodies are also shown at the bottom of the graph for reference. As discussed earlier, the wall temperature did not change at locations 2-mm bellow the back-plate tip and after this location lower wall temperatures are found in the case with CMC back plate. Due to low thermal conductivity of the CMC material, heat flux decreased significantly.

To understand the different aspects of the properties of the CMC materials, a numerical experiment was conducted by using two fictitious insulating materials. Results obtained with an insulation material (Ins. 1) whose thermal conductivity is very small (0.01 J/m/s/K) and density and specific heat are identical to those of stainless steel are shown in Fig. 5. In general, the flow and temperature fields are not changed noticeably due to the Ins. 1 back plate, except in the region very close to the back plate. While most of the back plate remained at temperatures < 500 K, the aft body also did not heat up beyond 900 K [Figs. 5(c) and 5(d)]. However, high temperature gradients have developed in the tip region of the back plate. The wall temperatures and the heat flux into the solid are compared to those obtained with SS back plate in Fig. 5(f).

Calculations were also made with another fictitious back plate whose thermal conductivity is identical to that of the CMC material but the density and specific heat are similar to those of stainless steel. Results in the form of instantaneous and time-averaged quantities are shown in Fig. 6. In this case also, the flow field is not noticeably different from the ones obtained for the previous cases. Interestingly, the back plate and aft body are at temperatures higher than those obtained with either the CMC or the stainless steel back plate. Because of these higher temperatures, the swirl velocity has also penetrated more into the main air [Fig. 6(e)]. A comparison of Figs. 4(f) and 6(f) suggests that heat transfer rate is lower with Ins. 2 back plate even though its thermal conductivity is same as that of CMC material and temperature is higher with Ins. 2 back plate even though its density and specific heat are the same as those of stainless steel. Further calculations need to be performed to understand these differences.

Summary

Preliminary studies on a Inner Turbine Burner were made to investigate the benefits of using CMC materials on cavity walls. A well tested two-dimensional CFD code, known as UNICORN, was used for the simultaneous simulation of reacting flow in the combustor and heat transfer in the metal parts. As the designed Inner Turbine Burner generates significant three-dimensional flow fields, a simplified geometry was proposed in this study for use with two-dimensional CFD codes. As observed in the experiment, almost all the fuel is burned in the cavity of this simplified geometry. Calculations made with stainless steel and CMC back plates suggested that a reduction in wall temperature can be achieved with the latter. Numerical experiments were performed by using fictitious metals with different material properties as back plates in the cavity to understand the role of individual properties on combustor performance. It is found that in the regions where the flow is in steady state, decrease in thermal conductivity from 53 to 2.5 J/kg/s/K did not help reducing the wall temperature. On the other hand, further reduction in thermal conductivity to 0.01 J/kg/s/K yielded cold walls.

Acknowledgments

This work was supported, in part, by Air Force Contract F33615-95-C-2507 and the Air Force Office of Scientific Research.

References

1. Rohsenow, W. M., Fink, C. H., and Pollis, S. R., Flow Through Two Orifices in Series, American Society of Mechanical Engineers Paper No. 51-A-87, 1951.
2. Migay, V. K., Study of Ribbed Diffusers (in Russian), Toploenergetika, No. 10, 1962, English translation issued as A.R.C. Paper 25,382, 1963.
3. Mair, W. A., The Effect of a Rear-Mounted Disc on the Drag of a Blunt-Based Body of Revolution, The Aeronautical Quarterly, Nov. 1965, pp. 350-360.
4. Little, B. H., and Whipkey, R. R., Locked Vortex Afterbodies, Journal of Aircraft, Vol. 16, No. 5, May 1979.
5. Roshko, A. and Koenig, K., Interaction Effects on the Drag of Bluff Bodies in Tandem, Presented at the symposium on Aerodynamic Drag Mechanisms of Bluff Bodies and Road Vehicles, General Motors Research Laboratories, Sept. 27-28, 1976.
6. Hsu, K. Y., Goss, L. P., Trump, D. D., and Roquemore, W. M., Performance of a Trapped-Vortex Combustor, AIAA Paper 95-0810, Washington, D. C., Jan. 9-12, 1995.
7. Sirignano W., et al. J. Propulsion & Power, Vol 14, No. 6, 1998.
8. Schauer, J., University of Dayton, Private Communication, June 1998.
9. Katta, V. R., and Roquemore, W. M., Numerical Studies on Trapped-Vortex Concepts for Stable Combustion, Trans. ASME: J. Eng. Gas Turb. Power 120, 60 (April 1998).
10. Katta, V. R., and Roquemore, W. M., Study on Trapped-Vortex Combustor--Effect of Injection on Flow Dynamics, AIAA J. of Propul. Power, Vol. 14, No. 3, 273-281, (1998).
11. John, R., Zawada, L. P., and Kroupa, J., Stresses Due to Temperature Gradients in Ceramic-Matrix-Composite Aerospace Components, Journal of American Ceramics Society, Vol. 82, No. 1, 161-168, (1999)
12. Roquemore W. M., and Katta, V. R., Role of Flow Visualization in the Development of UNICORN, Journal of Visualization, Vol.2, Nos. 3/4, 257-272, (2000).
13. Katta, V. R., Goss, L. P., and Roquemore, W. M., Numerical Investigations of Transitional H_2/N_2 Jet Diffusion Flames, AIAA Journal, Vol. 32, No. 1, 1994, p. 84.
14. Lenard, B. P., A Stable and Accurate Convective Modeling Procedure Based on Quadratic Upstream Interpolation, Computer Methods in Applied Mechanics and Engineering, Vol. 19, No. 1, 59-98 (1979)
15. Katta, V. R., Goss, L. P., and Roquemore, W. M., Int. J. Num. Meth. Heat Fluid Flow, 4:413 (1994)

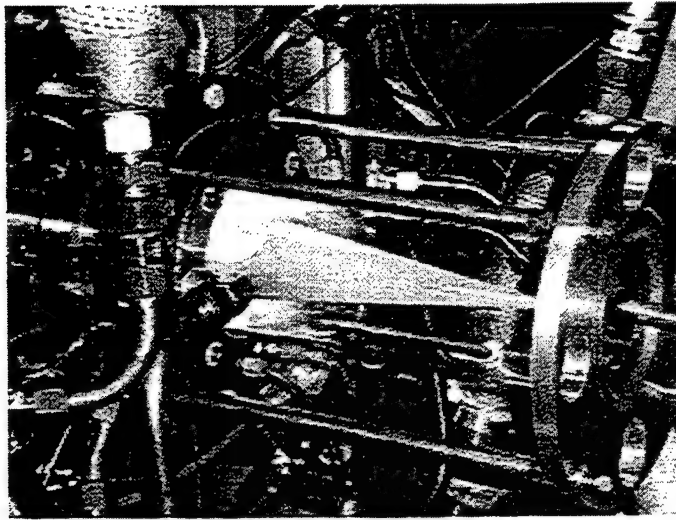


Fig. 1. Photograph of research Ultra Compact Combustor designed for studying benefits of using high-g conditions and enabling materials such as Ceramic-Matrix-Composite.

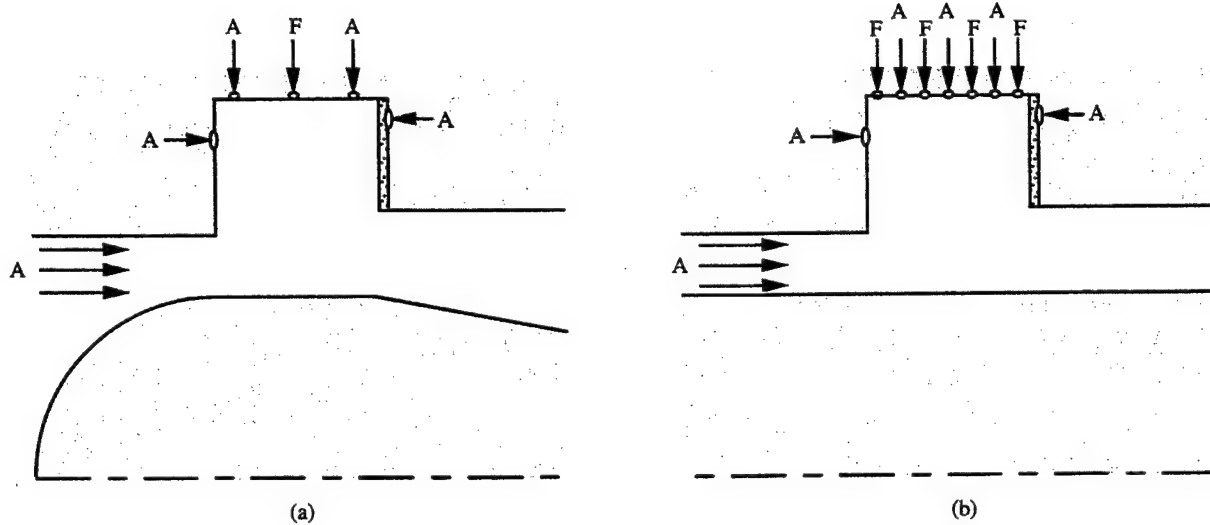


Fig. 2. Geometry of the research Ultra Compact Combustor. (a) Details of the actual annular combustor, (b) modified axisymmetric geometry developed to facilitate simulations using two-dimensional Computational-Fluid-Dynamics models.

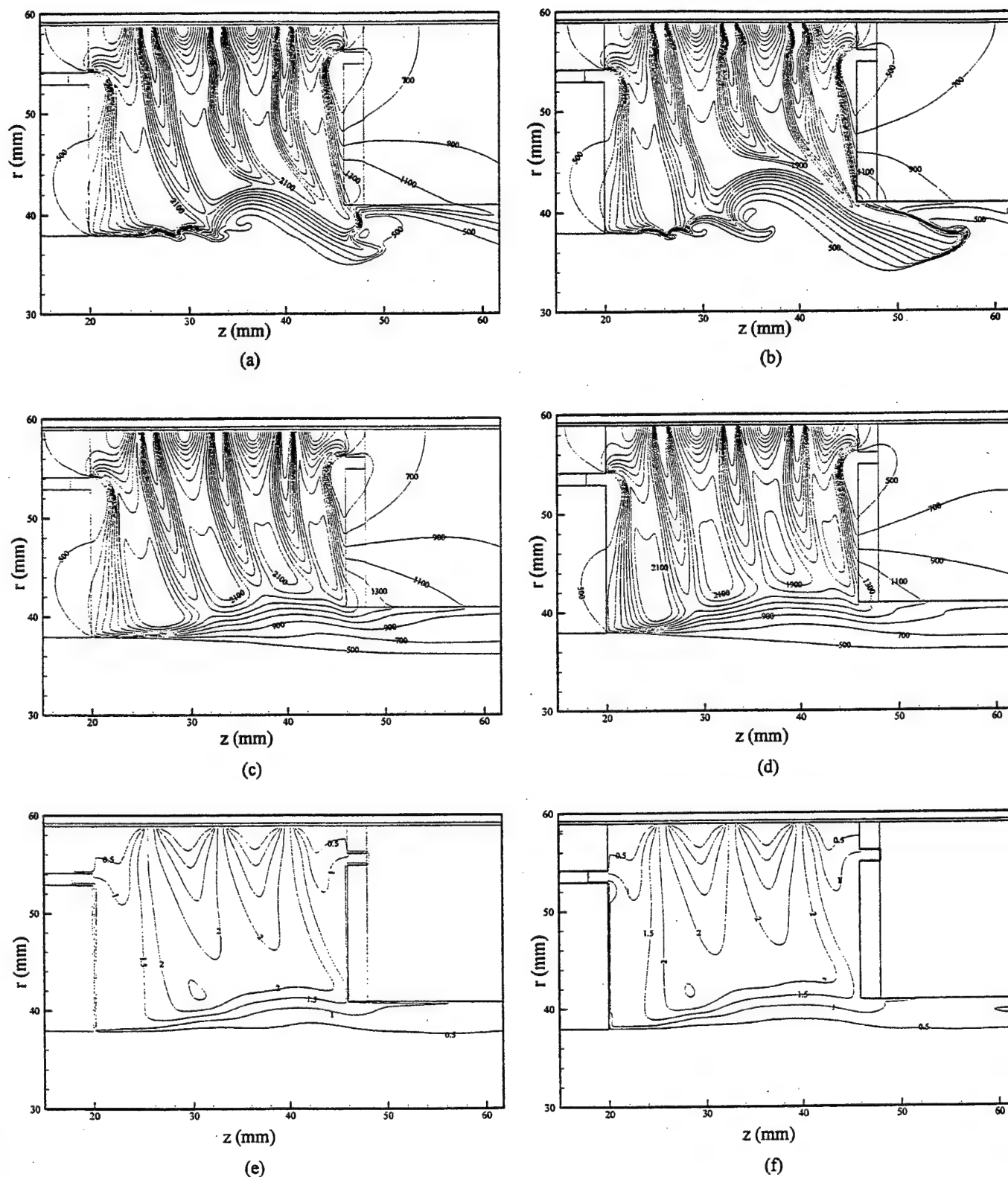


Fig. 3. Comparison of flowfields and temperature distributions inside cavity and temperature within metal parts obtained using two grid systems for the case with SS back plate. (a), (c), and (e) Results obtained using 251X141 grid system, and (b), (d), and (f) results obtained using 501X281 grid system. (a), (b) Instantaneous temperature fields, (c), (d) time-averaged temperature distributions, and (e), (f) time-averaged swirl velocity distributions.

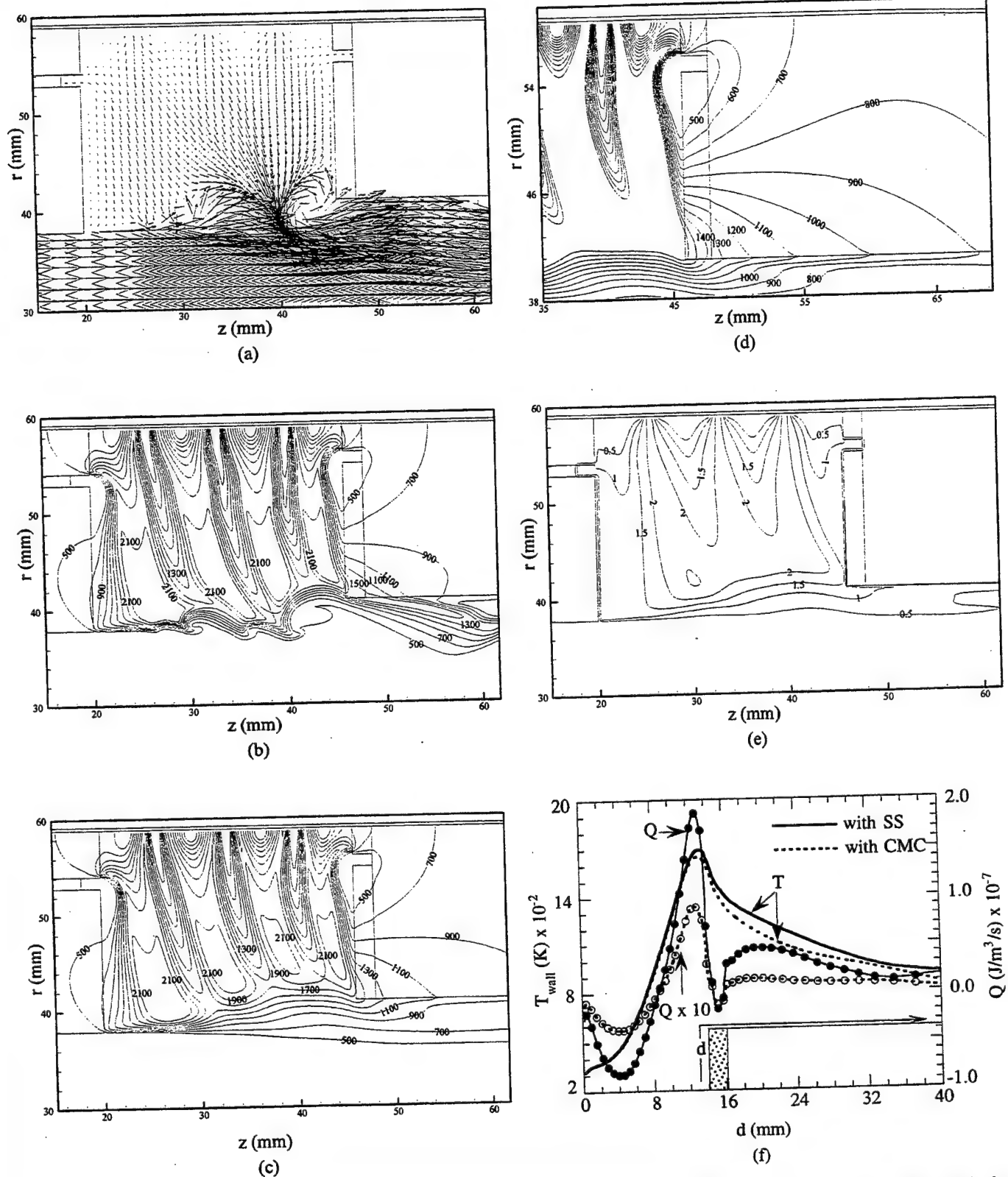


Fig. 4. Flowfield and temperature distribution inside cavity and temperature within metal parts for the case with CMC back plate. Instantaneous (a) velocity and (b) temperature fields, (c) time-averaged temperature, (d) close-up of temperature distribution within the back plate, (e) swirl-velocity distribution, and (f) comparison of wall temperature and heat transfer between the cases with SS and CMC back plates.

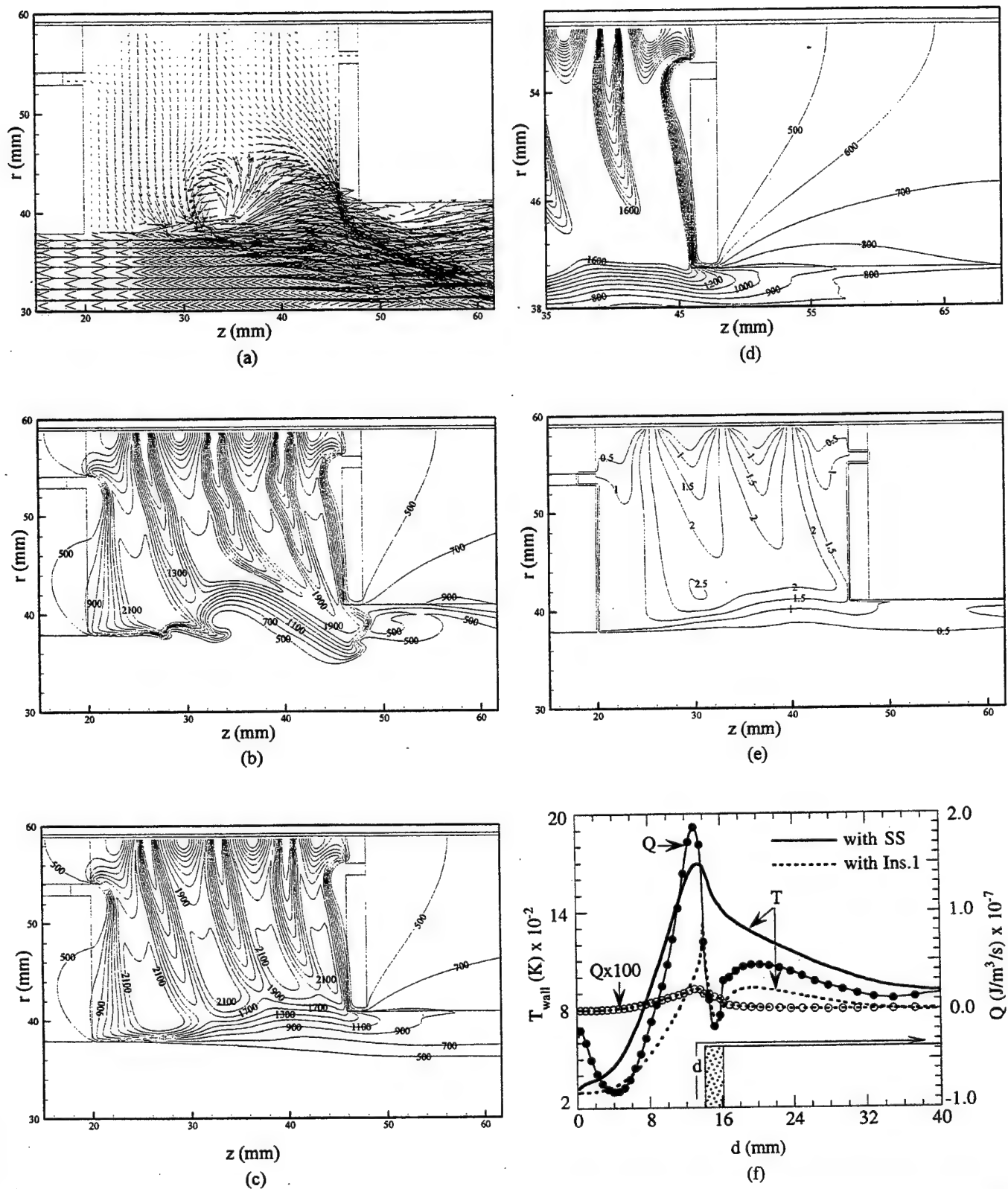


Fig. 5. Flowfield and temperature distribution inside cavity and temperature within metal parts for the case with Ins.1 back plate. Instantaneous (a) velocity and (b) temperature fields, (c) time-averaged temperature, (d) close-up of temperature distribution within the back plate, (e) swirl-velocity distribution, and (f) comparison of wall temperature and heat transfer between the cases with SS and Ins.1 back plates.

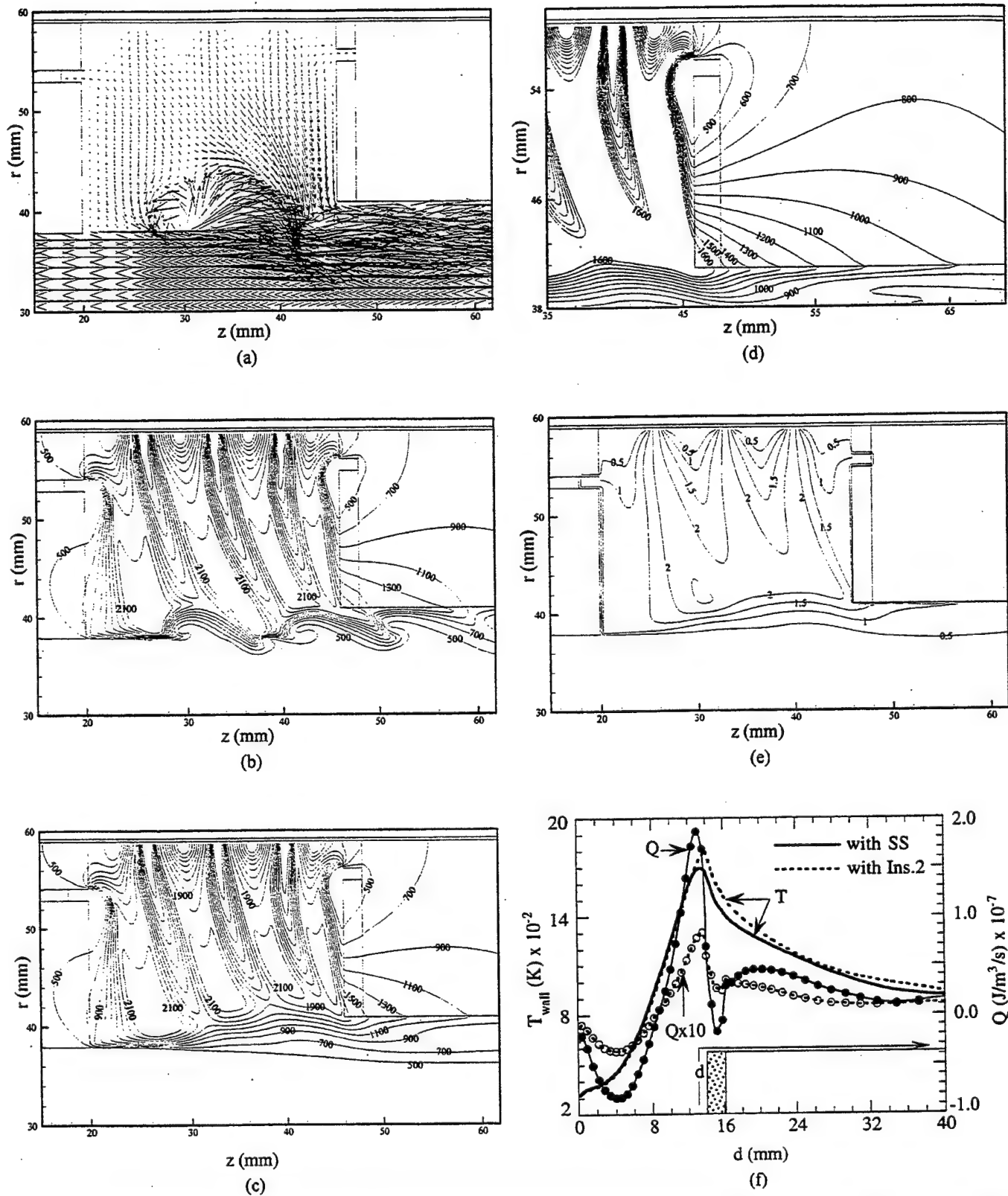
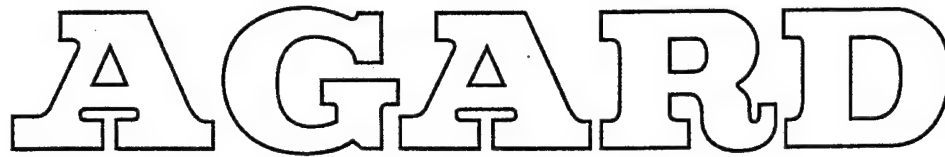


Fig. 6. Flowfield and temperature distribution inside cavity and temperature within metal parts for the case with Ins.2 back plate. Instantaneous (a) velocity and (b) temperature fields, (c) time-averaged temperature, (d) close-up of temperature distribution within the back plate, (e) swirl-velocity distribution, and (f) comparison of wall temperature and heat transfer between the cases with SS and Ins.2 back plates.

3.1.3.4 Active Combustion Control. A report entitled "Active Combustion Control for Propulsion Systems" (see pp. 572-622) summarizes the findings and conclusions of a four-day AGARD workshop. The objectives of the workshop were to (1) define the requirements of future combustors and combustion processes, (2) determine the status of active-combustion-control (ACC) systems, (3) assess the potential of ACC for meeting the performance goals of future combustors, and (4) determine near- and long-term ACC research and development.



ADVISORY GROUP FOR AEROSPACE RESEARCH & DEVELOPMENT

7 RUE ANCELLE, 92200 NEUILLY-SUR-SEINE, FRANCE

AGARD REPORT 820

**Active Combustion Control for
Propulsion Systems**

(le Contrôle actif de la combustion pour les systèmes de propulsion)

This Report was prepared at the request of the Propulsion and Energetics Panel of AGARD.
Papers were presented at a Workshop held in Athens, Greece, May 6-9 1996.

Authors

K. Schadow¹, V. Yang², F. Culick³, T. Rosfjord⁴, G. Sturgess⁵, and B. Zinn⁶

¹Naval Air Warfare Center Weapons Division ²Pennsylvania State University ³California Institute of Technology
⁴United Technologies Research Center ⁵Innovative Scientific Solutions, Inc. ⁶Georgia Institute of Technology

Original version first published by AGARD/NATO in R-820 - Active
Combustion Control for Propulsion Systems in September 1997
PUBLISHED WITH PERMISSION



North Atlantic Treaty Organization
Organisation du Traité de l'Atlantique Nord

The Mission of AGARD

According to its Charter, the mission of AGARD is to bring together the leading personalities of the NATO nations in the fields of science and technology relating to aerospace for the following purposes:

- Recommending effective ways for the member nations to use their research and development capabilities for the common benefit of the NATO community;
- Providing scientific and technical advice and assistance to the Military Committee in the field of aerospace research and development (with particular regard to its military application);
- Continuously stimulating advances in the aerospace sciences relevant to strengthening the common defence posture;
- Improving the co-operation among member nations in aerospace research and development;
- Exchange of scientific and technical information;
- Providing assistance to member nations for the purpose of increasing their scientific and technical potential;
- Rendering scientific and technical assistance, as requested, to other NATO bodies and to member nations in connection with research and development problems in the aerospace field.

The highest authority within AGARD is the National Delegates Board consisting of officially appointed senior representatives from each member nation. The mission of AGARD is carried out through the Panels which are composed of experts appointed by the National Delegates, the Consultant and Exchange Programme and the Aerospace Applications Studies Programme. The results of AGARD work are reported to the member nations and the NATO Authorities through the AGARD series of publications of which this is one.

Participation in AGARD activities is by invitation only and is normally limited to citizens of the NATO nations.

The content of this publication has been reproduced
directly from material supplied by AGARD or the authors.

Published September 1997

Copyright © AGARD 1997
All Rights Reserved

ISBN 92-836-1060-1



*Printed by Canada Communication Group Inc.
(A St. Joseph Corporation Company)
45 Sacré-Cœur Blvd., Hull (Québec), Canada K1A 0S7*

Active Combustion Control for Propulsion Systems

(AGARD R-820)

Executive Summary

Improving the combustion process is one of the most promising approaches for further improving the size/weight/power relationship in rockets, ramjets, afterburners, aero-engines, and stationary gas turbines for marine propulsion and power generation. Active control of combustion is being explored for various applications, including the civil industrial field. The workshop was organized to provide an overview of existing work and knowledge, and to discuss further possible strategies for the improvement of military equipment. There are very interesting prospects for the further enhancement of cooperation within the NATO nations, and other activities are planned. Areas for R&D needs have been identified.

Le contrôle actif de la combustion pour les systèmes de propulsion

(AGARD R-820)

Synthèse

L'amélioration du procédé de combustion est l'une des approches les plus prometteuses pour une optimisation plus poussée du rapport encombrement/masse/puissance dans les fusées, les statoréacteurs, les chambres de postcombustion, les moteurs d'avion et les turbomoteurs fixes pour la propulsion et la production d'énergie maritimes. Le contrôle actif de la combustion est à l'étude dans un éventail d'applications possibles, y compris dans le domaine industriel civil. Cet atelier a été organisé pour fournir un aperçu de l'état actuel des travaux et des connaissances dans ce domaine, ainsi que pour permettre de discuter plus avant des stratégies permettant l'amélioration du matériel militaire. Il existe des perspectives très intéressantes d'amélioration de la coopération entre les différents pays membres de l'OTAN. D'autres activités similaires sont prévues. Les domaines où il y aurait lieu de promouvoir les travaux de recherche et développement ont été identifiés.

Contents

	Page
Executive Summary	iii
Synthèse	iv
Recent Publications of the Propulsion and Energetics Panel	vi
1. Introduction	1
2. Background	4
3. Requirements for Future Combustors	6
3.1 Introduction	6
3.2 Aeroengine and Surface Power/Propulsion Gas Turbines	6
3.2.1 Aeroengine Gas Turbines	6
3.2.2 Premixed Surface Power/Propulsion Gas Turbines	8
3.3 Tactical Airbreathing Missile Propulsion	10
3.4 Rocket Propulsion	11
3.4.1 Solid-Propellant Rockets	11
3.4.2 Liquid-Propellant Rockets	12
3.5 Military Burners and Incinerators	12
4. Status of Active Combustion Control	13
4.1 Overview	13
4.2 Recent Results	17
5. Active Combustion Control Applications	21
5.1 Introduction	21
5.2 Surface Power Gas Turbines	22
5.3 Airbreathing Missiles	23
5.4 Solid-Propellant Rocket Motors	24
5.5 Military Burners and Incinerators	24
6. Research and Development Needs	24
6.1 Introduction	24
6.2 Understanding Fundamental ACC Processes	25
6.3 ACC Models	27
6.4 ACC Sensors	28
6.5 ACC Actuators	28
6.6 ACC Controller	29
6.7 ACC System Integration	31
7. Concluding Remarks	31
8. Collaborations	32
9. References	34
Appendix A	A
(List of Authors and Editors)	
Appendix B	B
Appendix C	C

Recent Publications of the Propulsion and Energetics Panel

CONFERENCE PROCEEDINGS (CP)

Interior Ballistics of Guns

AGARD CP 392, January 1986

Advanced Instrumentation for Aero Engine Components

AGARD CP 399, November 1986

Engine Response to Distorted Inflow Conditions

AGARD CP 400, March 1987

Transonic and Supersonic Phenomena in Turbomachines

AGARD CP 401, March 1987

Advanced Technology for Aero Engine Components

AGARD CP 421, September 1987

Combustion and Fuels in Gas Turbine Engines

AGARD CP 422, June 1988

Engine Condition Monitoring — Technology and Experience

AGARD CP 448, October 1988

Application of Advanced Material for Turbomachinery and Rocket Propulsion

AGARD CP 449, March 1989

Combustion Instabilities in Liquid-Fuelled Propulsion Systems

AGARD CP 450, April 1989

Aircraft Fire Safety

AGARD CP 467, October 1989

Unsteady Aerodynamic Phenomena in Turbomachines

AGARD CP 468, February 1990

Secondary Flows in Turbomachines

AGARD CP 469, February 1990

Hypersonic Combined Cycle Propulsion

AGARD CP 479, December 1990

Low Temperature Environment Operations of Turboengines (Design and User's Problems)

AGARD CP 480, May 1991

CFD Techniques for Propulsion Applications

AGARD CP 510, February 1992

Insensitive Munitions

AGARD CP 511, July 1992

Combat Aircraft Noise

AGARD CP 512, April 1992

Airbreathing Propulsion for Missiles and Projectiles

AGARD CP 526, September 1992

Heat Transfer and Cooling in Gas Turbines

AGARD CP 527, February 1993

Fuels and Combustion Technology for Advanced Aircraft Engines

AGARD CP 536, September 1993

Technology Requirements for Small Gas Turbines

AGARD CP 537, March 1994

Erosion, Corrosion and Foreign Object Damage Effects in Gas Turbines

AGARD CP 558, February 1995

Environmental Aspects of Rocket and Gun Propulsion

AGARD CP 559, February 1995

Loss Mechanisms and Unsteady Flows in Turbomachines

AGARD CP 571, January 1996

Advanced Aero-Engine Concepts and Controls

AGARD CP 572, June 1996

Service Life of Solid Propellant Systems

AGARD CP 586, May 1997

Aircraft Fire Safety

AGARD CP 587, September 1997

ADVISORY REPORTS (AR)

Producibility and Cost Studies of Aviation Kerosines (*Results of Working Group 16*)

AGARD AR 227, June 1985

Performance of Rocket Motors with Metallized Propellants (*Results of Working Group 17*)

AGARD AR 230, September 1986

Recommended Practices for Measurement of Gas Path Pressures and Temperatures for Performance Assessment of Aircraft Turbine Engines and Components (*Results of Working Group 19*)

AGARD AR 245, June 1990

The Uniform Engine Test Programme (*Results of Working Group 15*)

AGARD AR 248, February 1990

Test Cases for Computation of Internal Flows in Aero Engine Components (*Results of Working Group 18*)

AGARD AR 275, July 1990

Test Cases for Engine Life Assessment Technology (*Results of Working Group 20*)

AGARD AR 308, September 1992

Terminology and Assessment Methods of Solid Propellant Rocket Exhaust Signatures (*Results of Working Group 21*)

AGARD AR 287, February 1993

Guide to the Measurement of the Transient Performance of Aircraft Turbine Engines and Components (*Results of Working Group 23*)

AGARD AR 320, March 1994

Experimental and Analytical Methods for the Determination of Connected — Pipe Ramjet and Ducted Rocket Internal Performance (*Results of Working Group 22*)

AGARD AR 323, July 1994

Recommended Practices for the Assessment of the Effects of Atmospheric Water Ingestion on the Performance and Operability of Gas Turbine Engines (*Results of Working Group 24*)

AGARD AR 332, September 1995

LECTURE SERIES (LS)

Design Methods Used in Solid Rocket Motors

AGARD LS 150, April 1987

AGARD LS 150 (Revised), April 1988

Blading Design for Axial Turbomachines

AGARD LS 167, June 1989

Comparative Engine Performance Measurements

AGARD LS 169, May 1990

Combustion of Solid Propellants

AGARD LS 180, July 1991

Steady and Transient Performance Prediction of Gas Turbine Engines

AGARD LS 183, May 1992

Rocket Motor Plume Technology

AGARD LS 188, June 1993

Research and Development of Ram/Scramjets and Turboramjets in Russia

AGARD LS 194, December 1993

Turbomachinery Design Using CFD

AGARD LS 195, May 1994

Mathematical Models of Gas Turbine Engines and their Components

AGARD LS 198, December 1994

AGARDOGRAPHS (AG)

Measurement Uncertainty within the Uniform Engine Test Programme

AGARD AG 307, May 1989

Hazard Studies for Solid Propellant Rocket Motors

AGARD AG 316, September 1990

Advanced Methods for Cascade Testing

AGARD AG 328, August 1993

REPORTS (R)

Rotorcraft Drivetrain Life Safety and Reliability

AGARD R 775, June 1990

Impact Study on the use of JET A Fuel in Military Aircraft during Operations in Europe

AGARD R 801, January 1997

The Single Fuel Concept and Operation Desert Shield/Storm

AGARD R 810, January 1997 (*NATO Unclassified*)

Propulsion and Energy Issues for the 21st Century

AGARD R 824, March 1997

1. Introduction

This report summarizes the findings and conclusions of a four-day AGARD workshop on "Active Combustion Control for Propulsion Systems" that was held during May 6-9, 1996, in Athens, Greece. This workshop, organized in response to increased interest in application of active control in combustion systems, was attended by representatives from industry, government and universities in Europe and the United States.* The objectives of the workshop were to: (1) define the requirements of future combustors and combustion processes, (2) determine the status of active combustion control (ACC) systems, (3) assess the potential of ACC to meet the performance goals of the future combustors, and (4) determine near- and long-term ACC research and development needs. A special concern of the workshop was the confirmation of international collaborations between organizations working in this field.**

In contrast to passive control, the term 'active control' implies control of a system involving expenditure of energy from a source external to the system. Generally, the purpose is to minimize the difference or 'error' between the instantaneous desired and actual behavior of the system. Control may be exercised with feedback of information about the actual response of the system (closed-loop control) or without feedback (open-loop control). The field of active control of combustion is concerned both with control of dynamics, notably combustion instabilities, and with various forms of the 'regular' problem, for example maintaining operation to optimize some property of the performance. In any case open-loop control does not seem to be a useful strategy for the sort of applications envisioned for ACC.

Although the earliest proposals for active feedback control of combustors, and the initial experiments, were motivated by the intention to control combustion instabilities in rockets, ramjets, and afterburners, subsequent work has demonstrated other possible applications. Thus one can now conceive of situations in which the purpose of introducing ACC may be one or a combination of two or more of the following: (1) improve the performance of a combustor (e.g., reduce pollutant and/or noise emissions, reduce specific fuel consumption, increase combustion efficiency, improve pattern factors in gas turbine combustors, etc.); (2) permit modification of combustor design (e.g., reduce its length); (3) damp combustion instabilities; (4) increase combustor reliability; (5) extend operational limits of combustors (e.g., permit stable operation at lower equivalence ratios); and (6) improve performance of other military combustion processes such as shipboard incineration, and power and heat generation in the field. Because the practical problem of suppressing combustion instabilities has been the chief motivation for investigating ACC, it is useful to explain some broad aspects of the subject by considering feedback control of unsteady motions in a combustor. The essential reason for the presence of instabilities in a combustion system is the existence of internal feedback such that energy may be transferred to a

* A list of participants is provided in Appendix A.

** The agenda is provided in Appendix B. Information about requesting copies of viewgraphs presented at the workshop is given in Appendix C.

fluctuation at a rate dependent on the fluctuation itself. Passive control involves changes of design, (e.g., in the composition or types of reactants, injection system, chamber geometry) either (1) to reduce the rate at which energy is transferred to the unsteady motions or (2) to increase losses of energy, for example by the use of suitable resonators to introduce a dissipative process. Use of active control may be effective by causing either (1) or (2) to occur by sensing the instabilities and then using a feedback control loop to modify one or more input parameters. What may be possible, or what actually happens in a particular case, can be established only by understanding the system in question.

In the experimental work reported to date, relatively simple laboratory burners are typically used, having relatively large length/diameter ratios. The undesirable oscillations often have motions largely in the axial direction. Control has been exercised, or at least the levels of oscillations have been reduced, by applying several methods of actuation, the most common being: forcing the motion of a portion of the boundary, for example of the inlet; injecting acoustic waves with a loudspeaker; and modulating the primary or a secondary fuel supply. A typical arrangement for active control of combustion instabilities in a dump combustor is sketched in Figure 1 involving actuation, $A(t)$, achieved by modulating the flow through a fuel injector. The actual performance of the system is monitored by two pressure sensors, for the real-time, $s(t)$, and time-average, $\bar{s}(t)$, condition monitoring, respectively. Three different levels of ACC are shown. The first (marked 1) shows an open-loop operation in which the actuator is used without any feedback. The second (marked 2) adds a fast sensor to provide real-time feedback for control of the actuator signal. The third (marked 3) employs an additional sensor to detect the overall performance in a time-averaged sense. This sensor output is used to adjust the controller parameter to adapt to changes in operating conditions. In general more than two sensors could be used, distributed in space and measuring several properties of the motions, for example velocity and radiation in addition to the pressure.

For the control circuit 2 shown in Figure 1, the information acquired by the sensor must be processed and used within the feedback loop to activate a controller whose output drives the actuator according to a control law. Most demonstrations to date have used simple control laws which dictate oscillatory actuation at some phase relative to the sensed response of the system, and at some amplitude found to give best results, i.e., lowest amplitude of oscillations. That approach is a special form of classical PID (proportional/integral/derivative) control in which the control signal is proportional to the error itself, its time-integral, and/or its derivative. The conditions for optimal control influence have always been obtained experimentally with little preparatory design work, a consequence of the lack of knowledge of the systems under investigation. One example of such simple control systems is illustrated in Figure 2 for a ducted premixed-flame experiment. The phase-delayed signal from a microphone was used to drive the acoustic actuator in the flame plenum chamber for suppressing pressure oscillations. It should be emphasized that the unsteady flow motions can be effectively reduced using only a small fraction of the mechanical energy of the

oscillatory field, provided the control actions are exerted in regions that are most sensitive to actuations. In this flame experiment, the actuator suppresses velocity fluctuations at the flame base and thereby prevents the natural development of large-scale vortices responsible for driving instabilities. The evolution of vortex dynamics under conditions with and without external control forcing are shown in Figure 2 by means of the flame-radical flow visualization technique.

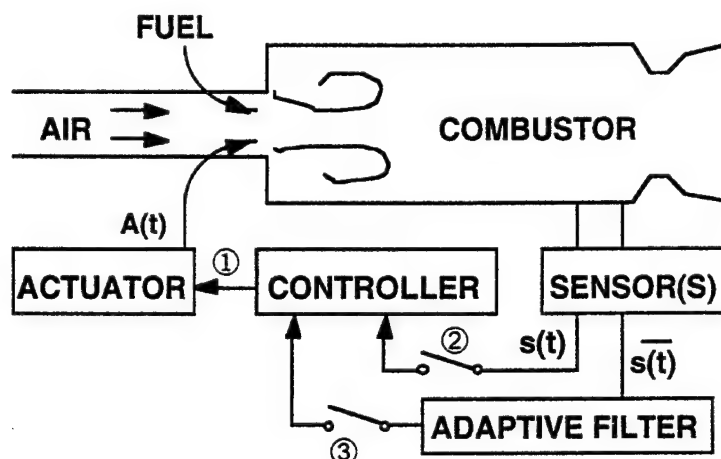


Fig. 1 Active Control Arrangement to Suppress Combustion Instabilities in Dump Combustor.

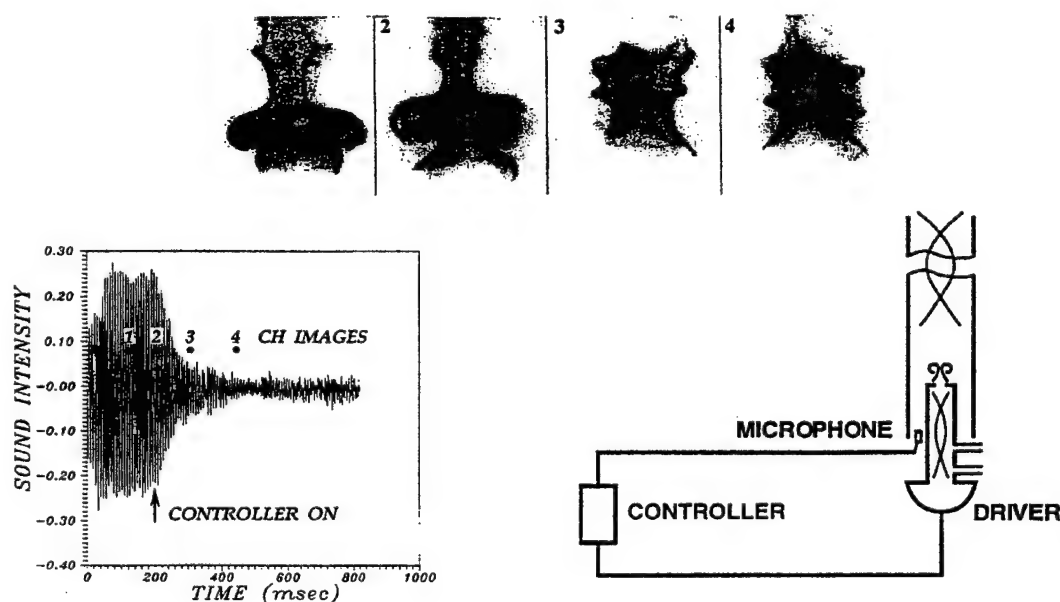


Fig. 2 Uncontrolled to Pressure Controlled Transition of Ducted Flame (Ref. 52).

According to the preceding remarks, there are broadly four areas in which research and development must proceed to form a firm basis for practical applications of ACC: sensing, actuation, formulation of control laws, and understanding of the systems to be controlled. As part of the progress required, it is essential to acquire understanding of the scaling laws, particularly with respect to the power density of a combustor. This report covers a broad range of issues ranging from future requirements of combustion systems to topics of basic research that must be addressed to realize the promise of active control of combustion.

2. Background

Although active feedback control had been posed and investigated for a restricted class of problems in the early 1950s for reasons cited in the preceding section, the idea was not pursued experimentally until the 1980s. It seems fair to recognize that the work at Cambridge University, supported by Rolls Royce with a view to application to afterburners, marked the beginning of the recent considerable activity in this area (see References 14 through 19 in Section 4). Indeed, the sequence of increasingly more elaborate experimental projects within the program introduced many of the novel ideas which have subsequently been vigorously pursued by a large number of research groups throughout the world. In particular, almost all of the types of sensing and actuation now being investigated were first used at Cambridge.

The general notion of active feedback control of combustion dynamics has recently attracted considerable interest of customers and manufacturers, mainly those producing systems for propulsion and stationary power generation. The chief reasons for this attention include: the trend toward higher combustor pressure (particularly in the past twenty years or so) not only for higher performance in some sense, but also for smaller size, improved efficiency, and reduced emissions of pollutants. While overall efficiency of a system has in the past been largely a matter of gaining a competitive advantage, independent of any regulatory practices, that is no longer the case. Increasingly stringent specifications on pollutant generation will likely be met not only by reducing the amount of pollution produced in combustion of a unit mass of fuel, but also by requiring less fuel to generate a unit of power output or thrust. Those requirements and the traditional methods of achieving desired improvement are discussed in Section 3. An implication of that discussion is that the customary methods of design changes (a strategy of 'passive' control) seem to be approaching their limits. Hence the interest in active control is a direct consequence of widespread practical motivations.

On the other hand, the subject of active control of combustion remains primarily a matter of research. Apart from a small number of relatively recent observations of emission levels, practically all work on ACC has been concerned with control of coherent pressure oscillations, i.e. combustion instabilities. There are however, no available reports of successful application of active control to suppression of combustion instabilities in full-scale systems of any sort. In fact, it appears that the available demonstrations of combustion instability control span a small range of

scales, both of geometry and power density. Consequently, almost nothing is known about the appropriate scaling laws.

The general reasons why research on active control of combustion dynamics has concentrated on control of combustion instabilities are easy to understand. First, it is generally true that as designs of combustors are pressed to give higher performance – normally a matter of raising power density – the likelihood is also raised that combustion instabilities will occur. Many examples exist for rockets, ramjets, and afterburners. Second, in the past several years, instabilities have become a serious problem in gas turbine combustors under quite different circumstances. In order to reduce production of nitrogen oxides, it is desirable to consume much of the fuel with lean burning to reduce the temperature. That implies operating a combustor as close to lean blow-out as possible. But then the global combustion process – the flame – tends to become unstable. The consequent unsteady motions can couple to global motions in the chamber, producing combustion instabilities.

Finally, there is a class of practical applications including heaters and incinerators of waste, for which intentionally pulsed combustion is effective for improved efficiency. Active control of pulsed combustion is attractive to ensure optimum operating conditions, avoiding, for example, inadvertent operation when the pulsations can cause unacceptable rates of surface heat transfer or reduced efficiency.

Several reviews or summaries of the various works on active control have been published, but no extended discussion of the subject has been given in the context of practical needs. Moreover, prior to this workshop there has been no opportunity for the international community of researchers to meet together and discuss the central issues. It became clear in early 1995 that both the research community and the potential users of active control methods for combustion systems would benefit significantly by joining to exchange information and ideas. The state of the field was such that merely presenting and publishing papers would not serve the purpose. A more informal situation was desirable, to allow extended discussions.

Work on ACC is applied research which if successful seems to have virtually immediate application to real systems. However, that view has not been proven. Despite the enthusiasm of all concerned there has been, on the one hand, a substantial gap between the appreciation of researchers for the actual situations in which ACC would be used – the requirements of industry; and on the other hand, users seem not to have a thorough understanding of (1) what really has been accomplished in ACC research, and (2) what one can reasonably expect to accomplish with applications in the near future. A major intention of the workshop was to clarify this situation. Due to the international nature of the communities involved, AGARD offered the best opportunities for achieving that goal. Moreover, it was a hope of the organizers that a workshop would promote collaboration with international partners.

3. Requirements for Future Combustors

3.1 Introduction

Active combustion control is a technology that has been demonstrated in the laboratory but has not been scaled up to the conditions and size of operational devices. As discussed in Section 6 of this report, research and development needs exist for all components of an active control system – sensor, actuator and controller. It is therefore appropriate to identify the projected needs and challenges for future combustors when determining the application opportunities for active control. This section provides a brief assessment of the requirements for future combustors as used in aeroengine and surface gas turbines, ramjets, rockets, and military burners and incinerators. Section 5 combines these future combustor requirements with the current status of active combustion control technology (Section 4) to identify near- and long-term applications.

3.2 Aeroengine and Surface Power/Propulsion Gas Turbines

Gas turbine engines have been developed for either aeroengine propulsion or surface power/propulsion. The aeroengine device, which is used for both military and commercial aircraft, always uses direct fuel injection in the combustor. That is, the liquid fuel is injected (often by an airblast fuel nozzle) into the combustor, where the physical processes of atomization, vaporization and fuel-air mixing occur. In contrast, surface power/propulsion devices, which can be used for ground power generation or ship propulsion, may utilize either direct-fuel-injection or fuel-air premixing. The former is identical to aeroengine combustors, but in the premixed arrangement, the aforementioned physical processes are essentially completed prior to entering the combustor. One consequence of fuel-air premixing is that the heat release is more concentrated. Because of the differences in fuel preparation, the requirements for aeroengines and premixed surface power/propulsion gas turbine combustors may be different.

3.2.1 Aeroengine Gas Turbines

Aeroengine gas turbines provide propulsion for aircraft, both military and commercial. In addition to requirements on performance and emissions that accompany any powerplant, there is a premium on achieving them in a compact, light-weight device that is very fuel efficient and highly reliable. These demands are projected to become increasingly severe for future aeroengine gas turbines. It is important to determine enabling technologies that might mitigate these challenges.

The basic performance trends for aeroengine gas turbines have been toward increasing thrust-to-weight ratio for military devices, and lower specific fuel consumption (i.e. fuel flow rate per pound of thrust) for commercial devices. The former is sought to increase maneuverability, while the latter supports reduced operating costs. Among the consequences common to both goals is the trend toward higher pressure ratios, with higher temperatures at both the combustor inlet and exit.

Based on these performance trends and mission-driven engine configuration studies, it is concluded that operating conditions for combustion systems will continue their historical trends toward increasing stringency. With long-term goals of doubling thrust-to-weight ratio and reducing specific fuel consumption by 25 to 50 pct, overall pressure ratios in the range of 50 to 75

are virtually certain, and values up to 100 are possible. For commercial applications, bypass ratios could increase to as high as 25 using gear-driven fans. For military applications bypass ratios will be more modest, but turbine inlet temperatures will increase significantly to values associated with combustor equivalence ratios of 0.5 - 0.7. These targets reflect the range of set-point operation over the power curve. The desire for military systems with shorter acceleration/deceleration response times imposes additional demands for more rapid transients between the set-point conditions. At times, the static stability of the combustor, and its adjacent components, will be exceeded.

These projected performance trends will impact the combustor design. Burning-length-to-dome-height ratios will approach 1.5, with a mean radius in the range of 216 to 250 mm (8.5 to 10 in.), regardless of engine airflow; dome heights will be in the range of 50 - 150 mm (2 to 6 in.) depending on the core engine airflow. Combustion intensities will range from 100 to 160 MW / m³ / bar (10 to 16 MBtu / hr / ft³ / atm). While the general combustor configuration will likely remain annular, the combustor inlet section diffuser may be changed for overall engine pressure ratios above 70. Specifically, passage heights in axial-flow compressors at very high pressures can become so small (depending on core engine airflow) that losses due to secondary flow begin to dominate, preventing final high efficiencies from being achieved. Under such circumstances, the final stages of compression might necessarily be done through one or more centrifugal-flow stages. This could have severe impacts on combustor configuration. At high pressures, secondary flow losses might also present difficulties for feeding shower-head cooling schemes in the leading edges of turbine inlet guide vanes. Therefore, shower-head cooling requirements might preclude the use of ultra-low pressure loss combustors in engines with very high overall pressure ratios. Also, the high fuel turndown ratio associated with high temperature turbines will make fuel-staged combustion systems common.

In order to cope with the requirements for future combustors, enabling technologies must be identified. For the demands discussed above, advances in high pressure fuel pumps, high temperature combustor liner materials, and fuel systems capable of handling super-critical fuels are required. Furthermore, in order to preserve and improve the combustor performance at these severe conditions, means are required for promoting the mixing of fuel, air, and combustion products in the burner, and for preserving stable operation under both steady-state and transient conditions. That is, the critical requirement for achieving the high combustion intensities associated with high pressure conditions, in reduced-size devices, is improved mixing of fuel and air inside the burner. Fuel-air premixing, such as used in some surface power/propulsion gas turbines, is precluded because of the very short autoignition time associated with very high pressure ratio cycles. While adequate mixing and an extremely high combustion efficiency is readily achieved for very fuel-lean operation, efficiency could become mixing-limited for higher equivalence ratios. Improved mixing is also necessary to minimize undesirable emissions of NO_x, CO, and smoke at higher equivalence ratios. Further, the increased combustion intensity at any

set-point may increase the likelihood of coupling with acoustic waves, promoting combustor dynamics problems. Such problems may also be exacerbated by faster transient responses.

The chemical reactions that determine energy release and pollutant formation occur on the molecular scale. However, the flow in a combustor is turbulent, and the mixing process must cascade down to the smallest eddy before molecular processes can become significant. The minimum turbulent length scale (Kolmogorov) determines the smallest mixing length scale. At atmospheric conditions, this scale is approximately 0.4 mm (0.015 in.) and decreases by three-orders-of-magnitude at 100 atm. In contrast, the dimension of the flow field structures are of the same order as the combustor geometry, which are on the order of 100 mm (4 in.). Hence, the mixing process must progress through an enormous dynamic range before molecular reactions can occur in significant amounts. While a wide range of eddies always exists in the combustor, achieving the stringent standards for efficiency and emission control requires that this mixing cascade occurs quickly and efficiently. That is, to achieve worthwhile improvements in mixing at fixed pressure loss will demand dramatic reduction in the characteristic "integral" turbulent length-scale associated with combustors. Radical geometric changes, such as reducing the combustor characteristic length scale by an order of magnitude, or greatly increasing the number of active shear layers to promote many length scales, appear to be essential.

3.2.2 Premixed Surface Power/Propulsion Gas Turbines

Surface power/propulsion gas turbines provide either ground power or propulsion for ships. Among the critical requirements for these gas turbines is high power density (power per occupied volume), high durability, and extremely low emissions. The latter is distinctively different than for aeroengine gas turbines, with allowed emission levels more than an order-of-magnitude lower. While this standard may not be required of all surface gas turbines (e.g. emission goals for ship propulsion are currently less strict than for ground power gas turbines), economics should drive manufacturers to develop only one surface gas turbine design. Since the lowest levels of emissions are obtained through the flame temperature control achieved with premixed combustion, and ground power gas turbines must strive for the lowest emissions levels to be competitive, the industry standard for new surface gas turbines is premixed combustion. The trend in development of surface gas turbines is toward lower emissions levels and higher cycle efficiencies. The former is driven by (real and anticipated) air quality regulations, while the latter affects operating cost (i.e. "cost of electricity"). Currently, many ground power gas turbines guarantee NO_x and CO exhaust concentrations limited to 25 ppm @ 15 pct oxygen (i.e. parts per million at a standard exhaust flow dilution to achieve 15 mole pct oxygen). Future products will strive for "single digit" (e.g. 9 ppm) guarantees. Depending on the application, such emission goals may result in engine cycles other than the "simple (Brayton) cycle" – cycles which, for example, extract heat of compression (i.e. "intercool") between two compressors.

The lowest level of emissions is achieved by employing a premixed combustion strategy. Generally, a fixed distribution of effective flow area divides the combustor airflow and delivers the

greatest fraction to the set of premixing fuel nozzles. The maximum airflow fraction, or leanest fuel-air mixture, is limited by the lean blowout (LBO) mixture, which is the leanest mixture which will sustain combustion. If the premixing airflow fraction is increased (starting from a high fuel-air ratio), then the fuel-air ratio, the flame temperature, and the formation rate of NO_x all decrease. However, as the fuel-air ratio approaches the LBO level, the flame temperature will not support sufficiently fast CO oxidation rates and its concentration in the combustor exhaust increases. That is, CO acts as a precursor to marginal stability, reflecting either globally reduced oxidation or the presence of sub-LBO fuel-air pockets which have extinguished. Hence, as depicted in Figure 3, there is a "window" of fuel-air ratio, and of corresponding flame temperature, that will simultaneously result in low NO_x and CO. The width of the window will depend on both the inherent combustor stability characteristics and the level of desired emissions control. The figure shows the window width for sub-25 ppm levels; the window is clearly narrower for lower limits. Generally, homogeneous (i.e. non-catalytic) combustion systems do not provide a window width covering the full mixture (or temperature) range experienced from low to baseload gas turbine power. Hence, to preserve ultra-low emissions over a wide power range will require shifting the premixing airflow fraction as the overall fuel-air ratio changes to remain within the desired flame temperature window. It is also true that as the fuel-air mixture approaches the LBO limit, thermoacoustic instabilities become more prevalent. Indeed, premixed combustion with its intense heat release gradients provides greater opportunities for coupling with the acoustics and fluid mechanics, and remedies to combustion instabilities are a common development challenge.

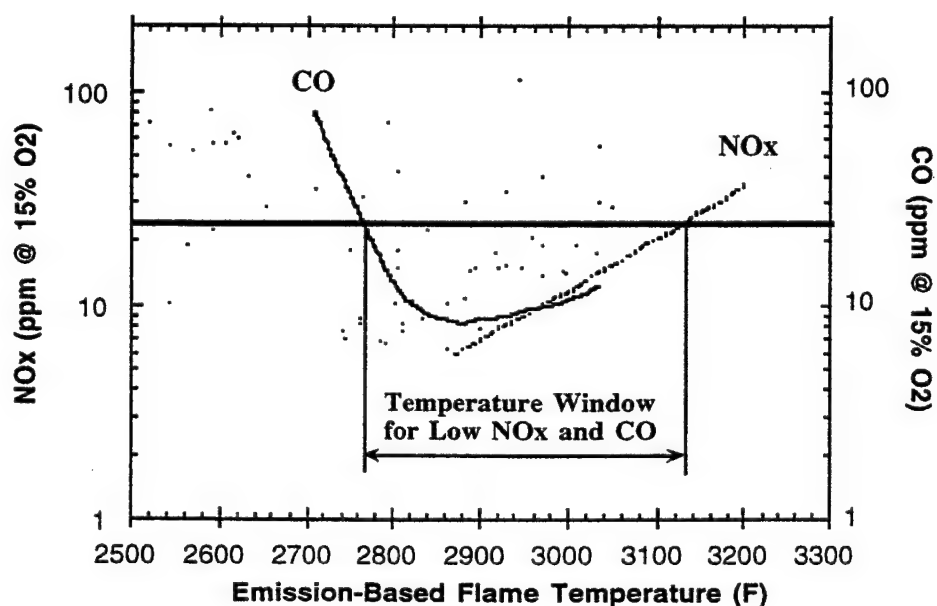


Fig. 3 Flame Temperature Window for Both Low NO_x and CO from Premixed Combustion.

3.3 Tactical Airbreathing Missile Propulsion

Airbreathing propulsion will receive increasing emphasis to meet future requirements for tactical missiles, with several different types of airbreathing propulsion systems being considered. Most attention is given to the liquid-fuel ramjets and gas-generator ramjets (ducted rockets). Liquid-fuel ramjets are operational in France (ASMP), Russia (Mosquito), and China (Silkworm), and advanced developments/demonstrations are currently being conducted in France (ASLP/ASMP) and USA (Low Drag Ramjet). Advanced development programs for ducted-rocket propulsion are being conducted in fewer countries, such as France (MPSR2) and USA (VFDR). Other potential systems are solid-fuel ramjets, scramjets, expendable turbine engines, and pulsed-detonation engines (PDE). The PDE is a device that can increase thermodynamic cycle efficiency by more than 30 pct compared to the constant pressure burn cycle (Brayton cycle) of the other systems, and has self-boost capability. Based on its advanced level of maturity, emphasis will be placed on discerning future combustor requirements for liquid-fuel ramjets based on mission demands.

Airbreathing propulsion has the potential for the highest performance per unit volume and weight and is considered for several different missions, including:

- (a) *Precision Strike* over long range with high sustained velocity and high warhead weight,
- (b) *Air Superiority* with increased range and maneuverability, and reduced time to target,
- (c) *Naval Surface Fire Support* with increased range of gun-launched missiles,
- (d) *Ship-Based Defense* with high velocities and reduced time to target, and
- (e) *Surface Air Warfare (Anti-Air)* with mission flexibility and long duration.

Generally, modern tactical weapons systems are being driven to longer ranges at minimum volume and weight. These general guidelines translate into specific requirements of: (1) increased kinetic performance to provide increased range and higher sustained and average velocity; (2) increased energy per volume and per weight to reduce weapons size and increase warhead weight; (3) increased propulsion energy management to enhance maneuverability and mission flexibility, (4) increased survivability through longer range launches, increased propulsion duration, higher velocities, and reduced plume signature, and (5) reduced cost.

As indicated in (2), the application of airbreathing propulsion to tactical missions drives the design to ever smaller combustors, which increases both the challenge to achieve high performance over a broad range of operational conditions, and the risk of combustion instabilities. The performance challenge derives from meeting the same high standards for combustion efficiency in higher through-put devices, over broader operational conditions, but with no increase in pressure loss. The risk of instability is a product of both broader operational conditions which drive the burner closer to blow-out, and increased energy release density which enhances the potential for its coupling with fluid dynamic and acoustic features of the burner.

A number of specific requirements can be identified for liquid-fuel ramjets. Future missions will require operation between sea level and 30 km (100,000 ft) altitude with a potential variation

of the equivalence ratio between 0.5 and 1.0. Highly efficient and stable combustion must be achieved over the entire operation envelope. For current combustors, efficiency is high at the high Mach number design point but falls off as the mission moves the fuel-air ratio toward either the lean or rich blow-off limits. Combustion instability is often encountered at either a medium frequency range (300 Hz corresponding to a longitudinal mode) or a high frequency range (3000 Hz corresponding to a tangential mode). Currently, the pressure oscillations and mechanical vibration arising from the instabilities (which also impose adverse fluid mechanical effects on the inlet margin) are solved by baffles, aerogrids, and tailored fuel distributions, but at the expense of combustion efficiency and pressure loss penalties. An enabling technology for current and future ramjet propulsion systems is a methodology to sustain stable operation, through either passive design or active control, over a wide range of operational conditions.

Alternative tactical missile propulsion systems include solid-fuel ramjets, scramjets, expendable turbine engines, and pulsed-detonation engines. Specific combustor requirements for ducted rocket propulsion systems are similar to those for liquid-fuel ramjets, while efficient ignition and combustion of liquid hydrocarbon fuels in dual-mode operation of compact designs are technical challenges for scramjets. Expendable turbine engines require increased performance per volume, possibly through the use of short L/D afterburners, highly energetic fuels, and shorter inlets. Liquid-fuel pulse detonation engines must enhance many features including fine-scale and large-scale mixing, fuel vaporization, two-phase detonation and shock-wave propagation, and continuous thrust generation. Clearly, these systems are not as mature as the liquid fuel ramjet.

3.4 Rocket Propulsion

Rocket propulsion systems have been developed for two applications – missile propulsion and space launchers. Each of these may be powered by either solid or liquid propellants. The propulsion systems are designed to deliver the maximum thrust with the minimal volume or weight. Hence the energy release densities are extremely high, often causing coupling with the combustor acoustic modes to produce combustion instabilities. As a consequence, the global requirement for future rocket propulsion systems is to achieve stable, high power-density operations. While both solid- and liquid-propellant systems have this common need, the controlling processes are not the same, and as such the means to achieve stable operation will be different.

3.4.1 Solid-Propellant Rockets

Solid-propellant rocket propulsion systems can be divided in three main applications – tactical missiles, strategic missiles and solid rocket motors (SRM) for large space launchers. This variety results in wide ranges of size and operational conditions, and hence in a wide range of conditions for instabilities. Potentially unstable frequencies can be well predicted from acoustic mode analyses, but identifying which frequencies become amplified, and the resulting oscillatory levels, remains a challenge, although predictions have been made for simple cases. Such predictions depend on non-linear influences of various phenomena which often depend on frequency (e.g.

propellant response, nozzle damping, particle damping, flow turning loss, vortex shedding driving). As a consequence, scaling rules are non-linear, and the extrapolation of results from smaller scale to larger scale devices can be uncertain. Recent CFD analyses of vortex shedding processes in solid-propellant rockets have increased an understanding of some of the influences.

Large segmented motors for space launchers (e.g., Space Shuttle SRB, Titan SRB and SRMU, Ariane 5 MPS P230) also display acoustic instabilities characterized by low-level pressure and thrust oscillations at the first acoustic modes. Such modes are experienced despite being predicted stable by conventional analyses. Attempts to expand classical acoustic-balance computer codes to include the vortex-shedding effects have shown some limitations that preclude their routine use. An ongoing work in France, carried out under the ASSM program supported by CNES, is attempting to validate a full numerical approach for instability prediction at conditions with vortex shedding. Moderate success has been achieved for axisymmetric conditions in a small scale research motor. However, the quality of these results is not sufficiently accurate for industrial purposes, especially considering the required extrapolation to larger scale where both under-predictions and incorrect trends have been obtained.

3.4.2 Liquid-Propellant Rockets

Liquid rocket motors are mainly used in space launchers. They use a variety of propellants, from storable propellants to cryogenic or semi-cryogenic propellants, and can be used for all stages of the launcher. The main challenges for liquid-propellant rockets include increasing performance and reliability, particularly of turbopumps, and decreasing costs and overall weight. Issues to be mastered include turbopump reliability, wall cooling, combustion efficiency and combustion instability. Techniques to eliminate liquid-propellant rocket instabilities are critical since their occurrence can be quickly catastrophic to the system. Modifications of injection designs and/or propellant formulation have been proposed as potential means to suppress the instabilities by altering the heat release distribution. Baffles have been used to shift the motor acoustic frequencies and to avoid the coupling between unsteady combustion and local flow oscillations. All of these approaches to eliminate instabilities are highly empirical. While CFD approaches to predict the modes and coupling mechanisms are being developed, their physical basis is immature.

3.5 Military Burners and Incinerators

The military will be required to comply with emerging regulations for all types of combustion devices, including burners and incinerators. Since these devices have common combustion features with propulsion systems, the use of ACC offers a viable solution to meet various future requirements.

Incineration is widely accepted for solid and liquid waste treatment on cruise ships. However, the US Navy has concluded that the present technology based on commercially available incinerators may significantly degrade military operations due to their physical volume and weight. Also, potential problems with emerging emission standards were cited and have caused a delay in implementing international regulations. The main requirements for future marine incinerators are

size and weight reduction, while maintaining pollutant emissions within acceptable levels, which are expected to be more strict than the present marine regulations for CO, NOx, and other hazardous species. In addition, continuous monitoring of selected species in real time may be required.

4. Status of Active Combustion Control

4.1 Overview

The concept of active combustion control has appeared in several forms over the past four decades. The first attempt was made by Tsien¹¹ in an effort to apply control theories to suppress the chugging instability in a liquid-propellant rocket engine. His analysis was based on a combustion model which considered a pressure-dependent time lag between the instants of propellant injection and burning. Stabilization of the combustion conditions was achieved by modulating the propellant injection rate through a capacitor controlled by a servomechanism with pressure feedback. The problem of intrinsic stability was studied using the Nyquist plot to determine the suitable servo coefficients. Similar approaches were used by Marble and Cox¹² and Lee et al.¹³ to control the low-frequency instabilities in bipropellant liquid rocket engines. However, no experimental results based on this "servo-stabilization" concept have been published, primarily because of the limitations of instrumentation at that time.

With recent developments in fast-response sensors and actuators, some interesting studies on the active control of various problems have been reported. Ffowcs-Williams¹⁴ described the concept of "anti-sound" — the elimination of unwanted oscillations in an acoustic field by means of acoustic interference. The basic idea is to first determine the characteristics of a given acoustic field, and then to use that information to manipulate a secondary source of sound which serves as an acoustic actuator. Control is achieved by producing waves out of phase with the unwanted oscillations. In principle, this wave-cancellation technique is applicable to combustion systems; however, implementation to a full-scale combustor is quite unlikely because the energy density of the oscillatory flow field may well exceed that which can be matched by such acoustic actuators as loudspeakers. Furthermore, as a result of the intrinsic richness of the thermo-acoustic interactions, implementation of a control system in a combustion chamber is much more complicated than for normal temperature and pressure environments.

Practical applications of the active control of combustion instabilities have been demonstrated in several research experiments. At Cambridge University, Dine¹⁵ showed that the instabilities of a flame burning on a gauze in a Rijke tube can be eliminated as follows. First, the light emitted from CH free radicals was monitored as a measure of the unsteady heat-release rate from the flame. This information was then processed and fed back to a loudspeaker placed near one end of the tube to increase the acoustic energy dissipation from the boundary. The same problem was studied by Heckl.^{16,17} However, instead of a photo-multiplier, a microphone was used as the sensor to excite the loudspeaker. Results indicated that instabilities can be suppressed over a wide range of phase

difference between unsteady oscillations and actuating pressure waves, provided the control gain is sufficiently large. This observation clearly demonstrated that the control of combustion instabilities can not be explained simply by the principle of anti-sound, which requires that the control excitation be precisely out of phase with existing oscillations.

More recently, Bloxsidge et al.^{18,19} reported the control of low-frequency combustion instabilities in a laboratory jet-engine afterburner. The mass flow into the combustion chamber was varied by oscillating a center body inserted in the choked inlet nozzle, thereby exerting the necessary modifications on the unsteady flow fields. The system was partially successful in suppressing the instabilities, with the amplitude of the fundamental mode reduced by fifty percent.

Lang et al.²⁰ and Poinso et al.^{21,22} explored the active control of instabilities in a small laboratory burner, using a loudspeaker as the control actuator. Both experiments used the same gaseous reactants, but with two different types of flame holders: a multiple orifice plate with 80 holes placed in a premixed propane-air stream; and an array of three rearward-facing steps through which fuel was injected into the air flow. Acoustic pressure was measured by a microphone located upstream of the chamber. The signal was then filtered, phased-shifted, amplified, and sent to a loudspeaker attached to the burner. In addition to the demonstration of instability control, their work showed that the active control technique can be used effectively to study the initial transient behavior of instabilities.

One feature common to the above approaches is that they all used mechanical means, such as loudspeakers or moving bodies, to suppress instabilities. For practical systems containing high energy density, implementation of these means may not be feasible due to the relatively large amount of power required to drive control actuators. It appears that the most direct method of control should be based on the manipulation of energy sources of oscillatory flow fields. Langhorne et al.²³ reported that pressure oscillations in a laboratory afterburner can be reduced significantly by a controlled secondary supply of fuel which is effective in generating the energy necessary for instability control. This method offers a promising solution to problems of low-frequency oscillations in full-scale combustors. Sivasegaram et al.,²⁴ Billoud et al.,²⁵ Wilson et al.,²⁶ and Schadow et al.²⁷ have all demonstrated experimentally the effectiveness of this technique. The theoretical study of Yang et al.²⁸ and Fung et al.²⁹ and the numerical simulations of Menon,³⁰ Shyy et al.,³¹ and Neumeier and Zinn³² have also demonstrated the viability of controlled fuel injection. For detailed reviews of active control of combustion instabilities, see Culick,³³ Candel,² and McManus et al.¹

In addition to its applications for propulsion systems, active control technology has been used to enhance mixing in incinerator afterburners and to increase the DRE (destruction and removal efficiency) for waste materials. Parr et al.⁹ have conducted a detailed study of the concept of utilizing vortex combustion for incineration in a small-scale gaseous fuel system and an extension to a more practical system using liquid fuels. Acoustic excitation was used to stabilize coherent vortices in the air flow, with the fuel modulated and introduced into the air vortex exactly at the

instant of vortex formation. This concept has demonstrated its effectiveness in improving waste destruction. The DRE for liquid benzene exceeded 99.999% for a afterburner/incinerator of 56 kW energy release, even when the waste surrogate constituted 17% of the total fuel content. The controller also reduced emissions: CO dropped from 2900 ppm to as low as 2 ppm and NO_x was reduced to 12 ppm. Parameters critical to the controller performance were the forcing level of the fuel injection, the fraction of the circumferentially entrained air, and the phase angle of the fuel injection with respect to the air vortex roll-ups.

The most common sensor used in ACC is the pressure transducer. For controlling combustion instability this is a natural choice, as the instability is characterized by the chamber pressure oscillations. Experimentally, photomultipliers have also been successfully used, since their signals can give a measure of the unsteady heat release which is at the root of the instability. The placement of either type of sensor is important. For example, the shapes of the chamber acoustic modes should be sufficiently well-known to avoid placing a pressure sensor at a pressure node point. Also, a photomultiplier's signal could be misleading if the sensor is positioned so that its field of view does not completely cover the entire range of motion of a spatially varying reaction zone. Recent advances in machine vision applied to an array of optical sensors may offer a solution, and also provide the controller with information regarding the global distribution of unsteady heat release. Of course, optical access (including interference by sooty flames) is another problem. Other optical sensors, such as laser-induced fluorescence for species measurement and LDV for velocity sensing are probably unfeasible for practical applications, but may be useful in experimental control systems. Optical sensors may be key in pattern factor control, since the temperature distribution throughout the cross section of a chamber is desired.

For combustion instability control, most ACC actuators attack either the acoustics (directly with mechanical acoustic actuation or indirectly through controlled fuel flow), or the hydrodynamics of a reacting shear layer in a dump combustor (by fluid dynamic forcing near the origin of the shear layer). The former approach is sensible in that chamber acoustics play a defining role in the energy feedback loop which causes high-frequency instabilities. The latter approach also has intuitive merit since the spatial and temporal unsteadiness of the heat release (source of energy for the instability) is strongly tied to the turbulent hydrodynamics of the shear layer. Both actuators have demonstrated varying degrees of success in closed-loop control, and shear layer actuation has exhibited positive influence in open-loop mode. Perhaps tandem acoustic and hydrodynamic actuation could accomplish more than either one alone.

In regard to controller design, most studies have used either fixed-parameter or adaptive approaches:

- (1) In a fixed parameter controller, the parameters which define the behavior of the controller do not change with time or with the state of the system. If a reliable model is available, the design of this type of controller can take advantage of well-developed and powerful control and optimization theories. The robustness issue is also most easily addressed for such control design.

Unfortunately, no complete model for practical combustors exists, and the closest approaches (i.e. CFD simulations) are far too complex for direct incorporation into viable controllers. Reduced-order models may be used to develop the controller,^{28,29,34,35} but these models usually contain unknown parameters. System identification can help to define these unknowns by effectively matching the behavior of the model to that of the actual system. Fundamental empirical studies may also aid in this way. Fixed-parameter controllers do not need to be model-based. For example, intuitive gain/phase relationships between the sensor measurements and required actuator signals have been assumed in many successful experiments. Although the controller gain and phase are adjusted for optimal damping of the combustion instability ("manual adaptation"), the controller would be essentially fixed-parameter in application. This approach was apparently also taken in Ref. 30, where a CFD-simulated "virtual combustor" was used to adjust the controller. This underscores the emerging value of CFD as a means of developing and testing controllers, as well as for increasing physical insight and understanding.

(2) An adaptive controller automatically adjusts its own parameters to achieve desired performance of the controller. In direct adaptation, the control parameters are changed based only on a measured performance function. First demonstration of this concept was reported by Billoud²⁵. This approach is demonstrated in Padmanabhan et al.,³⁶ where the Downhill Simplex method was used to seek control parameters which minimized the instability through shear layer actuation. In indirect adaptation, on-line system identification is performed continuously to maintain a locally accurate, updated model of the system; then the controller uses the model's parameters to adjust the control parameters and generate the actuator signal. The model in this case can be a generalized one detached from the physics of the problem (such as an FIR filter used by Billoud²⁵), or it can incorporate physical understanding. Although adaptive controllers are more complicated, their flexibility may be crucial for combustion instability control in the face of changing operating conditions, imperfect knowledge of the system, and changing or multiple modes of instability. Adaptive approaches have demonstrated practical success in the related field of noise control, and appear feasible in combustion control as well. More advanced control involving artificial intelligence techniques such as fuzzy logic and neural networks may eventually offer new solutions to the ACC problem. Although such schemes have been practically demonstrated in noise control, their ill-understood nature makes them unlikely candidates for systematic application in reliable ACC systems, at least in the near future.

Physical modeling can enhance the control design, and is a necessary component of some controllers. Many modeling efforts have concentrated on a specific process, such as acoustics or shear layer hydrodynamics. However, studies such as Cohen and Anderson³⁸ suggest that both acoustics and shear layer hydrodynamics are important in some instabilities. Instances of hysteresis in combustion chambers and significant changes in the nature of the unsteady heat release (such as the "pinching-off" of burning lumps of fuel²¹) also suggest acoustic/hydrodynamic interaction. The consideration of entropy modes may also be appropriate in some systems.

Although liquid fuel feed systems typically respond only to low-frequency (<100 Hz) chamber oscillations, the gas-filled volume of a premixer may respond to chamber acoustic modes, causing unsteady flow of fuel-air premixture into the chamber and hence feed-system like instabilities. In addition to the combustor itself, modeling the actuator can be an important issue, especially for injection of controlled fuel.³⁴

Finally, in any controller, it is important to squeeze the maximum amount of (accurate) information from the available sensor data to determine the state of the system being controlled. This issue of observer design has been explicitly addressed in Ref. 32. The presence of noise in a combustor, system uncertainties, and what information must be known a priori about the system are important considerations in observer design.

4.2 Recent Results

The status of the various ACC programs currently being conducted within the AGARD community was summarized at the workshop. These programs cover a broad spectrum of problems related to combustion instability and pollutant emissions. Schadow and his coworkers at the US Naval Air Warfare Center have been working on the detailed understanding of fluid dynamic/acoustics/combustion interactions. In particular, the effects of large-scale structures and their transition to fine-scale mixing are being considered. The ACC is applied to a variety of combustion devices, including ramjet dump combustors and incinerator afterburners. Both systems have similar combustion characteristics with flame stabilization at a backward facing step or dump region. For these flow conditions the development of jet shear layers is critical for the combustion processes, including flammability limits, combustion efficiency, and flame stability (combustion instability). The ACC work is therefore based on controlling jet shear-flow dynamics, which are characterized by flow instability frequencies associated with initial vortex shedding and subsequent vortex merging, as well as the jet preferred mode at the end of the jet core. The physical understanding of the relationship of these flow instability frequencies and acoustic driving frequencies is critical for the control process.

The initial vortex frequency is associated with the generation of small scale vortices, which are critical for molecular mixing and flame stability. Premixed flame experiments showed that open-loop forcing at the initial vortex shedding frequency, which scales with the momentum thickness and jet velocity, significantly extended the flame stability limits.⁵² The preferred mode frequency is associated with the generation of large-scale structures. When this flow instability frequency, which scales with the jet diameter and jet velocity, is near one of the acoustic resonant frequencies of the chamber, the large-scale structures are highly coherent and can cause periodic heat release. Under certain conditions this can lead to the driving of combustion instabilities. ACC was used to damp these oscillations using a variety of actuators, including acoustic drivers, pulsating fuel injection, and periodic secondary heat release. Both gaseous and liquid pulsed fuel injection⁵³ were used. The same technique is also used to enhance combustion efficiency.⁵⁴ In this approach gaseous and/or liquid fuel is injected at the right time into acoustically stabilized vortices using

ACC. Tests are being conducted to enhance efficiency in ramjet dump combustors and in incinerator afterburners. For the latter application it was shown that performance of an incinerator can be significantly increased, even when energy density of the system was reduced by a factor of 200 relative to present systems. The ACC mechanism was scaled up by a factor of 10 to a 50kW system and is currently being scaled up by a factor of 200 to a 1MW system.⁵⁵ In the present flame and combustor experiments simple time-delay controllers are being used. Also, limited experiments have been done with a neural net based controller.

The application of ACC to suppression of combustion instability was also employed by Zinn of the Georgia Institute of Technology.⁸ The system consists of an observer that uses an iterative, Fourier-like approach to determine the amplitudes, frequencies and phases of unstable combustor modes in real time. This information is sent to a controller where open-loop test data are used to determine the gain and phase shift that are added to each unstable mode. The modified modes are combined into a control signal that is delivered to a fast response fuel injector actuator that varies the length of a magneto-strictive material and, thus, modulates the injection rate of a secondary fuel stream into the combustor. The latter damps the unstable combustor modes by generating secondary heat addition oscillations out of phase with the pressure oscillations. To date, open loop tests have been performed to determine the frequency response of the fuel injector actuator, which was subsequently used in the closed-loop control tests. These tests showed that the developed system effectively damps large amplitude instabilities. For example, the amplitude of the most unstable combustor mode was damped by 26 dB within 40 milliseconds after activating the control.

In a research project sponsored by the US Navy, Yang and his colleagues of the Pennsylvania State University have been working on the development of integrated control methodologies for gas-turbine combustors in order to enhance performance in terms of lean blowout and combustion stability characteristics, while maintaining pollutant emissions within permissible limits.⁵⁶ A variety of active control techniques are systematically evaluated and implemented in a hierarchical approach. The control strategies are established at two levels. High-level control is carried out using modulated secondary fuel injection directly into the flame stabilization zone. Their process is appropriately synchronized with local heat release and pressure oscillations in order to stabilize the combustion flowfield and consequently extend the operating range. Low-level control is carried out using variable air swirl. This is used to change the degree of fuel-air mixing at the combustor inlet in order to achieve minimum emissions over the entire operating range of the combustor. The two-level strategy, together with appropriate combustion transient sensors, will be part of an ACC system which will extend the stable operating range of the combustor and reduce emissions. In addition, innovative concepts for diagnostic and prognostic decision-making will be incorporated into the control system to enhance engine reliability. Optimization of combustor operations will be conducted based on requirements for flame stability and pollutant emissions. When coupled with a

global engine control system, this combustor control system will allow for the development of fuel-efficient and clean gas turbine engines.

Several research groups have discovered the presence of hysteretic behavior in the vicinity of the stability boundary for oscillations in a dump combustor. The phenomenon is observed as the fuel air ratio is changed with all other parameters fixed. The existence of the hysteresis loop is the basis for a strategy of nonlinear control recently demonstrated by Culick⁵⁷ of the California Institute of Technology. When the system is operating on the upper branch of the hysteresis loop, the system can be forced to make the transition to the lower branch by injecting a single pulse of secondary fuel at the dump plane. Thus, by applying active control, the region of stable operation can be extended. Perhaps the most significant aspect of these results is that successful control has been achieved because the dynamics of the system are understood, and the control law was suitably constructed. It is particularly important to notice that the behavior treated with this method is intrinsically nonlinear. Application of linear control ideas would be inappropriate and much less successful. A fundamental matter is the extent to which truly nonlinear control can be extended outside the region of hysteresis.

California Institute of Technology also attempted to find chaotic behavior in an air-breathing combustor.⁵⁸ Sterling analyzed pressure records taken in a dump combustor showing no strange attractors that might indicate chaotic behavior. In contrast, a model, which was based on some of the characteristics of the pressure records, including a nonlinear combustion response with time delay, did produce chaotic behavior. Presently there is insufficient experimental data to rule out unequivocally chaotic behavior in combustors, but the available information suggests that the noisy background in combustors is due to stochastic sources such as flow separation and turbulence.

The ACC research conducted by Whitelaw and his associates at the Imperial College attempts to suppress combustion instabilities, extend flammability limits, and minimize emissions in a variety of geometric conditions.²⁴ These include ducted premixed flames behind one or more bluff-body stabilizers; a model of an industrial burner; a model of an annular gas turbine combustor; and an opposed jet flame. Discrete-frequency oscillations are imposed on the flows using actuators such as acoustic drivers, periodic spark ignition of part of the fuel, and devices to oscillate liquid and gaseous fuel flows and a spray of water. The frequency limitation of the injectors was overcome by fuel injection at half the dominant frequency and the sequential operation of injectors. Control of the oscillations also led to a reduction in NO_x emissions by 5% with oscillations of liquid fuel and by 50% with a spray of water. The latter is due to heat removal. The rich flammability limits of a model industrial burner was extended from an equivalence ratio of 1 to greater than 3 by the addition of oscillations by a loudspeaker. At the same time the flame was more stable and more compact. Imposed oscillations had an adverse effect on the lean flammability limits which was partly overcome by the dilution of the fuel with air.

Burkhardt of the Technical University in Hamburg-Harburg studied active combustion control of a bunsen burner flame using image processing sensors which can be superior to point sensors.⁵⁹

Using a CCD camera with 250000 diodes, it is possible to carefully characterize the state of the combustion process, for example, by analyzing turbulent and non-homogeneous reaction zones. In his experiments non-optimal burning states are recognized and corrected/optimized by closed-loop active control. Two different approaches, namely optimization techniques, and fuzzy logic and neural networks, were used to analyze changes in the image sequences. Both control strategies are able to "learn" an optimal state which is set up by a human expert and determine necessary actions for active control to optimize the reaction process. For the optimization technique, the image of a non-sooting flame was selected as the optimal burning state. By proper application of image processing techniques they continuously extract image features from the combustion process to compare with features from an optimum state obtained by a learning procedure. They use a quadratic, multispectral performance criterion to optimize on-line using the modified Newton-Raphson algorithm. For the fuzzy logic technique,⁶⁰ a small number of features (such as flame height and brightness) which are closely related to the state variables, are extracted. These features were compared with those obtained in the optimum combustion state, and the deviations are sent to the neural-network-based controller. The implementation of the fuzzy controller in the form of a neural network provides the possibility that the system can learn from the environment and improve the robustness against the environmental disturbances through updating of the network's weights. The system determines a control action by using a neural network which implements fuzzy inference. In this way, prior experts' knowledge can be incorporated easily.

ACC research is being conducted at UTRC under internal and DARPA funding on lean premix burners using both gaseous and liquid fuels. The focus of the research is on the control of combustion instabilities. The research is experimentally based, using a small scale atmospheric pressure rig for screening of actuation and control concepts, and a single nozzle rig running engine scale hardware at combustor operating pressures and temperatures. Actuation concepts involving fuel flow control are being evaluated. Methodology and hardware have been developed that have sufficient bandwidth to control instability frequencies up to about 200 Hz. Significant reductions in instability pressure levels have been demonstrated. For example, during screening tests on the atmospheric pressure rig operating on gas fuel, up to 8 dB reduction in combustion instability pressure oscillations were achieved using a pilot for control.

Active control has been investigated at Ecole Centrale de Paris as a means for reducing the level of nitric oxides emitted by liquid fuel combustors.^{61,62,63} Experiments carried out on a 25kW domestic boilers and on a 850 kW furnace indicate that reductions of up to 30% may be obtained by open loop control techniques. This demonstrates that active control principles may be used to improve combustion in practical systems.

Work on ACC has been carried out at IST, Lisboa, Portugal, aimed at suppressing oscillations and reducing NO and CO emissions. The technique used was the sinusoidal forcing of the gaseous fuel stream with phase shift control. A wall static pressure probe was used to detect the pressure in a tube and disc burner. It was shown that different disc sizes and geometries were

effective to reduce NO and CO production. This ACC work is related to earlier passive control work where pressure oscillations were reduced using different bluff body geometries.⁶⁴

ACC research has been conducted at the Munich University of Technology, Germany, for more than 10 years. The main aspect of this research, which was started with a joint project with Ecole Centrale de Paris,^{20,21} is the active suppression of self-excited combustion instabilities and exploring the onset of instabilities.⁶⁵ Current research includes the design and testing of practical actuators.^{66,67} The research is the basis for an industrial application of ACC to a full-size stationary gas turbine with an electric power output of 170 MW. This project is producing very encouraging results, which will be published at the ASME ASIA 97 Conference and the "18 Deutsch-Niederlaendische Flammentag."

5. Active Combustion Control Applications

5.1 Introduction

The review of future needs presented in Section 3 described several challenges which may limit the growth potential of combustion systems. For example, the evolution of aeroengine gas turbine combustors with very high pressure ratios may depend on achieving greatly accelerated mixing rates to preserve highly efficient operation at such high combustion intensity conditions. Some of the challenges may be mitigated by successful application of active combustion control methodologies. The following table depicts, for the major combustion systems, such challenges and the relative priority determined at the AGARD Workshop, based on a composite consideration of basic understanding, risk, and benefit. As indicated, a common combustion system challenge believed addressable by ACC was instability control; it was identified for all systems. The reason for "low" relative priorities assigned to aeroengine systems was because other systems had a more immediate need. A "low" relative priority for liquid-propellant rockets was assigned because the perceived risk was very high in order to achieve a successful active control application. The reason for "high" relative priority for instability control for both surface power gas turbine and airbreathing missiles was because it is an acknowledged developmental challenge for all manufacturers, and also laboratory demonstrations have shown the potential for active control to mitigate it. The "medium" relative priority for solid-propellant rockets instability control, as well as compact design for burner and incinerator emission control, reflected developmental needs and a belief that the key physical phenomena were known.

Together, instability controls in surface power gas turbines, airbreathing missiles, and solid fuel rockets were judged to be high impact applications for active combustion control. Successful application of active control methodology will expand the operational capabilities of each system to broader conditions while preserving attributes of high efficiency, stability, low emissions, etc. In pursuit of these applications, developments in sensor and actuator technology will be required to provide highly responsive, precise, and reliable devices. Further, it is important to expand the experience base for the applications from laboratory scale and conditions to realistic hardware and

conditions. For example, actuator capacity which may be suitable for atmospheric operating conditions may not function at elevated pressures and flowrates. Moreover, neither the identification of the key physical instability coupling phenomena, nor their scaling to other conditions, are known. Hence, the potential demonstrated at reduced conditions does not guarantee any payoff at real conditions. The logical development of all elements of the active control system, and their use in more realistic devices, will result in new options for the combustion system designer, and permit growth of the system's potential. In the following sections, active combustion control applications specific to surface power gas turbines, airbreathing missiles, solid propellant rockets, and military burners and incinerators are discussed.

Table 1. Relative Priority for Active Combustion Control

Combustion System	Operational Challenge Addressable by Active Control	Relative Priority
Aeroengine Gas Turbines	Enhanced Mixing	Low
	Instability Control	Low
Surface Power Gas Turbines	Instability Control	High
	Flame Temperature Control	Medium
Airbreathing Missiles	Instability Control	High
Solid Propellant Rockets	Instability Control	Medium
Liquid Propellant Rockets	Instability Control	Low
Burners/Incinerators	Compact Design for Emission Control	Medium

5.2 Surface Power Gas Turbines

Increasingly stringent emissions standards will raise the challenge for surface power gas turbines to operate stably. That is, in order to meet lower emissions goals for NO_x and CO, pre-mixed combustion systems will be used and operated at very lean fuel-air ratios. As previously discussed, the leanest mixture will be set by the stability characteristics of the combustor – both the static stability characterized by lean blowout and the dynamic stability characterized by lean-limit, acoustic-coupled instabilities. Both of these narrow the operational flame temperature window, and are currently encountered by most manufacturers of industrial gas turbines. Active combustion control is a technique believed capable of mitigating the lean-limit instabilities.

Subscale demonstrations of suppressed combustion instability have been performed at reduced pressure and temperature operating conditions. Such tests, performed for premixed and direct-injection systems, have shown that significant reductions in the combustor pressure oscillation can be achieved for instabilities experienced at frequencies up to approximately 300 Hz. While the

coupling driving the instabilities is often termed thermo-acoustic, a detailed understanding of the key processes is not available; successful demonstrations have not relied upon this knowledge. Generally the approach is to modulate a secondary fuel injection (or pilot) in a manner to either interfere with the coupling mechanism or cancel the pressure perturbations. Control algorithms often adapt to the instability because of the wide range over which stable operation must be preserved, and both electro-mechanical- and advanced material- (e.g. magnetostrictive) based actuators have displayed sufficient capacity and responsiveness for these demonstrations. While such subscale tests have shown the promise of achieving instability control of premixed combustion, these studies must be extended to realistic operating conditions. Both reliable, durable actuators with capacities consistent with real operating conditions, and control strategies capable of breaking the coupling mechanism, must be achieved. Further, the actuator authority must be sufficient such that any fuel perturbation does not compromise the combustor emissions goals. Ongoing studies suggest that the desired attributes of active stability control are achievable.

5.3 Airbreathing Missiles

Future requirements for tactical missiles will drive the design to even smaller combustors that must maintain high-level and stable combustion over even broader ranges of operation. Active combustion control has the potential to meet these challenges. In the near term, suppression of low-frequency combustion instabilities by active control should be achievable, while in the long term, the extension of lean blow-out limits may also be realized. This promising outlook is based on the fact that the critical role of shear-flow dynamics (or the development of large-scale structures and their break-down into fine-scale turbulence) for the combustion characteristics in ramjets (the airbreathing missile combustor) is well understood. While this is particularly the case for the center-dump combustors, an understanding of the underlying unsteady fluid dynamics found in annular and side dump combustors needs further research.

Methodology to suppress low-frequency combustion instabilities in center-dump combustors has been successfully demonstrated in laboratory tests, suggesting that its application to full-scale combustors is a realistic goal. The suppression of these oscillations are critical, because they can reduce the inlet margin, resulting in inlet unstart. While scale-up and transition to realistic operational conditions remain a technical challenge, current physical understanding and control strategies for vortex-driven combustion instabilities make near-term success likely. The demand on missile system actuators and sensors to control instabilities in the frequency range of 100 to 300 Hz is reasonably within capabilities. Higher frequency-response pressure and emission sensors and liquid fuel actuators for periodic fuel modulation are being explored in the current laboratory experiments. Simple fixed parameter controllers will be used for initial experiments to determine their adequacy, with neural net and model-based adaptive controllers being considered as future alternatives.

The role of shear-flow dynamics in influencing flame blow-out limits is less understood than for combustion instabilities. Therefore, the application of active control to extend blow-out

remains a longer term goal. In limited experimental experiences, flammability limits were extended by increasing fine-scale turbulence, and hence molecular mixing, by high-frequency acoustic excitation. However, practical actuators would require a higher bandwidth performance than for the combustion instability control.

5.4 Solid-Propellant Rocket Motors

Combustion instabilities remain a major concern in the development of solid-propellant rocket motors. This is particularly true for large motors including strategic missiles (about two meters in diameter) and space launchers (about three to four meters in diameter with large aspect ratio) loaded with metallized composite propellants, where modifications are more expensive and time-consuming. Active control may play an important role in curing the instability problems for this type of motor, since the pressure oscillations are dominated by low-frequency longitudinal modes, which are more accessible to control than higher-frequency oscillations associated with smaller motors. A concerted program for active control of combustion instabilities in large motors is currently being prepared by French laboratories with possible participation of a United States company or laboratory. The control strategy is based on modulated injection of liquid monopropellant at the head-end in a closed-loop system.

5.5 Military Burners and Incinerators

Successful application of ACC to military burners and incinerators will provide a promising opportunity to meet emerging emission standards. In particular, real-time monitoring of selected species should be included as an integral part of the control system. As demonstrated in a compact incinerator program, ACC implementation into burners with high energy densities can yield environmentally sound combustion processes which are not possible based on presently available technologies. Since the control strategy was established through detailed understanding of the combustion dynamics involved, the ACC approaches for incinerators can be readily applied to other burners for minimizing hazardous emissions.

6. Research and Development Needs

6.1 Introduction

Since the potential benefits of ACC are still uncertain, one of the main objectives of near term ACC research should be to demonstrate and quantify the advantages of ACC relative to other approaches. In this phase, the work should progressively shift to larger-scale devices featuring some or all of the conditions encountered in practice. Subsequent efforts should develop know-how to guide the development and optimization of practical ACC systems. Such information must be obtained from research and development programs which investigate problems unique to the systems at hand (e.g. rocket, gas turbine, and ramjet combustors and military incinerators), and from active control studies in related engineering applications (e.g., active noise and vibrations control). Combustor-related ACC studies may be used, for example, to investigate fundamental processes in uncontrolled and controlled combustors, develop sensors and actuators that

satisfactorily perform in the harsh combustor environment, and develop models of controlled combustors. Parallel studies will have to address more general issues such as development capabilities for real time data acquisition and analysis, microelectronics, computers, software, and nonlinear control. These research needs are discussed in the remainder of this section.

6.2 Understanding Fundamental ACC Processes

To effectively implement ACC, it is desirable to understand the fundamental aerothermochemical processes that must be controlled. In particular, detailed understanding of fluid dynamic processes, which are associated with large-scale structures and their breakdown into fine-scale mixing, should be first achieved as this opens up the potential for effective combustion control. Comprehensive information about these fluid dynamic processes and their passive and active control is available for combustion processes associated with shear layers generated at rear-facing steps (e.g., dump combustors) as illustrated in the following example. Research remains needed to develop the same level of understanding for other combustion processes, for example swirl stabilized flames.

It is well known that combustion instabilities in dump combustors are driven by a feedback process involving periodic vortex formation and combustion processes.³⁹⁻⁴¹ During an instability, a decrease in the combustor pressure increases the velocity of the reactants flow into the combustor. This is followed by the formation of coherent vortical structures that are ignited, after a time delay, as they entrain hot gases and/or burning gas pockets. Ignition is followed by a "sudden" vortex breakdown and nearly instantaneous heat release in phase with the local pressure oscillations, which provides the energy needed to drive the pressure oscillations, according to Rayleigh's criterion. The cycle repeats itself when a subsequent combustor pressure drop near the dump plane produces another increase in the reactant flow rate into the combustor and vortex formation. This understanding of the driving process could be used to guide the development of ACC approaches for controlling such instabilities. Candidate schemes include: developing a process that prevents periodic formation of vortices; generating a secondary, periodic, combustion process within the combustor (e.g., by periodic fuel injection^{1,2,8}) that damps the instability by releasing energy 180 degrees out of phase with respect to the unstable pressure oscillations; or using mechanical drivers (e.g., oscillating valves, speakers) to excite pressure oscillations out of phase with respect to the combustor pressure oscillations (i.e., anti-sound³). Research must be performed to determine which of these proposed (or other) approaches will provide the most effective ACC.

One important criterion for selecting control approaches is to minimize the energy input required to gain control authority on the physico-chemical processes involved. In the case of shear-layer control for preventing the development of large-scale vortices, it is important to identify the regions with high amplification of local flow disturbances. For dump combustors, these are the initial regimes of the shear-layer development, where seeding of small instability waves results in substantial changes in subsequent flow dynamics and combustion processes. In the case of

modulating fuel injection^{1,2,8} to control combustion instabilities, a fundamental understanding of the combustion process is critical, as discussed in the following.

Many ACC systems modulate the injection rate of a secondary fuel stream into the combustor, generally at the frequency of the unstable oscillation, to generate a secondary heat release process that damps the instability. Practical applications of this ACC technique will seek maximum damping with a minimum secondary (control) fuel flow rate. Therefore, the following questions must be addressed: (1) Does the secondary fuel injection modify the nonlinear combustion process that drives the instability and/or does it generate "another" (independent) combustion process that excites "separate" heat release oscillations out of phase with respect to the unstable pressure oscillations? (2) What is the optimum location(s) for secondary fuel injection? (3) What is the interaction mechanism of pulsed-sprays with large-scale flow structures in the combustor? (4) What is the optimum secondary fuel flow rate? (5) If a liquid fuel is used to damp the instability, what should be the characteristics of its spray to optimize damping? (6) What is the optimum number, diameter, orientation and velocity of the secondary fuel jets?

To realistically evaluate a proposed ACC approach, it should be initially investigated in a small scale experiment that closely simulates the full scale system design and operating conditions. Ideally, this could be accomplished by requiring that the following parameters be the same (or close) in the experimental and full scale setup: (1) the Mach, Reynolds and Strouhal numbers of the flows, (2) the reactants and injectors, (3) the Damkohler number of the combustion process, (4) the combustor's temperature, pressure, velocity and concentration fields distributions, and (5) the boundary conditions. The small scale studies should obtain complete information about the spatial and temporal variations of, for example, the fuel spray, reaction rate, and velocity, temperature, pressure and composition fields under controlled and uncontrolled operating conditions. This information together with results of visualization studies should then be used to identify specific characteristics of the combustor that could be controlled by ACC to improve its performance. Such characteristics may include the large and small scale vortical structures that drive combustion instabilities or enhance combustion, regions of slow mixing that impede combustion, and hot spots that enhance NOx emissions and/or distort the pattern factor causing damage to turbine blades.

The above discussions were primarily related to combustion devices using sudden flow expansions for flame stabilization, such as ramjets, military burners and afterburners for incineration, etc. Examples of additional ACC applications whose development requires further investigation of their controlling mechanisms include: (1) control of mixing, combustion, liner heating and ignition (i.e., relight)⁴² processes in gas turbines, which could result in safer operation, longer life time, reduction of combustor length and weight, emissions and liner heating, and improved pattern factor, (2) control of vortex formation in solid rockets to reduce the onset of combustion instabilities, (3) control of reactant feed processes, sprays and combustion processes in liquid rockets operating at sub- or super-critical conditions to increase combustion efficiency,

reduce combustion instabilities and prevent damage to the injector face and combustor walls, and (4) control of combustion problems in various propulsive devices to reduce signature. Investigations of these control problems will elucidate the fundamental processes in both the uncontrolled system, to help identify appropriate control approaches, and in the controlled system, to help in the optimization of ACC. The results of such studies will determine, for example, processes that must be excited or "canceled" within the combustor to attain the ACC goals, the time response of the ACC, and the types, number and locations of the actuators and sensors that will optimize the ACC performance. These studies will also indicate whether available sensors, controllers and actuators could be used in proposed ACC applications or whether new components must be developed.

6.3 ACC Models

There is also a need to develop models of actively controlled combustors. Such models, together with experimental data should be used to: (1) identify the fundamental processes that determine the performance of controlled combustors, (2) optimize the performance of ACC systems by, for example, predicting the optimal distributions and performance requirements of ACC sensors and actuators, (3) improve the design of ACC systems, and (4) develop ACC control approaches.

To pursue the above objectives, ACC models of various complexity will have to be developed. It is desirable to develop numerical simulations that fully account for all processes in controlled combustors; e.g., rapid time variations, three dimensionality of the flow, vortex dynamics, acoustics, turbulence, chemical kinetics, nonlinearities, flow-actuators interactions and effects of boundary conditions. Numerical predictions could be compared with experimental data to identify the mechanisms that determine the performance of controlled combustors. They could also serve as bench marks for the development of simplified (e.g., low order) models of controlled combustors that will be needed for ACC applications. The development of numerical simulations that can fully describe the behavior of controlled combustors will require additional research on such topics as efficient numerical solution techniques and efficient computational approaches (e.g., parallel computing).

Simplified ACC models must be developed to determine the instantaneous combustion chamber dynamics based on measured signals such as pressure and heat-release rate. The models shall not only provide the capability of monitoring the entire flowfields of concern in real time, but also serve as a basis for designing active control loops. The formulation should extend the nonlinear combustion dynamics model described in Refs. 29, 34, and 35 to include vortex formation and evolution. All three modes of flow motions (i.e., acoustic, vortical, and entropy waves) in practical systems need to be treated in such a unified fashion that the various processes involved in combustion chambers under external control actions can be investigated systematically. In addition, stochastic processes arising from combustion noise and intrinsic flow disturbances

should be included to provide a faithful description of the flow development, as well as to accommodate the effects of model uncertainties.

6.4 ACC Sensors

ACC sensors continuously measure specific system properties that are subsequently used to determine the state of the system. Fast response pressure transducers and/or photomultipliers have been used to measure pressure and radiation from radicals (e.g., CH or CC), respectively, in small-scale ACC experiments on combustion instability control. The measured data was used to determine the characteristics of the instability. It is expected, that as interest in ACC applications grows, the performance of existing sensors will have to be upgraded and new sensors will have to be developed to measure the temporal and/or spatial dependence of combustor properties (e.g., temperature, pressure, equivalence ratio, species and radical concentrations, and magnitudes of electric currents and magnetic fields). Any sensor must have a time response that is consistent with the goals of the ACC. For instance, fast response pressure transducers are required for active control of combustion instabilities, while slow response sensors are adequate for ACC systems that control pattern factor and emissions in gas turbines. ACC applications which require spatial resolution of combustor properties along with adequate time response may possibly employ proper distribution of sensors or MEMS (micro-electronic mechanical systems) sensor arrays. In all ACC applications, sensors will have to satisfy all or some of the following requirements: simple design, reliability, high robustness, high sensitivity, low weight, low cost, high frequency response, ability to continuously operate in harsh engine environments over long periods of time, and no or minimal need for optical windows.

Future developments of ACC will critically depend upon the availability of suitable sensors. Short term research should adapt existing sensors to practical ACC applications while long term research should develop novel sensors in response to evolving ACC needs. Examples of short term ACC sensors research include: (1) development of robust sensors for measuring various combustor properties (e.g., distributions of equivalence ratio, temperature and various species), (2) sensor miniaturization, (3) optical sensors⁴⁶ based on diode lasers (4) sensors materials, (5) sensors cooling methods, and (6) sensor arrays for measuring spatial distributions of properties. Long term research should address issues such as: (1) novel sensors and measurement techniques, (2) identification of optimum sensors for different ACC applications, and (3) development of approaches for combining sensor measurements with an appropriate model to determine spatial distributions of required properties (e.g., radial temperature distribution at the combustor exit for control).

6.5 ACC Actuators

The role of an ACC actuator is to "actively force" the combustor to bring about desired performance. ACC actuators that have been used to date include: (1) injectors that rapidly modulate the flow rate of a secondary fuel stream into the combustor for control of combustion instabilities,^{1,2,8,54} (2) valves that modulate the air flow rate into an unstable combustor to modify

its acoustics and/or increase its damping,⁴⁷ (3) speakers that excite sound within the combustor or near its boundary^{1,2} to cause destructive interference with unstable pressure oscillations, modify the instability driving process, or increase system damping,* (4) valves that vary the air flow rate in a blast atomizer to control the fuel spray characteristics,⁴⁸ (5) acoustic drivers that excite sound waves to control mixing processes,⁴⁹ (6) pulsed-combustion actuators that generate periodic heat release and sound waves,⁵³ (7) piezoelectric actuators that control boundary layer flow,⁵⁰ and (7) valves that produce phased, periodic air and/or waste injection to improve waste incineration.^{9,10}

In contrast to existing ACC sensors, which are generally based upon available combustion diagnostic techniques, the development of ACC actuators was stimulated by evolving needs of ACC. Future research in this area will have to determine the type of actuation needed for different ACC applications (e.g., piezoelectric, magnetostrictive, electric, magnetic, radicals injection, flow rate control). Such studies would help answer such questions as: should we use piezoelectric actuators or acoustic drivers to control mixing and, thus, emissions and the pattern factor in gas turbine combustors? Can we use electric or magnetic fields to control the combustion processes, or should we use air flow rate modulation or ultrasonic forcing to control the characteristics of the spray in air blast atomizers? Research is also needed to determine whether or not a MEMS-type array of actuators is required for a specific application, and if so, what its configuration would be to optimize ACC performance. For applications with individual actuators, the number and locations of the actuators should also be optimal.

Once developed, the performance of actuators will have to be evaluated in open and closed loop control experiments. The former will determine whether the actuators can force the system with adequate amplitude and time response; this will be an indication of the system's controllability.⁵¹ The latter will assess the actuators' capabilities and limitations for closed loop ACC. Once the actuators for a specific application have been chosen, their application will require additional efforts to address the actuators' scale-up, time response, reliability, robustness, weight, size, survivability in the harsh combustor environment, packaging and cost.

6.6 ACC Controller

The controller is the "brain" of an ACC system whose task is to determine the characteristics of the control signal to the actuator. These characteristics depend on whether the ACC operates in an open or closed loop control mode, and on the type of control. As stated earlier, the control signal in open loop ACC is independent of the state of the combustor and is determined a priori. In contrast, the control signal to the actuator in closed loop ACC depends upon the state of the system, which is determined from the sensor measurements.

Since open loop control is considerably simpler than closed loop control, the development of viable open loop ACC should be pursued. Such efforts will have to develop an understanding of the basic mechanisms involved in the process that needs to be controlled, and the manner in which

* In many instances, the mechanisms through which the actuator attains its objectives is not fully understood.

it can be optimally "forced" to attain the ACC objectives. For example, there is evidence suggesting that combustion instabilities can be damped by open loop ACC that excites pulsations within the combustor at a frequency not equal to any of the unstable combustor mode frequencies; the period of the forced oscillation need only be of the same order as either the periods of the unstable modes, or a multiple of the period of the most unstable mode. Research is needed to determine the feasibility of such control approaches and the optimum frequency and magnitude of the required forcing. It is also necessary to determine whether such approaches can satisfactorily stabilize combustors over wide ranges of operating conditions without producing adverse effects (e.g., undesirable signature).

Closed loop control generally consists of several steps. First, the signal measured by the sensors is used by the observer to determine the state of the system⁴⁹. Next, the observed state of the system is used to determine an "error" signal, representing the deviation from the desired state. The error signal is then used to determine the actuator's control signal, in a way determined by the controller design.

To attain effective closed loop control, the following two tasks must be accomplished: (1) the observer must determine the state of the system within a "relevant" time period that depends upon the controller's objective and characteristics of the controlled system, and (2) the controller must determine an appropriate control signal. Since the performance of practical combustors is generally described by a system of nonlinear partial differential equations (PDEs), the timely "observation" of its state would require the development of analytical/numerical approaches that can swiftly interpret the measured data in terms of the governing equations to determine the state of the system. The development of effective "observation" methods for ACC is urgently needed. These methods should account for multiple sensors in arbitrary number and locations, noise (e.g., turbulence), and the effects of process nonlinearities upon the accuracy of the "observed" state of the system. There is also a need for alternate "observation" approaches, which will not require solution of complex PDEs. Such approaches may use reduced order models or take advantage of qualitative understanding of the physics of the system. The latter approach was applied in Ref. 8 where a wavelet type analysis is used to "observe" the amplitudes, frequencies and phases of the unstable combustor modes in real time.

Improved algorithms for the determination of the control signals are also needed. Such studies should develop control approaches that take into account the effects of such phenomena as system nonlinearities and noise. There is also a need to investigate whether the controller should have constant parameters or adaptively varying parameters. The developed controllers will have to meet the ACC objectives within a specified time period* and with limited resource expenditures (e.g., actuator power input).

* In applications such as combustion instability it is mandatory that the ACC rapidly damp the instability before it causes system or mission failure.

Finally, possible application of newer control approaches such as neural network, fuzzy and chaotic control in ACC should be investigated.

6.7 ACC System Integration

Practical aspects of integrating an ACC system with the engine and flight vehicle must also be studied. Specific issues that should be addressed include: (1) the packaging of the ACC and space available for its installation in the engine, (2) protection (e.g., cooling) of the ACC in the harsh engine environment, (3) added weight of the ACC and its effect upon the system's overall performance, (4) integration of the ACC with the engine's and flight vehicle's control systems, and (5) the effect of the ACC upon the system's operation and maintenance.

Acceptance of ACC by the engineering community will require demonstration of its effectiveness under practical operating conditions. The performance of full scale ACC systems will have to be demonstrated on practical combustors in their real environments (e.g., shipboard incinerators, jet engines, rocket motors). Such tests will have to quantify the benefits of the ACC and demonstrate that it can survive in the harsh engine environment over periods of time comparable to the duration of the mission or life time of the combustor.

7. Concluding Remarks

This workshop was concerned broadly with three topics:

- (1) Possible applications of active control and the future requirements of combustors;
- (2) The current status of active control of combustor dynamics; and
- (3) The needs of research and development in order to close the gap between (1) and (2).

Participants came from all NATO countries and gave broad representation of industry, the research community, and government defense agencies. All three topics were addressed thoroughly by a group comprising most of the world's leading researchers and responsible officials from the user community.

With respect to the three topics, the participants agreed upon the following broad conclusions:

- (1) The demands to be placed upon the performance and behavior of future combustors are such that they likely cannot be met within the traditional design methods. All combustion systems offer problems or characteristics that seem to be candidates for application of active control.
- (2) To the present time, no full-scale applications of active control of combustion dynamics have been publicly reported, but several are planned. Consequently, forecasts of the future of ACC rest entirely on results of laboratory demonstrations; essentially nothing is understood about scaling laws.
- (3) The needs of research and development can reasonably be divided into near-term and long-term. The former must be based primarily on existing knowledge and resources, and consist mainly of well-defined demonstrations with specific types of systems, investigating feasibility and scaling laws. In the long-term, there is a wide array of

research needs comprising investigations of fundamental processes (both theoretically and experimentally) and development of sensors, actuators, and control laws.

For reasons which are clear from the discussion in Section 3, "Requirements for Future Combustors," and Section 5, "Applications," there is considerable enthusiasm for introducing methods of active control in virtually the entire spectrum of combustion systems. Moreover, that aggressive view by some potential users is encouraged by optimism flowing from a growing number of successful laboratory demonstrations, the majority of which have shown that active control can be used to reduce the amplitudes of oscillations in combustion instabilities. The emphasis on combustion instabilities is partly historical and partly because of pressing practical needs but should not be allowed to obscure the fact that other applications may be equally important. For example, some success has been achieved in using ACC to maintain an incineration process at optimum conditions.

There are some, however, who caution against full-scale tests too soon. Their reason is that, as stated several times in this report, the scaling laws are not known and any tests must be designed on the basis of results obtained in laboratory devices that have far smaller combustion energy densities than those in combustors intended for full-scale use. The primary and extremely important point to realize is that under these conditions, while success with a full-scale test would be an obvious advance, failure would not signify that ACC cannot be used – only that the particular instance was unsuccessful. Thus the financial and strategic costs must be carefully weighed.

It is quite clear that the matter of scaling is a central issue. Construction of the scaling laws can be done expensively by testing only, but practical considerations, and experience, demand that the most productive approach combine testing and theory. At the present time, theory and analysis lag far behind experimental work. And, as it happens, so also does understanding. There is, for example, no framework for interpreting quantitatively any of the experimental results reported to date. In particular, ACC has been used to reduce the amplitudes of various combustion instabilities, but no serious attempts have been made to predict the amplitudes before or after control is applied. That fact is symptomatic of the difficulties that must be recognized when full-scale tests are contemplated.

The field of active control of combustor dynamics has enormous potential. Sufficient favorable laboratory results have been generated to consider possible applications to full-scale systems. However, the state of progress in general is such that considerable research and development, both in theory and of hardware, will likely be required to achieve practical success. The workshop has shown that international collaborations promise to be highly effective to produce that success.

8. Collaborations

This first AGARD workshop provides the catalyst for future international collaborations to advance the ACC technology. With the decrease of available R&D funding, cooperation at both

national and international levels is gaining increasing importance for advancement of emerging technologies.

International collaboration can be accomplished through the following three activities:

- (1) additional workshops on ACC;
- (2) ACC R&D presentations at AGARD Symposia; and
- (3) special events.

The following actions have been taken following the first workshop:

A second workshop has been approved by PEP for Fall 1997 in conjunction with the AGARD Symposium "Advanced Non-Intrusive Instrumentation for Propulsion Engines" in Belgium. The workshop will be held at the Von Karman Institute from 17 and 18 October 1997.

A session for ACC presentations has been reserved at the AGARD Symposium "Gas Turbine Engines Combustion, Emissions, and Alternative Fuels" to be held in Lisbon, Portugal in October 1998. This will also provide an opportunity to present results of the first and second workshop to a wider audience.

To make R&D possibilities known to decision makers from industry, university, and government on a national and/or international basis, the status and the potential of active combustion control could be presented in special events. The new RTO of NATO can play a critical role in this regard. Possible arrangements of such events are under discussion.

9. References

1. McManus, K. R., Poinso, T. and Candel, S. M., "A Review of Active Control of Combustion Instabilities," *Progress in Energy and Combustion Sciences*, 1993, Vol. 19, pp. 1-29.
2. Candel, S. M., "Combustion Instabilities Coupled by Pressure Waves and Their Active Control," 24th Symposium (International) on Combustion, Sydney, July 1992.
3. Nelson, P. A. and Elliott, S. J., "Active Control of Sound," Academic Press, 1990.
4. Wang, K. W., von Flotow, A. H., Shoureshi, R., Hendricks, E. W. and Farabee, T. M., "Active Control of Vibration and Noise," ASME DE-Vol. 75, 1994.
5. Badmus, O. O., Chowdhury, S., Eveker, K. M., Nett, C. N. and Rivera, C. J., "A Simplified Approach for Control of Rotating Stall Part 1: Theoretical Development," AIAA 93-2229, 1993.
6. Epstein, A. H., Ffowcs Williams, J. E., and Greitzer, E. M., "Active Suppression of Compressor Instabilities," AIAA 86-1994, 1986.
7. Harje, D. T. and Reardon, F. H., "Liquid Propellant Rocket Combustion Instability," NASA SP-194, 1972.
8. Neumeier, Y. and Zinn, B. T., "Experimental Demonstration of Active Control of Combustion Instabilities Using Real Time Modes Observation and Secondary Fuel Injections," 26th International Symposium on Combustion, Naples, Italy, July 28, 1996.
9. Parr, T. P., Gutmark, E. J., Wilson, K. J., Yu, K., Smith, R. A., Hanson-Parr, D. M. and Schadow, K. C., "Compact Incinerator Afterburner Concept Based on Vortex Combustion," 26th International Symposium on Combustion, Naples, Italy, July 28, 1996.
10. Yu, K., Wilson, K. J., Parr, T. P. and Schadow, K. C., "Active Combustion Control Using Multiple Vortex Shedding," AIAA 96-2760, 1996.
11. Tsien, H. S., "Servo-Stabilization of Combustion in Rocket Motors," *ARS Journal*, Vol. 22, 1952, pp. 256-263.
12. Marble, F. E., and Cox, D. W. JR., "Servo-Stabilization of Low-Frequency Oscillations in a Liquid Bipropellant Rocket Motor," *ARS Journal*, Vol. 23, 1953, pp. 63-74.
13. Lee, Y. C., Gore, M. R., and Ross, C. C., "Stability and Control of Liquid Propellant Rocket Systems," *ARS Journal*, Vol. 23, 1953, pp. 75-81.
14. Ffowcs-Williams, J. E., "Anti-Sound," *Proceedings of Royal Society of London*, Vol. A395, 1984, pp. 63-88.
15. Dine, P. J., "Active Control of Flame Noises," Ph.D. Thesis, Cambridge University, Cambridge, England, 1983.
16. Heckl, M. A., "Heat Sources in Acoustic Resonators," Ph.D. Thesis, Cambridge University, Cambridge, England, 1985.
17. Heckl, M. A., "Active Control of the Noise from a Rijke Tube," *IUTAM Symposium on Aero- and Hydro-Acoustics, Lyon 1985*, Springer-Verlag, 1986, pp. 211-216.

18. Bloxsidge, G. J., Dowling, A. P., Hooper, N., and Langhorne, P. J., "Active Control of Reheat Buzz," AIAA Paper 87-0433, 1987.
19. Bloxsidge, G. J., Dowling, A. P., Hooper, N., and Langhorne, P. J., "Active Control of an Acoustically Driven Combustion Instability," *Journal of Theoretical and Applied Mechanics*, Vol. 6, 1987, pp. 161-175.
20. Lang, W., Poinot, T., and Candel, S., "Active Control of Combustion Instability," *Combustion and Flame*, Vol. 70, 1987, pp. 281-289.
21. Poinot, T., Bourienne, F., Candel, S., Esposito, E., and Lang, W., "Suppression of Combustion Instabilities by Active Control," *Journal of Propulsion and Power*, Vol. 5, No. 1, 1987, pp. 14-20.
22. Poinot, T., Veynante, D., Bourienne, F., Candel, S., Esposito, E., and Surget, J., "Initiation and Suppression of Combustion Instabilities by Active Control," *Proceedings of the 22nd Symposium (International) on Combustion*, 1988, pp. 1363-1370.
23. Langhorne, P. J., Dowling, A. P., and Hooper, N., "Practical Active Control System for Combustion Oscillations," *Journal of Propulsion and Power*, Vol. 6, No. 3, 1990, pp. 324-333.
24. Sivasegaram, S., Tsai, R. F., and Whitelaw, J. H., "Control of Combustion Oscillations by Forced Oscillation of Part of the Fuel Supply," *Combustion Science and Technology*, Vol. 105, 1995, pp. 67-83.
25. Billoud, G., Galland, M. A., Huynh, C., and Candel, S., "Adaptive Active Control of Combustion Instabilities," *Combustion Science and Technology*, Vol. 81, 1992, pp. 257-283.
26. Wilson, K. J., Gutmark, E., Schadow, K. C., and Smith, R. A., "Feedback Control of a Dump Combustor with Fuel Modulation," *Journal of Propulsion and Power*, Vol. 11, 1995, pp. 268-274.
27. Schadow, K. C., Gutmark, E., and Wilson, K. J., "Active Combustion Control in a Coaxial Dump Combustor," *Combustion Science and Technology*, Vol. 81, 1992, pp. 285-300.
28. Yang, V., Shinha, A., and Fung, Y. T., "State-Feedback Control of Longitudinal Combustion Instabilities," *Journal of Propulsion and Power*, Vol. 8, 1992, pp. 66-73.
29. Fung, Y. T., Yang, V., and Shinha, A., "Active Control of Combustion Instabilities with Distributed Actuators," *Combustion Science and Technology*, Vol. 78, 1991, pp. 217-245.
30. Menon, S., "Active Combustion Control in a Ramjet Using Large-Eddy Simulations," *Combustion Science and Technology*, Vol. 84, 1992, pp. 51-79.
31. Shyy, W., Thakur, S., and Udaykumar, H. S., "A High Accuracy Sequential Solver for Simulation and Active Control of a Longitudinal Combustion Instability," *Computing Systems in Engineering*, Vol. 4, 1993, pp. 27-41.
32. Neumeier, Y., and Zinn, B. T., *Active Control of Combustion Instabilities with Real Time Observation of Unstable Combustor Modes*, AIAA 96-0758, 1996.
33. Culick, F. E. C., *Combustion Instabilities in Liquid-Fueled Propulsion Systems*, AGARD-CP-450, Vol. 1, 1989, pp. 1-73.

34. Fung, Y. T., "Active Control of Linear and Nonlinear Pressure Oscillations in Combustion Chambers," Ph.D. Thesis, Dept. of Mechanical Engineering, Pennsylvania State University, University Park, PA, 1991.
35. Fung, T., T., and Yang, V., "Active Control of Nonlinear Pressure Oscillations in Combustion Chambers," *Journal of Propulsion & Power*, Vol. 8, 1992, pp. 1282-1289.
36. Padmanabhan, K.T., Bowman, C.T., and Powell, J.D., "An Adaptive Optimal Combustion Control Strategy," *Combustion and Flame*, Vol. 100, 1995, pp. 101-110.
37. Koshigoe, S., Komatsuzaki, T., and Yang, V., "Active Control of Combustion Instability with On-line System Identification," AIAA Paper 96-0759, 1996.
38. Cohen, J.M., and Anderson, T.J., "Experimental Investigation of Near-Blowout Instabilities in a Lean, Premixed Step Combustor," AIAA Paper 96-0819, 1996.
39. Gutmark, E., Parr, T. P., Hanson-Parr, D. M. and Schadow, K. C., "Synchronized Acoustic Excitation of Fuel and Oxidizer for Efficient Combustion," AIAA Aeroacoustics Conference, 1995.
40. Reuter, D., Hegde, U. G., Daniel, B. R. and Zinn, B. T., "Flame Driving of Longitudinal Instabilities in Dump Type Ramjet Combustors" *Combustion Science and Technology*, Vol. 55, pp. 125-138, July 1987.
41. Poinso, T. J., Trounev, A. C., Veynante, D. P., Candel, S. M. and Esposito, E. J., "Vortex-driven Acoustically Coupled Combustion Instabilities," *Journal of Fluid Mechanics*, 177, pp. 265-292, 1987.
42. Low, H. C., Wilson, C. W., Abdel-Gayed and Bradley, D., "Evaluation of Novel Igniters in a Turbulent Bomb Facility and a Turbo-Annular Gas Turbine Combustor," AIAA-89-2944, 1989.
43. Powell, E. A. and Zinn, B. T., "Nonlinear Combustion Instability in Liquid Propellant Rocket Engines," Proceedings of the 13th Symposium (International) on Combustion. The Combustion Institute, pp. 491-503, 1971.
44. Culick, F. E. C. and Yang, V., "Overview of Combustion Instabilities in Liquid-Propellant Rocket Engines," in *Liquid Rocket Engine Combustion Instability*, Progress in Astronautics and Aeronautics, Vol. 169, 1995.
45. Menon, S., "A Numerical Study of Secondary Fuel Injection Techniques for Active Control of Combustion Instability in a Ramjet," AIAA 92-0777, 1992.
46. Furlong, E. R., Baer, D. S. and Hanson, R. K., "Combustion Control and Monitoring Using a Multiplexed Diode-Laser Sensor System." AIAA 96-2763, 1996.
47. Langhorne, P. J., "Reheat Buzz: An Acoustically Coupled Combustion Instability. Part 1. Experiment," *Journal of Fluid Mechanics*, Vol. 193, pp. 417-443, 1988.
48. Brouwer, J., Ault, B. A., Bobrow, J. E. and Samuelson, G. S., "Active Control Application to a Model Gas Turbine Combustor," ASME 90-GT-326, 1990.
49. Matta, L. M., Zhu, C. and Jagoda, J. I., "Mixing by Resonant Acoustic Driving in a Closed Chamber," *Journal of Propulsion & Power*, Vol. 12, No. 2, pp. 366-370, March-April 1996.

50. Wiltse, J. M. and Glezer, A., "Manipulation of Free Shear Flows Using Piezoelectric Actuators," *Journal of Fluid Mechanics*, Vol. 249, pp. 261-285, 1993.
51. Ogata, K., *Modern Control Engineering*, 2nd Edition, Prentice-Hall Pub., 1990.
52. Gutmark, E., Parr, T.P., Hanson-Parr, D.M., and Schadow, K.C., "Active Control of a Premixed Flame", AIAA 90-2448, 1990.
53. Schadow, K.C., Gutmark, E.J., Parr, T.P., Wilson, K.J., and Yu, K., "Vortex Combustion with Synchronized Fuel Injection", presented at Twelfth International Symposium on Airbreathing Engines, September 10-15, 1995, Melbourne, Australia.
54. Yu, K., Wilson, K.J., Parr, T.P., Smith, R.A., and Schadow, K.C., "Characterization of Pulsating Spray Droplets and Their Interaction with Vortical Structures", presented at 34th Aerospace Sciences Meeting and Exhibit, January 15-18, 1996, Reno, NV.
55. Parr, T.P., Gutmark, E.J., Wilson, K.J., Hanson-Parr, D.M., K. Yu, Smith, R.A., and Schadow, K.C., "Compact Incinerator Afterburner Concept Based on Vortex Combustion", presented at Twenty-Sixth International Symposium on Combustion, July 28-August 2, 1996, Naples, Italy.
56. Yang, V., Santavicca, D.A., and Ray, A., "Intelligent Control of Gas Turbine Combustion Dynamics for Performance and Emission Improvement," Proceedings of the Ninth ONR Propulsion Meeting, 1996, pp. 286-292.
57. Knoop, P., Culick, F.E.C., and Zukoski, E.E., "Extension of the Stability of Motions in a Combustion Chamber by Nonlinear Active Control Based on Hysteresis," submitted to *Combustion Science and Technology*.
58. Sterling, James, *Combustion Science and Technology*, Vol. 89, pp. 167-179, 1993.
59. Burkhardt, H. and Strubenhoff, V., "Multispectral Vision-Guided Flame Control", presented at ECAPT '93: Karlsruhe 25-27 March 1993, Second Meeting of BRITE-EURAM Concerted Action on Process Tomography, Workshop on "Process Monitoring & Control".
60. Tao, W. and Burkhardt, H., "Application of Fuzzy Logic and Neural Networks to the Control of a Flame Process". In Proceedings of the 2nd IEEE Conference on "Intelligent Systems Engineering", Hamburg, September 1994.
61. O. Delabroy, E. Haile, D. Veynante, F. Lacas, and S. Candel (1996) *Revue Generale de Thermique*, 35, 475-489. Reduction de la production des oxydes d'azote (Nox) dans une flamme de diffusion a fioul par excitation.
62. O. Delabroy, F. Lacas, T. Poinso, S. Candel, T. Hoffmann, J. Hermann, S. Gleis, and D. Vortmeyer, "Combustion Science and Technology, Vol. 119, pp. 397-408. A study of Nox reduction by acoustic excitation in a liquid fueled burner.
63. E. Haile, O. Delabroy, F. Lacas, D. Veynante and S. Cander, "Structure of Acoustically Forced Spray Flame", 26th Symposium (International) on Combustion. The Combustion Institute, Pittsburgh, 1996.

64. E.J. Gutmark, K.C. Schadow, M.N.R. Nina, and G.P. Pita, "Suppression of Combustion Instability by Geometrical Design of the Bluff-Body Stabilizer", *Journal of Propulsion and Power*, Vol. 11, No. 3, pp. 456-463, 1995.
65. S. Gleiss, D. Vortmeyer, and W. Rau, "Experimental Investigations on the Transition from Stable to Unstable Combustion by Means of Active Instability Control," AGARD CP 479, pp. 22.1-22.7, 1990.
66. J. Hermann, S. Gleis, and D. Vortmeyer, "Active Instability Control (AIC) of Spray Combustors by Modulation of the Liquid Fuel Flow Rate," *Combustion Science and Technology*, Vol. 118, pp. 125, 1996.
67. C. Hantschk, J. Hermann, and D. Vortmeyer, "Active Instability Control with Direct Drive Servo Valves in Liquid-Fueled Combustion Systems, 26th International Symposium on Combustion, Naples, Italy, 1996.

APPENDIX A

AGARD WORKSHOP ON ACTIVE COMBUSTION CONTROL-Participants
May 6-9, 1996, Athens, Greece

FRANCE

Prof. S. Candel
Ecole Centrale de Paris
Laboratoire EM2C, UPR CNRS 288
Grande Voie des Vigner
92290 Chatenay-Malabry Cedex
France
Tel 33 1 44 13 1083
Fax 33 1 47 02 8035

Dr. P. Kuentzmann
Directeur Scientifique de L'Energetique
ONERA, BP72
92322 Chatillon Cedex
France
Tel 33 1 46 73 4300
Fax 33 1 46 73 4147

Dr. A. Laverdant
ONERA
Chemin de la Huniere
Et Des Joncherattes
F-91120 Palaiseau
France
Tel 33 1 69 93 6028
Fax 33 1 69 93 6161

Mr. C. Leboucher
SNECMA
77550 Moissy Cramayel
France
Tel 33 1 60 59 88 92
Fax 33 1 60 59 77 12

Mr. R. Deldalle
SNECMA
77550 Moissy Cramayel
France
Tel 33 1 60 59 86 44
Fax 33 1 60 59 86 76

Dr. F. Vuillot
ONERA
BP 72, F92322 Chatillon Cedex
Fort de Palaiseau
91120 Palaiseau
France
Tel 33 1 69 93 60 30
Fax 33 1 69 93 61 61

GERMANY

Dr. N. Brehm
BMW-RR, ET 3
Eschenweg 11
15872 DAHLEWITZ
Germany
Tel 49 33708 6 1433
Fax 49 33708 6 3279

Prof. W. Koschel
Institut Fur Strahlantriebe u. Turboarbeitsmaschinen
der RWTH Aachen
Templergraben 55
52062 AACHEN
Germany
Tel 49 241 80 5501
Fax 49 241 8888 228

Dr. B. Simon
MTU Motoren- und Turbinen-Union
Munchen GmbH
Dachauer Strabe 665
80995 Munchen
Germany
Tel 49 89 1489 2811
Fax 49 89 150 2621

Dr. S. Gleis
TU Munchen
Lehrstuhl B fur Thermodynamik
BotzmannstraÙe 15, D-85748
Germany
Tel 49 89 289 15776
Fax 49 89 289 15786

Prof. H. Weyer
Director, Institut fur Antriebstechnik
DLR
Postfach 90 60 58
W-5000 Koeln 90
Germany
Tel 49 2203 601 2249
Fax 49 2203 64395

Prof. H. Burkhardt
Technische Universitaet Hamburg-Harburg
Technische Informatik 1
Harburger Schloss-Str. 20
D-21071 Hamburg
Germany
Tel 49 40 7718 3025
Fax 49 40 7718 2911

GREECE

Prof. D. Papailiou
University of Patras
Mechanical Engineering Department
Energy Section
Laboratory of Applied Thermodynamics &
Statistical Mechanics
GR-28 110 Patras-Rion
Greece
Tel 30 61 997 272/991 497
Fax 30 61 997 271

ITALY

Prof. C. Bruno
Dip. Meccanica, University of Rome
Via Eudossiana 18
00184 Roma
Italy
Tel 39 6 458 5280
Fax 39 6 488 1759

Dr. Giancarlo Benelli
ENEL
Via Andrea Pisano, 120
56122 Pisa
Italy
Tel 39 50 535628
Fax 39 50 535021

PORTUGAL

Prof. M. Nina, IST
 Department of Mechanical Engineering
 Instituto Superior Tecnico
 Avenida Rovisco Pais
 1096 Lisboa Codex
 Portugal
 Tel 351 1 841 7369
 Fax 351 1 841 7365

Mr. E. Fernandes
 Instituto Superior Tecnico
 Seccao de Termodinamica Aplicada
 Pavilhao de Maquinas, 1 Andar
 Av. Rovisco Pais
 Lisboa Codex
 Tel 351 1 841 7379
 Fax 351 1 849 6156

UNITED KINGDOM

Mr. K. Garwood
 Rolls-Royce Limited
 Whittle House - WH 33
 P.O. Box 3
 Filton, Bristol BS12 7QE
 Great Britain
 Tel 44 117 979 57 99/1234
 Fax 44 117 979 0724

Dr. A. Taylor
 Department of Mechanical Engineering
 Imperial College of Science and Technology
 Exhibition Road, London SW7 2BX
 Great Britain
 Tel 44 171 594 7028
 Fax 44 171 589 3905

UNITED STATES

Prof. F. Culick
 California Institute of Technology
 Mail Stop 205--45
 Guggenheim Aeronautical Laboratory
 Pasadena, CA 91125
 Tel 1 818 395 4783
 Fax 1 818 449 2677

Prof. B. Zinn
 School of Aerospace Engineering
 Georgia Institute of Technology
 Atlanta, GA 30332
 Tel 1 404 894 3033
 Fax 1 404 894 2760

Dr. C. Jacobson
 Mail Stop 129-29
 United Technologies Research Center
 411 Silver Lane
 East Hartford, CT 06108
 Tel 1 860 610 7652
 Fax 1 860 610 7852

Dr. T. Rosfjord
 Mail Stop 129-16
 United Technologies Research Center
 411 Silver Lane
 East Hartford, CT 06108
 Tel 1 860 610 7418
 Fax 1 860 610 7669

Dr. J. Cohen
 Mail Stop 129-16
 United Technologies Research Center
 411 Silver Lane
 East Hartford, CT 06108
 Tel 1 860 610 7973
 Fax 1 860 610 7669

Dr. K. Schadow
 Code 4B3200D
 NAVAIRWARCENWPNDIV
 1 Administration Circle
 China Lake, CA 93555-6100
 Tel 1 760 939 6532
 Fax 1 760 939 6569

Prof. V. Yang
 Pennsylvania State University
 111 Research Building East
 University Park, PA 16802
 Tel 1 814 863 1502
 Fax 1 814 865 3389

Dr. G. Roy
 Office of Naval Research
 Code 333
 800 North Quincy Street
 Arlington, VA 22217-5660
 Tel 1 703 696 4406
 Fax 1 703 696 2558

Dr. G. Sturgess
 Innovative Scientific Solutions, Inc.
 3845 Woodhurst Court
 Beavercreek, OH 45430
 Tel 1 513 252-2706
 Fax 1 513 476 4652

APPENDIX B

AGARD WORKSHOP

Active Combustion Control for Propulsion Systems
May 6-9, 1996, Athens, Greece

OBJECTIVES:

1. Define Requirements for Future Combustors and Related Combustion
2. Determine Status of Active Combustion Control (ACC)
3. Discuss Potential of ACC to Meet Future Combustor Requirements
4. Determine Near- and Long Term R&D Needs for ACC
5. Publish AGARD Report
6. Explore Potential of International Collaborations
7. Establish AGARD Steering Group on ACC

WORKSHOP SUMMARY:

May 6	1030-1100	1. Introductions
	1100-1200	2. Requirements for Future Combustors and Related Combustion
	1330-1500	
	1530-1700	3. Current Status of Active Combustion Control
May 7	0830-1000	
	1030-1200	4. "Brainstorming"
	1330-1500	
	1530-1700	
May 8	0830-1000	5. Discussions
	1030-1200	
	1330-1700	Technical Tour
May 9	0830-1000	6. Wrap-up Discussions

AGENDA:

1. Introductions - 30 min.
2. Requirements for Future Combustors and Related Combustion - 2 hrs 30 min.

Session Chairmen: Weyer, GE, and Bruno, IT

- a. Gas Turbine - Sturgess, US (Enclosure (1))*
- b. Gas Turbine - Garwood, UK (Enclosure (2))
- c. Missile Propulsion (solid, liquid, airbreathing) - Kuentzmann, FR (Enclosure (3))
- d. General Comments - Culick, US (Enclosure (4)). Viewgraphs not available.)
- e. Summary - Bruno, IT (Enclosure (5))

*The information on enclosures is related to Appendix C.

3. Current Status of Active Combustion Control (Presentations and Discussions) - 3 hrs

Session Chairmen: Culick, US, and Vuillot, FR

- a. Candel, FR (Introduction, Overview) (Enclosure (6))
- b. Jacobson, US (Control Applications) (Enclosure (7))
- c. Gleis, GE (Control Applications) (Enclosure (8))
- d. Yang, US (Controller Aspect) (Enclosure (9))
- e. Zinn, US (Combustion Instabilities) (Enclosure (10))
- f. Schadow, US (Fluid Dynamic/Combustion Interactions) (Enclosure (11))
- g. Koschel, GE (Combustion Kinetics) (Enclosure (12))
- h. Yang, US (Modeling Aspect) (Enclosure (13))
- i. Taylor, UK (Control Experiments) (Enclosure (14))
- j. Nina, PO (ACC Research) (Enclosure (15))
- k. Benelli, IT (Gas Turbine Power Generation) (Enclosure (16))
- l. Burkhardt, GE (Image Sensors) (Enclosure (17))
- m. Papailiou, GR (LES) (Enclosure (18))
- n. Vuillot, FR (Summary) (Enclosure (19))

4. "Brainstorming" - 4 hrs and 30 min.

Session Chairmen: Brehm, GE, and Bruno, IT

- a. Physical Understanding/Modeling - Moderators: Candel, FR, and Taylor, UK
- b. System Integration - Rosfjord, US, and Simon, GE
- c. Controller - Yang, US, and Jacobson, US
- d. Sensor/Actuator - Gleis, GE, and Zinn, US
- e. Diagnostics/Experimental Methods - Cohen, US, and Gleis, GE
- f. Summary - Bruno, IT (Enclosure (20))

5. Discussions - 4 hrs

- a. Determine Current ACC Application Potential and Short Term R&D Needs
Rosfjord, US, and Taylor, UK
- b. Determine Long Term R&D Needs
Candel, FR

6. Wrap-up Discussions - 2 hrs

- a. Conclusions/ Recommendations - Rosfjord, US
- b. Summary Viewgraphs - Schadow, US (Enclosure (21))

APPENDIX C

**VIEWGRAPHS PRESENTED AT
AGARD WORKSHOP**

**ACTIVE COMBUSTION CONTROL FOR
PROPULSION SYSTEMS**

**6—9 MAY 1996
ATHENS, GREECE**

**FOR COPIES CONTACT:
KLAUS SCHADOW
CODE 4B3200D
NAVAL AIR WARFARE CENTER WEAPONS DIVISION
PHONE: (760) 939-6532
FAX: (760) 939-6569
E-MAIL: KLAUS_SCHADOW@IMDGW.CHINALAKE.NAVY.MIL**

REPORT DOCUMENTATION PAGE			
1. Recipient's Reference	2. Originator's Reference AGARD-R-820	3. Further Reference ISBN 92-836-1060-1	4. Security Classification of Document UNCLASSIFIED/ UNLIMITED
5. Originator Advisory Group for Aerospace Research and Development North Atlantic Treaty Organization 7 rue Ancelle, 92200 Neuilly-sur-Seine, France			
6. Title Active Combustion Control for Propulsion Systems			
7. Presented at/sponsored by A Workshop held in Athens, Greece, May 6-9 1996.			
8. Author(s)/Editor(s) Multiple			9. Date September 1997
10. Author's/Editor's Address Multiple			11. Pages 52
12. Distribution Statement There are no restrictions on the distribution of this document. Information about the availability of this and other AGARD unclassified publications is given on the back cover.			
13. Keywords/Descriptors <div style="display: flex; justify-content: space-between;"> <div> Combustion control Combustion chambers Optimization Rocket engines Ramjet engines Afterburners Aircraft engines Gas turbine engines </div> <div> Stationary engines Marine engines International cooperation Combustion stability Missile propulsion Rocket propulsion Incinerators </div> </div>			
14. Abstract <p>Active combustion control is one of the most promising approaches to further optimize the size/weight/power relationship in rockets, ramjets, afterburners, aero-engines, and marine propulsion. A workshop was organized in Athens in spring 1996 under the sponsorship of the AGARD Propulsion and Energetics Panel. It covered the existing knowledge, and further possible strategies for military equipment were discussed within the NATO nations. Further activities are planned.</p>			

3.1.3.5 Pulse Detonation Engines. Pulse Detonation Engines (PDEs) have potential for high thrust, low weight, low cost, high scalability, and a wide operating range. Thus, a research effort was initiated to investigate PDEs using a kerosene-based fuel. The paper entitled "AFRL In-house Pulse Detonation Engine Research Program" (see pp. 624-633) presents an overview of this research-and-development program. A companion paper entitled "Development of a Research Pulse Detonation Engine" (see pp. 634-643) summarizes the results of a computational and experimental program to investigate air-breathing PDE systems.

AFRL In-house Pulse Detonation Engine Research Program*

F.R. Schauer, J.S. Stutrud, and R.A. Anthenien
*Air Force Research Laboratory, Propulsion Directorate
Wright-Patterson AFB, OH 45433*

R.P. Bradley, L.P. Chin, and V.R. Katta
*Innovative Scientific Solutions, Inc.
Dayton, OH 45440*

An in-house computational and experimental program to investigate and develop an air breathing pulse detonation engine (PDE) that uses a practical fuel (kerosene based) is currently underway at the Combustion Branch of Propulsion Sciences and Advanced Concepts Division of the Air Force Research Laboratory (AFRL/PRSC). PDE's have the potential of high thrust, low weight, low cost, high scalability, and wide operating range; however several technological hurdles must be overcome before a practical engine can be designed. This research effort involves investigating such critical issues as: detonation initiation and propagation; valving, timing and control; instrumentation and diagnostics; purging, heat transfer, and repetition rate; noise and multi-tube effects; detonation and deflagration to detonation transition modeling; and performance prediction and analysis. An innovative, four-detonation-tube engine design is currently undergoing testing and evaluation. Preliminary data are obtained with premixed hydrogen/air as the fuel/oxidizer to demonstrate proof of concept and verify model predictions while avoiding the detonation initiation problems associated with more complex hydrocarbon fuels. Unique modeling of detonation propagation from a small channel to a larger channel (i.e. the predetonator concept) provides insight into the mechanisms responsible for transition from deflagration to detonation. Experimentally, new initiation methods are examined, and multi-tube effects are studied. This paper presents an overview of the AFRL/PRSC PDE development research program as well as a summary of the work performed to date.

Introduction

Recent renewed interest in pulsed detonation propulsion concepts has prompted a concerted effort being made by the U.S. Air Force (AFRL), U.S. Navy (NRL, ONR, and the Naval Post Graduate School), NASA, and several research contractors (Adroit Systems Inc., Advanced Projects Research, Inc., Pennsylvania State University, Enigmatics, and major engine manufacturers), to develop a low-cost, practical-fueled, pulse detonation

engine. Conceptually, pulse detonation engines (PDE) offer few moving parts, high efficiency, high thrust, low weight, low cost, and ease and of scaling are an attractive alternative to jet turbine engines for small disposable engines. A cartoon that illustrates the simplicity of the PDE cycle is provided in figure 1 below. The near constant volume heat addition process, along with the lack of a compression cycle lend to the high efficiency and specific impulse, simplicity, and low-cost

* Approved for public release; distribution is unlimited

of pulse detonation engines. Pulse detonation engines have the potential for operation at speeds ranging from static to hypersonic, with competitive efficiencies enabling supersonic

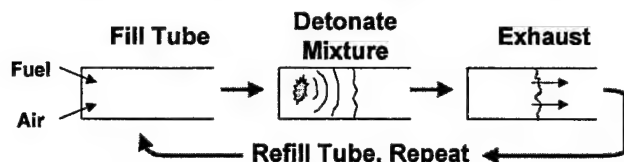


Figure 1. Conceptual pulsed detonation engine cycle.

operation beyond conventional gas turbine engine technology. Currently, no single cycle engine exists which has such a broad range of operability.

Pulsed detonation propulsion research has been funded by AFRL since the early 1990's, but most of the efforts have been performed out-of-house by contractors. In 1997, an AFRL/PRSC (the Combustion Branch of the Propulsion Sciences and Advanced Concepts Division, Propulsion Directorate at Wright-Patterson AFB, OH) in-house PDE research and development program was created. Our principal interests lie in the air-breathing arena; a similar pulsed detonation rocket engine (PDRE) program is conducted at our sister branch, AFRL/PRSA, at Edwards Air Force Base.

The in-house PDE program was established in order to make AFRL's unique resources available for the development of this technology. Traditionally, we have used our advanced computational modeling, diagnostic measurement techniques, and test facilities to work with government agencies and their contractor's on the development of advanced combustor concepts. As such, much of our work was focused on deflagration phenomena while trying to avoid detonations. In order to work with pulsed detonation phenomena, we have set out to develop the necessary facilities, diagnostics, modeling tools, and experience so that we can contribute and provide our unique resources for the maturation of pulse detonation technology.

The second motivation of the in-house program was to produce publishable PDE data. Currently, there is a great deal of dissension on PDE performance within the community ^[1]. Detonation physics and detonation engine blow-down are highly sensitive to initial conditions, boundary conditions, and multi-dimensional geometry effects. Most of the available data and models are proprietary and not shared across the community, making it difficult to assess the current status of PDE performance and capability. As part of AFRL's research, an in-house research PDE has been developed to provide publishable data from which codes and performance predictions can be anchored and/or benchmarked.

For the Air Force, a practical-fueled PDE means JP-air detonation. This requirement poses creates several technological hurdles which much be overcome in order to field such a PDE. Complex hydrocarbon fuels, and particularly liquid hydrocarbons, are difficult to detonate in air, typically requiring hundreds of kilo-joules to directly initiate a detonation ^[2]. For this reason, a practically fueled becomes a deflagration to detonation transition (DDT) minimization process since the fuel burned during detonation initiation does not produce thrust efficiently while it is burning at low pressures.

Furthermore, since thrust is generated with each detonation cycle of a PDE, it would be beneficial to raise the operating frequency in order to produce more thrust. Higher operating frequencies also have benefits from an unsteady inlet, nozzle, and noise generation perspective, but create complications in other areas including: valving, mixing, shortened residence time requirements, and increased heat loads.

In cooperation with other government organizations performing PDE research and as the developer of one of two government in-house PDE research engines, AFRL/PRSC

has attempted to establish a niche for itself in tackling the above issues. The ONR funded research engine at the Naval Post Graduate School in Monterey, California is directed towards liquid fuel injection, atomization, and mixing^[3] and AFRL's engine research is focused on detonation initiation and repetition. While there is crossover in the two programs, we are confident that if we can develop a premixed vapor fueled/air PDE, the Navy funded program will make it work on liquid fuels.

Approach

PRSC's unique resources^[4] have been used to develop three areas in which AFRL can contribute in-house to the development of PDE technology. In broad terms, these areas are: modeling, facilities and instrumentation, and research hardware development and testing. These three areas, and their applications to PDE research, are explained below.

Modeling

As discussed in the introduction, perhaps the biggest technological challenge for practical-fueled PDE is detonation initiation, which requires a DDT process for JP/air mixtures. An explicit 2nd-order MacCormack predictor-corrector technique with 4th-order FCT (Flux Corrected Transport) and two-step finite-rate chemistry has been used to study the extremely complex deflagration to detonation transition processes^[5]. The code is capable of reproducing the complex multi-dimensional detonation cellular structure as shown in the peak pressure traces of figure 2.



Figure 2. PDE model – peak pressure or 'smoke foil' with particle traces in a channel. Detonation propagation is from right to left.

In order to reduce the DDT time and volume to maintain the efficiency of a near-

constant volume combustion process, the detonation initiation section of a practical PDE must be optimized. Generally, a small-channel predetonator section is employed as the transition to detonation occurs more rapidly in a confined space. Largely through trial and error, an appropriate predetonator section is optimized. It is quickly apparent how a code capable of modeling DDT could be used to predict the effects of confinement, turbulence and mixing, obstructions, shock reflections, and other phenomena which impact the detonation initiation process. Unfortunately, thousands of detonation experiments can be done in the time it takes to accurately model a single detonation event. However, the only information available from the experiments is normally a pressure trace and, at best, high speed Schlieren images. This data usually only indicates if a given detonation phenomena did or did not occur, and can not explain why. Modeling can show the mechanisms of success and/or failure for detonation phenomena.

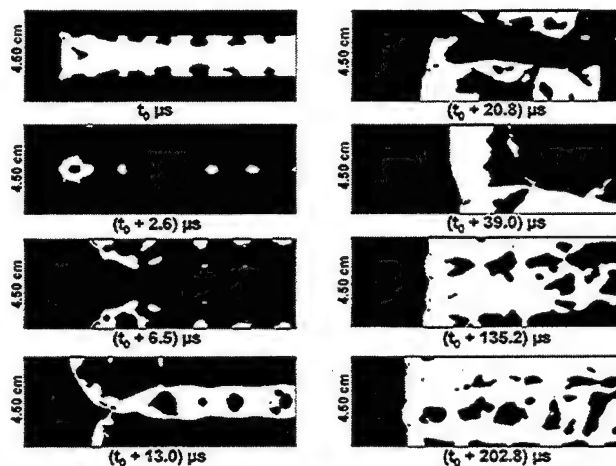


Figure 3. PDE model – detonation propagation from ~1" (22.5 mm) channel to ~2" (45.0 mm) channel. Direction of detonation propagation is from right to left and frame of reference is moving with combustion front.

The results from the code as shown in figure 2 can predict the detonation cell size that may be detected experimentally with smoke foil traces on the inside of a detonation tube. Results like these are instrumental in

helping with the design of predetonator and pulsed detonation components as the interaction of hardware geometry and propagating deflagrations/detonations can be observed.

Once a detonation is initiated in a small predetonator sections, it becomes a challenge to propagate that detonation to the main detonation tube section. A larger diameter tube is desirable from the standpoint of increased thrust per frontal area. However, propagation of a small tube detonation to a bigger tube will quench if the small tube is smaller than a critical diameter. Because this critical diameter is on the order of 10 cell widths, a small tube predetonator would have to be roughly a foot (300 mm) in diameter in order to successfully transition a detonation to a bigger tube. Hardware is being developed today in violation of this rule of thumb but the mechanism explaining successful propagation was previously unknown.

Using a model of a small channel to big channel transition, we were able to demonstrate the mechanism. Figure 3 shows frames with pressure isobars of the process of detonation propagation from a channel one cell-width to double that width. The detonation is propagating from left to right and the frame of reference is moving at the combustion wave front speed. In the upper left frame, a stable detonation is suddenly allowed to expand from the single cell-width channel. From this model, it is clear in the next frame that although the detonation does quench, the remnants of transverse waves in the detonation cellular structure reflect off the side walls in the third frame, creating high pressure/temperature hot spots. These hot spots, created by the reflecting transverse shock waves, accelerate the chemistry, and the enhanced heat release grows in magnitude yet again when the sidewall reflections meet in the middle of the channel. These colliding shock waves are then seen to coalesce, bouncing from sidewall to sidewall, growing in strength of heat release

as the pressure/temperature hot spots grow in magnitude until a stable cellular structure is re-established.

The mechanism of transverse wave reflections that is so evident in the models would be extremely difficult to detect experimentally. The detonation did quench, but the reflecting transverse waves re-initiated the detonation so quickly that the combustion process remains nearly constant volume and for all practical purposes, the detonation did successfully make the transition.

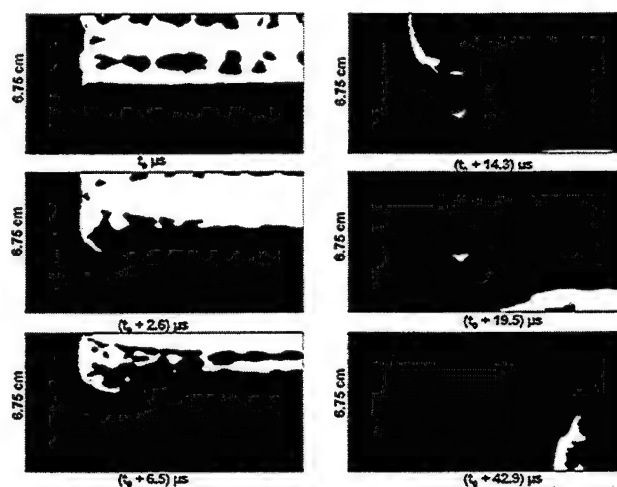


Figure 4. PDE model - detonation propagation and quenching from ~1.5" (36 mm) channel to ~2.6" (67.5 mm) channel. Direction of detonation propagation is from right to left and frame of reference is moving with combustion front.

In other cases, such as the one illustrated in figure 4, the detonation does not successfully propagate across the sudden expansion. In the case depicted in figure 4, the detonation is propagating down a 1 and 1/2 cell width channel and transitions to a deflagration during the sudden expansion to a channel that would have been 3 cell widths. In a recent series of detonation transition experiment, months of experimental testing were performed in order to isolate a failure to a .05" (1mm) change in geometry. The insights gained from the models illustrated herein explain the mechanism that produced the dramatic change in results from a seemingly insignificant change in geometry.

Pulsed Combustor/Detonation Engine Research Facility (D-Bay)

D-Bay is a formerly mothballed, full-scale, sea-level/static engine test facility that has been converted to perform both full-scale and component testing of pulsed combustors and/or detonation engines. The facility is explosion proof and can measure up to 60,000 pounds (268 kN) of static thrust. A damped thrust stand of 10 to 1,000+ lbf (45-4500+ N) average thrust capacity now sits on the static thrust stand for pulsed detonation engine testing.

Up to 6 lbm/sec (3 kg/sec) of 100 psi (680 kPa) air is available and high-capacity inlet and exhaust stacks are useful for self-aspirating designs and atmospheric exhaust. A direct connection to a liquid fuel farm via a high-pressure/high-capacity fuel pump retains the facilities ability to feed large-scale 60,000 lbf thrust engines. The facility test stand, damped thrust stand, with an installed research PDE are shown in figure 5. The damped thrust stand itself sits upon the large capacity static thrust stand and the roll-up door to the exhaust tunnel is visible on the right.

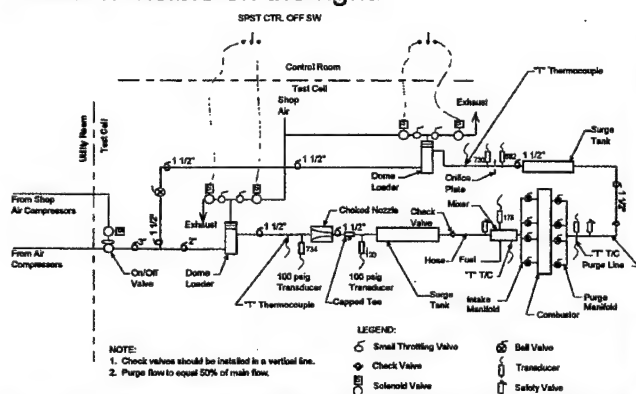


Figure 6. Pulsed combustor/detonation engine main combustion air and purge air systems; fuel system is similar.

Critical flow nozzles are used to obtain choked-flow measurements of air, purge air, and vapor fuels. These measurements are then available for accurate determination of the air/fuel ratio and flow rates going into a pulsed engine. These choke points isolate the

measurements from the downstream pressure oscillations of pulsed valves. Without such a scheme, accurate determination of the fuel/air ratio in pulsed engines has been largely a matter speculation. The air system is shown schematically in figure 6; note the independent control of main combustion air and purge air systems. The vapor fuel system has a similar scheme. Each system contains a pressure controller, a choked orifice plate or critical flow nozzle, and a surge tank to set and hold a required flow rate even with unsteady combustor valve flows. As long as the flow is choked, flow rate can be varied by changing the pressure and choked area. The depicted intake and purge manifolds allow for selection of from 1 to 4 detonation tubes.

A hardened remote-control room is adjacent to the 750,000+ ft³ test cell. A minimum of 2 feet of reinforced concrete is situated between the test cell and personnel during testing. Such precautions are necessary when dealing with the extremely hazardous noise levels associated with PDE operation. Control of all pulsed combustor/detonation engine operations and data acquisition is done via a LabVIEW based interface with duplicate manual emergency shutdown and safety system controls.

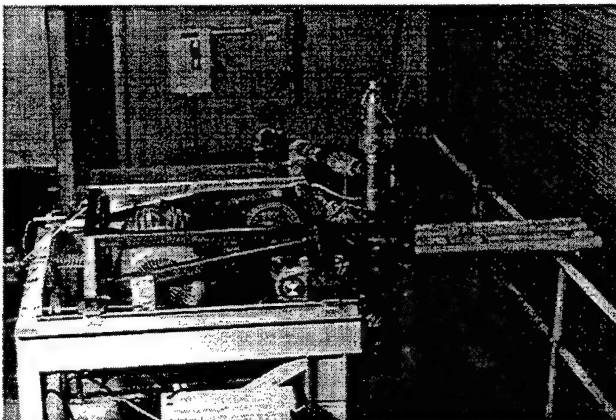


Figure 5. Pulsed combustor/detonation engine test stand, damped thrust stand, with installed research PDE.

In addition to conventional (low or kHz frequency) data acquisition and control systems which include intake, fuel, and purge system instrumentation, the facility is equipped

with up to 16 channels of high-frequency data acquisition at up to 5MHz. These may be used for high-frequency pressure transducers, thermocouples, photodiodes, or advanced laser diagnostics. A 1Mhz framing rate digital camera is also available for advanced laser diagnostics and imaging techniques^[6]. High frequency pressure transducers and photodiodes are currently installed with plans for digital Schlieren experiments to begin in the late fall of 1999.

Due to the nature of this facility, testing is not limited to small-scale PDE experiments. Conventional full-scale turbine engine tests are possible making hybrid turbo-PDE's a future research possibility in this facility. It is envisioned that several smaller scale (<1,000 pound thrust) experiments could take place across the test deck or a single large-scale (10,000+ pound thrust) engine test could be performed. As with most of PRSC's test facilities, easy swap-out of test hardware is expected and accounted for in the initial test-facility design.

Research Engine

Due to the critical timing issues in pulsed detonation engine operations, the high frequency valving tends to be both expensive and highly constrained. During the design of a research PDE, many options were considered that were either too expensive, had severe limitations in operating range, or both. The final design was based upon an extremely cheap, mass-produced valve system that was acquired from a salvage yard. It is based upon a General Motors Quad 4, DOHC cylinder head, as commonly found in the Pontiac Grand Am.

The operating conditions of PDE's are very similar to internal combustion engines and many of the components can be shared. By driving the overhead cams with an electric motor, the four valves in each of the four cylinders can be made to operate at between 0.5 and 50 Hz, with minor modifications

required to get the frequency limit up to 100 Hz. Provisions for lubrication, cooling, ignition, and fuel delivery are integral to the cylinder head/intake manifold assembly. The electric valve-train drive motor, which is grossly oversized but a scrounged component, is clearly visible on the left side of the frame in figure 5, along with the valve train drive parts.

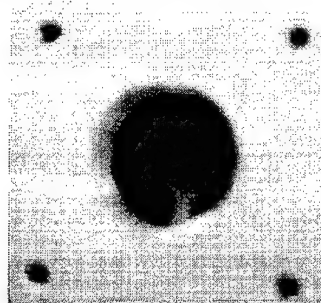


Figure 7. Research 'Quad 4' PDE detonation tube adapter plate with visible intake (upper) valve pair, purge air (lower) valve pair, and conventional spark igniter.

The two intake valves in each cylinder are used to feed premixed air and fuel into detonation tubes, which are attached to an adapter plate secured by the head bolts, visible in figure 7. In the current configuration, the head and detonation tubes are installed horizontally, and the intake valves are the upper pair. The exhaust valves are flowed in reverse with cold air used as a purge cycle to buffer hot products from igniting the next incoming charge and to convectively cool the inside of the detonation tube walls. The extra exhaust valve or valves in this four-valve-per-cylinder design could also be used for an axial predetonator or additional combustion air if necessary.

Somewhat uniquely, this PDE is operated premixed, minimizing mixing and stratification issues. The large pop-off valves and check valves visible in figure 5 are some of the precautions used to catastrophic failure in the event of an engine backfire through the premixed intake section. Up to four detonation tubes can be run at 90 degrees out of phase, with various diameters ranging up to ~3.5 inches (85mm). The main combustion air and purge air contain ball valves for each

detonation tube feed system so that the engine can be run with one tube, two tubes 180 degrees out of phase, or all four tubes. A rotary position sensor is adapted to the intake camshaft to provide both an index and relative position of the valve timing sequence. This signal serves as the master timing signal for the ignition and data acquisition systems.

Triggered off the rotary position sensor is an eight-channel igniter/fuel injection control box. Separate control of each detonation tubes igniter and/or fuel injector may be accomplished with this system, although currently vapor fuels are premixed with the combustion air via a separate critical flow nozzle and flow control system. Do to the hazardous noise levels associated with PDE testing, all controls and data acquisition are performed remotely from an isolated control room. All of the control systems and data acquisition systems are LabVIEW based and integrated into one 'virtual instrument' with back-up manual shut down and safety systems. This virtual control panel is extremely flexible and can control all aspects of the PDE's operation including: lubrication, operating valve drive motor control, fuel flow,

timing, ignition delays, and automatic shutdown in the event of a critical system failure. By changing the position of a few manual ball valves and pushing a few switches in the virtual control system, the engine configuration can be switched from one tube operating to four tubes in a matter of minutes.

Each of the four PDE tubes can operate from 0.5 to 100 Hz for an aggregate maximum frequency of 400 Hz. Petters predicted the inlet-neglected thrust of this configuration and the results are shown in figure 8 for four different engine configurations, including: single 2" (50 mm) diameter by 3' (900 mm) tube, single 3.5" (90 mm) diameter by 3' (910 mm) tube, and four tubes of each of the previous configurations^[7]. As is evident from the graph, significant thrust is developed even at these relatively low frequencies, further demonstrating the low thrust/cost ratio of this technology.

The engine is to be used for performance prediction validations and serve as a test-bed for research of: detonation initiation and DDT minimization, heat transfer, noise levels, pulsed ejector concepts, and multi-tube interactions. Initial testing and proof-of-concept is being done with hydrogen as the fuel due to the increased detonability versus practical liquid hydrocarbon fuels. A vapor propane fuel system has also been constructed in order to work with a complex-hydrocarbon that detonates much like kerosene based JP type fuels. This will eliminate the atomization and mixing of liquid fuel complications that increase the difficulty of practical PDE design and allow us to focus on detonation initiation and high frequency operation. As mentioned previously, ONR funded research is tackling the difficult problems of liquid fuel atomization and mixing for PDE applications^[3,8].

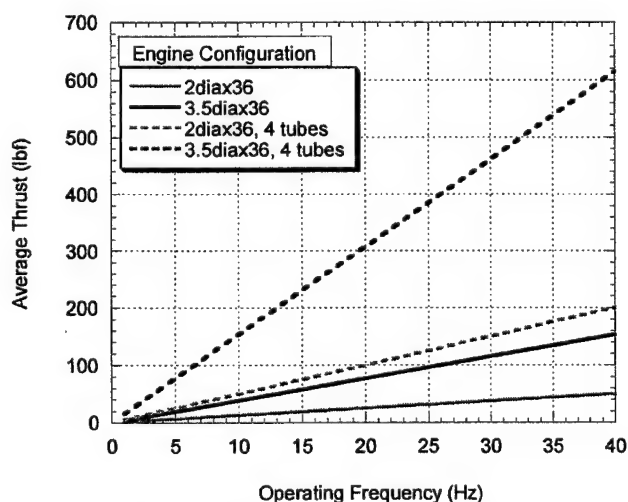


Figure 8. Research 'Quad 4' PDE detonation tube predicted thrust (inlet neglected) versus frequency for four different detonation tube configurations.

main combustion air flow, purge air flow,

Results and Discussion

Although this program was initiated two years ago and the test facility was an

abandoned, empty cell 9 months ago, we have successfully designed, built, and tested both the facility and the experimental research engine since that time. As described above, the modeling effort is already producing results and being published elsewhere^[5].

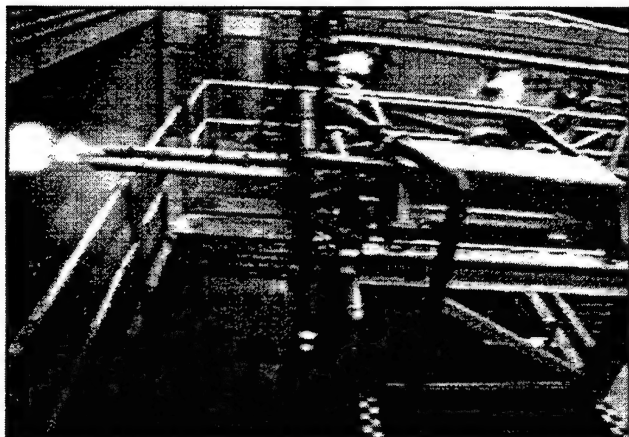


Figure 9. In-house research 'Quad-4' PDE, success on first attempt, 9 September, 1999: 91 second operation at 8Hz, single 2" diameter by 3' long tube, stoichiometric H₂/air, conventional ignition.

Cold flow testing of the systems began in early 1999, with the first hot firing on 9 September. This initial test was done at low fuel flow conditions to minimize the amount of hydrogen in the test cell in event of a failure. The first test was done with fully instrumented intake and purge systems, detonation tube surface temperature thermocouples, four high frequency pressure transducers along the length of the tube, damped thrust, and two black & white video cameras. An image extracted from one of the video cameras is shown in figure 9.

The initial testing produced very good qualitative results, with four runs of up to 91 seconds duration. These runs, which were un-cooled, were cut short because the tube surface thermocouples were epoxy mounted which began to melt. The thermocouples have since been re-affixed more robustly. The sharp 'CRACK' sound and flash of the exhaust were qualitative indicators of detonations which contrasted with the softer 'wumpff' sound and flame visible out the back when the

engine deflagrated due to off-stoichiometry conditions.

The high-frequency pressure transducers had not been tested until these initial hot-firings and did not produce publishable results. This is most likely due to gain settings and the in-ability of the data acquisition computer to keep up with the high data-streaming rate. A dual-processor PIII 600 MHz machine has been custom built to handle this task for future testing. The operating condition should have produced 10 pounds (45 N) of thrust, but the thrust stand was fully damped during these initial test runs. With damping, the static friction of the thrust stand has been measured at 20 lbf (90 N), which explains why no thrust was measured on the first runs. The dampers had been left on because it was not certain how long the engine would run and we wished to acquire a thrust measurement during the first 5 seconds of operation. Since the engine has demonstrated that it can run for much longer durations, the dampers will be removed for future tests with predicted thrust levels below 20 lbf (90 N).

Further testing results from this engine were not available at the time of this papers submission; they will be presented during the JANNAF meeting. Work in progress includes: higher frequency operation, multi-tube operation, alternative igniter schemes to minimize the DDT distance, additional high frequency instrumentation including thermocouples and more pressure transducers, and high frequency digital Schlieren visualization to evaluate the viscous boundary layer effects at the tube exit. Work on many of these areas has already begun and is documented elsewhere^[9].

Summary and Conclusions

Pulse detonation engines are an extremely promising alternative to small, disposable-jet turbine engines. The Air Force Research Laboratory has supported PDE

research for some time now, and an in-house program established by the Combustion Branch of the Propulsion Sciences and Advanced Concepts Division at Wright-Patterson AFB has been established to produce sharable benchmark performance data. In addition, the in-house program has been used to harness AFRL's unique resources in order to contribute to the development of pulsed detonation propulsion technology in the form of modeling, facility, and research components.

It is hoped that the contributions of our deflagration to detonation transition modeling can be used as a tool in the development and design of a practical-fueled detonation initiator. The pulsed combustor/detonation engine test facility has been developed as a cost-effective test resource that meets many of the unique needs required for PDE testing. The remote controls and high frequency data-acquisition systems have been assembled to provide test support for researchers working in collaboration with AFRL. The facility can handle everything from bench scale experiments from academia to full-scale hybrid engine concepts from engine manufacturers. Moreover, it is hoped that researchers will take advantage of this national resource.

A research PDE was successfully designed, built, and operated under the in-house program using an innovative valve system based upon a 16 valve Quad-4, four cylinder automobile engine from General Motors. The resulting engine is capable of a broad range of frequencies and configurations with up to four detonation tubes. Data from the engine will be published with the intent of providing non-proprietary PDE data against which performance codes and predictions can be benchmarked. The 'Quad-4' PDE serves as a research tool and test-bed for detonation initiation concepts, high frequency operation, heat transfer studies, multi-tube detonation engine operation, and pulsed ejector research. The engine, which was operated successfully

for the first time in the early fall of 1999, demonstrates the affordability and ease of scalability of PDE technology.

There is much work to be done in developing valving, detonation initiators, noise suppression techniques, thermal protection systems, intake and exhaust nozzles, and control systems before a JP/air fueled PDE becomes practical. AFRL/PRSC would like to invite the community to consider our resources for further PDE research. With high quality modeling, research facilities, and an in-house PDE engine, we can work with other organizations and contractors, as we have in the past with turbine engine technology, to mature and transition PDE technology to the field. to contribute to make practical

Acknowledgements

Special appreciation must be expressed to the technicians and support personnel, both in-house government employees and on-site contractors who made this work possible, particularly Dwight Fox (ISSI) who helped build much of the research PDE engine. We also wish to acknowledge the technical leadership of Dr. Mel Roquemore (AFRL/PRSC). Thanks go out to Dr. Dave Netzer and Dr. Chris Brophy of the Naval Postgraduate School for their shared experience and use of their facilities and hardware. Gratitude also goes to: Pennsylvania State University, ASI, APRI, Enigmatics, and the major automobile and airplane manufacturers for their contributions and continuing assistance.

References

1. K. Kailasanath, G. Patnaik, and C. Li, "Computational Studies of Pulse Detonation Engines: A Status Report," AIAA 99-2634 (1999).

2. J.E. Elsworth, P.J. Shuff, and A. Ungut. "Galloping' Gas Detonations in the Spherical Mode," in *Prog. Astronaut. Aeronaut.*, volume 94, pages 130-150, 1984.
3. Christopher Brophy, David Netzer, and Dave Forster, "Detonation Studies of JP-10 with Oxygen and Air for Pulse Detonation Engine Development," *AIAA 98-4003* (1998).
4. R.D. Hancock, J.R. Gord, D.T. Shouse, F.R. Schauer, V.M. Belovich, and W.M. Roquemore, "AFRL Combustion Branch (PRSC) Aeropropulsion Research and Development Activities," *Proceedings of the International Test and Evaluation Association (ITEA) Conference* (1999).
5. V.R. Katta, L.P. Chin, and F.R. Schauer, "Numerical Studies on Cellular Detonation Wave Subjected to Sudden Expansion," *Proceedings of the 17th International Colloquium on the Dynamics of Explosions and Reactive Systems*. Heidelberg, Germany (1999).
6. James R. Gord, Charles Tyler, Keith D. Grinstead, Jr., Gregory J. Fiechtner, Michael J. Cochran, and John R. Frus, "Imaging Strategies for the Study of Gas Turbine Spark Ignition," Presented at the SPIE's 44th Annual Meeting & Exhibition, Conference 3783 on Optical Diagnostics for Fluids/Heat/Combustion and Photomechanics of Solids, Denver CO, 23 Jul 99.
7. Dean Petters, Personal Communication, AFRL/PRST at Wright-Patterson AFB, OH (1999).
8. Gabriel D. Roy, "Pulsed Detonation Phenomena for Air Breathing Propulsion," *ISABE 99-7127* (1999).
9. R. A. Anthenien, F.R. Schauer, J.S. Stutrud, C.W. Frayne, R.P. Bradley, L.P. Chin, and V.R. Katta, "Development of a Pulse Detonation Research Engine," *Proceedings of First Joint Meeting of the U.S. Sections of the Combustion Institute*, Washington DC, 1999.

DEVELOPMENT OF A RESEARCH PULSE DETONATION ENGINE*

F.R. Schauer, J.S. Stutrud, and R.A. Anthenien
Air Force Research Laboratory, Propulsion Directorate
Wright-Patterson AFB, OH 45433

R.P. Bradley, L.P. Chin, and V.R. Katta
Innovative Scientific Solutions, Inc.
Dayton, OH 45440

ABSTRACT

An in-house computational and experimental program to investigate and develop an air breathing pulse detonation engine (PDE) that uses a practical fuel (kerosene based) is currently underway at the Combustion Branch of Propulsion Sciences and Advanced Concepts Division of the Air Force Research Laboratory (AFRL/PRSC). PDE's have the potential of high thrust, low weight, low cost, high scalability, and wide operating range; however several technological hurdles must be overcome before a practical engine can be designed. This research effort involves investigating such critical issues as: detonation initiation and propagation; valving, timing and control; instrumentation and diagnostics; purging, heat transfer, and repetition rate; noise and multi-tube effects; detonation and deflagration to detonation transition modeling; and performance prediction and analysis. An innovative, four-detonation-tube engine design is currently undergoing testing and evaluation. Preliminary data are obtained with premixed hydrogen/air as the fuel/oxidizer to demonstrate proof of concept and verify model predictions while avoiding the detonation initiation problems associated with more complex hydrocarbon fuels. Unique modeling of detonation propagation from a small channel to a larger channel (i.e. the predetonator concept) provides insight into the mechanisms responsible for transition from deflagration to detonation. Experimentally, new initiation methods are examined, and multi-tube effects are studied. This paper presents an overview of the AFRL/PRSC PDE development research program as well as a summary of the work performed to date.

INTRODUCTION

Recent renewed interest in pulsed detonation propulsion concepts has prompted a concerted effort being made by the U.S. Air Force (AFRL), U.S. Navy (NRL, ONR, and the Naval Post Graduate School), NASA, and several research contractors (Adroit Systems Inc., Advanced Projects Research, Inc., Pennsylvania State University, Enigmatics, and major engine manufacturers), to develop a low-cost, practical-fueled, pulse detonation engine. Conceptually, pulse detonation engines (PDE) offer few moving parts, high efficiency, high thrust, low weight, low cost, and ease of scaling are an attractive alternative to jet turbine engines for small disposable engines. A cartoon that illustrates the simplicity of the PDE cycle is provided in figure 1 below. The near constant volume heat addition process, along with the lack of a compression cycle lend to the high efficiency and specific impulse, simplicity, and low-cost of pulse detonation engines. Pulse detonation engines have the potential for operation at speeds ranging from static to hypersonic, with competitive efficiencies enabling supersonic operation beyond conventional gas turbine engine technology. Currently, no single cycle engine exists which has such a broad range of operability.

Pulsed detonation propulsion research has been funded by AFRL since the early 1990's, but most of the efforts have been performed out-of-house by contractors. In 1997, an AFRL/PRSC (the Combustion Branch of the Propulsion Sciences and Advanced Concepts Division, Propulsion Directorate at Wright-Patterson AFB, OH) in-house PDE research and development program was created. Our principal interests lie in the air-breathing arena; a similar pulsed detonation rocket engine (PDRE) program is conducted at our sister branch, AFRL/PRSA, at Edwards Air Force Base.

* Approved for public release, distribution is unlimited.

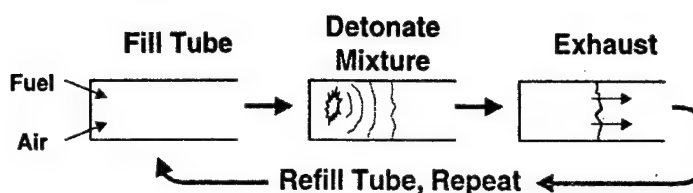


Figure 1. Conceptual pulsed detonation engine cycle.

The in-house PDE program was established in order to make AFRL's unique resources available for the development of this technology. Traditionally, we have used our advanced computational modeling, diagnostic measurement techniques, and test facilities to work with government agencies and their

contractor's on the development of advanced combustor concepts. As such, much of our work was focused on deflagration phenomena while trying to avoid detonations. In order to work with pulsed detonation phenomena, we have set out to develop the necessary facilities, diagnostics, modeling tools, and experience so that we can contribute and provide our unique resources for the maturation of pulse detonation technology.

The second motivation of the in-house program was to produce publishable PDE data. Currently, there is a great deal of dissension on PDE performance within the community^[1]. Detonation physics and detonation engine blow-down are highly sensitive to initial conditions, boundary conditions, and multi-dimensional geometry effects. Most of the available data and models are proprietary and not shared across the community, making it difficult to assess the current status of PDE performance and capability. As part of AFRL's research, an in-house research PDE has been developed to provide publishable data from which codes and performance predictions can be anchored and/or benchmarked.

For the Air Force, a practical-fueled PDE means JP-air detonation. This requirement poses creates several technological hurdles which much be overcome in order to field such a PDE. Complex hydrocarbon fuels, and particularly liquid hydrocarbons, are difficult to detonate in air, typically requiring hundreds of kilo-joules to directly initiate a detonation^[2]. For this reason, a practically fueled becomes a deflagration to detonation transition (DDT) minimization process since the fuel burned during detonation initiation does not produce thrust efficiently while it is burning at low pressures.

Furthermore, since thrust is generated with each detonation cycle of a PDE, it would be beneficial to raise the operating frequency in order to produce more thrust. Higher operating frequencies also have benefits from an unsteady inlet, nozzle, and noise generation perspective, but create complications in other areas including: valving, mixing, shortened residence time requirements, and increased heat loads.

In cooperation with other government organizations performing PDE research and as the developer of one of two government in-house PDE research engines, AFRL/PRSC has attempted to establish a niche for itself in tackling the above issues. The ONR funded research engine at the Naval Post Graduate School in Monterey, California is directed towards liquid fuel injection, atomization, and mixing^[3] and AFRL's engine research is focused on detonation initiation and repetition. While there is crossover in the two programs, we are confident that if we can develop a premixed vapor fueled/air PDE, the Navy funded program will make it work on liquid fuels.

APPROACH

PRSC's unique resources^[4] have been used to develop three areas in which AFRL can contribute in-house to the development of PDE technology. In broad terms, these areas are: modeling, facilities and instrumentation, and research hardware development and testing. These three areas, and their applications to PDE research, are explained below.

Modeling

As discussed in the introduction, perhaps the biggest technological challenge for practical-fueled PDE is detonation initiation, which requires a DDT process for JP/air mixtures. An explicit 2nd-order MacCormack predictor-corrector technique with 4th-order FCT (Flux Corrected Transport) and two-step finite-rate chemistry has been used to study the extremely complex deflagration to detonation transition

processes^[5]. The code is capable of reproducing the complex multi-dimensional detonation cellular structure as shown in the peak pressure traces of figure 2.

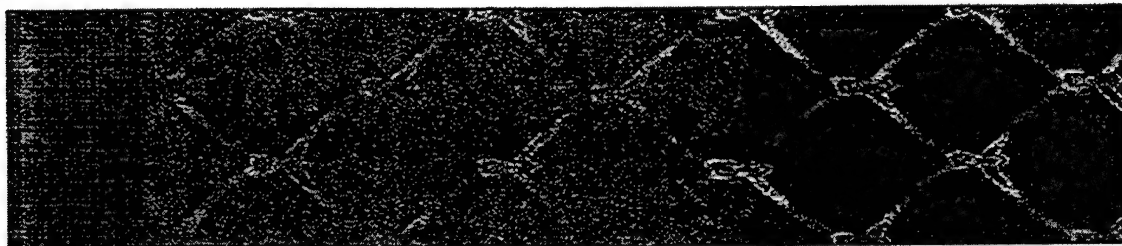


Figure 2. PDE model - peak pressure or 'smoke foil' with particle traces in a channel. Detonation propagation is from right to left.

In order to reduce the DDT time and volume to maintain the efficiency of a near-constant volume combustion process, the detonation initiation section of a practical PDE must be optimized. Generally, a small-channel predetonator section is employed as the transition to detonation occurs more rapidly in a confined space. Largely through trial and error, an appropriate predetonator section is optimized. It is quickly apparent how a code capable of modeling DDT could be used to predict the effects of confinement, turbulence and mixing, obstructions, shock reflections, and other phenomena which impact the detonation initiation process. Unfortunately, thousands of detonation experiments can be done in the time it takes to accurately model a single detonation event. However, the only information available from the experiments is normally a pressure trace and, at best, high speed Schlieren images. This data usually only indicates if a given detonation phenomena did or did not occur, and can not explain why. Modeling can show the mechanisms of success and/or failure for detonation phenomena.

The results from the code as shown in figure 2 can predict the detonation cell size that may be detected experimentally with smoke foil traces on the inside of a detonation tube. Results like these are instrumental in helping with the design of predetonator and pulsed detonation components as the interaction of hardware geometry and propagating deflagrations/detonations can be observed.

Once a detonation is initiated in a small predetonator sections, it becomes a challenge to propagate that detonation to the main detonation tube section. A larger diameter tube is desirable from the standpoint of increased thrust per frontal area. However, propagation of a small tube detonation to a bigger tube will quench if the small tube is smaller than a critical diameter. Because this critical diameter is on the order of 10 cell widths, a small tube predetonator would have to be roughly a foot (300 mm) in diameter in order to successfully transition a detonation to a bigger tube. Hardware is being developed today in violation of this rule of thumb but the mechanism explaining successful propagation was previously unknown.

Using a model of a small channel to big channel transition, we were able to demonstrate the mechanism. Figure 3 shows frames with pressure isobars of the process of detonation propagation from a channel

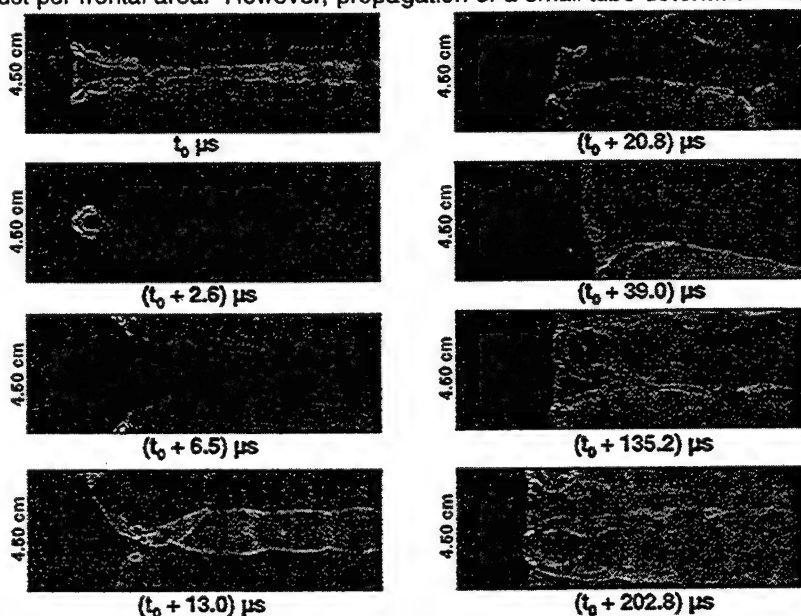


Figure 3. PDE model - detonation propagation from -1" (22.5 mm) channel to -2" (45.0 mm) channel. Direction of detonation propagation is from right to left and frame of reference is moving with combustion front.

one cell-width to double that width. The detonation is propagating from left to right and the frame of reference is moving at the combustion wave front speed. In the upper left frame, a stable detonation is suddenly allowed to expand from the single cell-width channel. From this model, it is clear in the next frame that although the detonation does quench, the remnants of transverse waves in the detonation cellular structure reflect off the side walls in the third frame, creating high pressure/temperature hot spots. These hot spots, created by the reflecting transverse shock waves, accelerate the chemistry, and the enhanced heat release grows in magnitude yet again when the sidewall reflections meet in the middle of the channel. These colliding shock waves are then seen to coalesce, bouncing from sidewall to sidewall, growing in strength of heat release as the pressure/temperature hot spots grow in magnitude until a stable cellular structure is re-established.

The mechanism of transverse wave reflections that is so evident in the models would be extremely difficult to detect experimentally. The detonation did quench, but the reflecting transverse waves re-initiated the detonation so quickly that the combustion process remains nearly constant volume and for all practical purposes, the detonation did successfully make the transition.

In other cases, such as the one illustrated in figure 4, the detonation does not successfully propagate across the sudden expansion. In the case depicted in figure 4, the detonation is propagating down a 1 and 1/2 cell width channel and transitions to a deflagration during the sudden expansion to a channel that would have been 3 cell widths. In a recent series of detonation transition experiment, months of experimental testing were performed in order to isolate a failure to a .05" (1mm) change in geometry. The insights gained from the models illustrated herein explain the mechanism that produced the dramatic change in results from a seemingly insignificant change in geometry.

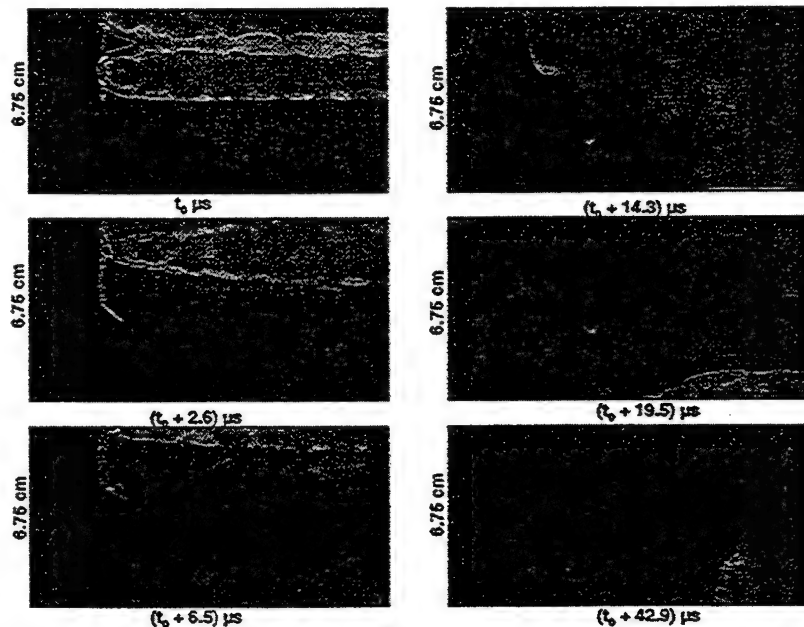


Figure 4. PDE model - detonation propagation and quenching from ~1.5" (36 mm) channel to ~2.6" (67.5 mm) channel. Direction of detonation propagation is from right to left and frame of reference is moving with combustion front.

Pulsed Combustor/Detonation Engine Research Facility (D-Bay)

D-Bay is a formerly mothballed, full-scale, sea-level/static engine test facility that has been converted to perform both full-scale and component testing of pulsed combustors and/or detonation engines. The facility is explosion proof and can measure up to 60,000 pounds (268 kN) of static thrust. A damped thrust stand of 10 to 1,000+ lbf (45-4500+ N) average thrust capacity now sits on the static thrust stand for pulsed detonation engine testing.

Up to 6 lbf/sec (3 kg/sec) of 100 psi (680 kPa) air is available and high-capacity inlet and exhaust stacks are useful for self-aspirating designs and atmospheric exhaust. A direct connection to a liquid fuel farm via a high-pressure/high-capacity fuel pump retains the facilities ability to feed large-scale 60,000 lbf thrust engines. The facility test stand, damped thrust stand, with an installed research PDE are shown in figure 5. The damped thrust stand itself sits upon the large capacity static thrust stand and the roll-up door to the exhaust tunnel is visible on the right.

Critical flow nozzles are used to obtain choked-flow measurements of air, purge air, and vapor fuels. These measurements are then available for accurate determination of the air/fuel ratio and flow rates going into a pulsed engine. These choke points isolate the measurements from the downstream

pressure oscillations of pulsed valves. Without such a scheme, accurate determination of the fuel/air ratio in pulsed engines has been largely a matter speculation. The air system is shown schematically in figure 6; note the independent control of main combustion air and purge air systems. The vapor fuel system has a similar scheme. Each system contains a pressure controller, a choked orifice plate or critical flow nozzle, and a surge tank to set and hold a required flow rate even with unsteady combustor valve flows. As long as the flow is choked, flow rate can be varied by changing the pressure and choked area. The depicted intake and purge manifolds allow for selection of from 1 to 4 detonation tubes.

A hardened remote-control room is adjacent to the 750,000+ ft³ test cell. A minimum of 2 feet of reinforced concrete is situated between the test cell and personnel during testing. Such precautions are necessary when dealing with the extremely hazardous noise levels associated with PDE operation. Control of all pulsed combustor/detonation engine operations and data acquisition is done via a LabVIEW based interface with duplicate manual emergency shutdown and safety system controls.

In addition to conventional (low or kHz frequency) data acquisition and control systems which include intake, fuel, and purge system instrumentation, the facility is equipped with up to 16 channels of high-frequency data acquisition at up to 5MHz. These may be used for high-frequency pressure transducers, thermocouples, photodiodes, or advanced laser diagnostics. A 1Mhz framing rate digital camera is also available for advanced laser diagnostics and imaging techniques^[6]. High frequency pressure transducers and photodiodes are currently installed with plans for digital Schlieren experiments to begin in the late fall of 1999.

Due to the nature of this facility, testing is not limited to small-scale PDE experiments. Conventional full-scale turbine engine tests are possible making hybrid turbo-PDE's a future research possibility in this facility. It is envisioned that several smaller scale (<1,000 pound thrust) experiments could take place across the test deck or a single large-scale (10,000+ pound thrust) engine test could be performed. As with most of PRSC's test facilities, easy swap-out of test hardware is expected and accounted for in the initial test-facility design.

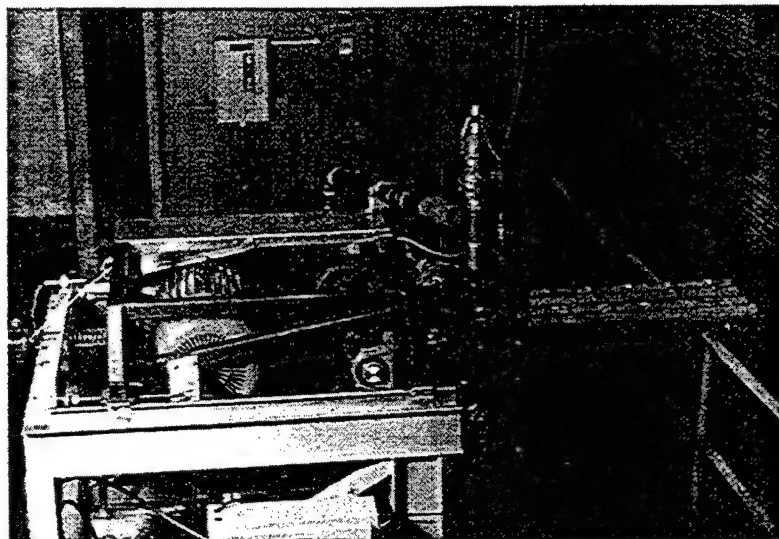


Figure 5. Pulsed combustor/detonation engine test stand, damped thrust stand, with installed research PDE.

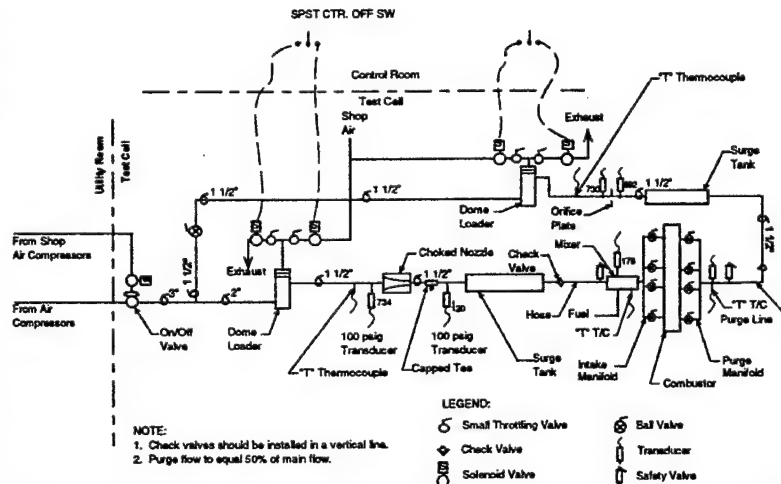


Figure 6. Pulsed combustor/detonation engine main combustion air and purge air systems; fuel system is similar.

Research Engine

Due to the critical timing issues in pulsed detonation engine operations, the high frequency valving tends to be both expensive and highly constrained. During the design of a research PDE, many options were considered that were either too expensive, had severe limitations in operating range, or both. The final design was based upon an extremely cheap, mass-produced valve system that was acquired from a salvage yard. It is based upon a General Motors Quad 4, DOHC cylinder head, as commonly found in the Pontiac Grand Am.

The operating conditions of PDE's are very similar to internal combustion engines and many of the components can be shared. By driving the overhead cams with an electric motor, the four valves in each of the four cylinders can be made to operate at between 0.5 and 50 Hz, with minor modifications required to get the frequency limit up to 100 Hz. Provisions for lubrication, cooling, ignition, and fuel delivery are integral to the cylinder head/intake manifold assembly. The electric valve-train drive motor, which is grossly oversized but a scrounged component, is clearly visible on the left side of the frame in figure 5, along with the valve train drive parts.

The two intake valves in each cylinder are used to feed premixed air and fuel into detonation tubes, which are attached to an adapter plate secured by the head bolts, visible in figure 7. In the current configuration, the head and detonation tubes are installed horizontally, and the intake valves are the upper pair. The exhaust valves are flowed in reverse with cold air used as a purge cycle to buffer hot products from igniting the next incoming charge and to convectively cool the inside of the detonation tube walls. The extra exhaust valve or valves in this four-valve-per-cylinder design could also be used for an axial predetonator or additional combustion air if necessary.

Somewhat uniquely, this PDE is operated premixed, minimizing mixing and stratification issues. The large pop-off valves and check valves visible in figure 5 are some of the precautions used to catastrophic failure in the event of an engine backfire through the premixed intake section. Up to four detonation tubes can be run at 90 degrees out of phase, with various diameters ranging up to ~3.5 inches (85mm). The main combustion air and purge air contain ball valves for each detonation tube feed system so that the engine can be run with one tube, two tubes 180 degrees out of phase, or all four tubes. A rotary position sensor is adapted to the intake camshaft to provide both an index and relative position of the valve timing sequence. This signal serves as the master timing signal for the ignition and data acquisition systems.

Triggered off the rotary position sensor is an eight-channel igniter/fuel injection control box. Separate control of each detonation tubes igniter and/or fuel injector may be accomplished with this system, although currently vapor fuels are premixed with the combustion air via a separate critical flow nozzle and flow control system. Due to the hazardous noise levels associated with PDE testing, all controls and data

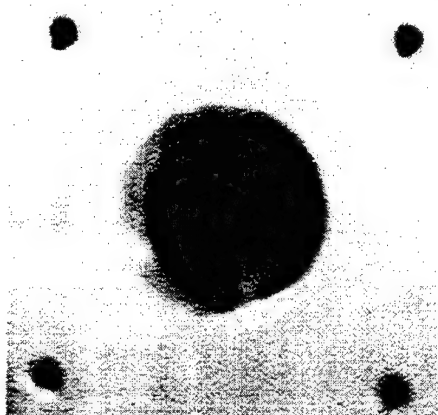


Figure 7. Research 'Quad 4' PDE detonation tube adapter plate with visible intake (upper) valve pair, purge air (lower) valve pair, and conventional spark igniter.

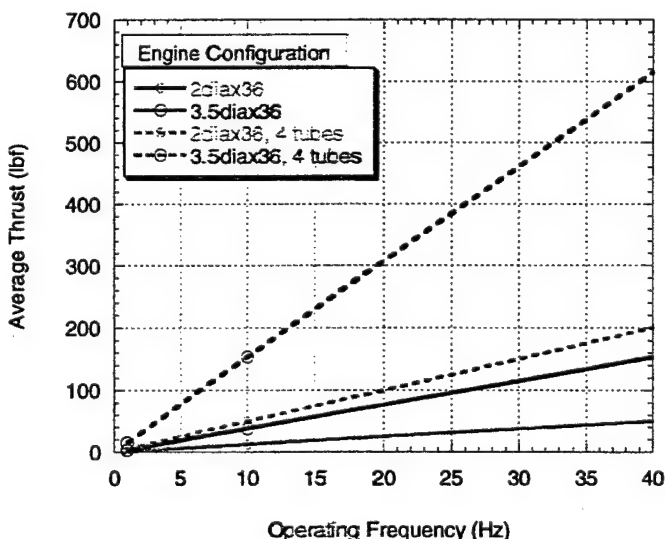


Figure 8. Research 'Quad 4' PDE detonation tube predicted thrust (inlet neglected) versus frequency for four different detonation tube configurations.

acquisition are performed remotely from an isolated control room. All of the control systems and data acquisition systems are LabVIEW based and integrated into one 'virtual instrument' with back-up manual shut down and safety systems. This virtual control panel is extremely flexible and can control all aspects of the PDE's operation including: lubrication, operating valve drive motor control, fuel flow, main combustion air flow, purge air flow, timing, ignition delays, and automatic shutdown in the event of a critical system failure. By changing the position of a few manual ball valves and pushing a few switches in the virtual control system, the engine configuration can be switched from one tube operating to four tubes in a matter of minutes.

Each of the four PDE tubes can operate from 0.5 to 100 Hz for an aggregate maximum frequency of 400 Hz. Petters predicted the inlet-neglected thrust of this configuration and the results are shown in figure 8 for four different engine configurations, including: single 2" (50 mm) diameter by 3' (900 mm) tube, single 3.5" (90 mm) diameter by 3' (910 mm) tube, and four tubes of each of the previous configurations^[7]. As is evident from the graph, significant thrust is developed even at these relatively low frequencies, further demonstrating the low thrust/cost ratio of this technology.

The engine is to be used for performance prediction validations and serve as a test-bed for research of: detonation initiation and DDT minimization, heat transfer, noise levels, pulsed ejector concepts, and multi-tube interactions. Initial testing and proof-of-concept is being done with hydrogen as the fuel due to the increased detonability versus practical liquid hydrocarbon fuels. A vapor propane fuel system has also been constructed in order to work with a complex-hydrocarbon that detonates much like kerosene based JP type fuels. This will eliminate the atomization and mixing of liquid fuel complications that increase the difficulty of practical PDE design and allow us to focus on detonation initiation and high frequency operation. As mentioned previously, ONR funded research is tackling the difficult problems of liquid fuel atomization and mixing for PDE applications^[3,8].

RESULTS AND DISCUSSION

Although this program was initiated two years ago and the test facility was an abandoned, empty cell 9 months ago, we have successfully designed, built, and tested both the facility and the experimental research engine since that time. As described above, the modeling effort is already producing results and being published elsewhere^[5].

Cold flow testing of the systems began in early 1999, with the first hot firing on 9 September. This initial test was done at low fuel flow conditions to minimize the amount of hydrogen in the test cell in event of a failure. The first test was done with fully instrumented intake and purge systems, detonation tube surface temperature thermocouples, four high frequency pressure transducers along the length of the tube, damped thrust, and two black & white video cameras. An image extracted from one of the video cameras is shown in figure 9.



Figure 9. In-house research 'Quad-4' PDE, success on first attempt, 9 September, 1999: 91 second operation at 8Hz, single 2" diameter by 3' long tube, stoichiometric H₂/air, conventional ignition.

The initial testing produced very good qualitative results, with four runs of up to 91 seconds duration. These runs, which were un-cooled, were cut short because the tube surface thermocouples were epoxy mounted which began to melt. The thermocouples have since been re-affixed more robustly. The sharp 'CRACK' sound and flash of the exhaust were qualitative indicators of detonations which

contrasted with the softer 'wumpff' sound and flame visible out the back when the engine deflagrated due to off-stoichiometry conditions.

The high-frequency pressure transducers had not been tested until these initial hot-firings and did not produce publishable results. This is most likely due to gain settings and the in-ability of the data acquisition computer to keep up with the high data-streaming rate. A dual-processor PIII 600 MHz machine has been custom built to handle this task for future testing. The operating condition should have produced 10 pounds (45 N) of thrust, but the thrust stand was fully damped during these initial test runs. With damping, the static friction of the thrust stand has been measured at 20 lbf (90 N), which explains why no thrust was measured on the first runs. The dampers had been left on because it was not certain how long the engine would run and we wished to acquire a thrust measurement during the first 5 seconds of operation. Since the engine has demonstrated that it can run for much longer durations, the dampers will be removed for future tests with predicted thrust levels below 20 lbf (90 N).

Further testing results from this engine were not available at the time of this papers submission; they will be presented during the JANNAF meeting. Work in progress includes: higher frequency operation, multi-tube operation, alternative igniter schemes to minimize the DDT distance, additional high frequency instrumentation including thermocouples and more pressure transducers, and high frequency digital Schlieren visualization to evaluate the viscous boundary layer effects at the tube exit. Work on many of these areas has already begun and it hoped that some of the results can be obtained at the oral presentation.

One concept being explored is the use of alternative ignition schemes to minimize the DDT distance in a predetonator. A total of eight successful tests have been conducted using a prototype ignition system and the preliminary results are very promising, with the DDT distance more than halved in the best scheme to date as shown in figure 10. In this data acquired in a cooperative effort between AFRL and the Naval Postgraduate School (NPS), the upper plot, which has a more conventional igniter, is just transitioning to near Chapman-Jouget (C-J) wave speeds by the later pressure transducer locations 12" (300 mm) axially down the tube.

The data in the lower plot was generated using the prototype igniter features to produce C-J wave speeds at the 6" (150 mm) axial tube location, which was the pressure transducer closest to the igniter end. The detonation wave may have been established well before this 6" (150 mm) point, but this was the extent of the available instrumentation for this limited study. The C-J wave speed for the conditions tested is estimated at ~6,500 ft/sec (~2,000 m/sec) and compares well with the experimentally observed stable C-J detonation speeds of ~6,900 ft/sec (~2,100 m/sec). Further information on these tests, which were performed in Monterey, California using the NPS JP/O₂ predetonator PDE section with AFRL supplied igniter hardware with support from both organizations, is available elsewhere^[9].

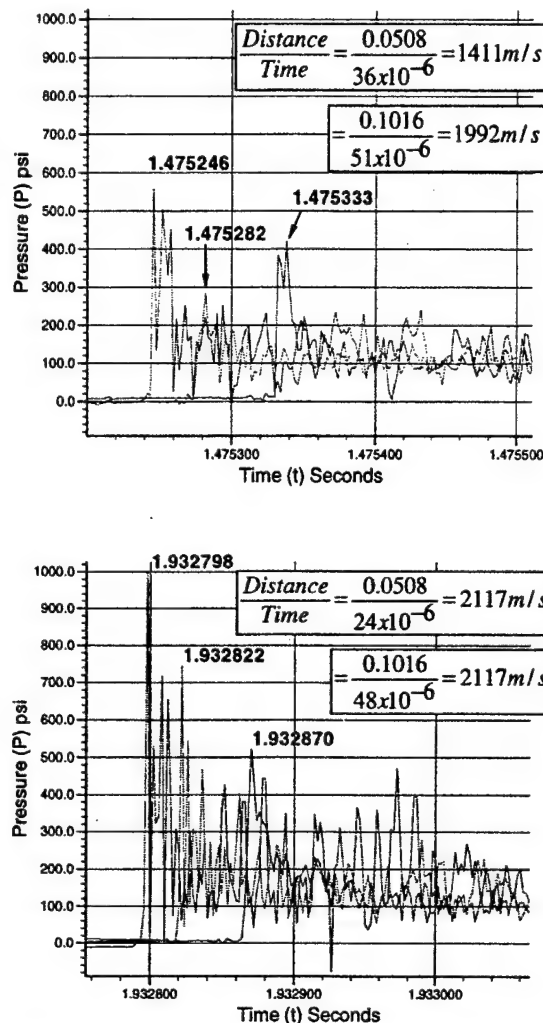


Figure 10. Impact of ignition upon DDT distance as indicated by time history of pressure transducer measurements. The lower plot has a much shorter DDT distance and attains near C-J detonation wave speeds in a shorter length by using a prototype ignition concept compared to the more conventional igniter results typical of the upper plot. Key to pressure transducer axial locations: Red 6" (150mm), Green 8" (200mm), Blue 12" (300mm).

SUMMARY AND CONCLUSIONS

Pulse detonation engines are an extremely promising alternative to small, disposable-jet turbine engines. The Air Force Research Laboratory has supported PDE research for some time now, and an in-house program established by the Combustion Branch of the Propulsion Sciences and Advanced Concepts Division at Wright-Patterson AFB has been established to produce sharable benchmark performance data. In addition, the in-house program has been used to harness AFRL's unique resources in order to contribute to the development of pulsed detonation propulsion technology in the form of modeling, facility, and research components.

It is hoped that the contributions of our deflagration to detonation transition modeling can be used as a tool in the development and design of a practical-fueled detonation initiator. The pulsed combustor/detonation engine test facility has been developed as a cost-effective test resource that meets many of the unique needs required for PDE testing. The remote controls and high frequency data-acquisition systems have been assembled to provide test support for researchers working in collaboration with AFRL. The facility can handle everything from bench scale experiments from academia to full-scale hybrid engine concepts from engine manufacturers. Moreover, it is hoped that researchers will take advantage of this national resource.

A research PDE was successfully designed, built, and operated under the in-house program using an innovative valve system based upon a 16 valve Quad-4, four cylinder automobile engine from General Motors. The resulting engine is capable of a broad range of frequencies and configurations with up to four detonation tubes. Data from the engine will be published with the intent of providing non-proprietary PDE data against which performance codes and predictions can be benchmarked. The 'Quad-4' PDE serves as a research tool and test-bed for detonation initiation concepts, high frequency operation, heat transfer studies, multi-tube detonation engine operation, and pulsed ejector research. The engine, which was operated successfully for the first time in the early fall of 1999, demonstrates the affordability and ease of scalability of PDE technology.

There is much work to be done in developing valving, detonation initiators, noise suppression techniques, thermal protection systems, intake and exhaust nozzles, and control systems before a JP/air fueled PDE becomes practical. AFRL/PRSC would like to invite the community to consider our resources for further PDE research. With high quality modeling, research facilities, and an in-house PDE engine, we can work with other organizations and contractors, as we have in the past with turbine engine technology, to mature and transition PDE technology to the field. to contribute to make practical

ACKNOWLEDGEMENTS

Special appreciation must be expressed to the technicians and support personnel, both in-house government employees and on-site contractors who made this work possible, particularly Dwight Fox (ISSI) who helped build much of the research PDE engine. We also wish to acknowledge the technical leadership of Dr. Mel Roquemore (AFRL/PRSC). Thanks go out to Dr. Dave Netzer and Dr. Chris Brophy of the Naval Postgraduate School for their shared experience and use of their facilities and hardware. Gratitude also goes to: Pennsylvania State University, ASI, APRI, Enigmatics, and the major automobile and airplane manufacturers for their contributions and continuing assistance.

REFERENCES

1. K. Kailasanath, G. Patnaik, and C. Li, "Computational Studies of Pulse Detonation Engines: A Status Report," *AIAA 99-2634* (1999).

2. J.E. Elsworth, P.J. Shuff, and A. Ungut. "'Galloping' Gas Detonations in the Spherical Mode," in *Prog. Astronaut. Aeronaut.*, volume **94**, pages 130-150, 1984.
3. Christopher Brophy, David Netzer, and Dave Forster, "Detonation Studies of JP-10 with Oxygen and Air for Pulse Detonation Engine Development," *AIAA 98-4003* (1998).
4. R.D. Hancock, J.R. Gord, D.T. Shouse, F.R. Schauer, V.M. Belovich, and W.M. Roquemore, "AFRL Combustion Branch (PRSC) Aeropropulsion Research and Development Activities," *Proceedings of the International Test and Evaluation Association (ITEA) Conference* (1999).
5. V.R. Katta, L.P. Chin, and F.R. Schauer, "Numerical Studies on Cellular Detonation Wave Subjected to Sudden Expansion," *Proceedings of the 17th International Colloquium on the Dynamics of Explosions and Reactive Systems*. Heidelberg, Germany (1999).
6. James R. Gord, Charles Tyler, Keith D. Grinstead, Jr., Gregory J. Fiechtner, Michael J. Cochran, and John R. Frus, "Imaging Strategies for the Study of Gas Turbine Spark Ignition," Presented at the SPIE's 44th Annual Meeting & Exhibition, Conference 3783 on Optical Diagnostics for Fluids/Heat/Combustion and Photomechanics of Solids, Denver CO, 23 Jul 99.
7. Dean Petters, Personal Communication, AFRL/PRST at Wright-Patterson AFB, OH (1999).
8. Gabriel D. Roy, "Pulsed Detonation Phenomena for Air Breathing Propulsion," *ISABE 99-7127* (1999).
9. R. A. Anthenien, F.R. Schauer, J.S. Stutrud, C.W. Frayne, R.P. Bradley, L.P. Chin, and V.R. Katta, "Development of a Pulse Detonation Research Engine," *Proceedings of First Joint Meeting of the U.S. Sections of the Combustion Institute*, Washington DC, 1999.

3.2 FUEL STUDIES

3.2.1 Overview

Since fuels are the primary heat sink in modern aircraft, an understanding of the propensity of fuels to produce either bulk or surface insolubles is essential. Development of fuel models can aid in predicting fuel behavior under complicated thermal- and oxidative-stress conditions that cannot be readily achieved in the laboratory; however, such models must be calibrated and evaluated using results from fundamental experiments. Such experiments must have objective criteria with which to rate different fuels, the effect of additives in a single fuel, and the effect of additives in a series of similar JP-8 fuels. Studies in this portion of the program were directed toward fundamental fuel thermal stability and additive evaluation. The results of efforts in each of these areas are discussed below.

3.2.2 Fuel Thermal Stability

3.2.2.1 Autoxidation of Jet-A Fuels. Surface fouling in aircraft fuel lines resulting from autoxidation of aviation fuel is a serious and very complicated problem. The role of surfaces in catalyzing aviation-fuel autoxidation in narrow-bore tubing and the possible ramifications with regard to surface fouling in aircraft fuel lines are reported in the paper entitled "Autoxidation of Aviation Fuels in Heated Tubes: Surface Effects." This paper was co-authored by E. G. Jones, L. M. Balster, and W. J. Balster and published in *Energy and Fuels*, Vol. 10, pp. 831-836 (1996). In the publication entitled "Surface Fouling in Aviation Fuels: An Isothermal Chemical Study" (see pp. 645-650), the effects of parameters such as reaction temperature, tube diameter, experimental test time, and fuel dopants are considered. The importance of bulk-fuel temperature in the formation of insolubles was assessed and the results reported in the paper entitled "Effects of Temperature on Formation of Insolubles in Aviation Fuels" (see pp. 651-655).

Surface Fouling in Aviation Fuels: An Isothermal Chemical Study

E. G. Jones¹

W. J. Balster

J. M. Pickard²

Systems Research Laboratories, Inc.,
An Operation of Calspan SRL Corporation,
2800 Indian Ripple Rd.,
Dayton, OH 45440

Surface fouling in aircraft fuel lines that results from autoxidation of aviation fuel remains a serious and very complicated problem. This area has been studied using two Jet-A fuels, POSF-2827 and POSF-2980. The results of a series of dynamic experiments conducted in a single-pass, tubular heat exchanger operated at very slow flow rates under near-isothermal conditions are reported herein. Such studies, by minimizing complications resulting from fluid dynamics and heat flow, constitute a simpler global approach to the chemistry of fouling. The basis for the selection of experimental test conditions is discussed, and data from measurements of dissolved oxygen and surface deposition as a function of fuel stress duration are presented. The effects of parameters such as reaction temperature, tube diameter, experimental test time, and fuel dopants are considered.

Introduction

Aviation fuels, when subjected to heat in the presence of oxygen, undergo degradation from autoxidation reactions, as summarized by Hazlett (1991). Insoluble products formed in these reactions tend to foul heated surfaces, causing reduced efficiency and possible blockage in heat exchangers, hysteresis in servocontrols, and changes in nozzle geometry. As the primary heat sink in modern aircraft, fuel will experience increased thermal stress as aircraft performance is enhanced (Edwards et al., 1992). Each fuel has a unique composition; thus, the chemical reactions describing the autoxidation of one fuel will be different from those of all other fuels. Similarly, the reaction steps from formation of the initial free radical to the final production of insoluble carbonaceous surface deposits or bulk insolubles are too complex to have been outlined for aviation fuels. Minor fuel constituents containing hetero-atoms such as sulfur and nitrogen have been identified either as the primary cause of insoluble formation or as the source of catalysis which can accelerate autoxidation. Also, the conditions of high fuel velocity and nonuniform wall and bulk-fuel temperatures present in fuel lines create complicated fluid-dynamic conditions that are difficult to simulate and that change during each segment of a flight cycle.

Simulating the fuel-stress conditions experienced in fuel lines during flight requires expensive full-scale rigs and large fuel batches. An alternative approach taken in this laboratory has been the use of a simpler near-isothermal flowing test rig (NIFTR) to simulate only the chemical conditions (i.e., the temperature and reaction time) by conducting experiments under near-isothermal conditions. The advantage of this approach is threefold: (1) Many complications from fluid dynamics are removed, (2) wall and bulk-fuel temperatures are the same, and (3) the global aspects of deposition can be described in terms of rate of deposition as a function of reaction time or fuel-stress duration. Since reactions are studied over 100 percent oxygen conversion, an inherent normalization occurs through the use

of a fixed amount of reactant, namely, the total amount of oxygen present in air-saturated fuel. It is assumed in this approach that 1 L of fuel stressed to 100 percent conversion will form the same quantity of insolubles as 1000 L of fuel stressed to 0.1 percent conversion. The latter condition more nearly approximates that experienced in an actual aircraft; however, if chemistry is a controlling factor, then the reaction chemistry in controlled isothermal experiments will be the same as that which occurs in the field. This forms the basis for the near-isothermal approach to the study of fuel fouling. Clearly, when isothermal conditions are used, the thermal behavior of fuel must be studied over a range of different temperatures to obtain a broad view of fuel thermal stability.

The goals of the isothermal approach are to (1) isolate the global-chemical processes, (2) collect experimental data that describe the fouling chemistry as a function of reaction time, and (3) compare the thermal behavior of different fuels and establish a baseline for evaluating the efficiency of additives in reducing or delaying surface fouling. Additives such as antioxidants for slowing oxygen consumption, metal deactivators for chelating dissolved metals or passivating tubing walls, and dispersants or detergents for increasing solubility would appear to hold the most promise from a thermal-stability standpoint. Martel (1987) has summarized jet-fuel additives including (in addition to the above) corrosion inhibitors, lubricity improvers, icing inhibitors, static dissipators, and pipeline-drag reducers. Changes introduced by the hindered-phenol antioxidant additive BHT in two Jet-A fuels are presented, and several possible criteria for rating fuels and additives based upon near-isothermal test results are reviewed.

Longer-term goals, not addressed in the current study but a simple extension of the current approach, are to collect data at several temperatures, to derive kinetic parameters that may ultimately describe surface-fouling processes over a broad temperature range, and to use these values in CFD models for predicting fouling under actual aircraft conditions that are difficult to achieve in the laboratory. Models such as those developed by Katta et al. (1993) have been successful in describing surface fouling for several rigs.

This paper describes progress toward obtaining baseline data at 185°C to reflect the surface fouling that occurs in two Jet-A fuels, POSF-2827 and POSF-2980. Included is the establishment of the optimum experimental conditions for studying fouling and for differentiating the fuels in a series. Experimental parameters such as tubing size, reaction-temperature range, sur-

¹ Current address: Innovative Scientific Solutions, Inc., 3845 Woodhurst Court, Beavercreek, OH 45430-1658.

² Current address: Kinetica, Inc., P. O. Box 182, Mound Advanced Technology Center, 1 Mound Rd., Miamisburg, OH 45343-0181.

Contributed by the International Gas Turbine Institute and presented at the 40th International Gas Turbine and Aeroengine Congress and Exhibition, Houston, Texas, June 5-8, 1995. Manuscript received by the International Gas Turbine Institute February 10, 1995. Paper No. 95-GT-45. Associate Technical Editor: C. J. Russo.

Table 1 Fuel properties

	POSF-2827	POSF-2980
Treatment	Straight Run	MEROX™-treated
JFTOT Breakpoint	266	288
Total Sulfur (%)	0.079	0.061
Freezing Point (°C)	-43	-44
Aromatics (% vol)	19	17
Total Acid No. (mg KOH/g)	0.001	0.001

face conditions, and test duration must be considered. For example, a 6-h test has been found to be adequate for quantifying insolubles and identifying reaction trends in POSF-2827 fuel (Jones and Balster, 1993); however, arguments presented herein indicate that, in general, longer tests of ~70-h duration may be preferable.

Experimental Arrangement

Some general properties of the two fuels are given in Table 1. Although both fuels contain a significant amount of total sulfur, they meet all USAF specifications. POSF-2980 fuel has been treated using the MEROX technique to reduce the mercaptan odor through oxidation to the corresponding disulfide. Both are Jet-A fuels representative of those in commercial service. The antioxidant BHT was obtained from DuPont. Fuels were used as received, with minimal filtration (15 μ m) for protection of the syringe pump.

The experiments were conducted using the NIFTR, which has been described previously (Jones et al., 1995; Jones and Balster, 1993). Figure 1 shows the heat exchanger as operated in the extended-pass mode to double the total reaction time. Fuel, which is saturated initially with respect to air and which contains 64 ppm (w/w) of oxygen, is pumped at a pressure of 350 psi through commercial stainless-steel (304) tubing clamped tightly in a 36-in. heated copper block. Most of the experiments were conducted using tubing with dimensions of 0.125-in.-o.d. and 0.085-in.-i.d.; in a few experiments larger tubing with dimensions of 0.25-in.-o.d. and 0.18-in.-i.d. was used. A pair of in-line Ag-membrane filters (0.45 and 0.2 μ m) collected the nonadhering bulk insolubles.

Deposition rates were measured in 6-h and ~70-h experiments that were run continuously at a fixed fuel-flow rate; reaction time or stress duration was determined from the flow rate, tube dimensions, and location along the tube axis. The calculated times were reduced by 15 percent to compensate for fuel expansion. When the total test time was increased tenfold, the total volume of fuel increased tenfold. At the end of each test, the heated tube was cut into 2-in. sections, and the quantity of carbon in the deposits was determined from surface-carbon burnoff (LECO RC-412). Deposition rates were determined from the amount of carbon in each 2-in. segment, the increment of stress time within that segment, and the total quantity of fuel used. Each section provides one data point, representing the rate averaged over the entire test time (i.e., 6–70 h). Deposition rate is expressed in units of micrograms of carbon per unit stress time per unit volume of fuel passed through the system. Nonadhering bulk insolubles were quantified by surface carbon burnoff of the in-line filters. Dissolved oxygen was measured in separate experiments using a 32-in. heated tube as a reaction

cell and GC detection (Rubey et al., 1992); stress duration was changed by varying the flow rate. Cleaned stainless-steel tubes were used for measurements related to 6-h deposition experiments where deposition occurs primarily on cleaned surfaces. In long-term tests, most deposition occurs on previously fouled surfaces; for comparison with deposition in this case, passivated tubes (Silcosteel, Restek Corporation) were used to minimize catalytic wall effects that occur during oxygen measurements.

Results and Discussion

Selection of Optimum Test Conditions

Temperature Range. In many fuels a close correlation exists between oxygen consumption and deposition; thus, the temperature ranges of interest for oxygen depletion and surface deposition overlap. Experimentally, oxygen depletion can only be measured over a limited temperature range of ~50–60°C for the following reason. At the high-temperature end, the reaction is very rapid, and higher fuel-flow rates are necessary for maintaining short residence times within the heated block. As a result the fuel does not achieve block temperature rapidly, i.e., the experiments depart significantly from isothermal. At the low-temperature end, the reaction is very slow, and residence times on the order of hours are necessary for complete consumption of the dissolved oxygen. Maintenance of GC-detector stability over extended periods of time can introduce significant errors into the measurements. Oxygen depletion in about 15 fuels has been studied in this laboratory, and dissolved oxygen has been found to be completely converted after 1–20 min of stressing at 185°C. The practical temperature range for oxygen measurements using the current techniques is 155–215°C.

Surface-fouling measurements are subject to similar temperature constraints. At the highest temperatures, reaction and subsequent deposition occur over a very narrow time interval; depending upon the fuel-flow rate, deposition occurs only in a limited region of the heated tube. Spatial deposition can be extended through higher flow rates, but at the expense of departure from isothermal conditions. At the lowest temperatures, very slow flow rates must be used for total reaction of the dissolved oxygen. The difficulty arises from the fact that in a 6-h test at 155°C, only about 25 ml of fuel are passed and a limited, minimal amount of deposit is collected. The practical temperature range for near-isothermal surface-fouling experiments is 145–225°C. A temperature of 185°C, the midpoint of the experimental range, was selected as the standard temperature for stressing neat jet fuels to obtain baseline surface deposition and dissolved-oxygen information.

Stress Duration. This parameter is controlled by rates of oxygen consumption and the deposition profile. The primary requirement is to provide sufficient residence time for completion of the oxygen reaction and subsequent deposition within the heated tube. Passing fuel through the heated block once or twice at a flow rate of 0.25 ml/min provides, respectively, 12 and 24 min of stressing at temperature. For the fuels studied, this time is sufficient for complete deposition to occur at 185°C within the heated block.

Test Time. This parameter was established for deposition experiments and determines the total amount of fuel passed through the system. The longer the test time, the greater the

Nomenclature

BHT = 2,6-di-tert-butyl-p-cresol, antioxidant

CFD = computational fluid dynamics

GC = gas chromatograph

JFTOT = jet-fuel thermal-oxidation test

NIFTR = near-isothermal flowing test rig

POSF-2827 = Jet-A fuel, straight run

POSF-2980 = Jet-A fuel, MEROX™-treated

USAF = United States Air Force

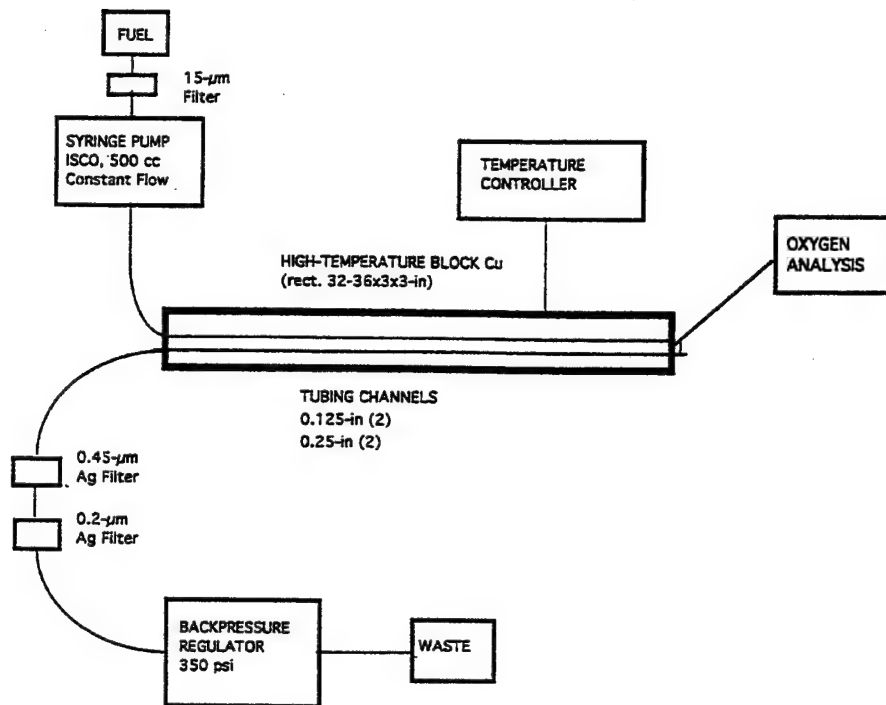


Fig. 1 Schematic diagram of apparatus (NIFTR)

quantity of insolubles formed and the greater the signal/noise ratio. The measured deposition rates represent averages over the total test time. It has been reported (Jones and Balster, 1994a) that the dependence of deposition rate upon stress duration for POSF-2827 aviation fuel changes as the test time is extended from 6 to 70 h. This observation was explained in terms of surface-dependent changes in the rate of oxygen consumption. The initial deposition on clean stainless-steel tubing is governed by a more rapid oxygen loss that is catalyzed by active sites on the cleaned surface. As deposits collect along the walls, active sites become covered, oxygen depletion is no longer surface catalyzed, and its rate and the rate of surface

deposition decrease. This is manifested by a reduced deposition rate and a shift in the deposition profile to slightly longer stress times, i.e., residence times. Once the surface is completely covered by deposits, the deposition profile becomes independent of test time.

Figures 2 and 3 show the deposition rate for POSF-2827 and -2980, respectively, as measured in 6-h (initial catalyzed rate) and in ~70-h tests (constant deposition). The rate plotted has been corrected by subtracting the effects of background surface carbon not related to autoxidation. Also shown is the corresponding decay in dissolved oxygen as measured in a cleaned stainless-steel tube and in an inert tube. In general,

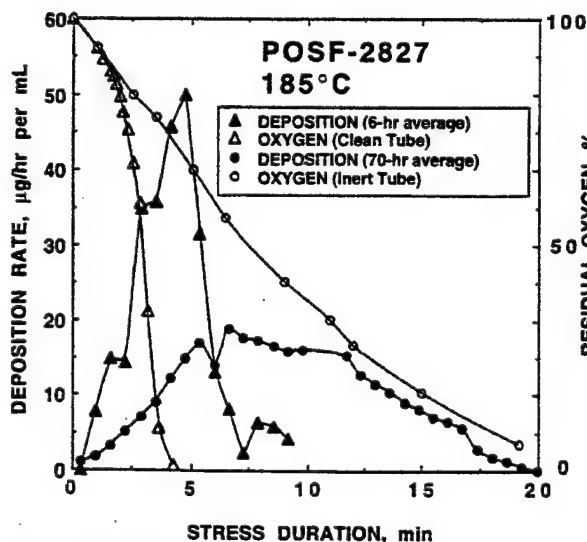


Fig. 2 Deposition rate and residual oxygen versus stress duration for POSF-2827 fuel measured in 0.125-in.-o.d. tubes

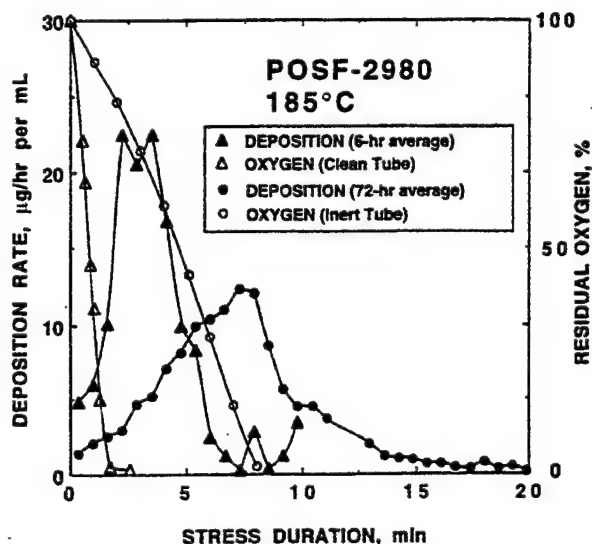


Fig. 3 Deposition rate and oxygen consumption versus stress duration for POSF-2980 fuel measured in 0.125-in.-o.d. tubes

Table 2 Advantages: short- versus long-term testing

Short Term (6 hr)	Long Term (~ 70 hr)
One-day experiment	Weekend experiment
Deposition on cleaned surfaces	Better signal-to-noise ratio
Faster oxygen reaction (catalyzed)	Deposition on fouled surfaces
Total insolubles per ml constant	Slower oxygen reaction (surface passivated)
	Reduced baseline correction to rate
	Total insolubles per ml constant

POSF-2980 has a slower deposition rate and a faster oxidation rate. The profiles pertain to different conditions. The first (6-h) describes deposition on cleaned stainless-steel tubing, and the second, the deposition mainly on previously fouled surfaces. Evidently POSF-2980 fuel displays deposition changes very similar to those reported for POSF-2827, namely, reduced rate and shift in the deposition profile as the test time is extended. The amount of deposition with POSF-2980 fuel is less and, hence, the surface coverage and passivation will be less than for POSF-2827. Also, regions exist near the entrance and exit of the tubes where deposition is minimal, and these surfaces may continue to catalyze autoxidation.

Table 2 outlines some of the distinct advantages associated with both short- and long-term tests. One of the major considerations is the signal-to-noise ratio. For the current treatment, long-term tests, which better reflect deposition on fouled surfaces were selected to simulate conditions encountered in actual aircraft fuel lines. However, fuels that leave few deposits may never lead to complete coverage of the original surfaces, even in 70-h experiments. It is doubtful that virgin clean surfaces would be common in fuel lines, except for servocontrols where very clean surfaces are required for minimization of hysteresis. In the latter case there may be cause for concern since autoxidation in both of the fuels under study is catalyzed by cleaned surfaces.

Tubing Size. Since deposition in isothermal tests is expressed as a function of stress duration rather than axial tube distance, the rate profiles should be similar in tubing with different internal diameters. The deposition measured for POSF-2827 fuel using larger diameter tubes is shown in Fig. 4. As the test time is extended, the trends observed are the same as those in Fig. 2. Rates are reduced by about a factor of two because of the reduced surface-to-volume ratio. For most studies 0.125-in.

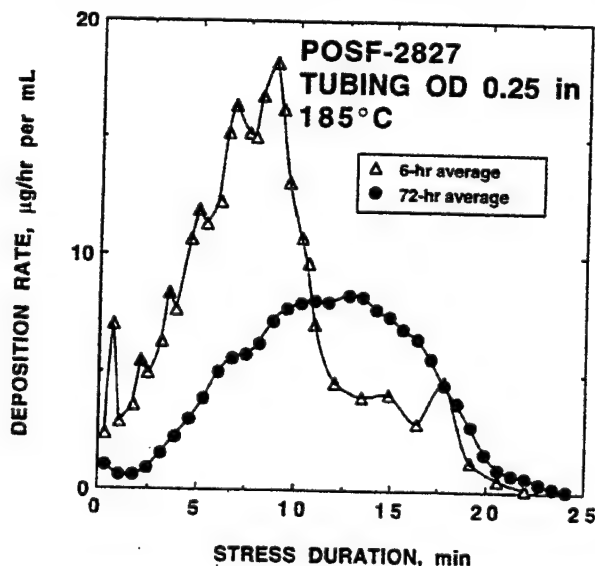


Fig. 4 Deposition rate versus stress duration for POSF-2827 fuel measured in 0.25-in.-o.d. tubes

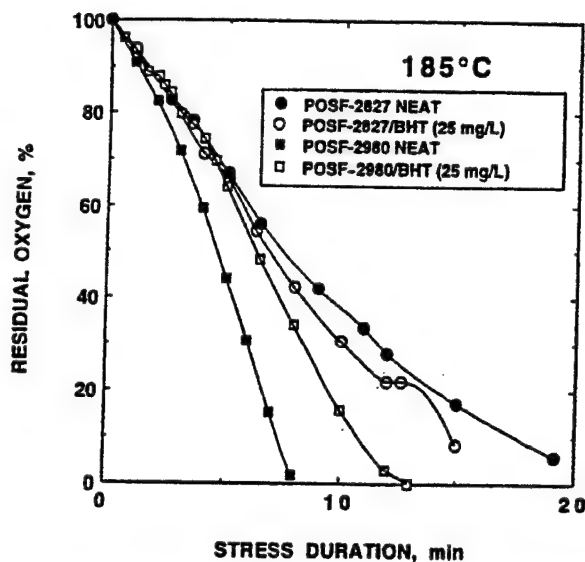


Fig. 5 Oxygen consumption in POSF-2827 and -2980 fuels, neat and with additives

tubes were selected to minimize fuel volume within the heated block and also to minimize the time needed to achieve isothermal conditions. For example, to achieve the same stress time within the heated section using tubing with twice the internal diameter would require a fourfold increase in flow rate. The higher the flow rate, the longer the time required to bring fuel to temperature and the greater the departure from isothermal reaction conditions.

Tubing Surface. The nature of the initial surface is a controlling factor in deposition in 6-h tests; however, once deposits have covered the metal surface, the deposition profile becomes constant. Thus, for long-term tests that produce deposits, the initial tubing surface is not a significant factor. It is for this reason that oxygen measurements were made using inert tubes.

Changes in Deposition Using Antioxidant BHT

POSF-2827 Fuel. The results of oxygen measurements at 185°C using the neat and additized fuel are shown in Fig. 5. Changes introduced by BHT at 25 mg/L fall within the reproducibility of the measurements. The rates are constant down to 30 percent residual oxygen, indicating oxygen nonlimited kinetics. Below 30 percent the rate becomes oxygen limited, as evidenced by tailing. Walling (1957) has summarized the rate expressions for the reaction of oxygen at high (oxygen-nonlimited) and low (oxygen-dependent) concentrations. The presence of certain types of sulfur compounds causes hydroperoxide concentration to remain low. Chain-breaking antioxidants such as BHT (hindered phenol) are ineffective in fuels containing large quantities of naturally occurring autoxidants. POSF-2827 fuel does produce hydroperoxides, but the measured steady-state concentration is very low ($<70 \mu\text{equivalents/L}$).

The corresponding deposition in the neat and additized fuel is given in Fig. 6. The two profiles are very similar. At this time it is not known whether the slight differences are real or whether they fall within experimental reproducibility. Based upon the similarity of the oxygen curves, it is concluded that BHT does not slow oxygen consumption, nor does it significantly change the surface deposition rate in POSF-2827 fuel.

POSF-2980 Fuel. In contrast to the results given above, BHT significantly slows the rate of oxygen consumption (see Fig. 5). The overall effect is a delay of ~2 min at 50 percent conversion and ~4-5 min at complete conversion. Clearly,

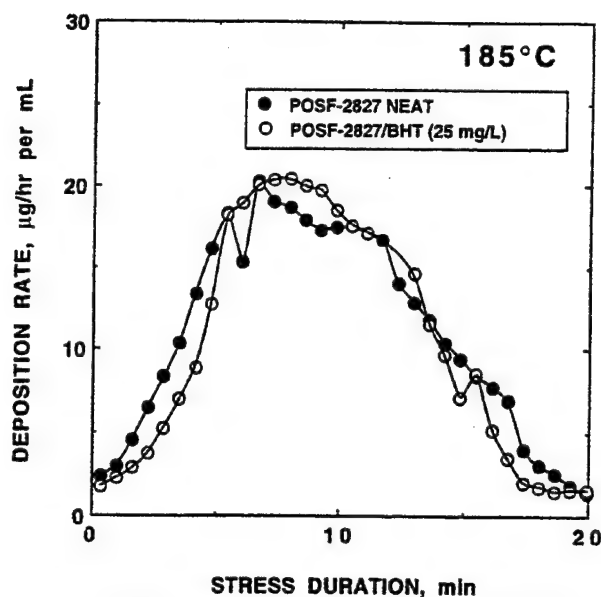


Fig. 6 Deposition rate in POSF-2827 fuel, neat and with additives

fundamental differences exist in the autoxidation of these two Jet-A fuels. The hindered-phenol antioxidant at a concentration of 25 mg/L has a negligible effect on POSF-2827 and yet is very efficient in retarding oxygen reaction in POSF-2980.

The effect of BHT on the deposition profile is shown in Fig. 7. BHT causes a dramatic delay in surface deposition, as might be expected from the oxygen behavior and previous reports of correlation between oxygen reaction and deposition in Jet-A fuels (Jones and Balster, 1994b). The delay in the maximum of the deposition profile is 3–4 min, in reasonable agreement with the oxygen-loss data. However, as with POSF-2827 fuel, the total quantity of deposit (integral under curves) is unaffected by BHT.

Criteria for Comparing Fuels and the Effect of Additives. Based on the previous considerations, two obvious criteria for comparing fuels are the rate of oxygen consumption and the

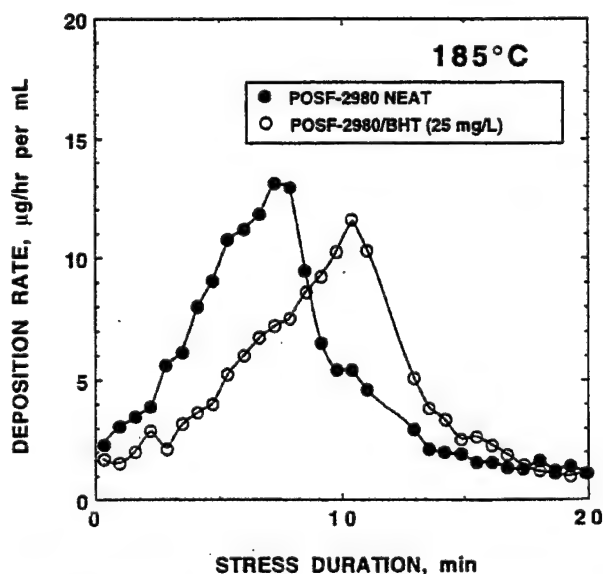


Fig. 7 Deposition rate in POSF-2980 fuel, neat and with additives

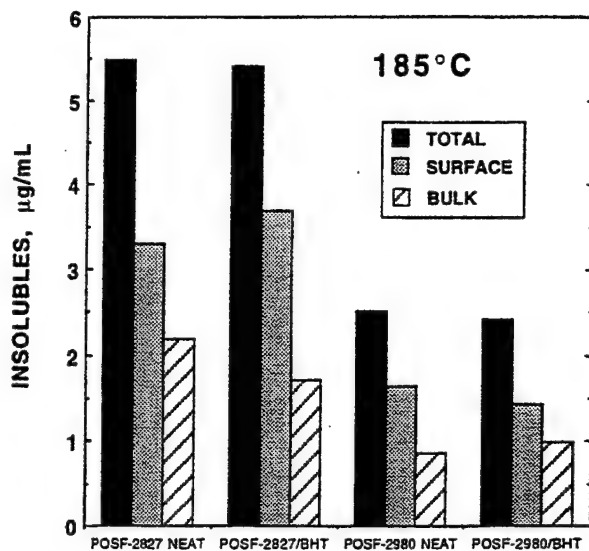


Fig. 8 Quantification of surface, bulk, and total insolubles

shape of the deposition-rate profile. Other quantitative criteria are the amount of bulk insolubles obtained directly from the in-line filters and the amount of surface insolubles obtained by integrating the area under the deposition profile. These quantities in units of micrograms per milliliter are summarized in the histogram in Fig. 8.

First, consider the impact of BHT. It does not reduce the amount of surface insolubles in POSF-2827 and causes a minor (10 percent) reduction in POSF-2980. BHT delays reaction in POSF-2980; but, given sufficient time to complete deposition, the total surface insolubles remain about the same. In actual service it is doubtful that all oxygen will be converted. This suggests that a more equitable way to assess the impact of BHT may be to compare surface insolubles formed after a limited stress duration, which is equivalent to considering the integral of the surface carbon as a function of stress duration; this is given in Fig. 9 for POSF-2980. Also plotted in this figure is the fractional reduction in surface deposits as a function of stress duration. After 10 min of stressing, BHT has reduced the

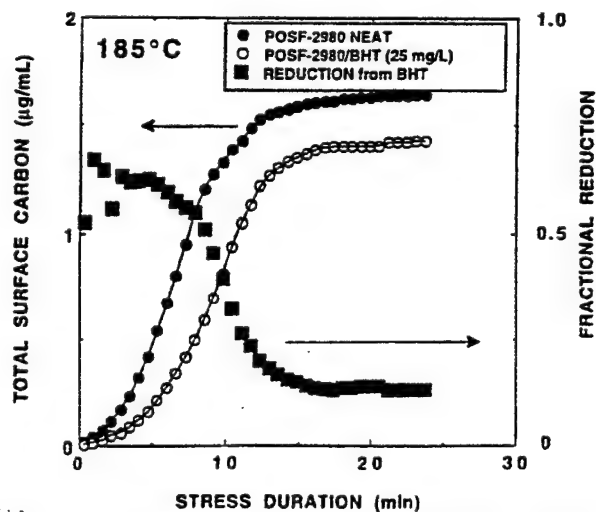


Fig. 9 Plot of total surface carbon (POSF-2980; neat and with additives) and fractional reduction versus stress duration

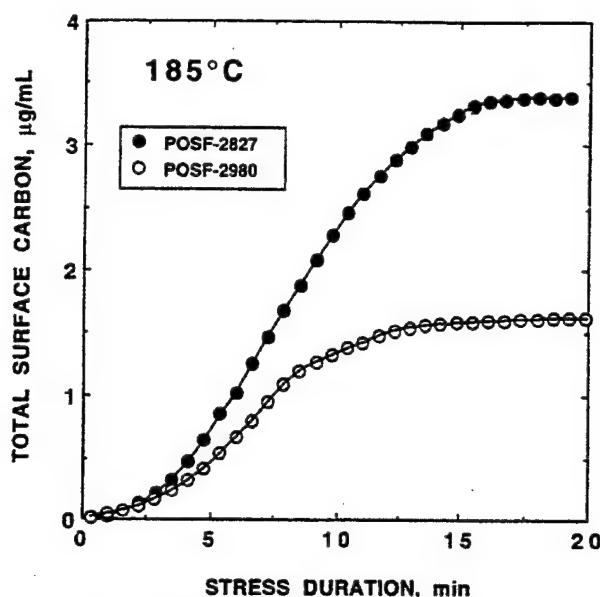


Fig. 10 Plot of total surface carbon versus stress duration at 185°C for POSF-2827 and -2980 fuels

total surface deposits by 35 percent; after only 5 min of stressing, the reduction is 60 percent. Clearly, comparison after shorter stress times best reflects the potential benefits of an antioxidant that serves primarily to delay reaction.

Second, compare the two Jet-A fuels. Figure 8 shows that POSF-2980 fuel produces less surface, bulk, and total insolubles at 185°C than POSF-2827 when these fuels are stressed to complete oxygen conversion and deposition. The difference is approximately a factor of two. However, if the comparison is based on the use of total surface carbon formed over limited stressing as shown in Fig. 10, then the difference between the two fuels is much less for a shorter stress duration. Isothermal test results provide information for comparing fuels using many criteria. It should be noted that all current comparisons relate only to reaction at 185°C. Data collected at other temperatures may rank fuels differently. For example, POSF-2827 fuel has an inverse temperature dependence for total surface insolubles (Jones and Balster, 1994b). It is not known whether POSF-2980 behaves similarly or has a very different temperature dependence. Clearly, refinement of a ranking scheme for fuels and additives is a complicated process.

Finally, Table 2 indicates that short- and long-term tests produce the same amount of insolubles when expressed per unit volume of fuel. For example, the bulk, surface, and total insolubles from 6-h tests with POSF-2827 fuel are 2, 3, and 5 µg/ml, respectively. The corresponding values for POSF-2980 are

0.83, 1.5, and 2.3. These sets of numbers are the same as the long-term values plotted in Fig. 8, within the experimental uncertainty of 10 percent.

Conclusions

Surface fouling that occurs at 185°C in two Jet-A fuels has been studied. Test conditions have been optimized to reflect fuel-dependent differences, and possible criteria have been outlined for ranking fuels and additives based on near-isothermal tests. Unique differences are observed both in the behavior of the neat fuels and in the impact of the antioxidant BHT. Autoxidation of both fuels is catalyzed by cleaned stainless-steel surfaces; the effect is greatly reduced or eliminated by surface passivation that occurs with the accumulation of surface deposits. Fuels that undergo surface catalysis may be of some concern under conditions where clean surfaces are encountered, as in servocontrols.

Acknowledgments

This work was supported, in part, by Wright Laboratory, Aero Propulsion and Power Directorate, Wright-Patterson Air Force Base, Ohio, under USAF Contract No. F33615-90-C-2033. The authors would like to thank Mr. Tim Gootee for performing the surface-carbon analyses, Ms. Lori Balster for making the oxygen measurements, and Mrs. Marian Whitaker for lending editorial assistance. The authors acknowledge valuable discussions with Dr. Larry Goss of SRL, Mr. Steve Anderson of the USAF, and Mr. Wayne Rubey of the University of Dayton Research Institute.

References

- Edwards, T., Anderson, S. D., Pearce, J. A., and Harrison, W. E., 1992, "High Temperature Thermally Stable JP Fuels—An Overview," AIAA Paper No. 92-0683.
- Hazlett, R. N., 1991, *Thermal Oxidation Stability of Aviation Turbine Fuels*, ASTM Monograph 1, American Society for Testing and Materials, Philadelphia.
- Jones, E. G., and Balster, W. J., 1993, "Phenomenological Study of Formation of Insolubles in a Jet-A Fuel," *Energy and Fuels*, Vol. 7, pp. 968-977.
- Jones, E. G., Balster, W. J., and Post, M. E., 1995, "Degradation of a Jet A Fuel in a Single-Pass Heat Exchanger," *ASME JOURNAL OF ENGINEERING FOR GAS TURBINES AND POWER*, Vol. 117, pp. 125-131.
- Jones, E. G., and Balster, W. J., 1994a, "Surface Fouling: Short- vs. Long-Term Tests," *Preprints—American Chemical Society, Division of Fuel Chemistry*, Vol. 39(3), pp. 952-957.
- Jones, E. G., and Balster, W. J., 1994b, "Formation of Insolubles in a Jet-A Fuel: Temperature Effects," *Preprints—American Chemical Society, Division of Petroleum Chemistry*, Vol. 39(1), pp. 78-81.
- Katta, V. R., Jones, E. G., and Roquemore, W. M., 1993, "Development of Global-Chemistry Model for Jet-Fuel Thermal Stability Based on Observations From Static and Flowing Experiments," AGARD Paper No. PEP-19.
- Martel, C. R., 1987, "Military Jet Fuels, 1944-1987," Air Force Wright Aeronautical Laboratory Technical Report AFWAL-TR-87-2062, Wright-Patterson Air Force Base, OH.
- Rubey, W. A., Tissandier, M. D., Striebig, R. C., Tirey, D. A., and Anderson, S. D., 1992, "In-Line Gas Chromatographic Measure of Trace Oxygen and Other Dissolved Gases in Flowing High-Pressure, Thermally Stressed Jet Fuel," *Preprints—American Chemical Society, Division of Petroleum Chemistry*, Vol. 37(2), pp. 371-376.
- Wallace, C., 1957, *Free Radicals in Solution*, Wiley, New York.

Effects of Temperature on Formation of Insolubles in Aviation Fuels

W. J. Balster

E. G. Jones

Innovative Scientific Solutions, Inc.,
2786 Indian Ripple Road,
Dayton, OH 45440-3638

Ten aviation turbine fuels (five Jet-A fuels, three JP-5, one JP-8, and one JPTS) were stressed at 185 and 225°C in a single-pass heat exchanger. On the basis of several criteria applied at 185°C, these fuels cover a broad thermal-stability range from lesser-quality fuels to the most stable JPTS fuel. Three of these fuels contain significant concentrations of dissolved metal (copper, >30 ppb). The surface and bulk insolubles formed from each fuel have been quantified using surface-carbon burnoff of tubing sections and of in-line filters. The total insolubles measured at 185 and 225°C fall in the range 0.3–7.5 µg/mL and 0.1–2 µg/mL, respectively. In general, the greater the quantity of insolubles formed at 185°C, the greater its reduction at 225°C. Possible explanations for this effect are offered, and implications relative to understanding surface fouling are discussed.

Introduction

Aviation fuel in modern military aircraft serves as the primary heat sink to cool subsystems; this application and its enhancement by fuel recirculation prior to combustion can lead to deleterious surface and bulk fuel fouling (Edwards et al., 1992). Below 300°C surface fouling originates as insoluble autoxidation products that collect on heat exchangers, nozzles, and servovalves. For understanding and reducing fouling, experimental methods are required for quantitative assessment of insolubles. The distribution of bulk fuel and wall temperatures under turbulent flow that exists in aircraft fuel lines results in complicated chemical test conditions. Simulations conducted under simpler, but well-defined, test conditions can be valuable in quantifying insolubles. One approach taken in this laboratory has been to study both autoxidation and fouling that occur during slow flow of fuel through a single-pass heat exchanger. In this manner, data interpretation is simplified by the imposition of flow conditions that are laminar and reaction conditions that are nearly isothermal. Quantification of surface and bulk insolubles is accomplished by surface-carbon burnoff of heat-exchanger tubing segments and in-line filters, respectively.

The effects of temperature on fuel-fouling kinetics are very complex. Autoxidation rates increase with temperature; however, the integrated quantity of insolubles does not necessarily increase. For example, studies in this laboratory (Jones and Balster, 1994) of one Jet-A fuel over the temperature range 145–225°C have shown surface insolubles to have a pronounced inverse temperature dependence. In order to assess the importance of bulk-fuel temperature in the formation of insolubles, we have conducted experiments to quantify insolubles formed in ten fuels at 185 and 225°C. The results of this temperature study are reported herein.

Experimental Arrangement

Ten aviation fuels covering a broad spectrum of thermal stability and currently of interest to the USAF are summarized in Table 1, along with some pertinent fuel properties. All experiments were conducted using the NIFTR single-pass heat exchanger, which has been described previously (Jones and Bal-

ster, 1993, 1995). The configuration consisted of a stainless-steel tube (0.318 cm o.d., 0.216 cm i.d.) clamped tightly within a copper block to maintain constant wall temperature. In order to maintain a single reaction phase, all studies were carried out at high pressure (>2.3 MPa). Autoxidation was studied using a gas-chromatographic technique developed by Rubey et al. (1995) for monitoring O₂. The disappearance of O₂ was tracked as a function of fuel residence time in a heated tube of fixed length (0.81 m) maintained at 185°C. Residence times were varied by changing the flow rate. Analogous experiments could not be performed at 225°C because of the short reaction times.

In fouling studies, fuel was pumped at a constant flow rate through a 1.8 m heated tube and Ag membrane in-line filters (0.45 and 0.20 µm). After the 72 h test period, the heated tube was cut into 5.1 cm segments. Tubes were then rinsed with heptane, treated for 24 h at 130°C in a vacuum oven, and subjected to conventional surface-carbon burnoff (LECO RC 412). Reaction time associated with each segment was calculated from tubing dimensions and flow rate, assuming plug flow. A flow rate of 0.25 mL/min provided ~23 min of isothermal stressing at 185°C for 1.08 L of fuel. A flow rate of 1.5 mL/min provided more than 3 min of stressing at 225°C for 6.48 L of fuel. Reaction conditions became isothermal at this higher temperature only after the reaction time exceeded that associated with the first three data points (~15 cm into the block). Reaction times allowed conversion of all dissolved O₂ and completion of the primary deposition processes at each temperature. Data are presented as the total integrated sum of tubing carbon (in units of micrograms per milliliter) as a function of stress duration. The quantity of surface carbon reproduces within 20 percent; the minimum detectable surface carbon is estimated to be 0.1 µg/mL.

Bulk insolubles were collected over the entire 72 h test period on in-line filters; the filters were rinsed with heptane and evaluated for surface carbon in the same manner as the tube segments. Total bulk insolubles (expressed in units of micrograms per milliliter) represented an average over the complete stress duration. Filter housings located ~10 cm from the heat exchanger remained at room temperature for the 185°C experiments and within 20°C of room temperature for the 225°C experiments. In both cases the measured filterables include additional contributions arising from fuel cooling. The dispersant additive obtained from Betz Laboratories was used at a concentration of 100 mg/L.

Contributed by the International Gas Turbine Institute and presented at the International Gas Turbine & Aeroengine Congress & Exhibition, Orlando, FL, June 2–5, 1997. Manuscript received by the ASME Headquarters July 1997. Paper No. 97-GT-218. Associate Technical Editor: H. A. Kidd.

Table 1 Fuel properties

fuel no.	class	JFTOT temp., K	total S ppm	dissolved metals, ppb*
3084	Jet-A	541	527	Cu, 35; Fe, <5
3119	Jet-A	(fails)	1000	Cu, 7; Fe, 26
2985	JP-5, Hydrotreated	535 (fails)	233	Cu, 14; Fe, 18
2962	JP-5		438	
2963	JP-5, Cu-Doped	505 (fails)	438	Cu, 98; Fe, 60
2827	Jet-A, Straight Run	539	790	Cu, <5; Fe, 8
2934	JP-8	539	755	Cu, 34; Fe, <5
2747	Jet-A, Hydrotreated	605	37	Cu, <5
2922	Jet-A, Hydrotreated	550	210	Cu, 7; Fe, <5
2976	JPTS	700	<5	

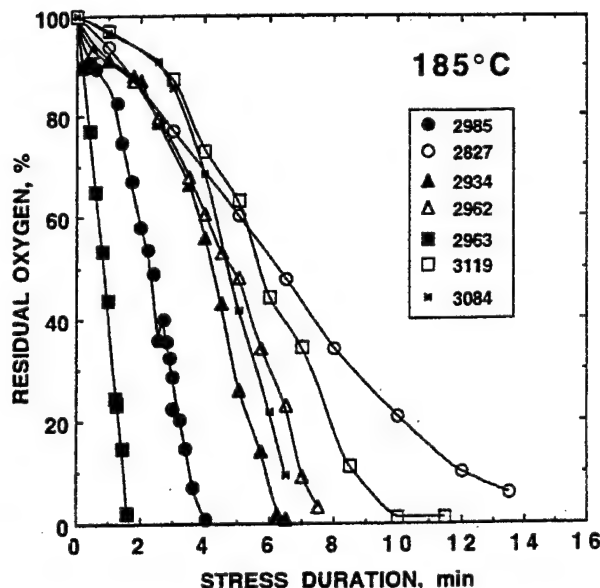
* Measurements made for USAF using graphite furnace Zeeman/5000 System Atomic Absorption Spectrometer by United Technologies, Pratt and Whitney.

Results and Discussion

Autoxidation and Insoluble Formation at 185°C. The disappearance of O₂ as a function of reaction time is given in Fig. 1 for seven of the ten fuels studied. The selected plots include the slowest and fastest oxidizing fuels and, for clarity in presentation, exclude the three most stable fuels. Time required for total reaction ranges from 1.5 min for the copper-doped JP-5 fuel to ~15 min for a straight-run Jet-A fuel. The integrated quantity of surface deposits, given in Fig. 2, shows a strong dependence on autoxidation, based on the fact that deposition occurs primarily during oxidation and becomes negligible soon after O₂ depletion. For example, deposition is complete after 2 and 15 min, respectively, for the two fuels mentioned above, which exhibited the largest difference in autoxidation rates.

The quantity of deposits is dependent on the nature of the fuel, the reaction temperature, and the amount of dissolved O₂ present. No simple dependence on the rate of autoxidation is apparent. Striebich and Rubey (1994) have found that the amount of dissolved O₂ in air-saturated fuel is approximately fuel independent; thus, the total amount of deposits and filterables evaluated for any fuel following complete O₂ conversion can be used as a relative measure of its thermal stability at that temperature (Jones et al., 1995). The quantity of bulk and surface insolubles increases markedly after a five-fold increase in dissolved O₂, as seen in Fig. 3. The higher concentration is obtained by sparging the initial fuel with pure O₂. Similarly, reductions by a factor of ~20 in surface insolubles from POSF-2827 fuel have been reported at this temperature after sparging of the initial fuel with helium (Jones and Balster, 1993).

Insoluble Formation at 225°C. Autoxidation at this temperature occurs too rapidly for measurement by our experimental methods. However, from reported Arrhenius parameters (Pickard and Jones, 1996), the slowest oxidizing fuel (POSF-2827) consumes all dissolved O₂ within 0.5 min. The deposition behavior of the seven selected fuels shown in Fig. 4 indicates two distinct regions. In the first, or major region, deposition occurs rapidly during the initial minute of stressing and corresponds to the time associated with O₂ depletion; this region encompasses the time needed for the fuel to achieve isothermal

Fig. 1 Depletion of dissolved O₂ at 185°C in air-saturated fuels

reaction conditions. In the second, or post-oxidation region, deposition occurs much more slowly and is negligible at 185°C. We attribute the first primarily to fast autoxidation reactions and the second to slow agglomeration of small particles coming out of solution.

Relative Comparison of Fuel Thermal Stability at 185 and 225°C. The integrated quantity of surface and bulk insolubles for the 10 fuels studied is summarized in Figs. 5(a) and 5(b) for reaction at 185 and 225°C, respectively. Fuels having the lowest thermal stability at 185°C (namely, POSF-3119, -3084, -2827, and -2934) also have the highest concentration of sulfur (see Table 1). Fuels containing many components having heteroatoms such as sulfur, nitrogen, and oxygen have lower thermal stability (Hazlett, 1991). This arises because such components are frequently aromatic and react during autoxidation to form polar products having reduced solubility. Sulfur-containing components are well known as inhibitors because of their ability to destroy hydroperoxides (ROOH) and, thereby, reduce self-initiation. The destruction of ROOH has been implicated in insoluble formation in kerosenes by Kendall and Mills (1986) and in jet-fuel blends by Jones et al. (1996a).

The large differences in thermal stability observed at 185°C are not apparent at 225°C. At the higher temperature all of the fuels, with the exception of JPTS, form similar quantities of insolubles within an experimental range of ± 0.5 $\mu\text{g/mL}$. The thermal stability of the more stable fuels does not change significantly with increasing temperature. However, that of the less stable fuels is relatively improved as the temperature increases. The data presented are consistent with autoxidation processes as the source of insolubles. This view is further supported by the fact that the copper-doped fuel, POSF-2963, forms surface deposits much faster than its undoped complement, POSF-2962,

Nomenclature

JFTOT = jet-fuel thermal-oxidation test
JPTS = thermally stable jet fuel
Jet-A = commercial kerosene fuel

JP-8 = kerosene fuel with additive package consisting of icing inhibitor, static-charge dissipator, and corrosion inhibitor
JP-5 = high-flash-point kerosene
NIFTR = near-isothermal flowing test rig

POSF = jet-fuel designation, see Table 1
QCM = quartz crystal microbalance
USAF = United States Air Force
8Q405 = proprietary dispersant from Betz Laboratories

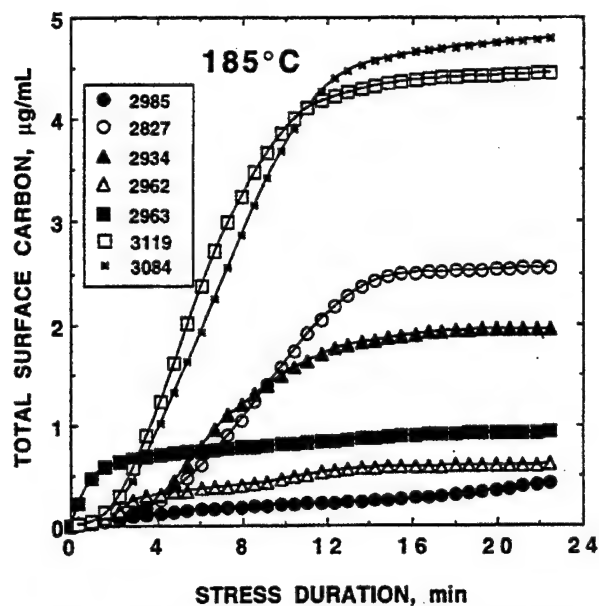


Fig. 2 Total surface deposition at 185°C in air-saturated fuels

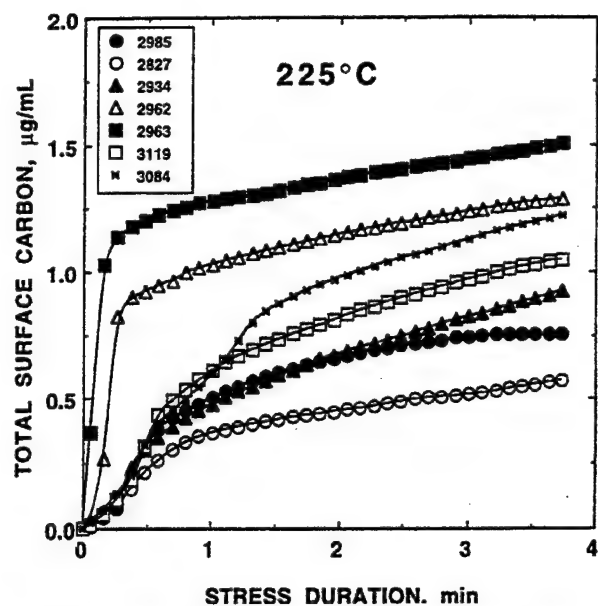


Fig. 4 Total surface deposition at 225°C in air-saturated fuels

or any of the other fuels. This can occur only as a result of the well-known catalytic role of metal cations in accelerating autoxidation by dissociating ROOH (Pedersen, 1949). Thus, any explanation of thermal-stability changes must involve ROOH and free-radical chemistry.

Effect of Dissolved Oxygen at 225°C. Considering the relatively small quantity of insolubles measured, it is important to investigate the importance of dissolved O_2 at 225°C. We have conducted tests after the initial fuel has been sparged with N_2 for 30 min. O_2 measurements under these conditions indicated ~15 percent of the air-saturated value. The deposition behavior of N_2 -sparged fuels is given in Fig. 6. Despite the large reduction in dissolved O_2 , the corresponding total insolubles were reduced

on an average only to 61 percent of the air-saturated values, with a mean deviation of 17 percent. The greatest observed reduction to 37 percent of the air-saturated value occurred for POSF-2934 and the least to 81 percent occurred for POSF-2962.

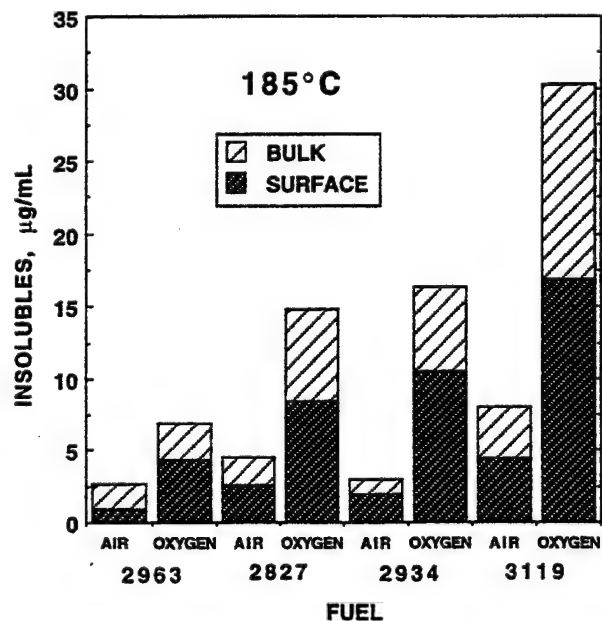


Fig. 3 Effect of dissolved O_2 on insolubles at 185°C

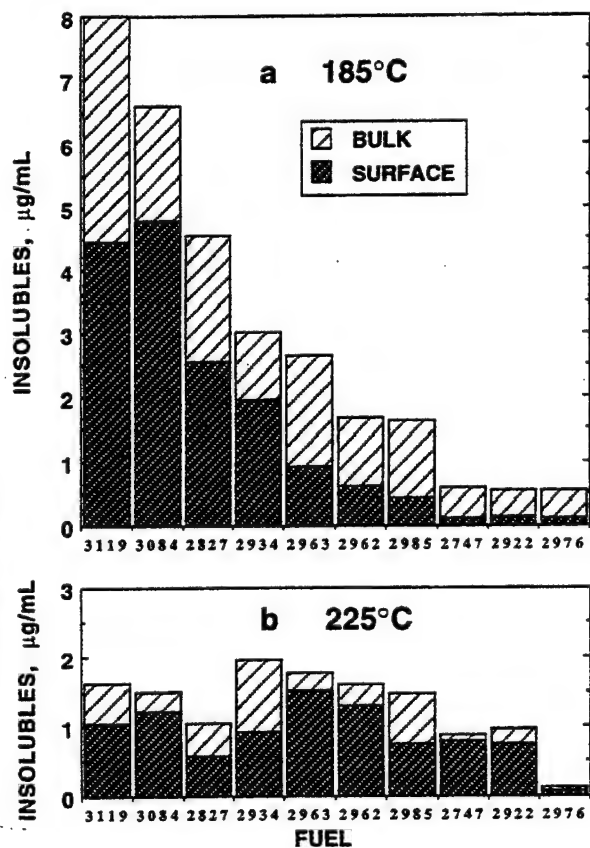


Fig. 5 Quantity of bulk and surface insolubles at 185 and 225°C

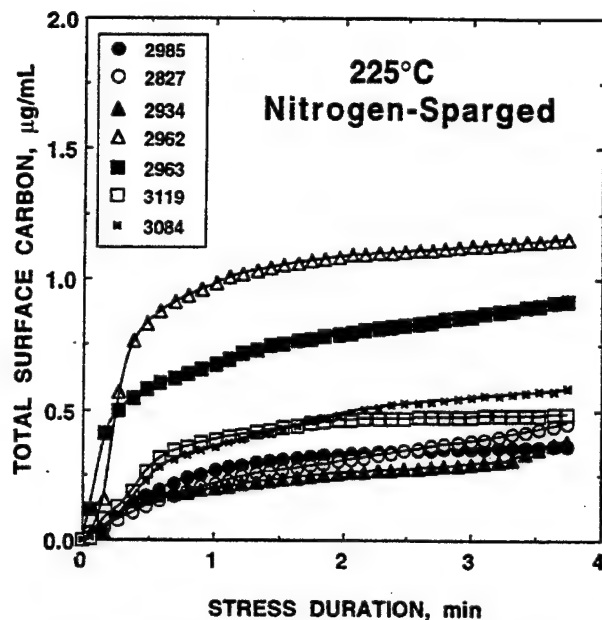


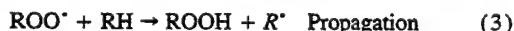
Fig. 6 Total surface deposition at 225°C in N_2 -sparged fuel

The dependence of total bulk and surface insolubles on dissolved O_2 is given in Fig. 7 for four fuels, including data for O_2 -sparging. It appears that for all of these fuels, some small amount of insolubles (on the order of 1 $\mu\text{g/mL}$) is formed—even under conditions of reduced O_2 . Taylor and co-workers in a series of papers (Taylor, 1974; Taylor, 1976; Taylor and Frankenfeld, 1978; Frankenfeld and Taylor, 1980) have addressed the effects of deoxygenation on deposition in fuels. The suppression of deposits by deoxygenation was found to vary considerably among fuels and was found to depend on the distribution of trace sulfur, nitrogen, and oxygen-containing components.

Deoxygenation and its ramifications are beyond the scope of this study, but some comments can be made based on the current results. First, most of the deposition involving N_2 -sparged or air-saturated fuel occurs primarily during oxidation and declines following O_2 depletion (see Figs. 4 and 6). This suggests that all deposition in the autoxidative region ($<300^\circ\text{C}$) requires the presence of some O_2 . The deoxygenation observations are explained according to the following reaction scheme:



Case 1. Sufficient O_2 (air-saturated; conventional autoxidation).



Case 2. Limited O_2 (N_2 -sparged).



Free radicals are first formed in the initiation reactions (1) and (5). In Case 1 (air-saturated fuel), insolubles from lesser quality fuels originate from the interaction of early autoxidation products such as peroxy radicals, ROO' , and $ROOH$ with polar fuel components as in reaction (6). The small amount of insolubles formed from hydrotreated fuels probably does not originate

from reaction (6) but rather from polar oxidation products. In Case 2 (N_2 -sparged fuel), some O_2 is necessary for the initiation reaction (1); but at such low O_2 concentrations, the initial free radicals do not undergo propagation reactions (2) and (3) to form ROO' and $ROOH$. They can, however, react with olefins in free-radical polymerization to produce insoluble oligomers that may contribute to surface fouling. Such polymerization reactions would not be significant at higher O_2 concentrations because O_2 serves as a polymerization inhibitor (Vollmert, 1973).

Possible Explanation of Dependence of Thermal Stability on Temperature. Two primary effects are proposed to account for the observed temperature dependence. The first is a chemical effect related to the least stable oxidation product, $ROOH$. Autoxidation in hydrotreated fuels is very similar to that in pure hydrocarbons and is dominated by the formation of $ROOH$, as in reactions (1)–(5). Because hydrotreatment removes natural antioxidants, hydrotreated or specialty fuels require the addition of synthetic antioxidants such as hindered phenols or phenylenediamines to improve storage stability (Turner et al., 1988). The absence of natural inhibitors in hydrotreated fuels reduces the importance of reaction (6), and only small quantities of insolubles are formed, as evidenced by the behavior of the treated fuels POSF-2747, -2922, and -2976. The lesser-quality fuels having heteroatom impurities such as sulfur react with ROO' and $ROOH$, slowing autoxidation and leading ultimately to insolubles. At higher temperatures, the homolysis reaction (5), dissociation of $ROOH$ on hot stainless-steel surfaces (Jones et al., 1996b), and other oxidation processes can compete with reaction (6), thereby limiting the quantity of insolubles. For hydrotreated fuels in which reaction (6) is not important, similar temperature effects would not be expected.

The second effect is a physical one, relating to the solubility and agglomeration of polar autoxidation products. Solubility is expected to increase with temperature, consistent with the current observations of reduced insolubles. The importance of agglomeration in deposition is demonstrated by observed reductions in insolubles with the use of detergent/dispersant additives at 140°C (Zabarnick and Grinstead, 1994) and at 185°C (Jones and Balster, 1995). There was, approximately, a 50 percent reduction observed using the dispersant additive 8Q405 at

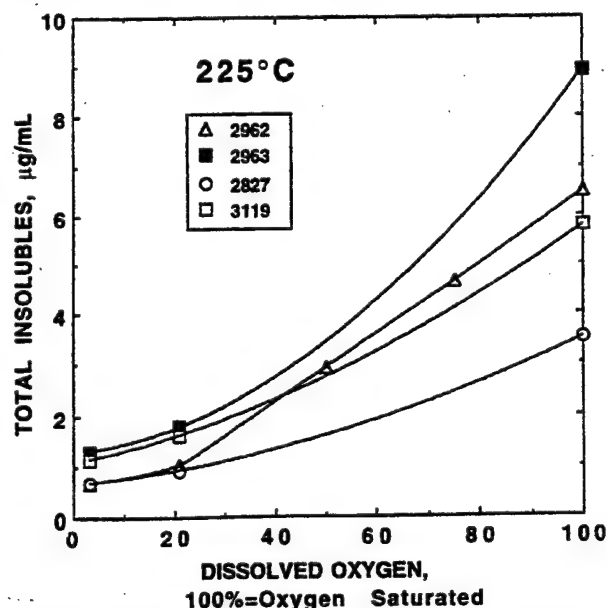


Fig. 7 Dependence of total insolubles on dissolved O_2 at 225°C

Table 2 Effect of 8Q405 (100 mg/L) at 225°C

fuel no.	surface, µg/mL	bulk, µg/mL	total, µg/mL
2963	1.50	0.27*	1.77*
2963, treated	0.80	0*	0.80*
2962	1.29	0.31	1.60
2962, treated	0.65	0.47	1.12
2827	0.57	0.46	1.03
2827, treated	0.29	0.28	0.57

* Correction made for inherent bulk insolubles.

185°C for fuels POSF-2827, -2934, -2980, -3084, and -3119. We have also studied 8Q405 at 225°C; the results, given in Table 2, indicate similar reductions at the higher temperature.

Summary and Conclusions

The formation of surface insolubles at 185 and 225°C is found to occur predominantly during O₂ depletion and is attributed to autoxidation reaction products. At 225°C, an increase in the dissolved O₂ results in a corresponding increase in insolubles; however, reducing dissolved O₂ to 15 percent of the air-saturated value effects only slight reductions. It is argued in the latter case that some small amount of O₂ is needed for free-radical initiation, but the mechanism of surface fouling under deoxygenation switches from autoxidation to free-radical polymerization. This situation is not anticipated to occur under normal fuel conditions unless deoxygenation efforts are made.

In cases where all dissolved O₂ is consumed, we find that a broad range of fuels produces 0.3–7.5 µg/mL of surface insolubles at 185°C and 0.1–2 µg/mL at 225°C. The inverse dependence on temperature occurs for fuels having lower thermal stability, and it is attributed to reduced steady-state concentrations of ROOH and increased solubility at the higher temperatures. This has implications for ranking fuels based on the relative quantity of insolubles measured isothermally. It would appear that quantification of insolubles at 225°C does not provide a sufficient dynamic range of either bulk or surface insolubles for identifying unstable fuels. Because of demonstrated ability to flag unstable fuels and to quantify the effectiveness of additives, lower-temperature isothermal methods such as the QCM at 140°C (Zabarnick and Grinstead, 1994) and the NIFTR at 185°C (Jones and Balster, 1995) are preferred.

Acknowledgment

The authors would like to acknowledge Ms. L. Balster for conducting the O₂ depletion experiments and Mrs. M. Whitaker for editorial assistance. This work was funded by Wright Laboratory, Aero Propulsion and Power Directorate, Wright-Pat-

erson Air Force Base, Ohio, under USAF Contract No. F33615-95-C-2507 and by the Air Force Office of Scientific Research.

References

- Edwards, T., Anderson, S. D., Pearce, J. A., and Harrison, W. E., 1992, "High Temperature Thermally Stable JP Fuels—An Overview," AIAA Paper 92-0683. Presented at the AIAA 30th Aerospace Sciences Meeting and Exhibit, 6–9 January, Reno, NV.
- Frankenfeld, J. W., and Taylor, W. F., 1980, "Deposit Formation from Deoxygenated Hydrocarbons, 4, Studies in Pure Compound Systems," *Industrial and Engineering Chemistry Product Research and Development*, Vol. 19, pp. 65–70.
- Hazlett, R. N., 1991, *Thermal Oxidation Stability of Aviation Turbine Fuels*, ASTM Monograph 1, American Society for Testing and Materials, Philadelphia, PA.
- Heneghan, S. P., and Zabarnick, S., 1994, "Oxidation of Jet Fuels and the Formation of Deposits," *Fuel*, Vol. 73, pp. 35–43.
- Jones, E. G., and Balster, W. J., 1993, "Phenomenological Study of the Formation of Insolubles in a Jet-A Fuel," *Energy and Fuels*, Vol. 7, pp. 968–977.
- Jones, E. G., and Balster, W. J., 1994, "Formation of Insolubles in a Jet-A Fuel: Temperature Effects," *Preprints-American Chemical Society, Division of Petroleum Chemistry*, Vol. 39, pp. 78–81.
- Jones, E. G., and Balster, W. J., 1995, "Surface Fouling in Aviation Fuel: Short vs. Long-Term Isothermal Tests," *Energy and Fuels*, Vol. 9, pp. 610–615.
- Jones, E. G., Balster, L. M., and Balster, W. J., 1995, "Quantitative Evaluation of Jet-Fuel Fouling and the Effect of Additives," *Energy and Fuels*, Vol. 9, pp. 906–912.
- Jones, E. G., Balster, L. M., and Balster, W. J., 1996a, "Thermal Stability of Jet-A Fuel Blends," *Energy and Fuels*, Vol. 10, pp. 509–515.
- Jones, E. G., Balster, L. M., and Balster, W. J., 1996b, "Autoxidation of Aviation Fuels in Heated Tubes: Surface Effects," *Energy and Fuels*, Vol. 10, pp. 831–836.
- Kendall, D. R., and Mills, J. S., 1986, "Thermal Stability of Aviation Kerosenes: Techniques to Characterize Their Oxidation Properties," *Industrial and Engineering Chemistry Product Research and Development*, Vol. 25, pp. 360–366.
- Pickard, J. M., and Jones, E. G., 1996, "Kinetics of the Autoxidation of a Jet-A Fuel," *Energy and Fuels*, Vol. 10, pp. 1074–1077.
- Pedersen, C. J., 1949, "Inhibition of Deterioration of Cracked Gasoline during Storage," *Industrial and Engineering Chemistry*, Vol. 41, pp. 924–928.
- Rubey, W. A., Striebig, R. C., Tissandier, M. D., Tirey, D. A., and Anderson, S. D., 1995, "Gas Chromatographic Measurement of Trace Oxygen and Other Dissolved Gases in Thermally Stressed Jet Fuel," *Journal of Chromatographic Science*, Vol. 33, pp. 433–437.
- Striebig, R. C., and Rubey, W. A., 1994, "Analytical Method for the Detection of Dissolved Oxygen," *Preprints-American Chemical Society, Division of Petroleum Chemistry*, Vol. 39, pp. 47–50.
- Taylor, W. F., 1974, "Deposit Formation from Deoxygenated Hydrocarbons, 1, General Features," *Industrial and Engineering Chemistry Product Research and Development*, Vol. 13, pp. 133–138.
- Taylor, W. F., 1976, "Deposit Formation from Deoxygenated Hydrocarbons, 2, Effect of Trace Sulfur Compounds," *Industrial and Engineering Chemistry Product Research and Development*, Vol. 15, pp. 64–68.
- Taylor, W. F., and Frankenfeld, J. W., 1978, "Deposit Formation from Deoxygenated Hydrocarbons, 3, Effects of Trace Nitrogen and Oxygen Compounds," *Industrial and Engineering Chemistry Product Research and Development*, Vol. 17, pp. 86–90.
- Turner, L. M., Kamin, R. A., Nowack, C. J., and Speck, G. E., 1988, "Effect of Peroxide Content on the Thermal Stability of Hydrocracked Aviation Fuel," *Proceedings of 3rd International Conference on Stability and Handling of Liquid Fuels*, Institute of Petroleum, London, pp. 338–349.
- Vollmert, B., 1973, *Polymer Chemistry*, Springer-Verlag, New York, NY, p. 62.
- Zabarnick, S., and Grinstead, R. R., 1994, "Studies of Jet Fuel Additives Using the Quartz Crystal Microbalance and Pressure Monitoring at 140°C," *Industrial and Engineering Chemistry Research*, Vol. 33, pp. 2771–2777.

3.2.2.2 Kinetics. The kinetics of the autoxidation of a Jet-A fuel were studied, and the results are reported in the paper entitled "Kinetics of the Autoxidation of a Jet-A Fuel," which was co-authored by J. M. Pickard (Kinetica, Inc.) and E. G. Jones and published in Energy and Fuels, Vol. 10, pp. 1074-1077 (1996). Inferences from the derived kinetic parameters suggest that initiation involves H-atom abstraction from either a vinyl or an aromatic fuel species. Results of experiments on the depletion of oxygen in air-saturated Jet-A fuel containing Fe_2O_3 were reported in the publication entitled "Catalysis of Jet-A Fuel Autoxidation by Fe_2O_3 ," which was co-authored by J. M. Pickard (Kinetica, Inc.) and E. G. Jones and published in Energy and Fuels, Vol. 11, pp. 1232-1236 (1997). Analysis of the surface insolubles for neat and doped fuel indicates that both the maximum and the magnitude of the surface deposition decrease for the Fe_2O_3 catalysis of the autoxidation and suggests that precursors for surface deposition are scavenged by Fe_2O_3 particles. The kinetics of oxygen depletion in an air-saturated paraffin blend were studied and the results reported in the paper entitled "Liquid-Phase Oxidation Kinetics: Paraffin Blends," which was co-authored by J. M. Pickard (Kinetica, Inc.) and E. G. Jones and published in Energy and Fuels, Vol. 12, pp. 1241-1244 (1998). The results are discussed with reference to kinetic parameters reported for conventional aviation fuels.

3.2.2.3 Fuel Blends. The potential impact on thermal stability of adding or blending secondary fuels was studied, and the results are reported in the paper entitled "Thermal Stability of Jet-A Fuel Blends," which was co-authored by E. G. Jones, L. M. Balster, and W. J. Balster and published in *Energy and Fuels*, Vol. 10, pp. 509-515 (1996).

Measurements of surface fouling in blends selected for their unusually slow oxidation indicate that the thermal stability of fuels can be improved by blending with a paraffinic/cycloparaffinic solvent. In the paper entitled "Autoxidation of Neat and Blended Aviation Fuels" improvements in the thermal stability of 1:1 blends are reported to be comparable to those achieved by introducing conventional fuel additives. This paper, co-authored by E. G. Jones, L. M. Balster, and W. J. Balster, was published in *Energy and Fuels*, Vol. 12, pp. 990-995 (1998). In the publication entitled "Autoxidation of Dilute Jet-Fuel Blends," it is reported that the similarity in the observed behavior of diluted fuels and hydrotreated fuels and the parallel of removing polar species either by dilution or by hydrotreatment led to classification of such diluted fuels as surrogate hydrotreated fuels. This paper, co-authored by E. G. Jones and L. M. Balster, was published in *Energy and Fuels*, Vol. 13, pp. 796-802 (1999).

3.2.2.4 Fuel Recirculation. In modern aircraft, jet fuel--in addition to providing combustion energy--is the major source of cooling for component systems such as the airframe, engine, lubricants, hydraulics, and gear boxes. Cooling applications can subject the fuel to severe thermal oxidative stress prior to combustion, leading to the undesirable buildup of deposits on heat exchangers and other sensitive fuel-line surfaces such as nozzles and servo-controls. In the paper entitled "Aviation Fuel Recirculation and Surface Fouling," the results of a thermal-stress experiment incorporating recirculation are reported. This paper, co-authored by E. G. Jones, W. J. Balster, and L. M. Balster, was published in *Energy and Fuels*, Vol. 11, pp. 1303-1308 (1997). The effects of recirculation (prestressing) for hydrotreated and straight-run fuels are discussed in the publication entitled "Extended Liquid-Phase Oxidation of Aviation Fuels" (see pp. 659-665). It was found that following extended oxidation (prestressing), hydrotreated fuel oxidizes more rapidly than in its neat form, resulting in part from formation of catalytic oxidation products such as hydroperoxides and depletion of synthetic primary antioxidants. In contrast, the straight-run fuel oxidizes more slowly following prestressing; this effect is ascribed to the formation of efficient secondary antioxidants and to depletion of radical initiators.



The Society shall not be responsible for statements or opinions advanced in papers or discussion at meetings of the Society or of its Divisions or Sections, or printed in its publications. Discussion is printed only if the paper is published in an ASME Journal. Authorization to photocopy for internal or personal use is granted to libraries and other users registered with the Copyright Clearance Center (CCC) provided \$3/article is paid to CCC, 222 Rosewood Dr., Danvers, MA 01923. Requests for special permission or bulk reproduction should be addressed to the ASME Technical Publishing Department.

Copyright © 1999 by ASME

All Rights Reserved

Printed in U.S.A.

PUBLISHED WITH PERMISSION

EXTENDED LIQUID-PHASE OXIDATION OF AVIATION FUELS

Lori M. Balster, Walter J. Balster, and E. Grant Jones

Innovative Scientific Solutions, Inc.

2766 Indian Ripple Road

Dayton, Ohio 45440-3638

ABSTRACT

Liquid-phase oxidation of two jet fuels classified as hydro-treated and straight-run (without dissolved metals) is studied at 185°C by measuring the depletion of dissolved oxygen in an isothermal, high-pressure flowing system. The goal is to simulate some of the effects of fuel recirculation by studying changes in oxidation that occur during the course of reaction. Recirculation of fuel is used in modern aircraft to optimize the ability of the fuel to dissipate heat from component systems. Following extended oxidation (prestress), hydrotreated fuel oxidizes more rapidly than in its neat form resulting, in part, from formation of catalytic oxidation products such as hydroperoxides and depletion of synthetic primary antioxidants. In contrast, the straight-run fuel oxidizes more slowly following prestressing; this effect is ascribed to the formation of efficient secondary antioxidants and to depletion of radical initiators. Results are discussed in terms of changes in the distribution of primary and secondary antioxidants and their effect on subsequent oxidation and the thermal stability of recirculated fuel.

NOMENCLATURE

BHT:	2,6-di-tert-butyl-p-cresol
NIFTR:	Near-Isothermal Flowing Test Rig
JFTOT:	Jet-Fuel Thermal-Oxidation Test
JPTS:	Thermally Stable Jet Fuel
Jet-A:	Commercial Kerosene Fuel
JP-8:	Kerosene Fuel with Additive Package Consisting of Icing Inhibitor, Static-Charge Dissipator, and Corrosion Inhibitor
JP-8+100:	JP-8 Fuel Protected by Antioxidant, Metal Deactivator, and Dispersant to Extend the Bulk Operation Temperature by 100°F
JP-5:	High-Flash-Point Kerosene
JP-900:	Future Jet Fuel Thermally Stable to 900°F

POSF: Jet-Fuel Designation
USAF: United States Air Force

INTRODUCTION

Jet or turbine fuel in modern military aircraft serves an important function in addition to providing combustion energy. It is the major source of cooling for subsystems such as the airframe, engine lubricants, hydraulics, and gearboxes (Edwards et al., 1992). This application elevates fuel temperature and, in the presence of dissolved oxygen, results in thermal oxidative stress of the fuel. In turn, reaction products from liquid-phase fuel oxidation can lead to deleterious surface and bulk fuel fouling. As surfaces of heat exchangers, nozzles, and servocontrols become fouled, performance degrades, necessitating expensive downtime for cleaning and replacement.

One potential solution involves slowing liquid-phase oxidation by the introduction of hindered-phenol synthetic antioxidants, thereby reducing the extent of the associated surface fouling. Oxidation of fuels that have not been hydrotreated is also influenced by the natural presence of O-, S- and N-containing species that can also act as antioxidants. These can be either primary antioxidants, which—like synthetic antioxidants—hinder or retard radical propagation by forming stable free radicals, or secondary antioxidants, which destroy the major source of radical initiation (hydroperoxides) without the formation of additional radicals. The former are thought to be H-atom donors such as phenols, thiols, and amines and the latter, mainly S-containing compounds, although their precise identity is not well known in complex fuels. Unfortunately, polar species that are good natural antioxidants have also been identified as playing key roles in surface-fouling processes (Kendall and Mills, 1986; Hazlett, 1991; Jones et al., 1996). Hence, refining processes such as hydrotreatment that reduce the concentration of most polar species greatly improve thermal stability.

Although the introduction of the synthetic antioxidant, BHT, slows oxidation, the overall effect on thermal stability is very fuel dependent. For example, reports by Morris et al. (1988) and Anderson et al. (1994) on several fuels, including POSF-2827, have found no net change in deposition, whereas others have found increased deposition (Jones et al., 1997a; Pande and Hardy, 1998).

Efficient management of on-board fuel includes consideration of combustion and heat-dissipation requirements during all phases of a flight, ranging from the condition of maximum thrust during which fuel is needed mainly for combustion to the condition of idle descent when combustion needs are minimal but heat-dissipation needs are critical. In the latter scenario, fuel may be used repeatedly for cooling by continually returning thermally stressed fuel to on-board fuel tanks. Experiments designed to simulate fuel recirculation have shown that thermal stability, as determined by direct measurements of surface fouling, is degraded for JP-8 fuels (Binns et al., 1995; Dieterle and Binns, 1995; Binns and Dieterle, 1996) and Jet-A fuels (Jones et al., 1997b, 1998a). Jones et al. (1997b) have identified three distinct sources of reduced thermal stability resulting from fuel recirculation: 1) depletion of primary antioxidants, 2) formation of catalytic reaction products (such as hydroperoxides), and 3) formation of deposition precursors.

The goal of the current study was to obtain empirical information related to changes in antioxidant concentration and oxidation that occur during extended oxidation resulting from fuel recirculation. Several reasons can be offered for selecting experimental conditions that allow extended oxidation. First, projections for advanced military aircraft indicate more extensive and aggressive fuel stressing at higher temperatures (Edwards et al. 1997). Second, fuel recirculation results in greater depletion of dissolved O_2 . Finally, future USAF use of JP-900 or endothermic fuels will result in the complete consumption of dissolved O_2 prior to attaining pyrolytic reaction temperatures (Edwards, 1998).

Since large differences have been observed in the oxidation of straight-run and hydrotreated fuels, the behavior of one representative of each fuel type is investigated in the current study. Two approaches are taken for studying the effects of extending oxidation. The first is to measure and compare O_2 depletion using air- and O_2 -saturated fuel. In principle, using fuel saturated with respect to O_2 and allowing the oxidation to proceed to completion, the reaction can be extended by approximately a factor of five over that achieved with air-saturated fuel. The second approach is to prestress fuel (O_2 -saturated) for 22 min at 185°C and then allow it to cool and re-establish saturation with respect to air. The depletion of O_2 in prestressed and in neat fuel can then be compared. If prestressed fuel oxidizes faster or slower than neat fuel, then the overall antioxidant effect has been, respectively, diminished or enhanced by prestressing. In this manner, one can track general changes in overall antioxidant effect and specific changes in primary antioxidants that occur during oxidation.

EXPERIMENTAL ARRANGEMENT

The two aviation fuels selected for study are POSF-2827 (straight-run) and POSF-2747 (hydrotreated). Some pertinent properties of these fuels are summarized in Table 1. Selection of these fuels offers certain distinct advantages. Oxidation is simplified since neither fuel contains detectable levels of Cu. Also, both are representative of their fuel class and have been extensively studied previously in neat and blended forms (Jones et al. 1996a). All experiments were conducted isothermally at 185°C under conditions of laminar flow using the NIFTR single-pass heat exchanger, which has been described previously (Jones et al., 1996). The configuration consisted of a tube (0.318-cm o.d., 0.216-cm i.d.) clamped tightly within a copper block to maintain constant wall temperature. To maintain a single reaction phase with no headspace, all studies were carried out at high pressure (> 2.3 MPa). Autoxidation was studied using a gas-chromatographic technique developed by Rubey et al. (1995) for high-pressure monitoring of O_2 . Depletion of O_2 was tracked as a function of fuel residence time inside a heated tube (0.81 m); to minimize problems from surface catalysis, tubes passivated by the Silcosteel process (Restek Corp.) were used. Residence times were varied by changing the flowrate. Exxsol D-110 obtained from Exxon Corporation was used as a paraffinic diluent for dilution experiments; it contains $< 1\%$ aromatics and no synthetic antioxidants. The concentration of hydroperoxides measured using the technique of Kauffman (1994) is less than 0.03 mM.

In fouling studies fuel was pumped at a constant flowrate of 0.25 mL/min through a 1.8-m heated tube. After the 72-hr test period, the heated tube was cut into 5.1-cm segments. Tubes were then rinsed with heptane, treated for more than 12 hr at 130°C in a vacuum oven, and subjected to conventional surface-carbon burnoff (LECO RC 412). Reaction time associated with each segment was calculated from tubing dimensions and flowrate, assuming plug flow. A flowrate of 0.25 mL/min provides ~ 22 min of isothermal stressing at 185°C. Data are presented as the total integrated sum of surface carbon (in units of micrograms per milliliter) as a function of stress duration. This quantity reproduces within 20%; the minimum detectable amount is estimated to be 0.1 $\mu\text{g/mL}$. Prestressing was achieved by passing O_2 -saturated fuel at a flow rate of 0.25 mL/min through a 1.8-m tube resulting in 22 min of stressing. The conditions of air- and O_2 -saturated fuel were achieved by initially sparging each fuel with air and O_2 , respectively, prior to filling the syringe pumps.

RESULTS AND DISCUSSION

Liquid-Phase Oxidation and Surface Fouling at 185°C

The disappearance of O_2 and the increase in total surface insolubles as a function of reaction time are given in Fig. 1 for the two fuel types. Representative of hydrotreated fuels, POSF-2747 oxidizes rapidly and has exceptional thermal stability, as

Table 1. Fuel Properties

	POSF-2747	POSF-2827
type	Jet-A-1	Jet-A
treatment	hydrotreated	straight run
JFTOT breakpoint (°C)	332	266
total sulfur (%)	0.004	0.079
mercaptan sulfur (%)	0.000	0.001
Cu (ppb)	<5	<5

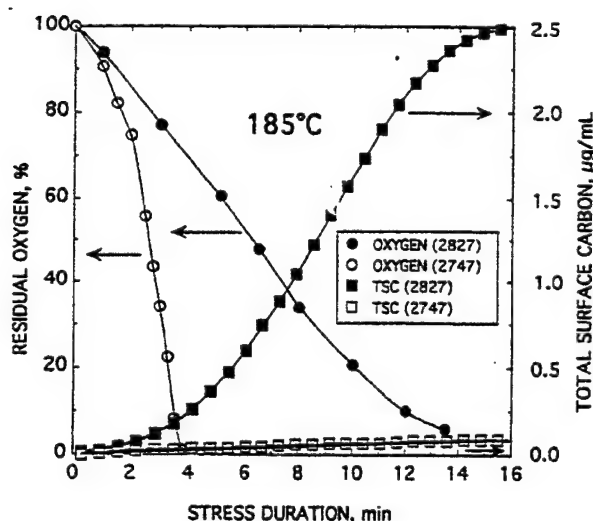


Fig. 1 Depletion of Dissolved Oxygen and Total Surface Deposition at 185°C Measured in Air-Saturated Fuels.

evidenced by total surface deposits $< 0.2 \mu\text{g/mL}$. The small delay time in oxidation arises from the introduction at the refinery of a hindered-phenol antioxidant to improve storage stability. Typically, BHT is added at concentrations up to 14 mg/L (Martel, 1987.) After depletion of some BHT, the concentration of hydroperoxides (ROOH) increases, and the reaction becomes, by definition, autocatalytic. Representative of straight-run fuels that do not contain metals, POSF-2827 oxidizes more slowly and has reduced thermal stability due to the presence of natural antioxidants. An excess of these natural antioxidants prevents the oxidation from becoming autocatalytic. In the following sections we discuss changes in these oxidation profiles resulting from increased concentration of dissolved O_2 and also from prestressing.

Effects of Increased Dissolved O_2

Hydrotreated Fuel. The O_2 -depletion results for air- and O_2 -saturated fuels are represented in Fig. 2 by the open symbols.

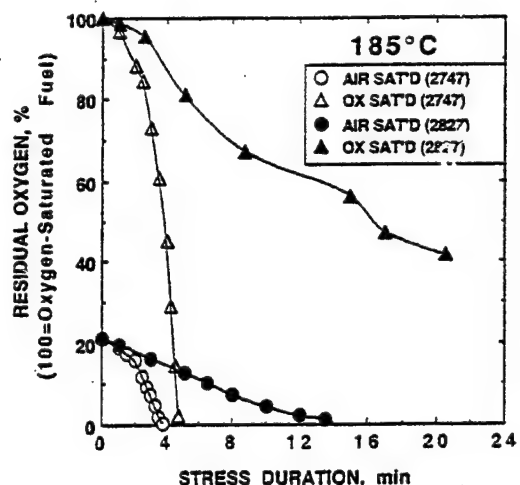


Fig. 2 Depletion of Dissolved Oxygen at 185°C Measured in Air- and Oxygen-Saturated Fuels.

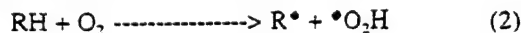
The oxidation behavior of POSF-2747 fuel is approximately independent of initial O_2 concentration. Again, once the synthetic antioxidant concentration is reduced, the oxidation rate accelerates. Because of the higher conversion of O_2 into ROOH, the rate of thermal initiation associated with reaction (1) increases



and the overall oxidation rate accelerates, as apparent in Fig. 2. This behavior is common in hydrotreated fuels, and very similar behavior has been reported for the JPTS fuel POSF-2976 (Jones and Balster, 1997) and the paraffinic/cycloparaffinic solvent Exxsol D-80 (Pickard and Jones, 1998). The thermal dissociation reaction (1) can be enhanced by additional contributions from metal ions, free radicals, or other molecules that can induce dissociation. Clearly, for hydrotreated fuels in which oxidation is dominated by ROOH, additional conversion associated with prestressing can greatly influence subsequent oxida-

tion. The major effects are depletion of synthetic antioxidants and the production of catalytic products such as ROOH.

Straight-Run Fuel. The oxidation results are represented by the closed symbols in Fig. 2. With increased initial O_2 , the initial rate of oxidation increases. Kinetic studies of this fuel (Pickard and Jones, 1996) have shown that the reaction order is 0.5 in O_2 . Initiation by a process such as reaction (2) or (3)



has been proposed for hydrocarbon initiation consistent with the observed 0.5 order in O_2 (Benson, 1976; Carlsson and Robb, 1966). It has been shown that the concentration of ROOH does not increase significantly in POSF-2827 (Jones et al., 1996). The exact reason for this is not well understood because peroxy radicals and presumably hydroperoxides could be generated following reaction (2) or (3). We have argued that secondary, or ROOH-decomposing, antioxidants prevent the increase in ROOH concentration (Jones et al., 1996). In either case, the contribution to initiation from reaction (1) is negligible and, hence, autocatalysis is not observed. The reaction rate slows at longer times and approaches that observed for air-saturated fuel. This behavior is consistent with a reduced concentration of initiating species O_2 or RH in reaction (2) or (3). Systems in which the rate slows with conversion may also be indicative of the formation of reaction products that can act as antioxidants, i.e., auto-inhibition. Similar auto-inhibition has been reported for POSF-3084—another straight-run fuel with added complexity from dissolved Cu (Jones et al., 1998b).

Effects of Prestressing

In our earlier study (Jones et al., 1997b) directed at thermal-stability measurements, realistic simulations of recirculation clearly demonstrated that prestressing is detrimental to thermal stability for POSF-2827 fuel. For exactly the same reasons it is presumed to be true for POSF-2747. Unfortunately, the complexity of the experimental configuration in the earlier study imposed serious limitations on simple measurements of O_2 depletion. The current study was designed to track detailed oxidation changes: it involves aggressive prestressing in order to exaggerate rather than to represent actual changes caused by fuel recirculation. One unfortunate consequence is the preclusion of meaningful experimental estimates of surface fouling from fuel prestressed to this extent.

Hydrotreated Fuel. Figure 3 (open symbols) illustrates differences in the oxidation of neat and prestressed air-saturated fuels. As mentioned above, both depletion of synthetic antioxidant and formation of catalytic reaction products such as ROOH that occur during oxidation are important considerations in recirculation of hydrotreated fuels. The reduced time necessary for complete O_2 consumption from 4 min in neat fuel to ~1 min in prestressed fuel attests to the complete consumption of synthetic primary antioxidants during prestressing. Without

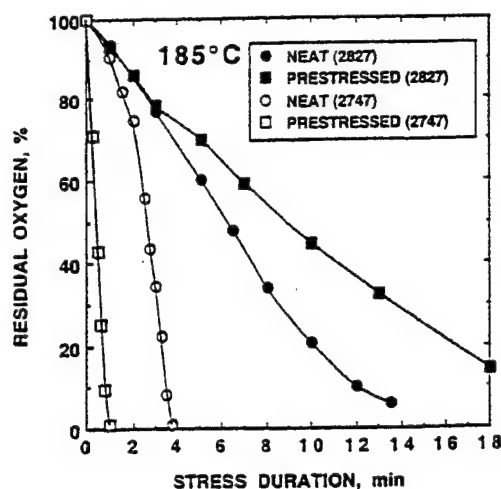


Fig. 3 Depletion of Dissolved Oxygen at 185°C Measured in Neat and Prestressed Air-Saturated Fuels.

any antioxidant protection and in the presence of ROOH (formed during prestressing), oxidation of prestressed fuel is extremely rapid and very similar to oxidation of simple hydrocarbons in which reaction (1) dominates radical initiation.

Recently we have used a dilution method as a means of estimating relative primary-antioxidant concentration (Jones and Balster, 1998). The rationale for use of this technique is that tenfold dilution of a jet fuel by a paraffinic solvent is equivalent to introducing one-tenth of the existing primary antioxidants into a paraffin. Dilution greatly simplifies oxidation because other species that influence oxidation by undergoing collision with ROOH are less important as a result of reduced concentration. Included are secondary antioxidants and dissolved metals. This technique is important in simplifying the oxidation of complex fuels by forcing them to oxidize in the same way as hydrotreated fuels but is less valuable when applied to hydrotreated fuels such as POSF-2747. Both dilution and prestressing reduce primary antioxidants to very low levels; as a result, combination of the two techniques essentially robs the fuel of antioxidant protection, as apparent in Fig. 4 for POSF-2747. Diluting prestressed fuel also serves to reduce the concentration of initiators (ROOH) in subsequent oxidation. Obviously, without antioxidant protection, the potential exists for rapid formation of hydroperoxides, negating the importance of previously formed initiators.

Straight-Run Fuel. As apparent in Fig. 3 and as suggested above with O_2 saturation, oxidation of prestressed fuel occurs at a slower rate than that of the neat fuel. A reduced concentration of radical initiators specific to reaction (1) or (2) may account for this effect. Studies of Balster et al. (1996) offered a similar explanation for slowed oxidation following the addition of small amounts of a paraffin to POSF-2827 fuel. Another possible explanation is the formation of antioxidants during oxidation,

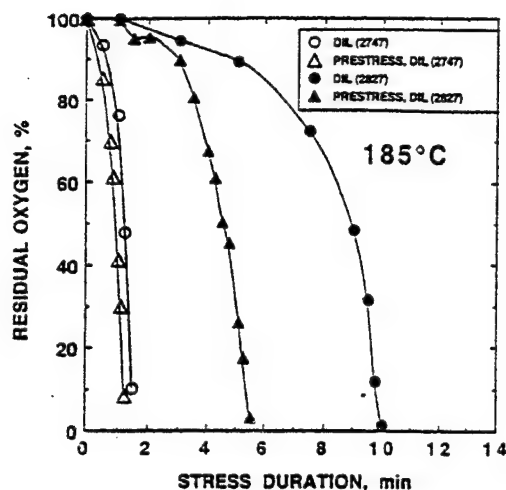


Fig. 4 Depletion of Dissolved Oxygen at 185°C Measured in Neat and Prestressed Fuels Following Tenfold Dilution with Exxsol D-110.

i.e., auto-inhibition. Considerable evidence exists in the literature of flask-test oxidation for secondary and tertiary oxidation products acting as antioxidants (Bol'shakov, 1974). For example, a strong acid or SO_2 can slow the reaction rate at higher O_2 conversion by catalytically decomposing ROOH without the formation of additional free radicals, i.e., efficient secondary antioxidants (Bridgewater and Sexton, 1977). The acid-catalyzed reaction of hydroperoxides generates an alcohol and a ketone; in the case of aromatic hydroperoxides, this same reaction yields phenols that when hindered are effective primary antioxidants. We cannot determine from Figs. 2 and 3 whether the observed inhibition occurring at extended conversion is due to the formation of primary or of secondary antioxidants.

The oxidation results following dilution with a paraffinic solvent, as shown in Fig. 4, do not indicate the presence of additional primary antioxidants as a result of prestressing. In fact, the primary-antioxidant effect has been clearly diminished. Unlike the hydrotreated fuel which experiences complete dissipation of primary antioxidants, the straight-run fuel still contains primary antioxidants but at reduced concentrations. An estimate of the residual antioxidant effect can be made by comparing the time delay necessary to achieve 50% depletion of dissolved O_2 in diluted prestressed fuel (~4.5 min) with that measured for a series of dilute blends of neat POSF-2827 fuel in the same paraffinic solvent. Utilizing the calibration plot in Fig. 5, we can estimate that approximately one-half of the primary antioxidant function has been lost as a result of prestressing. This finding supports the argument that the formation of secondary antioxidants during extended oxidation is responsible for the major changes in oxidation of prestressed fuel. The possible formation of phenols is obviously more than

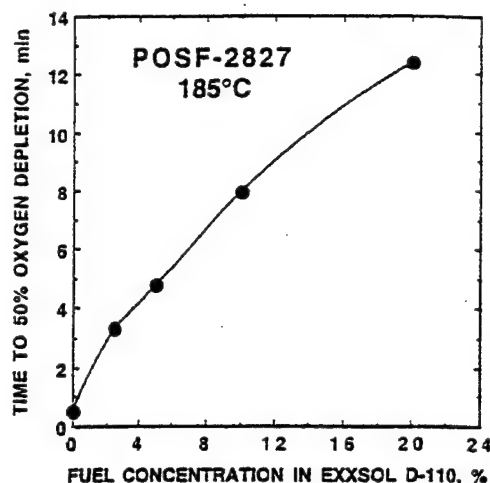


Fig. 5 Delay in Oxidation of Dilute Blends of POSF-2827 in Exxsol D-110. Delay is time to 50% Conversion of Oxygen at 185°C.

offset by depletion of other primary antioxidants during prestressing.

Implications to Recirculation of Jet Fuels

The current results have some important implications for oxidation of aviation fuels. First, the fact that primary or radical chain-terminating antioxidants are depleted in both hydrotreated and straight-run fuels during prestressing indicates that introduction of additional synthetic antioxidants may reduce the extent of oxidation. The JP-8+100 program initiated by the USAF utilizes the combined benefits of antioxidant (BHT), metal deactivator (MDA), and detergent/dispersant (Betz 8Q405) to improve thermal stability (Heneghan et al., 1996). The current results support our previous findings that additives that may be depleted during stressing associated with fuel recirculation should be introduced at higher concentrations (Jones et al., 1997b, 1998a). It is doubtful that fuels containing less than 100 ppb of dissolved metals will benefit from increasing the MDA concentration above 2 mg/L.

A related consequence of primary-antioxidant depletion is the formation and buildup of hydroperoxides that are known to attack polymeric O-rings and other fuel-tank sealants—a problem that is more serious when using hydrotreated fuels (Martel, 1987) and fuels with high Cu contamination (Pande and Hardy, 1997). These problems can also be solved by the early introduction of higher concentrations of synthetic primary antioxidant and MDA, respectively, for applications where significant fuel recirculation occurs.

The presence of hydroperoxides provides the major source of initiation for autoxidation. Because of the weak O-O bond, hydroperoxides that survive after the complete consumption of

O₂ also provide a lower temperature source of free radicals to participate in polymerization reactions associated with pyrolysis. The consequences of autoxidative reactions to subsequent pyrolysis are not simple. Edwards and Liberio (1994) have investigated surface and bulk fouling for fuels that have been N₂-sparged in order to reduce initial O₂ concentration. They have reported increased bulk fouling but decreased surface fouling in the pyrolytic regime.

SUMMARY AND CONCLUSIONS

Oxidation of two distinct classes of fuels (hydrotreated and straight-run) in the neat form and also following extended prestressing has been investigated to assess the impact of recirculating aviation fuels for efficient fuel management upon the rate of fuel oxidation. The hydrotreated fuel is found to experience detrimental acceleration in liquid-phase oxidation as a result of prestressing, the major reasons being formation of catalytic reaction products in the form of hydroperoxides and the depletion of synthetic antioxidants. The overall effect of these findings relative to surface fouling in the autoxidative regime may be negligible because of the high thermal stability of hydrotreated fuels; however, the role of hydroperoxides in radical initiation at higher temperatures may be more important. Because of the simplified oxidation of hydrotreated fuels, it is concluded that the observed behavior of POSF-2747 is representative of all hydrotreated fuels, including JPTS.

The straight-run fuel is found to oxidize more slowly following prestressing. On the basis of fuel-dilution experiments, this additional complication to oxidation has been ascribed to the formation of efficient secondary antioxidants and to depletion of radical initiators rather than formation of new primary antioxidants. From the standpoint of oxidation, recirculation of straight-run fuels that do not contain dissolved metals presents no problem. Although the behavior of POSF-2827 may be representative of a class of straight-run fuels, the oxidation of metal-containing fuels offers additional complexity that is not apparent in the current tests. From the standpoint of thermal stability or the tendency to foul surfaces, earlier studies of surface fouling for this fuel and other Cu-containing fuels have identified problems with precursor formation during stressing that are associated with fuel recirculation (Jones et al., 1997b).

Since both the hydrotreated and straight-run fuels used in this study exhibit loss of primary antioxidants, the oxidation of recirculated or prestressed fuel would be slowed by antioxidant replenishment. Thus, fuels protected by the JP-8+100 or similar additive packages may benefit from increased additive concentrations to offset the additional stressing associated with fuel recirculation.

ACKNOWLEDGMENT

This work was funded by Air Force Research Laboratory, Propulsion Directorate, Wright-Patterson AFB, OH, and the Air Force Office of Scientific Research under USAF Contract No. F33615-95-C-2507. The authors would like to acknowledge Mrs. Marian Whitaker for editorial assistance.

REFERENCES

- Anderson, S. D.; Jones, E. G.; Goss, L. P.; Balster, W. J., 1995, "Effect of Additives on the Formation of Insolubles in a Jet Fuel," in *Proceedings of the 5th International Conference on Stability and Handling of Liquid Fuels*; Giles, H. N., Ed.; U. S. Department of Energy: Washington, D. C., Vol. 1, pp 291-301.
- Balster, L. M.; Balster, W. J.; Jones, E. G., 1996, "Thermal Stability of Jet-Fuel/Paraffin Blends," *Energy Fuels*, 10, pp 1176-1180.
- Benson, S. W., *Thermochemical Kinetics*; Wiley: New York, 1976, p 239.
- Binns, K. E.; Dieterle, G. L.; Williams, T., 1995, "System Evaluation of Improved Thermal Stability Jet Fuels," in *Proceedings of the 5th International Conference on Stability and Handling of Liquid Fuels*; Giles, H. N., Ed.; U. S. Department of Energy: Washington, D. C., Vol. 1, pp 407-422.
- Binns, K. E.; Dieterle, G. L., 1996, "Evaluation of the JP-8+100 Additive Candidates in the Extended Duration Thermal Stability Test System," *Prepr.-Am. Chem. Soc., Div. Pet. Chem.*, 41 (2), pp 457-460.
- Bol'shakov, G. F., 1974, "The Physico-Chemical Principles of the Formation of Deposits in Jet Fuels," FTM-MT-24-416-74; Foreign Technology Division, Air Force Systems Command: Wright-Patterson AFB, OH, 8 April, Chapter 1.
- Bridgewater, A. J.; Sexton, M. D., 1977, "Mechanism of Antioxidant Action: Reactions of Alkyl and Aryl Sulphides with Hydroperoxides," *J. Chem. Soc. London, Perkin Trans. II*, pp 530-536.
- Carlsson, D. J.; Robb, J. C., 1966, "Liquid-Phase Oxidation of Hydrocarbons. Part 4. - Indene and tetralin: occurrence and mechanism of the thermal initiation reaction with oxygen," *Trans. Faraday Soc.*, 62, pp 3403-3415.
- Dieterle, G. L.; Binns, K. E., 1995, "Extended Duration Thermal Stability Test of Improved Thermal Stability Jet Fuels," ASME Paper No. 95-GT-69, Presented at the International Gas Turbine and Aeroengine Congress and Exposition, 5-8 June Houston, Texas.
- Edwards, T.; Anderson, S. D.; Pearce, J. A.; Harrison, W. E., 1992, "High Temperature Thermally Stable JP Fuels—An Overview," AIAA Paper 92-0683, Presented at the AIAA 30th Aerospace Sciences Meeting and Exhibit, 6-9 January, Reno, NV.
- Edwards, T.; Liberio, P. D., 1994, "The Relationship between Oxidation and Pyrolysis in Fuels Heated to ~590°C (1100°F)," *Prepr.-Am. Chem. Soc., Div. Pet. Chem.*, 39 (1), pp 92-96.
- Hazlett, R. N., 1991, *Thermal Oxidation Stability of Aviation Turbine Fuels*. ASTM Monograph 1: American Society for Testing and Materials: Philadelphia.
- Heneghan, S. P.; Zabarnick, S.; Ballal, D. R.; Harrison, W. E., III, 1996, "JP-8+100: The Development of High Thermal Stability Jet Fuel," AIAA Paper 96-0403, Presented at the AIAA 34th Aerospace Sciences Meeting and Exhibit, 15-18 January, Reno, NV.

Jones, E. G.; Balster, L. M.; and Balster, W. J., 1996, "Thermal Stability of Jet-A Fuel Blends," *Energy Fuels*, 10, pp 509-515.

Jones, E. G.; Balster, L. M., 1997 "Impact of Additives on the Autoxidation of a Thermally Stable Aviation Fuel," *Energy Fuels*, 11, pp 610-614.

Jones, E. G.; Balster, W. J.; Balster, L. M., 1997a, "Evaluation of the Effectiveness of a Metal Deactivator and Other Additives in Reducing Insolubles in Aviation Fuels," *ASME J. Eng. Gas Turb. Power*, 119, pp 830-835.

Jones, E. G.; Balster, W. J.; Balster, L. M., 1997b, "Aviation Fuel Recirculation and Surface Fouling," *Energy Fuels*, 11, pp 1303-1308.

Jones, E. G.; Balster, W. J.; Balster, L. M., 1998a, "Impact of Fuel Recirculation on Thermal Stability," in *Proceedings of the 6th International Conference on Stability and Handling of Liquid Fuels*; Giles, H. N., Ed.; U. S. Department of Energy: Washington, D. C., Vol. 1, pp 201-210.

Jones, E. G.; Balster, L. M.; Balster, W. J., 1998b, "Effects of Pre-stressing on the Autoxidation of Aviation Fuel," *Prepr.-Am. Chem. Soc., Div. Pet. Chem.* 43 (3), 346-348.

Jones, E. G.; Balster, L. M., 1998, "Autoxidation of Diluted Aviation Fuels," *Prepr.-Am. Chem. Soc., Div. Fuel Chem.* 43 (1), pp 44-48.

Kauffman, R. E., 1994, "Development of a Rapid, Portable Hydroperoxide Test for Jet Fuels," *Prepr.-Am. Chem. Soc., Div. Pet. Chem.* 39 (1), pp 42-46.

Kendall, D. R.; Mills, J. S., 1986, "Thermal Stability of Aviation Kerosenes: Techniques to Characterize Their Oxidation Properties," *Ind. Eng. Chem. Prod. Res. Dev.*, 25, pp 360-366.

Martel, C. R., 1987, "Military Jet Fuels, 1944-1987," Technical Report AFWAL-TR-87-2062; Air Force Wright Aeronautical Laboratories: Wright-Patterson Air Force Base, OH.

Morris, R. E.; Hazlett, R. N.; McIlvaine, 1988, C. L., "Effects of Stabilizer Additives on the Thermal Stability of Jet Fuel," *Ind. Eng. Chem. Res.* 27, pp 1524-1531.

Pande, S. G.; Hardy, D. H., 1997, "Comparison of the Effects of Storage in the Presence of Copper Using Laboratory vs Field Conditions on Jet Fuel Thermal Stability as Measured by the Gravimetric JFTOT," *Energy Fuels*, 11, pp 1019-1025.

Pande, S. G.; Hardy, D. H., 1998, "Effects of Extended Duration Testing and Time of Addition of N,N'-Disalicylidene-1,2-propanediamine on Jet Fuel Thermal Stability as Determined Using the Gravimetric JFTOT," *Energy Fuels*, 12, pp 129-138.

Pickard, J. M.; Jones, E. G., 1996, "Kinetics of the Oxidation of a Jet-A Fuel," *Energy Fuels*, 10, pp 1074-1077.

Pickard, J. M.; Jones, E. G., 1998, "Liquid-Phase Oxidation Kinetics: Paraffin Blends," *Energy Fuels*, 12, pp 1241-1244.

Rubey, W. A.; Striebich, R. C.; Tissandier, M. D.; Tirey, D. A.; Anderson, S. D., 1995, "Gas Chromatographic Measurement of Trace Oxygen and Other Dissolved Gases in Thermally Stressed Jet Fuel," *J. Chromatogr. Sci.*, 33, pp 433-437.

3.2.2.5 Fuel Pyrolysis. When fuels experience temperatures above the autoxidative regime, pyrolysis and related pyrolytic coking of fuel-line surfaces can take place in addition to autoxidative surface fouling. The results of pyrolytic studies of a long-chain n-alkane mixture representing JP-7 fuel are reported in the paper entitled "Effect of Pressure on Supercritical Pyrolysis on n-Paraffins" (see pp. 667-670).

Symposium on General Papers
Presented Before the Division of Petroleum Chemistry, Inc.
218th National Meeting, American Chemical Society
New Orleans, LA, August 22-26, 1999

Effect of Pressure on Supercritical Pyrolysis of n-Paraffins

E. Grant Jones, Lori M. Balster, and Walter J. Balster
Innovative Scientific Solutions, Inc.
2766 Indian Ripple Road
Dayton, OH 45440-3638

Richard C. Striebich
University of Dayton Research Institute
KL102, 300 College Park
Dayton, OH 45469-0132

INTRODUCTION

In future military aircraft, additional heat from component systems will be generated, resulting in heat-dissipation needs that exceed sensible cooling of onboard fuel within the autoxidative thermal-stability limits. As the primary coolant, fuel will experience temperatures above the autoxidative regime, causing pyrolysis and related pyrolytic coking of fuel-line surfaces in addition to the currently existing problem of autoxidative surface fouling (1). Saturated hydrocarbon fuels can undergo endothermic pyrolysis, and the additional heat sink associated with such endothermic fuels will become more important than sensible cooling.

In hydrocarbon systems C-C bonds are the weakest and are the major source of radicals. In free-radical chain mechanisms, the individual reactions fall into three categories — initiation, propagation, and termination. At high temperatures and low pressures, successive β -scission of C-C bonds in long n-alkanes leads to methane, ethane, and a series of alkenes, according to the Rice-Kossiakoff (R-K) Model (2). Under such low-pressure conditions, unimolecular and intramolecular rearrangement reactions dominate the product distribution. At higher pressures, intermolecular reactions compete with intramolecular reactions, resulting in more H-atom abstraction and a shift from alkene products to a distribu-

tion of alkanes and alkenes. The Fabuss, Satterfield, and Smith (F-S-S) modifications to the R-K mechanism account for these changes at elevated pressures (3). In summary, at low pressures both unimolecular and intramolecular reactions are important; at higher pressures, because of cage effects, the combination of unimolecular and intermolecular reactions becomes more important.

With the goal of optimizing the endothermic capabilities of fuel chemistry, this study addresses pyrolysis of a long-chain n-alkane mixture (Norpar-13) that represents a JP-7 fuel. Pyrolytic supercritical conditions of liquid fuels prior to combustion are simulated at temperatures up

to 615°C and pressures up to 16 MPa. In particular, we are interested in changes that impact endothermic fuels such as gas distribution, conversion from liquid to gaseous fuel components, endothermic cooling, and finally surface coking that can be attributed to changes in system pressure. For potential endothermic fuels, changes in the distribution of reaction products with pressure have been reported in experiments with tubular flow reactors (4, 5) and static systems (6).

EXPERIMENTAL

Experiments were conducted in a constant-heat-flux mode using a vertically mounted 42-in. tube (0.318-cm o.d. and 0.216-cm i.d.) which was electrically heated by a high ac current. Silcosteel tubing was used to suppress surface catalysis, including autoxidation (7) and the pyrolytic formation of filamentous carbon (8). The tubing was not insulated, and its external surface was painted with a flat-black high-temperature paint to maintain a constant emissivity for optical surface-temperature measurements (Omega pyrometer OS3707). Norpar-13 with a measured n-alkane composition of 0.7% undecane, 15% dodecane, 51.3% tridecane, 32.3% tetradecane, and 0.7% pentadecane was used for all experiments. Fuel was pumped (ISCO, Model D500) at a flow rate of 20 mL/min. Pressure changes were achieved by introduction of a series of mechanical back-pressure valves. Electrical current through the tube was initially adjusted to achieve an exit temperature of 615°C, and no further adjustments were made during the 3-hr test. Coking was evaluated by surface-carbon burnoff of 5.1-cm sections cut from

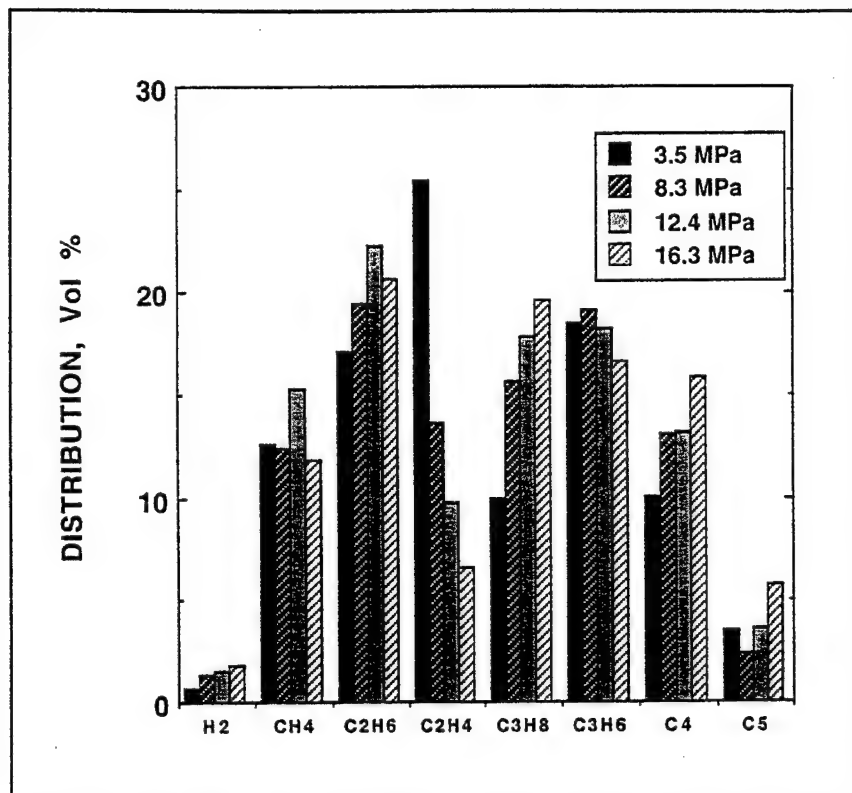


Figure 1. Effect of pressure on distribution of gases following supercritical pyrolysis of Norpar-13 (fuel exit temperature 615°C).

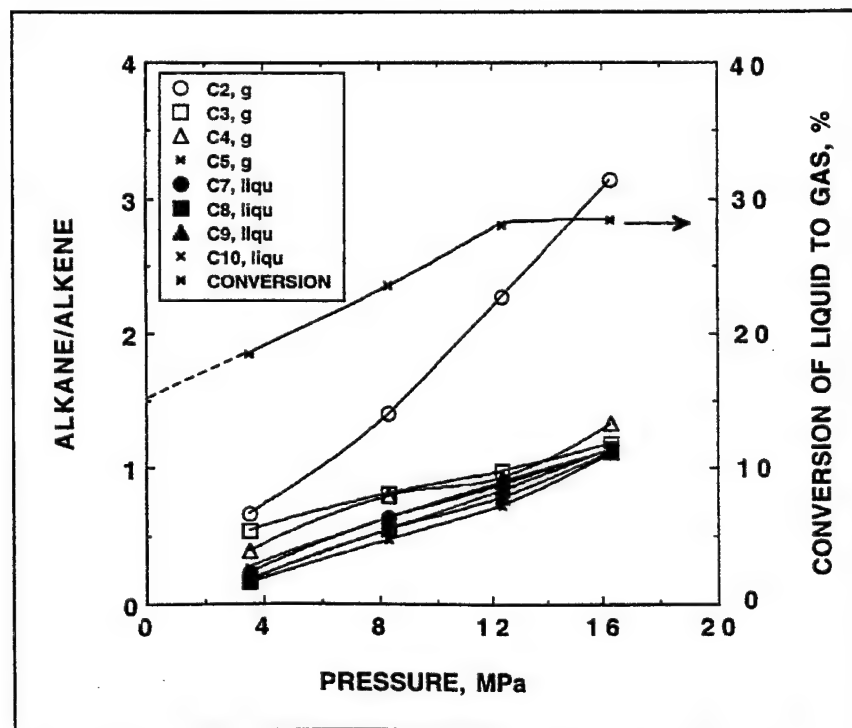


Figure 2. Effect of pressure on alkane/alkene ratio and conversion to gaseous products following supercritical pyrolysis of Norpar-13 (fuel exit temperature 615°C).

the heated tube. Gases were separated into a gas bag after the fuel was cooled to room temperature and were analyzed along with the stressed liquids using gas chromatography.

RESULTS AND DISCUSSION

Distribution of Products

The gas distribution at a series of pressures is shown in Figure 1. The most notable changes with pressure are a reduction in the amount of ethylene and an increase in propane. Such changes suggest a relative increase in alkanes as compared to alkenes. Figure 2 shows the alkane/alkene ratio for products that have cooled to room temperature. Ratios from gaseous products (C₂ to C₅) and liquid products (C₇ to C₁₀) display an increase with pressure and tend toward zero at the limit of zero pressure (gas phase). These changes in distribution are common to all carbon numbers, but C₂ is the most significantly affected.

Reaction Conversion

The original fuel is converted predominantly to gaseous and liquid products. The amount of solids collected on the tubing walls, although measurable, constitutes only a very small fraction of the converted liquid fuel. A very simple measure of conversion is the percentage of liquid lost in the reaction region, with the final quantity of liquid being determined after cooling to room temperature, as shown in Figure 2. Since initial bond cleavage is driven by temperature, most of the conversion to gas derives from heating the fuel to 615°C. By extrapolating the conversion to zero pressure, we can estimate that ~15% of the conversion arises from thermal effects. The additional 13% conversion at the highest pressures arises from the combination of thermal and pressure effects. Figure 2 shows that pressure alters not only the distribu-

tion of products but also the efficiency of conversion to small molecules that separate into the gaseous phase after the completion of pyrolytic stressing. Such fuel cracking has a beneficial impact on subsequent ignition and combustion efficiency (9).

Wall Temperatures

The external wall temperatures of the heated tubing are shown in Figure 3. Each data point represents an average of at least four readings during the course of the 3-hr experiment. Small, but reproducible, differences are observed as the pressure is increased, the most significant being wall cooling at the highest bulk temperatures. It should be noted that although the heat flux is equal at all points along the tube, radiative losses are at a maximum at the highest wall temperatures, i.e., at the downstream or top end of the heated tube. This effect, in part, accounts for the change in slope around 600°C. In addition to the expected radiative losses, a pressure-dependent suppression of wall temperature occurs at the hot end. In view of the observed changes in the quantity and the distribution of products, we attribute some of the decrease in wall temperature to additional endothermic processes that occur at the highest temperatures and pressures. This increased endothermicity associated with pressure changes is estimated to be in excess of 60 W (10). A common observation in wall-temperature measurements under these temperature and flow conditions is a sharp decrease in wall temperature corresponding to heat-flow changes at the onset of supercritical conditions. This feature tends to be lost in the averaging of several data sets but occurs between 10 and 15 in. along the tube under the current flow and power conditions.

Coking

Deposition is shown in Figure 4 as the integrated sum of surface carbon along the tube. The autoxidative thermal-stability fouling for paraffin

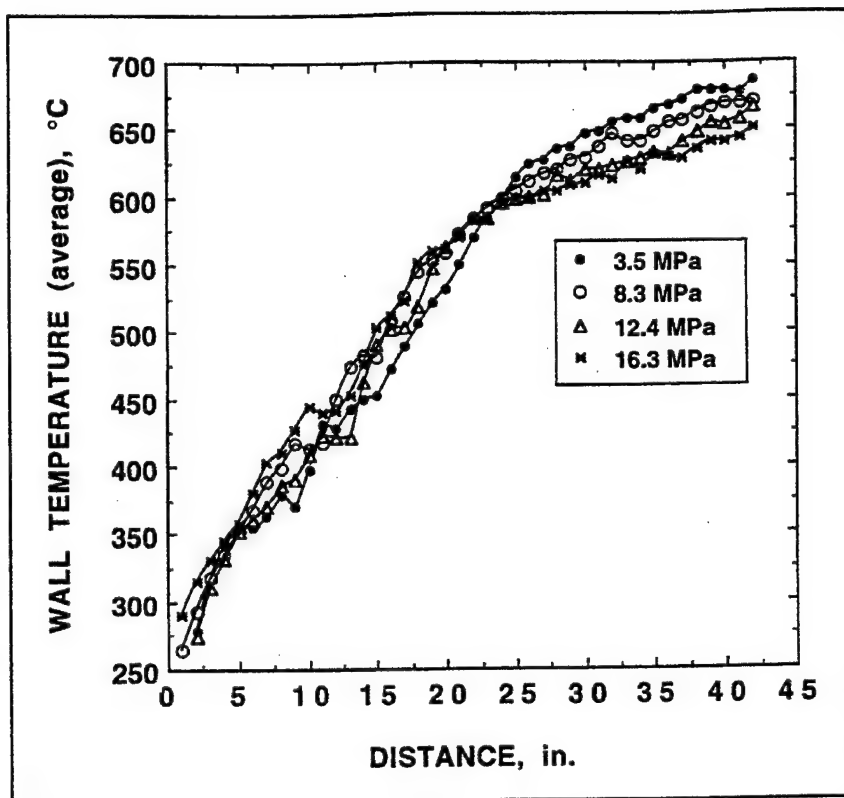


Figure 3. Effect of pressure on surface wall temperatures during supercritical pyrolysis of Norpar-13 (fuel exit temperature 615°C).

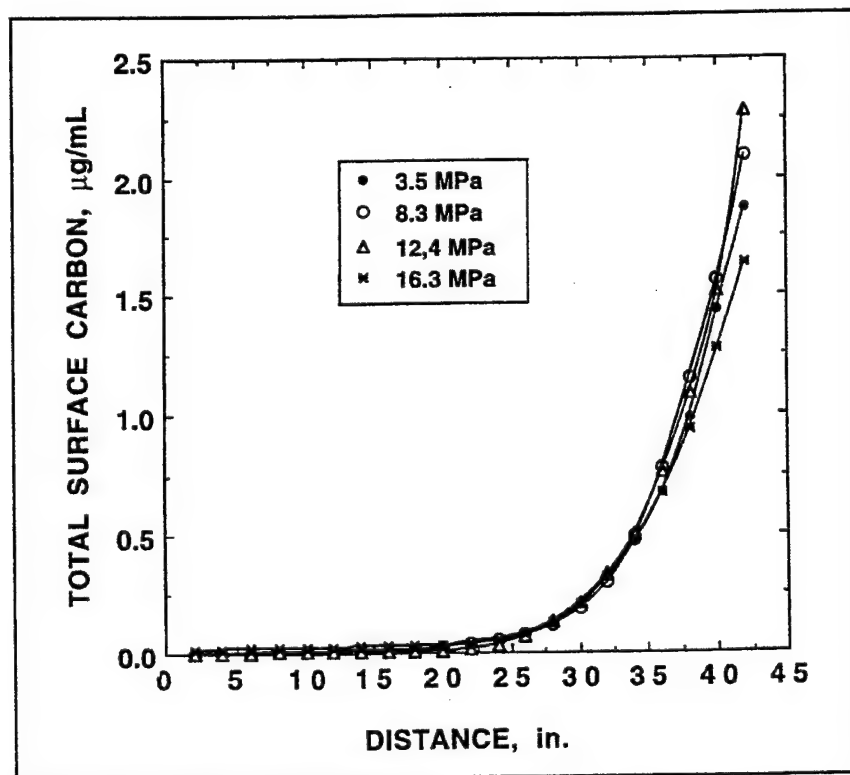


Figure 4. Effect of pressure on coking in supercritical pyrolysis of Norpar-13 (fuel exit temperature 615°C).

systems or JP-7 fuels is very high, resulting in the absence of significant surface fouling associated with autoxidation. The onset of pyrolytic fouling (coking) occurs around 25 in., and the amount of deposits increases toward the hot end of the tube. Within experimental reproducibility, surface fouling is independent of system pressure. This finding is important for maximizing endothermic cooling. No coking liability results from increased system pressure, despite changes approaching a factor of two in the distribution and quantity of liquid and gaseous products and enhanced endothermic cooling. These results suggest that coking does not depend on the extent of conversion to liquid or gaseous products but rather on a parameter that did not change significantly in the current series of experiments. The most obvious parameters are bulk-fuel and wall temperature. Previous modeling studies in this laboratory have suggested that wall temperature plays the essential role in pyrolytic deposition (11).

CONCLUSIONS

Supercritical pyrolysis studies of Norpar-13 have shown pronounced effects of pressure on: 1) the distribution of products, in particular, the alkane/alkene ratio, 2) the quantity of gaseous products, and 3) the reaction endothermicity. These are attributed to cage effects on the competition be-

tween intermolecular and intramolecular processes. The amount of coking is found to be independent of changes in pressure and the concomitant changes in conversion. The combination of increased conversion and endothermicity without increased coking suggests that the application of higher pressures may be a viable approach to achieving enhanced heat-sink capabilities while minimizing coking.

ACKNOWLEDGMENTS

This study was supported by the Air Force Research Laboratory (AFRL), Propulsion Directorate, Wright-Patterson Air Force Base, OH, under USAF Contract No. F33615-95-C-2507. The authors would like to acknowledge Mrs. M. Whitaker for editorial assistance.

LITERATURE CITED

- (1) Edwards, T., AIAA Paper 93-0807, 31st Aerospace Sciences Meeting and Exhibit, Jan 11-14, Reno, NV (1993).
- (2) Kossiakoff, A., and Rice, F. O., *J. Am. Chem. Soc.*, **65**, 590 (1943).
- (3) Fabuss, B. M., Smith, J. O., Lait, R. I., Borsanyi, A. S., and Satterfield, C. N., *Ind. Eng. Chem. Proc. Res. Dev.*, **1**, 293 (1962).
- (4) Khorasheh, F., and Gray, M. R., *Ind. Eng. Chem. Res.*, **32**, 1853 (1993).
- (5) Stewart, J., Glassman, I., and Brezinsky, K., *Am. Chem. Soc., Div. of Petrol. Chem., PREPRINTS*, **43**(3), 433 (1998).
- (6) Yu, J., and Eser, S., *Ind. Eng. Chem. Res.*, **36**, 574 (1997).
- (7) Jones, E. G., Balster, L. M., and Balster, W. J., *Energy Fuels*, **10**, 831 (1996).
- (8) Baker, R. T. K., and Harris, P. S., *Chemistry and Physics of Carbon*, Vol 14, P. L. Walker, Jr., and P. A. Thrower, Eds., Dekker, New York, **14**, p. 83 (1978).
- (9) Colket, M. B., III, and Spadacini, L. J., "Endothermic Fuels Autoignition Study," *Proc. 1998 JANNAF Propulsion Meeting*.
- (10) Sheu, J.-C. (CFDRC, Huntsville, AL), private communication.
- (11) Sheu, J.-C., Zhou, N., Krishnan, A., Jones, E. G., and Katta, V. R., *Am. Chem. Soc., Div. of Petrol. Chem., PREPRINTS*, **43**(3), 390 (1998).

3.2.2.6 Lubricants. The autoxidation reactions of fuels and lubricants are very similar. Stressing of jet fuels during aircraft cooling occurs with a limited amount of dissolved oxygen that severely limits conversion to products. The absence of similar restrictions in lubricant applications can result in extensive oxidation and necessitates the introduction of higher concentrations of antioxidants. In the paper entitled "Dilution Method for Estimating Concentration of Primary Antioxidants in Lubricants" (see pp. 672-675), a technique based upon oxygen depletion is identified for estimating antioxidant concentrations in lubricants.

Symposium on Recent Advances in the Chemistry of Lubricant Additives
Presented Before the Division of Petroleum Chemistry, Inc.
218th National Meeting, American Chemical Society
New Orleans, LA, August 22-26, 1999

Dilution Method for Estimating Concentration of Primary Antioxidants in Lubricants

E. Grant Jones and Lori M. Balster
Innovative Scientific Solutions, Inc.
2766 Indian Ripple Road
Dayton, OH 45440-3638

INTRODUCTION

Autoxidation Background

Oxidative degradation of hydrocarbon systems including fuels and lubricants occurs during field applications at higher temperatures. For example, fuels that are used as the primary heat sink in modern aircraft form insoluble oxidation products that foul critical fuel-line surfaces (1). Similarly, oxidation diminishes the beneficial physical and chemical properties of lubricants. Liquid-phase oxidation or autoxidation can be represented by a common sequence of free-radical reactions that require the presence of O_2 ; these reactions fall into three categories: initiation, propagation, and termination (2). Radical initiation may involve active surfaces, radiation, decomposition of hydrocarbon/oxygen complexes, or thermal bond cleavage. Primary antioxidants inhibit oxidation by the formation of radicals that are unreactive due to hindered or resonance-stabilized structures. Antioxidants increase the thermal oxidative stability; their depletion leads to rapid degradation of lubricant properties. Under conditions of simple inhibition, rapid or autocatalytic reaction is delayed by a time, t , that is proportional to the initial antioxidant concentration, $[AH]$, and inversely proportional to the rate of initiation (3). Many techniques have been developed for the determination of residual antioxidants or the remaining useful lubricant life (4). One of best methods involves titrating antioxidants with a free radical initiator during oxygen take-up experiments at low temperatures (5). The procedure outlined in this study is a variation on these earlier free-radical methods but derives from single-phase experiments on fuels conducted at an elevated temperature without added initiator.

Outline of Dilution Technique

The autoxidation reactions of fuels and lubricants are very similar. The stressing of jet fuels during aircraft cooling occurs with a limited supply of dissolved O_2 that severely limits conversion to products. The ab-

sence of similar restrictions in lubricant applications can result in extensive oxidation and necessitates the introduction of higher concentrations of antioxidants.

In the proposed technique O_2 -depletion measurements are made in

air-saturated hydrocarbons, using the fact that oxidation of complex hydrocarbon systems can be simplified experimentally by dilution with a paraffin or paraffin blend. The diluent replaces the fuel or lubricant as oxidizing species and its oxidation is inhibited or retarded by the reduced concentration of primary antioxidant. Oxidation in these cases is characterized by a well-defined delay time that corresponds to the time needed to deactivate the residual inhibitors. Antioxidant concentration can be assessed from inhibition times utilizing the proposed technique if the following requirements are met: 1) dilution is sufficient (> 10 fold) to ensure that the diluent is the major hydrocarbon, 2) the diluted-inhibitor concentration can be diminished by 1-2 mM of dissolved O_2 , and 3) depletion of O_2 occurs within an experimentally accessible time frame, which for our tests is < 30 min at $185^\circ C$. For antioxidants that are simple inhibitors, the second criterion can be met rigorously. Less efficient antioxidants (retarders) that are common to fuels will not be totally consumed during limited oxidation. However, their effectiveness may be negated, as apparent from the onset of reaction acceleration, by the conversion of 1-2 mM of dissolved O_2 . Ten-fold dilution has been found to satisfy these three criteria for fuels. Due to their higher initial antioxidant concentration, lubricants require more dilution (~ 600 fold). Dilution reduces the antioxidant concentration to a range that would correspond to 5-50 mg/L of a hindered phenol antioxidant such as 2,6-di-tert-butyl-p-cresol, BHT. The original antioxidant effect can be calculated from the delay time and the dilution factor. In this manner relative changes in origi-

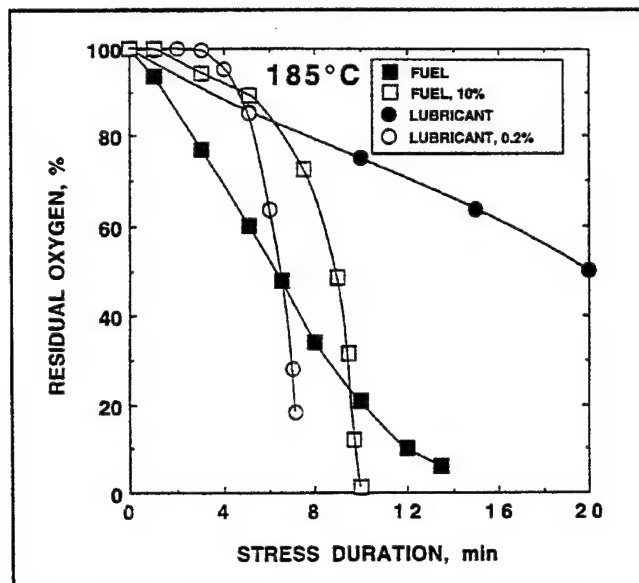


Figure 1. Depletion of dissolved oxygen measured at 185°C for fuel/lubricant in neat form and following dilution with paraffin blend.

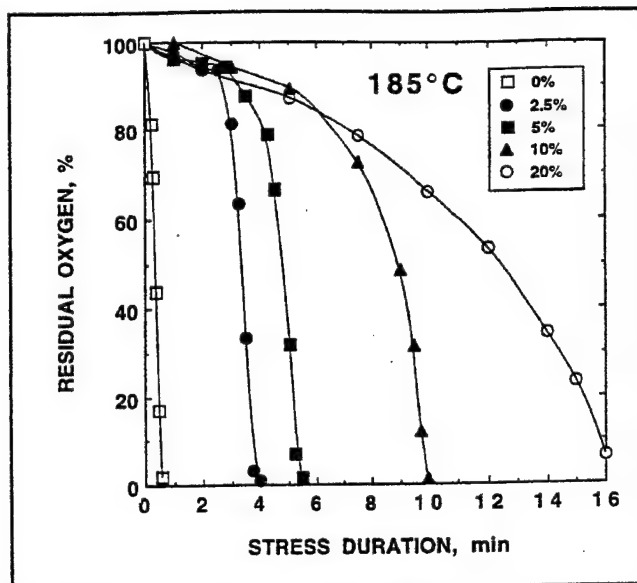


Figure 2. Depletion of dissolved oxygen measured at 185°C for POSF-2827 jet fuel diluted with paraffin blend.

nal primary-antioxidant concentration that occur during field stressing can be assessed. Calibration curves for known synthetic antioxidants in lubricants can be generated through diluent doping experiments. Since the distribution of natural primary antioxidants in fuels is not well known, calibration for naturally occurring antioxidants is not feasible.

EXPERIMENTAL

The experimental methods for measuring O_2 depletion at elevated temperatures and pressures were developed for studies of fuel oxidation and have been described previously (6). The neat fuel and lubricant are initially saturated with respect to air at room temperature, and each reacts with dissolved O_2 in a single liquid phase at 185°C under 2.3-MPa pressure. Reaction occurs during slow flow through 0.318-cm-o.d., 0.216-cm-i.d. tubing that is clamped tightly within a Cu-block heat exchanger. Dissolved O_2 is measured in-line at system pressure using a GC technique (6), after varied residence times in the heated tube. Tubing used in these experiments is passivated by the Silcosteel (8) process to minimize surface catalytic effects from the stainless-steel walls (9). Exxsol D-110,

a blend of paraffins and cycloparaffins with aromatic content <1%, was obtained from Exxon Corp. and used for dilution. Jet fuel dilution is given as vol/vol and lubricant dilution as w/vol. Diluted and undiluted samples are subjected to identical oxidation conditions. POSF-2827 is a straight-run Jet-A fuel of reduced thermal stability containing many natural antioxidants; 0-84-1 is a synthetic diester turbine-engine oil containing ~1% each of phenyl- α -naphthylamine (PANA) and dioctyl diphenylamine (Irganox 259, DODPA). Calibrants included the hindered-phenol antioxidant BHT obtained from Du Pont and the two amine antioxidants PANA and DODPA obtained from Du Pont and Ciba Geigy, respectively.

RESULTS AND DISCUSSION

Effects of Dilution on Oxidation

The oxidation behavior of the fuel and lubricant prior to dilution is shown in Figure 1 (closed symbols). Air-saturated concentration of dissolved O_2 (at room temperature) is represented by 100%. This value is ~60 ppm for fuels and is estimated for the current lubricant, based on relative GC signals, to be ~40 ppm. The

approximately linear decays are indicative of strongly inhibited oxidation without reaction acceleration due to ROOH formation. The oxidation behavior of the diluted samples (Figure 1, open symbols) is different from the neat samples, being characterized by a region of very slow or inhibited reaction, followed by a region of rapid or autocatalytic oxidation. The break estimated by the time to 50% O_2 depletion is indicative of consumption of residual antioxidants and the onset of ROOH formation. The effects of different dilution ratios (antioxidant concentration) on the oxidation curves for fuel and lubricant are given in Figures 2 and 3, respectively. The similarity in oxidation profiles at the highest levels of dilution shows that the three criteria outlined above are fulfilled and that straightforward estimates of inhibition times can be made for a range of dilution.

Calibration of Synthetic Antioxidants in Diluent

Figure 4 shows changes to the inhibition time of paraffin oxidation with the introduction of the two lubricant antioxidants and BHT. PANA and BHT have similar effectiveness on a weight basis, all three are similar

($\pm 20\%$) on a molar basis. This calibration covers the practical range of delay times for the diluted lubricant. Note that the observed delays are not linear in this concentration region at 185°C . Taking lubricant dilution at 1.5 g/L in Figure 3, the delay time is $\sim 6.5\text{ min}$. If PANA were the sole antioxidant, this time would correspond to the presence of 43 mg/L in the diluent or 43 mg in 1.5 g of original lubricant, i.e., 2.9% (w/w) antioxidant. This concentration is in the range expected for ester lubricants. The situation with the straight-run fuel is more complex since the identity of natural fuel antioxidants is unknown and, hence, no similar calibration can be conducted. However, a BHT equivalency can be estimated. For example, a 5% fuel blend equates to $\sim 35\text{ mg/L}$ of BHT, indicating very high natural antioxidant levels in the neat fuel.

Use of Dilution Method to Monitor Changes in Antioxidant Concentration with Stressing

To investigate how prestressing alters primary antioxidants in a fuel,

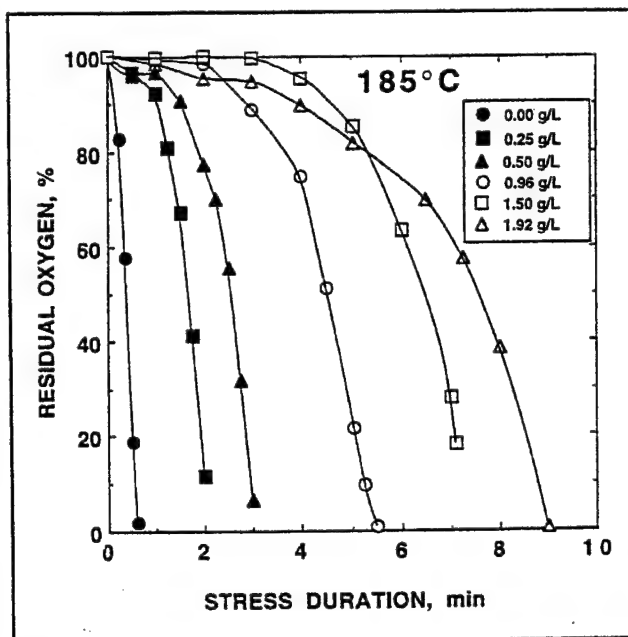


Figure 3. Depletion of dissolved oxygen measured at 185°C for lubricant diluted with paraffin blend.

POSF-2827 was prestressed in the same test rig for $\sim 21\text{ min}$ at 185°C , with the initial O_2 concentration being increased by a factor of five. These conditions were not representative of typical field-stressing but were chosen to be very aggressive. The oxidation profiles shown in Figure 5 for 10% blends of neat and prestressed fuel indicate about a factor-of-two

loss in the effectiveness of primary antioxidants.

The effects of lubricant prestressing were investigated by applying the dilution method to samples that had been prestressed for 24, 48, 60, and 72 hr at 204°C . The prestressing was not conducted in our laboratory; the University of Dayton Research Institute (UDRI) provided samples that were generated as part of a test program. Figure 6 shows the oxidation behavior of the diluted unstressed sample that represents the initial antioxidant condition, the four diluted prestressed samples, and the neat diluent that represents zero antioxidant concentration. Using the times needed to deplete O_2 by 50% , the relative change in primary antioxidant is plotted in Figure 7 as a function of prestress time at 204°C . Some residual antioxidant remains even after 72 hr of prestressing. Using a linear fit to the current data and extrapolating to zero concentration, it is estimated that 90 hr of prestressing would be required for complete dissipation of

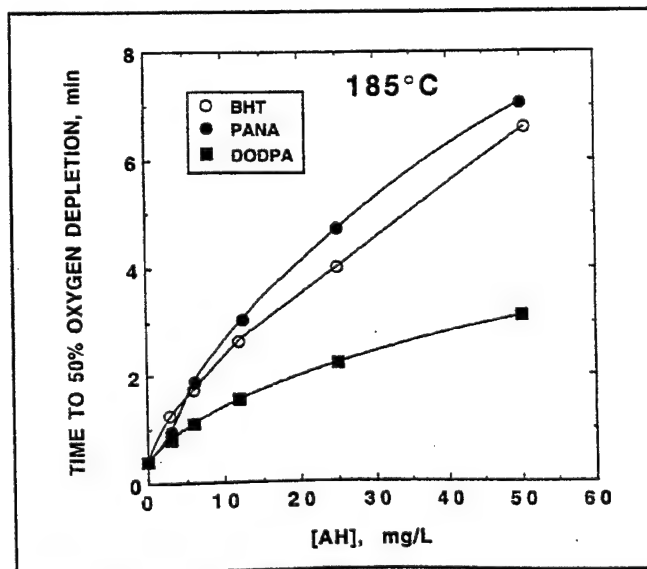


Figure 4. Changes in oxidation delay time at 185°C for synthetic antioxidants in paraffin blend.

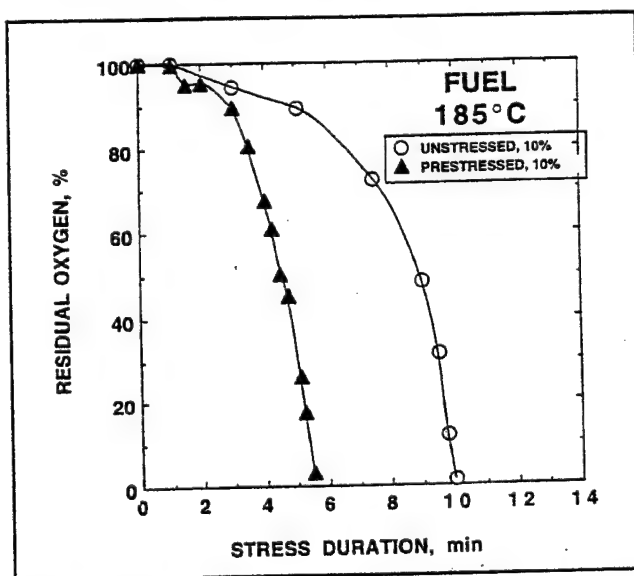


Figure 5. Changes in oxidation of neat and prestressed jet fuel at 185°C following ten-fold dilution with paraffin blend.

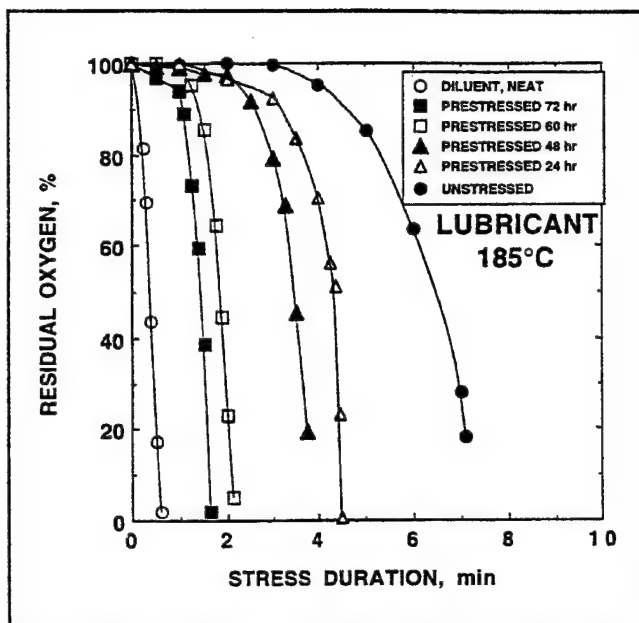


Figure 6. Changes in oxidation at 185°C following prestressing of lubricant at 204°C and dilution (1.5 g/L) with paraffin blend.

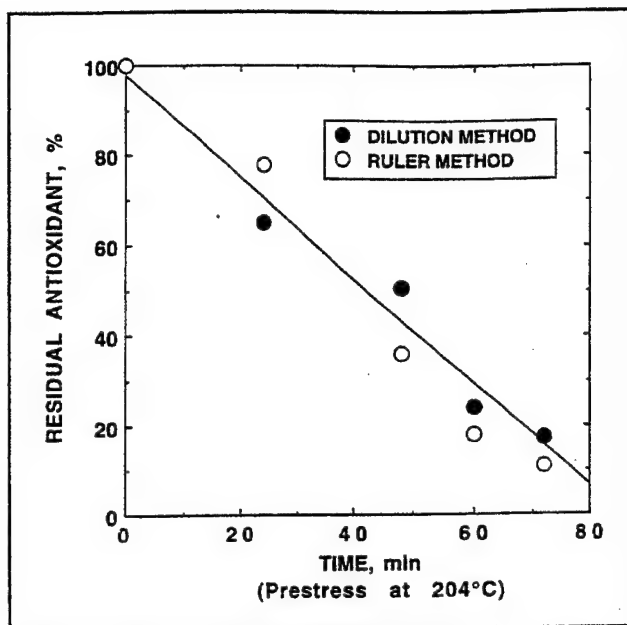


Figure 7. Reduction in antioxidants in lubricant as function of prestress time at 204°C. Closed circles: current data; open circles: RULER method described in Ref. 11.

primary antioxidants (10). The current results show good agreement with those from the RULER method developed by Kauffman (11).

CONCLUSIONS

A method has been described for estimating residual primary antioxidants in fuels and lubricants using O₂-depletion in paraffin-diluted samples.

ACKNOWLEDGMENTS

This study was supported, in part, by the Air Force Research Laboratory (AFRL), Propulsion Directorate, Wright-Patterson Air Force Base, OH, under USAF Contract No. F33615-95-C-2507. The authors would like to thank Dr. C. S. Saba (UDRI) for providing the stressed-lubricant samples and Mr. R. E. Kauffman (UDRI) for providing independent measurements with the RULER technique. One of us (EGJ) would like to thank Dr. R. L. Wright, Jr., AFRL Lubrication Branch, for many valuable discussions and Mr.

W. E. Harrison, III, AFRL Fuels Branch, for encouragement in this study. The authors would like to acknowledge Mrs. M. Whitaker for editorial assistance.

LITERATURE CITED

- (1) Hazlett, R. N., Thermal Oxidation Stability of Aviation Turbine Fuels, ASTM Monograph 1, American Society for Testing and Materials, Philadelphia (1991).
- (2) Walling, C., Free Radicals in Solution, John Wiley and Sons, Inc., New York (1957).
- (3) Tudos, F., Fodor, Z., and Iring, M., Oxidation Inhibition in Organic Materials, Vol. II, Chap. 5, ed. By J. Posposil and P. P. Klemchuk CRC Press, Boca Raton, FL, 1990.
- (4) See Kauffman, R. E., in CRC Handbook of Lubrication: Theory and Practice of Tribology, Vol III, Booser, E. R., Ed., CRC Press, Inc., Boca Raton, FL, 89 (1994) and references therein.
- (5) Mahoney, L. R., Korcek, S., Hoffman, S., and Willermet, P. A., Ind. Eng. Prod. Res. Dev., **17**, 250 (1978).
- (6) Jones, E. G., Balster, L. M., and Balster, W. J., Energy Fuels, **10**, 509 (1996).
- (7) Rubey, W. A., Striebig, R. C., Tissandier, M. D., Tirey, D. A., and Anderson, S. D. J. Chromatogr. Sci., **33**, 433 (1995).
- (8) Silcosteel tubing, Restek Corporation, Bellefonte, PA.
- (9) Jones, E. G., Balster, L. M., and Balster, W. J., Energy Fuels, **10**, 831 (1996).
- (10) A linear drop in antioxidant concentration is expected for simple inhibition (Ref 3).
- (11) Kauffman, R. E., Lub. Eng., **54**(1), 39 (1998).

3.2.3 Effects of Additives on Fuel Thermal Stability

Efforts were made to obtain fundamental information on the effects of a metal deactivator (MDA), an oxidant, and a dispersant added singly and in combination with two metal-containing fuels and to determine whether benefits arise from the inclusion of MDA in an additive package. The results are reported in the paper entitled "Use of MDA, BHT, and Dispersant Singly and in Combination as Jet-Fuel Additives" (see pp. 677-682). A reduction in surface fouling at elevated temperatures due to a Dupont jet-fuel additive package is documented in the publication entitled "Application of JFA-5 as an Antifouling Additive in a Jet-A Fuel." This paper, co-authored by E. G. Jones, W. J. Balster, and L. P. Goss, was published in *Industrial and Engineering Chemistry Research*, Vol. 35, pp. 837-843 (1996). An extensive study was conducted on the impact of additives on the thermal stability of aviation fuels; the results are documented in the paper entitled "Impact of Additives on the Autoxidation of a Thermally Stable Aviation Fuel." This paper, co-authored by E. G. Jones and L. M. Balster, was published in *Energy and Fuels*, Vol. 11, pp. 610-614 (1997). Potential advantages and disadvantages of using MDAs alone and in combination with other additives are addressed in the publication entitled "Evaluation of the Effectiveness of a Metal Deactivator and Other Additives in Reducing Insolubles in Aviation Fuels" (see pp. 683-688). The roles of natural and synthetic antioxidants in the liquid-phase oxidation of jet fuel are discussed in the paper entitled "Interaction of a Synthetic Hindered-Phenol with Natural Fuel Antioxidants in the Autoxidation of Paraffins." This paper, co-authored by E. G. Jones and L. M. Balster, was published in *Energy and Fuels*, Vol. 14, pp. 640-645 (2000).

Symposium on Structure of Jet Fuels IV
Presented before the Division of Petroleum Chemistry, Inc.
211th National Meeting, American Chemical Society
New Orleans, LA, March 24-29, 1996

Use of MDA, BHT, and Dispersant Singly and in Combination as Jet-Fuel Additives

Walter J. Balster and Lori M. Balster
Systems Research Laboratories
An Operation of Calspan SRL Corporation
2800 Indian Ripple Road
Dayton, OH 45440-3696

E. Grant Jones
Innovative Scientific Solutions, Inc.
3845 Woodhurst Ct.
Beavercreek, OH 45430

INTRODUCTION

Surface fouling in aircraft fuel lines resulting from autoxidation of aviation fuel leads to reduced efficiency as deposits collect on heat exchangers, nozzles, and servocontrols and may ultimately lead to system failure. Approaches taken to mitigate fouling include 1) additional refining techniques such as hydrotreatment, 2) innovative engineering of on-board fuel management to utilize additional fuel-sink capacity of the fuel, 3) introduction of individual additives and additive packages, including antioxidants to slow autoxidation, metal deactivators (MDA) to reduce the rate of initiation and possibly passivate metal surfaces, and dispersants/detergents to prevent agglomeration of insolubles. Dispersants and, to a lesser extent, antioxidants have been shown to improve thermal stability in USAF fuels (1, 2); however, the use of MDA is still under consideration. Experimental studies on the use of MDA in aviation fuels are extensive and have been reviewed and summarized by Hazlett (3). Metal deactivators have been reported (4) to operate via two distinct mechanisms: 1) chelation of metal ions and 2) surface passivation. Many reports in the literature support the role of chelation (5, 6); however, the role of surface passivation is less clear (5, 7). MDA has been proposed as a constituent to USAF fuel-additive packages.

The goals of the current study were 1) to obtain fundamental information on the behavior of an MDA, an antioxidant, and a dispersant added singly and in combination with two metal-containing fuels, and 2) to determine whether benefits arise

from the inclusion of MDA in an additive package. In order to emphasize only the metal-chelation role of MDA, we have chosen conditions where metal surface passivation effects would be minimal. Simple experiments to simulate fuel-line

fouling with a single-pass tubular heat exchanger operated under near-isothermal conditions have been conducted to study the thermal behavior of neat and additized jet fuels at 185°C. Comparison of the effectiveness of additive treatment is based on several criteria: 1) dependence of autoxidation on stress duration, 2) dependence of surface deposition on stress duration, and 3) total insolubles (bulk filterables and surface deposits). Potential advantages and disadvantages of using additives singly and in combination are discussed.

EXPERIMENTAL

Two metal-containing Jet-A fuels, POSF-3084 (Cu, 35 ppb; Fe, < 5 ppb) and POSF-3119 (Cu, 7 ppb; Fe, 26 ppb) of relatively poor thermal stability were investigated. The selected additives summarized in Table 1 were introduced at fixed concentrations. Neat and additized fuels were initially saturated with respect to air at room temperature and were passed through a 15- μ m filter before use. Reaction occurred as fuel was pumped through 0.318-cm- (0.125-in.-) o.d., 0.216-cm- (0.085-in.-) i.d. tubing, clamped tightly within a Cu-block heat exchanger at 185°C. System pressure was maintained at 2.3 MPa to ensure a single reaction phase. Two experimental arrangements were utilized, differing only in the length of the heat exchanger. Dissolved oxygen, O₂, was measured using the first or standard setup with the Near Isothermal Flowing Test Rig, NIFTR, which has been described in detail elsewhere (8) and will be reviewed here only briefly. For these experiments a fixed reaction path-length of 81.3 cm (32 in.) was used; stress duration or reaction

time was varied by changing the fuel flow rate. Dissolved oxygen was measured in-line at system pressure using a GC technique developed by Rubey and coworkers (9). Based on the difference between O₂ readings for the unstressed and stressed fuel, the percentage of residual O₂ was determined as a function of the calculated reaction time. The tubing selected for O₂ experiments was passivated by the Silcosteel process (10) in order to minimize possible surface catalytic effects.

Deposition experiments were conducted using the second experimental arrangement with an extended-length heat exchanger (NIFTR-2). Under fixed flow rates of 0.25 and 0.20 mL/min, this unit has a continuous, isothermal 183-cm heated path-length that provides 23 and 28 min, respectively, of stressing to accommodate the complete deposition profile of all fuels and most additized fuels used in this study. Deposits were collected over a relatively long test duration (72 hr), resulting in the passage of 864 - 1,080 mL of air-saturated fuel during the course of each experiment. Commercial stainless-steel (304) tubing was used for all deposition experiments; during the first few hours of each test, the original stainless-steel surfaces became covered with deposits and were considered to be passivated with respect to autoxidation (11). Thus, deposition and autoxidation experiments were conducted under similar test conditions, with minimal interaction of metal-tubing walls. Surface deposits were quantified by surface-carbon burnoff (LECO RC-412) of small tubing segments, and 72-hr average deposition rates were calculated for each segment as a function of stress (residence) time.

Bulk insolubles were collected over the entire 72-hr test period on two sets of in-line Ag-membrane filters (0.45 and 0.2 µm). The quantity of bulk insolubles from the two filter sets was summed and expressed in units of micrograms per milliliter,

Table 1.
Additives Studied

Class	Name	Chemical Name	Source	Conc. (mg/L)
Antioxidant	BHT	2,6-di-tert-butyl-p-cresol	DuPont	25
Metal Deactivator	MDA	N,N'-disalicylidene-1,2-propanediamine	DuPont	2
Dispersant	8Q405	Proprietary	Betz	100

representing an average over complete oxygen conversion. Filter housings located ~10 cm from the heat exchanger remained near room temperature; thus, measured filterables include additional contributions resulting from fuel cooling.

RESULTS AND DISCUSSION

Autoxidation

The disappearance of O₂ is given in Figures 1a and 1b for fuels POSF-3084 and POSF-3119, respectively. When used singly, all three additives slow autoxidation relative to the neat fuel. MDA, at a concentration of 2 mg/L delays autoxidation due to chelation of dissolved metals, thereby preventing metal-initiated autoxidation (12). The hindered phenol, BHT, present at 25 mg/L operates by a free radical chain-breaking mechanism to slow propagation and, thereby, slow autoxidation. The role of a dispersant in slowing autoxidation is unknown. In previous reports (2, 13), we noted that the dispersant 8Q405, present at 100 mg/L, does not slow autoxidation in fuels that do not contain dissolved metals (e.g., POSF-2827 and POSF-2980) but does introduce a delay in a Cu-containing fuel, POSF-2934. These facts coupled with the present observations indicate that the dispersant 8Q405 may operate to reduce the free-radical initiating effects of dissolved metals.

Additive pairs, in general, inhibit autoxidation more than any individual additive, and the combination of all three additives provides the best overall slowing of autoxidation. Benefits accrue from the use of multi-component additives, but the ab-

sence of overall effects greater than the sum of the individual effects indicates antagonism or overlap of additive function rather than synergism. For example, if the role of the dispersant is to reduce some of the catalytic initiation of dissolved metals, then its application in conjunction with MDA will result in a competitive rather than a cooperative interaction.

Deposition

To aid in visualizing differences resulting from the incorporation of additives and to reduce overlap in the differential-rate data, the deposition data are presented in the following format. The total surface carbon from each additized fuel is summed along the tube and is corrected by subtracting the corresponding sum obtained with the neat fuel. This results in the total surface carbon for each additive relative to the neat fuel (the latter being represented by a line along the x-axis); positive and negative values indicate, respectively, increased and decreased surface fouling caused by additive introduction. For example, the relative behavior upon introduction of the three individual additives is given in Figures 2a and 2b. The two fuels exhibit similar behavior. BHT causes negligible reduction in fouling (< 0.2 µg/mL) at short stress times and a pronounced increase (~ 2 µg/mL) for longer times. Despite the effectiveness of BHT in slowing autoxidation, its introduction does not correspondingly reduce surface deposition. Contrast this with the introduction of MDA which does effectively reduce fouling for short stress times, reflecting delays in autoxidation. For longer stress times, however, the situation is reversed, and

MDA causes the total deposition to increase relative to the neat fuels. The reasons for such reversals in surface fouling using MDA are not apparent. Finally, the dispersant provides the greatest reduction in surface fouling for all stress times.

The impact of the additives used in combination is given in Figures 3a and 3b. It was previously noted that all additive combinations delay autoxidation (see Figure 1) relative to the neat fuels. All combinations similarly reduce surface fouling relative to the neat fuels for the first 10 min of stressing. When used in pairs, MDA+8Q405 and BHT+8Q405 cause

the greatest reduction in surface fouling, and MDA+BHT causes the least reduction. The behavior of MDA+BHT is approximately equal to the average of the individual additive effects in improving thermal stability for short times, but the benefits disappear at higher conversion. The combination of antioxidant and MDA has been reported to improve long-term storage stability in Cu-containing diesel fuels (14), and it has recently been postulated that MDA is effective only when introduced at a concentration of 5.8 mg/L at the refinery, i.e., prior to Cu exposure (15). The dispersant appears to be the dominant component when these ad-

ditives are used in pairs. For example, its presence offsets some of the deleterious behavior of BHT and MDA particularly at longer stress times; however, the deposition behavior with all combinations does not differ significantly from that obtained with the dispersant alone. The combination of all three additives provides the greatest reduction in surface fouling, and this finding is consistent with the observed delays in autoxidation shown in Figure 1. The relative order of the additive and additive combinations in their ability to reduce fouling is MDA + BHT + 8Q405 > 8Q405 ~ BHT + 8Q405 ~ MDA + 8Q405 > MDA ~ MDA + BHT >> BHT.

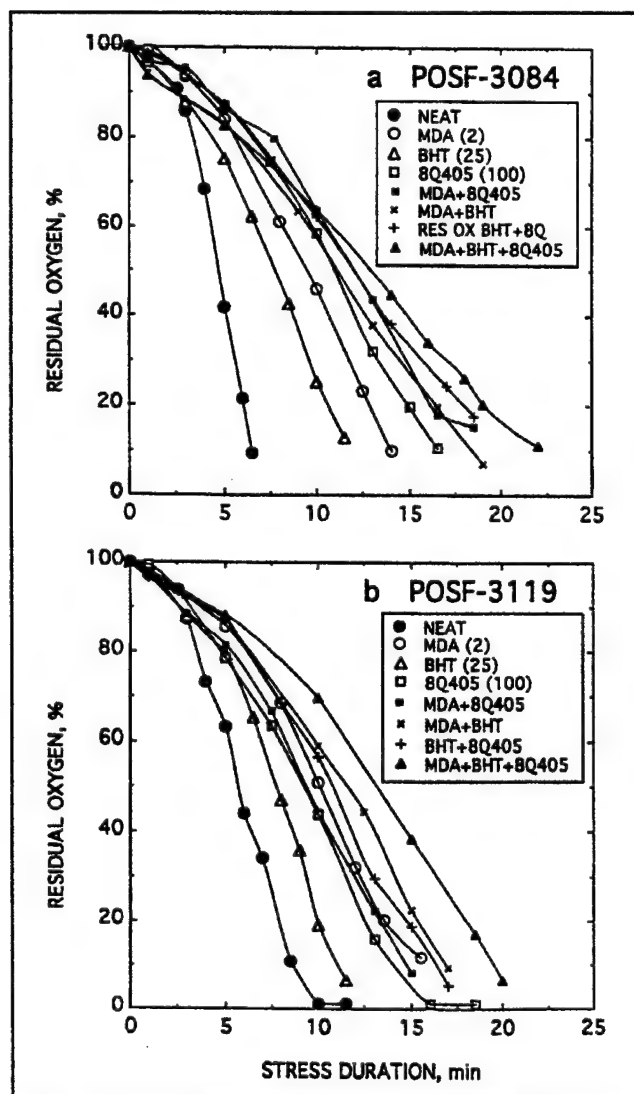


Figure 1. Autoxidation of POSF-3084 (a) and POSF-3119 (b): effect of additives.

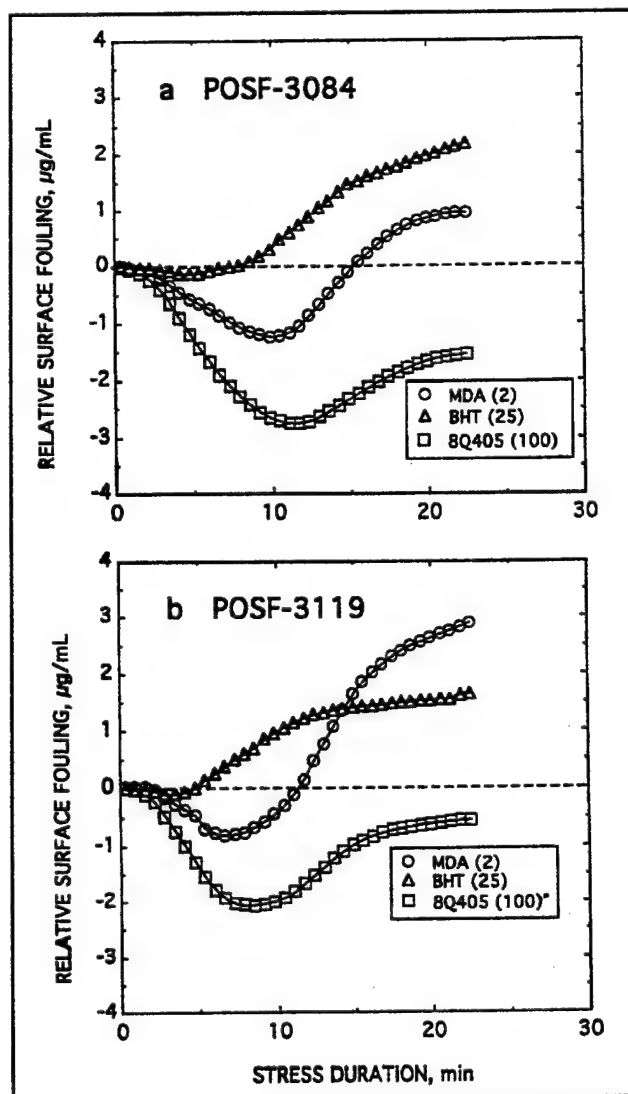


Figure 2. Relative surface fouling in POSF-3084 (a) and POSF-3119 (b): effect of additives used singly.

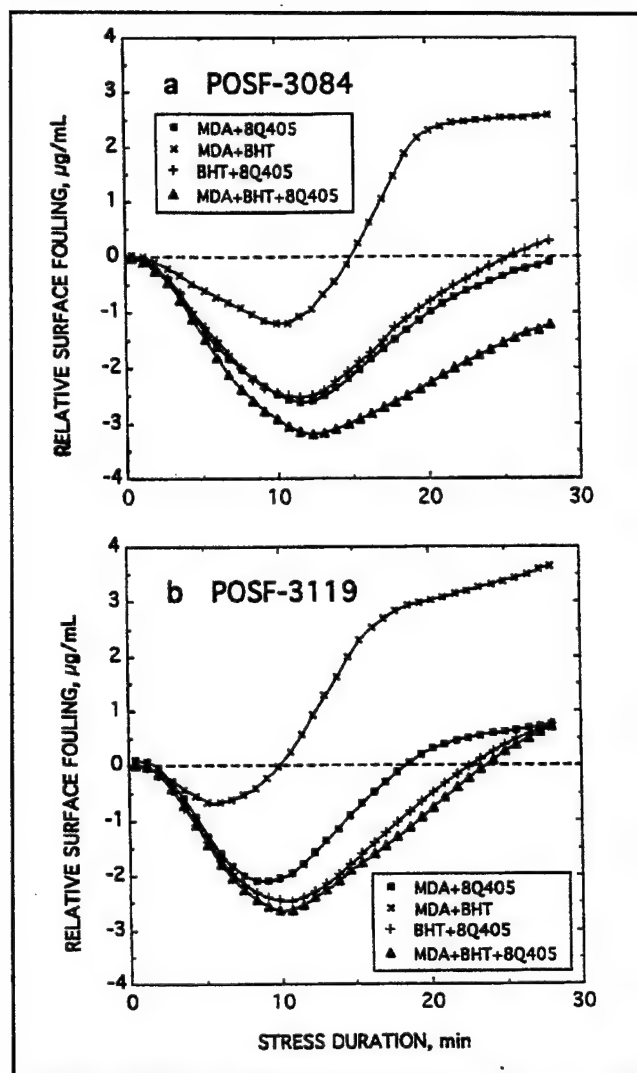


Figure 3. Relative surface fouling in POSF-3084 (a) and POSF-3119 (b): effect of additives used in combination.

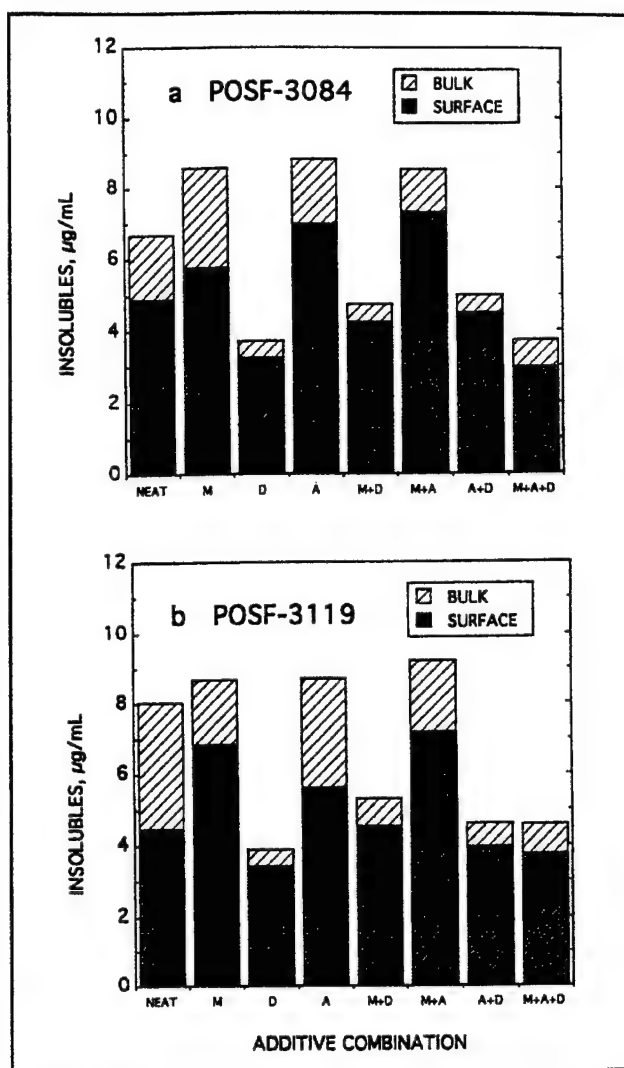


Figure 4. Insolubles formed after complete oxygen conversion in POSF-3084 (a) and POSF-3119 (b): effect of additives. M: MDA, D: Dispersant, A: Antioxidant.

Insolubles at Complete Conversion

Additives also impact the quantity of bulk insolubles collected on in-line filters. Filtration occurs following 23 - 28 min of stressing; thus, quantification relates only to the condition of complete oxygen conversion. The total quantities of surface and bulk insolubles evaluated at 185°C are given in Figures 4a and 4b for POSF-3084 and POSF-3119, respectively. Used singly, the dispersant 8Q405 exerts the greatest effect in reducing bulk and total insolubles, while neither BHT nor MDA has significant impact. Both BHT and MDA operate to slow autoxidation, the former by slowing free-radical propaga-

tion and the latter by slowing metal-catalyzed initiation; however, when fuels are evaluated following long-term stressing which permits all oxygen to react, i.e., completion of autoxidation and deposition, the impact of delays is negated. Dispersants operate by reducing agglomeration to keep particle size small; the current data indicate that this is an essential step for reducing the quantity of bulk insolubles. Since the two filters (0.45 and 0.20 μm) are in series, the partitioning of insolubles provides some quantitative information concerning particle size. The histograms in Figures 5a and 5b, giving the percentage of insolubles transmitted by the 0.45 μm filter for each additive combina-

tion, clearly indicate the impact of the dispersant in reducing particle size. POSF-3084 and POSF-3119 exhibit the same patterns, indicating that in cases where bulk insolubles are mitigated, the size of bulk particles has been reduced. The benefit of the dispersant is apparent for both limited and complete oxygen conversion.

CONCLUSIONS

A series of experiments has been conducted using a metal deactivator, antioxidant, and dispersant singly and in combination at fixed concentrations to study their effect on the thermal stability of two metal-containing aviation fuels. Thermal-sta-

bility evaluation was based on dissolved-oxygen measurements to monitor autoxidation and on surface-carbon measurements to monitor the rate of surface fouling under conditions where catalytic wall effects are minimized.

In autoxidation experiments it is found that 1) each additive used singly inhibits autoxidation, 2) each additive used in conjunction with MDA exerts a more pronounced effect, and 3) the three additives used together cause the greatest inhibition of autoxidation. Dispersants are known to prevent agglomeration, but the impact of 8Q405 in slowing autoxidation suggests a second—and, possibly, more important—role of dispersants, i.e., reducing metal-catalyzed free-radical initiation.

In deposition experiments the additive effect is found to be dependent on whether the evaluation is made after short or long stress times. For conditions of short stress times, all single and multiple additive combinations, with the exception of BHT, reduce surface fouling. The major improvement could be traced to the dispersant and, to a lesser extent, to MDA; but the three-additive combination caused the greatest reduction. Under conditions where the fuel is stressed for long times to allow complete O₂ conversion, surface deposits are not significantly reduced; however, the quantity of bulk insolubles is reduced markedly for all additive combinations containing the dispersant. These benefits are attributed to reduced agglomeration, based upon partitioning of bulk insolubles on the in-line filters.

Overall, the use of BHT does not cause a decrease in surface fouling;

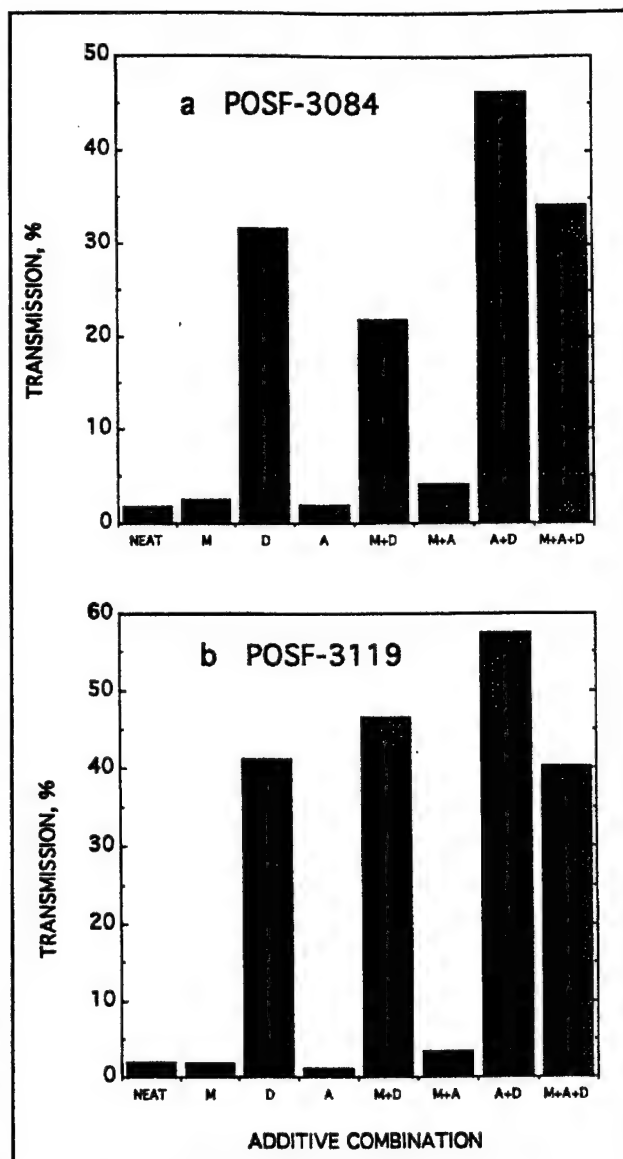


Figure 5. Percentage of bulk insolubles formed having diameters $< 0.45 \mu\text{m}$ (percent transmission through $0.45\text{-}\mu\text{m}$ filter) in POSF-3084 (a) and POSF-3119 (b) effect of additives. M: MDA, D: Dispersant, A: Antioxidant.

the use of MDA results in improvements, but only for short stress times; and the dispersant is the dominant additive. All combinations containing the dispersant improve thermal stability based on autoxidation, surface-fouling, and bulk-insoluble criteria. The greatest improvement in autoxidation (slowing) and in deposition (reduction) occurred with the use of the three-additive combination. This finding is ascribed not to synergism but to a nonlinear addition of individual effects. The current re-

sults indicate that the introduction of MDA into metal-containing fuels slows autoxidation and reduces surface fouling over short stress times at 185°C ; however, reversals in surface fouling for longer stress times raise concerns for the use of MDA as a single additive. When MDA is used in conjunction with an antioxidant and dispersant, additional benefits are obtained that are attributable primarily to the dispersant.

ACKNOWLEDGMENTS

This work was funded by Wright Laboratory, Aero Propulsion and Power Directorate, Wright-Patterson AFB, Ohio, under USAF Contract Nos. F33615-90-C-2033 (with SRL) and F33615-95-C-2507 (with ISSI). The current work was performed with the cooperation and encouragement of Mr. Steve Anderson (USAF) in his role as monitor of the JP-8+100 program. The authors would like to thank Mr. Tim Gootee for performing the surface-carbon analyses and Mrs. Marian Whitaker for lending editorial assistance.

LITERATURE CITED

- (1) Zabarnick, S., and Grinstead, R. R., *Ind. Eng. Chem. Res.*, **33**, 2771 (1994).
- (2) Jones, E. G., Balster, L. M., and Balster, W. J., *Energy Fuels*, **9**, 906 (1995).
- (3) Hazlett, R. N., *Thermal Oxidation Stability of Aviation Turbine Fuels*, ASTM Monograph

- 1, American Society for Testing and Materials, Philadelphia, Chapters VIII-IX (1991).
- (4) Clark, R. H., Proceedings of the 3rd International Conference on the Stability and Handling of Liquid Fuels (Institute of Petroleum, London, pp. 283-293 (1988).
- (5) Morris, R. E., and Turner, N. H., Fuel Sci. Technol. Int., 8, 327 (1990).
- (6) Mills, J. S., and Kendall, D. R., J. Eng. Gas Turb. Power, 108, 381 (1986).
- (7) Schreifeis, J. A., Morris, R. E., Turner, N. H., Mowery, R. L., and Hues, S. M., Energy Fuels, 5, 263 (1991).
- (8) Jones, E. G., and Balster, W. J., Energy Fuels, 7, 968 (1993).
- (9) Rubey, W. A., Striebich, R. C., Tissandier, M. D., Tirey, D. A., and Anderson, S. D., J. Chromatogr. Sci., 33, 433 (1995).
- (10) Restek Corporation, Bellefonte, PA.
- (11) Jones, E. G., and Balster, W. J., Energy Fuels, 9, 610 (1995).
- (12) Scott, G., Atmospheric Oxidation and Antioxidants, Elsevier, New York, p. 17 (1965).
- (13) Jones, E. G., Balster, W. J., and Balster, L. M., "Quantitative Evaluation of the Effectiveness of a Metal Deactivator in Reducing Insolubles in Aviation Fuels," to be presented at the 41st ASME Gas Turbine and Aeroengine Congress, Birmingham, United Kingdom, June 10-13, 1996.
- (14) Golubeva, I. A., Klinaeva, E. V., and Yakoviev, V. S., Chem. Technol. Fuels Oils, 30, 119 (1994).
- (15) Pande, S. G., and Hardy, D. G., Energy Fuels, 9, 177 (1995).

Evaluation of the Effectiveness of a Metal Deactivator and Other Additives in Reducing Insolubles in Aviation Fuels

E. G. Jones

W. J. Balster

L. M. Balster

Innovative Scientific Solutions, Inc.,
2786 Indian Ripple Road,
Dayton, OH 45440-3638

Surface fouling in aircraft fuel lines resulting from autoxidation of aviation fuel leads to reduced efficiency as deposits collect on heat exchangers, nozzles, and servocontrols and may ultimately lead to system failure. Metal surfaces and trace quantities of metals dissolved in the fuel exacerbate the surface-fouling problem because they can catalyze free-radical initiation, thereby accelerating autoxidation. Additives and additive packages containing antioxidants, dispersants, and metal deactivators (MDA) have been shown to reduce insolubles in some fuels. Because of metal chelation and possible metal-surface passivation, MDA has been proposed as an additive component to be included in all fuels, even those without dissolved metals. The goal of the present study was to obtain fundamental information on the behavior of MDA under conditions where surface-passivation effects are minimal. Experiments have been conducted to (1) study the effects of adding MDA to fuels containing a significant concentration of dissolved metals (i.e., chelation) and to those containing minor concentrations of dissolved metals and (2) investigate interactions when MDA is used in conjunction with an antioxidant and a dispersant. Simple fuel-line-fouling simulations with a single-pass tubular heat exchanger operated under near-isothermal conditions have been conducted to study the thermal behavior at 185°C of several neat and MDA-treated jet fuels as well as fuels treated with MDA plus other additives. Comparison of neat and treated fuels is based on several criteria: (1) dependence of autoxidation on stress duration, (2) dependence of surface deposition on stress duration, and (3) quantity of total insolubles (bulk filterables and surface deposits). Potential advantages and disadvantages of using MDA alone and in combination are discussed.

Introduction

Fouling of aircraft fuel lines that results from autoxidative and pyrolytic degradation of jet fuel is a significant problem for current aircraft and is projected to become more serious in the future, particularly for military aircraft (Edwards et al., 1992; Edwards, 1993). Approaches taken to mitigate fouling include (1) additional refining techniques such as hydrotreatment to remove trace polar components, (2) innovative on-board fuel management to utilize the additional fuel-sink capacity of the fuel, and (3) introduction of individual additives and additive packages, including antioxidants to slow autoxidation, metal deactivators to reduce the rate of initiation and possibly passivate metal surfaces, and dispersants/detergents to prevent agglomeration of insolubles. The use of these and other specific additives to inhibit corrosion, fuel icing, and static charge has been summarized by Martel (1987). As part of the USAF JP-8 + 100 program to improve fuel operating stability by 100°F (Edwards et al., 1993), the use of a generic additive package containing the antioxidant BHT, dispersant 8Q405, and metal deactivator MDA has been proposed.

Dispersants and, to a lesser extent, antioxidants have been shown to improve thermal stability in USAF fuels (Zabarnick and Grinstead, 1994; Jones et al., 1995); however, the use of MDA is still under consideration. Experimental studies on the use of MDA in aviation fuels are extensive and have been reviewed and summarized by Hazlett (1991). Metal deactiva-

tors have been reported (Clark, 1988) to operate via two distinct mechanisms: (1) chelation of metal ions and (2) surface passivation. Many reports in the literature support the role of chelation (Morris and Turner, 1990; Mills and Kendall, 1986); however, the role of surface passivation is less clear (Morris and Turner, 1990; Schreifels et al., 1991).

The goal of the current study was to use a very simple laboratory simulation of fuel-line fouling for (1) obtaining quantitative data for autoxidation and deposition at a fixed temperature (185°C) from several neat and MDA-treated aviation fuels, (2) making a comparison with similar data obtained from antioxidant- and dispersant-treated fuels, and (3) investigating possible benefits of using MDA, antioxidants, and dispersants in combination. The experimental conditions were specifically selected to discriminate against any metal-surface passivation mechanism by MDA and focus on the homogeneous function of MDA and other additives within the bulk fuel. In order to minimize possible complications from surface effects, autoxidation was studied for fuel reacting in tubing having inner surfaces passivated by the Silcosteel process. Also, deposition was studied using tests of long duration (72 h) in which inner wall surfaces became passivated by deposition early in the course of testing. The selection of 185°C for additive evaluation is predicated on the need for achieving isothermal reaction conditions in the absence of fluid-dynamic complications in order to simplify data interpretation. However, it should be noted that MDA may function quite differently if evaluated at higher temperatures under nonisothermal conditions of fast fuel flow.

Experimental Arrangement

The physical properties of the six fuels studied in this program are summarized in Table 1. Neat and additized fuels were

Contributed by the International Gas Turbine Institute and presented at the 41st International Gas Turbine and Aeroengine Congress and Exhibition, Birmingham, United Kingdom, June 10–13, 1996. Manuscript received at ASME Headquarters February 1996. Paper No. 96-GT-204. Associate Technical Editor: J. N. Shinn.

Table 1 Properties of aviation fuels

Fuel No.	Class	JFTOT Breakpoint Temp., K	Total S ppm	Dissolved Metals, ppb*
2827	Jet-A, Straight Run	539	790	Cu, <5; Fe, 8
2980	Jet-A, Merox-Treated	561	614	Cu, <5; Fe, <5
2962	JP-5		438	Cu, 10; Fe, <5
2934	JP-8	539	755	Cu, 34; Fe, <5
3084	Jet-A	541	527	Cu, 35; Fe, <5
3119	Jet-A	516	1000	Cu, 7; Fe, 26

*Measurements made for USAF using graphite Zeeman/5000 System Atomic Absorption Spectrometer by United Technologies, Pratt and Whitney.

initially saturated with respect to air at room temperature and were passed through a 15- μ m filter before use. Information on MDA and the other additives is given in Table 2. Reaction occurred as fuel was pumped through 0.318-cm- (0.125-in.-) o.d., 0.216-cm- (0.085-in.-) i.d. tubing, clamped tightly within a Cu-block heat exchanger at 185°C. System pressure was maintained at 2.3 MPa to ensure a single reaction phase. Two experimental arrangements were utilized, differing only in the length of the heat exchanger.

The concentration of dissolved oxygen, O_2 , was measured using the first or standard setup with the NIFTR, which has been described in detail elsewhere (Jones et al., 1993) and will be reviewed here only briefly. For these experiments a fixed reaction pathlength of 81.3 cm (32 in.) was used; stress duration or residence time was varied by changing the fuel flow rate and was calculated based on plug flow, with a 15 percent correction to accommodate fuel expansion at 185°C. Dissolved oxygen was measured in-line at system pressure using a GC technique developed by Rubey and co-workers (1995). Based on the difference between O_2 readings for the unstressed and stressed fuel, the percentage of residual O_2 was determined as a function of the calculated reaction time. The tubing selected for O_2 experiments was passivated by the Silcosteel process (Restek Corp.) in order to minimize possible surface catalytic effects. Reproducibility in oxidation data is estimated to be ± 5 percent.

Deposition experiments were conducted using the second experimental arrangement with an extended-length heat exchanger (NIFTR-2). Under fixed flow rates of 0.25 and 0.20 ml/min, this unit has a continuous, isothermal 183-cm heated pathlength that provides 23 and 28 min, respectively, of stressing to accommodate the complete deposition profile of all fuels and most additized fuels used in this study. Deposits were collected over a relatively long test duration (72 h), resulting in the passage of 864–1080 ml of air-saturated fuel during the course of each experiment. Commercial stainless-steel (304) tubing was used for all deposition experiments; during the first few hours of each test, the original stainless-steel surfaces became covered with deposits and were passivated with respect to autoxidation (Jones and Balster, 1995). Thus, deposition and autoxidation experiments were conducted under very similar test conditions, with minimal interaction of metal surfaces.

Because of the slow fixed flow rate used in deposition experiments, isothermal conditions prevail after fuel has passed ~ 5 cm into the block; thus, the reaction time is proportional to the

Table 2 Additives studied

Class	Name	Chemical Name	Source	Conc. (mg/L)
Antioxidant	BHT	2,6-di-tert-butyl-p-cresol	DuPont	25
Metal Deactivator	MDA	N,N'-disalicylidene-1,2-propanediamine	DuPont	2, 6
Dispersant	8Q405	proprietary	Betz	100

distance along the heated tube. Reaction time is calculated from tubing dimensions and flow rate, with corrections being made for fuel expansion. At test completion, the tube was cut into a total of 36 segments, each 5.1 cm long. Following heptane rinse and vacuum drying (130°C for 12 h), the carbon associated with the surface deposit was quantified by conventional surface-carbon-burnoff techniques (LECO RC-412). The surface-deposition rate on each tubing segment was calculated from the amount of carbon measured in burnoff, the fuel residence time within that tubing segment, and the total amount of fuel passed. Rate is expressed in units of micrograms of carbon/hour per milliliter of fuel, representing an average over the entire 72-h test period, and is plotted as a function of stress duration. The total surface carbon (μ g/ml) was obtained by integrating the differential-rate data. Reproducibility in deposition data is estimated to be ± 20 percent.

Bulk insolubles were collected over the entire 72-h test period on two sets of in-line Ag-membrane filters (0.45 and 0.2 μ m). The quantity of bulk insolubles from the two filter sets was summed and expressed in units of micrograms per milliliter, representing an average over complete oxygen conversion. Filter housings located ~ 10 cm from the heat exchanger remained near room temperature; thus, measured filterables include additional contributions resulting from fuel cooling.

Results and Discussion

Effect on Autoxidation and Deposition of Using MDA at a Concentration of 2 mg/L. The impact of adding MDA at a concentration of 2 mg/L to six fuels is shown in Fig. 1. Autoxidation in plots a–c for fuels that contain low concentrations of dissolved metals is only slightly delayed by MDA. On the other hand, autoxidation in plots d–f for fuels that contain greater concentrations of dissolved metals is significantly slowed by the chelating effects of MDA, as evidenced by the observed delays. The sensitivity of autoxidation, as measured in passivated tubing, to dissolved metals and to treatment with MDA makes comparisons such as those in Fig. 1 definitive in detecting the presence of metals.

The corresponding deposition rates are given in Fig. 2. For brevity, consideration has been limited to only two fuels of each category. Deposition in POSF-2827 shows no effect from introduction of MDA, while POSF-2980 with MDA shows some slight delay but virtually the same deposition profile. The response to MDA in the two metal-containing fuels is more pronounced. The deposition profiles broaden and are shifted to longer stress times. Such changes are anticipated from the slowed autoxidation that arises when chelation of the dissolved

Nomenclature

BHT = Hindered-Phenol Antioxidant, see Table 2

GC = Gas Chromatograph

JFTOT = Jet-Fuel Thermal-Oxidation Test

MDA = Metal Deactivator, see Table 2
NIFTR = Near-Isothermal Flowing Test Rig

POSF = Jet-Fuel Designation, see Table 1

USAF = United States Air Force
8Q405 = Dispersant, see Table 2

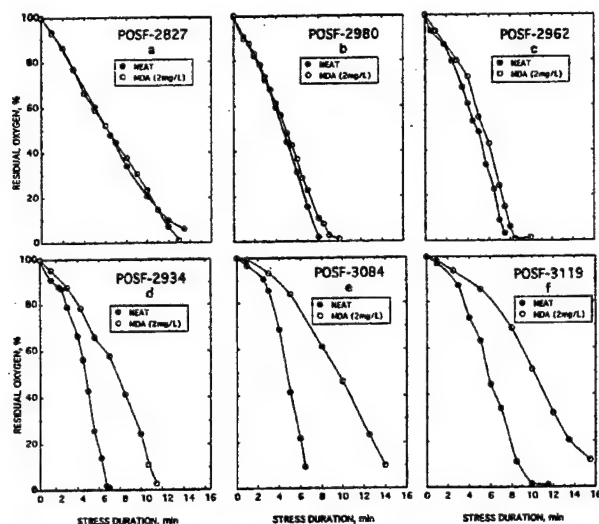


Fig. 1 Effect of MDA (2 mg/L) on autoxidation of fuels without dissolved metals (a, b, c) and with dissolved metals (d, e, f)

copper eliminates metal-initiated autoxidation (Scott, 1965). The beneficial reduction in fouling related to the autoxidation delay is noticeable; however, after deposition processes have been completed, more total deposits (area under profiles) have been produced in the MDA-treated fuels. Since fuels are rarely stressed to complete oxygen conversion, this latter point may be moot; however, it does raise questions as to what chemical or physical changes may be occurring in the MDA-treated fuels, leading to the observed increase in total deposits.

Effects on Deposition of Using MDA at a Concentration of 6 mg/L. A maximum of 5.8 mg/L of MDA is allowed in JP-8 aviation fuel, according to specification Mil-T-83133D; however, a concentration of 2 mg/L represents an excess of chelating agent for the current concentrations of dissolved metals. Thus, introduction of MDA at higher concentrations should not significantly alter either the autoxidation or surface-fouling behavior. This view is supported by the deposition data in Fig. 2 for POSF-3084. More significant changes are apparent with

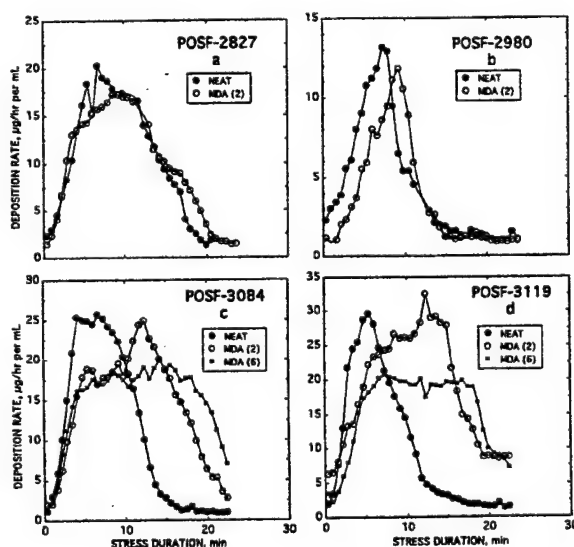


Fig. 2 Effect of MDA (2 mg/L) on surface deposition in fuels without dissolved metals (a, b) and of MDA (2 and 6 mg/L) in fuels with dissolved metals (c, d)

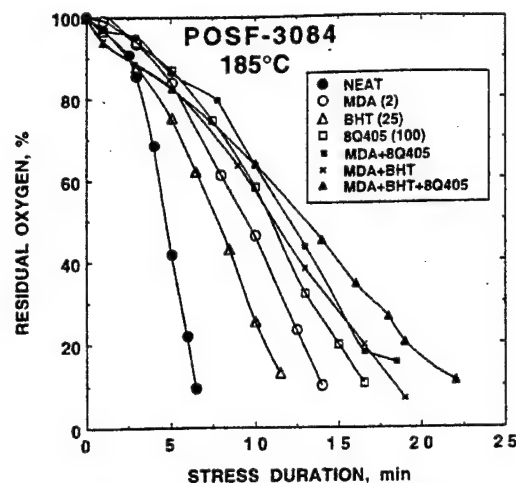


Fig. 3 Autoxidation of POSF-3084: effect of additives singly and in combination with MDA

higher MDA concentrations in POSF-3119, although it is not clear whether the observed differences fall outside experimental reproducibility.

Autoxidation in POSF-3084 and -3119; MDA, Antioxidant, and Dispersant Used Singly and in Combination. Two candidate additives that have been identified as effective in reducing surface fouling in fuels are the antioxidant BHT (25 mg/L) and the proprietary dispersant 8Q405 (100 mg/L). In the following sections the effect of additives is assessed only for the two metal-containing fuels POSF-3084 and -3119. The impact of the three additives used singly and in all combinations containing MDA is considered, maintaining fixed individual concentrations.

The autoxidation data for POSF-3084 are given in Fig. 3. When used singly, all three additives slow autoxidation relative to the neat fuel. As discussed above, MDA introduces a delay due to metal chelation; similar delays can arise from an antioxidant because the free-radical chain-breaking mechanism of hindered phenols slows the chain-propagation rate. However, the role of a dispersant in slowing autoxidation is unknown. In a previous report (Jones et al., 1995), we noted that the dispersant 8Q405 does not slow autoxidation in fuels such as POSF-2827 and -2980 that do not contain dissolved metals but does slow autoxidation in another Cu-containing fuel, POSF-2934. This suggests that the dispersant is operating to offset the free-radical initiating effect of the dissolved copper. Interestingly, autoxidation is slowed more by the dispersant than by either the antioxidant or MDA.

Additive pairs containing MDA inhibit autoxidation more than any individual additive. Incorporation of all three additives provides the optimum slowing of autoxidation. The current data are best explained by accumulating delays in autoxidation, which are less than their summed effects.

Similar to these observations, in POSF-3119 (Fig. 4) when all three additive types are introduced singly, autoxidation is slowed relative to the neat fuel. Use of BHT in conjunction with MDA slows autoxidation relative to that in the MDA-treated fuel. As was noted for POSF-3084, incorporation of all three additives provides an antioxidant effect that is greater than any individual or pair combination but not greater than the sum of the three individual effects. The two fuels when treated with the three-additive combination behave similarly, requiring ~21–23 min for total oxygen conversion. Again, benefits accrue from the use of multicomponent additives, but the absence of overall effects greater than the sum of the individual effects indicates antagonism or overlap of additive function rather than

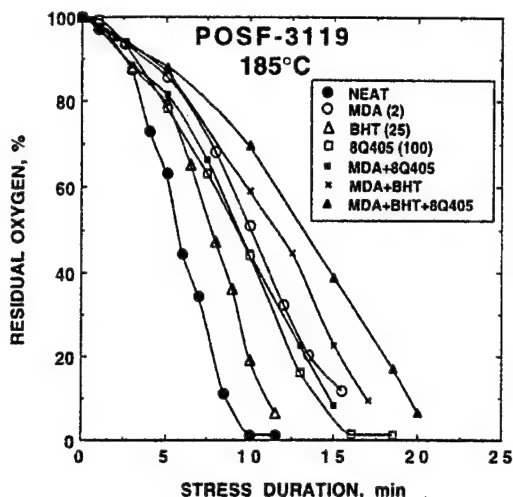


Fig. 4 Autoxidation of POSF-3119: effect of additives singly and in combination with MDA

synergism. For example, if the dispersant is functioning to cancel some of the catalytic initiation of dissolved metals, then its application with MDA will result in a competitive rather than a cooperative interaction.

Surface Deposition in POSF-3084 and -3119: MDA, Antioxidant, and Dispersant Used Singly. In order to better visualize differences resulting from the incorporation of additives and reduce overlap in the differential-rate data such as shown in Fig. 2, the deposition data are presented in the following format. The total surface carbon in each additized fuel is summed along the tube (integration under curves such as in Fig. 2) and is corrected by subtracting the corresponding sum obtained with the neat fuel. This results in the total surface carbon for each additive relative to the neat fuel; positive and negative values indicate, respectively, increased and decreased surface fouling caused by additive introduction. For example, the relative behavior upon introduction of the three individual additives is given in Figs. 5(a) and 5(b).

The two fuels behave similarly. BHT causes negligible reduction in fouling ($<0.2 \mu\text{g/mL}$) at short stress times and a pronounced increase ($\sim 2 \mu\text{g/mL}$) for longer times. Despite the effectiveness of BHT in slowing autoxidation, its introduction does not correspondingly reduce surface deposition. Contrast the introduction of MDA, which does effectively reduce fouling for short stress times, reflecting delays in autoxidation. However, for longer stress times the situation reverses, and MDA causes the total deposition to increase relative to the neat fuels. The reasons for such reversals in surface fouling using MDA are not apparent; this is a topic of current investigation in our laboratory. Finally, the dispersant provides the greatest reduction in surface fouling for all stress times. Based upon Figs. 5(a) and 5(b), the order of the individual additives with respect to their ability to reduce surface fouling in metal-containing fuels is $8\text{Q}405 > \text{MDA} \gg \text{BHT}$.

Surface Deposition in POSF-3084 and -3119: Antioxidant and Dispersant Used in Combination With MDA. The impact of the three additives used in combination for the same two fuels is given in Figs. 5(c) and 5(d). It was previously noted that all additive combinations delay autoxidation (see Figs. 3 and 4) relative to the neat fuels. All combinations similarly reduce surface fouling relative to the neat fuels for the first 10 min of stressing. When used in pairs, MDA + 8Q405 causes the greatest reduction in surface fouling, and MDA + BHT causes the least reduction. The behavior of MDA + BHT

is approximately equal to the average of the individual additive effects in improving thermal stability for short times, but the benefits disappear at higher conversion. This combination of antioxidant and MDA has been reported to improve long-term storage stability in Cu-containing diesel fuels (Golubeva et al., 1994), and it has recently been postulated that MDA is effective only when introduced at the refinery, i.e., prior to Cu exposure (Pande and Hardy, 1995). The impact of the dispersant is greater than that of the antioxidant and MDA. The combination of the three additives provides the greatest reduction in surface fouling, and this finding is consistent with the observed delays in autoxidation shown in Figs. 3 and 4. The relative order of the additive and additive combinations in their ability to reduce fouling in metal-containing fuels is $\text{MDA} + \text{BHT} + 8\text{Q}405 > 8\text{Q}405 > \text{MDA} + 8\text{Q}405 > \text{MDA} \approx \text{MDA} + \text{BHT} \gg \text{BHT}$.

Quantification of Surface and Bulk Insolubles for Complete Conversion: Additive Combinations With MDA. Additives also impact the quantity of bulk insolubles collected on in-line filters. Filtration occurs following 23–28 min of stressing; thus, quantification relates only to the condition of complete oxygen conversion. The total quantities of surface and bulk insolubles evaluated at 185°C are given in Fig. 6. Used singly, the dispersant 8Q405 exerts the greatest effect in reducing bulk and total insolubles, while neither BHT nor MDA has significant impact. Both BHT and MDA operate to slow autoxidation, the former by slowing free-radical propagation and the latter by slowing metal-catalyzed initiation; however, when fuels are evaluated based on long-term stressing, which permits all oxygen to react, i.e., completion of autoxidation and deposition, the impact of delays is negated. Dispersants operate by reducing agglomeration to keep particle size small; the current data indicate that this is an essential step for reducing bulk insolubles. Since the two filters (0.45 and $0.20 \mu\text{m}$) are in series, the partitioning of insolubles on them provides some quantitative information concerning the dimensions of the bulk particles. The histogram in Fig. 7, giving the percentage of insolubles transmitted by the $0.45\text{-}\mu\text{m}$ filter for each additive combination, clearly indicates the impact of the dispersant in reducing particle size. POSF-3084 and -3119 exhibit the same patterns in Figs. 6 and 7, indicating that cases where surface and bulk insolubles are mitigated are coincident

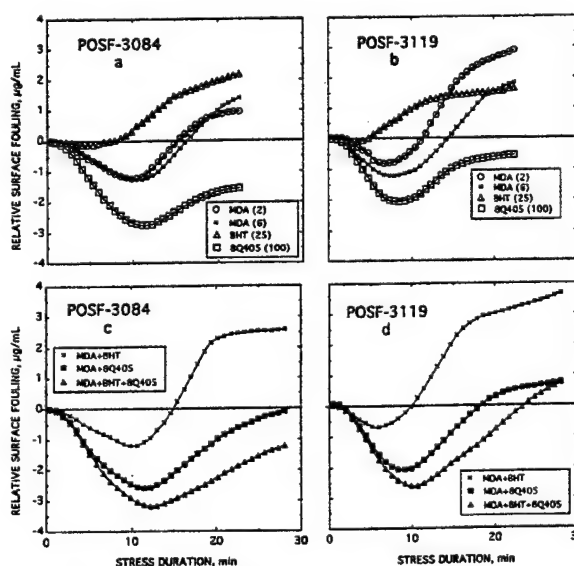


Fig. 5 Relative surface fouling in fuels with dissolved metals for additives used singly (a, b) and in combination with MDA (c, d)

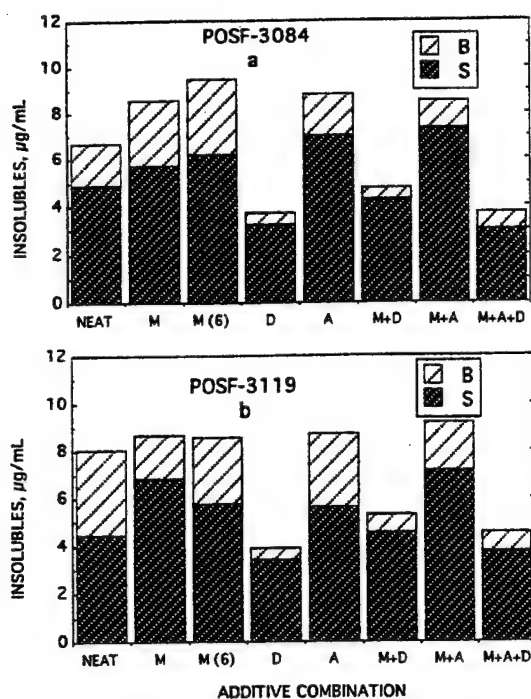


Fig. 6 Histogram of quantity of surface and bulk insolubles formed in neat and additized POSF-3084 (a) and -3119 (b) fuels evaluated for complete oxygen conversion. M: MDA, D: dispersant, A: antioxidant.

with cases where the size of bulk particles has been reduced. The benefit of the dispersant is apparent for both limited and complete oxygen conversion.

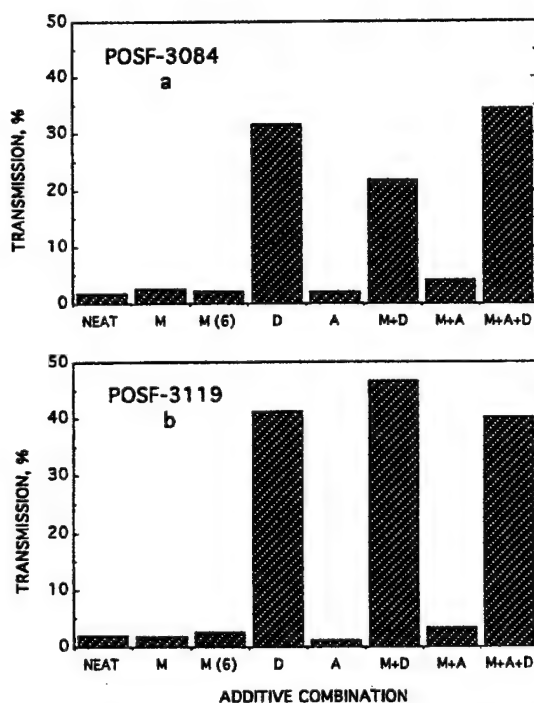


Fig. 7 Histogram showing percentage of bulk insolubles having diameters less than $0.45\ \mu\text{m}$ (percent transmission through $0.45\text{-}\mu\text{m}$ filter) in neat and additized POSF-3084 (a) and -3119 (b) fuels. M: MDA, D: dispersant, A: antioxidant.

Summary and Conclusions

A series of experiments has been conducted using MDA along with an antioxidant and a dispersant to study their effects on the thermal stability of aviation fuels when used singly and in combination at fixed concentrations. Thermal-stability evaluation was based on dissolved-oxygen measurements to monitor autoxidation and on surface-carbon measurements to monitor the rate of surface fouling. Autoxidation occurring in three fuels containing negligible concentrations of dissolved metals is minimally altered by MDA, whereas for three fuels containing metals, autoxidation is slowed significantly; this observation is consistent with dissolved-metal chelation by MDA. Similarly, MDA causes minor changes in surface-deposition rates in two fuels without dissolved metals but delays deposition in two fuels containing dissolved metals.

In autoxidation experiments using the two metal-containing fuels POSF-3084 and -3119, it was found that (1) each additive used singly inhibited autoxidation, (2) each additive used in conjunction with MDA exerted a more pronounced effect in POSF-3084, whereas delays were less obvious in POSF-3119, and (3) the three additives used together caused the greatest inhibition of autoxidation. Dispersants are known to prevent agglomeration, but the impact of 8Q405 in slowing autoxidation suggests a second—and, possibly, more important—role of dispersants, i.e., reducing metal-catalyzed free-radical initiation.

In deposition experiments with the same fuels, differences in the total additive effect are found to be dependent on whether the evaluation is made after short or long stress times. For conditions of short stress times, with the exception of BHT, all single and multiple additive combinations reduced surface fouling. The major improvement could be traced to the dispersant and, to a lesser extent, to MDA; but the three-additive combination caused the greatest reduction. Under conditions where the fuel is stressed for long times, surface deposits are not significantly reduced; however, the quantity of bulk insolubles drops for all additive combinations containing the dispersant. These benefits are attributed to reduced agglomeration based upon partitioning of bulk insolubles on the in-line filters.

Overall, the dispersant is the dominant additive, and all combinations containing it exhibit the greatest improvement in thermal stability based on autoxidation or surface-fouling criteria. The greatest improvement in autoxidation (slowing) and in deposition (reduction) occurred with the use of the three-additive combination. This finding is ascribed not to synergism, but to a nonlinear addition of individual effects.

The current results indicate that the introduction of MDA into metal-containing fuels slows autoxidation and reduces surface fouling over short stress times at 185°C ; however, reversals in surface fouling for longer stress times raise concerns for its use as a single additive. When MDA is used in conjunction with an antioxidant and dispersant, additional benefits are obtained that are attributable primarily to the dispersant.

Acknowledgments

This work was funded by Wright Laboratory, Aero Propulsion and Power Directorate, Wright-Patterson AFB, Ohio, under USAF Contract Nos. F33615-90-C-2033 (with SRL) and F33615-95-C-2507 (with ISSI). The current work was performed with the cooperation and encouragement of Mr. Steve Anderson (USAF) in his role as monitor of the JP-8 + 100 program. The authors would like to thank Mr. Tim Gootee for performing the surface-carbon analyses and Mrs. Marian Whitaker for lending editorial assistance.

References

- Clark, R. H., 1988, "The Role of a Metal Deactivator in Improving the Thermal Stability of Aviation Kerosines," *Proc. 3rd International Conference on the Stability and Handling of Liquid Fuels*, Institute of Petroleum, London, U. K., pp. 283–293.

- Edwards, T., Anderson, S. D., Pearce, J. A., and Harrison, W. E., III, 1992, "High Temperature Fuels—An Overview," AIAA Paper No. 92-0683.
- Edwards, T., 1993, "USAF Supercritical Hydrocarbon Fuels Interests," AIAA Paper No. 93-0807.
- Edwards, T., Roquemore, W. M., Harrison, W. E., III, and Anderson, S. D., 1993, "Research and Development in High Thermal Stability Fuels," Paper No. PEP-18, *AGARD Conference Proceedings 536, Fuels and Combustion Technology for Advanced Aircraft Engines*, Advisory Group for Aerospace Research and Development, Neuilly sur Seine, France.
- Golubeva, I. A., Klinaeva, E. V., and Yakoviev, V. S., 1994, "Stabilization of Blended Diesel Fuels by Combinations of Antioxidants and Metal Deactivators," *Chemistry and Technology of Fuels and Oils*, Vol. 30, pp. 119–122.
- Hazlett, R. N., 1991, *Thermal Oxidation Stability of Aviation Turbine Fuels*, ASTM Monograph 1, American Society for Testing and Materials, Philadelphia, Chaps. VIII and IX.
- Jones, E. G., and Balster, W. J., 1993, "Phenomenological Study of Formation of Insolubles in a Jet-A Fuel," *Energy and Fuels*, Vol. 7, pp. 968–977.
- Jones, E. G., and Balster, W. J., 1995, "Surface Fouling in Aviation Fuel: Short- vs. Long-Term Isothermal Tests," *Energy and Fuels*, Vol. 9, pp. 610–615.
- Jones, E. G., Balster, L. M., and Balster, W. J., 1995, "Quantitative Evaluation of Jet-Fuel Fouling and the Effect of Additives," *Energy and Fuels*, Vol. 9, pp. 906–912.
- Martel, C. R., 1987, "Military Jet Fuels, 1944–1987," Technical Report AFWAL-TR-87-2062, Air Force Wright Aeronautical Laboratories, Wright-Patterson Air Force Base, OH.
- Mills, J. S., and Kendall, D. R., 1986, "The Quantification and Improvement of the Thermal Stability of Aviation Turbine Fuel," *ASME JOURNAL OF ENGINEERING FOR GAS TURBINES AND POWER*, Vol. 108, p. 381.
- Morris, R. E., and Turner, N. H., 1990, "Influences Exerted by Metal Deactivator on the Thermal Stability of Aviation Fuels in the Presence of Copper," *Fuel Science and Technology International*, Vol. 8, p. 327.
- Pande, S. G., and Hardy, D. G., 1995, "Effect of Copper, MDA, and Accelerated Aging on Jet Fuel Thermal Stability as Measured by the Gravimetric JFTOT," *Energy and Fuels*, Vol. 9, pp. 177–182.
- Rubey, W. A., Striebig, R. C., Tissandier, M. D., Tirey, D. A., and Anderson, S. D., 1995, "Gas Chromatographic Measurement of Trace Oxygen and Other Dissolved Gases in Thermally Stressed Jet fuel," *Journal of Chromatographic Science*, Vol. 33, pp. 433–437.
- Schreifels, J. A., Morris, R. E., Turner, N. H., Mowery, R. L., and Hues, S. M., 1991, "Adsorption of a Metal Deactivator Additive Onto Metal Surfaces," *Energy and Fuels*, Vol. 5, pp. 263–268.
- Scott, G., 1965, *Atmospheric Oxidation and Antioxidants*, Elsevier, New York, p. 17.
- Zabarnick, S., and Grinstead, R. R., 1994, "Studies of Jet Fuel Additives Using the Quartz Crystal Microbalance and Pressure Monitoring at 140°C," *Industrial and Engineering Chemistry Research*, Vol. 33, pp. 2771–2777.

3.2.4 Icing Inhibitors

Because of the toxicity of current additives to fuel systems to inhibit icing, an immediate need exists for nontoxic, inexpensive, and biodegradable deicing compounds. The synthesis of polar sugar derivatives as alternatives to glycol-based additives was studied and the results reported in the paper entitled "Jet Fuel System Icing Inhibitors: Synthesis and Stability" (see pp. 690-693).

JET FUEL SYSTEM ICING INHIBITORS: SYNTHESIS AND STABILITY

^{a,b}George W. Mushrush, ^bErna J. Beal, ^bDennis R. Hardy, ^aWayne M. Stalick, ^aSubhash Basu, ^aDennis Grosjean, and ^aJohn Cummings

^aGeorge Mason University, Fairfax, VA 22030, ^bNavy Technology Center for Safety and Survivability, Washington, DC 20375, ^cInnovative Scientific Solutions Inc., 2786 Indian Ripple Road, Dayton, OH 45440, and ^dNaval Air-Warfare Center, Trenton, NJ 08628

ABSTRACT

The current fuel system icing inhibitor additives, used both by the military and commercial aviation, are ethylene glycol monomethyl ether (EGME) and diethylene glycol monomethyl ether (DiEGME). These deicing compounds are toxic at the concentrations that are required for effective deicing. This observation points to an immediate need for non-toxic, inexpensive, and biodegradable deicing compounds. The synthesis of polar sugar derivatives represents viable alternatives to glycol based additives. The synthesis and characterization of acetals, ketals, ethers, and esters of oxoacids will be discussed. These alternative deicing compounds are cheap, fuel stable, and exhibit similar icing inhibitor characteristics to EGME and DiEGME.

INTRODUCTION

The literature of deicing additives for jet fuels is rather sparse. Those articles that have appeared are related to concentration determination, stability in fuels, and health implications of these additives (1, 2). Currently the fuel icing inhibitor additives, ethylene glycol monomethyl ether (EGME) and diethylene glycol monomethyl ether (DiEGME), are mandatory in all military aircraft fuels and are optional in world-wide commercial aviation fuels depending on route, flight length, and season. Unfortunately, ethylene glycol based deicing compounds are toxic at the concentrations that are required for effective deicing (2). These additives are leached out of the fuel and into water bottoms and when this water is drained from fuel system sumps, filters and storage tanks it contains EGME and/or DiEGME thus creating a personnel health hazard. Also, glycols exert high oxygen demand for decomposition and when they get into the environment they cause the death of aquatic organisms as dissolved oxygen is depleted. These observations all point to an immediate need for non-toxic, inexpensive, and biodegradable deicing compounds. The approach of our laboratory is to utilize the large U.S. surplus of sugars as the basis for the synthesis of biodegradable deicing compounds. These potential deicing candidates must satisfy many constraints. They must be soluble in jet fuel, soluble in water, fuel stable during storage, and exhibit similar or enhanced ice inhibiting characteristics to currently used deicing compounds.

The latter of these constraints, concerning the behavior of deicing compounds in fuels, is being investigated in our laboratory since there are no readily available software programs to estimate either the physical or colligative properties of middle distillate fuels. A large number of physicochemical and toxicological properties are prerequisite to a reasonable hazard assessment of a chemical (1). However, environmental fate, and toxicity of chemicals can be estimated using computer models. These predicted values provide the guidance towards synthesizing safer icing inhibitors for this project.

EXPERIMENTAL

The general synthesis procedure followed for the synthesis of the glycerol acetals and ketals was that reported for the synthesis of the 2,2-dimethyl-1,3-dioxolane-4-methanol, compound I (3). The procedure was modified for the synthesis of the formaldehyde (compound II), and acetaldehyde (compound III), adducts. Acetone (232g, 4.5 moles), or acetaldehyde (197g, 4.5 moles), or formaldehyde (135g, 4.5 moles), was added to glycerol (100 g, 1.1 moles) in a toluene solvent (300 mL), containing 3.0 g *p*-toluene sulfonic acid and 255 g of 5A molecular sieves all in a 2,000 mL two-necked, round-bottomed flask fitted with a mechanical stirrer and a condenser. A freezing mixture of ethylene glycol and water at -25.0 °C was circulated through the condenser. The stirred reaction mixture was heated under gentle reflux for 33 hrs using a heating mantle. After reflux, the condenser was disconnected and excess acetaldehyde was allowed to evaporate. The acidic reaction mixture was neutralized with 3.0 g sodium acetate. The molecular sieves were separated by vacuum filtration using a Büchner funnel. The resulting liquid was distilled under vacuum. The colorless organic product distilling at 80-82°C/10 mm was collected for the acetone derivative to give a yield of 88%; for the acetaldehyde derivative the

product distilling at 85-90 °C/10mm was collected to give a yield of 80 %; and for the formaldehyde derivative the product distilling at 95-96°C/10 mm was collected (4).

Computational Methods. In order to estimate environmental fate and certain physical properties, a suite of programs developed by Syracuse Research Corporation was used (5). Well established computational methods are used in these programs.

DISCUSSION

The reaction products of aldehydes and ketones with glycerol have been known for more than 100 years. These compounds were usually regarded as intermediates in synthetic procedures and little interest was expressed in them. The compounds in this study are simpler than the carbohydrates and carbohydrate derivatives so they were the subject of this initial investigation. Acetal and ketal formation is catalyzed by either mineral acids or Lewis acids. The intermediate hemi-acetal or hemi-ketal is not usually isolated. The compounds were subjected to testing for deicing characteristics and compared to EGME, DiEGME, and dipropylene glycol. Dipropylene glycol was included because industries and the Federal Aviation Administration have recommended it as a replacement for the ethylene based deicers. The freezing point tests were conducted in a one gallon simulator rig. The data showed that both compounds II and III were effective deicers and closely paralleled the behavior of EGME and DiEGME(6). Compounds II and III show similar time vs temperature dependence. The compounds were also tested for fuel instability and incompatibility reactions. They were tested for storage stability by ASTM method D5304-92 in JP-8 (7).

Additives in this Study

These compounds, along with their estimated physical properties and environmental toxicity profile, are presented in Table 1. Compound I appears to have excellent potential properties as a deicing agent. This compound has been well characterized in the literature and is considered to be relatively non-toxic (8). It is used commercially as a solvent, plasticizer, and solubilizing and suspending agent in pharmaceuticals. Additionally, it is miscible in hydrocarbons, gasolines, turpentine, oils, and water; making it an ideal candidate as an icing inhibitor. Although Compound I has a higher dermal dose per event than current deicers this is countered by its lower toxicity and dermal permeability; due, perhaps in part, to its higher lipophilicity. Compound I is decomposed in the atmosphere at a rate comparable to current deicers. Like current deicers, it is not rapidly volatilized from aquatic systems. Upon ingestion, possibly at mouth pH but certainly at stomach pH, this compound is readily broken down into acetone and glycerol. Both of these compounds have relatively low toxicity and environmental concerns. The second of the compounds synthesized, compound III, exhibits a lower dermal permeability and dermal dose per event than any of the other compounds in this study. The decomposition products upon ingestion, which are glycerol and acetaldehyde, are also relatively non-toxic; acetaldehyde is even less toxic than acetone. Acetaldehyde is one of the metabolized products of ethanol.

Compound II was dismissed due to the formation of formaldehyde upon decomposition under mildly acidic conditions. Formaldehyde is a known toxic and carcinogenic agent and the use of formaldehyde adducts in this study was ceased for this reason. This concern aside, compound II exhibits similar properties to the other compounds in this study, with a lower dermal dose per event.

All three compounds were found to be soluble in jet fuel at the levels necessary for inhibiting the formation of ice; and closely paralleled the behavior of EGME and DiEGME(4). Accelerated fuel instability and incompatibility studies using ASTM method D5304-92 in JP-8 (7) showed negligible formation of solids (<0.01 mg) and no increased peroxidation.

CONCLUSION

Testing and evaluation of these new deicing compounds derived from sugars showed that they exhibited properties that make them ideal candidates for the next generation of deicing compounds. Both Compounds I and III are predicted to be environmentally benign and relatively nontoxic at the concentrations necessary for inhibiting ice formation. Compound I has been well characterized due to its current commercial applications, and the need for further investigation into the toxicity of Compound II is indicated. Other analogs from reduced sugars have been synthesized and evaluated and will be reported on in subsequent papers. The substituted forms of reduced sugars have the potential for the ideal combination of lipophilic and hydrophilic character necessary for deicing applications.

ACKNOWLEDGMENT

The authors would like to express appreciation to Syracuse Research Corporation, the Air Force Office of Scientific Research (AFOSR) under grant number 5-25016, and the Office of Naval Research for research support.

REFERENCES

- (1) Basak, S. C., Niemi, G. J., Veith, G. D. J. of Mathematical Chemistry. 4, 185 (1990).
- (2) U.S. Department of Health & Human Services, Agency for Toxic Substances and Disease Registry, Tech. Rpt for Ethylene Glycol/Propylene Glycol Rpt 205-88-0608, May 1993.
- (3) Organic Synthesis Collective Volume 3, ed. E.C. Horning, pp 502-504, Wiley:New York, 1965.
- (4) Mushrush, G.W., Stalick, W.M., Beal, E.J., Basu, S.C., Slone, J.E., Cummings, Petroleum Science & Technology. 15(3,4), 237 (1997).
- (5) Meylan, W., Syracuse Research Corporation.DERMAL for Windows, Version 1.23, (1996); (a). MPBP for Windows, Version 2.51, (1996); (b). WSKOW for Windows, Version 1.20, (1996); (c). HENRY for Windows, Version 2.51, (1995); (d) AOP for Windows, Version 1.80, (1996); (e).KOC for Windows, Version 1.57, (1995); (f) Estimation Program Interface for Windows, Version 2.00, (1995).
- (6) Stirling, K. Q., Ripley, D. L. Partition Coefficients of Icing Inhibitors in JP-4 and JP-5 Jet Fuel, U. S. Department of Energy and Naval Air Propulsion Center, Final Report DE-FC22-83FE60149, October 1990.
- (7) ASTM ?Standard Test Method for Assessing Distillate Fuel Storage Stability by Oxygen Over pressure,? Annual Book of ASTM Standards, ASTM:Philadelphia, Part 0.05.01, ASTM D5304-92, (1992).
- (8) Sanderson, M. D. J. Pharm. Pharmacol. 11, 150 (1959) and 11, 446 (1959).

	Compound I	Compound II	Compound III
Dermal permeability K_p , cm/hr	5.00×10^{-3}	6.94×10^{-4}	1.17×10^{-3}
Dermal dose per event (at concentration of 100 mg/cm ³ for 0.25 hr) in mg/cm ²	0.0430	0.0048	0.0079
log K_{ow} (lipophilicity)	1.07	-0.50	-0.09
Vapor pressure in mmHg	0.0647	0.2700	0.1140
Water solubility in mg/L	3.459×10^4	9.918×10^5	3.914×10^5
Henry's Law Constant in atm x m ³ /mol	1.91×10^{-9}	1.08×10^{-9}	1.44×10^{-9}
OH rate constant in cm ³ /molecules x sec	2.50420×10^{-11}	2.68248×10^{-11}	2.99376×10^{-11}
Atmospheric half-life in hrs.	5.125	4.785	4.287
Soil adsorption coefficient K_{oc}	1.00	1.00	1.00
Volatilization from model river in years (half-life)	60.30	94.712	75.62
Volatilization from model lake in years (half-life)	38.60	688.76	550.00
Biological Oxygen Demand in days (half-life)	2-15	2-15	2-15
LC ₅₀ in ug/L for <i>Pimephales Promelas</i>	1.67×10^7	2.36×10^7	-----
Bioconcentration factor for <i>Pimephales promelas</i>	1	1	1

Table 1. Compounds based upon the reduced sugar mannose

	Ethylene glycol mono- methyl ether (EGME)	Di(ethylene glycol) mono-methyl ether (DiEGME)
Dermal permeability K_p in cm/hr	4.98×10^{-4}	2.97×10^{-4}
Dermal dose per event (concentration of 100 mg/cm ³ for 0.25 hr) in mg/cm ²	4.66×10^{-3}	1.3×10^{-3}
log K_{ow} (lipophilicity)	-0.77	-1.18
Vapor pressure in mmHg	9.2200	0.2160
Water solubility in mg/L	1.000×10^6	1.000×10^6
Henry's Law Constant in atm	4.19×10^{-8}	6.50×10^{-10}
$\times m^3/\text{mol OH}$ rate constant in cm ³ / molecule \times sec	1.19983×10^{-11}	2.60139×10^{-11}
Atmospheric half-life in hours	10.698	4.934
Soil adsorption coefficient K_{oc}	1.00	1.00
Volatilization from model river in years (half-life)	11.32	6660.27
Volatilization from model lake in years (half-life)	82.30	4.4844×10^5
Biological Oxygen Demand (BOD) in days (half-life)	2-16	2-16
LC ₅₀ in ug/L for <i>Pimephales promelas</i>	2.15×10^7	2.96×10^7
Bioconcentration factor (BCF) for <i>Pimephales promelas</i>	1	1

Table 2. Estimated values for current FSII additives